

Sunday Afternoon, October 30, 2011

Biomaterials Plenary Session

Room: 108 - Session BP-SuA

Challenges in Biomaterials Analysis

Moderator: L. Gamble, University of Washington

3:00pm BP-SuA1 Wants, Needs, and Challenges in Biomedical Surface Analysis, *D.G. Castner*, University of Washington **INVITED**

Biomedical surface analysis has undergone significant and numerous advances in the past 30 years in terms of improved instrumentation, introduction of new techniques, development of sophisticated data analysis methods, and the increasing complexity of samples analyzed. Comprehensive analysis of surfaces and surface immobilized biomolecules (peptides, proteins, DNA, etc.) with modern surface analysis instrumentation provides an unprecedented level of detail about the immobilization process and the structure of the immobilized biomolecules. Results from x-ray photoelectron spectroscopy (XPS or ESCA), time-of-flight secondary ion mass spectrometry (ToF-SIMS), near edge x-ray absorption fine structure (NEXAFS), surface plasmon resonance (SPR) biosensing, atomic force microscopy, and sum frequency generation (SFG) vibrational spectroscopy provide important information about the attachment, orientation, conformation, etc. of biomolecules. However, even with the advances that have been achieved with these powerful surface analysis techniques, there still remains many significant challenges for biomedical surface analysis. These include characterizing the surface chemistry and structure of nanoparticles, determining the structure of protein bound to surfaces, and maintaining biomolecules and materials in a biological relevant state when using ultra-high vacuum based analysis techniques.

This talk will discuss the current challenges in biomedical surface analysis and what is being done to address them. Also discussed will be the role of well-defined standards to develop new biomedical surface analysis methods for characterizing more complex, biological relevant samples.

3:40pm BP-SuA3 Depth Profiling and 3D Analysis of Organic Surfaces, *A.G. Shard*, National Physical Laboratory, UK **INVITED**

Cluster ion impacts have been shown to sputter organic materials, whilst imparting low levels of damage to the freshly exposed surface. When coupled with a surface analytical technique, such as SIMS or XPS, it is possible to generate depth profiles with truly molecular information. Concurrent 2D spectroscopic imaging enables a three dimensional reconstruction of molecular distributions. This offers enormous potential for the label-free and multiplexed imaging of biological materials and medical devices.

The mechanism of cluster ion beam sputtering has been established over the past ten years and the most important factor that permits organic depth profiling is the large sputtering yield of organic material following a cluster ion impact. This is typically of the order of 100 nm³ of material per individual impact. However it has been shown that, for many materials, the sputtering yield changes as the cluster ion dose increases and therefore the interpretation of organic depth profiling data is, in general, not trivial. Additionally, this change in sputtering yield is often associated with sputter-induced roughening with a concurrent degradation of depth resolution. Recently, there has been a growing emphasis on the development of methods by which a wider range of materials can be depth profiled and a constant sputtering yield maintained. The most significant advances have been the use of sample cooling, low ion beam incidence angles and sample rotation. Large argon clusters appear to offer significant improvements over traditional cluster beams, such as C₆₀ in these regards.

The reliability of organic depth profiling was tested recently in two VAMAS interlaboratory studies. Results from these studies highlight the rapid developments that have recently been made. The application of this technique to medical devices and biological materials will be reviewed and the remaining challenges described.

4:20pm BP-SuA5 Nanoscale Surface Analysis of Living Cells using Atomic Force Microscopy, *Y.F. Dufrene*, Université catholique de Louvain, Belgium **INVITED**

The emerging new field of "live-cell nanoscopy" has revolutionized the way biologists explore the living cell to molecular resolution. Whereas far-field fluorescence nanoscopy enables to study the nanoscale localization and dynamics of biomolecules in cells, recent developments in atomic force microscopy (AFM) techniques offer unprecedented opportunities for imaging the supramolecular organization of cell surfaces, and for probing

the functional properties and interactions of their molecular machineries. In the past few years, AFM-based nanoscopy has enabled key breakthroughs in cell biology, including deciphering the nanoscale architecture of cell surfaces and their remodelling upon changing the cells functional state, understanding cellular mechanics and its functional implications, quantifying cell adhesion forces contributing to processes like tissue development and bacterial infection, unravelling the molecular elasticity of cellular proteins such as sensors and adhesion molecules, and elucidating how cells reassemble membrane receptors into nanodomains and modulate their functional state. In this talk, I will provide a survey of the recent work we have done using the AFM multifunctional toolbox, emphasizing its potential for understanding cell surface properties and interactions on the nanoscale.

References

- Nat. Chem. Biol., 5 (2009), 857-862.
- Nat. Commun., 1:27 (2010).
- Proc. Natl. Acad. Sci. USA, 107 (2010), 20744-20749.
- Nat. Methods, 8 (2011), 123-127.

5:00pm BP-SuA7 AVS 2011 Biointerphases Lecture - Tissue Engineering and Surface Science: 2D to 3D, Dry to Wet, Dead to Living and the Challenges to the Instrumentation, *B.D. Ratner**, University of Washington Engineered Biomaterials **INVITED**

The biointerface and related surface science ideas have had profound impact on biomaterials science since at least the 1960's. In the 21st century there is much discussion of tissue engineering, clearly a "3-D" phenomenon. This talk will review some history of the biointerface, illustrate modern trends, and show how biointerface ideas can be applied to tissue engineering and 3-D scaffolds. Techniques such as electron spectroscopy for chemical analysis (ESCA) and secondary ion mass spectrometry (SIMS) will be featured. SIMS has proven to be powerful for cell identification in culture dishes and for the analysis of decellularized extracellular matrix scaffolds. SIMS also provides much information on synthetic scaffold materials. There are now profound challenges in interpretation of complex spectra and in gleaned useful, biomedically relevant information from complex data sets. Finally, this talk will discuss healing, biointegration and regeneration, particularly in the context of new scaffolds made by a sphere-templating process.

* AVS 2011 Biointerphases Lecture

Monday Morning, October 31, 2011

Applied Surface Science Division

Room: 102 - Session AS-MoM

Quantitative Surface Chemical Analysis and Technique Development - Part I

Moderator: I.S. Gilmore, National Physical Laboratory, UK

8:20am **AS-MoM1 Characterization of Nano-structures from Analysis of the XPS Background: Automation and 3D-imaging.** *S. Tougaard*, University of Southern Denmark **INVITED**

The XPS peak intensity and its background of inelastically scattered electrons varies strongly with the depth distribution of atoms. This phenomenon is the basis for a widely used method for nano-structure analysis.¹ With the rapid increase in the application of XPS, there is a growing need for automated XPS analysis. To meet this demand, a modified simpler and less accurate algorithm, which however is suitable for automation was developed.² For each XPS peak, this algorithm determines just two numbers: the total amount of atoms within the outermost ~ 10 nm and the approximate depth of the atoms. The validity of the algorithm was demonstrated experimentally by comparison to more elaborate quantification methods.² The algorithm is thus of interest for automated XPS analysis. Another application of the algorithm is in XPS imaging, where thousands of spectra must be analyzed. Here automatic data-handling procedures are crucial. Software that can automatically analyze thousands of spectra corresponding to the situation in XPS imaging is now being developed. The method produces nondestructively a 3-D image of the surface with nanometer depth resolution. The practical applicability of this to XPS imaging was recently demonstrated.^{3,4}

In ref³ the algorithms ability to produce images of Ag taken from a series of samples with increasing thicknesses of plasma patterned Octadiene (2, 4, 6 and 8nm) on Ag substrates was demonstrated. The obtained images of the amount of Ag atoms in the outermost few nano-meters were in good agreement with the nominal thicknesses. Produced images of atoms at different depths clearly proved the potentials of the method for quantitative and nondestructive 3-D characterization of nano-structures. Spectral noise is a major limitation in imaging because the time allowed to acquire the spectrum at each pixel is typically ~1 sec. Different procedures for noise reduction were studied in ref³ and principal component analysis (PCA) was found to significantly improve the 3D images of a thermally patterned oxidized silicon where detailed 3-D images of the Si, O, and C atoms were determined on the nano-meter depth scale.

In the talk we will summarize the technique and discuss its limitations and potentials for both automation of conventional XPS data analysis and for 3D XPS imaging.

¹ S. Tougaard, Surf. Interf. Anal. 26 (1998) 249

² S. Tougaard, J. Vac. Sci. Technol., A21 (2003) 1081; A23(2005) 741

³ S. Hajati, S. Coultas, C. Blomfield and S. Tougaard, Surf. Interf. Anal. 40 (2008) 688

⁴ S. Hajati, J. Walton, N. Fairley, and S. Tougaard, Surf. Sci. 602 (2008) 3064

9:00am **AS-MoM3 Characterization of Model Gradient Inorganic Thin Films with XPS Spectral Modeling.** *L. Lohstreter*, Medtronic, Inc, *R. Sanderson, J. Dahn*, Dalhousie University, Canada

Information about the layer structure of surfaces at the angstrom level can be probed through X-ray Photoelectron Spectroscopy (XPS) by analyzing the structure of the entire spectrum, including the inelastic background. Model samples were prepared through a unique magnetron sputtering system to create thin film gradients ranging from two angstroms to hundreds of angstroms thick across a distance of seven centimeters. The system studied consisted of a titania wedge on a gold substrate. The samples were characterized using Variable Angle Spectroscopic Ellipsometry (VASE) to measure the thickness of the wedge along the sample at many points along the gradient. The thickness values from the XPS and VASE modeling were shown to have excellent linearity from two angstroms until the XPS photoelectron peak was extinguished. The effective attenuation lengths of the titania at the kinetic energies of the various gold photoelectron peaks were also measured and compared to theoretical values for inelastic mean free path. The values were within 29% of each other.

9:20am **AS-MoM4 Corrections for Backscattering Effects in Quantitative Auger Analyses.** *A. Jablonski*, Polish Academy of Sciences, Poland, *C.J. Powell*, National Institute of Standards and Technology

The backscattering factor (BF) has long been recognized as an important matrix-correction factor for quantitative AES. The BF definition ("fractional increase in the Auger current due to backscattered electrons" [1]) has been shown to be unsatisfactory since the "fractional increase" can be negative at low primary energies and more grazing-incidence of the primary electrons [2]. ISO/TC 201 is considering the definition of a new term, the backscattering correction factor (BCF), as a "factor equal to the ratio of the total Auger-electron current arising from ionizations in the sample caused by both the primary electrons and the backscattered electrons to the Auger-electron current arising directly from the primary electrons." NIST recently released a new BCF Database [3] for AES. This database provides BCFs from Monte Carlo simulations for two models, a simplified model based on the previous BF definition which is relatively rapid and an advanced model based on the proposed BCF definition which is more accurate but slower. BCFs can be determined for a solid of arbitrary composition, a user-specified instrumental configuration, and primary energies up to 30 keV.

Examples will be given of the dependence of the BCF for Pd M₅N₄₅N₄₅ Auger electrons on various instrumental conditions (primary energy, primary-beam angle of incidence (θ_0), and analyzer acceptance solid angle) [4]. BCFs calculated from the advanced model of electron transport in the surface region of the Pd sample varied weakly with analyzer half-cone angle for $\theta_0 = 0^\circ$ but more strongly for $\theta_0 = 80^\circ$ where there were BCF differences varying between 19% at a primary energy of 1 keV and 6% at a primary energy of 5 keV. These BCF differences are due partly to variations of the density of inner-shell ionizations within the information depth for the detected Auger electrons. The latter variations are responsible for differences larger than 10% between BCFs from the widely used simplified BCF model and those from the more accurate advanced model for primary energies less than about 5 keV for $\theta_0 = 80^\circ$. These and other BCF differences indicate that the simplified model can provide only approximate BCF values. In addition, the simplified model does not provide any BCF dependence on Auger-electron emission angle or analyzer acceptance angle. Comparisons will also be made with measured BCFs for elemental solids.

[1] ASTM E 673-03, "Standard Terminology Relating to Surface Analysis," in Annual Book of ASTM Standards, Vol. 3.06, 2010, p. 655.

[2] A. Jablonski, Surf. Science 499, 219 (2002).

[3] <http://www.nist.gov/srd/nist154.cfm>.

[4] A. Jablonski and C. J. Powell, Surf. Science 604, 1928 (2010).

9:40am **AS-MoM5 Effect of Monochromator X-ray Bragg Reflection on Photoelectric Cross Section.** *A. Herrera-Gomez*, CINVESTAV-Unidad Queretaro, Mexico

The photoelectric differential cross section plays a fundamental role for assessing the relative concentration of the various elements present within the XPS probing depth. Accounting for the different issues affecting the cross section is paramount not only for quantitative chemical studies (including angle-resolved XPS) but also for a proper comparison between the results obtained with different XPS tools, or in the same tool but with different X-ray sources. In XPS experiments employing monochromatized light, the X-ray Bragg reflection undergone by the beam at the monochromator crystal causes a partial polarization of the X-rays. The photoelectric cross section is affected since it depends on the angle between the electric field vector and the direction of the escaping electrons. An expression for the photoelectric differential cross section is presented that accounts for the effect of the monochromator and of the geometrical configuration of the XPS tool. The correction is as large as 9% for s-orbitals and reduces to up to 5% for orbitals with $\beta \sim 1$. The differences are directly related to the beta factor within the dipole approximation, which is the first order treatment of photoemission; i.e., they are not due to higher order quadruple terms.

10:00am **AS-MoM6 An XPS Investigation of CdS Based Photoresistor During Operation.** *S. Suzer, H. Sezen*, Bilkent University, Turkey

We have recently developed a technique for recording the shifts in the positions of the XPS peaks in response to different waveforms of electrical and/or optical stimuli for probing the dynamics of the developed electrical potentials originating from intrinsic or extrinsic (like doping) properties of semiconductive materials such as charging/discharging, photoconductivity, surface photovoltage, band-bending/flattening/inversion, etc.^{1,6} We have also shown that fast data acquisition (in the snapshot mode) and laterally spatial resolved XPS analysis (an area mapping mode) helps us to compare and

align extracted electrical behaviors and chemical information from the sample. For a better understanding of a realistic performance (or failure) of a device during operation, we have extended our measurements to a CdS based photoresistor, where we have mapped the position of the Cd3d peak over an area of 5 mm x 5mm while the device is under operation without and under photoillumination. This method allows us to detect defects and malfunctioning sites/domains. We will present our methodology with experimental results and an electrical circuit model.

- (1) Sezen H., Suzer, S. *Surface Science*, **2010**, 604, L59.
- (2) Suzer, S., Sezen, H., Ertas, G., Dâna, A. *Journal of Electron Spectroscopy and Related Phenomena* **2010**, 176, 52.
- (3) Sezen, H., Ertas, G., Suzer, S. *Journal of Electron Spectroscopy and Related Phenomena*, **2010**, 178-9, 373.
- (4) Sezen H., Suzer, S. *Journal of Vacuum Science and Technology A*, **2010**, 28, 639.
- (5) Sezen, H., Ozbay, E., Aktas, O., Suzer, S. *Applied Physics Letters* **2011**, 98, 111901.
- (6) Sezen, H., Suzer, S. *Journal of Spectroscopy and Dynamics* (in press).

10:40am **AS-MoM8 Coronene Ion Bombardment Effects in the Quantitative Analysis of Polymeric Materials by XPS**, *G.E. Hammer, L.J. Gamble, D.G. Castner*, University of Washington

XPS has long been a primary technique for the analysis of material surfaces, providing quantitative analysis of elemental atomic concentrations and chemical bonding states. When combined with ion sputter etching, it has provided a similar level of detail in depth profiling of metals, semiconductors, and inorganic compounds; however, the damage produced by ion bombardment precluded the depth profiling of organic and polymeric specimens. More recently it has been shown that sputter etching by carbon cluster ions significantly reduces the apparent damage to such materials, presumably the result of a combination of a reduced damage layer thickness and efficient removal of the damaged material. In this work we have used a coronene ($C_{24}H_{12}^+$) ion source to sputter etch a series of organic compounds and polymers, including trehalose, poly(amide), poly(glycolic acid), poly(lactic acid), poly(ethylene glycol), poly(methyl methacrylate), poly(acrylonitrile), poly(ethylene terephthalate), poly(vinyl chloride), and poly(tetrafluoroethylene). Specimens were sputtered to a steady-state condition and analyzed by XPS. Elemental composition and chemical bonding were compared to the original surface and the theoretical values. These data will be used to refine our understanding of cluster ion bombardment effects in polymers, and to interpret data from the analysis of future materials and devices.

11:00am **AS-MoM9 Using A C60 Ion Source For Routine Surface Chemical Analyses**, *W. Stickler, M.D. Johnson, D.K. Bilich*, HP ADL Corvallis, *C. Knutson, W. Wang, W. Cowell*, Oregon State University

C60⁺ ion sources are becoming one of the routinely used tools in the surface chemical analysis laboratory. While finding early acceptance and utility in the TOF SIMS community because of its direct applicability to organic systems, the C60 ion source is now a standard option for photoelectron spectroscopy tools. Routine use of this ion source requires characterization and understanding of the surface that is being created during the ion milling process. Such characterizations include the shape and roughness of the resulting surface, changes in chemistry of the surface created by the ion milling process and changes in the mechanical characteristics of the surface that might influence the interpretation of the surface analytical results. Full characterization requires the preparation of standards and also validation of the measurements. The characterization of the application of the C60 ion source for a variety of common polymers such as PMMA, SU8 and polycarbonate are discussed. Further, anticipating the examination of mixed mode systems, the application of the C60⁺ source for the characterization of inorganic materials such as titania, hafnia and alumina multilayered structures as well as metal-metal oxide layered structures is presented where sputter induced chemistry from the C60⁺ source is observed.

11:20am **AS-MoM10 Large Area Quantitative XPS Imaging for Small Feature Compositional Screening**, *S.J. Coultas, C.J. Blomfield, S.J. Hutton, A.J. Roberts*, Kratos Analytical Ltd, UK, *D.J. Surman*, Kratos Analytical Inc.

Many technologically important devices require nanometre level chemical characterisation over areas of several square mm, or even cm, for applications such as coating continuity and integrity or contamination monitoring.

The traditional approach when employing XPS for this application has been to acquire a number of small area spectra at different points. The advent of quantitative parallel XPS imaging introduced the possibility of faster

acquisition times and higher spatial resolution than the traditional small XPS probe approach.

Here we present an alternative approach whereby multiple features are simultaneously analysed over a large area using XPS imaging. Acquisition conditions and post acquisition data treatment to optimise this approach on a range of samples will be discussed

This approach provides both a faster and more easily interpreted graphical method for multiple feature analysis.

We present examples of this approach on a variety of samples.

11:40am **AS-MoM11 A New Type of Detector for Dynamic XPS Measurements**, *K. Winkler, P. Baumann, B. Kroemker, G. Pruemper, A. Feltz*, Omicron NanoTechnology, Taunusstein, Germany

Real time observation of fast processes occurring in a time window of a few milliseconds to a few minutes have been always difficult to observe by x-ray excited photoemission (XPS) studies under laboratory conditions. However the demand to understand the chemistry of surface processes e.g. during heating processes, electro migration and diffusion is of high relevance in various research fields.

In this contribution we will report on first results of a new multi-anode detector concept with 128 individual anodes, preamplifiers and counters. It has the capability to allow for quantitative XPS studies on fast time scales with good signal to noise ratio excited with a monochromated Al Ka laboratory source. The detector can be operated in snapshot XPS mode. This mode allows recording an energy window in the spectrum versus time with high repetition-rates and good energy resolution, e.g. a 15 eV detectable energy window with an approximate energy resolution of 0.5 eV.

As an early application we report on results of removing an in-situ grown SiO₂ layer on a Si substrate. The measurement was made during a sample temperature ramp from 600 to 900 degree Celsius within a time frame of one hour. The target of the experiment was to analyze the time window in which the oxide was removed.

Snapshot spectra have been recorded with an acquisition time of 0.5 seconds per spectrum to follow the evolution of the subcomponents Si4+ to Si0 during the heating process of the Silicon. The snapshot series with >5000 spectra shows the evolution of the peak versus time. The complete removal of the oxide occurred at a very small temperature window around 850°C. A closer look into the data revealed that the removal of the oxide from the silicon took place in about 2.5 minutes. Within this transition time 300 spectra have been recorded.

Biomaterial Interfaces Division
Room: 108 - Session BI-MoM

Biomolecules at Interfaces

Moderator: A. Rosenhahn, Karlsruhe Institute of Technology, Germany

8:20am **BI-MoM1 Cell Instructive Biomaterials by Non-Equilibrium Self-Assembly**, *R.V. Uljin, V. Jayawarna, S. Roy, M.J. Dalby*, The University of Strathclyde, UK, *S.L. McArthur*, Swinburne University of Technology, Australia

INVITED

Peptides are highly versatile building blocks for the production of supramolecular gels which mimic certain properties of biological systems but with minimal complexity. These gels may be ideally suited to interface synthetic systems with biology, and as such have attracted much interest in a range of areas including health care and energy related technologies. We have developed versatile gelator systems based on aromatic peptide amphiphiles, which self-assemble via a unique mechanism involving π -interlocked β -sheets. These systems display highly tunable supramolecular functionalities, giving rise to materials with controlled mechanical properties, nanotopography and bioactive properties. We will show that these properties can be controlled by exploiting non-equilibrium self-assembly which may involve the use of biocatalysts to control the self-assembly process. We will discuss progress in fundamental understanding of these systems as well as applications as matrices for stem cell differentiation.

References:

Nature Chemistry, 2010, 2, 1089-1094.; Chem. Soc. Rev. 2010, 39, 3351-3357.; Nanoscale, 2010, 2, 960-966.; Chemical Communications, 2010, 46,

3481-3483.; Nature Nanotechnology, 2009, 4, 19-24.; Langmuir, 2009, 25, 9447-9453.; Faraday Discussions, 2009, 143, 293-303.; Langmuir, 2009, 25, 7533-7539.; Acta Biomaterialia, 2009, 5, 934-943.; Biomaterials, 2009, 30, 2523-2530.; Soft Matter, 2009, 5, 1728-1734.; Small, 2009, 5, 587-590.; Adv. Mater., 2008, 20, 37-41.; Small, 2008, 4, 279-287.

9:00am **BI-MoM3 Lipid Vesicle Fusion for Studies of Cell Functions**, L. Simonsson, A. Gunnarsson, M. Kurczy, P. Jönsson, AS. Cans, F. Höök, Chalmers University of Technology, Sweden

Fusion of lipid vesicles and cells is a natural process which takes place in eukaryotic cells. It is a vital process, since it enables cells' communication with the outside, both via vesicle content release and through delivery of e.g. membrane proteins to the outer cell membrane. Exocytosis is still not fully understood and although attempts have been done to deliver membrane constituents to supported lipid bilayers, improvement in e.g. efficiency remains. In order to gain a deeper understanding of the mechanism of membrane fusion as well as improve the delivery of arbitrary membrane constituents including complete cell membrane fragments, to supported lipid bilayers, we have in this work developed two novel and powerful techniques.

To mimic exocytosis, we use giant unilamellar vesicles (GUVs) as a model of the cell membrane, cholesterol-DNA[1-3] as a mimic of the SNARE-proteins and small unilamellar lipid vesicles filled with easily oxidized catechol to represent the cellular vesicles. We probe the fusion process using a carbon fiber electrode, detecting the released catechol. By building this advanced but yet controllable model system of exocytosis, we believe that a wide range of studies can be made in order to decipher the process of exocytosis. Future applications are delivery of e.g. membrane proteins to GUVs, as well as for vesicular drug delivery to cells.

In order to deliver membrane constituents to SLBs, we use a controlled bulk flow through a microfluidic channel to move the front edge of a supported lipid bilayer and fuse it with vesicles adsorbed in front of it. The membrane constituents of the adsorbed vesicles are efficiently incorporated into the supported lipid bilayer and can be manipulated in 2D (accumulated and separated) by again using the bulk flow. We show that this method is perfectly compatible with cell membrane fragments derived directly from 3T3 fibroblast cells[4]. The method enables studies of e.g. receptor-ligand interactions as well as membrane protein separation in a native environment.

Simonsson et al., ChemPhysChem, (2010)

Stengel et al., J. Am. Chem. Soc., (2007)

Stengel et al. J. Phys. Chem. B, (2008)

Simonsson et al., Submitted

9:20am **BI-MoM4 Watching Biomineralization at Work: The Specific Interactions of Statherin with Hydroxyapatite Surfaces Probed at the Molecular Level**, T. Weidner, M. Dubey, K. Li, J. Ash, J.E. Baio, University of Washington, C. Jaye, D.A. Fischer, National Institute of Standards and Technology, G.P. Drobny, D.G. Castner, University of Washington

Biomineralization proteins act as nature's crystal engineers and adsorb onto crystal surfaces with high binding affinity and precision using specific substrate-surface binding motifs. Owing to the importance of the underlying physiological processes and a general interest in biomineralization mechanisms, the binding of regulatory proteins has attracted significant interest. We have studied statherin, which regulates the growth of hydroxyapatite (HAP) in bone and tooth enamel and prevents the buildup of excess HAP by inhibiting spontaneous calcium phosphate growth. A detailed understanding of the underlying molecular recognition mechanisms would help bioengineers and scientists to devise new biomimetic approaches for clinical applications and biomineral nanofabrication. Sum frequency generation (SFG) spectroscopy can probe protein orientation and secondary structure at the solid-liquid interface and we have recently shown it can address specific protein regions with atomic resolution when combined with isotopic labeling and solid state NMR (ssNMR) data.(1) We have combined both techniques with near edge X-ray absorption fine structure (NEXAFS) spectroscopy to characterize the structure of the binding domain of statherin, SN-15, on HAP. Protein adsorption was verified using XPS and ToF-SIMS. NEXAFS N K-edge spectra clearly show that hydrogen bonding is important for the binding of both peptides. SFG confirmed an α -helical secondary structure of SN-15 on HAP with the helix axis parallel to the surface. Deuteration was used to specifically probe the orientations of all hydrophobic side chains (leucine, isoleucine, phenylalanine) with SFG *in situ*. The leucine chain was tilted 120° from the surface normal (pointing towards the surface) and isoleucine was tilted 5° from the surface normal. We also employed fluorine labels to probe individual phenylalanine rings with NEXAFS spectroscopy. Measurements of ring orientations in combination with ssNMR surface distance and

rotamer dynamics data allowed us to develop a clear picture of the side chain structure.

1. Weidner T, Breen NF, Li K, Drobny GP, & Castner DG (2010) A Sum Frequency Generation and Solid-State NMR Study of the Structure, Orientation and Dynamics of Polystyrene-Adsorbed Peptides. *Proc. Natl. Acad. Sci. U. S. A.* 107:13288-13293.

9:40am **BI-MoM5 ECM Ordering Effects as a Marker for Early Tissue Formation on Artificial Substrates - A Sum-Frequency-Generation Spectroscopy Study**, M.-O. Diesner, P. Koelsch, Karlsruhe Institute of Technology (KIT), University of Heidelberg, Germany

The *in situ* monitoring of the interphase between a substrate and a cellular layer is of great interest as it allows determination of changes in surface properties and extracellular matrix (ECM) organization. The latter is an early indicator of major cellular processes like migration, adhesion, proliferation, metastasis, tissue formation, and gain or loss of differentiation occurring. Typically, ECM studies of adherent cells involve labeling and fixing cell samples, which may result in their disruption and in the loss of valuable information. In addition, the weak signal-to-noise ratio of fluorescent probes limits the probing capabilities at early stages of cell adhesion.

Recent work from our group has shown that sum-frequency-generation (SFG) spectroscopy can be used to interrogate the ordering of the ECM beneath adherent cells on an artificial substrate during these early stages.^{1,2} It turns out that SFG spectroscopy is suitable to probe the layer in between a solid substrate and living cells and that the information which can be obtained on such systems are twofold: first, changes of the surface coating can be investigated in real-time and *in vitro* on a molecular scale while cells adhere to it. Secondly, SFG spectroscopy is suitable for the determination of ordering parameters within the ECM without the need for labeling and processing.

In this contribution we will report on ordering phenomena occurring at early stages of rat and mouse embryonic fibroblasts adhesion on Au-coated Si wafers. Several phases observed during the adhesion process will be discussed and the results obtained by nonlinear optical spectroscopy will be correlated to classical tools including Western blot analysis of ECM constituents, fluorescent probes, and genetic screens blocking the formation of fibrils.

References

[1] M.-O. Diesner, C. Howell, V. Kurz, D. Verreault, and P. Koelsch. *In vitro* characterization of surface properties through living cells. *J Phys Chem Lett*, 1:2339- 2342, 2010.

[2] C. Howell, M.-O. Diesner, M. Grunze, and P. Koelsch. Probing the extracellular matrix with sum-frequency-generation spectroscopy. *Langmuir*, 24:13819-13821, 2008.

10:00am **BI-MoM6 Structure and Function of von Willebrand Factor on Synthetic Surfaces and Collagen**, E. Hillenmeyer, O. Yakovenko, R. Penkala, W. Thomas, D.G. Castner, University of Washington

von Willebrand Factor (VWF) is a soluble clotting protein responsible for binding platelets through the glycoprotein 1b platelet receptor. VWF can become activated and bind platelets when bound to collagen in an injured blood vessel or under increased shear.

VWF can also bind platelets when adsorbed to synthetic surfaces, specifically biomaterials. There is evidence that surface characteristics influence VWF adsorption. Previous AFM studies of VWF adsorbed to hydrophilic (mica) and hydrophobic (octadecyltrichlorosilane modified glass) surfaces showed differences in adsorbed topography¹. However, studies were not performed to relate adsorption differences to VWF function.

Previous studies in our lab have shown differences in function and structure of the platelet binding domain of VWF (A1 domain) when adsorbed to three surfaces: polystyrene (PS), tissue culture polystyrene (TCPS), and glass, with A1 most active when adsorbed onto PS. A1 function was tested by measuring platelet binding under flow. A1 surface structure was investigated using time of flight secondary ion mass spectrometry (ToF-SIMS) and binding of conformation-dependent antibodies in ELISA assays.

In the work presented here, we have used surface analysis techniques to obtain greater detail about structural differences of the VWF A1 domain adsorbed onto synthetic surfaces. We used near-edge x-ray adsorption fine structure (NEXAFS) to examine the amide backbone, corresponding to the pi* feature of the nitrogen edge NEXAFS spectrum. Differences were observed in the angle dependence of the spectra when A1 was adsorbed onto PS, TCPS, and glass, indicating significant structural differences in the protein when adsorbed onto different surfaces. Sum Frequency Generation (SFG) was also used to probe the structure of the amide backbone using amide I spectra.

In addition to examining VWF on synthetic surfaces, we have used ToF-SIMS to obtain structural information about A1 bound to collagen, as occurs during *in vivo* injury. Principal component analysis of ToF-SIMS data showed differences between A1 bound to collagen and A1 adsorbed directly onto polystyrene. This suggests that A1 adopts different conformations on the natural versus synthetic substrates, potentially leading to different mechanisms of activation.

In this work, we use surface analysis tools to increase our understanding of VWF behavior, both on synthetic surfaces and in complex, layered protein systems. Increasing our fundamental knowledge of VWF can improve our understanding of VWF interactions with biomaterial surfaces, as well as thrombosis during injury.

1. M. Raghavachari, et al. *Colloids Surf B* (2000) 19:315.

10:40am **BI-MoM8 ToF-SIMS Study of Orientation of FNIII₉₋₁₀ Fibronectin Fragment on Self-Assembled Monolayers**, *L. Árnadóttir, L.J. Gamble*, University of Washington

Fibronectin (FN) is an extra cellular matrix protein that is involved in many cell processes such as adhesion, migration and growth. The orientation and conformation of FN adsorbed onto surfaces can therefore have a critical effect on cell-surface interactions. Experimental orientation studies of model systems also provide an important benchmark for molecular simulations and are of great value for further development of force fields used in many theoretical studies of protein adsorption. In this study the adsorbed orientation of the 9-10 fragment of FNIII was studied on three different model surfaces (self-assembled monolayers (SAM) of C₁₁ alkanethiols on Au, -CH₃, -NH₂, and -COOH terminated SAMs.) The FNIII₉₋₁₀ fragment includes the two binding sites for the FN protein, a RGD site on segment 10 (seg10) and a synergy site on segment 9 (seg9). This fragment also has a significant asymmetry in its amino acid distribution with His found exclusively on seg9, Lys only on seg10 and three times more Tyr on seg10 than seg9. Taking advantage of this asymmetry, we use time of flight secondary ion mass spectrometry (ToF-SIMS) to study the different orientation on different surfaces and X-ray photoelectron spectroscopy (XPS) to determine the difference in surface coverage. While CH₃ and NH₂ have similar full coverage the highest COOH coverage is about half the maximal coverage observed for the two other surfaces. A ToF-SIMS comparison of the FNIII₉₋₁₀ on COOH and NH₂ at similar coverages shows significantly more His on the COOH and more Tyr on the NH₂ surfaces suggesting an opposite orientation of the fragment on these two surfaces. Results indicate that on the COOH surface the fragment is oriented with seg10 down while on the NH₂ surface seg9 is closer to the surface. Comparing similar coverages of the FNIII₉₋₁₀ on NH₂ and CH₃, the later has less Tyr signal (from seg10) suggesting that the seg10 is closer to the surface on CH₃ than on NH₂. In contrast, when FNIII₉₋₁₀ on CH₃ and COOH results were compared, the fragment on the CH₃ sample has less His signal suggesting that seg9 is closer to the surface compared to COOH.

11:00am **BI-MoM9 Single Protein Manipulation with STM**, *S. Khan, K. Clark, C. Henneken, E. Rauh, S.-W. Hla*, Ohio University

Scanning tunneling microscope (STM) is not only an instrument to image atomic landscape of material surfaces but also is a tool to manipulate individual atoms and molecules. If STM manipulation and spectroscopy can be applied to individual biomolecules, it will be advantageous for multiple research areas. Here we use a low temperature STM in an ultrahigh environment to image individual protein molecules with molecular resolution on Ag (111) surface at 4.6 K. A-b type amyloid precursor proteins molecules and various single chain proteins were deposited on atomically clean Ag (111) surface. STM images and tunneling spectroscopy enables direct sequencing of amino acid groups in these molecules. Moreover, using an STM manipulation procedure employing an attractive tip-molecule interaction, individual molecules were relocated on the surface; thereby their mechanical integrity can be tested. Protein folding is a major issue in biological processes. Here, we will demonstrate that folding of carbon back-bone in these proteins is possible using an STM manipulation procedure. This experiment presents a novel avenue of biological research where sequencing and manipulation may be performed one molecule-at-a-time. We acknowledge the financial support provided by US-DOE-DE-FG02-02ER46012.

11:20am **BI-MoM10 DNA Origami from Inkjet Synthesis Produced Strands**, *I. Saaem, A. Marchi, J. Tian, T. LaBean*, Duke University

High-throughput synthesis of quality mixed oligonucleotides (oligos) allows for exhaustive studies of DNA nanostructured material formation. In situ DNA synthesis was achieved with a custom piezoelectric inkjet system using phosphoramidite chemistry, on functionalized cyclic olefin copolymer (COC) as a chip substrate. When amplified off of the chip via strand displacement amplification (SDA), the oligos were eluted and used directly for constructing multiple DNA origami nanostructures in a one-pot

assembly. By performing SDA, each chip may be reused multiple times to produce pools of staple strands for repeated experiments. Two separate DNA origami structures were formed from a double-stranded scaffold strand. By redesigning specific staple strands, these structures can be connected to provide a larger nanostructured template.

11:40am **BI-MoM11 Solid State Electron Transport across Proteins**, *D. Cahen, M. Sheves, I. Pecht, L. Sepunaru*, Weizmann Institute of Science, Israel

We found that solid-state electron transport (Etp) studies are possible across non-modified 'dry' proteins, between two solid electrodes, using the light-induced proton pumping protein, Bacteriorhodopsin (bR), the electron transfer (ET) protein, Azurin (Az), and Bovine Serum Albumin (BSA). Clear differences between these proteins, where for bR and Az we can show that they preserve their structure in the solid state measurement configuration, were observed, with small tunneling decay constants for all three proteins, suggesting that incoherent transport is the dominant mechanism. Putting our data in perspective by comparing them to all known protein Etp data in the literature, we concluded that, in general, proteins behave more akin to molecular wires than to insulators. An important part of these studies was the modification of the proteins by, e.g., removing or disconnecting the retinal in bR and removing the Cu redox centre in Az.

We now report that, notwithstanding the above-noted earlier conclusion on hopping, which was based on the Etp efficiency, Az shows 9-360K temperature independent Etp, until its denaturation temperature. Removal of the Cu changes this behavior to Arrhenius-like thermally activated Etp, which becomes temperature independent below ~ 200K, a behavior that apo-Az shares, qualitatively with bR, its variants and with BSA.

This difference between bR and Az leads to the truly remarkable situation that above room temperature the non-ET protein bR shows significantly better Etp than ET protein Az.

Electronic Materials and Processing Division Room: 210 - Session EM-MoM

Dielectrics for Novel Devices and Process Integration Moderator: S. King, Intel Corporation

8:20am **EM-MoM1 Surface Cleaning and Monolayer Seeding for ALD of High-k Studied by In Situ STM, STS, and XPS**, *W. Melitz, T. Kent, J. Shen, A.C. Kummel*, University of California San Diego

Air exposed III-V surfaces nearly always defects which prevent full modulation of the Fermi level thereby impeding their use in practical semiconductor devices such as MOSFETs. For a high speed device, the air induced defects need to be removed to reduce trap states while maintaining an atomically flat surface to minimize interface scattering thereby maintaining a high carrier mobility. For silicon, the only commercial atomic layer deposition (ALD) high-k fabrication process is a replacement gate process to avoid processing induced damage. Surface channel III-V MOS devices can be fabricated with ALD high-K gate-first processes; while ALD is known to greatly reduce surface contaminants, contamination removal is not complete and the order of the surface after ALD cleanup is unknown. Using in-situ scanning tunneling microscopy (STM) and scanning tunneling spectroscopy (STS) the surface morphology of a multistep process was explored for gate-last unpinning of air exposed InGaAs and InP surface via cleaning with atomic H and ALD nucleating/passivating with trimethyl aluminum (TMA). STM of atomic H cleaned surfaces shows the dosing temperature and a post deposition anneal are critical to forming surfaces that resemble the decapped InGaAs or a highly ordered InP surfaces. For InGaAs(100), 300K H dosing can produce large multilayer etch features which cannot be annealed out; however by dosing at elevated temperatures these features can be avoided. After H cleaning at 380°C, the surface contains dark features consistent with monolayer etch pits, and these features are reduced by a factor ~50 with a post deposition anneal. The H cleaned and annealed surface can be unpinning by a half cycle dose of TMA followed by annealing because it generates an ordered dimethyl aluminum layer providing monolayer nucleation density, and an atomically flat surface, critical for aggressive EOT scaling. For InP, a low dose of H at similar temperatures and post deposition anneal generates a mixed surface reconstruction; however, with a higher dosing temperature around 440°C and post deposition anneal around 470°C, a single surface reconstruction is observed. A similar atomic H cleaning and TMA dosing procedure has been demonstrated to produced an ordered passivation layer on air exposed InP(100). It has been shown that for InGaAs and InP an oxide free surface can be achieved with atomic H dosing and annealing, however there is a dependence of surface roughness and defect densities on dosing and annealing conditions. The combination of atomic H cleaning and TMA

dosing provides a flat ordered surface ideal as a template for ALD of high-k gate dielectrics.

8:40am EM-MoM2 Selective Area Regrowth of Self-Aligned, Low-Resistance Ohmic Contacts on InGaAs, J.J.M. Law, A.D. Carter, G.B. Burek, B. Thibeault, M.J.W. Rodwell, A.C. Gossard, University of California, Santa Barbara

As electronic device areas scale with each generation by 1:4, resistances must remain constant, so contact resistivities must scale by 1:4. The high dopant concentrations achievable by molecular beam epitaxy (MBE) provide a method for creating low-resistance ohmic contacts; however, line-of-sight deposition and low desorption of atomic species may hinder the self-alignment of such regrowth. Careful control over growth conditions makes MBE a suitable technique for creating self-aligned, low resistance ohmic contacts to InGaAs.

Samples were grown by solid source MBE lattice matched to semi-insulating InP with layer structure as follows from the substrate: 400 nm InAlAs, 3 nm of Si-doped 2 and $3 \times 10^{19} \text{ cm}^{-3}$ InAlAs, and 25 and 15 nm of InGaAs, respectively. 300 nm of SiO₂ and 20 nm of Cr were deposited by PECVD and e-beam evaporation. A combination of electron beam and photolithography followed by ICP dry etching was used to define dummy spacer pillars. Oxidation and oxide removal of exposed InGaAs was done with UV o-zone and a dilute 10 H₂O:1 HCL dip. Samples were heated to 420 °C and treated with thermally cracked hydrogen ($\approx 1 \times 10^{-6}$ Torr) for 40 minutes prior to regrowth. 70 nm of 5×10^{19} Si-doped InAs was grown on the exposed InGaAs regions with quasi-migration enhance epitaxy (MEE) at 500 °C with V:III beam equivalent pressures of 4.0, 5.6, and 8.0. After regrowth, shorts over the dummy pillar were removed, and samples were metalized with lifted-off e-beam evaporated Ti/Pd/Au and mesa isolated. Contact resistances were extracted by transmission line measurements (TLM).

RHEED images during regrowth showed 4x2 surface reconstructions for regrowths with V:III ratios of 4.0 and 5.6 indicating a group In-rich surface reconstruction. SEM of regrowths at V:III ratios of 4.0 and 5.6 showed no faceting and fill-in to the dummy pillar edge. AFM showed roughened surfaces possibly due to high Si incorporation and lattice mismatch between InGaAs and InAs. Regardless of the V:III ratio during growth, 25 nm thick InGaAs channels showed contact resistances of 190 $\Omega \mu\text{m}$ while 15 nm thick InGaAs showed contact resistances of 105 $\Omega \mu\text{m}$. Metal-semiconductor contact resistances were 2.1 $\Omega \mu\text{m}$. Local electrode atom probe shows that the regrowth carries some of the Ga along with it creating a varying InGaAs alloy concentration throughout the regrowth.

9:00am EM-MoM3 Boron Nitride Development and New Applications for sub-20nm Device Fabrication, M. Balseanu, L.Q. Xia, V. Nguyen, M. Naik, D. Cui, K. Zhou, J. Pender, B. Mebarki, Applied Materials, Inc.

INVITED

The continuous need for films with lower dielectric constant, higher strength, and greater etch resistance drives the need to explore new materials. In this paper we present a study of boron nitride and other boron-based materials for multiple applications in semiconductor devices discussing the benefits and integration challenges.

As critical dimensions shrink and RC delay increases, the dielectric constant of the interconnect is a continuous area of focus. The current silicon carbonitride (SiCN) Cu barrier film has a dielectric constant greater than 5.0 and relatively poor step coverage. Significant advances have been made in recent years to develop a low k, conformal and manufacturable BN thin film for Cu barrier applications. The BN film was shown to have improved leakage, mechanical properties and insensitivity to UV cure relative to SiCN.

Back-end of line patterning has increased in complexity with the introduction of ultra-low k (ULK) dielectric materials. Dual hardmask (HM) patterning scheme eliminates the ULK damage caused by photoresist strip process. The TiN HM has faced challenges in extending below 20nm due to post etch residue and high stress leading to line bending. A boron-based HM material was developed to address those integration challenges. The new material has a low and tunable stress eliminating the line bending concerns. Boron content was optimized for the best selectivity to ULK without impacting the film stress. Significant defectivity and queue time improvement was observed with the boron-based HM due to volatility of the etch byproducts. 9% RC reduction relative to the conventional tri-layer patterning scheme was measured using 45nm 2-metal level electrical test structures.

Double or quadruple patterning technique is required for critical dimensions reduction due to the lack of manufacturable EUV lithography. Spacer-based double patterning (SADP) is one of the most adopted process flows to generate one-dimension regular array structures. Its implementation is impacted by the poor step coverage of the conventional PECVD SiN spacer leading to metal line cuts after final polishing step. A low temperature BN

film with superior step coverage, minimum pattern loading, good uniformity and low cost was developed for 20nm node and beyond. Its benefit for SADP was verified using a 20nm half pitch logic structure where a 200mm long serpentine yield was improved by 80%.

Evaluation of the boron-based thin films for Cu barrier and patterning applications has shown their potential to replace the conventional materials used today in the logic and memory process flow and thus enabling scaling below 20nm.

9:40am EM-MoM5 Novel Organosilicate Polymers for Ultralow-Dielectric Films with High Modulus, Low CTE, and Closed-Pore Morphology, D.Y. Yoon, J.H. Sim, Seoul National University, Korea, M. Liu, University of Michigan, H.W. Ro, C.L. Soles, National Institute of Standards and Technology, D.W. Gidley, University of Michigan

INVITED Novel organosilicate polymers are prepared using porogen bridged comonomers for ultralow-dielectric constant insulator applications. We synthesize silsesquioxane based terpolymers with methyltrimethoxysilane, ethylene bridged silane (1,2-bis(triethoxysilyl)ethane) and a porogen bridged silane comonomer via sol-gel reaction. The conventional route to generate nanoporous organosilicate films is to blend in a low molecular mass porogen that phase separates from the organosilicate network into isolated nanoscale domains that template the pores. However, using this approach it is difficult to achieve isolated nanopores with diameters below 2 nm when the total porosity becomes greater than 20 % by volume, which is essential for obtaining ultralow-k ($k < 2.2$) films. Our novel approach here is to covalently tether the both terminal ends of linear organic porogen to the trialkoxysilane monomers. This helps minimize the phase separation of the porogen during the thermal curing process of organosilicate polymers and keeps the resultant pores both smaller and less interconnected. For comparison we also prepare an analogous grafted version of this terpolymer series where only one end of the linear porogen is tethered to a trialkoxysilane monomer. The pore structures and porosities of this series of bridged and grafted porogen films are fully characterized with positron annihilation lifetime spectroscopy (PALS) and X-ray porosimetry (XRP). The resulting nanoporous films from the porogen bridged organosilicate polymers show much smaller pore sizes (1 nm to 2 nm), reduced interconnectivity of the pore structure, and superior mechanical properties in comparison with their analogs using the porogen grafting approach, especially at the high porosities (ca. 30 %) that are relevant for ultralow-k (2.0 to 2.2) insulators for advanced microprocessor applications.

10:40am EM-MoM8 Interface Traps and Low Subthreshold Swing in III-V Tunnel FETs, A. Seabaugh, S.-D. Chae, P. Fay, W.-S. Hwang, T. Kosel, R. Li, Q. Liu, Y. Lu, T. Vasen, M. Wistey, H. Xing, G. Zhou, Q. Zhang, University of Notre Dame, R.M. Wallace, University of Texas at Dallas

INVITED

Tunnel field-effect transistor (TFETs) are metal-oxide semiconductor (MOS) devices that use the gate electrode to control the band-overlap of a Zener tunnel junction. In TFETs, the subthreshold swing can be less than the thermal limit of 60 mV/decade in MOSFETs, allowing lower supply voltages for the same on/off current ratio, and lower power dissipation. Traps, however, at the high-k-dielectric/semiconductor interface act to terminate the gate field without contributing charge carriers to the channel and thereby degrade the subthreshold swing. This presentation will examine the relationship between interface traps and subthreshold swing and show, through impedance and transport measurements on InAs/AlGaSb TFETs, our current understanding of the interface, physics, charge control, and channel transport.

11:20am EM-MoM10 Impact of Vertical Structured Devices for Future Nano LSI, T. Endoh, Tohoku University, Japan

INVITED

For the past thirty years, the device downscaling has been the guiding principle in Si-LSI. The planar MOSFET has supported the expansion of the semiconductor industry; however, recently, the limit of planar MOSFETs is becoming apparent. As the feature size of planar MOSFETs approach the nano generation, it is becoming more difficult to improve its performance by SCE etc. Moreover, the process cost becomes expensive. In order to extend the scalability of CMOS technology to the nano generation; a new device structure is necessary. From above viewpoint, many new structured MOSFETs are proposed. The key points of next generation MOSFET are multi-gate structure, floating body structure and 3D structure. Therefore, proposed Vertical MOSFET [1-2] is emerging as one of the candidate to replace the conventional MOSFET.

In this paper, I will show the excellent performance of Vertical MOSFETs in comparison with others structured MOSFETs from viewpoints of high packing density and large driving current and good gate controllability etc. Moreover, I will show the impact of Vertical MOSFET for high density Memory [3]. Next, I will discuss that by using both proposed Vertical MOSFETs[4] and Spin device, Silicon ULSI can be evolved even if

becoming in nano generation in forces to Logic. Logic demands new scheme technology for realizing lower power operation and managing the total power consumption. On the other hands, Memory, especially non-volatile memory demands new cell technology for shrinking cell size and realizing high speed programming, low voltage operation and good reliability including endurance. From above viewpoint, we will show the excellent performance of both Logic-in-Memory Architecture [5-7] using MTJ, and MTJ based Vertical structured cell, as follows. First, it is shown that by Logic-in-Memory Architecture using MTJ, a compact LSI with a standby-power-free and immediate-power-up capability can be realized. Next, it is shown that by Vertical structured cell using MTJ, ultra high density non-volatile memory can be realized with utilizing both a capability of Vertical structure MOSFET such as large drive current, excellent gate controllability and compact footprint, and a capability of MTJ such as unlimited endurance and manufacturability integrated in backend metal line of Silicon CMOS technology. Finally, we discuss the impact of spintronic devices for future Nano Si-LSI.

- [1] T.Endoh,etal. IECE Trans.EL. E80-C, 1997
- [2] T.Endoh,etal. AWAD, 2008
- [3] T.Endoh,etal. IEEE IEDM, 2001
- [4] T.Endoh,etal. IECE Trans.EL. E92-C, 2009
- [5] A.Mochizuki, etal. IEICE Trans.EL E88-A, 2005
- [6] S.Matsunaga, etal. APEX 1, no.9, 2008
- [7] M.Kamiyanagi,etal. AWAD, 2009

Energy Frontiers Focus Topic

Room: 103 - Session EN+PS-MoM

Plasmas for Photovoltaics & Energy Applications

Moderator: S. Agarwal, Colorado School of Mines

8:20am **EN+PS-MoM1 Plasma Energy R&D at National Fusion Research Institute (NFRI): Fusion Energy, Silicon Quantum Dot Solar Cell, and Plasma-Enhanced Coal Gasification.** *S.J. Yoo*, National Fusion Research Institute, Republic of Korea **INVITED**

National Fusion Research Institute (NFRI) is a unique national laboratory dedicated to conducting research and development of the most powerful plasma energy application, the fusion energy, in Korea: We have constructed and a fully superconducting Tokamak device named KSTAR (Korea Superconducting Tokamak Advanced Research) which is now successfully in operation, and actively involved in the world's largest joint fusion project - International Thermonuclear Experimental Reactor (ITER), in which seven countries are participating to investigate engineering feasibility of fusion power commercialization.

Besides the fusion research, the NFRI has actively developed various plasma applications related to energy harvesting such as silicon quantum dot solar cells and plasma-enhanced coal gasification.

We have challengingly developed a new fabrication method of the silicon quantum dot solar cell by using hyperthermal neutral beams which are neutral beams with an energy range of 1 ~ 100 eV and very effective tools for thin film deposition at much lower substrate temperature without plasma-induced damages. The hyperthermal neutral beams can be effectively applied to each fabrication step of the silicon quantum dot solar cells: Deposition of a silicon thin film consisting of nano-crystal silicon and amorphous silicon matrix, then selective etching of the amorphous silicon matrix by keeping only nano-crystal silicon remained in order to obtain the silicon quantum dots, thereafter dielectric barrier coating on the silicon quantum dot surface, and then repetition of the procedure until a required thickness achieved.

We also have developed a steam plasma torch driven by microwave powers of 2.45 GHz and 915 MHz for effective gasification of various hydrocarbon materials and even low grade coals which can be hardly gasified by conventional thermal gasification methods since the steam plasma torch can produce much more abundant reaction catalysts such as O*, H*, OH*, H₂O₂, and O₃ than the thermal gasification methods. And, furthermore, the microwave plasma torch has a great advantage of the system life time compared to conventional arc plasma torches for which metallic electrodes are inevitable and thus easily eroded by the reaction catalysts produced for the coal gasification.

9:00am **EN+PS-MoM3 Synthetic Fuel Processing through Plasma-Assisted CO₂ Conversion.** *S. Welzel, S. Ponduri, F. Brehmer, M. Creatore, M.C.M. van de Sanden, R. Engeln*, Eindhoven University of Technology, Netherlands

Continuously increasing green house gas emissions and forthcoming (fossil) fuel depletion has stimulated research in novel fuel processing, cleaner combustion as well as CO₂ capturing and conversion. Conventional fuel processing usually aims at producing syngas (CO/H₂) mixtures that may be further converted into value-added hydrocarbons and oxygenates (C_xH_yO_z). Photocatalytic CO₂ hydrogenation is now considered as alternative approach which would simultaneously lead to a global green carbon cycle. It could reduce atmospheric CO₂ concentrations, while at the same time provide fuels on a renewable basis that can directly be supplied to our present energy infrastructure. Since the efficiency of such an artificial photosynthesis is low, we propose the plasma-assisted hydrogenation of CO_x into hydrocarbons.

This contribution focuses on the efficiency of CO₂ depletion and selectivity of CH₄ production in a low-temperature plasma expansion. The plasma is created from mixtures of argon and hydrogen while CO_x is injected into the expansion part where the dissociation mechanism might be radical- and/or ion-driven. Results on measurements of the (steady state) gas composition obtained by mass spectrometry and mid-infrared tuneable diode laser absorption spectroscopy will be reported.

Especially under argon rich conditions, where the chemistry is mainly driven by combined charge exchange with the Ar ions and dissociative recombination, a CO yield of 50 % was achieved. CH₄ formation was particularly detected at high hydrogen admixtures. C₂H_y hydrocarbons were in most cases absent while H₂O and CO turned out to be the main stable products. The results suggest an inherent syngas step during the plasma-assisted conversion approach, particularly a successive hydrogenation of CO.

9:20am **EN+PS-MoM4 Effective Light Trapping for Crystalline Silicon Solar Cells by Plasma Texturing.** *F.M.M. Souren*, Eindhoven University of Technology, Netherlands, *J. Rentsch*, Fraunhofer Institute for Solar Energy Systems (ISE), Germany, *M.C.M. van de Sanden*, Eindhoven University of Technology, Netherlands

Currently, in the photovoltaic (PV) industry, wet chemistry based etching is used for saw damage removal and surface texturing. It is known that plasma based dry etching leads to an improved light trapping on multi-crystalline silicon material and, therefore, it has the potential to increase the solar cell efficiency. However, up to now plasma based texturing has not been implemented in the PV industry, because of the very low etch rate (<1 μm/min) and the high cost of ownership. In this study, different front surface textures obtained by means of the Linear Microwave Plasma (LMP, commercialized by Roth&Rau) technique and the high rate Expanding Thermal Plasma (ETP, commercialized by OTB-Solar) technique, are investigated to reduce the overall reflection losses of mono-crystalline silicon solar cells and compared to KOH/IPA (Potassium hydroxide/Isopropanol) which is the standard process in solar cell manufacturing industry. The created textures employing the different etching techniques are characterized by reflectometry (250-1200 nm) to determine the weighted reflection and by Atomic Force Microscopy (AFM) to measure the surface topography so as to determine statistical roughness parameters. We have found that the average scatter angle, determined from the AFM measurements, shows a clear correlation to the measured weighted reflection. Effective light trapping has been obtained for two typical textures based on the described etching techniques. A texture which leads to a successive hit of the incident light ray towards the solar cell surface, can result in effective light trapping, as for example, the KOH/IPA process which creates a pyramidal texture. Efficient light trapping can also be obtained by the creation of a diffuse front surface (resembles the topography of "black silicon"), as for example by using the LMP technique, under the conditions used, which creates micro roughness. This micro roughness can be described as an effective medium with a refractive index between air and silicon and a typical thickness of up to (60±10) nm [1]. The micro roughness leads to an effective light trapping of a broad range of wavelengths from 250 nm up to 1200 nm. The light trapping of the wafer etched by the ETP technique is smaller than the as cut wafer and can be explained by a smaller average scatter angle compared to the as cut wafer. A short post treatment of the ETP textured wafer by the LMP technique, creates a diffuse front surface and results, therefore, in an improved light trapping. Moreover this combination shows great promise for a cost-effective approach towards plasma based texturing.

- [1] R.B. Stephens and G.D. Cody, Thin Solid Films 45 (1977) 19.

9:40am **EN+PS-MoM5 RF-PECVD Processes Excited by Asymmetric Voltage Waveforms**, *P.-A. Delattre, S. Pouliquen*, Laboratoire de Physique des Plasmas, France, *E.V. Johnson*, Laboratory of Physics of Interfaces and Thin Films, France, *J.-P. Booth*, Laboratoire de Physique des Plasmas, France

Voltage Waveform Tailoring (VWT) is a promising new technique for Radio-Frequency (RF) process plasma excitation. It is known that asymmetric waveforms resembling *peaks* (short positive and long negative voltage) or *valleys* (long positive, short negative voltage) can produce a voltage self-bias, even in a symmetrical reactor [1], known as the Electrical Asymmetry Effect (EAE). We have implemented a system to provide such voltage waveforms on the RF electrode of our Capacitively Coupled Plasma (CCP) reactor. For a peak to peak voltage (V_{pp}) of 300 V, we can control the self-bias from -190 V to 15 V, without changing any other process parameter. A new differential RF probe gives us the real-time current and voltage derivatives, and therefore, the instantaneous power. For a voltage waveform composed of a 15 MHz fundamental and three harmonics, instantaneous power changes from +1 kW to -1kW in 10 ns. Using a hairpin resonator probe in hydrogen at 13 Pa, we have measured an electron density of $2E8\text{ cm}^{-3}$ with a standard sine waveform, $2E9\text{ cm}^{-3}$ with a valleys waveform and $2E10\text{ cm}^{-3}$ with a peaks waveform (all with $V_{pp}=300\text{V}$). With a view towards photovoltaic applications, using a gas mixture of 4 % of SiH_4 in H_2 at 65 Pa, we have achieved a deposition rate of high-quality amorphous silicon of 1 Å/s for sine, 2.7 Å/s for valleys, and 3.8 Å/s for peaks voltage waveforms.

¹Brian G Heil *et al* 2008 *J. Phys. D: Appl. Phys.* **41** 165202

10:00am **EN+PS-MoM6 Spontaneous and High Rate Synthesis of Nanocrystalline Silicon by Expanding Thermal Plasma**, *İ. Doğan, N.J. Kramer, M.A. Verheijen*, Eindhoven University of Technology, Netherlands, *K. Dohnalova, T. Gregorkiewicz*, University of Amsterdam, Netherlands, *M.C.M. van de Sanden*, Eindhoven University of Technology, Netherlands

Silicon nanocrystals (Si-NCs) draw attention since they exhibit size dependent luminescence, improved charge storing capacity and increased surface reactivity. For instance, the size dependent optical properties of Si-NCs show great promise for increasing the efficiency of solar cells. Si-NCs could be used as spectrum down converters by converting the excess energy of a hot photon to generate multiple exciton pairs. For successful applications, the main issues on Si-NC synthesis are size control and surface engineering for improved optical properties, and high throughput. Among these points, the amount of throughput is highly critical for large scale applications however, it is not possible to achieve with current production techniques. Our research goal is to show that it is possible to fulfill these demands with a novel route by using the remote expanding thermal plasma (ETP) technique. Synthesis of Si-NCs in a remote Ar/ SiH_4 plasma occurs by means of a reaction sequence of ion- SiH_4 charge exchange and subsequent addition of SiH_4 molecules. This realizes spontaneous and nearly complete conversion of SiH_4 into Si-NCs with very high throughputs of about 25mg/min, the fastest deposition rate reported in the literature so far. Moreover, ETP has the freedom of tuning the size of the Si-NCs by controlling the flow rates of SiH_4 and Ar, i.e. the residence time in the plasma. Synthesized Si-NCs have a bimodal distribution of small (4-7nm) and large (50-80nm) sizes as confirmed by TEM, which is a consequence of the plasma expansion and reactor geometry. Bimodality has been analyzed with Raman spectroscopy by studying the asymmetry and shift in the transverse optical vibration mode of bulk-Si at 521cm^{-1} . Photoluminescence spectroscopy confirms the presence of monodisperse size distribution of small Si-NCs (4-7nm) leading to luminescence in the region 600-900nm. Observation of luminescence illustrates the quality of the nanocrystal surface passivated by the rapid native oxidation. Preliminary results show separation of the bimodal distribution can be controlled by means of geometrical isolation of the regions, in which small and large particles are formed.

10:40am **EN+PS-MoM8 SiH_4 and SiF_4 Dissociation in Matrix Distributed ECR Sources, and Potential for High Deposition Rate of Thin Film Silicon Alloys**, *S. Kasouti*, Total S.A, France, *P. Bulkin, P. Roca i Cabarrocas*, LPICM, France

Depositing at high rates and on ever larger areas are important objectives for the reduction of thin film silicon modules costs. High deposition rates have been achieved so far using different plasma sources but uniformity over large areas is still problematic. Matrix distributed electron cyclotron resonance (MDECR) systems consist of individual ECR plasma sources, which can be arranged in arrays with virtually no size limitations. Deposition rate of silicon alloys exceeding 10 nm/s, has been demonstrated, but little is known so far about the precursors' dissociation and species fluxes onto the surface.

We study here the dissociation of Silicon film precursors, using optical emission spectroscopy and quadrupole mass spectrometry, both in the plasma phase and in the fore line. We correlate the dissociation on the one hand to the electron density and temperature measured using Langmuir probes and microwave interferometry, and to film growth rate and structure on the other.

It is found that more than 90% of SiH_4 is used across a wide range of microwave powers, with a small dependence on gas residence time and pressure. Deposition rate depends primarily on the total flow of SiH_4 , and values above 3 nm/s are easily obtained. Transition from amorphous to microcrystalline silicon growth, on the other hand, occurs at high powers, and correlates to the electronic temperature and the high H/Si ratio observed in the gas phase. Direct dissociation of SiH_4 by electron impact, followed by deposition from atomic Si and subsequent crystallization by hydrogen is therefore a satisfactory explanation.

On the contrary, for deposition from SiF_4 , consumption is found to be lower than 60%, and independent of the gas residence time and microwave power. The deposition rate is also much lower, on the order of 0.3 nm/s. SiF_4 consumption increases with the total hydrogen flow rate added to the mixture. The total concentration of atomic Si in the gas phase varies linearly with the product of SiF and H species, estimated by actinometry, suggesting fluorine abstraction by hydrogen as a possible mechanism. Deposition rate is also proportional to the Si content in the plasma phase and increases with the hydrogen flow rate added to the plasma. We propose that film growth from MDECR plasmas of SiF_4/H_2 mixtures occurs through the deposition of atomic silicon, obtained from hydrogen abstraction of fluorine in the gas phase, direct electron impact dissociation of SiF_4 playing a smaller role.

This illustrates the importance of gas phase reaction for achieving high deposition rates, even in the case of high density low pressure plasma sources.

11:00am **EN+PS-MoM9 The Effects of Showerhead Hole Structure on the Deposition of uc-Si:H Thin Films by VHF PECVD**, *S.-S. Wi, Y.-G. Kim, H.-J. Lee*, Pusan National University, Republic of Korea, *D. Kim, D. Hwang, W.S. Chang*, LG Electronics, Republic of Korea

We present the characteristics of hydrogenated microcrystalline silicon thin films deposited from SiH_4/H_2 in 40 MHz plasma enhanced chemical vapor deposition (PECVD) equipped with multi-hole-array showerhead. The effects of hole array structure are analyzed in terms of their diameter and depth. Cross dependences between the hole structure and process parameters, such as SiH_4 concentration, rf power, pressure, substrate temperature and total gas flow rate, are also investigated. The results show that deposition rate is not a strong function of hole structure compared with other process parameters. However, it is found that uniformity can be controlled by varying the surface density of hole array. With decreasing total flow rate, faster increase in deposition rate is found at the multi-hole array compared with flat electrode. This may be attributed to the high electron density and longer residence time of within the holes. It is demonstrated that the multi hole array electrode can be used as an effective control variable for optimization of Si thin film solar cell PECVD process.

11:20am **EN+PS-MoM10 Plasma-Enhanced CVD and ALD Prepared Nanolayers for High-Efficiency Solar Cell Manufacturing**, *W.M.M. Kessels*, Eindhoven University of Technology, the Netherlands **INVITED** Photovoltaics has become a very innovative field of research and manufacturing due to the continuous improvement in the solar cell cost/performance ratio and its tremendous growth opportunities (past average annual growth rate of 40%). Several innovations with respect to the improvement of the cell efficiency lie in the field of thin film technology, not only for thin-film solar cells but also for crystalline silicon solar cells which are currently still dominating the market (87% market share in 2010). One particular trend is the application of ultrathin films or "functional nanolayers" for solar cell interface engineering. In crystalline silicon technology these nanolayers have as a main application the reduction of charge carrier recombination at interfaces through "surface passivation". Plasma-based deposition processes such as plasma-enhanced chemical vapor deposition (CVD) are key for the preparation of such films and recently the interest also shifted to (plasma-enhanced) atomic layer deposition (ALD) processes due to their precise growth control and their excellent uniformity and conformality [1]. Moreover, ultrathin films of < 10 nm have been found feasible in terms of reaching very-well passivated surfaces. In this contribution, the application of ultrathin films of various materials such as a-Si:H, a-SiN_x:H, SiO₂, and in particular Al₂O₃ will be addressed. The preparation methods will be described as well as the relevant surface reaction mechanisms during the film synthesis. Passivation and solar cell results will be presented with a main emphasis on the key mechanisms underlying the good passivation performance of the ultrathin

films. Also the market feasibility of new ALD technologies, e.g., in terms of high throughput processing, will be addressed.

[1] Atomic layer deposition: prospects for solar cell manufacturing, W.M.M. Kessels, et al., Proc. 33rd IEEE Photovoltaic Specialist Conference, San Diego, U.S.A. (2008).

Energy Frontiers Focus Topic

Room: 104 - Session EN-MoM

Industrial Physics Forum on Energy I

Moderator: R.A. Sears, Massachusetts Institute of Technology, B. Clark, Schlumberger

8:20am EN-MoM1 Energy Security and Energy Policy, *W.W. Hogan*, Harvard University **INVITED**

Energy security is broader and different than energy independence. Different definitions of energy security produce different policy prescriptions. A consistent framework for energy security must address basic principles.

9:00am EN-MoM3 Technology Innovation and China's Skyrocketing Demand for Energy, *E. Steinfeld*, Massachusetts Institute of Technology **INVITED**

9:40am EN-MoM5 Making Energy Sustainable – Scientific Challenges in Determining the Pathways to the Future, *E.D. Williams*, BP plc, UK **INVITED**

The scale and cost of the energy challenge are immense. Everyone wants secure, reliable, and affordable energy, but climate change, demand growth and, increasingly, resource scarcity, are transforming the energy landscape and it will continue to evolve.

There are many possible technical pathways to a low-carbon energy future, and each presents unresolved technical challenges that will influence the time, money and global-scale asset and infrastructure deployment that will take place over the next decades. BP's energy portfolio demonstrates many of the research challenges in this arena, and some examples from Carbon Capture and Storage and Biofuels will be discussed here specifically. Ultimately, research, technology, policies and partnerships will determine the pace of change.

10:40am EN-MoM8 Synthetic Biology for Energy and the Environment, *A.A.N. Patrinis*, Synthetic Genomics (SGI) **INVITED**

Synthetic biology is one of the major "tools" that are converting biology from a concept-driven scientific revolution to a tool-driven scientific revolution. This paradigm shift will enable significant applications of the new biology to major challenges in medicine, energy, and the environment.

11:20am EN-MoM10 Manufacturing Innovations for a Sustainable Energy Future, *R. Castro, O. Nalamasu*, Applied Materials, Inc. **INVITED**

Nanomanufacturing technology, the cost-effective and practical manufacturing solutions based on equipment and process solution platforms have been translating the promise of nanotechnology to reality in advancing transforming the electronics and display industries. Technology, Scale and Innovation would continue to be fundamental to meet the global inflections associated with Electronics and Display industries and more importantly, advances in nanomanufacturing technology are critical to solving the energy and environment challenges. In this presentation, I will detail the challenges and opportunities in building a sustainable energy future based on nanomanufacturing innovations.

Electron Transport in Low Dimensional Materials Focus Topic

Room: 209 - Session ET+EM+SS-MoM

Quantum Transport: From 0- to 2-Dimensions

Moderator: A.-P. Li, Oak Ridge National Laboratory, K. Varga, Vanderbilt University

8:20am ET+EM+SS-MoM1 Charge and Spin Transports at Surfaces of Strong Spin-Orbit-Coupling Materials, *S. Hasegawa, T. Hirahara*, University of Tokyo, Japan **INVITED**

Transports of charge as well as spin at crystal surfaces are now intensively studied by various kinds of experiments. Surface electronic states are generally decoupled from the bulk states and therefore intrinsically low-dimensional. Furthermore, space-inversion symmetry is broken down at crystal surfaces; one side of the surface is empty vacuum while other side is full of electrons in the crystal. These effects provide rich physics of transport, especially on surfaces of strong spin-orbit-coupling (SOC) materials. The surface-state bands are known to be spin-split of such strong SOC crystals such as Bi and Bi alloys, which is called by Rashba effect [1-4]. Similar effect is observed on a special kind of materials called topological insulators such as BiSb, BiSe, and BiTe alloys. Some of them have spin-split Dirac-cone type surface-state bands. This implies that spin-polarized current will flow at the surfaces of such materials.

In my presentation, by using samples of pure Bi [1-4], BiSb [5], BiSe [6,7], and BiTe, I will show that the surface-state bands are really spin-split and the Dirac-cone conductivity is directly measured by microscopic four-point probe method. An on-going project to detect the spin-polarization of surface current by using magnetic tips in a four-tip STM will be also introduced.

- [1] T. Hirahara, et al., Phys. Rev. Lett. 97, 146803 (2006).
- [2] T. Hirahara, et al., Phys. Rev. B 76, 153305 (2007).
- [3] T. Hirahara, et al., Appl. Phys. Lett. 91, 202106 (2007).
- [4] T. Hirahara, et al., New J. Phys. 10, 083038 (2008).
- [5] T. Hirahara, et al., Phys. Rev. B 81, 165422 (2010).
- [6] Y. Sakamoto, et al., Phys. Rev. B 81, 165432 (2010).
- [7] T. Hirahara, et al., Phys. Rev. B 82, 155309 (2010).

9:00am ET+EM+SS-MoM3 Electron Transport in Ferroelectric Domains and Walls, *A. Baddorf*, Oak Ridge National Laboratory **INVITED**

Ferroelectric tunneling, where electron transport is controlled by the polarization state, has recently been realized in a number of experiments. Polarization-controlled transport effects have been detected in tunnel junctions, thin films, single crystals and at domain walls. Yet, little analysis of data has undertaken to determine the transport mechanisms and their interaction with ferroelectric fields and domain boundaries involved in switching. We present seminal experimental observations of transport in thin films of $\text{Pb}(\text{Zr}_{0.2}\text{Ti}_{0.8})\text{O}_3$ (PZT) and BiFeO_3 (BFO). Earlier we have shown that both materials exhibit pronounced polarization-controlled electroresistance [1]. Temperature and voltage dependence of currents are not well fit by any one standard model. Instead a transition between surface and bulk limiting effects is observed. Upon close inspection, I-V curves exhibit a reproducible region of negative differential conductance associated with ferroelectric switching. Although this anomaly may originate from extrinsic processes, e.g. due to oxygen vacancies or charge injection, we have carried out a series of control experiments on PZT films that unequivocally connect variation of conductance with the size of the polarization domain in the plane of the surface. The I-V anomaly therefore originates from significant conductivity of the domain wall and a relatively slow expansion of the domain following polarization switching. However, our results do not imply simply that transport is through domain walls, but further that nanoscale domains formed by switching have fundamentally different conduction behavior [2]. We suggest that domains formed by tip-applied bias have curved walls and are consequently charged, modifying adjacent material much as charge accumulation modifies a semiconductor. Engineering the ferroelectric domain size produces a tunable conductance reminiscent of analogue memristors, providing a quasi-continuous spectrum of non-volatile resistive states, even though the PZT polarization itself is bistable. Ferroic memristive behavior, which based on our measurements is likely to be universal to ferroic semiconductors, is a striking departure from the conventional picture of discrete electron transport states in ferroelectrics.

Research was conducted at the Center for Nanophase Materials Sciences and sponsored by the Division of Scientific User Facilities, U.S. Department of Energy.

[1] P. Maksymovych et al., Science 324 (1421) 2009.

[2] P. Maksymovych et al., submitted.

9:40am **ET+EM+SS-MoM5 Electronic Instabilities, Fluctuations, and Transport in Epitaxial Nanowires, H.H. Weiering**, University of Tennessee and Oak Ridge National Laboratory **INVITED**

Quantum transport is at the heart of nanoscience and marries a fundamental law of nature — quantum mechanics — with applied electrical engineering and emerging materials technologies. Ultimately, nanoscale electronic devices will contain networks of wires whose cross sections will be so small as to represent one-dimensional conductors with novel transport properties. We have fabricated exceptionally long and uniform YSi₂ nanowires via self-assembly of yttrium atoms on Si(001). The wire widths are quantized in odd multiples of the Si substrate lattice constant. The thinnest wires represent one of the closest realizations of the isolated Peierls chain, exhibiting van Hove type singularities in the one-dimensional density of states and charge order fluctuations below 150 K. Conduction through individual nanowires follows an inverse Arrhenius behavior, indicative of thermally-assisted tunneling of small polarons between defect centers. Quantitative analysis of individual wire resistances, probe resistances, and negative differential resistances of nanowire networks indicates significant electronic interwire coupling below 150 K. The long-range coupling mechanism involves the dielectric polarization of the substrate, which induces current blockades in neighboring conduction channels.

This work is sponsored by the NIH/NHGRI and was partially conducted at the Center for Nanophase Materials Sciences, which is sponsored at Oak Ridge National Laboratory by the Office of Basic Energy Sciences, U.S. Department of Energy

10:40am **ET+EM+SS-MoM8 Grain Boundary Resistivity in Copper Nanowires, T.H. Kim**, POSTECH, South Korea **INVITED**

The reliable choice of the interconnect materials in current integrated circuits is copper because of its higher electrical conductivity and improved stability against electromigration among all possible candidates. However, as the width of interconnects is approaching a mean free path of the electrons, the resistivity of copper interconnects is known to increase dramatically. Typically, this increase in the resistivity of the narrow interconnect is attributed to enhanced sequential scattering of electrons from defect planes such as either grain boundaries (GB) or other surfaces/interfaces. But, it is very challenging to distinguish which scattering factor is dominant over others in such a small scale.

To answer such a fundamental question, theorists developed semi-empirical methods and the relative contribution of various electron scattering mechanisms has been understood largely by relying on the semi-empirical methods based on the theories of Fuchs-Sondheimer and Mayadas-Shatzkes. The direct measurements of the resistance of individual GBs have been surprisingly lacking mainly due to technical difficulty to access single GBs in a nanowire that could not be realized by conventional fabrication methods using a fixed electrical contacts. Recently, Y. Kitaoka *et al.* have observed a resistance change along a damascene Cu interconnect wire with four-probe scanning microscope. They successfully separated the GB scattering effect from other scattering sources; however, the direct correlation between the GB structure and the specific GB resistivity remained unclear.

Here we present the direct measurement of individual GB resistances and the critical role of GB structure in the increased resistivity in copper nanowires with a four-probe scanning tunneling microscope. The resistances of high symmetry coincidence GBs are then calculated using a first-principle method, which confirms that the coincidence GBs have orders of magnitude smaller resistance than those measured at the high-angle random GBs. As well, to explain high resistivity of random GBs, we used free-electron-with-random-point-scatterer (FERPS) model. In the FERPS model, we derived that the specific GB resistivity of random GB is independent of the specific structures of random GB such as orientation and is determined entirely by the Fermi wavelength of the bulk.

This research was conducted at the Center for Nanophase Materials Sciences, which is sponsored at Oak Ridge National Laboratory by the Office of Basic Energy Sciences, U.S. Department of Energy.

11:20am **ET+EM+SS-MoM10 Tunable Coulomb Blockade and Giant Coulomb Blockade Magnetoresistance in a Double Quantum Dot System, X.-G. Zhang**, Oak Ridge National Laboratory, T. Xiang, Chinese Academy of Sciences

We propose a Hubbard model to describe the tunneling effect of electrons in a double quantum dot system connected in the parallel circuit configuration to electrodes. The change in the interdot coupling is shown to dramatically influence the Coulomb blockade properties. For magnetic double dots, the interdot coupling can be tuned by the external magnetic

field, leading to a giant Coulomb blockade magnetoresistance. Possible detection of this effect in organic systems is discussed.

This research was conducted at the Center for Nanophase Materials Sciences, which is sponsored at Oak Ridge National Laboratory by the Office of Basic Energy Sciences, U.S. Department of Energy.

11:40am **ET+EM+SS-MoM11 Quantum Transport in Crossbar Devices, B. Cook, P. Dignard, K. Varga**, Vanderbilt University

Electronic devices with crossbar geometries have recently been fabricated with nanoscale features (Zhong. *et al.*, Science Vol. 302). Consisting of a two dimensional grid, devices have been formed with a variety of components including carbon nanotubes and semiconductor nanowires. These devices are assumed to operate classically, but as the dimensions of the device shrink consideration of quantum effects becomes necessary. We consider a single junction between two wires up to a four by four grid of wires. Through a series of calculations with atomistic first-principles, tight-binding and analytic models of multi-terminal devices we demonstrate the presence of unique behavior, such as interference effects, not present in classical models. It is expected that exploitation of these effects will be useful in the creation of circuit components.

Graphene and Related Materials Focus Topic Room: 208 - Session GR-MoM

Graphene Growth

Moderator: D.K. Gaskill, U.S. Naval Research Laboratory

8:20am **GR-MoM1 Atomic Layer Growth of Graphene, L. Colombo**, Texas Instruments Incorporated, C. Magnuson, Y. Hao, X. Li, R.S. Ruoff, University of Texas at Austin **INVITED**

Graphene has been shown to have unique electronic, chemical and physical properties over the past few years and this is opening many opportunities for its use. However, to date most of the experiments have been performed on graphene exfoliated from natural graphite and the graphene films have been rather small, hundreds of microns squared. Transport properties equivalent to those achieved on exfoliated graphene have also been achieved on layers of graphene on SiC; but this graphene is not easily transferred to other substrates. There is now a need to develop high quality, large area single crystal graphene. Li *et al.* discovered the growth of graphene on copper metal foils by chemical vapor deposition (CVD) using methane gas which led for the first time to the growth of meter square graphene. The current CVD process can indeed grow very large graphene films but the films are polycrystalline. The domain size for the baseline process is a few tens of microns in diameter and in principle there is pathway to achieving much larger domain size films. Large single crystals, 0.5 mm size, have recently been reported and perhaps we can learn from these results how to extend them to grow even large graphene films with higher quality. The growth mechanisms of graphene and single crystal growth of graphene will be presented and discussed together with a discussion of what the semiconductor industry would need to make graphene a reality.

9:00am **GR-MoM3 Graphene on Ni(111): Growth and Defects, M. Batzill**, University of South Florida, J. Lahiri, Brookhaven National Laboratory, I.I. Oleynik, L. Adamska, University of South Florida

Using scanning tunneling microscopy (STM), Auger electron spectroscopy (AES), and low energy electron microscopy (LEEM) we have investigated the growth of graphene on Ni(111) surfaces by carbon segregation from the bulk. We reveal two distinct growth modes for graphene growth. Between 480 and 650 °C graphene forms on clean Ni(111) and below 480 °C graphene grows by an in-plane conversion of a surface carbide phase [1,2]. This is the first time that graphene formation is observed by transformation of a surface carbide. STM indicates that a lattice-matched, one-dimensional in-plane domain boundary between graphene and the carbide forms. In the presence of the carbide graphene grows by replacing Ni-atoms with carbon at this interface. In addition to the growth of graphene we will also briefly discuss atomic-scale defects that can be synthesized in Ni-supported graphene. Different adsorption configurations of graphene on Ni will result in domain boundaries that exhibit pairs of pentagonal and octagonal carbon rings [3]. These line defects have similar electronic properties to graphene zig-zag edges but without the dangling bonds.

[1] J. Lahiri, T. Miller, L. Adamska, I.I. Oleynik, M. Batzill Nano Lett. 11, 518 (2011)

[2] J. Lahiri, T. Miller, A.J. Ross, L. Adamska, I.I. Oleynik, M. Batzill New J. Phys. 13, 025001 (2011).

[3] J. Lahiri, Y. Lin, P. Bozkurt, I.I. Oleynik, M. Batzill Nature Nanotechnol. 5, 326 (2010).

9:20am **GR-MoM4 Investigating Graphene Nucleation on C-Face SiC via Electron Channeling Contrast Imaging and Raman Mapping.** *J.K. Hite, J.D. Caldwell, J.L. Tedesco, R.L. Myers-Ward, C.R. Eddy, Jr., D.K. Gaskill*, U.S. Naval Research Laboratory

Epitaxial graphene (EG) has lately garnered enormous interest, due to its high free-carrier mobility and compatibility with semiconductor processing. Furthermore, EG RF field effect transistors have been demonstrated.¹ Current RF device work has been on the Si face (0001) semi-insulating 6H-SiC substrates as EG on this face mainly consists of mono- and bilayer graphene. In contrast, the C-face consists of up to a dozen or more graphene layers and has a rougher morphology. Even so, there is significant interest in obtaining few layer, smooth EG on the C-face of SiC due to its superior mobility (for similar charge density) as compared to growth on the Si-face. However, the growth mechanism of this material is not well understood. Recently, it was shown that C-face EG grown in an argon ambient slows the growth rate and, under certain conditions, results in localized growth of the graphene on the C-face.² These localized areas, referred to herein as graphene covered basins (GCBs), create the possibility of investigating the initial stages and mechanism of graphene growth on the C-face of SiC.

Previously, we had used electron channeling contrast imaging (ECCI) to investigate GCB morphology as a function of GCB size and growth conditions for EG growth on C-face SiC.³ Threading screw dislocations (TSDs) in the SiC substrate were found to be nucleation sites for GCBs. The TSDs were easily identified at the centers of small EG GCBs (<20 μm diameter). This work shows the evidence that the TSDs fade then disappear with increasing GCB size, suggesting that as the GCBs grow or coalesce to larger diameters the TSDs become buried. Concurrently, Raman mapping experiments determined graphene thickness and quality at GCB genesis; the maximum graphene thickness for TSD detection in the SiC by ECCI was also determined. Initial findings with Raman mapping confirm ECCI results showing that the graphene is thicker in the middle of the GCB. The small GCBs (<20 μm), which exhibit a strong TSD signal, are comprised of roughly 3-4 monolayers of graphene in the center, with decreased thicknesses near the edge. In addition, the Raman 2D spectral linewidth for these small GCBs were correlated with thickness. Atomic force and scanning electron microscopy of the same GCBs were used to obtain correlated morphological details. These results imply that graphene growth is complex on this polar surface of SiC.

¹J.S. Moon *et al.*, IEEE Electron Device Lett. **31**, 260, 2010.

²J.L. Tedesco *et al.*, Appl. Phys. Lett. **96**, 222103, 2010.

³J.K. Hite *et al.*, Nano Lett. **11**, 1190, 2011.

9:40am **GR-MoM5 Graphene Band Engineering on One-Dimensionally-Modulated SiC Substrate.** *K. Nakatsuji, T. Yoshimura*, University of Tokyo, Japan, *K. Morita, S. Tanaka*, Kyushu University, Japan, *F. Komori*, University of Tokyo, Japan

Engineering of the gapless graphene Dirac bands has been studied for understanding and useful applications of distinctive electronic properties due to their chiral nature. It has been theoretically shown that the group velocity of the bands can be tuned anisotropically by external potentials of a few tens nanometer scale. [1] A three-fold anisotropy of the conical band was found for a single-layer graphene modified by adsorbed metal clusters [2] while it was partly masked by the intrinsic trigonal warping of the bands. Here, we report uniaxial deformation of the Dirac cone of the single-layer graphene grown on a vicinal SiC(0001) substrate.

In the experiment, single-layer graphenes were thermally made by annealing in 5×10^{-5} Torr N_2 gas at 1970 K for 1 sec on Si-terminated surfaces of nitrogen-doped 6H- and 4H-SiC(0001) substrates vicinal to the [1-100] direction. The tilting angle was either 4 degree for the 6H substrate or 8 degree for the 4H substrate. The terraces were elongated as confirmed by scanning tunneling and atomic force microscopes. The terrace widths in the [1-100] direction were 21 and 13 nm for the 4- and 8-degree-off substrates, respectively, while the width perpendicular to the [1-100] direction was commonly 100 nm.

The shapes of the graphene π and π^* bands were studied using angle-resolved photoemission spectroscopy (ARPES) at 130 K. The graphene and reconstructed interface structures were confirmed by low energy electron diffraction (LEED) before the ARPES measurements, and we adjusted the orientation of the crystal axes using LEED. The Dirac point was 0.4 eV below Fermi energy E_F as previously observed graphene grown on flat SiC(0001) substrates. The spectrum width of the graphene on the 8-degree-off substrate is larger than that on the 4-degree-off substrate because of the electronic scattering at the curved area of graphene on the substrate step edges as discussed for the graphene on a SiC(0001) substrate vicinal to the [11-20] direction. [3]

The constant-energy ARPES intensity maps of the π and π^* bands for the graphene on the 4-degree-off substrate are trigonally warped, and almost agree with the previous reports. On the other hand, the intensity maps for the graphene on the 8-degree-off substrate are significantly elongate in the [1-100] direction. The group velocity of the π^* band in the G-K direction parallel to [1-100] is more than 20 % lower than the velocity in the other G-K directions. The velocity reduces in the direction parallel to the substrate slope in contrast to the theoretical prediction.[1]

References

1. C.-H. Park, L. Yang, Y.-W. Son, M. L. Cohen, and S. G. Louie, Nat. Phys. **4**, 213 (2008).

2. S. Rusponi, M. Papagno, P. Moras, S. Vlaic, M. Etzkorn, P.M. Sheverdyaeva, D. Pacile, H. Brune and C. Carbone, Phys. Rev. Lett. **105** 246803 (2010).

K. Nakatsuji, Y. Shibata, R. Niikura, F. Komori, K. Morita and S. Tanaka, Phys. Rev. **B82** 045428 (2010).

10:00am **GR-MoM6 Graphene Growth on Au(111).** *J. Wofford*, University of California at Berkeley and Lawrence Berkeley National Laboratory, *E. Starodub, N.C. Bartelt, K. McCarty*, Sandia National Laboratories, *O. Dubon*, University of California at Berkeley and Lawrence Berkeley National Laboratory

Studies on the growth of graphene on metal surfaces indicate that the strength of the interaction between the two materials plays a significant role in determining the evolution and final properties of the resulting film. A number of relatively strongly interacting graphene-metal systems, such as -Ru and -Ir, have been studied comprehensively, but the graphene-Cu system remains the only comparatively weakly interacting combination to have been so scrutinized [1]. Comparisons between graphene growth on Cu and Au provide an opportunity to systematically understand graphene growth on weakly interacting substrates. For example, both Cu and Au have low C solubility, but the mismatch between the lattice of graphene aligned with that of the metal's (111) surface is substantially larger for Au than for Cu. To examine what effect these differences have, we used low-energy electron microscopy (LEEM) to observe graphene growth on Au (111) in UHV by direct deposition of C from a heated graphite rod. Low-energy electron diffraction (LEED) analysis of the pre-growth Au (111) surface showed the characteristic "herringbone" reconstruction peculiar to Au. Graphene islands nucleate rapidly upon exposure to the C flux, suggesting a relatively low equilibrium C adatom concentration on the otherwise bare Au surface. The graphene islands nucleate simultaneously across the surface with a slight preference for nucleation along Au step edges rather than on terraces. The nucleation density is substantially higher than previously observed on other metals, causing inter-island impingement to begin at sub-micron sizes. Similar to Cu, no island growth due to C precipitation from the bulk of the Au occurs during sample cooling. We find that the graphene lattice prefers strongly to be aligned with the Au lattice with a small minority of the domains rotated by 30 degrees. The prevalence of the aligned graphene orientation is particularly surprising due to the substantial lattice mismatch involved and calculations predicting a 30 degree relative rotation is preferred [2,3]. We draw comparisons between the observed rotational structure and those predicted by first principle calculations.

Work at Sandia was supported by the Office of Basic Energy Sciences, Division of Materials Sciences and Engineering, U. S. Department of Energy under Contract No. DE-AC04-94AL85000. J.M.W. acknowledges support from the National Science Foundation Graduate Research Fellowship Program.

[1] J. M. Wofford, *et al.*, Nano Lett. **10**, 4890 (2010).

[2] M. Vanin, *et al.*, Phys. Rev. B **81**, 081408 (2010).

[3] C. Gong, *et al.*, J. Appl. Phys. **108**, 123711 (2010).

10:40am **GR-MoM8 Synthesizing Pristine Epitaxial Graphene and its Impact on Electronic Properties.** *V.D. Wheeler, G.G. Jernigan, N.Y. Garces, L.O. Nyakiti, R.L. Myers-Ward, C.R. Eddy, Jr., D.K. Gaskill*, U.S. Naval Research Laboratory

Epitaxial graphene (EG) enables wafer-scale production needed to realize graphene-based technologies. Since monolayer graphene is all surface, any impurities or adsorbed atoms can alter the graphene by doping, acting as scattering sites which decrease the mobility, and creating additional resistances that degrade device performance. Also, impurities and resist residues can increase ohmic contact resistance and impact the ability to deposit uniform gate dielectrics. Achieving pristine graphene surfaces allows ultimate control over future interface formations and thus improves device performance. In this work, an *in-situ* H_2 anneal is explored to attain the pristine epitaxial graphene required to fully realize the advantages of this material for future electronic applications.

EG was grown on semi-insulating, on-axis, (0001) 6H-SiC substrates in an Aixtron VP508 CVD reactor from 1575 to 1650°C for 60 to 180 min. Initially, samples were grown and cooled in a 100 mbar Ar ambient. Chemical analysis, using x-ray photoelectron spectroscopy (XPS), of the as-grown graphene surfaces showed the presence of both O and excess C impurities. These impurities can dope the EG and reduce the mobility, suggesting the need for methods to obtain pristine surfaces.

To address this need, several post-growth treatments were studied. Unlike exfoliated graphene¹, uncontaminated EG surfaces could not be obtained using a 400 °C Ar/H₂ anneal, and wet chemical cleans reduced the surface impurities. A pristine post-growth EG surface was only accomplished with a 1300 °C UHV anneal for 30 min.

Ex-situ UHV anneals are not practical for manufacturing graphene devices, so we explored a new technique incorporating a H₂ anneal during cool down from growth temperature. First, EG samples were cooled in Ar from growth temperature to 1000°C. Next, Ar was evacuated and H₂ introduced at constant pressure. Samples were annealed at 1000°C for 30 min., cooled in H₂ to 700°C, and then the chamber was evacuated. XPS analysis showed that the EG samples have no O impurities and reduced excess C impurities compared to Ar cooled samples. Also, the signal from the interfacial layer² is reduced, and both the graphene and SiC peaks are shifted to lower binding energies, suggesting a reduction in strain between the EG and the SiC substrate. These samples also had a more inert surface, showing only a small amount of adsorbed O (< 2%) after 3 days in atmosphere. Further, van der Pauw Hall measurements revealed a 2X increase in mobility over Ar cooled samples with no change in the sheet concentration magnitude.

1. Ishigami, et. al. *Nano Letters* **7(6)** 1643 (2007)

2. Jernigan, et. al. *Nano Letters* **9(7)** 2605 (2009)

11:00am **GR-MoM9 Growth and Characterization of Graphene Films on Cu(111)**, **Z.R. Robinson**, P. Tyagi, H. Geisler, C.A. Ventrice, Jr., University at Albany, H. Yang, T. Valla, Brookhaven National Laboratory, A.A. Bol, J.B. Hannon, IBM T.J. Watson Research Center

Previous studies have shown that monolayer graphene films can be grown on Cu substrates by the catalytic decomposition of various carbon containing molecules. These films are typically grown on poly-crystalline Cu foils, which have a tendency to recrystallize into a {100} texture during the growth procedure. Since graphene crystallizes in a hexagonal lattice and the {100} surface of a face centered cubic lattice has a square symmetry, this is expected to result in multi-domain graphene growth. Because the Cu(111) surface has hexagonal symmetry and a lattice mismatch of 3.7% with graphene, growth on this surface termination has potential for producing films with a lower defect density.

There have been relatively few studies of graphene growth on single crystal Cu substrates, owing to the fact that hydrocarbon source pressures in the range of 100 millitorr are needed, which is incompatible with most UHV systems. In this study, graphene films were grown on Cu(111) substrates by first preparing the clean surface in UHV by sputtering with inert gas ions followed by annealing. The sample was then transferred to a conventional tube furnace where the graphene film was grown by annealing in forming gas to reduce the surface oxide, followed by annealing in ethylene to produce the graphene film.

The growth morphology of the graphene overlayer was characterized using low energy electron microscopy (LEEM) and low energy electron diffraction (LEED). The LEEM shows a mesa-like surface texture with relatively flat terraces covered with graphene and valleys between the terraces with low carbon coverage. Micro-Raman spectroscopy of the terrace regions produces a signal characteristic of a well-ordered graphene overlayer, whereas the Raman signal in the valleys is much weaker and shows a distinct D-peak. The typical lateral dimension of the terraces was ~10 μm. Micro-LEED performed on the terrace sites shows a sharp Moiré pattern. Conventional LEED, which probes a lateral area of ~1 mm, shows a ring structure with increased intensity in the six high symmetry directions of the Cu(111) substrate lattice. This indicates that for this growth procedure there is a quasi-epitaxial relationship between the graphene overlayer and the Cu(111) substrate with rotational disorder of the graphene from mesa to mesa. Synchrotron-based angle-resolved ultraviolet photoelectron spectroscopy (ARUPS) measurements have been performed to probe the electronic band structure of the graphene overlayer. A linear dispersion has been measured in the K direction with the Dirac point located near the Fermi level.

11:20am **GR-MoM10 Graphene Growth on Cu(111)**, **S. Nie**, Sandia National Laboratories, J. Wofford, University of California at Berkeley and Lawrence Berkeley National Laboratory, N.C. Bartelt, Sandia National Laboratories, O. Dubon, University of California at Berkeley and Lawrence Berkeley National Laboratory, K. McCarty, Sandia National Laboratories

Large area graphene growth on copper foils has attracted considerable interest because of the low cost and high graphene quality. However, relatively little is understood concerning the effect of substrate crystallographic orientation on the morphological evolution of graphene islands. Complication arises by the fact that the foil surface texture depends on how the foil is manufactured. In previous work we have examined graphene growth on the commonly occurring (100) surface of cold-rolled Cu foil.¹ However, growth on the Cu(111) surface, another often observed orientation in textured Cu foil was not studied.

In this work we investigate graphene growth on single crystal Cu(111) in situ using a carbon evaporator in a low-energy electron microscope (LEEM). We find that graphene first nucleates at defects and impurities. A considerable fraction of the islands is misaligned in plane with the substrate, generating rotational boundaries upon inter-island impingement. Islands are dendritic with distinct lobes, similar to those reported on graphene/Cu(100).¹ However, instead of each lobe being a graphene sheet with a different orientation, all lobes in an individual island form a single crystal. We propose that these dendritic shapes are the result of diffusion-limited growth. Consistent with this, we find that new island nucleation caused by an increase in the carbon flux occurs equidistant from existing islands. Furthermore, we show that the growth velocity of each lobe is accurately predicted by simulations assuming diffusion limited growth. This diffusion limited growth is in stark contrast with the large carbon attachment barriers seen on Ru and Ir.² Unlike graphene growth on Ru(0001) and Ir(111),² large densities of carbon adatoms are not detected before island nucleation. Temperature plays an important role in the crystallographic alignment of the graphene film. At high growth temperature (> 900 °C), graphene islands are found closely aligned with Cu, while at low temperature (< 800 °C), increased disorder in the orientation of graphene with respect to Cu(111) is observed in the low-energy diffraction patterns.

Work at Sandia and LBNL was supported by the Office of Basic Energy Sciences, Division of Materials Sciences and Engineering, U. S. Department of Energy under Contracts No. DE-AC04-94AL85000 and No. DE-AC02-05CH11231 respectively. JMW acknowledges support from the National Science Foundation Graduate Research Fellowship Program.

1. Wofford, J. M.; Nie, S.; McCarty, K. F.; Bartelt, N. C.; Dubon, O. D., *Nano Lett.*, **10**, 4890 (2010).

2. Loginova, E.; Bartelt, N. C.; Feibelman, P. J.; McCarty, K. F., *New J. Phys.* **10**, 093026 (2008).

11:40am **GR-MoM11 Epitaxial Graphene Growth on Non-Polar 6H-SiC Substrates**, **L.O. Nyakiti**, R.L. Myers-Ward, V.D. Wheeler, F.J. Bezares, N.Y. Garces, J.K. Hite, C.R. Eddy Jr., J.D. Caldwell, D.K. Gaskill, U.S. Naval Research Laboratory

Graphene has attracted recent interest due to its unique electronic properties. Epitaxial graphene (EG) grown on different planes of 6H-SiC can have different morphological and electrical properties. For example, EG grown on the (0001) plane produces single or bilayer regions, step bunched heights of 5–10nm and lower carrier mobility compared to EG on the (000-1) plane that produces multilayer EG with ridge heights up to 80nm. Step bunching introduces conduction anisotropy¹ and poses a challenge to lithography at ≤100nm. To mitigate step heights and improve carrier mobility, we studied the formation of EG on non-/semi-polar surfaces, specifically the (10-10), (11-20), and (03-312). Here, we show the morphology of EG on these non-traditional planes is improved by an order of magnitude compared to vicinal plane growths.

EG samples (16x16mm²) were synthesized on non-polar (10-10), (11-20), and (03-312) substrates. Growth was carried out in an Aixtron VP508 chemical vapor deposition reactor. Prior to EG growth, substrates underwent an *in situ* H₂ etch at 1520°C for 50min., producing a controlled nucleating surface with average RMS of 0.1nm. Subsequent EG growth was conducted under a flowing Ar ambient of 20 standard liters per minute at 100mbar. Micro-Raman spectroscopy contour mapping was used to confirm the presence, thickness and strain variation of EG. Atomic force microscope (tapping mode) and scanning electron microscope was used to extract surface morphology variations.

Initial results show that 15min. of EG growth on (10-10) non-polar surface has horizontal wrinkles, indicative of multiple layers of graphene, peak-to-valley heights ≤5nm, and an RMS of ~0.73nm from a 10x10μm² AFM scan. Growth on (11-20) non-polar plane showed the presence of wrinkles (~3nm in height) and an average RMS of 1.1nm. Both (10-10) and (11-20) plane EG do not show the step bunch and terrace morphology typically associated with polar surfaces. While uniform terraces on the (0001) face can be up to

several μm wide, the (10-10) and (11-20) plane exhibits smaller terrace widths ~ 75 and $\sim 115\text{nm}$, respectively. Finally, EG grown on high order (03-312) plane was observed to have wrinkles as well as vertical ridges that were preferentially oriented parallel to each other and an average RMS of 1.17nm. The distance between the successive ridge peaks was $\sim 500\text{nm}$. Compared to the RMS values of 2.3 and 3.7nm for EG on (0001) and (000) planes, respectively, all EG films grown on non-/semi-polar orientations were markedly smoother. This work shows that the morphology of EG can potentially be controlled using different SiC orientations.

1. Yakes, M. Y., et al Nano Lett. **10**, 1559 (2010)

In Situ Spectroscopy and Microscopy Focus Topic Room: 106 - Session IS+AS+SS-MoM

In Situ Studies of Catalysis and Gas-Solid Reactions

Moderator: G. Rijnders, University of Twente, the Netherlands

8:20am **IS+AS+SS-MoM1 In Situ X-ray Studies of Model and Real Catalysts: Bridging the Complexity Gap.** *A.I. Frenkel*, Yeshiva University **INVITED**

In the last decade, there was a surge in advanced characterization methods to study catalytic materials at work. Most notable innovations in synchrotron-based techniques include the coupling of in situ/operando x-ray absorption and scattering methods to vibrational spectroscopies, empowered by improved time and energy resolutions. For example, in situ XAFS-XRD combination enables complementary studies of short and long range order in the same system, a great tool when multiple spatial dimensions evolve in a certain process, such as: modifications of both the catalyst and the support during catalytic reaction, the nucleation and growth of a nano-catalyst, oxidation/reduction of a bulk oxide. Combining in situ XAS or XRD with infrared or Raman spectroscopy is critical for understanding how the structural and electronic properties of a catalyst relate to its reactivity.

Although these are important new improvements in the way we currently study, and understand, processes in nanomaterials, they are done by methods that are not sensitive to local fluctuations in size, shape, structure of nanomaterials, that are present even in well-defined, model catalysts. Thus, in addition to the ensemble averaging that these and other commonly used methods provide, local information, such as one provided by electron microscopy, is needed. In this talk, I will focus on the new efforts in combining the local and average information by coupling the in situ x-ray absorption spectroscopy to in situ environmental transmission electron microscopy (E-TEM) for in situ investigations. Such experiments, done in two separate facilities (NSLS and CFN) at Brookhaven National Laboratory, revealed anomalous, mesoscopic phenomena in the electronic, structural and thermal properties of supported Pt nanoparticles. These systems have long been excellent model systems in catalysis research, yet, at a closer look, as our in situ measurements demonstrated, they turned out to be much more unstable and complex than previously perceived. These clusters exhibited unique physical properties, such as negative thermal expansion, increase in the Debye temperature, broad amorphous-to-crystalline transition zone, large surface strain, as well as charge exchange with support and adsorbates.

I will review recent works showing how such complex behaviors can be, in the case of Pt on γ -alumina and carbon supports, theoretically understood by separately studying the effects of their size, shape, support and adsorbates.

9:00am **IS+AS+SS-MoM3 Communicating Nanostructures: Spillover Processes Studied on Ceria-supported Platinum Nanoparticles.** *M. Happel*, Friedrich-Alexander-Univ., Germany, *Y. Lykhach*, *T. Staudt*, Friedrich-Alexander-Univ., Germany, *N. Tsud*, Charles Univ., Czech Republic, *T. Skála*, *K.C. Prince*, Sincrotrone Trieste, Italy, *V. Matolin*, Charles Univ., Czech Republic, *A. Migani*, Univ. de Barcelona, Spain, *G.P. Petrova*, Univ. of Sofia, Bulgaria, *A. Bruix*, *F. Illas*, *K.M. Neyman*, Univ. de Barcelona, Spain, *G.N. Vayssilov*, Univ. of Sofia, Bulgaria, *J. Libuda*, Friedrich-Alexander-Univ. Erlangen-Nuremberg, Germany

Ceria-based catalysts are technologically important for various applications, including automotive catalysis, SO_x scrubbers, and hydrocarbon transformation reactions. The complex surface chemistry and reaction kinetics in these systems are assumed to be strongly influenced by so-called metal-oxide (MO) interactions. We use a surface science-based model approach to obtain detailed insight into the origins of such effects at the microscopic level.

The model catalysts are based on ordered $\text{CeO}_2(111)$ films on $\text{Cu}(111)$, on which noble metal nanoparticles (e.g. Pt) are grown by PVD under UHV

conditions. The growth and geometric structure of the model catalysts are characterized by STM. Adsorption and reaction are followed by XPS, synchrotron radiation photoelectron spectroscopy (SR-PES), IRAS, and molecular beam (MB) methods, in combination with DFT calculations. Resonant PES (RPES) is used to monitor the changes in the cerium oxidation state with high sensitivity.

Two types of MO interaction are identified, electron transfer from the Pt nanoparticle to the support, and oxygen transfer (spillover) from ceria to Pt. Whereas electron transfer occurs on ceria supports irrespective of their morphology, oxygen transfer shows a pronounced structure dependency, i.e. it requires the presence of nanostructured ceria aggregates in close contact with Pt.[1]

Not only oxygen spillover, which is a key step in oxidative-self cleaning of carbon-poisoned catalysts, but also spillover and reverse-spillover of hydrogen and hydrocarbon fragments can be followed in detail by RPES. A particularly complex behavior is expected for SO_x , for which strong MO effects and spillover have been suggested in previous studies on powder catalysts. On the Pt-free model support we identify different sulfur species forming upon SO_2 exposure even at 150 K (sulfites, atomic sulfur, and potentially sulfates), formed via different adsorption, decomposition and disproportionation pathways. At higher temperature, these species transform into a bulk-like cerium oxysulfide. For interpretation of the sulfur-chemistry on Pt/ CeO_2 , reference experiments on Pt(111) were performed and numerous SO_x species were identified by IRAS and SR-PES. RPES for SO_2 adsorption on Pt/ CeO_2 provides direct evidence for spillover of SO_x to the Pt nanoparticles above 300 K. Between 300 K and 600 K Pt acts as a "sulfur-collector", before at even higher temperatures sulfur is finally transformed into a cerium oxysulfide species.

[1] G. Vayssilov, Y. Lykhach, A. Migani, T. Staudt, G.P. Petrova, N. Tsud, T. Skála, A. Bruix, F. Illas, K.C. Prince, V. Matolin, K.M. Neyman, J. Libuda, *Nat. Mater.* **2011**, *10*, 310.

9:20am **IS+AS+SS-MoM4 HPXPS Study of the Oxidation of 10 nm PdAg Nanoparticles.** *S. Blomberg*, *J. Gustafson*, *N.M. Martin*, *M.E. Messing*, *K. Deppert*, *J.N. Andersen*, Lund University, Sweden, *L.E. Walle*, *A. Borg*, Norwegian University of Science and Technology, Norway, *H. Grönbeck*, Chalmers University of Technology, Sweden, *M.E. Grass*, *Z. Liu*, Lawrence Berkeley National Laboratory, *E. Lundgren*, Lund University, Sweden

Due to the economic and environmental rewards, one goal in catalysis related research is to create cheaper catalysts. One way to realize this is to dilute the more expensive active catalyst material with a less costly one. This requires that the active material stays at the surface. This could be achieved by using a material which is less prone to interact with the reactant gases, such as a noble metal. In most catalysts, the active material is dispersed in a high area complex oxide support as nanoparticles. In order to maintain the high activity, it would be necessary to ensure that the active material is at the surface of the nanoparticle.

In the present contribution we report on our initial findings from attempts to produce PdAg alloy particles using an aerosol deposition technique [1]. The particles have a diameter of 10 nm distributed over a SiO_x wafer. The samples were characterized by high pressure XPS, SEM and TEM as was done previously for aerosol Pd particles [2,3]. By comparing to XPS data from a single crystal $\text{Pd}_{75}\text{Ag}_{25}(100)$ and from the X-ray Energy Dispersive Spectroscopy (XEDS) analysis we show that the PdAg particles have a similar alloy composition.

The *in-situ* high pressure XPS data from the 10 nm PdAg particles demonstrates that the Pd segregates to the surface in an oxygen rich environment and that the core of the particles are rich in Ag. Although a thin PdOx shell is formed, bulk oxidation is inhibited. The limited oxide formation is promising for the full oxidation of methane, since recent investigations [4] suggest that the PdO is less active for methane oxidation than the metallic Pd.

[1] M. E. Messing, K. A. Dick, L. R. Wallenberg, K. Deppert, *Gold Bull.* **42** (2009) 20.

[2] M. E. Messing *et al*, *J. Phys. Chem. C.* **114** (2010) 9257.

[3] R. Westerström *et al*, *Phys. Rev. B.* **83**, (2011) 115440.

[4] A. Hellman *et al.*, submitted.

9:40am **IS+AS+SS-MoM5 New Assignment for Ag(III) from In Situ XPS of Highly Oxidized Silver Films.** *T.C. Kaspar*, *T. Droubay*, *S.A. Chambers*, Pacific Northwest National Laboratory, *P.S. Bagus*, University of North Texas

For decades, it has been a goal to elucidate the mechanisms behind the unique chemistry of both oxygen-exposed silver metal and silver oxides. Silver compounds in bulk, thin film, and nanoparticle form are widely investigated for applications including industrially-relevant catalysis,

electrochemistry, transparent conducting oxides, and antimicrobial coatings. Determining the chemical state of both silver and oxygen is critical to developing a mechanistic understanding of the remarkable properties of these materials. *Ex situ* x-ray photoelectron spectroscopy (XPS) has been applied, starting in the 1970's, to determine the chemical state of Ag in various silver metal and silver oxide compounds. In contrast to most elements, Ag^{x+} (x>0) cations exhibit a negative binding energy (BE) shift relative to metallic Ag(0); thus, the lowest XPS core level binding energy observed for the Ag 3d peak, 367.3 eV, has been assigned to Ag(III) in AgO [Ag(I)Ag(III)O₂]. However, the XPS analysis has been hindered by the ease with which silver oxides form carbonate species upon atmospheric exposure, as well as the instability of silver oxides in vacuum. In this work, silver oxide films have been formed under very oxidizing conditions, by molecular beam epitaxy (MBE) deposition of silver metal in the presence of activated oxygen. *In situ* XPS was then collected in an appended chamber. For the most highly oxidizing deposition conditions, a substantially lower BE, 366.8 eV, was found for the Ag 3d peak, with an associated satellite located at 368.2 eV. This oxide species proved unstable in vacuum over several days, but could be recovered by further exposure to activated oxygen. Based on the decomposition behavior of the Ag 3d and O 1s spectra, the low BE species was assigned as Ag(III), while the previous peak position for Ag(III) was re-assigned as Ag(I). These assignments are supported in part by electronic structure calculations predicting the photoemission spectra of Ag(III). The combination of highly oxidizing deposition conditions and *in situ* characterization allowed identification of the true Ag(III) XPS spectrum for the first time. [1]

[1] T.C. Kaspar, T. Droubay, S.A. Chambers, and P.S. Bagus. *J. Phys. Chem. C* **114** 21562 (2010).

10:00am **IS+AS+SS-MoM6 The Oxidation of Methane Over Pd**, A. Hellman, Chalmers Univ. of Tech., Sweden, A. Resta, European Synch. Rad. Fac., France, J. Gustafson, N.M. Martin, Lund Univ., Sweden, A. Trincherio, P.-A. Carlsson, Chalmers Univ. of Tech., Sweden, O. Balmes, European Synch. Rad. Fac., France, J.N. Andersen, Lund Univ., Sweden, R. Feici, European Synch. Rad. Fac., France, E. Lundgren, Lund Univ., Sweden, H. Grönbeck, Chalmers Univ. of Tech., Sweden

An important goal in surface science is to provide fundamental information on gas-surface interactions for the design of cheaper and more efficient catalysts. For this purpose, the required minimum knowledge is the composition of a catalyst for a certain reaction under realistic reaction conditions. Although this information seems trivial it is surprisingly difficult to obtain due to the complex structural nature of a real catalyst and the sometimes high temperatures and pressures under reaction conditions.

In the case of the complete oxidation of methane using Pd as the catalyst, pure Pd metal, Pd surface oxides and bulk PdO have all been reported to be most efficient to convert CH₄ into CO₂ and H₂O [1-5]. This highlights the complexity of catalysis even for a relatively simple catalytic reaction.

In order to shed some light on the state of Pd during complete methane oxidation, we have performed in-situ Surface X-Ray Diffraction (SXRD) over a Pd(100) surface in a realistic reaction environment combined with DFT calculations. Our study demonstrates that significant roughening of the surface occur during the reaction, which increases the active surface area and thus affects the overall reactivity. Nevertheless, our study strongly suggests that the Pd metal is the most active phase for the full oxidation of methane.

[1] R. Burch, P. K. Loader, and F. J. Urbano, *Catalysis Today* **27** (1996) 243.

[2] R. F. Hicks, H. H. Qi, M. L. Young, and R. G. Lee, *J. Catal.* **122** (1990) 280.

[3] M. Lyubovsky and L. Pfefferle, *Catalysis Today* **47** (1999) 29.

[4] S. Oh, P. J. Mitchell, and R. Siewert, *J. Catal.* **123** (1991) 287.

[5] J. G. McCarthy, *Catalysis Today* **26** (1995) 283.

11:00am **IS+AS+SS-MoM9 The New Ambient Pressure X-ray Photoelectron Spectroscopy Instrument at MAX-lab - An Instrument also for Ultrahigh Vacuum Studies**, J. Schnadt, J. Knudsen, A. Pietzsch, N. Johansson, A. Olsson, F. Hennies, Lund University, Sweden, N. Mårtensson, H. Siegbahn, Uppsala University, Sweden, J.N. Andersen, Lund University, Sweden

Ambient pressure x-ray photoelectron spectroscopy (APXPS) is a technique, which dates back to the 1970s and 1980s, but which only during the past ten years has developed a very significant impact, driven forward especially by groups at the Advanced Light Source and BESSY. APXPS makes possible x-ray photoelectron spectroscopy (XPS) measurements

under realistic or close-to realistic conditions, while conventional XPS is limited to vacuum conditions of 10⁻⁶ mbar or better. APXPS thus contributes to closing the "pressure gap" of surface science, which has inhibited the understanding of processes and chemical reactions, for which the chemical potential of the gas atmosphere plays a decisive role. It also renders possible experiments on samples with a large vapour pressure, such as liquids or solid samples with a high degassing rate. Today, there exist a number of APXPS instruments around the world, including a small number of systems at synchrotrons. Common to these instruments is that they perform well at elevated pressures, but none of them is specifically designed to also allow studies under ultrahigh vacuum conditions. This complicates the connection to results from ultrahigh vacuum studies.

A new instrument for APXPS has just been installed at beamline I511 of the Swedish Synchrotron Radiation Facility MAX-lab. This instrument, which has been delivered by SPECS GmbH, Berlin, Germany, and which makes use of a PHOIBOS 150 NAP analyser, has been developed with the particular aim of building a strong link between ultrahigh vacuum and ambient pressure experiments and science. The instrument is capable of performing XPS measurements on the same sample in both types of environment. This is made possible by a unique design, which is based on the use of a retractable ambient pressure cell. For ambient pressure measurements at pressures of around 0.1 to 10 mbar the cell is docked to the electron energy analyser. Once the sample is loaded the cell is locked, and the only leak to the vacuum is through the nozzle of the analyser's lens system. Hence, even during ambient pressure measurements the vacuum remains intact in the analysis chamber. For UHV measurements the cell together with the nozzle is retracted into a separate chamber, and UHV XPS measurements can be performed normally. This entails also another attractive feature of the instrument, namely, that the high pressure cell easily can be replaced by dedicated cells for other sample environments.

In this contribution the design and concept of the APXPS instrument at MAX-lab will be discussed and first results shown. Also plans for an upgraded and dedicated new beamline at MAX-lab will be presented.

11:20am **IS+AS+SS-MoM10 In Situ XPS and STM Studies of Ge₂H₆ Interactions with the Si(100) Surface**, S. McDonnell, J.F. Veyan, University of Texas at Dallas, J. Ballard, J.H.G. Owen, J.N. Randall, Zyvy Labs, Y.J. Chabal, R.M. Wallace, University of Texas at Dallas

We present a study of the reactions between Ge₂H₆ and Si(100) surfaces. Ge₂H₆ is a potential precursor that could allow atomic layer epitaxy (ALE) on Ge(100) and Si(100) surface [1,2] which will be a vital component for atomically precise manufacturing (APM). We investigate the effects of various growth conditions such as substrate temperature, dosing pressure and post deposition annealing. We study the formation of seed layers for ALE along with the reactions on both the atomically clean and the hydrogen passivated surfaces, where we see evidence of Ge₂H₆ reacting with the dangling bonds.

To facilitate these studies, we utilize a UHV deposition/characterization tool. Chemical analysis of the surfaces is achieved using *in-situ* x-ray and ultraviolet photoelectron spectroscopy. Differences in the chemical states of germanium present on the surface under the various growth conditions are identified. This analysis is supplemented by *in-situ* scanning tunneling microscopy, which allows us to monitor the growth of germanium on silicon and confirm 2D or 3D growth. Comparisons are made with similar experiments carried out in a different UHV chamber where the surface is characterized with Fourier transform infrared spectroscopy (FTIR) and shows evidence of the digermane reacting with the surface at 173K as Ge₂H₅ rather than GeH₃.

This material is based upon work supported by the Defense Advanced Research Project Agency (DARPA) and Space and Naval Warfare Center, San Diego (SPAWARSYSCEN-SD) under contract N66001-08-C-2040. It is also supported by a grant from the Emerging Technology Fund of the State of Texas to the Atomically Precise Manufacturing Consortium.

[1] D.-S. Lin, K.-H. Huang, T.-W. Pi, and R.-T. Wu. *Phys. Rev. B*, **54** 16 (1996) 958

[2] K.-H. Huang, T.-S. Ku, and D.-S. Lin *Phys. Rev. B*, **56** 8 (1997) 4878

Marine Biofouling Focus Topic

Room: 105 - Session MB-MoM

Interfacial Aspects of Marine Biofouling

Moderator: D. Barlow, Naval Research Laboratory

8:20am **MB-MoM1 Fouling in the Face of a "Little" Surface Roughness**, R. Lamb, A. Wu, K. Cho, H. Zhang, The University of Melbourne, Australia **INVITED**

Nano-engineered superhydrophobic surfaces have been investigated for potential fouling resistance properties. Integrating hydrophobic materials with nanoscale roughness generates surfaces with superhydrophobicity that have water contact angles (θ) in excess of 160° and low hysteresis ($< 10^\circ$).

Small angle x-ray scattering (SAXS) was used to investigate the presence of air incursions at immersed superhydrophobic interfaces with varying nano/microscale architecture. This technique, sensitive to local changes in electron density, looks at the nanoscale wetting of the rough interface.

Three superhydrophobic coatings differing in their chemical compositions and architecture were analyzed using SAXS and tested against major fouling species (*Amphora sp.*, *Ulva rigida*, *Polysiphonia sphaerocarpa*, *Bugula neritina*, *Amphibalanus amphitrite*) in settlement assays.

Varying extents of attachment-inhibiting properties were observed across the tested coatings and appeared to correlate with the resistance to nanowetting rather than macroscopic contact angle measurements.

9:00am **MB-MoM3 Chemistry Depending Surface Conditioning and its Implication for Colonization by Microorganisms**, I. Thomé, Karlsruhe Inst. of Tech. (KIT), Germany, M.E. Pettitt, University of Birmingham, UK, S. Kirchen, T. Schwarz, S. Heissler, Karlsruhe Inst. of Tech. (KIT), Germany, M.E. Callow, J.A. Callow, Univ. of Birmingham, UK, G. Swain, Florida Inst. of Tech., M. Grunze, A. Rosenhahn, Karlsruhe Inst. of Tech. (KIT), Univ. of Heidelberg, Germany

Biofouling is a ubiquitously occurring phenomenon in tidal zones worldwide [1]. To prevent unwanted effects caused by biofouling, suitable non-toxic coatings for these environments are required. Changing the surface chemistry and the composition of a coating changes not only its properties but also the formation and composition of a conditioning layer. We use self-assembled monolayers (SAMs) on gold as highly controlled surface chemistries which allow to fine tune the physicochemical surface properties. In order to correlate colonization with surface conditioning, we varied the surface chemistry and thus their wetting properties. In agreement with previous work, chemical termination of the surface affects not only the settlement kinetics of spores of the macrofouler *Ulva linza* [2] but also the settlement of other species. As different SAMs have different affinity towards macromolecules, settlement is controlled by both, surface chemistry itself and an adsorbed conditioning layer. To disentangle both effects, formation of conditioning layers depending on the surface chemistry was investigated in greater detail by spectral ellipsometry and IRRAS. Organism settlement is significantly changed if pristine chemistries are compared to conditioned surfaces.

[1] M.E. Callow, J.A. Callow, J.D. Pickett-Heaps, R. Wetherbee, "Primary Adhesion of Enteromorpha (Chlorophyta, Ulvales) Propagules: Quantitative Settlement Studies and Video Microscopy", *J. Phycol.*, **1997**, *33*, 938.

[2] M. E. Callow, J. A. Callow, L. K. Ista, S. E. Coleman, A. C. Nolasco, G. P. López, "Use of self-assembled monolayers of different wettabilities to study surface selection and primary adhesion processes of green algal (*Enteromorpha*) zoospores", *Appl. Environ. Microbiol.*, **2000**, *66*, (8), 3249-3254.

9:40am **MB-MoM5 Probing Molecular Details of Marine Bioadhesion with In Situ Infrared Spectroscopy**, A.J. McQuillan, University of Otago, Dunedin, New Zealand **INVITED**

The critical step which triggers biofouling at interfaces is the initial adhesion of an invading species to a solid substrate. Of less importance in what occurs thereafter is growth of the species under the influence of nutrients and with the protection of its more sheltered environment. Understanding the factors determining the propensity of species to adhere to substrates is the key to developing new strategies aiming to more effectively inhibit the development of biofouling in many contexts.

Much of the thinking about biofilm formation and the adhesion of biological species to surfaces has been extrapolated from macroscopic observations about the aggregation of colloids. This has been largely based on the interplay between attractive dispersion forces and repulsive electrostatic forces and has given rise to adhesion descriptions in terms of reversible and irreversible stages. A major advance has been the use of in situ atomic force microscopy (AFM) to measure forces during adhesion of

microbes to substrates and evaluate their environmental influences. Nevertheless, this approach is unable to provide in situ molecular details of the chemical components which are suspected to play major roles in adhesion processes.

Vibrational spectroscopy is powerful to reveal the identity and environmental details of molecules in wet interface environments. Vibrational sum frequency spectroscopy and infrared spectroscopy are increasingly thus employed. However, attenuated total reflection infrared (ATR-IR) spectroscopy has the advantages of relative simplicity and greater general familiarity in spite of its use for wet surface situations having only recently been recognised. The ATR-IR approach employs total internal reflection at a high index refraction crystal such as ZnSe or diamond resulting in an evanescent wave sampling a few micrometers of material.

In this talk I will outline the principles of the ATR-IR method and how we have adapted them for studies of initial settling of live marine organisms settling onto surfaces under controlled temperature and environment conditions. Observations from recently published work on the settling of *Perna canalicula* mussel larvae and *Undaria pinnatifida* kelp spores will be presented and prospects for breakthrough studies of the settling and propagation of the freshwater diatom *Didymosphenia geminata*, invasive to New Zealand, will also be discussed.

10:40am **MB-MoM8 Relationships between Cement Production Cycles and Adhesive Strength of the Barnacle *Balanus Amphitrite***, D.K. Burden, D.E. Barlow, U.S. Naval Research Laboratory, B. Orihuela, D. Rittschof, Duke University Marine Laboratory, K.J. Wahl, U.S. Naval Research Laboratory

Marine organisms attach themselves to a wide variety of submerged surfaces. The barnacle is one of the most pervasive and persistent species to do so, securing itself by forming a thin film of permanent proteinaceous adhesive. For hard-shelled acorn barnacles like *Balanus amphitrite*, this process involves the recurring sequential release of two major secretions at the adhesive interface. We show that as the barnacle grows laterally, one of these cement precursor solutions, CPS1, is released on a fairly continuous basis, while the other, CPS2, is released cyclically. By utilizing the differences in secretion patterns, we have begun to deconvolve the contributions of these cement precursors to adhesion. Barnacles were resettled on CaF_2 substrates and release of the components at the interfaces was distinguished by optical and fluorescence microscopy. Shear detachment measurements of resettled barnacles showed that the release of CPS2 into the interface corresponded with a roughly twofold increase in adhesion versus CPS1 alone. AFM and FTIR also showed distinct differences in morphology, protein conformation, and chemical functionality for the CPS mixture versus CPS1. Possible ways in which the two components contribute to barnacle adhesion will be discussed based on these results.

11:00am **MB-MoM9 Micro to Nanostructured Stimuli-Responsive Surfaces for Study and Control of Bioadhesion**, G.P. Lopez, Duke University

This contribution will present recent results on the development and study of bioadhesion on stimuli responsive surfaces that are patterned on lateral length scales of the order of 10 microns and below. These length scales are commensurate with the sizes of the smallest creatures known to be problematic in marine biofouling. Model stimuli responsive surfaces include patterned polymer brushes and model marine organisms include marine bacteria grown in culture. Our previous studies have demonstrated that stimuli responsive materials can be used to control the adhesion of model marine organisms and this presentation will provide our latest advancements in this line of study, as regards to both molecular and cellular biointerfacial phenomena. Methods for preparing nanopatterns of stimuli responsive polymer brushes over areal scales necessary for biofouling studies will be presented, along with characterization of their structure and dynamic behavior.

11:20am **MB-MoM10 Surface Topographic Features to Control Biofouling**, L. Xiao, University of Heidelberg, Germany, M. Röhrig, Karlsruhe Institute of Technology, Germany, S.E. Thompson, M.E. Callow, J.A. Callow, University of Birmingham, UK, A. Rosenhahn, M. Grunze, University of Heidelberg, Germany

Marine biofouling is the undesirable accumulation of microorganisms, plants and animals on artificial surfaces immersed in the sea [1]. The increased hydrodynamic drag caused by fouling leads to higher operating costs of vessels. Studying the interaction between marine organisms and surfaces enhances the development of environmentally compatible approaches to control fouling [2]. Surface microtopography has been found to influence the settlement of cells and larvae [3]. We have studied the influence of surface topographic features on the biofouling process. Honeycomb gradient structures, inspired by the pattern found on the skin of

the pilot whale [4], were obtained by a hot embossing process, and the effect on the density of spores of the green alga *Ulva* that attached in laboratory assays was quantified. Spore settlement density was higher on the microstructured gradients than the smooth background. The highest density of spores was found when the size of the microstructures was similar to or larger than the size of a spore. With decreasing size of the honeycombs, spore settlement decreased to a level similar to that on the smooth background. In line with the results from the Brennan group [5], spore settlement correlated with Wenzel roughness.

[1] D. M. Yebra, S. Kiil, K. Dam-Johansen, "Antifouling technology – past, present and future steps towards efficient and environmentally friendly antifouling coatings", *Progress in Organic Coatings*, **2004**, *50*, 75-104.

[2] M. E. Callow, J. A. Callow, "Marine biofouling: a sticky problem", *Biologist*, **2002**, *49*, (1), 1-5.

[3] A. J. Scardino, R. de Nys, "Mini review: Biomimetic models and bioinspired surfaces for fouling control", *Biofouling*, **2011**, *27*, (1), 73-86.

[4] X. Cao, M. E. Pettitt, F. Wode, M. P. Arpa Sancet, J. Fu, J. Ji, M. E. Callow, J. A. Callow, A. Rosenhahn, M. Grunze, "Interaction of zoospores of the green alga *Ulva* with bioinspired micro- and nanostructured surfaces prepared by polyelectrolyte layer-by-layer self-assembly", *Adv. Funct. Mater.*, **2010**, *20*, 1984-1993.

[5] M. L. Carman, T. G. Estes, A. W. Feinberg, J. F. Schumacher, W. Wilkerson, L. H. Wilson, M. E. Callow, J. A. Callow, A. B. Brennan, "Engineered antifouling microtopographies – correlating wettability with cell attachment", *Biofouling*, **2006**, *22*, (1-2), 11-21.

11:40am **MB-MoM11 Biofouling: It's a Rough Business**, *A. Wu, R. Lamb, A. McDonald*, The University of Melbourne, Australia

The effect of minute changes in nanoengineered superhydrophobic surfaces on the attachment behaviour of several fouling species (*Amphora sp.*, *Ulva rigida*, *Bugula neritina*) was investigated.

Superhydrophobic surfaces were fabricated from latex-templated silica sol-gels¹. Nanoscale features of the surfaces were varied using two building blocks; silica nanoparticles ranging from 7 – 40 nm and PMMA templating latex ranging from 400 – 800 nm. The combination of these building blocks affords various roughness changes at the nanoscale. In maintaining surface chemistry identical, all fabricated surfaces exhibited superhydrophobic characteristics.

Attachment assays of each surface were conducted and a large variation in attachment-inhibition behaviour was observed. Correlating this behaviour against measured AFM roughness suggests that an intricate relationship exists between surface roughness and attachment behaviour. Data indicate that surface fabricated using small nanoparticles (7 nm) coupled with large templating latexes and high RMS roughness (> 130 nm) exhibited significant attachment inhibiting behaviour. This set of criteria also conforms to the definition of a fractal surface, where self-similarity is present different length scales.

Coupled with previous work² that linked pseudo-fractal dimension with nanowetting, this work strongly suggests that resistance to nanowetting has a key influence on attachment of marine organisms.

1 Cho, K. L., Wu, A. H. F., Lamb, R. N. & Liaw, I. I. *The Journal of Physical Chemistry C* **114**, 11228-11233, (2010).

2 Zhang, H., Lamb, R. N. & Cookson, D. J. *Applied Physics Letters* **91**, 254106, (2007).

Nanomanufacturing Science and Technology Focus

Topic

Room: 207 - Session NM+MS+NS+TF-MoM

ALD for Nanomanufacturing

Moderator: B. Lu, AIXTRON Inc.

9:00am **NM+MS+NS+TF-MoM3 Industrialization of Atomic Layer Deposition: From Design to Deposition**, *J.S. Becker, A. Bertuch, R. Bhatia, L. Lecordier, G. Liu, M. Sershen, M. Sowa, R. Coutu, G.M. Sundaram*, Cambridge NanoTech, Inc.

INVITED

The demonstrated benefits provided by Atomic Layer Deposition (ALD) in producing films of exceptional uniformity, and conformality, has set the stage for its use in large area, batch processing, and Roll-to-Roll applications. In this work we discuss the use of Computational Fluid Dynamics (CFD) as a means of gaining insight into the system performance of such industrial instruments, but also as a technique for refining system design. Additionally we describe the basic underpinnings of design for ALD systems operated under atmospheric conditions, (for Roll-to-Roll use),

along with the design factors which must be considered for zone separated ALD methods. Finally we will present film results taken from a zone-separated ALD system, and discuss the salient aspects of the deposition process.

9:40am **NM+MS+NS+TF-MoM5 Improved MOS Characteristics of CeO₂/La₂O₃ and MgO/La₂O₃ Gate Stacks Prepared by ALD**, *T. Suzuki, M. Kouda*, Tokyo Institute of Technology and AIST, Japan, *K. Kakushima, P. Ahmet, H. Iwai*, Tokyo Institute of Technology, Japan, *T. Yasuda*, AIST, Japan

La₂O₃ is one of the candidate materials for the next-generation high-k gate stacks because it can achieve sub-1 nm EOT by forming direct-contact La silicate with Si. There have been many ALD studies for La₂O₃, however, the performance of the MOSFETs incorporating ALD-La₂O₃ needs much improvement. Our previous studies using EB evaporation showed that capping the La₂O₃ dielectrics with an ultrathin layer of CeO₂ or metallic Mg (~1 nm) effectively improved the channel mobility [1,2]. In this paper, we report fabrication of CeO₂/La₂O₃ and MgO/La₂O₃ gate stacks by ALD/CVD for the first time, and demonstrate that these stacks show improved electrical properties (k value, channel mobility, etc.) as compared to single-layer ALD-La₂O₃.

The experiments were carried out using a multi-chamber ALD/CVD system which was capable of in-situ metallization and RTA. The CeO₂/La₂O₃ and MgO/La₂O₃ gate stacks were formed on H-terminated Si(100) using Ce[OC(Et)₂Me]₄, La(PrCp)₃, and Mg(EtCp)₂ metal sources. La₂O₃ and MgO films were formed by ALD using H₂O as an oxidant. The ALD temperature was set at a relatively low temperature of 175°C in order to ensure the self-limiting growth [3]. CeO₂ films were formed in the CVD mode via thermal decomposition of Ce[OC(Et)₂Me]₄ at 350°C. The gate electrodes were formed by sputtering of W. MOSFETs were fabricated by the gate-last process.

The effective k values for the CeO₂(1nm)/La₂O₃(3nm) and MgO(0.8nm)/La₂O₃(4nm) stack capacitors were approximately 16, which was significantly larger than those for La silicate without any capping layer (k=10~12). The k-value improvement by the CeO₂ capping is presumably due to the higher k value of CeO₂ (~23), whereas the improvement by the MgO capping is ascribed to suppression of excessive La-silicate formation.

We have also found that the CeO₂/La₂O₃ gate stack leads to excellent mobility characteristics. The mobility for the MOSFET with 1.43 nm EOT was 214 cm²/Vs at an effective field of 1.0 MV/cm, which was 85% of the Si universal mobility. The mobility improvement by the CeO₂ capping is attributed to the reduced fixed-charge density, since V_{th} approached to the ideal values by the CeO₂ capping. On the other hand, the MgO capping induced a negative shift in V_{th} and consistently degraded the mobility. These effects of ALD-MgO capping are qualitatively different from those observed for EB-evaporated Mg [2]. The mechanisms causing such a difference between EB evaporation and ALD are now under investigation.

This work was carried out in Leading Research Project for Development of Innovative Energy Conservation Technologies supported by NEDO.

References: [1] T. Koyanagi, et al., *JJAP*, **48**, 05DC02 (2009); [2] M. Kouda, et al., 2009 VLSI Symp., p. 200; [3] K. Ozawa, et al., 2010 ICSICT, p. 932.

10:00am **NM+MS+NS+TF-MoM6 Highly Uniform and Conformal Thin Film Metallization with Thermal and Plasma-Enhanced Atomic Layer Deposition**, *M. Toivola, J. Kostamo, T. Malinen, T. Pilvi, T. Lehto, C. Dezelah*, Picosun Oy, Finland

Ultra-thin, nanometer-scale metal or metallic films are a crucial component in e.g. several applications of modern MEMS/NEMS (Micro/NanoElectroMechanical Systems) and other advanced IC technologies, sensors, optical devices and catalyst manufacturing. When the component sizes keep diminishing and at the same time, the level of system integration increasing (for example the so-called "System-in-a-Package" multifunctional chip devices), it creates a drive from "conventional" 2D device architecture to 3D component integration. Through Silicon Vias (TSV) are a central structure in these 3D-stacked devices and there's often a need to produce highly uniform and conformal thin films of metals or otherwise conducting materials on the insides of the vias. Due to the often very high aspect ratio (AR) of the TSV structures, Atomic Layer Deposition (ALD) is one of the only methods with which reliably uniform and conformal material layers can be deposited on the via walls.

Industrially upscalable ALD processes were developed for several metals and metallic compounds, i.e. Pt, Ir, Ru, Cu, Ag, Au, TiN and TiAlCN. Deposition of metals can be done with thermal ALD and plasma-enhanced (PEALD). The main benefits of the PEALD technique are the possibility to use reductive processes instead of oxygen, lower deposition temperatures which decreases the thermal stress on the substrates, and a wider variety of precursor chemicals.

Inductively coupled remote plasma source system was further developed to reduce any possibility of plasma damage, which can often happen in the more conventionally designed, direct plasma devices. Instead of direct ion bombardment, our plasma system utilizes highly reactive radicals. Protective flows and separating metal precursor inlets shield the plasma source from getting short-circuited by films from precursor back-diffusion. E.g. N_2/H_2 , H_2/Ar , O_2 and mixed gas plasmas can be generated with the system.

Structural design solutions were optimized for ALD reactors. Top flow delivery of the precursor gases ensures even distribution of reactive molecules inside the reactor vessel. This is beneficial especially in the case of non-optimal processes with precursor decomposition or etching or poisoning of reactive sites by reaction by-products. Less impurity and thickness gradient can be achieved with the top flow, compared to the side-flow (cross-flow) design since all the area reacts at the same time leaving less reactive sites left for reaction with the by-products. Therefore, it is possible to get more challenging reaction chemistries working with the top-flow design, and also a forced flow for through-porous samples is possible. With modified stopped flow design, extended reaction time inside the chamber can be reached while still keeping the protective flows from the inlets on to prevent any back-diffusion of precursor and subsequent particle formation in the inlet lines.

Upscalable structure was specifically designed to bridge the gap between R&D and production. Smaller ALD tools can be used for process and chemical precursor development at for universities and research labs, whereas the larger, ALD tools can be fully automatized, upscaled and clustered into full scale high volume throughput industrial production unit capable of coating even several thousands of wafers per hour.

10:40am **NM+MS+NS+TF-MoM8 Atomic Layer Deposition for Continuous Roll-to-Roll Processing**, *S.M. George, P.R. P. Ryan Fitzpatrick*, University of Colorado at Boulder **INVITED**

Atomic layer deposition (ALD) is currently being developed for continuous roll-to-roll processing. This development is significant because roll-to-roll processing would allow ALD to address many applications in a cost effective manner. This talk overviews the approaches and progress to date. The original idea of ALD with moving substrates and constant precursor flows was presented in a patent by Suntola and Antson in 1977. This scheme involved rotating the substrate between alternating precursor sources and vacuum pumping regions. One current approach under development is based on moving the substrate close to a gas source head. The ALD precursors continuously flow through slits in the gas source head that are separated and isolated by inert gas purging. A second version of this design involves using a gas bearing to set the gap spacing between the gas source head and substrate. Another ongoing approach is based on moving the substrate through separate regions of precursor pressure and inert gas purging. Limited conductance between the regions prevents the gas phase reaction of the ALD precursors. The talk examines the issues and prospects for achieving ALD for continuous roll-to-roll processing. Additional details are presented for the dependence of precursor isolation on reactor parameters for a substrate under a model gas source head.

11:20am **NM+MS+NS+TF-MoM10 High Rate Continuous Roll-to-Roll Atomic Layer Deposition**, *E. Dickey*, Lotus Applied Technology **INVITED**

Atomic Layer Deposition (ALD) is a unique thin film deposition process, capable of producing coatings with unmatched quality and performance. Its unique attributes include high conformality and outstanding thickness precision, enabling the deposition of dense, continuous pinhole-free films, even when extremely thin, and even on highly imperfect substrate surfaces. These qualities have made the process attractive for applications on flexible substrates, including dielectrics and semiconductors for flexible electronics devices, and high performance gas diffusion barriers to encapsulate and protect environmentally sensitive devices such as OLED displays and lighting, and CIGS photovoltaic modules.

Until recently, ALD films have generally been deposited using conventional static processing, in which the individual precursors are sequentially introduced into and purged from a common volume containing the stationary substrate. This sequence, commonly called an ALD cycle, typically requires at least several seconds and results in the growth of approximately 0.1nm thickness. As a result, the time required to deposit films of reasonable thickness can be quite long. Furthermore, the static nature of the process makes roll-to-roll processing impractical. In this presentation, we discuss the development of a new ALD process based on substrate translation, with the ALD cycle elements enabled by transport of the flexible substrate back and forth between the precursor zones. Because no time is required for introducing, saturating, and removing precursors for each cycle, the deposition speed is dramatically increased. In addition, this configuration naturally provides the unique feature of film deposition only

on the substrate itself, as it is the only surface which is exposed to both precursors. In turn, this allows the use of steady-state plasma as the oxygen source, enabling a new technique of precursor isolation; "precursor separation by radical deactivation", in which the oxygen gas precursor actually mixes with the metal precursor, but is only reactive in the region of the plasma source. Together, this technology set has allowed the deposition of high quality ALD films on polymer substrates, including ultra-barrier films, at substrate speeds in excess of one meter per second.

Nanometer-scale Science and Technology Division Room: 203 - Session NS+EM-MoM

Nanowires and Nanoparticles I: Assembly and Devices Moderator: M. Hines, Cornell University

8:20am **NS+EM-MoM1 ZnO Nanowire Logic Inverter with the Difference of Two Gate Electrode**, *J.K. Kim, Y.T. Lee, R. Ha, H.J. Choi, S.I. Im*, Yonsei University, Republic of Korea

Recently, zinc oxide nanowires (ZnO NWs) have attracted much attention for high mobility and sensing properties. These advantageous give us strong possibility to use nanostructures as nanoelectronic device application; such as field effect transistors (FETs), diodes, and logic circuit devices.[1] In this work, we fabricated the logic circuit inverter using difference of gate electrodes which have the different work function.[2]

In order to fabricate the inverter devices, grown ZnO NWs were dispersed to the SiO_2/Si substrate by using a drop-and-dry method. The Ni/Ti source and drain electrodes were deposited by e-beam evaporator with a combination of photo-lithography and lift-off process. To make 30nm-thick Al_2O_3 gate insulator layer, we used Atomic Layer Deposition (ALD) system. And then, Pd and Ni/Ti top gate electrodes were deposited and these two devices were connected by wire bonding technique.

The threshold voltage of the Pd top gate ZnO NWs FET shows more positive value (~ 0 V) than that of the other FET (~ -1 V) with Ni/Ti top gate, and these transistors are able to be used as a driver and a load, respectively. The linear mobility of the driver shows about 119 cm^2/Vs at $V_D = 0.6$ V and the inverter device has high gain value of ~ 15 at $V_{DD} = 5$ V. Furthermore, the dynamic property of the logic inverter was measured under the 5 V square input voltages.

More details will be discussed in the meeting.

References

1. G.J, W. K. Hong, J.S. Maeng, M.H. Choe, W.J. Park, and T. K. Lee, *Appl. Phys. Lett.* **94** 173118 (2009)
2. K.M. Lee, J.H. Kim and S.I. Im, *Appl. Phys. Lett.* **88**, 023504 (2006)

8:40am **NS+EM-MoM2 Control of Growth Kinetics for Three-Dimensional III-nitride Nano-Heterostructures Towards Nanowire Devices**, *S.D. Carnevale, P.J. Phillips, T.F. Kent, J. Yang, M.J. Mills, R.C. Myers*, Ohio State University

The geometry of semiconductor nanowires (NWs) allows for both vertical and coaxial heterostructures, while only vertical heterostructures can be formed using planar structures. This is especially important for III-nitride NWs because crystallographic directions in which heterostructures are formed largely determine the magnitude of internal electric fields due to polarization. Here we describe a method to control the relative vertical and coaxial growth rates in catalyst-free GaN/AlN NW heterostructures grown on Si(111) substrates by plasma-assisted molecular beam epitaxy*.

A growth phase diagram is established relating NW density to substrate temperature and III/V ratio. This diagram reveals a reduction in effective growth rate and an increase in nucleation time caused by GaN decomposition. Using this information, a two-step method is developed to independently control NW density from NW deposition time. To begin we nucleate NWs until a small but appreciable density is reached. If deposition continues under these conditions, density will increase over time until reaching a saturation point. To suppress this increase, substrate temperature is increased upon completion of the initial nucleation time. NWs already nucleated continue to grow, but there is no new nucleation, thus controlling density. Additionally, the change in conditions alters growth kinetics, leading to purely vertical NW growth, which allows for the formation of NWs with arbitrarily large aspect ratios and small diameters (~ 20 nm). Kinetics that favor coaxial growth are also achieved. A low density, high aspect ratio NW array is prepared using the method described above then material is deposited at a lower substrate temperature. The relative coaxial growth rate increases due to lower Ga ad-atom mobility at the lower substrate temperature. Using this dynamic method, we demonstrate multiple

period GaN/AlN (2 nm / 2 nm) superlattices along either the vertical or coaxial NW axis, which exhibit atomically sharp compositional profiles. A coaxial, AlN/GaN resonant tunneling diode structure is presented. Large areas of nanowires are processed for electrical measurements without removing them from the Si(111) substrate. Preliminary electrical measurements are provided for both room temperature and low temperature conditions. This work is supported by the ONR under grant N00014-09-1-1153.

* S.D. Carnevale, J. Yang, P.J. Phillips, M.J. Mills, and R.C. Myers. "Three-Dimensional GaN/AlN Nanowire Heterostructures by Separating Nucleation and Growth Processes". *Nano Letters* 11, 2, pp. 866-871, Jan. 2011.

9:00am **NS+EM-MoM3 III-V Nanowire MOSFETs, L.-E. Wernersson, Lund University, Sweden** **INVITED**

III-V Nanowire transistors are considered possible candidates to extend the transistor scaling roadmap. The improved electrostatic control in the cylindrical geometry provides benefits for scaling and the advantageous transport properties of the III-V materials may be used to increase the drive current. Besides heterostructure design may be used to tailor the properties in the transistor channel.

In this talk, we will review some of the efforts made in Lund to realize high-performance III-V nanowire transistors using vertical nanowires grown by MOVPE. We will show how bottom-up technologies can be combined with top-down processing to realize nanowire-based RF-devices on Si 2" wafers. We use CV techniques to characterize the properties of the high-k material in vertical nanowire capacitors and compare the data to the 1/f-noise characteristics of scaled transistors to evaluate the influence of the high-k material on the transistor performance. We also show that the transistor channel may be reduced down to a diameter of 15 nm without degradation of the transport properties. Finally, we explore the use of novel materials in the transistor structures as we developed GaSb/InAs heterostructures with excellent Esaki diode characteristics to be used for TFET implementations.

9:40am **NS+EM-MoM5 Optimizing Quantum Efficiency in Quantum Dot Display, S.J. Lim, J. Kwon, Y. Oh, Seoul National University, Republic of Korea, B.L. Choi, K. Cho, Samsung Advanced Institute of Technology, Republic of Korea, Y. Kuk, Seoul National University, Republic of Korea**

In our previous study, we were able to fabricate full-color, 4-inch display made of colloidal quantum dot (QD). Despite such a demonstration of QD light emitting device which is one of candidates for next-generation display, understanding the interface characteristics between QD layer and electron (or hole) accumulation layer is still lacking and further study for improvement of quantum efficiency is essential. Here, we report on a study of scanning tunneling microscopy (STM), spectroscopy (STS) and cathode luminescence induced by tunneling current, performed on individually manipulated QD. We control the distance between two QDs using STM to reveal the mechanism of interaction between QDs. STS measurement showed shift of energy levels as manipulating the distance between two QDs. This result suggests that there exists the optimal distance between QDs for efficient light emission. Besides by making contacts between separated QDs and organic molecules, we simulated contacts between QD layer and electron (or hole) accumulation layer. From these experiments, we could understand excitonic behavior and carrier hopping from QD to QD or surrounding materials. Our findings thus suggest optimal configuration for QD application in display.

10:00am **NS+EM-MoM6 Polarization Engineered 1-Dimensional Electron Gas, D.N. Nath, P.S. Park, M. Esposito, Ohio State University, D. Brown, S. Keller, U.K. Mishra, University of California Santa Barbara, S. Rajan, Ohio State University**

One-dimensional electron gas (nanowire) based devices are of great interest due to their promise in high-performance electronics and other future device applications. However, synthesis and patterning of arrays of nanowires is a challenge in all material systems since both bottom-up and top-down approaches have their own merits and demerits.

Here we report on the demonstration of pure 1-dimensional arrays of electrons with current density up to 130 mA/mm and carrier confinement greater than 100 meV using lateral polarization engineering in N-polar vicinal AlGaIn/GaN heterostructures. The width of the atomic terraces characteristic of vicinal surfaces defines the dimensions of the nanowires which are found to exhibit sharp and clear signatures of 1-dimensionality at room temperature making them promising for novel device applications.

We report on devices fabricated on MOCVD grown N-polar AlGaIn/GaN HEMT structures on vicinal sapphire substrate (4° miscut towards a-plane)

with anisotropy in current and channel pinch-off voltages. Channels parallel to the miscut direction pinched off at higher negative gate biases than those perpendicular to the steps and carried more charge as measured by direction-dependent C-V profiling. An electrostatic model which predicts a saw-tooth energy band profile in the lateral direction has been proposed to explain the charge anisotropy. Each atomic terrace characteristic of the surface morphology of vicinal GaN with its corresponding saw-tooth energy profile is proposed to exhibit quasi-1D confinement. We will discuss the heterostructure/polarization design of structures demonstrating pure 1-D transport in direction parallel to steps.

Gated structures were fabricated to investigate the physics of the system as the Fermi occupation function is varied by varying gate bias. To confirm that the carriers are indeed 1-dimensional, we used direction-dependent small-signal capacitance voltage measurements to probe the density of state function and hence dimensionality of electrons as a function of gate bias. We developed a 2-band model consisting of one 1-D and one 2-D subband to describe the behavior of these wires at room temperatures. The variation of capacitance as well as charge density for a pure 1-D and a pure 2-D system as a function of applied gate bias as predicted by our 2-band model based on density of states matches very well with the data measured experimentally for 1-D and 2DEG respectively. This confirms that the channels created are indeed 1-dimensional in nature. Since 1-D channels are atomic terrace defined, they are promising for eliminating the disadvantages of both bottom-up and top-down approaches.

10:40am **NS+EM-MoM8 Adding New Capabilities to Silicon CMOS via Deterministic Nanowire Assembly, T.S. Mayer, M. Li, T. Morrow, J. Kim, B. Won, K. Sun, X. Zhong, K. Liddell, J.S. Mayer, C.D. Keating, Penn State University** **INVITED**

Integrating functionalized nanowires directly onto Si CMOS chips has the potential to combine highly selective and sensitive chemical and/or biological sensing capabilities with electronic signal processing in a single ultra compact, low power platform. Conventional integrated circuit manufacturing methods place considerable limits on the range of and number of different materials and molecules that can be incorporated onto Si chips, making it difficult to realize this goal. This talk provides an overview of a new deterministic assembly approach that uses electric field forces to direct many different types of bioprobe-coated nanowires to specific regions of the chip and to provide accurate registration between each individual nanowire and a specific transistor on the chip. This is achieved by synchronizing sequential injections of nanowires carrying different bioprobe molecules with a programmed spatially-confined electric field profile that directs nanowire assembly. Subsequent back-end lithographic and metal deposition processes are then used to electrically and mechanically connect all of the nanowire devices to the Si chip at the same time. Using this technique, individual nanowire device integration yields exceeding 90% have been demonstrated with a less than 1% mismatch across three populations of DNA-coated nanowires for arrays with densities of 106 cm⁻². The nanowire-bound DNA retained its ability to selectively bind complementary target strands following assembly and device fabrication showing that this process is compatible with these back-end manufacturing steps. The uniformity in the electrical properties of nanowire device arrays that were fabricated using this hybrid integration strategy will also be discussed.

11:20am **NS+EM-MoM10 Solid-State Dewetting of Direct Nanoimprinted Metallic Thin Films, R. Clearfield, North Carolina State University, J.D. Fowlkes, Oak Ridge National Laboratory, P.D. Rack, University of Tennessee Knoxville, N. Samatova, Oak Ridge National Laboratory, A.V. Melechko, North Carolina State University**

Heat applied to thin films below a critical thickness will generally cause transformation of the film into isolated particles. This process is known as dewetting. Solid state dewetting occurs below the melting temperature of the film and is governed by diffusive mass transport. Currently two mechanisms of dewetting are distinguished: hole nucleation and growth, and spinodal dewetting. Spinodal dewetting proceeds via film surface undulations that have characteristic wavelengths related to the thickness of the film. Lithographic patterning of thin films has been utilized to direct the dewetting instability development toward designed nanostructured geometry of nanoparticle arrays. Tailoring the geometry of thin film edge have been shown to affect both heterogeneous nucleation and spinodal dewetting regimes. Nanoimprint lithography, conventionally used for definition of the edges of thin films, is a fabrication method where a stamp is pressed into a thin normally monomer or polymer film at elevated temperatures. Nanoimprinting can also be conducted in direct mode where the stamp is pressed into a metallic film. Surface undulations characteristic for spinodal dewetting will be used to direct the stamp design. Such imprinting allows setting initial conditions, programming instability, in the thin metallic film that is linked to the spinodal surface instability. In this work we are presenting the results of the investigation into behavior of thin

films in which a 3D structure has been imprinted. We present observations on the effect of direct nanoimprint lithography on nanoscale Au and Ni films using periodic arrays of cylinders. Our focus is on the spatial distribution of the particles produced from dewetting of the nanoimprinted films. Particles in patterned regions are characterized in terms of their spacing, periodicity and size, and shape. The geometry of the dewetted patterns is compared to that of the 3D features created after direct nanoimprinting of the films. Analysis of spatial correlation of the final dewetted patterns to stamp patterns is presented.

Plasma Science and Technology Division Room: 201 - Session PS-MoM

Advanced FEOL / Gate Etching I

Moderator: A. Agarwal, Applied Materials, Inc.

8:20am **PS-MoM1 Impact of Synchronized Plasma Pulsing Technologies on Key Parameters Governing STI Etch Processes**, *M. Haass**, *M. Darnon*, *G. Cunge*, *P. Bodart*, *C. Petit-Etienne*, *M. Brihoum*, *L. Vallier*, LTM-CNRS, France, *S. Banna*, Applied Materials, Inc., *O. Joubert*, LTM-CNRS, France

Plasma etch processes are the only technological solution to address the critical dimension control at the nanometer range imposed by the continuous downscaling of CMOS device dimensions in microelectronics. However, the current processes are reaching their limits of controlling etch selectivity, defects, critical dimensions and uniformity. Lately, pulsed plasmas are increasingly used to overcome some of these limitations. On the basis of HBr/O₂ plasmas, dedicated to STI (Shallow Trench Isolation) etching, we discuss the role of the pulse parameters regarding the etched profiles, the reactive etch layer, the uniformity and the passivation layer. To investigate the passivation layer at various trench depths and CDs we developed a new XPS technique for quasi in-situ chemical topography analysis.

The experiments are carried out in a 300 mm AdvantEdge™ tool from Applied Materials Inc. The two generators to sustain the plasma (ICP) and to polarize the wafer (CCP), operated at 13.56 MHz, have been modified with the Pulsync™ system to allow pulsing at a wide range of parameters. However, only synchronous pulsing is studied here. Moreover, a Theta300 angle resolved XPS system from Thermo VG is connected under vacuum, allowing quasi in-situ analysis of an etched sample. Several additional diagnostic methods including time resolved UV-absorption, mass spectroscopy and ellipsometry are used to study the impact of pulsing the plasma on the surface and the gas phase compared to a continuous wave process.

We demonstrate that plasma pulsing can minimize the mask faceting and consumption which is due to a change in the ion energy distribution and the presence of larger molecular ion species. The duty cycle controls the formation of the passivation layer that governs in turn the form of the etched profiles. This correlation can partly be explained by less dissociated oxygen molecules in low duty cycle pulsing. Nevertheless, XPS analyses show that the chemical composition of the passivation layer changes little with height and trench CD while its thickness is directly linked to the aspect ratio of the analyzed part of the sidewall. Less thickness variation with respect to the aspect ratio is observed in pulsed mode, which explains an improved local uniformity in profile evolution. Furthermore, the time compensated etch rate with respect to the actual ON time of the plasma is increasing at low duty cycles due to a change of etch regime from more radical flux limited to ion flux limited. Nevertheless, the overall process etch rate is decreasing in pulsed mode which can be partly counteracted by increasing the source and the bias power.

8:40am **PS-MoM2 Effect of Si Damage on Shallow Source-Drain (SSD) Recess Structures**, *J. Guha*, *S. Sriraman*, Lam Research Corporation

Continued scaling in the semiconductor industry provides new challenges for critical Front-end-of-the-line (FEOL) process etch applications in front-end logic devices. One such application that is utilized in the PMOS transistor is the Strained Source Drain recess (SSD) structure that embeds an epitaxial strained SiGe thin film that significantly improves hole mobility in the channel region. Scale down of critical dimensions (CD) in current and future CMOS devices puts ever increasing emphasis in reducing post-etch Si surface damage in a source-drain (SD) recess structures. For a typical SSD application, the roughness of Si surface obtained after SD etch governs both the epitaxial growth of SiGe as well as the roughness of the SiGe layer, and ultimately determines the device performance. This paper

will discuss the factors that contribute to the Si surface roughness arising from a representative SD process etch step and its impact on the subsequent SiGe epitaxy and device performance. Typically, the SD etch sequence may consist of an anisotropic etch (halogen/oxygen based chemistry) followed by an isotropic etch (halogen/halogen based chemistry). Surface roughness of the etched silicon is quantified and spatially resolved through atomic force microscopy and surface haze measurements, and contributions of the anisotropic and isotropic etch steps to surface roughness are inferred. The effects of halogen ratio and relative halogen atom reactivity in the isotropic etch chemistry on surface roughness and the vertical-to-lateral (V/L) etch ratio in the SSD recess feature will be discussed and a surface reaction model proposed to characterize roughness evolution.

9:00am **PS-MoM3 Improving Etch Processes by using Pulsed Plasmas**, *M. Darnon*, *M. Haass*, *P. Bodart*, *G. Cunge*, *C. Petit-Etienne*, *M. Brihoum*, *R. Blanc*, CNRS-LTM, France, *T. David*, Cea Leti Minattec Campus, France, *E. Pargon*, *L. Vallier*, *O. Joubert*, CNRS-LTM, France, *S. Banna*, *T. Lill*, Applied Materials, Inc. **INVITED**

The etching processes for integrated circuits fabrication becomes extremely challenging when the devices dimensions are downscaling and the etch process has to stop on the ultra thin layers (less than 2nm) of materials. Perfect control of the passivation layers and mask erosion are required to precisely control the patterns profiles, which necessitates using flows and energies of plasma species in ranges which can not be attainable with current plasma technologies. In addition, limiting the plasma induced damage to thin layers requires very low ion energies which are not accessible in current plasma technologies. One promising solution is to pulse the plasma in conventional industrial reactors at very low duty cycle. Using this solution, the ratio of radicals and ions as well as their energy can be fine tuned in ranges that are unreachable otherwise, and very low energy ions are produced which strongly minimizes the damage to the thin layers exposed to the plasma.

Experiments are performed on a 300mm diameter Inductively Coupled Plasma chamber commercialized by Applied Materials (DPSII G5) equipped with the pulsinc system to enable plasma pulsing in an industrial reactor.

In this paper, we will show how plasma pulsing can be used to improve uniformity and pattern profiles by better controlling the passivation layer formed on the patterns sidewalls during the etching. In addition, we will demonstrate that the reduction of the average ion energy as well as the use of molecular ions decreases mask erosion, as well as damage to ultrathin etch stop layers. Morphological characterization, surface characterization and plasma diagnostics will be correlated to explain the mechanisms responsible for the process improvement.

9:40am **PS-MoM5 HfO₂ Etching by Pulsed BCl₃/Ar Plasma**, *P. Bodart*, *C. Petit-Etienne*, *G. Cunge*, *F. Boulard*, *M. Darnon*, *L. Vallier*, *E. Pargon*, CNRS-LTM, France, *S. Banna*, *T. Lill*, Applied Materials, Inc., *O. Joubert*, CNRS-LTM, France

Plasma etching of high-k materials, including HfO₂, has attracted much attention due to the necessity to integrate these materials in MOSFET transistor. After the metal gate patterning process, the high-k dielectric film must be removed from the source and drain regions of the transistor. It is today well established that HfO₂ can be etched selectively towards SiO₂ and Si in BCl₃/Cl₂ plasma. However, it remains difficult to minimize the plasma induced damages (Si amorphisation and recess) in the source/drain transistor regions in such processes. Since pulsed plasmas have shown a capability to minimize Si-recess in typical silicon gate oxide etching processes, we have investigated their potential for HfO₂ etching.

The experiments are performed in a 300mm DPS tool from Applied Materials. The chamber is modified to allow plasma diagnostic like UV-broad band absorption spectroscopy. The reactor is also connected to an Angle-Resolved X Ray Photoelectron Spectroscopy analyzer by a robotized vacuum chamber. The etching rate of HfO₂ sample (either 40 or 3.5nm-thick HfO₂ films with 8 Å SiO₂ interlayer deposited on Si substrates) and of SiO₂ samples (10 nm thick) are measured in real time by in situ multi-wavelength ellipsométrie.

We have evaluated the capability of pulsed plasmas to minimize the plasma induced damage of silicon during the etching of HfO₂ high-k gate dielectric. XPS analyses show that the perturbation of the bulk Si lattice is less pronounced with pulsed conditions, which is attributed to a lower ion bombarding energy. However, the formation of a BCl_x polymer selectively on the silicon (which is responsible for the HfO₂ to Si etching selectivity) is reduced when the plasma is pulsed leading to a loss of selectivity. VUV absorption spectroscopy indicates that the fragmentation of BCl₃ molecules, which leads to the formation of B-rich polymer precursors, decreases dramatically when the plasma is pulsed at low duty cycle. Therefore, as the duty cycle is reduced, the fluxes of B radicals to the wafer are reduced while the amount of Cl in the polymer increases. It follows that the polymer

* Coburn & Winters Student Award Finalist

deposition rate drops, eventually leading to a loss of selectivity at the lowest duty cycles.

However, there are several ways to retrieve the process selectivity in pulsed plasma, such as reducing the BCl_3 flow in the gas mixture or working at higher pulsing frequencies (up to 10 kHz) to enhance B formation in the gas phase. Pulsing the plasma is not a magic knob since it strongly changes the range of allowed new physics and chemistry ranges plasma parameters.

However, plasma pulsing reduces significantly the plasma induced damages after process optimization.

10:00am PS-MoM6 Study of Metallic Interfaces Etching for High-K Metal Gate stacks in CMOS 28 nm Technology. *F. Chave*, STMicroelectronics, France, *L. Vallier*, CNRS-LTM, France, *P. Gouraud*, *C. Vérove*, STMicroelectronics, France, *O. Joubert*, CNRS-LTM, France

In CMOS technology, the downscaling of the transistor gate dimension, driven by ITRS roadmap specifications for advanced technology, requires the introduction of new materials. Dry etching step of those new "High-K Metal Gate" (HKMG) stacks is critical for the electrical performances of the devices and needs very accurate process control to achieve correct profiles, with a good Critical Dimension control. Moreover, characterization tools are now dealing with thin materials thicknesses sometimes around the limit of one full atomic layer. In this work we focus on dry etching process of 28nm technology High-K Metal Gate stacks. Several issues, especially for Metal/Capping layer interfaces, are investigated to better understand and control physicochemical interactions.

Most of etching experiments are carried out in a 300mm DPS AdvantageEdge™ etch chamber from Applied Materials allowing in situ diagnostic, as reflectometry and spectroscopic ellipsometry. This modified tool permits to transfer wafer under vacuum to a customized Theta 300 XPS system from Thermo Fisher Scientific for quasi in-situ analysis without exposure to the environment. Samples were 300mm diameter Si wafer with full sheet and/or patterned deposited layers. Industrial 28nm photolithography & plasma etching process developed to gate first approach were employed.

Preliminary experiments have shown that foot and undercut effects are possible profiles deformations due to metallic interfaces, and we have to control these deviations.

Consequently, we focused first on the TiN/LaO interfaces which we highlight as a critical step. TEM analyses demonstrate that LaO capping layer acts as etch stop layer for current TiN etching chemistries. Therefore, a specific step for LaO removal is needed; otherwise etching residues are left over.

Layer thickness and step time in the specific removal of Lanthanum oxide are some parameters which directly impact the under-layer materials with the observation of pitting on nMOS open areas or residues on pMOS.

XPS characterizations were carried out. Etching results analyses for TiN/LaO/TiN interface reveal the fact that after the whole stack etching step, some LaO residues remain on the sample surface although TiN disappears as evidenced from XPS survey scan. The conclusion is that TiN looks totally removed as Lanthanum can be redeposit or for certain push-forward. Such as mechanisms were considered, and experiments were carried out to understand and complete this result.

Integration of thin metallic and capping layers in gate stacks challenge dry etching process. Those results highlight the trend of interactions all across the plasma etch process.

11:00am PS-MoM9 Double Patterning Challenges for the sub 22nm CMOS Nodes. *S. Kanakasabapathy*, *R. Jung*, *M. Hartig*, *S. Schmitz*, *Y. Yin*, IBM Research, *S. Raghunathan*, *L. Jang*, GlobalFoundries, *E. McLellan*, *S. Burns*, *S. Holmes*, *C.S. Koay*, IBM Research, *R.H. Kim*, GlobalFoundries, *G. Landie*, ST Microelectronics, *D. Horak*, IBM Research, *Y. Mignot*, ST Microelectronics, *S. Seo*, *S.T. Chen*, *J. Arnold*, *M. Colburn*, *B. Haran*, IBM Research

Wavelength and Numerical Aperture scaling in optical lithography have allowed CMOS density scaling to march along the Moore's Law curve for the past three decades. However, at the sub 22nm CMOS nodes, the print pitch faces a technological barrier at the 80nm mark for the Front, Middle and Back Ends of Line. Until further wavelength scaling becomes available through Extreme Ultraviolet (EUV), the industry's attention is focused on Double Patterning. Multiple Interdigitated Lithography and Sidewall Image Transfer (SIT) are the two broad categories of techniques under consideration. Interdigitated Lithography can be subdivided into approaches with and without multiple passes through etch. Both of these techniques present unique etch challenges in assembling looser pitch patterns into a composite mask and subsequent pattern transfer into the stacks of interest. We will review etch perspectives on the applicability of double patterning methods to various levels in the process flow.

In particular, Fins for FinFET technology represent the tightest pitch (approximately 40nm for the technology nodes in development at this time) and yield well to Sidewall Image Transfer. We will present the issues surrounding mandrel definition and spacer film properties for Fin definition. The Gate level poses competing requirements of overlay control between the simpler patterns and the need to attain multiple Critical Dimensions (CDs) and pitches. We will examine this and the challenges of etch into advanced gate stacks for the 14nm node. At the Interconnect levels, we will consider the challenges of transferring not only trenches but also self aligned via patterns at sub -40nm half pitch into ultra low-k (ULK) dielectrics.

11:20am PS-MoM10 Novel Etch Mechanism for High Selectivity Etching of Silicon Nitride over Silicon and Silicon Oxide for Spacer Applications. *S. Engelmann*, *J. Chang*, *E.A. Joseph*, *R.L. Bruce*, *N.C.M. Fuller*, *W.S. Graham*, *E.M. Sikorski*, *S. Balakrishnan*, *A. Banik*, *M. Gordon*, IBM T.J. Watson Research Center, *M. Nakamura*, *G. Matsuura*, ZEON Chemicals L.P., *H. Matsumoto*, *A. Ito*, Zeon Corporation

To continue scaling CMOS devices at the traditional pace following Moore's law, high selectivity of etch processes towards multiple materials is approaching nanoscopic dimensions. The spacer etch process is a very critical element in the CMOS device process flow as it ensures and enables the electrical isolation of source/drain and gate regions. Extremely high precision is needed to form a silicon nitride (SiN) spacer without damaging exposed Si, SiO₂, or other surfaces (SiGe or SiC for example). This process is even more challenging for non-planar devices (such as FinFETs and Trigate), where the plasma process needs to be able to form the spacer on the gate sidewall, but not the fin sidewall. At the same time the exposed SiO₂ and Si surfaces (if applicable) have to withstand the extended processing necessary to form the spacer.

Multiple etch gas chemistries have been evaluated and their impact on etch rates and selectivities for spacer applications have been evaluated. Surface analysis techniques such as XPS and FTIR have been applied in conjunction with OES analysis of the plasma to study the etch mechanisms leading to the observed etch rates. Fundamental differences in etch mechanism were found for different etch gas chemistries.

We observed that during conventional spacer processes, very little difference in plasma polymer deposition onto the respective substrates could be noted. A successful SiN spacer process was rather facilitated by a Si etch process that was selective to SiO₂, where excess oxidation lead to a conversion of Si to SiO₂. This also means that the etch rates of the SiN are limited by the simultaneous oxidation of the same. A potential solution to overcome this limitation would be to control the etch rate by polymer thickness, similar to high selectivity SiO₂ etching. An evaluation of this approach has yielded similar results as the general etch mechanism proposed by Schaepekens et al.[1] [#_ftn1] A novel etch chemistry was also evaluated that enables a different etch mechanism that cannot be described by the general model. The impact of the described mechanisms on actual CMOS devices will be discussed in detail.

[1] [#_ftnref1] M. Schaepekens et al., J. Vac. Sci. Technol. A 17, 26 (1999)

11:40am PS-MoM11 High-Aspect Silicon Trench Oxidation in Downstream of Surface-wave Oxygen Plasma. *Y. Taniuchi*, *H. Shindo*, Tokai University, Japan

A low temperature and low damage silicon oxidation technique is highly required in various technology fields, such as in ULSI insulation layer formations, MEMS (Micro-Electro-Mechanical System) processes and other material surface treatments. In particular, in ULSI, the shallow trench isolation (STI) technique is inevitable to realize further integrations. In this process, so-called, a liner oxidation, in which the trench bottom is directly oxidized, becomes more severe, as the trench aspect ratio is further increased with the integrations. In MEMS (Micro-Electro-Mechanical System) processes, on the other hand, deep silicon trench etching with high aspect ratios is one of key technologies, and to realize a deep trench etching with a good directionality, a side wall passivation by the trench oxidation is inevitable. In this work, a silicon trench oxidation is investigated by employing a microwave oxygen plasma downstream under the condition of radio-frequency bias as well as the DC. In particular, the radio-frequency bias and the DC are superimposed and applied onto the substrate with the trench structure, and the oxidation rates at various portions of trench with the aspect ratio of 2 to 6 are examined as a function of the superimposed substrate bias. The oxidation depth shows a maximum in a very downstream of further position from the microwave window, indicating that the oxidation is due to negative oxygen ions. The silicon trench oxidation mapping, in which the oxidation film thickness is two-dimensionally plotted for the radio frequency bias and DC bias voltages, clearly demonstrates that the maximum is brought about along the line of the substrate bias of +20 V just above the plasma potential. In particular, the silicon trench bottom

oxidation is just limited onto the higher radio frequency bias within the above condition. As for the dependence on the trench aspect ratio R, the oxidation at the trench bottom was attained 100 % of the trench top up to R=3, while at the trench bottom with R more than 4 it was only 60 %. The oxidation at the bottom of deep trench with the aspect ratio R= 6 was improved at the higher radio frequency bias. It is concluded that the oxidation is due to the negative oxygen ions in downstream.

Surface Science Division

Room: 109 - Session SS1-MoM

Water Films & Environmental Interfaces

Moderator: H. Fairbrother, Johns Hopkins University

8:20am SS1-MoM1 **Surface Science of Acetonitrile on Model Interstellar Ices and Grains**, *A. Abdulgalil, M. Collings, M. McCoustra*, Heriot-Watt University, UK

Physical and chemical processes occurring on the surfaces of icy dust grains in the cold, dense interstellar medium have a crucial role to play in the evolution of the modern Universe. The formation of simple hydrides, *e.g.* water, on grain surfaces explains the infrared astronomical observations of icy grain mantles and provides a reservoir of coolant molecules during the early stages of star formation that helps maintain the current rate of star formation and favours the formation of small, long-lived stars. Energetic processing of icy mixtures by short wavelength radiation and cosmic rays turns the icy grain mantles into chemical nanofactories producing increasingly complex organic molecules. Nitriles (RCN) represent a potential intermediate on the pathway to forming amino acids in these icy mantles. However, the formation of nitriles in and on icy grain mantles is not understood. Nor is the surface science of these simple species on models of the interstellar grain population. Acetonitrile (CH₃CN) is the simplest organic nitrile and is amongst the list of chemical species observed in the interstellar medium. This paper will report our recent investigations of the interaction of CH₃CN with model silica and water ice surfaces representative of bare and icy interstellar dust grains. We will report on the nature and strength of the interaction of CH₃CN with these substrates and on the thermal and non-thermal (electron-induced) desorption of CH₃CN from these surfaces as part of our on going programme in solid state and surface astrochemistry.

8:40am SS1-MoM2 **Energetic Xenon Sputtering and Embedding at Ice Surfaces**, *D.R. Killelea, K.D. Gibson, H. Yuan, S.J. Sibener*, University of Chicago

PLEASE NOTE YOU MUST IDENTIFY A DIFFERENT PRESENTER FOR THIS ABSTRACT. YOU MAY PRESENT ONE PAPER ONLY (ORAL OR POSTER) AT THE CONFERENCE. YOU ARE LISTED AS PRESENTER FOR ABSTRACT #278Energetic collisions between gas-phase atoms or molecules and ice surfaces are ubiquitous in nature. Such collisions occur under non-equilibrium conditions given the disparity between the temperature of the substrate and that of the incident species. Moreover, metastable absorption states can be accessed at sufficiently high collision energies, opening up enhanced channels for species collection and concentration. Here, we present results of a study where the energetically accessed absorption states of the network of molecules in an ice surface were probed with translationally activated gas-phase Xe atoms, focusing on sputtering, energy accommodation, and a new mechanism for the incorporation of volatile species into ice surfaces: collisionally activated embedding. Evidence for embedding comes from the observation of Xe desorption at temperatures nearly 100 K above the normal desorption temperature for xenon adsorbed onto an ice surface.

9:00am SS1-MoM3 **Composition and Chemistry at the Liquid/Vapor Interface of Aqueous Solutions: Liquid-Jet XPS Experiments Coupled with MD Simulations**, *J.C. Hemminger*, University of California, Irvine
INVITED

In spite of the importance of liquid/vapor interfaces to many real world problems our understanding of the composition and chemistry of liquid/vapor interfaces is limited. We have employed liquid micro-jet methods to obtain x-ray photoelectron spectra of the liquid/vapor interface of aqueous solutions at the BESSY II synchrotron. The variable photon energy characteristic of synchrotron light sources allows us to carry out experiments over a range of photoelectron kinetic energies—thus varying the probe depth of the experiment. The result is a depth profile of the composition of the liquid/vapor interface. We have focused our experiments

on aqueous solutions. In this talk I will describe results from recent experiments on the following systems: (1) aqueous nitric acid solutions, in which we demonstrate a large difference in the degree of dissociation at the surface compared to bulk solution. We have also been able to determine the degree of dissociation at the interface and in the bulk solution for a range of temperatures sufficient to determine the enthalpy of the dissociation reaction for the interface and the bulk, (2) aqueous solutions of monoethanolamine and monoethanolamine reacted with CO₂—aqueous monoethanolamine is widely proposed for CO₂ capture processes, (3) aqueous solutions of the organosulfur compounds DMS, DMSO, DMSO₂, DMSO₃—DMS is a major source of environmental sulfur compounds including in the atmosphere. In these systems we have been able to determine the relative propensity of each molecule for the liquid/vapor interface, (4) carboxylic acid solutions where we have been able to determine the relative surface activity of the dissociated and undissociated acid. For each of the above systems we have carried out molecular dynamics simulations. These simulations combined with our experimental depth dependent measurements have provided molecular level insight into the behavior of molecular solutes in aqueous solution.

9:40am SS1-MoM5 **In Situ Studies of Sulfuric Acid Aqueous Solutions by X-ray Photoelectron Spectroscopy**, *A. Margarella, T. Lewis*, University of California, Irvine, *M. Faubel*, Max-Planck-Institut für Dynamik und Selbstorganisation, Germany, *B. Winter*, Hemholtz-Zentrum Berlin für Materialien und Energie, Germany, *J.C. Hemminger*, University of California, Irvine

Sulfuric acid is amongst the most widely used acids in the chemical industry, as well as having an important presence in atmospheric aerosols. Using a micro-liquid jet, the chemistry at the liquid-vapor interface of aqueous solutions is explored in-situ by x-ray photoelectron spectroscopy (XPS). Experiments presented were performed at Beamline U41 at the BESSY II synchrotron facility. By tuning the energy of the incoming photons, the kinetic energy of the photoelectrons is varied, allowing measurements from different depths of solution. As a strong diprotic acid, an aqueous solution of sulfuric acid will have HSO₄⁻ and SO₄²⁻ present, and at high concentrations, (greater than 16M) undissociated H₂SO₄ is present. In XPS, all of these components are distinguishable using their S2p binding energy shifts. A series of sulfuric acid aqueous solutions with concentrations up to 16M is measured and using the peak areas in the XP spectra, the dissociation at the surface relative to the bulk can be determined for different solutions.

Additionally, the effect of solution temperature on the acid dissociation at the surface is explored.

10:00am SS1-MoM6 **Infrared Spectroscopy of Thin Water Films on TiO₂(110): Anisotropy and the Hydrogen-Bonding Network**, *G.A. Kimmel, M. Baer, N.G. Petrik, C.J. Mundy, R.J. Rousseau*, Pacific Northwest National Laboratory

The structure of water at interfaces is crucial for processes ranging from photocatalysis to protein folding. We have investigated the structure of thin water films adsorbed on TiO₂(110) using reflection-absorption infrared spectroscopy (RAIRS), temperature programmed desorption and *ab-initio* molecular dynamics simulations. Infrared spectra were obtained for light with the plane of incidence parallel and perpendicular to the [001] azimuth of TiO₂(110) for water coverages ≤ 4 monolayers (ML). The spectra indicate strong anisotropy in the water structure along the two major azimuths. For both 1 and 2 ML coverages, the water films form “strings” of water molecules parallel to the bridging oxygen rows on the (110) surface. Within the strings, each molecule participates in 4 bonds, such that the films have no dangling hydrogen bonds. The vibrational densities of states predicted by the *ab-initio* simulations for 1 and 2 monolayer coverages agree well with the observations. Despite extensive prior research, the structure of water films on TiO₂(110) has remained controversial. Our results provide crucial, molecular-level information about the structure of water films on this benchmark transition metal oxide.

11:20am SS1-MoM10 **Origins of the Molecular Volcano: Dewetting and Crystallization Effects Leading to Rapid Desorption from Amorphous Solid Water Overlayers**, *R.A. May, R.S. Smith, B.D. Kay*, Pacific Northwest National Laboratory

Amorphous solid water (ASW), a metastable phase of water occurring when water is deposited on a substrate cooled below 140K, is of fundamental interest for an array of applications including but not limited to desorption from interstellar ices and investigation of diffusion and solvation processes. When deposited over an immiscible substance, such as CCl₄, the underlayer desorption is dictated by the morphology of the ASW overlayer. This desorption process culminates in the rapid release of the underlayer commensurate with the development of crystallization induced cracks through the ASW. This episodic release is termed the “molecular volcano”.

Thus, the desorption event reports on changes in the structure of the ASW overlayer. Infrared spectroscopy combined with programmed desorption elucidates the complex interplay between the dewetting and crystallization processes which dominate the eruption event. The effects of the ASW deposition temperature and overlayer thickness on the CCl₄ desorption process will be presented and discussed.

This work was supported by the U.S. Department of Energy (DOE), Office of Basic Energy Sciences, Division of Chemical Sciences, Geosciences, and Biosciences. The research was performed using EMSL, a national scientific user facility sponsored by DOE's Office of Biological and Environmental Research and located at Pacific Northwest National Laboratory, which is operated by Battelle, operated for the U.S. DOE under Contract DE-AC05-76RL01830.

Surface Science Division

Room: 110 - Session SS2-MoM

Surface Chemical Dynamics

Moderator: L. Bartels, University of California, Riverside

8:20am SS2-MoM1 STM Dynamics Studies of Tip-Induced Reactions of Anthracene Derivatives on TiO₂(110). *D.V. Potapenko, R.M. Osgood*, Columbia University

In photocatalysis, reactions are driven by the charges that are generated in the bulk of the catalyst and then are transferred to the adsorbed molecules. Injection of electrons from the STM tip into the adsorbed molecules is a useful tool for surface dynamics studies as the energy the electrons as well as the adsorption state of the molecules could be precisely controlled. We have studied adsorption and tip-induced chemistry of anthracene and its derivatives on the TiO₂(110) surface. These molecules self-assemble on the rutile(110) surface at room temperature driven by electrostatic interaction. Applying electric pulses from the STM tip to individual molecules causes desorption and in some cases dissociation as indicated by the changes in the STM images. We have observed dissociative electron capture of 2-chloroanthracene molecules that leaves behind a surface chlorine atom. The energy threshold for dissociation found as ~ 3.1 V. We report on the dynamics of this tip-induced chemistry and propose a mechanism for the observed phenomena.

8:40am SS2-MoM2 Atom Specific Ultrafast Surface Chemistry using Soft X-ray Free Electron Laser: CO on Ru(0001). *M. Beye*, Helmholtz Zentrum Berlin, Germany, *R. Coffee*, SLAC Nat. Accel. Lab, *M. Dell'Angela*, Univ. of Hamburg, Germany, *A. Foehlich*, Helmholtz Zentrum Berlin, Germany, *J. Gladh*, Stockholm Univ., Sweden, *T. Katayama*, *S. Kaya*, *O. Krupin*, *A. Nilsson*, *D. Nordlund*, SLAC Nat. Accel. Lab, *H. Oberg*, Stockholm Univ., Sweden, *H. Ogasawara*, SLAC Nat. Accel. Lab, *H. Ostrom*, *L.G.M. Pettersson*, Stockholm Univ., Sweden, *W.F. Schlott*, *J.A. Sellberg*, SLAC Nat. Accel. Lab, *F. Sorgenfrei*, Univ. of Hamburg, Germany, *J.J. Turner*, SLAC Nat. Accel. Lab, *M. Wolf*, Fritz-Haber-Inst., Germany, *W. Wurth*, Univ. of Hamburg, Germany

New possibilities for the study of chemical reactions on surfaces using X-ray free-electron lasers (Linac Coherent Light Source, or LCLS, at SLAC National Accelerator Laboratory) will be presented. We induced the hot electron mediated excitation of CO on Ru(0001) with synchronized excitation by a femtosecond optical laser pulse. We have followed the ultrafast evolution of the bond distortions, weakening and breaking, using x-ray emission spectroscopy resonantly tuned to the oxygen core level with ultrashort x-ray pulses delivered from LCLS. We can directly study the time evolution of the molecular orbitals in an atom-specific way on a subpicosecond timescale. Different adsorption configurations explored have been characterized by comparing the measured time dependent energy shifts of the molecular orbitals in the valence band with theoretical results.

This research was carried out on the SXR Instrument on the Linac Coherent Light Source (LCLS) at the SLAC National Accelerator Laboratory. The SXR Instrument is funded by a consortium whose membership include the LCLS, Stanford University through the Stanford Institute for Materials Energy Sciences (SIMES), Lawrence Berkeley National Laboratory (LBNL), University of Hamburg through the BMBF priority program FSP 301, and the Center for Free Electron Laser Science (CFEL). The LCLS is funded by the U.S. Department of Energy's Office of Basic Energy Sciences.

9:00am SS2-MoM3 The Oxidation of Benzyl Alcohol on Gold and its Implications Towards a Gold-Mediated Conversion of Hydrocarbons, *J.C. Rodriguez-Reyes, C.M. Friend, R.J. Madix*, Harvard University

In order to understand alcohol conversion on gold, we have explored the mechanism of the oxidation of benzyl alcohol (C₆H₅-CH₂OH) on a Au(111) surface - a test reaction commonly used to determine the efficiency and selectivity of novel gold-based catalysts. Using adsorbed atomic oxygen as the active oxidizing species, we find that a high selectivity towards the conversion to aldehyde (benzaldehyde, C₆H₅-CHO) is achieved at low oxygen coverages. However, in excess oxygen the selectivity decreases dramatically, and benzaldehyde is readily transformed to adsorbed benzoate, which is eliminated as benzoic acid (C₆H₅-COOH) and CO₂. In addition, we show that the production of the ester produced by self-coupling (benzyl benzoate) does not require the separate presence of acid, as might be expected from acid-alcohol condensation reactions. These surface transformations are extremely facile and exhibit small kinetic barriers of the rate-limiting steps. Lastly, by comparing the mechanism of benzyl alcohol oxidation to that of toluene oxidation, we extract information of a model hydrocarbon-to-alcohol reaction (toluene to benzyl alcohol, C₆H₅-CH₃ to C₆H₅-CH₂OH). Our results suggest that due to the relatively large kinetic requirements for toluene conversion, the alcohol cannot be selectively produced on a gold surface; indeed, preliminary TPRS data indicates that the gold-mediated conversion of toluene yields benzoic acid and combustion gases.

9:20am SS2-MoM4 Determination of the Structure and Vibrational Dynamics of Methyl-Terminated Si(111) Using Helium Atom Scattering. *R.D. Brown, S.J. Sibener*, University of Chicago

MMethyl-terminated Si(111) interfaces are of great interest in the fields of solar energy, solar fuels, and electronics due to their superior electrochemical stability and device performance. Recent advances in synthetic techniques allow for the fabrication of high-quality, passivated organic-semiconductor hybrid interfaces on single-crystalline silicon substrates. This termination maintains the bulk electronic behavior of the underlying silicon, but eliminates surface trap states which hinder the performance of any device. We directly examined the structural and dynamical characteristics of the CH₃-Si(111) and CD₃-Si(111) interfaces using helium atom scattering. Helium atom scattering is a uniquely surface-sensitive technique which probes both atomic structure and dynamics. These results are the first measurements of this nature for an organic-semiconductor hybrid interface. Helium atom diffraction confirmed a high quality (1x1) methyl termination of the Si(111) substrate. We observed unusual dynamical characteristics for these interfaces through Debye-Waller attenuation measurements of helium atom diffraction peaks. These measurements characterized the thermal motion of the interface, and elucidated the surface Debye temperature and gas-surface interaction well depth. The Debye Waller measurements yielded temperature dependencies of the surface mean-square displacements displaying polarization dependence, and were similar to the thermal motion of local molecular vibrational modes. The effective surface Debye temperatures were much higher than expected, and correspond to the local vibrational modes of the C-Si bond. These two unusual results indicate that termination with the simplest monolayer organic film initiates a transition away from phonon dominated surface dynamics to dynamics dominated by local molecular vibrational modes. We also performed a series of high precision inelastic time-of-flight measurements to characterize the phonon band structure of these interfaces. Our measurements have clearly resolved multiple single phonon surface modes on CH₃-Si(111), and are the first observations of this nature on an organic-semiconductor hybrid interface.

9:40am SS2-MoM5 STM Insights into Single-Molecule Dynamics. *K. Morgenstern*, Leibniz University of Hannover, Germany **INVITED**

The development of molecular switches on the single molecule level is a major challenge on the path towards incorporating molecules as building units into nanoelectronic circuits. With a scanning tunneling microscope (STM) it is possible to induce chemical reactions on a single molecule basis by electrons tunneling inelastically from the STM tip into a molecule. The method is based on high-resolution imaging at low-temperature (5K) that allows us to identify different groups within the molecule. Chemical reactions are induced by injecting selectively electrons into specific parts of the molecule. The success of the manipulation is visualized in the recorded tunneling current during the manipulation and in STM images taken afterwards. We investigate isomerization of individual molecules adsorbed on metal surfaces. For chlorobenzene and azobenzene derivatives, the effects of different substitutional groups and different substrates are explored.

10:40am **SS2-MoM8 State-resolved Reactivity of Methane (v_2+v_4) on Ni(111)**, *N. Chen, Y. Huang, A. Utz*, Tufts University

Methane dissociation on transition metal surfaces is the rate-limiting step in the steam reforming reaction, which is the principal route for converting CH_4 to H_2 . Understanding the dynamics of energy flow during this process has both fundamental and practical impact. Experiments that measure the reactivity of methane prepared in select vibrational states reveal how specific nuclear motions promote methane dissociation. State-resolved measurements for methane reactivity on Ni and Pt surfaces show that molecules prepared in vibrationally excited states are more reactive than those without laser excitation, and the efficacies of vibrational energy in different excited states can differ significantly.

Here, we present state-resolved reactivity measurements of the v_2+v_4 bending combination vibration of CH_4 on Ni(111) as a function of translational energy. This state is a member of the pentad of vibrational states that can play an important role in the thermal activation of methane. We are able to quantify the state-resolved reactivity of methane in this particular vibrational state over a wide range of translational energies. We compare the efficacy for v_2+v_4 bend with that of the v_3 stretching and $3v_4$ bending states to gain insight into the ability of v_2 excitation to promote dissociative chemisorption. The result permits a detailed comparison of the role of stretch and bend excitation of methane dissociative chemisorption on Ni(111).

11:00am **SS2-MoM9 Molecular Beam Scattering of CO and CO_2 on CuO_x Nanoclusters Supported on Silica Fabricated by Electron Beam Lithography**, *M. Komarneni, U. Burghaus*, North Dakota State University
Adsorption dynamics of CO and CO_2 on 12 nm CuO_x nanoclusters supported on silica are studied by molecular beam scattering. Samples are fabricated by electron beam lithography. Scanning electron microscopy, auger electron spectroscopy, and x-ray photoelectron spectroscopy are used to characterize the sample. Cu clusters which are nearly metallic, partially oxidized, and fully oxidized are prepared by varying the sample treatment. The initial adsorption probability, S_0 , of both CO and CO_2 decreased with an increase in impact energy, E_i , and adsorption temperature, T_s , which is consistent with non-activated molecular adsorption. S_0 of CO approaches the values obtained for copper single crystals for E_i of 0.4 eV. This is a result of the so-called capture zone effect, where CO molecules are trapped on the support and subsequently diffuse to the metal clusters. S_0 of CO_2 is larger than for single crystals. The differences in S_0 for metallic and oxidic clusters can be explained by deviations in the mass matching. In contrast with CO_2 , S_0 of CO on metallic clusters is slightly larger than that of oxidic clusters. At low E_i and T_s , coverage dependent adsorption probabilities, $S(\theta)$, of CO and CO_2 on metallic clusters obeyed precursor-mediated Kisliuk-like dynamics. At large E_i , Langmuirian-like dynamics is seen for CO which is less pronounced for CO_2 on metallic clusters.

11:20am **SS2-MoM10 Precursor-Mediated Reactivity of Vibrationally Hot Molecules**, *D. DelSesto, E. Peterson, E. Dombrowski, A. Utz*, Tufts University

Methane's dissociative chemisorption is highly activated on a range of transition metal surfaces. Internal-state-averaged and state-resolved beam-surface scattering experiments show that vibrational energy (E_{vib}) can be highly effective in promoting dissociative chemisorption via a direct mechanism, but evidence for E_{vib} activation via a precursor-mediated mechanism on a metal surface remains scarce. We will present recent experimental results from our lab that demonstrate the ability of E_{vib} to promote methane dissociation via both direct and precursor mechanisms on Ir(111). These results build on prior studies of trapping-mediated reactivity on Ir(111) by exploring how E_{vib} in the incident methane molecule promotes reactivity, and they are consistent with the timescales and pathways of vibrational energy flow and damping on these surfaces.

1. Seets, D. C., C. T. Reeves, et al. (1997). "Dissociative chemisorption of methane on Ir(111): Evidence for direct and trapping-mediated mechanisms." *J. Chem. Phys.* **107**(23): 10229-10241.

11:40am **SS2-MoM11 Three-Dimensional Spatial Distribution of Desorbing N_2 and N_2O from Pd(211)**, *M. Sakurai, T. Kondo, J. Nakamura*, University of Tsukuba, Japan

Spatial distributions of N_2 and N_2O desorbing from Pd(211), Pd(S)-[3(111)×(100)], in temperature programmed desorption (TPD) were measured after the N_2O dosing on the surface at 60 K. About one-third of N_2O molecules on the surface are found to desorb as N_2 by the decomposition with sharp concentration to 25° ($\theta = -25^\circ$) (100) side from the normal direction of (211) plane at 108 K in the parallel plane to [211]

and [-111] directions at N_2O coverage of 1.0 ML. This indicates that N_2 desorbs without thermal equilibration by N_2O decomposition on Pd(211). From the preferential desorption direction ($\theta = -25^\circ$), the adsorption structure of N_2O just before the desorption is assigned as the bridge-structure at step-site, where O and terminal-N bonded with Pd at ontop (100) and 3fold hollow(111), respectively along the [-111] directions. On the other hand, the spatial distribution of desorbing N_2O obeyed cosine distribution directing the normal direction to the (211) plane, suggesting the existence of pre-desorption state on the surface.

Thin Film Division

Room: 107 - Session TF-MoM

Thin Films: Growth and Characterization I

Moderator: J.M. Fitz-Gerald, University of Virginia

8:20am **TF-MoM1 Heavy Ion Irradiation Effects on Ti/Al Multilayer Thin Films**, *R.S. Vemuri*, The University of Texas at El Paso, *T. Varga, S.V. Shutthanadan, S.V.N.T. Kuchibhatla, M.H. Engelhard, P. Nachimuthu, C.H. Henager, C.M. Wang, S. Thevuthasan*, Pacific Northwest National Laboratory, *C.V. Ramana*, The University of Texas at El Paso

There has been growing interest in thin bi-metallic multilayer films for the usage under extreme radiation conditions because of their radiation healing properties. Recent discovery and research indicate that materials can be hardened against radiation damage by building nanolayered structures with an optimized layer thickness to increase point defect recombination relative to a non-layered structure and that can self-heal. In this study, we investigate whether the internal interfaces can be manipulated at the nanoscale to enhance dynamic recombination of radiation-produced defects, or self-healing, so as to dramatically reduce radiation damage without compromising other properties using Ti/Al multilayer films.

Ti/Al multilayer films were fabricated on Si (100) and epi polished MgO (100) substrates using DC magnetron sputtering and Molecular beam epitaxy (MBE). The growth parameters for each method, for sputtering – pressure, power and substrate temperature deposition rate; and for MBE – deposition rate and substrate temperature were optimized to achieve high-quality thin films. The films were characterized using x-ray diffraction (XRD), x-ray reflectivity (XRR), Rutherford backscattering spectrometry (RBS), and x-ray photoelectron spectroscopy (XPS) measurements. The films show mostly polycrystalline structure with no elemental interdiffusion at the interfaces. Detailed structural and compositional analysis was also performed using high resolution TEM/STEM and atom probe tomography (APT). The films were irradiated using 1-8 MeV Au ions to understand the radiation effects. The damage peak, stopping range and ion distribution were simulated using binary collision approximation based Monte Carlo method (SRIM software program). Au ion energies, estimated from the simulation, were used to position the damage peak at the interested interfaces and away from the interfaces to obtain the complete picture at the interfaces and in the bulk of the films. The interface and crystal lattice damage, amorphization, and defect density were studied by RBS, HAADF-STEM and APT, and compared with those results from the pristine samples. The relationships between film properties and radiation healing characteristics will be presented and discussed.

8:40am **TF-MoM2 Flux and Surfactant-Assisted Physical Vapor Deposition: New Approaches for Improving Complex Oxide Thin Film Growth**, *J.-P. Maria, E.A. Paisley, B.E. Gaddy*, North Carolina State University, *M.D. Biegalski*, Oak Ridge National Laboratory, *D.L. Irving, A.R. Rice, R. Collazo, Z. Sitar*, North Carolina State University **INVITED**

Epitaxial integration of complex oxides with wide band gap polar semiconductors such as GaN (0002) presents the possibility for high-power, high-frequency, and high temperature GaN electronics by virtue of 2-D charge carriers at polar interfaces and possible access to non-linear dielectric properties. This work describes synthesis and characterization of such thin film heterostructures by MBE, with specific attention given to controlling film growth. Our previous work has shown growth of high-quality MgO (111) and CaO (111) films on GaN with measured valence band offsets > than 1 eV and conduction band offsets ~ 3.2 eV (MgO) and ~2.5 eV (CaO). However, the terminal 3D rocksalt growth surface is determined by the tendency for the high-energy (111) polar orientation to form (100)-oriented low-energy facets, and the interfacial symmetry between cubic MgO and hexagonal GaN. Therefore, realizing smooth oxide films on GaN requires the ability to overcome the rocksalt (001) faceting tendency through a surfactant growth method. In this presentation we will discuss a newly-developed surfactant approach to MBE growth of rocksalt oxides utilizing water vapor to hydroxylate CaO and MgO (111) surfaces *in situ*, which changes the equilibrium habit from cubic to octahedral,

eliminating the (100) faceting tendency. RHEED oscillations and AFM images of these films show 2D growth, suggesting that altering the surface chemistry during growth plays a critical role in determining the surface orientation. We demonstrate through electrical property measurements the impact of smooth (111) rocksalt surfaces as leakage current densities for thin CaO films are reduced by two orders of magnitude when films of equivalent thickness are grown using a 2-D vs. a 3-D mode. Finally, we will present a set of temperature *ab-initio* thermodynamic calculations of CaO surface energies with and without H-containing terminations that validate the surface-chemical mechanism of facet stabilization.

9:20am TF-MoM4 Initiated – Chemical Vapor Deposition of Organosilicones: from Growth Mechanism to Multilayer Moisture Diffusion Barriers. *G. Aresta, J. Palmans, M.C.M. van de Sanden, M. Creatore*, Eindhoven University of Technology, Netherlands

The state-of-the art approach in the encapsulation of high-end devices such as flexible (polymer) solar cells and organic light emitting diodes against water vapour permeation is an organic/inorganic multi-layer system. Although this approach allows increasing the lifetime of the encapsulated device, the optimization of a multi-layer is rather empirical as the mechanisms behind the improvement of the barrier performance are not yet unraveled. In particular, the role of the organic interlayer is rather controversial since effectively it does not act as a moisture vapor barrier, yet its application appears to be fundamental in the multi-layer solution. In this contribution, the role of the organic interlayer is investigated by selecting a system in which the barrier layer, a 100 nm-thick SiO₂ film, is plasma-deposited while the organic interlayer, a 200 nm-thick organosilicon film, is synthesized by means of initiated-chemical vapor deposition, i.e. via thermal decomposition of an initiator molecule promoting the polymerization of 1,3,5-trimethyl-1,3,5-trivinyl-cyclotrisiloxane (V₃D₃) at the substrate.

The implementation of *in situ* (real time) spectroscopic ellipsometry allows following the different growth stages in the V₃D₃ polymerization process. In particular, when applied to the polymer bulk growth, the determination of the growth rate allows monitoring the transition from a kinetic-limited (with activation energy of 65 ± 4 kJ/mol) to a mass transfer-limited regime. Furthermore, the deposition process is found to be monomer adsorption-limited with an activation energy of -39 ± 4 kJ/mol. When spectroscopic ellipsometry is applied to the initial monomer adsorption steps, isothermal adsorption/desorption studies provide insight into the microstructure of the underlying SiO₂ barrier layer, characterized by a residual open porosity in the micro/meso transition region (pore radius ≤ 2nm). The microstructure characterization by means of the above-mentioned studies implicitly points out the role of the i-CVD organic interlayer in multi-layer barrier structures, i.e. the filling of the open micro-meso porosity of the inorganic barrier layer, therefore, improving the intrinsic barrier quality of the underlying SiO₂ film. This outcome nicely correlates with the superior water vapor barrier performances (a barrier improvement factor of 2400 is reported with respect to the pristine polymer) of multi-layers based on the application of i-CVD organic interlayers with respect to fully-PECVD developed multi-layers.

9:40am TF-MoM5 Processing and Characterization of Iron and Fluorine Co-Doped Ba_{0.6}Sr_{0.4}TiO₃ Thin Films. *F. Stemme, H. Gesswein, C. Azucena*, Karlsruhe Institute of Technology (KIT), Germany, *M. Sazegar*, Darmstadt University of Technology, Germany, *J.R. Binder, M. Bruns*, Karlsruhe Institute of Technology (KIT), Germany

Barium strontium titanate (BST) is a very promising material for tunable microwave applications like phase-shifters and tuneable filters. Due to this the influence of e.g. annealing conditions and processes on thin film properties and their dielectric performance were largely investigated. But very few researchers have tried to change the sputtered BST thin film properties by using different dopants at the same time. Such iron and fluorine co-doped thin films can be achieved by RF magnetron sputtering, with a co-sputter target and a two step annealing process after deposition. The first annealing process provides the crystallinity of the films. In the second annealing process the fluorine co-dopant is introduced into the BST thin films by a diffusion controlled process.

The present contribution focuses on the processing and characterization of the iron doped BST thin films with various amounts of fluorine co-dopant. The characterization of the thin films by X-ray photoelectron spectroscopy (XPS) provides chemical binding states and film composition. XPS and time of flight secondary ion mass spectrometry (ToF SIMS) sputter depth profiles prove the chemical homogeneity and the film thickness. Grazing incident X-ray diffraction (XRD) and Raman spectroscopy validate the crystallinity and the identification of chemical phases. Furthermore film morphology is determined by scanning electron microscopy (SEM) and atomic force microscopy (AFM). Dielectric measurements, to investigate the influence of the donor and acceptor co-doping on the dielectric

performance, were carried out in metal insulator metal (MIM) structures with ground signal ground probes.

10:00am TF-MoM6 Advances in the Growth of Epitaxial Oxides for Neuromorphic Computing Applications. *J.D. Greenlee, W.L. Calley, W.A. Doolittle*, Georgia Institute of Technology

Present-day computing devices are approaching performance limits due to excess heat and parasitic capacitance degrading performance. One proposed solution, termed “neuromorphic computing”, is to perform computations similarly to the brain.

A key enabling device for neuromorphic computing is the lithium niobate (LiNbO₂) memristor[1]. Like synapses in the brain, LiNbO₂ memristors can exhibit excitatory or inhibitory behavior. This is due to the ability to produce both n and p-type LiNbO₂ memristors, a unique property for an oxide. As shown in Figure 1, when a voltage is applied across an n-type memristor (left), resistance increases over time, whereas a p-type memristor exhibits decreasing resistance (right). N-type memristors are grown with excess oxygen vacancies while p-type memristors are grown with excess lithium vacancies. N- and p-type films are very conductive, exhibiting resistances of 4.3x10⁻⁴ Ω-cm(p-type) and 3.9x10⁻⁴ Ω-cm(n-type) with carrier concentrations higher than 10²¹ cm⁻³ and Hall mobilities greater than 8 cm²/V-s.

The epitaxial growth of LiNbO₂ is the enabling technology for the memristors described above. Growths are conducted using an oxy-chloride MBE system in which metal-halide sources interact with lithium and oxygen [2]. Lithium acts as a getterer for the chlorine from the metal-halide, and the resulting LiCl is desorbed from the heated growth surface. The bare metal then oxidizes under the application of an oxygen plasma and combines with lithium. This growth chemistry has been used to produce dielectric/ferroelectric lithium niobate (LiNbO₃), semiconducting lithium niobate (LiNbO₂), and lithium cobalt oxide (LiCoO₂).

Insulating LiNbO₃ (Figure 2) and semiconducting LiNbO₂ (Figure 3) are grown using NbCl₅ and the phase of the material is controlled by the niobium to oxygen ratio delivered to the growth surface. Both single crystal LiNbO₃ and LiNbO₂ have been epitaxially grown on Al₂O₃ and SiC. LiNbO₃ is a promising lattice matched, ferroelectric transistor gate high-k oxide for its semiconducting sub-oxide, LiNbO₂. LiNbO₂ has a layered, lithium-intercalated structure [3] (Figure 4). When lithium is removed, holes are introduced which increases the conductivity of p-type material and decreases the conductivity of n-type material, thus producing the memristance effect described herein.

LiCoO₂ is grown on Al₂O₃ using CoCl₂ as the precursor (Figure 5). Like LiNbO₂, LiCoO₂ has a layered structure that facilitates lithium movement. The lattice spacing of LiCoO₂ is closely matched to LiNbO₂ (2.81 Å and 2.91 Å respectively), thus making it an attractive material for heterostructures of lithium-bearing semiconductor materials.

10:40am TF-MoM8 New Method to Produce High-Quality Epitaxial Ge on Si Using SiO₂-Lined Etch Pits and Epitaxial Lateral Overgrowth for III-V Multijunction Solar Cells. *D. Leonhardt, S.M. Han*, University of New Mexico

Integrating a high-quality layer of epitaxial Ge on Si has been a longstanding engineering challenge, despite its technological importance. The applications of Ge-on-Si include ‘virtual substrates’ for III-V multijunction solar cells, high-mobility field-effect transistors, and optical interconnects monolithically integrated with Si-based circuitry. The primary difficulties in achieving Ge films of sufficient quality stem from the lattice mismatch that leads to a large density (> 10⁹ cm⁻²) of threading dislocations (TDs) and the thermal expansion coefficient mismatch between Ge and Si that leads to microcracks or delamination of Ge film upon cooling from growth to room temperature. Herein, we present a new method to reduce the TD density, using a minimal number of standard microfabrication steps. The method begins with growing a 500-nm-thick epitaxial Ge layer on Si. A post-growth anneal step leads to a TD density of approximately 5x10⁷ cm⁻², as revealed by plan-view transmission electron microscopy (TEM) and etch pit density (EPD) measurements. The close agreement between EPD measurements and TEM shows that the EPD measurements reliably decorate all TDs. Etch pits are created around the dislocation cores in the Ge film. A 15-nm-thick layer of SiO₂ is subsequently deposited on the etch-pit-decorated Ge film. A thin layer of polymethyl methacrylate is then spin-coated onto the sample, which fills the etch pits and planarizes the Ge surface. Next, a reactive ion etching step is used to remove the polymer and SiO₂ from the planar regions of the sample surface surrounding the etch pits. An O₂ plasma is then used to selectively remove the remaining polymer, so that SiO₂ remains only within the etch pits. Lastly, a second layer of Ge is selectively grown on the exposed Ge surface and laterally over the SiO₂-lined etch pits until a fully coalesced Ge film is created. A final polishing step produces an atomically flat continuous Ge film. Ensuing EPD measurements reveal that the density of twin defects and TDs in the

upper Ge layer is approximately $1.7 \times 10^6 \text{ cm}^{-2}$, such that the overall defect density is reduced by a factor greater than 30 compared to that in the initial Ge layer. Both theoretical and experimental evidence suggest that the defect density in GaAs films on Ge/Si must be less than $2 \times 10^6 \text{ cm}^{-2}$ to have a minority carrier lifetime comparable to GaAs films grown on Ge and GaAs substrates. Therefore, our new method of using SiO_2 -lined etch pits to block the propagation of TDs in Ge may finally lead to device quality III-V materials integrated on Si substrates.

11:00am **TF-MoM9 Three Dimensional Reciprocal Space Measurements by X-ray Diffraction using Linear and Area Detectors: Application to Texture and Defect Determination in Oriented Thin Films and Nanoprecipitates**, *S. Gaudet, S. Lambert-Milot, P. Desjardins*, École Polytechnique de Montréal, Canada, *K. Dekeyser, C. Detavernier*, Ghent University, Belgium, *J.L. Jordan-Sweet, C. Lavoie*, IBM T.J. Watson Research Center

Very thin films grown or deposited on oriented substrates are often composed of highly oriented phases. Traditional x-ray diffraction approaches, scanning only limited portions of the reciprocal space, can fail to characterize some phenomenon occurring in those thin films. We developed an approach for the fast and efficient measurement of complete volumes of the reciprocal space by x-ray diffraction using linear and area detectors. In this presentation, we show how it allowed a detailed understanding of the solid-state thin film reaction to form contacts on transistors and of the growth of magnetic nanoprecipitates by metalorganic vapor-phase epitaxy. We first explain the procedures and scan strategies required for transforming raw scattering data into three-dimensional maps of the reciprocal space, and we present a complete open source software package for advanced data processing, analysis, and visualization. Case studies, chosen to highlight the overall capabilities of the technique, are then introduced. First, thermal diffuse scattering from a monocrystalline Si substrate is characterized. The presence of lines linking diffraction peaks in reciprocal space reflects the interaction of the x-ray beam with the phonon spectrum of the monocrystal. Second, a detailed investigation of texture in multiphase thin layers permits to reveal the unambiguous presence of fiber, axiotaxial, and epitaxial components in extremely oriented films. The visualization of the entire reciprocal space allowed us to identify unexpected metastable phases that could not be deduced or observed from measurements carried out in the Bragg-Brentano geometry. Finally, we present an investigation of defects in two thin film systems: planar defects in nickel silicide layers formed by solid-state reactions and microtwins in a GaP matrix containing coherent MnP precipitates. In summary, the systematic acquisition of significant volumes of the reciprocal space allows for the observation of behaviors that could otherwise remain undetected when restricting the analysis to typical measurement scans.

11:20am **TF-MoM10 Surface Characterization of Zr/Ti/Nb Tri-layered Films Deposited by Magnetron Sputtering on Si(111) and Stainless Steel Substrates**, *D.A. Tallarico*, Federal University of Sao Carlos, Brazil, *A.L. Gobbi*, Brazilian Synchrotron Light Laboratory, Brazil, *P.I. Paulin-Filho*, Federal University of Sao Carlos, Brazil, *A. Galtayries*, Ecole Nationale Supérieure de Chimie de Paris, France, *P.A.P. Nascente*, Federal University of Sao Carlos, Brazil

Titanium is a metal commonly used in medical implants, due to its interesting properties, such as high mechanical strength, good corrosion resistance in extreme conditions, and excellent thermal stability. Ti-6Al-4V is one of the main biomaterial alloys employed as implants, but the release of Al and V ions is associated to health problems and adverse tissue reactions. A new class of Ti alloys employs Zr for solid-solution hardening and Nb as β phase stabilizer. Metals such as Ti, Nb, and Zr, known as valve metals, usually have their surfaces covered by a thin oxide film spontaneously formed in air. This oxide film constitutes a barrier between the metal and the medium. The Ti-Nb-Zr alloys have mechanical and corrosion resistance characteristics which make them suitable for use as implants. Tri-layered films of Ti-Nb-Zr were deposited on both Si(111) and stainless steel substrates using a DC magnetron sputtering equipment, under an argon atmosphere. The films were deposited in the following manner: a 100 nm thick layer of Nb was deposited on a Si(111) substrate, then a 200 nm layer of Ti was deposited on top of Nb/Si, and lastly a 50 nm layer of Zr was deposited on top of Ti/Nb/Si. A similar Zr/Ti/Nb film was also grown on stainless steel substrate. The structure, morphology, and chemical composition of the films were analyzed by means of X-ray diffraction (XRD), atomic force microscopy (AFM), X-ray photoelectron spectroscopy (XPS), and time-of-flight secondary ion mass spectrometry (ToF-SIMS). The XPS results for the Zr/Ti/Nb layers deposited on Si(111) presented a predominance of ZrO_2 on the surface, and Nb_2O_5 and a small quantity of TiO_2 . For the layers deposited on stainless steel, only ZrO_2 and a small amount of niobium oxide were detected. The ToF-SIMS results indicated the formation of a three-layered film on Si(111), with each metal in a distinct layer and a well-defined interface between the layers, while the deposition

on the stainless steel substrate caused slight intermixing at the Nb/Ti and Ti/Zr interfaces. AFM images showed that the Zr/Ti/Nb tri-layer films presented nanostructured grains and low roughness, with the film deposited on stainless steel having the roughest surface.

11:40am **TF-MoM11 PECVD Synthesis of Hybrid Organic-Inorganic Nanolaminates**, *R. Patel, C.A. Wolden*, Colorado School of Mines

Hybrid organic-inorganic nanolaminates combine the functionality of an inorganic material with the flexibility and mechanical integrity provided by the organic polymer layer. They are integral components in various applications serving as advanced dielectrics, flexible barrier coatings, and as optical components. This work focuses on the low temperature synthesis of alumina/silicone nanolaminates by plasma-enhanced chemical vapor deposition (PECVD) in a single chamber for dielectric applications.

Self-limiting synthesis of alumina was accomplished via pulsed PECVD at the synthesis temperature of $\sim 100^\circ\text{C}$ using trimethyl aluminum (TMA) and oxygen as precursors. The deposition kinetics and film quality were evaluated as a function of precursor exposure, plasma power, substrate temperature, and pulse parameters. Film composition was assessed by using spectroscopic ellipsometry and Fourier transform infrared spectroscopy (FTIR). The deposition rate per pulse scaled with the degree of precursor exposure during the plasma off step. Through appropriate control of the TMA concentration and pulse duration, the depositing rate could be adjusted over a narrow range (1.6 – 2.8 Å/pulse). Alumina films deposited at 105°C contained a very small concentration of hydroxyl impurities. Polymeric silicone-like coatings were deposited using hexamethyldisiloxane (HMDSO) and oxygen as precursors. A wide range of coatings, from inorganic SiO_2 -like films to flexible polymeric films could be deposited by appropriate control of parameters including the rf power, substrate temperature and working pressure. Growth rates as high as 100 nm/min were obtained for polymeric silicone films.

Alumina/silicone nanolaminates were constructed as a function of nanolaminate composition and dyad thickness. Precise control of nanolaminate construction was confirmed through field emission scanning electron microscopy (FE-SEM) and transmission electron microscopy (TEM). The dielectric performance of these structures was examined by using capacitance-voltage and current-voltage measurements. The effective dielectric constant could be controlled by changing the alumina content of the nanolaminates, and modeling these structures as capacitors in series accurately described the observed variations in κ .

Vacuum Technology Division

Room: 111 - Session VT-MoM

Vacuum Measurement, Calibration & Primary Standards, Gas Flow and Permeation

Moderator: R. Garcia, SAES Getters

8:20am **VT-MoM1 Transportable NIST Traceable Vacuum Standards for Secondary Calibration Laboratories and International Key Comparisons**, *J.H. Hendricks, D.A. Olson, J.E. Ricker*, National Institute of Standards and Technology

Over the past decade, NIST has designed and built several high-stability transfer standard packages (TSPs) that have proven to be ideally suited for inter-laboratory comparisons in the atmospheric pressure and vacuum pressure range [1]. In the mid 1990's the development and use of micro electro mechanical systems (MEMS) enabled pressure sensor technology to make significant advances in both precision and accuracy. Resonant silicon gauges (RSGs) are MEMS sensors that are manufactured by micromachining silicon to produce silicon diaphragms nominally a few millimeters square by a fraction of a millimeter thick [2]. NIST has found that these gauges are very stable, rugged, and ideally suited as core technology for a high-stability precision pressure and vacuum standard. The RSG sensors with full-scale ranges of 10 kPa and 130 kPa have shown excellent stability [3]. However, one drawback of the RSGs is that they lack the sensitivity and resolution of capacitance diaphragm gauges (CDGs) with full-scale ranges of 133 Pa. The downside of only using these CDGs is their relatively poor calibration stability when compared to 10 kPa full scale range RSGs. The NIST solution has been to combine the high-resolution of the 133 Pa CDGs, with the high-stability of the 10 kPa RSGs into one transfer standard package. The RSG gauges are then used to determine the calibration drift in the CDGs at the time of use. A recently completed set of transportable NIST traceable vacuum standards with a range of 1 Pa to 10,000 Pa will be highlighted. These TSPs consist of pairs of 10 kPa RSGs and pairs of 133 Pa CDGs encased in temperature controlled enclosures that further enhance gauge performance. These standards will be used for an

upcoming international key comparison in absolute pressure from 1 Pa to 10,000 Pa.

[1] Hendricks, J.H., Olson, D.A., Physics World, Vacuum Challenges and Solutions (2009) 18-19.

[2] Harada, K. et al. 1999 Sensors and Actuators 73 261-266.

[3] Hendricks, J.H. et al. Metrologia 44 (2007) 171-176.

8:40am VT-MoM2 Extending the Range of the Spinning Rotor Gauge for Vacuum Measurements and Calibrations, M.L. Duncan, J.A. Keck, Oak Ridge National Laboratory
INVITED

The spinning rotor gauge (SRG) has long been the primary transfer standard used by metrology laboratories for providing traceability of measurements from field vacuum devices to primary vacuum standards maintained at national measurement institutes. The useful range of the SRG, in its current commercial form, is somewhat limited by several factors including the relatively small change in momentum of the rotating sphere caused by the adsorption/desorption of gas molecules as the gas pressure (and thus number of molecules adsorbing/desorbing) decreases. Current technology limits the low pressure end of this range to about $2E-5$ Pa with a $K=2$ uncertainty of approximately 1-3%.

Efforts are currently underway at the Oak Ridge National Laboratory to increase the range of the commercial SRG by approximately a decade by increasing the sensitivity of the rotor's momentum change to the low number of gas molecules available for adsorption/desorption at the lower pressures. Efforts are also underway to improve the uncertainty of the existing commercial SRG through better measurement and characterization of the thermal expansion of the spinning rotor itself. This paper will report on the progress of these efforts to date, some of the challenges discovered during the development process and plans to address those challenges

9:20am VT-MoM4 Cold Electron Source Used as Electron Source in Familiar Vacuum Measurement Devices, P.C. Arnold, Brooks Automation, Inc., G.A. Brucker, Brooks Automation, Inc., Granville-Phillips Products

Both a Bayard-Alpert type ionization gauge and a partial pressure analyzer have been fabricated and tested with cold electron sources. These vacuum measurement devices showed performance for their intended use generally similar to operation with thermionically heated hot cathode electron sources. The benefits from a cold cathode electron source are several: reduced heat input to the system, lack of electron emission failure due to detrimental gases of the environment, non-susceptibility to deposits of the chemistry of the environment, non-interaction with the environment which interaction could produce gas species other than that occurring as part of the activity of the chamber, and finally fast turn-on to the electron emitting state. Details of the constructions, using an electron multiplier as the electron source, as well as the methods of controlling the electron emission current itself will be described. Test models, test conditions, and test results will be shown for a recently designed autoresonant ion trap mass spectrometer and an otherwise nearly traditional Bayard-Alpert ionization gauge.

9:40am VT-MoM5 Review of Thermal Conductivity Vacuum Gauges, M. Wüest, INFICON Ltd, Liechtenstein

Thermal conductivity gauges are ubiquitous in vacuum industry. In the form of Pirani gauges they are a mainstay of cost-effective measurement in the fine vacuum range. Different realizations of the Pirani gauge will be discussed from the classical heated wire sensor to the newer micromachined sensors. We will review not only basic parameters such as measurement range and sensitivity but also topics interesting for industrial applications such as dynamical response, robustness and inertness in industrial processes.

10:00am VT-MoM6 Investigation of the Hot Cathode Ionization Vacuum Gauge; Stability and Reliability on the Point of View of Traceability, N. Takahashi, ULVAC Inc., Japan

Many hot cathode ionization gauges have been developed focused on the lower limit of the pressure measurement. We have also developed the Axial symmetric transmission gauge (AT gauge) which lower limit of the pressure measurement is lower than 10^{-10} Pa.

On the contrast, stability and reliability are important for the industrial field and metrological traceability field.

Traceability of the vacuum gauge in the range of 1 to 10^{-4} Pa is established by the spinning rotor vacuum gauge. The uncertainty of the spinning rotor vacuum gauge includes its stability is estimated 1 % to few %. However, the sensitivity of the ionization gauges, which usually are the calibration item of the reference spinning rotor vacuum gauge, changes few % to few tenth %. Sensitivity change was caused by following; geometry change of

the electrodes, change of the electron emission region on the hot cathode, contamination of the electrodes, etc.

We have investigated small all metal sealed triode type hot cathode ionization gauge on the contrast to the conventional glass bulbed triode type hot cathode vacuum gauge and all metal sealed BA gauge. The stability of the sensitivity of the small triode ionization gauge was less than 0.5% for 6 month before the huge earthquake happened in Japan. At the disaster, turbo molecular pump was crashed. We could report the sensitivity change of the gauge after the pump change.

We also demonstrate the benefit of the triode vacuum gauge in the contaminated vacuum system.

We will summarise the triode vacuum gauge is better characteristics than conventional glass bulbed triode vacuum gauge and BA gauge in the field of industrial field and metrological traceability field.

10:40am VT-MoM8 On the Stability of Capacitance-Diaphragm Gauges with Ceramic Membranes, K. Jousten, Physikalisch-Technische Bundesanstalt, Germany, S.P. Naef, INFICON Ltd, Liechtenstein

Capacitance-diaphragm gauges with ceramic membranes or diaphragms have been on the market for

about 15 years. The long-term stability of these devices with full scales from 13 Pa to 133 kPa

has been tested in the past decade by the calibration of gauges used by the manufacturer as reference

gauges on the production line. These reference gauges were calibrated annually on a primary

standard. It was found that the reproducibility of these devices depends on their full scale. For

13 Pa, the annual reproducibility near full scale varied between 0.02% and 0.05%, and for full scales

of 133 Pa and higher, it varied between 0.005% and 0.03% of full scale. The reproducibility of the

ceramic capacitance-diaphragm gauges for full scales of 133 Pa and 1.3 kPa was significantly lower

than the uncertainty of a primary standard applying the static-expansion method.

11:00am VT-MoM9 Thermal Transpiration Effects in Capacitance Diaphragm Gauges with Helicoidal Baffle System, M. Vargas, Institute of Mechanics - Bulgarian Academy of Sciences, M. Wüest, INFICON Ltd, Liechtenstein, S.K. Stefanov, Institute of Mechanics - Bulgarian Academy of Sciences

The Capacitance Diaphragm Gauge (CDG) is one of the most widely used vacuum gauges in low and middle vacuum ranges. This device consists basically of a very thin ceramic or metal diaphragm which forms one of the electrodes of a capacitor. The pressure is determined by measuring the variation in the capacitance due to the deflection of the diaphragm caused by the pressure difference established across the membrane. In order to minimize zero drift, some CDGs are operated keeping the sensor at a higher temperature. This difference in the temperature between the sensor and the vacuum chamber makes the behavior of the gauge to be non-linear due to thermal transpiration effects. This effect becomes more significant when we move from the transitional flow to the free molecular regime ($Kn > 0.1$). Besides, CDGs may incorporate different baffle systems to avoid the condensation on the membrane or its contamination.

In this work, the thermal transpiration effect on the behavior of a rarefied gas and on the measurements in a CDG with a helicoidal baffle system is investigated by using the Direct Simulation Monte Carlo method (DSMC). This technique is based on the discretization of the number of particles, the space and the time domains, and it combines deterministic aspects for modelling the particle motion with statistical aspects for computing the collisions between particles. The study covers the behavior of the system under the whole range of rarefaction, from the continuum ($Kn < 0.01$) up to the free molecular limit ($Kn > 100$), for various temperature differences and different temperature gradient configurations (with radial and axial components). Moreover, in order to analyse the dynamic response of the system to a change in the sensor temperature from an initial isothermal configuration, some non-steady state calculations are performed. In this way the evolution of the macroscopic properties of the gas is studied from the initial moments until the steady state is achieved.

11:20am VT-MoM10 Direct Conductance Measurements of Laser-Drilled Pinhole Apertures, J.A. Fedchak, D.R. Defibaugh, National Institute of Standards and Technology

A pinhole orifice with a known conductance can be used as a secondary flow standard. We are interested in using pinhole orifices to produce nitrogen gas flows into vacuum in the range of 10^{-11} mol/s to 10^{-6} mol/s (10^{-7} to 10^{-2} cm³/s; STP) for vacuum gauge calibrations because a flowmeter based upon an appropriate set of orifices is easy to operate and automate. Commercially available laser-drilled pinhole orifices with diameters from 1 μ m to 50 μ m can have molecular-flow conductances, C_0 , ranging from about 0.1 μ L/s to 230 μ L/s for N₂ at 23 °C, and can be used to produce gas flows in the range of interest by applying an upstream pressure in the range of 10 Pa to 100 kPa (0.1 to 760 torr). Accurate measurements of the orifice conductance, C , as a function of pressure are required to use the pinhole orifice as a basis of a flowmeter. The NIST bellows flowmeter is a primary gas flow standard that was used to directly measure the conductance of a pinhole orifice to better than 0.2 % over the entire pressure range of interest. We present results of the conductance measurements for nitrogen and other gases. One might expect that the differences among the gases would be mainly due to their different thermal velocities, and that those differences would disappear when the normalized reduced flow rate (C/C_0) is plotted as a function of inverse Knudsen number. However, this was not the case at higher pressures. For example, the reduced flow rate for nitrogen was smaller than for argon at the same inverse Knudsen number. Following a suggestion by Jitschen (Vacuum 76 (2004) 89-100), the effect of the heat capacity ratio on C/C_0 was investigated.

Monday Afternoon, October 31, 2011

Applied Surface Science Division

Room: 102 - Session AS-MoA

Quantitative Surface Chemical Analysis and Technique Development - Part II

Moderator: M.S. Wagner, The Procter & Gamble Company

2:00pm **AS-MoA1 Surface-based Model Systems of Biomolecular Hydrogels - From Supramolecular Organization and Dynamics to Biological Function**, N.S. Baranova, S. Attili, CIC biomaGUNE, Spain, R.P. Richter, CIC biomaGUNE & MPI for Intelligent Systems, Spain
INVITED

Nature has evolved complex materials that are exquisitely designed to perform specific functions. Certain proteins and glycans self-organize *in vivo* into soft and dynamic, strongly hydrated gel-like matrices. Illustrative examples of such biomolecular hydrogels are cartilage and mucus. Although biomolecular hydrogels are ubiquitous in living organisms and fulfill fundamental biological tasks, we have today a very limited understanding of their internal organization, and how they function. The main reason is that this type of assemblies is difficult to study with conventional biochemical methods.

In order to interrogate biomolecular hydrogels directly on the supramolecular level, we have developed an unconventional approach that draws on knowledge from several scientific disciplines. Exploiting surface science tools, such as supported lipid bilayers, we tailor-make model systems by directed self-assembly of purified components on solid supports. With a toolbox of surface-sensitive analytical techniques, including quartz crystal microbalance, ellipsometry, atomic force microscopy and microinterferometry, these model systems can be investigated quantitatively and in great detail. From the experimental data, combined with polymer theory, we develop a better understanding of the relationship between the supramolecular organization and dynamics of biomolecular hydrogels, their physico-chemical properties and their biological function. To illustrate this concept, I will present some of our recent work on the "sweet" jelly-like matrix that forms around the mammalian egg during ovulation (the so-called cumulus cell-oocyte complex matrix) and that is crucial for fertility, and on the proteoglycan-meshwork that contributes to the load-bearing and lubricating properties cartilage.

2:40pm **AS-MoA3 Soft Cluster-Induced Desorption and Ionization of Biomolecules - Influence of Surface Load and Sample Morphology on Desorption Efficiency**, M. Baur, B.-J. Lee, HS Esslingen, Germany, C.R. Gebhardt, Bruker Daltonik, Germany, H. Schröder, K.-L. Kompa, MPI for Quantum Optics, Germany, M. Durr, HS Esslingen, Germany

Neutral cluster-induced desorption and ionization is a very soft method for transferring surface-adsorbed biomolecules into the gas phase [1]. Using neutral SO₂ clusters seeded in a He beam, the method makes use of the dipole moment of the cluster's constituents which allows both for solvation and charge transfer processes in the cluster [2]. Thus the cluster provides not only the energy for the desorption process but also serves as a transient matrix. As a consequence, desorption and ionization of oligopeptides and proteins is observed at low energies of the impacting clusters and without any fragmentation of the biomolecules.

Here we show that cluster-induced desorption and ionization of biomolecules can be efficiently applied for a wide range of surface concentrations and configurations, i.e. from μm -thick films down to surfaces prepared with submonolayer surface concentration of biomolecules. Highest signal intensity in the respective mass spectra was observed from thick films, indicating an efficient desorption mechanism from bulk-like material. In the submonolayer regime, the ion signal of the desorbed biomolecules was found to depend nonlinearly on surface concentration of the wet-chemically applied biomolecules. The behavior is traced back to the formation of multilayered islands of biomolecules on the surface, as observed by means of SEM and AFM, and a dominant contribution to the ion signal from these islands even at low coverage. With the current set-up and preparation scheme, the lower detection limit was shown to be 10^{-13} mol.

[1] C. R. Gebhardt, A. Tomsic, H. Schröder, M. Dürr, and K.L. Kompa, *Angew. Chem. Int. Ed.* **48**, 2009, 4162.

[2] C. R. Gebhardt, H. Schröder, K. L. Kompa, *Nature* **400**, 1999, 544.

3:00pm **AS-MoA4 Sensitive Elemental Analysis of Materials via Femtosecond Ablation Time of Flight Mass Spectrometry**, J.F. Moore, MassThink, S. Milasinovic, Y. Cui, J.S. Penzak, Y. Liu, R.J. Gordon, L. Hanley, University of Illinois at Chicago

A new instrument is described which is capable of delivering ~ 70 fs pulses of 800 nm light to a 100 μm focus; this instrument can ablate small volumes (100-1000 μm^3) of material from a sample (e.g. a 10 μm spot to a depth of 3 μm) and analyze the ions formed in the ablation process by time of flight and quadrupole mass spectrometry. Some novel features of this instrument include (1) a variable pressure source that allows collisional cooling of ions from the ablation plume, (2) the ability to use fs pulse pairs as well as temporally shaped laser pulses with a variable delay line to provide control over the ablation and ion formation process, and (3) a high velocity sample stage combined with a rapid data acquisition system that allows rapid scanning of materials at kHz repetition rate (of ablation events). Results from the ablation of elemental samples (Mg, Al, Si, Cu, Mo, Ag, Ta, Au) and metal alloys will be presented along with microscopy of ablation craters and a discussion of fluence dependence, useful yield, and instrumental sensitivity. Although the current system provides analysis on the micron scale, plans to extend its capability to the nanometer scale and to apply ablation to nanoparticles are being made and will be addressed.

3:40pm **AS-MoA6 Interlaboratory Study on Consistency and Reproducibility of Sputter Rate Measurements**, M.H. Engelhard, D.R. Baer, Pacific Northwest National Laboratory

The method and procedures used by many researchers doing sputter depth profiling has evolved from the experience of many researchers using several generations of sputter ion guns. Often considerable instrument time is used to establish the sputtering rate for specific instrument configuration and operating conditions at the time of analysis. We have conducted an interlaboratory "round robin" study help identify the types of variations actually observed in sputtering systems in use today to help determine the time frame for which calibration may be needed, depending on the type of information required by the analysis. The depth of thin layers was identified as a major information need in surface analysis by surveys done for E42 and ISO TC201. This "round robin" was undertaken as an ASTM International Interlaboratory Study (ILS 229) The results obtained from this study will be used to determine a required frequency of ion gun sputter rate calibration and for the development of a guide or standard.

In this poster we present results obtained from seven ILS-229 participants. Each participant was sent a package containing 7 SiO₂ coupons with known thickness measured using a J. A. Woollam Co. α -SE Spectroscopic Ellipsometer. The participants were asked to perform 5 depth profiles using identical ion gun settings at different time intervals: Immediately after turning the ion gun filament (minimal warm up), after a 60 minutes filament warm up period (typical warm up), at the end of the day (filament on all day), the following day (typical filament warm up of 60 min.), and after one week (typical filament warm up of 60 min.) The sputter rates were determined from a plot of the Si and O intensity as a function of sputter time. The time needed to sputter through the entire SiO₂ layer (when the O signal drops to 50% of the plateau value) is identified as the sputter time. The sputter time t_{sp} is determined using ASTM Standard Practice E 1636-04 "Analytically Describing Sputter-Profile and Linescan Profile data by an Extended Logistic Function". The results demonstrate both the excellent consistency of sputter conditions for many ion gun systems, but also the need to have a process to actually determine the stability of a specific ion gun system and configuration.

4:00pm **AS-MoA7 Post-Acquisition Mass Resolution Improvement in Time-Of-Flight Secondary Ion Mass Spectrometry (TOF-SIMS)**, S.J. Pachuta, P.R. Vlasak, 3M Company

Time-of-flight secondary ion mass spectrometers employing pulsed primary ion beams provide excellent mass resolution, on the order of 10,000 (full-width-at-half-maximum) over most of the spectral range. Unfortunately, even with all instrumental parameters optimized, ultimate mass resolution can only be achieved by sampling a relatively small area on a smooth surface oriented perpendicular to the extraction optics, under a uniform electric field. It is often difficult to meet these four criteria simultaneously.

These criteria fall into two categories, geometric and electrical. Mass resolution degradation due to geometric factors is the result of a distribution of flight times for ions of the same mass, caused by secondary ions originating from different vertical and horizontal positions within the analysis area, and, for rastered primary ion beams, by differences in the flight times of primary ions across the rastered area. Partial correction of these problems can be achieved in real time through hardware and software compensation, but the instrument must be well-tuned. For insulators,

electrical effects may be convoluted with geometric factors and influence mass resolution in a number of unpredictable ways.

For data acquired in “raw” mode (full spectrum at every pixel), it is sometimes possible to correct for these real-world difficulties after data acquisition. Two approaches are employed. The first involves subdividing the analysis area into a regular grid of smaller regions and extracting mass spectra from each region. The extracted spectra are individually calibrated by an automated process, and all or an optimized portion of the spectra are summed to produce a new spectrum with higher mass resolution than the original total spectrum. Interestingly, the spectral calibration information can be used as a diagnostic tool for instrument alignment and tuning.

The second approach is effective for improving mass resolution in spectra of rough surfaces, such as fabrics. Unlike the first approach, the analysis area is not subdivided into a regular pattern. Rather, spectra are obtained from regions of similar height, identified by any of four methods ranging from manual selection of regions-of-interest to automated pixel selection using principal component analysis and multivariate curve resolution. The automated methods have the advantage of simultaneously optimizing the mass resolution and the spectral counts without having to take a trial-and-error approach.

With these methods, mass resolution improvements of 20% - 50% are typical for smooth surfaces, and much larger improvements can be achieved for rough surfaces.

4:20pm AS-MoA8 ToF-SIMS Analysis of Iron Oxide Particle Oxidation by Isotopic and Multivariate Analysis, *J. Ohlhausen, E. Coker, A. Ambrosini, J. Miller*, Sandia National Laboratories

A procedure for quantitative ToF-SIMS analysis of the re-oxidation of iron oxide particles in a ceramic matrix is discussed. Iron oxide is reacted with yttria stabilized zirconia (YSZ) to create a composite that facilitates the high temperature decomposition of CO₂ and H₂O. In the two step process, Fe₃O₄ is partially reduced to FeO by heating to high temperatures (>1300 °C) under inert atmosphere. It is then re-oxidized at < 1200 °C under CO₂ or H₂O yielding CO or H₂ respectively. The reactivity of this two step solar-thermochemical process is being investigated by varying the concentration of iron in YSZ up to and past its solid solubility point, thus affecting the size of iron oxide particles in the matrix, and hence their rate and extent of re-oxidation. For the SIMS experiment, the YSZ sample containing natural abundance iron oxide was mixed with an organic binder, isostatically pressed into a disc and calcined in air at 1450 °C. This disc (~ 10mm diameter, 2mm thickness) was thermally reduced at 1400 °C and then re-oxidized at 1100 °C in the presence of C¹⁸O₂. The ratio of ¹⁸O to ¹⁶O shows the extent of oxygen exchange for each iron oxide particle.

For ToF-SIMS analysis, samples are prepared by cross-sectioning and polishing by conventional metallographic preparation techniques followed by ion milling with Cs⁺ in the ToF-SIMS. ToF-SIMS data are acquired from the cross section only after surface contaminants are removed and a “bulk” condition exists on the exposed surface. Data are acquired in a fashion that maximizes the ability to correct for detector saturation, thus providing quantitative oxygen isotopic results with little error. Data analysis method uses a combination of multivariate analysis for particle identification and conventional analysis for quantitative isotopic ratioing. Details of analysis procedures will be discussed along with results for a range of iron oxide particle sizes.

Sandia National Laboratories is a multi program laboratory managed and operated by Sandia Corporation, a wholly owned subsidiary of Lockheed Martin Corporation, for the U.S. Department of Energy's National Nuclear Security Administration under contract DE-AC04-94AL85000.

4:40pm AS-MoA9 Informatics for SIMS: Identifying Molecules in Complex Mass Spectra, *I.S. Gilmore, F.M. Green, M.P. Seah, J.L.S. Lee*, National Physical Laboratory, UK

High-throughput screening using mass spectrometry for proteomics has driven the need to move from manual methods for protein identification to automated methods. Metabolomics has similar needs owing to the complex chemical mixtures studied. A combination of three important developments has allowed major progress in the automated interpretation of spectra to identify chemical and biological constituent substances. These are (i) the explosion in the amount of publicly available chemical information (PubChem¹, for example indexes over 71 million substances) (ii) advances in mass spectrometry search engines and fragmentation tools and (iii) rapid growth in high performance mass spectrometers (mass accuracy < 1 ppm and mass resolution > 100,000). These recent developments in informatics are the endeavours of a very much larger community than the surface analysis community. We can utilise this rich resource.

We show this in three parts. Firstly, we analyze the popular PubChem database in terms of the population of substances with mass when resolved with typical mass spectrometer mass accuracies². In general, in ToF-SIMS

the mass accuracy is ~ 30 ppm for an unknown substance. For a typical molecule (the modal mass in PubChem¹ is 385 u) there are ~ 30,000 substances within this mass tolerance². In high performance mass spectrometers (~ 1 ppm mass accuracy) this range reduces to ~ 1000 substances which may be further reduced to around 50 substances using isotope pattern matching. Clearly, the mass accuracy in organic SIMS needs to improve significantly to benefit from chemical databases in the same manner as the metabolomics community. Secondly, we have previously shown how G-SIMS simplifies spectra so that the most structurally significant peaks are dominant and we now show a new development called the g-ogram³. This gives a visually simple chromatographic method to interpret spectra and allows separation of, for example, substrate, polymer and molecule peaks based on the fragmentation energy. Thirdly, we show how the G-SIMS spectra are a bridge to the informatics methods used by the metabolomics community providing identification automatically linked to public chemical databases. Present challenges and future opportunities will be discussed.

References

- [1] *PubChem*; National Institute of Health, <http://pubchem.ncbi.nlm.nih.gov/> 2011.
- [2] F M Green, I S Gilmore & M P Seah, *Analytical Chemistry* 2011, dx.doi.org/10.1021/ac200067s
- [3] R. Ogaki, I. S. Gilmore, M. R. Alexander, F. M. Green, M. C. Davies and J. L. S. Lee, *Analytical Chemistry* 2011, dx.doi.org/10.1021/ac200347a

5:00pm AS-MoA10 keV Ion Impact Effect on the IonCCD™ Surface and Mass Spectra Peak Shape in Non-Scanning Sector-Field Instrument, *O. Hadjar, G. Kibelka, S. Kassan, C. Cameron, K. Kuhn*, OI Analytical

Particle-surface interactions are very important processes making physics practically impossible to apply without putting those interactions into the equation. For particle detection applications, the detection event is triggered by total or partial particle energy deposition upon impact on the detector. Mass spectrometry common ion detectors are Channeltrons and MCPs, which inherently destroy the particle upon measurement. The IonCCD, a product from the rapidly emerging technology will be characterized against keV ion impact when used in a dispersive mass analyzer.

The IonCCD is used as focal plane array in a sector field instrument of Mattauch-Herzog geometry (MH-MS). When miniaturized, MH-MS is best suited for low mass range applications (< 100 u). Differently from the two first detector families that most often operate in particle counting mode (time resolved detection) the IonCCD operates in an integration mode (charge integrator). In this case, dispersed ions neutralize on the electrode pixels for a well-defined time known as the integration time. While the potential energy of the detected ions is used for detection, the ion kinetic energy leads to ion-surface interaction, an artifact amplified at extreme low mass detection. This latter can be eliminated by floating the IonCCD or operating it in higher magnetic fields.

The artifact manifesting in the mass spectra as distortion (negative peak) due to keV ion impact induced secondary electron emission was modeled and investigated experimentally using electronic stopping power fingerprints. We demonstrate that the artifact increases linearly with ion impact velocity and is dependent in an oscillatory fashion on ion nuclear charge. Both findings are in agreement with the electronic stopping of keV ions with the TiN surface of the IonCCD. 3D simion modeling suggests efficient peak artifact suppression by operating the IonCCD in higher B-field (> 4000 G) and less elegantly by IonCCD-magnet face retarding field. Same model was used to enhance the performance of the instrument, confirming the dynamic mass range (Mmax/Mmin) increase from 16 to 70.

The potential IonCCD damage upon keV ion impact through the nuclear stopping effect was investigated by means of Atomic Force Microscopy and X-ray Photoelectron Spectroscopy. While AFM confirmed the expected increase in surface roughness, XPS showed no stoichiometry change due to implantation or preferential ion sputtering. The discoloration observed after extensive use was related to carbon layer formation in the roughened irradiated pixel area. Nuclear stopping effects do not seem to affect the detector performance at practical doses.

5:20pm AS-MoA11 First use of ToF-SIMS for Screening Assays: Enzymes Active on Wood, *R.E. Goacher, E.A. Edwards, C.A. Mims, E.R. Master*, University of Toronto, Canada

Proteomic and metagenomic studies are rapidly increasing the number of proteins available for enzymatic screening. However, current high-throughput enzyme assays have limited applicability for an important class of biochemical substrates – complex solid materials. The present work aims

to utilize the strengths of Time-of-Flight Secondary Ion Mass Spectrometry for the direct measurement of enzyme activity on solid substrates. Particularly, ToF-SIMS is applied to the detection of wood-modifying enzymes.

Proof-of-principle ToF-SIMS enzyme assays were performed by immersing extracted wood fibers in solutions of commercial cellulase and laccase enzymes (utilizing water/buffer and denatured enzymes for controls). The laccase enzyme was also tested with and without several small molecule mediators. Principle Component Analysis (PCA) clearly distinguished cellulase tests from controls through the loss of polysaccharide peaks and relative enrichment of lignin peaks. Additionally, PCA distinguished laccase test samples (with mediator) from controls through a shift in lignin-characteristic peaks. The active laccase was indicated by a relative decrease in guaiacyl-lignin and syringyl-lignin peak intensities and increase in generic aromatic peaks, resulting from the cleavage of hydroxyl and methoxy groups from lignin benzoid units.

These proof-of-principle assays demonstrate that ToF-SIMS is capable of providing yes/no screening information for enzyme activity on complex solid substrates, such as wood.

[1] R. E. Goacher, D. Jeremic, E. R. Master. Analytical Chemistry 83(3), 2011, 804-812.

Biomaterial Interfaces Division

Room: 108 - Session BI-MoA

Sensors and Fluidics for Biomedical Applications

Moderator: E. Reimhult, University of Natural Resources and Life Sciences, Austria

2:00pm BI-MoA1 Three-dimensional Microfluidic Flow Cell Array Integrated with SPR Microscopy for Multi-channel Bioassays, J.S. Shumaker-Perry, University of Utah **INVITED**

The expanding development and implementation of biotherapeutics to treat a wide range of diseases, including autoimmune diseases and cancer, have increased the need for immunogenicity assessment of these therapies. Immunogenicity is an immune system response of a patient to a drug. Anti-drug antibodies (ADAs) produced during the immune response may cause serious adverse effects such as reducing drug efficacy, altering pharmacokinetics, causing infusion reactions including anaphylaxis and serum sickness, and neutralizing native proteins. The complexity of immunogenicity analysis presents challenges in identifying and characterizing the neutralizing activity of ADAs. We have integrated a three-dimensional microfluidic flow cell array (MFCA) with surface plasmon resonance microscopy (SPRM) for a multi-channel, array-based approach to immunogenicity assessment. The microfluidic device provides 48 separate flow channels that can be used simultaneously for biomolecule immobilization and subsequent array-based biomolecule interaction analysis. Because the biomolecules can be immobilized *in situ*, exposure to harsh environments can be avoided, a major benefit for protein immobilization. In addition, the biomolecule immobilization process can be monitored in real time by SPR microscopy. This versatile, multi-channel biomolecule interaction analysis platform is being developed for ADA assessment which will benefit from the ability to implement controls, identify optimal assay conditions, and obtain detailed data about the nature of the biomolecule interactions. Characterization of the integrated system and initial investigations related to ADA assessment will be presented.

2:40pm BI-MoA3 Transport Properties of Proteins and Quantum Dots in Nanochannels in Multi-Gated Field-Effect-Transistor Configuration, L. Tribby, University of New Mexico, F. Van Swol, Sandia National Laboratories, C.F. Ivory, Washington State University, S.M. Han, University of New Mexico

The use of nanofluidic architectures as a means of concentrating and separating biomolecules, nanoparticles, and other small species of similar size scale may prove useful in developing new bioseparation and detection technologies. Recognizing this potential, a variety of nanofluidic devices have emerged that utilize enhanced electrokinetic control of fluid and molecular/particle motions at these scales. In our study, we have fabricated an array of slit-like nanochannels (100 nm w x 400 nm d x 15 mm l) in a multi-gated field-effect-transistor configuration, using interferometric lithography and conventional top-down fabrication techniques. Our main objective in developing such a dynamically controllable separation platform is to further increase our ability to rapidly concentrate and separate proteins (or nanoparticles) that have low abundance or require long separation time by conventional methods. In order to produce effective separation strategies, we have first experimentally characterized electrokinetic

transport properties of proteins and nanoparticles within our device. Based on this characterization and understanding, we report a technique to form highly concentrated protein bands in our nanochannels. We will also report observable differences in electrokinetic mobility for semiconductor nanocrystals in aqueous solutions whose surface is functionalized with organic ligands to assume different charges. These results and their implications towards nanofluidic separation techniques will be further discussed.

3:00pm BI-MoA4 High Sensitivity Recessed AlGaIn/GaN HFET Protein Sensors, X. Wen, H. Kim, P. Casal, S. Lee, W. Lu, The Ohio State University

We have demonstrated the improvement of sensitivity by biasing the AlGaIn/GaN HFET biosensors into the subthreshold regime. To bias the channel into the subthreshold regime, $V_g \approx -4$ V was. The gate voltage causes ions in the physiological buffer solution to move and result in measurement noise. To avoid side effects from a high gate voltage, we adopted the gate recess process to shift the subthreshold gate voltage to zero/near zero volt and retain high sensitivity.

The AlGaIn/GaN heterostructure used in this study has a 23 nm thick undoped AlGaIn barrier. The recession of AlGaIn barrier was conducted with an Oxford Plasmalab 100 system. A two-step recession process was used. The first step uses BCl_3 to etch the AlGaIn barrier and the second step uses a combination of $\text{Cl}_2/\text{N}_2/\text{O}_2$ to passivate the etched surface. To achieve zero/near-zero subthreshold gate voltage, we recessed devices with the first step duration to be 50, 55, 60, 65, and 70 sec respectively. We also fabricated diodes with the Schottky area recessed with the same conditions to check the material property changes. The measured C-V characteristics show that the threshold voltage shifts along the positive direction with the increase of etching time. With 70 sec etching time, the threshold voltage of Ni diodes achieve subthreshold regime at $V_a=0$ V. Extracted from C-V curves, the etched depths are 12.0, 11.6, 11.2, 9.7, and 8.8 nm respectively. AFM measurements of both recessed and original AlGaIn surfaces show that the surface smoothness is improved after recession processes.

The fabricated AlGaIn/GaN HFET biosensors have a recessed gate of 100 μm (L) \times 2 mm (W). To detect streptavidin, the AlGaIn surface was modified by silanization and biotinylation. The measured I_d - V_g curves of AlGaIn/GaN HFETs with (a) recession time of 65 sec, and without any recession. There are two major differences: 1) the threshold voltage of recessed device shifted to around 0 V; and 2) the off-state current of recessed device is 1-2 orders lower. The threshold voltage promises high sensitivity when the gate is floating or biased at a very low voltage. The decrease of the off-state current indicates that signal-to-noise ratio is improved. The difference between the threshold voltage of diodes and HFETs mainly because of 1) the diode Schottky metal is Ni and the HFET gate is PBS and 2) the HFET is treated with oxygen plasma for surface modifications. The detection of 25 pg/ml (473 fM) SA solution in 1X PBS shows that the drain current is decreased by 22.7% because SA carry negative charges in PBS solution. The sensitivity is increased by one order compared to our previously published results with non-recessed devices.

3:40pm BI-MoA6 AlGaIn/GaN HFETs for DNA Sensing: Charge Layer Distance Dependence, Y. Wang, W. Lu, The Ohio State University

AlGaIn/GaN heterostructure features two-dimensional electron gas which is highly sensitive to proximal charges and excellent stability against chemicals. These unique advantages imply the potential of AlGaIn/GaN based field effect transistor (FET) in facilitating various biological and chemical studies. We have previously reported the detection of hybridization between probe DNAs and fully complementary target DNAs with AlGaIn/GaN HFET biosensors. To further improve the sensitivity, comprehensive understanding of the working principle is necessary. In this work, we focus on a systematical investigation on the effects of the distance between the charged layer and the sensing surface, i.e., the distance from target DNA biomolecules to the AlGaIn surface. We immobilized a monolayer of single-strand probe DNAs modified with thiol groups on the Au-coated active gate surface of an AlGaIn/GaN HFET. Different target ssDNA molecules were designed so that distance between the hybridization sites and the AlGaIn surface varied. Experimental results show an explicit relationship between the detection sensitivity and the charge layer distance.

Six types of synthesized 25-mer oligonucleotides (Allele) solutions were prepared, including a probe DNA, a fully complementary target DNA, a 21-bp complementary DNA, a 13-bp complementary DNA, a 9-bp complementary DNA and a mismatched DNA. The amount of charges is assumed identical for DNAs with a constant length. The distance of the charge layer can be well controlled by varying the hybridization sites of target DNAs to the probe DNAs. For example, the 21-bp complementary DNA is 4-bp further away from the surface than the fully complementary DNA.

We compared the I_{DS} - V_{DS} characteristics of devices before and after hybridization. A decrease of drain current was noticed, revealing the binding of negatively charged DNAs. More importantly, the decreases in I_{DS} - V_{DS} demonstrated a clear dependence of charge layer distance by an observation of the current change ratio, defined by $\Delta I_{DS} / I_{DS}$, (gate bias: -1 V): 16.1% for fully complementary target DNA (0.1 μ mol), 14.9% for 21-bp complementary DNA, 10.9% for 13-bp complementary DNA, 6.89 % for 9-bp complementary DNA, and 0.75% for mismatch DNA, which was comparably insignificant. The current change decreases with the distance between the target DNA and sensing surface, although the amount of charges for the target DNA is constant. These results demonstrate that the detection sensitivity is significantly dependent on the charge layer distance. Theoretical analysis for varying charge layer distances of target DNAs will also be studied and compared with the experimental results.

4:00pm BI-MoA7 Effect of Analyte Flow Rate on the Sensitivity of Microcantilever Biosensors, R.P. Desikan, C.W. Van Neste, T.G. Thundat, University of Alberta, Canada

The past decade has witnessed the use of microcantilevers as mechanical transducers of molecular recognition and for the development of miniaturized and sensitive biochip platforms. Microcantilever based biosensors can be based on either mass adsorption or surface stress variation. The potential to operate a microcantilever sensor in liquid medium with extreme sensitivity makes it an ideal choice for the development of biological sensors. Selective detection is obtained by immobilizing receptor molecules on one side of the cantilever. Microcantilever based biological sensors predominantly operate in a liquid environment; this is done in order to retain the functionality of the biomolecules immobilized on the surface. Typically reference cantilevers serve to observe and analyze the effect of non specific interactions and fluid flow rate from specific biomolecular interactions. We have additionally observed that the interaction of analytes on the functionalized surface of the cantilever is influenced by the varying the flow rate of the solution used. The surface stress observed due to the adsorption of analyte molecules on to the receptors on cantilever surface in static condition is much higher compared to a dynamic condition where analyte molecules are allowed to flow across the cantilever surface with the help of a flow control system. Here we address the effect of flow rate on the biomolecular adsorption kinetics of the system and how it affects the sensitivity of Microcantilever based biological sensors.

4:20pm BI-MoA8 Fabrication of Nanowire FETs for pH Sensing, C. D'Emic, S. Zafar, A. Afzali, B. Fletcher, T. Ning, M.A. Guillorn, D.-G. Park, IBM T.J. Watson Research Center

Sensors for measuring pH are very important for understanding reactions of biological species such as proteins, enzymes and cells. While traditional sensors based upon such techniques as infrared spectroscopy, fluorescence and others have low sensitivity and slow response time, more recent nanowire field effect transistor sensors offer improved sensitivity and response time due to smaller size and increased surface areas. [1, 2]

We have fabricated nanowire FET sensors using conventional CMOS semiconductor processes. The nanowires were patterned by electron beam lithography and reactively ion etched into 30 nm thick silicon on insulator (SOI) substrates. The gate sensing surface is comprised of a hafnium oxide/silicon dioxide stack covering the nanowire, while the source/drain regions are comprised of boron activated SOI with nickel-platinum silicide contacts. The resulting 16 nm wide nanowire devices show high sensitivity for pH measurements. The FET drain current increases by a factor of eight per unit change in pH, while the subthreshold slope is ~ 77 mV/decade. The sensors operate at a reduced sensing voltage of 0.5 V, making them promising candidates for low power, bio-medical applications.

[1] E. Stern, J. Klemic, et al., Nature, 445 (2007) 519

[2] S. Zafar, C. D'Emic, et al, to be published

4:40pm BI-MoA9 La³⁺ doped TiO₂ Nano-engineered Platforms for Biosensor, R.R. Pandey, Centre for Cellular and Molecular Biology, India, K.K. Saini, National Physical Laboratory, India, M. Dhaval, Centre for Cellular and Molecular Biology, India

The use of nanotechnology tools has opened new opportunities to explore analytical applications of the nano-engineered materials which attracted great attention due to their unique morphology, extraordinary physical and chemical properties towards development of biosensors to facilitate the improvement of the selectivity and sensitivity of the current methods. In this work, the importance of semiconducting La³⁺ doped TiO₂ a metal-oxide-based nanostructure platform is highlighted for biosensors platforms. La³⁺ doped TiO₂ nanostructure having nanometer-scale inner-core cavity which were exposed to the outer surface with different oxidation states having possibilities for redox-activity can make them attractive for sensing uses. Therefore, the use of La³⁺ doped TiO₂ for the development of

electrochemical sensors will be discussed. These platforms has been characterized by XRD, XPS, FTIR, SEM, cyclic voltametry to determine structure, surface chemistry and electron transfer characteristics for biosensor applications. Cholesterol oxidase immobilized onto La³⁺ doped TiO₂-based nanostructured surfaces exhibited a pair of well-defined and quasireversible voltammetric peaks in CV measurements. We will also discuss the potential prospect of these surfaces as low cost stable platforms for biomedical diagnosis.

5:00pm BI-MoA10 Spray Deposition of Functional Antibody Films, J. Figueroa, S. Magana, D. Gomez, D.V. Lim, R. Schlaf, University of South Florida

Antibody films for the use in biosensors and assays are usually deposited via wet-chemical attachment methods. The presented experiments demonstrate that pneumatic spray deposition of antibody thin films from aqueous solution yields films of similar sensitivity and durability without special surface treatments and attachment chemistries. The experiments were performed using a commercially available low flow nebulizer in combination with a syringe pump and a substrate rotation stage to homogenize the coating.

In the experiments E. coli O157:H7 antibody was deposited on cleaned microscopy glass slides without any other pre-treatment. Standard wet-chemically prepared silanized glass slides using the avidin-biotin attachment scheme were also prepared for direct comparison of sensitivity and longevity of the spray based substrates. After incubation with GFP-labeled E. coli O157:H7 cells (ATCC 35150) ranging from 10⁴-10⁶ CFU/ml the slides were rinsed and AF647-labeled detector antibody was added and incubated. After rinsing and drying the slides were interrogated with a 635 nm laser and visualized using a CCD camera. Slides were also visualized by epifluorescence microscopy to examine antibody patterns and determine E. coli capture efficiencies.

The results of the experiments demonstrate that there is little difference between spray and standard protocol wet-chemically prepared substrates. This indicates that antibody films can be prepared via physisorption without complex attachment chemistries, and that antibodies can directly attach to glass slides, while retaining their functionality.

5:20pm BI-MoA11 Microfluidic Extraction of Human Chromosomal DNA from Single Cells, J. Topolancik, H.C. Tian, C.B. Wallin, D.R. Latulippe, J.J. Benitez, B.R. Cipriany, P.J. Murphy, P.D. Soloway, H.G. Craighead, Cornell University

Genome-wide analysis of single cells is important in life science research and modern medicine in applications ranging from cancer diagnosis to understanding tissue development. Microfluidic devices have been explored as a promising platform for single cell studies, providing superior handling of minute sample and reagent volumes in engineered microstructures. Isolation of nucleic acids from biological samples is an essential step of every type of genetic analysis. While numerous extraction methods have been explored, it remains rather challenging to isolate and analyze genomic DNA from small cell populations and individual cells. Traditional microfluidic devices utilize solid phase extraction (SPE), a method based on binding of DNA to chemically functionalized solid phase matrices for separation of nucleic acids from cell lysates. The binding affinity is sensitive to factors such as pH, temperature, and buffer composition which must be controlled, often dynamically, to minimize DNA losses. Even when the extraction process is optimized, it is difficult to ensure that all of the DNA fragments are adsorbed on the solid phase matrix and that the whole genome is represented in the purified extracts. An appreciable fraction of genomic DNA is often lost during the purification process when the cell debris is washed away. Additional DNA losses can be caused by incomplete lysis. State-of-the-art microfluidic devices for DNA separation from cell lysates exhibit rather modest extraction efficiencies of 60-85%. This is sufficient for genetic analysis of cell populations because multiple copies of every gene are present in the extract, which statistically guarantees complete genome coverage, but such losses are hardly acceptable when single-copy genes in a single cell need to be investigated. This work describes a valveless two-port microfluidic device for highly-efficient isolation and fluorescent analysis of DNA contents of single cells. Long strands of human chromosomal DNA released from the cell by chemical lysis loop around PDMS micropillars and are physically retained while the remaining cellular contents are washed away under hydrodynamic flow. DNA fragmentation is minimized by operating at low flow rates. Hydrodynamic entrapment of DNA in non-functionalized obstacle arrays allows separation of very large genomic DNA from cell debris and components such as proteins and membrane fragments as well as from much smaller mitochondrial DNA and RNA. The purified DNA was subsequently released from the device by enzymatic fragmentation with restriction endonucleases under continuous flow and collected for fragment-size analysis and evaluation of the extraction efficiency. Fluorospectrometric measurements indicate that the microdevice extracts

>95% of genomic DNA, which outperforms all alternative microchip-based extraction methods.

Electronic Materials and Processing Division

Room: 209 - Session EM1-MoA

Group III-Nitrides and Hybrid Devices

Moderator: K. Kavanagh, Simon Fraser University, L. Porter, Carnegie Mellon University

2:00pm **EM1-MoA1 Electrically-Monitored Gate-Recess for Normally-Off AlGaIn/GaN High-Electron Mobility Transistors**, *H. Kim, M. Schuette, W. Lu*, The Ohio State University

GaN-based power devices have been intensively investigated for high power switching applications as well as high power microwave applications. Particularly, high breakdown voltage and high saturation velocity of GaN-based heterostructures facilitate reduction in on-state loss and switching loss compared to currently dominant Si-based power devices. Moreover, normally-off GaN-based power field-effect transistors (FETs) offer their inherent safety, reduced power consumption, and diverse circuit functionality with normally-on ones. Recently, we developed a zero-bias Cl-based dry etching process to thin AlGaIn barrier with a minimal damage for enhancement-mode AlGaIn/GaN FETs. However, it has been difficult to control gate-recess process for normally-off GaN-based FETs due to strong polarization effects. Namely, 1 nm under- or over-etchings near the critical AlGaIn barrier thickness where the channel is pinch-off result in a negative threshold voltage (V_T) or a degraded transconductance (G_m), respectively. In this work, we report a methodology to control our Cl-based gate-recess for both positive V_T and high $G_{m,MAX}$ by relating electrical properties of the gate-recessed area before gate metallization to V_T and G_m in AlGaIn/GaN FETs.

Gate-recessed AlGaIn/GaN FETs were fabricated through fast etching with BCl_3 and slow etching with $\text{Cl}_2/\text{N}_2/10\%-\text{O}_2$ to thin AlGaIn barrier. The slow etching runs under inductively-coupled plasma mode only to minimize the damage. For monitoring purpose, resistance at 0 V (R_{0V}) and drain-to-source current ($I_{D,SAT}$) at 10 V between source and drain contacts were measured before gate metallization to correlate with V_T and G_m after gate metal deposition.

I_D - V_{GS} , G_m - V_{GS} , and capacitance-voltage characteristics of gate-recessed FETs with different AlGaIn thicknesses by doing $\text{Cl}_2/\text{N}_2/10\%-\text{O}_2$ etching for different times were measured and V_T values were extracted by linear extrapolation at $G_{m,MAX}$. V_T and $G_{m,MAX}$ were correlated with the monitoring parameters of R_{0V} or $I_{D,SAT}$. V_T and $G_{m,MAX}$ distributions with R_{0V} or $I_{D,SAT}$ guide us for monitoring as well as design of gate-recess process. For example, a recessed FET showing $R_{0V} = 1700 \text{ W}$ with 7 nm AlGaIn barrier exhibits V_T of 0.56 V and $G_{m,MAX}$ of 300 mS/mm. In addition, our recess process offers sufficiently long monitoring time (at least 4 minutes) to tune the gate recess for target V_T together with high $G_{m,MAX}$. Based on the distribution, the necessity of tuning process is determined and its progress is monitored by R_{0V} or $I_{D,SAT}$ before gate metallization until target R_{0V} or $I_{D,SAT}$ is met. Our electrically monitoring method allows gate recess process to be well-controlled for target V_T and $G_{m,MAX}$.

2:20pm **EM1-MoA2 Atom Probe Tomography Studies on Green Light Emitting InGaIn/GaN Multi Quantum Wells Grown on GaN Substrates**, *F. Liu, L. Huang*, Carnegie Mellon University, *S.V.N.T. Kuchibhatla, D.K. Schreiber*, Pacific Northwest National Laboratory, *M. Zhang*, University of Michigan, *E.A. Preble, T. Paskova, K.R. Evans*, Kyma Technologies, Inc., *L. Porter, R.F. Davis*, Carnegie Mellon University

Carrier delocalization in InGaIn/GaN multi-quantum wells (MQW) contained within green light-emitting diodes (LEDs) has been proposed as a contributor to LED efficiency droop. By contrast, interface roughness and fluctuations in composition within the MQWs may act to localize and confine carriers¹. In this study, InGaIn/GaN MQWs were grown on both (0001)GaN layers and on $\text{In}_x\text{Ga}_{1-x}\text{N}$ buffer layer with graded In mole fractions from 0 to 10%. Both heterostructures were grown on chemomechanically polished (0001)GaN substrates. Calculations using temperature-dependent photoluminescence spectra revealed a four-fold increase in the internal quantum efficiency (IQE) in the latter structure. A LEAP 4000X HRTM pulsed UV laser (355 nm at 200 kHz) atom probe tomograph was used to investigate the elemental and spatial characteristics of the interface of the $\text{In}_x\text{Ga}_{1-x}\text{N}/\text{GaN}$ MQWs. To establish consistent atom probe operation parameters for reliable comparison among different samples, a systematic study was conducted to optimize the evaporation rate and laser energy. The concentration profile of $\text{In}_x\text{Ga}_{1-x}\text{N}/\text{GaN}$ MQW showed slightly varied In fraction among different QWs, ranging from $x=0.21$ to $x=0.27$, while the XRD results showed an average In fraction in

all QWs of $x=0.25$. Furthermore, based on isoconcentration surface analysis and proximity histograms the upper surfaces of InGaIn QWs appear to be more diffuse than the lower surfaces. These results indicate surface roughening of the InGaIn layer. A detailed comparison of the two structures will be presented and the ability of 3-D atom probe tomography for such an analysis and the impact of the results on next generation LED technologies will be discussed.

1. J. Hader, J. V. Moloney and S. W. Koch, Appl. Phys. Lett. **96** (22), 221106 (2010).

2:40pm **EM1-MoA3 Local Surface Electrical Characterization of Polar GaN Surfaces**, *J.D. Ferguson, M.A. Reshchikov, A.A. Baski*, Virginia Commonwealth University

While GaN is a widely-used material in optoelectronic devices, localized surface-related electrical properties are not well-understood. These properties affect the operational performance and lifetimes of GaN-based devices. Here, several atomic force microscopy (AFM) techniques were used to characterize the Ga-polar, +c [0001], and N-polar, -c [0001 $\bar{1}$], surfaces of free-standing bulk GaN. Samples were prepared by either a chemical-mechanical polish (CMP) or mechanical polish (MP) of HVPE-grown GaN. AFM data showed that the Ga-polar surfaces (MP and CMP) were uniformly flat with rms roughness of less than 1 nm over a 5x5 micron image. In contrast, the N-polar surfaces were significantly rougher (~5 nm rms) with scratch-like features (100 nm wide, microns long), where the CMP treatment resulted in the presence of surface protrusions (~100 nm dia.) in proximity of the scratches. We then examined the local electrical properties using conducting AFM (C-AFM) to map surface conductivity and to obtain I-V spectra. C-AFM images at forward-bias (<6V) showed small contrast variations for all samples except the N-polar CMP surface. In that case, we observed less conducting behavior on the protrusions as compared to the surrounding surface. Local I-V data also revealed a higher forward-bias, turn-on voltage for the N-polar vs. Ga-polar samples. To investigate the local surface charging behavior, we used a two-step technique. First, a metallized AFM tip was used to locally charge the surface by applying a DC voltage, and then the resulting change in surface potential was monitored as a function of time with scanning Kelvin probe microscopy (SKPM). These surface charging data showed a smaller change in surface potential for the N- vs. Ga-polar samples, which appears to be consistent with the lower onset of conduction for the N-polar orientation. Finally, we measured the photo-induced changes in surface potential under UV light exposure (100W Hg lamp), otherwise known as the surface photovoltage effect (SPV). The N-polar samples had a smaller SPV compared to Ga-polar, which indicates a smaller amount of band bending at the surface. Additionally, N-polar GaN restored to dark-state conditions at a much faster rate, regardless of CMP or MP treatment. In summary, we observed differences in morphology and electrical behavior for the two polar, c-plane GaN surfaces, as well as differences in behavior due to CMP and MP treatments. These data suggest a less pronounced surface charging behavior on N-polar vs. Ga-polar GaN.

3:00pm **EM1-MoA4 The Effect of Ammonia - TMI Pulse Separation on the Structural Properties of InN Epilayers**, *R. Atalay*, Georgia State University, *M. Buegler*, Technische Universität Berlin, Germany, *S. Gamage, I. Senevirathna, A.G.U. Perera*, Georgia State University, *J.S. Tweedie, R. Collazo*, North Carolina State University, *N. Dietz*, Georgia State University

Over the last decade, significant research efforts have been devoted to understand and improve the properties of InN epilayers. However, even today, there is a significant lack of understanding of the InN surface and growth chemistry and its affect on the physical bulk properties. Crucial challenges in the growth of InN epilayers are the vast different partial pressures between indium and nitrogen and associated fragments of the utilized precursors trimethylindium (TMI) and ammonia (NH₃).

In this work, high-pressure chemical vapor deposition (HPCVD) is employed and explored in order to control and suppress the disassociation of InN alloys at higher growth temperatures. In order to reduce gas phase reactions and to control the surface chemistry, a pulsed precursor injection approach has been implemented, which provides additional process control parameters for the optimization of the physical epilayers properties.

In the pulsed precursor injection approach, the precursor separation times between the metal organic (MO) sources (TMI and TMG) and ammonia (S1), and ammonia and MO (S2) are two critical process parameters.

This contribution will present results on how the precursor separation times between the TMI and ammonia (S1) and ammonia and TMI (S2) affect the structural and optical properties of InN epilayers grown on GaN/sapphire templates and/or sapphire substrates. In this study, the separation times S1

and S2 have been varied from 1000 to 2500 ms and 250 to 500 ms, respectively. The results show that a longer S1 separation of around 1700 ms and short S2 separation of around 360 ms provide the best structural properties of InN epilayers.

The InN epilayers have been analyzed by Raman scattering, X-ray diffraction, IR reflection, and transmission spectroscopy. The Raman studies showed that the lowest FWHM of E2(high) vibrational mode with about 8 cm⁻¹ for a S2 separation time of 358 ms. XRD 2 θ - ω scans on these InN epilayers and the analysis of the InN (0002) Bragg reflex confirm the improved structural properties for the optimized S2 separation.

3:40pm EM1-MoA6 Neutron Scattering Provides a New Model for Optimal Morphologies in Organic Photovoltaics: Rivers and Streams, M. Dadmun, W. Yin, University of Tennessee, J. Ankner, K. Xiao, Oak Ridge National Laboratory

Organic Photovoltaics (OPVs) have attracted increasing interest as a lightweight, low-cost and easy to process replacement for inorganic solar cells. Moreover, the morphology of the OPV active layer is crucial to its performance, where a bicontinuous, interconnected, phase-separated morphology of pure electron donor and acceptor phases is currently believed to be optimal. In this work, we use neutron scattering to investigate the morphology of a model OPV conjugated polymer bulk heterojunction, poly[3-hexylthiophene] (P3HT) and surface-functionalized fullerene 1-(3-methoxyxycarbonyl) propyl(1-phenyl [6,6]) C₆₁ (PCBM). These results show that P3HT and PCBM form a homogeneous structure containing crystalline P3HT and an amorphous P3HT/PCBM matrix, up to ca. 20 vol% PCBM. At 50 vol% PCBM, the samples exhibit a complex structure containing at least P3HT crystals, PCBM crystals, and a homogeneous mixture of the two. The 20 vol% PCBM samples exhibit behavior consistent with the onset of phase separation after 6 hours of thermal annealing at 150 °C, but appears to be miscible at shorter annealing times. This suggests that the miscibility limit of PCBM in P3HT is near 20%. Moreover, for the 50 vol% PCBM sample, the interface roughens under thermal annealing possibly owing to the growth of PCBM crystals. These observations suggest a different morphology than is commonly presented in the literature for optimal bulk heterojunctions. We propose a novel 'rivers and streams' morphology to describe this system, which is consistent with these scattering results and previously reported photovoltaic functionality of P3HT/PCBM bulk heterojunctions.

4:20pm EM1-MoA8 Novel Boron Carbide-Based Semiconducting Polymers for Enhanced Electronic Properties, F. Pasquale, J. Kelber, University of North Texas

We report the controlled modification of valence band electronic structure of semiconducting boron carbides with sharply narrowed band gap, by combination of 1,4 diaminobenzene (DAB) with orthocarboranes to form a novel boron-carbide based semiconducting film. Semiconducting boron carbide films (B₁₀C₂H_x) and related materials formed from crosslinking of carborane icosahedra are of rapidly increasing interest in neutron detection, nanoelectronics, spintronics, and even conventional CMOS ULSI applications. The ability to modify the material's electronic structure in a controlled manner is of obvious interest in all these areas. We report x-ray and ultraviolet photoelectron spectra (XPS, UPS), demonstrating that electron-induced cross-linking of carborane and DAB results in a novel semiconductor with a significantly enhanced valence band density of states near the Fermi level, resulting in a shift, as determined by UPS, in the valence band maximum from ~ 4.3 eV to ~ 1.7 eV below the Fermi level. Importantly, this effect is relatively insensitive to total film thickness and for DAB/orthocarborane atomic ratios (determined by XPS) ranging from 1:4 to 1:1. Films were formed by condensation and cross-linking of alternating layers of orthocarborane and DAB precursors under ultrahigh vacuum (UHV) conditions, allowing precise control of relative DAB and carborane concentrations. This procedure also yielded films of systematically varied DAB/carborane concentration and film thicknesses between 20 Å and 100 Å average thickness, as determined by attenuation of Cu(2p_{3/2}) photoemission intensity from the substrate. The films exhibited shifts in the valence band spectra of ~ 0.2 eV to lower binding energies upon cross-linking, indicating a surface photovoltage effect, and the formation of a true *p*-type semiconducting film. The results demonstrate formation of a new semiconducting material based on carborane icosahedra but modified by the addition of an organic species. These data further indicate the potential for the development of a broad range of novel boron carbide-based polymers using carboranes and other organic additives, with film formation by a variety of methods, including photon or electron bombardment, or plasma-enhanced chemical vapor deposition.

4:40pm EM1-MoA9 Analysis and Application of Hybrid Electronic Structures Formed by Nanoscale Conductive Coatings on Textiles, J.S. Jur, W. Sweet, C.J. Oldham, G.N. Parsons, North Carolina State University

Electronic functionalization of complex fibrous systems is of interest for developing new hybrid electronic systems geared toward integrating biological detection and energy harvesting devices in textile materials. Reliable methods to evaluate the electrical properties of these textiles are necessary for future device design and performance improvement. This work investigates conformal, nanoscale coatings of zinc oxide and tungsten produced by atomic layer deposition (ALD) on natural and synthetic fibers structures, resulting in novel hybrid-based electronic structures. A modified 4-probe test method is introduced to evaluate the effective conductivity of these coatings. An applied normal force orthogonal to the current and field direction improves the fiber/fiber contact, resulting in consistent evaluation of the effective conductivity of the coatings across fiber systems and is a unique method of evaluating the mechanical behavior of these coated fiber structures. Optimization of the coatings has resulted in conductivity values as high as 40 S cm⁻¹ for zinc oxide coatings (~75 nm) on polypropylene and cotton fiber, as well as 1150 S cm⁻¹ for ALD tungsten (~50 nm) on quartz fiber matrices. Device application of these coated fiber matrices are benefited by their "all-fiber" structure, with characteristic high porosity and surface area. For example, a textile-based flow-through metal-insulator-metal capacitors fabricated from tungsten-coated quartz fibers is shown as an application in liquid chemical sensing. The mechanisms related to electron transport in a surface-coated textile fabric and implications on device fabrication and improvement will be discussed.

5:00pm EM1-MoA10 Quantum Dot Transfer using Patterned Self-Assembled Monolayers, S. Miller, A.J. Muscat, University of Arizona

Nano particles such as light emitting quantum dots offer many exciting new possibilities for device manufacturing. Along with the potential for low cost manufacturing, the ability to make quantum dot based solar cells and LEDs, has lead to the potential to make arrays of light detectors and nanometer scale patterned LEDs. Using two such devices together results in an optical switch, which may be employed in computer processing as a fast memory readout device. In addition ROM memories can be created using direct patterning of light emitting quantum dots on a disk. Because quantum dots of different size emit different wavelengths it is possible to code data in several wavelengths allowing the data from each wavelength to be written in the size limited area of focused light, dramatically increasing data storage. Many of the potential devices which can be made using nano particles require precise control over nano particle placement and layer thickness. We have found that it is possible to control quantum dot placement using a patterned self-assembled monolayer (SAM). Due to the hydrophobic properties of octadecyltrichlorosilane (OTS) it is possible to form an OTS SAM on which quantum dots will not deposit. This SAM layer can then be patterned using one of several methods. One approach is to use direct UV light exposure in air through a shadow mask, this will remove the OTS SAM in the open areas of the mask, allowing for quantum dot deposition to occur only in the open areas. OTS SAMs can also be formed on pre-made chemical patterns. Ultra high resolution patterns can be formed using nano-lithography including conductive atomic force microscopy, STM, and EBL. Arrays of conductive atomic force microscope tips can be used to pattern repeated patterns such as those required for detectors. Quantum dots or an alternate SAM can then be deposited directly into the open pattern areas. However, because of the time required for nano-lithography, it is desirable to use the patterned OTS SAM as a nano particle master stamp, where the quantum dots are transferred from the patterned OTS surface to a surface which chemically binds them. A self-assembled monolayer such as APTMS can be used to bind the quantum dots and remove them from the master patterned stamp, allowing the patterned OTS SAM to be repeatedly filled with quantum dots and stamped. This has been demonstrated using CdTe quantum dots with TGA ligands; however, there are a variety of nano particles with which this technique will work. Therefore by creating a patterned SAM and utilizing selective deposition and appropriate transfer chemistry it is possible to open a new realm of potential device manufacturing.

5:20pm EM1-MoA11 Solution Processed Quantum Dots for Infrared Imaging, J. Lewis, E.J.D. Klem, C. Gregory, G. Cunningham, D. Temple, RTI International

While InGaAs-based focal plane arrays (FPAs) provide excellent detectivity and low noise for short wave infrared (SWIR) imaging applications, wider scale adoption of systems capable of working in this spectral range are limited by high costs, limited spectral response, and costly integration with Si readout circuits (ROICs). RTI has demonstrated a novel photodiode technology based on a heterojunction between IR-absorbing, solution-processed PbS colloidal quantum dots (CQD) and C₆₀ fullerenes that can overcome these limitations of InGaAs FPAs. We have fabricated devices with quantum efficiencies exceeding 50%, and detectivities greater than

10¹² Jones, that are competitive with the performance of InGaAs photodiodes. Dark currents of ~2 nA/cm² were measured at temperatures compatible with solid state cooling. Additionally, by processing these devices entirely at room temperature we find them to be compatible with monolithic integration onto ROICs, thereby removing any limitation on device size. We will show early efforts towards demonstrating a direct integration of this sensor technology onto a Si ROIC IC and describe a path towards fabricating sensors sensitive from the visible to 1700 nm at a cost comparable to that of CMOS based devices. This combination of high performance, dramatic cost reduction, and multispectral sensitivity is ideally suited to expand the use of SWIR imaging in current applications, as well as to address applications which require a multispectral sensitivity not met by existing technologies.

Electronic Materials and Processing Division

Room: 210 - Session EM2-MoA

Dielectrics for Ultra Dense Memory Devices

Moderator: A.C. Kummel, University of California San

Diego

2:00pm **EM2-MoA1 Oxides for Spintronics**, *K.L. Wang, P. Khalili, F. Xiu*, University of California Los Angeles **INVITED**

Mainstream CMOS technology in today's electronics continues to scale down in its feature size. However, power dissipation per unit area and variability pose two major issues and challenges for the continuing scaling. Spintronics, as an emerging technology that exploits the intrinsic spin of the carriers, could potentially offer power savings, low variability and improved scalability. In the talk, we will address the importance of functional oxides such as MgO in field controlled spin FET devices and magnetic tunnel junctions.

Toward the realization of spin logic devices, electric-field manipulation of ferromagnetism offers a potential for achieving low power dissipation. The control of collection of spins is critical in accomplishing room - temperature spin field effect transistors for dilute magnetic semiconductors such as Mn_xGe_{1-x}. We found that by using high-quality MgO as gate oxide, the ferromagnetism of the quantum dots can be modulated up to 300 K, which opens the possibility to build room-temperature spin FETs. In addition, MgO was also shown to be effective for unpinning Schottky barrier height and improving the spin injection. Using an epitaxially grown Fe/MgO/n-Ge tunnel junction, we have obtained single crystalline and atomically smooth Fe/MgO on Ge. This high quality Fe/MgO/Ge junction not only passivates the Ge surface states to favor electronic transport, but also leads to an enhanced spin injection efficiency due to the symmetry induced spin filtering property of the MgO. By using this junction, we show electrical spin injection to bulk Ge.

We also studied the effect of MgO tunnel barrier thickness on the spin-transfer torque-induced switching of CoFeB-MgO-CoFeB magnetic tunnel junction (MTJ) devices used for nonvolatile memory. We studied the effect of MgO thickness on the resistance-area product (RA) and tunneling magnetoresistance (TMR) of the structures using both film-level current-in-plane tunneling (CIPT) and device-level electrical transport measurements. The TMR showed a large distribution for RA values lower than 4 Ω-μm² (corresponding to an MgO thickness ~0.85 nm), while it increased to ~150% for larger RA > 6 Ω-μm². The results allow for optimization of RA and MgO thickness for low write energy and high-density of magnetoresistive random access memory (MRAM) switched by spin-transfer torque (STT). We obtained switching times < 1 ns and write energies < 0.3 pJ for CoFeB-MgO-CoFeB MTJ devices. We also studied the effect of CoFeB free layer composition and thickness on device performance.

2:40pm **EM2-MoA3 Charge Trap Memories and 3D Approaches**, *G. Molas*, CEA Leti Minatec Campus, France **INVITED**

Charge Trap Memories and 3D Approaches

The standard planar Floating gate Flash memory has been scaled down over 20 years. However, many critical limitations are appearing (charge loss through the top or bottom dielectrics, cell to cell coupling interference, Random Telegraph Noise, reduction of the number of stored electrons, process induced variability...), making difficult further scaling of the memory device.

In this context, charge-trapping memories, based on the TANOS (TaN-Al₂O₃-Si₃N₄-SiO₂-Si) gate stack, are foreseen as the backbone of future

NAND technologies, allowing to reach the 20nm era with planar device structures and to overcome the 1X node when coupled to novel 3D vertical memory architectures. Nevertheless, to face this challenging Flash memory evolution, several process innovations are still required, and an in-depth physical understanding of the gate stack material properties, is needed.

This paper discusses the potentialities and limitations of charge trap memories, and proposes some paths of improvements to fulfil the stringent requirements of future memory generations.

First the engineering of the memory gate stack is investigated. In particular, engineered tunnel dielectrics, alternative charge trapping layers and improved control dielectric stacks are proposed, and their impact on the memory performances and reliability is debated. Experimental results are analyzed by means of models and simulations.

Then in a second part, the integration of charge trap memories in 3D architectures is studied. The various approaches investigated in the literatures are reported, and an original method to process stacked 6nm crystalline nanowires with gate all around SONOS configuration is proposed.

3:40pm **EM2-MoA6 A Survey of Cross Point Phase Change Memory Technologies**, *D. Kau*, Intel Corporation **INVITED**

This survey reviews the current advances in phase change memory and the integrated selector. Based on memory cell configuration in array, there are 3 basic array types, including 2-terminal cross point array [1-6], 3-terminal NOR array [7, 8], NAND string [9]. Among all the configurations, stackable thin-film cross point memory delivers the densest array, therefore the most compact die size. Combining its attributes in cost, performance and reliability, cross point phase change technologies stimulate potential opportunities in computing memory hierarchy.

[1] DerChang Kau *et al.*, *IEDM Technical Digest*, p617, S27.1 (2009)

[2] Y. Sasago, *et al.*, *Symposium on VLSI Tech.*, p24, T2B-1 (2009)

[3] K. Gopalakrishnan, *et al.*, *Symposium on VLSI Tech.*, p205, T19-4 (2010)

[4] Yi-Chou Chen *et al.*, *IEDM Technical Digest*, S37.4 (2003)

[5] J.H. Oh, *et al.*, *IEDM Technical Digest*, S2.6 (2006)

[6] Giorgio Servalli, *IEDM Technical Digest*, p113, S5.7 (2009)

[7] Y.N. Hwang, *et al.*, *Symposium on VLSI Circuits*, p173 (2003)

[8] Fabio Pellizzer, *et al.*, *Symposium on VLSI Technology*, p122, (2006)

[9] Y. Sasago, *et al.*, *Symposium on VLSI Tech.*, T5B-2 (2011)

4:40pm **EM2-MoA9 Resistive Switching in HfO₂ Metal-Insulator-Metal Devices (RRAM)**, *M. Bonvalot*, Laboratoire des Technologies de la Microélectronique (LTM), France, *C. Mannequin, P. Gonon, C. Vallee*, LTM-CNRS, France, *V. Jousseume, H. Grampeix*, Minatec, France

HfO₂ is attracting interest as a high-k dielectric for several applications in microelectronics, including transistor and Flash memory gate stacks, as well as Metal-Insulator-Metal (MIM) capacitors for DRAMs and rf circuits. As such, the assessment of HfO₂ reliability is of special importance.

In this work we investigate resistive switching of HfO₂-based devices. The HfO₂ thin films (10 and 20 nm thick) are deposited by the Atomic Layer Deposition (ALD) technique on TiN/Si or Pt/Si wafers (bottom electrode) and top Au electrodes. The MIM devices are subjected to a constant dc voltage stress (CVS) and the current is monitored as a function of time. During these experiments we observe transient leakage currents, followed by a progressive increase of conductivity. Phenomena are related to oxygen vacancy defects. Upon bias application oxygen vacancies drift (space charge limited transient currents) to form conducting filaments (leakage increase) through the HfO₂ thickness. Influence of the electrode is discussed since we found oxygen vacancies in MIM devices to be strongly correlated to the metal oxygen affinity [1]. Identical results have been recently found for TiO₂ RRAM devices [2].

We also proposed to modify the oxygen vacancies and study their effects on the RRAM electrical properties by applying post deposition plasma treatment. Different hydrogen-based (NH₃ and H₂) plasma annealing treatments of the HfO₂ dielectric are carried out in order to study the influence of the oxygen vacancies or defects on the subsequent switching behaviour before the deposition of the top electrode. The RRAM devices are then electrically and physically characterized. I(V) curves are then recorded and switching parameters such the SET voltage are compared for devices with and without plasma treatment. The modifications of switching properties are correlated to chemical analysis results, mainly Angle-resolved X-ray Photoelectron Spectroscopy, Attenuated Total Reflexion (ATR) and Spectroscopic Ellipsometry (SE) up to 8 eV, with special attention devoted to metal/oxide interface investigations.

[1] C. Vallée *et al.*, *Appl. Phys. Lett.* **96** (2010) 233504

Energy Frontiers Focus Topic

Room: 103 - Session EN+EM+NS-MoA

Nanostructured Materials for Third Generation Solar Cells

Moderator: W.A. Tisdale, Massachusetts Institute of Technology

2:00pm **EN+EM+NS-MoA1 Fabrication of Two-dimensional Array of Sub-10nm GaAs Nanodisk using Bio-template Neutral Beam Etching Process**, *S.-H. Lin, X.-Y. Wang, C.-H. Huang, Y. Ohno, M. Igarashi*, Tohoku University, Japan, *A. Murayama*, Hokkaido University, Japan, *S. Samukawa*, Tohoku University, Japan

Recently, 3-dimensional (3D) or 2-dimensional (2D) quantum dot superlattice are widely investigated to develop the new generation devices, such as quantum dot solar cell. Quantum dot superlattice consists of quantum dots with lower band gap energy in the matrix with higher band gap energy. For the device application, the structure requires high QD density, periodic QD array and uniform dot size and inter-dot spacing. Molecular beam epitaxy (MBE) and Metal-organic chemical vapor deposition (MOCVD) are two attractive methods among various bottom-up fabrication methods to fabricate quantum dots. However, there is limitation of bottom-up process to control the size, spacing and density of quantum dots. To breakthrough these problems, we have proposed the ultimate top-down process by combination of bio-template and damage-free neutral beam etching (NBE) for fabricating defect-free 2D array of quantum dots.

In this study, we developed a series of novel process for fabricating uniform size and high density 2D array of GaAs nanodisk with uniform inter-dot-spacing. Firstly, the hydrogen-radical treatment was used to remove the native oxide on GaAs surface. To utilize two-dimensional array of ferritin (protein including 7-nm-diameter iron core) as an etching mask, the formation of a hydrophilic 1-nm thick GaAs neutral beam oxidation film is key point. It is found that protein shell can be removed with oxygen-radical treatment at a low temperature of 280°C without thermal damage to GaAs. After protein shell removal, the iron oxide cores inside the ferritins remained on the surface. Then, using the iron core as an etching mask, neutral beam could etch the defect-free nanodisk structure of GaAs. Finally, we developed that iron oxide core was removed by wet etching with diluted hydrogen chloride and completed a fabrication process without inflicting any damage to GaAs. The result shows the quantum dot superlattice structure with a two-dimensional array of GaAs quantum dots with a diameter of ~7-nm, a height of ~10-nm, and a quantum dot density of more than $7 \times 10^{11} \text{cm}^{-2}$ was successfully demonstrated without any damage to GaAs.

This work is supported by the Core Research of Evolutional Science and Technology (CREST) of Japan Science and Technology Agency (JST).

2:40pm **EN+EM+NS-MoA3 Solution Processed Quantum Dots for Low Cost Photovoltaics**, *E.J.D. Klem, J. Lewis, C. Gregory, G. Cunningham, D. Temple*, RTI International **INVITED**

For solar energy to be a significant component of our energy supply new technologies are needed that enable the fabrication of low cost, high efficiency solar cells. Research into solar energy devices which incorporate carbon fullerenes and semiconducting polymers represent one such technology. One factor limiting their further advance is their lack of absorption in the infrared (IR). As half the sun's energy lies beyond 700 nm and one third beyond 1000 nm, low-cost device technologies are needed which capture this lost infrared potential. An additional factor limiting the further advance of these devices is the relatively poor electrical transport properties of most semiconducting polymers.

The use of solution processed quantum dots provides a potential route towards overcoming both of these limitations. Solution processed quantum dots can be tuned to absorb light well into the infrared, and quantum dot composite thin films have been shown to have charge carrier mobilities approaching that of amorphous silicon.

In this presentation we will present a brief overview of colloidal quantum dots and the field of quantum dot photovoltaics. We will discuss a range of device architectures and material systems that have been explored experimentally. This includes quantum dot-metal Schottky junctions, quantum dot heterojunctions, and quantum dot-metal oxide junctions.

We will also present a device architecture which is based on the heterojunction formed between infrared-sensitive PbS quantum dots and C₆₀ fullerenes. In this device pre- and post-deposition treatments to are used

passivate carrier traps and increase the conductivity of the quantum dot films. A device stack is presented that is designed to steer photo-excited charge carriers to the charge-separating interface, reducing recombination pathways and improving carrier extraction efficiency. Under simulated solar illumination the devices exhibit short circuit current densities greater than 20 mA/cm², power conversion efficiencies greater than 5%, and spectral sensitivity out to 1500 nm. This represents a significant step towards demonstrating the commercial viability of solution processed quantum dot technology

3:40pm **EN+EM+NS-MoA6 Role of Quantized and Mid-Gap States in "Dark" Charge Transport and Photoconductivity in Semiconductor Nanocrystal Films**, *P. Nagpal*, Los Alamos National Laboratory

Colloidal semiconductor nanocrystals (NCs) have attracted significant interest for applications in solution-processable devices such as light-emitting diodes and solar cells. However, poor understanding of charge transport in NC assemblies, specifically the relation between electrical conductance in dark and under light illumination, hinders their technological applicability. Here, we simultaneously address the issues of "dark" transport and photoconductivity in films of PbS NCs by incorporating them into optical field-effect transistors (OFETs), in which the channel conductance is controlled by both gate voltage and incident radiation. Spectrally resolved photoresponses of OFETs reveal a weakly conductive mid-gap band (MGB) which is responsible for charge transport in dark. The mechanism for conductance, however, changes under illumination when it becomes dominated by band-edge quantized states. In this case, the MGB still plays an important role as its occupancy (tuned by the gate voltage) controls the dynamics of band-edge charges. Our study has broad implications for NC-based electronics and optoelectronics, and specifically, suggests that design guidelines for NC devices might be different depending on whether they are intended for operation in dark (diodes and transistors) or under illumination (photodetectors and solar cells).

4:00pm **EN+EM+NS-MoA7 Using Surface Chemistry to Modulate the Bandgap of Ge Nanowires**, *S. Sivaram, M.A. Filler*, Georgia Institute of Technology

Small-diameter semiconductor nanowires are highly attractive building blocks for next generation photovoltaic devices because they exhibit highly tunable optoelectronic properties as a result of quantum confinement. Bottom up approaches, such as the vapor-liquid-solid (VLS) growth mechanism, are controllable down to ~20 nanometers but significant challenges exist at smaller length scales where property tuning is maximized. Furthermore, it is expected that the optoelectronic properties of quantum-confined nanowires will be heavily dependent on surface chemistry, yet there are no experimental studies that fundamentally probe this relationship. Germanium is an ideal system to study because of its large Bohr exciton radius, low rate of oxidation, and chemical similarity to silicon. In this work we controllably synthesize germanium nanowires with diameters from 5 to 20 nanometers using gold catalyst particles with a narrow size distribution. To obtain epitaxial Ge nanowires with uniform diameters and lengths, a two-step growth process is employed that includes a brief, high-temperature nucleation (390°C) above the Au-Ge eutectic point, followed by elongation at various process conditions, generally below the eutectic point (280 – 340°C, 1×10^{-7} – 1×10^{-4} Torr). To limit catalyst diffusion and formation of the $\sqrt{3} \times \sqrt{3}$ Au/Si reconstruction on the Si(111) surface, a key problem for controllable sub-20 nm growth, the substrate is passivated with -CH₃ groups prior to nanowire synthesis by introducing small quantities of methylgermane. Nanowire surface chemistry is probed with *in-situ* transmission infrared (IR) spectroscopy both during and after growth. We introduced different adsorbates (-H and -CH₃) and monitored their influence on the band gap as a function of surface coverage. We show that the band gap of Ge nanowires blue shifts with H passivation and red shifts with CH₃ termination.

4:20pm **EN+EM+NS-MoA8 Production of Multi-milligram Yields of Ternary II-VI Semiconductor Nanocrystals Under Non-coordinating Amine Activated Synthesis**, *M. Plaisant, P.H. Holloway*, University of Florida

Thermolysis of Zn and Cd precursors under a non-coordinating one-pot wet-chemical synthesis has successfully produced a heterogeneous ternary Cd_xZn_{1-x}Se alloy with an extensive spectral red shift of 200nm in the visible range. Large yields of twenty milligram of the Cd_xZn_{1-x}Se alloy are minimally required for inclusion of the material in the active layer of an inorganic/organic photovoltaic device. The facile synthesis of such large yields of ternary semiconductor nanocrystal alloys has not commonly been reported in the literature. Herein we discuss first the thermolytic synthesis of the material beginning from the ZnSe core through the inclusion of the Cd-precursor. We then discuss the production of the ternary II-VI semiconductor Cd_xZn_{1-x}Se material through a process of non-coordinating

synthesis with amine-activation to produce the high multi-milligram yields required for device inclusion.

4:40pm **EN+EM+NS-MoA9 Type-II ZnTe/ZnSe Quantum Dots for Intermediate Band Solar Energy Conversion**, *C. Chen, B. Juang, J. Hwang, S. Kim, X. Pan, J. Phillips*, University of Michigan

Intermediate band solar cells and impurity photovoltaics have been proposed to achieve high efficiency solar energy conversion by introducing electronic states within the bandgap of the host material. The intermediate electronic states provide enhanced photocurrent through the addition of sub-bandgap optical transitions while maintaining a voltage that follows the host material. Approaches to realize these solar cells include the incorporation of dopants/impurities, dilute alloys, and nanostructures such as quantum dots. Self-assembled quantum dots such as InAs/GaAs possess excellent optical properties and have been applied to numerous optoelectronic devices including demonstration of the intermediate band solar cell concept. The highly radiative transitions in these type-I materials result in short radiative carrier lifetimes – a feature that is desirable for light emitters, but can be problematic for photodetectors and solar cells. Semiconductor nanostructures with type-II band alignment result in spatially separated electron and hole wavefunctions, resulting in reduced oscillator strength and corresponding reduction in optical absorption, spontaneous radiative recombination rate, and increased radiative carrier lifetime. The tradeoff between carrier lifetime and optical absorption may be effectively used to provide a closer match to the generation-recombination rates desired for intermediate band solar energy conversion. In this work, ZnTe/ZnSe type-II quantum dots are proposed for intermediate band solar energy conversion. The theory of intermediate band solar energy conversion in this material system will be presented along with initial experimental results on the epitaxial growth, structural properties, and optoelectronic response of the materials. The ZnTe/ZnSe quantum dots were grown by molecular beam epitaxy, where three-dimensional island formation is observed via strained layer growth in the Stranski-Krastanow growth mode. Low temperature photoluminescence spectra reveal optical transitions from ZnSe (2.8eV), T_{esc} isoelectronic centers (2.6eV), and broad emission in the range of 2.0-2.4eV attributed to type-II quantum dots.

Energy Frontiers Focus Topic

Room: 104 - Session EN-MoA

Industrial Physics Forum on Energy II

Moderator: J.W. Rogers, Idaho National Laboratory, J.N. Hollenhorst, Agilent

2:00pm **EN-MoA1 The Role of Nuclear Energy in a Sustainable Energy Scenario**, *H.F. McFarlane*, Idaho National Laboratory **INVITED**

Only three primary energy sources power the planet for humankind's benefit. Though seldom identified as such, the most familiar is nuclear fusion, which provides the solar flux to warm the earth, power the renewable wind and water cycles, and drive photosynthesis for plant growth. Ancient carbon bonds, formed over millions of years and stored in the form of familiar fossil fuels—oil, natural gas, and coal—comprise plentiful resources that enable most of our transportation and electricity generation. Uranium powers the third, and to many people the most mysterious, energy source, nuclear fission.

Different groups define sustainable energy in different ways, the specific definition usually crafted to advance a particular point of view. In this discussion, I shall use sustainable to mean that the resource and its application are sustainable for hundreds of years, through multiple generations. Five years ago who would have thought that we would be talking about a 100-year supply of affordable natural gas, yet that is what new technology may have brought us—though the environmental consequences are still being sorted out. Renewable energy will serve us as long as we have a clear view of the sun, or until the solar plasma reaches out and kisses earth. Nuclear energy brings emotional baggage. Nuclear energy's sustainability yardstick is multi-dimensional, not merely a question of how long uranium resources will last under various scenarios.

One well-accepted international research, demonstration and development program addresses nuclear sustainability at its core—the Generation-IV International Forum. From 200 candidate technologies, the Forum selected six advanced nuclear systems for possible development. Each system is required to set stretch goals for safety, nuclear proliferation resistance, economic competitiveness, and sustainability. That said, nuclear's sustainability relies on success in the first three goals as well as public acceptance.

This talk will use the Generation-IV framework applied to existing as well as future infrastructure. It will provide a provocative perspective on resources, safety (including the Fukushima-Daiichi accident resulting from an overwhelming tsunami), and nonproliferation. Nuclear energy's potential role in providing a significant fraction of electrical generation as well transportation fuels will be explored.

2:40pm **EN-MoA3 What's So Smart about the "Smart Grid?"**, *J.G. Kassakian*, Massachusetts Institute of Technology **INVITED**

The "Smart Grid" has received considerable hype in Washington and the popular press. To some it means an automated metering infrastructure allowing consumers to participate in load management. To others it means the interconnection of distributed renewable resources and the introduction of electric vehicles. It is all of these and more. This presentation will provide an overview of the many dimensions of the smart grid vision, including anticipated technical innovations and policy changes necessary for realizing the vision.

3:40pm **EN-MoA6 Electrochemical Energy Storage for Renewable Integration and Grid Applications: Status, Challenges and Opportunities**, *Z.G. Yang*, Pacific Northwest National Laboratory **INVITED**

Growing concerns over the environmental consequences of burning fossil fuels and their resource constraints, along with the increasing world energy consumption, have spurred great interests in renewable energy from sources such as wind and solar. However, the power from these intermittent sources is constantly varied, making quite challenging for its use and dispatch through the aging electrical grid. One effective way to smooth out the intermittency is to employ electrical energy storage (EES). As such EES has been widely considered as a key enabler of the future grid or smart grid that is expected to integrate a significant level of renewable, while providing electricity or "fuel" to hybrid and electrical vehicles. Among the potential technologies are electrochemical energy storage technologies or batteries that are capable of storing a large quantity of electricity and releasing it according to demands. There remain significant challenges however for the current technologies to meet the performance and cost matrices for broad market penetration. This paper offers an overview on varied technologies, in particular batteries, and discusses the status, challenges and research needs.

Graphene and Related Materials Focus Topic

Room: 208 - Session GR+TF+ET-MoA

Graphene: Electronic Properties and Charge Transport

Moderator: L. Colombo, Texas Instruments Incorporated

2:00pm **GR+TF+ET-MoA1 Electronic and Magnetic Properties of a Graphene Line Defect**, *D. Gunlycke*, Naval Research Laboratory **INVITED**

Although graphene exhibits excellent electron and thermal transport properties, it does not have an intrinsic band gap, required to use graphene as a replacement material for silicon and other semiconductors in conventional electronics. The band structure of graphene, however, offers opportunities to develop non-traditional applications. One such avenue is to exploit the valley degeneracy in graphene. In this presentation, I will present a two-dimensional valley filter based on scattering of electrons and holes off a recently observed extended line defect. The transmission probability depends strongly on the valley and the angle of incidence of the incident quasiparticles. Quasiparticles arriving at the line defect at a high angle of incidence lead to a valley polarization of the transmitted beam that is near 100%.

I will also discuss results showing that the extended line defect gives rise to ferromagnetically coupled local moments. This ferromagnetism can be understood from a symmetry analysis of the boundary-localized eigenstates. The symmetry requires that the principal moments couple ferromagnetically both along and across the line defect, leading to approximately 2/3 more spin-up electrons and than spin-down electrons per repeat unit along the line defect.

This work was supported by the Office of Naval Research, directly and through the Naval Research Laboratory.

2:40pm **GR+TF+ET-MoA3 Hydrogenation Induced Graphene-Metal Contact - Observation of States at Fermi Level**, *S. Rajasekaran*, Stanford University, *S. Kaya*, *T. Annivey*, Stanford Synchrotron Light Source, *F. Yang*, *D. Stacchiola*, Brookhaven National Laboratory, *H. Ogasawara*, *A. Nilsson*, Stanford Synchrotron Light Source

Graphene has received tremendous interest due to its unique electronic structure. Manipulating its electronic structure has received considerable interest. Hydrogenating graphene to open a band gap has been proposed and certain groups have demonstrated hydrogenation induced band opening for graphene on metal substrates.

We employed carbon specific soft x-ray spectroscopy (X-ray photoelectron (XPS), X-ray absorption (XAS) and X-ray emission spectroscopy (XES)) and scanning tunneling microscopy (STM) to investigate how hydrogenation changes the geometric and electronic structure of graphene on Pt(111). Graphene growth on Pt(111) is accompanied with Moiré structure due to periodic rippling in the graphene overlayer due to lattice mismatch and weak interaction between graphene and Pt. Hydrogenation leads to complete disappearance of long range order, although STM indicates that ripple periodicity survives even after hydrogenation. We show that hydrogenation of the unit cell of Moiré nano-patterns is accompanied by pinning of the graphene layer to underneath metal substrate. Structural changes involved in the process of hydrogenation induce covalent graphene-metal interaction. Angle resolved XES and XAS make it possible to probe symmetry resolved states in σ and π bond geometry. XES-XAS indicates that the density of states (DOS) of graphene is very similar to that of graphite. Hydrogenation induces significant changes in the electronic DOS, most of which reflect the formation of C-H σ bonds. For disordered hydrogenated graphene, contrary to band opening, we observe states at the Fermi level after hydrogenation which we reason to arise due to graphene metal interaction and localized C-H bonds. This effect is proposed to be a way to tailor its electronic properties as a possible method to form better graphene-metal contact.

3:00pm **GR+TF+ET-MoA4 First-Principles Studies of Atomic and Electronic Structure of Graphene on Sn/Ni(111) Surface Alloy**, *L. Adamska*, *R.Q. Addou*, *A. Dahal*, *M. Batzill*, *I.I. Oleynik*, University of South Florida

Graphene-substrate interactions can be exploited to modify the electronic structure of free-standing graphene. Although most of the efforts were directed towards investigation of graphene on pure metallic substrates, less is known about properties of graphene grown on surface alloys. Sn/Ni(111) surface alloy is of particular interest because this structure has the surface lattice constant of Ni(111), i.e. almost a perfect match with graphene's lattice constant, and its surface is highly corrugated due to the substantially large atomic radius of Sn compared to Ni. Here we present results of first-principles density functional theory investigations of structural and electronic properties of graphene on $\sqrt{3}\times\sqrt{3}R(30^\circ)$ Sn/Ni alloy substrate. It was found that the presence of Sn atoms (1/3 monolayer) results in substantial weakening of graphene-substrate interactions, as is evidenced by large graphene-substrate separation. Nevertheless, the electronic structure of graphene is substantially affected by the underlying substrate as is seen on simulated STM images. The theoretical predictions for the atomic and electronic structures of graphene on Sn/Ni(111) substrate are compared with experimental results.

3:40pm **GR+TF+ET-MoA6 Charge Transport through Graphene: the Role of Metal Contacts**, *M.Y. Chou*, *M.E. Kindermann*, *S. Barraza-Lopez*, Georgia Institute of Technology

Graphene is a flat form of carbon only one-atom thick. Formed by two interweaving triangular sublattices, it has two atoms on its unit cell. Under normal conditions the charge carriers in graphene can be described with an effective single-particle picture. They display an isotropic and linear (i.e., conical) electronic dispersion around the charge neutrality level. This dispersion is described by a Dirac-like equation with a pseudo-spin (related to the sublattice degree of freedom) instead of the standard electron spin. The pseudo-spin is responsible in great part for the strongly suppressed back-scattering in graphene that results in coherent quantum charge transport on lengths up to the micrometer scale, making graphene a relevant material for electronic applications. Yet for applications and for electrical measurements metal contacts are patterned onto graphene. Then the two following questions naturally arise: (i) How graphene interacts with these metal contacts? (ii) How this interaction affects the conductance of a metal/graphene/metal junction in comparison with the hypothetical conductance of pristine (and contactless, infinite) graphene?

In this talk I will discuss quantitatively –within a single-particle description– the quantum transport of charges through graphene, with a focus on the signatures that metal/graphene interfaces imprint on the conductance features. The metals considered are normal (i.e., not superconducting), and spin unpolarized. A crucial observation is that not all

metal form covalent bonds to graphene. The conductance is obtained as a function of the separation between contacts, the width of the junctions, as well as the thickness of the metal layers when necessary. From these calculations we are able to extract the basic physics involved in transport for all normal metals [1]. Our studies aim towards a comprehensive modeling of graphene devices at the quantitative level.

[1] S. Barraza-Lopez, M. Vanevic, M. Kindermann, and M.-Y. Chou. "Effects of metallic contacts on electron transport through graphene." *Phys. Rev. Lett.* **104**, 076807 (2010); S. Barraza-Lopez, M. Kindermann and M.-Y. Chou. "Charge transmission through short two-terminal graphene junctions with normal bonding metal contacts." (In preparation.)

4:00pm **GR+TF+ET-MoA7 Layer Number Determination and Thickness-dependent Properties of Graphene Grown on SiC**, *W. Zhu*, *C. Dimitrakopoulos*, *M. Freitag*, *Ph. Avouris*, IBM T.J. Watson Research Center

The electronic properties of few-layer graphene grown on the carbon-face of silicon carbide (SiC) are found to be strongly dependent on the number of layers. The carrier mobility is larger in thicker graphene because substrate-related scattering is reduced in the higher layers. The carrier density dependence of the mobility is qualitatively different in thin and thick graphene, with the transition occurring at about 2 layers. The mobility increases with carrier density in thick graphene, similar to multi-layer graphene exfoliated from natural graphite, suggesting that the individual layers are still electrically coupled. The Hall coefficient peak value is reduced in thick graphene due to the increased density of states. A reliable and rapid characterization tool for the layer number is therefore highly desirable. To date, AFM height determination and Raman scattering are typically used since the optical contrast of graphene on SiC is weak. However, both methods suffer from low throughput. We show that the scanning electron microscopy (SEM) contrast can give similar results with much higher throughput.

4:20pm **GR+TF+ET-MoA8 Graphene: Scratching the Surface**, *M. Fuhrer*, University of Maryland at College Park **INVITED**

Graphene is of interest for its unique electronic structure: electrons in graphene obey the Dirac equation for massless particles, complete with a two-component spinor degree of freedom that mimics the spin of a relativistic particle. But graphene is also composed entirely of surface atoms, making the techniques of surface science useful in studying its properties. I will discuss experiments which combine ultra-high vacuum (UHV) surface science with electronic transport measurements to understand graphene and the adsorbed species on its surface. Surface science techniques can be used to controllably modify graphene's properties: potassium atoms can be deposited to form charged impurity scatterers; ice can be deposited to modify the dielectric environment of graphene and tune the electron-electron interaction strength; and ion irradiation can be used to create atomic vacancies which act as Kondo impurities. Graphene's transport properties are extraordinarily sensitive to surface adsorbates, and can be used to detect e.g. correlations in the positions of potassium atoms at concentrations below $1/1000^{\text{th}}$ of a monolayer, and phase transitions in few-monolayer water.

5:00pm **GR+TF+ET-MoA10 Metallic and Insulating Adsorbates on Graphene**, *K.M. McCreary*, *R.K. Kawakami*, University of California, Riverside

While several experiments have separately investigated the doping of graphene by metallic and insulating adsorbates, the transition from metallic to insulating behavior of the adsorbates has not yet been explored. We directly compare the effect of metallic titanium (Ti) and insulating titanium dioxide (TiO_2) on the transport properties of single layer graphene. The deposition of Ti results in substantial n -type doping and a reduction of graphene mobility by charged impurity scattering. Subsequent exposure to oxygen largely reduces the doping and scattering by converting Ti into TiO_2 . In addition, we observe evidence for short-range scattering by TiO_2 impurities.

5:20pm **GR+TF+ET-MoA11 Electron Transport in Carbon Nanotube - Graphene Contacts**, *B. Cook*, *W. French*, *K. Varga*, Vanderbilt University

Graphene and carbon nanotubes are two of the most promising materials for future applications due to their unique properties. Devices combining the two materials are expected to be particularly advantageous. The interface of carbon nanotubes and various metal electrodes has been previously studied, both experimentally (Chen et al. Nano Lett. 2005, Zhang et al. Nano Lett. 2007) and theoretically (Shan et al. PRB 2004, Zhu et al. APL 2006, He et al. APL 2009). These studies focus on the search for materials with a low p -type Schottky barrier. Hybrid graphene-carbon nanotube structures have been previously demonstrated (Tung et al. Nano Lett. 2009). We propose

the use of graphene as an electrode material for carbon nanotube based FET devices. To this end the carbon nanotube - graphene contact is investigated with first-principles calculations within density functional theory of the Schottky barrier height (SBH) and transport properties. Total energy and electronic structure calculations are carried out with a plane-wave basis set and the transport characteristics are calculated with a localized atomic orbitals basis within the non-equilibrium Green's function framework. We consider only the side-contact geometry, nanotubes laying atop graphene. The SBH for (5,0), (8,0) and (10,0) nanotubes on graphene is calculated. The transport characteristics of a combined graphene - nanotube device are considered. In the case of small diameter nanotubes (~0.6nm) a SBH of ~0.09 eV is found when graphene contacts are used, much lower than the typical reported values (0.3 eV and higher).

In Situ Spectroscopy and Microscopy Focus Topic

Room: 106 - Session IS+AS+SS-MoA

In Situ Characterization of Solids: Film Growth, Defects, and Interfaces

Moderator: M. Salmeron, Lawrence Berkeley National Laboratory

2:00pm **IS+AS+SS-MoA1 A New Approach to Defect Evolution Studies - Combined In Situ Experiments and Electron Tomography, I.M. Robertson, J. Kacher, G. Liu, University of Illinois at Urbana-Champaign**

INVITED

Electron micrographs are two-dimensional images capturing specific instances in the evolution of the microstructure and composition as well as the electronic and magnetic state. As these yields no insight as to how the state evolved, *a posteriori* knowledge is used to determine the most likely pathway. This challenge can be addressed by conducting experiments *in situ* in the transmission electron microscope, which allows direct observation and in some cases quantification of the reactions and interactions responsible for the evolved structure. The information, however, remains two-dimensional and with increasing use of this technique it is becoming apparent that lack of three-dimensional knowledge is hindering interpretation. Information in the beam direction can be recovered by applying electron tomography, but this is a relatively new technique to defect studies and despite its potential it remains a static snapshot. In this talk, I will illustrate how time-resolved deformation studies have improved our understanding of the behavior of dislocations and how this information has informed the development of new models. I will also demonstrate how three-dimensional images yield a better understanding of complex dislocation interactions and configurations. Finally, I will address the challenges faced in combining these two techniques such that three-dimensional snapshots of the evolving microstructure can be acquired periodically.

2:40pm **IS+AS+SS-MoA3 Real-time Oxide Growth Characterization using Atomic Force Microscopy, G. Rijnders, University of Twente, the Netherlands**

INVITED

Complex oxides have attracted great interest since they exhibit a rich spectrum of physical properties such as ferromagnetism, antiferromagnetism, colossal magnetoresistance, ferroelectricity, dielectricity, and superconductivity. Novel heteroepitaxial devices based on these complex oxides, like spin-polarized ferromagnetic tunnel junctions, superconducting devices and piezoelectric devices, have great potential and are currently under investigation in many groups.

The nature of the above-mentioned physical properties in complex oxides is determined by very small characteristic length scales, comparable to the unit cell lattice parameters of complex oxide. Because of these small characteristic length scales, growth control on an atomic level as well as understanding of the different mechanisms affecting the growth mode is essential for the fabrication of epitaxial heterostructures.

Two independent processes, i.e., nucleation and growth of islands, play an important role during vapor-phase epitaxial growth on an atomically flat surface. Here, nucleation causes the formation of surface steps and subsequent growth causes the lateral movement of these steps. Both processes are determined by kinetics, since they take place far from thermodynamic equilibrium. These kinetic processes affect the final surface morphology and are, therefore, extensively studied. I will demonstrate the applicability of high-pressure RHEED as well as Scanning Force Microscopy (SFM) to monitor to the growth of complex oxides during Pulsed Laser Deposition (PLD). Because of recent developments, SFM is nowadays also used to study dynamic processes, such as thin film growth and surface reaction mechanisms.

We have realized a system, in which SFM can be performed during Pulsed Laser Deposition (PLD). Deposition and force microscopy are performed in one vacuum chamber and via a fast transfer (in the order of seconds) the surface of a sample can be scanned. In our system we take advantage of the *pulsed* deposition process, because microscopy measurements can be carried out between the pulses. This provides real-time morphology information on the microscopic scale during growth. The transfer mechanism allows switching between microscopy and deposition with a reposition accuracy of ± 500 nm which gives new opportunities to study growth processes. Furthermore, it can provide information if RHEED is not possible, for example during amorphous and polycrystalline growth.

In this contribution, I will highlight recent advances in oxide thin film growth as well as the latest equipment developments.

3:40pm **IS+AS+SS-MoA6 An Auger Electron Analyzer System for In Situ MBE Growth Monitoring, W.L. Calley, Georgia Institute of Technology, P.G. Staib, Staib Instruments, J.E. Lowder, J.D. Greenlee, M.W. Moseley, W.E. Henderson, W.A. Doolittle, Georgia Institute of Technology**

Auger Electron Spectroscopy (AES) analysis is a surface sensitive technique for thin film analysis, able to detect nearly all elements [1]. Not only can AES help determine the species present at the surface, but AES can also yield information about the chemical bonding [1]. However, this analysis tool has historically been an *ex situ* technique with a few noted exceptions [2]. Herein we demonstrate the capabilities and usefulness of an Auger probe, the Staib *In situ* Auger Probe (SIAP) that has a sufficient working distance (tested up 82 mm) so as to not shadow beam fluxes allowing use during growth. The probe leverages an existing RHEED gun as an e-beam source for Auger electron excitation.

The configuration and operation of the SIAP has been described in detail [3]. The tool is installed on an MBE system configured for Terfenol growth, a miscible alloy of TbFe₂ and DyFe₂. Initial growths performed without Auger monitoring exhibited substantial oxidation even after Ar etched to remove surface contamination, figure 1. The SIAP was then employed to determine the sources of oxygen contamination.

Three sources of O were identified. The growth chamber had a high enough partial pressure of oxygen to oxidize the highly reactive rare earth elements. After 30 hours in the chamber, uncapped Tb showed a substantial increase in the ratio of O to Tb, figure 2. The Tb source material also delivered O and the rate of O delivery increased with cell temperature, figure 3. A final oxygen source was identified to be the Tb/SiO₂ interface as shown in the SIMS data in figure 4. Figure 5 shows the Si wafer with C and O present at the surface. After growth is initiated the C is not detected after 40 Å of deposition, however, the O can be detected until 200 Å are deposited, indicating intermixing with the SiO₂ interface.

Further tests were conducted starting with a layer of Dy and depositing part of a monolayer of Tb in 2% increments. Figure 6 shows a clear distinction between bare Dy and 2, 4, 6, 8, and 10% monolayer coverage of Tb on a Dy layer, demonstrating the SIAP's sensitivity is at least 2% of a monolayer for these heavy elements.

The SIAP is complementary to existing RHEED systems. While RHEED gives information about the crystal structure of the growing film, the SIAP provides chemical information. This is especially useful when working with films without line compositions. The SIAP coupled with a future closed loop control system may enhance growth of films with multiple oxidation states or other similar phase/chemical transitions. Finally this technique could give information about transitions between layers in multilayered films grown via MBE.

4:00pm **IS+AS+SS-MoA7 Quantum Size Effect Driven Structure Modifications of Bi-films on Ni(111), T.R.J. Bollmann, R. van Gastel, H. Zandvliet, B. Poelsema, University of Twente, The Netherlands**

We have investigated the initial growth of Bi/Ni(111) using Low Energy Electron Microscopy (LEEM) and Selected Area Low Energy Electron Diffraction (μ LEED). Bismuth represents an interesting material since 1) it has a tendency for allotropism, 2) it forms several ordered alloys with Ni and 3) with Bi being a neighbor of Pb in the periodic system, one may find evidence for quantum size effects in ultrathin Bi layers. Indeed we obtain ample evidence for Bi/Ni(111) as being a very rich system, even at a fixed substrate temperature of 474 K.

We find first that the deposition of Bi leads to the formation of a surface alloy with a ($\sqrt{3}\times\sqrt{3}$)-R30° structure at a Bi-coverage of 1/3. Continued Bi deposition leads to the formation of an incommensurate wetting layer with a continuously decreasing lattice parameter, finally ending in a (7x7) structure. From the variation of the step position at the buried interface, nicely accessible with LEEM, we conclude that the dealloying of the $\sqrt{3}$ phase is incomplete and that the (7x7) wetting layer in fact involves two layers with a small, but finite Bi content in the second layer. Upon further

Bi deposition elongated, 3-4 layers high nanowires emerge, with a p(5x2) structure and a width of about 80 nm, oriented along <110> and <100>-azimuths. Further deposition of Bi-leads to different (sometimes coexisting) structures: (3x3)-patches with a thickness of three atomic layers and patches with a matrix structure ($m_{11}=3$, $m_{12}=-1$, $m_{21}=1$, $m_{22}=2$) and a thickness of five atomic layers. This accurate height assignment is uniquely enabled by the analysis of LEEM-IV data.

The results are fully consistent with quantum size effect driven thin film morphology: the different film structures and their thicknesses nicely fit with integer numbers of nodes in their specific Fermi wave function, even for the seven layers thick (7x7) structure obtained at a lower temperature of 422 K. Tensor LEED calculations of the interlayer spacing of the different structures concur with this assignment.

The influence of the structure and morphology on electronic properties of various materials is well known. The interaction between electronic and crystal structure should be reciprocal. The Bi/Ni(111) system provides a nice and we think first illustration: electronic properties, in particular quantum size effects, actually drive the structure of the thin bismuth films.

4:20pm **IS+AS+SS-MoA8 Growth and Structure of Sm on an Ultrathin $\text{Al}_2\text{O}_3/\text{Ni}_3\text{Al}(111)$ Film: A Comprehensive Study**, J.F. Zhu, Q. Xu, S. Hu, X. Feng, D. Chen, University of Science and Technology of China

The growth and electronic structure of vapor-deposited Sm onto a well-ordered $\text{Al}_2\text{O}_3/\text{Ni}_3\text{Al}(111)$ ultrathin film under ultrahigh vacuum (UHV) conditions at room-temperature has been studied comprehensively using X-ray photoelectron spectroscopy (XPS), ultraviolet photoelectron spectroscopy (UPS), scanning tunneling microscopy (STM) and low electron energy diffraction (LEED). Our results indicate that at room temperature Sm grows in a layer-by-layer fashion for the first two layers, followed by three-dimensional (3D) growth. The interaction of Sm with Al_2O_3 thin films is so strong that deposited Sm is immediately oxidized at beginning. Both the oxidation states of Sm^{2+} and Sm^{3+} are found at low coverages (<1 ML) with the situation that the concentration of Sm^{2+} dominates below 0.2 ML and subsequently that of Sm^{3+} dominates. With increasing Sm coverage, the metallic state of Sm gradually appears. Annealing the film of 0.2 ML $\text{Sm}/\text{Al}_2\text{O}_3$ at $T < 500$ K results in further oxidation of the Sm species where all the Sm^{2+} species converts to Sm^{3+} . Further annealing at higher temperatures leads to loss of Sm from the surface via subsurface diffusion.

4:40pm **IS+AS+SS-MoA9 In Situ Study of the Reaction Mechanism Kinetics of Pt ALD from $(^{\text{Me}}\text{Cp})\text{PtMe}_3$ and O_2** , I.J.M. Erkens, A.J.M. Mackus, H.C.M. Knoops, F. Roozeboom, W.M.M. Kessels, Eindhoven University of Technology, Netherlands

Atomic layer deposition (ALD) of noble metals and noble metal oxides on high-aspect-ratio 3D nanostructures has a wide variety of potential applications in sensing and catalysis. Despite several studies,¹⁻³ much is still unknown about the reaction mechanism of Pt ALD using $(^{\text{Me}}\text{Cp})\text{PtMe}_3$ and O_2 , which can be considered a model system for noble metal ALD processes. Questions remain regarding the surface species and reactions, and the temperature dependence of the growth per cycle (GPC). In this contribution we expand the understanding of the Pt ALD mechanism by combining quadrupole mass spectrometry (QMS) and spectroscopic ellipsometry (SE). Using these in-situ techniques to study the process as a function of temperature between 100 and 300°C, we have gained a unique perspective, which has led to several new insights. The time-resolved QMS data for CH_4 and CO_2 show that combustion and other ligand reactions at the surface occur in sequence, while competing for the available carbon atoms. Quantification of the data showed that approximately 80% of the C atoms are combusted during the O_2 pulse. By performing the QMS measurements in a temperature series, valuable information was obtained on the rate of combustion of the hydrocarbon ligands at the Pt surface during the O_2 pulse. Using a combination of QMS and SE data, we were able to formulate a mechanism explaining growth inhibition at low temperatures. This mechanism manifests itself through three temperature dependent growth regimes: no growth below 100°C; limited growth between 100 and 250°C; and full growth between 250 and 300°C. Using results from surface science literature a likely explanation for these regimes was given. This involves the cyclopentadienyl ligands at the Pt surface forming reactive intermediates or being thermally decomposed. The mechanism was corroborated by QMS and SE data on post-plasma treatment cycles, by which catalytic activity was temporarily restored. We were therefore able to link the temperature dependence of the GPC to combustion kinetics. A detailed description of our methods and results will be given in our contribution.

1. Aaltonen *et al.*, *Electrochem. Solid-State Lett.* **6**, C130 (2003).
2. Kessels *et al.*, *Appl. Phys. Lett.* **95**, 013114 (2009).
3. Setthapun *et al.*, *J. Phys. Chem. C* **114**, 9758 (2010).

5:00pm **IS+AS+SS-MoA10 In Situ Surface Analytical Characterization of Electronic Devices: Thin Film Solar Cells and Lithium Ion Batteries as Examples**, A. Thissen, SPECS Surface Nano Analysis GmbH, Germany

Electronic devices have revolutionized everyday life in industrial countries over the last decades. Especially devices for energy conversion and storage like thin film solar cells and lithium ion batteries are of importance for the future. Recently two main tasks for research and development are dominant: miniaturization for sophisticated applications targeting at the nanoscale, and designing low cost large scale devices. In both fields the device performance is strongly determined by materials quality, composition, combination and last but not least by processes at materials interfaces. Nanostructures, minimization of material consumption and the need to improve device efficiencies consequently leads to the widespread focussing on thin film preparation. For thin film devices surface and interface analysis like photoelectron spectroscopy and surface (spectro-)microscopies are an important tools for material and device characterization. Classical well defined model experiments already reveal important insights using highly integrated vacuum systems for analysis and preparation. But analysis of materials and devices under near ambient conditions and even in situ during operation is an inevitable future development to improve the significance of data for development and quality management. In this respect the application of techniques like Near Ambient Pressure XPS, XPS from liquids and solid liquid interfaces, hard x-ray PES (HAXPS), Near Ambient Pressure SPM on solar cell and lithium ion battery materials is the challenging tasks for manufacturing companies of surface analytical equipment.

Marine Biofouling Focus Topic

Room: 105 - Session MB+BI+PS-MoA

Marine Antifouling Coatings

Moderator: A. Rosenhahn, Karlsruhe Institute of Technology, Germany

2:00pm **MB+BI+PS-MoA1 Advances in Sustainable Technologies for the Prevention of Marine Biofouling**, R. Deshmukh, University of Texas at Arlington, P. Sheth, University of North Texas Health Science Center, R.B. Timmons, University of Texas at Arlington, J.A. Schetz, University of North Texas Health Science Center **INVITED**

The cost associated with preventing the attachment of marine organisms to underwater surfaces (biofouling) is billions of dollars annually impacting numerous sectors including shipping, aquaculture, offshore drilling, and offshore tidal and wind power. Invariably the most effective biofouling control methods are ones that are biocidal in nature whereby a coating is impregnated with a toxin that leaches out over time. However, persistence and bioaccumulation of heavy metal-based and organic biocides, creates environmental and health problems that have resulted in their regulation. Vigorous hull cleaning, aimed at periodically removing biofouling organisms, disperses fine biocide-impregnated coating particles and this significantly increases biocide persistence in sediments where they are ingested by a variety of marine organisms and bioaccumulate.

Coatings that peel off under conditions of high shear, so called foul-release coatings, are another approach but such coatings are easily damaged, not amenable to grooming and ineffective against microfouling. Further, the most effective foul-release coatings are silicon-based and it is becoming increasingly apparent that leaching of toxic silicon oils from the coating matrix plays a role in their superior antifouling performance. Other approaches have been to develop durable coatings with little antifouling activity but that can withstand repeated intense grooming. One of our long term objectives is to identify coating materials with surface properties discouraging the settlement of biofouling organisms but also durable enough to withstand cleaning.

Here we report on the discovery of a transparent, conformal, pin-hole free, and plasma-polymerizable polymer coating made from an inexpensive monomer material that drastically reduces (>90%) algae (*Ulva*) sporeling settlement and biomass accumulation without any observable toxicity towards *Ulva* or a non-target brine shrimp species (*Artemia*). Further the unpolymerized monomer has no antifouling effect indicating that potential leaching of monomer from coated surfaces does not account for the observed antifouling activity. Rather the antifouling effect is believed to rely on the presence of a specific chemical moiety because chemical modification of that moiety abolishes antifouling activity. Testing of other marine antifouling species such as microfouling bacteria (*Cellulophaga*) and macrofouling mussels (*Ischadium*) suggests that the antifouling properties of the polymer surface are selective for algae. Potential unique

applications for this technology include the coating of algae bioreactor walls or light fixtures allowing for maximal illumination and easy cleaning.

3:00pm MB+BI+PS-MoA4 Development of a Comparative Protocol for Anti-Fouling Surfaces Based on Polymer Brushes, A. Serrano, S. Zürcher, S. Tosatti, SuSoS AG, Switzerland, N.D. Spencer, ETH Zurich, Switzerland

Marine surfaces are known to accumulate fouling material through the starting point of adhesion and settlement of proteins and cells. This effect can be manipulated through the modification and control of the substrate properties via surface functionalization. This approach has led to successful anti-fouling coatings based on biocidal agents containing copper or zinc compounds^[1,2]. The environmental toxicity of these latter materials, however, has increased the demand for less adverse coatings. The use of ultra-thin films consisting of polymer brushes has been considered a promising alternative and many studies have been published in this field^[3,4]. None, however, has focused on developing a protocol that allows a reliable comparison between the efficiency of different well-known anti-fouling polymers. This is one of the aims of this work and has been achieved by using a common, azide-terminated monolayer to which different non-fouling polymers, such as PEG, PEOXA, PVP and PVA, have been covalently bound. The different materials were compared by characterizing the structure-property relationship of the formed polymeric brushes. Also investigated was the role of the solvent used in the anti-fouling polymer solution as a key element to better control the surface homogeneity. A thorough analysis of the influence of this parameter on the conformation of the final polymer brush was based on ellipsometry, XPS and imaging ToF-SIMS. Finally, the anti-fouling surfaces were subjected to a comparative biological study by exposure to complex proteins solution and *Ulva* zoospores, in order to validate the developed protocol.

References:

- [1] Magin, C.M.; Cooper, S.P.; Brennan, A.B., *Materials Today*, **2010**, *13*, 36-44.
- [2] Chambers, L.D.; Stokes, K.R.; Walsh, F.C.; Wood, R.J.K., *Surface & Coatings Technology*, **2006**, *201*, 3642-3652.
- [3] Banerjee, I.; Pangule, R.C.; Kane, R.S., *Advanced Materials*, **2011**, *23*, 690-718.
- [4] Krishnan, S.; Weinman, C.J.; Ober, C.K.; *Journal of Materials Chemistry*, **2008**, *18*, 3405-3413.

3:40pm MB+BI+PS-MoA6 Surface Modification of Polymers via Self-Stratification: Decoupling of Bulk and Surface Properties, D.C. Webster, North Dakota State University

INVITED

Since materials interact with their surroundings via their surfaces, controlling the surface properties of a material are of critical importance. For materials to be used to mitigate biofouling, having the correct surface properties means the difference between a useful material and one that is unsuitable for the application. In many cases, the material properties of compositions which yield useful surface properties are not suitable for the bulk properties of the material. Thus, being able to decouple the surface and bulk properties is of interest in many areas.

Combining polydimethylsiloxane (PDMS) with other polymer systems generally results in materials covered with PDMS due to its low surface energy and incompatibility with other polymers. However, if the PDMS is not chemically bound into the system, it can be easily removed from the surface. Thus, forming a copolymer of the PDMS with the other polymer is required for a durable system. Since polyurethanes are known as tough polymers due to extensive internal hydrogen bonding, combining PDMS with a polyurethane could lead to a material which is tough, but has a low surface energy surface provided by the PDMS. Thus, we have found that incorporating a reactive PDMS into a crosslinked polyurethane system can result in a material which has a low surface energy which is stable when immersed in water. High throughput screening has been used to aid in the identification and optimization of PDMS molecular weight, composition of end groups, and the amount of PDMS in the coating. A unique coating was also identified having discrete domains of PDMS on the surface. Coatings having good fouling-release properties have been prepared and tested in ocean immersion testing.

4:20pm MB+BI+PS-MoA8 Antifouling Behavior on the Surface of Polyelectrolyte Brushes in Water, M. Kobayashi, M. Terada, Jst, Erato, Japan, A. Takahara, IMCE, Kyushu University, Japan

Nature utilizes super-hydrophilic surfaces under wetted state by water to achieve oleophobicity and self-cleaning behavior. For example, fish can maintain a clean body surface by surrounding a thin layer of mucus containing calcium phosphate and protein, which protects oil attachment, marine fouling, and adhesion of marine organisms. In this study, high-density hydrophilic polymer brushes were prepared on Si-wafer by surface-

initiated controlled radical polymerization of methacrylate monomers with ionic functional groups.[1] For example, poly(3-sulfopropyl methacrylate potassium salt) (PSPMK) and poly{2-(methacryloyloxy)ethyl phosphorylcholine} (PMPC) brushes with 50 - 100 nm thickness repelled both of air bubble and hexadecane droplet in water.[2] Even when the silicone oil was spread on the polyelectrolyte brush surfaces in air atmosphere, once the oil-sitting brush substrates were immersed in water, the oil quickly rolled up and detached from the brush surfaces due to the low adhesion force between the brush and oil caused by excellent affinity of polyelectrolyte brushes to water. Similar oil detachment behavior was observed on the hydrophilic poly(sodium methacrylic acid) (PMANa) and poly[3-{dimethyl(2'-methacryloyloxyethyl)ammonio} propanesulfonate (PMAPS) brushes,[3] whereas the oil still remained attached on the hydrophobic poly(2-perfluorooctylethyl acrylate) (PFA-C8) brush even though the PFA-C8 brush shows relatively oleophobic property under air atmosphere. These hydrophilic brush surfaces would contribute to the excellent self-cleaning, antifogging, and antifouling properties without any surfactants

[1] M. Kobayashi, M. Terada, Y. Terayama, M. Kikuchi, A. Takahara, *Macromolecules* **2010**, *43* 8409.

[2] M. Kobayashi, Y. Terayama, N. Hosaka, M. Kaido, A. Suzuki, N. Yamada, N. Torikai, K. Ishihara, A. Takahara, *Soft Matter* **2007**, *3*, 740.

[3] Y. Terayama, M. Kikuchi, M. Kobayashi, A. Takahara, *Macromolecules* **2011**, *44*, 104.

4:40pm MB+BI+PS-MoA9 Non-fouling Polymer Chemical Gradients for the Investigation of Marine Bioadhesion, O. Sterner, ETH Zurich, Switzerland, S. Zürcher, SuSoS AG and ETH Zurich, Switzerland, S. Tosatti, SuSoS AG and ETH Zurich, Switzerland, N.D. Spencer, ETH Zurich, Switzerland

The accumulation of marine organisms on submerged man-made structures (referred to as marine biofouling) has great economical and environmental impact [1]. Numerous strategies to prevent or lower the extent of marine biofouling have been developed, ranging from biocidal coatings to coatings that either prevent adhesion, lower the strength of adhesion or combinations thereof [2-4]. Surface gradients offer a high-throughput approach to investigate the potency of such coatings, and have the additional advantage of reducing the error in experiments by replacing a set of single samples, including positive and negative controls, with a single substrate [5]. In this project, polymeric ultrathin coatings have been prepared using a versatile surface functionalization system based on a self-assembled monolayer of poly(allyl amine) grafted with photo sensitive perfluorophenyl azide functional groups. Gradients have been prepared using a straightforward approach to control the extent of azide to nitrene conversion over the surface, forming a polymer density gradient. Gradients of poly(ethylene glycol), poly(2-ethoxy-2-oxazoline) and poly(vinyl pyrrolidone) have been prepared and investigated for non-fouling action against zoospores from green macrofouling algae *Ulva* and two strains of marine bacteria. The gradients reveal a drastic reduction in bacterial adhesion at low polymer densities for all polymers investigated. Gradients have been characterised with variable angle spectroscopic ellipsometry (VASE) and the properties of the polymer coatings have been evaluated with time-of-flight secondary ion mass spectroscopy (TOF-SIMS) and XPS.

References:

1. Schultz, M.P., *Biofouling*, **2007**, (5): p. 331-341.
2. Chambers, L.D., et al., *Surf Coat Tech*, **2006**, (6): p. 3642-3652.
3. Grozea, C.M. and G.C. Walker, *Soft Matter*, **2009**, (21): p. 4088-4100.
4. Krishnan, S., C.J. Weinman, and C.K. Ober, *J Mater Chem*, **2008**, (29): p. 3405-3413.
5. Morgenthaler, S., C. Zink, and N.D. Spencer, *Soft Matter*, **2008**, (3): p. 419-434.

5:00pm MB+BI+PS-MoA10 Development of Poly(silyl urethanes) with Tethered Quaternary Ammonium Biocides as Antifouling Marine Coatings, P.N. Coneski, N.K. Weise, J.H. Wynne, Naval Research Laboratory

Due to the significant economic burden posed by high operational and maintenance costs of biofouled ships, the design of environmentally benign, antifouling marine coatings has been a significant interest for many researchers since the ban on traditional coatings was enacted. Current approaches for developing new marine coating materials have primarily focused on the preparation of low surface energy materials, such as modified polydimethylsiloxane (PDMS) and fluorinated polymers. These materials have shown great promise for reducing the adhesion strength of various fouling organisms, thus allowing hydrodynamic forces to release the foulants as the ship moves through water. Unfortunately, no existing material has been shown to eliminate adhesion of all of the numerous

different fouling organisms, including zoospores, microalgae and diatomaceous species. As such, the development of marine coatings with multiple mechanisms of fouling prevention may be an important avenue of antifouling materials research. Poly(silyl urethanes) coatings have been developed via the reaction of various quaternary ammonium modified orthosilicates with polyisocyanates. Material properties including glass transition temperature, surface energy, and thermal stability have been investigated as a function of orthosilicate and polyisocyanate composition as well the inclusion or omission of low surface energy soft segments. The low surface energy of these materials should provide excellent fouling release properties, as has been seen with other PDMS-like materials, while the inclusion of bound quaternary ammonium biocides should further reduce the adhesion and propagation of fouling organisms at the material interface. Finally, the hydrolysable silyl ether crosslinking may prove to enhance the antifouling capabilities of these materials by allowing any fouled portions of the coating to slough away over time, generating a new active biocidal interface.

5:20pm **MB+BI+PS-MoA11 A Preliminary Study on Porous Pt-TiO₂/Ti Electrodes with Electrochemically Microbubble-Induced Superhydrophobic Surfaces for Drag Reduction and Antifouling.** *K.R. Wu, C.H. Hung, C.W. Yeh, J.C. Sun, J.K. Wu*, National Kaohsiung Marine University, Taiwan, Republic of China

We investigate a novel device that features a reduction in frictional resistance and antifouling hull surface of seagoing ships which are activated electrochemically by a series of porous Pt-TiO₂/Ti electrodes. This device includes of a series of anodic and cathodic porous Pt-TiO₂/Ti electrodes insulatedly mounted on the hull surfaces of which are electrically connected to a direct current (DC) power supply. The above-mentioned porous Pt-TiO₂/Ti electrodes are fabricated by two steps; porous TiO₂/Ti plates are firstly prepared on pure titanium plates via a micro-arc oxidation technique and Pt nanoparticles are thereafter deposited on the porous TiO₂/Ti samples using magnetron sputtering. The DC power supply provides an adequate DC bias to the Pt-TiO₂/Ti electrodes where hydrogen and oxygen microbubbles are electrochemically nucleated and formed herein in seawater. As a result, the microbubble-induced superhydrophobic surfaces are created and the reduction in frictional resistance and antifouling hull surface are obtained. Our preliminary tests reveal that no attachment organisms are found on the Pt-TiO₂/Ti electrodes after 15 days of field seawater tests at an applied potential of 1.2 V and an energy consumed rate of about 4 W/m². On the other hand, organisms, mainly *Crassostrea gigas* and barnacles, attached and grew on the Pt-TiO₂/Ti electrode that was not applied a DC potential. That is to say that attachment of organisms can be prevented. Furthermore, the Pt-TiO₂/Ti electrodes yields a gas production rate of 800 cm³/min m² by electrolysis of seawater at an energy consumed rate of about 18 W/m². Hence, the microbubble-induced superhydrophobic surfaces can be realized with this gas production rate for drag reduction of the ship hull.

Nanomanufacturing Science and Technology Focus Topic

Room: 207 - Session NM+MS-MoA

Challenges Facing Nanomanufacturing (All Invited Session)

Moderator: S. Rosenthal, Vanderbilt University, S. Butler, Texas Instruments Incorporated

2:20pm **NM+MS-MoA2 Sustainable Nanomanufacturing.** *M. Roco*, National Science Foundation **INVITED**

Nanomanufacturing has been defined as an approach to design, produce, control, modify, manipulate, and assemble nanometer-scale elements or features for the purpose of realizing a product or system that exploits properties seen at the nanoscale. Nanomanufacturing R&D has as its goal enabling the mass production of reliable and economical nanoscale materials, structures, devices, and systems. The current relatively rudimentary capabilities for systematic control and manufacture at the nanoscale are envisioned to evolve faster after 2011 as we develop new models and instrumentation and enter production of nanosystems for revolutionary new products and processes. We have estimated the global market of final products that incorporate nanotechnology increases by about 25 percent per year reaching \$1 trillion by 2015. This estimation made in 2000 [1] holds in 2011, after passing two thirds of the interval.

Three challenges of nanomanufacturing will be discussed: supporting innovation (beyond scaling), realizing efficiency (beyond new functions) and sustainability (of nanoscale processes and of global development). The

research trends and application opportunities in nanomanufacturing will be presented by considering four generations of products by 2020 [2]. Most of what has already made it into the marketplace is in the form of "First Generation" products (passive nanostructures with steady behavior) and more recently "Second Generation" (active nanostructures, such as advanced transistors, amplifiers, targeted drugs and chemicals, sensors, actuators, and adaptive structures), while embryonic "Third Generation" (nanosystems, such as bio-assembling; networking at the nanoscale, nanoscale robotics and multiscale architectures) products are in the pipeline. Concepts for the "Fourth Generation" products, including molecular nanosystems, are only in research. Convergence with modern biology, digital revolution, cognitive sciences and other areas is expected to accelerate nanotechnology manufacturing. The role of NNI Signature Initiative on Sustainable Nanomanufacturing will be discussed.

[1] Roco, M.C. and W. Bainbridge, Eds., "**Societal Implications of Nanoscience and Nanotechnology**", *NSF*, Springer (former Kluwer Academic Publishers), 350 pages, Boston, 2001.

[2] Roco, M.C., C.A. Mirkin and M.C. Hersam, "**Nanotechnology Research Directions for Societal Needs in 2020**", Springer, 2010 (www.wtec.org/nano2/)

3:40pm **NM+MS-MoA6 The National Nanomanufacturing Network: Opportunities, Challenges, and Strategies.** *M.T. Tuominen*, University of Massachusetts Amherst **INVITED**

Nanomanufacturing holds immense intellectual and economic potential for stakeholders who pursue it with a vigorous, long-term strategy. Although numerous nanomaterials are already in production and use, the breadth of possible applications and societal benefits is only in its infancy. To help nucleate and support communities of practice in the area of nanomanufacturing, the NSF provides funding for the National Nanomanufacturing Network (NNN), which facilitates cooperative activities between nanomanufacturing centers and projects in academia, industry and government, and provides a web-based information resource, InterNano. This presentation will distill key opportunities, challenges, and strategies emerging from thematic workshops, comprehensive summits, and other NNN activities focused on the issues associated with nanomanufacturing. Research, development, education and commercialization are all essential components of a robust nanomanufacturing value chain. Nanomanufacturing R & D both draws from and breaks away from conventional notions of manufacturing. Unique issues have emerged in the area of nanomanufacturing process development, scale-up, metrology, integrated nanosystems design for manufacturing, nanoinformatics, sustainable manufacturing, standards, and multiple issues associated with a robust national enterprise in nanomanufacturing.

4:40pm **NM+MS-MoA9 Nanomanufacturing: The Future of Manufacturing?** *K. Cooper*, Naval Research Laboratory **INVITED**

Nanomanufacturing is the fabrication of building blocks with nano-scale features and their integration into useful engineered systems. Through the precise control of materials and processes at the molecular- and nano-scale, new properties and functionalities, determined by nano-scale physics and chemistry, are possible. If successful, such a capability will have a profound impact on the future of manufacturing, which should lead to the emergence of new industries and products. The challenges for nanomanufacturing are achieving the desired functionality, product quality, process repeatability, production scalability and cost affordability. Another challenge will be to achieve manufacturing platforms capable of producing systems for a variety of applications. The ONR Manufacturing Science Program is meeting these challenges through basic research in novel nano-scale production. For example, the program supports research in direct digital nanomanufacturing, massively parallel nano-scale processing, and high-throughput (e.g., roll-to-roll) nanofabrication. It encourages system-level integration and cyber-enabled manufacturing approaches. These concepts along with a few research examples will be described.

Frontiers in Nanophotonics and Plasmonics

Moderator: N. Camillone III, Brookhaven National
Laboratory

2:00pm **NS-MoA1 Probing the Metal-Insulator Transition of Vanadium Dioxide using Gold Nanoantennas**, *D.W. Ferrara, J. Nag, E.R. MacQuarrie, R.F. Haglund*, Vanderbilt University

Vanadium dioxide (VO₂) films and nanostructures in contact with gold (Au) or silver nanostructures can form the building blocks of active metamaterials that can be modulated in response to various stimuli such as the presence of chemical agents, changes in temperature, or irradiation. The semiconducting-to-metal phase transition (SMT) of VO₂, — which can be induced thermally (T_c = 68°C), optically, or electrically — leads to a change in the dielectric function of the film. Since the localized surface plasmon resonance (LSPR) of the metal nanoantenna is sensitive to the local dielectric environment, the SMT allows the optical response of the metal:VO₂ nanocomposite to be tuned. Thus these Au:VO₂ nanocomposites are unique probes of strong-correlation physics because, during the phase transition, the electron-electron interactions in VO₂ that drive the SMT are coupled with the plasmonic excitation of the Au nanostructure.

We fabricated arrays of Au nanoparticles (NPs), 180 nm in diameter and 20 nm high on indium-tin-oxide coated glass by electron-beam lithography. Subsequently, the nanoparticle arrays were coated with a 60 nm VO₂ film by pulsed laser ablation of vanadium metal targets in 10 mTorr oxygen (O₂) background gas, then annealed for 45 minutes at 450°C in 250 mTorr of O₂. Using a Peltier heater and thermocouple mounted on a copper sample holder, temperature-dependent extinction of the array was measured using plain VO₂ film as a reference to determine the LSPR wavelength and linewidth during the SMT.

The LSPR wavelength of the NPs was 1000 nm in the semiconducting state and approximately 840 nm in the metallic state, thus overlapping the VO₂ electronic transitions from the occupied vanadium 3d_{||} band to the empty 3d_⊥ band centered at approximately 885 nm. As the film undergoes the SMT, the split 3d_{||} bands merge and, with the 3d_⊥ band, form the metallic VO₂ conduction band. Since the Au NPs are sensitive to changes in both the real and imaginary parts of the VO₂ local dielectric function, they serve as a direct probe of the SMT. The results show a 30% decrease in plasmon dephasing time during the transition due to an increase in carrier-carrier scattering in the VO₂. Both Maxwell-Garnett and Bruggeman effective-medium theories predict the decrease in dephasing time during the SMT; however, a linear theory is a more accurate model for the hysteresis in the LSPR wavelength.

2:20pm **NS-MoA2 Metamaterial Nanosensors based on the Metal-Insulator transition in VO₂**, *K. Appavoo, R.F. Haglund Jr.*, Vanderbilt University

The use of solid-solid phase transitions to modulate the plasmonic response of metal nanostructures is a promising approach to nanophotonic technologies, including sensors based on signal modulation in confined nanoscale volumes [1]. Consideration of phase-transforming materials has typically focused on composition, whereas relatively little attention has been paid to the question of size dependence in determining stable phases. However, size effects play a crucial role in determining the coupling with mechanical, optical, chemical or thermal input required to effect the phase transformation [2]. With rapid progress in nanofabrication techniques, size-dependent properties become relevant and systematic studies to assess both the role of nucleation in forming a new state and of the nanoscale dynamical effects are needed.

Here, we describe an example that shows how, by systematically varying the gap between the arms of split-ring plasmonic resonators, the in-arm coupling resonance in a split-ring metamaterial can be used to monitor the metal-insulator transition in discrete volumes of the strongly correlated VO₂. Moreover, this “plasmonic hysteresis” technique also provides a means to correlate the electronic phase-transition with its structural counterpart which was previously measured using SERS technique [3]. If the number of intrinsic nucleation sites is directly proportional to the interrogated volume (a reasonable assumption) [4], we have effectively shown that well-crafted plasmonic structures with well-understood modes can be a helpful tool to probe size-dependent effect [5]. Full field 3D finite-difference time-domain simulations show that the physical origins of these non-isotropic electron oscillations leads to concentration of the electromagnetic energy for focused interrogation and high sensitivity.

As an additional example, we briefly describe an investigation into the use of similar nanostructures as chemical sensors based on coupling of autocatalytic reactions at the gold-VO₂ interface and molecular recognition moieties. In this case, the detection method involves the change in optical transition of a metamaterial array incorporating VO₂ when the heat of decomposition is sufficient to initiate the metal insulator transition.

2:40pm **NS-MoA3 Enhanced Photoluminescence from Gd₂O₃:Eu³⁺ Based Core/Multi-shell Nanoparticles**, *J. Choi, M.R. Davidson, P.H. Holloway*, University of Florida

Core/shell and core/multi-shell nanoparticles with luminescent Gd₂O₃:Eu³⁺ were successfully synthesized by a high boiling-point alcohol (polyol) and solution precipitation methods, respectively. The hetero-structured nanoparticles with Eu doped Gd₂O₃ exhibited intense ⁵D₀-⁷F₂ photoluminescence (PL) from Eu³⁺ after calcination at 600 °C for 2h in air. Photoluminescence excitation (PLE) data showed that while a small fraction of the emission resulted from direct excitation of Eu³⁺, most of the excitation resulted from adsorption in the Oxygen to Europium charge-transfer band (CTB) between 225 and 275 nm. Gd₂O₃:Eu³⁺/Y₂O₃ core/shell nanoparticles exhibited PL intensities up to 40% larger than from bare Gd₂O₃:Eu³⁺ nanoparticles and SiO₂/Gd₂O₃:Eu³⁺/Y₂O₃ core/multi-shell samples showed quantum yield (QY) up to 72% larger than that of SiO₂/Gd₂O₃:Eu³⁺ core/single-shell nanoparticles. The increased PL and QY were attributed to reduced non-radiative recombination based on longer luminescence decay time. Potential applications of the nanoparticles as scintillation radiation detectors will be discussed.

3:00pm **NS-MoA4 Au|SiO₂|Yb:Er:Y₂O₃ Core|Shell Optical Nanoantenna: Experiment & Simulation**, *V. Jankovic, J.P. Chang*, University of California Los Angeles

The conversion of electromagnetic (EM) energy from free propagating radiation to localized energy and vice versa in the radio frequency (RF) and microwave domains is accomplished with the use of antennas. Optical antennas are analogous to their RF and microwave counterparts, but there are crucial differences in their physical properties and scaling behavior because metal is a highly dispersive material with finite conductivity at optical frequencies. Optical antennas are not driven by galvanic transmission lines like RF antennas, instead, localized oscillators such as atomic emitters are brought close to the feed point of the antennas, and electronic oscillations are driven capacitatively.

In this work, Au nanoparticles of different shapes (spheres, rods and stars) were used as antenna elements, Er³⁺ ions in an Y₂O₃ host matrix were used as atomic emitter antenna driving elements while the capacitative gap between the antenna element and the atomic emitter was controlled by deposition of an ultra-thin SiO₂ inner shell between the Au nanoparticle and the Yb:Er:Y₂O₃ outer shell. A 4-5nm silica spacer layer was deposited through a controlled TEOS hydrolyzation reaction and was shown to be effective in preventing quenching yet enabling energy coupling between the Au nanorod and the RE-ion doped oxides. Spatially and compositionally controlled Yb:Er:Y₂O₃ outer shells were deposited using both wet chemistry methods and radical enhanced atomic layer deposition (RE-ALD).

Upconversion (UC) spectral, power dependence and radiative lifetime measurements with 532nm, 750nm 980 nm and 1064nm laser excitation were used to assess the coupling of the Au optical antenna to the emitter ions as a function of antenna shape, spacer layer thickness and spectral and spatial mode overlap efficiency. Preliminary optical characterization showed a 2X earlier onset of upconversion with 980nm excitation for Yb:Er:Y₂O₃ coupled to an Au nanorod antenna compared to pure (uncoupled) Yb:Er:Y₂O₃ nanoparticles. Power dependence measurements with 980nm excitation showed a >5 slope indicating a multi-photon absorption induced luminescence process for the Au-coupled erbium and a <2 slope for the uncoupled erbium, indicating a two photon absorption (expected for erbium with 980nm excitation). These optical antenna core|shell particles have potential application in bio-imaging and light trapping for solar and sensor applications.

3:40pm **NS-MoA6 Gap-Mode Plasmonic Cavities: Engineering Light-Matter Interactions in Metallic Structures**, *E.L. Hu, K.J. Russell, T.-L. Liu, S. Cui, K. Yeung*, Harvard University

INVITED

Optical cavities can tightly confine light in the vicinity of optical emitters, enhancing the interaction of light and matter. The modes or optical states of the cavity can be precisely designed and engineered, and in recent years there has been remarkable progress in demonstrations of ‘cavity quantum electrodynamics (cQED)’ in solid state platforms. Such progress has been primarily for cavities fabricated in dielectric materials, with a steady improvement in cavity quality, with quality factors, Q, in excess of 10⁴ – 10⁶ realized for cavities with coupled emitters [1],[2]. These high Q-coupled emitter systems have demonstrated heralded single photon emission [3], ultra-low threshold lasing [4] and strong light-matter coupling [5],[6].

Metal-based optical cavities would have inherently lower Q's (and greater loss) than dielectrics; however, metal cavities utilizing surface plasmon polaritons (SPPs) can have sufficiently small mode volume to produce a substantial Q/V, the quantity relevant for high Purcell factors, a measure of the light-matter interaction. This talk will focus on such *plasmonic cavities*, with optical modes formed within the gap of the two metal layers which defined the cavity [7]. Initial structures comprised silver (Ag) nanowires (NW), 70 nm in diameter and 1 - 3 μm in length, placed into close proximity to a Ag thin film substrate, with the NW axis parallel to the substrate surface. Optically active material was interposed between the nanowire and the Ag substrate: this comprised one to two monolayers of PbS colloidal quantum dots, clad on top and bottom by thin dielectric layers of varying composition and thickness. The fluorescence spectrum of PbS quantum dots within the gap was strongly modified by the cavity mode, with peak position in quantitative agreement with numerical calculations, and demonstrating Q values of ~ 60 .

Such plasmonic cavities allow the easy incorporation of a variety of light-emitting active areas, and we have also explored the incorporation of various organic, dye-containing layers within the gap-mode plasmonic cavities. In addition these structures lend themselves to relatively simple modifications of geometry, allowing effective *tuning* of cavity modes, and also control of modes through the use of photonic crystal geometries, fabricated into metal.

The high Q/V possible for these cavities, and the range of organic and nanocrystalline emitters they can accommodate make these important building blocks for the exploration of light-matter interaction in the solid state.

References

- [1] S. Noda, M. Fujita, and T. Asano, *Nature Photonics* 1 (2007) 449.
- [2] B.-S. Song, S.-W. Jeon, and S. Noda, *Optics Letter* 36 (2011) 91.
- [3] P. Michler, et al. *Science* 290 (2000) 2282.
- [4] S. Strauf et al., *Phys. Rev. Lett.* 96 (2006) 127404.
- [5] J. Reithmaier et al. *Nature* 432 (2004) 197.
- [6] K. Hennessy, A. Badolato, et al. *Nature* 445 (2007) 896.
- [7] K. Russell and E. Hu, *Appl. Phys. Lett.* 97 (2010) 163115.

4:20pm NS-MoA8 Direct Characterization of Surface Plasmon Enhanced Electromagnetic Fields on Single Ag Nanostructure. *W.D. Wei, J. Wang, Y. Wang*, University of Florida, *G. Xiong, S. Peppernick, A. Joly, K. Beck, W.P. Hess*, Pacific Northwest National Laboratory

Using two-photon photoemission electron microscopy (2P-PEEM) we have directly explored the optical fields on a single Ag nanostructure and quantitatively measured the field enhancement factor (FEF). The 2PPE intensity from the Ag nanostructure is enhanced by 2 orders of magnitude with respect to the 2PPE intensity from a smooth and homogeneous Ag thin film. This enhancement is attributed to a localized surface plasmon excitation and resonance of the local field, and the FEF is determined to be around 4. The capability of directly correlating the field enhancement with nanostructures makes 2P-PEEM a promising tool to investigate the fundamental optical properties of nanomaterials.

4:40pm NS-MoA9 Comparisons of Optical and Magneto-Optical Properties between Core-Shell Fe-Ag and Co-Ag Nanoparticles based on Localized Surface Plasmon Resonance. *L. Wang, C. Clavero, K. Yang, A. Nelson*, College of William and Mary, *K. Carroll, Z. Huba, E. Carpenter*, Virginia Commonwealth University, *D. Gu*, Applied Research Center, *R.A. Lukaszew*, College of William and Mary

Magnetic transition nanoparticles (NPs) have been developed and studied by many researchers for bio-imaging and bio-sensing applications [1,2] due to their special optical and magneto-optical (MO) properties. Nevertheless, it is possible to enhance the MO effects of the magnetic NPs by combining them with other materials such as noble metals which exhibit intense localized surface plasmon resonance (LSPR) under certain conditions[3,4]. Here, we present our investigations on LSPR enhanced MO effect in magnetic metal core-noble metal shell NPs, such as core-shell Fe-Ag and Co-Ag NPs. These systems present strong Faraday rotation due to LSPR, nevertheless differences are found among them due to their different optical properties. A blue-shift is experimentally observed in the optical and MO spectra peaks from Fe-Ag to Co-Ag NPs with similar Ag shell concentrations and constant NPs sizes. Also, the absorption and Faraday rotation spectra of Fe-Ag NPs are broader than those of Co-Ag NPs. We explain such differences by means of theoretical studies based on an adaptation of the Maxwell-Garnet model to core shell nanoparticles yielding an excellent agreement with the experimental results. The possibility to understand and tune the properties of core-shell nanoparticles reported here will have significant impact in photonic and plasmonic applications.

This work was financed by DARPA under a grant for the development of novel sensors for bio-defense.

- [1] Gilles K. Kouassi and Joseph Irudayaraj, *Anal. Chem.*, 2006, **78** (10), pp 3234-3241.
- [2] Jae-Hyun Lee, Yong-Min Huh, Young-wook Jun, Jung-wook Seo, Jung-tak Jang, Ho-Taek Song, Sungjun Kim, Eun-Jin Cho, Ho-Geun Yoon, Jin-Suck Suh and Jinwoo Cheon, *Nature Medicine*, 2006, **13**, pp 95-99.
- [3] Lei Wang, Kaida Yang, Cesar Clavero, Andrew. J. Nelson, Kyler J. Carroll, Everett E. Carpenter, and Rosa. A. Lukaszew, *J. Appl. Phys.*, 2010, **107**, 09B303.
- [4] Lei Wang, Cesar Clavero, Zachary Huba, Kyler J. Carroll, Everett E. Carpenter, Diefeng Gu and Rosa A. Lukaszew, *Nano Lett.*, 2011, **11**(3), pp1237-1240.

5:00pm NS-MoA10 Plasmon Induced Current in Metal/Organic Hybrid Nanostructures. *D. Conklin, S. Nanayakkara, T. Park*, University of Pennsylvania, *J. Stetcher, M. Therien*, Duke University, *D.A. Bonnell*, University of Pennsylvania

Recently we demonstrated a new mechanism of plasmon-induced electronic transport in hybrid metal nanoparticle-molecular devices. The mechanism realizes enhancements of up to a factor of 200. The hybrid structures consist of arrays of gold nanoparticles linked by (porphinato)zinc(II) oligomers. Here we examine the role of metal particle size, spacing, and molecular length on the transport mechanisms. Understanding the charge transport through the structures allows the relative roles of nano antennae field focusing and hot electron distribution to the current enhancement to be compared. This phenomenon offers a pathway to wide ranging control of the opto electronic transport properties which enables concepts of energy harvesting, energy transduction and optoelectronic circuits.

5:20pm NS-MoA11 Direct-bandgap Infrared Light Emission from Tensilely Strained Germanium Nanomembranes. *J.R. Sanchez-Perez*, University of Wisconsin Madison, *C. Boztug*, Boston University, *F. Chen*, University of Wisconsin Madison, *F. Sudradjat*, Boston University, *D.M. Paskiewicz, R.B. Jacobson*, University of Wisconsin Madison, *R. Paiella*, Boston University, *M.G. Lagally*, University of Wisconsin Madison

Silicon, germanium, and related alloys, which provide the leading materials platform of electronics, are extremely inefficient light emitters because of their indirect fundamental energy bandgap. This basic materials property has so far hindered the development of group-IV photonic active devices, including diode lasers, thereby significantly limiting our ability to integrate electronic and photonic functionalities at the chip level. Here we show that Ge nanomembranes can be used to overcome this materials limitation. Theoretical studies have predicted that tensile strain in Ge lowers the direct energy bandgap relative to the indirect one. We demonstrate [1] that mechanically stressed nanomembranes allow for the introduction of sufficient biaxial tensile strain to transform Ge into a direct-bandgap, efficient light-emitting material that can support population inversion and therefore provide optical gain. [1] F. Chen, C. Boztug, J. R. Sanchez-Perez, F. Sudradjat, D. M. Paskiewicz, R. B. Jacobson, M. G. Lagally, and R. Paiella, *Direct-bandgap germanium pumped above optical transparency in tensilely strained nanomembranes*, submitted. Research supported in part by NSF and DOE

Plasma Science and Technology Division Room: 202 - Session PS+BI-MoA

Multiphase (Liquid, Solid, Gas) and Biological Related Plasmas

Moderator: A.M. Coclite, Massachusetts Institute of Technology

2:00pm PS+BI-MoA1 Atmospheric-Pressure Microplasmas for Novel Electrochemical Applications. *S.W. Lee, R.M. Sankaran*, Case Western Reserve University

Plasmas formed at sub-millimeter spatial scales operate stably and close to non-thermally at atmospheric pressure and are a source of ions, electrons, and other electronically excited states at ambient conditions. Overall, these features make microplasmas suitable for novel electrochemical applications where gas-phase species (e.g electrons) in the plasma can directly interact with ionic aqueous electrolytes to initiate redox reactions.

In this talk, we will present two approaches to microplasma-based electrochemistry that we have developed for nanoparticle synthesis. In one approach, microplasmas are formed at the surface of a liquid electrolyte and operated similar to an electrochemical cell with the plasma as the cathode and a solid metal immersed in the electrolyte as the anode [1]. Metal cations in solution such as Ag^+ are electrochemically reduced by the plasma to solid metal, resulting in the formation of metal nanoparticles without any chemical reducing agent. Alternatively, thin films of metal cations dispersed on a polymer are electrochemically reduced by a rastered microplasma [2]. This configuration allows microscale patterns of metal nanoparticles to be produced without the need for lithography. Recently, we have extended our patterning method to the reduction of metallopolymers which are novel molecular structures that can be used as a template for metal ion and metal particle formation [3]. This strategy has enabled patterns of metal nanoparticles to be prepared which are beyond lithographic limits. We will discuss our experimental techniques in detail, as well as the properties of the nanoparticles as assessed by UV-Visible absorbance spectroscopy, X-ray diffraction, and transmission electron microscopy.

1. C. Richmonds et al., Appl. Phys. Lett. 93, 131501 (2008).
2. S. W. Lee et al., Adv. Func. Mater., doi:10.1002/adfm.201100093
3. S. W. Lee et al., in preparation.

2:20pm **PS+BI-MoA2 Water Containing Non-Equilibrium Atmospheric Pressure Plasmas**, *P.J. Bruggeman*, Eindhoven University of Technology, the Netherlands **INVITED**

During the last decade water containing non-equilibrium atmospheric pressure plasmas have received a continuously increasing attention in view of their potential in biomedical, environmental, chemical synthesis and material processing applications. This evolution coincides with a strong need for improved diagnostics to enable us to unravel the complex physics and chemistry of water containing plasmas. Both discharges containing a liquid water phase and only water in the vapor phase will be addressed in this contribution.

We will give an overview of the physical and chemical properties of these discharges. The main plasma parameters such as the electron density, gas and electron temperature will be presented and the complications of the interpretation of the diagnostics to obtain these plasma parameters will be discussed. Water containing discharges produce high radical densities such as OH, which is a key radical in several applications. Due to the often high electron density of these discharges recombination reactions are very important not only for radical production but also to explain the optical emission of these discharges. Key differences between liquid water containing discharges and more conventional gas discharges will be discussed.

References:

- P. Bruggeman and C. Leys, Non-thermal plasmas in and in contact with liquids (topical review paper), J. Phys. D: Appl. Phys., 42 (2009) 053001
- P. Bruggeman, D.C. Schram, M.A. Gonzalez, R. Rego, M.G. Kong and C. Leys, Characterization of a direct DC-excited discharge in water by optical emission spectroscopy, Plasma Sources Sci. Technol. 18 (2009) 025017
- T. Verreycken, A. F. H. van Gessel, A. Pageau and P. Bruggeman, Validation of gas temperature measurements by OES in an atmospheric air glow discharge with water electrode using Rayleigh scattering, Plasma Sources Sci. Technol. 20 (2011) 024002
- P. Bruggeman, F. Iza, D. Lauwers and Y. Aranda Gonzalvo, Mass spectrometry study of positive and negative ions in a capacitively coupled atmospheric pressure RF excited glow discharge in He-water mixtures, J. Phys. D: Appl. Phys. 43 (2010) 012003

3:00pm **PS+BI-MoA4 Mechanism of Au Nanoparticles Formation in Solution Plasma**, *M.A. Bratescu, O. Takai, N. Saito*, Nagoya University, Japan

The Solution Plasma Processing (SPP) has been developed in our laboratory to synthesize nanoparticles and to improve surface properties of carbon nanomaterials by decorating with different nanoparticles or binding functional groups on the surface. The purpose of the present study is to investigate the mechanism of the Au nanoparticles (NP) formation in the SPP and to correlate the SPP properties with the Au NPs characteristics (morphology, size and surface functionalization). The investigation was conducted by changing the solution pH, using the same surfactant and keeping the same processing parameters.

The Au NPs were synthesis in an aqueous solution of 1 mM $\text{HAuCl}_4 \cdot 3\text{H}_2\text{O}$ used as precursor, 1 mM hexadecyltrimethylammonium chloride (CTAC) used as surfactant, and NaOH used to adjust the solution pH (3.2, 6.5 and 11.2). The plasma was produced by using a pulsed high voltage (HV) power supply with the peak voltage and current of 2 kV and 1 A, respectively and

the pulse width of about 1 μs . Plasma was characterized by optical emission spectroscopy (OES). The OES gives information about the presence of the relative number densities of the radicals as H, OH, O, and O_2 and from these data the electron temperature and density were evaluated.

On surface, in high vacuum environment, the Au NPs were characterized by Transmission Electron Microscopy (TEM), Secondary Ion Mass Spectrometry Time of Flight (SIMS - ToF) and X-rays Photoelectron Spectroscopy (XPS). In solution, as prepared, the Au NPs were characterized by UV-visible spectroscopy and Attenuated Total Reflectance Fourier Transform Infrared (ATR-FTIR) spectroscopy.

The size of the synthesized Au NPs depends on the initial pH of the solution. In a low pH solution, the particle size was around 15 – 20 nm diameter and in a solution with a higher pH value than 6, the NPs diameter was found to be 2 – 5 nm. The negative SIMS-ToF measurements reveals the presence of the Au^- , AuCl^- and AuN^- ions in the solution with a pH 3 and AuO^- in a solution with pH 11. In a solution before plasma processing, with a low pH value the negative ions Au_2Cl^- and Au_3Cl_2^- were detected, which can suggest an initial agglomeration of Au atoms in solution. The binding functional groups on the Au NPs are confirmed by the XPS analysis.

The correlation among information of the Au NPs morphology, the binding atoms on Au surface, plasma electron temperature and density and the formation of the Au complexes, during the Au NPs synthesis will be presented and discussed.

3:40pm **PS+BI-MoA6 Pulsed Plasma Studies of 2-chloro-p-xylene**, *I.C. Estrada-Raygoza, G. Padron-Wells, P.L.S. Thamban, L.J. Overzet, M.J. Goeckner*, University of Texas at Dallas

Chemical vapor deposited parylene-C is widely used for applications ranging from biomedicine to microelectronics. In our work, we use 2-chloro-p-xylene (2ClpX) as a precursor to deposit plasma polymerized Parylene C. Here we report data aimed at determining the dissociation mechanisms of the 2ClpX in the plasma. Specifically that data is from: in situ Fourier transform infrared spectroscopy (FTIR); plasma optical emission spectroscopy (OES); and electron beam OES. The main dissociation products are HCl, methane and acetylene. We also observe atomic and molecular hydrogen and chlorine, HCl ion, CH and the characteristic broad aromatic band in the 300 nm region. Both frequency and duty cycle have a strong effect in 2ClpX dissociation. When the pulse period is smaller than the diffusion time, the discharge behaves as continuous wave system, independent of the duty cycle used. When the pulse period is much larger than the diffusion time, the discharge behaves different and very little break up of the monomer is detected. When the pulse period is similar to the diffusion time, then the effect of duty cycle is considerable. This work is supported in part by NSF (Grant CBET- 0922962), Verity Instruments and CONACYT Grant 170201.

4:00pm **PS+BI-MoA7 Deactivation of Lipopolysaccharide and Lipid A by Ar/H₂ Inductively Coupled Plasma**, *E. Bartis*, University of Maryland, College Park, *T.-Y. Chung, N. Ning, J.-W. Chu, D.B. Graves*, University of California, Berkeley, *J. Seog, G.S. Oehrlein*, University of Maryland, College Park

Low temperature plasma (LTP) treatment of surfaces is a promising path toward sterilization of bacteria [1]. Past works have shown plasma-induced degradation of bacteria [2], but little knowledge exists regarding the plasma-induced chemical modifications in biomolecules that result in inactivation since various plasma species, e.g. ions, reactive radicals, and UV/VUV photons may aid in inactivation. Lipopolysaccharides (LPS) are a main component of the outer membrane of gram-negative bacteria and are difficult to remove from surfaces by conventional methods [3]. LPS is made up of a polysaccharide chain and lipid A and lipid A elicits an immune response in animals [1]. Previous studies have found that adding H₂ to an Ar plasma leads to a reduction of infrared bands originating from the aliphatic chains of lipid A, namely C-Hx stretching, C-O, and amide bands [4]. This study aims to distinguish the roles of physical sputtering, chemical attack by H-atoms, and plasma-generated VUV. LPS-coated silicon chips were exposed to LTP (Ar, H₂, and Ar/H₂ mixtures) to explore the effects of plasma composition/ion energy on the etch rates (ER) and chemical and optical properties of LPS. Real-time in-situ ellipsometry was used to monitor ER and changes in the LPS film's optical density during plasma exposure. The real-time data showed that Ar plasmas create a dense film on the surface that decreases in density with H₂ addition. The films were etched fastest in Ar discharges mixed with ~10% H₂ and were slowest in pure H₂. Since previous work [4] found that adding H₂ to an Ar discharge enhanced sterilization, these results may indicate that chemical modification rather than rapid erosion may be more important for inactivation. After LTP treatment, samples were characterized by vacuum-transfer to x-ray photoelectron spectroscopy (XPS) to measure the chemical modifications taking place in the LPS layer. With XPS, we measured a decrease in the

intensity of the C-C/C-H peak, which indicates that the aliphatic chains in lipid A were removed. The N/C ratio increases approximately equally in all discharges, which suggests that gas chemistry does not have a large impact on amides. Complementary studies with Lipid A will be presented as well as results of a VUV optical filter approach used to probe VUV-induced LPS modifications in real time by in-situ ellipsometry while protecting the material against ion bombardment.

- [1] A. von Keudell et al., *Plasma Process. Polym.* 7, 327 (2010)
- [2] H. Rauscher et al., *Chem. Phys. Chem.* 11, 1382 (2010)
- [3] E. T. Rietschel et al., *FASEB J.* 8, 217 (1994)
- [4] O. Kylian et al., *Plasma Process. Polym.* 5, 26 (2008)

4:20pm **PS+BI-MoA8 Development of Plasma Treated Mn Induced Nano-arrayed Structures in Sol-gel Derived TiO₂ Matrix for Biosensing Applications**, R.R. Pandey, Centre for Cellular and Molecular Biology, India, K.K. Saini, National Physical Laboratory, India, M. Dhayal, Centre for Cellular and Molecular Biology, India

We describe Mn doped TiO₂ nanomaterial-based biosensors modified by high pressure RF plasmas for biosensor applications which activates nanostructure matrix and greatly enhanced enzyme loading capacity for development of high sensitivity biosensors. As a test modal, effects of plasma treatment on a novel potentiometric urea biosensor for selective and quantitative recognition of urea by immobilizing urease onto Ti/urease-imprinted Mn induced TiO₂ film has been studied and monitoring the potentiometric response caused by the immobilized urease/urea reaction system was carried out. These platforms have been characterized by XRD, XPS, FTIR, SEM, cyclic voltammetry to determine the changes in structure, surface chemistry and electron transfer characteristics of platforms after plasma treatments and have been correlated with improved response of biosensor.

4:40pm **PS+BI-MoA9 Growth Promotion of Bread Yeast using Atmospheric Pressure Dielectric Barrier Discharges**, S. Kitazaki, K. Koga, M. Shiratani, Kyushu University, Japan, N. Hayashi, Saga University, Japan

Nonthermal atmospheric pressure plasmas have been employed for biomedical processing applications, because they provide high density radicals at a low gas temperature [1]. Recently, nonthermal atmospheric pressure plasmas as well as low pressure plasmas have been employed for growth promotion of plant cells [2,3]. In this study, we have developed a scalable atmospheric dielectric barrier discharge (DBD) device for biomedical processing in a large area and have applied the device to growth promotion of bread yeast. The device consisted of 20 electrodes of a stainless rod of 1 mm in outer diameter and 60 mm in length covered with a ceramic tube of 2 mm in outer diameter. The electrodes were arranged parallel with each other at a distance of 0.2 mm. The dry yeast was set at 1 mm under the electrodes. The discharge voltage and frequency were 10 kV and 10 kHz, respectively. The plasma treatment was carried out in the air. The treatment duration T_{on} was 50, 100 and 150 s. After the treatment, yeast was suspended in 0.5 ml yeast extract peptone dextrose (YPD) medium and agitated with a vortex mixer. 1 μ l of sample was mixed with 99 μ l YPD medium in a micro well plate and cultivated using a shaking incubator at 30 °C. To obtain growth curve of yeasts time evolution of 660 nm light absorbance of the samples was measured with a micro plate reader. For the control, the absorbance is almost constant until $t = 15$ hrs after the beginning of the cultivation, which corresponds to the lag phase, and then it exponentially increases with t , the exponential growth phase. For yeast with the plasma treatment, the absorbance increases from $t = 0$ hrs. At $t = 10$ hrs, the maximum absorbance for $T_{on} = 150$ s is 6.6 times as high as that for the control. From $t = 10$ to 15 hrs, the gradient of the absorbance becomes gradual. After $t = 15$ hrs, the absorbance increases exponentially with t . The plasma treatment reduces the lag phase of yeast growth and enhances the growth rate. The growth promotion tends to be enhanced with increasing T_{on} from 50 to 150 s. The growth promotion, therefore, depends on the dose of radicals produced by discharge plasmas.

- [1] M. G. Kong, M. Keidar, and K. Ostrikov, *J. Phys. D: Appl. Phys.* 44, 174018 (2011).
- [2] S. Kitazaki, D. Yamashita, H. Matsuzaki, G. Uchida, K. Koga, and M. Shiratani, *Proc. IEEE TENCON 2010, 1960* (2010).
- [3] Y. Akiyoshi, A. Nakahigashi, N. Hayashi, S. Kitazaki, T. Iwao, K. Koga, and M. Shiratani, *Proc. IEEE TENCON 2010, 1957* (2010).

5:00pm **PS+BI-MoA10 Plasma Deactivation of Pyrogenic Biomolecules: Vacuum Ultraviolet Photon and Radical Beam Effects on Lipid A**, T.-Y. Chung*, N. Ning, J.-W. Chu, D.B. Graves, University of California, Berkeley, E. Bartis, J. Seog, G.S. Oehrlein, University of Maryland, College Park

Conventional medical instrument sterilization methods are generally ineffective in completely removing harmful biological residues [1]. Biomolecules such as proteins and other pyrogens from bacterial residues are particularly resistant to elevated temperature and are not easily removed by conventional procedures [2, 3]. For example, the presence of lipopolysaccharide (LPS) in host tissue or blood circulation could lead to a generalized sepsis syndrome including fever, hypotension, and respiratory dysfunction and may lead to multiple organ failure and death [4]. Low temperature plasma is a promising technique for sterilization/deactivation of surgical instruments or medical devices, but its effectiveness against such targets is incompletely understood [5]. In this study using a vacuum beam system, we chose lipid A, the major immune-stimulating region of LPS, as a model biomolecule to study. Lipid A consists of a β -1,6-linked D-glucosamine (GlcN) disaccharide carrying two phosphoryl groups. This structure is attached to multiple acyl chains by ester or amide linkage [6]. After vacuum ultraviolet (VUV) photon exposure, loss of CH₂/CH₃, C=O ester, and P=O absorption peaks were observed by ex-situ transmission Fourier transform infrared (FTIR) spectroscopy, but the C=O amide absorption peak was only mildly affected. Monitoring photolysis products from lipid A films by in-situ mass spectrometry, we observed cracking patterns similar to those of alkanes/alkenes with a carbon number ~11-13. This result suggests that VUV photons remove phosphate groups and break ester linkages leading to desorption of acyl chains. Endotoxicity of lipid A is known to be primarily determined by the number and length of acyl chains as well as the phosphorylation state and the disaccharide backbone [6]. The present results therefore indicate that plasma-generated VUV reduces the endotoxicity of lipid A, in support of the hypothesis of Rossi et al. [7]. We report the effects of VUV and radical (H, O) exposures on endotoxicity based upon chemical structural change in Lipid A. Synergism of various beams is compared with plasma exposures and corresponding molecular dynamic (MD) simulations.

- [1] R. L. Baxter et al., *J. Hosp. Infect.* 63, 439 (2006)
- [2] T. Nakata, *J. Parenter. Sci. Technol.* 47, 258 (1993)
- [3] L. Moesby et al., *Eur. J. Pharm. Sci.* 26, 318 (2005)
- [4] J. Cohen, *Nature* 420, 885 (2002)
- [5] A. von Keudell et al., *Plasma Process. Polym.* 7, 327 (2010)
- [6] C. Erridge, E. Bennett-Guerrero, and I. R. Poxton, *Microbes Infect.* 4, 837 (2002)
- [7] F. Rossi et al., *New J. Phys.* 11, 115017 (2009)

5:20pm **PS+BI-MoA11 Charge Transfer Reactions at the Plasma-Liquid Interface**, M. Witzke, C. Richmonds, B. Bartling, S.W. Lee, J. Wainright, C.-C. Liu, R.M. Sankaran, Case Western Reserve University

Electrochemical reactions are normally studied at the interface of a solid metal electrode and an aqueous ionic electrolyte. A smaller number of experiments exist, dating back to more than 100 years ago¹, of plasmas formed at the surface or inside of liquids to initiate electrochemical reactions at the interface of a plasma electrode and a liquid electrolyte. Despite this long history, reactions at the plasma-liquid interface remain poorly understood. Plasmas that are formed at low pressures require liquids with extremely low vapor pressure, limiting previous studies to ionic liquids (i.e. molten salts)². In addition, plasmas are characterized by a complex environment (e.g. ions, electrons, UV, etc.) which has made it difficult to differentiate charge-transfer reactions from other non-faradaic reactions such as radical generation and chemical dissociation.

We have recently developed a novel microplasma source that allows a non-thermal, atmospheric-pressure plasma to be stably formed at the surface of aqueous ionic electrolytes^{3,5}, facilitating fundamental study of charge-transfer reactions at the plasma-liquid interface. Electron transfer reactions between the plasma and the liquid are studied by using the well-known ferricyanide-ferrocyanide redox couple. The electrochemical reduction of ferricyanide is monitored by UV-vis absorbance spectroscopy and cyclic voltammetry. We find that ferricyanide is indeed reduced by the plasma, confirming that charge transfer reactions can occur at the plasma-liquid interface. The rate of ferricyanide reduction is found to depend on the discharge current, which controls the electron flux delivered to the surface of the solution. By comparing the (discharge) current to the amount of ferricyanide reduced, we obtain a reduction efficiency of ~1%. To address the relatively low efficiency, we have measured the potential at the plasma-liquid interface to determine whether the potential is high enough for water

* Coburn & Winters Student Award Finalist

electrolysis and measured hydrogen generation by mass spectrometry. In this talk, we will present our overall methodology and discuss these results in detail.

1. J. Gubkin, *Ann. Phys.* **32**, 114 (1887).
2. S. Z. El Abedin, M. Polleth, S. A. Meiss, J. Janek, and F. Endres, *Green Chemistry* **9**, 549 (2007).
3. C. M. Richmonds and R. M. Sankaran, *Appl. Phys. Lett.* **93**, 131501 (2008).
4. W-H. Chiang, C. Richmonds, and R. M. Sankaran, *Plasma Sources Sci. Technol.* **19**, 034011 (2010).
5. F-C. Chang, C. Richmonds, and R. M. Sankaran, *J. Vac. Sci. Technol. A* **28**, L5 (2010).

Plasma Science and Technology Division

Room: 201 - Session PS+SE-MoA

Advanced FEOL / Gate Etching II

Moderator: A. Kadavanich, Mattson Technology

2:00pm **PS+SE-MoA1 Mechanical Analysis of the Line Edge Roughness in the sub-20nm Line Patterns**, *S.W. Park, K.H. Baek*, Samsung Electronics Co., Ltd, Republic of Korea, *S.H. Choi, J.S. Hong*, Lam Research Corporation, *K.S. Shin, Y.G. Shin, H.G. Kang*, Samsung Electronics Co., Ltd, Republic of Korea

In this study, the deterioration of line edge roughness during plasma etching process was analyzed to find possible control parameters. According to the aggressive design rule shrinkage of memory devices, the physical width of line patterns has become around 20nm. Controlling line edge and width roughness now became one of the biggest challenges in patterning process. Though a number of studies on this matter have done, the wiggling of line patterns is still making the migration slower. It is well known truth that the line edge and width roughness are mainly caused by the projection of poor photoresist patterns. However, the recent line patterns of around 20nm design rules experience severe wiggling added from the plasma etching process. This study focused on this etch-induced deformation that increased line edge roughness from the prior status. The final line edge roughness was assumed as the sum of the wiggling projected from that of mask pattern and the deformation during plasma process. The deformation part was explained with the equations of the mechanical beam theory assuming several stress sources originated from the plasma. This newly introduced approach could suggest the direction of process modification for more robust profile against deformation. Moreover, combining with the material properties of commonly used materials, this approach could estimate the extent of lateral deformation so that the ultimate size of line patterns could be expected in the aspect of line edge roughness.

2:20pm **PS+SE-MoA2 Dependence of ArF Photoresist Polymer Structure on Line-Edge-Roughness Formation during Plasma Etching Processes**, *T. Uesugi, A. Wada*, Tohoku University, Japan, *S. Maeda, K. Kato, A. Yasuda, S. Sakuma*, Mitsubishi Rayon, Japan, *S. Samukawa*, Tohoku University, Japan

ArF excimer laser (193nm) lithography technique is widely used in the fabrication of sub-50-nm devices. During plasma etching processes, however, the activated species radiated from plasma, such as ions, radicals, and photons, cause damages to ArF photoresist, resulting in low etching resistance and formation of line-edge roughness (LER). To solve these issues, we investigated the interaction between irradiated species from plasma and polymer structure of ArF photoresist. In our previous study, we found that improvement of stability of lactone group in side chain of ArF photoresist realized decrease in etching rate and reduction of the surface roughness of ArF photoresist.

In this study, to further improve the etching resistance and the surface roughness of ArF photoresist, we proposed a new polymer structure of ArF photoresist. Our newly developed ArF photoresist structure has acrylate group in main chain polymer structure, while usual ArF photoresist has methacrylate group in main chain polymer structure. We prepared silicon wafers coated by ArF photoresists with methacrylate group and acrylate group and etched them using chlorine plasma. As a result, these two types of photoresists had almost same etching rates. This result suggests that main chain structure of ArF photoresist does not affect its etching rate. On the other hands, the surface roughness of acrylate type photoresist after etching was drastically reduced in comparison with that of methacrylate type photoresist. It is considered to be due to stronger bonding energy of acrylate group than methacrylate group. From this result, it is concluded that the

acrylate type ArF photoresist structure is very effective to suppress the roughness formation in ArF photoresist.

2:40pm **PS+SE-MoA3 193nm Photoresist Pre-Treatments Before Plasma Transfer to Improve LWR Transfer and CD Control**, *E. Pargon*, CNRS-LTM, France, *L. Azarnouche*, ST Microelectronics, France, *M. Fouchier, K. Mengueli, O. Joubert*, CNRS-LTM, France

Linewidth roughness (LWR) is today one of the main parameters that limits our ability to shrink the transistor gate dimension down to 20nm. Indeed, LWR needs to be controlled down to 2nm to ensure good electrical performance of the future CMOS device, while state of the art patterning techniques only allows 4-3 nm gate LWR at best. The major issue in decreasing the gate LWR comes from the fact that the significant LWR of the resist pattern printed after 193nm lithography (about 6nm measured by CDAFM) is transferred into the gate stack materials during the subsequent plasma etching processes. One way to minimize the final gate LWR is to apply various pre-treatments to the resist patterns obtained right after lithography (before any plasma pattern transfer step).

In the present study, we have used CD-SEM and CD-AFM techniques to investigate the impact of different types of resist pre-treatments (combining plasma exposure (HBr, Ar, H₂ plasmas), vacuum ultra violet (VUV) light exposure, and annealing) on the photoresist LWR and profile. Many characterization techniques (FTIR and Raman spectrometries, ellipsometry, chromatography, DMA, TGA) have also been used to characterize the physico-chemical modifications of photoresist films responsible for the resist smoothing. We have also investigated the benefits of those resist pre-treatments on both LWR and CD control after pattern transfer in different stacks of materials.

We will show that all treatments generate resist chemical modifications that lead to a decrease in resist LWR while the etch resistance is not always improved. All treatments have in common the cleavage of the side groups (lactone group for plasma treatment and protecting group for annealing treatment) and a decrease of the glass transition temperature that seems to have a direct impact on the LWR decrease. But some other mechanisms compete according to the treatment used and its duration: main chain scission and crosslinking, leading to some different etch resistance improvement. Consequently even if some specific treatments (VUV light exposure, annealing) can improve the resist LWR before transfer, the subsequent plasma etching steps can degrade it and also induce a loss of CD control. We will show that by combining plasma exposure and annealing treatment the photoresist LWR could be decreased down to 2.6nm and that this LWR could be transferred into polysilicon gate without LWR and CD degradation.

3:00pm **PS+SE-MoA4 Plasma Smoothing of Extreme Ultraviolet Photoresist: LWR Reduction at 30nm Half Pitch**, *E. Atamirano-Sanchez, A. Pret Vaglio, R. Gronheid, D. Marc, W. Boullart*, IMEC, Belgium

Over the past years a tremendous amount of effort has been put on Extreme Ultraviolet lithography (EUVL) for printing the 16nm node. In 2010 imec's EUV alpha demo tool printed for the first time a 16nm node SRAM cell using state-of-the-art EUV photoresist (PR). In order to meet the line width roughness (LWR) requirements for the 16nm node, we have investigated plasma smoothing techniques on 30nm half pitch lines after exposure.

In this contribution we will report our findings on EUV PR plasma treatment (PT) using H₂, Ar and HBr for LWR reduction; and subsequent, in-situ PR encapsulation for preserving the improved LWR during subsequent pattern transfer. Currently we are investigating the vacuum UV role during the H₂ PT using MgF₂ windows. In parallel, we are characterizing a PR resist encapsulation carried out in-situ (in the etching chamber). The encapsulating layer is characterized through various analytical techniques, such as: XPS, Ellipsometry, mass metrology and TEM. These characterizations will provide understanding of how the H₂ plasma improves the LWR and of how the PR encapsulation preserves the PR pattern allowing a straight HM patterning profile.

This study was carried out on 300 mm silicon wafers with the following patterning stack, from top to bottom: 50 nm PR/20 nm under layer (UL)/15 nm SiOC/40 nm amorphous carbon layer (ACL). The dry etching was carried out in a ICP like reactor from Lam research (Kiyo C reactor TCPTM)

Power spectral density (PSD) analyses have shown that Ar and HBr plasmas do not improve the LWR of EUV PR as they do on 193i PR. Using the correct conditions in the ICP reactor, H₂ plasmas can improve LWR by ~30% without CD bias; in other words no PR reflow was detected.

After the H₂ plasma treatment, the pattern was transferred into the UL using a CH₂F₂/CF₄/O₂ gas mixture. This chemistry provides on the one hand a high PR passivation but on the other hand induces a PR pattern degradation, which is translated into higher LWR. A novel alternative for maintaining the improved LWR after H₂ PT was to deposit in-situ (in the ICP reactor) a silicon containing layer that encapsulates the PR and preserves the improved LWR when the pattern is transferred into the UL, the SiOC and the ACL.

3:40pm PS+SE-MoA6 Controlling Line Edge Roughness for Aggressively Scaled CMOS Devices by Reducing Organic Underlayer Deformation. *H. Miyazoe, S.U. Engelman, M. Glodde, M.A. Guillorn, M. Brink, A. Banik, W.S. Graham, E.M. Sikorski, N.C.M. Fuller*, IBM T.J. Watson Research Center

As the feature size in CMOS technology continues to shrink, control over line edge roughness (LER) and line width roughness (LWR) is approaching atomic scale for the 14 nm node and beyond. When the line/space patterns are decreased, deformation of the organic underlayer material occurs during plasma processing, which adversely impacts pattern transfer into substrate material to fail. We previously reported that vacuum ultraviolet (VUV) "curing" (modification) of the organic under layer material by plasma discharges is a promising approach to extend the process window for obtaining high fidelity pattern structures [1]. To understand the details of this approach in more detail, we exposed VUV light at various wavelengths corresponding to the absorption energies of various underlayer materials by synchrotron radiation on "unopened" and "opened" samples comprising stacks inclusive of the underlayer material. We found that exposing underlayers to certain absorption maxima of the patterning material maximize the curing effect. Specifically, for the underlayer material trademarked as NFC, absorption maxima at 155 nm had relatively large effect, reducing LER by as much as 37%. Curing treatments on "unopened" (post lithography) samples comprising varying underlayer materials effectively reduced the pattern deformation, though much less effective than on previously "opened" samples comprising the same. Similarly, chemical and physical effects of the plasma on underlayer material deformation were investigated. To investigate the changes based on chemical modification by plasma, we have generally found that the non-selective pattern transfer plasmas are better than highly selective processes to minimize the deformation. In addition, we also noticed that the ion energy of the discharge plays an important role in the deformation and found that the extent of pattern deformation decreased for lower energies. In addition, many commercially available organic underlayer materials were tested with respect to their composition and hardness. We found that the relative hydrogen content of the underlayer material seemed to correlate with the deformation behavior, while little effect was seen for hardness. These initial findings show that a close interlock between patterning materials, lithography and plasma processes has to be executed to minimize effects such as LER for future technology nodes.

[1] N.C.M. Fuller *et al.*, AVS presentation (2007).

4:00pm PS+SE-MoA7 Single Digit Nano Plasma Etching. *D.L. Olynick*, Lawrence Berkeley National Laboratory

One of our themes at the Molecular Foundry at LBNL is "Single-Digit Nanofabrication" (SDN) which describes our efforts to pattern materials with resolution, precision, and control at the sub-10 nm scale. At this scale, we enable research and applications in areas such as nanoelectronics, nanomagnetism, nanofluidics and plasmonics. For instance, the Molecular Foundry's work on graphene nanomeshes using SDN show a band gap opening with sub-bands.¹ However, the patterning and plasma pattern transfer for SDN present significant challenges and the question arises, "What are the limits?"

In this talk, I will survey nanoscale etching work from 30-3 nm to demonstrate the challenges and opportunities for plasma nanopatterning. High resolution patterns are made using a variety of materials and techniques including atomic layer deposition, directed self-assembly and electron beam and nanoimprint lithographies. Recent work with cryogenic etching and simulation in the SDN regime will be highlighted.

¹Liang, X.; Jung, Y.-S.; Wu, S.; Ismach, A.; Olynick, D. L.; Cabrini, S.; Bokor, J., *Nano Lett* **2010** 10, pp 2454-2460.

This work was performed at the Molecular Foundry, Lawrence Berkeley National Laboratory, and was supported in part by the U.S. Department of Energy under Contract No. DE-AC02-05CH11231

4:40pm PS+SE-MoA9 Ar and He Plasma Pretreatments of Organic Masking Materials for Performance Improvements during Plasma Pattern Transfer. *D. Metzler, F. Weinhoeck, N. Kumar, G.S. Oehrlein*, University of Maryland, *S. Engelmann, R.L. Bruce, N.C.M. Fuller*, IBM T.J. Watson Research Center

Plasma based pretreatments (curing) of organic masking materials have been shown to offer significant potential for reduction of surface, line edge and line width roughness during the subsequent pattern transfer process. Since one of the underlying mechanisms of roughness formation has been reported to be a synergistic effect of energetic ion bombardment, ultraviolet (UV) / vacuum ultraviolet (VUV) plasma radiation and increased temperature, a possible mechanism of organic mask curing may be the elimination of the above synergism by sequential exposures to VUV plasma radiation followed by ion bombardment dominated plasma etching. To examine this question, and establish the impact of pre-treatments on roughness introduction, etch resistance and pattern transfer fidelity during the pattern transfer process, we have studied pretreatments of 193nm PR and other organic masking materials in Ar and He discharges with pronounced UV/VUV emission. The impact of pretreatments and subsequent pattern transfer processes on the organic materials were monitored in real-time by in-situ ellipsometry. Multilayer modeling of these data allows determination of optical material density and film thickness of various layers, i.e. the surface layer densified by ion bombardment, the UV/VUV modified layer in the material bulk, and the rough surface layer. Additionally, post plasma characterization by Fourier transform infrared spectroscopy (FTIR) and atomic force microscopy (AFM) provides information on bulk material modifications and surface roughness improvements, respectively. UV/VUV spectroscopy combined with Langmuir probe characterization provides information on plasma parametric dependencies of photon and ion fluxes, respectively. Pretreatments in a He discharge reduced roughness introduction in a C₄F₈/Ar pattern transfer process by ~50% (RMS=4nm) while increasing film etch resistance by ~30% leading to only a slight increase in the total material removal when compared to the uncured material (pattern transfer only). Time resolved studies of this process allow detailed investigation of distinct stages and underlying mechanisms of materials modification, such as radiation induced changes in the materials bulk, ion crust formation at the film surface, and surface roughness development. Correlating these observations with post plasma characterization by AFM and FTIR allows a mechanistic understanding of plasma based pretreatments or organic materials and their impact on the subsequent pattern transfer process. The dependence of improvements in masking performance on Ar and He plasma based pretreatments and a description of the underlying mechanisms will be presented.

5:00pm PS+SE-MoA10 Sub-32nm Node Mask Patterning for Deep Silicon Trench Etch. *J. Yarmush, H. Haga, Y. Chiba, K. Kumar, P. Biolsi*, TEL Technology Center, America, LLC, *J. An, H. Hichri, B. Dirahoui, X. Li*, IBM Microelectronics, *R. Wise*, IBM Research

In the last several semiconductor device generations, one of the complexities in fabricating ever smaller feature sizes and increased density, has been the stringent requirements placed on photolithographic processes and mask scheme formation. The use of Immersion Lithography, reduced resist layer thicknesses and planarity requirements have driven the need for complex multilayer-multimaterial stacks that can be utilized for subsequent plasma Etching masks.

One requirement by manufacturers of Sub-32nm DRAM technology, utilizing deep silicon memory cells, is an extremely high aspect ratio mask that enables the anisotropic etch profile of the Silicon Trench. To meet both the needs of the photolithographic processes and the high aspect ratio mask requirements of the Silicon Trench etch, a complex Photo Resist, Silicon Anti-reflective coating, Optical Dispersive Layer, CVD Oxide layer is used. This deposited mask stack also sits on top of a Silicon-on-Insulator layer that must also be etched through anisotropically.

In this paper, we describe the unique requirements of etching each film stack in order to meet the overall physical requirements of this high aspect ratio mask patterning etch. It also describes the process capabilities of a commercially available Capacitively Coupled Plasma reactor that enables it to meet these advanced complex film stack requirements.

This work was performed by the Research and Development team at TEL Technology Center America in joint development with IBM Semiconductor Research & Development Center.

5:20pm PS+SE-MoA11 Quantitative Determination of the Mechanism of Anisotropic Silicon Etching. *M. Hines, M.F. Faggin, K. Bao, A. Gupta, B. Aldinger*, Cornell University

The production of atomically perfect surfaces by simple solutions is both intrinsically fascinating and technologically important. For over half a century scientists have known that many aqueous bases — so-called

“anisotropic etchants” — selectively attack all silicon faces except Si{111}. As a result, a macroscopic silicon sphere placed into one of these solutions spontaneously transforms into a polyhedron. Twenty years ago, the surface science community was rocked when researchers at Bell Labs showed that, in some cases, the etched surfaces are not just smooth, they are atomically flat and passivated by a single monolayer of H atoms. This type of highly precise but inexpensive chemical machining is used in diverse applications ranging from the production of ink-jet nozzles to the fabrication of ultrasmall transistors to the cleaning and polishing of silicon wafers; however, the chemical reactions that govern this behavior remain a source of controversy. We resolve this controversy and give the first quantitative, atomic-scale understanding of anisotropic etching across all silicon surface — not just Si(111).

The reactivity of a wide variety of Si(100) surface sites towards a prototypical anisotropic etchant, ammonium fluoride, is quantitatively determined from measurements of the atomic-scale morphology and chemical composition of etched surfaces. These measurements enable the effects of chemical strain, steric hindrance, and chemical structure to be separately determined. The high selectivity of the etchant is explained by the strain energy released during the chemical reaction; steric hindrance plays an important, but distinct, role. This pattern of reactivity is inconsistent with previously postulated mechanisms of aqueous silicon etching, which postulate insertion reactions across rigid, essentially immobile Si-Si backbonds. Instead, we propose that cleavage of the backbond occurs during the formation of a surface silanone which is driven by simultaneous interadsorbate strain release. On Si(100) surfaces, this hypothesis *quantitatively* explains the characteristic alternating-row etch morphology on both flat and vicinal surfaces, the observed site-specific reactivity, the unusual reaction kinetics, and the hydrogen termination of the etched surface without invoking an unreasonably strained reaction intermediate. This mechanism also explains the atomic-scale reactivity and relative etch rates of the three principal faces of silicon, thereby giving the first atomic-scale understanding of anisotropic silicon etching.

Surface Science Division

Room: 109 - Session SS1-MoA

Selectivity and Reactivity of Chemisorbed Species

Moderator: A.J. Gellman, Carnegie Mellon University

2:00pm SS1-MoA1 **Observation and Modeling of Chiral Modifier-Substrate Complexes on Pt(111).** *B. Hammer*, Aarhus University, Denmark, *V. Demers-Carpentier, P.H. McBreen*, Université Laval, Quebec, Canada

INVITED

We present a combined density functional theory (DFT) and scanning tunneling microscopy (STM) study of the complex formation between the chiral modifier naphthylethylamine (NEA) and the model substrate trifluoroacetophenone (TFAP) on a Pt(111) surface. The two molecules interact via a hydrogen bond between the amine group on the NEA and the carbonyl on the TFAP. Many different realizations of the hydrogen bond exist depending on the relative position and orientation of the two molecules. However, only very few are observed experimentally. These are all among the most stable structures found in DFT. The chemisorbed TFAP is prochiral and hydrogenation of the carbonyl would lead to a chiral product. The prochirality of TFAP when forming a complex with NEA is regiospecific, i.e., it depends on the position at which the TFAP is chemisorbed relative to the NEA. The origin of this regiospecificity is discussed.

2:40pm SS1-MoA3 **Enantiospecific Decomposition of Tartaric Acid on Spherically Curved Copper Single Crystals.** *B. Holsclaw, P. Kondratyuk, A. De Alwis, A. Reinicker, V. Pushkarev, A.J. Gellman*, Carnegie Mellon University

The kinetics and mechanisms of many catalytic surface reactions depend on the atomic level structure of surfaces. Detailed study and understanding of the influence of surface structure on a given reaction is experimentally arduous. The space of possible surface orientations spans a two-dimensional continuum. A detailed study of structure sensitive surface chemistry requires preparation and study of many different single crystal substrates, each with a different orientation. A new high-throughput methodology has been developed based on the use of Surface Structure Spread Single Crystals (S4C), spherically curved single crystals that expose a continuous distribution of different crystallographic planes across their surfaces. These S4C surfaces are being studied using surface analysis tools capable of spatially-resolved measurements that can sample the continuous space of surface orientations.

Six copper S4C surfaces have been produced in-house: three low Miller index centered surfaces, (100), (110), and (111); and three high Miller index surfaces, (821), (861), and (432). Each surface has been chosen and spherically curved so that the complete set of surfaces spans the entire stereographic triangle. The surfaces have been characterized using laser profilometry and oriented using x-ray diffraction and low energy electron diffraction. A benefit of the S4C surfaces is that they are naturally chiral, forming regions of either R- or S- chirality. The surface chemistry of a chiral molecule, such as tartaric acid, on a naturally chiral surface can be enantiospecific. Tartaric acid decomposition from copper surfaces shows very high enantioselectivity due to its highly nonlinear surface explosion kinetics. The nature and magnitude of the enantioselectivity of tartaric acid decomposition across the stereographic triangle is not currently well-understood. Copper S4C surfaces provide an opportunity to study tartaric acid decomposition on virtually all possible copper surface structures. This research is the first attempt to map surface enantioselectivity for any compound across the entire stereographic triangle in high detail.

3:00pm SS1-MoA4 **Reaction Pathways of Alcohols with Transition Metal Oxides: A Comparison between WO_3 and MoO_3 .** *Z.J. Li, Y.K. Kim, R.J. Rousseau, B.D. Kay, Z. Dohnálek*, Pacific Northwest National Laboratory

The reactions of C1-C4 aliphatic alcohols over cyclic $(\text{WO}_3)_3$ and $(\text{MoO})_n$ (n ranges from 3 to 6) clusters were studied experimentally and theoretically using temperature-programmed desorption, infrared reflection-absorption spectroscopy, and density functional theory. Three reaction channels, dehydration, dehydrogenation, and condensation, have been identified on $(\text{WO}_3)_3$ clusters while only dehydration and dehydrogenation have been observed on $(\text{MoO}_3)_n$. The desorption temperature of reaction products decreases with increasing alkyl chain length. The lack of a condensation channel on $(\text{MoO}_3)_n$ is attributed to the lower reactivity of alcohols with $(\text{MoO}_3)_n$ as compared to $(\text{WO}_3)_3$ and consequently a negligible concentration of the Mo(VI) centers coordinated with two alkoxy species required for this reaction are formed. DFT calculations provide a detailed explanation for the reactivity and relative selectivity among the reaction channels and W(VI) and Mo(VI) metal centers.

This work was supported by the U.S. Department of Energy Office of Basic Energy Sciences, Division of Chemical Sciences, Biosciences and Geosciences, and was performed at EMSL, a national scientific user facility sponsored by the Department of Energy's Office of Biological and Environmental Research located at Pacific Northwest National Laboratory (PNNL). PNNL is operated for the U.S. DOE by Battelle Memorial Institute under contract no. DE-AC06-76RLO 1830. Computational resources were provided at EMSL and the National Energy Research Scientific Computing Center at Lawrence Berkeley National Laboratory.

3:40pm SS1-MoA6 **Molecular Dynamics Simulations of Oligomer Film Stabilization through Ion-Beam Deposition.** *T. Kemper*, University of Florida, *D. Lee*, Lawrence Livermore National Laboratory, *S.R. Phillpot, S.B. Sinnott*, University of Florida

Ion-beam deposition is used to stabilize conducting oligomer films for use in organic photovoltaic devices. The goal is to prevent structural changes caused by chemical attack, disorder, or desorption, that are known to degrade device performance. The second-generation reactive empirical bond-order (REBO) potential has been successfully applied to the irradiation and modification of crystalline, polymer and nanostructures, such as carbon nanotubes. In this work the atomic-level processes involved in selective modification of oligomers for optoelectronic applications through thermal energy particle deposition are explored to identify the mechanisms by which different polyatomic ions and radicals assist in the stabilization of oligomer films. In particular, oligomer films of polythiophene are bombarded with incident H, CH_2 , C_2H and thiophene in the hyperthermal regime that involve incident energies of 4-50 eV. The results of classical molecular dynamics simulations with the REBO potential are compared to experimental findings, as well as linearly scaled density-functional theory molecular dynamics results. This work was supported by the NSF (CHE-0809376).

4:00pm SS1-MoA7 **Structure-Reactivity Relationships in the Electron Induced Reactions of Surface Bound Organometallics.** *H. Fairbrother, S. Rosenberg, J. Wnuk*, Johns Hopkins University, *C. Hagen, W. van Dorp, K. Landheer*, Delft University of Technology, Netherlands

Electron beam induced deposition (EBID) is a direct-write lithographic technique where volatile organometallic precursors are decomposed by a focused electron beam in a low vacuum environment to create metallic nanostructures. As a tool for nanofabrication, EBID offers an attractive and unique combination of capabilities including high spatial resolution and the flexibility to deposit free-standing three-dimensional structures without the need for resist layers. However, a major limitation of EBID is that

nanostructures deposited from organometallic precursors typically possess unacceptable levels of organic contamination. To overcome this limitation it is crucial to develop a more detailed and fundamental understanding of how adsorbed organometallics undergo electron stimulated decomposition. Using a selected suite of organometallic precursors used in EBID ($\text{CH}_3\text{CpPt}(\text{CH}_3)_3$, $\text{Pt}(\text{PF}_3)_4$ and $\text{W}(\text{CO})_6$) I will describe how a surface science approach has been used to provide mechanistic and kinetic insights into EBID and to identify key structure-reactivity relationships. Central to our findings is the observation that for many organometallic precursors, EBID is initiated by the cleavage of a single metal-ligand bond and the release of the free ligand into the gas phase. However, subsequent electron stimulated reactions are characterized by decomposition rather than desorption of the residual ligands. Rationale design criteria for new organometallics which will decompose to produce metallic nanostructures with greater metallic purity have also been developed, such as the need to avoid using cyclopentadienyl ligands. In related studies we have also identified and rationalized the often significant effect that substrate temperature exerts on the composition of EBID materials created from organometallic precursors. Specifically, increased purity is expected for EBID films deposited at high substrate temperatures and low electron fluxes; the same conditions that reduce growth rates.

4:20pm SS1-MoA8 Role of Substituents in Reactivity of Isocyanates Pre-Adsorbed on Ge(100)-2x1, K.T. Wong, S.F. Bent, Stanford University

Direct attachment of organic molecules to semiconductor surfaces offers the ability precisely control interfacial properties through tailoring of the organic molecule. This study focuses specifically on organic functionalization of germanium, as the ability to control its interfacial properties may enable devices to take advantage of its favorable electronic properties, as compared to silicon. Past studies have shown that a number of isocyanate-containing molecules react with the Ge(100)-2x1 surface in ultra-high vacuum by [2+2] cycloaddition across the C=N bond of the isocyanate. In this study, we use *in situ* Fourier transform infrared spectroscopy and X-ray photoelectron spectroscopy to investigate further reaction following [2+2] cycloaddition. Density functional theory calculations are also used to corroborate and help understand these experimental results. We show that phenyl isocyanate pre-adsorbed on Ge(100)-2x1 is highly sensitive to subsequent exposure to water vapor. Experimental evidence suggests that water reacts with the adsorbed isocyanates to form a diphenyl urea compound, similar to what is expected for the reaction of phenyl isocyanate and water in solution. Extending the analogy with classic organic chemistry in solution, we find that addition of methyl or methoxy substituents to the phenyl ring of phenyl isocyanate can significantly decrease the adsorbed isocyanate's reactivity towards water. Such ability to easily tune the reactivity of an adsorbate-covered surface using principles from organic chemistry demonstrates the flexibility of organic functionalization and could be of importance when using organic functionalization for various applications.

4:40pm SS1-MoA9 Investigation of Adsorbed Sodium Dodecyl Sulfate Films Formed on Charged and Hydrophilic Surfaces, S.-H. Song, T. Weidner, National ESCA and Surface Analysis Center for Biomedical Problems, M.S. Wagner, The Procter & Gamble Company, D.G. Castner, National ESCA and Surface Analysis Center for Biomedical Problems

Surfactants are important compounds used in many industrial applications, with sodium dodecyl sulfate (SDS) being one of the most widely used surfactants. This study uses sum frequency generation (SFG) vibrational spectroscopy and surface plasmon resonance (SPR) sensing to investigate the structure of SDS films formed from the adsorption of SDS onto positively charged and hydrophilic surfaces. The surfaces studied included CaF_2 as well as RF glow discharge deposited films of allylamine. The SDS films were prepared by adsorption of SDS from water solutions ranging in concentration from 0.067 to 20 mM. Since the water molecules above the SDS layer interact with the films, peaks from both the SDS molecules and water molecules were studied. SFG spectra of SDS adsorbed onto the positively charged CaF_2 surface exhibits two well resolved CH_3 peaks at 2877 and 2942 cm^{-1} , and two OH peaks at ~3200 and ~3400 cm^{-1} . At the 0.2 mM SDS concentration on the CaF_2 surface the intensity of both the CH_3 and OH peaks decrease to close to background levels and then increase as the SDS concentration is raised. As the SDS solution concentration continues to increase the CH_3 and OH go through a second intensity minimum. This second intensity minimum occurs between 3-6 mM for the CH_3 peaks and near 8 mM for the OH peaks. Previous studies have suggested these SFG intensity minima are due to the neutralization of positively charged CaF_2 surfaces by the anionic charged head group of SDS (1). Since the shape and, thus, the phase of the SFG peaks are affected by the molecular environment, fits of the SFG data were used to quantify the orientation and alignment of the SDS layers across the wide range of SDS solution concentration. Since SFG is sensitive to both orientational order and the amount of material adsorbed we used SPR to determine the SDS

coverage for the different solution concentrations in order to separate the two contributions. Combining SFG and SPR results provides a more detailed understanding of the structure and interactions of adsorbed SDS films.

(1) Becraft, K. A.; Moore, F. G.; Richmond, G. L. *Journal of Physical Chemistry B* **2003**, *107*, 3675.

5:00pm SS1-MoA10 Photon Stimulated Desorption of the Sub-Nanometer Size Clusters of Water, Methane, Ethylene, and Their Mixtures, I. Arakawa, D. Matsumoto, S. Takekuma, R. Tamura, T. Miura, Gakushuin University, Japan

Photon stimulated dynamics, such as desorption, dissociation, or chemical synthesis, at the water cluster which contains organic molecules have been studied in conjunction with the photochemistry at ice particles in cosmic space and in the atmosphere. In our experimental study, the clusters were prepared on the surface of a solid rare gas, which was condensed on the copper substrate cooled by liquid helium in an ultra high vacuum chamber. Our method has the advantage in controlling the cluster size and of high density of specimens in comparison with a molecular beam experiment. The clusters on the solid rare gas were excited by vacuum ultra-violet light with a photon energy between 12 and 108 eV with a pulse width of 10 ns, which was generated by a laser plasma light source [1]. The mass spectrum of photo-desorbed ions was measured by a time-of-flight (TOF) method. There are variety of species in the photo-desorbed ions from the co-adsorbed system of water and methane; protonated water clusters, $(\text{H}_2\text{O})_n\text{H}^+$, methane clusters, $(\text{CH}_4)_n\text{CH}_k^+$, hetero-clusters of water and methane, $(\text{H}_2\text{O})_n(\text{CH}_4)_m\text{CH}_k^+$, and synthesized species, methanol, CH_3O^+ .

It was found that the presence of a water molecule in a cluster substantially enhanced, or was almost essential for, the desorption of any species, even for CH_3^+ and CH_5^+ , observed in the spectrum. Dissociation of the water molecule plays a key role in the chemical reaction in the clusters. It was also found that the desorption yield of each species showed strong dependence on the composition and the size of the mother cluster on the substrate, which were controlled by the amount of adsorption of water and methane. Close and systematic investigation of their correlation has revealed the mother cluster which yields the each desorbed ions: $(\text{H}_2\text{O})(\text{CH}_4)$ clusters yield CH_3^+ , CH_4^+ , $(\text{H}_2\text{O})\text{CH}_3^+$, and CH_3O^+ while $(\text{H}_2\text{O})(\text{CH}_4)_2$ clusters yield CH_5^+ , $(\text{H}_2\text{O})\text{CH}_3^+$, and C_2H_4^+ . These specific behaviors were also the case for the clusters of water and ethylene.

[1] T. Tachibana et al, *Surf. Sci.*, **593**, 264-268 (2005).

5:20pm SS1-MoA11 Nanobonding between 2-nm β -cristobalite SiO_2 on $\text{OH}(1\times 1)\text{Si}(100)$ and SiO_x for Monolithic Electronics by Surface Smoothing via Wet Chemical and Spin Processing: TMAFM Study and Modelling of Interphases, S.D. Whaley, ASU, N.X. Herbots, ASU / SiO2 NanoTech Inc. / SiO2 Associates, LLC, J.D. Bradley, SiO2 Associates LLC / ASU, R.J. Culbertson, M.A. Hart, D.A. Sell, Q.X. Bradley, ASU, R.L. Rhoades, S.N. Drews, Entrepix, Inc., R.B. Bennett-Kennett, ASU

β -cristobalite nanofilms, 2-nm thick, are nucleated on $\text{OH}(1\times 1)\text{Si}(100)$ via the Herbots-Atluri (H-A) method [1,2] and form ultra-smooth, ordered, interphases that desorb at low temperatures ($T < \sim 200$ °C) [3] These ordered oxide nanophases on $\text{OH}(1\times 1)\text{Si}(100)$ promote oxidation at low temperatures in ambient, when in contact with oxygen-deficient phases of SiO_2 used in electronics. They can nucleate and grow a cross-bonding interphase between two substrates and achieve "nanobonding" [4] between various combinations Si and silica.

Nanobonding means forming cross-bonding molecules which condense into a continuous macroscopic bonding interphase between 2 smooth surfaces put into mechanical contact. For this to occur, the surfaces need to exhibit wide flat atomic terraces (width > 10 nm), low atomic step density (< 500 steps/ μm across atomic terraces direction) and very low particulate density (less than $1/100$ μm^2). This contrasts with the typical density of surface steps (~ 500 steps/ μm a.a.t.d.) and particulate density $> \sim 0.1$ - 1 μm^{-2} in as received wafers or post-processing. A surface step density ≥ 500 step/ μm a.a.t.d, typically found on $\text{Si}(100)$ with miscuts $< 0.025^\circ$ and particulates densities ≥ 0.1 μm^{-2} particulates results in 3-dimensional isolated bonding points of contacts as opposed to more uniform, 2-dimensional interphases that grow laterally as well as across is shown to occur in nanobonding. Wet chemical processing and SEZ spin technology are compared and combined to smoothen substrates via the H-A chemistry [1,2] via Tapping Mode Atomic Force Microscopy, before and after nanobonding. Our results show nanobonding can result in bonding strength larger than 10 MPa/cm² as measured by mechanical bond pull tests. Wafers fracture within the bulk of both Si and silicate substrates rather than interfacial delamination.

[1] US Patent 6,613,677, issued 9/2/03 "Long range ordered semiconductor interface phase and oxides." 6,613,677, Herbots, N.; Atluri, V. P.; Bradley J.D.; Swati, Banerjee; Hurst, Q.B.; Xiang, J.

[2] US patent 7,851,365 issued 12/14/10, "Methods for preparing semiconductor substrates & interfacial oxides there on" Herbots N., Bradley J.D., Shaw J.M., Culbertson and Atluri V.P.

[3] **Patent** Filed: 4/30/09, "Low Temperature Wafer Bonding and for Nucleating Bonding Nanophases. N. Herbots, R. J. Culbertson, J.D. Bradley, M. A. Hart, D. A. Sell and S. D. Whaley

[4] N. Herbots, Q. Xing, M. Hart, J. D. Bradley, D. A. Sell, R. J. Culbertson, Barry J. Wilkens; "IBMM of OH Adsorbates and Interphases on Si-based Materials". Nucl. Instr. and Meth. in Phys. Res., B. IBMM 17th International Conference Proceeds (Aug, 2010), accepted

Surface Science Division

Room: 110 - Session SS2-MoA

Molecular Ordering and Electrochemical Interfaces

Moderator: S.L. Tait, Indiana University

2:00pm **SS2-MoA1 Self-assembled Chains of 4,4'-azopyridine on Cu(100) Stabilized by Metal-Organic Coordination Interactions**, *H. Lim, S.L. Tait*, Indiana University

Understanding self-assembled molecular architectures at surfaces is essential to control and tune low-dimensional nanometer-scale organic structures. 4,4'-azopyridine (APY) has been vapor deposited on the clean Cu(100) surface in ultra-high vacuum and investigated using scanning tunneling microscopy and X-ray photoelectron spectroscopy. APY is chosen as a model building block for metal-organic frameworks, and for its conformational switching by the photoactive azo bridge. At low coverage, APY self-assembles into highly-ordered one-dimensional chains oriented along the low symmetry directions of the surface, many of which grow from the Cu step edges and some of which form tee junctions with other chains. Careful analysis of high resolution STM images points to pyridyl-Cu interactions being responsible for the high chain stability at room temperature. The related molecule, azobenzene, forms 1D chains on Au(111), but these grow side-to-side by hydrogen bonding at the azo bridge nitrogens and are only observed at cryogenic temperatures [1]. At higher coverages, APY chains align in a parallel fashion to form 2D islands, which increase in size with annealing.

[1] A. Kirakosian, M. J. Comstock, J. Cho, M. F. Crommie, *Phys. Rev. B* **71**, 113409 (2005).

2:20pm **SS2-MoA2 Molecular Self-assembly of Terephthalic Acid and Sodium Chloride on the Cu(100) Surface**, *D. Skomski, S. Abb, S.L. Tait*, Indiana University

To expand the catalogue of available interactions for the efficient self-assembly of highly-ordered nanoscale structures, we have investigated the formation of new supramolecular networks of terephthalic acid (TPA) and sodium chloride (NaCl) on the copper (100) surface. The mixture of this organic species with salt is prepared by vapor deposition in an ultra-high vacuum system and represents a model system for ionic self-assembly in two-dimensions. Several structures have been observed by means of scanning tunneling microscopy molecular resolution imaging. Chemical shifts in the sodium 1s photoelectron peak have been observed by X-ray photoelectron spectroscopy upon addition of TPA to the surface, confirming a direct interaction. Our research indicates that TPA and sodium produce new structures due to favorable ionic interactions between sodium cations and the negatively charged carboxylate groups in TPA's deprotonated form. Interactions with the metal surface and organic molecules appear to be sufficient to break the ionic bonds of the NaCl lattice. The formation of new TPA-Na structures illustrates the interplay between adsorbate-substrate and ionic interactions and opens new possibilities for ionic self-assemblies at surfaces with highly ordered structure and specific chemical function.

2:40pm **SS2-MoA3 Characterization of Azulene-Based Self-Assembled Monolayer Films**, *C.L. Berrie, M. Barybin, B. Neal, A. Dela Rosa*, University of Kansas

Azulene has been predicted to have attractive electronic properties for potential use in molecular electronics applications. However, examples of self-assembled monolayers (SAM) of azulene-based molecules are rare. Characterization of a variety of azulene based SAM films has been carried out using ellipsometry, contact angle, FTIR, and AFM. The role of the functional linker group on the structural properties of the film as well as the electronic properties has been investigated. In addition, the interactions with gold surfaces of azulene-based molecules with different functional groups has been studied. Specifically, the competition between isocyanozulenes and mercaptoazulenes for binding at the Au(111) surface has been examined.

3:00pm **SS2-MoA4 Formation of Closed Shell Quantum Dots as a Driving Force for Molecular Ordering**, *L. Bartels, J. Wyrick, Z. Cheng, D. Sun, D. Kim*, University of California, Riverside, *T.L. Einstein*, University of Maryland

Anthraquinone self-assembles on Cu(111) into a giant honeycomb network with exactly three molecules on each side. Here we propose that the exceptional degree of order achieved in this system can be explained as a consequence of the confinement of substrate electrons in the pores, with the pore size tailored so that the confined electrons can adopt a noble-gas-like two-dimensional quasi-atom configuration with two filled shells. Formation of identical pores in a related adsorption system (at different overall periodicity due to the different molecule size) corroborates this concept. A combination of photoemission spectroscopy with density functional theory computations (including van der Waals interactions) of adsorbate-substrate interactions allows quantum mechanical modeling of the spectra of the resultant quasi atoms and their energetics.

The resultant pores have about 4 nm in diameter. In this study we explore how the behavior of adsorbates inside them differs from that on extended terraces. CO molecules and adlayers exhibit properties under such nanoscale confinement that markedly depart from those of extended adlayers: a) the confinement stabilizes dislocation lines (anti-phase domain boundaries) in the adlayer that affect roughly 1/4 of the adsorbed molecules; b) confinement prevents the formation of dense islands of adsorbed molecules, depending on coverage either causing dispersion of vacancies in the adlayer or preventing the growth of molecular islands; c) at a coverage of just a few molecules on the facet, we observe that a molecular shell structure is formed, resembling in its underlying mathematics the atomic model. Confined structures are an ideal test bed for measurement of the coverage dependence of molecular diffusion and in this study we find a reduction of the diffusion barrier at a slope of 57%/ML.

3:40pm **SS2-MoA6 Redox Activity and Structural Transitions at Electrochemical Interfaces**, *K.R. Wandelt*, University of Bonn, Germany
INVITED

Ordered layers of organic molecules play an increasing role in modern material science. Their electrochemical deposition from solution has several important advantages: i) Thermally unstable organic molecules which are not intact volatile may be deposited under mild conditions, ii) unlike vacuum deposition electrochemical adsorption may be performed near equilibrium, and iii) the electrochemical potential is an extra parameter which enables a controlled switching of the redox-state of the adsorbed molecules and, thereby, structural transitions of the layers. This lecture concentrates on the correlation between redox-activity and structural properties of viologen and porphyrin layers at metal – electrolyte interfaces. The selfassembly of the molecules is studied as a function of i) the nature and symmetry of the substrate (Cu(111), Cu(100), Au(111) and Cu/Au(111)), ii) the nature of the accompanying counter ions (Cl, Br, I, SO₄), iii) the concentration of the solution, and, most importantly, iv) the potential dependent redox state of the adsorbed molecules, by using in-situ ElectroChemical Scanning Tunneling Microscopy (EC-STM), in-situ Infrared Reflection Absorption Spectroscopy (IRRAS) as well as ex-situ Synchrotron X-ray Photoelectron Spectroscopy (SXPS) after air- and contamination-free transfer from the solution into the UHV analysis chamber. The lecture not only provides a deep insight into the properties of the investigated model systems but also demonstrates the status of modern electrochemical surface science.

4:20pm **SS2-MoA8 Influence of Solvent on the Chiral Resolution of Organic Molecules on Au(111): EC-STM Study of Biphenyl Dicarboxylic Acid on Au (111) in an Aqueous Environment**, *B.I. Kim, J.A. Hanson, M.W. Turner, L.J. Reeder*, Boise State University

Adsorption induced chiral resolution of organic molecules is important due to its potential applications in stereo-selective catalysis. We studied the adsorption induced chiral resolution using a model achiral molecule of 4,4'-biphenyl dicarboxylic acid (BPDA) on Au (111) in 0.1 M perchloric acid (HClO₄) by scanning tunneling microscopy (STM). The BPDA molecules are known to have chiral resolution on Au(111) in an ultrahigh vacuum (UHV). However, our experimental data show that the molecules form island structures with distinctive preferred orientations at the length scale of the molecular size, whereas they have no orientation order at the length scale bigger than the molecular size. We calculated angle dependent binding energy between the substrate and a BPDA molecule, the intermolecular interactions between the BPDA molecules and their interactions with water molecules. The calculation suggests that the absence of chiral resolution in the aqueous environment may originate from the increase of effective rotation energy barrier of the BPDA molecules due to its hydrogen bonding with the surrounding water molecules. The strength hydrogen binding between BPDA molecules is sufficient to overcome the energy barrier for chiral resolution through rotational motion in UHV, but not in an aqueous environment.

4:40pm **SS2-MoA9 Surface and Interface Forces between Dissimilar Surfaces in Aqueous Solution: The Effect of Electrochemical Surface Potentials, Surface Roughness and Hydration Layers**, *M. Valtiner, K. Kristiansen, G.W. Greene, J.N. Israelachvili*, University of California, Santa Barbara

With the rapid progress in the design and fabrication of micro- and nanometer-scaled devices at smaller and smaller length scales, a fundamental understanding of, and the ability to control the interfacial interactions between materials across ultra small distances plays a critical role in advancing these technologies. The ability to 'tune' the forces in various device components remains a critical hurdle to optimizing device performance and reliability of, for example nanofluidic and lab-on-a-chip systems, aqueous-based MEMS, sensor devices; as well as devices where adhesion and adsorption can be controlled, surface contacts and wetting properties tuned, and single molecules and bi-layer interactions manipulated. Surface morphology (including roughness) and electrostatic potential-dependent interaction forces significantly affect the physical and mechanical properties of surfaces and play a critical role in all of these systems.

We present novel setups for both an improved electrochemical AFM [1] and a newly developed electrochemical surface force apparatus [2], and compare the two techniques. We describe the results of the first surface force measurements under electrochemical potential control between a metal and a ceramic surface across a liquid medium (water). Our experiments also reveal how increasing levels of surface roughness and dissimilarity in the surface potentials of the interacting surfaces influence the strength and range of electric double layer, van der Waals, hydration, and steric forces, and how these contribute to deviations from DLVO theory, particularly at distances less than two Debye lengths, or 2-3 times the rms roughness, whichever is greater.

[1] Markus Valtiner, G. Anka, A. Bashir and F. Renner, *Rev. Sci. Instrum.* **82**, 023703 (2011)

[2] Markus Valtiner, Kai Kristiansen, George W. Greene, Jacob N. Israelachvili, *Advanced Materials*, DOI: 10.1002/adma.201003709 (2011)

5:00pm **SS2-MoA10 Diffusion of Single Water and Hydrogen Sulfide Molecules on Ag(111): A DFT Study**, *D.-J. Liu*, Ames Laboratory - US DOE

Diffusion of water (H₂O) and hydrogen sulfide (H₂S) on metal surfaces can be more complicated than single adatom diffusion, even for simple hopping mechanism. Additional degree of freedom, such as rotation and tilting of the molecule, must be considered. Due to the asymmetry of the molecule, and therefore the potential energy surface, the saddle points generally deviate from any high symmetry adsorption site. We carry out a systematic study based on the density-functional theory for diffusion of H₂O and H₂S on Ag(111). For both molecules, the most stable configuration for adsorption is nearly flat and on top of a Ag atom. As it approaches the bridge site, the molecule can tilt, and in the case of H₂S, also rotate, to lower its energy. We also find that in this case, zero point vibrations contribute significantly to diffusion of the molecule.

5:20pm **SS2-MoA11 The Structure of Methylthiolate and Ethylthiolate Monolayers on Au(111): Absence of the ($\sqrt{3}\times\sqrt{3}$)R30° Phase**, *L. Tang*, University of Birmingham, UK, *F. Li*, University of Birmingham, UK & Northwestern Polytechnical Univ., P.R. China, *W. Zhou*, Northwestern Polytechnical Univ., P.R. China, *Q. Guo*, University of Birmingham, UK

Surface structures of self-assembled methylthiolate and ethylthiolate monolayers on Au(111) have been imaged with STM. For saturation coverage at room temperature, the well-known ($\sqrt{3}\times\sqrt{3}$)R30° phase routinely observed for longer chain alkanethiolates does not appear under any conditions for adsorbed methylthiolate and ethylthiolate. Instead, both thiolate species organize themselves into a well-ordered 3×4 structure with a coverage equal to 0.33 ML. We thus conclude that the stable structure for saturation coverage of methylthiolate/ethylthiolate on Au(111) at RT is 3×4, not ($\sqrt{3}\times\sqrt{3}$)R30° as generally believed.

We performed experiments by imaging methylthiolate and ethylthiolate monolayers in ultra-high-vacuum (UHV) using high-resolution STM. The methylthiolate monolayer was prepared by exposing a gold single crystal in vacuum to 10⁻⁸ mbar of dimethyl disulfide (DMDS) vapour at RT for 15 minutes. It is known that DMDS adsorb dissociatively on Au(111) at RT by forming methylthiolate. Ethylthiolate monolayer was prepared by exposing a (111) oriented gold film to 5×10⁻⁵ mbar of ethanethiol vapor at room RT for 2 hours. The much higher exposure required for ethanethiol is due to the very low dissociation probability of this molecule.

When the 3×4 phase is subjected to a gentle thermal annealing to 320 K, partial desorption takes place and a striped phase with coverage equal to 0.27 ML appears. The striped phase for ethylthiolate resembles that observed for propylthiolate and other long chain thiolates, but the striped

phase for the methylthiolate takes a unique structure of its own. Our findings suggest that the general belief that all alkanethiols form at least one common structural phase is not true and new theoretical modeling is urgently required to address the chain-length dependent property of alkanethiol monolayers.

Thin Film Division

Room: 107 - Session TF-MoA

Emerging ALD Applications

Moderator: G. Scarel, James Madison University

2:00pm **TF-MoA1 Atmospheric ALD of Al₂O₃ for a High Throughput c-Si Solar Cell Passivation**, *V.I. Kuznetsov, P. Vermont, E.H.A. Granneman*, Levitech BV, Netherlands **INVITED**

Surface passivation of advanced solar cells becomes more important with decreasing silicon wafer thickness (increased surface to bulk ratio). The International Technology Roadmap for Photovoltaics predicts that the thickness of wafers processed in mass production will be 100 μm by 2020. By 2012 new processes with lower Cost of Ownership (CoO) and better passivation properties will be needed [1].

It is widely accepted that Al₂O₃ layer has excellent surface passivation capabilities [2]. Solar cells with Al₂O₃ layers < 10 nm demonstrate the best results: higher efficiency and more stable structures when annealed at high temperatures [3,4]. ALD is an ideal technique for the deposition of thin layers. However, conventional ALD equipment can not be used in the PV industry because of the low throughput and associated high CoO. A suitable way to reduce the tool cost per cell is to increase the throughput of the system. The ITRPV requires a minimum throughput of production tools from 3600 wph in 2012 to 7200 wph in 2020.

We developed an ALD tool which meets these throughput requirements and is capable to process at a cost of 3-4 cent per wafer. In this tool we implemented a new approach: atmospheric, spatial ALD. Silicon wafers are transported in a linear track passing areas with TMA and H₂O precursor gas curtains. N₂ purges in between these curtains separate the different precursors thereby avoiding deposition on the track walls. The wafers are transported on a gas bearing (levitate) inside a narrow track. The Levitrack system operates in-line and has a length of ~10 m for the deposition of 10 nm of Al₂O₃. At the conference Levitrack tool details and process results will be presented. Some items are:

- Passivation quality: effective lifetime of 6.1 ms in mono-silicon 10 Ω cm at injection level of 3E15 cm⁻³.
 - Layer characteristics: 1σ uniformity <3% on 156x156 mm wafers, intrinsic layer charge of -4E12 cm⁻²
 - Tool options: deposition on both or one side of the wafer (N₂ flow protects the back side of the wafer against Al₂O₃ deposition)
 - Tool automation (automated wafer loading/unloading, 100 wafer cassettes and use inline, control of process, safety, and other parameters)
 - Tool reliability (reliable performance at marathon runs with throughput of ~4000 wph)
 - Current solar cell results (efficiency obtained for p-type crystalline silicon cell is 16.6% and for n-type is 18.3%. Improvement of 1-2% is expected to be achieved by optimizing local BSF below metal contacts and contact/shunt resistances)
1. ITRPV.net, 2nd edition, 2011
 2. S.Chunduri, Photon Int., p.146, 2011
 3. P.Brand, 37th IEEE PV Conference, Seattle, 2011
 4. I.G.Romijn, 25th. EU PVSEC, 2010

2:40pm **TF-MoA3 Atomic Layer Deposition of Al₂O₃ for Quantum Computing**, *A.C. Kozen, M. Khalil, B. Sarabi, K.D. Osborn*, University of Maryland, College Park, *C. Musgrave*, University of Colorado, Boulder, *C. Lobb, G.W. Rubloff*, University of Maryland, College Park

Josephson junctions (JJ) are a primary building block of superconducting quantum computers. The JJ structure is a superconductor-dielectric-superconductor stack, with the conventional dielectric layer fabricated by thermal oxidation of an aluminum metal electrode. The coherence time of these qubits is limited by high loss tangents in the dielectric layer thought to be due to defect-related quantum two level systems (TLS) inherent in the Al₂O₃. We have identified the -OH rotor TLS associated with hydroxyl species in the Al₂O₃ as a prime defect candidate based on TLS energetics. Simulations indicate that replacement of the -OH defect with the -OD defect will reduce the dielectric loss in these systems. We demonstrate the

fabrication of Al₂O₃ dielectric thin films using atomic layer deposition (ALD) from trimethylaluminum and both H₂O and D₂O precursors as a function of substrate temperature and precursor dose. ALD enables precise control of film growth at the atomic scale, while comparison of H₂O vs. D₂O as the oxidation precursor enables isotopic defect loading in the Al₂O₃ and replacement of the –OH defect with the –OD defect. We have developed the D₂O based ALD process, and characterized both D₂O and H₂O based ALD Al₂O₃ thin films by SIMS, XPS and spectroscopic ellipsometry. Our resulting Al₂O₃ films are physically identical with the exception of –OH and –OD defects, making this system an ideal platform for the study of TLS defect related dielectric loss in JJ qubits. To this end we have fabricated MIM capacitor test structures and superconducting resonators using Re and Al electrodes and performed electrical measurements. Correlation between these data and low temperature superconducting microwave resonator performance will be discussed.

3:00pm TF-MoA4 Supported Core-Shell Pt-Pd Nanoparticles Synthesized by Atomic Layer Deposition, M.J. Weber, A.J.M. Mackus, Eindhoven University of Technology, Netherlands, M.A. Verheijen, C. van der Marel, Philips Innovation Services, Netherlands, W.M.M. Kessels, Eindhoven University of Technology, Netherlands

Recently, atomic layer deposition (ALD) has become the subject of great interest as a new way to synthesize supported metallic nanocatalysts (1, 2). In comparison to their single-metal counterparts, bimetallic nanoparticles (NPs) can present a higher selectivity and an enhanced catalytic activity. In this contribution, we present an innovative ALD process enabling the synthesis of supported bimetallic core-shell NPs. Although ALD was primarily developed to deposit conformal thin films, metals have the tendency to form nanoclusters on the substrate during the initial cycles of the process. In this work, Platinum-Palladium core-shell NPs were successfully deposited on Al₂O₃ using ALD of Pt and Pd. The selective growth property of noble metal ALD (3) has been exploited to cover Pt nanoclusters with a Pd shell. An ALD process using MeCpPtMe₃ and O₂ has been used to deposit Pt nanoclusters, and ALD with Pd(hfac)₂ and H₂ enabled to selectively cover them with a Pd shell. High Angle Annular Dark Field (HAADF) TEM images confirm the fact that bimetallic core-shell NPs of 3-4 nm were synthesized (on Al₂O₃ covered TEM windows). Information on the chemical state of the Pd and Pt was obtained from XPS analysis. Average values of the Pd shell thickness as obtained by a model analysis of the XPS data were found to be in agreement with the TEM data. This new process is expected to be also applicable to other Platinum group metals. The tailoring of such NPs by changing the ALD process parameters in order to obtain different particles sizes and compositions is also addressed. It is expected that the fuel cells industry, but also advanced sensors technologies, can benefit considerably from an enhancement of catalytic activity and selectivity of nanocatalysts prepared by ALD.

1: Stair, *J. Chem. Phys.* **2008**, 128, 182507

2: Christensen et al., *Small* **2009**, 5, No. 6, 750-757

3: Mackus et al., *J. Appl. Phys.* **2010**, 107 (11), 116102-1/3

3:40pm TF-MoA6 Photoluminescence Characteristics of TiO₂ Film Deposited on Vertically Oriented Si Nanowire by Remote Plasma Atomic Layer Deposition, J.S. Lee, T.Y. Park, Y.B. Ko, H.Y. Jeon, J.G. Park, J.H. Ryu, H.T. Jeon, Hanyang University, Republic of Korea

Titanium dioxide (TiO₂) has been regarded as one of the most promising photocatalysts for environmental protection because of its high photocatalytic activity, high chemical stability, low toxicity, and low cost. Anatase and rutile structures of TiO₂ are two main phases with band gap energies of 3.3 and 3.1 eV, respectively. The structures of both anatase and rutile consist of chains of TiO₆ octahedra. However, two crystal structures are obviously different. It is well-known that the difference in crystal structures causes different mass density (3.894 g/cm³ for anatase and 4.250 g/cm³ for rutile) and electronic band gap. The anatase phase has a more negative conduction band edge than that of the rutile phase. It results in superior photocatalytic activity of anatase phase than that of the rutile phase. Therefore, the structure of TiO₂ films and high surface area are heavily important factors in photocatalytic efficiency.

In this study, TiO₂ film was deposited by remote plasma atomic layer deposition (RPALD) and its phase formation temperature, impurity concentration, and chemical states of the were characterized by various analyses such as Auger electron spectroscopy (AES), X-ray diffractometry (XRD), X-ray photoelectron spectroscopy (XPS), and transmission electron microscopy (TEM). The TiO₂ film was deposited on the flat Si substrate and vertically oriented Si nanowire by using remote plasma atomic layer deposition (RPALD) method. RPALD method has advantage to deposit thin film with uniform thickness on the 3-dimensional structure like vertically oriented Si nanowire. In addition, the RPALD method is possible to reduce damage by high energetic ion and to enhance the chemical reactivity between metal-organic precursor and reactant gas for deposition of high

quality film. The vertically oriented Si nanowire was fabricated by Ar-annealing of Si substrate with Au nanocrystal at 1000 °C. And we have compared the photoluminescence (PL) features of these TiO₂ films with these two different specific surface areas. We have found that TiO₂ film deposited vertically aligned Si nanowire has higher PL intensity than that of TiO₂ deposited flat Si substrate due to large area density of vertically oriented Si nanowire.

4:00pm TF-MoA7 Fast Atomic Layer Deposition for High Throughput and Low Temperature Applications, P. Poodt, A. Illiberi, M. Smets, R. Knaapen, TNO, Netherlands, F. Roozeboom, TNO & Eindhoven University of Technology, Netherlands, A. van Asten, TNO, Netherlands

Atomic Layer Deposition is a deposition technique capable of producing ultrathin conformal films with control of the thickness and composition of the films at the atomic level. The major drawback of ALD is its low deposition rate (~ 1 nm/min). Recently, fast ALD concepts were developed based on the *spatial* separation of the half-reactions, instead of temporal, combined with gas-bearing technology¹. With this technique, deposition rates for Al₂O₃ of more than 1 nm/s have been reported². This has led to the development of the high-throughput, industrial scale ALD tools for surface passivation of crystalline silicon solar cells^{3,3}.

A new field of applications for fast ALD are flexible electronics⁴, including system-in-foil, flexible displays, OLEDs and solar cells. Flexible electronics are slowly but surely evolving from lab-scale to industrial production. This opens up new possibilities for fast ALD as high-throughput production tool for functional layers such as transparent oxide (semi)conductors (e.g. ZnO) and moisture barriers (e.g. Al₂O₃). One important prerequisite is that these applications require low temperature processes (below 100°C), as they are often temperature sensitive. We present two approaches for low temperature Fast ALD; low temperature *thermal* fast ALD and atmospheric plasma enhanced fast ALD.

A *low temperature thermal fast ALD* process for alumina from tri-methyl aluminum and water has been developed. It was observed that the kinetics of the water half-reaction is significantly different than at high temperatures (>200°C). Multilayer adsorption of water molecules at low temperatures seems to hinder the self-limiting nature of the ALD process at temperatures below 75°C. Nevertheless, if very low temperatures are not required, low temperature thermal fast ALD is a very suitable technique. Potentially lower deposition temperatures could be achieved by *atmospheric plasma enhanced fast ALD*. We have integrated an atmospheric plasma source in our reactor in which an He/O₂ plasma is created to act as the oxidant half reaction. However, the chemistry of atmospheric plasmas is different than that of conventionally used low pressure plasmas and has a lower reactivity that can limit the throughput.

Another important aspect of fast ALD for flexible electronics is the processing of flexible substrates, either sheet-to-sheet or roll-to-roll. Approaches for roll-to-roll fast ALD, their challenges and possible solutions will be briefly discussed.

¹ P. Poodt et al., *Adv. Mater.* 22 (2010) 3564.

² www.solaytec.com .

³ I. Cesar, et al., *Proc. 35th IEEE PVSC*, Honolulu, Hawaii (2010), in press

⁴ J. van den Brand et al., *Microelect. Rel.* 48 (2008) 1123

4:20pm TF-MoA8 Industrial ALD Equipment for PV and OLED Applications, M. Putkonen, Beneq Oy, Finland

Atomic Layer Deposition (ALD) has been successfully applied to antireflection, buffer and passivation layers for PV as well as moisture barriers for OLED packaging. In these applications ALD offers superior performance compared to the corresponding layers deposited with other methods. Outside IC manufacturing ALD has largely been confined to laboratories so far due to non-availability of larger scale, high throughput ALD systems. For example, ALD is widely seen as the desired manufacturing technology for producing high quality functional layers into solar cells: e.g. buffer layers into CIGS and surface passivation into both p-type and n-type c-Si solar cells, but ALD commonly considered too slow for high throughput manufacturing.

In this presentation we introduce commercial high capacity ALD tools for PV and OLED diffusion barrier applications as well as discuss more about the requirements for high throughput industrial ALD tools. Conventional ALD deposition parameters and characteristics, such as stability of precursor temperatures even with extremely high precursor doses and optimising the flow path are needed before strict coating requirements can be fulfilled.

The TFS 1200 deposition system is designed to improve efficiency of CuInGaSe₂ (CIGS) type thin film PV cells using Zn(O,S) buffer layer. It has throughput in inline and off-line configurations of 12 and 24 modules/hour, respectively. (substrate size 120 x 120 cm², 20 nm Zn(O,S))

We have obtained thin film thickness uniformity of $\pm 3\%$ with the cycle time of 2.0 s. With $60 \times 120 \text{ cm}^2$ substrate size these numbers will be doubled to 24-48 modules/hour. These values fulfill the throughput requirements of CIGS production lines (20-60 modules/h). Even higher throughputs can be obtained using batch type tools for CIGS buffer layers.

TFS NX 300 is a fully automated cassette to cassette ALD manufacturing system for Al_2O_3 surface passivation. It consists of 4 processing tubes each with the capacity for a 500 wafer batch. For this application we have modified thermal ALD-process for Al_2O_3 which has a higher growth rate than the conventional thermal (TMA/ H_2O) ALD process and the film quality is equal to plasma assisted ALD film quality giving throughput of >3000 wafers/h.

The Beneq TFS 600 is a vacuum-line integrated ALD system for OLED moisture barrier coating. Reaction chamber is designed for batch processing up to 35 substrates measuring $500 \text{ mm} \times 400 \text{ mm}$. For this application we have been developing low-cost multilayer barrier structure giving WVTR $<10^{-6} \text{ g/m}^2/\text{d}$.

4:40pm TF-MoA9 Conductive Coatings on Nonwoven Fiber Mats by Atomic Layer Deposition. *W. Sweet, J.S. Jur, G.N. Parsons*, North Carolina State University

Conductive fiber mats offer unique possibilities in the development of many sensing and protective electronic systems. In this work, atomic layer deposition (ALD) is applied to produce conformal coatings of conductive ZnO on complex fiber systems such as nonwoven polypropylene and nylon. The conductivity of these materials were evaluated using a modified 4-probe method specific for fabric structures and correlated with the overall mass gain of the fabric samples after ALD processing. This analysis provided a detailed evolution of the conductive films on the fabric mats. For example, nonwoven polypropylene coated with ZnO showed a significant initial mass increase, eventually becoming linear with increasing ALD cycles. The corresponding conductivity of these films remained low ($< 3 \text{ S cm}^{-1}$), even after 500 ALD ZnO cycles. Inserting a thin insulating ALD Al_2O_3 layer prior to the ZnO growth, linear ZnO mass gain was achieved after low ALD cycles. Transmission electron microscopy shows that the Al_2O_3 barrier reduces the penetration of the ZnO vapor phase reactants into the polypropylene. As a result, a higher effective conductivity ($> 25 \text{ S cm}^{-1}$) was achieved after 200 ALD ZnO cycles that corresponded well with measurements from simultaneous ZnO growth on a planar silicon oxide surface. For comparison, ZnO deposition on nonwoven nylon-6 exhibits uniform growth without Al_2O_3 pretreatment and the conductivity again changes significantly with the Al_2O_3 pretreatment. Implications of the deposition temperature, film thickness, and the use of aluminum doping, on the chemical, mechanical, and electrical properties of ZnO films deposited on polypropylene and nylon nonwovens will be discussed.

5:00pm TF-MoA10 ALD IrOx Thin Film to Improve Microelectrode Array Performance in Stem Cell Applications. *T. Ryyänen, J. Lekkala*, Tampere University of Technology, Finland, *L. Ylä-Outinen, S. Narkilahti*, University of Tampere, Finland, *J. Hämäläinen, M. Leskelä*, University of Helsinki, Finland

We promote atomic layer deposition (ALD) and especially ALD deposited iridium oxide (IrOx) thin film [1] as a novel alternative to improve electrical characteristics of microelectrode arrays (MEAs) used in stem cell and other tissue engineering applications. The additional microelectrode coating on microelectrode base material is traditionally used to decrease impedance and noise levels, and to increase charge transfer capacity of microelectrodes in MEAs. However, most of the common microelectrode coatings suffer from certain drawbacks. For example 1) electrochemical activation used to decrease the impedance of sputtered IrOx by one decade is not applicable for long term cell measurements due to rather fast deactivation, 2) widely used electrodeposited platinum (Pt black) suffers often from poor adhesion on underlying microelectrode base material, and 3) lately actively studied carbon nanotube (CNT) coatings still have unsolved issues related to difficult fabrication processes and concerns about biocompatibility and long term adhesion. Thus there is obvious demand for another stable solution in addition to sputtered titanium nitride (TiN) thin film favored by one of the leading commercial MEA manufacturers.

In our initial studies the about 120 nm thick ALD IrOx layer decreased the impedance of 30 μm diameter titanium microelectrodes down to 450 k Ω at 1 kHz, which is several times less than without the coating and consistent with the impedance reported for unactivated sputtered IrOx coated microelectrodes [2]. Stem cell growth experiments performed with human embryonic stem cell derived neuronal cells (hESC-N) [3, 4] showed that in field potential measurements ALD IrOx thin film decreases the noise level significantly compared to non-coated microelectrodes. Also, no biocompatibility or adhesion problems were detected. Even if already as such the ALD IrOx thin film clearly improves the MEA performance, we expect that by optimizing the thin film thickness and ALD process

parameters from the default 3000 cycles of Ir(acac)₃ and ozone, the impedance level of the ALD IrOx coated microelectrodes can be decreased even further. Thus impedance levels of 100 k Ω and below could be reached, which would make ALD IrOx thin film a strong competitor for the other commonly used microelectrode coatings. In addition to offering an economical, easily controllable, and highly reproducible fabrication process for a thin film improving the electrical characteristics of MEAs, ALD technology may in the future offer also other interesting coating solutions for cell culturing platforms, for example controlling cell growth via functionalized coatings.

[1] J. Hämäläinen *et al.*, Chem. Mater. 20 (2008) 2903.

[2] S. Gawad *et al.*, Front. Neuroeng. 2 (2009) 1.

[3] R. Lappalainen *et al.*, Regen. Med. 5 (2010) 749.

[4] T. Heikkilä *et al.*, Exp. Neurol. 218 (2009) 109.

**Vacuum Technology Division
Room: 111 - Session VT-MoA**

Optical and Mass Spectroscopy for Gas Analysis and Pump Modeling

Moderator: R. Versluis, TNO Science and Industry, The Netherlands

2:00pm VT-MoA1 Low Uncertainty Measurements of Trace Water Vapor Based on Cavity Ring-Down Spectroscopy. *T. Hodges*, National Institute of Standards and Technology

INVITED

I will discuss how cavity ring-down spectroscopy (CRDS) can be applied to accurately measure the concentration of residual water vapor which is present in a vacuum system or process gas stream. In CRDS, a monochromatic laser beam is injected into an evacuated or sample-gas-containing optical resonator and the transient decay of light exiting the cavity is monitored to quantify the optical losses. For water detection, the laser wavelength is tuned to probe characteristic rotation-vibration absorption features of the water molecule. The sample absorption coefficient is determined from observations of the ring-down cavity decay time and laser frequency, both of which can be precisely measured. Also, because CRDS uses a resonant optical cavity, extremely long effective optical pathlengths (up to tens of km) can readily be achieved in the laboratory. These properties make CRDS a high-spectral resolution, species-selective method, with relatively small combined uncertainty, and high sensitivity. I will show that when CRDS measurements are combined with first-principles spectroscopic models, this technique can yield concentration measurements with sub-percent-level relative uncertainty for absolute concentrations as low as 10^{11} cm^{-3} . I will present examples of CRDS-based trace water detection in vacuum and ultra-high purity gas systems, and I will talk about recent CRDS measurements of the vapor pressure of ice over the temperature range 0 deg C to -100 deg C.

2:40pm VT-MoA3 Comparison of Cavity Ring-Down Spectroscopy, Oscillating Quartz Crystal and Electrical Impedance Technologies for Trace Water Vapor Detection below 100 ppb. *M.W. Raynor, J. Feng, Matheson*

Control of trace water vapor in high purity process gases at low ppbv levels is critical to the performance of many micro-electronic and photonic devices [1]. Consequently a variety of measurement technologies, have been developed to detect water below 100 ppb. However, the performance characteristics of each technology can vary and this is not always well understood by users. In this presentation three different approaches are considered: Oscillating quartz crystal microbalance (QCM), Al_2O_3 based electrical impedance sensor and laser induced cavity ring-down spectroscopy (CRDS). QCM technology, developed in the early 1960's, is still widely applied today. It is based on adsorption of water vapor on the hygroscopic coating of the QCM, which causes an increase in the mass of the crystal, and in turn, decreases its oscillation frequency. CRDS is a laser absorption technique based on the light decay in a high finesse optical cavity. The high resolution laser $\sim 1\text{-}2 \text{ MHz}$ ($\sim 10^5 \text{ cm}^{-1}$), high reflectivity mirrors (~ 0.99998) results in a long effective path-length which enables high selectivity and sensitivity for H_2O detection. Impedance-based sensors for trace water vapor detection have typically suffered from drift and equilibration issues. However, recently an impedance-based Al_2O_3 sensor chip with integrated heater for cycling the temperature within 60°C to 200°C has been developed. Water vapor is measured dynamically as impedance changes during wet-up of the sensor resulting in rapid response. In this work, we present and discuss data showing the performance of the above

detection technologies with respect to sensitivity, speed of response and measurement stability in the <100 ppbv range.

[1] H.H. Funke et al., Rev. Sci. Instrum., 74 (9) 2003, 3909-3933.

3:00pm **VT-MoA4 Commercial Applications and Benefits of Continuous-Wave Cavity Ring-Down Spectroscopy**, *Y. Chen*, Tiger Optics

Continuous-Wave Cavity Ring-Down Spectroscopy (CW-CRDS) is a laser-based state-of-the-art detection technique. Based on first principles, it directly derives the absolute optical loss due to absorption inside the cavity from a simple time measurement, independent of laser intensity noise and optical detector drift.

This highly sensitive absolute absorption measurement technique was first commercialized by Tiger Optics for sub parts-per-billion (ppb) level detection of moisture in inert gases. More than a dozen national metrology labs now use this technique as their moisture transfer standard. Several of these key national labs recently concluded a multi-year project comparing the performance of their different moisture standard generators by using two Tiger Optics CW-CRDS devices as their "referees", shipping them around the globe across three different continents. Inter-comparison data from this comprehensive study will be presented.

With over 1000 measurement points worldwide, CW-CRDS has gained widespread acceptance and growing use in a series of challenging, real-world industrial applications, well beyond trace moisture in simple matrices. We will demonstrate the strong capability of CW-CRDS for a diverse group of analytes over a large dynamic range and under widely varying application conditions. In addition, starting with ultra-high-purity, sub or low parts-per-billion measurement, this technology is now increasingly sought for higher parts-per-million applications as well. Taking maximum advantage of its exceptional dynamic range, with a variety of flexible configurations, CW-CRDS-based instruments address these various applications with a self-verifying measurement solution that is fast and sensitive, yet extremely robust and simple to operate.

3:40pm **VT-MoA6 Vacuum Quality Measurement at UHV Levels with AutoResonant Ion Trap Mass Spectrometers**, *G.A. Brucker*, Brooks Automation, Inc., *J. Rathbone*, *B.J. Horvath*, Brooks Automation, Inc., Granville-Phillips Products

Autoresonant Ion Trap Mass Spectrometers (ART MS) have recently become commercially available and are rapidly finding applications in many areas of the vacuum technology industry. One of the biggest benefits of ART MS sensors is their ability to provide fast and sensitive data at ultrahigh vacuum levels (UHV). The ability to operate the sensor remotely, i.e. with the electronics unit away from the gauge head, has also made ART MS technology the gas analysis instrumentation of choice for hard radiation environments. The performance of ART MS sensors under UHV conditions is discussed. Test results for gas analysis measurements performed under UHV conditions are shown and compared against similar results obtained with legacy instrumentation including quadrupole-based residual gas analyzers. Different approaches available to improve the performance of an ART MS instrument under UHV conditions are explored and explained based on the basic principles of operation of the technology.

4:00pm **VT-MoA7 Reducing Uncertainties for Hydrogen Loading Determination of 1,4-bis(phenethyl)benzene (DEB) Using GC/MS Instead of the Traditionally-used CHN Analysis Method**, *S.M. Thornberg*, *J.M. Hochrein*, *M.I. White*, Sandia National Laboratories

Hydrogen getters are used in many industries including aerospace, defense, and electronics (e.g., MEMS packaging) to control levels of hydrogen in sealed atmospheres and vacuum systems. In this research, we explore not only the products formed during the hydrogenation process but also the product distribution resulting from differing rates of hydrogenation. This work focuses on the analysis of hydrogenation products of 1,4-bis(phenethyl)benzene (DEB) using GC/MS and a method for creating samples with known hydrogenation levels. This information can then be used to calculate the remaining capacity of the getter by determining the ratios of saturated, partially saturated, and unsaturated products.

DEB has a molecular formula of C₂₂H₁₄ (MW=278 amu) and has a capacity for four moles molecular hydrogen per mole of DEB. The analysis of pure DEB (unhydrogenated) showed no contamination from partially hydrogenated products and only one chromatographic peak (from DEB). As hydrogenation proceeds, a series of products is formed with nominal masses 280, 282, 284, and 286 amu (282, 286, 290 and 294 amu for deuterium). Hydrogenation experiments were performed from 0% to 100% hydrogenation (calculated by molar ratios) with hydrogen mixed with a buffer gas (nitrogen) to slow the uptake reaction rate. After hydrogenation, the resultant solid was homogenized, dissolved in methylene chloride, and filtered. The stock solutions, diluted appropriately, were then analyzed

using gas chromatography (Agilent, model 6890N) for product separation, and a high-resolution mass spectrometer (Jeol MStation, model JMS-700) for product identification.

In this talk, a comparison between the GC/MS method presented here and the traditional CHN analysis method will be presented. Round robin samples between three labs were used to assess the performance of each method.

Sandia is a multiprogram laboratory operated by Sandia Corporation, a Lockheed Martin company, for the U.S. Department of Energy's National Nuclear Security Administration under Contract DE-AC04-94AL85000.

4:20pm **VT-MoA8 Sampling Equilibration Times of Chemical Species for Different Capillary Surfaces**, *R. Ellefson*, REVac Consulting, *D. McClelland*, Mound Technical Solutions, Inc.

Gas sampling through long, small-bore capillary tubing has long been used as a method to reduce the atmospheric pressure (or higher pressure) process gas to a low pressure for analysis by a mass spectrometer (MS). With care of sampling system design and operation, the species integrity of the process gas can be preserved in the sampling which enables accurate compositional analysis. The gas dynamics of the gas stream within the capillary tube equilibrating with the capillary wall and measured at the MS leads to a stable composition at the MS when equilibrium is achieved. A model that includes the wall material interaction is presented with prediction of stabilization time for various gas species. Data from four different capillary materials or surfaces are given to show the interaction process. The capillaries tested are: 304SS, 304 Sulfinert[®] SS, PEEK (polymer) and fused silica tubing. All capillaries have 0.25 mm i.d. and a 2 m length for direct comparisons. Composition profiles versus time are measured for a dry nitrogen sample followed by room air (50% RH) which shows the gas dynamics of the equilibration of adsorbed gases (e.g. H₂O and CO₂) with the various interior surfaces of each capillary. The effect of capillary length and i.d (defining the surface area to be equilibrated) is included in our model and measurements. Equilibration times of 50 sec for H₂O are seen at room temperature for a 2 m capillary with 10 sccm flow rate. Longer times are needed to reach the low H₂O concentration in the nitrogen (drying the capillary surface). Raising the temperature of the capillary reduces equilibration time as expected.

The exit end of the capillary flows into the low pressure region created by the sampling forevacuum with a port to the MS for analysis. The effect on equilibration time of a Silcotek[®] surface treatment of interior surfaces of the inlet to the MS is measured and compared with equilibration time for the regular 304SS surface of the machined inlet.

4:40pm **VT-MoA9 Numerical Methods for the Design of Vacuum Systems with Examples**, *R. Kersevan*, ITER International Organization, France **INVITED**

The paper deals with the issue of the numerical computation of relevant properties of vacuum systems under ultra-high vacuum (UHV) conditions, i.e. when molecular flow conditions are in place. Properties of interest, among others, are pressure profile, angular profiles, conductances, transmission probabilities, effective pumping speed, sputtering deposition profiles.

Many modern research tools need UHV conditions in order to function properly. The size of the system is not an issue, it can be very small (electronic packaging; gauge calibration benches, for instance) or very large (ITER torus, cryostat and ancillary systems; particle accelerators; spectrometers, etc...). The availability of relatively cheap computing power has in recent years brought at the forefront of research new software tools which allow the simulation of complex geometries and working conditions.

The paper quickly reviews the existing algorithms and tools [1], and then moves on to show examples of calculations, with particular emphasis on the Molflow+ code [2].

[1] R. Kersevan, "Analytical & Numerical Tools for Vacuum Systems", Proc. CAS - CERN Accelerator School and ALBA Synchrotron Light Facility : Course on Vacuum in Accelerators, Platja d'Aro, Spain, 2006 - Downloadable at <http://cdsweb.cern.ch/record/923393>

[2] R. Kersevan, J-L. Pons, "Introduction to MOLFLOW+: New graphical processing unit-based Monte Carlo code for simulating molecular flows and for calculating angular coefficients in the compute unified device architecture environment", J. Vac. Sci. Technol. A 27, 1017 (2009);

5:20pm **VT-MoA11 Numerical Modeling of Compact Siegbahn Molecular Drag Stages**, *H. Telib*, Politecnico di Torino, Italy, *R. Arpa*, Optimad Engineering s.r.l., Italy, *L. Campagna*, *I.F. Cozza*, *E. Emelli*, Agilent Technologies s.p.a., Italy

In the frame of an optimization of single/multi-stage disk-type vacuum pumps, characterized by spiral channels a comprehensive but efficient

numerical analysis of performances has to be founded on a careful modeling of the local gas flow features, such as pump leakage and development of the rarefied gas flow along the curved channels. Here, gas flows are in general considered three-dimensional, because of the spiral groove curvature, and driven by pressure gradients and the applied rotation speed as well as inertial forces (centripetal and Coriolis effects), which play the most important role.

Following the assumptions made for a Holweck model by Sharipov et al., we propose a lower-order model for steady flows in spiral molecular drag stages, based on the solution of the Boltzmann Equation (BE) with a BGK closure, in general curvilinear coordinates (properly fitted to the geometrical design of the channel), where the inertial effects explicitly appear in the governing equation. The order of the 3D original problem is reduced in the physical space (2D), by introducing assumption of “locally” known flow development of the distribution function along the spiral channel. Thus, 2D-BE calculations of the flow rates and stresses will be performed in a finite number of sections, suitably positioned along the spiral channel, from the outlet up to the inlet, in order to recover the pressure and torque distribution. In particular, the 2D Boltzmann equation is linearized in the most significant parameters (local rotation speed and pressure gradients along the pump radial direction), and solved in the reference section. The local values of pressure and torque are obtained consistently by enforcing the mass flow conservation constraint.

A Discrete Velocity Method (DVM) is used to solve the Boltzmann Equation, with an explicit pseudo-time dependent technique to relax the flow up to its stationary solution. In order to decrease the computational time employed, the solver is designed to work on parallel architectures (MPI).

The performance prediction of the model will be assessed using test cases from the literature and compared to the available experimental data, on both Holweck and Siegbahn geometries. A further verification test will be carried out, to test prediction capabilities in the continuum regime by direct comparison with results obtained by a Navier-Stokes solver, with slip-boundary conditions.

Tuesday Morning, November 1, 2011

Applied Surface Science Division

Room: 102 - Session AS-TuM

Imaging and 3D Chemical Analysis

Moderator: V.S. Smentkowski, GE-GRC, X. Dong, Eli Lilly and Company

8:00am **AS-TuM1 Recent Applications of GCIB Depth Profiling with XPS and TOF-SIMS**, T. Miyayama, N. Sanada, ULVAC-PHI Inc., Japan, J.S. Hammond, Physical Electronics **INVITED**

The development of new electronic devices incorporating organic materials, such as Organic Light Emitting Diodes (OLED's) and Organic Photovoltaics (OPV's) is rapidly increasing. To control quality, performance and lifetimes of these devices, it is necessary to characterize the layer structures and the dopant distributions in the thin organic materials. Conventional surface analysis techniques such as XPS and TOF-SIMS, combined with mono-atomic ion beam sputtering, have been widely used for chemical depth profiling of inorganic thin films. However, this approach has not been successful for the depth profiling of organic materials due to the loss of chemical information during the sputtering process. Recent cluster ion beam developments utilizing C₆₀ and Coronene ions have also had limited success for the XPS and TOF-SIMS depth profiling of OLED and OPV structures due to similar modification of chemical and molecular information as a function of sputter depth.

The chemical depth profiling of organic layers with thicknesses greater than one micron has also been problematic utilizing XPS and TOF-SIMS with C₆₀ cluster sources. The implementation of new cluster ion sources that could extend chemical depth profiling of organics to more than several microns should also expand the applications of the XPS and TOF-SIMS techniques.

Recent studies have shown the successful use of a GCIB (gas cluster ion beam) source on XPS (X-ray photoelectron spectroscopy) instruments to quantify the chemical depth profile of polyimide films without sputter induced chemical degradation^[1, 2]. Based on these earlier experiments, additional GCIB depth profiling applications of organic and biomaterials with XPS and TOF-SIMS will be discussed. Examples will be presented for the characterization of ultra-thin organic electronic layers in OLED's and OPV's. The successful organic depth profiling to depths of several tens of microns will also be discussed.

1. Takuya Miyayama, Noriaki Sanada, Mineharu Suzuki, John S. Hammond, S.-Q. D. Si and Atsushi Takahara, *J. Vac. Sci. Technol. A* 2010, A 28(2), L1

2. Takuya Miyayama, Noriaki Sanada, Scott R. Bryan, John S. Hammond and Mineharu Suzuki, *Surf. Interface Anal.* 2010, 42, 1453-1457.

9:00am **AS-TuM4 Advances in Organic Depth Profiling for Polymer Devices**, J.L.S. Lee, I.S. Gilmore, National Physical Laboratory, UK, A. Licciardello, University of Catania, Italy

Knowledge of the distribution of organics within an organic matrix is important to the innovation and manufacture of many advanced technologies including polymer electronics and photovoltaics, medical devices, ink-jet printing technologies and drug delivery systems. Organic depth profiling using sputtering with cluster ions and imaging by SIMS or XPS have revolutionised the analytical capability for these important systems, providing uniquely detailed 3D chemical information. However, despite recent progress, organic depth profiling is not yet routinely applied to industry problems. The principal reason for this is that organic sputtering only works for a limited set of materials [1] and unfortunately it fails completely for many industrially important materials, such as conjugated polymers in the organics electronics industry. Consequently, an important recent development is the use of nitric oxide (NO) flooding [2] as a radical scavenger to reduce ion induced cross-linking during depth profiling.

In this study, we use model polymer layers, including polystyrene and industrially relevant conjugated polymers, to demonstrate the benefits of using NO flooding for polymers that do not sputter under normal conditions and evaluate the basic metrology. Understanding the mechanisms for damage, cross-linking, radical generation and radical reaction is vital in developing this technique to work with industrial materials. Using C₆₀²⁺ as a sputtering ion beam, it is found that NO flooding combined with sample cooling [3] significantly reduce the disappearance cross-section for characteristic fragments. For polystyrene model systems, the steady state intensity of C₇H₇⁺ can be increased from typically < 0.1% of the initial intensity at normal experimental conditions to 50% when NO flooding is used in conjunction with cooling. We also demonstrate successful depth

profiles on 1 μm thick polymer material, showing high and constant sputtering yields with ~ 30 nm depth resolution to the interface. Our results show a dramatic improvement for the depth profiling of difficult type II polymers. NO flooding may be used along with other developments e.g. large argon cluster ions [4], sample cooling and sample rotation [3], and has the potential to provide a step change in analytical capability for industrial samples.

[1] C. M. Mahoney, *Mass Spectrom. Rev.*, 2010, 29, 247

[2] N. Tuccitto, I. Delfanti, V. Spampinato and A. Licciardello, presented at SIMS XVII, Toronto, 2009.

[3] P. Sjövall, D. Rading, S. Ray, L. Yang and A. G. Shard, *J. Phys. Chem. B*, 2010, 114, 769.

[4] J. L. S. Lee, S. Ninomiya, J. Matsuo, I. S. Gilmore, M. P. Seah and A. G. Shard, *Anal. Chem.* 2010, 82, 98.

9:20am **AS-TuM5 TOF-SIMS Depth Profiling and 3D Analysis of Polymer Materials Using C₆₀ and Ar Cluster Ion Beams for Sputtering**, D. Rading, ION-TOF GmbH, Germany, N. Havercroft, ION-TOF USA, Inc., R. Moellers, E. Niehuis, ION-TOF GmbH, Germany

Preservation of molecular information under high-dose sputtering conditions has become increasingly important. It is not only a pre-requisite for depth profiling and 3D analysis of organic materials, but also extends the survival of sample material beyond the static SIMS limit in high lateral resolution imaging. In this respect, the use of a high energy cluster ion beam for sputtering such as SF₅ [1] and C₆₀ [2-4] has aroused considerable interest. With the beam energies typically applied, the total energy is high enough for reasonable sputter rates whereas the energy per atom, of about several 100 eV, is considered low enough to minimize sample damage. However, it has been demonstrated that a variety of organic compounds cannot be profiled in a satisfactory way and characteristic molecular secondary ion signals are lost [5-7]. In this respect it has been shown recently that massive argon cluster ions can be successfully applied as primary projectiles in SIMS [8,9].

We equipped a TOF-SIMS 5 instrument with a Bi_n, C₆₀ and an Ar_n cluster ion source in order to compare the possibilities and limitations of these projectiles for depth profiling of polymer materials. In this contribution, we will focus on dual beam depth profiling where the analysis is done with Bi_n and the sputtering with C₆₀ and Ar_n cluster ion beams, respectively. Stability and intensity of characteristic high mass molecular ion signals as well as sputter yields and depth resolution will be compared. For this purpose different beam energies resulting in 2 - 10 eV/atom for Ar_n and 167 - 667 eV/atom for C₆₀ sputtering have been applied to various polymer samples. From our experiments we can conclude that most of the limitations C₆₀ sputtering suffers from could be successfully overcome and that the Ar GCIB seems to be a more universal tool for sputtering of organic materials.

[1] C.M. Mahoney, S.V. Roberson, G. Gillen, *Anal. Chem.* 2004, 76, 3199-3207

[2] N. Winograd, *Anal. Chem.* 2005, April 1, 143A-149A

[3] J. Cheng, A. Wucher and N. Winograd, *J. Phys. Chem. B*, 2006, 110, 8329-8336

[4] J.S. Fletcher, X.A. Conlan, J.C. Vickerman, N.P. Lockyer, *Appl. Surf. Sci.* 2006, 252, 6513-6516

[5] M.S. Wagner, *Anal. Chem.* 2005, 77, 911-922

[6] R. Möllers, N. Tuccitto, V. Torrisi, E. Niehuis, A. Licciardello, *Appl. Surf. Sci.* 2006, 252, 6509-6512

[7] H.-G. Cramer, T. Grehl, F. Kollmer, R. Moellers, E. Niehuis, D. Rading, *Appl. Surf. Sci.* 2008, 255, 966

[8] N. Toyoda, J. Matsuo, T. Aoki, I. Yamada, D.B. Fenner, *Nucl. Instr. and Meth. in Phys. Res.* 2002, B 190, 860-864

[9] S. Ninomiya, K. Ichiki, H. Yamada, Y. Nakata, T. Seki, T. Aoki, J. Matsuo, *Rapid Communications in Mass Spectrometry* 2009, 23, 1601-1606

9:40am **AS-TuM6 The zcorrectorgui for 3D ToF-SIMS Depth Profiles**, D.J. Graham, M. Robinson, D.G. Castner, University of Washington

ToF-SIMS imaging is a powerful technique for obtaining chemically specific maps of the surface of a wide range of samples including polymers, metals, tissues, and cells. When combined with the sputtering capabilities of modern ToF-SIMS instruments, one can obtain chemically and biologically specific 3D depth profiles, as well as track chemical signatures throughout a sample volume. This is done with a dual beam approach by taking an image of the surface, sputtering away a given amount of the material and then taking a new image of the freshly exposed area. This process is repeated until the object of interest is gone or the desired depth is reached.

When working with surfaces with significant topography such as the surface of a cell, the z axis of the resulting data cube is not correct. This is

due to the fact that each image slice of the surface is displayed as a 2-D image taken from a 3-D surface. This results in a type of inverted topography of the 3D structure within the ToF-SIMS image volume. To correct for this, the National ESCA and Surface Analysis Center for Biomedical Problems NESAC/BIO (Seattle, WA) has developed a Matlab (Mathworks, Natick MA) toolbox to correct the z-axis of cell depth profiles and display the data properly.

Since the shape and topography of a cell can be complex, we have created a set of features of known chemistry and controlled geometry in order to test and validate that the zcorrectorgui is accurately correcting the z-axis. For this, microsphere templating was combined with capillary force lithography to create features of known size and shape. The features sizes were chosen to correspond with the sizes of typical eukaryotic cells. Topographical images of these features were obtained by AFM. After AFM analysis the features were depth profiled by ToF-SIMS. The resulting depth profile data was then imported into the zcorrectorgui and processed. In this presentation we will highlight the results from this study and show example data obtained from a real cell depth profile processed with the zcorrectorgui.

10:40am **AS-TuM9 3D Analysis of Organic Multilayer Structures by TOF-SIMS Using Ar Cluster Ions**, *R. Moellers*, ION-TOF GmbH, Germany, *R. Kersting*, TASCION GmbH, Germany, *D. Rading*, *E. Niehuis*, ION-TOF GmbH, Germany

Organic multilayer systems are of increasing importance in many technological fields. The entry of the OLED technology into commercially available multi-color displays is one example. Optimization of this technology in terms of lifetime and efficiency requires a detailed knowledge of the layer and interface composition.

From the analytical point of view, these OLED multilayer structures are quite challenging. A detailed analysis requires the identification of complex high mass organic molecules in thin layers of only several nanometer thickness with a lateral resolution in the micrometer range. In particular the identification of the molecular composition is challenging for SIMS as molecular information does usually not survive high dose sputtering conditions.

In the past different projectiles such as low energy Cs⁺ [1] and keV C₆₀⁺ cluster [2-4] have been explored for their depth profiling capabilities on organic layers. For some materials molecular information survives but for the majority of organic molecules depth profiling using these projectiles fails. Recently the application of large Ar clusters for the non-destructive removal of organic matter has been discussed in the SIMS community. The GCIB (gas cluster ion beam) technique was developed by the group of Isao Yamada [5] at the University of Kyoto and has already demonstrated some potential in this field of application [6].

We used a TOF-SIMS 5 instrument equipped with a Bi cluster ion gun for the analysis and an Ar GCIB as well as a C₆₀ cluster ion gun providing both analysis and sputter gun capabilities. In this contribution we will focus on the variation of the sputter projectile, the energy dependence of the resulting depth resolution and the survival of specific molecular ion signal under high dose sputtering conditions. For this purpose a well-defined multilayer model sample similar to a working OLED device was used. The knowledge about the optimum analysis conditions gained on the model system was transferred to a 3D analysis of an OLED display device using an Ar GCIB for sputtering.

[1] N. Mine, B. Douhard, J. Brison and L. Houssiau, *Rapid Commun. Mass Spectrom.* **2007**, 21, 2680-2684

[2] N. Winograd, *Anal. Chem.* **2005**, April 1, 143A-149A

[3] J. Cheng, A. Wucher and N. Winograd, *J. Phys. Chem B.* **2006**, 110, 8329-8336

[4] J.S. Fletcher, X.A. Conlan, J.C. Vickerman, N.P. Lockyer, *Appl. Surf. Sci.* **2006**, 252, 6513-6516

[5] I. Yamada, J. Matsuo, N. Toyoda, A. Kirkpatrick; *Materials Science and Engineering: R-Reports: A Review Journal*; **34**, **2001**, 6, 231-295

[6] S. Ninomiya, K. Ichiki, H. Yamada, Y. Nakata, T. Seki, T. Aoki, J. Matsuo, *Rapid Communications in Mass Spectrometry* **2009**, 23, 1601-1606

11:00am **AS-TuM10 Molecular Imaging of Cells and Tissues with Novel Ion Beams**, *J. Matsuo*, QSEC, Kyoto University, CREST, Japan, *K. Ichiki*, *T. Yamamoto*, *Y. Yamamoto*, Kyoto University, Japan, *S. Ibuki*, QSEC, Kyoto University, CREST, Japan, *T. Aoki*, *T. Seki*, Kyoto University, CREST, Japan

The field of secondary ion mass spectrometry (SIMS) for biological material analysis is receiving much attention nowadays, because molecular, structural and chemical information is considered to be invaluable. However, for large biomolecules the sensitivity of SIMS needs to be improved. Cluster ion beams have been reported to enhance the yields of secondary ions, because of the high-density energy deposition and multiple

collisions near surfaces. SF₅, C₆₀, Au₃ and Bi₃ were found to be quite useful for SIMS of organic materials.

We have proposed using a large Ar cluster beam for organic SIMS. This beam has a number of advantages over other cluster beams for molecular depth profiling of various polymers, and it provides new opportunities for sputtering molecules without inducing significant damage [1]. Biomolecules are also very fragile and thus difficult to sputter with conventional ion beams; therefore, a large Ar cluster beam would be quite suitable for biological material analysis. However, molecular imaging requires a focused Ar cluster beam, and we developed a new Ar cluster ion gun aiming to obtain a fine-focused beam of several mm diameter. An orthogonal acceleration time-of-flight (oa-TOF) mass spectrometer, which allows the use of a continuous beam, was also combined in the system, and a mass resolution higher than 6000 was obtained. Because there was no need to use the ion-bunching technique in this system, there was no tradeoff between beam diameter and mass resolution. This is another advantage of this molecular imaging system over the conventional TOF instrument. This novel system is quite useful for both molecular depth profiling and imaging.

The latest results of this system and its performance in molecular imaging of cells and tissues will be presented and discussed.

[1] J. Matsuo, S. Ninomiya, H. Yamada, K. Ichiki, Y. Wakamatsu, M. Hada, T. Seki and T. Aoki, *Surf. Interface Anal.* (2011) 42, 1612

11:20am **AS-TuM11 High Resolution TOF-SIMS Imaging of Barrier Layers in Mouse Skin Stratum Corneum**, *I. Ishizaki*, ULVAC-PHI inc., Japan, *A. Kubo*, Keio University, Japan, *Y. Ohashi*, *A. Yamamoto*, ULVAC Inc., Japan, *J.S. Hammond*, *G.L. Fisher*, *S.R. Bryan*, Physical Electronics

The stratum corneum (SC) is the outermost layer of epidermis that acts as a barrier to keep foreign objects out of the body and to keep water in. It is composed of multi-layered sheets of dead cells containing keratin that continuously fall off and are regenerated from live cells in the underlying layers. The total thickness of the SC layer is less than 40 μm. In order to study the barrier properties of the SC and how this function fails in certain skin disorders, it is necessary to visualize the distribution of different biomolecules within the multi-layered SC structure. It is also valuable to compare the penetration of various foreign chemicals into the SC layer in mice with and without the skin disorder. In this initial study, we applied TOF-SIMS imaging using a bismuth cluster ion beam to characterize the multi-layer structure of mouse skin. Samples were prepared by quick freezing of mouse tails followed by cross-sectioning by cryostat. TOF-SIMS imaging provided the spatial resolution and molecular specificity to clearly visualize dead cell layers and living layers of the epidermis. By using peaks characteristic of specific molecules, it was possible to image the distribution of amino acids, cholesterol, and lipids within the SC. The results suggest that SC might contain several chemically distinct layers. Skin samples were also depth profiled using GCIB sputtering. Imaging of cross-sections and depth profiling from the skin surface will be compared for obtaining molecular profiles within the SC structure.

Biofabrication and Novel Devices Focus Topic **Room: 105 - Session BN+NM-TuM**

Biofabrication Applications

Moderator: G.F. Payne, University of Maryland, College Park

8:20am **BN+NM-TuM2 Electrically Controlled Biofabrication with Stimuli-Responsive Polysaccharide and Their Visualization in Microfluidic Devices**, *Y. Cheng*, *X.L. Luo*, *J. Betz*, *C.Y. Tsao*, *H.C. Wu*, *G.F. Payne*, *W.E. Bentley*, *G.W. Rubloff*, University of Maryland, College Park

Stimuli-responsive polysaccharides, such as chitosan and alginate, are useful biomaterials that can be induced to undergo a reversible sol-gel transition to generate biologically-relevant scaffolds. The recent discovery that their gelation can be triggered by imposing an electrical signal opens many avenues for the creation of biologically functional hybrid structures and their localization onto and within microfabricated devices for biofabrication and biosensing applications. Here we report two different mechanisms for creating polysaccharide hydrogels in microfluidics by electrical signal. The cathodic electrodeposition of the cationic chitosan hydrogel was achieved by electrochemically generated OH⁻ ions at the cathode surface, creating a localized pH gradient at the sol-gel interface. The anodic electrodeposition of calcium alginate hydrogel was achieved by electrical-signal-mediated release of Ca²⁺ ions as a result of electrochemically generated H⁺ ions at the anode surface reacting with suspended CaCO₃ particles in alginate solution. Localization of the

hydrogels in transparent microfluidic devices makes them highly accessible through optical imaging and spectroscopy. The processes of *in situ* gel formation are simple, scalable, spatially controllable, and electroaddressable. Applications in protein immobilization and cell assembly with electroaddressing capability were further demonstrated. With the advantage of spatiotemporal control of gel formation coupled with microfabrication techniques, a variety of novel and useful structures such as multi-layer, multi-address, and even site-programmable arrays of biological components can also be achieved.

8:40am **BN+NM-TuM3 Biofabrication for Interrogating Cell Signaling**, *W.E. Bentley, T. Gordonov*, University of Maryland, College Park **INVITED**

The biological signal transduction process is the means by which external signals are incorporated into information that directly or indirectly alters gene expression and ultimately, phenotype. The hierarchical structure of signal transduction processes is a topic of intense research. Microbial quorum sensing (QS) is responsible for a variety of phenotypes and is rich in diversity and modes of action. As such, quorum sensing represents a "guide" for learning how signals can be translated into altered phenotype.

As microbial communities occupy a confined space over time, concentrations of extracellular signaling molecules accumulate, providing stimulus for unique and varied cellular responses as well as protection from competing microbial communities. Referred to as "quorum sensing" for it's often reported and coincident dependence on high population density, extracellular signaling provides a new basis for control over molecular and cellular processes as well as population behavior, perhaps in a manner more consistent with that of native machinery. Among behaviors guided by QS are the establishment and persistence of bacterial infections.

Our laboratory has uncovered many of the molecular features of the QS autoinducer-2 (AI-2) system using traditional methods that probe bacterial physiology and by exploiting newer principles of biofabrication. That is, we employed electrodeposition methods to assemble complex biological subsystems onto specific sites on microfabricated devices and within microfluidic channels via programmable electrical signals. We have also used genetic engineering techniques to create signal activated fusion tags that covalently link proteins to the device/bio interface. We have designed and synthesized "biological nanofactories" that provide small signal molecule generation at the surface of targeted and captured cells - enabling programmable control of cell function.

Using these methods, we have discovered attributes of the natural switching mechanism that can be exploited for developing next generation antimicrobials. That is, we decomposed elements of the QS "switch" via mutation and a mathematical model of the regulatory elements and coupled this understanding with devices designed to appropriately interrogate these molecular features. Finally, we have developed alkyl analogs of AI-2 that elucidate structural detail and have potential for affecting behavior in natural environments. Correspondingly, these serve as the basis for creating next generation antimicrobials that target the communication between bacteria rather than their survival mechanisms.

9:20am **BN+NM-TuM5 Surface Modified Magnetic Microparticles for Bioreactor Applications**, *A. Khaing, E. Milkani, A. Maziarz, C. Lambert, W. McGimpsey*, Worcester Polytechnic Institute

A magnetically-stabilized, continuous-flow bioreactor was designed and applied for the controlled growth of rat aortic smooth muscle cells (RASMC) in a pre-determined shape in a three-dimensional environment. The cells were immobilized on magnetic agarose beads (MABs) and grown into a tube-shaped tissue. By adjusting the experimental parameters, the size of the MABs were controlled. The surfaces of the MABs were biochemically modified and RASMC cell growth on the modified MABs was tested. Initial RASMC tissue rings with MABs grew in the magnetic field inside the continuous flow of culture medium in the first few days. The RASMC tissue tube was formed in a week, and allowed to mature up to about a month before removing from the bioreactor to characterize it. Histological staining of RASMC tissue tube showed that RASMC were circumferentially aligned perpendicular to the direction of the flow of culture medium. The majority of the cells in the RASMC tissue tube grown out of the MABs stabilized in the magnetic field in the continuous flow were healthy and highly proliferating. The system has applications in the fields of tissue regeneration, pharmaceutical production, stem cell amplification and biofuel production.

9:40am **BN+NM-TuM6 Bacterial Communication in Controlled 3D Microenvironments**, *X.L. Luo, H.C. Wu, C.Y. Tsao, Y. Cheng, J. Betz, G.W. Rubloff, W.E. Bentley*, University of Maryland

Antibiotic resistance is a growing and widely recognized public health issue. Today, more than 70% of bacteria are resistant to at least one of the most commonly used antibiotics. Bacteria evolve with increasing antibiotic resistance due to the selective pressure that administration of conventional antibiotics creates on cell viability, wherein those bacteria that survive antibiotics become dominant. The emergence of "super" bacteria that carry multiple resistant genes calls for the development of novel antimicrobial strategies that place *less* selective pressure on the target bacteria. Rather than killing bacteria with antibiotics, interruption of bacterial communication networks - or quorum sensing (QS) - might delay the population-scale behaviors of target bacteria in gene regulation and buy time for the host immune system to fight back. Microfluidic environments provide a controlled and attractive opportunity to study bacterial QS and to explore these strategies.

Here we report *in vitro* signaling between localized, spatially distinct cell populations in controlled 3D fluidic microenvironments. First, a freestanding chitosan membrane was fabricated by using pH gradients generated at the flow interface of two converging flows. Next, alginate membranes were fabricated by cross-linking alginate sequentially on both sides of the chitosan membrane using diffusion of calcium ions through the semi-permeable chitosan membrane. Finally, cell assembly was achieved by suspending cells in the alginate solution to embed the target cells into the alginate scaffolds, realized as a micro-sandwich structure of cells in alginate on both sides of the chitosan membrane. Signal molecules transmitted *in situ* from one cell population were transported either by diffusion to (1) surrounding cells and (2) nearby segregated cell population, or by convection to (3) cell populations that are relatively far away in a separated microchannel. Induced quorum sensing responses, the production of fluorescence proteins functionally linked to QS genes, were observed for all three configurations. Importantly, these membrane-based 3D scaffolds offer convenient top-down visualization and easy access to both sides of the scaffolds. These approaches provide a versatile and powerful platform to understand and modulate collective and interruptive cellular responses in bacterial quorum sensing.

10:40am **BN+NM-TuM9 "Body-On-A-Chip": Combining Microfabrication, Cell Cultures, and Mathematical Models**, *M.L. Shuler*, Cornell University **INVITED**

We seek to understand the response of the human body to various pharmaceuticals. Our platform technology is an *in vitro* system that combines microfabrication and cell cultures and is guided by a computer model of the body. We called this *in vitro* system a micro cell culture analog (microCCA) or a "Body-on-a-Chip". A microCCA device contains mammalian cells cultured in interconnected micro-chambers to represent key body organs linked through the circulatory system and is a physical representation of a physiologically based pharmacokinetic model. ^(1, 2) MicroCCAs can reveal toxic effects that result from interactions between organs as well as provide realistic, inexpensive, accurate, rapid throughput toxicological studies that do not require animals. The advantages of operating on a microscale include the ability to mimic physiological relationships more accurately as the natural length scale is order of 10 to 100 microns.

We have used a microCCA to test potential combination therapies (Tegafur and uracil) for colon cancer. ⁽³⁾ Tegafur is a prodrug for 5-FU and uracil an inhibitor of DPD, an enzyme which deactivates 5-FU. Simple microwell plates cannot probe this system, but the microCCA predicts the types of responses observed experimentally. A "pumpless" system that would be easy to utilize has been demonstrated with Tegafur also. ⁽⁴⁾ We have coupled these body modules with a micro model of the GI tract to examine the response to oral exposure of drugs, chemicals, or nanoparticles. ⁽⁵⁾

Overall, we believe that *in vitro*, microfabricated devices with cell cultures provide a viable alternative to animal models to predict toxicity and efficacy in response to pharmaceuticals.

References

1. Sin, A., K.C. Chin, M.F. Jamil, Y. Kostov, G. Rao, and M.L. Shuler. The Design and Fabrication of Three-Chamber Microscale Cell Culture Analog Devices with Integrated Dissolved Oxygen Sensors. *Biotechnol. Prog.* (2004), 20:338-345.
2. Khamsi, R. Meet the Stripped Down Rat. *Nature* (2005), 435(5 May):12-13.
3. Sung, J.H. and M.L. Shuler. A Micro Cell Culture Analog (microCCA) with 3-D Hydrogel Culture of Multiple Cell Lines to Assess Metabolism-Dependent Cytotoxicity of Anti-Cancer Drugs. *Lab Chip* (2009), 9:1385-1394.

4. Sung, J.H., C. Kam, and M.L. Shuler. A microfluidic device for pharmacokinetic-pharmacodynamic (PK-PD) model on a chip. *Lab Chip* (2010) 10: 446-455.

5. Mahler, G.J., M.B. Esch, R.P. Glahn, and M.L. Shuler. Characterization of a gastrointestinal tract microscale cell culture analog used to predict drug toxicity. *Biotechnol. Bioeng.* (2009) 104:193-205.

11:20am **BN+NM-TuM11 Simultaneous Bacterial Transformation and Localization within a Microfluidic Device**, *J. Betz, Y. Cheng, C.Y. Tsao, G.F. Payne, W.E. Bentley, G.W. Rubloff*, University of Maryland

Transformation, the process by which a bacterium takes up and incorporates extracellular DNA, is one of the primary enabling technologies in the biotechnology field. This allows a researcher to program bacteria, equipping them with a complement of genes to accomplish a task, such as producing a molecule of interest or acting as a sensor. We describe the simultaneous transformation and localization of *Escherichia coli* bacteria in response to an electric signal within a microfluidic device. We demonstrate that these transformed bacteria can act as fluorescent sensors of isopropyl β -D-1-thiogalactopyranoside (IPTG), a chemical stimulus, or low dissolved oxygen levels, an environmental stimulus.

This method focuses on bacterial transformation with the added benefit of simultaneous entrapment within an alginate hydrogel at a desired electrode address. This offers the ability to create microfluidic cell-based sensors in a single, simple step. To transform and deposit bacteria, the device was filled with a mixture of electrocompetent cells, 200ng plasmid, 0.5% alginate, and 0.125% CaCO₃ and subjected to a 30V/cm DC electric field for 3 minutes on ice. The cells were allowed to recover at 37°C for an hour, cultured for 16 hours, and induced with a chemical signal, IPTG, for 4 hours. This resulted in increased expression of DsRed, a red fluorescent protein.

Dissolved oxygen is an important parameter for many cell culture experiments. To create a dissolved oxygen sensor, *E. coli* were transformed with a plasmid that causes production of green fluorescent protein (GFP) in response to decreased dissolved oxygen concentration in the surrounding medium. Following the above transformation and culturing method, the cells were induced with media that had been deoxygenated in a vacuum chamber, resulting in an increase in GFP expression.

This method is versatile in terms of creating microfluidic cell-based sensors. We envision many exciting applications of this work, including the development of dynamically reconfigurable microfluidic biosensors and high-throughput screening methods for plasmid libraries generated by protein engineering and directed evolution experiments.

Electronic Materials and Processing Division

Room: 210 - Session EM+TF-TuM

High-k Dielectrics for MOSFETs Part 1

Moderator: R.M. Wallace, University of Texas at Dallas

8:20am **EM+TF-TuM2 In Situ TMA Pre-Treatment Study of GaAs and In_{0.53}Ga_{0.47}As Surfaces**, *B. Brennan, D.M. Zhernokletov, H. Dong, R.V. Galatage, J. Kim, E.M. Vogel, R.M. Wallace*, University of Texas at Dallas

One of the major issues preventing the integration of high mobility III-V semiconductors into next generation CMOS devices is the formation of high levels of interfacial defects at the high-k/III-V interface. These can have the effect of pinning the Fermi level and preventing optimal operation of the devices. Engineering the interface between these materials therefore becomes of critical importance to try and reduce the defect density. Identification of the individual defects however is not a trivial matter with correlation between electrical data and physical measurement techniques rarely seen. This study aims to investigate the effect of *in-situ* chemical treatments prior to Al₂O₃ deposition on (NH₄)₂S treated GaAs and InGaAs surfaces, in terms of both physical characterization by X-ray photoelectron spectroscopy (XPS) and electrical measurements from MOS capacitors.

The reduction of interfacial oxides through a “clean up” effect by a ligand exchange mechanism with the tri-methyl aluminum (TMA) precursor for atomic layer deposition (ALD) of Al₂O₃ is well known, [1,2] however little work has been carried out to optimize this process and determine whether variations in the effect are seen as a result of changes in the number of TMA cycles or pulse time prior to oxide deposition. Variations in the presence of arsenic surface features, (i.e. As-As bonding or surface dimers) come under particular focus. The effect of post deposition annealing is also investigated specifically in terms of the potential role hydrogen could play in passivating defects at the interface. [3]

[1] C. L. Hinkle, A. M. Sonnet, E. M. Vogel, S. McDonnell, G. J. Hughes, M. Milojevic, B. Lee, F. S. Aguirre-Tostado, K. J. Choi, H. C. Kim, J. Kim, R. M. Wallace, *Appl. Phys. Lett.* 92, 071901, (2008)

[2] B. Brennan, M. Milojevic, H.C. Kim H.C., P.K. Hurley, J. Kim, G. Hughes, R.M. Wallace, *Electrochem. Solid-State Lett.*, 12, 6, (2009)

[3] H. D. Trinh, E. Y. Chang, P. W. Wu, Y. Y. Wong, C. T. Chang, Y. F. Hsieh, C. C. Yu, H. Q. Nguyen, Y. C. Lin, K. L. Lin, M. K. Hudait, *Appl. Phys. Lett.* 97, 042903 (2010)

8:40am **EM+TF-TuM3 Half-cycle Atomic Layer Deposition Studies of HfO₂ on the GaSb(001) Surface**, *D.M. Zhernokletov, H. Dong, B. Brennan, J. Kim, R.M. Wallace*, University of Texas at Dallas

Since GaSb(001) is a candidate surface channel material for p-MOSFET and an interfacial passivation layer for buried channel quantum well and tunneling FETs (GaSb static dielectric constant of ~ 16), it is necessary to understand its interface with high-k dielectric materials which would act as gate dielectrics in these devices[1]. An *in-situ* half-cycle atomic layer deposition/X-ray photoelectron spectroscopy (ALD/XPS) study is conducted in order to investigate the evolution of the HfO₂ dielectric interface with the GaSb(001) surface after sulfur passivation procedures and HCl etching designed to remove the native oxides. Monochromatic XPS is used to examine the surfaces following the various surface treatments and then without breaking vacuum, after each individual ALD pulse of tetrakisdimethyl-amino-hafnium (TDMA-Hf) and deionized water (DIW) precursors (i.e. single TDMA-Hf pulse/XPS scan; single DIW/XPS scan; etc.) for two full cycles and finally after 1 nm of HfO₂ deposition to determine whether there is any “clean up” effect of the native oxides due to the ALD process. The various surface preparation techniques are compared to determine which is more effective at minimizing native oxides. The behavior of the sulfides and the effect of HCl surface cleaning procedure upon HfO₂ deposition are discussed as well as a comparison to previous results from half cycle Al₂O₃ deposition on GaSb [2]. This work is supported by the Semiconductor Research Corporation FCRP MSD Focus Center, the Nanoelectronics Research Initiative and the National Institute of Standards and Technology through the Midwest Institute for Nanoelectronics Discovery (MIND) and the NSF (ECCS-0925844).

[1] A. Nainani, T. Irisawa, Z. Yuan, Y. Sun, T. Krishnamohan, M. Reason, B.R. Bennett, J.B. Boos, M. Ancona, Y. Nishi, K.C. Saraswat, International Electron Devices Meeting, (IEDM) Tech. Dig. (2010).

[2] S. McDonnell, D. M. Zhernokletov, A. P. Kirk, J. Kim, and R. M. Wallace. *Applied Surface Science Letters*, submitted (2011).

9:00am **EM+TF-TuM4 Remote Phonon and Surface Roughness Limited Universal Electron Mobility of In_{0.53}Ga_{0.47}As Surface Channel MOSFETs**, *E.M. Vogel, A.M. Sonnet, R.V. Galatage*, University of Texas at Dallas, *P.K. Hurley, E. Pelucchi, K. Thomas, A. Gocalinska*, Tyndall National Institute, *J. Huang, N. Goel, G. Bersuiker*, SEMATECH, *W.P. Kirk, C.L. Hinkle*, University of Texas at Dallas **INVITED**

The inversion layer electron mobility in n-channel In_{0.53}Ga_{0.47}As MOSFET's with HfO₂ gate dielectric with several substrate impurity concentrations (~1×10¹⁶ cm⁻³ to ~1×10¹⁸ cm⁻³) and various surface preparations (HF surface clean, (NH₄)₂S surface clean and PECVD a-Si interlayer with a HfO₂ gate dielectric) have been studied. The peak electron mobility is observed to be strongly dependent on the surface preparation, but the high field mobility is observed to be almost independent of the surface preparation. A detailed analysis of the effective mobility as a function of electric field, substrate doping, and temperature was used to determine the various mobility components (surface roughness, phonon, and coulombic scattering limited mobility components). For the substrates with high doping concentration, the electron mobility at low vertical electric field is dominated by Coulomb scattering from the substrate dopants, whereas, for lower substrate doping the Coulombic scattering is dominated by the disorder induced gap states. Low temperature measurements were used to determine the surface roughness scattering and phonon components. The results show that room temperature mobility of In_{0.53}Ga_{0.47}As surface channel MOSFETs with HfO₂ gate dielectric at high electric field is limited primarily by remote phonons whereas the Al₂O₃ gate dielectric is limited by surface roughness scattering.

9:40am **EM+TF-TuM6 Structural Characterization of Ultra-thin High-k Gate Oxide Films through a Multi-technique Approach**, *E.J. Bersch, J.D. LaRose, I.B. Wells*, University at Albany, *S.P. Consiglio, R.D. Clark, K.N. Tapily, G.J. Leusink*, TEL Technology Center, America, LLC, *A.C. Diebold*, University at Albany

High-k HfO₂-based gate oxides have recently been put into production in CMOS-based integrated circuits, and their future use in this capacity depends on how well they can continue to be downscaled. To this end,

efforts to increase the dielectric constant (k) of HfO₂-based gate oxides are ongoing. Recent work has shown that by tailoring annealing procedures, k values for HfO₂ films of greater than 30 have been obtained.¹ These higher k values for HfO₂ occur for the metastable tetragonal and cubic crystalline phases, while the thermodynamically preferred monoclinic phase has a lower k value (~20). To evaluate the crystalline structure of ultra-thin (< 100 Å) HfO₂ films which have undergone various annealing treatments, we used several techniques, including grazing incidence in-plane X-ray diffraction (GIIXRD), X-ray and UV photoemission spectroscopy (XPS and UPS, respectively) and spectroscopic ellipsometry (SE). GIIXRD measurements showed that ~60 Å HfO₂ films grown with a sequence of depositions and anneals (so-called DADA process²) were monoclinic, while those which were post deposition annealed (PDA) were in a mixture of monoclinic and either tetragonal or orthorhombic phases. Pole figure measurements of these films showed that the DADA film had a monoclinic (-111) fiber texture, while the PDA film was randomly oriented. For HfO₂ films with thicknesses of ~25 Å, GIIXRD measurements showed that DADA films were tetragonal or orthorhombic, while PDA films were also tetragonal or orthorhombic, but also possibly with a monoclinic component. XPS and UPS measurements of the valence bands of HfO₂ films were found to be useful in distinguishing between crystalline and non-crystalline films, but were not useful in distinguishing between crystalline phases.³ SE has been shown to be useful in identifying crystallinity in HfO₂ through a feature that appears in the HfO₂ extinction coefficient curve at the absorption edge. We have observed this absorption edge feature for films that were crystalline and strongly monoclinic, but not for films that were only weakly crystalline or mostly non-monoclinic, in keeping with previous work.⁴

References:

- [1] S. Migita, *et al.*, 2008 Symposium on VLSI Technology, 152-153(2008).
- [2] R.D. Clark, *et al.*, *ECS Trans.*, **35(4)**, 815-834 (2011).
- [3] S. Toyoda, *et al.*, *J. Appl. Phys.*, **97**, 104507 (2005).
- [4] J. Schaeffer, *et al.*, *J. Electrochem. Soc.*, **150** (4), F67 (2003).

10:40am **EM+TF-TuM9 Research Advances on III-V and Ge MOS/MOSFETs Beyond Si CMOS**, *T.D. Lin, M.L. Huang, Y.C. Chang, W.C. Lee*, National Tsing Hua University, Taiwan, Republic of China, *T.W. Pi*, National Synchrotron Radiation Research Center, Taiwan, Republic of China, *J. Kwo*, National Tsing Hua Univ. and National Taiwan Univ., Taiwan, Republic of China, *M. Hong*, National Tsing Hua University, Taiwan, Republic of China

INVITED

Metal-oxide-semiconductor (MOS) and MOS field-effect-transistors (MOSFETs) of high k dielectrics on high carrier mobility channels of InGaAs and Ge have been feverishly studied, as they are now strongly considered for technologies beyond Si complementary MOS (CMOS) integrated circuits (ICs). The post Si CMOS research is now facing unprecedented challenges in materials and physics, as key material/electrical/processing issues have to be met/solved in order to realize the new advanced devices; these include equivalent oxide thickness (EOT) < 1 nm, interfacial density of state (Dit) $\leq 10^{11}$ eV⁻¹cm⁻², high-temperature thermal stability for self-aligned process, low parasitic, and integration with Si. Using *in-situ* ultra high vacuum (UHV) and *in-situ/ex-situ* atomic layer deposited (ALD) high k 's of Ga₂O₃(Gd₂O₃), Al₂O₃, and HfO₂ on InGaAs and Ge, this research group has made advances in achieving an EOT of 0.5 nm, Dit of low 10¹¹ eV⁻¹cm⁻² (with a flat distribution versus energy within the semiconductor bandgap), and high-temperature stability of the MOS structures (rapid thermal annealing to 800-900°C and 500-600°C for the high k 's/InGaAs and /Ge, respectively). Atomic manipulation to perfecting the high k 's/InGaAs and /Ge interfaces is the key for the above achievements. Probing of the interfaces and gaining insightful understanding of the electronic properties was made possible using our uniquely designed experiments of *in-situ* synchrotron radiation photoemission. High-performance self-aligned inversion-channel high k 's/InGaAs MOSFETs in achieving record-high drain currents and transconductances, and record-low sub-threshold swings, and high k 's/Ge MOSFETs without employing interfacial passivation layers will also be discussed.

11:20am **EM+TF-TuM11 SiO₂ Interlayer Thickness Dependence of the Density and Polarity of Charges in Si/SiO₂/Al₂O₃ stacks**, *N.M. Terlinden, G. Dingemans, M.M. Mandoc, M.C.M. van de Sanden, W.M.M. Kessels*, Eindhoven University of Technology, Netherlands

In this contribution, we investigate the influence of the SiO₂ thickness on the density and polarity of built-in charges in SiO₂/Al₂O₃ stacks deposited on Si(100). Such charges lead to the development of a space-charge region (SCR) in the Si at the dielectric interface, having consequences such as flat band voltage shifts in MOS devices and electric-field induced passivation in optoelectronic devices like solar cells. We have employed the nonlinear

optical technique of second-harmonic generation (SHG) to probe the Si(100) SCR electric field through the effect of electric-field-induced SHG (EFISH). Using this non-intrusive and contactless technique we found previously that the built-in charge density at the SiO₂/Al₂O₃ interface is independent of the Al₂O₃ thickness down to ~2 nm.¹ Here we report on the influence of the interfacial SiO_x layer, present between the Si(100) substrate and the atomic layer deposited (ALD) Al₂O₃ film, addressing the origin, density, and polarity of the charges. For this reason, we have synthesized SiO₂/Al₂O₃ stacks with intentionally grown SiO₂ interlayers having a thickness in the range ~1.4-150 nm using various deposition methods (e.g. thermal oxidation, PECVD, ALD). Spectroscopic SHG measurements were carried out with a femtosecond pulsed Ti:sapphire laser tunable in the 1.33-1.75 eV photon energy range. From the obtained spectra we found that the charge density is highly influenced when increasing the SiO₂ thickness, dropping from 10¹³ to 10¹¹ cm⁻², with the polarity switching from negative to positive. These measurements were confirmed by *C-V* measurements and surface voltage measurements employing corona charging of the stacks. On the basis of the observations the mechanism and consequences of charge trapping in Si/SiO₂/Al₂O₃ stacks will be addressed.

¹ Terlinden *et al.*, *Appl. Phys. Lett.* **96**, 112101 (2010)

11:40am **EM+TF-TuM12 Study of the Interface Barrier of Atomic Layer Deposited (ALD) Al₂O₃ on GaN**, *M. Esposito, S. Krishnamoorthy, D.N. Nath, S. Bajaj, S. Rajan, T.-H. Hung*, Ohio State University

We report on the deposition and energy band diagram analysis of high-quality low-leakage Al₂O₃/GaN using atomic layer deposition. As GaN-based transistors are scaled to achieve higher frequency operation, atomic layer deposition techniques offer a promising way to achieve low leakage while scaling gate-to-channel distance. In addition, applications of GaN in power switching systems require ultra-low leakage that can be achieved using metal-insulator-semiconductor (MISHEMT) structures. In this work, we have made quantitative estimates of conduction band offsets and interface charge density.

MIS structures with varying oxide thickness were fabricated on an n+/n-GaN sample grown by RF plasma MBE on low dislocation density Lumilog GaN templates. Three Al₂O₃ layers of nominal 6 nm, 12 nm, and 18 nm were deposited by atomic layer deposition at 300°C, using trimethylaluminum (TMA) and H₂O as precursors. The pre-deposition treatment of the surface consisted in a 10:1 HF-dip for 15s. All three samples were then annealed at 600°C in forming gas for 1min. A new ALD deposition procedure was also developed to achieve low leakage in these structures.

A quantitative analysis of the interface barrier of Ni/Al₂O₃/GaN capacitors was carried out to determine conduction band discontinuity, interface fixed charge and pinning effects. The I-V measurements show extremely low current density for thin dielectric films. A quantitative energy band diagram was estimated from capacitance voltage (C-V) measurements by extracting the apparent charge profiles of the MIS capacitors taking into account the spontaneous polarization in GaN and doping. The extracted flat-band voltages were -0.36 V, -1.55 V and -2.73 V for the 6 nm, 12 nm and 18 nm-thick oxide respectively. The hysteresis in the C-V profile for the 6nm-thick capacitor pointed out a D_{it} charge density of approximately 5x10¹¹ cm⁻² and higher for the thicker capacitors. This was because the deposition and post deposition annealing conditions were optimized for very thin oxide layers (~ 5-6 nm). A linear relationship between the flat-band voltage and the oxide thickness was experimentally observed, indicating absence of Fermi-level pinning at the Al₂O₃/GaN interface. The conduction band offset at the Al₂O₃/GaN interface was calculated to be 2.66 eV. In addition, we estimate that a non-zero field of approximately 2 MV/cm exists in the oxide under flat band conditions in the semiconductor. This non-zero field is attributed to a fixed charge density at the Al₂O₃/GaN interface of 2.79x10¹³ cm⁻².

Energy Frontiers Focus Topic

Room: 103 - Session EN+NS-TuM

Ultrafast Charge and Energy Transfer in Nanomaterials

Moderator: J.B. Baxter, Drexel University

8:00am **EN+NS-TuM1 Controlled Deposition of Nanocrystal Quantum Dots on Silicon Surfaces: Demonstration and Application of Forster Resonant Energy Transfer**, *O. Seitz, H.M. Nguyen, Y.N. Gartstein, A.V. Malko*, University of Texas at Dallas, *Y.J. Chabal*, The University of Texas at Dallas

Studying Forster resonant energy transfer (FRET) at semiconductor surfaces has been a challenge because of difficulties in grafting reliably nanocrystal quantum dots (NQDs) onto electronically passivated substrates.

Poor control has often resulted in formation of aggregates (3D growth), inhomogeneity, and poor adhesion. In this study, combining IR absorption spectroscopy (IRAS) and X-ray photoelectron spectroscopy (XPS), photoluminescence, atomic force microscopy (AFM) and electrical measurements, we have grafted self-assembled monolayers (SAMs) on both oxidized and oxide-free silicon surfaces with appropriate functionality to obtain dense monolayer of NQDs and to study FRET. SAMs that are directly attached to the silicon via Si-C bonds display a high interface quality with a low density of interface states. This makes it possible to prepare systems with tunable thicknesses necessary for FRET investigation. The time evolution of the fluorescence intensity is in good agreement with the predicted thickness dependence. We are currently developing 3D structures to enhance energy collection for a given surface area. Such hybrid colloidal NQD/Silicon optoelectronic structures could potentially be attractive for both photovoltaic as well as light emitting applications.

8:20am EN+NS-TuM2 Orbital-dependent Charge Transfer Dynamics in Potential Molecular Wires, *H. Hamoudi*, Universität Heidelberg, Germany, *S. Nepl*, Technische Universität München, Germany, *P. Kao*, Penn State University, *B. Schüpbach*, Universität Frankfurt, Germany, *P. Feulner*, Technische Universität München, Germany, *A. Terfort*, Universität Frankfurt, Germany, *D.L. Allara*, Penn State University, *M. Zharnikov*, Universität Heidelberg, Germany

Continued progress in technologically important fields such as molecular and organic electronics as well as organic photovoltaics depends on reliable information about the charge transport (CT) through individual molecular groups, above all so-called molecular wires, since these represent important building blocks of a variety of devices. In this context, femtosecond CT dynamics in a series of self-assembled monolayers with oligo(phenyleneethynylene) and oligo(phenyl) backbone, which are prototypes of potential molecule wires, was addressed by resonant Auger spectroscopy using the core hole clock method. The length of the molecular backbone was varied to monitor the respective dependence of the CT time. The CT pathway was unambiguously defined by resonant excitation of the nitrile tailgroup attached to the backbone. Due to the conjugation of the electronic systems of this group and the adjacent terminal phenyl ring of the backbone, a splitting of the degenerated unoccupied molecular orbital (MO) of nitrile occurred, resulting in two different MOs which could be selectively addressed by X-rays and used as the starting points for CT. The characteristic CT times were found to depend strongly on the character of the MO which mediates the CT process. This demonstrates that the efficiency and rate of CT in molecular wires can be controlled by resonant injection of the charge carriers into specific MOs.

8:40am EN+NS-TuM3 Photophysics of Semiconductor Nanostructures in Relation to Problems of Solar Energy Conversion, *V.I. Klimov*, Los Alamos National Laboratory **INVITED**

This presentation provides a brief overview of research activities in the Center for Advanced Solar Photophysics with focus on spectroscopic properties of semiconductor nanocrystals studied from the prospective of solar energy conversion. One process, which can be used for boosting a photocurrent of solar cells, is carrier multiplication (CM) or multiexciton generation. Our recent activities in this area include the development of reliable methods for efficient screening of CM performance using photon counting with superconducting nanowire detectors, the studies of the impact of "extraneous" processes on CM measurements, and the evaluation of the effects of the nanocrystal composition, dimensions, and shape on CM yields. As part of our effort on controlling excited-state dynamics, we study hot-electron transfer in nanocrystals. We find that the efficiency of this process can approach 10% even with incidental impurity-like acceptors, suggesting that even higher probabilities are possible with engineered acceptors designed for testing the ideas of hot-electron extraction. We also apply spectroscopic tools for probing the physics of charge transport in nanocrystal assemblies using exploratory devices such as optical field-effect transistors (OFETs). The OFET studies help to understand the nature of conducting states in dark and under illumination and to rationalize many previously unexplained observations including a weak sensitivity of conductance to particles' polydispersity and a significant difference in a photovoltage compared to a nominal band-gap energy. These studies illustrate how key insights into the performance of nanoscale materials are gained through close integration of spectroscopic, materials and device efforts across the Center.

9:20am EN+NS-TuM5 Hot Electron Transfer from Semiconductor Nanocrystals, *W.A. Tisdale*, Massachusetts Institute of Technology **INVITED**

In conventional semiconductor solar cells, absorption of photons with energies greater than the semiconductor band gap generate "hot" charge carriers that quickly "cool" before all of their energy can be captured – a process that limits device efficiency. Semiconductor nanocrystals (or

quantum dots) have been touted as promising materials for photovoltaics because discretization of their electronic energy levels can slow down this cooling process, which might enable the extraction of photogenerated charge carriers before their excess energy is converted to heat.

In this talk, I will demonstrate hot electron transfer from PbSe nanocrystals to delocalized conduction band states of TiO₂ and the concomitant excitation of coherent surface vibrational modes associated with this ultrafast process. In order to make these measurements, we developed the use of optical second harmonic generation (SHG) for femtosecond time-resolved studies of interfacial charge separation. I will discuss the information we obtain from this technique as well as the effect of temperature, nanocrystal size, and surface chemistry, and how these observations inform our understanding of electronic coupling at interfaces between confined states and bulk materials.

10:40am EN+NS-TuM9 Single Molecule Study of Charge Transfer in 6T-TBrPP-Co Molecular Complex, *Y. Zhang*, *U.G.E. Perera*, *S.-W. Hla*, Ohio University

When two molecules having tendency to donate or accept electronic charge are put together, charge transfer between the molecules can take place. By a suitable selection of donor and acceptor molecules, it is possible to engineer an entire class of materials having metallic, semiconducting, insulating, or even superconducting properties [1, 2]. Here, we present a low temperature scanning tunneling microscopy and spectroscopy study of single molecule level charge transfer process between α -sexithiophene(6T) and TBrPP-Co molecules on a Cu(111) surface. We form molecular clusters composed of both molecular species on Cu(111). The charge transfer between the molecules is directly evident in the tunneling spectroscopy data, which reveals the shift of 6T HOMO towards the surface Fermi level indicating donation of charge from 6T to TBrPP-Co. This work is supported by the US-DOE-DE-FG02-02ER46012 grant.

Reference:

[1] F. Jackel, U. G. E. Perera, V. Iancu, K.-F. Braun, N. Koch, J. P. Rabe, and S.-W. Hla, *Phys. Rev. Lett.* 100, 126102 (2008).

[2] K. Clark, A. Hassanien, S. Khan, K.-F. Braun, H. Tanaka and S.-W. Hla, *Nature Nanotechnology*, Vol.5, April, 2010.

11:00am EN+NS-TuM10 NEGF Quantum Simulation of Nanotip Thermionic Emitters for Direct Energy Conversion, *T.D. Musho*, *D.G. Walker*, Vanderbilt University

Wide band-gap diamond nanotip field emission devices have been experimentally shown to have superior performance and lifetime. However, theoretical studies of the electronic emission from these devices using standard Fowler-Nordheim (FN) theory does not fully capture the physics as a result of the fitting parameters inherent to the FN approximation. The following research computationally models wide band-gap nanotip field emission devices from a quantum point of view, using a novel non-equilibrium Green's function (NEGF) approach previously applied to modeling the transport in solid-state electronic devices. In this research the IV characteristics of a single square tip diamond emitter are investigated under several bias conditions. Those bias conditions include both field emission in response to a potential bias and thermionic emission in response to a temperature bias. The NEGF model calculates the ballistic transport using a self-consistent Schrödinger-Poisson solver, calculating the transmission at discrete energy levels which is then used by the Landauer formalism to determine the total current. Ultimately, this model allows the inherent quantum mechanical transport to be captured without any fitting parameters. Findings from this research have confirmed non-linearities in the FN curve and have demonstrated the experimental transport trends. Additionally, thermionic emission trends suggest that select geometric parameters are target for enhanced emission.

11:20am EN+NS-TuM11 Mechanisms of Heterogeneous Charge Transfer at the Quantum Dot-Organic Interface, *A. Morris-Cohen*, *M. Frederick*, *L. Cass*, *E.A. Weiss*, Northwestern University **INVITED**

We examine the rates and mechanisms of electron transfer between colloidal semiconductor quantum dots (QDs) and viologen derivatives using ultrafast transient absorption spectroscopy. Viologens accept electrons from photoexcited QDs on the femtosecond-to-single picosecond timescale. Modifications of the chemistry by which the ligands link to the QD surface, and the density of ligands on the QDs, facilitates control of charge separation and recombination rates, and determination of the operative mechanisms of charge transfer.

Energy Frontiers Focus Topic
Room: 108 - Session EN-TuM

Industrial Physics Forum on Energy III

Moderator: D.G. Seiler, National Institute of Standards & Technology, J.S. Murday, University of Southern California

8:00am **EN-TuM1 Materials for Low Risk Nuclear Reactors, T.R. Allen**, University of Wisconsin, Madison **INVITED**

Advanced reactor concepts have been proposed for many reasons that could be attributed to "risk reduction." Risk reduction could mean improved safety margins, more certain economic performance, greater resistance to proliferation, or reduction of risk of exposure during the long-term storage of waste. For many of the envisioned advanced reactor concepts that have been proposed to reduce some form of risk, the ultimate deployment hinges on overcoming challenges in fuels and materials performance. The limits of performance unique to nuclear systems are typically associated with either radiation damage from high-energy particles or due to high-temperature corrosion or stress corrosion cracking. This presentation will provide an overview of the unique operating conditions in proposed reactor concepts and special challenges associated with structural materials operation. Then an overview of two approaches to improve material performance will be presented, specifically use of nanoparticles to improve high temperature strength in radiation fields and the use of tailored systems of grain boundaries to improve corrosion and stress corrosion cracking resistance.

8:40am **EN-TuM3 Battery 500 - the Li-Air Battery Opportunity, S.A. Swanson**, IBM Almaden Research Center **INVITED**

In 2009, IBM started a project to develop rechargeable Li-air batteries for electric cars with a range of 500 miles per charge. This type of high density energy storage technology could become a game changer for the widespread adoption of electric vehicles but it also presents enormous technical challenges. Published work on Li-air batteries has only reported small fractions of the theoretical limit with limited rechargeability. Many aspects of the technology, including the lithium-oxygen electrochemistry, appear to have been poorly understood.

This presentation will give an overview of Li-air battery technology. We will describe our ongoing research including our investigation into the decomposition of carbonate based solvents during cell discharge using Differential Electrochemical Mass Spectrometry, the characterization and identification of the cathode electrodeposits, and enhanced cell capacities achieved using alternative aprotic solvents.

9:20am **EN-TuM5 Advanced Thermoelectric Technology for Waste Heat Recovery, G.P. Meisner**, General Motors Research & Development **INVITED**

In today's internal combustion engine based vehicles, more than two-thirds of the fuel energy is lost as waste heat. At General Motors Global Research & Development, we aim to demonstrate a viable thermoelectric (TE) generator system to recover that waste heat by converting it into useful electricity using advanced TE technology and thereby reduce vehicular fuel consumption. Essential to the long term success of TE technology in the automobile industry, and for waste heat recovery applications in general, is new materials research, specifically fundamental physics and materials research aimed at discovering and understanding new high performance TE materials, and the development of those materials into robust and high performance TE devices. Our work, which is generously supported by the U. S. Department of Energy's Vehicle Technologies Program, focuses on (1) bulk TE materials (e.g., filled skutterudites) and their temperature dependent physical, mechanical, and TE properties, and (2) TE device and module development, TE generator design, and prototype TE generator fabrication, assessment, and validation. We have made significant progress on constructing working prototype automotive TE generator and testing it on a GM production vehicle.

10:40am **EN-TuM9 Improving Solar Energy Conversion with Nanoscale Materials, S.F. Bent**, Stanford University **INVITED**

With the intensifying global need for alternative energy, there is strong interest in new approaches to materials for sustainable energy devices. A variety of different energy technologies must work in concert to produce, store, and consume the 20 TW of energy that humans will soon demand. Underlying the diverse set of energy conversion devices are similar physical and chemical phenomena, many of which can be controlled with nanoscale materials. This talk will describe research on nanoscale materials for solar photovoltaics and solar fuel production. Synthetic strategies including atomic layer deposition are used to generate nanoscale materials with a high level of control over composition, structure, and thickness. The materials

are then tested in energy conversion devices. The prospects and challenges for such materials to contribute to higher energy conversion efficiencies will be discussed.

Electron Transport in Low Dimensional Materials Focus Topic

Room: 209 - Session ET+EM+NS+GR-TuM

Electron Behaviors in Nanoelectronics, Interconnect, and Carbon-based Materials

Moderator: J. Wendelken, Oak Ridge National Laboratory, A. Swan, Boston University

8:00am **ET+EM+NS+GR-TuM1 Electron Transport Study of Graphene on SiC Using Scanning Tunneling Potentiometry, K. Clark, S. Qin**, Oak Ridge National Laboratory, *G. He*, Carnegie Mellon University, *G. Gu*, The University of Tennessee, *R.M. Feenstra*, Carnegie Mellon University, *A.-P. Li*, Oak Ridge National Laboratory

The unique electronic and transport properties of graphene have helped this material emerge as a perspective graphene based electronic system. Single layers of graphene formed on SiC look to be a promising system for the realization of graphene electronics. To utilize the full potential of graphene on SiC a complete understanding of the physical and electronic properties of this system is needed. This study uses Scanning Tunneling Microscope (STM) images along with scanning tunneling spectroscopy to characterize the sample surface. STM images clearly show the distinction between 1 monolayer (ML) and 2ML regions. The 1ML to 2ML transition is further confirmed by point spectroscopy measurements and spectroscopic mapping across the boundary. Defects, grain boundaries, step edges and other potential scattering centers are thought to play a major role in the electronic properties, especially in transport, along the graphene sheets. Using a low temperature four-probe scanning tunneling microscope, potentiometry measurements are performed on epitaxial graphene grown on 4H-SiC. Potentiometry maps spanning the transition from 1ML to 2ML graphene layers show a contrast change indicating a potential change at this interface. Preliminary results of the transport along this potentially revolutionary new electronic system will be presented. This research was conducted at the Center for Nanophase Materials Sciences, which is sponsored at Oak Ridge National Laboratory by the Office of Basic Energy Sciences, U.S. Department of Energy.

8:20am **ET+EM+NS+GR-TuM2 Engineering the Electronic States of CVD Grown Few Layer Graphene by Twisting and Lattice Distortion, M.H. Pan**, Oak Ridge National Laboratory, *X.T. Jia*, *S. Bhaviripudi*, Massachusetts Institute of Technology, *V. Meunier*, Rensselaer Polytechnic Institute, *M.S. Dresselhaus*, *J. Kong*, Massachusetts Institute of Technology
Few layer graphene (FLG) can have advantages over single layer graphene because it has a larger current-carrying capacity and the electronic properties are sensitive to more engineerable system parameters. In particular, Hass et al. have demonstrated that orientational disorder is normally present in carbon-face SiC epitaxial FLG samples.[1] Recently both theoretical and experimental studies suggest that strain can be used to engineer graphene electronic states through the creation of a pseudo-magnetic field. [2] Here we present both scanning tunneling microscopic/spectroscopic (STM/S) studies of chemical vapor deposition grown few layer graphene samples. There indeed exists a twisting between the stacked graphene layers, confirmed by both high-resolution STM images and low temperature spectroscopic measurements. Our results show that, by stretching graphene along three symmetry directions, a strain-induced pseudo magnetic field can lead to the formation of different Charge Density Wave (CDW) states at the top layer of graphene.

[i] Hass, J., Varchon, F., *Phys. Rev. Lett.* **100**, 125504(2008)

[ii] Levy, N. et al., *Science* **329**, 544 (2010).

8:40am **ET+EM+NS+GR-TuM3 Unique One- and Two-Dimensional Phenomena Observed in Carbon Nanotubes and Graphene, S. Cronin**, University of Southern California **INVITED**

Our ability to fabricate nearly defect-free, suspended carbon nanotubes

(CNTs) has enabled us to observe several phenomena never seen before in CNTs, including breakdown of the Born-Oppenheimer approximation[1], mode selective electron-phonon coupling[2], leading to negative differential resistance (NDR) and non-equilibrium phonon populations, and a Mott

insulator transition[3]. In this work, Raman spectroscopy is used to measure individual, suspended CNTs under applied gate and bias potentials. Raman spectroscopy of periodic ripple formation in suspended graphene will also be reported. As will be shown, preparing clean, defect-free devices is an essential prerequisite for studying the rich low-dimensional physics of CNTs and graphene.

1. Bushmaker, A.W., Deshpande, V.V., Hsieh, S., Bockrath, M.W., and Cronin, S.B., "Direct Observation of Born-Oppenheimer Approximation Breakdown in Carbon Nanotubes." *Nano Letters*, 9, 607 (2009).
2. Bushmaker, A.W., Deshpande, V.V., Bockrath, M.W., and Cronin, S.B., "Direct Observation of Mode Selective Electron-Phonon Coupling in Suspended Carbon Nanotubes." *Nano Letters*, 7, 3618 (2007).
3. Bushmaker, A.W., Deshpande, V.V., Hsieh, S., Bockrath, M.W., and Cronin, S.B., "Large Modulations in the Intensity of Raman-Scattered Light from Pristine Carbon Nanotubes." *Physical Review Letters*, 103, 067401 (2009).

9:20am **ET+EM+NS+GR-TuM5 Probing Surface Band Conduction through Back-Gated Conductance Measurements on Si Nanomembranes**, *W.N. Peng**, *J. Endres*, *S. Scott*, *Z. Aksamija*, *D.E. Savage*, *I. Knezevic*, *M.G. Lagally*, *M. Eriksson*, University of Wisconsin Madison

Silicon-on-insulator substrates provide large-area Si nanomembranes (SiNMs) mechanically supported by bulk handle wafers. Because of the intervening oxides, SiNMs are also electrically isolated from the substrates. The typical membrane thickness is less than a few hundred nanometers. Because they are so thin, SiNMs display interesting transport phenomena influenced by surface effects. Here, we demonstrate a novel method to probe surface transport via conductance measurements on SiNMs. When contacts are placed on the front surface, a current flows between the source and the drain via the membrane body as well as its surface. By utilizing an underlying back gate (the Si handle substrate), the conductance through the membrane can be continuously tuned and made smaller than the surface contribution, enabling experimental determination of the surface conductance. We measure the membrane conductance as a function of both the membrane thickness and the backgate voltage in ultra-high vacuum. In contrast to H-terminated Si surfaces, clean reconstructed Si(001)(2×1) surfaces show a constant-conductance regime when the backgate voltage is varied, and the conductance in this regime does not depend on membranes thickness. We demonstrate that the constant conductance (on the order of 10^9 Siemens) stems from an additional conduction channel through the dimer-reconstructed surface π^* band. By comparing the experimental results to numerical simulations, the surface band mobility is determined to be in the range 10-50 cm^2/Vs .

Research supported by NSF [UW MRSEC, award DMR-0520527, as well as awards 0937060 (subaward CIF-146) and ECCS-0547415] and DOE

9:40am **ET+EM+NS+GR-TuM6 Ferroelectric Field-Effect Transistor Behavior in CdS Nanotetrapods**, *S. Qin*, Oak Ridge National Laboratory, *W. Fu*, *L. Liu*, Chinese Academy of Sciences, *T.H. Kim*, Oak Ridge National Laboratory, *S.L. Hellstrom*, Stanford University, *W. Wang*, *W. Liang*, *X. Bai*, *E. Wang*, Chinese Academy of Sciences, *A.-P. Li*, Oak Ridge National Laboratory

Complex nanostructures such as branched semiconductor nanotetrapods are promising building blocks for next-generation nanoelectronics. Here we report on the electrical transport properties of individual CdS tetrapods in a field-effect transistor (FET) configuration with a ferroelectric $\text{Ba}_{0.7}\text{Sr}_{0.3}\text{TiO}_3$ film as high- κ , switchable gate dielectric. A cryogenic four-probe scanning tunneling microscopy is used to probe the electrical transport through individual nanotetrapods at different temperatures. A p -type field effect is observed at room temperature, owing to the enhanced gate capacitance coupling. And the reversible remnant polarization of the ferroelectric gate dielectric leads to a well-defined nonvolatile memory effect. The field effect is shown to originate from the channel tuning in the arm/core/arm junctions of nanotetrapods. At low temperature (8.5 K), the nanotetrapod devices exhibit a ferroelectric-modulated single-electron transistor behavior. The results illustrate how the characteristics of a ferroelectric such as switchable polarization and high dielectric constant can be exploited to control the functionality of individual 3-dimensional nano-architectures. **Acknowledgement:** The research at the Center for Nanophase Materials Sciences is sponsored at Oak Ridge National Laboratory by the Office of Basic Energy Sciences, U.S. Department of Energy. The research in Beijing is supported by MOST and CAS of China.

10:40am **ET+EM+NS+GR-TuM9 Probing Electron-Electron Correlations in Quantum Dots Using Transport: Quantum Monte Carlo Studies**, *H.U. Baranger*, Duke University **INVITED**

Strong electron-electron correlations occur in nanoscale systems in a variety of contexts – when electrons form a crystal at low density, for example, or in correlations between quantum dots. Nanoscale systems introduce in addition an unprecedented level of control over the physical parameters determining such correlations. As electron transport is one of the primary probes of nanosystems, the effect of e-e correlations on transport is a key issue. I shall discuss an example in which we used quantum Monte Carlo (QMC) techniques to calculate the conductance:

Consider a system of four quantum dots designed to study the competition between three types of interactions: Heisenberg, Kondo, and Ising. We find that the competition produces a rich phase diagram containing two sharp features: a quantum phase transition (QPT) between charge-ordered and charge-liquid phases, and a dramatic resonance in the charge liquid visible in the conductance. The conductance is calculated using a world-line QMC method: extrapolation of the imaginary time QMC data to zero frequency yields the linear conductance, which is then compared to numerical renormalization group results in order to assess its accuracy. The QPT is of the Kosterlitz-Thouless type with a discontinuous jump in the conductance at the transition. We connect the sharp resonance phenomenon with the degeneracy of three levels in the isolated quadruple dot and argue that this leads to an emergent symmetry. I shall end by discussing the sensitivity to parameter variation and possible experimental realizations in laterally gated quantum dots as well as carbon nanotubes.

This work was done in collaboration with Dong E. Liu and Shailesh Chandrasekharan (Duke University).

11:20am **ET+EM+NS+GR-TuM11 Resistivity Increase due to Electron Scattering at Surfaces and Grain Boundaries in Metal Thin Films and Nanowires**, *J.S. Chawla*, *D. Gall*, Rensselaer Polytechnic Institute

The effect of surface and grain boundary scattering on the resistivity of Cu thin films and nanowires is quantified using (i) *in situ* transport measurements on single-crystal, atomically smooth Cu(001) layers, (ii) textured Cu(111) layers and patterned Cu wires with independently varying grain size, thickness and line width, and (iii) *in situ* grown interfaces including Cu-Ta, Cu-MgO, Cu-SiO₂ and Cu-oxygen. In addition, the electron surface scattering is also measured *in situ* for single-crystal Ag(001) and TiN(001) layers. These findings are important for the development of future generation narrow low-resistivity Cu interconnects and TiN metal gates.

Cu(001), Ag(001), and TiN(001) layers with a minimum continuous thickness of 4, 5 and 1.8 nm, respectively, are grown by ultra-high vacuum magnetron sputter deposition on MgO(001) substrates and are found to be atomically smooth single crystals by a combination of x-ray diffraction θ - 2θ scans, ω -rocking curves, pole figures, reciprocal space mapping, Rutherford backscattering, x-ray reflectometry, transmission electron microscopy, and *in-situ* scanning tunneling microscopy. Polycrystalline Cu layers with a 111-texture are deposited on thermally grown SiO₂, with and without Ta barrier layer. Subsequent *in-situ* annealing at 350°C followed by sputter etching in Ar plasma yields Cu layers with independently variable thickness and grain size. Cu nanowires, 50 to 150 nm long, 70 to 350 nm wide, and 45 nm thick, are patterned using electron beam lithography and sputter etching.

In-situ electron transport measurements at room temperature in vacuum and at 77 K in liquid nitrogen for single-crystal Cu and Ag layers is consistent with the Fuchs-Sondheimer (FS) model and indicates specular scattering at the metal-vacuum boundary with an average specularly parameter $p = 0.6$ and 0.4, respectively. In contrast, layers measured *ex-situ* show completely diffuse surface scattering due to sub-monolayer oxidation. Electron transport measurements for polycrystalline Cu/Ta layers and wires show a ~10% and ~11% decrease in resistivity, respectively, when increasing the average lateral grain size by factor 2. *In-situ* deposition of 0.3 to 8 nm thick Ta barrier layers on Cu(001) leads to a resistance increase that indicates a transition from $p = 0.8$ to $p = 0$, independent of the Ta thickness. *In-situ* exposure of Cu(001) layers to O₂ between 10⁻³ and 10⁵ Pa-s results in a sequential increase, decrease and increase of electrical resistance which is attributed to specular surface scattering for clean Cu(001) and for surfaces with a complete adsorbed monolayer, but diffuse scattering at partial coverage and after chemical oxidation.

* NSTD Student Award Finalist

11:40am **ET+EM+NS+GR-TuM12 Control of Contact Formation via Electrodeposition on GaAs Nanowires**, *C. Liu, O. Einabad, S. Watkins, K.L. Kavanagh*, Simon Fraser University, Canada

Copper (Cu) electrical contacts to as-grown gallium arsenide (GaAs) nanowires have been fabricated via electrodeposition. The nanowires are zincblende (111) oriented grown epitaxially on n-type Si-doped GaAs(111)B

substrates by gold-catalyzed Vapor Liquid Solid (VLS) growth in a metal organic vapour phase epitaxy (MOVPE) reactor. The epitaxial electrodeposition process, based on previous work with bulk GaAs substrates, consists of a substrate oxide pre-etch in dilute ammonium hydroxide carried out prior to galvanostatic electrodeposition in a pure Cu or Fe sulphate aqueous electrolyte at 20C. The conductivity of wires was controlled via the addition of carbon tetrabromide (CBr₄) during growth. For nominally undoped GaAs nanowires, we find that Cu or Fe has a preference for growth on the gold catalyst avoiding the sidewalls. After etching the gold, both metals still preferred to grow only on the tops of the nanowire, consistent with the location of the largest electric field. Core-shell GaAs nanowires with highly conductive carbon-doped shells were fabricated via changing the Ga precursors from triethylgallium to trimethylgallium for radial growth. Increasing the conductivity of the nanowires in this way, not surprisingly; meant that Cu nucleation and growth began to occur on the sidewalls as well as on the gold catalyst. Finite element simulations will be compared to our electrodeposition results towards the calibration of nanowire conductivity.

Graphene and Related Materials Focus Topic

Room: 208 - Session GR+EM-TuM

Graphene: Optical Properties, Optoelectronics and Photonics

Moderator: P.E. Sheehan, U.S. Naval Research Laboratory

8:00am **GR+EM-TuM1 Graphene Optoelectronics: From Ultrafast Lasers to Flexible Displays**, *A.C. Ferrari*, University of Cambridge, UK
INVITED

The richness of optical and electronic properties of graphene attracts enormous interest. So far, the main focus has been on fundamental physics and electronic devices. However, we believe its true potential to be in photonics, plasmonics and optoelectronics, where the combination of its unique optical and electronic properties can be fully exploited, the absence of a bandgap can be beneficial, and the linear dispersion of the Dirac electrons enables ultra-wide-band tunability [1]. The rise of graphene in photonics and optoelectronics is shown by several recent results, ranging from solar cells and light emitting devices, to touch screens, photodetectors and ultrafast lasers. Despite being a single atom thick, graphene can be optically visualized [2]. Its transmittance can be expressed in terms of the fine structure constant [3]. The linear dispersion of the Dirac electrons enables broadband applications. Saturable absorption is observed as a consequence of Pauli blocking [4,5]. Chemical and physical treatments enable luminescence [1,6]. Graphene-polymer composites prepared using wet chemistry [4-6] can be integrated in a fiber laser cavity, to generate ultrafast pulses, down to 100fs with up to 1 W average power, and enable broadband tunability [4,5]. Graphene-based mode-locked laser are a near term application for this extraordinary material, and can provide simple, low-cost, and convenient light sources for metrology, sensing, medicine and micromachining. Graphene is an ideal transparent flexible conductor. A flexible electrically switchable smart window will be reported, with over 230 contrast ratio, as well as an electro-tactile screen for mobile phone applications. The optoelectronic properties of graphene can be enhanced by combination with plasmonic nanostructures [7], for example in plasmonic-enhanced photovoltage generation [8]

1. F. Bonaccorso et al. *Nature Photonics* 4, 611 (2010)
2. C. Casiraghi et al. *Nano Lett.* 7, 2711 (2007).
3. R. R. Nair et al. *Science* 320, 1308 (2008).
4. T. Hasan, et al. *Adv. Mat.* 21,3874 (2009)
5. Z. Sun et al. *ACS Nano* 4, 803 (2010); *Nano Research* 3, 653 (2010)
6. T. Gokus et al. *ACS nano* 3, 3963 (2009)
7. F. Schedin, *ACS Nano* 4, 5617 (2010).
8. T.J. Echtermeyer et al, submitted (2011)

9:00am **GR+EM-TuM4 Quantum Mechanics-Based Exploration of Graphene-Like Systems to Model Magnetic Resonators**, *X.W. Sha, E.N. Economou, D.A. Papaconstantopoulos*, George Mason University, *M.R. Pederson, M.J. Mehl*, Naval Research Laboratory, *M. Kafesaki*, University of Crete, Greece

Quasi-circular pieces of graphene as well as nanotubes offer the possibility of acting as magnetic resonators to be used in negative refractive index optical metamaterials. The advantage of these graphene pieces is twofold: (a) they are stable even when their size reaches the tens of nanometers; (b) the induced currents in the presence of an AC magnetic field perpendicular to the graphene plane cancel each other in all the interior hexagons and only an edge circular current remains. This current is expected to be ballistic in nature with almost zero resistance. This analog of the split (in the split ring resonators) is expected to be achieved by the substitutional insertion of foreign atoms (e.g. nitrogen atoms). To explicitly and reliably check these ideas we have used the NRLMOL, a first-principles DFT code, in the presence of an AC magnetic field, to calculate the response of various configurations of quasi-circular pieces of graphene with or without the presence of substitutional foreign atoms. In order to be able to extend our calculations to larger systems, of the order of tens of thousands of atoms, we used the NRL-TB method, in which the TB matrix elements were fitted so as to reproduce the energy levels of our DFT approach. Results for the energy levels, some selected eigenfunctions, and the current distribution for several configurations will be presented and evaluated vis-a-vis the intended use as almost lossless magnetic resonators.

9:20am **GR+EM-TuM5 Infrared Optical Conductance of CVD-grown Graphene**, *J.W. Weber, M.C.M. van de Sanden*, Eindhoven University of Technology, Netherlands

The infrared optical conductance of chemical vapour deposited (CVD) graphene is determined from near normal incidence reflection and transmission Fourier transform infrared measurements in the spectral range of 370-7000 cm⁻¹. The real part of the conductance, up to 2500 cm⁻¹, shows both the effect from doping and finite temperature that was shown for exfoliated graphene.^{1,2} The conductance for the range 2500-7000 cm⁻¹ is increasing from the value for the universal optical conductance ($\pi e^2/2h$) to 1.5 times this value. This could imply that graphene and bilayer graphene have grown in a 1:1 ratio. The graphene is grown via CVD of methane and hydrogen on Cu-foil and transferred to a glass substrate following the procedure of Li *et al.*³ A three-phase optical model (air/graphene/glass) is used to simultaneously fit the reflection and transmission data and extract the (Kramers-Kronig consistent) optical conductance. The conductance will be used to compare it with the conductance of CVD-graphene that is exposed to a hydrogen plasma.

¹Mak *et al. Phys. Rev. Lett* **101**, 196405 (2008)

²Li *et al. Nat. Phys.* **4**, 532 (2008)

³Li *et al. Science* **324**, 1312 (2009)

9:40am **GR+EM-TuM6 Optical Properties of Graphene on MgO and SiC Polytypes Determined by Spectroscopic Ellipsometry**, *A. Boosalis, T. Hofmann, S. Schoche, P.A. Dowben*, University of Nebraska - Lincoln, *S. Gaddam, C. Vamala, J. Kelber*, University of North Texas, *V. Darakchieva*, Linköping University, Sweden, *D.K. Gaskill*, U.S. Naval Research Laboratory, *M. Schubert*, University of Nebraska - Lincoln

Wafer-scale production of epitaxial graphene has been demonstrated recently. It has been observed, however, that the highest quality graphene is achieved from exfoliation, while epitaxial graphene exhibits less desirable electronic and optical characteristics. Identifying substrate effects on epitaxial graphene is of paramount contemporary interest for future device production.

We have determined the complex dielectric function of graphene deposited on a number of different substrates using multiple growth techniques. The investigations were performed in the spectral range from 1.5 to 9.5 eV using spectroscopic ellipsometry. The samples studied here include graphene grown on (111) MgO using chemical vapor deposition (CVD) and graphene grown on SiC by sublimation of silicon from the substrate at high temperature. Several different SiC polytypes, including 4H, 3C, and 6H SiC were studied. Distinct differences in the complex dielectric function of graphene are observed as the underlying substrate differs in material composition and polytype. In particular in the spectral region of the exciton absorption peak (4 eV) the complex dielectric function is sensitive to both substrate and growth parameters. We compare our results with those of recent publications of graphene grown by CVD on SiO₂.

10:40am **GR+EM-TuM9 Plasmon Resonance in Individual Nanogap Electrodes Studied Using Graphene Nanoconstrictions as Photodetectors.** *S.-F. Shi*, Cornell University, *X. Xu*, University of Washington, *P.L. McEuen*, *D.C. Ralph*, Cornell University

A plasmonic nanostructure can act like an optical antenna, concentrating light into a deep sub-wavelength volume and enabling manipulation of light-electron interactions at the nanometer scale. Achieving efficient coupling from such antennas to functional electrical devices has been challenging, because the region of field enhancement is so small. We achieve direct electrical read out of the wavelength and polarization dependence of the plasmon resonance in individual gold nanogap antennas by positioning a graphene nanoconstriction within the gap as a localized photodetector. The polarization sensitivities can be as large as 99%, while the plasmon-induced photocurrent enhancement is 2-100. The plasmon peak frequency, polarization sensitivity, and photocurrent enhancement all vary between devices, indicating the degree to which the plasmon resonance is sensitive to nanometer-scale irregularities.

11:00am **GR+EM-TuM10 Large Area Graphene Growth for Optoelectronic Applications.** *C. Edwards*, *C.L. Berrie*, *J. Liu*, *J. Wu*, University of Kansas

Graphene shows great promise for numerous applications within the field of optoelectronics due to its high charge mobility, high optical transmittance, chemical inertness, and flexibility. We are focused on developing large-area graphene sheets that sustain or enhance these characteristics currently present in small-area growth. Chemical vapor deposition of graphene onto various copper substrates has been investigated to understand the role of the substrate in graphene epitaxy and its deposition mechanism. With this understanding it will be possible to use the substrate structure to control the density of surface defects, which is high in current methods for large area fabrication. Also, the effect of nanopatterning and doping graphene grown by chemical vapor deposition has been investigated, and observed improvements in light transmittance and electrical conductivity suggest the potential to favorably modify graphene optical and electrical properties for these applications.

11:20am **GR+EM-TuM11 Stable Chemical Doping of Graphene: Transport, Raman Spectroscopy, SEM, and Transmittance Studies.** *K. Berke*, *S. Tongay*, *M. Lemaitre*, *Z. Nasrollahi*, *D.B. Tanner*, *B.R. Appleton*, *A.F. Hebard*, University of Florida

Since becoming experimentally available by mechanical exfoliation, graphene has been used in various devices such as field effect transistors (FETs), Schottky based solar cells and sensing applications. Although graphene based devices with modest characteristics have been reported, in some of the device geometries a lower graphene sheet resistance with different Fermi level values is still desired. To achieve these ends, graphene's physical properties have been adjusted by *n*- or *p*- chemical doping using AuCl₃, Br₂, N₂, and organic solutions. However, these techniques have several drawbacks which prevent their use in devices, namely: environmental instabilities, aging effects and a reduction in optical transparency. Here, we describe our use of a hydrophobic organic complex dopant with strong electronegativity, tight bonding, environmental stability and high optical transmittance which is spin cast onto CVD-prepared graphene films. We observe a typical 75% reduction in sheet resistance upon chemical modification of the graphene. Resistance vs. temperature / magnetic field and Hall measurements imply that the modified graphene sheets are doped, and time-dependent resistance measurements show excellent stability. Using a Horiba Micro Raman instrument we confirm the doping of graphene sheets from the shifts in G and 2D peak positions and intensity ratios. We show transmittance and SEM characteristics of the graphene sheets before and after doping. The presented results may serve as a guide for modification of graphene's properties as desired for various applications.

In Situ Spectroscopy and Microscopy Focus Topic
Room: 106 - Session IS+AS+SS-TuM

In Situ Studies of Organic and Soft Materials and Liquid-Solid Interfaces

Moderator: A.I. Frenkel, Yeshiva University

8:00am **IS+AS+SS-TuM1 Solid-Vacuum, Solid-Gas, and Solid-Liquid Interfaces: Structure and Dynamics under Environmentally Relevant Conditions.** *M. Salmeron*, *C. Escudero*, Lawrence Berkeley National Laboratory **INVITED**

Surfaces play a fundamental role in many of today's frontier topics, such as clean and renewable energies, efficient and highly selective chemical processes (green catalysis), high capacity rechargeable batteries and fuel cells, and also environmental problems. To advance our For this it is imperative to develop new fundamental approaches to the study of the interface of solid materials with gases, liquids and solids, because it is in these environments that crucial processes occur that need to be understood to enable game-changing discoveries.

One way to control the structure of interfaces and their properties is through the design of materials of nanoscale dimensions, with specific shape, size and composition. It is equally imperative to develop and use techniques for in situ atomic level structural and spectroscopic characterization of the interfaces. New advances in instrumentation are fulfilling this need. I will illustrate this with examples from research carried out in my laboratory, which include scanning tunneling microscopy (STM), photoelectron and x-ray absorption spectroscopies (PES) under ambient conditions, for studies of catalyst models, thin films, single crystals and nanoparticles, for applications in catalysis and electrochemistry. The results obtained so far demonstrate that the information obtained with these new techniques is unique and could not have been obtained or extrapolated from other more traditional surface sensitive techniques.

8:40am **IS+AS+SS-TuM3 Imaging Tagged Proteins in Whole Eukaryotic Cells in Liquid with Scanning Transmission Electron Microscopy.** *N. De Jonge*, *D.B. Peckys*, Vanderbilt University School of Medicine **INVITED**

We have recently introduced a novel electron microscopy technique for the imaging of whole cells in aqueous media using scanning transmission electron microscopy (STEM) [1, 2]. Eukaryotic cells in liquid were placed in a microfluidic chamber with a thickness of 5 - 10 μm contained between two ultra-thin electron-transparent windows. On account of the atomic number (Z) contrast of the STEM, nanoparticles of a high-Z material (e.g., gold) were detected within the background signal produced by a micrometers-thick layer of a low-Z liquid (e.g. water, or cellular material). Nanoparticles specifically attached to proteins can be used to study protein distributions in whole cells in liquid, similar as proteins tagged with fluorescent labels can be used to study protein distributions in cells with fluorescence microscopy.

COS7 fibroblast cells were labeled with gold nanoparticles conjugated with epidermal growth factor (EGF). Intact fixed cells in liquid were imaged with STEM with a spatial resolution of 4 nm and a pixel dwell time of 20 microseconds [1]. In test experiments we demonstrated a maximal spatial resolution of 1.5 nm on gold nanoparticles placed above a water layer of a thickness of 3 micrometer, consistent with theoretical predictions, and with Monte Carlo simulations of the STEM imaging [3]. The use of quantum dots (QDs), which are fluorescent nanoparticles, allowed STEM images to be correlated with fluorescence images [4]. Eukaryotic cells were grown directly on microchips for the microfluidic chamber, fixed, and imaged with fluorescence microscopy. The intact cells were then imaged in liquid with STEM. The STEM images showed individual QDs, and their locations were correlated with the cellular regions, as imaged with fluorescence microscopy. We have also demonstrated the imaging of nanoparticle uptake in live cells [5], and the ultrastructure of pristine yeast cells was studied [6]. Liquid STEM presents an innovative approach for the imaging of whole cells, with significantly improved spatial resolution and imaging speed over existing methods.

URL: <http://www.mc.vanderbilt.edu/labs/dejongelab/>

References

- [1] de Jonge, N., Peckys, D.B., Kremers, G.J. & Piston, D.W., Proc. Natl. Acad. Sci. 106, 2159-2164, 2009.
- [2] Peckys, D.B., Veith, G.M., Joy, D.C. & de Jonge, N., PLoS One 4, e8214-1-7, 2009.
- [3] Dukes, M.J., Peckys, D.B. & de Jonge, N., ACS Nano 4, 4110-4116, 2010.

[4] de Jonge, N., Poirier-Demers, N., Demers, H., Peckys, D.B. & Drouin, D., *Ultramicroscopy* 110, 1114-1119, 2010.

[5] Peckys, D.B. & N. de Jonge, *Nano Lett.* 11, 1733-1738, 2011.

[6] Peckys, D.B., Mazur, P., Gould, K.L. & de Jonge, N., *Biophys. J.*, in press, 2011.

9:20am **IS+AS+SS-TuM5 Imaging Live Cells in Liquid with Scanning Transmission Electron Microscopy**, *D.B. Peckys, N. De Jonge*, Vanderbilt University School of Medicine

We have applied a novel electron microscopy technique, referred to as liquid scanning transmission electron microscopy (liquid STEM) [1, 2] for the imaging of live eukaryotic cells. In two separate experiments, we studied a) nano particle (NP) uptake in COS-7 cells [3], a green monkey kidney fibroblast cell line, and, b) the ultrastructure of *Schizosaccharomyces pombe* cells [4], also known as fission yeast. The cells were confirmed to be alive at the onset of the liquid STEM imaging using specific fluorescent, live indicating dyes and correlative fluorescence microscopy. For the STEM imaging in liquid the cells were placed (in liquid) in a microfluidic chamber. The chamber had two ultra-thin electron-transparent windows allowing the passage of electrons and photons. The dimensions of the COS-7 cells required a thicker liquid filled space in the microfluidic chamber compared to the experiments with the fission yeast cells, and contrast was mainly obtained on the gold NP's. However, the thinner *S. pombe* cells allowed a thinner liquid layer, and images were recorded of the cellular ultrastructure.

Despite the fact, that the cells were not anymore alive after the STEM imaging, we consider the first STEM images taken from a cell or a specific cellular region, to represent the unperturbed and therefore physiological state. We derived this assumption after evaluation of the STEM images for signs of radiation damage at the achieved resolution. Our STEM results were found to be consistent with known data about intracellular NP trafficking and storage in mammalian cells and data about the dimensions and distribution of organelles in fission yeast.

In conclusion, we have demonstrated the feasibility of STEM imaging live eukaryotic cells. The advantages of this approach are a) a several-fold higher resolution than live cell imaging with conventional light microscopy, b) a much faster (hours versus days) sample preparation than needed for conventional transmission electron microscopy (TEM) imaging of cells, c) absence of artifact introduction associated with conventional TEM sample preparation, and d) no need for introducing any kind of labels in order to achieve a similar range of resolution as possible with the new nanoscopic imaging techniques.

References

[1] de Jonge, N., Peckys, D.B., Kremers, G.J. & Piston, D.W., *Proc. Natl. Acad. Sci.* 106, 2159-2164, 2009.

[2] Peckys, D.B., Veith, G.M., Joy, D.C. & de Jonge, N., *PLoS One* 4, e8214-1-7, 2009.

[3] Peckys, D.B. & N. de Jonge, *Nano Lett.* 11, 1733-1738, 2011.

[4] Peckys, D.B., Mazur, P., Gould, K.L. & de Jonge, N., *Biophys. J.*, in press, 2011.

9:40am **IS+AS+SS-TuM6 Microscopic Imaging of Biological Samples using Coherent Soft X-rays from Free-Electron Laser and Synchrotron Sources**, *T. Gorniak, T. Senkbeil, M. Beckers, C. Christophis*, University of Heidelberg, Germany, *K. Giewekemeyer*, University of Göttingen, Germany, *M. Grunze*, University of Heidelberg, Germany, *T. Salditt*, University of Göttingen, Germany, *A. Rosenhahn*, University of Heidelberg, Germany

Coherent X-ray microscopy of hydrated biological samples – especially in the so-called water window of 284-540 eV – is of tremendous interest for life sciences due to the high contrast of organic matter with respect to the aqueous background. Especially free-electron lasers can provide highly intense and coherent pulses, which allow single pulse imaging to overcome resolution limits set by radiation damage. We present the first holographic microscopy images of dehydrated biological material acquired in the water window with higher harmonic radiation provided by the free-electron laser FLASH. In order to increase the photon flux we used high efficiency zone plates instead of pinholes to create the divergent light cone for holography. The results pave the way to the vision of holographic imaging of hydrated biological samples with single FEL pulses. We supplement single pulse imaging experiments byptychographic imaging with synchrotron radiation at BESSY II. This method uses coherent diffraction imaging at different sample positions while maintaining a fixed spatial overlap between the fields of view. By introducing this spatial redundancy to the data an additional constraint for the iterative reconstruction algorithm is achieved. This enhances the convergence of phase retrieval drastically. The spatial resolution of below 50 nm and the imaging properties were characterized

using lithographic and biological test samples. We also show results on resonant imaging with chemical contrast caused by both, absorption and phase shifts, in the vicinity of core level absorption edges.

10:40am **IS+AS+SS-TuM9 Surface Chemistry of Amino Acids at Near Ambient Pressure of Water Vapor**, *A. Shavorskiy*, Lawrence Berkeley National Laboratory, *T. Eralp*, The University of Reading, UK, *F. Aksoy*, Nigde University, Turkey, *M.E. Grass, Z. Liu, H. Bluhm*, Lawrence Berkeley National Laboratory, *G. Held*, The University of Reading, UK

The co-adsorption of water with organic molecules under near-ambient pressure and temperature conditions opens up new reaction pathways on model catalyst surfaces that are not accessible in conventional ultra-high vacuum surface-science experiments. The surface chemistry of glycine and alanine at the water-exposed Cu{110} and Pt{111} interface was studied both in situ and in UHV using ambient-pressure photoemission and X-ray absorption spectroscopy techniques [1,2]. At water pressures above 10⁻⁵ Torr a significant pressure-dependent decrease in the temperature for dissociative desorption was observed for both amino acids on Cu{110}[3]. On Pt{111}, on the other hand, desorption temperature does not depend significantly on the presence of water vapor. The most likely reaction mechanism of decomposition involves dehydrogenation induced by O and/or OH surface species resulting from the dissociative adsorption of water on Cu{110}, but not on Pt{111}.

The linear relationship between the inverse decomposition temperature on Cu{110} and the logarithm of water pressure enables determination of the activation energy for the surface reaction, between 213 and 232 kJ/mol, and a prediction of the decomposition temperature at the solid-liquid interface by extrapolating towards the equilibrium vapour pressure. Such experiments near the equilibrium vapour pressure provide important information about elementary surface processes at the solid-liquid interface, which can neither be retrieved under ultra-high vacuum conditions nor from interfaces immersed in a solution.

[1] H. Bluhm, et al. *J. El. Spec. Rel. Phenomena* 150 (2006) 86.

[2] G. Jones, L. B. Jones, F. Thibault-Starzyk, E.A. Seddon, R. Raval, S. Jenkins, G. Held, *Surf. Sci.* 600 (2006) 1924.

[3] A. Shavorskiy, F. Aksoy, M.E. Grass, Z. Liu, H. Bluhm, G. Held, *J. Am. Chem. Soc.* 133 (2011) 17

11:00am **IS+AS+SS-TuM10 STM Tip Catalyzed Adsorption of Thiol Molecules and Functional Group-Selective Adsorption of Bi-Functional Molecule Using This Catalysis**, *Y.H. Min, S. Kim, S.J. Jung, Y.-S. Youn*, Korea Advanced Institute of Science and Technology, Republic of Korea, *D.H. Kim*, Daegu University, Republic of Korea, *E.H. Park*, Korea Advanced Institute of Science and Technology, Republic of Korea

In this study, in contrast with cases in which Scanning Tunneling Microscopy (STM) tip-induced reactions were instigated by the tunneling electrons, the local electric field, or the mechanical force between a tip and a surface, we found that the tungsten oxide (WO₃) covered tungsten (W) tip of a STM acted as a chemical catalyst for the S-H dissociative adsorption of phenylthiol and 1-octanethiol onto a Ge(100) surface. By varying the distance between the tip and the surface, the degree of the tip-catalyzed adsorption could be controlled. We have found that the thiol head-group is the critical functional group for this catalysis and the catalytic material is the WO₃ layer of the tip. After removing the WO₃ layer by field emission treatment, the catalytic activity of the tip has been lost.

3-mercapto isobutyric acid is bi-functional molecule which has two functional groups, carboxylic acid group and thiol group, at each end. 3-Mercapto Isobutyric Acid adsorbs at Ge(100) surface only through carboxylic acid group at room temperature and this adsorption was enhanced by the tunneling electrons between a STM tip and the surface. Using this enhancement, it is possible to make thiol group-terminated surface where we desire. On the other hand, surprisingly, the WO₃ covered W tip of STM was found to act as a chemical catalyst to catalyze the adsorption of 3-mercapto isobutyric acid through thiol group at Ge(100) surface. Using this catalysis, it is possible to make carboxylic acid group-terminated surface where we want. This functional group-selective adsorption of bi-functional molecule using the catalysis may be used in positive lithographic methods to produce semiconductor substrate which is terminated by desired functional groups.

Min, Y. H.; Jung, S. J.; Youn, Y. -S.; Kim, D. H.; Kim, S. *J. Am. Chem. Soc.* **2010**, *132*, 9014.

11:20am **IS+AS+SS-TuM11 CO₂ Capture in Aqueous Monoethanolamine Solutions: Role of the Solution Interface Investigated with X-ray Photoelectron Spectroscopy.** *T. Lewis*, University of California, Irvine, *B. Winter*, Helmholtz-Zentrum Berlin für Materialien und Energie, Germany, *M. Faubel*, Max-Planck-Institut für Dynamik und Selbstorganisation, Germany, *J.C. Hemminger*, University of California, Irvine

Aqueous monoethanolamine (MEA) solutions are commonly used to capture CO₂ emitted into the atmosphere from industrial processes. It is likely that interactions between MEA and CO₂ at the aqueous solution surface are important to this process, yet surprisingly very few studies have explicitly addressed the role of the solution-gas interface. In the present study, interfacial chemistry of CO₂ capture is studied by surface sensitive photoelectron spectroscopy measurements from a liquid microjet of CO₂-reacted MEA solutions with carbon loadings of 0.1 to 0.9 mol/mol. These experiments determine the spatial distribution of MEA and reaction products into the solution as a function of CO₂ loading. Results show that neutral MEA exhibits a propensity for the solution surface, whereas protonated MEA and reaction products prefer bulk solvation, suggesting enhanced reactivity at the solution interface, especially at high CO₂ loading. These observations indicate that a detailed understanding of the chemistry of CO₂ at the liquid/vapor interface and interface to bulk transport of the products will be important in understanding CO₂ capture.

11:40am **IS+AS+SS-TuM12 Fundamental Aspects of Organic Heterostructure Formation Examined using Supersonic Molecular Techniques and *In Situ* Real Time X-ray Synchrotron Radiation.** *E.R. Kish*, *T.V. Desai*, *A.R. Woll*, *J.R. Engstrom*, Cornell University

Over the past several years significant advances have been made concerning our understanding of the growth of crystalline small molecule organic thin films consisting of a single component. An important challenge in organic electronics, photonics and photovoltaics is to develop and improve methods to integrate both *p*-type and *n*-type small molecule organic semiconductors into the same device microstructure. Thus, developing an understanding of the molecular scale events that lead to heterojunction formation is essential in these systems consisting of multiple components. Here we report on our examinations of the nucleation, growth, and dynamics of adsorption of a *n*-type organic semiconductor, *N,N'*-ditridecylperylene-3,4,9,10-tetracarboxylic diimide (PTCDI-C₁₃), on SiO₂ surfaces modified by self-assembled monolayers (SAMs) and on a pre-deposited monolayer of pentacene (a *p*-type semiconductor) using supersonic molecular beam techniques, *in situ* synchrotron x-ray scattering and *ex situ* atomic force microscopy. From real-time x-ray scattering we find that PTCDI-C₁₃ exhibits prolonged layer-by-layer growth for approximately the first 10 monolayers (MLs) of deposition on all three SAMs examined. Concerning the kinetics of growth we find that the adsorption probability of PTCDI-C₁₃ on itself is similar to that observed on two SAMs that possess aromatic endgroups, but it differs significantly to that observed on a relatively short, methyl-terminated SAM. These differences could reflect mechanisms such as direct molecular insertion of PTCDI-C₁₃ into either the existing PTCDI-C₁₃ film, or the longer chain SAMs with aromatic endgroups. Concerning growth in the submonolayer regime, we find that nucleation is homogeneous, and that the absolute density of islands depends on the nature of the surface, while the relative change of the island density with increasing growth rate is essentially independent of the underlying SAM. From the latter we find that a critical island size of a single molecule of PTCDI-C₁₃ can describe all the data. Finally, we will discuss our most recent results concerning the growth of heterostructures composed of a few to several monolayer stacks of PTCDI-C₁₃ and pentacene. In this work we find that PTCDI-C₁₃ grows in a smooth layer-by-layer fashion on pentacene, but the opposite is not true—pentacene grows in a purely 3D mode when deposited on PTCDI-C₁₃. We will discuss the implications of this observation concerning the growth of organic heterostructures for applications in electronics, photonics and photovoltaics.

Nanomanufacturing Science and Technology Focus Topic

Room: 207 - Session NM+MN+MS+TF-TuM

Lithography Strategies for Nanomanufacturing

Moderator: T.S. Mayer, Penn State University

8:00am **NM+MN+MS+TF-TuM1 A SANE Approach to Programmable Soft Lithography.** *T.W. Odom*, Northwestern University
INVITED

The prototyping of nanoscale features has rarely been separated from the scaling of them. In order to create arbitrary patterns, serial techniques such

as e-beam lithography or focused ion beam milling must start from scratch every time; also, the patterns cannot be generated over large areas. In contrast, parallel fabrication methods such as molding, imprint lithography and soft lithography can scale patterns, but they are limited to transferring the same pattern on the mold. The development of new tools that can combine the strengths of serial approaches (prototyping patterns, high resolution) with those of parallel ones (high throughput, large patterned areas) is critical for next-generation applications based on nanostructures.

This talk will describe an all-moldable nanofabrication platform that can generate—from a single master—large-area nanoscale patterns with programmable densities, fill factors, and lattice symmetries. Solvent-assisted nanoscale embossing (SANE) can increase the spacing of patterns up to 100% as well as decrease them down to 50% in a single step by stretching or heating a thermoplastic substrate. In addition, SANE can reduce critical feature sizes as small as 45% compared to those on a master by controlled swelling of patterned molds with different solvents. SANE can also produce different and reconfigurable lattice symmetries, which enables new opportunities to manipulate the electronic, photonic, and magnetic properties of nanomaterials.

8:40am **NM+MN+MS+TF-TuM3 Micromolding Surface-Initiated Polymerization: A Versatile Route for Microscale Replication onto a Solid Support.** *C.A. Escobar*, *J.C. Tuberquia*, *N. Nizamidin*, *G.K. Jennings*, Vanderbilt University

This presentation will introduce the use of confined surface-initiated ring-opening metathesis polymerization (SI-ROMP) of perfluoroalkyl or alkyl norbornene monomers from solid substrates to synthesize surface-bound polymer structures with tunable physical and chemical properties that accurately replicate those exhibited by Nature's engineered, microscopically rough, and highly functional surfaces. This approach not only allows mimicking of highly evolved and functional surface architectures but also provides versatility in that it introduces a wide variety of chemical compositions available in materials chemistry, including partially fluorinated polymers with ultralow critical surface tensions. Optical microscopy and scanning electron microscopy confirm growth of the polymer structures and the precise replication of the microscale and nanoscale features exhibited by the target natural surface with the added freedom to expand beyond Nature's chemical building blocks. Contact angle measurements show that the surface architectures exhibit both hydrophobic and oleophobic behavior, and in some cases, superhydrophobic properties. This approach is not limited to natural surfaces and could be applied in a straightforward manner to a variety of synthetic surfaces that have microscale features.

9:00am **NM+MN+MS+TF-TuM4 Si Mold Etching with Hard Mask for Bit-Patterned Media.** *M. Kurihara*, Hitachi, Ltd., Tokyo, *M. Satake*, *Y. Tsuchiya*, *T. Nishida*, Central Research Laboratory, Hitachi, Ltd., Japan, *Y. Tada*, *H. Yoshida*, Hitachi Research Laboratory, Hitachi, Ltd., Japan, *N. Negishi*, Central Research Laboratory, Hitachi, Ltd., Japan

Bit-patterned media (BPM) is one of the promising candidates for hard disk media with areal density greater than 1.0Tb/in². Nanoimprint lithography (NIL) for BPM has also been investigated as a patterning technique to reduce the production cost. One of the critical issues in NIL mold fabrication is the etching selectivity between silicon and the organic mask pattern due to the following two reasons. One is a significant decrease of pattern thickness to meet the photo-lithography requirements. This decrease remained when applying the self-assembly polymer process to fine patterning. The other is the micro-loading effect that causes the etching rate drop with pattern size shrinking.

In this work, we have developed a hard mask process to compensate for the low etching selectivity. First, the micro-loading effect in the HBr/Cl₂/O₂ gas chemistry was evaluated with a SiO₂ hard mask of 20-nm thickness. This SiO₂ hard mask was patterned from 30 to 50 nm by EB lithography and etched with CHF₃ gas chemistry. The coefficients of micro-loading in silicon etching were evaluated based on the relationship between hole depth and etching time with a hole diameter of 30, 40, and 50 nm respectively. With increase of the sidewall taper angle, the micro-loading effect could be improved by about 60%. We also confirmed that there was a hole with a depth of 87 nm with a diameter of 30 nm. Extrapolating this micro-loading effect, it is expected that a hole with a depth greater than 80 nm with a diameter of 10 nm will be achieved. This result will satisfy the pattern aspect ratio of 2, which is required in NIL. We will also demonstrate the Si mold etching with a hard mask by applying the self-assembly polymer in which the areal density is greater than 1.0Tb/in².

9:20am **NM+MN+MS+TF-TuM5 Directed Assembly of Block Copolymers to Advance the Performance of Conventional Lithography, P.F. Nealey**, University of Wisconsin **INVITED**

Our research program aims to integrate self-assembling block copolymers into current manufacturing practice. The fundamental concepts of the approach are that 1) the most advanced production-oriented exposure tools (e.g. 193 nm, EUV, or electron beam lithography) and resist materials are used to create patterns of differing chemical functionality on the substrate, and 2) films of block copolymers can be directed to assemble in the presence of the chemical pattern into predictable and desirable morphologies, thereby augmenting and enhancing the lithographic process. In comparing the pattern in resist to the pattern of domains induced to assemble in the block copolymer film, directed assembly has been demonstrated to achieve high degrees of pattern perfection, placement of features at the precision of the lithographic tool used to make the chemical pattern, improved dimensional control of features, improved line edge and line width roughness, and resolution enhancement by factors of two to four. In addition, the approach has been demonstrated to robustly achieve non-regular device-oriented geometries used in the fabrication of integrated circuits also with resolution enhancement by multiplication of feature density by interpolation on low duty cycle chemical patterns. After describing current capabilities, remaining technological questions and pathways towards implementation in specific applications will be discussed.

10:40am **NM+MN+MS+TF-TuM9 Measured Backscattered Electron Profile for Optimized Proximity Effect Correction, D.A. Czaplewski, L.E. Ocola**, Argonne National Laboratory

Electron beam (e-beam) lithography has been used to create nanoscale patterns in myriad of resists with features as small as single nanometers. When creating resist features on the single nanometer length scale, the process window to create the desired resist structure becomes increasingly small. Overdosing or under dosing of critical features causes changes in critical dimensions. In addition to the dose required for a single feature, the contribution of additional dose due to proximity of nearby features must be considered. To solve this problem, finite element analysis software packages are available for adjusting dose assignments for different features based on size, shape, and placement with respect to other features. The FEM software can only work as good as the input parameters. These parameters come from the backscattered electron profile. Here, we present the measured electron backscattered profile using a negative e-beam resist. In order to measure the backscattered profile, we use a pattern of intersecting lines surrounded by a large annulus. The lines are measured while the annulus provides a circularly symmetric backscattered electron dose. The lines and annuli are written with varying doses. By measuring the thickness of the resist, the contribution from both the lines and the annulus can be determined for different doses and different shapes by using the resist contrast curve. By using the contrast curve to assign doses to specific resist thicknesses, the specific resist and developer effects are removed from the data. The resultant backscattered electron profile can be used as input into the FEM model to create more accurate resist dose assignments for proximity effect corrected patterns for all resists.

11:00am **NM+MN+MS+TF-TuM10 CMOS Density Scaling in Non-Planar Multi-Gate Devices: A Patterning Perspective, M.A. Guillorn, J. Chang, S. Bangsaruntip, C.-H. Lin, W.E. Haensch**, IBM T.J. Watson Research Center **INVITED**

The use of planar Si CMOS device technology may continue beyond the 22 nm node. However, the requirements for the gate dielectric and junction depth needed to maintain control of short channel effects might prove to be unobtainable in devices scaled to meet the integration density requirements of the 14 nm node and beyond. Consequently, an additional method for improving the electrostatics of the device is required. This realization has driven a steady increase in research on non-planar multi-gate CMOS devices over the past 5 years. Raising the Si channel out of the plane of the substrate creates the opportunity to form the gate electrode around multiple sides of the channel. This geometry results in a superior situation from an electrostatics standpoint compared to a planar device where the gate electrode is present only on the top surface of the channel.

In this talk, we will discuss the challenges of fabricating three non-planar multi-gate devices from Si on insulator (SOI) substrates: (1) the FinFET, where the gate controls two sides of a thin Si mesa or fin (2) the Trigate where the gate controls three sides of a Si fin and (3) a gate-all-around nanowire transistor where the gate electrode surrounds all sides of a suspended Si channel. We will present experimental results from advanced prototypes of these devices fabricated at dimensions and densities relevant to 14 and 10 nm node technology. An emphasis will be given to the unique role lithography and patterning play in determining the electrical behavior of these devices. These results offer insight into what may lie ahead for Si CMOS scaling and how it will impact the demands placed on patterning and metrology.

11:40am **NM+MN+MS+TF-TuM12 High Resolution Dry Development, D.L. Olynick, D.G. De Oteyza, P. Perera, P. Kulshreshtra, P. Ashby, M. Schmidt, S. Dhuey, B.D. Harteneck, R.M. Falch, A. Schwartzberg, P.J. Schuck, S. Cabrini**, Lawrence Berkeley National Laboratory

As feature sizes continue to shrink, new approaches are required to overcome roadblocks toward high-resolution lithographic patterning. One significant roadblock towards miniaturization is pattern collapse due to capillary forces during drying.[1] We have invented a dry development method for creation of high resolution and high aspect ratio resist features. We use resists that undergo an optical absorption change after exposure to high-resolution radiation (here we use electron beam lithography). This optical change allows the material to be selectively laser ablated such that the resolution is defined by the high-resolution radiation and not limited by the laser spot size. Using methyl-acetoxy calix[6]arene, a CW 532 nm laser, and spot sizes ~300 nm, we have produced features down to 10 nm in a film 120 nm thick, with pitch resolution down to 30 nm (Fig. 1). Calixarene was introduced as a high resolution electron-beam resist [2] and has demonstrated 12.5 nm half-pitch in extreme ultra-violet lithography.[3] Typically, films are spun thin to prevent high-resolution pattern collapse in thicker films but using the dry development, the patterns are well defined even in the thick films. Note, the resist acts negative with solvent development, as the cross-linked material can not be removed, whereas it is positive under laser dry development at the same electron-beam dose conditions. This is in contrast to the thermal dry development process where calixarenes are developed in negative tone.[4] With thermal development, patterns were demonstrated at 25 nm half-pitch in a 25 nm film (1:1 aspect ratio).

We have systematically studied the optical absorption contrast behavior as a function of electron beam dose, laser wavelength, and laser dose. At 532 nm laser wavelength, we identified that the absorption is a two photon process and found one functional group which is responsible for the optical contrast. We will discuss the options for materials beyond calixarenes.

This work was supported by the U.S. Department of Energy under Contract No. DE-AC02-05CH11231.

References

- [1] T. Tanaka, M. Morigami, N. Atoda, *Jpn. J. Appl. Phys.* 32 (1993) 6059-6064.
- [2] J. Fujita, Y. Ohnishi, S. Manako, Y. Ochiai, E. Nomura, T. Sakamoto, S. Matsui, *Jpn. J. Appl. Phys.* 36 (1997) 7769-7772.
- [3] H.H. Solak, Y. Ekinici, P. Kaser, S. Park, *J. Vac. Sci. Technol. B*, 25 (2007) 91-95.
- [4] V. Auzelyte, A. Langner, H.H. Solak, *J. Vac. Sci. Technol. B*, 27 (2009) 2990-2992.

Nanometer-scale Science and Technology Division Room: 203 - Session NS-TuM

Nanowires and Nanoparticles II: Characterization and Synthesis

Moderator: U.D. Schwarz, Yale University

8:00am **NS-TuM1 Formation of Metallic Glass Nanofiber, K.S. Nakayama, Y. Yokoyama, T. Wada, N. Chen**, Tohoku University, Japan

Metallic glasses have been receiving significant attention because their superior mechanical properties are attractive to structural materials. However, far less attention has been paid to metallic glass nanostructures though they have exciting potential for catalysis applications due to the expanding of metallic surface area. Progress has been hindered by the lack of bottom-up methodologies to produce self-assembly nanostructures. Recently, we show that the instantaneous fracture process of a bulk metallic glass produces amorphous nanostructures [Nakayama et al., *Nano Lett.* 8, 516 (2008)] and the simple tensile draw under viscous deformation leads to the formation of individual amorphous nanowires [Nakayama et al., *Adv. Mater.* 22, 872 (2010)]. However, these approaches are unsuitable for massive production because the amount of nanowires is limited. In this talk, we first report an approach to the synthesis of metallic glass nanofibers that exploits a conventional gas atomization which is a central technique in powder metallurgy. We found that the nanofiber forming ability is closely related to the super liquid cooling region of the alloys and the atomizing gas pressure.

8:20am **NS-TuM2 Plasma-assisted Dissociation of Organometallic Vapors for Continuous, Gas-Phase Preparation of Multimetallic Nanoparticles**, *R.M. Sankaran, P. Lin*, Case Western Reserve University

Metal nanoparticles (NPs) are desired for novel optical, magnetic, electric, and catalytic applications. Recently, there has been growing interest in *multimetallic NPs*, a special class of metal NPs composed of two or more distinct metal elements with alloyed, core-shell, or other architectures. Despite the development of numerous synthetic routes for metal NP synthesis, the preparation of multimetallic NPs with controlled size, composition, morphology, and purity remains a significant challenge.

Here, we present a single-step, continuous, gas-phase process that is capable of producing a wide range of size- and compositionally-tuned multimetallic NPs [12]. Our approach is based on plasma-assisted dissociation of metal-organic vapors which is a well-established technique for chemical vapor deposition (CVD) of thin films of metals. In our case, these same precursors are dissociated in a continuous-flow, atmospheric-pressure microplasma to homogeneously nucleate metal NPs. To synthesize multimetallic NPs, more than one precursor is mixed in the microplasma reactor. The size of the multimetallic NPs is controlled by the total vapor concentration of the precursors while the atomic-scale composition is controlled by the relative ratio of the different metal precursors. Bimetallic and trimetallic NPs of various metals including Ni, Fe, Cu, and Pt, have been produced by this approach. In this talk, we will discuss our experimental method in detail, as well as the structural properties of the NPs as determined by *in situ* aerosol measurements, high-resolution transmission electron microscopy (HRTEM), energy-dispersive spectroscopy (EDS), and X-ray diffraction (XRD).

References

1. W-H. Chiang and R.M. Sankaran, *Adv. Mater.*, 4857 (2008).
2. P. A. Lin and R. M. Sankaran, submitted.

8:40am **NS-TuM3 Electrical Characterization of III-V Semiconductor Freestanding Nanowires with Scanning Tunneling Microscopy**, *O. Persson, D. Suyatin, J. Wallentin, L. Samuelson, A. Mikkelsen, R. Timm*, Lund University, Sweden

Semiconductor nanowires show great characteristics for implementations in a broad range of applications, e.g. optoelectronic devices [1]. The increased possibilities of using different materials to realize tailored *p-n*-junctions or bandgaps and the inherent property of low density of defects make the nanowire the perfect candidate to realize new electronic devices.

Vast arrays of freestanding nanowires are used in many applications such as LEDs and solar cells. The electronic properties of such wires are essential to investigate for understanding and further developing the devices. The prevalent method used to make electronic measurements on nanowires is complex and challenging. It consists of several processing steps where the nanowire has to be deposited onto a substrate, localized, and then contacts need to be defined and deposited [2]. The range of nanowire material systems and doping levels for which this method can provide good Ohmic contacts is strongly limited.

Here we show a novel technique for investigating the electronic properties of freestanding nanowires by utilizing a scanning tunneling microscope (STM). We can exactly obtain the position of individual freestanding nanowires by scanning them from the top [3]. By contacting the Au-seed particle on the top of the nanowire with the STM tip in a controlled manner, a well-defined point contact is established. The sample substrate will act as a back contact establishing a well-defined system in an ultra-high vacuum.

We have previously performed a variety of successful STM measurements on III-V nanowires [3,4]. Here we show that *I-V* measurements on single as-grown wires can be done reproducibly and consistently. GaAs wires with a doping concentration of 10^{18} cm^{-3} and a diameter of 80 nm are analyzed with this method and they consistently show a resistivity of approx. 700 Ω . Measurements on InP and InAs wires confirm the reliability of this new technique by revealing nanowire conductivities which agree well to the corresponding doping level. We will also present first results on individual nanowire *p-n*-junctions and Schottky diodes.

The main advantages of our method are that we get a well-defined contact, the measurements are done on as-grown nanowires, and we have a good control of the wire surfaces due to UHV conditions. To determine the chemical surface composition of these wires, the *I-V* studies are complemented by high intensity X-ray photoemission spectroscopy at the MAX-II synchrotron in Lund.

- [1] Li *et al.*, *Mater. Today* **9** (10), 18 (2006)
- [2] Suyatin *et al.*, *Nanotechnology* **18**, 105307 (2007)
- [3] A. Fian *et al.*, *Nano Lett.* **10**, 3893 (2010)
- [4] E. Hilner *et al.*, *Nano Lett.* **8**, 3978 (2008)

9:00am **NS-TuM4 Semiconductor Nanowires: From Materials Physics to Devices**, *L. Samuelson*, Lund University, Sweden **INVITED**

The field of self-assembled growth of semiconductor nanowires has emerged as a powerful way to form advanced materials and devices on the 10nm-scale. In this talk I will review the state of the art of the field, exemplified by our recent progress in growing ideal and defect-free III-V and III-nitride nanowires, on either III-V or silicon as substrates. I will discuss the hot materials physics aspects of structural control and the influence of zincblende vs wurtzite crystal structures on materials properties. I will then review recent progress in realizing various electronic as well as opto-electronic devices, such as nanowire field-effect transistors, tunnel devices, solar-cells as well as light-emitting diodes.

9:40am **NS-TuM6 Self-Catalyzed Growth of InP_{1-x}Sb_x Nanowires on InP(111)B**, *C. Ngo, M. Pozuelo, M. Mecklenburg, H. Zhou, B.C. Regan, R.F. Hicks, S. Kodambaka*, University of California Los Angeles

Group III-V semiconductors possess high carrier mobilities and small band gaps, making them applicable to nanoelectronics and optoelectronics.[1] Properties of these materials can in principle be controllably tuned by the fabrication of low-dimensional structures, such as nanowires. Nanowires are most commonly grown via the vapor-liquid-solid (VLS) process using Au as the catalyst. A variant of this approach is the self-catalyzed VLS process, where one of the elements of the growing material promotes the one-dimensional growth can also yield nanowires. Recent studies show that InP and InP_{1-x}Sb_x nanostructures can be grown via metalorganic chemical vapor deposition (MOCVD) using indium and indium-antimonide droplets as catalysts.[2] In this talk, we present results from studies focused on understanding the influence of metalorganic precursor flow rates on the compositional and structural evolution of InP_{1-x}Sb_x alloy nanowires.

All of our samples are grown via MOCVD using trimethylindium (TMIn), tertiarybutylphosphine (TBP), and trimethylantimonide (TMSb) as precursors, with liquid indium droplets as the catalysts and InP(111)B as substrates. The as-grown structures are characterized using scanning and transmission electron microscopies, selected area electron diffraction, energy dispersive x-ray spectroscopy, and scanning TEM to determine their morphology, crystallinity, and composition.

We demonstrate the successful growth of InP_{1-x}Sb_x alloy nanostructures of desired Sb content that is tunable with substrate temperature and TMSb flow rate. Interestingly, doubling the precursor flow rates, at a given temperature, leads to crystallization of pure wurtzite-structured InSb at the catalyst-wire interface. We attribute this phenomenon to the precipitation of excess Sb present in the indium droplets during InP_{1-x}Sb_x alloy growth. By taking advantage of the differences in growth kinetics of InP and InSb, we demonstrate the formation of compositionally-abrupt interfaces in InP/InSb axial nanowire heterostructures.

- [1] M. Pozuelo, S.V. Prikhodko, R. Grantab, H. Zhou, L. Gao, S.D. Sitzman, V. Gambin, V.B. Shenoy, R.F. Hicks, and S. Kodambaka, "Zincblende to Wurtzite Transition During the Self-catalyzed Growth of InP Nanostructures" *J. Crystal Growth* **312**, 2305 (2010).
- [2] H. Zhou, M. Pozuelo, R.F. Hicks, and S.Kodambaka, "Self-catalyzed vapor-liquid-solid growth of InP_{1-x}Sb_x nanostructures" *J. Crystal Growth* **319**, 25 (2011).

10:40am **NS-TuM9 The Surface Hydrogen-Controlled Crystal Structure of Group IV Nanowires**, *N. Shin, M.A. Filler*, Georgia Institute of Technology

Semiconductor nanowires offer exciting opportunities to fabricate high performance devices for energy conversion, photonics, and quantum computation. The precise control of crystal structure and geometry is required to achieve a desired behavior, especially in highly confined nanoscale systems. Unfortunately, a fundamental understanding of the surface chemistry that controls surface energetics is currently lacking, despite its critical importance for robust synthesis. Although hydrogen is prevalent during the hydride-based vapor-liquid-solid growth of semiconductor nanowires, its role is largely unknown. To this end, we systematically studied the effect of hydrogen during the growth of Si nanowires and confirmed its influence on crystal growth direction, catalyst ripening, and sidewall faceting for the first time. *In-situ* transmission infrared (IR) spectroscopy was used to identify the presence and bonding of hydrogen on Si nanowires as a function of growth conditions. Si nanowires were grown via a two-step process: (1) brief nucleation at high temperature (550°C) and low pressure (5×10^{-5} Torr) followed by (2) elongation under different conditions (400 – 500°C, 5×10^{-5} – 5×10^{-3} Torr). Vertically-oriented epitaxial Si nanowires with uniform densities, diameters, and lengths were obtained with this method. *In-situ* IR data recorded in real-time reveals the evolution of surface Si-H stretching modes near 2090 cm^{-1} and 2075 cm^{-1} . Our data indicates that surface-bound hydrogen is responsible for changes in crystal orientation even for relatively large diameter nanowires. More specifically, the surface energy of the nuclei-vapor interface near the triple-

phase-boundary is dramatically reduced by hydrogen adsorption and drives a transition from $\langle 111 \rangle$ to $\langle 112 \rangle$ oriented growth. We propose a simple nucleation model that explains this observation. This knowledge is then applied to rationally fabricate nanowire superstructures through the judicious incorporation of small quantities of Ge during growth. This work demonstrates the important role that surface chemistry plays in the growth of semiconductor nanowires, and the extensive use of hydride chemistries for most group IV and III-V semiconductor nanowire syntheses suggests significant implications for many materials systems.

11:00am NS-TuM10 Inhomogeneous Longitudinal and Radial Dopant Distribution Measurements in Si Nanowires Using Scanning Auger. *J.S. Hammond, D.F. Paul, Physical Electronics, U. Given, Northwestern University*

The incorporation of electrically active dopants into nanowires (NW) is essential to the development of semiconductor NWs based electronic devices. The ability to engineer the electrical properties of nanowires grown by the vapor liquid solid (VLS) process is currently limited by our incomplete understanding of the doping mechanism. Recently, several studies have shown evidence of inhomogeneous radial dopant distributions in Si NWs and the resulting effects on their electrical properties [1-2]. However, the longitudinal dopant profile has not been addressed to the same extent. Studies employing both indirect and direct measurement techniques (such as scanning photocurrent microscopy, Kelvin probe force microscopy and atom probe tomography) have addressed variations in longitudinal dopant profiles in Si NWs and related them to radial dopant variations induced by the growth process [3-4]. There have not yet been direct measurements of dopant concentrations along VLS grown nanowires. We have measured the longitudinal and radial doping profiles of phosphorus doped, untapered Si NWs using scanning Auger. We have found order of magnitude enhancements in the dopant concentration toward the NW's base as expected from previous indirect measurements. Importantly, the physical dopant profile is not identical to the active dopant profile, as shown by comparison with scanning photocurrent microscopy and Kelvin probe force microscopy measurements. The resolution and sensitivity of scanning Auger as an analytical tool for dopant concentration measurements will be compared to the other available techniques to indicate unique capabilities that can advance our understanding of nanowire doping.

[1] E. Tutuc, J. O. Chu, J. A. Ott, and S. Guha. *Appl. Phys. Lett.* 2006, 89, 263101

[2] P. Xie, Y. Hu, Y. Fang, J. Huang and C.M. Lieber, *Proc. Natl. Acad. Sci. USA* 2009, 106, 15254-15258; E. Koren, N. Berkovich, and Y. Rosenwaks, *Nanoletters*, 2010, 10, 1163-1167.

[3] J. E. Allen, D. E. Perea, E. R. Hemesath, and L. J. Lauhon. *Adv. Mater.* 2009, 21, 3067-3072.

[4] E. Koren, Y. Rosenwaks, J. E. Allen, E. R. Hemesath, and L. J. Lauhon. *Appl. Phys. Lett.* 2009, 95, 092105.

11:20am NS-TuM11 Crystal Structure Engineering of Ge Nanowires. *I.R. Musin, M.A. Filler, Georgia Institute of Technology*

Semiconductor nanowire engineering provides a promising route to achieve next generation energy conversion, photonic, and electronic materials. In order to enable the appropriate function for a particular application, control of nanowire crystal structure (e.g. lattice, orientation, faceting) is critical. Unfortunately, this remains a challenging task with bottom-up nanostructure syntheses. To this end, we rationally control Ge nanowire crystal structure for the first time via the addition of bifunctional alkylgermanes, which adjust the interface energetics near the three-phase line. More specifically, Ge nanowires are grown using the vapor-liquid-solid (VLS) technique with germane combined with methyl-, ethyl- or tertbutyl-germane. Scanning electron microscopy (SEM) and high resolution transmission electron microscopy (TEM) reveal that nanowires transition to a new growth direction upon addition of an alkylgermane, but remain single crystalline throughout. For the case of methyl-germane, nanowires transition from the $\langle 111 \rangle$ to $\langle 110 \rangle$ crystal growth direction. A significant reduction in tapering is also observed in all cases. Infrared spectroscopy (IR) shows that nanowire sidewalls are alkyl terminated and X-ray photoelectron spectroscopy (XPS) indicates this termination reduces the rate of oxidation. The impact of alkylgermane identity and surface coverage on crystal growth direction will be discussed in detail. The control of interface chemistry demonstrated by this work provides an important new handle for controlling nanowire structure and properties. Furthermore, the ability to effectively passivate nanowire sidewalls during growth is expected to enable more robust doping profiles by only permitting precursor incorporation through the catalyst tip.

11:40am NS-TuM12 Towards an Understanding of Ligand Selectivity in Nanocluster Synthesis. *S. Hong, G. Shafai, University of Central Florida, M. Bertino, Virginia Commonwealth University, T.S. Rahman, University of Central Florida*

Gold nanoclusters have been known to have a high catalytic reactivity. However, the difficulty in the synthesis of monodisperse nanoclusters (typically consisting of fewer than 100 atoms) in large amounts has been a considerable hurdle to catalytic research. Recently, bidentate ligands of the general formula $P(Ph)_2-(CH_2)_M-P(Ph)_2$ {labeled LM}, where Ph = phosphine and M is the length of the aliphatic chain separating the P atoms, is found to remarkably have the size selecting capacity for gold nanoclusters depending on M. To investigate the origins of size selectivity of the diphosphine ligands towards small-sized Au clusters, we performed scalar relativistic density functional theory (DFT) calculations using the projector augmented wave scheme (PAW). We find that a diphosphine with long spacer such as L5 can relieve a strain induced by the spacer more easily than can one with short spacer such as L3. Hence, while L5 can interact effectively with a broad range of gold clusters of various sizes, L3 can interact only with a narrow range of gold clusters demonstrating its size-selecting power towards small gold clusters such as Au₁₁₊₃. Based on these results, we propose a two-body ligand system for an ideal, highly-selective ligand, in which one part of the ideal ligand provides a high reactivity towards the broad range of gold clusters and the other part of the ideal ligand provides the control over the reactivity, which could be the form of a short length of spacer, as in diphosphine, but not necessarily limited to, or any type of controllable, reactivity-poisoning component. The controllable competition between the two components of an ideal, highly-selective ligand system will produce a desirable selectivity for the generation of monodisperse nanoclusters of interest through tailoring process.

This work is supported in part by US-DOE under Grant No.DE-FG02-07ER46354.

**Plasma Science and Technology Division
Room: 202 - Session PS+MN+TF-TuM**

Plasma Processing for Disruptive Technologies

Moderator: M.C.M. van de Sanden, Eindhoven University of Technology

8:00am PS+MN+TF-TuM1 Scallop Free TSV Etching Method for 3-D LSI Integration. *Y. Morikawa, T. Murayama, T. Sakuishi, S. Toyoda, K. Suu, ULVAC, Inc., Japan*

INVITED

Thru silicon via (TSV) etch process for deep and high-aspect ratio structure has been studied thoroughly for applications such as MEMS and CMOS devices. Recently, TSV used in 3D-LSI devices for logic devices may be a few microns in diameter and about 50 μm deep. On the other hand, TSVs used in stacking memory devices, the via diameter and depth would be several tens of microns. Therefore, development of TSV etching process is very important for realizing these applications. In this study, a large via size etching in a high-pressure process was focused by using very high frequency capacitive coupled plasma (VHF-CCP) with an ultra self-confined system. This plasma system is simple parallel plate CCP about 100Pa or more process. High-pressure process was carried out on the plasma confined, because mean free pass is very short. And, ion energy distribution (IED) is also controllable by high-pressure process with VHF bias. The bimodal IED changes under high-pressure. The peak of high-energy side is reduced, and a charge exchange peak appears. It is considered that the charge exchange is important to anisotropic Si etching of large size TSV with VHF bias.

And next, the high-density and small size of TSV below 10 μm diameter is indispensable to the utilization and improvement in high performance of 3D-LSI. We have developed a new etching system for TSV application for small size and high aspect ratio via. This system is a planer type magnetic neutral loop discharge (NLD) plasma. For high rate silicon etching, it is very important to understand not only the high density of the ICP plasma generation but also the high density of fluorine atoms. In this study, a novel RF antenna 'Multi Stacked rf Antenna' has been developed for highly accurate and high rate etching process. This antenna consists of multistage spiral turn rf antennas to reduce self-inductance (L). The L of this antenna is below 1.0 μH and it is a lower than the standard spiral antenna. As a result of performing the electron density measurement of the planer NLD plasma using this MS antenna, it succeeded in the high-density plasma production of $1 \times 10^{12} / \text{cm}^3$ by the process pressure of 7 Pa. Next, the Si etching process development was performed using the advanced NLD etcher. As a result, the etching rate improved 4 times more compared to the standard cylindrical NLD plasma. Finally, the diameter of 2 μm was attained by the anisotropic

etching of 5 $\mu\text{m}/\text{min}$, and the aspect ratio is above 10 using the planer NLD etcher. VHF CCP and planer NLD etching processes are non-cycle etch methods, and these processes were demonstrated about smooth sidewall TSV formation.

8:40am **PS+MN+TF-TuM3 Deep Silicon Etching of 0.8 μm to Hundreds of Microns Wide Trenches with the STiGer Process.** *T. Tillocher, W. Kafrouni*, GREMI, France, *J. Ladroue*, STMicroelectronics - GREMI, France, *P. Lefauchaux*, GREMI, France, *M. Boufnichel*, STMicroelectronics, France, *P. Ranson, R. Dussart*, GREMI, France

The STiGer process is designed to achieve high aspect ratio features in silicon. Like the Bosch process, passivation steps (SiF_4/O_2 plasmas) and etching steps are cycled to get vertical structures. The etching steps can be purely isotropic (SF_6 plasmas) or anisotropic (SF_6/O_2 plasmas). It is required to cool the silicon substrate with liquid nitrogen to form a SiO_xF_y passivation layer. It desorbs and disappears when the substrate is heated back to room temperature. Thus, there is no need to clean neither the microstructures nor the chamber walls after each process run. Then, the robustness of the process is enhanced in comparison with standard cryoetching: the profiles are less sensitive to temperature or flow rate variations. But, like in Bosch etching, a scalloping is present on the sidewalls.

Submicron trenches having critical aperture of about 0.8 μm can be etched with high aspect ratios (> 40). In these cases, the average etch rate is around 1.8 $\mu\text{m}/\text{min}$. These features exhibit both undercut and a special defect, which is called "extended scalloping". This defect is composed of anisotropic cavities developed on the feature sidewalls, just below the mask. It originates from ions scattered at the feature entrance that hit the top profile and remove locally the passivation layer. This defect is observed only for high aspect ratios (typically above 10). Thus, we will also investigate the role of trench critical dimension (from 0.8 μm to 100 μm). A mechanism explaining the formation of the extended scalloping will be proposed.

We have studied the influence of both the duty cycle (etch/(etch+passivation)) and the chamber pressure on the profiles and the extended scalloping. Basically, when the duty cycle increases, etching dominates passivation, which leads to higher defects. Pressure is a way to tune the slope of the sidewalls. Actually, decreasing the chamber pressure helps to shift from positively tapered features to more vertical profiles, and even negative slopes, hence with dovetailed shape.

This will be correlated with plasma analysis by means of mass spectrometry and optical emission spectroscopy. Actually, it is relevant to investigate how changes in the plasma chemistry can modify the trench profiles.

These trends have been used to optimize two methods that can help to reduce the extended scalloping. The first consists in adding a low oxygen flow in the etch cycle, favouring a low additional passivation. The second technique consists in gradually increasing the SF_6 flow from a low value to the nominal value. Consequently, the process starts with a low etch rate and a more efficient passivation, which helps to limit the extended scalloping.

9:00am **PS+MN+TF-TuM4 Evaluation of Alternative Passivation Chemistries for TSV Applications.** *E.A. Joseph*, IBM T.J. Watson Research Center, *G. Matsuura*, ZEON Chemicals L.P., *S. Engelmann*, IBM T.J. Watson Research Center, *M. Nakamura*, ZEON Chemicals L.P., *N.C.M. Fuller*, *E.M. Sikorski*, *M. Gordon*, *B.N. To*, IBM T.J. Watson Research Center, *H. Matsumoto*, *A. Itou*, Zeon Corporation

With the current advent of 3D integration for advanced interconnect and packaging applications, there has been a renewed focus on deep silicon etch technology to satisfy the need for Through Silicon Via (TSV) patterning. The most common etch method used to fabricate said devices is a time-multiplexed (BoschTM) process, based on years of maturity in the MEMS field.[i] However, issues such as scalloping, mask undercut and limited etch rates are becoming more pronounced as feature sizes scale to meet the ITRS roadmap requirements. This has prompted efforts to attempt to either develop a more conventional etch process[ii][iii] or to modify the Bosch process to circumvent these issues.[iii][iv] [v] In this work, we explore a novel polymerizing feedgas chemistry for the deposition step of the Bosch process to improve mask undercut while simultaneously increasing TSV etch rate. Initial results indicate a 5x larger deposition rate as compared to C4F8 (under nominal conditions) and under optimized conditions, enables a 50% decrease in undercut along with 10% increase in TSV etch rate. Optical emission spectra also differ substantially between the two feed gases, indicating different dissociation pathways and radical densities. Further results and a detailed characterization of the deposition properties of

the novel chemistry will also be discussed leading to a proposed mechanism for the profile improvements as compared to C4F8. [i] B. Wu, A. Kumar and S. Pamarthy, J. of Applied Physics 108, 051101 (2010) [ii] I. Sakai, N. Sakurai and T. Ohiwa, J. Vac. Sci. Technol. A 29(2), Mar/Apr 2011 [iii] N. Ranganathan et al, Proceedings of the Electronics Components and Technology Conference, 2005 [iv] H. Rhee et al, J. Vac. Sci. Technol. B 27(1), Jan/Feb 2009 [v] S.-B. Jo et al, J. Vac. Sci. Technol. A 23(4), Jul/Aug 2005

9:20am **PS+MN+TF-TuM5 Wafer Scale Hermetic Packaging of MEMS.** *C.S. Gudeman*, IMT **INVITED**

The explosion of MEMS in automotive and cell phone markets has been enabled by low cost wafer level packaging (WLP) technology that provides a robust and hermetic enclosure for an otherwise delicate device. The more obvious advantage of WLP is greatly improved reliability, because the device is protected from organic and particulate contaminants while in the hands of the end user. A less obvious advantage is the protection provided by WLP during the manufacturing process, which often produces the highest levels of stress that a MEMS device experiences. These processes include wafer grinding, wafer dicing, and chip solder re-flow attachment to circuit boards and other chips. Firstly in this talk, wafer level packaging technologies will be outlined, focusing on the truly hermetic methods -- alloy, glass frit, Au-Au thermo-compression, anodic, and fusion bonding. Secondly the integration of Through Silicon Vias (TSV) with WLP will be discussed. Finally the performance of these technologies will be compared from a manufacturing perspective, including yield and thermal budget.

10:40am **PS+MN+TF-TuM9 Challenges in Plasma Etch for NVM: Scaling and Materials.** *M. Kiehlbauch*, Micron Technology, Inc. **INVITED**

With advances in non-volatile memory, the major challenge confronting plasma etch is the introduction of new materials while simultaneously shrinking critical dimensions. This talk will address key development aspects including profile control, feature level uniformity, and plasma microdamage. Plasma microdamage is not the traditional, charge/voltage/current based impact to, for example, gate oxides. Rather, it is the changes to the atomic scale morphology in the sidewall or landing film of a plasma etch process. This results in a disruption of local stoichiometry, film defects, and other issues that impact device performance. The etch process and hardware changes to address this will be presented.

11:40am **PS+MN+TF-TuM12 Mechanisms of Selective Etching for Magnetic Materials: Ni, Co and Ta Etching by Carbon Monoxide/Methyl Alcohol Based Plasmas.** *K. Karahashi*, *T. Ito*, *S. Hamaguchi*, Osaka University, Japan

Dry etching of magnetic thin films is a crucial step in micro fabrication of magnetic random access memories (MARMs) and read/write heads for magnetic data storages. Argon (Ar) ion milling seems to be almost the only etching technique available in the current manufacturing processes. However Ar ion milling is incapable of achieving anisotropic and selective etching of magnetic films (Ni, Co etc.) over hardmasks (Ta etc.) and therefore highly selective reactive ion etching (RIE) of magnetic thin films is a highly sought-after technology. RIE processes based on CO/NH_3 or CH_3OH is a candidate for selective etching of magnetic thin films. In this study, we have examined etching processes of Ni, Co and Ta thin films by energetic CO^+ , O^+ or OH^+ ions, which are considered to be major etchants of CO/NH_3 or CH_3OH plasmas. We have determined the etching yields and analyzed surface reactions, using a mass-selected ion beam system. The ion beam system is designed to inject mono-energetic single-species ions into a sample surface in ultra-high vacuum conditions. The reaction chamber, where the sample is placed, is equipped with an X-ray photoelectron spectroscopy (XPS) for in-situ chemical analyses of irradiated surfaces. The ion beam energy used in this study is in the range of 150-1000 eV. The etching yields are determined from measured depth profiles of irradiated surfaces and ion fluxes. The etching yields of Ni and Co by CO^+ ions are higher than that by O^+ ions but lower than the yields of possible physical sputtering, which are estimated from interpolation of sputtering yield data of inert atom ions (He^+ , Ne^+ , Ar^+ , Kr^+ etc.). From XPS analysis for O^+ irradiated Ni and Co surfaces, oxidation is found to occur under O^+ irradiation, which suggests that the oxide layer hinders sputtering by ion bombardment. It is found that little oxidation occurs on Ni or Co surfaces under CO^+ ion irradiation and etching by CO^+ ion bombardments proceeds. On a Ta surface, on the other hand, in the both cases of O^+ and CO^+ irradiations, oxidation occurs and its etching yield is far smaller than the yield of its possible physical sputtering. Therefore we have found that high selectivity of Ni and Co etching against hard masks (Ta, TaN) arises from the prevention of sputtering by mask oxidation. Etching characteristics by OH^+ irradiation were also studied in a similar manner. This work was

supported by the Semiconductor Technology Academic Research Center (STARC).

Plasma Science and Technology Division Room: 201 - Session PS-TuM

Advanced BEOL / Interconnect Etching I

Moderator: A. Balakrishna, Applied Materials, Inc.

8:00am **PS-TuM1 Narrow Pitch Dual Damascene Patterning using EUV Lithography in Association with a Spin-On Trilayer Resist System**, *F. Lazzarino, V. Truffert, B. Vereecke, S. Demuyneck*, IMEC, Belgium

Extreme ultraviolet lithography (EUVL) is one of the leading candidates for the 22-nm node device manufacturing. However, a major issue is the necessity to use thin photoresist (between 55-nm and 80-nm after development) because of resolution requirement and limited depth of focus. In addition, its low etch resistance does not allow high aspect ratio pattern transfer. In this context, a new hardmask strategy called spin-on trilayer resist system has been considered.

In this work, we mainly focus on the etch patterning capability of narrow pitch dual damascene structures by using EUVL combined with a spin-on trilayer resist system. The latter consists of three layers. The photoresist on top is used to pattern a thin spin-on glass layer which is then used to pattern a thick spin-on carbon layer (SOC). The SOC has two functions. It is used for its good gap-filling capability to avoid patterning over nonplanar surfaces but it also acts as a hardmask to pattern the dielectric stack (150-nm of oxide on top of 15-nm of SiCO and 5-nm of SiCN). Regarding the dual damascene architecture, two different approaches have been considered: the via-first and the trench-first. Despite few challenges such as the well-known fencing issue, the via-first approach has been chosen as it is less sensitive to misalignment. In this scheme, two lithography and etch steps are needed, first to form the via then to pattern the trench and etch the barrier layer. In this study, we compared the via opening by using the standard PECVD carbon layer and by using the SOC layer. As expected, the PECVD carbon layer has a better process window compared to the SOC layer. The selectivity is greater and allows many chemistry variations to fine tune for instance the profile. To get similar process window with the trilayer resist system, we introduced C4F8 and CO to substitute C4F6 and O2 in the original chemistry. This modification clearly improved the process by having a better control on the passivation layer formation. Regarding the trench opening, we observed a significant line wiggling of the SOC hardmask for 50-nm half-pitch structures and beyond. We characterized this instability thanks to stress measurements and we kept it under control by changing three different process parameters: the bottom electrode temperature, the baking conditions after coating and the film thickness. Each of them has an impact but the best result came from combining all three together.

To conclude, we demonstrated that narrow pitch dual damascene structures can be obtained by using EUVL in association with a spin-on trilayer resist system. The structures formed in this way shows good electrical characteristics.

8:20am **PS-TuM2 TiN Hard Mask Integration Line Wiggling Onset: Etching Time Dependence**, *G.A. Delgado*, Lam Research Corp.

Cu resistivity increase at smaller geometries and the use of lower κ dielectrics forced several changes on BEOL integration. Susceptibility of ULK material to strip damage drove the adoption of TiN hard mask integration starting with a few players at 65nm node to full adoption at 32nm for advance logic.

TiN hard mask demonstrated good selectivity during dielectric etch but concerns arise as we move to smaller pitch: 1- TixFy residues may compromise metallization of small features and 2- Residual compressive stress in the TiN may induce line wiggling. This last concern is the focus of this work.

We develop a simple analytical model based on Energy balance to predict wiggling onset based on geometrical and mechanical properties of the materials. We showed that the wiggling onset aspect ratio reduces with the pitch. We also shown that even when at the end of the process the no-wiggling condition is satisfied, wiggling might have occurred during etch causing feature distortions.

8:40am **PS-TuM3 Surface Reaction Control for BEOL Application**, *M. Fukasawa, T. Tatsumi*, Sony Corporation, Japan **INVITED**

Increasingly there are more challenges of controlling the plasma processes for BEOL integration, which include the Cu/low-k interconnects, contact hole etching, etc. The presentation will give an overview of the surface reaction control during plasma processes. The main focus is damage reduction and suppression of process fluctuations.

Reducing the damage to low-k dielectrics caused by plasma exposure is one of the key issues. O₂-based plasma has been widely used for ashing the photoresist on low-k SiOCH. H₂-based plasma is employed for the etching of organic low-k film as well as the ashing of photoresist. The origin of damage generation is classified by ions, radicals, and UV/VUV radiation. It was found that not only the ions but also the synergy of radicals and UV/VUV radiation cause a significant amount of damage in the SiOCH, measured by using the pallet for plasma evaluation (PAPE).¹ Hence, precise control of incident ions, radicals, and UV/VUV radiation is required for controlling the surface reactions.

In addition to the precise control of incident species, the optimization of subsequent processes (wet treatment, annealing, etc.) are very important to obtain sufficient electrical yields and reliabilities. The remaining damaged layer after wet treatment degrades the Cu and SiOCH surface and corrupts the interface between the Cu and barrier metal. For instance, the desorbed H₂O from the SiOCH damaged layer causes the oxidation of barrier metal, which results in a shorter EM lifetime. The surface modification during SiCN and SiN etching by CH_xF_y-based plasma and its impact on the electrical yields will also be discussed.

The suppression of fluctuation is also required in the advanced interconnects. Although statistical prediction is one of the approaches to realize stable processes, there is a limitation of prediction accuracy for purely statistical predictions due to the lack of physical models. Thus, the combination of statistical and physical models for highly accurate prediction has become an emerging trend in mass production. We will demonstrate a novel statistical etch rate prediction model by considering the fluctuation caused by the plasma-wall interactions.²

The developed prediction model is one of the approaches to realize stable processes. Changes in the spatial distribution of reactive species in the etching chamber are, however, very difficult to detect in current mass production tools. Thus, greater progress of the *in-situ* monitoring tools and prediction methods based on the physical model (simulation) are strongly required in the near future.

1. S. Uchida et al., JAP 103, 073303 (2008).

2. M. Fukasawa et al., JJAP 48, 08HC01 (2009).

9:20am **PS-TuM5 Trench First Metal Hard Mask RIE for the 22 nm Node and Beyond**, *Y. Feurprier, R. Gaylord, Y. Chiba, K. Kumar, D. Trickett*, TEL Technology Center, America, LLC, *Y. Mignot*, ST Microelectronics, *R. Srivastava, T. Kwon, R. Koshy, C. Labelle*, GlobalFoundries, *Y.J. Park*, Samsung, *E. Wormyo, S. Allen*, IBM Research, *E. Soda*, Renesas Electronics, *D. Horak, Y. Yin, J. Arnold*, IBM Research, *M. Ishikawa, H. Tomizawa*, Toshiba America Electronic Components

Trench First metal Hard Mask (TFmHM) integration scheme for BEOL has gained traction over recent years because it can mitigate many challenges that are inherent with Via First Trench Last (VFTL) scheme. This integration scheme was more recently shown to enable Self-Aligned Via (SAV) patterning. The SAV patterning implies a pretty drastic change of the via process as, on top of the usual via requirements, the via patterning process needs to be selective to the metal HM. Key process parameters including temperature, gas chemistry, power and pressure were investigated. The required selectivity of the materials and tight CD control capability necessitate temperature controllable chucks eventually allowing greater process flexibility for both via and trench patterning.

The simultaneous control of via, trench and chamfer profiles (i.e. Critical Dimensions, depth, taper profile, etc), implies the need for better control of the metal HM selectivity during both SAV and trench patterning and the need for flexible adjustment of the ion energy and control of the flux of ions and active neutrals. Low-k material damage control is always pertinent in the RIE process as dimensions get smaller. As the direct result of such tight process guidelines, the hardware challenges arise and new dimensions in process controls are needed.

In this paper, the RIE efforts on process controls of the via and trench profiles, the metal HM selectivity, associated hardware solutions and future process flow options under TFmHM scheme will be discussed.

This work was performed by the Research and Development team at TEL Technology Center America in joint development with IBM Research Alliance Teams in Albany, NY 12203. This work has also been supported by the independent Bulk CMOS and SOI technology development projects at the IBM Microelectronics Div. Semiconductor Research & Development Center, Hopewell Junction, NY 12533.

9:40am **PS-TuM6 Plasma Processing of Ti and TiN Metal Hardmasks for Dielectric Etch.** *F. Weilnboeck**, *E. Bartis*, *S. Shachar*, *G.S. Oehrlein*, University of Maryland, College Park, *D. Farber*, *T. Lii*, *C. Lenox*, Texas Instruments Incorporated

Ti and TiN metal hardmasks are of interest for plasma-based pattern transfer into low-k materials due to their expected improvements of etch performance and process flow relative to resist masks. We have studied the performance of Ti and TiN in CF₄/Ar and C₄F₈/Ar discharges along with organosilicate glass (OSG) - a reference low-k material. Plasma processes were characterized in real-time by in-situ ellipsometry and provided information on erosion stages, etch rates (ER) and selectivity (SEL), i.e. ER(OSG)/ER(hardmask). Post plasma characterization was performed by vacuum transfer x-ray photoelectron spectroscopy (XPS). Plasma parameters investigated were: 1) ion energy, 2) pressure, 3) Ar dilution, 4) O₂ addition and 5) N₂ addition to fluorocarbon/Ar mixtures. Furthermore, we have studied chamber wall contamination and surface reactions upon atmospheric exposure of processed Ti/TiN hardmasks. Ellipsometric multilayer modeling of real-time measurements showed three hardmask erosion stages: 1) initial removal of surface oxides, 2) steady state erosion with F-saturated hardmask surfaces (TiF_x, x~3) covered with a FC film (0.8-1.6nm depending on plasma conditions) and 3) small amounts of Ti remaining on the underlayer after erosion of the hardmask layer. For all plasma conditions, Ti provides systematically lower ERs and higher SELs (~15) than TiN (~11). The higher ERs of Ti over TiN can be explained by the rapid removal of N by formation of NF₃ and the smaller Ti-atom number density of TiN compared to Ti. Surprisingly, the more polymerizing C₄F₈ conditions lead to lower SELs than CF₄. This observation is explained by FC layer-induced OSG ER reduction, whereas for the hardmasks materials ER are limited by product volatility and the FC surface layer effect is reduced, e.g. as compared to conventional organic masking layers. Chamber contamination studies have shown that only small amounts of Ti (<1%) are deposited together with FC on the chamber wall. Overall, metal hardmasks, especially Ti, showed excellent performance as a masking material in low-k etch and provide high SEL (~15) which can be further increased by systematically optimizing discussed plasma parameters.

11:00am **PS-TuM10 Superposition of High Negative DC Voltage in Capacitively Coupled Plasma.** *A. Ranjan*, *A. Metz*, *A. Lisi*, *Y. Chiba*, *W. Li*, *Y. Feuprier*, *K. Kumar*, *P. Biolsi*, TEL Technology Center, America, LLC, *L. Chen*, *P. Ventzek*, *R. Sundararajan*, Tokyo Electron America

The effects of applying a negative DC voltage to capacitively coupled plasmas (CCP) were investigated using PIC-MCC simulation and experiment. High energy secondary electrons, originating at the electrode with high negative DC voltages (DC electrode), are generated due to ion impact as well as electron-impact. These secondary electrons are accelerated away from the DC electrode by the sheath voltage drop. These secondary electrons gain energy equal to DC voltage drop across the sheath and travel to wafer electrode or get trapped between electrodes. Trapping and dumping of ballistic electrons depends on the voltages on the electrodes. Ballistic electrons alter the bulk electron energy distribution function of the plasma (EEDF). EEDF at wafer, high energy electron flux to wafer and plasma density profiles. Simulation shows that center to edge uniformity, plasma density and EEDF can be tuned by applying negative DC voltage in CCPs. Bulk plasma volume can be modulated by applying negative DC voltage giving us a very effective knob for an "effective" variable gap CCP without moving chamber parts in vacuum. The change in EEDF alters the plasma chemistry, the result of which can be observed by optical emission spectra and blanket etch rate data, validating the changes in chemistry due to superimposed negative DC voltage. Various other interesting aspects will also be presented.

11:20am **PS-TuM11 Evaluation of C5HF7: A High Etch Selectivity Hydrogen-Containing Fluorocarbon Gas for Oxide Etch.** *R.L. Bruce*, IBM T.J. Watson Research Center, *M. Nakamura*, ZEON Chemicals L.P., *S. Engelmann*, *E.A. Joseph*, IBM T.J. Watson Research Center, *G. Matsuura*, ZEON Chemicals L.P., *N.C.M. Fuller*, *E.M. Sikorski*, *W.S. Graham*, *Y. Zhang*, IBM T.J. Watson Research Center, *A. Itou*, Zeon Corporation

A high etch selectivity hydrogen-containing fluorocarbon gas, C5HF7, was evaluated for high aspect ratio dielectric etch. Plasma etching with Ar/C5HF7/O₂ chemistry was shown to have significant advantages over Ar/C4F6/O₂ in terms of oxide-to-organic mask etch selectivity and line-edge roughness. The mechanism behind the high etch selectivity of C5HF7 originated from the different thickness and composition of steady-state fluorocarbon (FC) layers generated on oxide and organic mask materials during plasma etch. We also determined that hydrogen addition to the Ar/C4F6/O₂ feedgas did not reproduce C5HF7 etch behavior, presumably

due to the difference in atomic hydrogen formation between molecular H₂ dissociation versus intramolecular H dissociation (from C5HF7). This latter phenomenon facilitated a wider window for "etch stop" margin. Profile evaluation showed larger bowing for C5HF7, compared to C4F6, and was linked to a higher sticking coefficient of CxHy radicals. This was verified and remedied by increasing the substrate temperature, which reduced the radical sticking coefficient and eliminated bowing, while maintaining the high etch selectivity. We also demonstrated reduced low-frequency line-edge roughness when etching with C5HF7. We showed that less surface roughness was generated using C5HF7 since less organic mask thickness was removed. In addition, since a major contribution of line-edge roughness was the transfer of organic mask surface roughness into the sidewalls of the dielectric, overall lower line-edge roughness was observed.

11:40am **PS-TuM12 Etch Uniformity Improvement Using Mid-Gap Capacitively Coupled Plasma.** *C. Cole*, *A. Ko*, *A. Ranjan*, *T. Enomoto*, *A. Metz*, *K. Kumar*, *P. Biolsi*, TEL Technology Center, America, LLC, *E. Wornyo*, *H. Yusuff*, *S. Allen*, *R. Wise*, IBM Research, *C. Labelle*, *T. Chen*, GlobalFoundries, *S. Kanakasabapathy*, IBM Research, *Y. Mignot*, STMicroelectronics

As device dimensions continue to shrink, uniformity of etch rate/feature depth and critical dimension becomes very important. Capacitively coupled plasma (CCP) sources have advantage in terms of uniformity over non-planar sources in addition to design simplicity, reliability and wide process window. Wide-gap CCPs have been used for front-end etch applications where as small-gap CCPs are work-horse for back-end dielectric etch. Recently, studies on mid-gap CCPs indicates that inter-electrode spacing of ~100mm is best suited for etch rate and CD uniformity. In our studies, for tri-layer mask etch and TiN hard-mask etch, mid-gap CCP achieved uniformity of <1nm (3σ) CD and ~1% (3σ) etch rate. Mid-gap CCPs have 20-30% higher etch rate compared to wide-gap CCPs. Power on top electrode can be divided to center and edge for control of plasma density distribution. Design changes in pumping port assembly effectively create uniform confined plasma without plasma leaking through pump-port. Plasma confinement helps in creating denser plasma at relatively lower RF power. Using above-mentioned "knobs", flat etch rates and CDs were achieved in mid-gap CCPs.

This work was performed by the Research and Development team at TEL Technology Center America in joint development with IBM Research Alliance Teams in Albany, NY 12222. This work has also been supported by the independent Bulk CMOS and SOI technology development projects at the IBM Microelectronics Div. Semiconductor Research & Development Center, Hopewell Junction, NY 12533.

Surface Science Division

Room: 109 - Session SS1-TuM

Chemisorption & Surface Reactions

Moderator: D.A. Chen, University of South Carolina

8:00am **SS1-TuM1 XANES and EXAFS Analysis of the Effects of Cobalt Incorporation Into Silica Supports for Fischer-Tropsch Synthesis.** *B.M. Goundie*, *I.T. Ghampson*, *M.C. Wheeler*, *W.J. DeSisto*, *B.G. Frederick*, *R.W. Meulenber*, University of Maine

The growing need for non-petroleum based fuel sources has led to an increase in research into Fischer-Tropsch synthesis (FTS), which can be used to convert biomass into fuels. We have developed several silica supported cobalt catalysts to investigate the role of pore size on phase and reactivity. Cobalt based catalysts produce high molecular weight hydrocarbons in FTS, and there has been increased research into the characterization of such catalysts. The catalysts have been previously characterized using several techniques including x-ray diffraction (XRD), nitrogen porosimetry, and transmission electron microscopy/selected area diffraction (Ghampson IT, et al. Effects of pore diameter on particle size, phase, and turnover frequency in mesoporous silica supported cobalt Fischer-Tropsch catalysts. *Applied Catalysis A - General*. 2010; 388(1-2)).

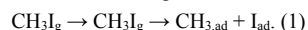
In this presentation we will discuss x-ray absorption near edge structure (XANES) and extended x-ray absorption fine structure (EXAFS) measurements of three different MCM-41 supported cobalt catalysts. These materials include incorporation of cobalt into the silica framework (Co-MCM-41), and cobalt impregnated catalysts, via wet impregnation, onto the pure (Co/MCM-41) and cobalt in the framework (Co/Co-MCM-41) supports. We analyzed the XANES and EXAFS at three different stages in the catalyst history: after calcination, after temperature programmed reduction, and after Fischer-Tropsch synthesis. Evidence suggests that the

* Coburn & Winters Student Award Finalist

presence of cobalt in the framework affects the reducibility of the cobalt species. The data also suggests mixed phases of cobalt metal and cobalt monoxide in the reduced and post FTS samples. The as prepared samples show only the Co₃O₄ phase, while the post FT and post TPR show both CoO and Co metal. The good agreement between XAS and XRD measurements demonstrates the use of these techniques to quantitatively determine the cobalt phase composition.

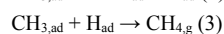
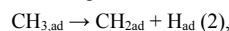
8:20am **SSI-TuM2 Measurement of the C-Pt Bond Energy for Adsorbed Methyl on Pt(111) by Methyl Iodide's Dissociative Adsorption Energy**, E.M. Karp, T.L. Silbaugh, C.T. Campbell, University of Washington

Knowing the bond energies of molecular fragments adsorbed to surfaces is an important ingredient in the fundamental understanding needed for rational design of heterogeneous catalysts. This study utilizes the ultrahigh vacuum technique of single crystal adsorption calorimetry to study the energetics of adsorbed methyl (CH_{3,ad}) on Pt(111), using measurements of the dissociative adsorption energy of methyl iodide (CH₃I) on Pt(111). At temperatures above 250 K, adsorbed CH₃I on Pt(111) is known to undergo C-I bond scission to form CH_{3,ad} and adsorbed iodine (I_{ad}). At 270 K, the rate of C-I scission is fast relative to the 100 ms time of calorimetric measurement, so that it provides the enthalpy for the net, two-step dissociative adsorption reaction:



The integral heat of Reaction (1) is -224 kJ/mol at a coverage of 0.05 ML. Through the use of a simple thermodynamic cycle and other known adsorption energies, this provides a heat of formation of CH_{3,ad} of -63 kJ/mol and a Pt-CH₃ bond energy of 209 kJ/mol.

Mass spectrometer measurements taken during experiments at 300 K and 320 K indicate that methane is produced. Previous studies indicate that at these temperatures, adsorbed methyl both decomposes to form adsorbed methylene (CH_{2,ad}) and hydrogen (H_{ad}) and reacts with H_{ad} to form methane according to the reactions :



where CH_{4,g} is gas phase methane. The microcalorimetric measurements performed at 300 K and 320 K, along with information on the rates of Reactions (2) and (3) available in the literature, allowed for the decoupling of Reactions (1)-(3) and an analysis of the energetics of all three reactions as a function of surface coverage, and the heat of formation of CH_{2,ad}.

8:40am **SSI-TuM3 A DFT Study of Methanol Reaction Pathways on the Au₁₃/TiO₂(110) Surface**, S. Hong, University of Central Florida, D.A. Chen, University of South Carolina, T.S. Rahman, University of Central Florida

We have performed density functional theory calculations to understand the reaction pathway selection for methanol decomposition on clean and Au₁₃ deposited TiO₂(110) surface. We find that when methanol adsorbs on the *clean* and *reduced* TiO₂(110) surface, it decomposes spontaneously into methoxy, which adsorbs on the O-vac site and desorbs as methyl leaving behind O-br on the TiO₂(110) surface. On the *stoichiometric* TiO₂(110) surface, we find that while methanol decomposition has a small activation energy of 0.2 eV, methoxy decomposition (i.e. formaldehyde formation) is not possible because of high activation energy of 3 eV. Nevertheless, once the surface is oxidized formaldehyde formation becomes *spontaneous*, through C-H bond scission by surface oxygen species. These results confirm the experimental results of methyl formation on the *reduced* and formaldehyde formation on the *oxidized* TiO₂(110) surface. Turning to the case of partially reduced Au/TiO₂(110) surface, our DFT calculations show that the adsorption of methanol and its intermediate methoxy does not occur on gold sites but on TiO₂ sites. Methoxy, in fact, forms at the Au-titania interface as a result of O-H bond scission by lattice oxygen (O-br), and its optimized tilted structure makes C-H bond scission -- through H abstraction by lattice oxygen near the interface site -- much easier than that for a vertical, non-tilted structure of methoxy in a non-interfacial site. Moreover, depending on the reduction level of the TiO₂(110) surface, the adsorption site preference for methanol and methoxy species on the Au/TiO₂(110) surface is: O-vac > interfacial Ti-cus > stoichiometric Ti-cus site. This hierarchy implies that the major product will switch from methyl on the fully-reduced surface, to formaldehyde on the partially-reduced or oxidized Au/TiO₂(110) surface. This conclusion is in full agreement with experiment.

This work is supported in part by US-DOE under Grant No. DEFG02-07ER15842.

9:00am **SSI-TuM4 Turning Aluminum into a Noble-metal like Catalyst for Low Temperature Molecular Hydrogen Activation**, I. Chopra, University of Texas at Dallas, S. Chaudhuri, Washington State University, J.F. Veyan, Y.J. Chabal, University of Texas at Dallas

There has been an ongoing quest to find cheaper hydrogen activation routes based on aluminum. Despite theoretical suggestions^{1,2} it has been difficult to obtain unambiguous experimental evidence for such catalytic activity towards hydrogen activation.

We demonstrate here that aluminum doped with very small amounts of Ti can activate molecular hydrogen at temperatures as low as 90K. The method is based on the ability to introduce a high flux of molecular hydrogen seeded with a *guest molecule to probe the catalytic activity and H₂ dissociation*. Once dissociated, hydrogen forms a complex with adsorbed CO (CO-H), characterized by a substantially and uniquely blue-shifted CO internal frequency. This complex is metastable, and is removed at a temperature (115K). We find that CO does not adsorb even weakly on H-covered Al, and use this finding to clearly show that, once dissociated, hydrogen diffuses away from the catalytic site onto Al sites (i.e. spills over). We use this new method to determine the dependence of the catalytic activity of aluminum surfaces on Ti coverage. Finally we show that the complex with activated hydrogen leads to further reactions at remarkably low temperatures (115K), such as formation of formyl (HCO), formaldehyde (HCHO) or methanol. These results provide the first direct evidence that Ti-doped Al can perform the quintessential first step of molecular hydrogen activation under nearly barrier-less conditions, thereby challenging the monopoly of noble metals in hydrogen activation.³

References:

- [1] Chaudhuri, S. & Muckerman, J. T. First-principles study of Ti-catalyzed hydrogen chemisorption on an Al surface: A critical first step for reversible hydrogen storage in NaAlH₄. *Journal of Physical Chemistry B* **109**, 6952-6957 (2005).
- [2] Chaudhuri, S., Graetz, J., Ignatov, A., Reilly, J. J. & Muckerman, J. T. Understanding the role of Ti in reversible hydrogen storage as sodium alanate: A combined experimental and density functional theoretical approach. , 11404-11415 (2006). B. Author, Nano. Bio. Info. Sci. **001**, 1234 (3001).
- [3] Chopra, I. S., Chaudhuri, S., Veyan, J.-F., and Chabal, Y. J., Nature materials (submitted) 2011.

9:20am **SSI-TuM5 On the Role of Hydrogen in Heterogeneously Catalyzed Reactions**, M. Mavrikakis, University of Wisconsin Madison **INVITED**

Hydrogen is a frequent participant in several heterogeneously catalyzed reactions, including Fischer-Tropsch Synthesis (FTS) of fuels, ammonia synthesis, oxygen reduction reaction (ORR), NO reduction, preferential oxidation of CO in the presence of H₂ (PROX), etc. Having analyzed the detailed aspects of the reaction mechanism for a number of these reactions on various transition metal and alloy surfaces using first-principles methods, some common principles governing the role of hydrogen in a wide range of catalytic transformations begin to emerge. In this presentation, we will discuss these common mechanistic principles by examples, including FTS^{1,2}, NO-reduction, ORR³, PROX^{4,5}, through an analysis of the energetics of alternative elementary reaction steps and the resulting potential energy diagrams. Connections to observations from experimental studies provide an invaluable perspective for the evaluation of our theoretical assessments.

References

1. M. Ojeda, R. Nabar, A. U. Nilekar, A. Ishikawa, M. Mavrikakis, E. Iglesia, *Journal of Catalysis* **272**, 287 (2010).
2. M. Ojeda, A. Li, R. Nabar, A. U. Nilekar, M. Mavrikakis, E. Iglesia, *Journal of Physical Chemistry C* **114**, 19761 (2010).
3. D. C. Ford, A. U. Nilekar, Y. Xu, M. Mavrikakis, *Surface Science* **604**, 1565 (2010).
4. A. U. Nilekar, S. Alayoglu, B. Eichhorn, M. Mavrikakis, *Journal of the American Chemical Society* **132**, 7418 (2010).
5. S. Alayoglu, A. U. Nilekar, M. Mavrikakis, B. Eichhorn, *Nature Materials* **7**, 333 (2008).

10:40am **SSI-TuM9 Prediction of Surface Ensembles in Au-based Bimetallic Alloys using Combined DFT and Monte Carlo Simulations**, J.A. Stephens, H.C. Ham, G.S. Hwang, University of Texas at Austin

Bimetallic materials have shown great promise for the development of superior catalysts. The recent surge of new interest in catalysis by gold has led researchers to investigate the effects of adding gold to other metals. While mechanisms underlying the alloying effect are still not understood in detail, recent evidence suggests that the enhanced reactivity of bimetallic catalysts can be attributed to a combination of metal-metal interactions

(ligand effect) and unique mixed-metal surface sites (ensemble effect). The ability to accurately predict the arrangements of constituent atoms in a surface alloy is indispensable to unraveling the roles played by the ensemble and ligand effects in the performance of bimetallic model catalysts. We have developed a scheme to predict the equilibrium arrangement of atoms in surface alloys in the presence of adsorbates at finite temperatures. It is based on the Ising model and is capable of reproducing DFT-predicted total energies to within no more than a few meV per surface atom. We have used it successfully to predict the populations of monomers, dimers, and other, larger ensembles in Au-Pd and Au-Pt fcc (111) and (100) surface alloys. The scheme will be presented in detail, as well as what we have learned about the effects of temperature, composition, and the presence of adsorbates on ensemble formation in both fcc (111) and (100) surface alloys. We will also discuss how the atomic arrangements affect the reactivity of gold-based alloy surfaces, particularly towards oxygen reduction and carbon monoxide oxidation.

11:00am **SS1-TuM10 Adsorption and Electron-induced Dissociation of CO₂ on TiO₂(110)**, *J. Lee, X. Deng, D. Sorescu*, National Energy Technology Laboratory

Adsorption and electron-induced reaction of CO₂ on the TiO₂(110) surface has been investigated using scanning tunneling microscopy (STM) and dispersion corrected density functional theory (DFT). At low coverage the adsorption of CO₂ takes place at the oxygen vacancy defect. At higher coverage the CO₂ starts to adsorb on the Ti rows. The DFT results show that the CO₂ at the oxygen vacancy defect is in a tilted configuration and the molecular axis is perpendicular to the bridging oxygen row. On the Ti row, the DFT results confirm that the CO₂ adsorbs in a flat configuration with its axis parallel to the bridging oxygen row. Electron injection from the STM tip into the CO₂ at the oxygen vacancy defect induces the dissociation of CO₂. The oxygen vacancy defect is found to be healed by the O atom released during the CO₂ dissociation process. Statistical analysis shows that the dissociation of CO₂ is a one-electron driven process with a threshold voltage of 1.4 eV above the conduction band minimum of TiO₂. The formation of a transient negative ion by the injected electron is considered to be the key process in the CO₂ dissociation.

11:20am **SS1-TuM11 Adsorption and Dissociation of Propane-1, 3-diol Molecules on Reduced TiO₂(110) Surface- A Scanning Tunneling Microscopy Study**, *D. Acharya, X. Lin, B.D. Kay, Z. Dohnálek, Z. Zhang*, Pacific Northwest National Laboratory

Rutile TiO₂(110) surface is one of the most studied model systems for the fundamental investigations of a variety of processes on metal oxide surfaces, including heterogeneous catalysis, greenhouse gas reforming, solar cells, photodecomposition of organic pollutants, and photoinduced water splitting. It is widely accepted that the surface chemistry of the oxide surfaces are mainly influenced by the defects sites, particularly oxygen vacancies. Here we study the adsorption of propane-1,3-diol molecules on partially reduced rutile TiO₂(110) surface using variable temperature scanning tunneling microscope (STM). STM images obtained before and after in-situ dose of propane-1,3-diol molecules at room temperature shows that the molecule preferentially binds at the bridging oxygen vacancies via bond scission of one of the OH groups. The hindered rotation of the 3-hydroxypropoxide species was seen at room temperature, while the diffusion and dissociation of the species were observed at elevated temperatures. The experiment was carried out at the Environmental Molecular Science Laboratory, a National Scientific user facility supported by the U.S. Department of Energy, Office of Biological and Environmental Research at Pacific Northwest National Laboratory.

11:40am **SS1-TuM12 Oxygen-Vacancy Assisted Formation of Enolate Species on Reduced CeO₂(111) Surfaces**, *F.C. Calaza, Y. Xu, D.R. Mullins, S.H. Overbury*, Oak Ridge National Laboratory

Enolate species are key intermediates proposed in a number of important organic reactions heterogeneously catalyzed by metals and metal oxides, but enolate has been difficult to identify on active catalytic surfaces due to difficulties of isolating it in the keto-enol equilibrium.

Reflection absorption infrared spectroscopy (RAIRS) was coupled with density functional theory (DFT) to study the adsorption of acetaldehyde, a simple \geq C2 aldehyde, on CeO_{2-x}(111) surfaces of different extent of oxidation (where $x = 0 - 0.5$). It is found experimentally that the molecule adsorbs weakly on the fully oxidized surface ($x=0$) at low temperatures and desorbs without further reaction near 215 K. The molecule bonds to *c.u.s.* Ce⁴⁺ cations through the oxygen lone pair electrons in the carbonyl group with its C-C bond perpendicular to the surface plane and the acyl hydrogen tilted slightly towards one of the lattice oxygen anions of the first layer.

On the reduced surfaces ($x=0.1 - 0.4$), acetaldehyde interacts more strongly with the surface upon adsorption at low temperatures by losing its carbonyl bond character and adsorbing as 1,1-dioxyethane and forming dimers and

polymers. Heating the surface to 400 K leads to desorption of some amount of these strongly adsorbed species as acetaldehyde and the appearance of hydroxyl and yet a different organic species.

The identities and structures of the different intermediates on the CeO₂ and CeO_{2-x} surfaces have been determined by their characteristic signatures in RAIRS and by DFT calculations. Our observations for the CeO_{2-x} surfaces are consistent with the vacancy-promoted dehydrogenation in the original methyl position of acetaldehyde and the formation of enolate (CH₂=CHO-Ce). Experiments with isotopically labeled acetaldehyde have verified the vibrational assignments for the enolate species and are in excellent agreement with DFT results. The assignment of the enolate species is furthermore consistent with C 1s XPS and C k-edge NEXAFS results.

Research sponsored by the Division of Chemical Sciences, Geosciences, and Biosciences, Office of Basic Energy Sciences, US Department of Energy. Use of the National Synchrotron Light Source, Brookhaven National Laboratory, was supported by the US Department of Energy, Office of Science, Office of Basic Energy Sciences.

Surface Science Division

Room: 110 - Session SS2-TuM

Self Assembled Monolayers and Networks

Moderator: J.E. Reutt-Robey, University of Maryland

8:20am **SS2-TuM2 In Situ UHV Growth and XPS/NEXAFS Characterization of Aromatic Self-Assembled Monolayers on Gold Substrates**, *A. Nefedov*, Karlsruhe Institute of Technology, Germany, *H. Muzik*, University of Bielefeld, Germany, *M. Naboka*, Karlsruhe Institute of Technology, Germany, *A. Turchanin*, A. Götzhäuser, University of Bielefeld, Germany, *C. Wöll*, Karlsruhe Institute of Technology, Germany

Aromatic self-assembled monolayers (SAMs) on gold show high potential for applications in nanobiotechnology [1]. Although the SAMs are typically prepared by immersing gold substrates in a solvent, their growth by vapor deposition in vacuum has various advantages both for the technological applications and fundamental studies [2, 3]. Thus, it is possible to characterize in detail the monolayer growth by various UHV compatible surface science techniques such as, e.g., electron spectroscopy. Here, we employ a new endstation of the HESGM beamline at BESSY II to study the *in situ* growth of 4'-nitro-1,1'-biphenyl-4-thiol (NBPT) SAMs on gold/mica substrates by X-ray photoelectron spectroscopy (XPS) and near edge X-ray absorption fine structure spectroscopy (NEXAFS). XPS C1s, N1s, O1s and S2p spectra as well as NEXAFS CK-, NK- and OK-absorption edge spectra were analyzed. These results demonstrate the formation of NBPT SAMs by vapor deposition in UHV with a similar packing density and molecular orientation as usually obtained in solvents. Moreover, we analyze the electron-radiation-induced modification of NBPT SAMs, that is widely employed in chemical nanolithography [4]. By varying the dose of electron irradiation we study two effects: (i) mechanisms of the electron-induced cross-linking [5] and (ii) conversion of the nitro groups into amino groups [6]. We analyze these transformations and compare the experimental NEXAFS data with calculations made by the StoBe software package.

[1] A. Turchanin, A. Tinazli, M. Ei-Desawy, H. Großmann, M. Schnietz, H. H. Solak, R. Tampé and A. Götzhäuser, *Adv. Mater.* **20**, 2008, 471.

[2] L. Kankate, H. Großmann, U. Werner, R. Tampé, A. Turchanin, A. Götzhäuser, *Biointerphases* **5**, 2010, 30.

[3] L. Kankate, A. Turchanin, and A. Götzhäuser, *Langmuir* **25**, 2009, 10435-10438.

[4] A. Götzhäuser, W. Eck, W. Geyer, V. Stadler, T. Weimann, P. Hinze, M. Grunze, *Adv. Mater.* **13**, 2001, 806.

[5] A. Turchanin, D. Käfer, M. Ei-Desawy, Ch. Wöll, G. Witte and A. Götzhäuser, *Langmuir*, **25**, 2009, 7342.

[6] W. Eck, V. Stadler, W. Geyer, M. Zharnikov, A. Götzhäuser, M. Grunze, *Adv. Mater.* **12**, 2000, 805.

8:40am **SS2-TuM3 Structure, Bonding and Electronic Properties of Self-assembled 2D Organic Nanostructures at Surfaces: Negatively Charged TCNQ Networks and Other Systems**, *S.L. Tait*, Indiana University

INVITED

Interfaces between organic materials and inorganic supports are critical for the design and function of new organic-based technologies (e.g., OLEDs, organic photovoltaics, and molecular electronics) as well as novel routes to chemical sensors and catalysts. There are vast opportunities for designing structure-function relationships in these systems due to the immense library of organic compounds and metal-organic chemistries available. Molecular self-assembly at surfaces by covalent, metal-organic, ionic, and weaker

interactions are active fields of research, but much remains to be determined with regard to the complex interplay of intermolecular and adsorbate-substrate interactions and how these impact structure and function. TCNQ undergoes a charge transfer from a Cu surface to adopt a bond conformation to the surface that enables stable adsorption and the self-assembly of highly ordered 2D structures via surface-mediated attractive interactions. These structures are stable at room temperature. Addition of Mn triggers a structural transformation to a highly-ordered porous network with Mn centers in a high spin state. These studies have allowed new insight into organic / metal interfaces by collaborative work involving high-resolution scanning tunneling microscopy, photoelectron spectroscopy methods, synchrotron measurements, other UHV surface experiments, and density functional theory calculations. Recent progress on other 2D and multilayer organic systems in our group lends further evidence to the significance of direct organic-surface interactions in such systems, the problems those interactions may pose, and solutions for balancing them at a desired level. We are making progress towards tailored chemical function by rational design of molecular architectures at surfaces and tuning such function through supramolecular design strategies.

9:20am **SS2-TuM5 Ultrafast Self-Assembly of 1-Adamantanethiol and *p*-Terphenylthiol on Au(111)-surface.** *V.V. Korolkov, S.A. Allen, C.J. Roberts, S.J.B. Tendler*, The University of Nottingham, UK

Study of organic thiols adsorption on noble metals continues to be a subject of many research papers within the last three decades. Such steady interest arises mainly from the possibility to design metal surfaces with predefined chemical and physical properties that makes them suitable for a whole range of theoretical and applied studies.

Here we propose and investigate an idea that thiols with rigid or spherical hydrocarbon moieties should self-assemble on Au-surface much quicker than those with long-chain moieties. To support this idea we have investigated adsorption dynamics and monolayer structure for 1-adamantanethiol¹ (AdSH) and [1,1':4',1''-terphenyl]-4-thiol (TPT) molecules self-assembled on Au(111)-surface at 393K. We have demonstrated that both thiols form defect free and uniform SAMs almost instantly at elevated temperature. It takes ~1sec for AdSH to self-assemble on gold. In case of TPT ~90% of the monolayer forms within the first ~10 seconds of adsorption, and then it takes ~60 seconds to develop into a well-ordered structure. Both SAMs on Au were characterized with ambient STM up to a single-molecule level, X-ray photoelectron spectroscopy and spectroscopic ellipsometry. We were able to obtain near atomic resolved STM images for AdSH SAM on Au. They clearly showed that all AdSH molecules adsorbed in the same conformation with the molecular tilt and the twist angles being 114° and 0° correspondingly. We have also demonstrated that most AdSH molecules are arranged in a head-to-tail orientation, with some molecules having a head-to-head orientation without forming a disulfide bond.

Molecular resolved STM images of TPT SAM/Au clearly demonstrated that within first seconds of adsorption the Au-surface is equally covered with two different phases (α - and β -). β -phase dominates on the Au-surface from ~10 sec of exposure and onwards. A closer inspection of the β -phase on a single molecule level allowed us to propose an upright conformation for TPT molecule on Au with the tilt angle of 0±5°. We also estimated the tilt angle for the α -phase to be within 10-20°. For both systems STM and XPS analysis suggest a high chemical and structural quality of the monolayers.

Overall we have proposed a simple and straightforward protocol for ultrafast fabrication of AdSH and TPT SAMs on Au-surface, which we believe can be readily extended for other similar molecular systems.

¹*Korolkov et al. J. Phys. Chem. C, Vol. 114, No. 45, 2010*

9:40am **SS2-TuM6 Role of van der Waals Interaction in the Binding of 1,4 diaminebenzene to the Au(111) Surface.** *D. Le, M. Aminpour*, University of Central Florida, *A. Kiejna*, University of Wroclaw, Poland, *T.S. Rahman*, University of Central Florida

The physisorption of 1,4 diaminebenzene (BDA) molecule on Au(111) surface is studied within the generalized gradient approximation of the density functional theory with the PBE [1], vdW-DF [2], and vdW-DF2 [3] exchange correlation functionals. The binding energy of an isolated BDA adsorbed on Au(111) surface calculated from vdW-DF (vdW-DF2) is 0.78 eV (0.84 eV) in better agreement with the experimental value (1.0 eV) [4] than that from PBE (0.37 eV), while the alignment of the molecule along the surface obtained from PBE (20°) is closer to the experimental value of 24° [4] than that of about 5° derived from vdW-DF (or vdW-DF2). On the other hand, when interactions between the BDA molecules is included in the calculations, as would be the case if the molecules were to self-assemble, say in the form of a linear line structure on Au(111), inclusion of vdW interactions gives excellent agreement with experimental observations. In particular vdW-DF and vdW-DF2 predict the BDA tilt angles to be 23° and 21°, respectively. The binding energy of a BDA on Au(111) in this case

is 0.70 eV and 0.71 eV, respectively. As is to be expected, PBE does not account for intermolecular interactions and does not give good agreement with the data. We suggest the presence of such alignment of molecules along the surface in the experiments, and that they are governed by hydrogen bonding between N and H atoms of neighboring BDA molecules. We compare our results also with unpublished STM data for the system.

[1] J. P. Perdew, K. Burke, and M. Ernzerhof, **Phys. Rev. Lett.** 77, 3865 (1996).

[2] M. Dion, H. Rydberg, E. Schröder, D. C. Langreth, and B. I. Lundqvist, **Phys. Rev. Lett.** 92, 246401 (2004)

[3] K. Lee, É. D. Murray, L. Kong, B. I. Lundqvist, and D. C. Langreth, **Rev. B82**, 081101 (2010).

[4] M. Dell'Angela, G. Kladnik, A. Cossaro, A. Verdini, M. Kamenetska, I. Tamblyn, S. Y. Quek, J. B. Neaton, D. Cvetko, A. Morgante, and L. Venkataraman, **Nano Lett.** 10, 2470-2474 (2010)

*Work supported by DOE Grant DE-FG02-07ER15842.

10:40am **SS2-TuM9 Conformational Chirality, Chiral Switching and Chiral Induction in Self-Assembled Molecular Structures.** *T.R. Linderoth*, University of Aarhus, Denmark **INVITED**

Chiral self-assembled structures formed from organic molecules have been subject to intense investigation, motivated both by applications such as enantiospecific heterogeneous catalysis as well as by fundamental interest e.g. in relation to the origin of biomolecular homochirality. Chirality on surfaces may arise both for intrinsically chiral molecules and for prochiral molecules that become chiral due to reduced symmetry upon adsorption. However, chiral effects originating from conformational degrees of freedom have received relatively little attention.

Here we use a combination of organic synthesis and UHV-STM experiments to address how rational design of molecular building blocks allows transfer of chirality from the molecular to the supra-molecular level. We investigate a class of custom-designed molecules based on a linear oligo-phenylene-ethynylene backbone and characterize their adsorption structures on the Au(111) surface. Most of these compounds are prochiral and display conformational chirality in the sense that they can adsorb in different chiral conformations distinguished by the positions of two tert-butyl side-groups. A novel chiral switching mechanism, involving a conformational change where the terminal groups rotate around the molecular axis, is directly revealed from time-resolved STM. We demonstrate that it is possible through control of the terminal group functionalization to steer the molecular backbones into surface assemblies that are either mirror symmetric or display pronounced organizational chirality in the form of a characteristic windmill motif. We furthermore achieve control over the absolute chirality of windmill assemblies by synthesizing an intrinsically chiral variant where the tert-butyl side pendant is replaced by a chiral (*S*)-*sec*-butyl group. This intrinsically chiral compound is finally used in co-deposition experiments as an induction seed to control the chirality of assemblies formed from the original prochiral compound.

Chiral switching by spontaneous conformational change in adsorbed organic molecules

S. Weigelt, C. Busse, L. Petersen, E. Rauls, B. Hammer, K.V. Gothelf, F. Besenbacher, and T.R. Linderoth, **Nature Materials**, 5 11 (2006)

Steering organizational and conformational surface chirality by controlling molecular

chemical functionality

C. Bombis, S. Weigelt, M. M. Knudsen, M. Nørgaard, C. Busse, E. Lægsgaard, F. Besenbacher,

K. V. Gothelf, and T. R. Linderoth, **ACS NANO** 4, 297 (2010).

Controlling chiral organization of molecular rods on Au(111) by molecular design

M. Knudsen, N. Kalashnyk, F. Masini, J. Cramer, E. Lægsgaard, F. Besenbacher, T. R. Linderoth, K. Gothelf, **Journ. Am. Chem. Soc.** 133 4896 (2011).

11:20am **SS2-TuM11 Electronic Structure and Charge Injection Barriers of Self Assembled Peptide Nucleic Acid Monolayers on Au.** *M.A. Wolak*, University of South Florida, *A. Balaeff*, Duke University, *S. Gutmann*, *M.M. Beerbom*, University of South Florida, *E. Wierzbinski*, *D.H. Waldeck*, University of Pittsburgh, *S. Bezer*, *C. Achim*, Carnegie Mellon University, *D.N. Beratan*, Duke University, *R. Schlaf*, University of South Florida

Peptide nucleic acids (PNA) are a promising alternative to DNA for bio-sensing applications as well as for strategies for self assembly based on nucleic acid hybridization. This potential is a result of the PNA's neutral pseudopeptide backbone, which eliminates inter-strand electrostatic

repulsion. In recent years charge transfer through PNA molecules has been a focus of research due to potential applications in self-assembled molecular circuits. This makes it interesting to investigate the electronic structure of PNA interfaces to electrode materials. A widely used strategy to 'connect' PNA molecules to metallic electrodes is through thiol-Au bonds using a terminal cysteine appended to PNA oligomers. This motivated the here presented research where the electronic structure of self-assembled PNA monolayers on Au substrates was investigated. Cys-appended PNA 7-mers of thymine (Cys-T7) were incubated on Au substrates in a nitrogen glove box attached to a photoemission spectrometer. Ultraviolet and x-ray photoemission spectroscopy (UPS and XPS) measurements on the resulting SAMs revealed the hole injection barrier at the interface and the interface dipole. Electronic structure calculations based on molecular dynamics sampling of the PNA structure yielded the band gap and the electronic density of states for PNA. Combined with the UPS data, the theoretical calculation enabled the estimate of the electron injection barrier at the interface, as well as the assignment of individual UP spectral features to specific molecular orbitals. Control measurements on Cys-appended, abasic PNA backbone 7-mers allowed the identification of the emissions related to the PNA backbone in the UP spectra. The orbital line-up at the interface between the Au substrate and the Cys-PNA indicates a significant interface dipole resulting in the alignment of the Au Fermi level near the center of the PNA HOMO-LUMO gap. This alignment causes large charge injection barriers for both holes and electrons, and thus impedes charge transfer from Au into the Cys-PNA SAM.

11:40am **SS2-TuM12 Immobilization of Single-Stranded DNA Probe on InAs Surfaces for Biosensor Application**, *E.K. Cho*, University of Wisconsin, *A. Brown*, Duke University, *T.F. Kuech*, University of Wisconsin

We study the immobilization of single-stranded DNA (ssDNA) probe on indium arsenide (InAs) surface and its characterization for diagnostic application. In contrast to other semiconductors, the Fermi level in InAs is typically pinned above the conduction band minimum, resulting two-dimensional electron gas (2DEG) located immediately below the surface. The InAs based system forms the basis of a DNA sensing platform because hybridization of complementary DNA sequence with the immobilized DNA probes on InAs surface causes the conductivity changes due to negativity charges on the phosphorus backbone of DNA sequences. The DNA immobilization was done using weakly basic solution and characterized by X-ray photoelectron spectroscopy (XPS) and hall measurement. The DNA probe is modified with thiol for 5' end to anchor the DNA probes on InAs surface and fluoro adenosine for 3' end to reveal the existence of DNA on the InAs surface. The XPS spectrum of F 1s and N 1s peaks verify that the DNA is successfully attached on InAs surfaces. The As 3d peak shows that there are considerable amount of As-S observed with no As-Ox after exposing the basic DNA solution. In contrast, In-S is not found in the In 3d core-level. The XPS data suggest that the DNA probes are attached to the InAs surface exclusively via thiolate bonds to As atoms and the DNA functionalization effectively removes InAs oxide as well. This result is not consistent with what has been observed on InAs (100) surfaces, where the thiolate bond is predominantly anchored to Indium atoms. For example, it has been shown a predominance of In-S bonds of alkanethiols and thioacetamide self-assembled monolayer (SAM) on InAs [1, 2]. However, the bonding chemistry of thiolate to III-V surface has been of great debate in literature [3]. The predominance of As-S bonds has been shown with octadecanethiol SAM on GaAs (100) surfaces driven by kinetic competitions [3] even though Ga-S bonds are energetically more favorable than As-S bonds [4]. In addition, the sheet resistivity of initial InAs surface and DNA immobilized surface is measured, and the response of a DNA functionalized InAs surface with complimentary DNA sequence is monitored.

- [1] D. Y. Petrovykh et al., *Surf. Interface Anal.* 2005, 37, 989-997.
- [2] D. Y. Petrovykh et al., *Langmuir* 2009, 25, 12185-12194.
- [3] C. L. McGuinness et al., *J. Phys. Chem. C* 2007, 111, 4226-4234.
- [4] T. Scimeca et al., *Phys. Rev. B* 1991, 44, 12927-12932.

Thin Film Division

Room: 107 - Session TF+EN-TuM

ALD for Energy

Moderator: W.M.M. Kessels, Eindhoven University of Technology, the Netherlands

8:20am **TF+EN-TuM2 Controlling the Dispersion and Size of Platinum Nanoparticles Using Pt Atomic Layer Deposition and Surface Treatments**, *V.R. Anderson*, University of Colorado, Boulder, *N. Leick*, Eindhoven University of Technology, Netherlands, *K.E. Hurst*, National Renewable Energy Laboratory, *A.S. Cavanagh*, University of Colorado, Boulder, *S. Kocha*, *K. Jones*, *A.C. Dillon*, National Renewable Energy Laboratory, *S.M. George*, University of Colorado, Boulder

Platinum nanoparticles are used as the catalyst on the cathodes of proton exchange membrane (PEM) fuel cells. Controlling the dispersion and size of the Pt nanoparticles is important for efficient and cost-effective fuel cells. When Pt atomic layer deposition (ALD) is performed on oxide or carbon substrates, nucleation difficulties and the high surface energy of Pt lead to Pt nanoparticles rather than continuous films. This research explored strategies to control the dispersion and size of Pt nanoparticles using Pt ALD together with various surface treatments. Pt ALD was performed using Pt hexafluoroacetylacetonate Pt(hfac)₂ and formalin as the reactants. Titanium oxide (TiO₂) and tungsten oxide (WO₃) were explored as the substrates. We used *in situ* transmission Fourier transform infrared (FTIR) spectroscopy to monitor the surface species during Pt ALD. Surface poisoning by hfac species was observed during the nucleation of Pt ALD on TiO₂, in agreement with our previous studies of Pd ALD [1]. Trimethylaluminum (TMA) was able to remove the hfac species from TiO₂ and promote more facile nucleation of Pt ALD, also as expected by our earlier work on Pd ALD [2]. We then used hfacH adsorption prior to Pt ALD to block surface sites, delay Pt ALD nucleation and decrease Pt nanoparticle dispersion. In addition, we used TMA exposures after Pt(hfac)₂ exposures to facilitate Pt ALD nucleation and increase Pt nanoparticle dispersion. The Pt nanoparticles were detected by the rising absorbance baseline of the FTIR spectrum, and transmission electron microscopy images of Pt nanoparticles on TiO₂ and WO₃ particles. The size of the Pt nanoparticles was dependent on the number of ALD reaction cycles.

1. D.N. Goldstein & S.M. George, *Thin Solid Films* (In Press).
2. D.N. Goldstein & S.M. George, *Appl. Phys. Lett.* **95**, 143106 (2009).

8:40am **TF+EN-TuM3 Nucleation & Growth of Continuous and Ultrathin Pt ALD Films for Improved Oxygen Reduction Activity in Fuel Cells Using W ALD Adhesion Layers**, *L. Baker*, *A.S. Cavanagh*, *S.M. George*, University of Colorado, Boulder, *A. Kongkanand*, *F.T. Wagner*, General Motors Research & Development

Transition metals, such as Pt, are important as catalysts in fuel cells. The cost of Pt requires that this metal be utilized as efficiently as possible. Previous studies have demonstrated that flat, continuous Pt surfaces have an activity for the fuel cell oxygen reduction reaction (ORR) per surface Pt atom that is 5-10 times larger than the activity of 3 nm Pt nanoparticles on carbon-supported electrocatalysts. Consequently, very thin continuous Pt layers are needed to achieve high activity per mass of Pt and favorable economics.

Pt has a high surface energy and does not readily wet low surface energy oxide and carbon material surfaces. Instead, Pt nanoclusters are formed during the nucleation of Pt ALD on these low surface energy supports. A continuous Pt film is possible only after the coalescence of the nanoclusters when the film thickness is >5 nm. One possible route to obtain a continuous and ultrathin Pt film is to deposit on an adhesion layer that has a higher surface energy than Pt. In this case, the Pt will wet the adhesion layer because the deposited Pt film will lower the surface energy. One material that has a higher surface energy than nearly all other metals, including Pt, is tungsten (W).

W ALD using WF₆ and Si₂H₆ is known to nucleate and grow rapidly on Al₂O₃ ALD surfaces [1]. The surface chemistry of W ALD is able to form chemical bonds to the underlying Al₂O₃ substrate that overcome the surface energy differences. In this study, Pt ALD is performed using MeCpPtMe₃ and H₂ plasma on W ALD adhesion layers grown on Al₂O₃ ALD films. X-ray photoelectron (XPS) and x-ray reflectivity (XRR) studies have demonstrated that Pt ALD nucleates nearly immediately on the W ALD adhesion layers. The XPS and XRR data are consistent with a layer-by-layer growth model. Pt ALD films can be deposited that are 1 nm thick, conformal and continuous. Initial electrochemical measurements on these

thin films have yielded a large proportion of the anticipated ORR activity benefit.

[1] R.A. Wind, F.H. Fabreguette, Z.A. Sechrist and S.M. George, "Nucleation Period, Surface Roughness and Oscillations in Mass Gain per Cycle during W Atomic Layer Deposition on Al₂O₃", *J. Appl. Phys.* 105, 074309 (2009).

9:00am TF+EN-TuM4 Engineering Li_xAl_ySi_zO Ion Conducting Thin Films by Atomic Layer Deposition for Lithium-ion Battery Applications, Y.-C. Perng, J. Cho, D. Membreno, N. Cirigliano, B. Dunn, J.P. Chang, University of California Los Angeles

Lithium (Li)-ion batteries have drawn much attention for their outstanding performance in portable electronics applications. However, formation of the solid electrolyte interphase (SEI) layer on the surface of electrodes during the charge-discharge cycling can reduce battery capacity and the long-term reliability of current battery technology. The use of solid electrolyte layers can effectively suppress formation of the SEI. Another application for thin solid electrolytes is in microbatteries, especially those based on the engineering of electrodes into 3D architectures involving high aspect ratio pillars. To realize this potential, an ultra-thin and highly conformal electrolyte layer is needed to coat the 3D electrode array. The ionic conductor lithium aluminosilicate (LiAlSiO₄) synthesized by atomic layer deposition (ALD), is a promising candidate for these battery applications. The material exhibits high ionic conductivity along its c-axis because of channels formed by the alternating tetrahedra of aluminum-oxygen (Al-O) and silicon-oxygen (Si-O).

The self-limiting characteristic of ALD allows for precise control of thickness and composition of complex oxides and results in a highly conformal and pinhole-free coating suitable in 3D micro-battery applications or electrolyte surface coatings. The metal precursors used in this work are tetraethyl orthosilicate (TEOS), trimethylaluminum (TMA) and lithium t-butoxide (LTB). These precursors, along with water vapor as the oxidant, were used to deposit SiO₂, Al₂O₃ and Li₂O, with deposition rates in the range of 0.8–2 Å/cycle, respectively. The deposition rate of stoichiometric LiAlSiO₄ was ~5 Å/cycle at a temperature of 290°C. The concentration of each metal element in Li_xAl_ySi_zO (LASO) thin films is found to correlate closely to ALD cycles and the associated incubation times. Complex impedance measurements show that the ionic conductivities of as-deposited LASO films are in the range of 10⁻⁷ to 10⁻⁸ S/cm and directly related to the lithium content in the film. The LASO ALD coating on 3D features, such as NWs and nanoparticles (NPs), were confirmed to be conformal and uniform by transmission electron microscopy (TEM) imaging. Further electrochemical tests to check pinhole-free coatings on 2D and 3D features were performed as well. The crystallinity of the films after post-deposition rapid thermal annealing (RTA) was a function of cation concentration. The epitaxial relation of LASO to silicon, a potential anode material, was found to be β-LiAlSiO₄ (-1 2 -1 0) || Si (400) and β-LiAlSiO₄ (1 0 -1 0) || Si (004).

9:20am TF+EN-TuM5 ALD: Enabling Designer Nanostructures for Energy Applications, G.W. Rubloff, University of Maryland **INVITED** Nanostructures will dominate next-generation energy technologies. Progress in nanofabrication increasingly allows design flexibility control of structural geometry and material combinations to achieve high performance multifunctional 3-D nanostructures for energy harvesting and storage. Such designs derive advantage from high surface areas, ultrathin films, structures with high aspect ratios, heterogeneous materials combinations, and control over 3-D profiles of material compositions and nanostructure shapes. Self-assembly, self-alignment, and self-limiting reactions enable both nanofabrication of desired energy nanostructures and their scaling to unprecedented levels of integration.

Atomic layer deposition (ALD) plays a pivotal role in this paradigm because of its intrinsic attributes: thickness control at the atomic scale; exceptional conformality to apply this control in the most demanding of nanogeometries; and a growing portfolio of ALD materials choices from new precursors and processes. As a result, ALD is becoming common, even pervasive, in nanostructure-based energy research, spanning applications from heterogeneous nanowires to passivating electrochemical layers and high-efficiency catalytic nanostructures.

Two primary challenges will determine whether ALD's potential is realized in next-generation energy technology.

First, integration of ALD with other processes into suitable process sequences determines how well nanostructure designs can be fabricated and

tailored for the energy application. For example, in high aspect ratio trenches, pores, or aperiodic porous materials, ALD films can be highly conformal or tapered "top-down" to thinner layers deeper in the structure, while electrodeposited films can be grown "bottom-up" from a working electrode at the bottom, together offering more design flexibility in vertical profiles than does either process alone.

Second, scaleup of ALD equipment, processes, and control is required for cost-effective ALD manufacturing. Significant efforts are already underway to develop these technologies, notably including roll-to-roll and other high throughput approaches, as well as atmospheric pressure ALD to circumvent the cost and complexity of vacuum-based equipment.

* Supported by the US Department of Energy, Office of Basic Energy Sciences as part of an Energy Frontier Research Center, and by the Laboratory for Physical Sciences.

10:40am TF+EN-TuM9 Functionalized Quartz Fibers by Atomic Layer Deposition for Dye-Sensitized Solar Cells, D. Kim, H.J. Koo, M. Woodroof, J.S. Jur, B. Kalanyan, K. Lee, C.K. Devine, G.N. Parsons, North Carolina State University

Dye-sensitized solar cells (DSCs) are a promising alternative to Si-based photovoltaic cells because of their high efficiency, low cost, and simple processing. To improve the efficiency, the light harvesting properties of the DSC photoanode structure should be improved.

This work shows the ability to improve DSCs efficiency by the incorporation of quartz fiber mats functionalized by ALD with a conformal nanoscale TiO₂ coating for the photoanode. The TiO₂ atomic layer deposition allows precise nanoscale thickness control throughout the quartz fiber mat. In addition, thermal stability of the quartz fiber also enables the annealing of TiO₂ films at high temperatures in order to obtain anatase crystallinity, which is the preferred TiO₂ phase in DSCs due to faster electron transfer kinetics. As a result, we obtained very stable anatase TiO₂ on quartz fibers by annealing at as high as 1050 °C. The micro-sized randomly oriented structure of coated quartz fibers caused high light scattering effect inside the photoanode, so that it increased the photon adsorption. At the same time, TiO₂-coated quartz fibers were successfully sensitized by more dye molecules compared to bare quartz fibers.

The use of the dye-sensitized quartz fiber mats in a DSC framework produces devices with overall efficiency exceeding 7% in our laboratory, compared to ~6% for similar devices without the coated fiber scattering layer. We will present X-ray diffraction, morphological changes, and optical properties of TiO₂-coated quartz fibers, as well as I-V and IPCE data for the DSCs. The effects of various integration schemes for introducing quartz fibers into the DSC photoanode will be discussed. Moreover, it is believed that the combination of quartz fiber and ALD is very attractive especially to energy research fields where they need finely tuned nanostructures to meet intricate requirements.

11:00am TF+EN-TuM10 Angle Dependent Electromotive Force in an Al₂O₃/Al/Thermoelectric Power Generator System Interacting with Infrared Radiation, A.J. Vincent-Johnson, K.A. Vasquez, James Madison University, A.E. Masters, Custom Thermoelectric, X. Hu, G. Scarel, James Madison University

We present a fundamental study of the interaction between infrared radiation and an Al₂O₃ film on Al sheet placed on a thermoelectric power generator (system 1). We compare the results with those obtained for a system consisting in an Al sheet on a thermoelectric power generator (system 2). The Al₂O₃ film in system 1 is prepared using atomic layer deposition, which provides smooth and well defined air/film and film/substrate interfaces. Infrared spectra show that Al₂O₃ films on the aluminum foil absorb an increasing amount of infrared radiation at increasing angle of incidence. This behavior, known as the Berreman effect, is caused by the radiative surface polaritons excited close to the frequencies of longitudinal optical phonons by the infrared radiation at the interfaces of Al₂O₃/Al. Our work demonstrates that a similar trend occurs when infrared radiation is absorbed by system 1: as the infrared radiation starts illuminating system 1 in its initial condition, the electromotive force jumps up to a maximum (EMF_{max}) and then decays exponentially. The EMF_{max} value and its amplitude increase with the increasing incidence angle of the infrared radiation. Since system 2 exhibits only a weak dependence of the EMF_{max} value and amplitude on the incidence angle of the infrared radiation, we conclude that the behavior of the electromotive force during the transient in system 1 is caused by radiative surface polaritons in Al₂O₃/Al. This research is at a seminal stage and needs further understanding. However many routes can be investigated to enhance the efficiency of the electromotive force production. The results are relevant to

energy generation from radiation, sensors, and electromagnetic wave detectors.

Thin Film Division

Room: 104 - Session TF+SE-TuM

Glancing Angle Deposition (GLAD) I

Moderator: T. Karabacak, University of Arkansas at Little Rock

8:20am **TF+SE-TuM2 Progress in Glancing Angle Deposition Technology for Practical Applications, M. Suzuki**, Kyoto University, Japan **INVITED**

Recently, advanced top-down processes for the fabrication of nanostructures have been developed; however, these processes are long predated by the process of shadowing growth by glancing angle deposition (GLAD), which affords the fabrication of the self-assembled nanostructures over a much larger area at significantly lower costs. In the past two decades, significant progress has been made in the development of 3D nanomorphologies well-controlled by the GLAD such as the zigzag and helix morphologies. Much effort has also been expended to gain a theoretical and numerical understanding of the growth mechanism of nanostructures in order to improve their morphology. Many researches are being carried out in academia to investigate the useful properties of nanocolumnar thin films, such as magnetic anisotropy, birefringence, dichroism, and optical activity *induced by nanoshapes*; high-performance catalysis and electrodes *using large surface area*; and various *size effects*. On the other hand, most companies seem hesitant to introduce the GLAD technique in the factory because of the prejudice that obliquely deposited thin films are not durable and reproducible. However, some products of obliquely deposited thin films are already being manufactured, although their production processes have not necessarily been disclosed. In this presentation, we discuss the previous products and investigations of GLAD thin films and demonstrate that this prejudice can be overcome. In addition, we introduce our recently commercialized products manufactured by GLAD, namely, surface enhanced Raman substrate¹ and low-reflectivity wire-grid polarizers². Because GLAD films have the great potential of enabling humankind to overcome the energy and environmental problems it confronts, it is important to encourage the industry to adopt GLAD by removing the prejudice against GLAD films.

[1] M. Suzuki *et al.*, "Au Nanorod Arrays Tailored for Surface-Enhanced Raman Spectroscopy," *Analytical Sciences* **23**, 829 (2007).

[2] M. Suzuki *et al.*, "Low-Reflective Wire-Grid Polarizers with Absorptive Interference Overlayers," *Nanotechnology* **21**, 175604 (2010).

9:00am **TF+SE-TuM4 Engineering Columnar Nanostructures for Organic Photovoltaics, R.T. Tucker**, Univ. of Alberta, Canada, *D.A. Rider*, NRC-Nat. Inst. for Nanotech., Canada, *J.G. Van Dijken*, *M. Thomas*, *B.J. Worfolk*, *A. Lalany*, *K.M. Krause*, Univ. of Alberta, Canada, *M.D. Fleischauer*, NRC-Nat. Inst. for Nanotech., Canada, *M.T. Taschuk*, Univ. of Alberta, Canada, *K.D. Harris*, NRC-Nat. Inst. for Nanotech., Canada, *J.M. Buriak*, *M.J. Brett*, Univ. of Alberta, Canada

Organic photovoltaics (OPVs) represent one possible route to widespread adoption of solar energy production [1]. The most promising OPV technology to date has been the bulk heterojunction, a photoactive mixture which bridges the gap between exciton diffusion lengths (~15 nm) and typical device length scales (~200 nm). However, bulk heterojunctions are typically disordered, which can limit charge extraction and thereby reduce OPV performance. The ideal OPV bulk heterojunction structure has been identified as ordered interpenetrating columnar electron donor and acceptor layers [2]. The interface morphology of such structures may be fabricated with glancing angle deposition (GLAD), a well-developed, robust nanostructuring technique that has been demonstrated for numerous materials at the length scales required for high quality OPV devices.

Here we present a summary of organic solar cell research utilizing GLAD at the University of Alberta. GLAD's flexibility lends itself to structuring both the transparent conductor layer as well as the donor and acceptor photoactive layers. We have demonstrated GLAD structuring of indium tin oxide (ITO), copper (II) phthalocyanine (CuPc), and fullerene (C60). ITO nanopillars fabricated by GLAD have been incorporated as three dimensional high surface area electrodes in organic photovoltaic devices [3]. The nanostructured electrodes demonstrated 30% improved performance compared to planar ITO anodes, due to increased optical absorption and high surface area. Typical OPV donor and acceptor materials, CuPc and C60, have also been successfully structured by the

GLAD technique [4,5]. Advanced motion control algorithms, designed to form thinner columns, were used to optimize the material nanostructures and produce highly desirable ordered bulk heterojunctions when coupled with complementary polymers. In the case for GLAD C60 devices, the short-circuit current was double that of bulk heterojunction devices. The GLAD technique has proven to be an incredibly useful method for fabricating and tuning electrode and bulk heterojunction morphologies in OPVs.

[1] H. Spanggaard and F.C. Krebs, *Sol. Energy Mater. Sol. Cells* **83** 125-146 (2004)

[2] F. Yang and S.R. Forrest, *ACS Nano* **2** (5), 1022-1032 (2008)

[3] D.A. Rider *et al.*, *Nanotechnology* **22** (8), 085706 (2011)

[4] J.G. Van Dijken *et al.*, *J. Mater. Chem.* **21** (4), 1013-1019 (2011)

[5] M. Thomas *et al.*, *ACS Appl. Mater. Interfaces* (in press, 2011)

9:20am **TF+SE-TuM5 Enhanced Photoconductivity Response of Glancing Angle Deposited Indium Sulfide Nanorod Arrays for Photodetector Device Applications, H. Is, M.F. Cansizoglu, T. Karabacak**, University of Arkansas at Little Rock

Photoconductivity (PC) in semiconductors can be detected by measuring the change in electrical conductivity when the material is exposed to light. Photosensitive materials with high PC response can be useful especially for photodetector applications. Compared to conventional thin film geometry, semiconducting nanostructures can provide enhanced photoresponse due to their low dark conductivity and superior capability of absorbing light, which leads to an enhanced PC response even to the minimal changes in light intensity. Glancing angle deposition (GLAD) provides a unique capability of producing nanostructured arrays of various materials with controlled shapes, size, and separation. In this study, we fabricated semiconducting indium sulfide nanorod arrays by GLAD on ITO coated glass substrates in various lengths and capped them with a silver film as metal contact to form a proof-of-concept photodetector device. PC response of these devices was measured at different wavelengths with altered light intensities. We show that GLAD nanorods have a superior PC response than conventional thin film, which is believed to be mainly due to their enhanced light trapping and high optical absorption property.

10:40am **TF+SE-TuM9 Catalytic Nanomotor Control: Design Techniques Using Dynamic Shadowing Growth, J.G. Gibbs, Y.P. Zhao**, University of Georgia

Catalytic nanomotors with nanometer-to-micrometer dimensions convert chemical energy into mechanical work via catalysis allowing for autonomous self-propulsion. They are an emerging nanotechnology field and promise important technological advances in drug delivery, transport, assembly, and other processes at the nano-scale. Catalytic nanomotors are inorganic analogues of cellular motor proteins that convert chemical energy into work through stored energy. One of the greatest challenges in this field is the manipulation and direct control of motion and swimming behaviors.

We focus upon the geometric design of catalytic nanomotors to modulate motion behaviors. To achieve this goal, a dynamic growth technique must be implemented. Most research uses template-directed electroplating (TDEP) allowing only simple geometries. We use dynamic shadowing growth (DSG) for fabrication which is a dynamic process allowing for construction of a much wider range of structures and shapes.

Depositing different materials and controlling the overlapping area is the first method of motion modulation used. To alter the swimming speed of a spherical nanomotor, Au is overlapped with the Pt-catalyst to varying degrees; the Au surface area A is changed systematically. The average moving speed u is found to follow the scaling relationship, $u \propto A^{-1/2}$, which agrees with the self-electrophoresis mechanism.

Swimming behaviors can also be altered by geometrical design, easily implemented by DSG making the technique useful to engineer different types of motion. Various swimming behaviors are exhibited by altering the geometry, and/or changing the location of the Pt catalyst accomplishable. Two very similar structures were fabricated and move based upon the location of the catalyst. Multi-component rotational nanomotors consisting of Pt coated TiO₂ nanoarms grown upon ~2.01 μm diameter silica microbeads are designed by dynamic shadowing growth. When exposed to hydrogen peroxide, H₂O₂, the structures rotate about an axis through the center of the microbead and perpendicular to the TiO₂ nanoarm at a rate of 0.15 Hz per % H₂O₂ concentration. The other nanomotors are tadpole-like structures that swim in large sweeping circular trajectories. The swimming trajectories are fine-tuned by altering the arm length and orientation exploiting geometry-dependent hydrodynamic interactions at low Reynolds number. The curvature, angular frequency, and radius of curvature of the

trajectories change as a function of arm length. Simulations based on the method of regularized Stokeslets are also described and correctly capture the trends observed in the experiments.

11:00am **TF+SE-TuM10 Fabrication of Cr-doped TiO₂ Nanorod Arrays by Oblique Angle Co-Deposition and Their Photocatalytic Properties**, *G.K. Larsen*, University of Georgia, *R. Fitzmorris, J.Z. Zhang*, University of California Santa Cruz, *Y.P. Zhao*, University of Georgia

In order to achieve efficient photocatalytic behavior in the visible light range, transition metal ions are often doped into TiO₂. Of these transition metal dopants, Cr appears superior in extending the photoresponse of TiO₂ into the visible range. However, different fabrication methods have produced mixed results regarding the effect of the Cr dopant on photocatalytic efficiency. In this study, a unique fabrication method, oblique angle co-deposition (OACD), is used to deposit a well-aligned array of Cr-doped TiO₂ nanorods that exhibit optical absorption in the visible region. These films are compared with TiO₂ nanorod arrays fabricated by oblique angle deposition (OAD). Due to the similarity of fabrication methods, the effect of the dopant on the structural, optical, and photocatalytic properties of TiO₂ can be isolated. The Cr dopant alters the TiO₂ lattice structure, with an increase in the crystallization temperature of the anatase phase and a decrease in the rutile crystallization temperature. Additionally, Cr is found to segregate out of the TiO₂ matrix and migrate to grain boundaries and the surface of the nanorods. The photocatalytic efficiency and IPCE of the Cr:TiO₂ films is reduced when compared to intrinsic TiO₂ due to changes in the photocatalyst's surface and charge transport properties as a result of the formation of intergranular Cr(VI) oxide clusters. The presence and the effects of the Cr(VI) phase is the result of exceeding the solubility limits of Cr within the TiO₂ lattice.

11:20am **TF+SE-TuM11 Optimal Conditions for Visualization of Fingerprints with the Conformal-Evaporated-Film-By-Rotation Technique**, *D.P. Pulsifer, S.A. Muhlberger, R.J. Martin-Palma, R.C. Shaler, A. Lakhtakia*, Pennsylvania State University

The conformal-evaporated-film-by-rotation (CEFR) technique was investigated for use as a development technique to visualize sebaceous fingerprints of forensic importance. A variation on oblique angle deposition, the CEFR technique requires the substrate holder to rapidly rotate about a perpendicular axis. The combination of an obliquely directed, collimated vapor flux and rapid rotation of the substrate gives rise to a conformal coating on the residue left behind on a substrate by the friction ridges of the finger. The coating has a closely packed nanocolumnar morphology. We conducted a systematic study of various deposition parameters in order to identify those conditions which are optimal for the development of fingerprints with the CEFR technique. We varied: base pressure during deposition, vapor flux angle with respect to the substrate plane, substrate rotation rate, deposition rate, and final film thickness. By qualitatively comparing fingerprints before and after development for various values of each deposition parameter, we were able to identify optimal conditions for development. For all depositions chalcogenide glass of nominal composition Ge₂₈Se₆₀Sb₁₂ was used to coat sebaceous fingerprints placed on glass microscope slides. We found the optimal conditions to be: a vapor flux angle of 10 deg as measured from the substrate plane, a rotation rate of 3 rps, a deposition rate of 1 nm/s, a final film thickness of 500 nm, and a deposition pressure of 0.1 mTorr. These values are close to those reported previously for CEFR coating of fingerprints with the exception of the base pressure. An optimal base pressure of 0.1 mTorr significantly relaxes the vacuum requirements of an evaporation chamber to be used for this purpose, making the technique very accessible to forensic scientists and law enforcement agencies. This work was supported by Grant No. 2010-DN-BX-K232 from the U.S. Department of Justice.

Vacuum Technology Division

Room: 111 - Session VT-TuM

Accelerator and Large Vacuum System Design, Outgassing and Pumping

Moderator: Y. Li, Cornell University

8:00am **VT-TuM1 Continued Work toward XHV for the Jefferson Lab Polarized Electron Source**, *M.L. Stutzman, P.A. Adderley*, Thomas Jefferson National Accelerator Facility

The Jefferson Lab DC, high voltage polarized electron source utilizes deep-UHV pressures to limit photocathode damage due to ionization and acceleration of residual gasses into the photocathode, as well as preserve the surface chemistry necessary for electron emission. Continued efforts toward improving and quantifying pressures below 5×10^{-12} Torr for electron source

vacuum chambers will be presented, including operational experience with the newly available Watanabe Bent-Belt Beam (BBB) gauge, and the incorporation of a bakable cryopump into the pumping configuration.

8:20am **VT-TuM2 Status of National Synchrotron Light Source II Vacuum Systems**, *H.C. Hseuh, A. Blednykh, L. Doom, M.J. Ferreira, C. Hetzel, J.P. Hu, S. Leng, C. Longo, V. Radindranath, K. Roy, S. Sharma, F. Willeke, K. Wilson, D. Ziggrosser*, Brookhaven National Laboratory

INVITED

National Synchrotron Light Source II is a new medium energy, ultra low emittance, high flux and high brightness synchrotron radiation facility. NSLS-II consists of a 200-MeV linac, a 3-GeV booster synchrotron, and a 3-GeV 500-mA storage ring with a circumference of 792 meter and over 60 beam lines. The construction of NSLS-II started in 2009 and will be ready for users in 2014. The storage ring vacuum chambers are made of extruded aluminium, with ante-chamber for photon extraction and for distributed NEG pumping. The precision machined extrusions are welded to aluminium-to-stainless bi-metallic flanges using robotic welding machines. Due to the high heat loads, all the photon absorbers are made of GlidCop. The details of the storage ring vacuum system will be presented and compared with those of similar facilities. The challenges encountered in the fabrication of vacuum chambers, photon absorbers and RF shielded bellows will be described. The status of the project will also be summarized.

9:00am **VT-TuM4 The Large Cryopump System for the Heating Neutral Beam Injection of ITER**, *S. Hanke, M. Scannapiego, X. Luo, C. Day*, Karlsruhe Institute of Technology (KIT), Germany, *F. Fellin, P. Zaccaria*, Consorzio RFX, Italy

The ITER Neutral Beam Injection system (NBI) is one of the heating systems to achieve the required plasma temperatures to start the fusion process. Thereby, the NBI system is basing on the principle of provision and acceleration of deuterium and protium ions and the re-neutralization of the high energy ions to be injected into the plasma through the confining magnetic fields. Each heating NBI is designed to insert 16 MW of heating power to the plasma and presents major technical and physical challenges.

In order to solve these and to demonstrate the achievement of the required parameters, a robust R&D program is under way. A central milestone for this development is the establishment of a full scale test facility, which will be built on site of Consorzio RFX, Padova. Part of this test facility is MITICA (Megavolt ITER Injector and Concept Advancement), the test bed for the entire neutral beam injection system. Karlsruhe Institute of Technology (KIT), which is the lead party in design and R&D of the ITER cryopumps since more than a decade, is supporting this project with the development of a customized cryopump design which ensures that the requested density profiles for optimum beam performance can be produced.

The main operational task which has to be provided by the cryogenic pump at a speed of ~ 5000 m³/s is to handle very high gas loads of protium and deuterium. As basic pumping concept, cryosorption was chosen and the cryopump is operated with supercritical helium at 4.5 K for the adsorbing and gaseous helium at 80 K for the shielding circuit. As demonstrated in other NBI applications, cryosorption provides a wide and robust operational window at acceptable cryogenic loads to the cryoplant. The design was driven by two competing requirements: The high thermal heat loads ask for a closed pump, whereas the need for a high pumping speed asks for an open structure. To reconcile both objectives in an optimized geometry, modeling simulations were performed using the Test Particle Monte Carlo code MOVAK3D. To properly describe the density distribution in the NBI vessel with large thermal and pressure gradients, the time-of-flight cell code ProVac3D was developed.

Additional to the design activities for an optimized cryopump, a considerable effort has been spent to investigate the thermal hydraulic properties of the cryopump during the different operational and failure modes.

9:20am **VT-TuM5 Design and Construction of the Vacuum System for SuperKEKB**, *Y. Suetsugu, K. Shibata, H. Hisamatsu, M. Shirai, T. Ishibashi, K. Kanazawa*, KEK, Japan

The upgrade project of KEKB B-factory, that is SuperKEKB, has started last year. The SuperKEKB is a two-ring electron-positron collider with 7.0 GeV electrons and 4 GeV positrons aiming a goal luminosity of 8.0×10^{35} cm⁻²s⁻¹, which is approximately 80 times higher than that of KEKB. In order to realize the unprecedented luminosity, the stored beam currents are increased to 2.4 A and 3.6 A for electrons and positrons, respectively. The vertical beam sizes at the collision point are also squeezed to approximately 60 and 50 nm with the beam emittances of 5/13 and 3/9 nm/pm (horizontal/vertical) for electrons and positrons, respectively. The vacuum system is accordingly improved to achieve the challenging goal. Beam pipes with antechambers are adopted for the reduction in the beam impedance of beam channel and also in the irradiation power density of

synchrotron radiation from intense stored beams. Various vacuum components adaptable to the antechamber scheme with low beam impedance and high thermal strength had been developed. The bellows chambers, for example, have a comb-type RF-shield, and the main vacuum pump is NEG strips inserted into one of antechambers. Special attention is paid for the mitigation of the electron cloud issues in the positron ring to avoid unwanted increase in the beam emittance. In order to reduce secondary electron emission, the inner surface of beam pipes is coated with TiN, the grooved surface is prepared in dipole magnets, and the newly developed clearing electrodes are introduced in wiggler magnets. The antechamber scheme is also effective to suppress the photoelectron effect. The beam pipes in drift spaces, furthermore, are wound by solenoid coils. The design of vacuum system has been mostly completed, and the mass production of beam pipes has started. Copper beam pipes with clearing electrodes for wiggler magnets had been already delivered. Aluminum beam pipes for arc section of positron ring are under manufacturing, together with bellows chambers, gate valves, NEG pumps, and so on. The installation to the ring will start next year after TiN coating, expecting the start of commissioning from 2014. The overall vacuum system design and some key issues for SuperKEKB together with the present status will be reported here.

9:40am **VT-TuM6 New Perspectives in UHV-XHV via a Novel Combination of NEG and Sputter Ion Pump Technologies**, *F. Siviero, A. Conte, L. Viale, A. Bonucci, P. Manini, L. Caruso*, SAES Getters, Italy, *L. Di Giacomo, G. Santella*, SAES Advanced Technologies, Italy

Current vacuum trends driven by end users requirements are demanding vacuum pumps with better performance in smaller packages. This is driving pump manufacturers to redesign their pumps and/or to consider new ways to combine pumping technologies more efficiently. In response to this trend it has been found it may be advantageous in UHV-XHV systems to use Non Evaporable Getter (NEG) pump as the main pumping element and complement it with a small ion pump to remove inert gases and methane. A novel design of such a combination, called NEXTor[®][1], was first introduced in 2010 at this conference.

Since the introduction, extensive studies have been carried out indicating the success of this configuration. Also, a broader range of pump models has been introduced, featuring pumping speed from 100 to 500 l/s (H₂).

The result of the vacuum characterization carried out on the pumping performances for a variety of gases of interest for UHV-XHV applications is discussed in this paper. Pumping speed measurements, pump down, rate of rise and out-gassing tests have been conducted and in some cases compared with traditional pumping approaches based on large sputter ion pumps. The advantages coming from the synergic integration of the NEG and the ion pump elements are highlighted and discussed. Examples of applications showing how this novel family of pumps can simplify the design and operation of vacuum systems are also presented and critically reviewed.

[1] NEXTor is an International Trademark registered by the "Madrid System" property of SAES Getters S.p.A.

10:40am **VT-TuM9 Modeling Hydrogen Outgassing in a Small Vacuum Chamber**, *R.F. Berg*, National Institute of Standards and Technology

Reports of hydrogen outgassing usually involve large vacuum chambers made of stainless steel. Typically, the chambers were baked at temperatures up to 400 °C, but the outgassing was measured only at room temperature. In contrast, the chamber used for the present measurements had a volume of only 29 cm³, with a correspondingly large surface-to-volume ratio, and the outgassing rate was measured at temperatures as high as 250 °C.

The present outgassing measurements were compared with a numerical model that included (1) diffusion of hydrogen atoms in the steel, (2) recombination at the surface into hydrogen molecules (plus the reverse process), and (3) release of hydrogen from traps. A trap is a site, such as a dislocation or a grain boundary, where the hydrogen is bound more strongly than in the surrounding metal. Traps allow stainless steel to hold much more hydrogen than implied by the small solubility of hydrogen in pure iron. The larger binding energy means that increasing the temperature does more than speed up diffusion; it also increases the amount of mobile hydrogen in the steel.

The model used the values obtained by Grant, Cummings, and Blackburn for the diffusivity, recombination, and permeation of hydrogen in stainless steel. If one assumes a plausible value for the initial hydrogen concentration, it gives outgassing rates in rough agreement with the measurements.

11:00am **VT-TuM10 Modelling and Simulation of the ITER Cryopumping Systems**, *C. Day*, Karlsruhe Institute of Technology, Germany **INVITED**

A cryopump is probably the most versatile and flexible vacuum pump. In large R&D applications where cryopumps are anyway available and high pumping speeds at high throughputs are requested, it is often advantageous to exploit a directly cryogen-supplied cryopump. The nuclear fusion project ITER is a perfect example for such a project, which triggered the development of customized cryopumps. To name just two advantages of this approach, a cryopump can be designed to perfectly fit the available space, and can be installed in-situ without any conductance losses, if regeneration frequency allows for that.

Karlsruhe Institute for Technology (KIT) is developing tailor-made cryosorption pumps for fusion applications over the last 20 years. This has been associated with an extensive design supporting R&D programme which has provided a broad parametric database and stimulated the development of modeling and design tools.

This paper will delineate the essential steps one has to consider when designing a cryosorption pump. The design process of a customized cryopump starts with the proper identification of the set of requirements, which defines the requested integral pumping speed at the given pump location and space. The tools needed for individual cryopump design are described and typical examples are given. This includes the calculation of capture coefficients and distributed pumping on the cold surfaces by means of Test Particle Monte Carlo methods.

Cryopump examples are taken from the area of large cryopumps for ITER, such as the torus cryopumps (~ 80 m³/s) and the cryopumps for high energy neutral beam injection development (~ 5000 m³/s). Although being cryogenic pumps, these applications are characterised by relatively moderate vacua due to the high gas throughputs during pumping. This also leads to the fact that transitional flow conditions prevail inside the pump, which results in additional challenges with regard to modelling and operation. Both pump types are currently in the stage of build-to-print design finalization and prototypes will be manufactured to validate this design in dedicated testbeds at KIT and Padova, Italy.

11:40am **VT-TuM12 Design and Construction of the Ultrahigh Vacuum System for the 3 GeV TPS Accelerator**, *G.Y. Hsiung, H.P. Hsueh, C.L. Chen, J.R. Chen*, National Synchrotron Radiation Research Center, Taiwan, Republic of China

The ultrahigh vacuum system for the electron storage ring of the 3 GeV Taiwan Photon Source (TPS) accelerator has been started the construction since 2010. The critical vacuum components with lower impedance design including the bellows with spring-finger rf-contact, the metal gate valves with comb-finger rf-contact, pulsed magnet kicker ceramic chambers, beam position monitors, crotch absorbers, and the precise machined sector bending chambers and BPM chambers, have been manufactured. The large aluminum alloy (Al-) bending chambers for the arc-cells have been precisely machined with oil-free machine tools in the clean room, and undergoing the ozonate water cleaning after with the precisely in-house welding. Mass production of the vacuum equipments including the ion gauges, ion pumps, NEG pumps, and gate valves, has been contracted out and partially delivering following the schedule of the cell assembling. Each cell, contains two short Al-straight chambers and two Al-bending chambers, has been started the assembling and on-site welding on the pre-aligned girders in clean room forming an one-piece vacuum vessel about 14 m in length following by the vacuum baking to the ultra-high vacuum. The progress of prototyping development and the status of construction for the TPS ultrahigh vacuum system will be described in this paper.

Tuesday Lunch, November 1, 2011

Exhibitor Technology Spotlight

Room: West Exhibit Hall - Session EW-TuL

Exhibitor Technology Spotlight

Moderator: Langley

12:20pm **EW-TuL2 New Developments in Surface Analysis from Thermo Fisher Scientific**, *T.S. Nunney, R.G. White, A. Bushell, P. Mack*, Thermo Fisher Scientific, UK

Surface structure and chemistry are crucial to the successful production and operation of innumerable devices, materials and coatings. X-ray photoelectron spectroscopy, with its high surface specificity and chemical state sensitivity, is an ideal tool for the evaluation of material composition. XPS depth profiling allows the identification of chemical variations in materials from the surface to bulk, and facilitates characterisation of complex layer structures. Recent advances in ion source design have seen the introduction of noble gas cluster ion beams for depth profiling applications, which allow materials that are unstable under monatomic ion bombardment to be analysed.

Solutions to structural and chemical problems using the full range of state-of-the-art, fully integrated X-ray photoelectron spectrometers from Thermo Fisher Scientific are presented. These include the characterisation of thin film polymer coatings, and determination of the structure of multilayer stacks. The effectiveness of the analyses, and the automated data refinement processes using new features of the award-winning Avantage datasystem, are shown for each of these examples.

12:40pm **EW-TuL3 A Complementary Approach to the Chemical and Structural Characterization of Graphene with Raman and X-ray Photoelectron Spectroscopy**, *T.S. Nunney, R.G. White*, Thermo Fisher Scientific, UK, *M. Wall*, Thermo Fisher Scientific, *K. Bolotin*, Vanderbilt University, *H.M. Meyer III*, Oak Ridge National Laboratory

The application potential of graphene is currently being extensively explored by the materials science community. Its utility as a transparent conductive electrode for the microelectronics industry is already being exploited. More recent progress has demonstrated how the unique combination of electronic, chemical, and structural properties of graphene will have a significant impact on the development of next-generation thin film transistors. Additional applications of graphene to molecular sensors are underway. In all stages of development there is a critical requirement for materials characterization and analysis: from the initial research stages through to testing of the finished devices. Because most materials need to be analyzed for compositional homogeneity both across the surface and through the thickness of a given sample, a complementary approach involving several techniques is often required.

In this presentation we will discuss how a multi-technique approach using Raman spectroscopy and XPS can address the problems associated with the analysis of ultra thin film materials. Raman microscopy is a vibrational technique that is very sensitive to small changes in a molecule's geometric structure and its environment. This sensitivity allows Raman to be used as a probe for a number of properties important to a specific graphene sample. These properties include, but are not limited to layer thickness, the presence or absence of defects, and local strain. XPS enables complete characterization of thin graphene films with respect to chemical modification, in addition to the chemical interaction between the film and the substrate. The combined XPS/Raman measurement approach will be applied to graphene produced by both exfoliation and CVD methods, providing a full comparison of the chemical and structural information offered by each technique.

1:00pm **EW-TuL4 Optimized XPS Depth Profiling of Organic Materials using Polyatomic Ion Sources**, *D. Surman*, Kratos Analytical Inc., *C. Blomfield, A. Roberts, S. Page*, Kratos Analytical Ltd., UK

Over the last several years multiple methods have developed for the depth profile analysis of organic materials using a variety of different polyatomic species as the sputtering ion. It has also become clear that different classes of polymers require quite different sputtering parameters to be effectively profiled with no loss of chemical information. In this presentation we discuss a variety of approaches that have developed in order to effectively sputter profile a wide range of materials. These approaches utilize differences in ion beam energy, impact angle and sample temperature in order to achieve an effective sputter profile.

1:20pm **EW-TuL5 Advances in XPS Chemical Imaging and Depth Profiling**, *J.S. Hammond, D.G. Watson, P.E. Larson, S.N. Raman*, Physical Electronics

Optimized scanning x-ray microprobe technology has been shown to provide superior sensitivity with minimal data artifacts for micro-area XPS. To improve the chemical state sensitivity, computation methods have been developed to provide a 10X improvement in count rate for chemical state spectroscopy with reduced x-ray damage. Utilizing the unscanned analyzer mode of operation, a user selectable number of data channels are now available for optimized chemical state imaging and chemical state depth profiling. Examples of these new computational methods will be presented for XPS chemical state imaging of patterned semiconductor and polymer samples as well as organic XPS depth profiling.

Tuesday Afternoon, November 1, 2011

Applied Surface Science Division

Room: 102 - Session AS-TuA

Imaging and 3D Chemical Analysis - Part II

Moderator: W. Stickle, HP ADL Corvallis

2:00pm **AS-TuA1 Integration of an External Cavity Quantum Cascade Laser Into a Scattering-Type Infrared Scanning Near-Field Optical Microscope**, *A.S. Lea, M.S. Taubman, M.C. Phillips*, Pacific Northwest National Laboratory, *M. Raschke*, University of Colorado, Boulder

Molecular nanostructures, polymer and supramolecular assemblies, proteins, biomembranes, correlated systems, and many other natural and synthetic materials gain their unique functionalities from intra- and intermolecular interaction and electron correlations on mesoscopic length scales of 10's of nm. Gaining a molecular level understanding of the materials structure and function has remained a major experimental challenge. This is due to the lack of experimental techniques that can routinely provide a chemically specific spectroscopic identification with simultaneous nanometer spatial resolution on the relevant length scale associated with the size and interactions of the molecular building blocks: within the 10 – 100 nm range. We have developed an instrument for spectroscopic infrared vibrational near-field nanoimaging capable of ultrahigh spatial resolution down below 10 nm, vibrational spectral information in the 14 to 2 um range, sensitivity down to the molecular level, and applicability under ambient and environmental conditions. There are few instruments that can provide near field IR nanoimaging at high resolution, but except for the aforementioned instrument, none are broadly tunable over a large spectroscopic range nor has resolution that approaches 10nm.

We are integrating a Quantum Cascade Laser to the new instrument as a complementary IR light source to the femtosecond OPO chain. QCLs are a monopolar semiconductor laser devices that can be fabricated to cover significant regions of the mid IR spectrum, specifically 3.5 to 20 microns. Moreover, these devices work extremely well in the molecular fingerprint region (8 to 12 microns), which will be of particular use in this instrument as this is where many fundamental vibrational bands are found, where MCT IR detectors work best, and the region is relatively free from water interference. The rapid scanning capabilities of External Cavity QCLs (ECQCLs) in the 100s of Hz, will allow IR spectra to be taken point by point across the sample, allowing rapid spectral data coverage. This is to be compared with the Hz-rate scanning of the OPO chain. The second significant advantage of QCL incorporation will be its ease of use (permitting wide-spread usage), low cost and ruggedness. This presentation will cover the integration of an ECQCL into the existing scattering-type IR scanning near-field optical microscope and demonstrate its ability to provide spatially resolved IR spectroscopic signatures on a sub-100nm scale. Ultimately, we anticipate this instrument will be able to provide chemical binding information of molecular adsorbates on nanostructured materials.

2:20pm **AS-TuA2 An Investigation Into the Aging of Paintings using Surface Analysis Techniques**, *T.S. Nunnay*, Thermo Fisher Scientific, UK, *J.J. Boon*, AMOLF, Netherlands, *E.S.B. Ferreira*, Swiss Institute for Art Research (SIK-ISEA), Switzerland

The understanding of the processes involved in the aging of artworks is of considerable importance in maintaining these pieces for future generations. Delamination of paint layers, chemical reactions of constituents in and between paint layers, interactions with the material that the paint was applied to, and the influence of the environment on the works can all have an effect on their appearance. By understanding these processes, conservators can attempt to retain the appearance as the artist intended.

Surface analysis has been used to investigate a cross-section sample taken from "Autumn in Schwand" (1906) by Cuno Amiet (1868-1961). The painting has become lighter in certain areas, and the cause of this was investigated. EDS analysis indicated that a higher proportion of lead had accumulated near the surface of the outer paint layer. XPS imaging of the sample in conjunction with multivariate statistical analysis of the data allows the chemical state of the individual components to be distinguished, from lead carbonate (or "lead white" pigment) to the lead soaps that are causing the change in the appearance of the painting, and the copper, chromium and arsenic pigments that form the paint layers. These analyses were compared with spectra from reference pigments to identify the original paints used. Further investigation using Raman and FTIR microscopy was used to complete the analysis.

2:40pm **AS-TuA3 Probing Insect Tissue by NEXAFS Imaging: A Chemical Characterization of Cuticle from an African Flower Scarab (*Eudicella gralli*)**, *J.E. Baio*, University of Washington, *C. Jaye*, National Institute of Standards and Technology, *E. Sullivan*, Woodland Park Zoo, *D.A. Fischer*, National Institute of Standards and Technology, *D.G. Castner*, *T. Weidner*, University of Washington

Insect cuticle is a matrix of structural proteins and long chain polymers of chitin. The chemical composition of the cuticle is dictated by the biomechanics of the insect. Regions of the exoskeleton where extra stiffness is required - this matrix become mineralized and form sclerites. Elastic portions of the cuticle are rich with pliable structural proteins. While engineers have set out to copy these biomineralization processes and design materials that mimic the extraordinary structural capabilities of these exoskeletons – a complete understanding of the structure of this chitin/protein/mineral matrix does not currently exist. In this study, we set out to spatially resolve the chemistry, at the cuticle surface, of an African Flower Scarab (*Eudicella gralli*) by near edge x-ray adsorption fine structure (NEXAFS) imaging. The NEXAFS images are produced by a new parallel process magnetic field electron yield optics detector, and a full field incident soft X-ray beam on the sample. The rapid parallel process magnetic field electron yield optics detector (LARIAT: Large Area Imaging Analytical Tool) produces a series of two-dimensional NEXAFS spatial images as the incident soft X-ray energy is scanned above a K or L absorption edge. A spatially resolved view of cuticle surface chemistry was created by mapping spectral features within the carbon (270-370 eV), nitrogen (380-430 eV), and oxygen (520-580 eV) K-edge spectra. Distributions of protein and chitin rich regions around the beetle were defined by changes in intensity of π^* (284.5 eV) and C-H* (290 eV) within the C K-edge spectra. Regions of high mineralization were observed around the edges of the beetle's head and were assigned by tracking the intensities of the calcium (330-360 eV) and iron (700-740 eV) L-edges. These images also showcase the strengths of NEXAFS imaging, which unlike other photoelectron spectroscopy modalities, allowed us to collect high quality spectra over a large field of view (12 mm x 18 mm) at a range of x-ray incidence angles, with little beam damage to the tissue.

3:00pm **AS-TuA4 Surface Cleaning of Organic and Inorganic Materials with Argon Cluster Ion Beams**, *A.E. Wright*, *P. Mack*, *O. Greenwood*, Thermo Fisher Scientific, UK

Surface analysis of many materials can be impeded by the presence of contaminant substances at the surface. Signals from these contaminants can dominate a photoelectron spectrum, leaving little contribution from the underlying material of interest. Spectroscopic analysis of contaminated samples can be a considerable challenge in surface science, so methods of cleaning samples are of some importance. One common method of removing contamination *in vacuo* is argon ion sputtering, which can be effective at removing surface materials. Damage to the underlying material can be substantial with argon ions, however, particularly at high impact energies. Ion impacts can disrupt polymer structures and reduce inorganic oxides, so that the surface after cleaning does not closely resemble the intact material.

The recent development of argon cluster ion beam sources promises significant improvements in depth profiling of soft materials. Cluster beams can offer exceptionally gentle sputtering, and so may be ideally suited to removal of contaminants and surface modifications from a variety of samples.

In this presentation, we evaluate the utility of argon cluster ions for the surface cleaning of various materials, in combination with the Thermo Scientific ESCALAB250Xi surface analysis instrument for characterisation of the samples. The results of gas cluster profiling on polymeric and inorganic materials will be presented, with spectroscopic and imaging analyses showing the benefits of this method.

4:00pm **AS-TuA7 Structure Determination of Heterogeneous Materials through 3D Imaging using XPS and Multivariate Analysis**, *K. Artyushkova*, The University of New Mexico, *S.J. Coultas*, *S.J. Hutton*, *A.J. Roberts*, Kratos Analytical Inc.

The sputtering of solids with ion beams followed by analysis with photoelectron spectroscopy has been widely used as it offers a powerful strategy for the in-depth characterization of complex inorganic materials. The combination of imaging techniques with depth profiling to create three-dimensional information is an obvious and exciting extension of these experiments. Recent introduction of cluster ion beams, such as coronene,

into XPS instrumentation offers capabilities in quantifying the chemical and molecular gradients in the near surface region of soft materials, such as polymers and biomaterials. XPS data can be acquired as a function of sputter depth into organic materials while maintaining molecular integrity.

There are only a handful number of studies combining XPS imaging and depth sputtering. One of the biggest problems when dealing with 3D imaging data sets is visualizing the lateral distribution of chemical moieties as a function of depth. When multispectral images are acquired at each sputtered depth, four-dimensional datasets can result with a full spectrum acquired at each voxel of the space. These datasets represent a huge amount of data which can only be interpreted with assistance of Multivariate Analysis.

In this research we report on application of various types of MSA methods such as two-step PCA and two-step MCR-ALS, PARAFAC, MFA, Tucker and 3D MCR-ALS to multispectral XPS imaging data acquired as a function of sputtering depth for different heterogeneous biomaterials and polymers. The component images extracted from MSA, which show the spatial distribution of the various chemical components, will be visualized in 3D individually or together representing an overall chemistry of individual layers.

4:20pm AS-TuA8 Interface Orientation Dependent Field Evaporation Behavior in Multilayer Thin Films, J.G. Brons, University of Alabama, A.A. Herzog, K.L. Henry, I.M. Anderson, National Institute of Standards and Technology, G.B. Thompson, University of Alabama

Intermixing between thin film layers can alter mechanical and thermal transport properties, phase stability and growth textures. Quantification of the degree of intermixing is crucial to identify the mechanisms of intermixing and their scaling effect on properties as listed previously. Atom probe tomography has received considerable attention for this type of characterization because of its ability to identify and provide reconstructions of atoms with near atomic spatial 3D resolution. In general, these atom probe reconstruction algorithms assume a constant evaporation field across the surface of the specimen. In reality, chemical inhomogeneity (i.e. discrete interfaces) modulates the evaporation field at the specimen surface. This introduces reconstruction artifacts and degrades the spatial resolution of the atom probe tomography technique. Multilayer thin films provide ideal specimen geometries to measure and quantify these artifacts since thin films can be deposited with near atomic layer precision and can exhibit large planar surfaces with various degrees of intermixing across the interfaces. A series of Fe/Ni and Ti/Nb multilayers with bilayer repeat distances of 4 nm have been sputter-deposited onto n-doped Si [001] substrates. The multilayers were annular focus ion beam milled into the required needle-shaped geometry for the atom probe analysis with the film interfaces oriented with the bilayer chemical modulations parallel and perpendicular to the specimen apex. This was done to compare field evaporation behavior at these limiting geometries. The atom probe compositional profiles were then compared to Electron Energy Loss Spectroscopy (EELS) compositional profiles to determine the fidelity of the reconstructions through cross-comparison microscopy. The best agreement between the profiles was seen for Fe/Ni (similar field strengths) in a perpendicular-to-the-apex orientation.

4:40pm AS-TuA9 Atom Probe Tomography and Spectroscopic Analysis of Wide Bandgap Nanostructures, N. Dawahre, G. Shen, W. Baughman, S. Balci, S. Wilbert, N. Harris, L. Butler, S. Kim, P. Kung, University of Alabama

Wide bandgap ZnO based semiconductors are materials of great importance in an increasingly large number of optoelectronic devices for energy applications, including high efficiency low cost photovoltaics, solid-state lighting, ultraviolet light emitting and laser diodes, transparent electronics, transparent conducting windows that can be a potentially cheaper and more abundant substitute to ITO for photonic devices, and higher performance scaffold than TiO₂ in sensitized solar cells. The material's wide bandgap, large exciton binding energy, and piezoelectricity can now be exploited at the nanoscale through the realization of nanobelts, nanoribbons and nanowires, leading to a dramatically expanded range of applications (e.g. chemical sensors and mechanical energy harvesting devices, etc). Enhancing our understanding of the chemical purity of ZnO nanostructures and understanding of the interfaces in ZnO based nano-heterostructures with atomic resolution is essential in order to enable the development of novel devices while further improving the performance of existing ones.

In this talk, we report the use and development of atom probe tomography (APT) in order to image the chemical composition of well aligned ZnO nanowires synthesized by thermal chemical vapor deposition and its relation to other material spectroscopic characteristics. The ZnO nanowires used were on various substrates, including sapphire, GaN and Si. The nanowires were single crystalline, 0.5-20 um long with a diameter controllable from 50 to 150 nm and a density on the order of 10⁸ per cm².

We subsequently discuss the sample preparation techniques employed and the influence of various APT measurement parameters on the quality of the data collected. Atoms probe tomography (APT), which combines a field ion microscope and a time-of-flight mass spectrometer, is an analytical technique which is unmatched in identifying composition at the atomic scale and in 3D. However, proper interpretation of the APT data required thorough analysis of the mass spectra. Data analysis was also carried out in correlation with the nanowire synthesis conditions (e.g. carrier gas and dopant) and with other characterization techniques aimed at assessing the nanowire optical and electrical properties. These included high resolution transmission electron microscopy along with energy dispersive spectroscopy mapping, confocal Raman spectroscopy and imaging, confocal photoluminescence and imaging, as well as terahertz time domain spectroscopy.

5:00pm AS-TuA10 Probing 3D-Semiconductor Structures, Vandervorst, IMEC, Belgium INVITED

The trends in advanced semiconductor devices and technologies call for the ability to probe compositional and impurity distributions with a depth resolution approaching near-atomic resolution. At same time, quantitative interpretation is of utmost importance in particular in multilayer structures and at interfaces such as local silicide composition and phase, interfacial interactions high k metal gate, etc.. At the same time one must admit that the advent of nanoscale devices and three-dimensional structures like Finfets, nanowires necessitates techniques which provide 3D-resolution. In this paper we will discuss recent approaches in extracting local 2D, 3D information on dopant distributions, carrier distribution, defects in thin dielectrics, phase and composition analysis, detection of small voids in ultra narrow interconnect lines (> 15 nm) as well as in (large, > 50 micron!) Cu-interconnects (TSV's).

For nanoscale 1D and 2D characterization we presently rely on concepts such as EXLE-SIMS for ultra high depth resolution dopant profiling, SSRM for 2D- carrier analysis, C-AFM for dielectrics, (S)TEM (+ELNES, EDX, HAADF) for quantitative composition analysis. 3D-characterization represents a serious challenge and one must rely on concepts like the tomographic Atom Probe to extract 3D-composition analysis on the nm-scale or Tomographic TEM. We will show examples for both cases and address the issues of Atom Probe in particular as the latter, although very appealing, does contain many artifacts as well. The latter are linked to sample preparation, laser-tip interaction, and reconstruction artifacts as well as issues inherently linked to instrument performance (mass resolution, sensitivity,...) and underlying physics (linked to sample heterogeneity). For analysing 3D-dopant distributions in Finfets, this can be complemented with tomographic SSRM and SIMS through Fins.

For back-end applications, the detection voids in narrow Cu-lines (15-30 nm) can be done using EDX whereas their analysis in the very large Cu TSV's requires sophisticated ion milling approaches (plasma based FIB, slcie and view) as excessive milling times and surface topography evolution (curtaining) can hide the required information.

Biomaterial Interfaces Division

Room: 105 - Session BI-TuA

Protein-Membrane Interactions

Moderator: L.J. Gamble, University of Washington

4:00pm BI-TuA7 Membrane Binding, Structure and Regulation of the PTEN Phosphatase, M. Lösche, Carnegie Mellon University and National Institute of Standards and Technology INVITED

Phosphatase and tensin homologue deleted on chromosome 10 (PTEN) is an important regulatory protein and tumor suppressor that performs its phosphatase activity as an interfacial enzyme at the plasma membrane-cytoplasm boundary. Acting as an antagonist to phosphoinositide-3-kinase (PI3K) in cell signaling, it is deleted in many human cancers. Despite its importance in regulating the levels of the phosphatidylinositoltriphosphate PI(3,4,5)P₃, there is little understanding of how PTEN binds to membranes, is activated and then acts as a phosphatase. The interaction of the protein with membranes is highly dynamic and is at least partially controlled by the in-plane fluidity of the bilayer. PTEN function requires multiple, lipid-specific interactions with the target membrane. These interactions regulate enzyme activity as well as lateral and subcellular distribution of the enzyme. From studies of the membrane association of PTEN under well-defined conditions in model systems, we report recent insights in the structural and functional basis for PTEN membrane binding and regulation.

4:40pm **BI-TuA9 Biomimetic Lipid Membrane Systems Applied to HIV-1 Neutralization**, *G. Hardy, M. Alam, S. Zauscher*, Duke University

Evidence suggests that lipid membrane interactions with rare, broadly neutralizing antibodies (NABs), 2F5 and 4E10, play a critical role in HIV-1 neutralization. The **objective** of this research is to understand how lipid membrane properties, such as chemical head groups, lipid domain organization, and lipid diffusivity contribute to 2F5/4E10 membrane interactions and antigen localization at the membrane interface, with the ultimate vision of guiding immunogen designs. Recent immunization studies have shown that induction of antibodies that avidly bind the gp41-MPER antigen is not sufficient for neutralization. Rather, it is required that antigen designs induce polyreactive antibodies that recognize MPER antigens as well as the viral lipid membrane. However, the mechanistic details of how membrane properties influence NAb-lipid and NAb-antigen interactions remain unknown. **Methods:** To understand how membrane properties contribute to 2F5/4E10 membrane interactions, we have engineered biomimetic supported lipid bilayers (SLBs) and have developed a surface plasmon resonance (SPR) spectroscopy based assay that monitors antibody binding to thiol monolayers, which mimic salient surface chemical properties of lipid membranes.

Our **results** showed that 2F5 and 4E10 bound preferentially on charged and hydrophobic thiol surfaces. This supports the theory that NABs interact with lipid head groups before embedding into hydrophobic tail regions. We have also engineered supported lipid bilayers (SLBs) whose compositions mimic both the host cell membrane and the HIV-1 envelope. These SLBs have planar surfaces that facilitate quantitative surface-characterization techniques such as high-resolution scanning-probe imaging, detection of fluorescence recovery after photobleaching, and neutron reflection measurements. Using these characterization techniques we have begun to i) visualize domains of lateral membrane organization; ii) determine SLB domain diffusivity; iii) determine differences in adhesion force (surface energy) of domains; and iv) correlate these membrane properties with NAb-membrane binding and NAb/antigen localization.

Our research is **significant** in that it provides a biologically relevant system to screen interactions of lipid-reactive antibodies with a broad range of diagnostic tools. Because current 2F5/4E10 immunogens have not yet elicited antibodies with the required membrane reactivity it is important to reveal the role of lipids underlying antibody-antigen binding. This information will elucidate how membrane properties can enhance antigen recognition and thus enable the design of next generation HIV-1 immunogens.

5:00pm **BI-TuA10 Interactions between the Norovirus and Glycosphingolipids Studied with Cell Membrane Mimics**, *M. Bally*, Chalmers University of Technology, Sweden, *G. Larson*, University of Gothenburg, Sweden, *F. Höök*, Chalmers University of Technology, Sweden

The determining initial step of viral infection is mediated by highly specific recognition events between the viral shell and ligands on the host cell surface. Detailed understanding of virus-membrane interactions is therefore of central importance to the development of new antiviral therapies, new vaccines and high-performance diagnostics platforms. In this context, assays based on cell-membrane mimics have a considerable potential, as they offer the possibility to study interactions between controlled ligand mixtures with surface-sensitive techniques, while presenting the ligand in a more native configuration. Potentially relevant characteristics such as membrane fluidity, ligand mobility and their ability to organize into microdomains can be preserved [1].

In this work we investigate the interactions between norovirus capsids and phospholipid bilayers containing glycosphingolipids (GSL). The norovirus is well known as the major causative agent of acute viral gastroenteritis, but its human target cells and the precise mechanism for viral entry are still poorly understood.

In a first example, we identify galactosylceramide - a major glycosphingolipid in the small intestine- as a ligand for Norovirus-like particles (VLP) from the Dijon strain. Quartz Crystal Microbalance and Atomic Force Microscopy studies on GalCer-containing supported lipid bilayers reveal that a clustered arrangement of the glycosphingolipids plays a crucial role in promoting a firm attachment of the pathogen to the lipidic membrane, most likely via the establishment of multiple contacts between the particle and the membrane [2].

We further investigated the interaction between individual fluorescent GSL liposomes and surface immobilized VLPs with single virus particle sensitivity. Besides representing the ultimate sensitivity for diagnostics purposes, our method makes it possible to study weak interactions. Kinetics analysis of vesicle residence times over large time scales reveals a highly heterogeneous behavior and yields information on multivalency, on the presence of domains and the role of cell-membrane curvature.

As exemplified here, simplified membrane models have a unique potential in providing fundamental understanding on the contribution of individual components to complex biological processes [3].

[1] Bally et al. "Liposome and Lipid Bilayer Arrays Towards Biosensing Applications", SMALL, 2010.

[2] Bally et al. "Interaction of Single Virus-like Particles with Vesicles Containing Glycosphingolipids", submitted.

[3] Bally et al. "Norovirus GII.4 virus-like particles recognize galactosylceramides in microdomains of planar supported lipid bilayers", submitted.

5:20pm **BI-TuA11 Binding of C-reactive Protein to Lipoprotein Nanoparticle Mimics: A Gel Electrophoresis Study**, *M.S. Wang, S.M. Reed*, University of Colorado Denver

C-reactive protein (CRP) is an acute phase serum protein involved in inflammation that recognizes pathogenic agents, and activates complement. Because CRP levels can increase by over 1000-fold from basal levels within 72 hr in response to inflammation, it has been used as a biomarker to predict the risk for cardiovascular disease (CVD). In addition, CRP has been shown to bind oxidized low density lipoprotein (oxLDL) through the phosphatidylcholine (PC) headgroup that is exposed on the surface of oxLDL and has been found to co-localize with atherosclerotic lesions. It is suggested that CRP was deposited in these lesions when engulfed by macrophage while it is still bound to oxLDL. Because LDL and the other lipoprotein particles (LPPs) have diameters (d) in the nanometer range, they can be considered as biological nanoparticles. In fact, LPPs are classified into four major categories according to their size and density: high density lipoprotein (d=8-13nm), LDL (d=20-30nm), intermediate density lipoprotein (d=30-40nm), and very low density lipoprotein (d>40nm). Moreover, the physiological functions of LPPs are greatly influenced by the size. For example, the presence of sdLDLs (d<25.5nm) are associated with increased risk of coronary artery disease (CAD) and diabetes; while increased levels of HDL are considered to be atheroprotective. Therefore, LPP profiling has emerged as a tool to more accurately assess the development of metabolic risk factors such as CAD. While the PC moieties on oxLDL are likely ligands for CRP recognition, it is still unclear why CRP binds only oxLDL although PC is expressed on native LDL and on all cell membrane. In this work, we correlated the effects of particle size (i.e. membrane curvature) to CRP binding using LPP mimics. To this end, we engineered LPP mimics using lipid-coated gold nanoparticles (PC-AuNPs) to explore the influence of LPP size on CRP binding. Binding analysis of CRP to the mimics was performed using gel electrophoresis (GE). The migration of CRP and PC-AuNP was directly visualized after electrophoresis, and the presence of CRP was confirmed using Western blots. The overlapping bands from the gel and Western blot confirmed that CRP bound to the PC-AuNPs and co-migrated during GE. Together, we demonstrated that 1) PC-AuNPs are size-separable, 2) the lipid layer around the PC-AuNP remained intact during GE, and 3) CRP binds to a relevant LDL-sized PC-AuNP mimic. This is, to our knowledge the first use of GE to separate lipid-coated nanoparticle and to evaluate non-covalent binding of protein-nanoparticle interactions.

Biofabrication and Novel Devices Focus Topic
Room: 105 - Session BN-TuA

Biofabrication Methods and Devices

Moderator: L. Gamble, University of Washington

2:00pm **BN-TuA1 Microengineered Hydrogels for Stem Cell Bioengineering and Tissue Regeneration**, *A. Khademhosseini*, Brigham and Women's Hospital, Harvard Medical School, MIT, and Harvard University **INVITED**

Micro- and nanoscale technologies are emerging as powerful tools for controlling the interaction between cells and their surroundings for biological studies, tissue engineering, and cell-based screening. In addition, hydrogel biomaterials have been increasingly used in various tissue engineering applications since they provide cells with a hydrated 3D microenvironment that mimics the native extracellular matrix. In our lab we have developed various approaches to merge microscale techniques with hydrogel biomaterials for directing stem cell differentiation and generating complex 3D tissues. In this talk, I will outline our work in controlling the cell-microenvironment interactions by using patterned hydrogels to direct the differentiation of stem cells. In addition, I will describe the fabrication and the use of microscale hydrogels for tissue engineering by using a 'bottom-up' and a 'top-down' approach. Top-down approaches for fabricating complex engineered tissues involve the use of miniaturization

techniques to control cell-cell interactions or to recreate biomimetic microvascular networks within mesoscale hydrogels. Our group has also pioneered bottom-up approaches to generate tissues by the assembly of shape-controlled cell-laden microgels (i.e. tissue building blocks), that resemble functional tissue units. In this approach, microgels were fabricated and seeded with different cell types and induced to self assemble to generate 3D tissue structures with controlled microarchitecture and cell-cell interactions.

2:40pm **BN-TuA3 Nanoscale Architectures for Probing Cell Mechanics**, S. Wind, M. Schwartzman, M. Palma, M. Biggs, T. Fazio, R. Piqueras Jover, M. Sheetz, Columbia University

The physical properties of a cell's environment are important factors in determining cell behavior and ultimately, phenotype. Two key factors that have been associated with major changes in cell morphology and behavior are (1) spatial organization of extracellular matrix (ECM) molecules and (2) rigidity. In order to understanding how cells sense these factors at the nanoscale and how these factors affect cell function, we have developed new nanofabricated surfaces in which these physical characteristics of the ECM are simulated.

The first type of surface combines nanoimprint lithography with selective biofunctionalization to precisely control the placement and geometric arrangement of integrin binding sites. The binding sites consist of sub-10 nm metallic nanodots functionalized with ECM binding ligands, designed so that each site can accommodate only a single integrin molecule. Cell spreading and motility assays were performed using 3T3 fibroblasts on arrays in which binding site spacing, density and number were independently varied. Cell spreading efficiency was markedly enhanced for clusters comprising at least 4 liganded sites spaced ≤ 60 nm apart, with little or no dependence on global density. This points to the existence of a minimal matrix adhesion unit defined in space and stoichiometry.

A second type of surface consists of elastomeric substrates with locally variable rigidity. We have found that exposure of poly(dimethylsiloxane) (PDMS) to an electron beam alters the rigidity of the elastomer, with the modulus of the exposed regions increasing with the applied electron dose. In addition to planar surfaces, pillared substrates can be patterned with no measurable change to the pillar dimensions. Immortalized mesenchymal stem cells plated on soft PDMS surfaces patterned in this manner displayed a distinct preference for the more rigid, exposed regions, forming focal adhesion nearly exclusively there. Furthermore, focal adhesion formation diminished significantly as the size of the exposed features was reduced below 1 μm , indicating that there is a length scale for cellular rigidity sensing, with the critical length in the range of a few hundred nanometers.

By adapting the tools of nanomanufacturing to cellular systems, we are able to define important parameters that can control aspects of cell function and behavior and will help identify conditions under which these functions may be altered. Potential applications range from therapeutic treatments that block metastasis to the development of new adoptive immunotherapies, as well as the development of new guidelines for the design of tissue scaffolds that can optimize healing without scarring.

3:00pm **BN-TuA4 Production of Functionalized 3D Micro Environment for Cell Culture**, J. Nowak, D. Mehn, P. Colpo, M. Zurn, T. Martin, F.J. Rossi, European Commission, JRC Institute for Health and Consumer Protection, Italy

One of the main challenges for the robust *in-vitro* studies is to obtain adaptable 3D culture systems that may mimic the tissue environment. Unfortunately the universal condition used in 2D cell culture techniques may hinder the full functionality of cells and generate misleading results.

Fabrication of firm and flexible micro-structures from organic polymers offers benefits for making smart 3D environments capable of driving cell behavior and surpassing the limitations of the 2D systems. These 3D bio-scaffolds can be employed to study various aspects of cell biology. Furthermore upon functionalization with the extra-cellular matrix proteins or signaling molecules they can be used as platforms for governing stem cell differentiation into the specialized cell types.

Here we present the straightforward approach to generate 3D bio-scaffolds that can facilitate cell growth under controlled geometrical and chemical conditions.

The technique involves UV cross-linking of the polymeric precursors to create the micro-well structures. The geometrical features of the structures are obtained by introducing a physical mask in contact with a liquid precursor, therefore restricting the region of the polymerization. We used PDMS mold as a physical mask to direct the polymerization of the PEG-DA and epoxy based polymers. However the technique can be used with various UV-sensitive polymeric materials.

The chemical and geometrical properties of the structures were characterized by XPS and microscopic techniques.

The features of the scaffolds lead to the development of a geometrically defined neuronal network when applied as platforms in a primary-neuron culture. Cell morphology and expression of the neuronal markers were characterized by fluorescent microscopy.

Electronic Materials and Processing Division Room: 210 - Session EM-TuA

High-k Dielectrics for MOSFETs Part 2

Moderator: A.C. Kummel, University of California San Diego

2:00pm **EM-TuA1 High Mobility Channel Materials and Novel Devices for Scaling of Nanoelectronics beyond the Si Roadmap**, M. Heyns, IMEC, Belgium **INVITED**

The introduction of high-k dielectrics and metal gates in advanced CMOS has opened the door to Ge and III-V compounds as potential replacements for Si to further increase the device performance. Using MOCVD the selective area growth of low-defect InP and InGaAs layers in submicron trenches on Si was demonstrated. These virtual Ge-III/V substrates can be processed in a standard CMOS line. Short channel Ge pMOS devices with high drive currents were fabricated. Strain engineering using GeSn source/drain areas allows to boost the performance of these devices so that they can outperform their strained Si counterparts. One of the key problems in developing III/V devices is the near midgap Fermi level pinning associated with the high density of defect states present at the high-k/III-V interface. The origin of these states is still under debate but there are clear indications that there exists a strong relationship with native antisite point defects. Various sulfide and other treatments were investigated to passivate the surface. The measured distribution of interface states and border traps on typical III/V MOS structures has some special consequences on the electrostatic operation of different transistor designs. Since inversion mode devices do not seem to be the appropriate choice for III/V based logic applications, other device types have been explored. The Implant-Free Quantum Well (IF-QW) device enables VLSI-compatible processing by self-aligned source/drain definition. Strained Implant Free Quantum Well Ge-based pFETs show excellent short channel control and record drive currents. The concept was also used to demonstrate high mobility n-channel InGaAs devices. For III/V pMOS devices GaSb is at present the material of choice. Very encouraging results have been obtained on direct heteroepitaxy of GaSb epilayers on InP(001) combined with *in-situ* deposition of an Al_2O_3 high-k gate dielectric. The introduction of these advanced materials also allows the development of new device concepts that can fully exploit the properties of these new materials. Tunnel-FETs, where the III/V material may be either introduced only in the source or in the complete device, can provide superior performance at lower power consumption by virtue of their improved subthreshold behavior, allowing to reduce the supply voltages. Vertical surround gate devices can be produced from III/V nanowires directly grown on silicon, allowing the introduction of a wide range of III/V materials and functionalities on Si. This illustrates some of the possibilities that are created by the combination of new materials and devices to allow scaling of nanoelectronics beyond the Si roadmap.

2:40pm **EM-TuA3 Local Profile of the Dielectric Constant Near the Oxygen Vacancy in the GeO_2 Films**, J. Nakamura, M. Tamura, The University of Electro-Communications (UEC-Tokyo), Japan

Ge-based metal-oxide-semiconductor (MOS) devices are focused as complementary-MOS devices for the next-generation in the post-Si technology. However, the dielectric properties of GeO_2 gate ultrathin films have not been clarified yet in detail. Our purpose is to clarify the spatial variation of the local dielectric constant for the GeO_2 thin films using first-principles ground-state calculations in external electric fields [1,2]. In particular, we reveal the local profile of the dielectric constant near the oxygen vacancy in the film, focusing on the crystal phase dependence.

We have adopted quartz (0001) and rutile (001) films with/without oxygen vacancies, in which Ge atoms at the topmost surfaces are terminated with H atoms. We have evaluated the optical and the static dielectric constants that are attributed to the electronic polarization and both the lattice and electronic polarizations, respectively.

From the local profile of the dielectric constants for the ideal films, it has been clarified that the dielectric constants change gradually from the surface and approach constant values at the center of the film. Such features have also been confirmed for the Si and SiO_2 films [1,2]. The dielectric constant for the defective model of the quartz film becomes larger locally "at" the oxygen vacancy site compared with that for the ideal model, but at "adjoining" oxygen sites to the vacancy for the rutile film. Such features

stem from the difference in the fashion of the chemical bonding between Ge and O atoms: The dielectric constant for the defective quartz model becomes large at the vacancy site where the covalent Ge-Ge bonding is formed. For the rutile, on the other hand, the Ge-O bondings surrounding the vacancy site are softened because of their less ionic character, which results in the larger displacement in external electric fields, leading to the larger lattice polarization around the vacancy.

[1] J. Nakamura *et al.*, J. Appl. Phys. 99, 054309 (2006); Appl. Phys. Lett. 89, 053118 (2006)

[2] S. Wakui *et al.*, J. Vac. Sci. Technol. B 26, 1579 (2008); *ibid* 27, 2020 (2009).

3:00pm **EM-TuA4 Two Step Passivation and ALD Monolayer Nucleation on Ge(100)**, T. Kaufman-Osborn, J.S. Lee, K. Kiantaj, W. Melitz, A.C. Kummel, University of California San Diego, A. Delabie, S. Sioncke, M. Caymax, G. Pourtois, IMEC, Belgium

Germanium is a promising channel material for next generation MOSFET. The best method to passivate Ge(100) is to form a layer of GeO₂, free of Ge suboxides, using high pressure O₂ or O₃. However, there are three challenges: (1) it is difficult to keep a stoichiometric GeO₂ monolayer (ML) at elevated temperatures, (2) the thermal oxidation process creates a rough interface degrading mobility at high field, and (3) scaling the passivation layer to only 1 ML is a challenge. This study presents a process to form a 1/2 ML of Ge-H and 1/2 ML of Ge-OH bonds without disrupting the Ge(100) surface. In-situ scanning tunneling microscopy (STM), in-situ scanning tunneling spectroscopy (STS), and in-situ X-ray photoelectron spectroscopy (XPS) were employed to determine the atomic and electronic structure of the passivation monolayer.

Using a differentially-pumped H₂O dosing system, an ordered, flat monolayer of H₂O chemisorption sites on Ge(100) was formed with a low density of unreacted dangling bonds at 300K. STS data showed that the Ge-H and Ge-OH sites removed the bandgap states from the Ge(100) dangling bonds. Annealing the surface between 20°C and 250°C gradually decreased the coverage of H₂O sites. However, even at 300K, the H₂O surface is highly reactive to trimethyl aluminum (TMA) since it contains a half monolayer of Ge-OH which catalyzes the breaking of Al-CH₃ bonds thereby inducing the formation of Al-O bonds, and the Ge-H sites block ALD ligand chemisorptions. STM experiments showed that the H₂O chemisorbed Ge surface provides a half monolayer of nucleation centers with approximately 0.5 nm spacing for TMA dissociative chemisorption at 300K. High resolution XPS experiments indicated that thermally unstable Ge-OH bonds were converted to thermally stable Al-O bonds. Furthermore, passivating the surface with H₂O prior to TMA dosing doubles the aluminum coverage compared to the TMA only dosed Ge(100) surface. The higher nucleation density from the two step functionalization process, TMA + H₂O, should be favorable for pinhole reduction. DFT calculations are consistent with the data showing TMA reaction with either -Ge-H and -Ge-OH is exothermic, but the reaction of TMA on the -Ge-OH site has both a low activation barrier and higher exothermicity (-41.4 kcal/mol) compared to TMA reaction on the -Ge-H site (-10.8 kcal/mol). The calculation is consistent with the key to full monolayer nucleation, the formation of a full monolayer of Ge-OH chemisorption sites, which is being studied with HOOH dosing.

4:00pm **EM-TuA7 Bilayer High-k Gate Stacks on Ge and InGaAs**, P.C. McIntyre, Stanford University **INVITED**

Research on novel channel materials such as Ge and InGaAs for high performance MOSFETs prompts interest in alternative high permittivity gate dielectrics because the thermal stability requirements that led to the adoption of HfO₂-based high-k dielectrics on silicon are relaxed for such channels. We have focused recently on ALD-grown TiO₂/Al₂O₃ bilayer dielectrics that combine large band gap Al₂O₃ interfacial layers (1-2 nm in thickness) with physically thicker but very high k TiO₂ gate dielectrics as a means of scaling gate capacitance and gate leakage current. This bilayer structure relies on the electrical passivity of the Al₂O₃/channel interface to achieve high performance. This presentation will summarize the scaling potential of these bilayer dielectric structures and methods by which low defect density Al₂O₃/Ge and Al₂O₃/InGaAs interfaces can be prepared.

4:40pm **EM-TuA9 Effect of Post Deposition Anneal on the Characteristics of InP MOS Capacitors with High-k Dielectrics**, R.V. Galatage, B. Brennan, H. Dong, D.M. Zhernokletov, C.L. Hinkle, R.M. Wallace, E.M. Vogel, The University of Texas at Dallas

Due to high defect density between III-V semiconductors and high-k dielectrics, buried channel structures with InP barrier layers are being considered for CMOS applications^{1,2}. It has been observed that sulfur passivated InP is thermally stable up to ~460° C³. However, little work has been performed to understand the thermal stability of the high-k/InP interface. In this work, the effect of dielectric post deposition anneal (PDA)

on InP MOS capacitors with high-k dielectrics was studied. Temperatures above 450° C result in an increase of the interface trap density.

MOS capacitors were fabricated on both n-type and p-type InP substrates with HfO₂ and Al₂O₃ dielectrics. Room temperature ammonium sulfide was used for surface passivation prior to ALD. Various temperatures ranging from 400° C to 500° C were used for PDA and a control sample without any PDA was used. The surface Fermi level is severely pinned for the p-InP substrate and the device does not go into accumulation. This behavior is not observed for the n-InP substrate. Room temperature C-V characteristics for HfO₂/n-InP devices show increased interface trap response for the samples with PDA above 450° C. However, low temperature (77 K) C-V measurements show that the samples with PDA have similar equivalent oxide thickness (EOT) and their interface trap response can be compared directly. A semi quasi-static method is used to calculate the Dit distribution across the InP band gap. Details of the technique will be presented. The Dit distribution shows a peak located at mid gap for all of the samples which increases with increasing temperature. A similar trend is observed for Al₂O₃/InP MOS capacitors. Correlation of these results to X-ray photoelectron spectroscopy (XPS) analysis will be presented.

This work is sponsored by SRC FCRP MARCO Materials Structures and Devices Center and the National Science Foundation.

[1] M. Radosavljevic *et al.*, IEDM Tech. Dig., pp.13.1 (2009).

[2] H. Zhao, Y. Chen, J. Yum, Y. Wang, F. Zhou, F. Xue, and J. Lee, Appl.Phys. Lett. 96, 102101(2010)

[3] Anderson, G. W.; Hanf, M. C.; Norton, P. R.; Lu, Z. H.; Graham, M. J., Appl.Phys. Lett, vol.65, no.2, pp.171-173, Jul 1994

[4] Hyoung-Sub Kim, I. Ok, M. Zhang, F. Zhu, S. Park, J. Yum, H. Zhao, Jack C. Lee, and Prashant Majhi, Appl. Phys. Lett. 93, 102906 (2008)

5:00pm **EM-TuA10 ALD Half Cycle Study of HfO₂ on InP by In Situ XPS**, H. Dong, D.M. Zhernokletov, B. Brennan, J. Kim, R.M. Wallace, University of Texas at Dallas

InP attracts significant attention as a high mobility channel material for Metal-Oxide-Semiconductor Field Effect Transistors (MOSFETs)-with many excellent electrical measurements reported on InP based devices. It is well known that one of the electrical limitations of surface channel III-V MOSFETs comes from the interface defects generated from surface/interface oxidation between high-k dielectrics and III-V materials, which can cause Fermi level pinning [1]. InP is also considered as a potential buffer layer material for quantum well FETs, which is in direct contact with a gate dielectric [2]. To examine the interfacial chemistry for high-k/InP, we present a half cycle Atomic Layer Deposition (ALD) study on native oxide and wet chemically treated InP (100) samples with Hf (TDMA-Hf precursor) and water by *in-situ* monochromatic X-ray photoelectron spectroscopy (XPS). The “clean up” effect is examined and compared to the results for ALD Al₂O₃ on InP. The significant reduction of interfacial oxides by pre-ALD wet chemical treatments and the detailed growth rate of HfO₂ on various samples are also discussed.

This work is supported by the FCRP MSD Focus Center and NSF (ECCS-0925844).

[1]. W. Wang, C.L. Hinkle, E.M. Vogel, K. Cho, R.M. Wallace, Microelectron. Eng. (2011) doi: 10.1016/j.mee.2011.03.053.

[2]. M. Radosavljevic *et al.*, IEDM, Tech. Dig., pp.13.1 (2009).

5:20pm **EM-TuA11 Nonvolatile Memresistive Nano-Crossbar Switches in Pt/Ta₂O₅/Cu Solid Electrolytes**, P.R. Shrestha, K.P. Cheung, National Institute of Standards and Technology (NIST), H. Baumgart, Old Dominion University

Metal filament resistive memory is an excellent candidate for a nanoscale crossbar switch, and such two terminal “memresistive” devices are being considered for next-generation non-volatile memory due to the inherent simplicity, scalability and low cost (1). Additionally, these devices show potential to replace static random access memory (SRAM) as high performance switches for reconfigurable devices .

Memresistive devices operate by changing resistance from high (R_{off}) to low (R_{on}) values in response to an applied voltage. Despite a tremendous amount of work in the scientific literature, the actual underlying switching mechanism has yet to be fully explained. Few studies, most of which lack measurement details, have reported on the transient current response and high speed switching characteristics of memresistive devices. The papers suggest the presence of the variety of active current and thermal dissolution of the low resistance filament while switching OFF. The switching ON has been attributed to the movement of the metal ions towards the cathode and being neutralized by the electrons to form the metal filament. Transient current measurements for switching ON have not yet been analyzed in detail in the literature. Another crucial problem in measurements of these

devices is due to the preferred values of $R_{on} (<1k\Omega)$ and $R_{off} (>1G\Omega)$. Thus the key obstacle preventing fundamental understanding has been the lack of reliable and accurate measurements of the transient response while switching ON (from R_{off} to R_{on}). In this work, we developed a new measurement capability that enables reliable and accurate investigation of the transient switching response, monitoring change from low R_{on} to high R_{off} .

In order to address the need to reliably and accurately monitor the device I-V transient response extremely fast, we have designed an amplifier with low-gain and high bandwidth (1.7 GHz) to accommodate much faster (and realistic) "program" voltage pulses. For switching purposes, this amplifier allows for fast transient current monitoring during programming with proficiency but not limited to follow 2 nsec of pulse rise time. The high gain bandwidth of the amplifier allows us to monitor change from low current (R_{off}) to high current (R_{on}) accurately.

1. R. Waser, R. Dittmann, G. Staikov, K. Szot, *Advanced Materials* 21, 2632 (2009).

5:40pm **EM-TuA12 Metrology for Interfaces and Mass Transport in C-MOS Related Nanofilms**, *A. Herrera-Gomez, A. Sanchez-Martinez, O. Ceballos-Sanchez, M.O. Vazquez-Lepe*, CINVESTAV-Unidad Queretaro, Mexico, *P. Lysaght*, SEMATECH

Interface layers play a fundamental role in determining the electrical properties of CMOS devices because their thicknesses are of a magnitude comparable to that of the dielectric layers currently employed. The main (top) techniques traditionally used for characterizing the chemical depth profile of MOS structures have been XPS-Sputter and Back-Side TOF-SIMS. However, they lack the appropriate resolution to characterize the thickness and composition of nano or sub-nano layers. Due to the lack of appropriate metrology methods, the structure of interface layers is usually assessed indirectly through their effect on the device's capacitance. Another important issue in the processing of MOS devices is the diffusion control of chemical species. To quantify or to simply observe displacements on the order of 2 or 3 nm of low concentration elements with those techniques is *close to impossible*. The semiconductor industry will greatly benefit from a metrology method capable of: (a) characterizing the thickness and composition of the various layers constituting a MOS device, including the interface layers; (b) assessing the effect of process driven diffusion of various critical chemical species present in the film. There is a growing consensus that X-Ray Photoelectron Spectroscopy (XPS), specifically Angle-Resolved XPS (ARXPS), has the appropriate chemical and depth resolution for assessing the depth profile of films between 0 and 8 nm. The precise methodology for applying the technique, however, varies wildly among different groups. In many cases the analysis algorithms of ARXPS data are highly susceptible to noise. Because of this, ARXPS is frequently regarded as qualitative techniques. In this talk we briefly describe a robust ARXPS analysis methodology that *minimizes* the sensitivity to noise. This methodology has been successfully applied to characterize various systems. One example that will be addressed regards the failure mechanism for the degradation of the electrical performance of TiN/HfO₂/InGaAs devices during thermal processing. We investigated the change on the structure caused by annealing, such as the possible formation of As, Ga or In oxides, accumulation of these elements in the dielectric, formation of metallic arsenic, and/or any other change on the structure that could be correlated to device degradation. ARXPS experiments were performed on those samples and analyzed using the robust methodology. One important finding was that indium diffuses through the dielectric all the way into the metallic layer upon annealing.

Energy Frontiers Focus Topic

Room: 103 - Session EN+NS-TuA

Nanostructured Materials for Thermophotovoltaics, Thermoelectrics & Plasmonics

Moderator: P. Nagpal, Los Alamos National Laboratory

2:00pm **EN+NS-TuA1 Thermal Plasmonics as a Route to Photovoltaics?**, *D.J. Norris*, ETH Zurich, Switzerland **INVITED**

Patterned metallic films allow the generation and manipulation of special electromagnetic waves known as surface plasmons that propagate along a metal interface. Because these waves allow the concentration of light in nanometer-scale volumes, they have implications for fundamental phenomena as well as applications such as imaging, sensing, and solar cells. Thus, the field of plasmonics has arisen to study and utilize surface plasmons. While light is typically used to create these waves, in some cases it would be more convenient to have a non-optical source for surface

plasmons. One route is thermal excitation (*i.e.*, heat). Here, we will explore hot plasmonic structures for obtaining new optical behavior. For example, we will examine metallic films patterned with a series of circular concentric grooves (a bull's eye pattern). We show that, when heated, these films can emit light that is amazingly narrow, both in terms of its spectrum and its angular divergence. Thus, a simple metallic foil can generate a highly directional beam of monochromatic light by a thermal process. This effect has implications for creating efficient thermophotovoltaic devices, which convert heat into electricity. During these studies, we also developed a simple, high-throughput method for obtaining ultrasoft patterned metal films. Previously, roughness in such films has hindered the field of plasmonics. Therefore, our approach solves a critical problem and allows many high-quality plasmonic structures to be available for the first time.

2:40pm **EN+NS-TuA3 Nanocrystal Assemblies: A Modular Approach to Materials Design**, *D.V. Talapin*, University of Chicago **INVITED**

Colloidal nanocrystals can combine the advantages of crystalline inorganic semiconductors with the size-tunable electronic structure and inexpensive solution-based device fabrication. Single- and multicomponent nanocrystal assemblies, also known as superlattices, provide a powerful general platform for designing two- and three-dimensional solids with tailored electronic, magnetic, and optical properties. Unlike atomic and molecular crystals where atoms, lattice geometry, and interatomic distances are fixed entities, the nanocrystal arrays represent ensembles of "designer atoms" with potential for tuning their electronic structure and transport properties. Generally speaking, nanocrystal assemblies can be considered as a novel type of condensed matter, whose behavior depends both on the properties of the individual building blocks and on the interparticle exchange interactions.

The ability to assemble precisely engineered nanoscale building blocks into complex structures is opening the door to materials where components and functionalities can be added, tuned or combined in a predictable manner. I will show how self-assembly of nanocrystals can lead to a palette of unprecedented phases including superlattices isostructural with the Archimedean tilings and dodecahedral quasicrystals.

Efficient charge transport is crucial for performance of nanocrystal-based electronic and optoelectronic devices. The insulating nature of surface ligands traditionally used for nanocrystal synthesis results in the poor electronic coupling between individual nanocrystals. To facilitate charge transport in nanocrystal solids, we introduced the concept of inorganic ligands for colloidal nanocrystals. These ligands, namely metal chalcogenide complexes, can be applied to a broad range of inorganic nanomaterials. I will demonstrate the power of this approach on several examples of prospective electronic, thermoelectric and photovoltaic materials.

4:00pm **EN+NS-TuA7 Photonic and Plasmonic Crystals for Thermophotonics and Energy Conversion**, *R. Biswas*, Iowa State University & Ames Laboratory - US DOE **INVITED**

Photonic and plasmonic crystals that have various energy-related applications will be discussed. Metallic plasmonic crystals consisting of an array of nano-holes or nano-pillars on common substrates, with pitch at infrared length scales, have very sharp absorption properties at infrared wavelengths. Such arrays have diverse applications to sensors and thermophotonic applications. The absorption, thermal emission, and angular characteristics from these plasmonic arrays will be described with rigorous scattering matrix simulations and compared to measurements. I will also survey the rich physics underlying plasmonic nano-arrays at optical length scales, and a few energy related applications.

4:40pm **EN+NS-TuA9 Molecular and Hybrid Solution Processible Thermoelectrics**, *R.A. Segalman, S. Yee*, University of California, Berkeley, *N. Coates, J. Urban*, Lawrence Berkeley National Laboratory **INVITED**

Thermoelectric materials for energy generation have several advantages over conventional power cycles including lack of moving parts, silent operation, miniaturizability, and CO₂ free conversion of heat to electricity. Excellent thermoelectric efficiency requires a combination of high thermopower (S , V/K), high electrical conductivity (σ , S/cm), and low thermal conductivity (κ , W/mK). To date the best materials available have been inorganic compounds with relatively low earth abundance and highly complex, vacuum processing routes (and hence greater expense), such as Bi₂Te₃. Molecular materials and hybrid organic-inorganics bring the promise of inexpensive, solution processible, mechanically durable devices. While highly conductive polymers are now common place, they generally demonstrate low thermopower. Our work on molecular scale junctions suggests that nanostructuring of organics allows them to act as thermionic filters between inorganic junctions which can lead to enhanced thermoelectric properties. We have taken inspiration from this fundamental

understanding to design material systems in which we combine a high electrical conductivity, low thermal conductivity polymer with a nanoparticle that contributes high thermopower. Additionally, the work functions of the two materials are well-aligned which introduces the possibility of thermionic filtering at the interface and an additional boost to the power factor. The combination of these effects results in a new hybrid, solution processible material with a thermoelectric figure of merit approaching those of Bi₂Te₃. In this talk, I will discuss both the use of thermoelectric measurements to gain insight to molecular junctions and how this insight translates to design principles for polymer and hybrid thermoelectrics.

5:20pm **EN+NS-TuA11 Semiconductor Nanowire Networks as Thermoelectric Platforms**, *A.J. Lohn**, University of California Santa Cruz, *E. Coleman, G.S. Tompa*, Structured Materials Industries, Inc., *N.P. Kobayashi*, University of California Santa Cruz

Current energy production mechanisms for electrical power and transportation are plagued by inefficiencies which results in most of the energy source being lost as heat. In most cases that heat is found in the form of low-grade heat with temperatures below approximately 200 degrees C. Unfortunately, typical methods such as the Rankine cycle for converting heat to electricity suffer from poor efficiency for low-grade heat. Direct thermoelectric conversion is currently struggling to match the efficiency of the Rankine cycle at high temperatures but offers advantages in terms of reduced maintenance and form-factor which enable energy scavenging in places such as the exhaust line of a vehicle where larger systems could not be implemented.

Dominated by recent progress in nanostructured materials, the unitless thermoelectric figure of merit ZT has been increased to well beyond 1 such that efficiencies are reaching a range which makes them cost effective. Typically thermoelectric materials include elements such as lead or tellurium which are toxic and rare therefore alternative materials are being sought. Recent progress in silicon nanowire thermoelectric has shown a reduction in thermal conductivity, and therefore an increase in ZT of two orders of magnitude, making them viable candidates in the thermoelectric marketplace. Decreased cost and toxicity of silicon as compared to conventional thermoelectric materials make it an attractive candidate but to date nearly all studies on thermoelectricity of nanowires have focused on nanowires in isolation. Our platform based on interconnected 3-dimensional nanowire networks grown directly on metallic substrates provides large area thermoelectric modules capable of scavenging low-grade heat for low cost. The materials properties comprising ZT: thermal conductivity, electrical conductivity and Seebeck coefficient will be discussed for undoped, p-type and n-type silicon nanowire networks with particular emphasis on electrical conductivity and Seebeck coefficient within the temperature range of low-grade heat.

5:40pm **EN+NS-TuA12 Diamond as an Electrode Material for the Direct Conversion of Thermal to Electrical Energy through Thermionic Emission**, *W.F. Paxton, J.L. Davidson, W.P. Kang*, Vanderbilt University

Introduction

Thermionic energy conversion is a candidate technology for the efficient conversion of thermal energy directly to electrical energy. In a thermionic converter, thermally excited electrons are emitted from the surface of a heated cathode into a vacuum gap. These electrons are then collected by a cooler anode and driven through an external load back to the cathode. The thermionic emission current density of a heated cathode can be described by the Richardson Equation (Eq. 1).

$$J = AT^2 e^{-\Phi/kT} \quad (1)$$

where: J: Thermionic emission current density (A/cm²); A: Richardson constant (A/cm² T²); T: Temperature (K); Φ : Material's work function (eV); and k: Boltzmann constant (eV/T)

It can be seen from Eq. 1 that a material with a lower work function, Φ , can achieve higher current densities at lower temperatures than a material with a higher work function, which implies lower work function values translate into better energy converters. Prior attempts to construct efficient thermionic converters were limited by available materials with work function values ranging from 3.5eV to 5eV requiring extreme cathode temperatures in order to achieve useable output power values. In this study, the thermionic emission properties of nitrogen-incorporated diamond films are examined as a potential electrode material to enhance the efficiency of such a device.

Experimental

Polycrystalline diamond films were synthesized on molybdenum substrate via Microwave Plasma-Enhanced Chemical Vapor Deposition (MPCVD). The source gasses were H₂, CH₄, and N₂, microwave power was 1.5KW, and the nominal pressure was 50Torr. Scanning electron micrographs of the samples demonstrated uniform film coverage and a thickness of ~100 μ m.

Thermionic emission characterization was performed in a vacuum environment with a base pressure of 1 x 10⁻⁷ Torr. The diamond films were resistively heated and the temperature was constantly observed by a dual color pyrometer. Electron emission current was collected with an electrically isolated anode biased at a constant voltage of 100V positioned 0.5cm above the heated cathode.

Results and Discussion

Observation of the electron emission current above the noise level began at 600°C and increased exponentially with temperature up to 800°C. Analysis of this data demonstrated agreement with the Richardson equation with a correlation coefficient of 0.99. From this data, the nitrogen-incorporated diamond samples were determined to have a work function value less than 2eV which is considerably lower than previously mentioned materials. These results exhibit diamond's potential as an interesting cathode material for a thermionic energy converter.

Energy Frontiers Focus Topic

Room: 108 - Session EN+TF-TuA

Thin Films for Solar Cells

Moderator: C.A. Wolden, Colorado School of Mines

2:00pm **EN+TF-TuA1 Thin Film Silicon Approaches to Future Generations of PV Materials**, *P.C. Taylor*, Colorado School of Mines

INVITED

Silicon is a material of choice for photovoltaic (PV) applications for several reasons. First, there is perhaps more known about the properties and processing of Si than any other semiconductor due to its prominence in electronic devices. In addition, Si is a non-toxic, abundant element that is potentially inexpensive to produce in large quantities. The major problems with Si for use in future PV applications are the inefficient absorption of light due to its electronic band structure and a fundamental limit on the efficiency of any single junction bulk device due to transmission of photons below the optical band gap energy and loss of energy to heat for photons above the optical gap energy (so-called Shockly Queiser limit). Nanostructured films of Si have the potential to overcome these problems by decoupling the absorption length for photons from the collection length for carriers and by introducing additional optically excited carriers due to the quantum confinement in nanostructured films. The most promising possibilities for more efficiently exciting and collecting carriers include the production of more than one electron-hole pair per absorbed photon for photon energies greater than twice the optical gap energy, the absorption of photons of below gap energies by the introduction of an intermediate band of states within the optical energy gap due to the inclusion of quantum confined structures with the appropriate properties, and the collection of excited carriers before they lose their energy to phonons. Progress in utilizing these mechanisms for dramatically increasing the efficiencies of future PV devices based on Si will be discussed.

2:40pm **EN+TF-TuA3 On the Influence of the Amorphous Silicon Microstructure on the Crystallization Kinetics Towards Polycrystalline Silicon for Solar Cells**, *M. Creatore, K. Sharma, M.C.M. van de Sanden*, Eindhoven University of Technology, the Netherlands

Polycrystalline silicon (poly-Si) is considered to be a promising candidate for thin film PV, coupling the high quality crystalline Si technology with large area and low-cost manufacturing. Our initial studies [1] on poly-Si layers have shown grains extending through the whole thickness (1 μ m) upon solid phase crystallization (SPC) of high growth rate plasma deposited amorphous silicon (a-Si:H) films. Furthermore, larger grains are promoted by an increase in the a-Si:H microstructure parameter R* [2], which represents the order (low R*)/disorder (high R*) in the matrix according to the Si-H bond distribution in mono-/di-vacancies (low stretching mode-LSM) and nano-sized voids (high stretching mode-HSM), and it is quantified by the integrated IR absorption band ratio $I_{HSM}/(I_{LSM}+I_{HSM})$.

The SPC of a-Si:H follows the steps of incubation, nucleation and grain growth. With the purpose of providing insight on the crystallization process, this contribution addresses a detailed crystallization kinetic study of plasma deposited a-Si:H films by means of in-situ X-ray diffraction (XRD). a-Si:H films having R* in the range of 0.05-0.6, with an hydrogen content of 5-14 at. %, were annealed at 600 °C.

* NSTD Student Award Finalist

The medium range order (MRO) of the a-Si:H layers, quantified by the XRD line-width, and representing the most ordered regions in the matrix (up to 15-25 Å from the mono-vacancies), is found to affect the incubation time (t_0), in agreement with [3]: low R^* and high MRO promote a faster nucleation (t_0 in the range of 50-100 min), since the most ordered regions act as nucleation centers; as the structural disorder increases, the MRO decreases and the incubation step is delayed up to 450 min. However, for $R^* > 0.3$ and an hydrogen content above 9%, the incubation time unexpectedly decreases. Therefore, the R^* and the MRO evolutions during the annealing step are studied. High R^* layers, characterized by hydrogen mainly bonded to nano-sized voids, are more prone to hydrogen out-diffusion upon annealing, as inferred by the quantitative decrease of the HSM mode with respect to the LSM mode. The hydrogen evolution is then followed by the rearrangement of the a-Si:H into more ordered regions, as witnessed by the increase of the MRO upon annealing, promoting a decrease in incubation time. In conclusion, next to the established role of the MRO, the nano-sized voids play also a role in the crystallization kinetics, as they affect the overall microstructure and medium range order upon annealing.

[1] Illiberi et al., *Material Letters* **2009**, 63, 1817.

[2] Sharma et al., *Advanced Energy Materials* **2011**, DOI: 10.1002/aenm.201000074

[3] Mahan et al., *Adv. Funct. Mater.* 2009, 19, 2338.

3:00pm **EN+TF-TuA4 Deposition of Microcrystalline Silicon Thin Films by Radio Frequency PECVD using Voltage Waveform Tailoring.** *S. Pouliquen, P.-A. Delatre, E.V. Johnson, J.-P. Booth*, Ecole Polytechnique (Palaiseau), France

This paper shows the feasibility of depositing thin films of hydrogenated microcrystalline silicon ($\mu\text{-Si:H}$) for photovoltaic applications by radiofrequency discharge using voltage waveform tailoring. Contrary to typically used sinusoidal waveforms, the films were deposited using asymmetric voltage waveforms, resembling “peaks” and “valleys”, composed of a fundamental frequency of 15 MHz and three harmonics. Such waveforms lead to an electrical asymmetry effect in the plasma, and a different ion bombardment energy on each electrode. For these experiments, we used a gas mixture of silane diluted in hydrogen (from 1-4%), a total flow rate less than 100 sccm, and a range of pressure from 100 up to 1000 mTorr. We show that the chemical, optical and structural properties - as measured by FTIR, spectroscopic ellipsometry, Raman scattering and profilometry - are strongly determined by the shape of the voltage waveform, and therefore the ion bombardment energy. We observe this effect on the Si-Si bond configuration (microcrystalline vs amorphous peaks in Raman scattering between 480 and 520 cm^{-1}) as well as on the Si-H bond configuration (FTIR peaks at 2000-2100 cm^{-1}). We examine the strength of the effect for varying process parameters, including pressure, total gas flow, voltage amplitude, and SiH_4/H_2 dilution ratio. For the range of parameters used, a growth rate for highly microcrystalline silicon of up to 3 Å/s was achieved without exceeding a pressure of 100 mTorr.

4:00pm **EN+TF-TuA7 Amorphous and Nanocrystalline Silicon Thin Film Photovoltaic Technology on Flexible Substrates.** *B. Yan, A. Banerjee, J. Yang, S. Guha*, United Solar Ovonic LLC **INVITED**

Because of the rapid increase of energy demand and growing concern of environmental impact, renewable energy from photovoltaic (PV) has gained a great deal of attention in the last decade. Various PV technologies have been developed. However, solar panels using conventional crystalline silicon have dominated the market. Thin film silicon is one of the so-called second generation PV technologies. Nowadays, majority of thin film silicon PV products are made with hydrogenated amorphous silicon (a-Si:H) and amorphous silicon germanium (a-SiGe:H) alloy. The advantages of a-Si:H based technology are low cost, capability of large scale manufacturing, abundance of raw materials, and no environmental concerns. One disadvantage of a-Si:H PV technology is its lower efficiency than solar panels made of crystal silicon and compound crystal thin film semiconductors. To resolve the low efficiency issue, significant effort has been made by the researchers. In order to use the solar spectrum effectively, multi-junction structures are normally used by incorporating a-SiGe:H in the bottom cell. In recent years, hydrogenated nano-crystalline silicon (nc-Si:H) has been used as a potential replacement of a-SiGe:H bottom cell in multi-junction structures. The pros of nc-Si:H are its stability under sun light, high photocurrent capability, and no Ge-containing gases required in the process; the cons are thick intrinsic layer that needs high rate deposition and technical challenges for large-area deposition. United Solar has been heavily involved in research and development of a-Si:H and nc-Si:H based PV technology. We have made significant progress in efficiency improvements of a-Si:H and nc-Si:H multi-junction solar cells and modules. We have achieved (i) a 15.4% initial active-area ($\sim 0.25 \text{ cm}^2$) solar cell efficiency, (ii) an NREL measured stable total area ($\sim 0.25 \text{ cm}^2$) efficiency of

12.5%, and (iii) NREL measured initial and stable module ($\sim 400 \text{ cm}^2$) efficiencies of 12.0% and 11.4%, which all set new record efficiencies achieved by a-Si:H, a-SiGe:H, and nc-Si:H multi-junction cell structures. Based on these achievements, we have started working on the development of roll-to-roll manufacturing technology for a-Si:H and nc-Si:H multi-junction structures on flexible substrates. We expect to launch 12% stable aperture area a-Si:H and nc-Si:H product in 2012. In this presentation, we will review the progress made by the community and challenges a-Si:H and nc-Si:H PV technology face.

4:40pm **EN+TF-TuA9 High Efficiency, Large Area Silicon Thin Film Solar Modules.** *L. Li, T. Guo, Y. Meng, Z. Xu, F. Dai, F. Zhang, W. Li, Z. Lei, C. Cai, H. Li, B. Tang, D. Zhou*, ENN Solar Energy Co. Ltd. **INVITED**
Hydrogenated amorphous and microcrystalline silicon based thin film solar cells have long shown great potential for various photovoltaic applications due to its better electricity generation under low light and high temperature, shorter energy payback time and greener manufacturing processes, as well as unique applications for BIPV. However, this technology hasn't fully realized its market potential, as low module efficiencies at mass-production level being one of the major limiting factors. In this paper we report over 9% stabilized module efficiencies in volume production achieved on 5.7 m² substrates from a-Si:H/nc-Si:H tandem junction solar modules, which reflects significant efficiency improvement by process tuning of silicon thin films, back contact, and device structure, etc.. Several application case studies are also reported which demonstrate excellent field performance of ENN silicon thin film solar modules.

5:20pm **EN+TF-TuA11 Metal-Modulated Epitaxy Growth of InGaN/GaN p-i-n Solar Cells.** *B. Gunning, M.W. Moseley, J.E. Lowder, W.A. Doolittle*, Georgia Institute of Technology, *J. Wierer, S. Lee, D. Koleske, Q. Li*, Sandia National Laboratories

InGaN alloys have great potential in the field of photovoltaics due to their excellent light absorption and tunable bandgap (0.7-3.4eV) which spans the visible spectrum. However, the growth of this material remains a challenge due to thermal decomposition, indium surface segregation, and phase separation. To combat these issues, low substrate temperatures and high growth rates must be implemented in combination with in situ surface monitoring via RHEED. Metal modulated epitaxy (MME) has been shown to achieve single-phase InGaN alloys throughout the miscibility gap with sub-nm RMS roughness.

In this study, MME is applied to the growth of n-GaN/i-InGaN/p-GaN solar cells. Unintentionally doped InGaN layers 50/200nm thick with 16% In composition are grown on a 3 μm n-type GaN template. The topmost layer consists of p-type GaN with varying hole concentrations. Transient RHEED signals are monitored closely during InGaN growth to prevent indium surface segregation and ensure a smooth film.

The absorption characteristics are determined as shown in Figure 1, and the material is characterized via AFM, XRD and PL prior to being fabricated into device structures. The InGaN layers are found to be approximately 80% strain relaxed as determined by XRD analysis of the (20-25) reflection (Figure 2). During device testing, the solar cells exhibit low turn-on voltages below the expected value, as well as low external quantum efficiency. These inconsistencies indicate carrier loss due to electrical shorts and defects. The scanning TEM images in Figure 3 show striations in the InGaN layer similar to those in a superlattice structure but with a period that does not correspond to the shutter cycles. Even though the x-ray diffraction indicates predominantly relaxed epitaxy, TEM images are unable to resolve individual threading dislocations. It is not clear at present if this is indicative of extremely large dislocation density or a new method of relaxation related to the above mentioned striations. Finally, post-growth annealing processes are explored as possible ways to improve device performance.

The work at Georgia Tech was supported by Air Force Office of Scientific Research, under a basic science grant managed by Kitt Reinhardt.

Sandia National Laboratories is a multi-program laboratory managed and operated by Sandia Corporation, a wholly owned subsidiary of Lockheed Martin Corporation, for the U.S. Department of Energy's National Nuclear Security Administration under contract DE-AC04-94AL85000.

Exhibitor Technology Spotlight
Room: West Exhibit Hall - Session EW-TuA

Exhibitor Technology Spotlight
Moderator: Langley

3:20pm **EW-TuA5 Selecting the Best Metrology Method for Monitoring Thin Film Deposition, T. Ballinger, Bruker**

This presentation will include a discussion of traditional metrology techniques, in addition to recent innovations in metrology technology for monitoring thin film deposition. Measurement techniques to be discussed include contact methods such as stylus profilometry and non-contact methods such as white light interferometry and confocal microscopy, as well as scanning probe microscopy. A comparison of the various technologies will be provided, as well as the advantages and disadvantages of each metrology method for thin film measurements. This presentation is designed to provide attendees with the information necessary to determine the best metrology technique to monitor thin films below one micron (down to 1 nanometer) and thick films over 10 microns. The hardness, softness or optical properties of the films and substrates will be addressed, on how they can influence the decision in selecting a metrology method for a particular application. Also included in the presentation will be a description of thin film stress and how tensile or compressive stress in the film can adversely affect the film adhesion and cause other defects and product failures if not properly and accurately measured and controlled.

Graphene and Related Materials Focus Topic
Room: 208 - Session GR+MI-TuA

Graphene: Magnetic Properties and Spin-Dependent Phenomena

Moderator: A.C. Ferrari, University of Cambridge, UK

2:00pm **GR+MI-TuA1 Magnetic Impurities on Graphene, K. Kern, Max Planck Institute for Solid State Research, Germany** **INVITED**

Hybrid systems consisting of transition metal (TM) atoms in contact with graphene are expected to show outstanding magnetic effects, from Kondo screening to long range ferromagnetism due to the large Fermi wavelength in graphene. First recent experimental evidence supports this scenario, however, little is known about the nature of the chemical interaction between TM atoms and graphene, which is the necessary starting point for any advanced application. Here we present recent X-ray Absorption Spectroscopy (XAS) and X-ray Magnetic Circular Dichroism (XMCD) experiments probing the electronic configuration and magnetism of Fe, Co and Ni impurities on graphite and various graphenes. We find a rich physical scenario with marked differences between graphite and silicon oxide supported graphene on one hand and few layer epitaxial graphene on the C-face of silicon carbide on the other hand.

2:40pm **GR+MI-TuA3 Electron Spin Transport in Exfoliated and Epitaxial Graphene Grown on SiC, J. Abel, A. Matsubayashi, J.J. Garramone, University at Albany, C. Dimitrakopoulos, A. Grill, Sung, IBM T.J. Watson Research Center, V.P. LaBella, University at Albany**

Graphene is an ideal candidate for the transport channel in future spintronic devices due to its long spin lifetimes at room temperature. The long lifetime arises due to the small intrinsic spin orbit coupling and low hyper-fine interaction of the electron spins with the carbon nuclei. Non-local Hanle measurement devices were fabricated on epitaxially grown graphene on SiC, provided by IBM, and multi-layer exfoliated flakes. Spin injection and detection were achieved in these devices using cobalt nano-magnets directly deposited on the graphene. Spin precession was observed and the spin lifetimes for the epitaxial graphene were found to be comparable to those found in the exfoliated multi-layer flake. We will also present our measurements of spin relaxation as a function of temperature. The temperature dependence in the spin lifetime observed in the exfoliated flake show a coupling between the magnetic contacts and graphene channel. This is expected due to the lack of a tunnel barrier contact. The comparable spin relaxation times measured in epitaxial graphene fabricated with similar contacts and the multi-layer flake is believed to be caused by a large contact induced relaxation due to the contacts coupling with the graphene channel. The strong coupling effectively removes the spin from the channel.

3:00pm **GR+MI-TuA4 Landau Levels of Dirac Fermions Observed at Zero External Magnetic Fields on Modified Graphite by STS, T. Kondo, D. Guo, T. Machida, T. Suzuki, K. Iwatake, S. Okada, J. Nakamura, University of Tsukuba, Japan**

Under the external magnetic field, carriers of graphene are quantized to show an unusual Landau level (LL) energy spectrum due to mass-less Dirac fermions (DFs).¹ The LL energies are not equally spaced and include a characteristic zero-energy state (the $n = 0$ LL) contrary to the case of normal metals or two-dimensional electron gases. As a result, anomalous quantum Hall effect of graphene has been observed.^{2, 3} The quantization of the graphene carrier also occurs without external magnetic field if the appropriate strain is induced.^{4,5} Here, we report spontaneous LLs formation of mass-less DFs on potassium intercalated graphite (K-Graphite) and nitrogen-doped graphite (N-Graphite) under zero external magnetic field with the use of scanning tunneling spectroscopy (STS). On the basis of the calculation with the density functional theory, the top-most graphene layer is found to be decoupled with the graphite due to the partial intercalation of potassium atom or nitrogen-doping on graphite. Partially decoupled graphene layer has a sufficient strain to generate the pseudo-magnetic field with about 280 T and 60 T for K-Graphite and N-Graphite, respectively, leading to the LLs formation on the top-most graphene layer on graphite.

1. A. H. Castro Neto et al., Rev. Mod. Phys. 81 (2009) 109.
2. K. S. Novoselov et al., Nat Phys. 2 (2006) 177.
3. K. S. Novoselov et al., Science. 306 (2004) 666.
4. F. Guinea et al., Nat Phys. 6 (2010) 30.
5. N. Levy et al., Science. 329 (2010) 544.

4:00pm **GR+MI-TuA7 Tunneling Spectroscopy of Adsorbed Iron Phthalocyanine on Epitaxial Graphene on SiC(0001), A.A. Sandin, D.B. Dougherty, J.E. Rowe, North Carolina State University**

Graphene may be an ideal material for spin field effect transistors because of its high charge carrier mobility and long spin relaxation times due to small spin-orbit coupling.¹ However, efficient spin injection into graphene requires overcoming conductivity mismatch through the use of tunnel barriers and/or spin filters.² It is possible that organic films can serve as tunnel barriers/spin filters with highly tailorable properties. In particular, metal phthalocyanines have recently been shown to exhibit spin dependent interfacial coupling on magnetic electrodes.³ A study of the coupling and morphology of such molecules on graphene is a crucial first step to understand potential spin enhanced interfaces.

We deposit monolayer iron phthalocyanine (FePc) on both single layer and bilayer epitaxial graphene on the Si-terminated polar face of SiC, named SiC(0001). Scanning tunneling microscopy reveals an adsorbed molecular lattice periodicity of 1.8 nm, close to that of the graphene/SiC buffer layer corrugation periodicity. This lattice spacing is larger than that of FePc adsorbed on a graphite surface that shows a smaller spacing of ~1.4 nm. This implies a stronger interaction of the FePc with epitaxial graphene than expected and is possibly due to the modification of graphene by the SiC substrate. Tunneling spectroscopy has been used to study the occupied and unoccupied electronic states of the adsorbed monolayer FePc. Broad unoccupied states indicate significant electronic coupling between the molecules and the graphene and suggest a promising future for molecular strategies for spin injection.

*Supported by the NSF Center for Chemical Innovation: Center for Molecular Spintronics under CHE-0943975.

1. Y. G. Semenov, K. W. Kim and J. M. Zavada, Appl. Phys. Lett. 91 (15), 3 (2007).
2. W. Han, K. Pi, K. M. McCreary, Y. Li, J. J. I. Wong, A. G. Swartz and R. K. Kawakami, Phys. Rev. Lett. 105 (16), 4 (2010).
3. C. Iacovita, M. V. Rastei, B. W. Heinrich, T. Brumme, J. Kortus, L. Limot and J. P. Bucher, Physical Review Letters 101 (11), 116602-116604 (2008).

4:20pm **GR+MI-TuA8 Atomic Scale Determination of the Bilayer Graphene Energy Gap, S. Jung, N.N. Klimov, D.B. Newell, N.B. Zhitenev, J.A. Stroscio, NIST**

We have performed scanning tunneling spectroscopy measurements on a gated bilayer graphene device. In graphene bilayer, a potential asymmetry between the layers induces an energy gap in the electron spectrum. The formation of the energy gap is investigated as a function of carrier density and magnetic field. We found that in zero magnetic field, the reliable determination of the gap can be complicated because of disorder scattering. However, in the quantum Hall regime, the energy gap can be quantitatively determined by measuring the layer-polarized low index Landau levels.

Our scanning tunneling spectroscopy measurements reveal that the microscopic nature of the bilayer gap is very different from what was

observed in previous macroscopic measurements or expected from current theoretical models. The potential asymmetry varies spatially in both magnitude and sign on a nanometer length scale, showing strong correlation with the disorder potential. This random pattern of alternating dipole fields is qualitatively consistent with the reduced disorder-induced density fluctuations in the top layer.

4:40pm **GR+MI-TuA9 Atomic, Electronic, and Magnetic Properties of Metal-Graphene Interfaces**, *I.I. Oleynik, L. Adamska, Y. Lin*, University of South Florida, *A. Ross*, Saint Anselm College, *M. Batzill*, University of South Florida

Metal/graphene interfaces play an important role in both surface science studies of the epitaxial growth of graphene on metallic substrates, as well as in metal/graphene contacts in graphene nanoelectronic devices. We present results of first-principles density functional theory (DFT) investigations of structural, electronic, and magnetic properties for graphene/Ni(111) and graphene/Cu(111) interfaces relevant to experimental studies of graphene growth on metallic substrates. The favored interface geometries and binding sites for different interface configurations were identified. Additional adlayers of Ni and Cu were either adsorbed on top of the graphene/metal interface, or placed between the graphene and substrate to model processes of metal intercalation. It was also found that the interaction between graphene/Ni(111) and the top Cu adlayer is much weaker compared to that for a Ni adlayer. The atomic, electronic, and magnetic properties of these interfaces, including induced magnetic moments in graphene/Ni(111), Ni/graphene/Ni(111) systems, are also discussed.

5:00pm **GR+MI-TuA10 Spin-Dependent Scattering from Gated Potential Obstacles in Graphene Systems**, *M. Asmar, S. Ulloa*, Ohio University

We study the scattering of Dirac fermions in a sheet of graphene from potential obstacles created by external gates in the presence of both intrinsic and extrinsic spin-orbit (SO) interactions [1]. Obtaining analytical solutions in a real-space representation for the eigenvectors allows us to calculate the phase shifts generated by a finite-size obstacle in the presence of SO interactions [2]. From the phase shifts extracted from these solutions we can calculate the differential, total and transport cross sections. The knowledge of these quantities allows us to obtain the spin-flip and momentum relaxation times. The dependence of both relaxation times on the strength of the SO interaction was analyzed showing comparable relaxation times for relatively large values of energy, while displaying a big difference for small values of energy. The relaxation times of the injected electrons exhibit a number of resonances in energy associated with the structure of the scattering obstacle. In the presence of SO, new resonances appear at energies that depend on the strength of the SO interactions, and as such contain spectroscopic information on the system. It has been shown that the main scattering mechanism in graphene is due to strong defects [3]. Therefore, the analysis performed in our work can help understand the role of SO interactions in the scattering processes in these and related experiments.

[1] C. L. Kane and E. J. Mele, PRL 95, 226801 (2005).

[2] A. H. Castro Neto and F. Guinea, PRL 103, 026804 (2009).

[3] M. Monteverde, C. Ojeda-Aristizabal, R. Weil, K. Bennaceur, M. Ferrier, S. Gueron, C. Glattli, H. Bouchiat, J. N. Fuchs, and D. L. Maslov, PRL 104, 126801 (2010).

5:20pm **GR+MI-TuA11 Suppression of Weak-Localization Effect in Strained CVD-grown Graphene**, *X. Miao, S. Tongay, M. Lemaire, B.R. Appleton, A.F. Hebard*, University of Florida

We investigate the magnetic field and temperature-dependent transport properties of CVD-grown graphene subjected to different strains. The graphene is transferred to kapton substrates to which a blending force can be applied. In zero magnetic field, the prefactor to the logarithmic-in-temperature conductivity correction decreases by an approximate factor of 3 for strains as high as 0.6 %. There is also a concomitant decrease in diffusivity by a factor of 6. At 5 K we observe negative magnetoresistance for fields up to 0.5 Tesla followed by positive magnetoresistance at higher fields. We attribute the low field negative magnetoresistance to weak-localization and find that it is well described by theory. The strains resulting from the applied blending force inhibit the intervalley scattering more than an order of magnitude and decrease the phase coherence length, thereby leading to a suppression of weak-localization.

5:40pm **GR+MI-TuA12 Simulation of Electron-Ion Dynamics in Pristine and Functionalized Graphene in External Fields**, *S. Bubin, K. Varga*, Vanderbilt University

In the framework of real-time real-space time-dependent density functional theory (TDDFT) we have studied coupled electron-ion dynamics in small

fragments of graphene, graphane, and fluorinated graphene subjected to short (a few femtoseconds) intense laser pulses or irradiated by energetic ions. The goal of this study is to investigate the possibility of defect creation in graphene and desorption of hydrogen/fluorine from graphene surface. We will present the results of our simulations, discuss the mechanisms that take place, and identify the parameters of the laser or energetic ions necessary for those processes to occur.

Graphene and Related Materials Focus Topic
Room: 209 - Session GR-TuA

Graphene on Dielectrics, Graphene Transfer to Novel Substrates

Moderator: A. Turchanin, University of Bielefeld, Germany

2:20pm **GR-TuA2 A Scanning Tunneling Microscopy and Spectroscopy Study of Artificially Modified Bilayer Graphene**, *H. Baek, J. Ha, B. Hwang, J. Kwon*, Seoul National University, Republic of Korea, *J.A. Stroscio*, National Institute of Standards and Technology, *Y. Kuk*, Seoul National University, Republic of Korea

Bilayer graphene has drawn considerable attention due to deviation from Dirac Fermion picture such as anomalous quantum hall effect and a tunable band gap in their spectrum. While a pristine Bernal (AB) stacked bilayer graphene can be synthesized by mechanical exfoliation, growth on a SiC single crystal and epitaxial growth on metal substrates, separate control of the top and the bottom layers has seldom been performed. In this study, artificially modified 2D layers were demonstrated with individually stacked bilayer graphene. Large-area graphene was grown on a Cu foil by chemical vapor deposition (CVD). CVD-grown graphene layers were transferred successively onto insulating substrates with minimum chemical process for realizing bilayer graphene. In this method the mosaic spread between the top and the bottom graphene layers could be varied and an additional thin layer structure could be inserted between the two layers. Artificial bilayer graphene was investigated using scanning tunneling microscopy and spectroscopy. In topographic images and spatially resolved spectrums of local density of states, defect scattering and the misorientation between two graphene layers suggesting weak interaction compared to the AB stacking were found.

3:00pm **GR-TuA4 Dry Transfer of Single Layer Graphene to Polymers**, *E.H. Lock, S.G. Walton, M. Baraket, M. Laskoski, S. Mulvaney, W.K. Lee, P.E. Sheehan*, Naval Research Laboratory (NRL), *D. Hines*, Laboratory for Physical Sciences (LPS), *J.T. Robinson*, Naval Research Laboratory (NRL), *J. Tosado, M. Fuhrer*, University of Maryland, College Park

The ability to grow and transfer large area single-layer graphene is critical from both fundamental and applied points of view. The transfer of large area samples will facilitate fundamental studies of graphene's unique properties. It can also allow for the fabrication of three-dimensional structures, electrically insulated graphene bilayers, graphene on previously unexplored substrates and "curved" graphene with non-trivial geometry. Currently, single layer graphene grown via CVD on metal foils is transferred to other substrates via chemical etching of the foil. The transfer process is time consuming, generates chemical waste, and destroys the foils.

We have developed method for direct dry transfer of graphene grown on Cu foils to polymers. The method relies on the differential adhesion between graphene, the metal foil, and the receiving polymer. A successful print results when the adhesion of graphene to the polymer surface is stronger than its adhesion to the metal foil. Plasma treatment of polymers allowed for the attachment of perfluorophenylazide (PFFA) linker molecule. The transfer printing was performed by placing the PFFA treated polymer surface in contact with graphene covered Cu foil and applying heat and pressure. Then, the polymer substrate with transferred graphene was separated from the Cu foil. In this talk, details of the printing process along with graphene film characterization will be discussed.

This work was supported by the Office of Naval Research. M. Baraket appreciates the NRL/NRC postdoctoral research fellowship.

4:00pm **GR-TuA7 Studies on Ozone Based Atomic Layer Deposition of High-k Dielectrics on Graphene**, *S. Jandhyala, G. Mordji, B. Lee, J. Kim*, University of Texas at Dallas, *P.-R. Cha*, Kookmin University, Korea
Graphene, being a two dimensional material, is one of the most promising alternative channel materials for post-Si generation [1-3]. However, being just one atom thick and having an inert surface, it poses a huge challenge to develop a top-gate dielectric process for graphene-based devices. Several

techniques are currently being explored for depositing dielectrics including physical-vapor deposition (PVD), chemical-vapor deposition (CVD) and atomic layer deposition (ALD) after chemical ‘functionalization’ of graphene (using NO₂ or O₃) or after depositing nucleation layers (such as Al, PTCA, PVA) on graphene [3].

Here, we will present a novel technique developed by our group for depositing ALD high-k dielectrics such as Al₂O₃ on graphene through ozone functionalization [4]. Physisorption of ozone has been claimed to be the plausible mechanism for functionalizing the graphene surface [5]. Based on Langmuir adsorption equation, the amount of ozone adsorbed on graphene can be increased by increasing the partial pressure of ozone. By utilizing this, we have been able to precisely control the dielectric thicknesses and successfully scale dielectrics on graphene down to a thickness of ~3 nm. We employed both AFM on HOPG/graphene and in-situ electrical characterization of graphene-FETs in order to understand the adhesion mechanisms of ozone with graphene, enabling the deposition of ALD dielectrics. For in-situ electrical characterization, we used package-level devices with back-gated graphene devices to detect molecules adsorbed on graphene surface. The observed charge scattering mechanisms and effect on mobility due to the interaction of ozone with graphene as a function of temperature and amount of ozone will be presented. In-situ studies regarding the role of TMA (Tri-methyl Aluminum) will also be discussed based on experiments in actual ALD chambers.

Acknowledgement

NRI-SWAN (Theme # 1464.012) and Korea-US International R/D program by MKE

References

- [1] P. Avouris, Nano Lett. 10 (11), pp. 4285-4294 (2010)
- [2] V. V. Cheianov, et al., Science 315 (5816), pp. 1252-1255 (2007)
- [3] S. K. Banerjee, et al., Pro. of IEEE, 98 (10), pp. 2032-2046 (2010)
- [4] B. Lee, et al., Appl. Phys. Lett., 97 (4), 043107 (2010)
- [5] G. Lee, et al., Jour. Phys. Chem. C, 113 (32), pp. 14225-14229 (2009)

4:20pm GR-TuA8 Fluorine Functionalization of Epitaxial Graphene for Uniform Deposition of Ultrathin High-k Dielectrics, V.D. Wheeler, N.Y. Garces, L.O. Nyakiti, R.L. Myers-Ward, J. Culbertson, C.R. Eddy Jr., D.K. Gaskill, U.S. Naval Research Laboratory

Thermal atomic layer deposition (ALD) is a viable approach to attain high-quality ultrathin dielectric films needed for graphene devices, but the hydrophobic nature of the graphene surface inhibits direct application of thermal ALD oxides. Several methods have been explored to render the surface more susceptible to ALD[1-3], but these techniques often result in graphene mobility degradation and/or shifts in the Dirac voltage due to charge in the gate stack. In this work, we investigated a simple dry chemical approach using XeF₂ to functionalize the graphene surface prior to ALD which results in conformal ultrathin high-k oxides without degradation of the underlying graphene electrical properties. Epitaxial graphene samples were grown on semi-insulating, on-axis (0001) 6H-SiC substrates using an Aixtron VP508 SiC reactor at 1650°C for 120 min. Fluorination of the graphene was performed in a Xactix X₃ etcher operating in pulse mode. Optimum fluorine exposure conditions consisted of six, 20s pulses with constant XeF₂ and N₂ carrier gas partial pressures of 1 and 35 torr, respectively. X-ray photoelectron spectroscopy (XPS) was used to chemically analyze the functionalized surface prior to oxide deposition. ALD Al₂O₃ and HfO₂ films (≤ 15 nm) were deposited at temperatures between 150 - 225 °C using TMA or TEMAHF and deionized (DI) water precursors. Growth was initiated with 20 DI water pulses. Oxide coverage was characterized with atomic force microscopy and scanning electron microscopy, while graphene mobility changes were observed with van der Pauw Hall measurements. Capacitance-voltage (C-V) measurements were conducted on Ti/Au C-V dots to extract the dielectric constant and electrical quality of the oxide. Initial results show that 15 nm conformal, uniform Al₂O₃ and HfO₂ films are obtained with an optimized XeF₂ surface treatment prior to ALD. XPS showed that the optimum XeF₂ treatment resulted in ~6% fluorine on the surface and the presence of only C-F bonds which provide ALD reaction sites needed for uniform oxide deposition. Graphene mobilities were maintained, and occasionally increased, implying little impact of the XeF₂ treatment or ALD oxide on the underlying graphene properties. Raman spectroscopy reveals no change in the D/G ratio after XeF₂ and oxide deposition, verifying that the graphene lattice quality is maintained. The viability of the fluorination method for achieving ultrathin films (<10 nm) will be presented along with electrical C-V data to show the electronic quality of the ALD oxides.

1. Robinson, et al. *ACS Nano* **4**(5) 2667 (2010)
2. Farmer, et al. *Nano Letters* **9**(12) 4474 (2009)
3. Lee, et al. *ECS Transactions* **19**(5) 225 (2009)

4:40pm GR-TuA9 Improving Performance of CVD Graphene Field Effect Transistors by Reducing Water Trapped at the Graphene/Substrate Interface, J. Chan, A. Venugopal, A. Pirkle, S. McDonnell, D. Hinojos, The Univ. of Texas at Dallas, C. Magnuson, R.S. Ruoff, The Univ. of Texas at Austin, L. Colombo, Texas Instruments Inc., R.M. Wallace, E.M. Vogel, The Univ. of Texas at Dallas

Graphene grown by chemical vapor deposition (CVD) provides a promising pathway for large area fabrication of graphene field effect transistor (FET). However, the performance of CVD graphene FETs reported to date is poorer than FETs fabricated using exfoliated graphene. CVD graphene FETs often exhibit strong hysteresis accompanied with low mobility, large positive Dirac point (V_{Dirac}) and large intrinsic carrier concentration. CVD graphene is exposed to a number of aqueous solutions and deionized water when it is transferred to a device substrate. We find that the large V_{Dirac} shift and strong hysteresis observed in CVD graphene FET are largely due to water trapped in the graphene/substrate interface during the transfer process.

In this study, CVD graphene grown on copper is transferred to SiO₂ substrates with the following three interfacial conditions: i) normal hydrophilic SiO₂, ii) SiO₂ with 20nm of Al₂O₃, and iii) a hydrophobic surface prepared by coating hexamethyldisilazane (HMDS). Device performance, including mobility, V_{Dirac} and intrinsic carrier concentration are compared in ambient as well as in vacuum. Gate hysteresis is analyzed by measurement of time-resolved channel resistance at various back-gate bias voltages. We find that the gate hysteresis is partially reduced by transferring the graphene onto a substrate coated with HMDS. Vacuum pump down and low temperature (80 °C) annealing can remove the remaining gate hysteresis and V_{Dirac} shift. The resulting hole mobility is 5,420cm²/Vs, which is high compared to most of the CVD graphene mobility values reported in the literature.

As a control experiment, the CVD graphene FET fabricated on untreated SiO₂ shows a smaller mobility, a larger V_{Dirac} and a stronger hysteresis compared to the HMDS coated sample. Under vacuum the hysteresis is reduced but remains significant. We believe the remaining hysteresis is due to adsorbates trapped at the substrate/graphene interface. A graphene FET prepared on a substrate with an Al₂O₃ interface shows less hysteresis than the sample fabricated on an untreated SiO₂ surface but more than that of the HMDS coated surface. In order to study the influence of water trapped between the graphene and the substrate, water is intentionally replaced by isopropanol at the end of the transfer process before drying. In samples prepared using this method, hysteresis and V_{Dirac} point shift are both reduced. These results indicate that efforts to prevent trapping of water molecules at the graphene/substrate interface during the transfer process will improve the performance of CVD graphene FETs.

This work was supported by the NRI SWAN center, ONR, NSF and Sandia's LDRD program.

5:00pm GR-TuA10 Improved Performance of Top-Gated Graphene-on-Diamond Devices, A.V. Sumant, Argonne National Laboratory, J. Yu, G. Liu, A. Balandin, University of California, Riverside

Since the discovery of graphene and realization of its exceptional electronic properties in suspended form, there have been many efforts in fabricating FET-type devices based on single and bilayer graphene on SiO₂ substrate. However, performance of these devices is found to be inferior to the expected intrinsic properties of graphene. It has been observed that apart from carrier mobility in graphene, which is sensitive to trapped charges, and surface impurities at the graphene-oxide interface, breakdown current density in graphene depends sensitively on the heat dissipation property of the underlying supporting substrate. Although graphene has extremely high intrinsic thermal conductivity, it is reported that in graphene devices, more than 70% of the heat dissipates through the 300 nm SiO₂ on silicon directly below the active graphene channel while the remainder is carried to the graphene that extends beyond the device and metallic contacts. Such a distribution of heat in to the substrate cause undesirable effects on the overall performance of the device. We show for the first time that by the use of thin CVD-grown ultrananocrystalline diamond thin films on silicon in graphene-on-diamond configuration, the heat dissipation can be improved substantially leading to the higher breakdown current density of more than 50% as compared to conventional graphene-on-oxide substrates. We also describe the fabrication of the top-gate graphene-on- diamond devices and discuss their performance. The obtained devices had the carrier mobility ~ 2354 cm²V⁻¹S⁻¹ for holes and ~1293 cm²V⁻¹S⁻¹ for electrons. The obtained results are promising for developing high-performance graphene-on-diamond devices and interconnects for future electronics.

Use of the Center for Nanoscale Materials was supported by the U. S. Department of Energy, Office of Science, Office of Basic Energy Sciences, under Contract No. DE-AC02-06CH11357. The work in Balandin group at UCR was supported, in part, by DARPA – SRC Center on Functional Engineered Nano Architectonics (FENA).

5:20pm **GR-TuA11 Growth of Turbostratic Graphene on Sapphire.** *S. Rothwell, P.I. Cohen*, University of Minnesota, *M. Kumar*, National Physical Laboratory, India

Large area turbostratic graphene was grown on the (0001) plane of sapphire by thermal decomposition of acetylene. Sapphire is an attractive substrate since it has a symmetry match and close coincidence lattice match to graphene. It is a good insulator, appropriate for electronics applications, and large single crystal wafers are readily available. We have found that only after overcoming nucleation barriers, high quality graphene can be grown directly on sapphire without transfer. The sapphire was first heated to about 1400 C to obtain a reconstructed sqrt 31x31 R9 surface structure. The reconstruction was monitored in real time via reflection high energy electron diffraction, which was possible due to the low Debye-Waller factor. After obtaining a clean reconstructed surface, the sample was cooled to near room temperature and exposed to 10 Torr of acetylene. The sample was then heated to 1400 C in the presence of acetylene, in order to nucleate growth. At these pressures, sufficient acetylene coverage for growth was maintained during the ramp to high temperatures. Continued exposure to acetylene at 1400 C did not result in further growth. We speculate that at high temperature there is not sufficient residence time for incorporation, thus lower temperature is needed for further growth. Controlling pressure and temperature during a cool down phase becomes the fine control for film thickness. For example, 10 nm thick graphene samples were obtained by cooling in 1 - 7 E-7 Torr of acetylene. Transmission electron diffraction showed very sharp, nearly continuous rings, indicating large domains and no preferential azimuthal rotation between planes. X-ray diffraction showed an increased layer separation of 0.345 nm compared to graphite. Electron energy loss spectroscopy showed bulk-like plasmons or interband transitions, indicative of multilayer graphene. Raman spectra showed 2D/G peak intensity ratios of 0.5 to 1, comparable to literature values for turbostratic graphene. The spectra also exhibit the expected broader highly symmetric 2D peak. Thicker films could be easily lifted from the substrate. Films greater than 100 nm thick exhibited macroscopic ripples while 10 nm thick films were flat. Hydrogen was explored as a means to control growth but was found to rapidly etch graphene and to passivate the room temperature reconstructed sapphire surface. The growth was modeled with a simple rate equation analysis. These results offer a route to large area graphene grown directly on single crystal sapphire wafers.

Partially supported by the University of Minnesota IREE and by the National Physical Laboratory, India

5:40pm **GR-TuA12 Scanning Tunneling Microscopy and Nanomanipulation of Graphene-Coated Water on Mica.** *J.D. Wood, K.T. He, E. Pop, J.W. Lyding*, University of Illinois at Urbana Champaign

Graphene on ultraflat substrates such as hexagonal boron nitride has shown to suppress charge puddle formation and give high carrier mobility [1,2]. Transfer of graphene to other ultraflat substrates such as muscovite mica might bring about similar transport characteristics. To that end, we place graphene on mica for scanning tunneling microscopy (STM) studies. We grow monolayer graphene on Cu by chemical vapor deposition and support it with polymethyl methacrylate (PMMA). We clean the film with water baths and transfer it to mica. In contrast to previous atomic force microscopy (AFM) experiments of dry-transferred exfoliated graphene on mica [3,4], our graphene films trap multiple water layers. After a 700 °C *in situ* degas, we achieve atomic resolution of graphene on water on mica, and we notice that there are at least 3 layers of ordered, bound water on mica [5], due to the wet transfer and the highly hydrophilic mica. We can atomically image graphene monolayers, bilayers, and grain boundaries regardless of the underlying water structure. Additional water layers on top of the bound water are rough, weakly bound, and amorphous. We notice up to 5 layers of graphene-encapsulated water on mica. Using the STM tip, we can nanomanipulate these amorphous layers at high tunneling conditions (>6 V, 1 nA). These water patterns are highly stable, invariant after several days of scanning. Water nanomanipulation under graphene could help elucidate water's complex bonding structure and charge transfer from graphene to encapsulated species. Further, graphene-coated water can assist in STM-based research of other aqueous-suspended nanostructures.

[1] Xue *et al.*, *Nature Mat.* **10**, 282 (2011); [2] Dean *et al.*, *Nature Nano.* **5**, 722 (2010); [3] Xu *et al.*, *Science* **329**, 1188 (2010); [4] Lui *et al.*, *Nature* **462**, 339 (2009); [5] Park *et al.*, *Phys. Rev. Lett.* **89**, 85501 (2002).

Helium Ion Microscopy Focus Topic
Room: 106 - Session HI+AS-TuA

Basics of Helium Ion Microscopy

Moderator: A. Gölzhäuser, University of Bielefeld, Germany, V.S. Smentkowski, GE-GRC

2:00pm **HI+AS-TuA1 Principles of Helium Ion Microscopy.** *J.A. Notte, L. Scipioni, L.A. Stern*, Carl Zeiss NTS **INVITED**

The Helium Ion Microscope (HIM) consists of an interesting blend of long established technologies and recent state of the art engineering designs that enable superior charged particle scanning microscopy capabilities. They are capable of providing sub-nanometer spatial resolution with remarkable surface information and a unique ability to image insulating samples. HIMs share many similarities with Scanning Electron Microscopes (SEMs), but also embody new principles that uniquely differentiate HIM hardware and applications from traditional SEMs.

The most significant hardware difference of the HIM compared to SEM is the ion source. On the macroscopic scale the source appears very similar to a standard electron field emission source. However, the detailed tip geometry allows for much higher electric fields to be produced in the vicinity of the tip than what is found in traditional SEM field emission sources. The higher field enables ionization of the neutral helium gas which surrounds the tip, producing the needed helium ion beam. In addition to the high electric field requirement, it is necessary to keep the tip and surrounding imaging gas at cryogenic temperatures. The implementation of source cryogenics while operating the tip at ~ 35 keV, and also maintaining mechanical motion for both source translation and tilting, introduces significant engineering challenges in the design of a HIM.

Due to fundamental differences between helium ion and electron interactions with the sample under observation, the HIM is capable of producing images that are significantly different from those produced by traditional SEM. Since the entire electron population created due to an incident helium ion is of very low energy, only those electrons near the point of helium incidence are capable of escaping from the sample, resulting in images that are rich with surface information and possess superior spatial resolution. Due to the much higher secondary electron yield associated with helium bombardment of a sample relative to electron bombardment, and the fact that the incoming particles are positively charged, the net charge state of the sample is always positive, unlike the SEM case. Furthermore, due to the strong affinity of a helium ion to capture an electron, the net charge on the sample always exists as a surface charge. The positive surface charge can be easily neutralized with an electron flood gun, thus enabling charge free imaging on highly insulating samples. These various unique imaging principles make the HIM a versatile and unique imaging instrument.

2:40pm **HI+AS-TuA3 Design and Performance of a Near Ultra High Vacuum Helium Ion Microscope.** *R. van Gastel*, University of Twente, The Netherlands, *L. Barriss, J.A. Notte, Carl Zeiss NTS, G. Hlawacek*, University of Twente, The Netherlands, *L. Scipioni, A.P. Merkle, D. Voci*, Carl Zeiss NTS, *C. Fenner*, L'Vestus Energy Inc., *H. Zandvliet, B. Poelsema*, University of Twente, The Netherlands

The advent of He Ion Microscopy (HIM) as a new technique to image materials and microstructures has enabled a new look at materials that is based on the interaction of swift light ions with matter, as opposed to that of more commonly used high (and low) energy electrons [1]. Initial Carl Zeiss Orion® He Ion Microscope instruments have demonstrated high-resolution imaging, combined with great surface sensitivity, the ability to neutralize charge very efficiently, and with enhanced materials contrast when ion induced secondary electrons are used for imaging. The use of Rutherford backscattered ions to form images has provided a new imaging modality that emphasizes differences in elemental composition and it can also be used to probe samples in-depth.

The HIM provides obvious benefits in terms of novel modes of contrast, surface sensitivity, lateral resolution, depth of field and charge compensation. To achieve ultimate performance, the chamber vacuum of the existing platform may be improved. For instance, carbon deposits due to beam interaction are readily seen due to the surface sensitivity of the technique. At sufficiently high current densities the sharply focused He ion beam may very efficiently decompose or cross-link residual hydrocarbons that are present in the instruments vacuum, more so than an electron beam in a SEM setup. Not only can this obscure a clear view of the sample, thereby negating the benefits of the small spot size, it also limits the available acquisition time for spectroscopic measurements. In addition to this, some materials (Au in particular) have yielded unexpectedly high

sputtering rates. On the one hand, this has proven extremely useful in the field of nanopatterning for sensors, plasmonics or other device fabrication applications at the sub-10nm level when operating at high doses. On the other hand, it is undesirable when the instrument is used for materials characterization.

In this presentation we will discuss the basic considerations that went into the design of a Near-UHV (NUHV) Orion Plus® He Ion Microscope. We will detail how the improved vacuum level is anticipated to alter those processes that are directly relevant to the imaging performance of the instrument such as beam interaction in the surface region and the emission of secondary electrons. First applications that the instrument was used for will be highlighted and its impact in the areas of surface physics, notably catalysis, corrosion, and other research areas that require increased imaging sensitivity, both laterally and in depth, will be discussed.

References

[1] B. Ward, J. Notte, and N. Economou, *J. Vac. Sci. Technol.* 24, 2871 (2006).

3:00pm **HI+AS-TuA4 Sub-10 nm Scanning Helium Ion Beam Lithography**, K. van Langen, E.W.J.M. van der Drift, Delft University of Technology, Netherlands, E. van Veldhoven, D.J. Maas, TNO, Netherlands, P.F.A. Alkemade, Delft University of Technology, Netherlands

Since the launch of the novel sub-nanometer helium ion microscope by Zeiss / Alis in 2006 nanofabrication with this tool has gained a lot of interest [1]. Key characteristic in this matter is the directional interaction of the helium ion with matter with negligible backscattering. In ion milling it enables very steep structuring when compared to the Ga⁺ ion equivalent [2]. In a similar comparison helium ion beam-induced deposition in a precursor gas ambient yields tall and smooth nanostructures [3], partially also because the sputtering by helium ions is at least an order of magnitude lower than by gallium ions.

The present contribution deals with scanning helium ion beam lithography (SHIBL). Thusfar two initial SHIBL studies on hydrogensylsesquioxane (HSQ) resist were reported [4,5]. In the present work performance of SHIBL is compared with state-of-the-art electron beam lithography (EBL). As resist materials we explored HSQ, polymethylmethacrylate (PMMA), and the inorganic resist of aluminumoxide. The latter material choice is motivated by the need for enhanced mask selectivity in pattern transfer in the sub-10-nm area.

The results for HSQ and PMMA can be summarized as:

- smallest feature size of 5 nm, equivalent to the best EBL performance [6]
- clear pattern densities up to 10 nm full-pitch, which is better than in EBL
- sensitivity 1-2 orders of magnitude better than in EBL.

As for the inorganic resist, 5-nm features have been realized.

In a semi-quantitative and comparative approach the results will be explained and future prospects will be outlined.

1 R. Hill, F.H.M. Faridur Rahman, *Nucl. Instr. and Meth. A* (2010), doi:10.1016/j.nima.2010.12.123, in press

2 L. Scipioni, D. C. Ferranti, V. S. Smentkowski, R.A. Potyrailo, *J. Vac. Sci. Technol. B* (2010) 28: C6P18

3 P. Chen, E. van Veldhoven, C.A. Sanford, H.W.M. Salemink, D.J. Maas, D.A. Smith, P.D. Rack, and P.F.A. Alkemade, *Nanotechnol.* (2010) 21: 455302

4 V. Sidorkin, E. van Veldhoven, E. van der Drift, P. Alkemade, H. Salemink, D. Maas, *J. Vac. Sci. Technol. B* (2009) 27: L18

5 D. Winston, B.M. Cord, B. Ming, D.C. Bell, W.F. DiNatale, L.A. Stern, A.E. Vldar, M.T. Postek, M.K. Mondol, J.K.W. Yang, K.K. Berggren, *J. Vac. Sci. Technol. B* (2009) 27: 2702

6 H. Duan, D. Winston, J.K.W. Yang, B.M. Cord, V.R. Manfrinato, and K.K. Berggren, *J. Vac. Sci. Technol. B.* (2010) 28: C6C58

4:00pm **HI+AS-TuA7 Contrast Performance in Helium Ion Microscopy**, D.C. Bell, Harvard University **INVITED**

In order to achieve ultra high resolution imaging with secondary electron imaging, it is critical that the electric potential of the specimen surface is well controlled. For electrically conductive samples this can be achieved by simply grounding the specimen. However, imaging of electrically insulating specimens can provide challenging or impossible to image due to uncompensated charge resulting from the electron or ion beam interaction with the specimen surface. The main reason for the uncompensated charge is that the insulating specimen has insufficient conductivity through

mobility of either electrons or holes to quickly restore the neutrality of the scanned area. The buildup charge causes significant deflection and distortion of the ion or electron beam. Which is more appropriate, to use charge compensation with high kV helium ions or employ a low kV SEM image to obtain the required surface information? This paper will present a systematic examination of the surface information provided by both techniques, including SEM charge compensation mechanisms.

One key advantage of the Helium Ion Microscope technology in the case of imaging highly charging specimens is the electron flood gun can be utilized to neutralize the positive charge buildup and facilitate high-resolution imaging. A flood gun is used to charge the surface to a negative potential (using electrons as the neutralizing particles). When utilizing the electron flood gun, the electron beam and He ion beam are synchronized and adjusted with respect to one another, so that the low energy electrons are not interfering with the secondary electron imaging.

Some of our research from the past year has been surprising and may provide a foundation for a change in analysis techniques of different materials. The nature of the Helium ion beam interactions with the sample shows enhanced edge contrast which is especially useful for critical dimension measurements; one particularly interesting development is the imaging of non-conducting materials showing a contrast due to three apparent mechanisms simultaneously - atomic number, channeling contrast and a possible enhanced edge contrast. The advantages of Helium ion microscopy is still being investigated and still are proving some exciting results.

5:00pm **HI+AS-TuA10 Helium Ion Beam Induced Deposition Examined using a 3D Monte Carlo Simulation**, D.A. Smith, P.D. Rack, University of Tennessee Knoxville, P.F.A. Alkemade, H. Miro, Delft University of Technology, The Netherlands

The growth of nanostructures has traditionally been dominated by electron beam induced deposition (EBID) or gallium ion beam induced deposition (Ga-IBID). While EBID provides smooth sidewalls and good resolution for nanopillar growth, the cross-section for dissociation is low and etching is difficult as sputtering is negligible. Ga-IBID is a relatively faster method of producing nanostructures, however it suffers from lower resolution, alters deposited materials, and leaves an etching residue. A new tool in this field has been recently explored: the helium ion beam microscope. This tool has been modified to perform IBID using high energy helium ions. It has been found that He-IBID combines the high resolution of EBID with the speed of Ga-IBID. Moreover, there is less implantation damage and minimal sputtering compared to Ga beams.

To examine this process, a 3-dimensional Monte Carlo simulator has been designed based ion-solid-precursor interactions. This simulation system, named EnvisION, can provide useful knowledge of how user-controlled parameters can be optimized for highly efficient growth of nanostructures using this tool. In this work, an in-depth explanation of the simulation will be presented, including an example of its use examining the growth efficiencies of nanopillars grown on a silicon substrate using the (CH₃)₃Pt(CpCH₃) precursor via He-IBID. Furthermore we compare how the morphology changes with dwell times, refresh time, precursor coverage and surface diffusion in order to span the range of growth regimes from mass-transport limited to reaction-rate limited deposition. The simulated morphologies predicted using the EnvisION simulator are compared to experimentally grown pillars to validate the simulation.

5:20pm **HI+AS-TuA11 TEM Specimen Preparation with Light Ions**, L. Giannuzzi, L.A. Giannuzzi & Associates LLC

Much research with light energetic ions such as He⁺ and Ne⁺ from gas field ionization sources has focused on imaging and nano-machining. It is a natural progression to question to the viability of TEM specimen preparation using these light ions. Of vital importance for TEM specimen preparation quality is the understanding of surface ion implantation and amorphization damage. Theoretical calculations using SRIM indicate that there may be a damage trade off between vacancy formation, ion range, and dose. That is, the range of light ions is much greater than conventional heavy ions (e.g., Ga⁺), and can indeed penetrate directly through a TEM specimen. While this may indicate the possibility of light ions damaging the entire TEM specimen thickness, light ions produce far less vacancies per ion compared to heavy ions for the same dose. However, since the sputter yield of light ions is smaller than heavy ions, a larger dose of light ions may be necessary to achieve sufficient material sputtering. This theory will be supplemented with experimental results.

5:40pm **HI+AS-TuA12 The Possibilities of the HIM for Imaging and Nanopatterning of EUVL Masks**, *D.J. Maas, E. van Veldhoven, N.B. Koster*, TNO, Netherlands, *P.F.A. Alkemade, E.W.J.M. van der Drift*, Delft University of Technology, Netherlands

Although Helium Ion Microscopy (HIM) was introduced only a few years ago [1], many new application fields are emerging. Key issue is the directional interaction of the primary helium ion beam with the sample at and just below its surface with negligible backscattering. The sub-nanometer sized probe of the 10-35 keV ion beam generates Secondary Electrons (SEs) that have a typical energy between 0 and 20 eV. Taking all together the SE signal stems from an area that is very well localized around the point of incidence of the primary beam. This makes the HIM well-suited for both high-resolution imaging as well as high resolution nanofabrication [2]. We explore the possibilities to use the HIM simultaneously for imaging and nano patterning of EUVL masks.

The HIM is a high-resolution surface imaging tool. In practice, the optimum dose for imaging is a balance between maximizing S/N ratio, while minimizing sample damage. Imaging work at TNO van Leeuwenhoek Laboratory (VLL) [3] focuses at sensitive materials such as e.g. DUV and EUV resists and EUV masks, which are difficult to image in a SEM due to their charging behavior. An electron flood gun in the HIM offers effective charge cancellation, which enables high-resolution imaging of insulation structures and for pin pointing defects on a EUV reticle. In this presentation we will show images of particles down to 5 nm on reticles.

Furthermore, to explore the possibilities of the helium ion microscope as a nanofabrication tool, the HIM at the TNO VLL is equipped with a pattern generator and a gas injection system (GIS). This presentation will show our latest nano structuring results made with Helium Ion Beam Induced Processes: deposition and etching. It is expected that the unique capabilities of the HIM in combination with the GIS are suited for EUV mask repair. These capabilities offer the possibility of circuit repair in the latest and smallest semiconductor technology nodes (beyond 22 nm). In both cases sub-surface damage due to scattered He ions is a matter of concern and topic of investigation. At this moment we are capable of etching 13 nm lines with 25 nm spacing on a EUV dummy mask with approximately 80 nm of TaN absorber. Furthermore we demonstrate Pt deposited lines of 13 nm width at a 16 nm spacing.

References

- [1] J. Morgan, J. Notte, R. Hill, and B. Ward, *Microscopy Today* 14, (2006) 24
- [2] D.J. Maas et al., *Proc. SPIE Vol. 7638, 763614* (2010) 1-8
- [3] <http://www.vanleeuwenhoeklab.com/>

Nanomanufacturing Science and Technology Focus Topic

Room: 207 - Session NM+NS+MS-TuA

Manufacturable Nanoscale Devices and Processes

Moderator: R. Maboudian, University of California at Berkeley, R. Mu, Fisk University

2:00pm **NM+NS+MS-TuA1 Assessing Nanotechnologies for Volume Manufacturing**, *B.E. Goodlin, S. Butler, L. Colombo, R. Doering*, Texas Instruments Incorporated **INVITED**

Over the past several years, we have seen significant advances in nanotechnology. Much of the underlying purpose of "nanotechnology" research and development, at least as it applies to the electronics industry, is to revolutionize mainstream technology through the use of unique properties and capabilities of nanomaterials, like Si nanowires, graphene, CNTs, in an effort to provide advantages that could not be otherwise obtained thru evolutionary technology scaling. However, the ultimate goal of adopting such technologies into volume manufacturing will most certainly rely on the same tried and tested principles that govern adoption for mainstream manufacturing. Such principles include: performance (does the process hit the desired target?), cost (is it more/less costly as compared to alternatives?), capability (how reproducible is the process?), throughput (how many product can be produced and at what rate?), yield/defectivity, reliability, controllability/metrology (can the process be controlled and what measurements are needed?), maintainability (is equipment/process required easy to maintain?). Do these same governing manufacturing principles truly apply for nanotechnologies? If so, how do some of the current nanotechnologies fare? What gaps exist? Is sufficient focus being applied to address these gaps? Can we even provide adequate answers to these questions yet? Prior to addressing these questions, one must first step back and clearly identify the important, unique requirements (process, materials,

equipment) that exist for a given nanotechnology to enable delivery of the desired performance. Also, one must consider interactions and compatibility of the processes with upstream and downstream processes that are necessary for the final product. Have such requirements and interactions been thought out clearly for various nanotechnologies? If so what are the requirements? What are the interactions? This talk will seek to investigate answers to these questions in an effort to assess various emerging nanotechnologies and their capabilities for eventual adoption into volume manufacturing.

2:40pm **NM+NS+MS-TuA3 Material and Tool Design Challenges for Taking ALD to High-volume Production Beyond 30nm Node**, *B. Lu, Z. Karim, S. Ramanathan*, AIXTRON Inc. **INVITED**

Atomic Layer Deposition enables conformal coating of high-quality thin film on complex nano-scale structures. It has been the preferred choice of deposition technology for high-k and metal films in high-aspect ratio capacitor structure for memory applications. Maintaining 25 fF/cell in sub 30nm DRAM devices poses multiple challenges: (a) structural - very high aspect ratio (~100:1) capacitor cell structures and (b) material - the need for advanced Hi-k oxides beyond ZrO₂, which are typically multi-component oxides. Chemical precursors for a majority of the promising new high-k materials are typically low vapor-pressure liquids or even solids. Achieving excellent composition control inside these high aspect ratio structures using low vapour pressure precursors is a significant challenge. These challenges are pushing ALD technology to its limit and are testing its production-worthiness for high volume manufacturing of sub 30nm devices. Innovative technology in precursor delivery, reactor design, and platform architecture are required to overcome these challenges. This presentation will discuss the new developments in equipment design to meet the technology needs as well as practical manufacturing targets (such as throughput and cost of ownership) in order to provide a production-worthy ALD solution. Applications in new high-k oxide (La/Sr/Ba oxides), metals, and PCRAM materials (such as GST) will be discussed.

4:00pm **NM+NS+MS-TuA7 The Metal-Oxide-Metal Vacancy Drift Memristor - A CMOS Compatible, High Speed, Non-Volatile Switch for Universal Memory and Storage**, *R.S. Williams, J.P. Strachan*, Hewlett-Packard Labs **INVITED**

The existence of the fourth passive circuit element was proposed by Prof. Leon Chua of UC Berkeley in 1971 from fundamental symmetry arguments to augment the familiar resistance, inductance and capacitance equations. Although he showed that such a 'memristor' had many interesting and useful circuit properties, until 2008 no one knew if such a circuit element existed or not. In fact, researchers had been making and studying memristors for decades without knowing it - examples are resistive RAM devices, STTRAM devices and phase change memory devices. At HP, we have focused primarily on metal-oxide-metal bipolar resistive switches. Memristance arises naturally in these systems via coupling of electronic and ionic transport in thin semiconducting metal-oxide films under an external bias voltage. Simple analytical models show that memristance becomes much more important as the thickness of the active device region decreases, and thus memristors are mainly nanoscale structures. Memristor theory serves as the foundation for understanding a wide range of hysteretic current-voltage behavior, including both unipolar and bipolar switching, observed over the past 50 years. We have built nanoscale titanium dioxide and tantalum pentoxide memristors in our laboratory and have demonstrated both their fundamental electrical properties and several potential uses. They can be integrated into electronic circuits using conventional fabrication techniques and materials available in standard CMOS fabrication facilities. I will discuss recent results on such topics as device switching speed, endurance, measurements required to parameterize a physics-based SPICE model, and 3D stacking of memristive crossbars.

4:40pm **NM+NS+MS-TuA9 Large Scale Graphene: Progress and Challenges**, *R.S. Ruoff*, The University of Texas at Austin **INVITED**

Graphene-based materials hold promise due to their electronic and thermal transport properties, mechanical properties, high specific surface area, and that they can act as an atom thick layer, barrier, or membrane. Here, I focus on growth of large area graphene on metal substrates and the structure and thermal and mechanical properties of such graphene. A history of experimental work on graphene (from its discovery in 1969 until 2010) is provided at:

<http://bucky-central.me.utexas.edu/>

Support of our work by The WM Keck Foundation, DARPA, ONR, SWAN NRI, NSF, ARO, AEC, and Graphene Energy, Inc., is appreciated.

5:20pm **NM+NS+MS-TuA11 Laser-Assisted Electron-Beam Induced Deposition and Etching**, *N.A. Roberts*, University of Tennessee and Omniprobe, Inc., *J.D. Fowlkes*, Oak Ridge National Laboratory, *P.D. Rack*, University of Tennessee and Oak Ridge National Laboratory, *G.A. Magel*, *H.M. Marchman*, *C.D. Hartfield*, *T.M. Moore*, Omniprobe, Inc.

Focused electron-beam induced deposition (EBID) and etching (EBIE) are direct-write nanofabrication techniques that allow localized deposition or etching of materials without the need for resists. These deposition and etching processes are controlled by electron-beam dissociation of a precursor gas. In both cases, by-product species are created, and if the unwanted byproduct is not desorbed from the surface it will be incorporated into the deposit or reduce the etch rate for deposition and etching, respectively. Substrate heating has been used in experiments to enhance desorption by reducing the residence time of the by-product. The substrate heating has the same impact on the residence time of the precursor gas and therefore reduces the growth or etch rate of the process. *Ex situ* treatments of deposits have also been investigated to remove impurities with some success, but these treatments result in void formation and shape changes. *In situ* laser processing at short pulse widths is ideal for electron-beam induced processing because desorption of the by-products can be achieved by local heating of the sample, but the narrow pulse width results in a short heating time and cooling time. Thus the by-products can be effectively desorbed and adequate recovery time for fresh reactant to re-adsorb.

Laser-assisted EBID and EBIE processes are made possible through the use of the OptoProbe™, which is an optical imaging and processing system that can be attached to an SEM and used in conjunction with an appropriate gas injection system. The design of this port-mounted optical accessory enables simultaneous optical imaging and delivery of laser irradiation to a sample within the SEM, without interfering with normal SEM/FIB imaging and processing modes. The optical system is mounted on a 3-dimensional nanomanipulator so that precision alignment and focusing is easily achieved. For this work, the OptoProbe™ has been optimized to deliver a high-irradiance near-infrared laser spot to provide localized time-dependent sample heating for enhancing focused electron-beam induced deposition and etching. In this presentation, we will discuss recent experimental results as well as modeling of laser-assisted EBID of Au and EBIE of SiO_x using XeF₂.

5:40pm **NM+NS+MS-TuA12 Channel SiGe Selective Epitaxy Process for DRAM High K Peripheral Transistors**, *J. Yeo*, *H. Hwang*, *S. Lee*, *W. Yoo*, *S. Ahn*, *I. Jeon*, *B. Kim*, *S. Nam*, *S. Kim*, *K. Jung*, *J. Lee*, *S. Jang*, *T. Lee*, *K. Huh*, *S. Yamada*, Samsung Electronics Co., Ltd, Republic of Korea
As the DRAM technology evolved towards the sub 2x era, the need for high performance transistor grows higher for the DRAM peripheral transistors. The novel technologies such as embedded SiGe, high K gate oxide, or 3-dimensional transistor technologies are indispensable in a near future. Especially, to scale the gate oxide further and to meet the gate oxide leakage constraint at the same time, high K gate dielectrics should be adapted. For a successful application of high K dielectrics to DRAMs, it is essential to realize the effective work-function (EWF) for both n, pMOSFETs, where this EWF should be maintained even after huge back-end thermal budget of DRAM process. Therefore, so called 'gate-first approach' has been examined, i.e. LaO, or MgO capping layers for NMOS [1,2], and AlO capping layer, F implantation, and ion implantation on metal for PMOS [2,3], respectively. A SiGe channel has been also examined by many research groups [4-7]. When SiGe epitaxial layer is introduced to the PMOS channel, interface trap density (D_{it}) has been increased by order of magnitudes, which consequently results in the degradation of transistor performance and reliability [4]. To control this interface degradation, Si capping layers often deposited on the SiGe channels, which reduces the V_t gain that can be gained by SiGe only. In this research, SiGe selective epitaxial growth (SEG) condition has been set-up first, Si capping condition has been optimized by tuning growth temperature, process pressure, and Cl/Si ratio in a LPCVD chamber. The process pressure was precisely controlled to grow Si capping layer 'selectively' as well as to avoid SiGe migration. When we increased the process pressure, surface atomic mobility can be decreased, which effectively reduced SiGe migration. However, when the pressure is increased too high, resulting in growth rate too high, selective growth condition fails. HCl/SiH₄ flow rates were also tuned to get a margin for selective growth condition. When introduced to DRAM peripheral transistors, a SiGe channel reduces PMOS V_{th} by 290 mV, and Si capped SiGe channel by 170 mV, respectively, which has good agreement with the expected value by Energy Band Simulation. This reduced V_t controllability could be recovered by increasing Ge content of SiGe channel. To conclude, the channel SiGe channel SEG process has been successfully applied for DRAM integration, and robust pMOSFET V_t tuner method was realized.

Nanometer-scale Science and Technology Division
Room: 203 - Session NS+AS-TuA

Frontiers in Nanoscale Imaging and Characterization
Moderator: E.I. Altman, Yale University

2:00pm **NS+AS-TuA1 Proximity, Phonon in Nanometer Size Superconducting Nb Islands : A STM Study**, *S. Jeon*, Seoul National University, Republic of Korea, *H. Suh*, Samsung Advanced Institute of Technology, Republic of Korea, *Y. Oh*, *S. Kim*, *Y. Kuk*, Seoul National University, Republic of Korea, *M. Machida*, Japan Atomic Energy Agency, Japan

Despite successful macroscopic picture on a conventional superconductor niobium(Nb), not much were reported on nanometer scale objects. One may have to consider quantum mechanical size effect, fluctuation, and quantum phase slip in a nanometer scale superconducting object. In this study, quantum size effect of superconducting niobium(Nb) nano-islands grown on a tungsten(W) surface was investigated with scanning tunneling microscopy(STM) and scanning tunneling spectroscopy(STS). Various size (30nm ~ 200nm) of niobium islands were formed on a W(110) surface after making several layers of wetting layer. STS measurement at 4.2K showed that the Nb island have a BCS-like superconducting gap of about 2meV around the Fermi level. The critical temperature is much lower than that of the bulk value. In addition, We found spatial dispersion of DOS (density of states) outside of the superconducting gap. Spatially-resolved scanning tunneling spectroscopy(SR-STs) data taken inside and outside of the niobium islands reveal unique dispersion. That can be understood by quantum size effect based on Bogoliubov - de Gennes equation.

2:20pm **NS+AS-TuA2 Spin Excitation Spectroscopy**, *D. Eigler*, IBM Almaden Research Center
INVITED

The energies and relaxation times of spin excitations are traditionally measured using the classic spin resonance techniques, Nuclear Magnetic Resonance (NMR) or Electron Spin Resonance (ESR). The measurement of spatial variations of spin relaxation times is of profound practical importance as they are often used as the primary contrast mechanism in magnetic resonance imaging. It has been an outstanding challenge to extend the spatial resolution of these spectroscopies to the atomic scale. We have developed a new kind of spin spectroscopy, *Spin Excitation Spectroscopy*, that achieves this goal. Through a combination of inelastic tunneling spectroscopy and pump-probe techniques, we have extended the capability of the scanning tunneling microscope to interrogate both the energetics and dynamics of spin systems on the atomic scale. We anticipate that this will have application in a broad range of studies concerned with nanometer-scale magnetic systems, how they may be understood, and how they may be engineered to have a desired functionality.

Work done in collaboration with Cyrus Hirjibehedin, Andreas Heinrich, Christopher Lutz, Jay Gupta, Markus Ternes, Alexander Otte, Sebastian Loth and Bruce Melior

3:00pm **NS+AS-TuA4 Atom-Specific Interaction Quantification and Identification by Combined Scanning Tunneling and Atomic Force Microscopy**, *M.Z. Baykara*, *H. Mönig*, Yale University, *T.C. Schwendemann*, Southern Connecticut State University, *M. Todorovic*, *R. Perez*, Universidad Autónoma de Madrid, Spain, *E.I. Altman*, *U.D. Schwarz*, Yale University

On surfaces, forces extending into the vacuum direct the behavior of many scientifically and technologically important phenomena such as corrosion, adhesion, thin film growth, nanotribology, and surface catalysis. To advance our knowledge of the fundamentals governing these subjects, it would be desirable to simultaneously determine a surface's structure, map electron densities, quantify force interactions, and identify chemical species. For example, in the case of a catalytically active surface, this would allow study of the role and effectiveness of surface defects such as vacancies, steps, kinks, impurities, and domain boundaries as active sites.

In this talk, we will show the example of an oxygen/copper(100) surface phase that much of this information can be derived from combining the new method of three-dimensional atomic force microscopy (3D-AFM) [1,2], a variant of noncontact atomic force microscopy, with simultaneous scanning tunneling microscopy. The surface oxide layer of Cu(100) features domain boundaries and a distinct structure of the Cu and O sublattices that is ideally suited for such model investigations. By combining experimental results with theoretical simulations, we will show how 3D data sets enable the site-specific quantification of force interactions and tunneling currents, how different chemical species can be imaged using different tips, different tunneling conditions, and different interaction mechanisms, and how

structure-induced stress fields and their influence on the local chemical activity and topographical deformation can be studied.

- [1] B. J. Albers et al., *Nature Nanotechnology* **4**, 307 (2009).
[2] M. Z. Baykara et al., *Advanced Materials* **22**, 2838 (2010).

4:00pm NS+AS-TuA7 The Role of Surface States in Inelastic Electron Tunneling Into Metal Surfaces, P. Maksymovych, M.H. Pan, Q. Li, Oak Ridge National Laboratory

A small fraction of electrons tunneling across a vacuum junction will undergo inelastic scattering, exciting surface phonons, molecular vibrations, magnons and plasmons in the contact leads. Although the study of surface phonons is a most straightforward inelastic electron tunneling spectroscopy (IETS) experiment, relatively few systematic studies have been done to date. One of the most surprising observations was that of atomic resolution in the IETS of Au(111) [1], and an equally intriguing variation phonon energy from 20 meV to 9 meV depending on the vertical stacking across the $22 \times \sqrt{3}$ reconstructed surface.

To investigate the origin of these effects on Au(111), we have carried out systematic IETS measurements using a home-built scanning tunneling microscope operating in the temperature range from 20K to 77 K. Particular emphasis was put on understanding of the role of the surface state in the electron-phonon coupling, judged from the intensity of the IETS signal and the energy of the observed vibrational modes.

We have found that largely independent of the measurement temperature, IETS spectra feature a broad peak centered around 18 meV, representing a weighted average of the phonon density of states within the Brillouin zone. Lower lying surface phonon bands (with energies from 7 to 9 meV) were resolved, but the majority of spectra are dominated by the peak at 18 meV, corresponding to the bulk phonon modes at the zone boundary. Although the spectrum remained largely unchanged across the surface, in contrast to earlier observations, the IETS intensity markedly dropped at the step edges. Furthermore, the IETS intensity exhibited long-range oscillations, the wavelength of which coincided with the Friedel oscillations of the surface state in the vicinity of the defects. Combined, the observations attest to the important role of the surface state in electron-phonon coupling [2], likely emphasizing the critical enhancement in the lifetime of hot electrons that tunnel into surface states relative to bulk states. We will also discuss the important role of tip effects in the IETS measurement. Tip-sensitivity may produce significant variations in the IETS spectrum across the herringbone reconstruction because of selectivity toward a particular phonon mode due to the convolution of the tip-surface interactions and heterogeneity of the surface state across the surface.

Research was conducted at the Center for Nanophase Materials Sciences and sponsored by the Division of Scientific User Facilities, U.S. Department of Energy.

- [1] H. Gawronski, M. Mehlhorn, K. Morgenstern, *Science* **319** (2008) 930-933.
[2] Q. Li, P. Maksymovych, M. Pan et al, to be submitted (2011)

4:20pm NS+AS-TuA8 2011 AVS Medard Welch Award Lecture - Inelastic Electron Tunneling Spectroscopy and Imaging of Single Molecules, W. Ho*, University of California, Irvine INVITED

The transformation of matter invariably involves energy transfer and redistribution. By probing matter and its coupling to external perturbations at the atomic scale with the scanning tunneling microscope (STM), it is possible to gain a broad range of new knowledge that would be difficult to achieve by other techniques. Through high precision measurements of inelastic phenomena inside single molecules with the STM, chemical and physical properties of molecules are obtained by probing their response to electrons, photons, and an external magnetic field. The STM is used to measure the electronic and vibronic states, vibrational and spin excitations, and optical transitions in single molecules. New features emerge when measurements are carried out at increasingly extreme conditions of vacuum, temperature, magnetic field, and pulse duration of light while maintaining the atomic-scale spatial resolution. The inelastic processes can result in nuclear motions such as molecular rotation, diffusion, conformational change, bond dissociation, and bond formation. By studying a wide range of systems from atomic hydrogen to large molecules such as metal porphyrins and phthalocyanines on metal and thin oxide surfaces, the new knowledge obtained by the STM can be applied to the understanding and advancement of numerous technologies such as chemical catalysis, information storage, nanophotonics, alternative energies, and environmental remediation. Underlying these longer range applications is the immediate gain in the

fundamental scientific understanding of matter that can be derived from these studies.

5:00pm NS+AS-TuA10 Two-Color Ultrafast-Laser-Assisted STM, A. Dolocan, D. Acharya, P. Zahl, P. Sutter, N. Camillone, Brookhaven National Laboratory

Substrate-adsorbate charge transfer and carrier-mediated substrate-adsorbate energy transfer are central to photoinduced surface chemistry. To investigate fundamental links between surface electron dynamics and heterogeneous photocatalysis we are developing an ultrafast-laser-excited scanning tunneling microscopy approach to probing surface electron dynamics with simultaneous subnanometer spatial and subpicosecond temporal resolution. Historically, thermal effects associated with laser power variations have presented a major hurdle to progress. In particular, thermal load modulations due to optical interference have been a barrier to observing dynamics at timescales on the order of the temporal width of the laser pulses. In this talk we present results from a new two-color method that completely eliminates this interference. We will show results for two cases: (1) where the tip is retracted from the surface far enough to prohibit tunneling, and (2) where the tip is within tunneling range of the surface. A delay-modulation technique isolates the two-color photo-emission from concurrent one-color two-photon photoemission and the conventional tunneling current, and also enables subpicosecond time-resolved detection of the photoexcited surface electrons. Advantages of the two-color approach are highlighted by comparison with the one-color case where optical interference causes current modulations that are orders of magnitude larger than the desired signal. The two-color approach represents an important step toward the ultimate goal of simultaneous subnanometer and subpicosecond measurement of surface electron dynamics.

5:20pm NS+AS-TuA11 High Precision local electrical Probing: A New Low Temperature 4-Tip STM with Gemini UHV-SEM Navigation, B. Guenther, A. Bettac, M. Maier, M. Oertel, Omicron NanoTechnology, Germany, F. Matthes, C.M. Schneider, Forschungszentrum Juelich, Germany, A. Feltz, Omicron NanoTechnology, Germany

A major challenge in the development of novel devices in nano- and molecular electronics is their interconnection with larger scale electrical circuits required to control and characterize their functional properties. Local electrical probing by multiple probes with STM precision can significantly improve efficiency in analyzing individual nano-electronic devices without the need of a full electrical integration. Among a very few commercial approaches, the Omicron *UHV NANOPROBE* has been established as a suitable instrument for local electrical probing in UHV on nano-structures down to structure sizes in the 10 nm range. The mayor technical requirements for such sophisticated instrumentation are:

- Rapid and simultaneous SEM navigation of four local STM probes on small structures
- Localization of nanostructures by high resolution SEM (UHV Gemini)
- Individual probe fine positioning by atomic scale STM imaging
- STM based probe approach for "soft-landing" of sharp and fragile probes and controlled electrical contact for transport measurements
- Preparation techniques towards sharp and clean and STM tips
- Suitable low noise signal re-routing for transport measurements with third party electronics

Although the *UHV NANOPROBE* has been successfully used for various applications, today's scientific requirements motivated the development of the next generation probing system. We will present the newly developed *LT NANOPROBE* which takes experimental capabilities one step further and opens up new research opportunities in nano-electronics, spintronics, and molecular electronics. Besides SEM/STM probe fine navigation and imaging, the excellent STM performance level of the *LT NANOPROBE* expands applications to tunneling spectroscopy and even the creation or modification of nano-structures by an ultimately precise STM probe. The R&D project has been driven by the following major milestones:

- Operation at temperatures of $T < 5$ K for STM imaging and STM based probing
- SEM navigation at base temperature $T < 5$ K
- Simultaneous operation of STM and SEM at base temperature
- Thermal equilibrium of sample and probes for (i) extremely low thermal drift and electrode positioning accuracy in time and (ii) defined temperature of the local electrical contact and
- Performance and stability level of each individual STM Probe suitable for STM spectroscopy and atom manipulation

First evaluation measurements with the system installed at the Forschungszentrum Jülich will be presented: STM on Au(111) with pm

* Medard W. Welch Award Winner

stability, STS revealing the superconducting gap of a Nb tip with approx. 3meV gap size, and transport measurements on nanowires at T<5K.

5:40pm NS+AS-TuA12 Spin-Polarized VLEED: Experimental Access to the Spin-Dependent Surface Barrier, K. Wulff, A.B. Schmidt, Westfälische Wilhelms-Universität Münster, Germany, J. Braun, Ludwig-Maximilians-Universität München, Germany, M. Donath, Westfälische Wilhelms-Universität Münster, Germany

The spin-dependent reflectivity of very-low-energy electrons from ferromagnetic surfaces has recently been utilized in a new type of electron spin detector [1,2]. The underlying effect is a result of electron scattering from a spin-dependent substrate potential as well as from a spin-dependent surface-potential barrier.

We present the first spin-polarized very-low-energy electron-diffraction (SPVLEED) measurements on a ferromagnetic system. Our data on Co/Cu(001) reveal a significant spin dependence of the reflected intensities that varies strongly with electron energy, polar and azimuth angle of incidence.

In these intensity vs. energy spectra $I(V)$, additionally, fine structures appear [3], which are caused by the surface-potential barrier. Their particular intensities and energy positions are very sensitive to the shape of the surface-potential barrier. On the vacuum side far from the surface, the barrier resembles the well-known Coulomb potential, while, on the crystal side, it converges to the inner potential. In theoretical calculations, the transition region is usually described by a parameterized phenomenological model. Our experiment provides access to exactly this transition region.

We could determine the spin-dependent shape of the surface-potential barrier of Co/Cu(001) from the dispersion of the fine structure as a function of polar and azimuth angle.

[1] T. Okuda *et al.*, Rev. Sci. Instrum. **79** (2008) 123117 ; [2] A. Winkelmann *et al.*, Rev. Sci. Instrum. **79** (2008) 083303 ; [3] R.O. Jones, P.J. Jennings, Surf. Sci. Reports **9**, 165 (1988)

Plasma Science and Technology Division Room: 202 - Session PS1-TuA

Advanced BEOL / Interconnect Etching II Moderator: S. Sriraman, Lam Research Corp.

2:00pm PS1-TuA1 Feature Profile Evolution for HARC Etching in SiO₂, P. Moroz, Tokyo Electron US Holdings Ltd., S.-Y. Kang, Tokyo Electron Ltd., Japan

Feature profile control for HARC etching is a very important issue. Possible profile defects such as bowing, necking, variations in depth and shape, among others, become critical for the next technological steps with ever shrinking dimensions of the features. Using numerical simulations as a tool, we studied HARC etching of SiO₂ by the fluorocarbon-argon-oxygen plasma in a capacitive-type plasma system. The first step in our simulations involved estimation of neutral and ion fluxes, and their angle-energy distributions for most important species involved into processing in the systems chosen for comparison. Then the feature profile simulator FPS-3D [1] was run to estimate various chemical and physical effects on HARC profile evolution during processing. The difficult part in those simulations was taking into account deposition of polymer films and etching through those films. The final results come as a competition between counteracting effects of etching and deposition. Important effects of ions for etching at the bottom of the contact holes, and of polymer films for protecting sidewalls from further etching, were investigated. Possible bowing and necking effects were considered in detail. Calculations were carried out for different sizes of the features, different gas compositions, and different RF powers leading to different ion energies. Published data for the underlined reaction mechanisms were analyzed and used for tuning the chemical reactions database in the FPS-3D code. Comparison of simulations with different experiments and the corresponding analysis of HARC etch processing are presented. The authors are thankful to Masanobu Honda and Akira Tanabe for providing experimental data.

[1] P. Moroz, 57th AVS Int. Symp., PS1-ThA10, Albuquerque, NM, October, 2010.

2:20pm PS1-TuA2 Hybrid Strip Process to Minimize Low-k Dielectric Damage, E.A. Hudson, T. Choi, K. Takeshita, S. Sirard, B. Ji, M. Kato, M. Moravej, O. Turmel, G.A. Delgado, S. Heo, A.D. Bailey III, Lam Research Corp.

INVITED

Integration of materials with low dielectric constant into microelectronics interconnect structures has presented significant challenges for several years. As structures and materials have evolved, there has been a consistent concern that plasma processing damages the low-k material, especially during process steps intended to strip organic mask films. For efficiency, it is convenient to remove organic films *in situ*, as part of a sequence of etch steps in the etch reactor. But plasma strip conditions may remove carbon from the dielectric film, causing an increase in dielectric constant and other issues. This is an increasing concern as the target dielectric constant is reduced with successive device generations, and the films become more sensitive.

For via-first integration schemes which use an embedded metal hard mask to define the trench pattern, organic mask stripping is required only after the vias are partially defined in the dielectric. This approach protects the trench sidewall by eliminating the post-trench strip, but may lead to localized regions of dielectric damage in the final structure, corresponding to the remaining material which was exposed to post-via strip.

For *in situ* plasma strip processes based upon CO₂ gas, damage to the dielectric film is mainly induced by reactive neutral species at the via sidewall. There are several strategies to reduce this damage while maintaining the ability to strip the targeted organic mask layer. One is to minimize the radical to ion ratio, in order to reduce the damage rate while preserving strip rate. Another method is the "hybrid strip" in which a protective layer of polymer is deposited on the via sidewall prior to strip. This barrier reduces the influence of strip plasma species on the underlying dielectric film. Damage reduction is achieved using passivation based either upon hydrocarbon or fluorine-containing polymers.

Because the strip plasma tends to remove the passivation from the sidewall, and because the damage rate increases in the final part of the strip process, better results can be achieved if the protective films is periodically re-applied. A cyclic process which alternates between passivation and strip conditions minimizes the strip-induced damage at the via sidewall. To facilitate an efficient hybrid strip process, the etch reactor design can be optimized for rapid switching between the two different plasma conditions. This requires minimization of both the gas exchange time and the RF coupling stabilization time.

3:00pm PS1-TuA4 Model for High Aspect Ratio Dielectric Etch Process in a Capacitively-Coupled Plasma, J.A. Kenney, A. Balakrishna, A. Agarwal, N. Misra, S. Rauf, K. Collins, Applied Materials, Inc.

Etching of high aspect ratio (HAR) features in dielectric substrates is a challenging process, growing increasingly difficult with each new device generation. A common approach uses a multi-frequency capacitively-coupled plasma (CCP) reactor with high bias power and a dilute mixture of fluorocarbon and oxygen feed gases. Here, F atoms are the primary etchant, assisted by high energy ions to penetrate the fluorocarbon polymer layer formed by CF_x radicals. [1] Oxygen atoms act to suppress excessive polymerization. The high energy ions give directionality to the etch process, with sidewalls remaining protected by the fluorocarbon polymer.

Due to the complexities involved in developing processes for each new application, many efforts have been made to model HAR etch processes (e.g., [2]). These necessarily involve at least two fundamental parts: (1) a plasma model of the CCP, which ideally includes the effects of power, generator frequencies, gas composition and flow, pressure, and reactor geometry, and (2) a model of the surface mechanism, which considers fluxes of relevant species, ion energies, and a simplified description of the competing deposition and etching processes. Complicating matters are the difficulties in obtaining systematic experimental data by which to validate either model so as to gain confidence in their predictive capabilities.

In this paper, we present models of an HAR dielectric etch process in a CCP, where the surface mechanism has been developed using experimental etch rate data generated on blanket oxide wafers. We focus on low pressure processes in an Ar/C₄F₆/O₂ mixture, using a multi-frequency CCP with very high frequency (VHF) source and dual radiofrequency (RF) bias. Experimental data were collected for multiple pressures (15 – 80 mT), source powers (500 – 900 W), bias powers (3500 – 7100 W in different frequency mixtures), and flows of feed gases. The same processes were modeled using CRTRS, Applied Materials' 2/3D reactor-scale plasma simulation tool, giving fluxes and energies of etch-relevant ion and neutral species. A surface mechanism based on that of Schaepekens *et al.* [1] was then developed, using the plasma simulation output and experimental etch rate data for calibration of parameters. Finally, this mechanism was used in a string-based feature profile evolution tool to quantify the impacts of varying the above process parameters.

[1] Schaepekens *et al.*, JVSTA 17, 26 (1999).

4:00pm **PS1-TuA7 Plasma-induced Damage Reduction in Porous SiOCH Dielectrics by Replacement of H₂ and N₂ by CH₂F₂ and Ar in Fluorocarbon Based Plasmas, L. Souriau, F. Lazzarino, L. Carbonell, I. Ciofi, P. Verdonck, J.F. de Marneffe, M. Baklanov, IMEC, Belgium**

With the scaling of devices and related interconnects, the integration of dielectric materials with a k-value lower than 2.5 is greatly required. In particular hybrid porous SiOCH low-k materials are considered as promising candidates. However, such low-k dielectrics generally have a poor resistance to plasma damage due to their high connected porosity. It is therefore important to develop less damaging etching chemistries as well as more resistant low-k materials. During the discharge, ion bombardment, active radicals and VUV radiations are responsible for the degradation of the low-k. Mainly, -CH₃ groups are removed from the film resulting in its hydrophilization and consequent moisture uptake which has a severe impact on the final k-value after patterning.

In order to limit the damage during plasma etch, fluorocarbon-based chemistries allow a thin protective etch polymer film to be deposited on the surface of the low-k film during plasma etch and therefore effectively prevents possible damage by penetration of active radicals. We have evaluated the etching of a SiOCH dielectric with a k value of 2.0 using CF₄ in combination with either C₂H₄ or CH₂F₂ and using H₂, N₂ or Ar as tuning gas. The plasma damage has been evaluated by measuring the loss of -CH₃ groups and -OH uptake by FTIR and by measuring the k-value variation by forming MIS planar capacitor. Starting from a CF₄/H₂/N₂ plasma, it has been found that the damage is reduced by substituting H₂ by N₂. H is able to diffuse deep into the low-k film and probably remove -CH₃ groups by forming CH₄. Switching to a CF₄/C₂H₄/N₂ plasma further allows to decrease the damage, most probably through the formation of a thicker passivation layer on the low-k. Plasma damage can be further reduced by replacing N₂ by Ar, leading to a CF₄/C₂H₄/Ar plasma. Possibly, N₂ is causing damage by extracting C from the low-k film by forming HCN by-product. However the replacement of N₂ by Ar resulted in a reduction of the etch rate which could be recovered by finally replacing C₂H₄ by CH₂F₂ while maintaining a low damage level.

Finally, 90nm half pitch trenches have been patterned into the SiOCH dielectric film using a dual hard mask approach (spin-on glass and spin-on carbon films). The influence of the hard mask on the plasma composition required optimization of the etch conditions in order to obtain straight profiles. Integrated k-value after complete processing will be discussed.

In conclusion, we have showed that H₂ and N₂ were responsible for the low-k damage during etch in fluorocarbon based plasmas. Switching to a CF₄/CH₂F₂/Ar plasma allows to reduce damage while maintaining good patterning capability.

4:20pm **PS1-TuA8 Using Pulsed Power to Control Etch Properties of SiO₂ in Ar/CF₄/O₂ Capacitively Coupled Plasmas, S.-H. Song, M.J. Kushner, University of Michigan**

Feature scale etch or deposition properties in plasma processing of microelectronic devices are determined by the energies and fluxes of radicals and ions to the wafer. These fluxes are ultimately controlled by controlling and customizing the electron energy distribution function $f(\epsilon)$ which determines the dissociation patterns of feedstock gases and the relationship between applied power and sheath potential. One way to customize $f(\epsilon)$ in dual frequency capacitively coupled plasmas (CCPs) is using pulse power for either or both of the high frequency or low frequency. Pulsed power in CCPs is attractive for controlling $f(\epsilon)$ and plasma properties as it provides a means for producing combinations of fluxes (e.g., magnitude, identity and energy) not otherwise attainable using continuous wave excitation. In these systems, the choices of duty cycle and pulse repetition frequency (PRF) are important in determining the cycled average value of $f(\epsilon)$ and $f_i(\epsilon)$ due to the role of thermalization of electrons during the afterglow. The ability to control $f(\epsilon)$ and $f_i(\epsilon)$ may have both clear and subtle effects on the critical dimensions (CD) of etch features. For example, charge accumulation in the feature and the angular spread of ions may be controlled by the choice of duty cycle and PRF, both of which affect the etch profile. This enables some ability to control, for example, the sidewall slope of high-aspect-ratio (HAR) features by pulse-power formats. To demonstrate the ability to control feature profiles through control of $f(\epsilon)$ and $f_i(\epsilon)$ using pulsed plasmas, simulations were performed separately in two regions – on the equipment scale using the Hybrid Plasma Equipment Model (HPEM) and on the feature scale using the Monte Carlo Feature Profile Model (MCFPM). The fluxes of radicals and ions to the wafer from the HPEM are transferred to the MCFPM to calculate the etch properties. Plasma properties, $f(\epsilon)$ and $f_i(\epsilon, \theta)$, and ratios of fluxes to the wafer for an Ar/CF₄/O₂ gas mixture in a 2-frequency CCP will be discussed. The tuning of etch rates and profiles of HAR features in SiO₂ resulting from these fluxes will then be summarized.

4:40pm **PS1-TuA9 Chemical Mechanisms for Dielectric Product Development, A. Balakrishna, A. Agarwal, J.A. Kenney, S. Belostotskiy, S. Rauf, K. Collins, Applied Materials, Inc.**

Smaller technology nodes in the semiconductor industry place increased emphasis on etch productivity requirements, such as etch rate and critical dimension. Modeling and simulation is playing a central role in new developments (design of new hardware and exploration of novel processing options) to address the concurrent demand for improved performance and shorter development cycle. Validation against experimental data is a critical step in making these models a mature development tool. Monte Carlo, level set and string based feature scale models have been used to investigate processing issues within nanoscale features. Due to the complexity of surface and sub-surface processes, these models generally use empirically developed mechanisms which fit the model predictions to measured profiles and film characteristics. In this paper, we apply and refine the above method to develop a validated dielectric etch mechanism and feature scale model.

We obtained experimental data for etching of blanket SiO₂ wafers in a c-C₄F₈/O₂/Ar plasma over a wide range of pressures (25-150 mTorr), bias powers (500-1500 W), and c-C₄F₈ and O₂ flows in a dual-frequency capacitively coupled plasma etcher. The etch rate increased with bias power and c-C₄F₈ flow rate, weakly decreased with increasing O₂ flow rate, and moderately increased with pressure. The reactor scale simulations were performed using CRTRS, a 2/3-dimensional fluid plasma model. The plasma simulations provided fluxes of various fluorocarbon polymerizing species, atomic oxygen and atomic fluorine. We also calculated fluxes and energies of the ions impacting the wafer. These values were used to calibrate an etch mechanism, whose main features are (a) a polymer thickness determined by the balance between polymer deposition (by C_xF_y species) and polymer removal (by ion sputter and O etch), (b) an exponential decay in ion energy through the polymer, and (c) reactive ion etching at the polymer-dielectric interface.[1] The etch rates and their trends with bias power, c-C₄F₈ flow rate and O₂ flow rate were captured well in this model. The calculated polymer thicknesses also exhibited the expected trends, decreasing with bias power and O₂ flow rate and increasing with c-C₄F₈ flow rate. Our mechanism was not able to capture the etch rate trends with pressure, which is likely due to deficiencies in our plasma chemistry mechanism for Ar/c-C₄F₈/O₂ gas mixture. Finally, the calibrated mechanism was used in a string based feature profile model to investigate the influence of control parameters on dielectric etch process in a dual-frequency capacitively coupled plasma tool.

[1] Schaepkens et al, JVST A, 17, 26 (1999).

5:00pm **PS1-TuA10 Optimization of CF₃I Process for Low-K Etching, A.J. Gildea, J.C. Long, E. Eisenbraun, College of Nanoscale Science and Engineering, The University at Albany-SUNY, V. Omarjee, F. Doniat, N. Stafford, C. Dussarrat, American Air Liquide – Delaware Research and Technology Center**

Semiconductor manufacturing is facing major integration challenges. The introduction of ultra low-k materials (k=2.5 and below) in BEOL processing combined with the always shrinking dimensions increased the number of film parameters such as LER or species diffusion that need to be perfectly mastered. In particular, the use of porous dielectrics to reduce permittivity is done at the expense of film chemical and mechanical robustness. With films having porosity ranging from 15 to 30%, patterning collapse, impurity diffusion and other defects are becoming serious issues. A negative impact on interconnect reliability and performance is observed unless tight process controls and/or new approaches are employed. To overcome the defects created during the low-k patterning, one approach that is considered here is the use of new etch gases. Among the possible choices, CF₃I has seen increased momentum over the past years. When the first studies >10 years ago demonstrated some interesting features of CF₃I such as a GWP<1, the benefits were still too marginal to consider a fundamental change for dielectric etching in the semiconductor industry. Recently, with the increasing challenges to be overcome when etching the low-k, alternatives such as CF₃I are receiving increased attention.

In this talk we will present a comparison of the etching performance such as etch rate and selectivity of CF₃I alone or in combination with standard fluorocarbons such as CF₄ and C₄F₈.

Etching rate measurements performed on blanket porous low-k films (k=2.4) showed comparable values between CF₃I and the standard gases; therefore demonstrating no loss of throughput. Possible iodine incorporation during the process was carefully monitored and found to be negligible. Iodine, if detected, is usually at the detection limit of the tools (<0.4 at.%) and concentrated at the film surface therefore could be easily removed during the subsequent ashing and cleaning steps.

Patterned structure etch testing was performed and optimized using a DOE approach. CF_3I was found to be suitable to obtain nicely etched features. In many cases, better etched structures and higher selectivity were obtained using CF_3I compared to the standard gases.

5:20pm **PS1-TuA11 Mechanism of Highly Selective SiO_2 Etching over Si_3N_4 , Si and Photoresist Using Hydro-Fluorocarbon Gases**, Y. Miyawaki, Y. Kondo, K. Asano, M. Sekine, K. Ishikawa, T. Hayashi, K. Takeda, H. Kondo, M. Hori, Nagoya University, Japan

Highly selective etch of dielectric films is one of the key technologies in integrated circuits fabrications. We achieved extreme high SiO_2 selectivity against Si_3N_4 , Si and ArF photoresist using hydro-fluorocarbon gas, C_3HF_7 and O_2 , Ar gas mixture [1] in a dual frequency (60 MHz / 2 MHz) capacitively coupled plasma (CCP). The selectivity over Si_3N_4 seemed to be infinite because selective fluorocarbon deposition occurred on Si_3N_4 . The surface roughness that leads to line edge roughness was reduced by the selective deposition. The selective etch mechanism among plasma etch using fluorocarbon gases with and without hydrogen in gas molecule was investigated by the diagnostics of gas phase species and etched surfaces. As comparing $CxFy$, $CxFyO$ and $CHxFy$ gases, it was found that the hydrogen containing species with larger molecular weight play an important role for forming thick and carbon-rich polymer film especially on Si_3N_4 , Si as well as on Si, photoresist. For the $CHxFy$ gas plasma, the density of F radical that degrades the selectivity was inclined to be lower. $CHxFy$ species act as an etchant for SiO_2 that contains oxygen, similar to the conventional selective etch scheme of SiO_2 by fluorocarbon plasma [2]. On the other hand, it could be deposition species to reduce the etch rates after some etch reaction on the surfaces of Si_3N_4 , Si and photoresist that have no or less oxygen content. This means that the $CHxFy$ species are etchants at the very beginning and turn to species for fluorocarbon polymerization just on Si_3N_4 , Si and photoresist. Here, we need some sacrifice layer to initiate that selective deposition. The photoresist surface suffered roughness formation in the beginning, then the roughness was cured by the further deposition with ion bombardment [3]. This protective and roughness curing deposition on photoresist should occur for $CxFy$ gas plasma in some condition (e.g. higher gas-mixing ratio of $CxFy/Ar$), however it also forms a thick polymer on SiO_2 to stop etching. The temperature dependence for the etching and deposition properties [4] suggested that the difference of sticking coefficient for species with and without hydrogen was not so important. It is also speculated that the thick polymer formation on Si_3N_4 , Si and photoresist while less reducing the SiO_2 etch rate is due to the relative large flux of specific hydrogen containing species in C_3HF_7 plasma.

Acknowledgement: Tokyo Electron Ltd., ZEON Corp., JSR Corp.

References: [1] Y. Miyawaki, et al.; Proc. 32nd Int'l. Symp. Dry process, P.181 (The Japan Society of Applied Physics, Tokyo, 2010). [2] M. Sekine; Applied Surface Science **192**, (2002) 270. [3] K. Asano, et al.; The 72nd Fall Meeting of JSAP, 31a-M-6 (The Japan Society of Applied Physics, Yamagata, 2011). [4] Y. Miyawaki, et al.; *ibid.*, 31a-M-4

Plasma Science and Technology Division

Room: 201 - Session PS2-TuA

Plasma Diagnostics, Sensors and Control I

Moderator: V. Nagorny, Mattson Technology, Inc.

2:00pm **PS2-TuA1 Prediction of Ion Sheath Shape and Ion Trajectory during Plasma Etching Processing using On-Wafer Monitoring Technique**, R. Araki, K. Miwa, T. Kubota, Tohoku University, Japan, T. Iwasaki, K. Ono, Mizuho Information & Research Institute, Inc., Japan, S. Samukawa, Tohoku University, Japan

Precise plasma processes are indispensable for the fabrication of ULSI and MEMS devices. Some MEMS devices have larger scaled 3D structures comparable to the ion sheath thickness on the surface in plasma processing. In such cases, because of distortion of sheath shape due to the MEMS structure, ions trajectory are distorted to the surface and it causes etched shape anomaly. In order to solve these problems, we are developing a system to measure sheath thickness and to predict sheath shape, ion trajectory, and etched shape by fusion of a new on-wafer monitoring data and computer simulation. Our newly developed on-wafer sheath shape sensor can measure the surface potential and ion saturation current at wafer surface. Based on these results, the sheath thickness, shape, and ion trajectory were calculated by using our developed simulation. In this study, we could measure the sheath thickness, and then calculate the sheath shape deformation around a structure having large step in the case of using SF6 inductively coupled plasma. We found that the sheath thickness was about 1 mm and ion trajectory was bent near the large steps on the wafer surface. This result was completely corresponding to the actual etching pattern

profile near a structure having large step. It is suggested that our proposed fusion system of on-wafer monitoring data and computer simulation is very effective to predict real etched shape during plasma etching processes.

2:20pm **PS2-TuA2 Measuring Electron Density, Electron Temperature, and Plasma Potential with RF Frequency Probes**, D.R. Boris, R.F. Fernsler, S.G. Walton, Naval Research Laboratory (NRL)

Plasma density measurements are an essential tool in understanding and controlling processing plasmas across a wide range of applications. Charge collection probes (Langmuir probes) are of limited utility in depositing plasmas, high pressure applications or in processes that require the use of reactive gases, as these environments result in unreliable data acquisition. Plasma frequency probes are an attractive alternative to Langmuir probes in such applications since they do not suffer significant performance degradation in these environments. This work presents frequency probes measurements of plasma density over a range of 10^9 to 10^{12} cm^{-3} in a variety of processing plasma chemistries (N_2 , CH_4 , NH_3 , O_2 and SF_6). In addition to electron density measurements frequency probes are also useful for measuring plasma potential, electron temperature, and electron energy distribution functions in the gas chemistries mentioned above.

2:40pm **PS2-TuA3 Effects of Wire Thickness, Neutral Pressure and Gas Composition on the Inflection Point Technique**, B. Dechawatapanisal, N. Hershkowitz, J.P. Sheehan, CS. Yip, University of Wisconsin-Madison

The inflection point technique in the limit of zero emission determines the plasma potential by fitting a straight line to the graph of the emission current versus the inflection point of the emissive probe I-V traces. The plasma potential is determined by extrapolating the line to the limit of zero emission. The effects of wire thickness, gas composition, neutral pressure and position on the technique were investigated. Experiments were performed in a multi-dipole filament discharge. Wire thicknesses of 0.013, 0.025, 0.05 and 0.1mm were studied. Experiments were done in Argon, Xenon and Helium plasmas with neutral pressures ranging from 0.5mTorr to 3mTorr. Measurements were performed from the bulk of the plasma to its sheath edge near a 10cm diameter negatively biased plate.

This work is supported by U.S. DOE under the Grant and Contract Nos. DE-FG02-97ER54437 and No. DE FG02- 03ER54728, DE SC0001939 and by the National Science Foundation Grants under the Grant and Contract Nos. CBET-0903832, and No. CBET-0903783.

3:00pm **PS2-TuA4 A New Diagnostic Tool System of Radio-Frequency Plasmas by Employing Floating-Emissive Probe**, Y. Taniuchi, M. Utsumi, Tokai University, Japan, M. Yanagisawa, Landmark Technology Corporation, Japan, H. Shindo, Tokai University, Japan

A new diagnostic tool to measure plasma parameters as well as Electron Energy Distribution Function (EEDF) by a floating-emissive probe has been proposed[1], and a diagnostic system has been newly developed and applied to radio-frequency (RF) plasmas. It is generally difficult for a conventional probe method to measure EEDF in RF plasmas, because of the plasma potential fluctuation, particularly in the capacitive mode. The present method has an advantage that there is no need of an external compensation circuit and all measurements can be made in the floating condition. The method is based on measurement of the functional relationship between the floating potential change ΔV_F and the heating voltage V_H of emissive probe. If the plasma electrons are in Maxwellian, the equation can be obtained for the value of ΔV_F as a practical and useful formula.[1]

It is important to know that the value of ΔV_F contains information of electron energy distribution. In the experiment, the data of V_F and ΔV_F was measured in a 13.56 MHz RF plasma produced by single-loop antenna[2], as a function of V_H . In the conditions of high RF power, the plasma mode was ICP and the measured values of ΔV_F were in agreement with the theoretical value, stating that the plasma electron was in Maxwellian. The electron temperatures thus obtained were very consistent with those measured by Langmuir probe. The electron density was also obtained from the value of ΔV_F near the plasma space potential and they were consistent with Langmuir probe data. Consequently, by using a new diagnostic system one can obtain the electron temperature and density, the plasma space potential and floating potential, as well as the EEDF in the floating condition of the probe. It should be stressed that this is the first success of floating probe to be able to measure all plasma parameters. One can also expect that the present method is applied to plasmas which are produced in insulated vessels.

References:

- [1] K.Kusaba and H.Shindo, Review of Scientific Instruments, **78**, 123503-1(2007).
- [2] Y.Jinbo and H.Shindo, Applied Physics Express, **2**, 016001-1(2009).

4:00pm **PS2-TuA7 A Comparison of Emissive Probe Techniques for Electric Potential Measurements in a Complex Plasma**, *J.P. Sheehan**, University of Wisconsin-Madison, *Y. Raitses*, Princeton Plasma Physics Laboratory, *N. Hershkowitz*, University of Wisconsin-Madison, *I. Kaganovich*, *N.J. Fisch*, Princeton Plasma Physics Laboratory

Accurate measurements of the plasma potential is a critical challenge especially for complex plasmas such as magnetized and flowing. We compare various emissive probe techniques for measurements of the plasma potential. The measurements were conducted in a low-pressure magnetized discharge of the Hall thruster. The thruster was operated with xenon gas in subkilowatt power range and the discharge voltage range of 200-450 V. The probe was placed at the channel exit where, the electron temperature is in the range of 10 to 60 eV and the plasma potential is in the range of 50 to 250 V. The floating point method is expected to give a value $\sim T_e/e$ below the plasma potential. The experimental results are consistent with these expectations. Specifically, it is shown that the floating potential of the emissive probe is $\sim 2T_e/e$ below the plasma potential. It is observed that the separation technique varies wildly and does not give a good measure of the plasma potential.

This work was supported by US Department of Energy grants No. DE-AC02-09CH11466, No. DE-FG02-97ER54437, and No. 3001346357 and the Fusion Energy Sciences Fellowship Program administered by Oak Ridge Institute for Science and Education under a contract between the U.S. Department of Energy and the Oak Ridge Associated Universities.

4:20pm **PS2-TuA8 Probe Diagnostics Instrument for Laboratory and Industrial RF Plasmas**, *V. Godyak*, RF Plasma Consulting

Contemporary probe diagnostics of low pressure rf discharge non-Maxwellian plasmas implies the measurement of electron energy distribution function, EEDF and variety of plasma parameters found as the corresponding EEDF's integrals. There are four major problems in implementing of meaningful probe diagnostics in rf plasma reactors. They are: a) large frequency spectrum with significant amplitudes of the plasma rf potential corresponding to source and bias fundamental frequencies and their harmonics; b) low frequency noise due to plasma instability and ripples in an rf power source, c) too high impedance between the plasma and grounded chamber due to limited surface of the chamber and its contamination or/and an artificial protective coating, and d) contamination of the probe surface with a low conductive layer of the reaction products. The probe characteristic distortion caused by these factors are hardly recognized when one just follows Langmuir procedure to infer plasma parameters assuming Maxwellian EEDF, since distorted and undistorted probe characteristics look similarly. But the problem becomes apparent after double differentiation of the distorted probe characteristics (to infer the EEDF) due to error augmentation inherent to differentiation procedure. A probe diagnostic system VGPS[®] [1], addressing the aforementioned problems has been designed and tested in the variety of rf plasmas in basic research experiment and in different rf plasma reactors. Examples of EEDF measurements with high energy resolution (small fraction of T_e) and large dynamic range (3-4 orders of magnitude) in laboratory and industrial rf plasmas, are given in this presentation.

4:40pm **PS2-TuA9 Ion Energy Distributions in Pulsed Plasmas with Synchronous DC Bias: Effect of Noble Gas**, *W. Zhu*, *H. Shin*, *V.M. Donnelly*, *D.J. Economou*, University of Houston

Ion energy distributions (IED) on the substrate electrode were measured in a Faraday-shielded inductively coupled plasma. Narrow distributions with well-controlled ion energy were obtained by pulsing the plasma and applying a synchronous DC bias on a "boundary" electrode during the afterglow. The peak ion energy was controlled by the DC bias, as the plasma potential and the electron temperature decayed drastically in the afterglow. IED measurements were performed in Ar, Kr and Xe plasmas, using a retarding field energy analyzer. A Langmuir probe was also used to measure time- and space-resolved plasma density and electron temperature during a pulse as a function of power and pressure. The quasi-steady electron temperature (late in the active glow) followed the order $Ar > Kr > Xe$ i.e., the gas with the highest ionization potential had the largest electron temperature. The opposite order of T_e ($Xe > Kr > Ar$) was observed in the afterglow, as the decaying electron temperature was controlled by diffusion cooling, and the diffusivity is lower for heavier gas. The full width at half maximum (FWHM) of the IEDs followed the order $Xe > Kr > Ar$. Higher electron temperature in the afterglow correlated with larger FWHM. The width of the IED could also be controlled by varying the pulsed plasma frequency and duty cycle, or the time window of the application of the DC bias during the afterglow. Small additions (up to 5% by volume) of chlorine gas resulted in IEDs that were similar to those in the corresponding pure noble gas plasma, except that the peak ion energy was lower by a few eV.

* Coburn & Winters Student Award Finalist

Work supported by the DoE Plasma Science Center and NSF.

5:00pm **PS2-TuA10 2011 AVS John A. Thornton Award Lecture - As Device Dimensions Continue to Shrink... A Journey Through Thirty Years of Plasma Etching Diagnostics and Mechanisms**, *V.M. Donnelly†*, University of Houston

With each new generation of integrated circuits and reduction in transistor and interconnect dimensions, plasma etching of fine features in silicon, aluminum and insulating thin films encounters new sets of challenges. Over the past thirty years, our understanding and control of plasma etching processes has greatly improved, due to the advances in diagnostic techniques and basic mechanistic studies, combined with advanced modeling methods. This talk will review studies, mostly from our laboratories, spanning this era with an emphasis on the connections between studies, the influence of other fields, and the interactions between collaborators and colleagues. Some old controversies will be revisited and perhaps revived.

Advanced Surface Engineering Division

Room: 104 - Session SE+TF-TuA

Glancing Angle Deposition (GLAD) II

Moderator: N.A. Beckers, University of Alberta

2:00pm **SE+TF-TuA1 Evolution of Crystal Orientation during Oblique Angle Deposition**, *G.-C. Wang*, *T.-M. Lu*, Rensselaer Polytechnic Institute

The oblique angle deposition (OAD) has attracted attention due to the shadowing effect that results in interesting morphology of isolated nanostructures. These artificial nanostructures have rich textures depending on the growth conditions such as the angle of incidence, substrate temperature, deposition rate, and substrate rotation speed or mode. These OAD films often have biaxial textures even on amorphous substrates because the in-plane symmetry is broken under the off-normal incidence of the deposited atoms on the substrate. The most frequently used characterization technique for biaxial texture films is x-ray pole figure analysis. However, the texture obtained by x-ray is an average texture from the entire thickness of the film due to the x-ray's few micron penetration depth. As the texture of a film often changes during growth, information on the basic mechanisms that control the final texture is often lost. In this talk we will show how we can use our newly developed reflection high energy electron diffraction (RHEED) surface pole figure technique to probe the surface texture evolution of the growth front from the initial stage (a few nm thick) to the later stage of thick films [1] either *in situ* or *ex situ*. Examples of biaxial texture evolution of CaF_2 [2], Mg, W [3] and Mo nanostructures as a function of thickness, incident angle, and rotation schemes, will be presented. The surface sensitive RHEED pole figure technique reveals that biaxial texture can be formed at thickness as small as 20 nm. In some cases, surface texture at the growth front is seen to be quite different from the bulk texture measured by x-ray pole figures. We also show that these biaxial textured films can be used as buffer layers to grow near-single crystal semiconductor films which may find important applications in energy conversion devices.

Work was supported by NSF-0506738.

[1] F. Tang, T. Parker, G.-C. Wang, and T.-M. Lu, "Surface texture evolution of polycrystalline and nanostructured films: RHEED surface pole figure analysis", *Journal of Physics D: Applied Physics* 40, R427 (2007).

[2] C. Gaire, P. Snow, T.-L. Chan, W. Yuan, M. Riley, Y. Liu, S.B. Zhang, G.-C. Wang and T.-M. Lu, "Morphology and texture evolution of nanostructured CaF_2 films on amorphous substrates under oblique incidence flux", *Nanotechnology* 21, 445701 (2010).

[3] R. Krishnan, Y. Liu, C. Gaire, L. Chen, G.-C. Wang and T.-M. Lu, "Texture evolution of vertically aligned biaxial tungsten nanorods using RHEED surface pole figure technique", *Nanotechnology* 21, 325704 (2010).

2:40pm **SE+TF-TuA3 Vapor-Liquid-Solid Glancing Angle Deposition (VLS-GLAD): A New Way of Shaping Crystalline Nanowires**, *A.S. Alagoz*, *T. Karabacak*, University of Arkansas at Little Rock

Vapor-liquid-solid (VLS) is a powerful method enabling fabrication of single crystalline semiconductor nanowires in feature sizes ranging from nano to micro scales. On the other hand, control of nanowire growth direction by using VLS technique is still challenging. In this presentation, we demonstrate a new approach, called vapor-liquid-solid glancing angle

† John A. Thornton Memorial Award Winner

deposition (VLS-GLAD), of fabricating crystalline semiconductor nanowire arrays with controlled geometry. VLS-GLAD is a physical vapor deposition based nanowire fabrication technique which relies on selective deposition of source atoms onto metal catalyst nanoislands placed on a crystal wafer. In this technique, collimated obliquely incident flux of source atoms selectively deposit on catalyst islands by using "shadowing effect". Geometrical shadowing effect combined with VLS growth mechanism leads to the growth of crystalline semiconductor nanowire arrays. In this work, we show the morphological and structural properties of tilted single crystal semiconductor nanowire arrays fabricated by utilizing a conventional thermal evaporation system for VLS-GLAD.

3:00pm SE+TF-TuA4 Lithographic Processing of Nanostructured Thin Films Grown Using Oblique Angle Deposition Method, P. Shah, University of Dayton Research Institute, A. Sarangan, University of Dayton
It is known that exposing structured thin films (STF) grown using oblique angle deposition (OAD) to liquids such as DI water or any common solvents permanently deforms the physical structure of the thin films and alters their properties. This is a severe limitation of STFs because the films cannot be patterned into useful devices using conventional wet lithographic processes. In this work, we overcome this challenge and propose to demonstrate conventional i-line lithography technique for patterning STF's grown using OAD. The ability to selectively fabricate STF in chosen areas of the active devices will be beneficial for numerous applications. It is shown that the structure of these thin films is preserved after lithographic processing. Processing limits in terms of dimensions of the devices or patterns that may possibly be fabricated are discussed.

4:00pm SE+TF-TuA7 Automated Measurement Technique for Growth Scaling in Glancing-Angle Deposited Films, J.M. Siewert, J.M. LaForge, M.T. Taschuk, M.J. Brett, University of Alberta, Canada
With growing application of glancing-angle deposition (GLAD) thin films, there is increasing need to understand and engineer GLAD growth mechanics. Devices that make use of GLAD films, such as RH sensors, optical filters, and solar cells require precise knowledge and control of GLAD nanostructure. Typically, GLAD vertical post diameters are described by a power law, $d = w_0 h^p$, where d is column diameter, h is height, and w_0 and p are material dependent constants which describe column diameter and broadening, respectively [1, 2]. Based on theoretical growth models, p is expected to range from 5/16 to 1/2. While many GLAD materials have been characterized for p , reliable trends have not yet been obtained [2,3,4,5].

Most groups measure p from cross-sectional SEM images, recording diameters of clearly distinct posts as a function of height. This technique is labour-intensive and large scatter in the data has been observed [4]. One alternative, focused ion-beam cross sections of GLAD films [5], produces very precise measurements but is impractical for characterizing the ensemble properties of a GLAD film. In both cases, the limited number of measurements restricts what can be learned about GLAD films.

To eliminate this limitation, we have been developing an automated characterization method for GLAD posts that enables effective measurement of thousands of posts. Using this technique, we have measured p and w_0 as a function of pitch for 1500 nm TiO₂, 81° deposition angle, vertical post films. We examine post growth for "extinct" and full height posts, discovering markedly different growth scaling behaviors. Characterization of phi-sweep slanted post structures is underway. We will present the optimized technique, current experimental results, and comparisons of automated measurements with existing measurement methodologies.

[1] T. Karabacak, J. Singh, Y.-P. Zhao, G.-C. Wang, and T.-M. Lu, *Phys. Rev. B*, vol. 68, Sep. 2003.

[2] C.M. Zhou and D. Gall, *J. Appl. Phys.*, vol. 103, Jan. 2008, p. 014307.

[3] C. Buzea, G. Beydaghyan, C. Elliott, and K. Robbie, *Nanotechnology*, vol. 16, Oct. 2005, pp. 1986-92.

[4] M.T. Taschuk, K.M. Krause, J.J. Steele, M.A. Summers, and M.J. Brett, *J. Vac. Sci. Technol. B*, vol. 27, 2009, p. 2106.

[5] K.M. Krause, D.W. Vick, M. Malac, and M.J. Brett, *Langmuir*, vol. 26, Nov. 2010, pp. 17558-67.

4:20pm SE+TF-TuA8 Heterogeneous Nanorod Arrays Fabrication by a Two-Source Dynamic Shadowing Growth System, Y.P. He, Y.P. Zhao, University of Georgia

There are increasing interests in designing and engineering nanostructured materials to improve their performances in various applications. Among many nanostructure fabrication and synthesis techniques, the dynamic shadowing growth can offer an unique advantage by sculpturing nanorod-based structures through computer programming using the self-shadowing

effect. The geometry shadowing effect is the dominant growth mechanism resulting in the formation of topologically engineered nanostructure arrays, such as tilted, C-shape, S-shape, L-shape, zigzag, matchstick, helical, and vertical nanorods, by programming the substrate rotation in polar and/or azimuthal directions. Such a topological design can be further advanced through compositional engineering. A co-deposition provides a way to evaporate two or more materials simultaneously to form homogeneous composite/doped nanostructures by controlling the relative ratio of the deposition rates of two or more sources. Recently, we have constructed a two-source dynamic shadowing growth (DSG) and demonstrated that various topologically and compositionally engineered nanostructures can be designed by multilayer glancing angle deposition (GLAD) and/or glancing angle co-deposition (GLACD) techniques. Here, we will highlight some of the recent progress in designing heterostructured nanorod arrays through a two-source dynamics shadowing growth system. In particular, Vanadium catalyst doped Mg nanorod arrays fabricated through the oblique angle co-deposition show very different morphology compared to the Mg nanoblades formed by oblique angle deposition. The kinetics of the hydrogen storage performance of the doped Mg nanostructures can be greatly improved compared to that of the Mg nanoblades. The composition-graded CuSi nanorod array can be designed through dynamically changing the deposition rates of the two sources. The Li⁺ battery performance of these nanostructures compared to that of pure Si nanorods will be discussed.

Surface Science Division

Room: 110 - Session SS+EM-TuA

Organic Electronic Interfaces

Moderator: J.R. Engstrom, Cornell University

2:00pm SS+EM-TuA1 The Effect of Structure on Interfacial Energy, F. Stellacci, EPFL, Switzerland **INVITED**

In this talk I will highlight recent result on solid-liquid interfaces where the solid has a nanostructure with a characteristic length scale that is only a few liquid molecule wide. The talk will start with the presentation of a new scanning probe technique able to measure interfacial energy (work of adhesion to be precise) with atomic/molecular resolution. It will then show how surfaces with alternating stripe-like domains a few nanometer thick have a structural component to their work of adhesion that can account for as much as 20% of the total energy. Finally novel self assembly approaches to achieve such surfaces will be discussed.

2:40pm SS+EM-TuA3 Interfacial Electronic Structure of Dipolar Organic Semiconductors, O.L.A. Monti, M.P. Steele, N. Ilyas, L.L. Kelly, D.A. Rucke, University of Arizona

We present an investigation of the evolution of the electronic structure at the interface of the dipolar organic semiconductor vanadyl naphthalocyanine with both highly oriented pyrolytic graphite and Au (111). Using angle-resolved two-photon photoemission and other photoelectron spectroscopies we observe both excitonic as well as strictly interfacial states in both ground and excited state manifolds, with large differences between the two surfaces. Simple electrostatic considerations provide a chemisorption model that is capable of quantitatively describing long- and short-range interface-mediated intermolecular coupling, significantly altering the molecular electronic structure. Additional insights are available from full-scale first-principles calculations at these interfaces. As a consequence, we show that electrostatic multipoles can significantly influence molecular and interfacial electronic structure, with direct and observable impact on interfacial charge-transfer dynamics. Interfacial electrostatic fields may therefore be used to manipulate in a concrete fashion processes of critical importance to solar energy conversion such as photoinduced interfacial electron transfer.

3:00pm SS+EM-TuA4 Characterization of Quinonoid Zwitterion Molecular Films on Metal Surfaces, L. Routaboul, P. Braunstein, Lab. de Chimie de Coordination (UMR 7177 CNRS), France, B. Doudin, Inst. de Phys. et Chimie des Mat. de Strasbourg, France, J. Xiao, Z. Zhang, Nebraska Ctr. for Mat. & Nanosci., Y.B. Losvyj, O. Kizilkaya, The J. Bennett Johnston Sr. Ctr. for Adv. Microstructures & Devices, L.G. Rosa, Univ. of Puerto Rico-Humacao, P.A. Dowben, Nebraska Ctr. for Mat. & Nanosc.

There is considerable interest in the functionalization of metal surfaces by molecules with large dipoles. For this purpose, *p*-benzoquinonemonimine-type zwitterions represent ideal candidates. These zwitterions can be anchored on gold surfaces where they form homogeneous thin films with the dipole preferentially oriented along the surface normal.^[1] Some zwitterions will selectively adsorb on patterned gold substrates from

solution while selective deposition of the zwitterions onto specific ferroelectric domains has been demonstrated. This represents an attractive approach to pattern molecular deposition on optically transparent planar substrates through electrostatic dipolar interactions or orientation dipole controlled surface chemistry. Taking advantage of the high solubility of two zwitterions in both organic solvents and water, we studied the influence of the solvent on the functionalization of surface.^[2] The goal is to control both packing and selective deposition on a variety of substrates through zwitterion solvent combination.

Acknowledgement. This research was supported by the CNRS and the Ministère de la Recherche et des Nouvelles Technologies, the ANR (07-BLAN-0274-04), the National Science Foundation (grants CHE-0909580 and DMR-0851703), and the Nebraska Center for Materials and Nanoscience at the University of Nebraska-Lincoln.

4:00pm SS+EM-TuA7 Directed Organization of C₇₀ Kagome Lattice by TiOPc-Monolayer Template, J.E. Reutt-Robey, Y. Wei, University of Maryland

Abrupt molecular semiconductor interfaces between titanyl phthalocyanine (TiOPc) and C₇₀ were prepared by physical vapor deposition and characterized by UHV-STM. Molecular TiOPc is a highly anisotropic molecule with a 3.5 dipole moment. Ordered TiOPc monolayer films of the honeycomb phase thus represent a regular 2-d dipolar lattice, which was investigated as an electrostatic template for the growth of the highly polarizable C₇₀. Films of C₇₀ grown layer-by-layer revealed the directed formation of a Kagome lattice. Atomically detailed structural models were obtained for the 0-6 nm C₇₀ thickness (up to 5 ML) range over which the ordering influence of the TiOPc dipolar substrate persists. Unusually low-density C₇₀ molecular packing arrangements result from the ellipsoidal shape, curved surfaces and high polarizability of C₇₀. While Kagome lattices have been frequently observed in colloidal and magnetic systems, this appears to be the first electrostatically-induced Kagome lattice involving a molecular film.

This work has been supported by the National Science Foundation under Surface Analytical Chemistry grant CHE0750203 and under the University of Maryland MRSEC DMR-05-20471

4:20pm SS+EM-TuA8 Solvation - Assisted Growth of ZnPc and 4NO₂-ZnPc Monolayer Films on Au(111), L. Tskipuri, Q. Shao, J.E. Reutt-Robey, University of Maryland, College Park

The UHV spray-jet molecular beam deposition technique marries the chemical versatility and efficiency of solution-film processing with the atomic-level control and analytical tools of UHV surface science. Here we show how the solvent used in aerosol deposition can be used to fine tune film morphology. Thin films of ZnPc and 4NO₂-ZnPc are grown on a Au(111) support with a newly developed spray-jet molecular beam deposition source and characterized in situ via UHV-STM. Phthalocyanes are delivered to the Au(111) surface in a series of N₂-entrained μ-sized solvent droplets of variable surface residence time. The formation of submonolayer films with corresponding density variations demonstrates the impact of the ~nm-thick solvation layers on growth kinetics. Phthalocyanine film registration to the herringbone reconstruction of the Au(111) substrate, indicative of thermodynamically-favored structure, is observed only for aromatic solvents with long residence times. Vacancy cavities in monolayer films from solvent memory are eliminated with mild annealing, yielding film structures that rival PVD grown films. Results are interpreted through solvation-mediated kinetics.

4:40pm SS+EM-TuA9 Direct Observation of NO₂ Adsorption onto CuPc Monolayers with STM, J.H. Park, J. Royer, S. Lee, T. Kent, W. Trogler, A.C. Kummel, University of California San Diego

Copper phthalocyanine (CuPc) thin film devices have been widely studied for use as chemical vapor sensors; however, the molecular scale sensing mechanism remains undetermined. This study presents molecular scale observation of NO₂ adsorption onto CuPc monolayers using ultra-high vacuum (UHV) scanning tunneling microscopy (STM). CuPc monolayers were deposited on Au (111) surfaces by organic molecular beam epitaxy in ultra-high vacuum (UHV) and subsequently exposed to different NO₂ concentrations at atmospheric pressure. After annealing at 50 °C to improve STM imaging, for low NO₂ doses (1 ppm for 5min) the STM images reveal NO₂ molecules arranged as islands primarily along the domain boundaries. The NO₂ molecules almost completely desorb from the CuPc monolayer after annealing at 100 °C for 1 hr. Conversely, at high NO₂ doses (10 ppm for 5 min), the NO₂ exhibit irreversible reactions with the CuPc surface. After annealing at 50 °C, the domain boundaries act as nucleation centers for semi-ordered NO₂ adsorbates. As the annealing temperature is increased to 150 °C, the islands of NO₂ molecules diffuse from the domain boundaries to the CuPc terraces to form ordered structures on the terraces. After annealing at 250 °C for 1 hr, the CuPc monolayer becomes disordered and

has numerous vacancies. The data is consistent with that NO₂ inducing CuPc decomposition. The behavior of NO₂ dosed CuPc monolayers suggests that NO₂ undergoes molecular chemisorption with the CuPc metal center at low exposures. However, at high exposures, NO₂ not only undergoes molecular chemisorption with the metal center, but also induces decomposition of the CuPc. This direct observation for NO₂ dosed CuPc monolayers with STM can give an insight into reversible versus dosimetric sensing in CuPc organic thin film chemical sensors (chemFETs). While nearly all weakly bonding analytes give reversible mobility sensor responses on CuPc chemFETs, some strong oxidants are observed to give reversible mobility responses at short exposures and dosimetric irreversible threshold voltage responses for longer exposures. This is consistent with the larger doses saturating the reversible chemisorption sites and inducing an oxidative decomposition of the CuPc which induces a dosimetric response via formation of uncompensated positive charge in the CuPc film. Therefore, the data is consistent with two chemisorption mechanisms of a strong oxidant on a single molecule given two different classes of sensor response.

5:00pm SS+EM-TuA10 Tunneling Spectroscopy of Benzoic Acid Monolayers: The Role of the Metal-Molecule Interface, J. Kreil, P. LeClair, G.J. Szulcowski, The University of Alabama

A series of self-assembled monolayers were prepared from para-substituted benzoic acids (X-C₆H₄CO₂H where X = H, F, Cl, Br, I, and CN) onto oxidized Al films and characterized by x-ray photoelectron spectroscopy and contact angle measurements. The acids adsorb to the oxide as a carboxylate group with the plane of the aromatic ring largely perpendicular to the surface, which places the para-substituent away from the surface. Tunnel junctions were made by vapor deposition of Ag and Pb films as the top electrodes onto the monolayers. Four point probe electrical measurements were made from 4 to 300K. At 4 K the superconducting gap of Pb was observed and unequivocally demonstrates tunneling through a barrier without metallic shorts. When Ag was the top electrode, differential conductance [G(V) = dI/dV] measurements at 4 K showed a quadratic dependence on the applied bias voltage and no zero-bias anomalies. These low temperature measurements suggest the monolayers form pin-hole free tunnel barriers. Two trends emerge when comparing G(V) versus bias voltage for junctions with Ag and Pb top electrodes. When Pb was the top electrode the minimum in G(V) versus bias voltage is offset from zero bias for each monolayer, which scales in a systematic manner with the polarity of the para C-X bond. However, when Ag was the top electrode there was no offset the tunneling conductance. The origin of the different tunneling behavior observed for Pb and Ag top electrodes will be discussed in detail.

5:20pm SS+EM-TuA11 Interfacial Engineering of Organic Light Emitting Diodes with Sputter Treated Molybdenum Oxides as Hole Injection Layers, C.I. Wu, P. Wang, I. Wu, National Taiwan University, Republic of China

In this paper, the mechanisms leading to the enhancement of organic light emitting diodes (OLEDs) with molybdenum oxide MoO₃ incorporated in as hole injecting layers (HILs) will be discussed. The first one is the lowering of hole injection barrier between anodes and organic layers when a thin film of MoO₃ is inserted. The high work function of MoO₃ serves as a carrier ladder which decreases misalignment between the Fermi level of electrodes and highest occupied molecular orbital (HOMO) level of hole transport layers, such as N,N'-di(naphthalene-1-yl)-N,N'-diphenyl-benzidine (NPB). The second model is the formation of gap states above the valence band edge of MoO₃ to the Fermi level of electrodes when NPB molecules are deposited on MoO₃ layers. These gap states enhance the conductivity of MoO₃ and provide transition paths of carrier to assist the injection of hole from indium tin oxide (ITO) anodes to NPB layers. The third mechanism is the p-type doping effect of MoO₃ doped in NPB layers. This p-type doping increases hole concentration in NPB layers and reduces the energy difference between the Fermi level of electrodes and the HOMO of NPB.

We will also demonstrate an effective method to improve the current injection efficiency of OLEDs by modifying the oxidation states of as-deposited MoO₃ as HILs with in-situ argon ion (Ar⁺) sputtering. The injection current of devices incorporating this method is enhanced by one order of magnitude, as compared to that of devices without sputter treatment. The luminance of the devices is also improved. Beside device characterization, X-ray photoemission spectroscopy (XPS) and ultra-violet photoelectron spectroscopy (UPS) were carried out to obtain the chemical and electronic information of MoO₃ thin films treated with Ar⁺ sputter and to unveil the origins of improvement in device performance. It is found that, with slight sputter treatments, MoO₃ layers represent lower oxidation states and show metallic characteristics in energy band structure, which remarkably elevates the carrier injection efficiency from ITO to NPB.

5:40pm **SS+EM-TuA12 Probing Surface Photovoltage Development by Dynamical XPS Measurements**, *S. Suzer*, Bilkent University, Turkey

Various semiconducting, photoactive and insulating materials have been investigated using XPS where the data is collected in a dynamic mode. This is achieved by recording the spectrum while applying an electrical signal in the form of ± 5 or 10 V d.c. bias, and/or square-wave pulses, without and under photoillumination using different lasers. This method enables us to probe and sort out the effects and contributions of the three fundamental processes operating; **Charging, Photovoltage-Development, and Photoconductivity** in a **chemically specific fashion**. Accordingly, the chemical shift differences between the n- and p-doped semiconductors are amplified due to the effect of the photovoltage operating in the opposite directions. Time and/or frequency dependence of various processes adds a new dimension to XPS for sorting out the effects of external stimuli (electrons, ions, photons, etc.) as well as the chemical nature of the material under investigation. Experimental results and various applications will be presented and discussed.

Surface Science Division

Room: 109 - Session SS-TuA

Catalysis on Metals and Alloys

Moderator: G. Fisher, University of Michigan

2:00pm **SS-TuA1 La_{1-x}Ce_xMnO₃ Perovskites: Structural Features and Performance for Preferential CO Oxidation Reaction**, *S.S. Maluf*, Federal University of Sao Carlos, Brazil, *B.E. Hayden*, University of Southampton, UK, *C.R.M. Afonso*, Federal University of Sao Carlos, Brazil, *E.M. Assaf*, University of Sao Paulo, Brazil, *P.A.P. Nascente*, Federal University of Sao Carlos, Brazil

The perovskite structure is characterized by a large capacity to stabilize unusual valence states of different metal ions and can also accommodate variable amounts of different lattice defects. Several lanthanum transition metal based perovskites, represented as La_{1-x}A_xMO₃, have been known as very good oxidation catalysts in a variety of reactions. Particularly, LaMnO₃ perovskites have shown to be the most active. The catalytic activity of these compositions in different reactions can be further enhanced by the substitution of lanthanum by cerium. The catalysts were prepared by coprecipitation method, from aqueous solutions of La, Mn, and Ce nitrates with Na₂CO₃/NaOH solution (pH 10). The prepared samples were La_{1-x}Ce_xMnO₃ (x = 0, 0.05, and 0.10) and were characterized by EDS-SEM, surface area-BET method, X-ray diffraction (XRD), and temperature programmed reduction (TPR). The catalytic activity was tested over the temperature range of 130–230°C in a fixed-bed tubular glass micro-reactor, with 200mg of catalyst. The reaction products were analyzed in-line by gas chromatography. The amounts of the constituent metals obtained by EDS were in agreement with expected values; the presence of cerium did not change the surface area of the samples (26–27 m² g⁻¹). The X-ray diffraction lines corresponded to cubic LaMnO₃ structure; the replacement of La did not change the diffractograms. Peaks of cerium oxide were not observed, suggesting the incorporation of Ce ions into the LaMnO₃ lattice. The sample with the highest content of cerium presented an increase on thermal stabilization of Mn³⁺ ions, and Mn⁴⁺ species were reduced to lower temperatures. The SEM results indicated that the presence of cerium decreased slightly the grain size (from 56 to 43 nm) and the range of distribution sizes is homogeneous and the most grains are spherical. All samples presented the same catalytic behavior, starting their activities at 130°C, and their activities increased with the temperature. At 150°C, the sample with 5% of Ce presented a slight advantage compared to other samples, and this was more significant at 230°C, indicating that the promoter effect of cerium can be observed for higher reaction temperatures. The results suggested that the replacement of La by Ce caused an increase of cationic/anionic vacancies and also in the Mn⁴⁺/Mn³⁺ ratio change, and consequently the catalytic behavior for CO oxidation changed, facilitating the CO adsorption.

Acknowledgements

The authors thank FAPESP for financial assistance, Ilika Technologies and University of Southampton for the XRD analyses.

2:20pm **SS-TuA2 Faceted Metal Surfaces: Surface Chemistry and Growth of Metallic Nanoclusters**, *W. Chen, Q. Shen, R.A. Bartynski*, Rutgers University

In this work, surface faceting is used to prepare a nanoscale model catalyst for surface reactions and a nanoscale template for growth of metallic nanoclusters. Faceting occurs when an initially planar surface converts to a “hill and valley” structure exposing new crystal faces of nanometer scale dimensions. Nanoscale three-sided pyramids exposing (311), (31-1) and

(110) faces with tunable facet sizes are formed on an initially planar Ir(210) surface upon annealing in O₂ and a clean faceted Ir(210) surface can routinely be prepared in situ by heating in H₂. Surface reaction of NO+CO has been carried out on clean planar Ir(210) and clean faceted Ir(210) with varying facet size (5–14nm). Both planar and faceted Ir(210) favor reduction of NO by CO with high selectivity to N₂, which is accompanied by simultaneous oxidation of CO. The reaction is not only structure sensitive on faceted Ir(210) versus planar Ir(210) but also exhibits size effects on faceted Ir(210) for average facet size ranging from 5nm to 14nm without change in facet structure. Strong interaction between NO and CO at high NO exposure and 1ML CO pre-coverage results in “explosive” evolution of N₂ and CO₂ on planar Ir(210). Annealing Ru(11-20) in NO₂ leads to formation of ridge-like faceted surface exposing (10-11), (10-1-1), (01-11) and (01-1-1) faces. Faceted O/Ru(11-20) facilitates growth of nanoscale metallic clusters at room temperature which preferentially nucleate within valleys of the faceted surface.

Supported by DOE contract No. DE-FG02-93ER14331

2:40pm **SS-TuA3 Modeling the Complexities of Heterogeneous Catalysts**, *D.W. Goodman, Matt Lundwall*, Texas A & M University
INVITED

In the past several decades, surface science methodologies have contributed significantly to our understanding of reaction mechanisms of heterogeneous catalysts. From fundamental studies on metal single crystals to investigations of metal oxide supported metal clusters, the relative complexities of model catalyst systems have continued to evolve in complexity and likeness to industrial catalysts. Studies on metal single crystals have aided researchers in understanding the effect of surface structure on catalyst reactivity and selectivity for a number of important reactions. More recently model systems consisting of metal clusters deposited on planar oxide surfaces under ultra high vacuum conditions have facilitated the study of metal particle size and support effects. These model systems are useful for carrying out kinetic investigations, yet are amenable to surface spectroscopic techniques, thus enabling investigations under realistic pressures and at working temperatures. This talk will present selected investigations of catalytic reactions on single crystal and model supported catalysts with emphasis on recent work addressing the nature of the active site in structure sensitive reactions.

4:00pm **SS-TuA7 Nanocatalysis: New Developments in Catalytic Performance of Size- and Shape-Controlled Metal Nanoparticles**, *B. Roldán Cuenya*, University of Central Florida

Tailoring the chemical reactivity of nanomaterials at the atomic level is one of the most important challenges in catalysis research. In order to achieve this elusive goal, fundamental understanding of the geometric and electronic structure of these complex systems at the atomic level must be obtained. To study these effects, homogeneous size- and shape-selected Pt nanoparticles (NPs) were synthesized by means of diblock copolymer encapsulation.

The influence of the nanoparticle *shape* on the reactivity of Pt nanocatalysts supported on nanocrystalline γ -Al₂O₃ will be described. Nanoparticles with similar size distributions (~0.8–1 nm) but with different shapes were found to display distinct reactivities for the oxidation of 2-propanol. A correlation between the number of undercoordinated atoms at the nanoparticle surface and the onset temperature for 2-propanol oxidation was observed, demonstrating that catalytic properties can be controlled through shape-selective synthesis. Furthermore, the complex interaction between catalysts and reactants was investigated under *operando* conditions via X-ray absorption fine-structure spectroscopy. Platinum oxides were found to be the active species for the partial oxidation of 2-propanol (<140°C), while the complete oxidation (>140°C) was catalyzed by oxygen-covered metallic Pt NPs. Our findings highlight the decisive role of the nanoparticle structure and chemical state in oxidation catalytic reactions.

4:20pm **SS-TuA8 Oxidative-Coupling Reactions via Nucleophilic Attack on Gold Surface**, *B. Xu*, C.M. Friend, R.J. Madix*, Harvard University

Metallic gold owes its centuries-old mystique and intrinsic value to its chemical inertness toward bulk compound formation. In the past decade, however, it has been discovered that the surface of gold is far from inert, and that gold can catalyze important chemical transformations – particularly with the assistance of molecular oxygen or other oxidizing agents. These processes are of particular significance because they may occur at remarkably low temperatures and pressures, suggesting the possibility of energy efficient and environmentally benign reaction conditions using metallic gold catalysts. Recently, there has been a focus on selective

* Morton S. Traum Award Finalist

oxidation of alcohols to aldehydes, oxidative self-coupling of alcohols to form esters and, most recently, acylation via amine-formaldehyde coupling. Our work under ultra-high vacuum (UHV) condition on the well defined model system of Au(111) surface has unequivocally proved that surface adsorbed atomic oxygen is critical in facilitating a range of nucleophilic coupling-reactions among alcohols, aldehydes and amines. A general reaction mechanism for this class of coupling-reactions is established: surface alkoxy or amide is formed via the deprotonation of the corresponding alcohol or amine by surface atomic oxygen, which can subsequently nucleophilically attack the aldehydes (formed in situ from alkoxy or introduced directly) and produce the corresponding ester or amide. The product distribution of our low-pressure experiments match remarkably well with gas phase reactions carried out in the ambient condition as well as liquid phase reactions, proves the generality of the mechanism.

4:40pm SS-TuA9 Understanding the Enhanced Activity for Methanol Reaction on Titania-supported Au Clusters, D.A. Chen, S.A. Temney, B.A. Cagg, M.S. Levine, University of South Carolina, S. Hong, T.S. Rahman, University of Central Florida

The growth and chemical activity of Au clusters deposited on rutile TiO₂(110) were studied by scanning tunneling microscopy, temperature programmed desorption and density functional theory calculations. Methanol reaction on 0.25 ML Au clusters produces formaldehyde as the major product at 535 K with methanol desorption observed at the same temperature; water and hydrogen evolution are detected below room temperature, as well as methyl radical evolution at 575 K. On the titania surface itself, methanol reaction also produces methyl radical around 600 K. Formaldehyde production reaches its maximum value between 0.25 and 2 ML but decreases dramatically as the coverage is increased to 5 ML. This behavior suggests that formaldehyde is produced at the Au-titania interface since formaldehyde production does not occur at pure Au sites. STM experiments confirm that the 0.25 ML Au coverage has the greatest number of Au-titania interfacial sites at the perimeter of the clusters. For higher coverages of 2 and 5 ML, cluster coalescence diminishes the number of Au-titania sites, and this is consistent with the decreased formaldehyde yield at higher Au coverages. When the titania surface is reoxidized with ¹⁸O₂ prior to Au deposition and exposure to methanol, lattice oxygen is incorporated into the water that is evolved at low temperature. We propose that the role of the titania support is to facilitate the formation of the reactive methoxy intermediate via abstraction of the hydroxyl hydrogen in methanol by lattice oxygen. Density function theory calculations also indicate that methoxy is the intermediate formed at the Au-titania interface after O-H bond scission is induced by lattice oxygen.

5:00pm SS-TuA10 Oxygen Chemisorption, Formation, and Thermal Stability of Pt Oxides on Pt Nanoparticles Supported on SiO₂/Si(001): Size-Effects, L.K. Ono, J.R. Croy, H. Heinrich, B. Roldan Cuenya, University of Central Florida

The changes induced in the structure and chemical state of size-selected Pt nanoparticles (NPs) supported on ultrathin SiO₂ films upon exposure to oxygen have been investigated by atomic force microscopy, transmission electron microscopy, in situ X-ray photoelectron spectroscopy (XPS), and temperature-programmed desorption (TPD). For low atomic oxygen dosings, chemisorbed oxygen species were detected on all samples. Exposure to higher atomic oxygen coverages at room temperature lead to the formation and stabilization of PtO_x species (PtO₂ and PtO). On all samples, a two-step thermal decomposition process was observed: PtO₂ → PtO → Pt. For NPs in the 2-6 nm range, the NP size was found to affect the strength of the O-binding. Contrary to the case of Pt(111), where no oxides were detected above 700 K, 10-20% PtO was detected on the NP samples via XPS at the same temperature, suggesting the presence of strongly bond oxygen species. In addition, for identical atomic oxygen dosings, decreasing the NP size was found to favor their ability to form oxides. Interestingly, regardless of whether the desorption of chemisorbed oxygen species or that of oxygen in PtO_x species was considered, our TPD data revealed higher O₂ desorption temperatures for the Pt NPs as compared to the Pt(111) surface. Furthermore, a clear size-dependent trend was observed, with an increase in the strength of the oxygen bonding with decreasing NP size.

5:20pm SS-TuA11 Alloy Surface Reactivity on Cu_xAu_yPd_{1-x-y} Composition Spread Alloy Films, A.J. Gellman, J.B. Miller, P. Kondratyuk, D. Priyadarshini, Carnegie Mellon University, B.D. Morreale, National Energy Technology Laboratory

The key features of Cu-Au-Pd alloys relevant to their application as hydrogen purification membranes are the ability to dissociatively adsorb H₂ and the ability to transport H atoms through their bulk. We have developed tools for the preparation of Cu_xAu_yPd_{1-x-y} composition spread alloy films (CSAFs) as libraries for high throughput study of their catalytic surface properties. These ternary Cu_xAu_yPd_{1-x-y} CSAFs expose a broad and

continuous distribution of compositions for spatially resolved analysis of their properties. Electron backscatter diffraction has been used to verify the structure of the films across their composition spread and to demonstrate that they have the atomic structure expected on the basis of their phase diagram. LIES has been used to study surface segregation as a continuous function of composition, (x,y), demonstrating that segregation is preferred in the order Au>Cu>Pd at the clean alloy surfaces. A multichannel microreactor array has been used to spatially resolve the surface activity for H₂ dissociation by measuring the kinetics of H₂-D₂ exchange as a function of alloy composition. This reveals that while both Cu and Au poison surface activity, Cu is more effective than Au at suppressing H-D exchange activity. This work demonstrates the potential value of CSAFs as platforms for study of alloy surface chemistry and for comprehensive study of their properties across composition space.

5:40pm SS-TuA12 Pd Ensemble Effects on Enhancing Low Temperature CO Oxidation and Tolerance on AuPd Alloys: A First Principles Study, H.C. Ham, J.A. Stephens, G.S. Hwang, University of Texas at Austin

In the oxidation reaction of fuels such as CO-contained hydrogen, methanol and formic acid at the low temperature region (300 ~ 400K) at the anode side of polymer electrolyte membrane fuel cell, the precious catalysts such as Pd and Pt have suffered the gradual loss in the catalytic activity due to the blocking of active sites (Pd/Pt) by CO molecules (the so-called CO poisoning effect). To handle this issue, alloying precious catalysts by other transition metals has been suggested as one of solutions since the synergetic alloying effects such as the creation of unique mixed-metal surface sites [ensemble effect] and electronic structure change by metal-metal interactions [ligand effect] can provide an avenue for preventing CO poisoning and enhancing CO oxidation at the low temperature.

In this talk, we will present our recent first-principles results on the role of Pd ensembles on the AuPd alloy in enhancing CO oxidation and tolerance at the low temperature. Using spin-polarized DFT-GGA calculations, for the first time, we elucidate that the reactivity toward CO+O₂ oxidation at the low temperature on various CO-precovered Pd ensembles (such as monomer, dimer, trimers and tetramers) is a strong function of surface Pd arrangements on the AuPd surface. In particular, the small-sized ensembles like dimer or compact trimer are responsible for enhancing the low temperature CO+O₂ oxidation by the increased availability of free Pd sites and facile O₂ activation on CO-precovered Pd ensembles. We will also show the importance of the interplay of ensemble and ligand effects in reducing the CO poisoning of the catalysts through the comparison study on the energetics, charge transfer, geometric and electronic structures of CO between Pd and Pt ensembles. Finally, we will present geometric parameter effects (such as strain and facet) on the CO tolerance of Pd ensembles, which can provide the proper criteria for designing the nano-sized Au-based bimetallic catalysts.

This study hints on how the surface arrangements of atoms and the influence of ensembles on the reaction kinetics and energetics can offer insight to properly tailor CO-tolerant Au-based bimetallic catalysts for fuel cell applications.

Thin Film Division

Room: 107 - Session TF-TuA

ALD: Fundamental Reactions and Film Properties

Moderator: S.M. George, University of Colorado, Boulder

2:00pm TF-TuA1 Indium Oxide Atomic Layer Deposition Facilitated by the Synergy between Oxygen and Water, J.A. Libera, J.N. Hryn, J.W. Elam, Argonne National Laboratory

This study describes how In₂O₃ films can be prepared by ALD using alternating exposures to cyclopentadienyl indium (InCp) and combinations of H₂O and O₂, even though H₂O and O₂ are ineffective when used individually. Nanostructured photovoltaics would benefit enormously from the capability to deposit conformal indium-tin oxide (ITO) films inside of high aspect ratio structures. For instance, our previous In₂O₃ ALD method using InCp and O₃ enabled ITO growth inside of anodic alumina membranes producing higher photocurrents through radial charge collection in dye-sensitized solar cells. However, this process yielded poor thickness conformality due to the In₂O₃-catalyzed thermal decomposition of O₃, and this shortcoming motivated our search for an O₃-free process. We were surprised to discover that when H₂O and O₂ were used together, either as a simultaneous exposure (SE) or in the sequence H₂O-O₂ (WO) or O₂-H₂O (OW), very uniform, highly conducting In₂O₃ films were deposited at 1.0-1.6 Å/cycle over large areas (12"x18") at temperatures as low as 100°C. *In-situ* quartz crystal microbalance, mass spectrometry, and Fourier transform

infrared measurements revealed that the H₂O and O₂ work synergistically to facilitate the In₂O₃ ALD. Each molecule performs a necessary but distinct role in the growth mechanism. Next, we conducted a thorough study of this process for all three growth modes (SE, WO, OW) over the temperature range 100-250°C using spectroscopic ellipsometry, ultraviolet-visible transmission, X-ray diffraction, scanning electron microscopy, and Hall probe measurements. These measurements identified a remarkable correlation between the film structure and electrical properties around an amorphous-to-crystalline phase transition near the deposition temperature of 140°C.

2:20pm TF-TuA2 Engineering AlN Thin Films by Atomic Layer Deposition on Wide Bandgap Semiconductors as Gate Dielectric, Y.-C. Perng, J.P. Chang, University of California Los Angeles

Wide bandgap semiconductors, such as SiC and GaN, are known as base materials in electronic devices operating under high temperatures and high electric fields. Aluminum nitride (AlN) is a promising interfacial layer or dielectric material for SiC and GaN due to its material properties, such as wide bandgaps, similar atomic arrangement and small lattice mismatch (1.3% and 2.6%). Although various deposition methods, such as chemical vapor deposition (MOCVD) and molecular beam epitaxy (MBE), have been used, synthesizing high quality AlN thin films for those applications is still an issue, especially in the view of controllability in atomic scales. Atomic layer deposition (ALD) is used to synthesize AlN thin layer on SiC, GaN and Si to achieve atomic controllability and assess the possibility to extend this deposition method to nitride growth and how the substrate properties affect the interface quality and corresponding electrical properties of the synthesized film

The AlN thin films were synthesized at 400~600°C via a chamber with the base pressure as 10⁻⁷ torr, using trimethylaluminum (TMA) and blue grade ammonia (NH₃) as precursors. The surface structure during the deposition was monitored via *in-situ* RHEED and the growth rate was 0.5~2Å/cycle as a function of the deposition temperature. The surface composition, including the impurities, was found to be correlated to the deposition temperature, verified by *in-situ* x-ray photoelectron spectroscopy (XPS). The surface morphology of the films was studied by transmission electron microscopy (TEM) and atomic force microscope (AFM) and found to be conformal because the rms value was found to be less than 10Å on SiC, which is the same as that of the substrate surface roughness. The capacitance/conductance-voltage characteristics were measured to determine the dielectric constant of the ALD film and interpret the interface states density, which were 8 and on the order of 10¹² cm⁻²eV⁻¹, respectively, comparable to that reported for MBE synthesized AlN.

2:40pm TF-TuA3 Paul Holloway Award Lecture - Gas-Surface Interactions during Atomic Layer Deposition, S. Agarwal*, Colorado School of Mines **INVITED**

Atomic layer deposition (ALD) is an ideal technique for depositing amorphous and polycrystalline films that require atomic layer control over the film thickness and chemical composition, and can provide conformal coverage with sharp interfaces on high-aspect-ratio nanostructures. ALD has been used to deposit oxide, nitride, elemental and compound semiconductors, and metal films for various applications. The primary challenges in ALD are control over the film's microstructure and residual impurities, which in turn affect their structural, electrical, and transport properties. To overcome these problems, an understanding of atomic-scale events that occur during growth is required. In this presentation, we will discuss the mechanisms of the surface reactions of radicals and molecular precursors supplied during growth using a suite of *in situ* diagnostic tools. We will specifically discuss the reaction mechanisms during plasma- and ozone-assisted ALD of TiO₂, Al₂O₃, and SiO₂, and how such reactions influence the film properties.

4:00pm TF-TuA7 Mechanical Properties of ALD Thin Films, H. Baumgart, Old Dominion University **INVITED**

Atomic Layer Deposition (ALD) is recognized as the preferred method to deposit technologically important thin films of novel high-k dielectric metal oxides or semiconducting metal oxides for CMOS and MEMS technology with Angstrom accuracy. Large bodies of extensive studies exist on the electrical characterization of ALD films, however, there exists a lack of systematic studies regarding the mechanical properties of ALD grown thin films. Elevated temperatures cause phase changes in many ALD metal oxide films, which affect the mechanical properties and surface morphologies. Little is known about the impact of those phase changes on the nanomechanical properties of ALD HfO₂. Phase change of ALD HfO₂ impacts the mechanical and electrical properties of high-k dielectric gate insulators depending on whether a Gate First or Gate Last process

integration has been adopted. Nanoindentation is the most appropriate testing mechanism that accurately investigates the mechanical properties of extremely thin film specimens such as microcrystalline ALD thin films. Nanoindentation testing was conducted to investigate the impact of the different phase changes of HfO₂ on the mechanical properties. We have deposited ALD HfO₂ at low temperature and measured the mechanical properties of the various phase changes of HfO₂ following various thermal annealing cycles. After crystallization by annealing in a rapid thermal annealing (RTA) chamber, the modulus was found to decrease from 370±20GPa to 240±20GPa as the HfO₂ films transition from amorphous to polycrystalline structure past the phase change transition temperature of 600°C. Similarly, the hardness measurements reveal a high value of 18±1GPa for amorphous HfO₂ films and a decrease to 15±1GPa following the transition temperature to polycrystalline HfO₂ films.

Piezoelectric films such as ALD ZnO are finding applications in microelectromechanical systems (MEMS), piezoelectric transducers and oscillators, micro-resonators, gyroscopes, and energy harvesters. Since piezoelectricity of ZnO involves internal generation of electrical charge resulting from an applied mechanical force deforming the static structure of the ZnO crystals, studying the mechanical properties of novel ALD thin films of ZnO is important for these technical applications. Obtaining a better understanding of the structural and mechanical properties of novel ALD ZnO films is essential to improve key performance parameters of MEMS micro-devices.

An overview of the measured mechanical properties of selected ALD thin films will be presented. The mechanical properties of ALD thin films differ significantly from published values of bulk material.

4:40pm TF-TuA9 Effect of Atomic Layer Deposition on the Mechanical Properties of Synthetic Nonwoven and Electrospun Polymer Fibers, C.K. Devine, C.J. Oldham, J.S. Jur, G.N. Parsons, North Carolina State University

Nonwoven fiber mats and electrospun nanofiber films have been widely researched for their use in filtration, sensing, scaffolding for biological applications, and in many other areas. Nano- and microscale fibers can be functionalized using thin coatings deposited using ALD to impart mechanical strength, catalytic character, and increase conductivity while maintaining the fiber structure. We are interested in the mechanical properties of ALD coated micro and nano-sized fibers. Increasing the mechanical strength of these fibers allows for their use in more robust applications; however it is desirable for the fibers to maintain their flexibility. For this study, nylon nanofibers formed by electrospinning were coated with either TiO₂ or ZnO at temperatures between 60 and 75°C, and the mechanical tear resistance was characterized by optical microscopy under the application of lateral strain. For the TiO₂ coated samples, the tear resistance remained the same when coated with smaller cycle numbers. As the films become thicker the mechanical properties are more dependent on the character of the coating. Specifically, after oxide coating, the fibers show a more brittle response to bending, resulting in visible cracking under optical microscopy after bending by less than 5° for thicker coatings. Similar trends are observed when nylon nanofibers are coated with ZnO or Al₂O₃, however, using our technique, the measurable change in mechanical response was observed at lower cycle numbers for ZnO and even lower for Al₂O₃, consistent with very different reactions between the nylon and the various ALD precursors. The difference in the tear resistance between these materials may be a result of the reactivity of the ALD precursors. Choosing a more robust and less brittle material to deposit on the fiber mats should improve their mechanical properties will maintaining the fiber structure and flexibility.

5:00pm TF-TuA10 In Situ Studies of Oxide ALD for Crystalline Oxide Growth on Silicon, B.G. Willis, H. Wang, University of Connecticut, C. Zhang, Chinese Academy of Sciences, China, X. Jiang, University of Connecticut **INVITED**

Thin films of crystalline oxides integrated with silicon are of interest for novel electronic devices that utilize a rich variety of functional properties of oxide materials. These useful properties include piezoelectricity and ferroelectricity among others. Growth of crystalline oxides on silicon requires careful control of a nanometer thin transition region between the film and substrate to avoid deleterious side reactions such as oxidation of the substrate. Submonolayer surface reconstructions of alkaline earth metals such as Sr are critical for controlling the interface for successful growth. In this paper, we show how atomic layer deposition (ALD) can be used to precisely control the interface reactions for epitaxial growth. X-ray photoelectron spectroscopy and *in-situ* spectroscopic ellipsometry are used to monitor the growth and interface evolution of oxides deposited by ALD. Ellipsometry provides real time feedback on sequential adsorption cycles including precursor adsorption and oxidation. X-ray photoelectron spectroscopy provides detailed insight into the evolution of the interface structure during annealing and oxide desorption. Using this high degree of

* Paul Holloway Award Winner

control enables the successful deposition of critical Sr/Si reconstructions for heteroepitaxy. The results show that ALD crystalline oxide heteroepitaxy is promising.

5:40pm **TF-TuA12 Nucleation and Interface Formation of Al₂O₃ on HF-treated InGaAs(100) by Atomic Layer Deposition**, *A.J. Muscat, B. Granados, F.L. Lie*, University of Arizona

III-V compound semiconductors are alternative channel materials for high-speed, low-power digital logic devices because their electron transport and breakdown properties are superior to that of Si. However, robust surface passivation processes and thermodynamically stable interfaces are barriers to its wider adoption. Additionally, the scaling down of integrated circuits has prompted the use of alternative high-*k* dielectric films to replace SiO₂ as the gate in metal-oxide-semiconductor field effect transistors (MOSFETs). Recent work demonstrated oxide removal and passivation of III-V surfaces by depositing high-*k* dielectrics using atomic layer deposition (ALD).

In this study, the ALD of Al₂O₃ was investigated on liquid and vapor HF-etched In_{0.53}Ga_{0.47}As(100) samples. Both half and complete ALD cycles of trimethylaluminum (TMA) and H₂O at 170°C were used to better understand nucleation and film growth. Aqueous HF etching was performed by a 49% HF dip 1 min and 15 s water rinse. *In situ* gas phase HF/H₂O etching was run at 29°C and 100 Torr with an HF to water partial pressure ratio of 1.23.

The initial 8.0±1.4 Å-thick native oxide contained 21% In, 27% Ga, and 52% As oxides and was reduced to a 4.3±1.5 Å-thick oxide containing 91±7% As by aqueous HF. In contrast, the gas phase HF produced ~7 Å-thick mixed oxide and fluoride overlayer containing 30% In, 40% Ga, and 30% As.

Large reductions of substrate oxides were observed after the first TMA pulse on both liquid and gas phase HF-treated samples. The intensity of the O 1s XPS peak was constant but the peak shifted by 1 eV to higher binding energy (BE) due to the conversion of the oxide to Al₂O₃. On the gas phase HF-treated samples removal of In, Ga and As atoms in the fluoride-rich overlayer layer was also observed after the first TMA pulse. The intensity of the F 1s peak was reduced and the peak shifted by 2.2 eV to higher BE, indicating the etching of fluoride as well as the conversion of the bonding from substrate fluorides to Al-F.

Subsequent H₂O and TMA pulses up to three cycles of TMA/H₂O revealed a systematic peak shift of the overlayer atom signals. F 1s, O 1s and Al 2p peaks shifted 0.9 eV, 0.4 eV and 0.2 eV, respectively, towards lower BE after a H₂O pulse and shifted back to their original positions after a TMA pulse. The systematic shifts could be attributed to the change in surface termination after every half-cycle reaction, methyl termination after the TMA pulse and hydroxyl termination after a water pulse. Understanding surface reactions involved in the nucleation phase and early cycles of ALD is important in achieving control of the III-V-dielectric interface.

Vacuum Technology Division

Room: 111 - Session VT+MN+NS+SS+AS-TuA

Surface Science for Future Electronic Materials and Accelerator Applications

Moderator: M. Wüest, INFICON Ltd, Liechtenstein

2:00pm **VT+MN+NS+SS+AS-TuA1 New UHV Low Temperature Scanning Probe Microscopy Facility for the Study of Future Electronic Materials**, *J.A. Stroscio*, National Institute of Standards and Technology
INVITED

Since the beginning of the last century new frontiers in physics have emerged when advances in instrumentation achieved lower experimental operating temperatures. Notable examples include the discovery of superconductivity and the integer and fractional quantum Hall effects. New experimental techniques are continually adapted in order to meet new experimental challenges. A case in point is scanning tunneling microscopy (STM) which has seen a wealth of new measurements emerge as cryogenic STM instruments have been developed in the last two decades. In this talk I describe the design, development and performance of a scanning probe microscopy facility operating at a base temperature of 10 mK in magnetic fields up to 15 T [1]. The STM system can be connected to, or disconnected

from, a network of interconnected auxiliary UHV chambers used for sample and probe tip preparation. Results from current measurements on graphene and topological insulators will be described.

[1] *A 10 mK Scanning Probe Microscopy Facility*, Y. J. Song, A. F. Otte, V. Shvarts, Z. Zhao, Y. Kuk, S. R. Blankenship, A. Band, F. M. Hess, and J. A. Stroscio, *Rev. Sci. Instrum.* **81**, 121101 (2010).

2:40pm **VT+MN+NS+SS+AS-TuA3 Contact Resistance of RF MEMS at a Randomly Rough Surface in the Presence and Absence of Adsorbed Organic Monolayers**, *D. Berman, J. Krim, M.J. Walker*, North Carolina State University

Understanding of current flowing through the asperities is interesting for many applications: in RFMEMS, Molecular electronics, Nanotube tunneling etc.

Previous results [2] suggest that the films are displaced from the contacts themselves, but remain present in nearby regions. The increase in resistance is associated with elimination of vacuum electrical tunneling currents in those regions. This raises the question of the relative proportions of contact resistance (*R_c*) and effective tunneling resistance (*R_t*).

Measurements on the gold on gold contacts adhered in the closed position, where the contamination film cannot possibly be placed inside the contacts are reported, to investigate vacuum tunneling current contributions to the total current at the contact. Electrical Contact Resistance measurements are reported for RF micro-electromechanical switches with Au/Au and Au/RuO₂ contacts, situated within an ultrahigh vacuum system equipped with *in situ* oxygen plasma cleaning capabilities. Fused Au/Au switch resistance increases by 3-5% (which corresponds to 20W tunneling resistance in parallel) after adding pentane to the switch environment. Moreover, the results are repeated with a different substrate (Ruthenium rather than Au), known for higher resistance, to change the resistance values with almost the same work function. If this is tunneling, the same effective tunneling resistance is expected, because tunneling depends on the work functions of the tip and substrate, which are close for gold and ruthenium oxide. In addition, the results are investigated for two different adsorbates, pentane and dodecane. Measurements have been recorded as the function of film coverage and the same tunneling resistance impact is observed. This is consistent with elimination of vacuum tunneling when adsorbed films are present.

Theoretical analysis of two possible mechanisms of the impact of molecular uptake is performed to interpret the experimental results: a) parallel connection of contact resistance and effective tunneling resistance before molecular adsorption, followed by molecules blocking the tunneling current; b) in series connection of contact resistance and pentane layer after adsorption. The data are more consistent with model a).

This work was supported by US National Science Foundation, AFOSR MURI and DARPA. We are grateful to C. Nordquist at Sandia National Lab and J. Hammond at RF Micro Devices for providing the experimental switches.

[1] D. Berman, M. Walker, C. Nordquist, J. Krim, *in preparation for Journal of Applied Physics*

[2] M. Walker, C. Nordquist, J. Krim, *in preparation for Tribology Letters...*

3:00pm **VT+MN+NS+SS+AS-TuA4 Surface Issues for Solid Niobium SRF Accelerator Cavities**, *M. Kelley*, College of William and Mary

The world-wide physics community looks forward to a slate of accelerator projects of unprecedented magnitude and diversity. Certainly its sheer size makes the International Linear Collider the most visible to the public eye, with 16,000 solid niobium cavities performing at historically high gradient, and built (and operated) for historically low unit cost. Net performance makes superconducting radiofrequency (SRF) technology the approach of choice.

Solid niobium is the material most widely used for construction of SRF cavities because it has the highest critical transition temperature (*T_c* = 9.2 K) of the pure metals, sufficiently high critical magnetic field (*H_c* > 2 k Oe) for SRF applications, and metallurgical properties adequate for fabrication and service load. Studies of the SRF performance of niobium cavities began to be reported more than 30 years ago and continue now with the application of improved experimental techniques. Niobium metal superconductivity is a nanoscale, near-surface phenomenon because of the shallow RF penetration. Considerable evidence indicates that cavity interior surface chemistry and topography strongly impact SRF accelerator performance, motivating investigation of how they are affected by post-fabrication treatments.

Current status and prospects are discussed with respect to accelerator needs and opportunities.

4:00pm **VT+MN+NS+SS+AS-TuA7 Examples of Surface Related R&D on Nb Samples and SRF Cavities for Particle Accelerators at JLab, A.T. Wu,** Thomas Jefferson National Accelerator Facility

This contribution will review some examples of surface related R&D on small and flat niobium (Nb) samples and single cell Nb superconducting radio frequency (SRF) cavities done at Jefferson Lab in the past few years. Most of the surface measurements were performed via the experimental systems available in the surface science lab that was set up¹ at JLab to study the various problems on the Nb surfaces in the SRF field.

The first topic is about a new Nb surface polished technique called buffered electropolishing (BEP) that was developed at JLab². This technique can produce the smoothest surface finish ever reported in the literature³. It was also demonstrated that under a suitable condition, a Nb removal rate higher than 10 $\mu\text{m}/\text{min}$ could be realized. Efforts have been made to try to understand the polishing mechanism through experiments with a well defined experimental geometry on small flat Nb samples. A unique versatile vertical polishing system was constructed to perform BEP on Nb single cell cavities. Small flat samples, Nb dumbbells and Nb single cell cavities were also studied and treated at CEA Saclay in France and Peking University in China and the cavities were RF tested at JLab. Experimental results will be analyzed and summarized. It is shown that BEP is a very promising candidate for the next generation surface polishing technique for Nb SRF cavities.

A second topic will deal with a new Nb surface cleaning technique employed gas cluster ion beam (GCIB)⁴. This is a result of collaboration with Epion Corporation, Fermi Lab, and Argonne Lab. Beams of Ar, O₂, N₂, and NF₃ clusters with accelerating voltages up to 35 kV were employed in this technique to bombard Nb surfaces. The treated surfaces of Nb flat samples were examined by several surface experimental systems such as SEM, EDX, AFM, SIMS, and 3-D profilometer. The experiments revealed that GCIB technique could not only modify surface morphology of Nb, but also change the surface oxide layer structure of Nb and reduce the number of field emission sites on the surface dramatically. Computer simulation via atomistic molecular dynamics and a phenomenological surface dynamics was employed to help understand the experimental results. A system was set-up at Epion Corporation to do treatments on Nb single cell cavities and then RF-tested at JLab. The experimental results will be summarized and the perspective of this technique for real applications is discussed.

Finally, I will show two typical examples of surface studies of Nb using a high resolution transmission electron microscope⁵ and a home-made scanning field emission microscope⁶ respectively.

4:20pm **VT+MN+NS+SS+AS-TuA8 Early Stages of Nb Growth on Cu for SRF Accelerator Applications, C. Clavero,** The College of William and Mary, *N.P. Guisinger*, Argonne National Laboratory, *R.A. Lukaszew*, The College of William and Mary

Among the large range of possible applications for superconducting Nb thin films, coatings for superconducting radio-frequency (SRF) cavities in linear accelerators have greatly aroused the interest of researchers in the last years^[1]. Superconducting thin films and multilayer coatings are expected to increase further the maximum field gradients that SRF cavities can withstand, pushing them above 100 MeV/m^[2]. In this regard, Nb coated Cu cavities have been proposed as a prototypical system for this purpose since they combine the better thermal stability of Cu due to its much higher thermal conductivity and the superconducting properties of Nb thin films^[3]. Nevertheless, it is well known that structural dislocations and localized surface resistive defects on the thin films have a dramatically negative influence on their superconducting properties and resonator quality. Indeed, the quality of the films is strongly conditioned by the growth mode below the single atomic layer coverage at the very early stages of growth, and thus special attention needs to be devoted to this range. Here we present a complete study on the early stages of growth of Nb on Cu(111). Different growth and annealing temperatures ranging from room temperature (RT) to 600 °C were used in order to investigate the characteristic growth mode of Nb in the sub-monoatomic coverage range. Scanning tunneling microscopy (STM) and scanning tunneling spectroscopy (STS) were used to investigate morphology and chemical composition of the surfaces with atomic resolution. Growth of sub-monolayer coverages at RT leads to amorphous Nb islands with 1 and 2 AL heights. Annealing at 350 °C gives rise to crystallization of the islands pseudomorphically with the substrate, *i.e.* Nb(111). Further annealing at 600 °C promotes interdiffusion of Nb atoms into the Cu substrate and alloying of the islands. Growth of higher coverages above 1 AL at 350 °C reveals preferential Volmer-Weber growth mode.

1. H. Padamsee, Annual Review of Nuclear and Particle Science, 635 (1993).

2. A. Gurevich, Applied Physics Letters (1), 012511 (2006).

3. C. Benvenuti, S. Calatroni, I. E. Campisi, P. Darriulat, M. A. Peck, R. Russo and A. M. Valente, Physica C: Superconductivity (3-4), 153-188 (1999).

4:40pm **VT+MN+NS+SS+AS-TuA9 Epitaxial Niobium Thin Films for Accelerator Cavities, W.M. Roach, D. Beringer, C. Clavero,** College of William and Mary, *C. Reece*, Thomas Jefferson National Accelerator Facility, *R.A. Lukaszew*, College of William and Mary

The currently proven superconducting radio frequency (SRF) technology used in linear accelerators is based on bulk niobium cavities. Since this has a high cost and these cavities are approaching the maximum field gradients that they can withstand^[1], development of a suitable, reliable, cost effective alternative to bulk niobium SRF cavities is needed. Attempts have been made to replace bulk niobium cavities with niobium-coated copper cavities since the thermal conductivity of a suitable base material such as copper is better than bulk niobium^[2]. Coating niobium on SRF cavities is a promising but also challenging path, since there are several difficulties associated with various thin film deposition techniques and a lack of systematic studies pertinent to niobium thin film nucleation and growth leading to surfaces of greatest benefit.

Our systematic studies show that the transport properties, in particular the residual resistance ratio (RRR), are improved when niobium is epitaxially grown on crystalline ceramic substrates such as MgO and Al₂O₃, compared to niobium grown on (001) copper templates. Since grain boundaries are typically one of the main obstacles to superconducting transport, we show how the increased number of crystallographic domains that can occur during epitaxial niobium growth onto copper surfaces leading to higher density of grain boundaries can explain our results. We will discuss a route to improved transport properties while maintaining thermal efficiency by using alternative seed-layers grown on copper templates that can limit increased grain boundary density. We will show our correlated studies of microstructure and surface morphology (RHEED and AFM) and the resulting transport/magnetic properties (four point probe and SQUID magnetometry) illustrating possible mechanisms to improve SRF cavity performance of such niobium films.

This work is funded by HDTRA1-10-1-0072 from the Defense Threat Reduction Agency as well as a subcontract from Thomas Jefferson National Accelerator Facility under contract DE-AC05-06OR23177 from the Department of Energy as supplemented by ARRA funds.

References:

[1] P. Kneisel *et al.*, Proceedings of 2005 Particle Accelerator Conference, Knoxville, TN, TPPT076 (2005).

[2] S. Calatroni, Physica C **441**, 95 (2006).

5:00pm **VT+MN+NS+SS+AS-TuA10 Development via Energetic Condensation of Niobium Thin Films Tailored for Superconducting RF Applications, A.-M. Valente-Feliciano,** Jefferson Lab

For the past three decades, bulk niobium has been the material of choice for SRF cavities applications. In the recent years, RF cavities performances have approached the theoretical limit for bulk niobium. For further improvement of RF cavity performance for future accelerator projects, an interesting alternative has been recently proposed by Alex Gurevich with the Superconductor-Insulator-Superconductor multilayer approach, using the benefit of the higher critical field H_{c2} of higher-T_c superconductors without being limited with their lower H_{c1}.

JLab is pursuing this approach with the development of multilayer structures based on NbTiN via magnetron sputtering and High Power Impulse Magnetron Sputtering (HiPIMS). Insulators such as, AlN, Al₂O₃ and MgO are being investigated as candidates for the insulator layers.

This paper presents the characteristics of NbTiN and insulator layers produced and results on NbTiN-based multilayer structures on bulk Nb and thick Nb films.

5:20pm **VT+MN+NS+SS+AS-TuA11 Evaluation of Secondary Electron Emission Yield Suppression Coatings at CEsrTA, Y. Li, X. Liu, J. Calvey, J. Conway, J.A. Crittenden, M.A. Palmer, J.P. Sikora,** Cornell University, *S.De. Santis*, Lawrence Berkeley National Laboratory

The performance of particle accelerators may be significantly limited due to buildup of electron cloud (EC) in the vacuum chambers. The EC buildup intensity is strongly affected by secondary electron emission from interior surfaces of the chambers. Application of coatings with reduced secondary electron yield (SEY) onto vacuum chamber interior surfaces is one of the

most economical EC suppression techniques. As a part of the International Linear Collider (ILC) R&D program, the Cornell Electron Storage Ring (CESR) has been successfully reconfigured as a Test Accelerator (CesrTA) to study EC buildup and suppression techniques. During the CesrTA program, various passive SEY-reduction coatings (TiN, amorphous-carbon and diamond-like carbon thin films) have been applied to diagnostic vacuum chambers in CESR in order to evaluate the efficacy of the EC suppression and the vacuum performance of these coatings in an accelerator environment. These chambers are equipped with both vacuum instrumentation (ion gauges and residual gas analyzers), as well as EC diagnostics (retarding field analyzers and RF-shielded pickups). In this paper, we present the results of studies of the vacuum conditioning and EC mitigation performance of these coatings.

5:40pm **VT+MN+NS+SS+AS-TuA12 Electron Cloud Mitigation for the Large Hadron Collider (LHC)**, *V. Baglin, G. Bregliozi, P. Chiggiato, P. Costa Pinto, J.M. Jimenez, G. Lanza, M. Taborelli, C. Yin Vallgren*, CERN, Switzerland

One of the main issues for the vacuum system of the Large Hadron Collider (LHC) is the build-up of electron clouds generated by electron multipacting in presence of beams. The occurrence of spatially distributed negative charges can lead to beam instabilities and emittance blow-up, pressure rises with a consequent background growth in the experimental areas, and increased thermal load in the cryogenic sections. The development of electron clouds depends on beam intensity and structure, magnetic field, and, in particular, the secondary electron emission of the beam pipe walls. With respect to this latter point, electron clouds can be eradicated whenever the maximum secondary electron yield becomes lower than a critical threshold. In the LHC the problem has already been tackled at the design phase by introducing TiZrV non-evaporable getter thin film coatings as the baseline for most of the room temperature sectors of the ring. After activation by in situ heating, this material provides maximum secondary electron yield lower than 1.1. In addition, during operation, dedicated scrubbing runs are carried out by generating intentionally electron clouds and electron impingement onto the non-coated vacuum chambers, in a way to reduce their secondary electron yield. Recently magnetron sputtered carbon coatings have been also studied because they can reach exceptionally low secondary electron emission without any heating; their application in the LHC injectors and future LHC components is under investigation.

The effect of electron clouds in the pressure variations during the first months of LHC operation will be presented, together with the effects ascribed to the mitigation techniques.

Tuesday Afternoon Poster Sessions

Applied Surface Science Division
Room: East Exhibit Hall - Session AS-TuP

Applied Surface Science Poster Session

AS-TuP2 An Electrostatic Analytical Microscope for SEM/SAM Surface Studies with 3nm-7nm Spatial Resolution, A.R. Walker, M. Rignall, Shimadzu Research Laboratory (Europe) Ltd., UK

A very high spatial resolution all electrostatic, ultra high vacuum, electron optical column has been developed for fast Nano analysis of specimen surfaces. The electron optical column does not project any electric or magnetic fields to the analysis region or beyond.

The electrostatic column operates with a beam energy range of 1-10keV, at a specified working distance of 10mm, for all survey and analytical modes of operation. Spatial resolutions of 4-7nm for Auger Nano analysis and 3nm for a SEM mode correspond to probe currents that range from 1nA to 0.25nA. Other modes of operation are available and these include operation at intermediate spatial resolutions <100nm with high probe currents of 100's nA and a very useful wide survey mode of ~5mm field of view at lower spatial resolutions <1 μ m. The electron optical column, having no magnetic lens components and therefore no hysteresis effects, is able to switch fast between these different modes.

Key to the electron optical column specification is the design of the probe forming electrostatic objective lens which operates in an accelerating mode. This lens design is a compact truncated cone with 80° apex angle at the analysis position (10mm WD) which enables a wide angular access (50°) to the specimen surface. Its electron optical design is an Einzel lens of asymmetrical electrode structure and operates with a positive potential of up to 50kV applied to its central electrode. The lens operation is extremely stable with no detectable electrical instabilities.

To aid the development of the electrostatic lens we use simulation software to calculate the lens parameters. At the objective lens WD of 10mm and object at infinity, low values of spherical aberration (75mm) and chromatic aberration (19mm) were computed. These values are comparable to the best magnetic lenses of similar external dimensions and working distance.

The column is mounted on a small analytical chamber for test purposes. We have demonstrated a 3nm SEM spatial resolution at beam energies of 10keV with 250pA of current. At a beam energy of 3keV with 150pA of current, we achieved and 7nm SEM spatial resolution.

An Auger signal was detected using a new form of hyperbolic field parallel energy analyser. A Gold Au (64eV) line scan demonstrated an edge resolution of 4.1nm using a primary probe of 10keV energy and 400pA of current.

For conventional energy analyzers, a probe current of 1nA is more appropriate and the spatial resolutions have been measured as 5nm and 7nm for respective beam energies of 10keV and 7keV.

AS-TuP3 Core Level Shift from Experiment and First-Principles-Theory – A Comparison, B. Kiefer, New Mexico State University, B. Halevi, K. Artyushkova, University of New Mexico

The knowledge of geometries and chemistry of functional motifs that causes particular materials behavior is crucial for the rational development of novel materials and materials based technologies. X-ray photoelectron spectroscopy (XPS) measures the binding energy (BE) changes that are induced on an atom by its surrounding ligands and by comparing to them to databases. However, in many cases the reference materials available in the databases are limited to limited to common/model compounds, while actual materials designed may have more complicated chemistries. Furthermore, the big spread in the reported values of BE due to various ways to charge calibrate spectra and also sensitivity of BE to secondary environments present a big problem for accurate identification of unknown peaks in spectra.

Being able to calculate binding energy shifts based on molecular structure can be very important tool for identifying structural motifs in materials. There are only a few studies reporting density-functional-theory (DFT) calculations of BE energies due to challenges that are associated with the treatment of core electrons. Their high kinetic energy can require to include relativistic effects especially for heavy elements and absolute values of binding energies cannot be expected to be accurate. Furthermore the differences in reference state complicate the direct comparison between experiment and theory.

A possible solution to these challenges is to compare BE to a reference system that is accessible both in experiment and theory. We will report on BE shift that have been calculated and compared to experimentally obtained values for metallic, bimetallic and covalent systems. For metallic Pd (111) system, surface layers have lower binding energy, while sub-surface is bulk like. For bimetallic PdZn system, Pd(3d) and Zn(2p) shift upward with respect to fcc-Pd(3d) and for hcp-Zn(2p), respectively. Magnitudes of shifts are very similar to that obtained experimentally. For covalent system, such as metal-less and metal-containing porphyrins, shift for N 1s BE in Co 2p environment compared to N 1s without metal is also very close to that obtained experimentally.

AS-TuP4 Evaluation of C₆₀ Depth Profiling Conditions for XPS Organic Films Analysis, S. Alnabulsi, S.R. Bryan, J. Moulder, Physical Electronics

Type-II organic materials can be successfully depth profiled by XPS using C₆₀ ion beam sputtering at room temperature. Success is defined by achieving steady state composition as a function of depth. However, depth profiling of Type-I polymers have been marginally successful due to rapid sample damage under C₆₀ bombardment. The use of high C₆₀ beam energy at a glancing angle has been shown to extend the maximum depth of successful depth profiling, yet it eventually fails due to sample roughening, concomitant carbon build up, and a strong reduction in sputter rate.

Zalar (azimuthal) rotation has been shown to minimize sputter induced roughness formation, improve depth resolution in multi-layer film structures, and allow depth profiles to be extended to even greater depths. Cooling of the sample to below its glass transition temperature is expected to reduce the mobility and reactivity of free radicals that are formed during the sputtering process.

The purpose of this study is to evaluate the relative importance of using Zalar rotation and sample cooling to characterize standard organic thin film structures and to quantify the benefit to using them simultaneously.

AS-TuP5 Development and Application of Novel Electron Energy Analyzers for Chemical Analysis of Surfaces, D. Cubric, Shimadzu Research Laboratory (Europe) Ltd., UK, N. Kholine, Institute for Analytical Instrumentation, RAS, Russian Federation

Various instruments have been developed previously for analyzing the spectrum of energies of beams of charged particles emanating from surfaces and described in numerous publications [1]. Among all those instruments the concentric hemispherical analyser (CHA) and the cylindrical mirror analysers (CMA) have been the most often used instruments both commercially and for various devices developed by different laboratories. At first sight, geometry of the two analyser types is very different. However, topologically their geometries are very similar. This paper presents a line of thought where geometries of both analysers are just particular examples of a more general geometry that in turn provides numerous analyser configurations, that we now call spheroid energy analysers (SEA), often having excellent electron optical characteristics [2]. The SEA instrumental concept enables electron optical exploration of various new analyser embodiments, particularly well suited for chemical analysis of surfaces and surface nano-features. Progress in this instrumentation development and example spectra will be presented. **References** [1] D. Roy and D. Tremblay, Design of electron spectrometers, Rep. Prog. Phys. 53 (1990) 1621-1674 [2] D. Cubric, N. Kholine and I. Konishi, doi:10.1016/j.nima.2010.12.146

AS-TuP6 Extreme Brightness: Reaching the Ultimate Limits of the Electron Beam, J.D. Jarvis, J.L. Kohler, B. Ivanov, N. De Jonge, B.K. Choi, A.B. Hmelo, C.A. Brau, Vanderbilt University

We report recent results from field emission microscopy studies of multiwall carbon nanotubes (MWCNT) and from energy spectrum measurements of beams from diamond field emitters (DFE). As expected, resonant tunneling through adsorbed species on the emitter surface is an important and sometimes dominant effect. For diamond emitters our observations include order-of-magnitude emission enhancement without spectral broadening, complex spectral structure, and sensitivity of that structure to the applied electric field. For carbon nanotubes we have observed electron beams from individual adsorbates which are estimated to approach the maximum beam brightness allowed by Pauli exclusion.

The development of CNTs as field emitters for the purposes of microscopy, lithography, radiation generation, and display production has been a protracted endeavor. Working in their favor, CNTs have excellent emission stability, high activation energy for thermal migration, excellent current throughput capacity, and a high degree of chemical inertness. Not

surprisingly, these properties extend to other covalent-carbon structures such as CVD diamond field emitters. DFEs have shown great promise as high-brightness electron-beam sources in recent years. One of the more exciting revelations regarding CNTs and DFEs has been the realization that resonant tunneling through adsorbed species can be exploited for the generation of multi-microamp-level beams with perfect transverse coherence.

For resonant tunneling through a single molecule the electron source size is on the order of the electron wavelength. Estimates of the transverse momentum spread of the resulting electron beams suggest that the transverse emittance is Heisenberg limited. Such beams have been produced using single atom tungsten, or single atom noble-metal field emitters, however the relatively weak binding of the metal atoms has limited the total current that can be extracted to the sub-microamp regime. In this paper we will discuss our efforts to generate, stabilize, and characterize, multi-microamp beams from individual molecules on CNTs

AS-TuP8 Surface Characterization of Disposable Laboratory Gloves by X-ray Photoelectron Spectroscopy (XPS). *B.R. Strohmeier, C. Bailly, T.S. Nunney*, Thermo Fisher Scientific, UK, *A. Plasencia*, Thermo Fisher Scientific, *J.D. Piasecki*, RJ Lee Group, Inc.

Disposable elastic gloves are ubiquitous in scientific laboratories and are also widely used in many industries during handling of critical surfaces. Disposable gloves are typically made from nitrile, latex, neoprene, or other polymers and offer their users protection from various aqueous acids and bases, biological fluids, organic solvents, and other potentially harmful chemicals. A second major application of disposable gloves is to protect manufactured products and analytical samples from contamination caused by the transfer of skin cells, oils, salts, or other residues resulting from contact with bare hands. However, disposable gloves can also be a potential source of contamination. In addition to the primary polymer structure, many types of common laboratory gloves also contain a variety of inorganic materials in the glove formulation. Mold-release agents that allow the gloves to be easily stripped from the glove formers during fabrication may be present on glove surfaces. Furthermore, many types of disposable gloves have polymeric surface coatings that provide improved donning properties. Contamination resulting from surface residues on gloves can adversely affect materials used in industries where surface cleanliness is essential for optimum product performance and can also interfere with the analysis of samples depending on the specificity and sensitivity of the analytical technique. X-ray photoelectron spectroscopy (XPS) is a qualitative and quantitative surface sensitive technique that can be used to evaluate the surface composition of disposable gloves and to determine if contamination transfer occurs from gloves in a specific process. In this study, XPS was used to characterize the surface compositions of a variety of common laboratory gloves. The transfer of surface components from gloves to other material surfaces and changes in the surface composition of gloves following exposure to several common laboratory solvents were also investigated.

AS-TuP10 Large Area Cross Sectional Microstructural Characterization of ToF-SIMS Depth Profile Crater Walls. *V.S. Smentkowski, D. Ellis*, GE-GR

Focused Ion Beam (FIB) techniques are widely used in order to generate cross sections of samples which can then be analyzed using a variety of analytical instrumentation in order to obtain microstructural information. In order to rapidly generate FIB cross sections, small areas (typically 5 to 10 microns) are milled. Time of Flight Secondary Ion Mass Spectrometry (ToF-SIMS) is a powerful surface analytical technique that is able to measure low concentrations of sub surface species. ToF-SIMS depth profile measurements are collected by eroding a large area (50 to 1,000 microns in size) of a sample using an ion beam for a certain amount of time, pausing the erosion, analyzing a smaller (central) region of the eroded area, and repeating the cycle until the desired depth has been reached. Ion images are often recorded at each depth and a full mass spectrum is saved at every volume element allowing for 3 D analysis. Often times, both ToF-SIMS depth profile analysis and high resolution microstructural SEM characterization are required on the same sample. Ideally, these complimentary analyses would be performed in the same region of a sample. In this presentation, we will demonstrate that FIB techniques can be used to clean up the large area craters produced by ToF-SIMS depth profile analysis thereby enabling microstructural characterization over larger areas of samples.

Advantages of this approach are: larger FIB cross sections can be prepared since a significant amount of material was removed during the erosion cycles in the ToF-SIMS analysis, combining the chemical information provided from the ToF-SIMS analysis with the large area microstructural characterization provided by FIB-SEM analysis, and having both the ToF-SIMS and the large area cross sectional analysis performed in the same region of the sample. The ToF-SIMS depth profile craters have a slope of

about 45 deg (the ion column is positioned at an angle of 45 deg from the sample normal), and hence an advantage of performing the FIB clean up at this angle is the enhancement in the layer thickness that will be available for microstructural analysis.

AS-TuP11 Microphase Separation of Various Diblock Copolymers Investigated by TOF-SIMS Depth Profiling. *Y. Lee*, Korea Institute of Science and Technology, Republic of Korea, *J. Lee*, Korea University, *W.C. Lim*, Korea Institute of Science and Technology, *K. Shin*, Sogang University, Korea, *K.-J. Kim*, Korea University

Diblock copolymers, composed of two distinct homopolymers covalently bonded together at one end, exhibit a microphase separation from a disordered state to an ordered state on cooling or heating. The microphase separation of diblock copolymers has been investigated by many different research groups for many years, because of the increasing use of diblock copolymers as compatibilizers, dispersants, impact modifiers, nanocarriers, and templates. Investigation of the phase behaviour of a family of diblock copolymers between styrene and a homologous series of methacrylates or acrylates has revealed that significantly different phase behaviours are seen for these materials, depending on the temperature, molecular weight, and alkyl side chain length. In this work, we characterized the morphology from various diblock copolymers of poly(styrene-*b*-alkyl acrylate)(PS-PAA), where PS block was perdeuterated, near the copolymer/air and copolymer/substrate interfaces and in the bulk using time-of-flight Secondary Ion Mass Spectrometry (ToF-SIMS). ToF-SIMS Depth Profiling was obtained for the lamellar morphology of PdS-PAA which is found to orient parallel to the surface of the substrate. This preferential orientation resulted in a periodic variation in the composition of each block that continued through the entire copolymer film. Temperature- and chain length-dependent annealing studies on PdS-PAA thin films on the silicon substrates were performed to investigate the order-to-disorder transition (ODT) properties of diblock copolymers.

AS-TuP12 Analysis of Passivated Surfaces for Mass Spectrometer Inlet Systems by Auger Electron and X-Ray Photoelectron Spectroscopy. *H.M. Ajo, D.W. Blankenship, E.A. Clark*, Savannah River National Laboratory

Stainless steel coupons approximately 0.5" in diameter and 0.125" thick were passivated with five different surface treatments and an untreated coupon was left as a control. These surface treatments are being explored for use in tritium storage containers. These coupons were made to allow surface analysis of the surface treatments using well-known surface analysis techniques. Depth profiles using Auger electron spectroscopy (AES) and X-ray photoelectron spectroscopy (XPS) were performed on these coupons to characterize the surface and near surface regions. Scanning electron microscope (SEM) images were collected as well. All of the surface treatments studied here appear to change the surface morphology dramatically, as evidenced by lack of tool marks on the treated samples. In terms of the passivation treatment, Vendors A-D appeared to have oxide layers that were very similar in thickness to each other (0.7-0.9 nm thick) as well as the untreated samples (the untreated sample oxide layers appeared to be somewhat larger). Vendor E's silicon coating appears to be on the order of 200 nm thick.

AS-TuP13 Surface Characterization of Gunshot Residue (GSR) by X-ray Photoelectron Spectroscopy (XPS) and High Resolution Electron Microscopy. *A.J. Schwobbe*, RJ Lee Group, Inc., *B.R. Strohmeier*, Thermo Fisher Scientific, *K.L. Bunker, D.R. McAllister, J.P. Marquis, Jr., J.D. Piasecki, N.M. McAllister*, RJ Lee Group, Inc., *W. Sgammato*, Thermo Fisher Scientific

Discharged firearm cartridges produce unique microscopic particles referred to as gunshot residue (GSR). GSR is primarily composed of the products of combustion of the cartridge primer materials and typically contains varying amounts of Pb, Sb, and Ba, plus other elements. GSR particles can range in size from tens of nanometers to hundreds of micrometers. Because of the high temperatures (~1,500-3,600 °C) and pressures (~14,000-65,000 psi) that result within 1 millisecond of discharging a firearm cartridge, highly complicated chemical interactions are likely to occur that will affect the chemical composition of the GSR particles. Computer-controlled scanning electron microscopy (CCSEM) is the method preferred by the forensic community for the automated analysis of GSR. With CCSEM, large populations of potential GSR particles in the size range of ~1-10 µm are rapidly screened for the characteristic presence of combinations of Pb, Sb, and Ba using energy dispersive X-ray spectroscopy (EDS). Determining the presence of these three elements fused together in a single particle having the correct morphology is all that is normally required for the positive identification of GSR. CCSEM, however, does generally not provide information regarding the population of particles much less than 1 µm. In addition, little is presently known regarding the surface chemistry of GSR. Because of its nanometer-scale sampling depth and the ability to provide

detailed chemical state information, X-ray photoelectron spectroscopy (XPS) can provide important information regarding the surface chemistry of GSR. This work examines the fine fraction of GSR particles with high resolution electron microscopy methods and complements the microscopy data with surface chemistry information obtained from XPS.

AS-TuP14 Analysis of Graphene and Other Graphitic Materials using XPS and AES, H.M. Meyer III, Oak Ridge National Laboratory

Synthesis and characterization of advanced carbon materials, including graphene, has accelerated over the past several years at the Oak Ridge National Laboratory. Projects include, among others, the development of nanostructured carbon materials for batteries, fuel cells and as supports for revolutionary catalysts. The past year has also brought to ORNL new projects related to the growth, characterization and application of graphene. This poster will highlight x-ray photoelectron spectroscopy and scanning Auger microanalysis of a variety of important carbon materials from several of these research projects, including nano-sized carbon powders for battery applications, graphitic carbon powders used in fuel cells, graphene flakes synthesized for supporting catalyst materials and CVD grown graphene. In particular, an approach for curve fitting highly graphitic materials will demonstrate internally consistent results, giving insight into the sp^2 vs. sp^3 type carbon atoms present in the material.

Research sponsored by the Assistant Secretary for Energy Efficiency and Renewable Energy, Office of FreedomCAR and Vehicle Technologies, as part of the High Temperature Materials Laboratory User Program, Oak Ridge National Laboratory, managed by UT-Battelle, LLC, for the U.S. Department of Energy under contract number DE-AC05-00OR22725.

AS-TuP15 Investigation of Precious-Metal/Metal-Oxide-Support Interactions in Automotive Catalytic Converters using a Pd/Ce_{0.7}Zr_{0.3}O₂ Model Planar Catalyst System, O.K. Ezekoye, University of Michigan, M.I. Nandasiri, Western Michigan University, T. Varga, P. Nachimuthu, W. Jiang, S.V.N.T. Kuchibhatla, S. Thevuthasan, Pacific Northwest National Laboratory, X. Pan, G.W. Graham, University of Michigan

Ceria-zirconia mixed oxide (CZO) has been incorporated into automotive catalysts as a support material for precious metals (Pt, Rh, Pd) due to its highly desirable redox properties. However, at high operating temperatures, certain interactions between CZO and precious metal particles may adversely affect the performance of the catalytic converter. Thus, it is important to investigate the CZO/precious-metal interactions under redox conditions. Here, the preparation of Pd/CZO thin films as model planar catalyst systems will be described together with a systematic study of an important adverse interaction, the encapsulation of Pd particles by CZO, using a combination of x-ray diffraction (XRD) and high resolution transmission electron microscopy (HRTEM).

Ceria-zirconia ($Ce_{0.7}Zr_{0.3}O_2$) thin films with thickness ranging from 10-200 nm were grown on (111) yttria-stabilized zirconia (YSZ) by oxygen plasma assisted molecular beam epitaxy (OPA-MBE). The epitaxial layer growth of CZO on YSZ(111) was confirmed by in-situ reflection high energy electron diffraction (RHEED). Atomic force microscopy (AFM) images revealed the smooth surface of the films with low roughness values (3-8 Å). Rutherford backscattering spectrometry (RBS) data along channeling and random geometries showed the minimum yield (χ_{min}) of 13% for Ce with no inter-diffusion of metal atoms at the film/substrate interface. The single crystal nature of the film with CZO(111) orientation was confirmed by XRD data. Following the growth and characterization of thin films, ~1 monolayer of Pd was deposited on CZO(111) by thermal evaporation in a UHV chamber. After air calcination at 600 °C, the Pd/CZO films were reduced in 1% H₂/N₂ at 200°C, followed by annealing in N₂ at 700 °C. Due to the additional reduction-induced compressive stress, the 10 nm and 40 nm films broke up and formed a rough surface with 10-20 nm CZO mesas, as observed by HRTEM. However, films with a thickness above ~50 nm were stable, and Pd particles that formed on the surface became partially encapsulated by migration of CZO. In the films with a thickness above ~50 nm, the native compressive stress induced by the lattice mismatch between the film and substrate was relaxed by misfit dislocations at the interface, as revealed by high resolution scanning TEM images, to varying degree, depending on film thickness, but the extent of encapsulation appeared to be about the same for all film thicknesses. These results suggest that the driving force for the partial encapsulation resides in the nature of CZO, and is not simply a consequence of the lattice-mismatch-induced compressive stress in the films.

AS-TuP17 Cleaning and Characterization of InP Surface using Atomic Hydrogen and STM, W. Melitz, J. Shen, T. Kent, University of California San Diego, R. Droopad, Texas State University, P.K. Hurley, Tyndall National Institute, A.C. Kummel, University of California San Diego

Metal oxide semiconductor field effect transistors (MOSFETs) are the dominant logic device in modern electronics. Due to the challenges of scaling Si-MOSFETs alternative materials are being explored to improve device performance. III-V semiconductors are of interest for use in MOSFETs due to their high mobilities, but in order to make these devices competitive the semiconductor-oxide interface needs to have a low density of interfacial traps (D_{it}) in order to minimize subthreshold swings and also be atomically flat to allow high mobility at high field strengths. Current Si-MOSFET fabrication uses a gate last process which is an attractive method because it minimizes the gate oxides exposure to harsh processing conditions. In order for gate last processing to provide a nearly defect free semiconductor-oxide interface for surface channel devices, the channel surface must be in pristine condition before the oxide layer is deposited. In addition the oxide deposition process cannot introduce any defects. Recent advances show that a thin indium phosphide layer deposited on top of the InGaAs channel may provide superior electronic performance because the InGaAs/InP interface is defect-free and flat while the defects at the oxide/InP interface are less detrimental to device performance than the defects at the oxide/InGaAs interface.

In order to facilitate gate last processing of the InP/InGaAs channel stack, a four step process was investigated to clean and nucleate atomic layer deposition (ALD) of an InP/InGaAs surface. Samples were grown with an undoped 2 nm InP layer on ~1 μm InGaAs layer doped with $4 \times 10^{18} \text{ cm}^{-3}$ of Si on an InP wafer. Using in-situ atomic imaging (scanning tunneling microscopy), electronic measurements (scanning tunneling spectroscopy), and XPS a four step in-situ process was developed for converting an air-exposed InGaAs(100)-4x2 surface into a flat, electronically passivated, mono-layer nucleation template for ALD of gate oxides. The optimized process includes a small dose of atomic hydrogen, annealing to reduce surface roughness, TMA dosing to functionalize the surface, and a final annealing to induce a highly ordered ALD nucleation layer. Following atomic hydrogen cleaning at 380°C and annealing at 470°C, the surface was exposed to $\sim 1 \times 10^{-2}$ Torr of TMA at room temperature and annealed to 270°C. The TMA induces a surface reconstruction consistent with a bulk like bonding configuration between the Al atoms and the surface P atoms. The TMA passivation layer has horizontal rows of DMA. The cleaning and nucleation process does not disrupt the InP surface thereby providing a path for further scaling of the InP layer and the gate oxide.

AS-TuP18 Highly Selective and Low Damage Etching of GaAs/AlGaAs Heterostructure using Cl₂/O₂ Neutral Beam, J.S. Oh, K.S. Min, C.K. Kim, G.Y. Yeom, Sungkyunkwan University, Korea

Highly selective and low damage etching of the GaAs cap layer on AlGaAs is essential in fabricating devices such as heterojunction superlattices, field effect transistors, injection lasers, and solar cells, etc. The GaAs on AlGaAs was etched using a low energy Cl₂/O₂ neutral beam and the schottky device characteristics fabricated on the exposed AlGaAs were compared with those fabricated after the etching using wet etching and a Cl₂/O₂ ion beam. The wet etching was conducted by a mixture of H₂O₂ and H₃PO₄. For the Cl₂/O₂ neutral beam etching, a neutral beam system composed of three-grid inductively coupled plasma (ICP)-type ion gun and a reflector installed just in front of the ion gun was used. Using a low energy Cl₂/O₂ ion beam or a Cl₂/O₂ neutral beam, highly selective etching of the GaAs cap layer to AlGaAs similar to wet etching could be achieved through the formation of Al₂O₃ on the exposed AlGaAs during the etching. When the electrical characteristics of the schottky devices were compared, the devices fabricated after the etching using the neutral beam showed the best electrical characteristics such as electrical stability, low leakage current, higher barrier height, etc. by showing low damage to the exposed AlGaAs surface.

AS-TuP19 TiO₂ Nanotube Growth Mechanism Studied with Scanning Auger Spectroscopy, D.F. Paul, Physical Electronics, S. Berger, F. Schmidt-Stein, S.P. Albu, H. Hildebrand, P. Schmuki, University of Erlangen-Nürnberg, Germany, J.S. Hammond, Physical Electronics

Anodic TiO₂ nanotubes offer unique properties for a wide range of applications including energy conversion, photocatalysis and biomedical devices^{1,2,3}. It is widely accepted that the initial growth of the nanotubes is based on the formation of a compact anodic oxide followed by the formation of etching grooves and pores in the oxide^{4,5}. The mechanism of steady state growth of the nanotubes from the embryonic pores has, however, remained a topic of debate. To evaluate a flow model^{1,6} for the formation of the tubular structures, high spatial resolution Scanning Auger Spectroscopy data is used to elucidate the compositional variations across TiO₂ nanotube layers grown in a fluoride containing ethylene glycol electrolyte. The layers were fractured parallel to the axes of the nanotubes

and quantitative spectra, line scans and elemental maps were acquired along the walls of the nanotubes. The Auger data indicates the presence of a fluoride rich layer located between the tube walls, and in particular, the triple points of the hexagonally ordered nanotube arrays. This data supports fluoride dissolution as the reason for a transition from a porous oxide layer to tubular structures. This data also supports a flow model as a mechanism for the formation of the tubular morphology.

AS-TuP20 Effect of Annealing TiN/Al₂O₃ Nanofilms Grown on InGaAs. *O. Ceballos-Sanchez, A. Sanchez-Martinez, M.O. Vazquez-Lepe, CINVESTAV-Unidad Queretaro, Mexico, P. Lysaght, SEMATECH, A. Herrera-Gomez, CINVESTAV-Unidad Queretaro, Mexico*

III-V compounds are candidates to replace Si as the semiconductor in complementary metal-oxide-semiconductor (CMOS) devices.¹ The extensive research for over 40 years in the field of III-V semiconductors reflects the efforts that have been made to find new materials that meet the technological needs. InGaAs is one of the most promising compounds because of its high electron mobility and flexible bandgap as compared to Si.² However, one difficulty associated to III-V semiconductors is the lack of high-quality and thermodynamically stable gate dielectric insulators that passivate the interface. Growing Al₂O₃, HfO₂ and ZrO₂ by atomic layer deposition (ALD) on InGaAs or III-V semiconductors have shown the removal of native oxide and the passivation of the high-*k*/III-V interface.³ However, the high temperatures (~850°C) required for the activation of some dopant in the device induce structural changes that degrade the properties of the interface.⁴ The appearance of oxides, defects or even the diffusion of atoms within the material are issues that primarily affects the device performance. The poor ultimate resolution achieved with some of the characterization techniques traditionally employed for the assessment of the chemical depth profile of thin films limits the quantitative analysis of the structure and composition of the films. In this work we present an analysis by angle-resolved x-ray photoelectron spectroscopy (ARXPS) of TiN/Al₂O₃/In_xGa_{1-x}As nanofilms with different thermal treatments (no-annealing, 500 °C for 2 min, and 700 °C for 10 s). The purpose of the study was to investigate possible reasons of the interface degradation. Through a self-consistent approach based on a multilayer model (MLM), a quantitative study was performed for the composition and thickness of the TiN/Al₂O₃/InGaAs nanofilms. The results clearly show that indium diffuses towards the metal layer as a consequence of heat treatments, suggesting a possible failure mechanism. [1] Han Zhao, Jeff Huang, Yen-Ting Chen, Jung Hwan Yum, Yanzen Wang, Fei Zhou, Fei Xue, and Jack C. Lee, *Appl. Phys. Lett.* **95**, 253501 (2009). [2] F. S. Aguirre-Tostado, M. Milojevic, C. L. Hinkle, E. M. Vogel, R. M. Wallace, S. McDonnell, and G. J. Hughes, *Appl. Phys. Lett.* **92**, 171906 (2008). [3] Y. Xuan, H.C. Lin, and P.D. Ye, *Appl. Phys. Lett.* **88**, 263518 (2006). [4] Y. Xuan, P.D. Ye, and H.C. Lin, *Appl. Phys. Lett.* **89**, 132103 (2006).

AS-TuP21 Comparison between the Continuous and Discrete Model to Assess the Thickness of SiO₂ Layers on Si with XPS Data. *M.O. Vazquez-Lepe, P.G. Mani-Gonzalez, A. Mendoza-Galvan, A. Herrera-Gomez, Cinvestav Queretaro Mexico*

X-ray Photoelectron Spectroscopy (XPS) is a valuable tool for assessing the thickness of surface layers in the 0 to 8 nm range. The prediction of a core-level XPS signal from a solid requires assuming a specific volumetric distribution of such core levels. Since the core levels are spaced close to the atomic nucleus, a possible approximation is to model their volumetric distribution as a sum of delta functions at the atomic sites. Another approach is to consider that the source of the photoelectrons is uniformly distributed within the volume of the solid. The latter is called the *continuous approximation* (CA) and the former the *discrete approximation* (DA). The CA is widely employed; it leads to an expression for the XPS signal proportional to $c\lambda \sin \alpha$, where c is the volumetric density, λ is the effective attenuation length, and α is the take off angle. The DA applied to crystalline structures leads to an expression proportional to $s[1 - \exp(-a/(\lambda \sin \alpha))]^{-1} \exp(-a/(2\lambda \sin \alpha))$, where a is the spacing of the atomic planes parallel to the surface, and s is the atomic plane surface concentration ($s/a = c$) [1]. When $a/\lambda \ll 1$, the DA expression reduces to the corresponding to CA. Applying the DA to amorphous materials requires defining an "effective" or "average" atomic spacing (a_e) and surface concentration (s_e). In this paper we compare the differences on the thickness of silica layers on Si[001] calculated with these two approaches. The analysis was done by employing XPS data at one angle or at various angles (ARXPS). The samples employed were thermally grown silica at 800 °C for 16 s, 75 s, 145 s, 212 s and 7 min. The results are also compared to more standard methods [2], such as that employing the parameter R (ratio of the Si 2p XPS intensities for clean Si and thick SiO₂). The thickness of the silica layers were also assessed from Transmission Electron Microscopy (TEM) images and correlated to Ellipsometry measurements. It was found that the approach employing the DA and various angles better reproduced the TEM measurements.

[1] "Self consistent ARXPS analysis for multilayer conformal films with abrupt interfaces." A. Herrera-Gomez. Internal Report 2007 (<http://www.qro.cinvestav.mx/~aanalyzer/arxpsAnalysisSharpInterfaces.pdf>)

[2] Cumpson P.J. *Surf. Interface Anal.* 2000; 29: 403.

AS-TuP22 Electrical and Surface Studies of the High-*k* Gate Dielectrics Al₂O₃, HfO₂, and Al_xHf_{1-x}O₂ on Silicon via Atomic Layer Deposition. *S. Hogan, G. Hernandez, R. Candler, S. Franz, Y.S. Lin, UCLA*

As the demand for high speed electronics remains ever increasing, the dimensions of MOSFET technology are continuously scaled down to the smallest possible levels. Traditional gate dielectrics such as SiO₂ are unable to effectively stop electron tunneling from degrading device performance at thicknesses below 1-1.2 nm. We propose using high dielectric materials instead, which can effectively limit leakage current and have a band gap close to SiO₂. This study will focus on the dielectrics Al₂O₃, HfO₂, and Al_xHf_{1-x}O₂ deposited using ALD. Several ratios of aluminum and hafnium in the Al_xHf_{1-x}O₂ compound will be investigated to find a level that maximizes both electrical and physical properties of the film. The electrical properties of each dielectric will be characterized by XPS, AFM, spectroscopic ellipsometry, and by taking IV and CV measurements of fabricated transistors and capacitors. We will also investigate the effects of different annealing and deposition temperatures on the interface by TEM.

AS-TuP23 Enhanced Green Emission from UV Down-Converting Ce³⁺-Tb³⁺ Co-Activated ZnAl₂O₄ Phosphor. *K.G. Tshabalala, University of the Free State, South Africa, S. Cho, J. Park, Korea Institute of Science and Technology, Republic of Korea, H.C. Swart, O.M. Ntwaeaborwa, University of the Free State, South Africa*

Ce³⁺-Tb³⁺ co-activated ZnAl₂O₄ nanocrystal phosphors were prepared by a solution combustion method using urea (CH₄N₂O, 99.0–99.5%) as a fuel. The samples were annealed at 700°C for 4 hrs, in a tubular furnace, in a reducing atmosphere containing a mixture of 4% H₂ and 96% N₂. The X-ray diffraction (XRD) and high resolution transmission electron microscopy (HRTEM) data showed that a well known cubic normal spinel structure of ZnAl₂O₄ was crystallized. In addition, the HRTEM data showed that the particles were spherical with some degree of faceting. Auger electron spectroscopy (AES) and X-ray photoelectron spectroscopy (XPS) were used respectively to analyze the chemical composition of the phosphors and electronic states of individual elements. The XPS data demonstrated that there was structural readjustment of ZnAl₂O₄ from normal to spinel inversion due to annealing. An enhanced down-converted green emission associated with the ³D₄→⁷F₅ transitions of Tb³⁺ was observed at 543 nm from the ZnAl₂O₄:Ce³⁺, Tb³⁺ powders with different concentrations of Ce³⁺ and Tb³⁺. It was confirmed from the fluorescence decay data that the enhancement was due to energy transfer from Ce³⁺ to Tb³⁺ ions. Possible mechanism of UV down-conversion will be discussed. In addition, cathodoluminescence (CL) intensity degradation was evaluated for possible application of this material as a green emitting phosphor in field emission displays.

AS-TuP24 Characterization of Al_xGa_{1-x}N Thin Film Light Emitting Diode (LED) Device by Spectroscopic Ellipsometry. *K. Uppireddi, L. Yan, HORIBA Scientific*

The demand for efficient energy usage for lighting at industry viable production costs catalyzing the rapid growth of global LED market. LED lighting is widely in use from LED-backlit TVs to solid-state lighting. The wall-plug efficiency, which characterizes its performance depends on the design and material properties of thin film LED structure. The accurate determination of thickness and composition of the well and barrier layers is desired for quality control in the production. The Sapphire/AlN/Al_xGa_{1-x}N structure was characterized using a phase modulated spectroscopic ellipsometer (PMSE) at an angle of incidence of 70 degree across the spectral range 0.6-6.5 eV. Using a three layer structure we accurately modeled the thickness of the layers in the spectral range from 0.6 to 4.5 eV and Al_xGa_{1-x}N optical constants. The PMSE delivers both unique performance and proven reliability for on-line quality control of production process.

Biofabrication and Novel Devices Focus Topic Room: East Exhibit Hall - Session BN-TuP

Biofabrication and Novel Devices Poster Session

BN-TuP1 Photoluminescence Characterization of Polythiophene Films Incorporated with Highly-Functional Molecules Such as Metallophthalocyanines, *H. Kobe, K. Onaka, H. Kato, S. Takemura, T. Hiramatsu, K. Shimada, K. Matsui*, Kanto Gakuin University, Japan

Conducting polymer polythiophene (PT) films incorporated with highly-functional molecules such as phthalocyanines with different center metals were synthesized and characterized by x-ray photoelectron spectroscopy (XPS) measurements, photoluminescence measurements (PL) and time correlated single photon counting (TCSPC) measurements in order to obtain fundamental photoluminescence properties of various PT-phthalocyanine complexes prepared by different solvents. The electrochemical polymerization was performed in acetonitrile containing thiophene monomer and $(\text{ET})_4\text{NBF}_4$ as a supporting electrolyte and the polymerization on an indium tin oxide (ITO) was conducted by applying positive voltage to the anode. The dopant molecules were iron phthalocyanine (FePc), copper phthalocyanine (CuPc), magnesium phthalocyanine (MgPc), lithium phthalocyanine (Li_2Pc) and cobalt phthalocyanine (CoPc). Those molecules were doped in the polymer film by the diffusion method. The solvents used in the doping process were acetonitrile and toluene. At first, it was confirmed by XPS measurements that the metallophthalocyanines were introduced in the PT films. In the photoluminescence measurement, emission peaks were different in intensity and wavelength according to the additional dopant molecules. Those peaks were influenced by Soret and Q bands. The solvent used in the doping process also influenced the emission characteristics. In the case of CuPc using acetonitrile as a solvent, emission peaks which originated from Soret and Q bands were observed in the photoluminescence emission spectrum. On the other hand, emission peaks only due to Q band were observed in the cases of FePc, MgPc, Li_2Pc and CoPc. Using toluene as a solvent drastically changed the emission characteristics. In the case of FePc, Li_2Pc and CoPc, the emission peaks only due to Soret band were observed. As for CuPc, an emission peak due to Soret band was dominated. In the TCSPC measurements, it was confirmed that the number of life time components fitted to the decay curve ranged from 3 to 5 with several nanoseconds to several hundreds of nanoseconds. The life time and the number of components depended on the center metals of the doped phthalocyanine and the solvent used in the doping process. The present work clarified that the photoluminescence emission peak position, intensity and life time were varied by solvents and center metals of phthalocyanines.

BN-TuP3 Towards F_1 -ATPsynthase Based Hybrid Nanobiodevice Fabrication, *J.K. Settle, M.L. Richter, C.L. Berrie*, University of Kansas

Incorporation of biomolecules into nanoscale devices, termed nanobiodevices, requires control over biomolecule placement within the device. Nonspecific adsorption of the tiny molecular motor, F_1 -ATPsynthase (ATPase), results in a variety of protein orientations on the surface. To improve the functionality of the immobilized protein, only one orientation (γ unit upright) is desired. Therefore, controlling orientation is also imperative in increasing the number of functional molecules. Several techniques have been utilized to study and control this adsorption process. Atomic force microscopy was used to graft a dithiol into a resist matrix monolayer, exposing a thiol group. Through maleimide chemistry, a maleimide-nitroloacetic acid (NTA) group can be attached to the terminal end of the dithiol pattern. NTA will coordinate with nickel ions, which then coordinates with the histidine tag on the ATPase, thus controlling orientation. This process has also been studied via surface plasmon resonance. By coordinating these efforts with nanoelectrode construction, a functional nanobiodevice may be engineered.

Graphene and Related Materials Focus Topic Room: East Exhibit Hall - Session GR-TuP

Graphene and Related Materials Focus Topic Poster Session

GR-TuP2 Solution Plasma Assisted Surface Decoration of Chemically Converted Graphene Sheet with Various Metallic Nanoparticles, *K. Sadasue, N. Zettsu, T. Ueno, O. Takai, N. Saito*, Nagoya University, Japan

Like the other newly discovered carbon nanomaterials, such as fullerenes and carbon nanotubes, graphene, a monolayer graphite, and its composites have been widely applied to the field of electrocatalysis due to that

graphene have unique structures and inherent properties including high specific surface areas, chemical and electrochemical inertness, easy surface modification, higher electron mobility and broad electrochemical windows. Thus, the use of graphene as substrates of catalysts provides a new opportunity for designing and constructing next-generation catalysts. Especially, graphene decorated with metallic nanoparticles can be employed as fuel cell electrocatalysts, in which they play an important role in improving the charge-transfer efficiency and decreasing the overpotential of electrochemical reactions such as methanol oxidation and oxygen reduction.

However, there are still unresolved issues in practical use, such as durability. In situ growth method is the most widely used method for preparing graphene/metallic nanoparticle composites. Hydrophobic and/or electrostatic interactions are the main driving forces of adsorbing metallic nanoparticles on graphene surfaces. These relatively weak binding interaction often gave rise to desorption of the nanoparticles from the graphene surface during charging and discharging operation at high temperature.

Very recently, we reported a fabrication of Pt catalysts supported on carbon nanoballs, as well as characterization of their electrochemical activities (Saito et al.,

J. Vac. Sci. Technol. A, 27(4) pp.826-830). Plausible mechanism has remained a mystery, Pt catalysts were strongly attached to the carbon nanoball surface. The resultant products showed relatively higher durability compared with that of catalysts prepared by conventionally used approaches. In this work, we demonstrate surface decoration of chemically converted graphene with various metallic nanoparticles by the originally-developed solution plasma processing. Structural characterization and electrochemical activities of the all product was performed by a combination with TEM, XRD, AFM, Raman spectroscopy, and measurements of oxidation-reduction potential [[file:///C:/Users/%E5%AE%9A%E6%9C%AB%E4%BD%B3%E7%A5%90/AppData/Roaming/EdMax/Attachment/20110504_133844_dtub14/AVS%20%E3%82%A2%E3%83%96%E3%82%B9%E3%83%88%E3%83%88%E3%83%88%EF%BC%88%E5%AE%9A%E6%9C%AB%EF%BC%89_revised_zettsu0504.docx](file:///C:/Users/%E5%AE%9A%E6%9C%AB%E4%BD%B3%E7%A5%90/AppData/Roaming/EdMax/Attachment/20110504_133844_dtub14/AVS%20%E3%82%A2%E3%83%96%E3%82%B9%E3%83%88%E3%83%88%E3%83%88%E3%83%88%EF%BC%88%E5%AE%9A%E6%9C%AB%EF%BC%89_revised_zettsu0504.docx)].

GR-TuP3 Synthesis of Carbon Nanoballs, Covered by CNTs with Metallic Conductivity, *K. Ohno, N. Zettsu, T. Ueno, O. Takai, N. Saito*, Nagoya University, Japan

Carbon nanostructures, due to their unique electronic and extraordinary mechanical properties, have been receiving much attention for a wide variety of applications. Especially, highly-conductive carbon nanostructures is a promising candidate supports for heterogeneous catalysts, for use in fuel cells and in metal-air sources of current. Synergetic interaction of the catalyst-nanoparticles with carbon nanostructures exhibits better catalytic parameters than application of carbonaceous materials.

Very recently, we demonstrated a fabrication of platinum catalysts supported on carbon nanoballs (CNBs), as well as characterization of their electrochemical activities (Saito et al., *J. Vac. Sci. Technol. A*, 27(4) pp.826-830). Originally-developed CNB is a highly crystallized nanosized carbon powder with spherical shape. The CNBs can be synthesized by thermal decomposition of ethylene and hydrogens under argon stream. Diameter of CNB can be tuned from 200 to 700nm by changing the mixing ratio of H_2 . Platinum nanoparticles were densely loaded on the CNBs surface under modified solution plasma processing of CNBs and Pt ions with stabilizing agents. We obtained 1.6-fold increase in the electrochemical activity of Pt/CNBs system ($0.26\text{cm}^2/\text{mg}$) compared with that of conventionally-used Pt/C system ($0.16\text{cm}^2/\text{mg}$).

In this work, we propose newly developed CNBs, covered by carbon nanotubes (CNTs) with metallic conductivity in order to reduce contact resistance between neighboring CNBs in electrodes. We grew CNTs from various shaped Fe, Ni nanocrystals deposited onto an individual CNB, and subsequently decorated the surface of the CNBs with Pt nanoparticles as a catalyst by using solution plasma processing. The ratio of metallic to semiconducting CNTs of our all products was evaluated by Raman spectroscopy.

GR-TuP5 Soluble Precursor Synthesis of Graphene and Graphene Nanoribbons, *L.M. Tolbert, C.L. Henderson, J. Vargas, J. Baltazar, J. Kowalik*, Georgia Institute of Technology

Graphene is currently produced typically through one of three routes: (1) some combination of mechanical and chemical exfoliation of graphite, (2) high temperature processing of SiC, or (3) through high-temperature catalytic methods on metal surfaces using simple carbon precursors such as methane. We are investigating and developing methods for synthesis of graphene through a molecular approach, in which the molecular precursors used already possess most of the C=C bonds necessary for graphene formation. A limitation of such approaches is that many of the precursors, e.g., pentacene, are only sparingly soluble and thus have difficulty being solution coated or have low volatility that prevent vapor phase deposition.

Thus we have been investigating the use of soluble precursor molecules which form the graphene templates at higher temperatures or in the presence of catalysts. In particular, one approach toward solubilization that is under investigation is the use of reversible Diels-Alder chemistry to produce soluble grapheme precursor adducts. After solution coating of the materials onto appropriate substrates, the cycloaddition can be reversed at modest temperatures to produce the desired polyaromatic precursor and subsequently processed into grapheme through a further chemical or thermal consolidation. This presentation will review our progress to date in developing such techniques and will demonstrate the ability to form graphene from such approaches at relatively moderate temperatures. A discussion of the effect of choice of precursor on the ability to consolidate the material into graphene and its resulting quality will be presented.

GR-TuP6 Formation of Graphene Films and Patterned Structures through Deposition of Graphene Oxide on Patterned Aminosilane Monolayers, C.L. Henderson, L.M. Tolbert, H.-W. Chu, J. Baltazar, J. Kowalik, Georgia Institute of Technology

Graphene is currently produced typically through one of four routes: (1) some combination of mechanical and chemical exfoliation of graphite, (2) oxidation of graphite to form grapheme oxide which is subsequently deposited onto surfaces and reduced to grapheme, (3) high temperature processing of SiC, or (4) through high-temperature catalytic methods on metal surfaces using simple carbon precursors such as methane. Some applications for grapheme would benefit from low temperature methods (<400 °C), and the first two methods mentioned above can inherently provide access to such low processing temperatures. However, simple exfoliation of graphite has only been demonstrated to produce relatively small, poorly controlled grapheme flakes that are not easily processed due to their limited solubility in solvents and lack of methods for further assembly into larger structures. Therefore, we have been investigating the ability to utilize grapheme oxide (GO) flakes as a soluble grapheme precursor that can be assembled onto surfaces to form both continuous grapheme films and directly form patterned grapheme microstructures. We will present a process in which we deposit and pattern aminosilane monolayers on a substrate, pattern them using lithographic techniques, and utilize such aminosilane patterns to control where GO assembles on the surface and subsequently is reduced to form grapheme. It will be demonstrated that by producing aminosilane monolayers that are dense and which possess a large fraction of non-hydrogen bonded amine terminal groups, continuous grapheme oxide and grapheme films and microstructures can be assembled on substrates. It will be shown that by subjecting the resulting assembled grapheme on such aminosilane layers to modest thermal treatments, that stable n-doped grapheme can be produced. The materials produced via such methods will be discussed in terms of their spectroscopic (e.g. Raman) and electrical properties (e.g. I-V curves for FET devices, carrier concentrations, mobilities, etc.)

GR-TuP7 Graphene Layer-By-Layer Growth on Co₃O₄ (111) at 1000 K by Molecular Beam Epitaxy, M. Zhou, F. Pasquale, J. Kelber, University of North Texas, A. Boosalis, M. Schubert, P.A. Dowben, University of Nebraska - Lincoln

We report layer-by-layer growth of macroscopically continuous and uniform graphene sheets on Co₃O₄(111) at 1000 K by carbon molecular beam epitaxy (MBE) from a graphite rod source. The direct growth of graphene on dielectric substrates is an essential step in the practical and scalable production of graphene-based devices. Co₃O₄(111) films 3 monolayers (ML) thick were formed from surface segregation of dissolved oxygen after deposition ~ 40 Å Co grown on Al₂O₃(0001) substrates at 750 K in UHV. Epitaxial Co₃O₄(111) films, as characterized by Auger spectroscopy and LEED, were formed by subsequent annealing to 1000 K in UHV, and exhibit th a O-O surface nearest neighbor distance of 2.8 Å, in good agreement with literature. The evolution of the Auger electron C(KVV) lineshape during carbon MBE indicates sp² hybridization, and layer-by-layer growth up to at least 3 ML average thickness. LEED spectra indicate that the sp² (111) graphene overlayer is incommensurate with the Co₃O₄(111) substrate. The graphene-related diffraction spots remain sharp from a coverage of 0.4 ML up to 3 ML, indicating that the graphene sheets are azimuthally in registry with each other. Exposure of the 3 ML graphene/Co₃O₄(111)/Co(111) sample to ambient results in no observable change in Auger or LEED spectra, indicating macroscopically continuous graphene sheets. Subsequent acquisition of XPS spectra in a separate chamber yields a graphite-characteristic asymmetric C(1s) peak at 284.9 eV binding energy, indicating graphene → oxide charge transfer, as observed for graphene/SiC and graphene/MgO. A π → π* satellite feature is also observed. Spectroscopic ellipsometry measurements carried out in a separate system confirm the presence of a π → π* resonance, and similarities with the optical absorption of graphene/SiC are observed. Raman spectra acquired at different, macroscopically separated sample areas indicate a uniform 3ML graphene film thickness. These results also

strongly suggest that other non-polar (111) transition metal oxide surfaces with similar O-O nearest neighbor distances may act as suitable substrates for graphene growth at moderate temperatures, opening the way to controlled direct growth of high quality graphene on a variety of dielectric substrates, with materials and processing temperatures readily compatible with Si CMOS integration.

**Helium Ion Microscopy Focus Topic
Room: East Exhibit Hall - Session HI-TuP**

Aspects of Helium Ion Microscopy Poster Session

HI-TuP1 From HIM to NIM: The Prospects of a Neon Ion Microscope, F.H.M. Rahman, L.A. Stern, J.A. Notte, Carl Zeiss NTS

From the time of its conception, the gas field ion source (GFIS) was operated with a variety of gas species - each considered for some particular virtue that depended on the particular application. However, practical issues such as vibration, cost, and stability prevented the commercial introduction of the GFIS for 50 years. The one gas species that was deemed to be most suitable was helium, and this was recently offered as a commercial product in the form of the ORION helium ion microscope in 2006. Now with several years of continued learning, the neon GFIS is being reconsidered in order to determine its suitability for the GFIS and the applications that it might enable.

The virtues of neon arise from its intermediate mass, one third the mass of gallium, and five times the mass of helium. While the helium probe offers minimal damage under normal imaging dosages (10¹⁵ ions/cm²), the neon beam can sputter at much higher yield (typically 10 times the rate of helium – nearly half the yield of gallium). Compared to helium, the neon ions also penetrate less deeply, and produce many fewer sub-surface dislocations per surface sputtering event. For example, with a helium beam normally incident upon aluminum at 30 keV, there are about 1200 vacancies per sputtered atom according to SRIM. Under these same conditions, the neon beam produces just about 212 vacancies per sputtered atom, and these are located much closer to the surface. Also, the distribution of sputtering atoms is more localized to the incident beam location when neon is used. Compared to gallium, neon is expected to offer a much smaller probe size, and permit nanofabrication with much higher fidelity.

Experimental results will be presented to characterize the basic properties of the focused ion beam from our prototype neon GFIS system. Images will be provided to demonstrate our first cross-section milling and imaging characteristics.

(See supplementary PDF online)

HI-TuP2 Helium Ion Microscope (HIM) Milling of Solid-State Nanopores for Single-Molecule Detection Devices, A.R. Hall, University of North Carolina Greensboro, J. Yang, D. Ferranti, L.A. Stern, J. Huang, J.A. Notte, Carl Zeiss NTS

We report the formation of solid-state nanopores using the highly focused ion beam and lithographic capabilities of a scanning Helium Ion Microscope (HIM). We will discuss several aspects of the fabrication process, offering the advantage of high sample throughput along with fine control over nanopore dimensions. We will compare characteristics of the resultant devices with those made by the established technique of transmission electron microscope milling and demonstrate the utility of our nanopores for biomolecular analysis.

HI-TuP3 Imaging and Identification of Self Assembled Monolayers using HIM, G. Hlawacek, A. George, J.E. ten Elshof, R. van Gastel, H. Zandvliet, B. Poelsema, University of Twente, The Netherlands

Helium Ion Microscopy (HIM) is a new and versatile tool for imaging and characterizing surfaces, buried interfaces, thin films and tackling many other problems in modern material science. HIM utilizes ionized Helium to scan the specimen surface. Secondary electrons created by the impinging ions allow to record morphology images with an unmatched lateral resolution of less than 0.35 nm. In addition, back-scattered ions carry the elemental information of the scattering partner – allowing for a elemental identification of the surface composition.

Here, we report on the visualization of thin self assembled monolayers (SAM) deposited on (001) silicon wafers, covered by a thin native oxide. In particular, SAMs formed by (3-Mercaptopropyl)trimethoxysilane (MPS) and Triethoxy-1H,1H,2H,2H-tridecafluoro-n-octylsilane (TDFOS) have been patterned into a rectangular stripe pattern using a two step gas-phase silanization process. The clever use of channeling into the underlying bulk (001) silicon, together with a work-function based evaluation of the

secondary electron data allows a clear assignment of different sample areas to the different chemical species. This is possible for both the electron and the ion generated image. The importance of channeling to distinctly and visibly tag the different SAMs will be demonstrated.

HI-TuP4 Analysis of Metal Nanoparticles in Biological Tissues Specimens Using the Helium Ion Microscope, V.S. Smentkowski, L. Denault, D. Wark, GE-GRC, L. Scipioni, D. Ferranti, Carl Zeiss SMT

The Helium Ion Microscope (HIM) is a newly introduced instrument that has a number of beneficial characteristics that are of importance for the analysis of biological/tissue samples, including: (1) the ability to perform high lateral resolution imaging, (2) high depth of field, (3) and the ability to analyze charging samples. In this poster, we summarize the first HIM analysis of spleen tissue samples that have been treated with a metal contrast agent. We show the advantages of HIM over techniques such as Scanning Electron Microscopy (SEM). The HIM analysis are complimented by surface analysis using Time of Flight Secondary Ion Mass Spectrometry (ToF-SIMS) in order to demonstrate that the contrast observed by HIM is indeed associated with the contrast agent.

HI-TuP5 Fabrication of Carbon Nanomembranes by Helium Ion Beam Lithography, X. Zhang, H. Vieker, A. Beyer, A. Götzhäuser, Bielefeld University, Germany

A helium-ion microscope can be used as beam writing tool on electron beam photoresists, such as hydrogen silsesquioxane (HSQ). It has been demonstrated to have a high resolution, a high sensitivity and a low proximity effect.

Here we report the fabrication of carbon nanomembranes from aromatic self-assembled monolayers (SAMs) with a helium ion beam as direct writing tool. Cross-linking of SAMs is achieved by exposure with helium ions which results in the formation of mechanically stable carbon nanomembranes. The required doses for cross-linking with helium ions are approximately one order of magnitude lower than with electrons. The cross-linked SAMs were transferred to either silicon substrates with an oxide layer for optical characterization or transmission electron microscopy (TEM) grids for preparing free-standing carbon nanomembranes.

With helium ion based cross-linking we fabricated patterned nanomembranes as well. Furthermore, the proximity effect and the sample damage on the nano-scale pattern is investigated and discussed.

HI-TuP6 Layer Thickness Homogeneity Determination via Rutherford Backscattering in Helium-Ion Microscopy, H. Vieker, K. Rott, A. Beyer, G. Reiss, A. Götzhäuser, University of Bielefeld, Germany

The recently developed helium-ion microscope allows remarkable surface resolution with the secondary-electron (SE) detector. Simultaneously, backscattered ions can be detected that allow imaging with a substantially higher elemental contrast. This Rutherford backscattered (RBS) ion contrast depends mainly on the elemental composition of the investigated sample surface. The escape depth of RBS ions is much larger than for secondary electrons. Thus whole layers with a wide range of thicknesses will contribute to a RBS ion image, whereas the SE image is far more surface sensitive, i.e. insensitive to buried parts under the sample surface.

In this contribution we examine RBS ion imaging as tool to characterize thickness variations of layered samples with well defined compositions. In a model example the homogeneity of a gold layer on a silicon substrate is investigated. The achievable spatial resolution for detecting buried inhomogeneities is analyzed. Furthermore we present examples with multiple layers.

HI-TuP7 Multi-Technique Approach to Study the Degradation Mechanism of used JLab Photocathode Samples, V. Shuthanandan, Z. Zhu, M.I. Nandasiri, S.V.N.T. Kuchibhatla, S. Thevuthasan, W.P. Hess, Pacific Northwest National Laboratory, C. Hernandez-Garcia, Jefferson Lab

Degradation of the photocathode materials in accelerator-based photoinjectors represents a challenge for sustained beam delivery in proposed fourth generation light sources. The quantum yield in most existing photocathodes degrades over time leading to machine downtime for quantum yield replenishing and in some instances to photocathode replacement. Several photocathode degradation processes have been proposed including ion back bombardment, photochemistry of surface adsorbed species and irradiation-induced surface and bulk defect formation. At present, no consensus exists within the user community as to the mechanisms of photocathode damage. Better understanding of degradation mechanisms of existing photocathode materials could lead to improved emission properties and longer operating lifetime. Existing photocathode materials range from metallic (e.g. copper) to semiconducting (e.g. GaAs) with various structures, dopants, and surface preparations. Photocathode

emission requirements include high electron yield and low thermal emittance at high repetition rate. The goal of this work is to thoroughly characterize the used photocathode samples obtained from Jefferson lab using helium ion microscope (HIM), Rutherford backscattering spectrometry (RBS) in channeling and random directions, secondary ion mass spectrometry (SIMS), atom probe tomography (APT) and atomic force microscopy (AFM) to understand the degradation mechanism. Four different GaAs samples (two control including one as prepared and the other as annealed but not used, and two used to delivered 1000 and 7000 Coulombs) were analyzed using these techniques. HIM images obtained at the damaged spot from the 7000 C sample clearly show that the surface at this spot is severely damaged. In addition, some cracks are clearly visible on the surface. HIM images collected at the tilt angle of 20° clearly show that these damage features are protruding above the surface of the photocathode samples at the center region of the spot. Stylus profilometer measurement on this spot reveals that the spot has peaks and valleys; the height of the main peak is around 7000 nm while the depth of the valleys ranges from 1000 to 3000 nm. It appears that the material in this area is melted. HIM images collected from all four samples clearly show that there is a systematic variation in the topography of the samples as a function of prolonged use of the photocathodes. The larger the usage time the smaller the structures are. Detailed analysis of these samples using RBS, SIMS together with HIM will be discussed.

**In Situ Spectroscopy and Microscopy Focus Topic
Room: East Exhibit Hall - Session IS-TuP**

In Situ Spectroscopy and Microscopy Focus Topic Poster Session

IS-TuP1 In Situ Infrared Spectroscopy of Oxidation Process of Amorphous Carbon Film, Depending on Substrate Temperatures, M. Shinohara, Y. Takaki, K. Hara, Y. Takami, Y. Matsuda, H. Fujiyama, Nagasaki University, Japan

There has been much interest in amorphous carbon films because they have a lot of useful properties: mechanical hardness, chemical inertness, and changeable electrical properties. The films can be deposited at low temperatures by using plasma process. The films have been used as coating materials for mechanical apparatus. The property of the film surface can be change with the addition of the other atoms on the surface. The addition of oxygen atoms to the surface leads the surface hydrophilic. The hydrophilic property on the surface has advantages to the further surface treatment. Therefore, it is important to understand the oxidation process of amorphous films. One of the effective oxidation methods is oxygen plasma exposure. We investigated the plasma oxidation process with in-situ infrared spectroscopy in multiple internal reflection geometry (MIR-IRAS). In this presentation, we focus on the dependence of oxidation process on the substrate temperatures. Infrared spectroscopic studies indicated that the oxygen plasma exposure induced the generation of OH components in the film. It means that carboxyl group would be formed by the exposure. With the increases of the substrate temperatures, the formation of OH components in the film was suppressed; moreover, the hydrophilic property was decreased with the substrate temperatures. On the other hand, the etching rate due to the oxygen plasma exposure was increased with the substrate temperatures. It is suggested that the etching rate is increased with substrate temperature, compared with the preservation of the OH components in the film.

IS-TuP3 In Situ TEM Studies of Nanoparticle Growth in a Fluorozirconate (ZBLAN) Glass Matrix, J. Johnson, University of Tennessee Space Institute

ZBLAN glass-ceramic materials are being developed as x-ray imaging plates. The materials are doped with europium and chlorine and can be heat treated in such a way that they form a novel nanocomposite material containing barium chloride nanocrystals, with the ability to convert x-rays into stable electron-hole pairs. The image can be read out afterwards with a scanning laser beam in a photostimulated luminescence process.

The ZBLAN glass only acts as an imaging plate upon annealing. As the annealing temperature and annealing time are increased, so a higher degree of nucleation of BaCl₂ crystallites inside the glass matrix is observed. As a result, more crystallites are available to incorporate Eu²⁺ and hence increase the fluorescence intensity. However, a higher annealing temperature and a longer annealing time also lead to a larger degree of crystal growth, resulting in bigger nanoparticles. This leads to a decrease in spatial resolution of a ceramic-glass storage phosphor. The optimal annealing condition thus needs to compromise between the fluorescence intensity and the spatial resolution.

Here we present *in situ* TEM studies of ZBLAN glasses, being carried out to further understand the growth of nanoparticles inside a glass matrix under various heating conditions.

Nanomanufacturing Science and Technology Focus Topic

Room: East Exhibit Hall - Session NM-TuP

Nanomanufacturing Science and Technology Poster Session

NM-TuP1 Nanoscopic Polymerization of Polyaniline on the Nanostructured Alumina Surface and the Nano-Contact Transfer of the Nanofabricated Polyanil. *Y. Watanabe, T. Mori, H. Kato, S. Takemura, T. Hiramatsu*, Kanto Gakuin University, Japan

The aim of the present study is to present what types of nano-size structures and patterns made of polyaniline can be created in local polymerization in nanoscopic area such as nano-size crater or trench. The authors also intend that the fabricated polyaniline patterns can be transferred to other substrate such as silicon wafer by a nano-contact method. Nanoscopic polymerization of polyaniline was conducted locally in nanoscale craters or highly-oriented line pattern with nanoscale trenches fabricated on an aluminum surfaces by combined process of chemical treatments and anodization. Nanoscopic polymerization process was performed by a wet method. Aniline monomer solved in pure water, which was added by oxidation agent ammonium peroxodisulfate (APS) solved in HCl in a test tube, was dropped on the nanostructures as a droplet with a micropipette and was extended on the surface. Aniline monomer was being polymerized in a test tube under those conditions. As for the linked-crater structure, the size of the crater ranged from 50 nm to 100 nm by dynamic force microscopy (DFM) measurements. On the other hand, as for the highly-oriented line structure, the line distance was estimated at 30-40 nm. Nanoscopic polymerization was conducted on the two types of nanostructured templates. DFM observation and the cross section analysis were conducted on pre-deposited and deposited surfaces. For the nanoscale polymerization on the linked-crater structure, one of the characteristic patterns was a polyaniline dots pattern. The DFM image showed that each crater was filled with polyaniline creating polyaniline dots. It was also found that binding small dots formed a tree-like network made of polyaniline covering the linked-crater surface. In the case of lower concentration of APS, dots became smaller. Preliminary stage of nanowire growth was also observed. On the other hand, as for the nanoscale polymerization on the highly-oriented line structure, one of the characteristic patterns was polyaniline line pattern where polyaniline polymerized in each trenches. At the next stage, nano-contact transfer of the fabricated polyaniline patterns to Si wafers was tried. In the case of the line pattern template, it was found that a polyaniline line pattern could be transferred to a Si wafer for the lower concentration of aniline monomer. It was also confirmed that the transferred pattern was changed into dots pattern for the higher concentration of aniline. By atomic force microscopy-current imaging tunneling spectroscopy (AFM-CITS) measurements, the obtained IV characteristics indicated the gap became broaden on the transferred polyaniline pattern.

NM-TuP2 Dielectric Performance of Post Deposition Treated Al₂O₃ Films Prepared by Using Parallel-Plate Electrode PEALD. *C.C. Yu, National Applied Research Laboratories, Taiwan, Republic of China, H.D. Trinh, National Chiao Tung University, Taiwan, Republic of China, B.H. Liu, C.C. Kei, C.N. Hsiao, D.P. Tsai, National Applied Research Laboratories, Taiwan, Republic of China*

In this study, self established plasma enhanced atomic layer deposition system (PEALD) was successfully used to deposit Al₂O₃ films at room temperature. Trimethylaluminum (TMAI) and ionized oxygen ions have used as metal precursors and oxidant, respectively. PEALD cycles comprised TMA pulsing and O₂ plasma treatment steps, and all the steps followed by purging nitrogen gas for 5 second. Parallel electrodes and DC power supply have applied to ignite O₂ plasma during ALD cycles. Effects of plasma power output have investigated by preparing Al₂O₃ films with different O₂ plasma power ranged from 7 – 50 W. Film thickness measurement has been carried out by using x-ray reflection analysis (XRR), and self limiting behavior has been investigated which verified PEALD growth mechanism. Growth rate of PEALD Al₂O₃ films that analyzed by XRR was ranged from 0.8 – 1.7 Å/cyc. Microstructure analysis of PEALD Al₂O₃ films have been characterized by using scanning electron microscope (SEM) and transmittance electron microscope (TEM) and revealed pin-hole free structures with excellent interfaces between films and substrates. Results of atomic force microscope (AFM) measurement show that PEALD cycle number varied from 100 – 500 cycles would lead to the smooth

surface roughness of films ranged from 0.184 – 0.35 nm. Dielectric behavior of high-k capacitors has measured by using HP4284A LCR impedance analyzer. The relations between D_{it} values and plasma power output have characterized and evaluated. The results of C-V measurement show shifted C-V curves and hint that the films deposited with different plasma power lead to varied D_{it} values. This phenomenon implies that higher plasma power causes higher amount of interfacial charge traps on the substrate surface. To study the effects of interfacial conditions on performances of capacitors, post treatment has been used to modify the film properties. Post deposition annealing technique has been applied by using rapid thermal annealing furnace (RTA). The adopted annealing temperatures were ranged from 300 – 500 °C for 30 seconds in nitrogen atmosphere. Improvements of Shifted C-V curves were investigated and carried out the varied D_{it} values as 10⁶ – 10¹⁸ / cm² - eV.

Key : PEALD, Direct plasma, High-k material, C-V, I-V, D_{it}, Parallel electrode

NM-TuP3 Effect of Growth Temperature on Optical Properties of TiO₂ Films by Atomic Layer Deposition. *M.H. Chan, C.C. Kei, C.N. Hsiao, W.-H. Cho, C.C. Yu, B.H. Liu, W.C. Chen, D.P. Tsai*, National Applied Research Laboratories, Taiwan, Republic of China

Titanium dioxide (TiO₂) films were deposited on Si and B270 glass substrates by a horizontal-flow atomic layer deposition (ALD) system. Titanium tetrachloride and deionized water were used as metal precursor and oxidant, respectively. Precursors were separately introduced into the reactor for a pulse length of 40 ms, and the working pressure was kept at 1 torr. Deposition temperature of TiO₂ films was varied between 100 and 300°C. Absorption coefficient and refractive index were obtained by using spectroscopic ellipsometry. Crystal structure of TiO₂ films was acquired by using X-ray diffractometry. Film thickness was obtained by scanning electron microscopy. Curve-fittings of ellipsometric data was also applied to evaluate the film thickness and growth rate of TiO₂ films. It was found that the crystallinity of Rutile TiO₂ films was significantly improved as increase the processing temperature from 150 to 300 °C. This might be the reason for an increasing refractive index of TiO₂ films prepared at a higher temperature. Beside, increase of precursors' reactive rate would result in a lower absorption coefficient for samples prepared at a higher temperature. The growth rate of TiO₂ film prepared at various temperatures is around 0.6 Å/cycle. However, a slight decrease in the growth rate can be observed due to the faster desorption rate of precursors at higher temperatures.

NM-TuP4 Fabrication of Double Nanohoneycombs (Pt/ZnO) with Controllable Size using Nanosphere Lithography and Plasma Enhanced Atomic Layer Deposition. *C.-T. Lee, W.-H. Cho, B.H. Liu, C.C. Kei, D.P. Tsai*, National Applied Research Laboratories, Taiwan, Republic of China

The double nanohoneycombs (Pt/ZnO) on glass and Si substrates were fabricated by nanosphere lithography (NSL) and plasma enhanced atomic layer deposition (PEALD). The first nanohoneycomb (ZnO) was fabricated by controllable size with NSL and magnetron sputtering. In this study, platinum thin films were deposited on ZnO nanohoneycomb by using PEALD using MeCpPtMe₃ and oxygen plasma as precursors. The effects of the thickness of platinum thin films on the structural and optical properties of the double nanohoneycombs (Pt/ZnO) were investigated by field emission scanning electron microscopy, X-ray diffraction and spectrometer. X-ray diffraction analysis revealed that the platinum thin films are polycrystalline with a preferred orientation along (111). This technique forming double nanohoneycombs, especially with desired period, is expected to be a candidate for wide nanostructure applications such as field emission, sensors, etc.

NM-TuP7 Fabrication of Nanopattern Sapphire Substrate by Nanosphere and Nanoimprint Lithography Technology. *C.M. Chang, M.H. Shiao, D.Y. Chiang*, National Applied Research Laboratories, Taiwan, Republic of China, *C.T. Yang*, Industrial Technology Research Institute, Taiwan, Republic of China, *M.J. Huang*, National Applied Research Laboratories, Taiwan, Republic of China, *W.J. Hsueh*, National Taiwan University, Taiwan, Republic of China

In this study, nanosphere lithography (NSL) and nanoimprint lithography (NIL) methods were used to fabricate metal pit and polymer pillar etching masks for sapphire substrate etching process, respectively. The metal mask contains 500 nm hole array and polymer pillar array mask which each pillar's size was 350 nm in diameter and height. Then inductively-coupled-plasma reactive ion etching (ICP-RIE) technique was used to etch sapphire substrate, which introduced both boron trichloride (BCl₃) and Argon (Ar) mixture etchant gases with 1 : 6 flow rate ratio. After etching processes were finished, two types of nanopattern structure were obtained on the sapphire substrate surface. One type of sapphire substrate was nano-pit array structure with 400 nm in diameter and 200 nm in depth, another type

of sapphire substrate was nano-cone array structure with 400 nm diameter and 100 nm in thickness. The contact angles of two patterned sapphire substrates were measured to be 101.02° and 98.14° for nano-pit array and nano-cone array structure, respectively. From the contact angle measurement results, it can be found that the surface property of sapphire substrate changed from hydrophilic, which contact angle was 24.46°, to be hydrophobic.

NM-TuP8 Fabrication of Single-Electron Transistor Utilizing Multi-Coated Self-Assembled Monolayer. *N. Kwon, K. Kim, I. Chung,* Sungkyunkwan Univ., Republic of Korea

We have fabricated quantum dots with the precise sizes from 30 nm to sub-10 nm at the controllable position. First, Au electrodes with the unique shape were obtained using a conventional lithography. Then, self-assembled multilayers, composed of alternating layers of α , ω -mercaptoalkanoic acids (~2 nm) and copper (II) ions, were deposited on Au electrode patterns to form the controllable gap between adjacent Au electrodes. After reaching to nanometer-scale gap, the second Au was deposited again. Finally, lift-off both e-beam resist and molecular resist were removed by lift-off, thereby resulting in quantum dot with nano-gap between gold electrodes. The physical properties were analyzed using scanning probe microscopy (SPM) and field emission scanning electron microscopy (FE-SEM). The electrical properties were evaluated using Keithley-4200.

NM-TuP9 Photoluminescence Studies of Nanostructured Alumina Surfaces Coated by Polythiophene Film and Copper Phthalocyanine. *A. Ishii, R. Nakashima, H. Kato, S. Takemura, H. Kobe, Y. Watanabe, T. Hiramatsu,* Kanto Gakuin University, Japan

Photoluminescent properties of the nanostructured alumina surfaces and the surfaces coated by polythiophene (PT) nanofilm and Copper phthalocyanine (CuPc) were investigated. Nanostructures such as linked-crater structure and highly-oriented line structure were prepared on an Al surface by a combined process of chemical and electrochemical treatments. The nanoscale linked crater structure was fabricated on an Al surface by treatment with Semi Clean and successive electrochemical anodization in H₂SO₄ solution created a nanoscale finer linked-crater structure on the surface. The crater size was estimated at 80-150 nm in diameter by dynamic force microscopy (DFM) measurements. Regarding the highly-oriented line structure, the anodization process applied to the original fiber-like surface structure on the Al plate. The anodization fabricated the finer line structure on the Al surface. The line distance was estimated at 40 nm. The fabricated nanostructured surfaces were identified as alumina by Fourier transform infrared spectroscopy (FT-IR) and x-ray photoemission spectroscopy (XPS) measurements. Conducting polymer polythiophene nanofilm growth on the nanostructured Al surface was conducted by an electrochemical synthetic method in an electrochemical cell. Polythiophene nanofilm was polymerized on the nanostructured Al used as an anode in acetonitrile containing thiophene monomer and (Et)₄NBF₄ by applying positive voltage to the anode. It was observed by DFM that nanofilm was grown along the crater structures or the line structures. CuPc deposition on the nanostructured surfaces was carried out by casting method. Photoluminescent properties of the nanostructured alumina surfaces and the surfaces topped by the nanofilm and CuPc were investigated. It was shown that characteristic ripples of several emission peaks appeared in the wavelength range of 350-550 nm in both cases of linked-crater and highly-oriented line structures while no ripple-shaped emission peaks were observed in the case of the original native Al oxide surface. The emission spectral profile was different in peak positions, number of ripples and intensities between two types of nanostructures. Photoluminescence measurements on the polythiophene nanofilm-grown linked-crater structure also showed that the rippled emission peaks clearly appeared. It was also clearly confirmed that the observed rippled emission patterns were significantly enhanced in both cases of CuPc deposited and nanofilm-coated nanostructures. The mechanism of generation of the rippled peaks and the enhancement were discussed by considering nanosize effects and Al-O vibration modes.

NM-TuP11 Optimization of Criss-Cross Photolithography for 3D NAND. *J. Germain, J. Smith, J.M. Kim, K.Y. Ko,* Applied Materials, Inc.

The patterning of small contact holes is an ever present challenge in the field of photolithography. Recently, the importance of this challenge has expanded both because of the development of 3D NAND architectures such as BiCS and because of the need to pattern even smaller contact holes for DRAM applications.

As the required critical dimensions and pitches of contact holes become smaller, the methods typically used for lithography become insufficient. One approach to solving this problem is the use of criss-cross lithography. In criss-cross lithography, two sets of lines are patterned perpendicular to each other, and a freeze step is used to bind them in place. In the first

portion of this work, criss-cross lithography is used to pattern 60 nm holes, with an argon freeze applied to harden the first layer of polymer before patterning the second layer. In this application, two types of problems were discovered: underexposure which causes patterns to become unstable due to gaps at the bottom of the structure and non-optimized dosing which results in patterns which, while circular before etch, exhibit X/Y directionality when any of a wide range of etch processes is applied to the pattern. We explain the causes of these two problems and demonstrate a consistent relationship between etch depth and X/Y directionality for these types of patterns.

In the later portion of this work we demonstrate the applicability of an alternate technique, thermal freeze, to the patterning of 60 nm contact holes. This technique has been applied and optimized such that it enables the criss-cross patterning approach to produce patterns that are consistent and circular even after the etch process. Along with demonstrating that thermal freeze can be used to produce criss-cross wafers, we also identify the exposure relationships required to achieve circular patterns.

**Nanometer-scale Science and Technology Division
Room: East Exhibit Hall - Session NS-TuP**

**Nanometer-scale Science and Technology Division Poster
Session**

NS-TuP1 Electromigration Assisted Single Silver Nanowire Ammonia Sensing. *W. Xing, S. Kung, R. Penner,* University of California, Irvine

Due to small size, high sensitivity, and low power consumption, 1 dimensional nanowire sensors have attracted a lot of attention and may substitute for traditional thin film sensors in the future. To further improve the sensitivity, there is an obvious need to make sensors with a single nanowire and some seminal work has already been done using semiconductor nanowires in this direction. In this work, a single silver (Ag) nanowire was prepared on glass surface using Lithographically Patterned Nanowire Electrodeposition (LPNE) method. The produced Ag nanowire had a mean grain size of around 30nm and a height and width in the range from 20-80nm and 100-400nm, respectively. Chemiresistor type sensors were fabricated from these single electromigrated Ag nanowires with 4 probe contacts, and their resistances upon exposure to different concentrations of NH₃ gas were investigated at room temperature. Furthermore, electromigration was used to create a narrow junction inside the nanowire, which enhanced the sensing performance dramatically. The electromigrated sensors showed a resistance change, $\Delta R/R_0$, that was large (90% for 7% NH₃), fast (<30s) and reversible with a detection limit of approximately 200ppm. In addition, the characterization of these nanowires by AFM, TEM, and SEM will be presented.

NS-TuP2 Inhomogeneous Density Distribution of Silicon Dioxide Thin Film Thermally Grown at 1000 °C on Si (100) Surface. *K. Odaka, A. Kurokawa, Y. Azuma, L. Zhang, T. Fujimoto,* National Institute of Advanced Industrial Science and Technology (AIST), Japan

We would report on the XRR (X-ray reflectivity) analysis to observe the density distribution of the SiO₂ thin film which is thermally grown on Si (100) at 1000 °C. The results show the non-uniform distribution in depth, and once the high density SiO₂ was formed during ramp-up it would remain under the following 1000 °C oxidation.

Experimental We measured XRR using an apparatus equipped with a shower of high purity N₂ to protect a specimen from contamination for a few hours of measurement. We analyzed the data with a fitting method [1], [2] which is well established to evaluate thicknesses, densities, and surface roughness of laminated layers of a specimen. We assumed a two-layer-fitting model consisting of a transition layer and an upper layer where each had uniform density in it. We oxidized a H-terminated Si (100) specimen of 15x15 mm² in dry O₂ flow at 1 atm. with a quartz tube furnace. The ramp rate was 33 Kmin⁻¹. We kept specimens at 1000 °C for 0 through 120 min to form SiO₂ films of 7.4 through 95.9 nm.

Results We measured XRR for the as grown samples. Then we etched the 95.9 nm sample with dilute HF solution and measured XRR at some thicknesses. The densities of the etched samples as a function of the thickness coincided with those of the as-grown samples. The transition layer was 1 nm thick and about 2.46 gcm⁻³ in density for all the samples. The upper layer density changed from 2.35 to 2.25 gcm⁻³ as the thickness increased. The upper layer density obtained above was an averaged value in its thickness according to our assumption. The density between the two-neighboring-measured points of the etched data might correspond to the real density distribution in depth. The results were as follows. The pre-formed layer of 7.4 nm including the transition layer which grew during the ramp-

up process had density of 2.35 gcm^{-3} or more. The density of the main layer formed at $1000 \text{ }^\circ\text{C}$ decreased rapidly to 2.25 gcm^{-3} at 20 nm , however the non-uniformity occurred mainly within 10 nm . The pre-formed layer remained stable at $1000 \text{ }^\circ\text{C}$ in 1 atm. O_2 for 120 min . The thermal SiO_2 films had stoichiometric composition. [3] The non-uniformity might be caused by change in structure of SiO_2 -network.

Conclusions The XRR analysis revealed the non-uniform density distribution of the thermally grown SiO_2 thin films which may originate from structural change in SiO_2 -network near SiO_2/Si interface region.

[1] Paratt, L. G., Phys. Rev. **95** (1954) 359. [2] Awaji, N., Ohkubo, S., Nakanishi, T., Sugita, Y., Takasaki, K., and Komiya, S., Jpn. J. Appl. Phys. **35** (1996) 67. [3] Kurokawa, A., Odaka, K. and Ichimura, S., Abstract 47th Ann. Meeting Vac. Soc. Jpn. (2006) in Japanese.

NS-TuP3 Growth and Characterization of Au-implanted MBE Grown CeO_2 Thin Films for Plasmonic Based Chemical Sensors. *N.A. Joy*, University of Albany-SUNY, *M.I. Nandasiri*, Western Michigan University, *T. Varga*, *V. Shuthanandan*, *W. Jiang*, *P. Nachimuthu*, *S.V.N.T. Kuchibhatla*, *S. Thevuthasan*, Pacific Northwest National Laboratory, *M.A. Carpenter*, University of Albany-SUNY

Au doped cerium oxide (CeO_2) material system has exhibited high activity, good selectivity and stability for low-temperature catalytic reactions. Recently, highly dispersed Au nanoparticles supported on metal oxides including CeO_2 have attracted a great deal of attention due to their high catalytic activity. Au nanoparticles are also promising candidates for plasmonic applications due to the sensitivity of their surface plasmon resonance (SPR) band to changes in the environment. In this study, we report the growth, characterization, and gas sensing properties of Au nanoparticles embedded in CeO_2 as optical beacons for the detection of H_2 , CO and NO_2 in harsh environment.

CeO_2 thin films were grown on $\text{Al}_2\text{O}_3(0001)$ by oxygen plasma-assisted molecular beam epitaxy (OPA-MBE). Following the MBE growth and in-situ characterization by reflection high energy electron diffraction (RHEED), as-grown CeO_2 thin films were irradiated by 2.0 MeV Au^{2+} ions generated in a tandem accelerator with high fluence of $1 \times 10^{17} \text{ ions/cm}^2$ at 600°C . Subsequently, Au implanted ceria films were annealed at 600°C for 10 hours in air to form well defined Au nanoclusters. As-grown, irradiated, and annealed CeO_2 thin films were characterized by Rutherford backscattering spectrometry (RBS), x-ray photoelectron spectroscopy (XPS), and x-ray diffraction (XRD) techniques. The streaky RHEED patterns from the as-grown films indicate the epitaxial growth of the CeO_2 thin films. Glancing incidence XRD (GIXRD) pattern of the as-grown 300 nm thick ceria film indicates the presence of some polycrystalline material. Following the Au implantation at 600°C , GIXRD pattern shows the Au peaks and the reflections associated with ceria-alumina inter-mixing phase (CeAlO_3) in addition to CeO_2 peaks. It suggests the inter-diffusion of metal atoms at the ceria-alumina interface, which is possibly due to the bombardment of high energy Au^{2+} ions. RBS data of the Au-implanted CeO_2 sample also confirmed the inter-diffusion of the metal atoms at the film/substrate interface. Furthermore, the broader x-ray rocking curve of the $\text{CeO}_2(111)$ reflection after Au implantation confirm the crystalline disorder of the CeO_2 film caused by irradiation. Despite the inter-diffusion and poor crystalline quality, both CeO_2 and Au crystallites are highly-oriented in (111) direction. After annealing and ex-situ characterization of Au/ CeO_2 sample, SPR analysis and gas exposure experiments were performed in a high temperature optical transmission cell. The ppm level gas exposure experiments with the Au/ CeO_2 sample has shown promising sensing characteristics towards the detection of H_2 , NO_2 and CO in an air background at 500°C .

NS-TuP4 Facile Metal Oxide Nanosheet Synthesis using Atomic Layer Deposition. *K. Lee*, *G.N. Parsons*, North Carolina State University

Two dimensional nanosheets have attracted great interest due to their unique thermal and electrical properties. For example, graphene nanosheets which are exfoliated from graphite or synthesized using a chemical solution have shown the potential applications as an electrode, catalysts, and electrochemical sensors. In addition to graphene, various kinds of materials such as MoS_2 , MnO_2 , and MgO nanosheets have been studied extensively. This work demonstrates that atomic layer deposition (ALD) is a facile but effective technique for fabrication of metal oxide nanosheets precisely controlling thickness and chemical composition. We spin-coated a substrate with polymer such as PMMA, PVA, and PAA as a sacrificial layer, then coated the polymer with TiO_2 or ZnO ALD. We made small cuts through the metal oxide/polymer film, and then dissolved the polymer in solvent to release nanosheets from the substrate. We successfully attained two dimensional TiO_2 nanosheets with several hundred μm in lateral size and less than 10 nm in thickness. In addition to single material nanosheets, we can effectively form heterogeneous nanosheets with two metal oxides such as TiO_2/ZnO , where each layer thickness is individually controlled. We

confirmed the thickness with AFM and compositions with EDX. We are exploring possible applications for these materials, and available results will be presented and discussed.

NS-TuP6 Nanoscale Surface Patterning for Controllable Metal Deposition. *G. Smith*, *C.L. Berrie*, University of Kansas

Nanoscale patterning techniques using an atomic force microscope on self-assembled monolayers (SAMs) are used to controllably form metal nanostructures on gold and silicon surfaces. Nanoetching and nanografting are done on methyl-terminated SAMs to pattern in molecules with carboxyl termination. Oxidative lithography is used to electrochemically oxidize nanopatterns into methyl-terminated SAMs to achieve similar results. These nanopatterns are then treated with an electroless metal plating solution to form metal nanostructures selectively on the patterns. The patterns and features are characterized with atomic force microscopy. Controllable metal nanostructure formation has implications in nanoelectronics and nanodevice construction.

NS-TuP7 Probing the Size-Induced Electronic Structures of CdSe Quantum Dots. *P. Nachimuthu*, *A.S. Karakoti*, *S.P. Sanghavi*, *P. Yang*, *V. Shuthanandan*, *L.J. Terminello*, *S. Thevuthasan*, Pacific Northwest National Laboratory

The CdSe quantum dots have been studied for various applications ranging from biomedical imaging and sensing to hybrid solar cells. When the size of the nanocrystals reduces below the exciton Bohr's radius, the energy levels become discrete (quantized). Consequently, the band gap of quantum dots increases with decreasing the size of the dots. This is inherently reflected in the electronic structures of these quantum dots. In addition, these CdSe quantum dots are known to exhibit a phase transition from a stable hexagonal phase in larger dots to a metastable cubic phase at smaller dot sizes during their synthesis. As the size of quantum dot decreases, the number of surface atoms and the energy associated with the surface increase leading to creation of vacancies, which results in the non-stoichiometric CdSe. However, the mechanism is not clear at atomic level. Therefore, we took a systematic approach to study the size-induced structural and electronic properties of CdSe quantum dots in toluene and drop-casted on Si by various in-situ and ex-situ imaging, spectroscopy and diffraction techniques to obtain the correlation between the quantum confinement and the corresponding stoichiometry, crystalline phases and the effect of surface ligands. The CdSe quantum dots capped with trioctylphosphine oxide (TOPO) or hexadecylamine (HDA) in toluene exhibit predominantly wurtzite crystal structure, which undergoes a phase transformation to zinc blende crystal structure following drop casting on Si and this phase transition increases with decreasing the size of the CdSe quantum dots. A systematic increase in the core level binding energies of Cd 3d and Se 3d, the band gap and the Cd/Se ratio is found as the size of the quantum dots decreases from 6.6 nm to 2.1 nm . This is attributed to the quantum confinement of CdSe crystallites by the capping ligands in toluene which increases with decreasing the size of the quantum dots thereby increasing the Se vacancies. However, drop-casting of CdSe quantum dots on Si alters the arrangement of capping ligands on the quantum dots which facilitates significant phase transformation. To gain further insights in understanding these transitions we are seeking first principles investigation on model CdSe particles using density functional theory (DFT). The relative stability between the two phases as a function of particle sizes will be reported.

NS-TuP8 Plasmon-Enhanced Emission With GLAD-Functionalized ZnO Nanowires. *D.C. Mayo*, *A.T. Mayo*, *A. Ueda*, *Z. Pan*, *R. Mu*, Fisk University

ZnO has increasingly been the focus for optical emission studies due to both its wide band gap of 3.37 eV and high thermal stability. In this research, vertically oriented ZnO nanowires (NWs) are grown upon silicon substrates using a novel, modified vapor-solid method within a vertical furnace. Electron-beam evaporation is then used with glancing angle deposition (GLAD) to functionalize the sides of the ZnO NWs with both Ag and MgO:Ag . Comparative characterization is then performed using photoluminescence measurements at varying angles to examine both surface-plasmon-enhanced emissions and to study the underlying coupling mechanisms responsible for the enhancements. This research may serve as the foundation for applications which range from high-efficiency LEDs to optoelectronic plasmon waveguides.

NS-TuP9 Fabrication of High-Performance Carbon Nanotube Field-Effect Transistors with Semiconductors as the Source/Drain Contact Material. *Z. Xiao*, Alabama A&M University, *F.E. Camino*, Brookhaven National Laboratory

We report fabrication of high-performance single-walled carbon nanotube field-effect transistors (CNTFETs) using semiconductors as the source/drain contact material and defining submicron-meter gate within the source and

drain, without overlapping the source and drain. Common problems in the fabrication of carbon nanotube field effect transistors (CNTFETs) include the positioning of tubes across electrodes and poor device electrical performance due to the presence of metallic nanotubes intermixed with semiconducting ones. To circumvent these problems, dielectrophoresis (DEP) will be used for tube alignment, while semiconducting electrodes such as Sb_2Te_3 and $\text{Bi}_2\text{Te}_{3-x}\text{Se}_x$, instead of metal electrodes in CNTFETs will be employed to selectively turn off metallic nanotubes resulting in improved device electrical characteristics. The submicron-meter gates within the source and drain in the fabrication of CNTFETs will be fabricated using the ion beam assisted deposition capability of the dual electron/ion beam system. The electrical measurements on the CNTFETs will be performed and the measurement results will be reported.

NS-TuP11 Preparation of Triethylamine Stabilized Silver Nanoparticles for Low-Temperature Sintering. *S.L.C. Hsu, J.T. Wu,* National Cheng-Kung University, Taiwan, R.O.C.

In this research, silver nanoparticles were synthesized by chemical reduction from silver nitrate using triethylamine as the protecting and reducing agents simultaneously. The average size of the silver nanoparticles was less than 5 nm, which allowed low-temperature sintering of the metal. X-ray diffraction (XRD), thermogravimetric analysis (TGA), and energy dispersive spectrometric (EDS) analysis results indicate that silver nitrate has been converted to silver nanoparticles completely. Using a 20 wt% silver nanoparticles suspension with thermal treatment at 150 °C, silver films with a resistivity of 8.09×10^{-5} W cm have been produced, which is close to the resistivity of bulk silver.

NS-TuP12 Selective Growth and Characterization of a SnO_2 Nano-Wire by Employing DNA-templated Gold Nanoparticle Chains. *J.H. Heo,* Korea Institute of Materials Science, South Korea, *H.J. Kim,* Sungkyunkwan University, South Korea

Recently, the Tin-oxide (SnO_2) has been widely used in the fabrication of various gas (O_2 , CO , NO_x) detecting sensor. Basically, the SnO_2 is n-type semiconductor which has a wide band gap, about 3.99eV. Also, thin film of SnO_2 has been known as a transparent electrode and it is applicable for a various electronic parts. Nowadays, research on SnO_2 nano-wire characterization is very actively performed because it is able to realize a micro-sensor array with conventional Silicon processing. However, it isn't easy to align a single SnO_2 nano-wire on the specific site for the fabrication of integrated gas sensor device. To achieve a high-performance gas-sensor with SnO_2 , we need to make integrated single SnO_2 nano-wire 2 electrode devices. In this study, we employed DNA-templated alignment using a combination of molecular combing and surface-patterning techniques to form a Au nanoparticle chain as a catalyst. It is possible to obtain parallel and latticed nanostructures consisting of DNA molecules and thus DNA-templated Au nano-wires aligned at 400nm intervals.[1,2] After that, a single SnO_2 nano-wire which had been synthesized on the Au nanoparticle by a thermal process.[3,4] By using the AFM probing technique, a Rh coated conducting cantilever can approach a single SnO_2 nano-wire in nano scale and get the I-V curves with sweeping applied voltage between Au electrode and cantilever with a controlled concentration of Oxygen in measuring chamber to change the ionosorption rate. From the results of such experiments, we selectively grow SnO_2 nano-wires and verified Oxygen detecting ability which would be necessary for the realization of micro-sensor array.

[1] Hyung Jin Kim, Yonghan Roh, Seong Kyu Kim and Byungyou Hong, "Fabrication and characterization of DNA-templated conductive gold nanoparticle chains", J. of Applied Physics 105, 074302 (2009)

[2] Hyung Jin Kim, Yonghan Roh and Byungyou Hong, "Selective Formation of a Latticed Nanostructure with the Precise Alignment of DNA-Templated Gold Nanowires", Langmuir article 26(23),18315-18319 (2010)

[3] R.S. Wagner and W.C. Ellis, "Vapor-liquid-solid mechanism of single crystal growth", Appl. Phys. Lett. 4, 89 (1964)

[4] Y. Wu and P. Yang, "Direct Observation of Vapor-liquid-solid nano-wire growth", J. Am. Chem. Soc. 123, 3165 (2001)

Neutron Scattering Focus Topic
Room: East Exhibit Hall - Session NT-TuP

Neutron Scattering Poster Session

NT-TuP1 High Pressure and High Temperature Neutron Reflectometer Cell for Solid-Fluid Interface Research. *P. Wang, D. Hickmott, A. Lerner, J. Majewski,* Los Alamos National Laboratory

To understand the interfacial behaviors of materials under high pressure (P) and temperature (T) are of great importance and interest since lots of natural phenomena and practical applications involve those conditions. For instance, mineral surface/fluid interactions control success or failure of many attempts to engineer Earth's subsurface for energy and/or environmental applications. The corrosion of metals and alloys in high subcritical aqueous systems, and especially in supercritical environments is an important safety issue in nuclear power plants.

However, due to the fact that most interface characterization techniques are difficult to implement at elevated P-T, little experimental attention has focused on solid/fluid interfaces at high P-T.

Neutron reflectometry (NR) is increasingly being used as a characterization tool to study the surface/interface of planar substrates. SPEAR at Lujan center is a Time-of-Flight (ToF) NR facility which is specifically designed to study solid-liquid interface and is able to in-situ monitor the surface/interface behavior with a space resolution of a few angstroms. The obtained real space model from reflectivity curve fitting can provide a lot of physical and chemical information about the interface.

One key gap to study the interfacial behaviors of materials under high P-T conditions is the lack of well designed pressure cell capable of handling P-T conditions close to or above supercritical conditions. To build up the capability of studying high P-T surface/interface, Lujan Center developed a special designed pressure cell which allows us to reach 200 MPa and 250 °C (in the future such cell will be equipped with *in-situ* spectroscopic Raman and IR capabilities). Neutron is highly penetrating, which is able to "see through" high P-T aluminum cell walls and examining the surface/interface properties. Besides the pressure cell itself, the high P-T cell system includes three other subsystems: temperature, pressure and sample chamber environment control systems.

NT-TuP2 Polarized Neutron Reflectivity of Exchange Inversion Layers. *H. Lee, J. Yu, N. Pachauri, S. Keshavarz, P. LeClair, G.J. Mankey,* University of Alabama, *H. Ambaye, V. Lauter,* Oak Ridge National Laboratory

Bulk FeRh undergoes an antiferromagnetic to ferromagnetic phase transition as it is heated above room temperature. The addition of Pd lowers the phase transition temperature so that, in thin film form, the details of the phase transition can be studied while maintaining the same structural and morphological properties of the as-deposited film. The FeRhPd thin film was prepared by DC magnetron sputtering in an ultraclean sputtering system. A FeRhPd/Pt/FeRhPd trilayer was grown at 600°C on an a-axis sapphire substrate with a Rh seed layer and a Pt buffer layer. The epitaxial orientation of this 111-oriented thin film was confirmed by X-ray diffraction methods including standard high-angle diffraction, rocking curve analysis and pole figure analysis. The first-order metamagnetic phase transition and thermal hysteresis of the magnetic moment were examined by vibrating sample magnetometry. To study the detailed magnetic structure of a trilayer with a Pt spacer between two epitaxial films we applied polarized neutron reflectivity (PNR). PNR is used to detect the magnetic moment distribution in layered structures. Temperature-dependent PNR showed the dependence of ferromagnetic spin-splitting for the neutron reflectivity of the two spin polarization channels. Fitting of the PNR data shows a change of the spin splitting that is consistent with vibrating sample magnetometry data. PNR measurements at two different applied magnetic fields of 1 T and 0.5 mT revealed the dependence of magnetic splitting on applied magnetic field and a modification of the thermal hysteresis. This data confirms the strong field dependence of the magnetically stable state. Analysis of the off-specular neutron reflectivity data will show how the magnetic domains change with experimental conditions. The authors gratefully acknowledge financial support from DOE award DE-FG02-08ER46499. Research at Oak Ridge National Laboratory's Spallation Neutron Source was sponsored by the Scientific User Facilities Division, Office of Basic Energy Sciences, U.S. Department of Energy.

Advanced Surface Engineering Poster Session

SE-TuP2 Fabrication of Multilayer X-ray Gratings on Staircase Substrates, C. Liu, Argonne National Laboratory, **S. Lynch,** National Heart, Lung, and Blood Institute, **L. Assoufid,** Argonne National Laboratory, **H. Wen,** National Heart, Lung, and Blood Institute

Classical hard x-ray transmission gratings fabricated using lithography are limited by a small aspect ratio of less than 20 when the grating periods are smaller than 2 microns. State of the art X-ray phase contrast imaging techniques require high density transmission gratings with smaller periods and higher aspect ratio to cover larger energy range for thicker samples. This problem may be addressed with a sliced multilayer technique, similar to that used in multilayer Laue lenses and multilayer transmission mask gratings. To increase the acceptance area of the grating, it was proposed [1] to use a thin Si substrate that is asymmetrically etched to a staircase with each stair supporting a multilayer parallel to its surface. Using an X-ray beam shining through the layers at an oblique angle to the substrate and parallel to the layer surfaces, one hopes to have a large-area transmission grating with small multilayer periods. The first fabrication test is completed using W/Si multilayers with dc magnetron sputtering deposition. The layer thickness d is designed to be (stair height)/ $2N$, where $2N$ is the total number of layers. Preliminary results and challenges are presented.

[1] S. K. Lynch and H. H. Wen et al. "Multilayer-Coated Micro-Grating Array for X-Ray Phase-Contrast Imaging," SPIE Proceedings 2011, submitted.

* This work is supported by the U. S. Department of Energy, Office of Science, Office of Basic Energy Sciences, under Contract No. DE-AC02-06CH11357. SKL and HHW are supported by Division of Intramural Research, National Heart, Lung and Blood Institute, National Institutes of Health.

SE-TuP3 Investigations on Physical Processes for Low Temperature Plasma Activated Wafer Bonding, T. Thomas Plach, K. Hingerl, Johannes Kepler University, Austria, **V. Dragoi, M. Wimplinger,** EV Group, Austria

Direct wafer bonding is a straightforward method of directly connecting wafers, with suitable (in terms of micro-roughness, flatness and cleanliness) surfaces, permanently to each other, by bringing them into contact and subsequently annealing them or simply storing them. The conventional process for hydrophilic oxidized Silicon surfaces (native as well as thermal oxide) is well understood, and explained the following way [1]:

Up to 100°C the substrate surfaces are held together via van der Waals interaction which is mediated by a few monolayers of water. In the range of 100-200°C the water diffuses away from the interface both along the interface and through the oxide into the crystalline bulk, where it reacts with the silicon and forms oxide. The increase of the bond strength from 50% to 100% of Si bulk strength is usually attributed to a closing of gaps at the interface, which starts at the softening temperature of the thermal oxide at around 900-1000°C, depending on whether dry or wet oxide was used.

Low temperature plasma activated direct wafer bonding is a process that lowers the required annealing temperatures necessary for reaching high bond strength. One example for such an improvement is a pair of native oxide – thermal oxide wafers, where bulk strength can be realized by plasma activation with subsequent annealing at temperatures below 200°C. At this temperature conventional wafer bonding reaches half of Si bulk strength, and is limited by gaps at the bonding interface. The mechanism behind this improvement compared to the non activated process is still under discussion.

To clarify the mechanism for this commercially available process, different bonding experiments were performed to evaluate the lifetime of the surface activation and the achievable bond strength when varying some of the boundary conditions of the process (substrates with different orientations, various plasmas, and lowering the annealing temperature).

By partly covering wafers during plasma activation, comparisons between the activated and non-activated regions could be made on single wafers. Therefore the influence of the slightly different substrates could be eliminated. Such wafers were then analyzed by atomic force microscopy, by spectroscopic ellipsometry, by Auger analysis and by X-ray photoelectron spectroscopy.

Finally a model for the mechanism, which was derived from the model for the conventional bonding process, and which explains the experimental results will be presented.

SE-TuP4 Crystalline Thin Film Materials with Ultra-Low Thermal Conductivity, C. Muratore, V. Varshney, A. Reed, J. Hu, J. Bultman, T. Smith, A.A. Voevodin, Air Force Research Laboratory

Transition metal dichalcogenide (TMD) crystals are characterized by their distinct layered atomic structures, with strong covalent bonds comprising each layer, but weak van der Waals forces holding the layers together. The relationship between chemical bonding in a material and its thermal conductivity (k) is well-known, however the thermal properties of TMD thin films with such highly anisotropic chemical bonds have only recently been investigated with remarkable results, such as ultra-low k_z . Materials with very low thermal conductivity in the z-axis, but higher k_x and k_y have potential as next-generation thermal barrier or heat spreading materials. Molecular dynamics (MD) simulations predicted $k_x=k_y=4k_z$ for perfect TMD crystals (MoS₂ in this case). Experiments to determine $k_{x,y}$ and k_z were conducted by developing processes to grow crystalline TMD thin film materials with strong (002) (basal planes parallel to surface) or (100) (perpendicular basal planes) preferred orientation. Initially, no correlation between structure and thermal conductivity was apparent, as water intercalation and reactivity to ambient air resulted in a thermal "short-circuit" across basal planes, such that the time between deposition and k measurement had a stronger impact on thermal conductivity than film orientation. Experiments to measure intrinsic thermal conductivity of MoS₂ revealed values approximately one order of magnitude lower than those predicted using MD simulations, however, measurement of $k_x=k_y=4k_z$ was consistent with simulation results. Simulations to evaluate the dependence of thermal conductivity on grain size were evaluated, which correlated well to measured values. Comparison of measured k values for MoS₂, WS₂, WSe₂ and other materials with analogous crystal structures are discussed in the context of the Slack Law, which accounts for intrinsic physical properties of the crystal, but not film microstructure. Alternatives to TMDs, with less environmental sensitivity, will also be illustrated.

SE-TuP5 Investigation on the Nanoindentation Research Trend in the Surfacing and Joining Technologies, H.T. Kim, S.C. Kil, Korea Institute of Science and Technology Information, Republic of Korea

The research trend on the nanoindentation testing in the surfacing and joining/welding technologies has been reviewed. The increasing interest in the mechanical properties of modern surfacing and joining/ welding structures is placing stringent demands on the manufacturing techniques and performance requirements, and the manufacture employs the high quality and efficiency testing devices to produce best quality products. Nanoindentation testing which enables to evaluate hardness, yield/tensile strength, and residual stress plays an important role in measuring the mechanical properties for relatively small and local volumes, so that it is very useful in obtaining profiles or maps of mechanical properties in the narrow zone of coating and HAZ of weldment. This has led to an increasing attention to the field of surfacing and joining/welding structures. This paper covers recent technical trends of nanoindentation testing technologies of surfacing and joining/welding including the COMPENDEX DB analysis of published papers, research subject and research institutes.

Surface Science Division

Room: East Exhibit Hall - Session SS-TuP

Surface Science Poster Session

SS-TuP1 Oxidative-Coupling Reactions via Nucleophilic Attack on Gold Surface, B. Xu, C.M. Friend, R.J. Madix, Harvard University

Metallic gold owes its centuries-old mystique and intrinsic value to its chemical inertness toward bulk compound formation. In the past decade, however, it has been discovered that the surface of gold is far from inert, and that gold can catalyze important chemical transformations – particularly with the assistance of molecular oxygen or other oxidizing agents. These processes are of particular significance because they may occur at remarkably low temperatures and pressures, suggesting the possibility of energy efficient and environmentally benign reaction conditions using metallic gold catalysts. Recently, there has been a focus on selective oxidation of alcohols to aldehydes, oxidative self-coupling of alcohols to form esters and, most recently, acylation via amine-formaldehyde coupling. Our work under ultra-high vacuum (UHV) condition on the well defined model system of Au(111) surface has unequivocally proved that surface adsorbed atomic oxygen is critical in facilitating a range of nucleophilic coupling-reactions among alcohols, aldehydes and amines. A general reaction mechanism for this class of coupling-reactions is established:

surface alkoxy or amide is formed via the deprotonation of the corresponding alcohol or amine by surface atomic oxygen, which can subsequently nucleophilically attack the aldehydes (formed in situ from alkoxy or introduced directly) and produce the corresponding ester or amide. The product distribution of our low-pressure experiments match remarkably well with gas phase reactions carried out in the ambient condition as well as liquid phase reactions, proves the generality of the mechanism.

SS-TuP2 Many-Body Interactions in Quasi-Freestanding Graphene. *D.A. Siegel, C.H. Park*, University of California, Berkeley, *C.G. Hwang*, Lawrence Berkeley National Laboratory, *J. Deslippe*, University of California, Berkeley, *A.V. Fedorov*, Lawrence Berkeley National Laboratory, *S.G. Louie, A. Lanzara*, University of California, Berkeley

Until recently it had been extremely difficult to experimentally address one of the most fundamental questions about graphene: How do the quasiparticles behave in neutral graphene, i.e. when the chemical potential coincides with the Dirac point energy? Here we address this question by investigating graphene on a particularly interesting substrate, the carbon face of SiC, with high-resolution angle-resolved photoemission spectroscopy (ARPES). We present the first direct measurements of the self-energy in graphene near the neutrality point, and show that the many-body physics in graphene differ from those of an ordinary metal. These exciting findings set a new benchmark in our understanding of many-body physics in graphene and a variety of novel materials with Dirac fermions.

SS-TuP3 Edge Termination of Modified Graphene Oxide during Thermal Exfoliation. *M. Acik, Y.J. Chabal*, The University of Texas at Dallas

Nanopore formation in carbon materials (e.g. exfoliated nanostacks of graphite) has been widely studied through mechanical exfoliation, intercalation, electrochemical separation, chemical or thermal exfoliation of graphite oxide (GO) via expansion with partial oxygen removal. Amongst all these methods, exfoliation of modified graphene (GO), a solution-processable precursor compound where aromatic and heterocyclic rings with embedded oxygen functionalities exist, by thermal processing still remains elusive for the following reasons: (1) poor control of GO composition (initial oxygen content), (2) poor understanding of the chemical composition, (3) unknown role of oxygen, adjoining oxygen interactions, and edge termination with oxygen. Infrared absorption spectroscopy coupled with *in-situ* thermal annealing process [1] makes it possible to examine the chemical changes taking place during thermal reduction to identify and understand interacting molecular environment and the edge functionalization. To unravel the complex mechanisms leading the removal of oxygen in GO, we have performed *in-situ* transmission infrared absorption spectroscopy (IRAS) measurements of graphene/graphite oxide (GO) thin and bulk films upon thermal annealing (60-850°C) in vacuum (10^{-3} - 10^{-4} Torr). Control of the edge geometry of finite-sized modified graphene flakes depends very much on the control of the processing methods. This edge reconstruction further determines electronic, electric, optical and mechanical properties of the exfoliated modified graphene flakes. Therefore, we not only perform studies deriving a thermal reduction mechanism, but also examine the edge reconfiguration with oxygen. We report here the observation of a surprisingly strong IR absorption band that occurs only upon thermal reduction of GO. After annealing at 850°C in vacuum, the strong enhancement of the new IR active absorbance band is observed at ~ 800 cm^{-1} [2]. The intensity of this band is 10-100 times larger than what is expected for the oxygen content of the reduced GO, namely between 5 and 8 at.%. This band is assigned to a specific oxidation state, involving oxygen located in the basal plane (forming C-O-C bonds) and at *atomically straight* edges of reduced graphene. The large enhancement in IR absorption is attributed to the direct participation of electrons, induced by the asymmetric C-O-C stretch mode displacement. These findings open new possibilities in the field of nanoelectronics for all sensor and energy storage applications. [1] M. Acik, *et al.* J. Am. Chem. Soc. (2011), *in preparation*. [2] M. Acik, *et al.* Nat. Mater. 9, 840-845 (2010).

SS-TuP4 Electrocatalytic Surfaces: Structure, Reactivity and Nanotemplating. *X.F. Yang**, Lehigh University, *B.E. Koel*, Princeton University

Electrocatalysis in energy related applications such as fuel cells and hydrogen production impacts and possibly defines the future energy technology picture. Pt-based electrocatalysts are widely used because of their exemplary performance, but these catalysts have serious drawbacks, e.g., cost, modest efficiency, and low durability, which limit fuel cell development. Our research explores non-Pt electrocatalysts or ultrathin-Pt film electrocatalysts to gain insight and discover materials that can replace

Pt or greatly reduce Pt loadings while retaining or even increasing activity and/or stability. Our approach is to use model electrocatalyst surfaces with well-defined composition and structure to simplify and exert control on the system to improve our understanding of the surface phenomena that control electrocatalytic reactions. In this work, four types of model electrocatalysts were prepared in UHV: (i) Pd₃Fe(111), (ii) Au/Pd₃Fe(111), (iii) Pt on a faceted C/Re(11-21) nanotemplate, and (iv) Pt/HfI₃ (poly). These surfaces were characterized using LEED, XPS, LEIS, and AES, and then their electrocatalytic activity for the oxygen reduction reaction (ORR), the hydrogen evolution reaction (HER), and ethanol oxidation (EO) reaction was measured.

Significant surface segregation of Pd was discovered after clean Pd₃Fe(111) was annealed at high temperatures in UHV. The surface structure strongly depends on the annealing temperature, with the formation of an atomically smooth, random substitutional alloy by heating to 1000 K, and the formation of Pd monomer and dimer adatoms by heating to 1250 K. The annealed Pd₃Fe(111) surfaces exhibit higher ORR reactivity than pure Pt. When a submonolayer amount of Au was deposited on Pd₃Fe(111), the Au/Pd₃Fe(111) surface was found to be highly active for the ORR. The activity was strongly dependent on the Au coverage, with the highest activity found at 0.6-ML Au. A Pt monolayer deposited on a nanofaceted C/Re(11-21) surface had a catalytic activity higher than Pt(111) for the HER. In addition, a Pt monolayer on a polycrystalline HfI₃ substrate displayed great improvement in reactivity for electrochemical ORR and EO. In summary, we have investigated a range of non-Pt and ultrathin-Pt film model electrocatalysts that are more active than pure Pt and that point to new materials that could be used to reduce cost and improve activity by nanoengineering novel electrocatalysts.

SS-TuP5 Characterization and Chemical Activity of Pt-Au and Ni-Au Bimetallic Clusters on TiO₂(110). *S.A. Tenney*, *B.A. Cagg*, *W. He*, *M.S. Levine*, *R.P. Galhenage*, *D.A. Chen*, University of South Carolina

Oxide-supported bimetallic Pt-Au and Ni-Au clusters were studied as model catalysts for low temperature oxidation reactions. The growth, composition, and chemical activity of Ni-Au and Pt-Au clusters deposited at 300 K on TiO₂(110) were investigated using scanning tunneling microscopy (STM), low energy ion scattering (LEIS), X-ray photoelectron spectroscopy (XPS), and temperature programmed desorption (TPD). The importance of the Au-titania interface for low temperature oxidation was illustrated by a series of TPD and STM experiments that show a direct correlation between the number of Au-titania interfacial sites and the activity on the surface. Bimetallic clusters were grown by first depositing Ni or Pt onto the surface in order to seed the more mobile Au at existing Ni or Pt clusters. The surfaces of the bimetallic clusters are significantly enriched in Au and are almost entirely pure Au for clusters with > 50% bulk Au composition. TPD of methanol and CO on bimetallic clusters that are highly enriched in Au at the surface still show significant activity characteristic of Ni or Pt at the surface, suggesting that methanol and CO are able to induce the diffusion of Ni and Pt to the surface of the clusters. Heating the bimetallic clusters above 600 K results in the selective encapsulation of Pt or Ni by a thin film of titania. Pre-annealed Pt-Au and Ni-Au bimetallic clusters show promise for enhanced activity towards the conversion of methanol to formaldehyde.

SS-TuP6 Pattern Formation through Leveled Copper Etching after Dysfunctional Electropolishing. *A.D. Paoric*, *P. Kruse*, McMaster University, Canada

Electropolishing is a common industrial practice whereby a metallic surface is subjected to an anodic potential in an appropriate electrolyte to produce a microscopically smooth surface. It is typically performed in concentrated acid with cell potentials ranging from between 1.3 and 2.3V. However, little research has been conducted in the parameter space outside the electropolishing regime. Previous research in our group using deviations from electropolishing conditions has characterized a wide range of fascinating surface structures including terraces, oxide nanotubes, stripes, and dimples. Our current work involves using the copper/phosphoric acid system as a model system to study deviations from electropolishing conditions and the resultant surface features.

Upon exposing copper substrates to a high applied cell potential in concentrated phosphoric acid, etched surface patterns up to over a micron in depth are observed. Characterization of the patterns includes the use of atomic force microscopy (AFM), scanning electron microscopy (SEM), and surface enhanced Raman spectroscopy (SERS). The surface patterns evolve with variation in temperature and phosphoric acid concentration. A distinguishing feature is that the patterns are etched into rather than grown upon the copper substrate, promoting mechanical stability. Additionally, the tops of the surface features are level with respect to their surroundings. Potential applications include electrodes, current collectors for lithium ion batteries, catalysts, micro-cooling, and substrates for the fabrication of other surface morphologies.

* Morton S. Traum Award Finalist

SS-TuP7 Surface Chemistry of Atomic Layer Deposition of Manganese Thin Films, H. Sun, X. Qin, F. Zaera, University of California, Riverside
Manganese thin films can potentially be used as Cu diffusion barriers in microelectronic devices, and may possibly be grown by atomic layer deposition (ALD), to produce highly uniform thin films with good conformality in high aspect-ratio structures. Here, the early stages of film growth of two precursors, methylcyclopentadienyl manganese tricarbonyl (CH₃C₅H₄)Mn(CO)₃ and dimanganese decacarbonyl (Mn₂(CO)₁₀), were investigated by X-ray photoelectron spectroscopy (XPS) to assess their viability for ALD of manganese thin films. In most cases, only oxidized manganese could be deposited on silicon substrates covered with their native oxide layer. Only in depositions using (CH₃C₅H₄)Mn(CO)₃ at relatively high temperatures (>300°C) it was possible to detect a low binding energy feature in the Mn 2p XPS that could be assigned to metallic Mn (although it is also possible to come from manganese silicate). It was also determined that that low-binding-energy manganese species appears only after the growth of a layer of oxidized manganese, and seems to form in the sub-surface. Electron-induced deposition was also studied and compared with the thermal process. The Mn₂(CO)₁₀ precursor was much more reactive, and could lead to multilayer deposition by itself at temperatures as low as 200°C

SS-TuP8 Spin Effects on Metal Surface Reactions: O₂ on Ferromagnetic Pt, M.C. Escano, N.T. Quang, H. Nakanishi, Osaka University, Japan, E. Gyenge, The University of British Columbia, Canada, H. Kasai, Osaka University, Japan

We studied O₂ chemisorption on Pt surface in the need to promote O₂ activation. Activation, in this case, is defined as lowered activation barrier for O₂ dissociation but minimized O adatom (O_{ad}) binding energies; or a significantly stretched O-O bond in a loosely bound molecular O₂. This kind of reaction is not easy to attain since O₂ may present the same affinity to surface in its reaction path. However, such unique reaction is often sought in many electrochemical/chemical systems (i.e. fuel cell cathode catalyst, three-way automotive catalyst). Here, we show how the magnetic state of Pt can achieve this desired reaction. The model system involves a non-magnetic Pt layer pseudomorphically laid on top of magnetic surface (M=Fe(001), Co(001)). The *ab-initio* calculation based on spin-polarized density functional theory, suggests that the magnetic ground state of the system is a ferromagnetically coupled Pt-M layers[1]. The induced spin moment of 0.50μ_B in the Pt layer is in agreement with X-ray Magnetic Circular Dichroism (XMCD) [2]. The hybridization of Pt-5d with the M-3d states give characteristic exchange splitting similar to the spin-resolved inverse photoemission spectroscopy [3]. Using the Heisenberg spin Hamiltonian to determine the exchange interaction, we note that strong inter-layer coupling of the Pt-M spins gives a transition temperature of Pt layer higher than room temperature, in agreement with [2,3].

Potential energy surfaces obtained for O₂ dissociative adsorption on ferromagnetic Pt layer show much lower activation barrier for dissociation and also lowered O_{ad} binding energy. For molecular adsorption, the O₂ vibrational frequency is lower on ferromagnetic Pt as compared to paramagnetic Pt, despite the much lower binding energies on the former. We note that spin effects played significant role rather than charge transfer effects on the over-all structure and binding of the O₂ at transition state and on the surface [4]. This will be discussed in the meeting in terms of local density of states, charge transfer and spin density, and other parameters involved in the bonding and magnetic interactions.

References

1. M.C. Escano, T.Q. Nguyen, H. Nakanishi, H. Kasai, J. Phys.: Condens. Matt. 21 (2009) 49221.
2. J. Lyubina, I. Opahle, M. Richter, O. Gutfleisch, K. Muller and L. Schultz Appl. Phys. Lett. 89 (2006) 032505
3. R. Bertacco and F. Ciccacci, Phys. Rev. B, 57 (1998) 96.
4. M.C. Escaño, H. Nakanishi and H. Kasai, J. Phys. Chem. A 113 (2009) 14302.

SS-TuP9 X-ray Diffraction Study on Hydrogen-Induced Pd(110) Surface Reconstruction, M. Takahasi, S. Fujikawa, W. Hu, Japan Atomic Energy Agency, H. Tajiri, Japan Synchrotron Radiation Institute

Absorption of hydrogen into a substrate begins with dissociated adsorption of hydrogen molecules. The mechanism of the transition from adsorption to absorption is an important knowledge for improving the performance of hydrogen storage materials. The aim of the present study is to verify the hydrogen absorption model in atomic scale through quantitative determination of structures of hydrogen-adsorbed Pd(110) by synchrotron X-ray diffraction.

Experiments were performed at a synchrotron beamline 13XU at SPring-8 using a surface X-ray diffractometer integrated with a UHV chamber equipped with a cryostat. The sample was Pd(110) single crystal which was

10 mm in diameter and 3 mm in thickness. The clean Pd(110)-(1x1) surface was prepared by electrochemical etching in HCl solution and cycles of Ar-sputtering and annealing at ca. 900 K in UHV. For the hydrogen adsorption experiments, the hydrogen pressure was carefully controlled with a needle valve and a nude ion gauge.

We measured five crystal truncation rod (CTR) profiles with increasing substrate temperature to room temperature from 57 K after the substrate was exposed to 10⁻⁶ Torr s hydrogen. Before and after hydrogen adsorption at 57 K, the CTR profiles changed only slightly. More distinctive changes were observed when the sample temperature reached 180 K. At room temperature, the CTR profiles were accounted for by a structure model with disordering of surface atoms. According to past Low-energy electron diffraction, He diffraction and thermal desorption spectroscopy studies, hydrogen adsorption below a substrate temperature of 120 K induced the (1x2) surface reconstruction with 1.5 monolayer (ML) hydrogen through the (2x1) structure at a hydrogen coverage of 1 ML. When the temperature is raised to 200 K, the (1x2) reconstruction returns to a low-coverage 2x1 phase without hydrogen desorption. A comparison with our X-ray diffraction results and these past studies shows that the change of the CTR profiles at 180 K corresponds to the transition from the (2x1) to (1x2) reconstructions and concomitant incorporation of hydrogen into subsurface. These results provide us with an atomic-scale picture that explains how adsorbed hydrogen is absorbed into the Pd bulk.

SS-TuP10 Single Molecule Force Spectroscopy Studies on Nanoclay Surfaces, B. Ozkaya, G. Grundmeier, University of Paderborn, Germany

Sequential adsorption of oppositely charged polyelectrolytes leads to multilayered thin films via electrostatic self-assembly. Incorporation of sheet-like inorganic nanoparticles is a promising method to improve barrier and ion transport properties, as well as mechanical properties in such films. The interface chemistry between the nanosheets and the polyelectrolyte segments plays a crucial role on design of thin coatings with tailored properties. In the present study, we have investigated the effects of pH and ionic strength on the adsorption of single polyelectrolyte molecules on natural clay (Na-Montmorillonite) platelets by means of AFM-based single molecule force spectroscopy (SMFS). SMFS is one of the few methods where in-situ experiments can be performed to obtain precise and quantitative information on interaction forces at a molecular level. In order to perform SMFS on clay platelets (lateral size: 50-300 nm), a heterogeneous model surface has been obtained via electrostatic immobilization of exfoliated clay platelets on template stripped ultra-flat Au(111) surfaces. Probe molecules (polyallylamine) were covalently attached to the gold coated AFM cantilever. Equilibrium desorption plateaus of constant force were obtained from the successive force-distance measurements. By adjusting the ion valency in the electrolyte, selective information from clay platelets could be obtained. In the presence of monovalent ions, desorption plateaus of constant force in the range of ~50 pN were obtained from pH 3 to pH 7. At pH values above the pK_b value of polyallylamine, -confirmed with polarization modulation infrared reflection absorption spectroscopy (PM-IRRAS) measurements on cast polyallylamine- no detectable desorption event took place. The constant negative surface charge of clay platelets simplifies the evaluation of effects of electrical double layer and polymer line-charge density on adsorption of the polyelectrolyte molecules. Overall, the results of pH and ionic strength dependent de-adhesion measurements provide valuable information on the interplay between surface properties and polyelectrolyte adsorption giving the basis for an improved understanding of the behavior of silicate nanoparticles in polyelectrolyte films.

SS-TuP11 Atomic Structure of Aluminum on Si(110): STM and First-principles Study of “4 × 6” Reconstruction, M. Yoshimura, D. Matsuoaka, Toyota Technological Institute, Japan

With the miniaturization of semiconductor devices, low-dimensional structures such as quantum wires and quantum dots have recently attracted much attention. The “16 × 2” on a clean Si(110) surface has been noticed as an effective and unique substrate for the fabrication of low-dimensional nanostructures, because the one-dimensional undulated terrace structure of monatomic height and of about 2.5 nm width are formed. Because the hole mobility of Si(110) surface is about 1.5 times as large as that of Si(100) typically used as substrates of present semiconductor devices, higher speed operation is expected [1]. Thus, the interaction between Si(110) and metal is very important [2,3]. Aluminum is the typical metal forming Schottky barrier with silicon and the Al-adsorbed structures have been well examined on Si(111) or Si(001) plane [4,5]. In contrast, little is known about the structures of the Al/Si(110), particularly in real-space. In this study Al/Si(110) surfaces are investigated in real space using STM and first-principle calculation.

The experiments were carried out in an ultrahigh vacuum (base pressure: 2.0 × 10⁻⁸ Pa). First-principles calculation was performed using VASP program [6]. Aluminum was deposited on a clean Si(110)- “16 × 2” at 600

°C for 10 min to prepare a “4 × 6” reconstruction [7]. In the empty state, alternative arrangement of zigzag rows and straight rows is visible in empty states. In filled states, bright spots are prominent at the position of defects in the zigzag row. They are assumed to be silicon substitutional defects, as is the case for Al/Si(111) [8]. Thus we conclude Al and Si atoms formed zigzag and straight rows, respectively. In addition, the straight row of the silicon was composed of the silicon pentagon [9] as revealed by high-resolution STM. Based on the above observation, an atomic structural model is proposed and discussion will be made based on the theoretical calculation.

[1] T. Sato et al., *Phys. Rev.* **B4** (1971) 1950. [2] Y. Ohira, Master Thesis, Toyota Tech. Inst. (2007). [3] Y. Ohira et al., *Jpn. J. Appl. Phys.*, **47** (2008) 6138. [4] M. Yoshimura et al., *Phys. Rev.* **B47** (1993) 13930. [5] H. Itoh et al., *Phys. Rev.* **B48** (1993) 14663. [6] G. Kresse et al., *Phys. Rev.* **B54** (1996) 11196. [7] A. V. Zotov et al., *Surf. Sci.* **277** L77 (1992). [8] R. J. Hamers, *Phys. Rev.* **B40** (1989) 1657. [9] T. An et al., *Phys. Rev.* **B61** (2000) 3006.

SS-TuP12 Adsorption Dynamics of Ethylene on Si(001). *M.A. Lipponer, N. Armbrust*, University of Marburg, Germany, *M. Durr*, HS Esslingen, Germany, *U. Hofer*, University of Marburg, Germany

The functionalization of semiconductor surfaces by means of organic molecules is of great interest due to possible applications in the field of nanoelectronics. However, only little information on the reaction dynamics of these systems is available. In this work, the adsorption dynamics of ethylene on Si(001) has been investigated. With ethylene being the most simple unsaturated organic molecule, the system serves as a model system for non-activated adsorption on semiconductor surfaces. In order to investigate its reaction dynamics, we employed a supersonic molecular beam which allows for the control of the kinetic energy of the impinging molecules. Additionally, surface temperature and the excitation of internal degrees of freedom were varied when measuring the sticking coefficients as a function of relative surface coverage by means of King and Wells techniques.

With increasing kinetic energy of the impinging molecules, we find a decrease of the initial sticking coefficient as it is typical for non-activated reaction channels; the excitation of the internal degrees of freedom is shown to have a minor impact on the reactivity. With increasing surface temperature, a decrease of the initial sticking coefficient is observed. Surprisingly, the maximum surface coverage also decreases with increasing surface temperature. The results are discussed in the context of a reaction channel via a mobile precursor with long lifetime at low temperatures.

SS-TuP13 Surface Characterization of Polymeric Materials using TOF-SIMS and XPS, *J. Lee, K.-J. Kim*, Korea University, Republic of Korea, *Y. Lee*, Korea Institute of Science and Technology, Republic of Korea

TOF-SIMS and XPS are very useful techniques for the analysis of solid surfaces composed of organic and polymeric species. In order to widen the application of TOF-SIMS and XPS to archeology and plasma process, we analyze the dyed fabrics and the fluorocarbon thin films. First, the fabrics dyed with natural dyes and synthetic dyes were investigated with TOF-SIMS and XPS. Dyes investigated belong to various chemical groups, which include indigo, carthamin, crocin, shikonin, curcumin, purpurin and alizarin. TOF-SIMS and XPS spectra for the dyed textiles showed specific molecular ions and fragment ions from organic dyes as well as elemental ions from metallic mordants. Several ancient fabrics were also analyzed to identify the natural dyes. Secondly, Fluorine-containing hydrophobic thin films were obtained by two different plasma methods: inductively coupled plasma (ICP) and pulsed plasma (PP). Three kinds of fluorine-containing gases such as C₂F₆, C₃F₈, and *c*-C₄F₈ were used to generate hydrophobic plasma polymer films. Process parameters for plasma polymerization such as gas ratio, gas pressure, pulse frequency, and processing time were investigated. Surface analytical instruments such as TOF-SIMS, XPS, and AFM were used to characterize the fluorocarbon thin films generated by ICP and PP. In this work, TOF-SIMS was used to provide useful information about the chemical properties including surface composition and XPS was used to examine the chemical structure of dyed fabrics and fluorocarbon films.

SS-TuP14 Links Between the Surface Atomic Arrangement and Catalytic Properties of Bimetallic Alloys: A First Principles-based Investigation, *J.A. Stephens, H.C. Ham, G.S. Hwang*, University of Texas at Austin

Catalysts composed of more than one metallic element often exhibit remarkable activity and selectivity compared to their monometallic constituents. These synergistic properties often can be explained in terms of two kinds of effects: modification of catalyst electronic structure due to interactions between dissimilar metal atoms (ligand effects) and the

presence of mixed-metal surface sites that, because of their size and shape, promote some chemical reactions more than others (ensemble effects). Understanding in detail how ligand and ensemble effects operate in particular cases is an important step toward realizing the longer term goal of rational catalyst design. Experimental study has provided valuable insight into this problem, but progress has been hampered by the difficulty of studying reacting systems with atomic resolution. We employ the tools of molecular simulation in a two-pronged approach to complement these efforts. First, we use density functional theory to explore how particular atomic arrangements in the surfaces of bimetallic alloys influence their catalytic function. We have found, for example, that the experimentally-observed ability of Au-Pd catalysts to promote the direct synthesis of hydrogen peroxide may depend on the presence of surface Pd monomers surrounded by Au. Our calculations indicate that on larger Pd ensembles, O-O bond scission can more readily occur, leading to the formation of water. We have similarly studied the oxygen reduction reaction and carbon monoxide oxidation on Au-Pd alloys. In the second prong of our work, we attempt to predict how the metal atoms in catalyst surfaces are actually arranged using a combination of density functional theory, the cluster expansion method, and Monte Carlo simulation. From these simulations, we have obtained the temperature- and composition-dependent ensemble size and shape distributions for the (111) and (100) surface facets of Au-Pd and Au-Pt alloys. Our results are in good agreement with available experimental observations.

SS-TuP15 Nitrogen-Rich Heterocycles and Stimulus-Induced Switching Imaged by Liquid STM, *B.E. Hirsch, K.P. McDonald, A.H. Flood, S.L. Tait*, Indiana University

Supramolecular motifs that provide controllable functionalization of surfaces on a nanometer scale offer significant advances in organic solar cells and other surface supported systems. Based on recent advances in two-dimensional organic self-assembly at the liquid/solid interface, we are developing complex surface architectures based on versatile nitrogen-rich heterocycles. This work focuses on the molecular design and subsequent adsorption of this class of compounds onto graphite (HOPG) utilizing liquid scanning tunneling microscopy to resolve the packing of the individual molecules. Current molecular design includes extended alkyl chains and other substituents including amide linkages to facilitate intermolecular ordering. Exploration of photo-activated, tip-induced, and chemically stimulated switching of these molecules is underway to enable manipulation of patterning and packing.

SS-TuP17 Electrical, Physical, and Chemical Properties of the Metal to Amorphous Hydrogenated Boron Carbide Interface, *M.S. Driver, S. Karki, A.N. Caruso*, University of Missouri - Kansas City

Boron carbide (BC), as a semiconducting material, has been under scrutiny for several decades for its use in heterostructure devices toward applications in solid-state neutron detection and thermoelectric energy conversion. The heterostructure devices are typically heterojunctions in which p-type amorphous hydrogenated boron carbide (a-B₃C:H_x) is deposited onto n-type Si, and a Cr/Au contact is applied at the a-B₃C:H_x surface. Traditionally it has been believed that Cr forms an ohmic contact at the a-B₃C:H_x interface and that the heterostructure current-voltage rectification is a classical function of the p-n junction. However, we have found through photoemission studies of Cr overlayers on a-B₃C:H_x that a complex series of interfaces is formed, involving various oxides and borides, which are likely convoluting—and could be dominating—the observed rectification. To follow up the Cr findings, we have explored Al, Cu, Au, Ag, and Ti using the same set of studies. This talk will provide an overview of the electronic, physical, and chemical interfaces between the above metals and a-B₃C:H_x in the context of understanding the *I(V)* characteristics of the presumed p-n junction.

SS-TuP22 Electron Stimulated Reactions on Graphene-Coated Ru: Relevance to Extreme Ultraviolet Lithography (EUVL), *B.V. Yakshinskiy, R.A. Bartynski*, Rutgers University

The contamination of optical surfaces in EUVL exposure tools, operating at 92 eV photon energy, results in degradation of the mirror reflectivity. We report studies of the thermal and electron-induced interaction of benzene and toluene vapors, typical background gases, with the Ru surface, as model cap layer for multilayer mirrors (MLM), using temperature programmed desorption (TPD), X-ray photoelectron spectroscopy (XPS), low energy ion scattering (LEIS), electron stimulated desorption (ESD), low energy electron diffraction (LEED), and scanning tunneling microscopy (STM). A low energy electron source (100 eV) is used to simulate radiation excitations on the surface produced by EUV photons. Heating of adsorbed hydrocarbons leads to a stepwise dehydrogenation and buildup a self-limited carbon monolayer. Electron bombardment of the bare Ru surface in the presence of gas phase hydrocarbons inevitably results in rapid accumulation of 1 ML of carbon or carbonaceous species. Subsequent

contamination growth is determined by the electron-stimulated surface chemistry on the graphitized surface. Graphene monolayer and bilayer formation on Ru(0001) by hydrocarbon pyrolysis or by carbon segregation from the sample bulk is examined as a possible way to reduce the surface contamination rate. Graphene buildup was confirmed by the presence of corresponding superstructures in LEED patterns and STM images. The binding energy of the hydrocarbon molecule is found to be smaller on a graphene layer than on disordered carbon. Electron irradiation of both bare and graphene covered Ru surface in the presence of benzene and toluene vapors leads to C-buildup. However, in a case of low irradiation density, when the electron flux is rate-limiting parameter, graphene monolayer exhibits its protective properties by slowing down carbon accumulation initially, until sufficient thick overlayer is formed. But in a case of high electron flux, when the adsorption of hydrocarbons is rate-limiting parameter, the carbon accumulation rate is invariant to the surface morphology.

The work is supported by Intel and DOE.

SS-TuP23 Photoelectron Spectroscopy Studies of Superconducting Mo₂B and Mo₂BC. *L. Huerta*, Universidad Nacional Autonoma de Mexico, *R. Falconi*, Universidad Juárez Autónoma de Tabasco, Mexico, *M. Flores*, Universidad de Guadalajara, Mexico, *A. Duran*, *R. Escamilla*, Universidad Nacional Autonoma de Mexico

The effect of carbon in the structure of Mo₂B is increasing the superconducting transition temperature from 5.8 K to 7.5K. Polycrystalline samples of the Mo₂B and Mo₂BC were synthesized by the arc melting technique. The samples were characterized by x-ray diffraction (XRD), x-ray photoelectron spectroscopy (XPS) and ultraviolet photoelectron spectroscopy (UPS). XRD results shown that when carbon atoms are added to the structure of the Mo₂B compound a transition structural from body centered tetragonal to face centered orthorhombic is induced forming the Mo₂BC compound. XPS spectra revealed the presence of the Mo 3d, C 1s, and O 1s core levels associated to the chemical states Mo₂B and Mo₂BC. In order to explain the increase of transition temperature in the Mo₂B doped with carbon, we measured the valence band spectra (XPS and UPS), the results were compared with the density of states at the Fermi level $N(E_F)$ of Mo₂B and Mo₂BC.

SS-TuP24 Electrical and Photo-Functional Properties of Copper Oxide Thin Films Prepared by Reactive Magnetron Sputtering. *A. Shukur*, *H. Shukur*, *M. Sato*, *I. Takano*, Kogakuin University, Japan

Copper oxide-based materials have been widely investigated due to their potential application in many technological fields. Cupric oxide (CuO) is a monoclinic n-type semiconductor with a band gap of 1.2-1.5 eV, whereas cuprous oxide (Cu₂O) is cubic p-type semiconductor with a band gap of 2.0 eV [1]. Copper oxides have been employed as a heterogeneous catalyst for several environmental processes, e.g. NO selective reduction, CO oxidation and NO₂ decomposition and it is a very promising material for the development of photovoltaic devices like solar cells.

Copper oxide thin films were prepared by reactive magnetron sputtering. Firstly the sputtering chamber was pumped down to 1.2×10^{-5} Pa. The substrate was a corning glass (#1737) and mirror finishing stainless steel (304ss). The Ar gas was kept at 15sccm and the substrate temperature was kept at 300°C. The amount of oxygen flow rate was varied at 0-10sccm and also the deposition power was varied at 10-40W in order to prepare films with different structures. The structure of the deposited films was measured by X-ray diffraction method (XRD: MAC Science. Co, Ltd). The surface morphology was observed by atomic force microscopy (AFM). The resistivity, mobility and carrier concentration were measured by employing the Hall Effect measurement system. The optical properties of the films were determined by a UV-VIS spectrophotometer (Shimadzu).

In this study, the copper oxide thin films were deposited by a reactive DC magnetron sputtering method. Single Cu₂O and CuO phase can be obtained by controlling the sputtering power. The p-type Cu₂O thin films were prepared with 30-40W. The n-type CuO was observed at power 10-20W. Low electrical resistivity of 90.18Ωm was obtained for the thin film formed at sputtering power of 30W. The thin film was showed a band gap of 2.5eV attributed to Cu₂O at sputtering power 30W whereas the band gap of 10w is 1.9eV. Our experimental investigation indicated that the sputtering power and oxygen flow rate has a significant influence on the electrical properties and optical band gap of the films.

SS-TuP25 Influence of Crystal Structure for Electrochromism of WO₃ Thin Films Prepared by Reactive Magnetron Sputtering. *H. Suzuki*, *H. Shukur*, *S. Ibrahim*, *I. Takano*, Kogakuin University, Japan

WO₃ is known as the material with an n-type semiconductor characteristic showing electrochromism (EC). The amorphous WO₃ thin film especially is used for a display device or a high-speed reaction sensor using electrochromism. WO₃ thin films for electrochromism have been fabricated

by various film formation methods such as reactive sputtering and vacuum evaporation. The relationship between Ar gas and O₂ gas introduced during the film formation is the important condition for the structure of WO₃ thin film. The structure decides the electrochromic characteristic of the WO₃ thin film. In the reactive sputtering method Ar/O₂ gas flow rate especially induces the structure change of WO₃ thin film and the surface morphology.

In this study, WO₃ thin films were deposited by reactive magnetron sputtering with a W target in the condition of changing an Ar/O₂ gas flow rate. In the condition the WO₃ thin films with various crystal structures were fabricated. The relationship between the crystal structure and the electrochromic property were investigated with the great interest.

The WO₃ thin films were deposited by the multi process system with the helicon sputtering source on an Indium-tin oxide (ITO) coated glass and stainless steel (304SS) used as a substrate. The formation conditions of the WO₃ thin film were changed from 5 to 10 sccm in Ar gas flow rate and from 10 to 20 sccm in O₂ gas flow rate under a constant DC source power. The substrate temperature was kept at 473 K using an infrared lamp. The crystal structure and electrochromic property were investigated by X-ray diffraction (XRD) and UV-VIS spectrometer respectively. The crystal structure turned from the WO₃ thin film with the peak (112) to the WO₃ thin film with the peak (002), (112) and (022) with increasing Ar gas flow rate, while increase of O₂ gas flow rate gradually turned up the main peak (112). The maximum efficiency of electrochromic property was obtained at 7.5 sccm in Ar gas flow rate and 15 sccm in O₂ gas flow rate.

SS-TuP26 The Friction Properties of F-Doped DLC Thin Film Prepared in a C₇H₈ Atmosphere by the Ion-Beam Assisted Method. *M. Kurosu*, *I. Takano*, Kogakuin University, Japan

DLC (Diamond-Like Carbon) is known as amorphous carbon including hydrogen and has a characteristic between graphite and diamond. DLC film has been prepared by various methods of chemical vapor deposition (CVD) or physical vapor deposition (PVD) including the sputtering method. The property of DLC shows wear resistance, high hardness and low friction coefficient. DLC is applied in various fields such as motor parts, tools and molds.

In this study, DLC films were prepared by the ion-beam assisted method that was the PVD method allowing a low-temperature formation. In this method the mixing layer which led to high adhesion was formed between the substrate and the DLC thin film. PTFE-Doped DLC (F-DLC) films were prepared by He⁺ ion irradiation in the toluene (C₇H₈) gas. He⁺ ion beam was irradiated at a current density of 5 μA/cm² with a constant accelerating voltage of 5 kV. PTFE doping was performed by using the electron-beam deposition method with PTFE evaporation rate from 0.05 to 0.2 nm/sec. The film thickness measured using QCM was kept at 200 nm. Film composition and microstructure were investigated by X-Ray photoelectron spectroscopy and Raman spectroscopy, respectively. The hardness was measured by an indentation method with a Knoop indenter. The friction coefficient was measured for an SUJ2 ball with a constant load of 0.98 N until the sliding distance reached to a length of 100 m. The friction coefficient property under the vacuum was measured in 5×10^{-4} Pa.

Frictional properties changed under the vacuum and the atmosphere. Friction coefficient of the F-DLC thin film with PTFE deposition rate of 0.2 nm/sec showed 0.25 at a sliding distance of 100 m. Friction coefficient property of the F-DLC thin film under a vacuum showed 0.12 at a sliding distance of 100 m. It was found that F-DLC indicated a low friction coefficient in a vacuum. F-DLC can be expected to be used as one of space materials in the future.

SS-TuP27 Photo-functional Properties of Cu-Added Titanium Dioxide Thin Films Prepared by Reactive Magnetron Sputtering. *S. Arahara*, *H. Shukur*, *M. Sato*, *I. Takano*, Kogakuin University, Japan

TiO₂ has been known as one of a promising photocatalyst and is already used in various practical applications, such as the degradation of environmental pollutants and the self cleaning of glasses. Furthermore, the surface of TiO₂ exhibits high hydrophilicity under ultra-violet (UV) light irradiation. A crystal form of TiO₂ is classified according to structure as anatase, rutile and brookite. TiO₂ shows relatively high reactivity and chemical stability under UV light whose energy exceeds the band gap of 3.2eV in the anatase crystalline phase. The sun can provide an abundant source of photons. However, UV energy accounts for only a small fraction (~5%) of the sun's energy compared to the visible region (45%). Many techniques have been examined to improve this problem by the doping of transition metals into TiO₂.

In this study, TiO₂ films were prepared by reactive magnetron sputtering using a Ti target in an Ar/O₂ gas mixture. Cu addition was performed by Cu sputtering onto those TiO₂ films. It was considered that the charge separation between an electron and a hole was improved by adding Cu to the TiO₂ surface. Composition and microstructure of these films were investigated by X-ray photoelectron spectroscopy and X-ray diffraction,

respectively. Chromatic change of a methylene blue solution was applied to a photocatalytic property. Light irradiation to TiO₂ films in a methylene blue solution was carried out by using a commercial sterilizing lamp as ultraviolet light and an artificial sun light as visible light. Transmittance of a methylene blue solution was measured by a spectrophotometer. Furthermore, photocurrent between the TiO₂ film and a platinum electrode was measured by a volt-ampere characteristic using an unresisted ammeter in a KCl solution of 0.5 mol/l.

The crystal structure of TiO₂ turned from a rutile type into an anatase type with increase of O₂ gas flow rate. Photocatalytic property and photocurrent property of an anatase type of TiO₂ showed the high value. The effect of the Cu addition exhibited different behavior according to each crystal structure. As for the photocatalytic property, the effect of the Cu addition was observed in rutile type, while on the photocurrent property the effect of the Cu addition was observed in anatase type. It was considered that the charge separation between an electron and a hole was enhanced by adding Cu to the TiO₂ surface.

SS-TuP28 Deviation from Wulff Structures for Pt Nanoparticles Supported on TiO₂(110): A STM Study, F. Beharid, B. Roldan Cuenya, University of Central Florida

This study reports the shape of micellar platinum nanoparticles (NPs) supported on TiO₂(110) resolved by scanning tunneling microscopy (STM). Since micellar NPs are initially spherical in shape at room temperature, the 3D faceted shapes obtained after high temperature annealing display structures typical of thermodynamic equilibrium, in contrast with kinetic shapes of physical vapor deposited NPs, which are normally 2D and dominated by the diffusion of metal atoms on the support. All of the NPs resolved show an epitaxial relationship with the support, evident by TiO₂(110)[001] direction being one of the symmetry axis of the NPs. Analyzing these shapes reveals that in addition to hexagonal top (type A) and square top (type B) NPs reported for evaporated NPs, there are two additional categories of shapes observed for micellar NPs (Type C and D). Type A and B consist only of 111 and 100 facets at the interface with the support and the free top surface. However, type C and D feature also 110 facets either at the interface with the support or at the free surface. This facet orientation was not observed before in other studies due to its instability and high surface energy. The ratio of 100/111 facets obtained for these shape deviates from the Wulff structure. This deviation could be attributed to size effects, interface-induced strain, and/or possible TiOx adsorbates on exposed facets.

SS-TuP29 Slope Selection in Au Growth Fronts by Protrusion Interactions, J.L. Sacedón, A. González González, J.A. Aznárez, E. Rodríguez Cañas, E. Vasco, Consejo Superior de Investigaciones Científicas, Spain

Growth fronts of polycrystalline films composed by paraboloid-like surface protrusions (SPs) have been recently decomposed into elemental paraboloidal meridian zones, which allow a comprehensive statistical analysis of the film surface [1]. Using this analysis, local height distribution curves have been synthesized [2] and the interface width expressed as function of the statistical parameters [3]. The method evidences that the average value of the slopes obtained at the SP border remains constant during the growth [2]. The analysis of distribution curves of the terrace width (~ the inverse of the slope) at the SP borders provides three terrace-width limit values [4]: two of them in close agreement with the predicted ones within the frame of the standard slope selection theory, which is based on the balance between downhill/uphill surface currents for the A,B flanks of preferential (111) fcc growth (an intra-SP mechanism); and the third one has been interpreted as a result of an external interaction between SPs and the borders of crystalline plates on which the SPs grew. In the selected slope theory formalism, the surface current balance is the condition to keep constant a characteristic terrace width along a straight infinite flank formed by uniform terraces. In this work, we show that it is possible to obtain limit terrace-width values close to those observed experimentally for limited and curved profiles by using, at the SP border terraces, an external interaction parameter and upward "Pav" coefficients predicted by the theory [5]. Finally, we will propose a general self-organization formalism, which applied as an inter-SP mechanism to the over-growing and under-growing protrusions, allows to predict limit values of terrace widths for the A and B flanks, in a reliable agreement with the experimental ones.

[1] E. Rodríguez-Cañas, J. A. Aznárez, A. I. Oliva, and J. L. Sacedón, Surf. Sci. **600**, 3110 (2006)

[2] J. L. Sacedón, E. Rodríguez-Cañas, C. Munuera, A. I. Oliva, and J. A. Aznárez, Phys. Rev. B **72**, 195413 (2005)

[3] E. Rodríguez-Cañas, E. Vasco, and J. L. Sacedón, Appl. Phys. Lett. **90**, 013112 (2007)

[4] E. Rodríguez-Cañas, E. Vasco, J. A. Aznárez, A. Ruiz, C. Munuera, A. González-González, and J. L. Sacedón, Surf. Sci. **604**, 974 (2010)

[5] J. Yu, and J. G. Amar, Phys. Rev. B **69**, 045426 (2004)

SS-TuP30 UV Induced Photodesorption of O₂ on Rutile TiO₂(110): An Angular Imaging Study, D.P. Wilson, M.D. Kershis, Brookhaven National Laboratory, M.G. White, Stony Brook University and Brookhaven National Laboratory

The binding states of oxygen on TiO₂(110) are important for many reactions, including the degradation of organic compounds and photodesorption. Experimental data and theoretical calculations have shown many different configurations for O₂ on TiO₂(110), including O₂⁻, O₂²⁻, and O₄⁻. Defect sites in titania (bridging oxygen vacancy, Ti³⁺ interstitial), while necessary for the adsorption of oxygen, also play a role in the initial binding states. In this experiment, the angular distributions and images of oxygen photodesorption from a rutile TiO₂(110) surface are studied under UHV conditions using a pump-probe Time-of-Flight (TOF) detection scheme to help determine the initial binding states of oxygen on this surface. Excitation occurs via exposure to 3.7 eV photons followed by one-photon ionization using 13.05 eV photons. The delay time between the lasers can be varied according to the maximum desorption velocity of the oxygen molecules. Ions were detected using a dual microchannel plate and a phosphor screen. A CCD camera positioned behind a phosphor screen captured the light emission of the phosphor, allowing for the imaging of the desorbing neutral O₂ molecules. SimION 3D was used to simulate the motion of the ions through a Time-of-Flight (TOF) mass spectrometer to generate a probability distribution for detection that was used to compare images at different delays.

Previous experiments on the oxygen velocity distribution on TiO₂ (110) showed 3 different "channels" for desorption, with two being "fast" and one being "slow". The velocity distribution for the slow channel tracked with surface temperature, indicating that a trapping desorption mechanism dominated this channel. The two "fast" channels, however, did not depend on temperature and were attributed to two different oxygen binding states on TiO₂ (110). Many different binding states of oxygen have been predicted and it is unclear which state is responsible for which channel. Images of the fastest channel and comparisons at different coverage and photon flux are shown.

The methyl radical velocity distributions from 4 different ketones (acetaldehyde, acetone, butanone, and acetophenone) were also investigated. For ketones where methyl radical desorption is not the preferred pathway (butanone), a 2+1 REMPI scheme was used for signal enhancement. Using these model systems allows for direct comparison of different properties of each molecule.

Thin Film Division

Room: East Exhibit Hall - Session TF-TuP

Thin Films Poster Session

TF-TuP1 Spatially Varied Orientation Selective Epitaxial Growth of CeO₂(100) and (110) Areas on Si(100) Substrates by Reactive Magnetron Sputtering Utilizing Electron Beam Irradiation, T. Inoue, S. Shida, Iwaki Meisei University, Japan

Cerium dioxide is of great interest due to favorable properties as an electronic material, such as high dielectric constant of 26, high chemical stability, transmission in visible and infrared regions, and high efficient ultra-violet absorption. Epitaxial growth of CeO₂ layers on Si substrates has been studied making the best use of a close lattice parameter matching relation. Recently, we have found that orientation selective epitaxial (OSE) growth of (100) and (110) oriented CeO₂ layers on Si(100) is capable by controlling surface potential distribution in reactive magnetron sputtering. Non-polar CeO₂(110) grows on Si(100) with usual non-modified surface potential, whereas polar CeO₂(100) grows on Si(100) with adequately bent surface potential. We are studying two OSE control methods, one is substrate bias application[1] and the other is low energy electron beam irradiation.[2,3] The latter has the attractive possibility of spatially varied two dimensional control of OSE grown regions.[4] This paper describes experimental results of electron beam induced OSE growth with patterned scanning of 90 eV electron beams. The size and position of the electron beam irradiation area were controlled using absorbed electron current image observation. RHEED and XRD analyses proved the realization of two dimensionally controlled OSE growth of CeO₂(100) and (110) areas in electron beam irradiated and non-irradiated areas, respectively. Precise XRD peak profile measurements revealed that there are considerably wide transition regions in between the above two areas, which contain both orientation components. For the application to two dimensionally patterned

hybrid orientation technology, the transition region width should be reduced significantly. Our experiments clarified that the width of the transition region reduces proportionally with the logarithm of underlying Si substrate resistivity, reflecting the surface spread of potential distribution. These results will lead to sophisticated microelectronics devices using hybrid orientation technology. This work was supported by KAKENHI (20560024). A part of this work were conducted at the AIST Nano-Processing Facility, supported by "Nanotechnology Network Japan" of the MEXT, Japan.

[1] T. Inoue, N. Sakamoto, M. Ohashi, S. Shida and A. Horikawa, *J. Vac. Sci. Technol.*, **A22**, 46 (2004).

[2] T. Inoue, T. Saito and S. Shida, *J. Cryst. Growth*, **304**, 1 (2007).

[3] T. Inoue, H. Ohtake, J. Otani and S. Shida, *J. Electrochem. Soc.*, **155**, G237 (2008).

[4] T. Inoue, N. Igarashi, Y. Kanno and S. Shida, *Thin Solid Films*, to be published.

TF-TuP2 Influence of Growth-Rate on the Epitaxial Orientation and the Crystalline Quality of CeO₂ Thin Films Grown on Al₂O₃(0001) by Molecular Beam Epitaxy, *M.I. Nandasiri*, Western Michigan University, *P. Nachimuthu*, *T. Varga*, *V. Shuthanandan*, *W. Jiang*, *S.V.N.T. Kuchibhatla*, *S. Thevuthasan*, Pacific Northwest National Laboratory, *S. Seal*, University of Central Florida, *A. Kayani*, Western Michigan University

Cerium oxide (CeO₂) is one of the extensively studied rare earth oxides; however, it continues to attract attention because of its potential use in medical biology, catalysis, intermediate temperature solid oxide fuel cells (IT-SOFC), and resistive oxygen gas sensors. Driven by the need for fundamental understanding of its unique properties, CeO₂ thin films grown on various substrates by different methods at different experimental conditions have been extensively studied. However, the influence of growth-rate on the orientation and the crystalline quality of the CeO₂ thin films is relatively unexplored. While understanding the influence of growth-rate, we evaluated the ability to tailor the orientation and the epitaxial quality of CeO₂ films on Al₂O₃(0001).

CeO₂ thin films were grown on Al₂O₃ (0001) substrates at 650 °C with different growth-rates (1-10 Å/min) by oxygen plasma assisted molecular beam epitaxy (OPA-MBE). The growth rate induced epitaxial orientations and crystalline quality of CeO₂ thin films were studied by in-situ reflection high energy electron diffraction (RHEED), atomic force microscopy (AFM), and x-ray diffraction (XRD) techniques. CeO₂ grows as three-dimensional (3-D) islands and two-dimensional (2-D) layers at growth-rates of 1-7 Å/min and ≥9 Å/min, respectively. AFM images show average surface roughness of 5-10 Å, indicating the high-quality surfaces of CeO₂ thin films. The formation of epitaxial CeO₂(100) and CeO₂(111) thin films occurs at growth rates of 1 Å/min and ≥9 Å/min, respectively. Glancing incidence XRD measurements have indicated that the films grown at intermediate growth rates (2-7 Å/min) consist of some polycrystalline CeO₂ along with CeO₂(100). As indicated by x-ray pole figure measurements, the CeO₂ thin film grown at 1 Å/min shows six in-plane domains, characteristic of well-aligned CeO₂(100) crystallites. When increasing the growth rate from 1 Å/min to 2-7 Å/min, poorly-aligned CeO₂(100) crystallites start to coexist along with well-aligned crystallites. The content of the poorly-aligned CeO₂(100) crystallites increases with increasing growth rate from 2 Å/min to 7 Å/min, and three out of six in-plane domains gradually decrease and eventually disappear. At growth rates ≥9 Å/min, CeO₂(111) film with single in-plane domain was identified. The formation of CeO₂(100) 3D-islands at growth rates of 1-7 Å/min is a kinetically-driven process unlike at growth rates ≥9 Å/min, which result in an energetically and thermodynamically more stable CeO₂(111) surface.

TF-TuP3 Influence of Target Type on Surface Texture-etched AZO Films Prepared by Magnetron Sputtering for Solar Cell Transparent Electrode Applications, *T. Minami*, *T. Miyata*, *T. Hirano*, *Y. Noguchi*, *J. Nomoto*, Kanazawa Institute of Technology, Japan

This paper describes the influence of sintered oxide targets on the surface texture formation as well as light management obtainable by wet-chemically etching transparent conducting Al-doped ZnO (AZO) thin films prepared by different types of magnetron sputtering depositions (MSD). For transparent electrode applications in thin-film solar cells based on CuIn_{1-x}Ga_xSe₂ and Si, transparent conducting AZO thin films require an appropriate surface texture to improve photovoltaic properties through induced light scattering and subsequent light trapping. It was found that the suitability of the light scattering characteristics for thin-film solar cell applications was considerably dependent on both the type of AZO target and the type of MS deposition used.

The surface texture-etched AZO thin films were prepared by a d.c.- or r.f. (13.56 MHz) power-superimposed d.c.- magnetron sputtering deposition

(dc-MSD or rf+dc-MSD) with sintered AZO targets that was followed by a heat treatment with rapid thermal annealing (RTA) and a subsequent wet-chemical etch. Five types of commercially available high-density-sintered rectangular AZO targets were used. The suitability of the light scattering characteristics for thin-film solar cell applications was evaluated by carrying out surface texturing of the samples with wet-chemical etching in a 0.1% HCl solution conducted after the heat treatment with RTA (at a temperature of 300-500°C for 1-5 min in air). It was found that the obtainable surface texture as well as the haze value in the range from visible to near infrared were considerably affected by not only the AZO target used but also the type of MSD; the dc- and rf+dc-MSD were conducted using the five types of targets with properties that depended on the supplier. The surface-textured AZO thin films prepared by rf+dc-MSD and etched to an appropriate depth after RTA were found to exhibit a higher haze value and a lower resistivity than the values exhibited by equivalent films prepared by dc-MSD. It was also found from X-ray diffraction analyses that the as-deposited AZO thin films prepared by rf+dc-MSD exhibited better crystallinity than those prepared by dc-MSD; also, the crystallinity of AZO thin films, such as the c-axis orientation, was slightly improved by the RTA treatment. A high haze value generally above 70% in the range from visible to near infrared (at wavelengths up to 1200 nm), which is suitable for thin-film solar cell applications, was obtained in the best surface-textured AZO thin films: film thickness of 2 μm prepared by rf+dc-MSD with an appropriate AZO target and etched to a depth of approximately 300 nm after RTA at approximately 500°C for 5 min.

TF-TuP4 XPS and ToFSIMS Characterization of Laser Modified Films for Li-Ion Battery Cathodes, *M. Bruns*, *R. Kohler*, *J. Proell*, *C. Ziebert*, *W. Pfleging*, Karlsruhe Institute of Technology, Germany

The development of novel electrode materials for lithium-ion batteries has become subject of great interest in recent years due to the necessity of improved performance for future mobile applications and energy storage systems. Therefore, a great deal of effort has been spent to develop strategies for the enhancement of battery lifetime, capacity, and cyclability. A self-evident goal to improve the electrochemical properties of cathode materials is to enhance the lithium intercalation rate by increasing the surface to bulk ratio. For this purpose, a very promising approach is the laser-assisted surface modification and structuring of commonly as a cathode material used lithium cobalt oxide and lithium manganese oxide.

The present study focuses on the characterization of non-structured and laser modified films before and after electrochemical cycling using a combination of complementary surface analytical methods. For this purpose rf magnetron sputtered lithium cobalt oxide and lithium manganese oxide were structured with laser radiation leading to a surface microstructure with increased active surface area. In particular, high repetition excimer laser radiation with a pulse width of 4-6 ns and 248 nm wavelength was used. Self-organized conical microstructures were formed using laser fluences between 0.5 J/cm² and 2.0 J/cm². A subsequent annealing process using high power diode laser radiation at 940 nm wavelength enables the adjustment of the required crystallinity.

X-ray photoelectron spectroscopy (XPS) provides the chemical composition in a non-destructive manner. The in-depth distribution of the electrode constituents and the solid electrolyte interface after cycling was studied by time-of-flight secondary mass spectrometry (ToFSIMS) and XPS sputter depth profiles. In addition, the conical topography was shown by scanning electron microscopy (SEM) and crystallinity was proven by X-ray diffraction.

TF-TuP5 Effect of Temperature on the Native Oxide Consumption during the ALD of Ta₂O₅ and TiO₂ on GaAs (100) Surfaces, *L. Ye*, *T. Gougousi*, UMBC

Thermal ALD processes for the deposition of TiO₂ and Ta₂O₅ have been developed using amide precursors and H₂O as reagents. The TiO₂ films were deposited from tetrakis dimethyl amido titanium and H₂O and the Ta₂O₅ films were deposited from pentakis dimethyl amido tantalum and H₂O. The growth rate for both processes was ~0.6 Å/cycle at 200°C and 250°C respectively. These temperatures represent the so-called ALD minimum. At these temperatures the existence of a reaction that leads to the consumption of the surface native oxides during depositions on GaAs (100) surfaces has been confirmed using x-ray photoelectron spectroscopy and high resolution transmission electron microscopy. To investigate the effect of temperature on the native oxide consumption rate two sets of samples with thickness 2 and 3 nm have been prepared at temperatures ranging from 100 to 350°C. For both ALD chemistries a significant enhancement in the gallium and arsenic oxide consumption rate was observed for process temperatures above 300°C. For depositions performed at temperatures more than 50°C below the ALD minimum the consumption reaction is significantly slower.

TF-TuP7 Influence of Doped Al Content on Electrical Properties and Light Management Obtainable by Texture-etched AZO Films Prepared by DC Magnetron Sputtering. *J. Nomoto, T. Miyata, T. Hirano, T. Minami,* Kanazawa Institute of Technology, Japan

Al-doped ZnO (AZO) thin films that would be suitable for transparent electrode applications in thin-film Si-based solar cells must necessarily attain not only a decrease of plasma resonance frequency by lowering the carrier concentration while retaining a resistivity on the order of 10^{-4} Ω cm, but also a significant scattering of light incident on the film by surface texturing. In this paper, we describe the influence of doped Al impurity content on the electrical properties as well as the light management obtainable by surface texture-etched AZO thin films that were prepared with various Al contents by a dc magnetron sputtering (dc-MS) deposition and wet-chemically etched after a rapid thermal annealing (RTA) treatment. In addition, the stability of the resulting electrical properties for practical use in various environments was investigated for these AZO films prepared with various Al contents.

Transparent conducting AZO thin films were prepared with a thickness up to $2\mu\text{m}$ by a dc-MS deposition using sintered AZO targets that had various Al contents. The basic sputter depositions were carried out on OA-10 glass substrates at a temperature of 200°C in a pure Ar gas atmosphere at a pressure of 0.4Pa and a power of 200W. Surface texturing of the AZO thin films was carried out by wet-chemical etching in a 0.1mol/l HCl solution after the thin films were heat treated with RTA at a temperature of $300\text{--}500^\circ\text{C}$ for 1-5min in air. It was found that the obtainable surface texture and electrical properties in texture-etched AZO thin films were considerably affected by the RTA treatment conditions as well as the Al content doped into the films. The transmittance in the near-infrared region of the resulting AZO thin films exhibited a tendency to improve as the RTA temperature was increased. A high transmittance above 80% at a wavelength of $1.2\mu\text{m}$ was obtained in $1\text{-}\mu\text{m}$ -thick-AZO thin films prepared under the following conditions: an Al content (Al/(Al+Zn) atomic ratio) of approximately 0.5at.% when the thin films were heat treated without RTA and an Al content below 1.5at.% when the thin films were heat treated with RTA. In addition, when the thin films were heat treated with RTA at 500°C for 3-5min, increasing the Al content doped into the AZO films enhanced the transmittance in the near infrared region, irrespective of the film thickness. However, it should be noted that the optimal Al content doped into texture-etched AZO thin films that would be suitable for transparent electrode applications in thin-film Si-based solar cells was considerably dependent on the obtainable crystallinity in the films as well as whether the thin films were heat treated with RTA or not.

TF-TuP9 Structure and Photo-Functional Properties of N^+ Ion Irradiated TiO_2 Thin Film under Various Substrate Temperatures. *H. Shukur, M. Sato,* Kogakuin University, Japan, *I. Nakamura,* Tokyo Metropolitan Industrial Technology Research Institute, Japan, *I. Takano,* Kogakuin University, Japan

Titanium dioxide (TiO_2) has been fundamentally used as a photocatalytic application to decompose environmental pollution materials. TiO_2 can generate active oxygen by exposing to sunlight and also is harmless to the environment and the low cost material, so that it is expected to use as an element of a clean energy system in the future.

TiO_2 shows relatively high reactivity and chemical stability under UV light whose energy exceeds the band gap of 3.2 eV for the anatase crystalline phase and 3.0 for the rutile crystalline phase. Many techniques has been examined to increase its activity under visible light region.

N^+ ion irradiation method has been used by many researchers because it can provide an activated TiO_2 in both of visible and UV light. However the collision between ion and film causes a defect in film structure as causing a decline in photo-functional property.

In this study structural, chemical and photo-functional properties of TiO_2 thin film with a rutile structure were studied after irradiation by various doses of N^+ ion beam under various temperatures. Reactive magnetron sputtering method was employed to prepare TiO_2 thin film on glass substrate (corning #1737). Ti-O was sputtered from Ti target in an Ar / O_2 gas and the substrate was heated at 300°C . The total film thickness was around 180 nm with a deposition rate of 0.025nm/sec. N^+ ion was irradiated to TiO_2 thin film under 15 keV in acceleration voltage, and $40 \mu\text{A}/\text{cm}^2$ in ion current density with a various implantation doses. Substrate temperature was set at a room temperature (25°C), 100, 200 and 300°C through ion irradiation processes. The structure was determined by X-ray diffraction (XRD: MAC Science High quality XG M18XCE) with $\text{CuK}\alpha$ (0.154nm) radiation at an incident angle of 0.3° , and the composition was characterized by X-ray photoelectron spectroscopy. The photocatalyst property was measured by a MB immersion test. The spectrophotometer (SHIMADZU UV-2550) was used to measure the difference in light absorption at a wave length of 665nm.

The increasing in the Full Wave Half Maximum (FWHM) of XRD measurements with N^+ ion irradiation under 25°C refers to declining of the crystal structure of the TiO_2 thin film. On the other hand HMFWD decreased by increasing the substrate temperature and closed to the value of the as-deposited film prepared under 300°C . Thus the improvement of photocatalytic property under visible light was increased from 9.1% at 25°C to 25.7% at 300°C under the same N^+ irradiation (2.5×10^{15} ions/ cm^2).

TF-TuP11 Study of Electronic Structure in In-Ga-ZnO Amorphous Semiconductor Films, *Y. Li, Z. Liu, X. Hu, J. Ren,* Xi'an Jiaotong University, China

Amorphous oxide semiconductor In-Ga-ZnO (IGZO) has unique electron transport properties such as large electron mobility ($10\text{--}30 \text{ cm}^2/\text{Vs}$) and good uniformity for active-matrix flat panel display applications [1-2]. Theoretical studies indicate the high electron mobility in amorphous IGZO is due to spherically spread orbitals of metal cations forming unaffected electron transport path. It has been proposed amorphous IGZO has strong ionic electronic structure compared to the covalent electronic structure in amorphous Si [3]. However, the transport mechanism to result in high electron mobility in amorphous structure has not been experimentally explained yet. The focus of this study is to use surface probe, optical as well as Raman spectroscopic techniques to investigate the electronic structure in IGZO. Amorphous IGZO thin films are being grown at room temperature by pulsed laser deposition. Initial Hall effect measurements indicate that amorphous IGZO films have electron concentration of $9 \times 10^{19} \text{ cm}^{-3}$ with Hall mobility of $16.8 \text{ cm}^2/\text{Vs}$. Raman spectroscopy is being used to analyze the lattice arrangement, i.e. the amorphous state and the bonding properties in IGZO films. During film processing, hydrogen is being introduced into the material system to modulate the defect state levels and band gap structure in IGZO. X-ray photoelectron spectroscopy is being used to obtain the valence band spectrum of IGZO films. The energy state within the band gap is being analyzed using deep level transient spectroscopy. The correlation of growth parameters on optical properties as well as electronic structure will be described in this work.

[1] K. Nomura, H. Ohta, K. Ueda, T. Kamiya, M. Hirano, H. Hosono, Science 300,1269 (2003).

[2] K. Hoshino, J.F. Wager, IEEE Trans. Electron Devices 31,818 (2010).

[3] T. Kamiya, H. Hosono, NPG Asia Mater. 2, 15 (2010).

Vacuum Technology Division

Room: East Exhibit Hall - Session VT-TuP

Vacuum Technology Poster Session & Student Poster Competition

VT-TuP1 Measurement of Molar Mass and Viscosity of a Viscous Flowing Gas with a Resonant Vibrating Sensor. *A. Kurokawa,* National Institute of Advanced Industrial Science and Technology (AIST), Japan, *H. Hojo, T. Kobayashi,* VPI Co., Japan

We would show that a quartz tuning-fork type resonator can measure the viscosity and the molar mass of the gas in which the resonator is vibrating. The vibrating resonator has two kind of outputs which are frequency change (Δf) and impedance change (ΔZ). The Δf and ΔZ are defined as the shift from their origin measured at high vacuum. We reported that the Δf and ΔZ given as a function of pressure are independent, and then the measurement of Δf and ΔZ will give the gaseous viscosity with no need to measure the gaseous pressure [1, 2]. In this report we will show that the molar mass of the measurement gas can be given by measurement of Δf , ΔZ and pressure.

In this experiment the temperature controlled measurements were essential because Δf and ΔZ are sensitive to the temperature variation. The measurement apparatus, such as the vibrating sensor, driving circuit for oscillation, mass flow controllers, gas accumulator and the pressure gauges, are in a temperature controlled chamber by $29 \pm 0.02^\circ\text{C}$. The impedance of the resonator was evaluated by the current passing through the sensor under constant driving AC voltage. The frequency of the resonator was 32kHz. The measured gas was Ne, Ar, N_2 , O_2 . The Δf and ΔZ were measured for the pressure between 120 kPa and vacuum. The absolute pressure was measured with a capacitance manometer.

The results showed that the $\Delta Z(P)$ and $\Delta f(P)$, give as a function of pressure, are larger for higher pressure. The $\Delta Z(P)$ and $\Delta f(P)$ for Ar, N_2 , O_2 gases do not have the intersection. However Ne gas, having smaller molar mass but larger viscosity, crossed the other curves. So we cannot distinguish the gas species simply by $\Delta Z(P)$ or $\Delta f(P)$ measurements. To discriminate the gas

species with their viscosity the ΔZ - Δf plot is useful. We found that the characteristic curves of ΔZ - Δf lied in the descending order of the viscosity, i.e., Ne, Ar, O₂, and N₂. These curves do not cross each other above 1 kPa.

We found the molar mass can be derived with the vibrating sensor. The product of molar mass and pressure can be evaluated without pressure measurement. The molar mass can be given with additional pressure measurement. The results showed that above 10kPa of the gas pressure the deviation of measured molar mass is less than a few percent.

[1] A. Kurokawa, H. Hojo, T. Kobayashi, AVS 57th Int. Sympo. Exhibi. (2010, Albuquerque).

[2] A. Kurokawa, H. Hojo, T. Kobayashi, Appl. Phys. Express 4 (2011) 037201.

VT-TuP3 Pumping Performance of Scroll Pump, F.C. Hsieh, P.H. Lin, J.C. Lu, F.Z. Chen, National Applied Research Laboratories, Taiwan, Republic of China

Scroll pumps are widely used in solar-optic and semiconductor industry for backing purpose. The performance of scroll pump could affect significantly the performance of pumping station. The performance of a scroll pump was predicted by using VacTran commercial software and the experiment were conducted to verify the prediction in this study. Specifically, the delivered pumping speed, conductance and delivered throughput of the pump were investigated. The experimental delivered pumping speed increased as the inlet pressure increased and reached to 291.05 L/min at 11.62 mbar. As the inlet pressure increased, the conductance increased to 4.58×10^3 L/min at 1.18×10^2 mbar. The analysis delivered throughput increased obvious from 3.77×10^2 mbar and reached its maximum value at 1.2×10^2 mbar. The standard deviation between analysis and experimental delivered pumping speed was less than 15% in the pressure ranges from 1.9×10^{-1} mbar to 45.3 mbar.

VT-TuP4 A System for Vacuum Gauge Calibration in the Pressure Range of 10^5 to 10^5 Pa, Y.W. Lin, C.P. Lin, C.N. Hsiao, National Applied Research Laboratories, Taiwan, Republic of China

A vacuum gauges calibration system for wide-range pressure was developed, and the measurement uncertainty associated with the system. The design of the system took into consideration of influencing factors that include uniformity of gas distribution and the geometric location of the gauge to be calibrated. The system operates following the procedure stipulated in the comparison vacuum gauge calibration method. The calibration may range from 10^5 to 10^{-5} Pa. The system makes use of capacitor vacuum gauge, SRG and hot cathode thermion vacuum gauge to estimate the degree of uncertainty associated with the system. The data collected from the gauge calibration tests indicated that if the background pressure of the system had reached 10^{-7} Pa, the uncertainty associated with the system were as follows: less than 4 % in the pressure range of 10^{-5} to 10^{-2} Pa, less than 2 % in the pressure range of 10^{-2} to 10^5 Pa. The present research has demonstrated the high stability of the vacuum calibration system, and its capabilities of conducting calibration for vacuum gauge with great efficacy.

VT-TuP5 Application of AutoResonant Ion Trap Mass Spectrometry (ART MS) to Vacuum Quality Measurement, P.D. Acomb, G.A. Brucker, J. Rathbone, B.J. Horvath, Brooks Automation, Inc., Granville-Phillips Products

Autoresonant Ion Trap Mass Spectrometers (ART MS) have demonstrated significant benefits when applied to vacuum quality measurement at ultra-high vacuum (UHV) levels. Vacuum quality monitors based on ART MS technology are known to deliver more accurate gas analysis at UHV levels than any other competitive mass spectrometry technology presently used for residual gas analysis. The speed, accuracy and remote-sensing capabilities of ART MS technology for vacuum quality measurement at UHV levels will be explained and several application examples will be presented. The low outgassing rates associated to ART MS sensors will be justified and explained in terms of surface area and power dissipation considerations. Gas analysis results, data-acquisition rates and detection limit values will be listed and compared against similar results obtained with legacy instrumentation including quadrupole-based residual gas analyzers. Instrument optimization strategies for UHV applications will be disclosed.

VT-TuP6 Combination of NEG and Sputter-Ion Pumps for Particle Accelerator Vacuum Systems, P. Chiggiato, J.M. Jimenez, S. Meunier, I. Wevers, CERN, Switzerland, A. Bonucci, A. Conte, P. Manini, SAES Getters

NEG and sputter-ion pumps are usually combined in particle accelerators to attain UHV pressure specifications. NEG pumps provide very high

pumping speed at a reasonable cost for most of the residual gases except CH₄ and rare gases, which amount to less than an hundredth of the total outgassing rate. Sputter-ion pumps remove all gases, though with a lower pumping speed. As a consequence, an optimized design should be based on NEG assisted by sputter-ion pumps for the gases that are not adsorbed chemically. Two examples of such configuration are here described. In the first, a commercial NEG lump pump is installed on a dedicated set-up together with sputter-ion pumps of different nominal pumping speeds. We show that the ultimate pressure achieved in the system does not depend on the applied sputter-ion pump nominal pumping speed in the range 30 to 400 ls⁻¹, and that values in the XHV range can be reached. In the second, we consider the vacuum system of the long straight section of the Large Hadron Collider (LHC) where most of the vacuum pipes were coated by magnetron sputtering with thin Ti-Zr-V films using Kr as discharge gas; the guidelines for the choice of the location and quantity of the sputter-ion pumps are reviewed in term of sectorization criteria and CH₄ and Kr outgassing rates.

VT-TuP7 Cryogenic Viscous Compressor Design and Development for the ITER Vacuum System, S.J. Meitner, L.R. Baylor, C.N. Barbier, S.K. Combs, R.C. Duckworth, T.D. Edgemon, M.P. Hechler, D.A. Rasmussen, Oak Ridge National Laboratory, R. Kersevan, M. Dremel, R.J.H. Pearce, ITER International Organization, France

A specialized cryopump known as a cryogenic viscous compressor (CVC) is being developed for the ITER vacuum system to pump the regenerated, hydrogenic, fusion reaction gases from the torus cryopumps and neutral beam cryopumps, to the tritium exhaust processing facility. Several of these pumps will operate in parallel and are staged to maintain continuous pumping during plasma operation. The CVC's regenerate at a higher pressure (500 mbar) than the torus and neutral beam cryopumps, which allows the regenerated gas to be pumped by a tritium compatible scroll pump train, with sufficient speed to maintain the regeneration duty cycle. The CVC's are cooled to operating temperatures by precooling the inlet gas with a 80K helium cooled chevron heat exchanger, followed by a tube bank heat exchanger cooled with supercritical helium at 4.5K. Hydrogenic gas is frozen on the inner tube bank walls while helium impurity gas, a byproduct of the fusion reactions, passes through the CVC and is pumped by conventional vacuum pumps.

A conceptual design of the CVC has been developed and a representative prototype has been designed, fabricated, and is undergoing testing to verify the concept of a full scale CVC before detailed design is completed. While cooling is provided by either cold helium gas or supercritical helium, hydrogen with trace amounts of helium gas is introduced into the central column of the cryopump at 100 Pa and 80 K at flow rates of 8 mg/s. Heat transfer between the laminar flowing gas and the cold pump tube is being enhanced with the use of internal petal fins. Temperature and pressure measurements are made along the pump gas stream in order to benchmark with design heat transfer characteristics. Comparison with a fluid dynamics code is under way. Modeling of the gas flowing into the pump and through the precooler heat exchanger and freezing zones is accomplished with the CFX computational fluid dynamics code [1]. The flows into the pump are at low pressure (~1mbar) and are in a laminar, low Reynolds number regime, ($Re < 300$) that is handled well with the CFX code. As the gas begins to desublimates in the cold zone of the pump, it reaches a rarified gas regime where the CFX model for flow and heat transfer breaks down. The modeling results are being compared with the prototype testing and will be used to further optimize and ensure reliable operation of the full CVC in the ITER application.

[1] ANSYS CFX, ANSYS, Inc., Canonsburg, PA 15317, USA

* This work was supported by the Oak Ridge National Laboratory managed by UT-Battelle, LLC for the U.S. Department of Energy under Contract No. DE-AC05-00OR22725.

VT-TuP9 Development of Niobium Thin Films Tailored for SRF Applications, J.S. Spradlin, A.-M. Valente-Feliciano, Jefferson Lab

Over the years, Nb/Cu technology, despite its shortcomings due to the commonly used magnetron sputtering, has positioned itself as an alternative route for the future of superconducting structures used in accelerators. Recently, significant progress has been made in the development of energetic vacuum deposition techniques, showing promise for the production of thin films tailored for SRF applications. JLab is pursuing energetic condensation deposition via techniques such as Electron Cyclotron Resonance and High Power Impulse Magnetron Sputtering (HiPIMS). As part of this project, the influence of the deposition energy on the material and RF properties of the Nb thin film is investigated with the characterization of their surface, structure, superconducting properties and RF response. It has been shown that the film RRR can be tuned from single digits to values greater than 400. This paper presents results on surface impedance measurements correlated with surface and material

characterization for Nb films produced on various substrates, monocrystalline and polycrystalline as well as amorphous.

VT-TuP10 Bulk-like Nb Films might be Possible with Coaxial Energetic Deposition for Superconducting RF Cavities, *T. Tajima*, High Energy Accelerator Research Organization (KEK), Japan and LANL, *N.F. Haberkorn*, *L. Civale*, Los Alamos National Laboratory, *E. Valderrama*, *M. Krishnan*, Alameda Applied Sciences Corporation

B_{pen} , the magnetic field at which magnetic vortices start to penetrate into Nb films prepared by coaxial energetic deposition (CED) technique was measured with a SQUID magnetometer. Unlike the films prepared by conventional sputtering technique that showed $B_{pen} \sim 94$ mT at 2.5 K, the CED films showed B_{pen} of 180-190 mT at 2.5 K, a value that is very close to the number for bulk Nb used for SRF cavities. This corresponds to an accelerating gradient (E_{acc}) of approximately 45-48 MV/m for the SRF cavities with $B_{peak}/E_{acc} \sim 4$ mT/(MV/m) such as those for the European XFEL or the ILC projects. These samples were coated on MgO, Sapphire and Borosilicate with RRR ranging between 21(Borosilicate) and 540 (MgO). The next step will be to coat on copper. If it is possible to fabricate Nb coated copper cavities that have similar performance to bulk Nb high-gradient cavities, this will lead to a significant cost saving since the cost of copper is about 2 orders of magnitude less than Nb. It will also have other benefits such as better thermal stability due to high thermal conductivity of copper and less susceptibility to ambient magnetic field than bulk Nb cavities as has already been shown by LEP Nb/Cu cavities at CERN.

Wednesday Morning, November 2, 2011

Applied Surface Science Division

Room: 102 - Session AS+BI+NS-WeM

Advances in Scanning Probe Microscopy

Moderator: S.A. Allen, The University of Nottingham, UK

8:00am AS+BI+NS-WeM1 High-Speed Atomic Force Microscopy for Filming Biomolecular Processes, T. Ando, Kanazawa University, Japan

INVITED

Vital phenomena are engendered through the dynamic activity of biological molecules. Therefore, observing the dynamic behavior of biological molecules in action at high spatiotemporal resolution is essential for elucidating the mechanism underlying the biological phenomena. The dynamic biomolecular processes are now widely studied using single-molecule fluorescence microscopy. However, the fluorescently labeled biological molecules themselves are invisible in the observations even using super-resolution fluorescence microscopy. The structure of biological molecules has been studied using x-ray crystallography, NMR, electron microscopy, and atomic force microscopy (AFM) but the obtained structures are essentially static. Thus, the simultaneous assessment of structure and dynamics is infeasible. To overcome this long-standing problem and make it possible to simultaneously record the structure and dynamics of biological molecules, we have been developing high-speed AFM for more than 15 years and at last it is now coming of age. Various AFM devices and control techniques were optimized or invented for high-speed scanning and low-invasive imaging. As a result, the imaging rate now reaches 10-30 frames/s for the scan range $250 \times 250 \text{ nm}^2$, 100 scan lines, and the spatial frequency of a sample surface corrugation 0.1/nm [Prog. Surf. Sci. **83**, 337-437 (2008)]. Remarkably, even delicate protein-protein interactions are not disturbed by the tip-sample contact. With this capacity of high-speed AFM, some biological processes are successfully captured on video, such as walking myosin V molecules along actin filaments [Nature **468**, 72-76 (2010)], photo-activated structural changes in bacteriorhodopsin [Nat. Nanotechnol. **5**, 208-212 (2010)], and cooperative GroEL-GroES interactions. The high-resolution movies not only provide corroborative 'visual evidence' for previously speculated or demonstrated molecular behaviors but also reveal more detailed behaviors of the molecules, leading to a comprehensive understanding of how they operate. Thus, the high-speed AFM imaging of functioning biological molecules has the potential to transform the fields of structural biology and single-molecule biology.

8:40am AS+BI+NS-WeM3 Integrated Imaging: Probing Molecular Interactions by Correlated Atomic Force Microscopy Approaches, C. Yip, University of Toronto, Canada

INVITED

The development of powerful single molecule functional imaging tools has been critical to our understanding of molecular dynamics and structure-function relationships in (bio)molecular systems. Our lab's focus on the design, implementation, and application of coupled imaging and spectroscopy is providing intriguing insights into the mechanisms of membrane disruption, receptor oligomerization, and protein-membrane interactions. We have devised several correlative approaches based on the integration of in situ atomic force microscopy with fluorescence and vibrational spectroscopies for extracting the orientation, conformation, and association dynamics of membrane-associated proteins in model membranes and in live cells. Some of the key challenges and opportunities afforded these new tools will be discussed.

9:20am AS+BI+NS-WeM5 Visible Light Emission from Fluorescent Proteins on Silver Substrate Induced by Tunneling Electrons, T. Yamada, RIKEN, Japan, T. Iwaya, S. Matsunaga, M. Kawai, The University of Tokyo, Japan

We detected the characteristic visible light emission from fluorescent protein molecules deposited on metallic silver (Ag) upon injection of tunneling electrons generated by a standard scanning tunneling microscope (STM) in ambient condition. A series of fluorescent proteins originating from jellyfish or coral, nowadays engineered to generate various colors of fluorescence by gene technology, is characterized with a β -barrel structure insulating the chromophore electronically from the surrounding. We purchased green, yellow, red and infrared fluorescent proteins (GFP, YFP, RFP, HcRed, molecular diameter $\approx 5 \text{ nm}$), deposited on a bare Ag surface, and used a Ag tip set on a STM setup to obtain images and to generate fluorescence. Light from the gap was collected by an optical fiber and introduced to a grating spectrometer with a liquid N₂-cooled CCD detector. On bare Ag surfaces, visible light was detected with the STM bias voltage within $\pm 1.8 \text{ V}$ in a modestly moisturized N₂ atmosphere. The spectra were

unstable in general, indicating light emission upon excitation of local plasmon [1], which depends on the changeable geometry of Ag tip. The wavelength onset of emitted light was equivalent to the STM bias voltage within $\pm 3.0 \text{ V}$, obeying the law of quantum energy conservation. The fluorescent proteins were dissolved in pure water, drop-cast on the Ag substrate and air-dried to form multilayers. STM images mostly showed flat terraces with steps composed of the protein molecules. Within a $200 \text{ nm} \times 200 \text{ nm}$ scanning area, the light emission spectra apparently involved the characteristic fluorescence peaks of proteins (GFP = 540 nm (2.30 eV), YFP = 550 nm (2.25 eV), RFP = 650 nm (1.91 eV), HcRed = 660 nm (1.88 eV)) over a background of weakened Ag plasmon spectrum. The same experiment with Au tips and Au(111) substrates was with almost no detection for the characteristic fluorescence of all the proteins. For clean Au(111), although visible light was detected, the above-mentioned plasmon energy conservation stood for the bias voltage only within $\pm 1.9 \text{ V}$. The maximum energy of local plasmon on Au(111) is too small to excite the fluorescent proteins electronically. The characteristic fluorescence from proteins is considered aided by the plasmon excitation of the Ag substrate. The protein β -barrel structure reserves the lifetime of excited state towards light emission, insulating electronically from the metallic substrate against the radiationless de-excitation process of the present surface-adsorbate system.

References:

[1] F. Rossel, M. Pivetta, W.-D. Schneider, *Surf. Sci. Rep.* **65**, 129 (2010).

9:40am AS+BI+NS-WeM6 Characterization of Peptide Nanotubes by Atomic Force Microscopy, J.L. Remmert, M.C. Vasudev, Air Force Research Laboratory, L. Eliad, E. Gazit, Tel Aviv University, Israel, T.J. Bunning, R.R. Naik, A.A. Voevodin, Air Force Research Laboratory

This work investigates the properties of aromatic dipeptides, which are of interest due to their ability to self-assemble into nanotubes and nanowires. Peptide nanotubes have been used to template inorganic materials¹ and construct nanochannels in microfluidic devices². The mechanical, thermal, and electronic transport properties of these nano-structures are desired to evaluate their potential use for biomolecular electronics³ and other applications. Atomic Force Microscopy (AFM) offers multiple modes to interrogate the response of discrete nanotubes. For instance, AFM with dry sample heating has established the thermal stability of peptide nanotubes up to $100 \text{ }^\circ\text{C}$ ⁴ with a spring constant of 160 N/m at room temperature⁵. A separate study targeting a single nanowire bridging two electrodes revealed semiconductor characteristics under repeated bias cycling⁶. We have similarly sampled detached nanotubes among peptide bundles and vertically aligned 3D arrays. Peptide nanotubes were synthesized by either Plasma Enhanced Chemical Vapor Deposition (PECVD) or solvent phase growth in 1, 1, 1, 3, 3, 3 Hexafluoroisopropanol (HFP), using approaches similar to that described by Reches et al¹. The nanotubes were observed by SEM to vary between 85-100 nm in diameter and up to 50 μm in length. Sample density was controlled by suspension and dilution in various solvents, including HFP and water, prior to deposition on a variety of substrates. AFM studies have revealed details of the tubular outer shell with tapping and electrostatic force modes (EFM), while also probing the mechanical integrity and thermal response to localized tip-side heating.

¹M. Reches, E. Gazit, "Casting Metal Nanowires within Discrete Self-Assembled Peptide Nanotubes", *Science* **300** 625 (2003)

²N. Sopher, Z. Abrams, M. Reches, E. Gazit, Y. Hanein, "Integrating peptide nanotubes in micro-fabrication processes", *J Micromech Microeng* **17** 2360 (2007)

³V. Dinca, E. Kasotakis, J. Catherine, A. Mourka, A. Ranella, A. Ovsianikov, B. Chichkov, M. Farsari, A. Mitraki, C. Fotakis, "Directed Three-Dimensional Patterning of Self-Assembled Peptide Fibrils", *Nano Lett* **8** 538 (2008)

⁴V. Sedman, L. Adler-Abramovich, S. Allen, E. Gazit, S. Tendler, "Direct Observation of the Release of Phenylalanine from Diphenylalanine Nanotubes", *J Am Chem Soc* **128** 6903 (2006)

⁵N. Kol, L. Adler-Abramovich, D. Barlam, R. Shneck, E. Gazit, I. Rouso, "Self-Assembled Peptide Nanotubes Are Uniquely Rigid Bioinspired Supramolecular Structures", *Nano Lett* **5** 1343 (2005)

⁶J. Lee, I. Yoon, J. Kim, H. Ihee, B. Kim, C. Park, "Self-Assembly of Semiconducting Photoluminescent Peptide Nanowires in the Vapor Phase", *Angew Chem Int Edit* **50** 1164 (2011)

10:40am **AS+BI+NS-WeM9 Determination of Molecular Polarization at Protein-Electrode Interfaces with Combined Optical, Transport, and Dielectric Scanning Probe Microscopy.** *X. Chen, K. Kathan-Galipeau, B.M. Discher, D.A. Bonnell*, University of Pennsylvania

Bio-molecule integrated electronic devices are of great interest recently. For such systems to be designed and fabricated, the optoelectronic properties of protein molecules in ambient environment must be understood at a fundamental level. Here we demonstrate a new scanning probe based technique: torsional resonance nanoimpedance microscopy (TR-NIM), which simultaneously probes transport and dielectric properties in conjunction with optical excitation. To make a controlled interface, we start by designing a peptide molecule with ability to control protein/electrode interface interactions, as well as incorporation of several different optically active cofactors, and we successfully patterned peptides on HOPG substrates. Using TR-NIM electronic transport and the effect of optical absorption on dielectric polarizability in oriented peptide single or multiple molecular layers is determined. This approach enables quantitative comparisons of the change in polarization volume between the ground state and excited state in both single and multiple molecular layers.

11:00am **AS+BI+NS-WeM10 Scanning Local Capacitance Measurements with High Spatial and Dielectric Resolution.** *M.J. Brukman, S. Nanayakkara, D.A. Bonnell*, University of Pennsylvania

Spatial variation of dielectric properties often dictates the behavior of devices ranging

from field effect transistors to memory devices to organic electronics, yet dielectric

properties are rarely characterized locally. We present methods of analyzing 2nd

harmonic-based local capacitance measurements achieved through non-contact atomic

force microscopy. Unlike contact-based methods, this technique preserves tip

shape and allows the same probe to realize high-resolution topographic imaging and

scanning surface potential imaging. We present an improved analysis of the electrical

fields between tip and sample, yielding high sensitivity to the capacitance-induced

frequency shift.

The techniques are applied to thin-film strontium titanate and mixed-phase self-

assembled monolayers to illustrate application to high dielectric constant hard materials

and lower dielectric constant organic films. Conversion from frequency shift signal to

dielectric constant κ is demonstrated on both samples, with sub-5 nm spatial resolution

and dielectric constant resolution between 0.25 and 1.

11:20am **AS+BI+NS-WeM11 Parallel Momentum Conservation of Hot Electrons across a Metal Semiconductor Interface.** *J.J. Garramone, J. Abel, R. Balsano, V.P. LaBella*, College of Nanoscale Science and Engineering, the University at Albany-SUNY

Parallel momentum of electrons is a conserved quantity as the electron traverses a barrier between two materials which lead to refraction like effects in the electrons trajectories. Ballistic electron emission microscopy (BEEM) is a scanning tunneling microscopy (STM) based technique that injects hot electrons ($E > EF$) into a metal-semiconductor Schottky diode[1]. A small fraction of these electrons will traverse the metal with little to no scattering and make it into the semiconductor and counted as BEEM current. This makes it an ideal technique to study parallel momentum conservation. However, direct observation of this effect has been rather elusive. To observe this effect the dependence of the attenuation length with hot electron energy of Ag on both the Si(001) and Si(111) substrates has been measured.

Samples consisted of nanometer thick Ag films that were deposited on HF cleaned Si(001) and Si(111) wafers and capped with 10 nm Au to prevent oxidation of the films. Attenuation lengths were extracted by measuring the BEEM current as a function of the metal overlayer thickness. The dependence of the attenuation length with tip bias (electron energy) displayed a sharp increase as the energy approached the Schottky barrier height for the Si(001) substrates and a slight decrease for the Si(111)

substrates. This contrast is a direct result of parallel momentum conservation and the lack of zero parallel momentum states at the Si(111) interface when compared to the Si(001) interface. Additional insight into the relative contribution of both elastic and inelastic scattering can be obtained by fitting the data to a Fermi liquid based model.

[1] L. D. Bell, et al., Phys. Rev. Lett. **61** 2368 (1988).

11:40am **AS+BI+NS-WeM12 High Resolution Scanning Probe Imaging of 2D-Supramolecular Networks on Au(111), Graphite and Molybdenite.** *V.V. Korolkov, S. Allen, C.J. Roberts, S.J.B. Tendler*, The University of Nottingham, UK

Chemical decoration of surfaces with various molecules and supramolecular structures has been a major strategy for introducing new properties to both organic and inorganic materials. Amongst these properties are wettability, biocompatibility, sensing properties, catalytic activity, optical properties and adhesion. Most of methods for surface modification include molecules binding to the surface via stable chemical bond. Recently methods have been developed to modify atomically flat surfaces with periodical porous molecular structures, termed 2D-supramolecular networks. The networks are commonly composed of two types of molecules serving different functions e.g. joints and ribbons. Such 2D-structures bring forward a unique surface property - a spatially controlled adsorption with almost single molecule precision.

Most networks reported in the literature have been studied using UHV STM on metal substrates and, to a lesser extent, on HOPG and non-conductive substrates. Here we present a study, utilizing both ambient STM and AFM, of 3,4,9,10-perylene-tetracarboxylic diimide (PTCDI) - melamine networks deposited on Au(111), HOPG and MoS₂ substrates. AFM imaging was performed using PeakForce Tapping AFM (Bruker Inc.) and Torsion Resonance (TR)-AFM. Both STM and AFM were able to resolve a clear periodical network structure for all substrates after exposure to a solution of PTCDI and melamine molecules in dimethylformamide at 373K. AFM images show that the network forms a monolayer on both HOPG and molybdenite substrates, and also that most of the HOPG surface is covered with network structure, with some minor defects. In contrast the Au(111) surface was mostly covered with network multilayers as suggested both by TR-AFM and STM. AFM also revealed that the network structure on HOPG and molybdenite remains intact for several hours in the ambient and can be stored in N₂-ambient for up to ~24h.

Biomaterial Interfaces Division

Room: 108 - Session BI-WeM

Cells at Interfaces

Moderator: M.R. Alexander, University of Nottingham, UK

8:00am **BI-WeM1 Real Time Analysis of Polymer Film Integrity Upon Exposure to Bacteria and Aqueous Medium.** *D.E. Barlow, J.C. Biffinger*, Naval Research Laboratory, *E.R. Petersen*, Nova Research, Inc., *J.N. Russell, P.E. Pehrsson*, Naval Research Laboratory, *W.J. Goodson*, Air Force Research Laboratory

Polymer coatings are of great importance for protecting and imparting specific properties at the surfaces of man-made structures, but can be affected in many ways by the natural environments they must withstand. We have studied the effects of aqueous medium exposure and biofilm formation on antistatic polyurethane coatings in real time using in situ ATR-FTIR. The results show that the coatings are susceptible to water permeation and swelling, and deuterium exchange was also shown to occur within the films upon D₂O exposure. When exposed to *Pseudomonas fluorescens* in M9 minimal medium, the coating interface became compromised as the pyruvate carbon source was depleted. Reasons for these changes will be discussed, including the role of water permeation and the potential for the bacteria to use the coating as a carbon source. While ATR-FTIR has been used in the past to study biofilm growth, these results also demonstrate the effectiveness of the method for assessing substrate impact, an often overlooked factor.

8:20am **BI-WeM2 Early Stages of Bacterial Biofilm Formation – A Numerical Study of Bioadhesion on Biomaterials.** *D. Siegmund, A. Schroeter, S. Schuster, M. Rettenmayr*, Friedrich Schiller University Jena, Germany

Biomaterials for implant purposes are increasingly applied in modern medicine e.g. to recover human body functions or for tissue substitution in general. Infections of these implants, called Biomaterial-centered infections

(BCI), are among the fundamental challenges in biomaterials science. They are primarily initiated by adhesion of bacteria on the biomaterial's surface. The subsequent formation of a bacterial biofilm requires a total implant replacement in the majority of cases.

The adhesion of bacteria is thus the first crucial step for biofilm formation that is only incompletely understood. Interactions of bacteria with the surface are controlled by surface properties such as surface energy, surface chemistry and topography.

In the present work, a model for bacterial adhesion is introduced that describes the early stages of biofilm formation as a function of the surface properties. A two-dimensional Cellular Automaton (CA) / Finite Difference (FD) adsorption model is combined with the predictions of the extended DLVO (Derjaguin, Landau, Verwey, Overbeek) theory that accounts for the interaction energies between the bacteria and the material's surface. The model describes the mass transport of bacteria in an aqueous solution towards the material's surface and the adsorption and desorption process, depending on the surface properties.

The adhesion process of different human pathogenic bacteria (*Enterococcus faecalis*, *Staphylococcus aureus*, *Escherichia coli*) on different biomaterial surfaces (titanium, stainless steel, polyethylene, polymethylmethacrylate, polytetrafluoroethylene) has been simulated. Results are the surface coverage with bacteria and, where applicable, clustering of the bacteria due to their migration on the surface.

Excellent agreement with experimental findings from the literature and own adhesion experiments concerning the kinetics of the adsorption process is found. In addition, a realistic bond strengthening mechanism of bacteria on surfaces, as described in the literature, is reproduced by the model. By using a spatial pattern analysis of our own experimental data we show that physical processes occurring during initial stages of the adhesion process are essentially correctly incorporated in the model.

8:40am BI-WeM3 A Library of Polymer Gradients for Understanding Bacteria-Material Interactions, A.L. Hook, J. Yang, C.-Y. Chang, University of Nottingham, UK, **D.G. Anderson, R. Langer,** Massachusetts Institute of Technology, **S. Atkinson, P. Williams, M.C. Davies, M.R. Alexander,** University of Nottingham, UK

Biofilm formation leads to a 1000 times increase in antibiotic tolerance compared with planktonic bacteria and is associated with 80% of hospital acquired infections, resulting in \$3.0 billion in excess health-care costs each year in the U.S alone. Thus, new materials for biomedical devices that prevent biofilm formation would offer enormous benefits to the health industry and improve patient welfare. However, our current understanding of bacteria-material interactions limits scope for rational design of such materials. Polymer microarrays are emerging as a key enabling technology for the discovery of new biomaterials.¹ A method for forming polymer microarrays has been developed using contact printing to deposit nanolitre volumes of premixed acrylate monomer and initiator to defined locations on a poly(HEMA) coated glass slide with UV photo-initiation.² This platform enables a large combinatorial space to be rapidly screened by a biological assay to identify new materials that fulfil a given performance criterion.³ A library of polymer gradients that enables the systematic investigation of biology-material interactions can be created by producing polymers from monomers mixed at hundreds of different concentrations. Utilising a high throughput surface characterisation approach the surface chemical and physical properties of each material can be characterised and related to the biological performance.⁴ We have developed a high throughput bacterial attachment assay based on three pathogens (*Pseudomonas aeruginosa*, *Staphylococcus aureus* and *Escherichia coli*) expressing green fluorescent protein, which is compatible with the polymer microarray format. This study provides novel insights into the bacteria-material interactions, highlighting chemical moieties that both support and resist bacterial attachment. Specifically, superior efficiency to prevent bacterial attachment has been demonstrated for hydrophobic moieties on a polyacrylate backbone that contains weakly polar ester groups, which represent an amphiphilic chemical nature.

¹ Hook, A. L. et al., High throughput methods applied in biomaterial development and discovery. *Biomaterials* **31** (2), 187 (2010).

² Anderson, D. G., Levenberg, S., and Langer, R., Nanoliter-scale synthesis of arrayed biomaterials and application to human embryonic stem cells. *Nature Biotechnology* **22** (7), 863 (2004).

³ Mei, Y. et al., Combinatorial development of biomaterials for clonal growth of human pluripotent stem cells. *Nature Materials* **9** (9), 768 (2010).

⁴ Urquhart, A. J. et al., High throughput surface characterisation of a combinatorial material library. *Advanced Materials* **19** (18), 2486 (2007).

9:00am BI-WeM4 Developing Tools to Observe Microbial Metabolic Exchange in 2D and 3D, J. Watrous, University of California, San Diego, **T. Alexandrov,** University of Bremen, Germany, **W.-T. Liu, A. Lamsa, D. Gonzalez, N. Bandeira, M. Hamby, R. Kersten, K. Pogliano, B. Moore, P.C. Dorrestein,** University of California, San Diego **INVITED**

From the early days of bacterial culturing over a century ago, microbiologists have known that microorganisms respond to their surroundings. Unicellular organisms rely on natural product mediated metabolic exchange to adapt to environmental stresses, sense colony density, and form biofilms. However, studies of the chemistry and phenotypes that correspond to signaling behavior have largely been disconnected and measured indirectly. To connect the chemistry and phenotypes, imaging mass spectrometry (IMS) methodologies are developed to observe metabolic exchange mediated within pair-wise interactions and microbial communities in two- and three dimensions. IMS provides the ability to correlate the presence of metabolites to phenotypic changes and to detect new biological phenotypes. Many of such phenotypes cannot be observed by the naked eye.

9:40am BI-WeM6 Analysis of Cancer Cell Lines with ToF-SIMS and PCA, M. Robinson, University of Washington, **F. Morrish, D. Hockenberry,** Fred Hutchinson Cancer Research Center, **L.J. Gamble,** University of Washington

Time-of-flight secondary ion mass spectrometry (ToF-SIMS) has been increasingly utilized for examining biological samples including biomaterials, cells, and tissues. The primary advantage of this MS technique is that it produces a chemical map of a sample, which includes hundreds of peaks that are detected in parallel. The advent of cluster ion sources has allowed the detection of many high mass lipid species that can be used to characterize biological surfaces [1]. In conjunction with principal component analysis (PCA), we use ToF-SIMS to determine differences in the chemical makeup of the outer membrane of two different cancer cell lines: MDA-231 and MCF-7 cells. There is similar work currently being done that uses Ultra Performance Liquid Chromatography-MS and gene sequencing to start characterizing lipid membrane metabolism in breast cancer tumor tissue [2]. The separation of the two cell lines across PC1 can be clearly seen in Figure 1. The entirety of the loads for PC1 can be seen in Figure 2, with cholesterol strongly loading towards the MDA-231 cells and many diacylglycerol (DAG) species loading towards the MCF-7 cells. Key differences were found in the levels of certain lipid constituents of the cell membrane, which may play a role in the ability of one cell type to be more drug resistant than the other. There are a variety of lipid components that have similar trends which are not discussed in this abstract but may play an important role in understanding this system.

This work is the foundation for future studies using human tumor biopsy samples that will help elucidate the link between fatty acid composition within a tumor and the potential drug resistance of that tumor.

10:40am BI-WeM9 Engineering Stem Cell Differentiation via Material Properties, T. McDevitt, Georgia Institute of Technology **INVITED**

Stem cell differentiation is sensitive to a variety of global and local environmental cues that impact cell fate decisions. Pluripotent stem cells (i.e. ESCs & iPSCs) are capable of recapitulating many aspects of early development and can serve as a robust cell source for the development of cell-based diagnostics and regenerative medicine therapies. ESCs are commonly differentiated as three-dimensional multi-cellular aggregates referred to as "embryoid bodies" (EBs), because of their ability to mimic the early morphogenic transformation of pluripotent cells into derivatives of the three germ lineages (ecto-, endo-, and mesoderm). In order to better understand and ultimately control ESC morphogenesis, we have focused on systematically engineering biochemical and biophysical parameters of the 3D EB microenvironment via the integration of different biomaterials and examining the emergent results on stem cell differentiation. Microparticles (MPs) of varying size (1-20 μm) and chemistries (i.e. PLGA, agarose, gelatin) were incorporated within 3D stem cell aggregates in a dose-dependent manner (~1 particle / 10 cells) without adversely affecting cell viability. Interestingly, the mere presence of relatively small numbers of different types of materials alone could modulate stem cell phenotype as evidenced by gene expression profiling and immunophenotype analyses. Delivery of morphogenic factors, such as retinoic acid (RA), bone morphogenic protein 4 (BMP4) or vascular endothelial growth factor (VEGF), to ESCs from incorporated MPs significantly impacted the differentiation of the cells to different lineages and was more efficient than comparable soluble treatment methods. Altogether these results suggest that engineered biomaterials can direct the differentiation of stem cells through modulation of biochemical and/or biophysical properties of the 3D microenvironment. It is expected that the development of inherently scalable techniques to direct pluripotent stem cell differentiation will benefit

the biomufacturing of stem cell derivatives for regenerative cellular therapies and *in vitro* cell based diagnostic technologies, as well as enable engineering of tissues directly from stem cells.

11:20am **BI-WeM11 Adhesion and Rolling of Leukemic Cells on Immobilized Hyalurons**, *A. Rosenhahn*, Karlsruhe Institute of Technology, Germany, *C. Christophis, I. Taubert, G.R. Meseck, A.D. Ho, M. Grunze*, University of Heidelberg, Germany

Adhesion and rolling on vessel walls are two processes which are relevant for the homing of hematopoietic cells. Especially in the case of acute leukemia, one key in successful therapy is the homing of the hematopoietic stem cells (HSC) to the bone marrow after transplantation. We investigated the interaction of HSC with the hyaluron binding motive and quantitatively studied the interaction of different leukemic cells with synthetic polysaccharide surfaces. For the experiments we applied a microfluidic shear force assay recently developed in our group [1]. Leukemic Jurkat and Kasumi-1 cells lacking CD44-expression showed no adhesion or rolling on the polysaccharides whereas CD44 expressing leukemic cells KG-1a, HL-60, and K-562 attached and rolled on hyaluronan. We find that at weak flow cells have a poor tendency to adhere and only if shear forces above a threshold are present, adhesion is mediated. While this effect is well known for leukocytes on hyaluronan expressing feeder layers, it is the first demonstration that the mechanism also occurs in leukemic progenitor cells towards synthetic hyaluronan coated surfaces. We also extended the study to hematopoietic progenitor cells and saw for the first time that also HPCs with high degree of stemness show a flow induced interaction with hyalurons.

[1] C. Christophis, M. Grunze, A. Rosenhahn, Phys. Chem. Chem. Phys. (2010) 12, 4498

Electronic Materials and Processing Division

Room: 210 - Session EM-WeM

Low-k Materials and Devices

Moderator: B. French, Intel Corporation

8:20am **EM-WeM2 Feature-Scale Modeling of Diffusion Barrier and Metal Seed Physical Vapor Deposition Processes**, *R.A. Arakoni, J.-P. Trelles, D. Kim, M. Khabibullin, S. Nikonov, D. Zierath*, Intel Corporation

The continuous reduction of critical dimensions and the increasing complexity of interconnect structures has stressed the process requirements of metallization steps (i.e., deposition of diffusion barrier and metal seed, electroplating, chemical-mechanical polishing). Particularly, physical vapor deposition (PVD) of the barrier and seed relies on a limited number of process parameters (e.g., target and bias power, reactor pressure) to satisfy increasingly tighter film requirements (e.g., coverage over high aspect ratio features, control of barrier thickness, proper aperture of the seed to prevent void formation during electroplating). Computational modeling has proven an efficient means to aid the design and development of PVD metallization steps by allowing pre-silicon analysis of the effects of feature geometry and process parameters (e.g., see [1]). A continuum-based process simulator, based on a level-set solver for multi-material topography evolution, is applied to the analysis of 2 successive metallization steps, namely the PVD of barrier-over-ILD and of seed-over-barrier. Primary (e.g., distributed along the domain boundary) as well as secondary (e.g., emitted and reflected from surfaces) fluxes are accounted for through a ray-tracing technique that ensures mass conservation. In contrast to Monte-Carlo methods, which allow the description of gas phase kinetics, our solver is based on the specification of finite-rate surface reactions, which provides smooth topography evolution and is suitable for the analysis of extended domains encompassing multiple features, as needed for the analysis of within-die pattern effects. Sputtering, attachment, and neutralization reactions are accounted for between all the neutral and ionic species and the entire set of surface and bulk species in the film to allow the description of inter-material interactions (e.g., re-deposition of sputtered barrier species over the seed). The simulator is used to analyze the effects of neutral and ionic flux distributions (e.g., athermal neutrals, directional ions dependent on bias power) and the sputtering yield characteristics (i.e., energy and angular dependence) on the obtained film. Figure 1 presents snapshots of simulation results of the two-step process over a dual damascene structure. The results show that the simulation of consecutive steps is essential for the realistic description of inter-process effects.

[1] P. J. Stout, D. Zhang, and P. L. G. Ventzke, J. Vac. Sci. Technol. A 21(3), May/June 2003

8:40am **EM-WeM3 Ultralow-k PECVD pSiCOH Dielectrics and their Implementation in VLSI Interconnects**, *A. Grill, S.M. Gates*, IBM Research, *E.T. Ryan*, GlobalFoundries, *S. Nguyen*, IBM Research **INVITED**
The performance of integrated circuits and their density has been improved continuously through the shrinking of the active devices according to Moore's law. At the 0.25 μm technology node it became clear that new materials had to be introduced to reduce the RC of the interconnect which became a barrier to further improvement of the VLSI performance.

After IBM introduced Cu in 1997, low-k PECVD SiCOH dielectrics with a dielectric constant $k=3.0$ were introduced in 2003-2004 at the 90 nm node, after many other low-k dielectrics failed integration. Reduction or even maintaining of the interconnect capacitance at the decreasing dimensions of later technology nodes required the development of porous ultralow-k pSiCOH. The first generation of pSiCOH dielectrics with $k=2.4$ has been successfully integrated by IBM in 45 nm products, such as the Power 7 chip released in 2010. Material extendibility of porogen based pSiCOH has been demonstrated to k values as low as 2.0. However, the reduction of the dielectric constant is achieved for a given chemistry by increasing porosity in the films, resulting in a decrease of mechanical properties, degraded integrability of the dielectric, and potentially reduced reliability of the interconnect.

The original chemistry produced the pSiCOH films having a skeleton of mainly O-Si-O bonds, with nanometer sized pores stabilized by Si-CH₃ groups (V1 type). These films are damaged by the integration processes and the degree of damage increases with decreasing k and decreasing pattern dimensions with each new technology node. To reduce these problems we developed pSiCOH films using precursors containing Si-CH₂-Si bonds, enabling the fabrication of high-carbon (V2 type) films whose skeleton comprises Si-CH₂-Si bonds in addition to the Si-O-Si. The high-carbon pSiCOH films have reduced degrees of porosity and improved pore structures as compared to the V1 type films of same k and, as a result, have higher resistance to processing damage and provide improved dimension control during integration compared to V1 pSiCOH of identical k values.

The talk will discuss the evolution of the low-k and ultralow-k dielectrics, the effects of the chemistries on the properties of the different types of the porous pSiCOH, and the behavior of such dielectrics during integration processing.

This work was performed by the Research Alliance Teams at various IBM Research and Development Facilities.

9:20am **EM-WeM5 Limitations in Dielectric Constant Scaling for low-k a-SiC(N):H Diffusion Barriers in Nanoelectronic Applications**, *S. King, D. Jacob*, Intel Corporation, *M. Liu, D.W. Gidley*, University of Michigan

As the semiconductor industry strives to keep pace with Moore's Law, new materials with extreme properties are increasingly being introduced and tighter control of these material properties is being demanded. Low dielectric constant (i.e. low-k) materials are one specific example. Lower k (< 6) a-SiC(N):H materials are desired to replace a-Si₃N₄:H ($k > 6.5$) as the Cu capping diffusion barrier layer in order to reduce resistance-capacitance (RC) delays in nano-electronic Cu interconnect structures. Typical methods for producing low-k a-SiC(N):H materials consist of introducing controlled levels of nano-porosity via carbon doping during plasma enhanced chemical vapor deposition (PECVD) of a-Si₃N₄:H matrix materials. While lowering k , the introduction of nano-porosity can seriously compromise the moisture and Cu diffusion barrier performance of these materials. In this presentation, we demonstrate that critical thresholds in nano-porosity exist for the diffusion of water through low-k materials. Specifically, we utilize Fourier Transform Infra-Red (FTIR) spectroscopy, to show that the concentration and size of nano-pores formed in low-k a-SiC(N):H dielectric materials is controlled by the concentration of terminal Si-CH₃ bonding versus Si-C/N network bonding. We further combine moisture diffusivity measurements with x-ray reflectivity (XRR) and positron annihilation lifetime spectroscopy (PALS) to demonstrate that low-k a-SiC(N):H dielectrics become poor moisture diffusion barriers at mass densities $< 2.0 \text{ g/cm}^3$ and when the pore size approaches that for the molecular diameter of water. The implications of these critical nano-porosity thresholds on continued dielectric constant scaling of low-k a-SiC(N):H diffusion barrier materials will be discussed as well as methods for overcoming these limitations.

9:40am **EM-WeM6 Fundamental Characterization of Amorphous Hydrogenated Boron Carbide Toward its use as a Low-k Dielectric Material**, *B.J. Nordell, S. Karki, C. Clayton, M.S. Driver, M.M. Paquette, A.N. Caruso*, University of Missouri-Kansas City

The development of stable and low-dielectric-constant (i.e., low-k) materials for interlayer dielectrics (ILDs) in ultra-large-scale integrated circuits has become an essential target for the semiconductor industry. Toward this end, several low-Z boron-based materials (e.g., boron nitrides

and boron carbonitrides) have been studied due to their exceptional thermal, mechanical, and chemical stability, which have exhibited k values as low as 1.9–2.4. Amorphous hydrogenated boron carbide, in turn, may be an even more promising low- k boron-based material on the basis of the lower polarity of B–C bonds relative to B–N bonds and the mesoscopically porous icosahedral cage structure of boron-rich carbides which can exhibit significantly lower free volume, particularly for the low-density amorphous hydrogenated variants. Moreover, amorphous hydrogenated boron carbide films grown by plasma-enhanced chemical vapor deposition (PECVD) methods from carborane precursors exhibit resistivity's $>1 \times [10]^{-10}$ ohm-cm. This talk will describe the causal relationship between the measured dielectric constant, resistivity, breakdown voltage, hardness, Young's Modulus, and mass/density as a function of the PECVD growth parameters (power, pressure, substrate temperature, and gas flow) and film composition (notably hydrogen and oxygen content) in the context of establishing and optimizing amorphous hydrogenated boron carbide as a next-generation durable and resilient low- k ILD.

10:40am **EM-WeM9 Robust PECVD Ultra-Low- k Dielectric ($\kappa \leq 2.55$) Development for sub-28nm Generations.** *D. Kioussis, E.T. Ryan, GLOBALFOUNDRIES, S.M. Gates, IBM T.J. Watson Res. Ctr., A. Madan, N. Klymko, C. Parks, S. Molis, IBM, R. Augur, GLOBALFOUNDRIES, H. Masuda, Toshiba America, D. Restaino, IBM, Z. Sun, GLOBALFOUNDRIES, S. Hosadurga, IBM, S. Cohen, IBM T.J. Watson Res. Ctr., K. Virwani, IBM Almaden Res. Ctr., A. Grill, IBM T.J. Watson Res. Ctr.* **INVITED**

In the demanding microelectronics industry there is a constant need to increase circuit density in multilevel Copper (Cu) back-end-of line (BEOL) interconnects to improve the operating speed and reduce power consumption. With successive node-on node scaling, one approach to meet the capacitance-resistance (RC) requirements for the BEOL is through the introduction of organo silicate glass (SiCOH) materials with low dielectric constants (κ -value) as interlevel dielectrics (ILD). At the 45 nm node, porosity was first introduced into the BEOL interconnect structures in the form of porous organo silicate glass films (p-SiCOH) with ultra low- κ (≤ 2.55) to further minimize the RC delay. These ULK materials incorporate a large number of methyl groups and pores into Si-O based network structures, although the initial precursors and final properties may vary. Both the SiCOH and pSiCOH ILD films are commonly deposited by plasma-enhanced chemical vapor deposition (PECVD). Since their introduction nanoporous ULK films have significantly increased the Cu BEOL fabrication complexity. For example, porous ULK films are mechanically weak and tend to crack as a result of elastic mismatch with the substrate. Meanwhile, pore collapse and carbon depletion occur when ULK is exposed to RF-plasma during etching or ashing. Subsequent moisture adsorption leads to the increase of effective κ -value in Cu interconnects degrading RC performance. Therefore, the integration challenges of ULK are significant, such as plasma damage, chip packaging interaction, and dielectric/metal barrier compatibility issues. Careful optimization of the ULK properties is crucial for successful process integration in the 28 nm BEOL node and beyond.

This presentation will report on the ability to tune the material properties of ULK films with $\kappa \leq 2.55$ through the use of new chemical precursors and simple processing optimization steps to meet the specific integration requirements. Three ULK material classes were evaluated, optimized, and characterized to compare electrical and mechanical properties, pore characteristics, FTIR, XPS, and thermal stability. The effect of UV Cure dose on the ULK film properties and correlation of the degree of plasma damage to the ULK chemical, physical, and structural properties will be discussed. We will show that balancing composition of the film to minimize damage for successful integration needs to be coupled with improving electrical and mechanical integrity for packaging compatibility.

11:20am **EM-WeM11 Molecular Strengthening Mechanisms for Low- k Dielectrics.** *R.H. Dauskardt, Stanford University* **INVITED**

Hybrid organic-inorganic glass films processed from small organosilane precursors exhibit unique electro-optical properties while maintaining excellent thermal stability. Processed using either sol-gel or plasma-enhanced chemical vapor deposition they have application in emerging CMOS, nanoscience and energy technologies. A fundamental challenge for their integration, however, remains their inherently mechanically fragile nature that derives from the oxide component of the hybrid network and the presence of terminal hydroxyl and organic groups that reduce network connectivity. Also, to achieve ultra-low dielectric properties (i.e. $k < 2.4$) nanoporous forms of the hybrid films are required which further reduce mechanical properties. We describe the development of computational methods to address the fundamental relationship between molecular structure and resulting mechanical and fracture properties of organosilicate glasses. Using molecular dynamics and a simulated annealing approach, large distortion-free hybrid glass networks with well-controlled network

connectivity can be generated. With this capability along with a novel fracture model and molecular dynamics simulations of elastic deformation, we elucidate the critical effect of network connectivity and nanoporosity on mechanical properties. The accuracy of our computational tools is confirmed through comparison to synthesized hybrid films where the molecular structure, connectivity and nanoporosity is carefully controlled. Having predictive models for how molecular structure affects mechanical properties offers the opportunity for computational design of new glasses and provides a quantitatively accurate rationale for guiding precursor selection. Thus in addition to the fundamental insights gained regarding structure-mechanical property relationships, we will present our efforts to apply these tools to design new neat and nanoporous glasses with exceptional mechanical properties and low density.

Energy Frontiers Focus Topic

Room: 103 - Session EN+EM+NS-WeM

Quantum Dot and Nanowire Solar Cells

Moderator: K. Leschkes, Applied Materials Inc.

8:00am **EN+EM+NS-WeM1 Hybrid Quantum-Dot/Organic Solar Cells Based on Silicon Nanocrystals.** *U. Kortshagen, C.Y. Liu, Z. Holman, J. Yang, University of Minnesota* **INVITED**

Organic solar cells based on bulk heterojunctions between acceptor and donor semiconductors have attracted significant attention due to their low cost, compatibility with roll-to-roll processing, and relative lack of health and environmental concerns. However, the stability of organic semiconductors under solar irradiation remains to be a challenge. Producing bulk heterojunction solar cells based entirely on inorganic materials thus has become an attractive proposition.

In a first step into this direction, we have produced solar cells from silicon nanocrystals (Si NCs) and poly-3-hexylthiophene (P3HT). Silicon NCs 3–5 nm in diameter were synthesized by dissociating silane gas in a nonthermal radio frequency plasma, and collected on a mesh downstream of the plasma. The silicon-hydride terminated NCs were dispersed with P3HT in 1,2-dichlorobenzene. Films of this blend with thicknesses of 100–200nm were spin-cast onto an indium tin oxide (ITO) substrate pre-coated with 50 nm of poly(3,4-ethylenedioxythiophene)/poly(styrenesulfonate) (PEDOT:PSS). Metal electrodes (2mm wide, 100 nm thick) were then evaporated on top of the Si NC/P3HT film.

The Si NCs were found to be efficient electron acceptors. The optimal weight ratio of Si NC to P3HT was 50 wt%. The effects of annealing and different metal electrodes on Si NC/P3HT hybrid solar cells were studied. After annealing at 150 °C, Si NC/P3HT solar cells exhibited power conversion efficiencies as high as 1.47%. The hole mobility in the P3HT phase extracted from space-charge-limited current measurements of hole-only devices increased from 2.5×10^{-10} cm²/V-s to 1.1×10^{-9} cm²/V-s after annealing, resulting in better transport in the solar cells. A quenching of the open-circuit voltage and short-circuit current was observed when high work function metals are deposited as the cathode on Si NC/P3HT hybrid devices.

Devices with silicon-hydride terminated Si NCs were plagued by poor film morphology. Hence we studied functionalized Si NCs with organic ligands. Functionalization with 1-octene and 1-dodecene led to improved film morphology but the transport in the Si NC network became worse. However, excellent stability with respect to air exposure of these cells was observed. Efforts to improve the dispersability of Si NCs without inhibiting transport in the Si NC network are in progress.

This work was supported primarily by the MRSEC Program of the National Science Foundation under Award Number DMR-0819885 and by the DOE Energy Frontier Research Center for Advanced Solar Photophysics.

8:40am **EN+EM+NS-WeM3 Precision Engineering of Semiconductor Nanowires for Advanced Photovoltaic Devices.** *N. Shin, I.R. Musin, S. Sivaram, M.A. Filler, Georgia Institute of Technology* **INVITED**

Semiconductor nanowires offer exciting opportunities to engineer light absorption and carrier transport for ultrahigh efficiency photovoltaic devices. The precise control of crystal structure and geometry is required to achieve a desired behavior, especially in highly confined nanoscale systems. In the ideal situation, the combination of nanowire diameter, lattice structure (e.g. diamond cubic, wurtzite), crystal orientation (e.g. $\langle 111 \rangle$ vs. $\langle 110 \rangle$), and sidewall faceting that yields the most robust device performance would be known and could be rationally synthesized. Unfortunately, an inadequate understanding of nanowire chemistry-structure and structure-property relationships prevents the accomplishment of this task with bottom-up syntheses at the present time. This presentation

will provide an overview of our recent efforts to bridge this knowledge gap. In our research, *in-situ* infrared spectroscopy is combined with an ultrahigh vacuum growth environment to fundamentally correlate nanowire chemistry with photophysics, while circumventing the sample degradation that can obscure the intrinsic properties of nanoscale structures. Group IV nanowires and their heterostructures are a model system and are fabricated with the vapor-liquid-solid (VLS) growth technique. The critical influence of surface-bound species near the three-phase boundary and their impact on nanowire crystal structure will be discussed in detail. This fundamental knowledge opens a generic and highly tunable route to engineer multiple classes (e.g. group IV and III-V, etc.) of semiconductor nanowires, heterostructures, and superstructures for advanced photovoltaic device applications.

9:20am **EN+EM+NS-WeM5 Electrophoretic Deposition of CdSe Nanocrystals in Quantum Dot Sensitized Solar Cells**, *N.J. Smith*, Middle Tennessee State University

Electrophoretic deposition (EPD) of nanocrystal thin films from the solution phase has received increasing attention due to its simplicity and ability to rapidly create controlled thickness films. In this presentation, we will discuss the impact of solvent choice, deposition time, and electrode voltage on the properties of CdSe nanocrystal films deposited by EPD for solar cell applications.

While hexanes are a commonly used solvent for depositing CdSe nanocrystals, resulting film formation by EPD is often not reproducible for different batches of nanocrystals. In this work, we report that adding acetone to solutions of nanocrystals in hexanes enables the consistent deposition of CdSe nanocrystal thin films of controllable thickness. These films form within a few seconds and require comparatively low electrode voltages for the deposition process. The addition of acetone appears to mitigate the effects of impurities in the precursor chemicals, the presence of solvents left over from nanocrystal synthesis, and variable environmental conditions that may otherwise compromise the quality of the resulting EPD nanocrystal films.

Quantum dot sensitized solar cells have been fabricated using the EPD process with CdSe nanocrystals solvated in hexanes with acetone. By modifying the EPD parameters, both the density and thickness of the nanocrystals films deposited on titanium dioxide coated ITO slides were affected. We will discuss the relationship between the EPD parameters and the resulting I-V characteristics and efficiency of the CdSe nanocrystal sensitized solar cells. Preliminary studies suggest that proper choice of EPD parameters can lead to more than one order of magnitude improvement in the solar cell performance metrics.

9:40am **EN+EM+NS-WeM6 Selective and Highly Efficient Photo-Induced Activity Over Nano-Scale Sites in Porous Silicon: Potential Application for Hybrid Organic-Silicon PV**, *M. Asscher*, The Hebrew University of Jerusalem, Israel, *G. Toker, A. Nahor, O. Berger, S. Yitzchaik, A. Sa'ar*, Hebrew University, Israel

Photo-induced processes over solid surfaces are of great basic and technological interest with applications in e.g. photolithography, sensing, catalysis and photovoltaics. Photo activity within porous silicon (PSi) following UV (193-266nm) irradiation has been studied. Unusually efficient, non-thermal, morphology and wavelength dependent photo-induced desorption (PID) of Xe was recorded. It is a selective process, revealing more than 3 orders of magnitude enhancement within pores, at the vicinity of nano-scale silicon tips, over atoms adsorbed on top of flat surfaces. Remarkably large cross sections up to $\sigma_{\text{PSi}} = 2 \cdot 10^{15} \text{cm}^2$ were recorded, significantly larger than any previously published photo-induced events on solid surfaces at this wavelength range. Long lived, photo-induced positive charges (holes) located at inner surface nano-tips is proposed to stabilize transient negative Xe adsorbate ions as the precursor for this new photo-desorption process.

These results were utilized for the construction of hybrid conducting polymer-porous silicon photovoltaic cell. Proof of concept and preliminary results are discussed.

10:40am **EN+EM+NS-WeM9 High-Performance, Low-Cost Nanopillar Array Photovoltaics**, *A. Javey*, University of California Berkeley **INVITED**

Semiconductor nanowires (NWs) hold great promise for fabrication of high-performance, low-cost solar cells. These materials have been extensively studied, both computationally and experimentally. The key advantage of NW solar cells resides in the ability to grow single crystalline NWs non-epitaxially on support substrates. Additionally, by varying the NW

geometry, the electrical, optical and mechanical properties of the solar cells can be controlled, providing opportunities unavailable to planar thin-film solar cells. Here we discuss our work on bottom-up CdS/CdTe nanopillar (NPL) solar cells, optical engineering of NPL arrays, and top-down fabrication of InP solar cells.

Bottom-up NPL solar cells were fabricated on anodized aluminum oxide (AAO) templates. Due to the 3-D geometry, the templated NPL architecture orthogonalizes the light absorption and carrier collection directions, enabling cells to be optimized even for poor quality materials. First-generation CdS/CdTe solar cells on low-cost Al foil exhibited 6% efficiency, 0.6 V open circuit voltage, V_{OC} , and 21 mA/cm² short circuit current, J_{SC} , despite significant (>30%) optical reflection from the top contact. Additionally, detailed electronic simulation was used to examine the design trade-offs involved with the NPL architecture. We found that even for a poor quality CdTe absorber layer, through proper design, moderate efficiencies of ~15% could be achieved. Additionally, all the processes used to fabricate the cell were roll-to-roll compatible. Thus, the combination of experiment and modeling show the promise of this method for fabrication of low-cost, high-performance solar cells.

The AAO templated growth enables a high degree of control over the geometry and dimensions of the NPL arrays. For single-diameter Ge NPL arrays embedded in AAO, increasing the Ge material filling ratio both increases the reflectance and decreases the transmittance. The absorbance of an array is shown to strongly increase for increased diameter NPL arrays. Thus, by fabricating arrays of dual-diameter Ge NPLs, ~99% of incident light was absorbed with a film only 2 μm thick. This behavior is caused by the smaller NPL diameter at the interface between the material and incident light, and the higher diameter base then absorbs the light.

Finally, radial p-n junction solar cells are fabricated from InP NPLs generated from a top-down etching procedure. The main challenge with radial p-n junctions is the ability to form ultra-shallow and conformal junctions along the radial axis. By utilizing a sulfur monolayer doping scheme, conformal junction depths of <10nm with high electrically active dopant concentrations ($\sim 10^{19} \text{cm}^{-3}$) are achieved. The fabricated solar cell exhibited a power conversion efficiency of 8.1%, a $V_{\text{OC}}=0.54 \text{ V}$, and a $J_{\text{SC}}=25 \text{ mA/cm}^2$.

In summary, we have presented both top-down and bottom-up approaches for fabricating NPL solar cells, from both crystalline starting materials as well as low-cost Al foil. The templated AAO growth method also enabled optical engineering of NPL arrays, allowing a single material to maximize absorption and minimize reflection. Finally, the utilization of a previously-developed conformal, ultra-shallow doping scheme was shown to enable radial InP solar cells.

11:20am **EN+EM+NS-WeM11 Extremely Thin Absorber Solar Cells Based on CdSe-Coated ZnO Nanowires**, *H. Majidi, T.P. Le, G.W. Gugglietta, J.B. Baxter*, Drexel University

Solar cells can provide an abundant, clean, and sustainable source of electricity, but high costs have limited their implementation. The use of sensitized nanostructured architectures may enable both low-cost processing and high efficiency by decoupling the functions of light harvesting and charge transport into different materials. Sensitized solar cells consist of a bicontinuous interpenetrating network of electron- and hole-transporting materials with an interfacial absorber layer. In this architecture, interfacial recombination is the dominant loss process, so controlling the interfacial chemistry during deposition is critical.

We report on the use of n-type ZnO nanowire arrays sensitized with thin CdSe coatings and covered with p-type CuSCN in extremely thin absorber (ETA) solar cells. Low temperature, solution deposition methods were used for each material, offering the potential for inexpensive and scalable nanomanufacturing. Nanowire arrays provide direct pathways for electron transport as well as sufficient surface area for sensitization. The electrodeposited CdSe coatings are nanocrystalline and conformal with well-controlled thickness. CuSCN is electrodeposited into the pore volume between nanowires. Morphology and microstructure of CdSe and CuSCN depend sensitively on bath chemistry and deposition potential. By controlling nucleation and growth rates, conformal and void-free materials can be deposited.

A combination of solar cell measurements and ex situ materials characterization for both planar thin film stacks and nanowire arrays have been used to direct the selection of optimal ETA cell architectures. For example, ultrafast transient absorption spectroscopy demonstrates that interfacial electron transfer from photoexcited CdSe to the ZnO is much faster than recombination (~3 ps vs ~50 ps) for thin coatings. Planar solar cells were used to identify the optimal coating thickness of ~70 nm for these materials. External quantum efficiency measurements show efficient sensitization throughout the visible region of the solar spectrum. However, interfacial recombination limits overall energy conversion efficiencies.

11:40am EN+EM+NS-WeM12 **Hybrid Photovoltaics Devices Based on Quantum Dot Functionalized ZnO Nanowire Arrays Embedded in a Polymer Matrix**, N. Harris, L. Butler, G. Shen, N. Dawahre, S. Wilbert, W. Baughman, S. Balci, P. Kung, S. Kim, University of Alabama

There is an increasing need to develop new low-cost materials and architectures for high efficiency solar cells in an attempt to provide a cost effective alternative to fossil fuels. Dyes, polymers and quantum dots have received tremendous amounts of attention due to their potential for solution processing and high absorption coefficients. Polymers and quantum dots are an attractive option for replacing dyes as the next generation low-cost absorber material due to their improved electronic properties and increased longevity. Bulk-heterojunction polymer based cells suffer from low carrier mobility and short carrier lifetimes which lead to high recombination rates. Quantum dots are promising sensitizing material because they potentially have improved stability over polymers and can potentially generate multiple excitons per photon. However, charge transport in solar cells based solely on quantum dots is generally accomplished through the hopping-mechanism and leads to increased recombination rates.

In this talk, we present a hybrid photovoltaic device structure based on quantum dot (QD)-functionalized single crystalline ZnO nanowire arrays embedded into a polymer matrix in order to achieve improved charge collection efficiencies from the QDs and transport through the cell. A number of issues need to be addressed, such as the enhancement of the coverage of the nanowires with quantum dots to increase photon absorption, as well as implementing a hole-transport medium that does not degrade the quantum dots and can potentially serve as a secondary absorber material that could potentially greatly improve device longevity, reproducibility and efficiency.

In this work, the specific photovoltaic device structure consisted of an InP/ZnS core-shell QD functionalized ZnO nanowire array that is embedded into a poly-3(hexylthiophene) (P3HT) hole transport matrix. The QD sensitized ZnO nanowires were characterized by optical absorption, confocal Raman and photoluminescence spectroscopy, as well as high resolution and scanning transmission electron microscopy. In addition, interface between QDs and ZnO NWs were studied by Atom Probe Tomography. QDs with different absorption bands were concurrently functionalized onto the same nanowire arrays in order to broaden the final device absorption bandwidth. The ZnO:P3HT matrix was then planarized using inductively coupled plasma etching. The performance of planarized, quantum dot functionalized devices was subsequently compared to as-deposited and non-functionalized devices and the effect of QDs on device efficiency is presented. These include the study of the charge transfer mechanism using terahertz time domain spectroscopy.

Energy Frontiers Focus Topic

Room: 209 - Session EN+NS-WeM

Organic Photovoltaics

Moderator: R.A. Quinlan, Naval Surface Warfare Center, Carderock Division

8:00am EN+NS-WeM1 **Sol-gel Prepared Ca Doped ZnO and Its Application in Polymer-Oxide Bilayer Hybrid Solar Cells**, M. Wang, I. Hill, Dalhousie University, Canada

Conjugated polymer/metal oxide hybrid photovoltaic devices have received considerable attention in recent years due to their potential for scalable, low-cost manufacturing. To improve device efficiency, most research has focused on increasing the fill factor and short circuit current. In this article, calcium doped zinc oxide ($Zn_xCa_{1-x}O$) is used as electron acceptor in the hybrid poly(3-hexylthiophene) / $Zn_xCa_{1-x}O$ bilayer solar cells to modify the band offsets and increase the open circuit voltage. XRD results show the sol-gel prepared Ca doped ZnO films have a hexagonal wurtzite phase with no indication of calcium separation. Atomic force micrographs indicate the $Zn_xCa_{1-x}O$ surface becomes decorated with interconnected ridges approximately 100 nm in height. The rms surface roughness increases with increasing Ca. The band gap obtained from UV-vis absorption spectra widens from 3.20 to 3.60 eV as the Ca concentration increases from $x=0$ to $x=0.12$. The work function of the $Zn_xCa_{1-x}O$ films measured by Kelvin probe is seen to decrease with increasing Ca composition for values of x up to 0.12, which indicates a decrease in electron affinity. The open circuit voltage of hybrid P3HT/ $Zn_xCa_{1-x}O$ devices increases from 570 mV at $x=0$ up to 800 mV for $x=0.10$. Work is under way to incorporate Ca doped ZnO nanoparticles into bulk heterojunction solar cells to optimize device efficiency.

8:20am EN+NS-WeM2 **The Influence of ITO Surface Treatments on Spatially Localized Photocurrent Variation in Organic Photovoltaic Devices**, B.J. Leever, Air Force Research Laboratory, I.P. Murray, Northwestern University, M.F. Durstock, Air Force Research Laboratory, T.J. Marks, M.C. Hersam, Northwestern University

The fabrication process for bulk heterojunction (BHJ) organic photovoltaic (OPV) devices nearly always includes anode modification steps ranging from solvent cleaning to haloacid treatments to the deposition of interfacial layers such as polymer blends or transition metal oxides. The role of these treatments is not yet fully understood, but they are thought to modify the anode work function, contribute to electron-blocking, alter the anode surface energy, and prevent shunts among other functions. In separate work, conductive atomic force microscopy (AFM) and derivative techniques have been used to simultaneously probe both the morphological and electrical properties of BHJ photovoltaic layers. Previous work has demonstrated a correlation between BHJ nanostructure and properties such as photocurrent at the same scale (~ 20 nm) as the phase separation in these films. Photocurrent variability has also been observed at a length scale orders of magnitude larger the domains in the BHJ layer, and this variation has been speculated to have an origin in the anode or interfacial layers in the OPV architecture.

In this work, a correlation between indium tin oxide (ITO) surface treatment and spatially localized photocurrent variation has been found in OPV devices with a poly(3-hexylthiophene):[6,6]-phenyl-C-61-butyric acid methyl ester (P3HT:PCBM) BHJ layer. Atomic force photovoltaic microscopy (AFPM) was used to scan arrays of functioning 2 μ m solar cells with varied ITO surface treatments. The standard deviation of the average photocurrent was found to be 11.4% for devices fabricated on untreated ITO, 8.6% for devices with a poly(3,4-ethylenedioxythiophene):poly(styrene sulfonate) (PEDOT:PSS) interlayer, and 6.7% for devices with a HCl-treated ITO surface. These results suggest that conductive non-uniformity in the ITO surface is transferred through the P3HT:PCBM film and that improving the anode conductive uniformity could be an important role of OPV interfacial layers or anode surface treatments.

8:40am EN+NS-WeM3 **Electronically Monodisperse Single-Walled Carbon Nanotube Thin Films as Transparent Conducting Anodes in Organic Photovoltaics**, T.P. Tyler, R.E. Brock, H.J. Karmel, T.J. Marks, M.C. Hersam, Northwestern University

Carbon nanomaterial thin films are being increasingly investigated for use as transparent electrodes in a variety of optoelectronic devices [1-3]. These flexible and solution-processible films are ideal candidates for organic electronics, including organic photovoltaics (OPVs), where low production costs and mechanical robustness are essential. While carbon nanotube networks have begun to be explored in such devices, the inherent polydispersity of the samples—namely the mix of both semiconducting and metallic species—has prevented the realization of their full potential in these devices and convoluted a complete understanding of their implications on device operation. Herein we report the use of single-walled carbon nanotubes (SWNTs) sorted by electronic type via density gradient ultracentrifugation as the transparent anode in poly(3-hexylthiophene) (P3HT) [6,6]-phenyl-C₆₁ butyric acid methyl ester (PCBM) organic photovoltaic devices. Through a combination of dip coating and nitric acid treatment we achieve film roughnesses comparable to typical transparent oxides such as indium tin oxide. While carbon nanotube films are often electronically doped during processing, either intentionally or as a byproduct of roughness-reducing acid treatments, we find that the application of the quintessential electron-blocking interlayer poly(3,4-ethylenedioxythiophene):poly(styrenesulfonate) (PEDOT:PSS) removes sufficient adsorbed dopant groups to return the semiconducting nanotubes to their original state, vastly reducing their contribution toward current collection and transport. This is observed by both sheet resistance increases and UV-vis-NIR spectrophotometry. Further investigation using X-ray photoelectron spectroscopy reveals that the weakly-bound nitric oxide groups on the surface are almost entirely removed by PEDOT:PSS. By varying the semiconducting and metallic content in the electrodes, we find that metallic content greater than 70 percent yields devices with efficiencies 50 times greater than those comprised of almost entirely semiconducting SWNTs. This observation is counterintuitive considering that freshly acid-treated semiconducting SWNT films often possess a lower sheet resistance than their metallic counterparts [4]. This underscores the advantage of using metallic-enriched populations for transparent conductors, where unstable doping of semiconducting carbon nanotubes complicates processability and ultimately reduces device performance.

[1] T. M. Barnes; et al. *Appl. Phys. Lett.* **2010**, *96*, 243309.

[2] S. Kim; et al. *Adv. Funct. Mater.* **2010**, *20*, 2310.

[3] J. Li; et al. *Nano Lett.* **2006**, *6*, 2472.

[4] J. L. Blackburn; et al. *ACS Nano* **2008**, *2*, 1266.

9:00am **EN+NS-WeM4 In Situ Characterization of Lifetime and Morphology in Operating Bulk Heterojunction Organic Photovoltaic Devices by Impedance Spectroscopy**, *B.J. Leever, C.A. Bailey*, Air Force Research Laboratory, *T.J. Marks, M.C. Hersam*, Northwestern University, *M.F. Durstock*, Air Force Research Laboratory

Numerous reports have established that improving the performance of bulk heterojunction (BHJ) organic photovoltaic (OPV) devices requires not only the development of materials systems with improved spectral response and higher charge carrier mobility but also the ability to understand and tailor the morphology of these systems. Approaches for morphological characterization have included microscopic techniques such as scanning electron microscopy, transmission electron microscopy, and various atomic force microscopy techniques. Other methods have provided indirect information about active layer morphology by enabling the determination of charge carrier lifetimes. These approaches have included transient absorption spectroscopy, transient photovoltage, and time-of-flight techniques among others. While these methods have proven quite informative, the relationships between nanoscale morphology, device performance, and the underlying electrical characteristics of functioning devices are not yet fully understood.

Recently, impedance analysis has begun to be applied to BHJ OPV devices. These reports demonstrate that the impedance analysis framework established for dye-sensitized solar cells can, to some extent, be extended to bulk heterojunction devices in order to calculate average charge carrier lifetime, electron densities-of-states, and charge carrier concentrations. However, a detailed analysis of the impedance response of active devices, and its dependence on device processing history, morphology, and operating conditions is still needed. In this work we acquire and analyze the impedance behavior of operating P3HT:PCBM bulk heterojunction devices and its dependence on illumination and bias conditions, active layer composition, and annealing history. We also report a simplified equivalent circuit model that successfully describes bulk heterojunction devices over a range of illumination conditions and applied biases. We use this model to extract relevant device performance characteristics such as average electron lifetime and find, in agreement with other reports, that bimolecular recombination losses play a significant role in these devices. To this end, we demonstrate a correlation between device efficiency and lifetime, and describe how values extracted from the present equivalent circuit model can be used to optimize device performance with new materials systems.

9:20am **EN+NS-WeM5 Singlet Exciton Fission in Tetracene and Diphenyltetracene**, *P. Jadhav, A. Mohanty, J. Sussman, M. Baldo*, Massachusetts Institute of Technology

INVITED

Singlet exciton fission is a process by which a high energy singlet spontaneously decomposes into two low energy triplets. It is an example of a multi-exciton generation process that could allow the efficiency of solar cells to reach beyond the Shockley-Queisser limit. In this talk we examine singlet exciton fission in solar cells based on tetracene and diphenyltetracene (DPT). Notably we find that the photocurrents in each cell have opposite dependencies on the application of a magnetic field, suggesting that fission increases the photocurrent in tetracene-based solar cells, but decreases the photocurrent in DPT-based solar cells.

We report an organic semiconductor solar cell using tetracene and CuPC (Copper Phthalocyanine) as donors, and C60 as the acceptor. Tetracene absorbs photons in the 450-550-nm region, generating high energy singlets which split into two lower energy triplets, potentially doubling the photocurrent in this part of the spectrum. CuPC extends the absorption of the solar cell to the red part of the spectrum. We also demonstrate bulk heterostructure tetracene-C60 devices and tested them for singlet exciton fission.

We observe that: (i) The addition of the CuPC layer does not affect the flow of excitons from tetracene to the CuPC - C60 junction significantly because of similarities in triplet energies of tetracene and CuPC, (ii) The application of a .5T magnetic field shows ~1.5% change in photocurrent, confirming singlet fission, (iii) Low temperature quantum efficiency measurements show a drop in the tetracene IQE (internal quantum efficiency), and a singlet fission yield of 72% at room temperature. The drop in performance at low temperature is expected since singlet exciton fission in tetracene is a thermally activated process. (iv) Singlet exciton fission has a very high yield even in bulk heterostructure devices and can be potentially used to improve the performance of polymer solar cells.

In comparison, we observe that solar cells consisting of DPT-C60 exhibit a large positive (+5%) effect of the magnetic field on the photocurrent, +5% at ~.4T. We explain the anomalous magnetic field effect and demonstrate that it can be increased beyond 100% by biasing the device close to open circuit, potentially leading to applications as an anisotropic magnetic field detector.

10:40am **EN+NS-WeM9 Charge Separation and Relaxation in Phthalocyanine-C₆₀ Photovoltaic Systems**, *G.J. Dutton*, University of Maryland -College Park, *S.W. Robey*, National Institute of Standards and Technology

Organic photovoltaic (OPV) structures depend on charge transfer processes occurring within 10's of nanometers of donor-acceptor interfaces. Charge generation in these devices involves successive steps of (1) optical absorption to create excitons, (2) diffusion of the exciton population to the donor-acceptor interface, (3) exciton dissociation and charge transfer at the interface and (4) charge transport and collection at electrodes. The charge separation step depends critically on electronic level alignment between the donor and acceptor. Also, because exciton diffusion to the interface occurs on timescales of several to 10's of picoseconds (ps), relaxation processes occurring on sub-ps and ps timescales as the exciton diffuses can impact the energy available for charge separation at the interface. We have investigated the exciton relaxation and charge separation processes close to phthalocyanine (Pc)-C₆₀ interfaces by combining time-resolved two-photon photoemission (TR-2PPE) with organic MBE to form donor-acceptor interfaces layer-by-layer. Pc $\pi \rightarrow \pi^*$ transitions are excited by a pump pulse to generate singlet (S₁) excitons. The resulting population dynamics are then probed with a time-delayed UV pulse to follow the relaxation and charge separation as a function of energy. For CuPc /C₆₀ interfaces, we compared the decay dynamics as a function of CuPc thickness, and thus distance from the C₆₀ interface, to allow determination of the rate of charge transfer at the interface. We find a charge transfer rate of $\approx 8 \times 10^{12} \text{ sec}^{-1}$ for the initial exciton population formed immediately after pumping. For CuPc, the exciton population also undergoes vibrational relaxation and intersystem crossing (ISC) on a timescale of $\approx 1-2 \text{ ps}$, ultimately resulting in the production a triplet exciton population at significantly lower energy. By again comparing results for thin and thick Pc layers we estimate that the charge transfer rate of this lower energy triplet population is reduced by at least a factor of ≈ 1000 , giving charge transfer rates closer to $8 \times 10^9 \text{ sec}^{-1}$. We will also discuss measurements for the case of H₂Pc and C₆₀ where ISC of the Pc singlet excitons to triplet levels is negligible. Our results will be discussed within the context of the Marcus theory of charge transfer and connections will be made to calculated charge transfer rates for similar donor-acceptor interfaces.

11:00am **EN+NS-WeM10 Low Energy Ion-Assisted Modification of PbS Nanocrystal-Sexithiophene Composite Films**, *F.D. Pleticha*, University of Illinois at Chicago, *L. Donghwa*, University of Florida, *I.L. Bolotin*, University of Illinois at Chicago, *S.R. Phillpot*, *S.B. Sinnott*, University of Florida, *L. Hanley*, University of Illinois at Chicago

The properties of semiconductor nanocrystal-organic films are of interest for applications in photodetectors, light-emitting diodes and photovoltaics. The versatility of these films arises from the ability to tune the bandgaps by adjusting the PbS nanocrystal size. Nanocrystalline photoelectric properties are also strongly affected by the chemical environment presented to them and by their bonding to the surrounding organic films. PbS nanocrystals are simultaneously deposited under vacuum into an organic matrix of evaporated α -sexithiophene while concomitantly modulating the film interface with 50 eV acetylene ions. Cluster beam deposition has been shown to allow the preparation of PbS nanocrystals that are surface terminated with either Pb or S [1]. Surface polymerization on ion assisted deposition (SPIAD) has shown an ability to increase the conjugation of oligothiophenes and otherwise lead to their chemical modification [2-4]. Cluster beam deposition and SPIAD are combined here to modulate the interface between the PbS and the organic matrix by introducing acetylene ions during the formation of the film. X-ray photoelectron spectroscopy analysis shows chemical shifts indicative of acetylene ion modulated interaction between the nanocrystals and sexithiophene. The deposition process was also simulated by a linearly scaled density functional theory method. These computer simulations indicate chemical bonding between the nanocrystals and sexithiophene, which is consistent with the chemical shifts observed by XPS.

1. A. M. Zachary, I. L. Bolotin, D. J. Asunskis, A. T. Wroble, and L. Hanley ACS Appl. Mater. Interf. 1 (2009) 1770

2. S. Tepavcevic, A. M. Zachary, A. T. Wroble, Y. Choi, and L. Hanley, J. Phys. Chem. A 110 (2006) 1618

3. S. tepavcevic, Y. Choi, and L. Hanley, Lang. 20 (2004) 8754

4. W. -D. Hsu, S. Tepavcevic, L. Hanley, and S. B. Sinnott, J. Phys. Chem. C 111 (2007) 4199

11:20am **EN+NS-WeM11 Molecular Modulation of Solar Cells: Where Inorganic, Molecular and Organic Electronics Meet**, *D. Cahen*, *R. HarLavan*, *O. Yaffe*, Weizmann Institute of Science, Israel

Organic materials present a promising direction for potentially cheaper solar cells. One way to use them and increase our understanding (e.g., define basic physical cell performance limits), is hybrid, organic / inorganic

photovoltaics (PV). We explore 2 main directions to hybrid PV - with molecules as dipolar films, i.e., use electrostatics
- with molecular monolayers as electronic transport medium.

While we find that incomplete partial dipolar monomolecular films can control solar cell behavior for /single, poly- and nano-crystalline cells, for current to pass through the molecules, we need dense monolayers. Alkyl chain monolayers help form near-ideal Metal-Insulator-Semiconductor (MIS) diodes, with significant PV activity. Surprisingly, though we can actually make *MIS* cells without a separate *I*(nsulator) layer, suggesting that 'MIS' effects are at least partly more "chemical than is often thought.

In this way we demonstrate a near-ambient, simple, potentially low-cost approach to make and modify semiconductor solar cells, using a monolayer of molecules, as short as two carbons, that self-assembles onto the semiconductor (absorber) surface, passivating and buffering it. Good passivation is necessary to express the molecule-induced interface dipole, which can change the semiconductor electron affinity by up to 1 eV.

Good, stable interface passivation along with strong inversion allows minority carriers, generated by absorbed light, to move laterally within the semiconductor top layer, for collection by a minimal-area grid, deposited on the conducting polymer and also minimizes photo-current losses, due to sheet resistance. Thus, ≤ 1 nm thick organic molecules appear to convey a unique advantage over inorganic passivation or buffer layers.

11:40am **EN+NS-WeM12 Correlation of Interfacial Electronic Structures and Open Circuit Voltages in Organic Solar Cells, M.H. Chen**, National Dong Hwa University, Taiwan, Republic of China, *W.H. Tseng, J.Y. Wang, C.T. Tseng, C.I. Wu*, National Taiwan University

In this study, the interfacial electronic structures and energy band diagrams of polymer/fullerene bulk heterojunction (BHJ) solar cells are investigated. To study the device performance influenced by the interlayer, poly(3-hexylthiophene) (P3HT) mixed with 6,6-phenyl C61-butyric acid methylester (PCBM) are used as an active layer and bathocuproine (BCP) and calcium (Ca) are incorporated respectively with the cathodes. Since the mechanisms leading to the improvement of power conversion efficiency are more chemically and electronically complicated and have not been understood, the ultraviolet and x-ray photoemission spectroscopy (UPS and XPS) are used to investigate the properties of energy band, electronic structures and the interface chemistry at the interface. For the devices incorporated with BCP, highest occupied molecular orbital (HOMO) level of PCBM is pulled down about 0.3 eV with respect to the Fermi level after the deposition of BCP. It indicates that the BCP layer could modify the energy band by shifting the energy level of acceptors, causing the increase of built-in potential (V_{bi}). Thus, the open circuit voltage (V_{oc}) attributed to the increase of V_{bi} resulted from BCP could be enhanced. Moreover, AFM image indicates that BCP molecules cannot form a uniform layer on the active layer surface, pointing out the band modulation is the key reason to the V_{oc} improvement. For the devices with Ca as cathodes, the UPS results with deposition of Ca illustrate a 0.8 eV-downward shift in energy levels of P3HT, but not in those of PCBM. Therefore, the energy difference between the HOMO of P3HT and the LUMO of PCBM is widened, resulting in the increase of V_{oc} and the enhancement of device efficiency. Moreover, from the XPS spectra, there is an extra new peak appear at the lower binding energy about 162 eV, which suggests that the addition of electrons around the reactive sulfur (S) atoms in P3HT molecules after Ca deposition. The combinations of S and Ca spectra imply that the formation of Ca-S bonding at the Ca/P3HT interface, which is in good agreement with the findings of UPS spectra.

Exhibitor Technology Spotlight

Room: West Exhibit Hall - Session EW-WeM

Exhibitor Technology Spotlight

Moderator: D. Surman, Kratos Analytical Inc.

10:20am **EW-WeM8 Using the Apple IPAD with your PVD System Maintenance, C. Malocsay**, Semicore

Rarely does one item change several industries at once like the Apple IPAD or other tablet computers. Semicore has followed other major companies that have taken this device and applied it to increase productivity and reduce costs. Not a replacement for your PC but considered as an extension of your computer just like a wireless mouse. Applications available at little or no cost can increase the users effectiveness in Thin film vacuum deposition systems and their day to day operation.

Graphene and Related Materials Focus Topic Room: 208 - Session GR+MN-WeM

Graphene: Mechanical and Thermal Properties, Graphene MEMS and NEMS

Moderator: J. Rabe, Humboldt University Berlin, Germany

8:00am **GR+MN-WeM1 Graphene Atomic Membranes: From Patchwork Quilts to Atomic Drums, P.L. McEuen**, Cornell University
INVITED

Graphene is the world's first atomic membrane, a robust, one-atom thick freestanding layer of sp²-bonded carbon. The physical properties of these membranes straddle the border between soft and hard condensed matter. They are strong but highly flexible, with bending stiffness comparable to a lipid bilayer but stretching stiffness similar to diamond. Meter-scale polycrystalline graphene films can now be produced cheaply and easily, opening the door to applications in both science and technology. In this talk we will present new results on the structural and physical properties of this remarkable 2D material, including the first STEM images of graphene grain boundaries and the patchwork-quilt-like structure of graphene grains. We also discuss experiments on atomic drums made with graphene membranes that can be actuated and probed either electrically or optically. Unlike for traditional MEMs and NEMs, we find that stiction and entropy are key parameters in determining the drum's vibration frequency.

8:40am **GR+MN-WeM3 Nanomechanics of Graphene: Non-Linear Response, Fracture, and Crack Propagation, R. Perriot, Y. Lin**, University of South Florida, *X. Gu*, Aalto University School of Science and Technology, Finland, *V.V. Zhakhovskiy, I.I. Oleynik*, University of South Florida

Recent nanoindentation experiments on graphene have revealed its exceptional strength, making it an excellent candidate for the design of nano devices such as MEMS and pressure sensors. Therefore, it is critical to understand the mechanical properties of graphene, and its response to a wide range of loading pressures beyond the elastic regime. In this work we performed molecular dynamics (MD) simulations of the nanoindentation of graphene membranes by a spherical indenter. The indentation curves (load vs. indentation depth) obtained from simulations revealed two regimes of response: linear for smaller, and non-linear for larger indentation depths respectively. The MD results are in good agreement with the theory of elastic plates and recent experiments. Using the kinetic theory of fracture, we were able to determine the breaking strength of graphene and its dependence on the indenter radius. MD simulations also provided an atomic-scale description of the breaking process, which occurs through crack formation and propagation in graphene.

9:00am **GR+MN-WeM4 The Effect of the Environment on Electrical and Mechanical Properties of Graphene, K. Bolotin**, Vanderbilt University

Every atom of graphene, a monolayer of graphite, belongs to the surface. Therefore, the environment of graphene -- the substrate onto which graphene is deposited and the coating on top of graphene -- intimately affects the properties of graphene. In this talk, we demonstrate that both mechanical and electrical properties of graphene can be tuned by varying the environment of graphene.

To study the mechanical properties of graphene, we developed a novel technique that is based on measuring the temperature-dependent deflection of a "bimetallic" cantilever composed of graphene and silicon nitride or gold layers. We demonstrate that the built-in strain, the substrate adhesion force and even the thermal expansion coefficient of graphene depend on the substrate under it.

To study the electrical properties of graphene in various environments, we developed a technique to fabricate electrically contacted multiterminal *suspended* graphene devices that are submerged into liquids. We explore the dependence of electron mobility of graphene on dielectric constant and ionic concentration of liquids surrounding graphene. We find that ions in liquids can cause strong scattering in graphene and that very large values of mobility ($>40,000$ cm²/Vs) can be achieved in ion-free liquids.

9:20am **GR+MN-WeM5 Nanoscale Friction and Adhesion Behavior of Graphene: The Effect of Sliding History, X.-Z. Liu, Q. Li, B. Zhang, R.W. Carpick**, University of Pennsylvania

As a prominent example of a two-dimensional (2-D) material, graphene has drawn much attention because of its extraordinary physical properties. However, in contrast to its electronic and thermal properties, the mechanical and tribological properties of graphene remained poorly understood. These properties are interesting scientifically because of the extremely high

strength and low defect density of the bonds, and the intrinsically wrinkled structure of graphene. These properties are important for integrating graphene with devices. We studied the friction and adhesion between nanoscale single-asperity tips and exfoliated graphene sheets using atomic force microscopy (AFM). We have previously reported that friction on few-layer graphene (and other 2-D materials) depends on the number of layers[1], whereby the friction is higher for fewer layers. The layer-dependence is associated with the presence of a “strengthening” effect, where the static friction force builds up as scanning proceeds, most evident for the thinnest layers. This suggested that the increase was due to the build-up of a puckered area in front of the tip due to the high compliance of the graphene and adhesion with the tip. However, adhesion between the tip and graphene, measured by regular AFM force-displacement spectroscopy, does not change appreciably when the layer number changes. This result agrees with trends obtained from finite element method (FEM) simulations. However, we observed that both friction and adhesion exhibit a contact history dependence. For friction on single layer graphene, the strengthening is not present initially, but rather, it gradually builds up as the tip is rastered over the surface. This suggests that the puckered structure requires repeated scanning before it geometrically develops to a point where friction is enhanced. In addition, we find that adhesion is enhanced if it is measured without breaking the tip-graphene contact after sliding the AFM tip over the same area for a sufficient distance. This sliding-history dependence was not observed on bulk graphite or SiO₂ substrates, and thus appears to be yet another unique feature of the tribological behavior of atomic sheets. These two observations strongly suggest that the geometric structure of the sheet and the contact area it makes with the tip is significantly affected by the sliding history.

[1] Lee, C., Q. Li, W. Kalb, X. Liu, H. Berger, R. Carpick, and J. Hone, *Frictional Characteristics of Atomically Thin Sheets*. Science, 2010. **328** (5974): p. 76.

10:40am **GR+MN-WeM9 Molecular Dynamics Simulations of Melting of Graphene**, *B. Steele, V.V. Zhakhovskiy, R. Perriot, I.I. Oleynik*, University of South Florida

It has long been predicted by Peierls, Landau, and Mermin that infinite two-dimensional solids are unstable and should melt at any finite temperature. The stability of graphene, a two-dimensional layer of carbon atoms, is thus explained by the presence of an additional degree of freedom that allows it to buckle in the third direction normal to the 2-D perfect plane. We performed large-scale molecular dynamics (MD) simulations of graphene melting in order to provide a fundamental insight into the stability of graphene, as well as to investigate the nature of the defects naturally created by thermal excitations at high temperatures. We will discuss the types of defects appearing before melting, the atomic-scale mechanisms of melting, and the nature of the resulting carbon melt. In addition, the graphene melting in 3D space *versus* 2D-constrained melting is also discussed. The importance of a proper description of chemical bonding in graphene at high temperatures is illustrated using different interatomic potentials: the reactive bond order (REBO) potential and the newly developed screened environment dependent SED-REBO. Comparisons with other recent simulations of graphene melting (including those using the LCBOPII potential for carbon) are also presented.

11:00am **GR+MN-WeM10 Inhomogeneous Strain in Monolayer Epitaxial Graphene**, *D.A. Schmidt*, Ruhr-University Bochum, Germany, *T. Ohta, L.B. Biedermann, T.E. Beechem, S.W. Howell, G.L. Kellogg*, Sandia National Laboratories

We report a large in-plane compressive strain (up to 0.5%) and its inhomogeneous variation at micrometer length scale in single layer graphene films on silicon-carbide (SiC) (0001). The strain, due to the difference in lattice constants and thermal expansion coefficients of graphene and SiC substrate, is probed using Raman scattering. We show that both the growth mechanism and the relaxation along the mismatched symmetry of the graphene and underlying substrate can affect the exact amount of local strain. The large compressive strain implies that monolayer graphene is tightly grafted to the underlying interface layer and SiC substrate; otherwise it would delaminate to relieve the strain. The magnitudes of the structural strain and its local variation are significant and need to be taken into account for electronics applications based on the graphene-SiC(0001) system.

The Raman microscope was supported under BMBF grants 05KS7PC2. D. A. S acknowledges support within the BMBF funded projects 05KS7PC2 and 05K10PCA. The work was also supported in part by the LDRD

program at SNL and the US DOE Office of Basic Energy Sciences' Division of Materials Science and Engineering (Contract No. DE-AC04-94AL85000). Part of this work was performed at CINT (Contract No. DE-AC04-94AL85000). SNL is a multi-program laboratory managed and operated by Sandia Corporation, a wholly owned subsidiary of Lockheed Martin Corporation, for the U.S. Department of Energy's National Nuclear Security Administration under contract DE-AC04-94AL85000.

Helium Ion Microscopy Focus Topic Room: 106 - Session HI+AS+BI+NS-WeM

Nano- and Bio- Imaging with Helium Ion Microscopy
Moderator: A. Götzhäuser, University of Bielefeld, Germany, V.S. Smentkowski, GE-GRC

8:40am **HI+AS+BI+NS-WeM3 Helium Ion Microscopy Techniques for Imaging and Characterization of nano-Device Materials and Structures**, *S. Ogawa, T. Iijima*, National Institute of Advanced Industrial Science and Technology (AIST), Japan **INVITED**

This paper presents several imaging modes for nano-devices fabrication that may make HIM a tool of particular value to soft materials such as low-k dielectrics (low-k) with less transformation and more materials contrast which reflects damaged areas, and copper interconnect buried in dielectrics, and shows luminescence induced by the focused helium ion beam using the HIM for the first time.

Imaging of -100 nm pitch patterned low-k is important for LSI Cu/low-k interconnect processes, while SEM imaging results in changes to the low-k line edge roughness and shape by damage during an electron beam irradiation. The HIM could provide low-k dielectric secondary electron (SE) image with nm order resolution, deeper focus depth, less transformation because of three order magnitude lower thermal energy transfer into a unit volume of the low-k than the SEM under an appropriate operation condition¹⁾.

During the imaging, even at very low helium ion current, surfaces of samples were atomically etched off, as in a graphene patterning, and then blistering or physical etch occurred with the increase of the helium ion current. This makes the interpretation of the HIM SE imaging difficult but helpful. Damaged areas at side walls of the low-k regions in a 140 nm pitch interconnect were successfully seen with a different contrast from non-damaged low-k regions at an “optimized” helium ion beam condition²⁾, which was similar to a TEM/Valence EELS result. On the other hand, using the SEM, the damaged areas contrast in the low-k regions could not be imaged.

A new imaging mode, through the inter-level dielectric, of the underlying copper, was explored. Cu interconnect was seen through a 130 nm thick low-k dielectrics. The incident helium ions might generate secondary electrons (SEs) at the buried Cu surface and the SEs of 1-2 eV energy passed through the dielectric of a few eV band gap without any energy transfer, and then the image was obtained. Helium ion channeling at the Cu surface area varied the secondary electron quantity, and it might generate a crystal orientation contrast of the buried Cu metal.

Luminescence induced by the focused helium ion beam was studied using the HIM³⁾. Helium ion beam of a few pA current was irradiated to a SiO₂ film, and peaks in a spectrum were observed at around 281, 447, and 672 nm; these positions were different from those by a conventional SEM cathode luminescence. The further study will be presented.

L.Stern, W.Thompson and J.Notte of Carl Zeiss are acknowledged for their discussions in the Cu / low-k works.

1) S. Ogawa, et al, Jpn. J. Appl. Phys., 49 (2010) 04DB12, 2) S. Ogawa, et al, Proc. of 2011 IEEE IITC (2011)

9:20am **HI+AS+BI+NS-WeM5 He Ions Image the Au (111) Herringbone Reconstruction**, *V. Veligura, G. Hlavacek, R. van Gastel, H. Zandvliet, B. Poelsema*, MESA+ Institute for Nanotechnology, University of Twente, Enschede, The Netherlands

The herringbone reconstruction of the Au(111) surface was directly visualized using an Ultra High Vacuum Helium Ion Microscope. Ion channeling phenomena arise from the different atomic ordering in the outermost layer of the crystal. First, we investigated the channeling contrast from the bulk Au fcc structure by imaging polycrystalline Au on glass films. The contrast that was observed as a function of crystal orientation was found to conform to what is calculated from a simple hard sphere model. Consequently, the herringbone reconstruction was investigated. It is a periodic zigzag structure of the three different types of crystal stacking (fcc, hcp and bridge sites connecting these regions) and, ideally, has a

period of 6.3 nm. The different stacking of the atoms that constitute the surface reconstruction leads to lateral variations of the secondary electron yield that can be resolved in HIM imagery. The existence of the herringbone reconstruction on the sample was independently confirmed through STM measurements and the quantitative details from both techniques are similar, but seem to be affected by the differences in vacuum conditions. An influence of both the ion beam and vacuum environment on the visibility of the herringbone reconstruction is observed in our UHV-HIM system.

9:40am **HI+AS+BI+NS-WeM6 Imaging of Graphenoid Nanomembranes with Helium-Ion Microscopy, A. Beyer, A. Turchanin, A. Götzhäuser, University of Bielefeld, Germany**

Helium-ion microscopy is known for its high surface sensitivity. Here we present a study about imaging extremely thin nano-scale objects: graphenoid nanomembranes which consist exclusively of atoms near the surface. Such freestanding nanomembranes with a thickness of 1 nm are made from self-assembled monolayers (SAMs) by cross-linking and subsequent transfer to transmission electron microscopy (TEM) grids or other suitable substrates. We show that these nanomembranes exhibit a substantially higher contrast in helium-ion microscopes as compared to electron microscopes.

Cross-linking of SAMs is performed by large area exposures with electrons or photons which yield extended nanomembranes. On the other hand, patterned exposures allow the fabrication of nanosieves, i.e. perforated nanomembranes. Advantages in imaging such patterned cross-linked SAMs as well as freestanding nanosieves with the helium-ion microscope will be discussed.

10:40am **HI+AS+BI+NS-WeM9 Nanofabrication and Biological Imaging with the Helium Ion Microscope, D.S. Pickard, National University of Singapore** **INVITED**

The Helium Ion Microscope (HIM) is a new imaging technology based on a high brightness and stable Gas Field Ion Source (GFIS). The GFIS employed exhibits a low energy spread (<1 eV), small virtual source size (<0.3 nm) and a high brightness $> 4 \times 10^9$ A/cm².sr [1]. This, in conjunction with the shallow escape depth (<1 nm) of the secondary electrons generated by the incident 30 keV helium ions, contribute to the HIM's primary advantage in the imaging of solid samples: its high spatial resolution (0.25 nm) [2]. We have applied this novel technology across a broad spectrum of multidisciplinary applications (from basic materials science and semiconductor applications to the biological sciences) to assess its utility and possible advantages over alternative techniques.

One area where our investigations have gained significant traction is in the imaging of biological specimens. The utility of this instrument in addressing topics of the biological sciences is due in part to the HIM's high spatial resolution. However, in the context of biological specimens, it is the ability to image non-conductive samples without the application of a metal (or other conductive) overcoat and without the need of a background gas (both of which degrade resolution and surface details), which has proven to be a distinguishing attribute. This opens up a whole new range of biological problems that can be solved rapidly and with less risk of artifacts.

An equally compelling application is in the field of nano-structuring. The focused helium ions have the ability to directly modify the sample surface under a high ion flux (via surface sputtering). This enables the direct patterning of structures and promises great utility in the fabrication of sub-10 nm devices. It also provides a mechanism for high resolution patterning on nonconventional substrates (such as suspended graphene membranes), where resist-based lithographic techniques are not feasible. Our experiences in sub-10 nm pattern transfer for both graphene and plasmonics applications will be presented.

1. B. Ward, J. Notte, and N. Economou, J. Vac. Sci. Technol. B, Vol. 24, No. 6, Nov/Dec 2006

2. Application Note, Carl Zeiss SMT, "Ultra-High Resolution Imaging in ORION[®]PLUS", PI No. 0220-2008-ENG, Nov. 21, 2008

11:20am **HI+AS+BI+NS-WeM11 Imaging and Characterizing Cellular Interaction of Nanoparticles using Helium Ion Microscopy, B.W. Arey, V. Shutthanandan, Y. Xie, A. Tolic, G. Orr, Pacific Northwest National Laboratory**

The helium ion microscope (HeIM) probes light elements (e.g. C, N, O, P) with high contrast due to the large variation in secondary electron yield, which minimizes the necessity of specimen staining. A defining characteristic of HIM is its remarkable capability to neutralize charge by the implementation of an electron flood gun, which eliminates the need for coating non-conductive specimens for imaging at high resolution. In addition, the small convergence angle in HeIM offers a large depth of field ($\sim 5x$ FE-SEM), enabling tall structures to be viewed in focus within a single

image. Taking advantage of these capabilities, we investigate the interactions of engineered nanoparticles (NPs) at the surface of alveolar type II epithelial cells grown in culture. The increasing use of nanomaterials in a wide range of commercial applications has the potential to increase human exposure to these materials, but the impact of such exposure on human health is still unclear. One of the main routes of exposure is the respiratory tract, where alveolar epithelial cells present a vulnerable target. Since the cellular interactions of NPs govern the cellular response and ultimately determine the impact on human health, our studies will help delineating relationships between particle properties and cellular interactions and response to better evaluate NP toxicity or biocompatibility.

The Rutherford backscattered ion (RBI) is a helium ions imaging mode, which backscatters helium ions from every element except hydrogen, with a backscatter yield that depends on the atomic number of the target. Energy-sensitive backscatter analysis is being developed, which when combined with RBI image information, support elemental identification at helium ion submicron resolution. This capability will enable distinguishing NPs from cell surface structures with nanometer resolution.

11:40am **HI+AS+BI+NS-WeM12 Application of Helium Ion Microscope on Semiconductor Surface Imaging and Metrology, H.X. Guo, National Institute for Materials Science, Japan, H. Itoh, National Institute of Advanced Industrial Science and Technology (AIST), Japan, K. Onishi, T. Iwasaki, D. Fujita, National Institute for Materials Science, Japan** Scanning electron microscope (SEM) has been used in the semiconductor surface imaging and metrology for more than 50 years. Now, a new tool, Helium ion microscope (HeIM), is developed and applied to this work. SEM and HeIM are the same in some fundamental characteristics. But, the latter has advantages in smaller probe size, higher resolution, and greater depth of field. These abilities enhance the performance of the HeIM in the semiconductor surface imaging and metrology, such as imaging of low- k materials [1] and measurement of critical dimension of the semiconductor devices [2].

A standard sample for scanning probe microscope tip characterization [3, 4] was measured by using HeIM and atomic force microscope (AFM) as shown in Fig. 1 and Fig. 2. Line profile of the HeIM image in Fig. 1 shows high accuracy in edge definition of the sample. The contrast of the image is related to morphology and materials of the sample [5], the probe size of the Helium ion beam, direction of the sample and beam, charge distribution, and so on. All the aspects will be analyzed in our presentation. The AFM image of the sample shown in Fig. 2 is a dilation of the real surface topography of the sample due to the finite-size AFM tip [6]. With an erosion algorithm, the surface of the sample was reconstructed to be compared with HeIM measurement.

[1] S. Ogawa, W. Thompson, L. Stern, L. Scipioni, J. Notte, L. Farkas, and L. Barriss, Jpn. J. Appl. Phys., 49, 04DB12(2010)

[2] M. T Postek, A. Vladar, C. Archie and B. Ming, Meas. Sci. Technol., 22, 024004 (2011)

[3] H. Itoh, C. Wang, H. Takagi, Proc. of SPIE, 7971, 79711A-1, (2011).

[4] H. Takenaka, M. Hatayama, H. Ito, T. Ohchi, A. Takano, S. Kurosawa, H. Itoh, and S. Ichimura, Journal of Surface Analysis, 17, 264, (2011).

[5] Y. Sakai, T. Yamada, T. Suzuki, T. Sato, H. Itoh, and T. Ichinokawa, Appl. Phys. Lett., 73, 611 (1998)

[6] M. Xu, D. Fujita, and K. Onishi, Rev. Sci. Instrum., 80, 043703 (2009)

Magnetic Interfaces and Nanostructures Division

Room: 105 - Session MI-WeM

Fundamental Problems in Magnetism

Moderator: C. Clavero, College of William and Mary

8:00am **MI-WeM1 Fundamental Problems in Magnetism, W.H. Butler, The University of Alabama** **INVITED**

In this presentation, we shall attempt to describe the fundamental magnetic properties, the physics that controls and limits them and the practical implications of possible improvement. The most important fundamental properties of magnetic materials are Curie temperature, saturation magnetization, and magnetic anisotropy. The maximum Curie temperature (Co) and maximum saturation magnetization (Fe₆₅Co₃₅) at room temperature have not increased in a century. We shall discuss the reasons for this and speculate on the prospects that either may be increased. The magnetic anisotropy is somewhat less refractory. We shall discuss the prospects and implications of significant increases. Although higher room temperature saturation magnetization would be very useful, there would also be interesting applications for a magnetic material with very low

magnetization, but very strong spin dependence of its transport properties. There are also interesting potential applications for insulating ferromagnets.

8:40am **MI-WeM3 Progress toward Understanding the Sign of Spin-Polarization at Interfaces in Organic Spin-Valves**, *G.J. Szulczewski*, University of Alabama

In this talk I will present results from a systematic study to understand the role of LiF, Al₂O₃, and MgO tunnel barriers in organic spin-valves. The overall aim of this work is to better quantify the degree of spin-polarized electron injection and extraction at ferromagnetic metal/organic semiconductor interfaces. In general we find that spin-valves made with two ferromagnetic transition metals has a positive magnetoresistance. However, when one of the ferromagnetic metals is exchanged with La_{0.67}Sr_{0.33}MnO₃, the sign of the magnetoresistance is inverted. In addition the spin-polarized tunneling measurements the structural, electronic, and magnetic properties of these interfaces have been thoroughly investigated by cross-sectional transmission microscopy, photoelectron spectroscopy, and polarized neutron reflectometry. These results will be compared to other findings in the literature in order to summarize the current status of spin-polarized electron transport across organic semiconductor/insulator/ferromagnetic metal interfaces.

9:00am **MI-WeM4 Rational Design of New Spintronics Materials: From Topological Insulators and Spin Torque Applications**, *C. Felser*, Johannes Gutenberg University Mainz, Germany **INVITED**

Heusler compounds are a remarkable class of intermetallic materials with 1:1:1 (often called Half-

Heusler) or 2:1:1 composition comprising more than 1500 members [1]. Today, more than a century after their discovery by Fritz Heusler, they are still a field of active research. New properties and potential fields of applications emerge constantly; the prediction of topological insulators is the most recent example [2]. Surprisingly, the properties of many Heusler compounds can easily be predicted by the valence electron count or within a rigid band approach. Their extremely flexible electronic structure offers a toolbox which allows the realization of demanded but apparently contradictory functionalities based on a virtual lab approach. The subgroup of more than 250 semiconductors is of high relevance for the development of novel materials for energy technologies. Their band gaps can readily be tuned from zero to 4 eV by changing the chemical composition. Thus, great interest has been attracted in the fields of thermoelectrics and topological insulator research. Ternary materials based on multifunctional properties, i.e. the combination of two or more functions such as superconductivity and topological edge states will revolutionize technological applications. The design scheme for topological insulators from the view point of bands and bond will be presented.

The wide range of the multifunctional properties of Heusler compounds is reflected in extraordinary magneto-optical, magneto-electronic, and magneto-caloric properties. Tetragonal Heusler compounds Mn₂YZ as potential materials for STT applications can be easily designed by positioning the Fermi energy at the van Hove singularity in one of the spin channels [3]. A high calculated magnetic anisotropy energy (MAE) is the sufficient condition for a material with perpendicular magnetocrystalline anisotropy (PMA). Materials with saturation magnetizations of 0.2 – 4.0 μ_B, high Curie temperatures of 380 – 800 K, high spin polarizations, PMA, and required lattice constant matching with MgO can be realized with ferri- or ferromagnetic Heusler-related compounds. Such materials are strongly recommended for the spin transfer torque magnetic random access memory (STT-MRAM) data storage and the spin torque oscillators (STO) for telecommunication. Additionally the first spin gapless semiconductor is realized in Mn₂CoZ.

9:40am **MI-WeM6 Interfacial Effect on the Magnetic Properties of Core-Shell Co/Pt Supported Nanodots**, *P. Campigilo, N. Moreau, V. Repain, C. Chacon*, Lab. Mat. et Phénomènes Quantiques, France, *H. Bulou, F. Scheurer*, Inst. de Phys. et Chimie des Mat. de Strasbourg, France, *P. Ohresser*, Synchrotron SOLEIL, France, *H. Maignan*, Service de Phys. et Chimie des Surfaces et Interfaces, France, *E. Fonda*, Synchrotron SOLEIL, France, *J. Lagoute, Y. Girard*, Lab. Mat. et Phénomènes Quantiques, France, *C. Goyhenex*, Inst. de Phys. et Chimie des Matériaux de Strasbourg, France, *S. Rousset*, Lab. Mat. et Phénomènes Quantiques, France

Core-shell nanoparticles have been receiving an increasing attention in order to practically employ magnetic clusters in devices [1]. The shell permits to protect the magnetism of the core, which readily oxidize in environmental conditions. Moreover, the shell can donate to the particle new chemico-physical functionalities which, combined with magnetism, permit to obtain multifunctional systems. Cobalt self-organized supported nanodots are promising candidates for applications as very high density magnetic recording media. However, it is necessary to improve the

magnetic stability of such small nanostructures against thermal excitations. The capping with a non-magnetic metal of magnetic nanostructures induces different interfacial phenomena which together lead to a modification of the magnetic behavior of the system.

In the present work, the growth and the magnetism of Co/Pt core-shell have been studied. Pt has been deposited as over layer on Co self-organized on Au(111) template. The structural properties have been addressed by combining Scanning Tunneling Microscopy (STM) and Surface Extended X-ray Absorption Fine Structure (SEXAFS) measurements with molecular dynamics calculations. Magneto-Optic Kerr Effect (MOKE) and X-ray Magnetic Circular Dichroism (XMCD) have been coupled in order to identify the main magnetic phenomena acting at the Co/Pt interface. In the submonolayer regime, Pt forms metal rims around Co nanodots, and the Co magnetic anisotropy decreases. On the other hand, if more than one monolayer of Pt is deposited, the Co dots are completely covered and their magnetic anisotropy is enhanced. Furthermore, the Pt capping is found to have a minor effect of the cobalt magnetic moments. By changing the deposition conditions and by comparing the effect of Pt and Au capping [2], we identified three principal phenomena at the Co/Pt interface: intermixing, magnetoelasticity and band hybridization. Our results indicate that the principal one is band hybridization, which is responsible for the observed increasing of magnetic anisotropy. Intermixing and magnetoelasticity have rather the opposite effect and tend to decrease the magnetic anisotropy energy. The knowledge of the interplay between these different phenomena is fundamental in order to tune the magnetic properties of nanoparticles for precise applications, from data storage to biomedical research.

[1] A. Lu, E. Salabas, and F. Schüth, *Angew. Chem. Int. Ed.* 46, (2007) 1222.

[2] Y. Nahas, V. Repain, C. Chacon, Y. Girard, J. Lagoute, G. Rodary, J. Klein, S. Rousset, H. Bulou, and C. Goyhenex, *Phys. Rev. Lett.*, 103 (2009) 067202.

10:40am **MI-WeM9 Spin-Split Bands in Non-Magnetic Systems**, *E. Vescovo*, Brookhaven National Laboratory **INVITED**

For fundamental and technological reasons materials with a spin-split electronic band structure in proximity of the Fermi level are highly attractive. The possibility of separately manipulating the two spin channels introduces novel functional behaviors without counterpart in the corresponding spin-degenerate systems. A promising approach in this field consists in the exploitation of the spin-orbit interaction, which couples spin and orbital degrees of freedom. The Rashba interaction offers particularly interesting perspectives: at the surface of a crystalline material the breaking of the full translational symmetry gives rise to an effective (Rashba) electric field which splits in k-space the valence electrons with opposite spin orientations. For heavy elements, such as Bi, the Rashba interaction results in spin-polarized surface bands, detectable in angle-resolved photoemission experiments [1]. In this talk various cases of such systems will be presented. Bi-Ag(110) surface alloy allows to study the anisotropy of splitting induced by the anisotropic electric fields of the (110) – surface. The system Bi-Ag(111)/ Fe(110) provides direct evidence of the interplay between the Rashba splitting of the Bi-Ag alloy and the ferromagnetic splitting of the Fe bands.

[1] Yu. M. Koroteev, G. Bihlmayer, J. E. Gayone, E. V. Chulkov, S. Blügel, P. M. Echenique, and Ph. Hofmann, *Phys. Rev. Lett.* 93, 046403 (2004); T. Hirahara, T. Nagao, I. Matsuda, G. Bihlmayer, E. V. Chulkov, Yu. M. Koroteev, P. M. Echenique, M. Saito, and S. Hasegawa, *Phys. Rev. Lett.* 97, 146803 (2006).

11:20am **MI-WeM11 Unoccupied Electron States in Rashba Systems Studied by Spin-Resolved Inverse Photoemission**, *M. Donath*, *S.N.P. Wissing*, *A. Zumbülte*, *C. Eibl*, *A.B. Schmidt*, Muenster University, Germany

We present the first spin-resolved inverse-photoemission measurements of the unoccupied part of the Rashba-split surface state on Au(111). This Shockley-type state is considered as the prototype of a Rashba-split electron state on a metallic surface. The spin splitting of the occupied part of this state was first indicated by spin-integrated photoemission data [1]. This pioneering work was followed by a spin-resolved study, which directly proved the spin structure of the state [2].

Our study complements the information on the spin character by following the surface state into the unoccupied energy region. The state crosses the Fermi energy as a function of the wave vector parallel to the surface and finally leaves the bulk-band energy gap. Our spin-resolved inverse-photoemission experiment stands out from conventional systems thanks to an improved energy and **k** resolution [3]. Our data confirm the spin character of the surface state, as far as it does not overlap with bulk states.

In addition, we show how the spin character is altered when the surface state becomes degenerate with bulk states.

Further Rashba systems with even larger spin splittings as well as topological insulators are currently investigated with our spin-resolved inverse-photoemission apparatus. We will provide a status report on our latest results.

- [1] LaShell *et al.*, Phys. Rev. Lett. **77**, 3419 (1996)
- [2] Hoesch *et al.*, Phys. Rev. B **69**, 241401(R) (2004)
- [3] Budke *et al.*, Rev. Sci. Instrum. **78**, 083903 (2007)

11:40am **MI-WeM12 MBE Growth of Topological Insulator Bi₂Se₃ on Epitaxial Graphene on 6H-SiC(0001)**, *Y. Liu**, *M. Weinert*, *L. Li*, University of Wisconsin-Milwaukee

In this work, we report results on the MBE growth of Bi₂Se₃, a prototypical topological insulator, on epitaxial graphene on 6H-SiC(0001). In situ scanning tunneling microscopy indicates spiral growth, characterized by atomically smooth terraces 10 to 50 nm in width, separated by steps of 1-2 quintuple-layers in height. X-ray diffraction shows only the (003) family of diffraction peaks with a full width at half maximum of 0.1 degree. Raman spectroscopy reveals two characteristic peaks at 130.21 and 171.48 cm⁻¹, corresponding to the in-plane Eg2 and out-of-plane A1g2 vibrational modes, respectively. The close resemblance of the positions and line shapes of both these peaks to those of bulk Bi₂Se₃ attest to the very high quality of the film. These results and their impact on the properties of the topologically protected surface states of the Bi₂Se₃/graphene heterostructure will be presented at the meeting.

*Ying Liu applied for postdoctoral fellow award

Nanomanufacturing Science and Technology Focus Topic

Room: 111 - Session NM+AS+MS-WeM

Nanomanufacturing Issues: Metrology and Environmental Concerns

Moderator: J. Johnson, University of Tennessee Space Institute, W. Collins, Fisk University

9:00am **NM+AS+MS-WeM4 Particle Characterization Issues in Evaluating the Toxicity and Environmental Impact of Manufactured Nanomaterials**, *K.W. Powers*, University of Florida

Nanostructured materials and nanoparticles promise to revolutionize many key areas of science and technology, however, the environmental effects of nanomaterial enabled products need to be considered throughout their lifecycle, from manufacture to environmental disposal. As nanomaterials become more commonplace in commercial applications, there is a need to assess the potential health and safety effects on human and other biological organisms. Materials at the nanoscale often possess properties that are different from the equivalent bulk or molecular scale. It is clearly shortsighted to assume that toxicological profiles of nanomaterials are the same as in the bulk or molecular forms. As they address these issues, toxicologists often need assistance in understanding and accommodating many of the unique attributes of nanoscale materials as they begin to assess potential health and environmental effects. Though the interpretation of the biological markers of toxicity are well developed, there are a number of issues relating to dosage, size, shape, detection and characterization that are problematic. There is a growing consensus that the complexity of these issues requires a multidisciplinary approach to nanoparticle toxicology that includes medical personnel, environmental and physical scientists as well as engineers trained in particle technology.

Keywords: nanoparticles, nanocharacterization, nanotoxicology, toxicity,

9:40am **NM+AS+MS-WeM6 Sampling for Airborne Nanoparticles and Selecting Respiratory Protection**, *S.M. Hays*, Gobbell Hays Partners, Inc., *J.R. Millette*, MVA Scientific Consultants

As the manufacture and use of nanomaterials continue to increase, appropriate questions are raised about the release of airborne nanoparticles into the general environment and specifically into the breathing zone of people. The development of monitoring procedures specific to carbon

nanotubes and other nanoparticles is crucial in determining the effectiveness of engineering controls and personal protection. This presentation will review experiments conducted to determine the efficacy of using asbestos air sampling methodology for sample collection with standard membrane filter cassettes and analysis using transmission electron microscopy (TEM). Tests done to evaluate the use of cartridge style respirator filters in carbon nanotube aerosols will also be presented. These laboratory tests will be discussed in relation to air samples collected in a variety of actual field use situations. Proposed methodology for the analysis for nanotubes in settled dust will be presented. Finally, one author is chairing an ASTM committee that is developing a consensus method to collect and analyze airborne nanotubes. The current state of that committee's work will be summarized.

10:40am **NM+AS+MS-WeM9 Local Probes Enabling Science and Manufacturing**, *D.A. Bonnell*, University of Pennsylvania **INVITED**

The last decade has witnessed significant advances in measuring nanoscale phenomena. These advances have enabled scientific discovery and provided a framework to support some nanomanufacturing processes. Nevertheless, both scientific advance and to a greater extent manufacturing are limited by our current capabilities in nanoscale metrology. This talk will highlight some of the exciting advances in probe based metrology, project future developments and outline the challenges that are critical to realizing a robust nanomanufacturing sector. The outcome of a recent global assessment of Nano Metrology will also be summarized.

11:20am **NM+AS+MS-WeM11 The Influence of Surrounding Materials on the Optical Properties of Nanoscale Films: An Unforeseen Complication in Nanoscale Metrology**, *A.C. Diebold*, *V.K. Kamineni*, University at Albany

Optical measurement of film thickness requires knowledge of the complex refractive index (dielectric function) of each material in the film stack. Practical experience has shown that the dielectric function changes with film thickness for many poly crystalline metal films and single crystal semiconductor layers. (1, 2) Previous studies pointed to quantum confinement induced changes in the dielectric function of thin silicon nanofilms between 10 nm and 2 nm. Extra Thin silicon on insulator (ET-SOI) films were used for this study. These films are often referred to as crystalline silicon quantum wells (c-Si QW). Our most recent study shows that the dielectric function of c-Si QWs can be further altered by the presence of a dielectric layer above the nano silicon top layer.(3) Based on an elastic theory description of the acoustic phonon modes, the dielectric function of the c-Si QWs is found to be strongly influenced by electron – phonon scattering. We illustrate this point using low temperature measurements of the dielectric function of a series of c-Si QWs and by comparing room temperature measurements of the dielectric function of 5 nm c-Si QWs with native oxide, 10 nm SiO₂, and 10 nm HfO₂.

1. Observation of quantum confinement and quantum size effects, A.C. Diebold and J. Price, Phys. Stat. Sol. (a) **205**, No. 4, (2008), pp 896–900.
2. Optical Metrology of Ni and NiSi thin films used in the self-aligned silicidation process, V. K. Kamineni, M. Raymond, E. J. Bersch, B. B. Doris, A. C. Diebold, J. Appl. Phys., **107**, (2010), pp 093525 1-8.
3. Evidence of phonon confinement effects on the direct gap transitions of nanoscale Si films, V.K. Kamineni and A.C. Diebold, submitted

Nanometer-scale Science and Technology Division Room: 203 - Session NS-WeM

Carbon-Based Nanomaterials

Moderator: M.C. Hersam, Northwestern University

8:00am **NS-WeM1 Characterization of Large Area Graphene Crystallites Grown on Cu Foil Substrates**, *P. Tyagi*, *Z.R. Robinson*, *H. Geisler*, *C.A. Ventrice, Jr.*, University at Albany, *H. Yang*, *T. Valla*, Brookhaven National Laboratory, *Y. Hao*, *R.S. Ruoff*, University of Texas at Austin

Graphene growth on Cu foils by catalytic decomposition of methane forms predominately single layer graphene films due to the low solubility of carbon in Cu. One of the key issues for the use of CVD graphene in device applications is the influence of defects on the transport properties of the graphene. In particular, the presence of grain boundaries within the graphene film will increase the probability for scattering of carriers, resulting in reduced mobilities. Therefore, an important goal is to develop techniques for growing graphene films with crystallites that have lateral dimensions of a few millimeters or larger. There are several factors that influence the size and orientation of the graphene crystallites such as the size and orientation of the grains within the metal foil, temperature

* Postdoc Award Finalist

gradients during growth, the hydrocarbon source pressure, and the growth temperature. By growing the graphene films using methane source pressures less than 50 millitorr, preanneal times of approximately an hour, growth temperatures of 1035 °C, and a tented Cu substrate geometry within a conventional tube furnace, graphene crystallites larger than a millimeter in size have been achieved.

Measurements of the graphene growth morphology and surface topography of the Cu substrate have been performed using scanning electron microscopy (SEM). The graphene crystallites show a dendrite pattern, and the Cu substrate typically shows a somewhat faceted structure at this growth temperature. Low energy electron diffraction (LEED) measurements show sharp diffraction spots but with multiple zero-order reflections, which results from the faceted structure of the Cu substrate after growth. Electron backscatter diffraction (EBSD) measurements have been performed on the Cu substrates to determine the crystallographic orientation and size of the substrate grains. Before growth, the average grain size is ~10 μm with a random orientation. After growth, the Cu substrate grain size is on the order of centimeters with a typical orientation towards the {100} surface termination. Synchrotron-based angle-resolved ultraviolet photoelectron spectroscopy (ARUPS) measurements have also been performed to probe the electronic band structure of the graphene. A linear dispersion has been measured in the K direction with the Dirac point located near the Fermi level.

8:20am NS-WeM2 Gas Adsorption on Pt-Clusters Supported by Graphene, J. Knudsen, Lund University, Sweden, *T. Gerber*, University of Cologne, Germany, *E. Graanäs*, Lund University, Sweden, *P.J. Feibelman*, Sandia National Laboratories, *K. Schulte*, Lund University, Sweden, *P. Stratman*, *C. Busse*, *T. Michely*, University of Cologne, Germany, *J.N. Andersen*, Lund University, Sweden

Model systems of real catalysts consisting of nanoparticles deposited on substrates often have a broad size distribution, making it difficult to link the adsorption properties to the atomic scale structure of the nanoparticles using averaging techniques. Metal nanoparticles grown on a graphene/Ir(111) moiré film, however, show exceptionally well ordered arrays of nanoparticles with an extremely narrow size distribution [1, 2]. Further, it is possible to control the cluster size precisely by adjusting the amount of deposited material, since each moiré unit cell contains one cluster. The narrow size distribution and the easy control of cluster size make metal particles supported by graphene an ideal model system for adsorption studies with averaging techniques.

In this contribution we report on our studies on CO adsorption on such an ideal model system consisting of Pt-clusters grown on a graphene/Ir(111) moiré film using photoemission X-ray spectroscopy (XPS), scanning tunnelling microscopy (STM), and density functional theory (DFT) [3].

For Pt/graphene without CO we observe pinning of the graphene film, as a shoulder at the high binding energy side of the C 1s peak observed for pristine graphene. DFT calculations reveal that this shoulder should be assigned to carbon atoms positioned below and in the vicinity of the Pt clusters, which all are displaced towards the Ir(111) surface.

Upon CO adsorption we observe C 1s and the O 1s peak positions consistent with preferential adsorption in atop sites at the cluster step edges. We also observe that the pinning-induced shoulder in the C 1s spectrum diminish upon CO adsorption, and interpret this as unpinning of the graphene film when CO adsorbs on the clusters step edges. From real time STM movies taken during CO dosing we show that the unpinning of the graphene film leads to coalescences of the Pt clusters, when the clusters are smaller than approximately 10 atoms.

References:

- [1] A. T. N'Diaye, S. Bleikamp, P. J. Feibelman, et al., *Phys. Rev. Lett.* **97** (2006)
- [2] A. T. N'Diaye, T. Gerber, C. Busse, et al., *New Jour. Phys.* **11** (2009)
- [3] J. Knudsen, P. J. Feibelman, T. Gerber, E. Grånäs, K. Schulte, P. Stratman, C. Busse, J. N. Andersen, T. Michely (in manuscript)

8:40am NS-WeM3 Seeding Atomic Layer Deposition of High-k Dielectrics on Epitaxial Graphene with Organic Self-Assembled Monolayers, J.M.P. Alaboson*, *Q.H. Wang*, *J.D. Emery*, *A.L. Lipson*, *M.J. Bedzyk*, Northwestern University, *J.W. Elam*, *M.J. Pellin*, Argonne National Laboratory, *M.C. Hersam*, Northwestern University

The development of high-performance graphene-based nanoelectronics requires the integration of ultrathin and pinhole-free high-*k* dielectric films with graphene at the wafer scale. Here, we demonstrate that self-assembled monolayers of perylene-3,4,9,10-tetracarboxylic dianhydride (PTCDA) act as effective organic seeding layers for atomic layer deposition (ALD) of

HfO₂ and Al₂O₃ on epitaxial graphene on SiC(0001). The PTCDA is deposited via sublimation in ultra-high vacuum and shown to be highly ordered with low defect density by molecular-resolution scanning tunneling microscopy. Whereas identical ALD conditions lead to incomplete and rough dielectric deposition on bare graphene, the chemical functionality provided by the PTCDA seeding layer yields highly uniform and conformal films. The morphology and chemistry of the dielectric films are characterized by atomic force microscopy, ellipsometry, cross-sectional scanning electron microscopy, and X-ray photoelectron spectroscopy, while high-resolution X-ray reflectivity measurements indicate that the underlying graphene remains intact following ALD. Using the PTCDA seeding layer, metal-oxide-graphene capacitors fabricated with a 3 nm Al₂O₃ and 10 nm HfO₂ dielectric stack show high capacitance values of ~700 nF/cm² and low leakage currents of ~5 × 10⁻⁹ A/cm² at 1 V applied bias. These results demonstrate the viability of sublimated organic self-assembled monolayers as seeding layers for high-*k* dielectric films in graphene-based nanoelectronics.

9:00am NS-WeM4 Graphene-based Electronics and Optoelectronics, Ph. Avouris†, IBM T.J. Watson Research Center **INVITED**

Graphene a two-dimensional, single atomic layer material with linear electron dispersion has rather unique electrical and properties¹. There is currently strong interest in taking advantage of these properties for technological applications². In my talk I will review some of the key properties of graphene, how these are affected by environmental interactions and how they can be utilized in electronics and optoelectronics.

Specifically, I will discuss high frequency (>100 GHz) graphene transistors^{3,4}, their fabrication and operation, as well as related device physics aspects, such as carrier transport mechanisms, electrical contacts, temperature effects, energy dissipation, etc. Simple integrated graphene circuits will also be presented. I will then discuss key optical properties of graphene and how they can be combined with its excellent electrical properties and used in optoelectronics applications. Specific examples involving ultrafast graphene photodetectors⁵ and their applications in the detection of optical data streams⁶ will be presented.

[1] Geim, A.K. *Science* **3**, 1530 (2009).

[2] Avouris, Ph., *Nano Letters* **10**, 4285 (2010).

[3] Lin, Y.-M.; Dimitrakopoulos, C.; Jenkins, K.A.; Farmer, D.B.; Chiu, H.-Y.; Grill, A.; Avouris, Ph. *Science* **327**, 662 (2010);

[4] Wu, Y.; Lin, Y.-M.; Bol, A.; Jenkins, K.; Xia, F.; Farmer, D.; Zhu, Y.; Avouris, Ph., *Nature*, on-line April 6 (2011).

[5] Xia, F.; Mueller, T.; Lin, Y.-M.; Valdes-Garcia, A.; Avouris, Ph. *Nature Nanotechnology* **4**, 839 (2009).

[6] Mueller, T.; Xia, F.; Avouris, Ph. *Nature Photonics* **4**, 297 (2010).

9:40am NS-WeM6 Plasma-based Approach to Controlling the Properties of Graphene, S.C. Hernández, *M. Baraket*, *S.G. Walton*, *W.K. Lee*, *C.R. Tamanaha*, *P.E. Sheehan*, *J.T. Robinson*, *V.D. Wheeler*, *R.L. Myers-Ward*, *L.O. Nyakiti*, *Eddy*, *D.K. Gaskill*, Naval Research Laboratory (NRL)

Graphene has attracted a widespread of interest because of its unique structural and electronic properties however, manipulation of these properties is necessary before realizing its full potential as the next generation material in a broad range of electronic and sensing applications. Specifically, tailoring the surface chemistry of graphene by the addition of functional groups is an attractive way to simultaneously manage the conductivity and reactivity of this material. This work discusses the use of electron-beam generated plasmas to controllably functionalize graphene synthesized from different methods. Electron-beam generated plasmas, produced in a variety of background gases (e.g. N₂, O₂, SF₆, NH₃) were used to introduce functional groups in a range of atomic densities at the graphene surface, without damage to the underlying graphene structure. Plasma processing conditions and characteristics, as well as the resulting chemical, structural, and electrical properties of the functionalized graphene were examined. This work is supported by the Office of Naval Research.

10:40am NS-WeM9 Solution Plasma-Assisted Surface Functionalization of Chemically Converted Graphene Sheet toward an Enhancement of Solubility in Solution, N. Tsuda, *T. Ueno*, *N. Zetsu*, *S. Cho*, *O. Takai*, *N. Saito*, Nagoya University, Japan

Graphene, a one-atom layer of graphite, possesses a unique two-dimensional structure and excellent mechanical, thermal, and electrical properties. Thus, it has been regarded as an important component for making various functional composite materials. Graphene can be prepared through micromechanical exfoliation, epitaxial growth, and chemical vapor

* NSTD Student Award Finalist

† NSTD Recognition Award

deposition and electrochemical approaches. Different from these approaches, chemical synthesis of graphene using graphite, graphite oxide (GO) or other graphite derivatives as starting materials were tested to be effective for producing chemically converted graphene (CCG) from various precursors, such as graphite, carbon nanotubes, and polymers, in large scale and at low costs. Therefore, CCG is more suitable for synthesizing high-performance graphene based composites.

Graphene oxide can be chemically reduced to CCG. Hydrazine monohydrate was most widely used, mainly due to its strong reduction activity and the stability in aqueous media. Upon reduction with hydrazine, most oxygen-containing functional groups of graphene oxide are eliminated and the π -electron conjugation within the aromatic system of graphite is partially restored. As a result, the reduced graphene oxide (or CCG) is usually precipitated from the reaction medium because of the recovered graphite domains of CCG sheets increased their hydrophobic property and π -stacking interaction. The use of hydrazine as reducing agent also has several disadvantages. The trace residual may strongly decrease the performance of CCG in devices.

In this work, we demonstrate solution plasma-assisted surface functionalization of chemically converted graphene sheet in order to enhancement of solubility in both aqueous and organic solvent. Solution plasma (SPP) is a plasma discharge in solution, which is expected a higher reaction rate under low-temperature conditions, and the greater chemical reaction variability since the molecular density of liquid is much higher than that of gas phase.

A colloidal graphene oxide sheets was treated with SP in ammonium containing aqueous solution in order to make reduced CCG and functionalize CCG surface with primary amine group. A glow discharge was produced at bipolar-pulsed voltages with pulse width and frequency of 2 ms and 15 kHz, respectively. The all products were characterized by IR, Raman, spectroscopy, AFM, XRD, and TEM. Furthermore, we also demonstrate an introduction of organic and polymeric molecule as a second component onto the aminated CCG surface to insulate hydrophobic property and π -stacking interaction of neighboring CCG sheets in aqueous solution, and to be organic solvent solubilization.

11:00am NS-WeM10 Horizontally Aligned Carbon Nanotubes on Quartz Substrate for Electrolyte-Gated Chemical and Biological Sensing. S. Okuda, Y. Ohno, K. Maehashi, K. Inoue, K. Matsumoto, Osaka University, Japan

Electrolyte-gated carbon nanotube field-effect transistors (CNTFETs) based highly sensitive chemical and biological sensors were demonstrated. Dense, well-aligned CNTs grown on quartz substrates were utilized as channels of CNTFETs. Using the large number of CNTs is a simple strategy to realize excellent performance of CNTFETs. First, the pH dependence of CNTFETs was measured in buffer solution ranging from pH 4.0 to 8.3 by monitoring the drain current (I_D) in the CNTFET. Clearly and stepwise increases in I_D were observed against the change in pH in the solution. The detection limit for changes in pH was estimated to be 0.015, which is a superior characteristic to that of conventional CNTFETs. The result indicates that CNTFETs on quartz substrates can be used as highly sensitive pH sensors. Moreover, label-free biomolecule sensing was demonstrated. The target protein was a class of antibody, immunoglobulin E (IgE). To achieve the electric detection of IgE, we used aptamer-modified CNTFETs with multichannel. Then, binding event of target IgE onto the aptamers was detected. IgE-concentration dependence measurements revealed that we succeeded in detection of nM quantities of IgE. In conclusion, electrolyte-gated multichannel CNTFETs will be useful for highly sensitive chemical and biological sensors.

11:20am NS-WeM11 Gas-phase Studies and Growth of Well-Defined Carbon Nanotubes. A. Kumar, P. Lin, R.M. Sankaran, Case Western Reserve University

Carbon nanotubes (CNTs) have attracted interest for a wide-range of technological applications including nanoelectronic, energy storage, and energy conversion devices. In many of these applications, the nanotube structure must be sufficiently controlled at the growth stage; however, current growth methods typically produce mixtures of tubes, including multi-walled, single-walled, and a range of different chiralities, that must be purified and separated to facilitate applications.

We are interested in controlling the properties of CNTs at the growth stage. We have recently developed a two-step process [1-3] to study and grow CNTs consisting of a microplasma reactor that controls the size- and composition of the nanoparticle catalysts and a flow furnace that nucleates and grows the nanotubes. In addition, the nanotubes are monitored *in situ* by aerosol measurements to provide real-time feedback and allow the reactor conditions to be rapidly optimized. By tuning the size of our catalyst, we have found that the fraction of single-walled CNTs in the as-

grown product can be varied. Similarly, by tuning the composition of the catalyst, we have found that the chirality distribution of the as-grown nanotubes is changed. Here, we will present results for Ni-based bimetallic catalysts and the influence of the catalyst size and composition, as well as other growth parameters such as carbon feedstock and growth temperature, on nanotube growth. In addition to aerosol measurements, the nanotubes are collected and characterized by micro Raman spectroscopy and UV-Vis-NIR absorbance spectroscopy. The structure and properties of the nanotubes and their relationship to the catalyst and other growth parameters will be discussed in detail.

1. W-H. Chiang et al., Appl. Phys. Lett. 91, 121503 (2007).
2. W-H. Chiang et al., J. Phys. Chem. C 112, 17920 (2008).
3. W-H. Chiang et al., Nat. Mater. 8, 882 (2009).

11:40am NS-WeM12 Visualizing Defect Distributions in Carbon Nanotubes using Linear Dichroism Signals in Scanning Transmission X-ray Microscopy (STXM) and TEM-EELS. E. Najafi, A.P. Hitchcock, D. Rossouw, G. Botton, McMaster University, Canada

The X-ray Linear Dichroism (XLD) signal in spatially resolved X-ray absorption spectromicroscopy of individual carbon nanotubes (CNT) [1] has been shown to be sensitive to the local density of sp^2 defects along the nanotube. This dichroic signal is as strong for single-walled [2] as for multi-walled CNT, which is rather surprising given the much higher curvature in SWCNT than MWCNT. The link between the strength of the XLD of the C 1s $\rightarrow \pi^*$ peak at 285.2 eV and defect density within the sampled area has been verified by intentionally inducing sp^2 defects by ion bombardment [3]. This XLD signal is potentially useful for guiding optimization of CNT synthesis and preservation of the quality of nanotubes through various processing steps used to make functional devices where defect distribution and character play an important role. However STXM has limited spatial resolution; 10 nm, state-of-art while this work was performed at ~ 25 nm. Recently we have demonstrated that Electron Linear Dichroic (ELD) signals similar to XLD can be measured in q-dependent C 1s electron energy loss spectroscopy carried out in an aberration compensated, monochromated transmission electron microscope. The signals are detected by operating in STEM mode, carefully arranging the conditions such that the spectrometer accepts a narrow range of off-axis scattered electrons (with a specific location, identified in diffraction mode), and using a tilt stage to change the orientation of the CNT relative to the incident and outgoing electron directions. STEM-EELS maps measured with 2 nm sampling over a portion of a MWCNT, and over a range of tilt angles provide quantitative maps of the ELD signal. The experimental conditions will be described and the defect mapping capability of this method will be demonstrated.

STXM measurements were carried out at the SM beamline at the Canadian Light Source, which is supported by the Canada Foundation for Innovation (CFI), NSERC, Canadian Institutes of Health Research (CIHR), National Research Council (NRC) and the University of Saskatchewan. We thank Chithra Karunakaran, Jian Wang and Martin Obst for their expert support of the CLS STXM. TEM-EELS was performed with the Titan-1 system of the Canadian Centre for Electron Microscopy which is supported by CFI and NSERC.

- [1] E. Najafi, D. Hernández Cruz, M. Obst, A. P. Hitchcock, B. Douhard, J.J. Pireaux, A. Felten, Small, 2008, 4, 2279–2285.
- [2] E. Najafi, J. Wang, A.P. Hitchcock, J. Guan, S. Denommee and B. Simard, J. Am. Chem. Soc. 2010, 132, 9020-9029.
- [3] A. Felten, X. Gillon, M. Gulas, J.-J. Pireaux, X. Ke, G. Van Tendeloo, C. Bittencourt, E. Najafi and A.P. Hitchcock, ACSNano 2010, 4, 431–4436

Neutron Scattering Focus Topic Room: 207 - Session NT+AS+MI-WeM

Applications of Neutron Scattering I Moderator: V. Lauter, Oak Ridge National Laboratory

8:00am NT+AS+MI-WeM1 A Deeper Look into Spintronic Material Systems with Neutrons and Synchrotron Radiation. T. Brueckel, Forschungszentrum Jülich, Germany **INVITED**

The discovery of the Giant Magnetoresistance GMR effect triggered the evolution of Spintronics, i.e. information storage, information processing and information transport using the spin of the electron. While the first Spintronic devices were merely transition metal multilayers, the interest has shifted to include transition metal oxide systems, laterally structured films and magnetic nanoparticles. Scattering techniques applied to model systems

are ideal to provide fundamental microscopic information on the spin and domain structure.

In this contribution, we will give an overview highlighting the capabilities of modern neutron and synchrotron x-ray techniques. We will show that neutron scattering under grazing incidence is able to provide unique depth resolved information on magnetization, magnetic correlations and magnetization dynamics relevant for basic and applied research on nanostructured magnetic materials and how synchrotron x-ray scattering can provide complementary element specific information. Examples for current research on patterned metallic multilayers, thin transition metal oxide films and magnetic nanoparticles will be given.

8:40am NT+AS+MI-WeM3 Magnetic Properties of FePtRh Films and Multilayers Studied by Neutron Scattering. *D. Lott, J. Fenske, Helmholtz-Zentrum Geesthacht, Germany, G.J. Mankey, Univ. of Alabama, W. Schmidt, K. Schmalzl, Forschungszentrum Juelich, Germany, E. Tartakowskaya, National Academy of Science, Ukraine, H. Amabye, ORNL, F. Klose, A. Mulders, ANSTO, Menai, Australia, A. Schreyer, Helmholtz-Zentrum Geesthacht, Germany, V. Lauter, ORNL*

Ordered FePt alloys with $L1_0$ structure are known as materials with FM order and a high magnetic moment of Fe providing a large magnetization. The large atomic number of Pt on the other hand results in a high magnetic anisotropy. If grown in thin films, the high anisotropy often results in perpendicular magnetization which is the preferred orientation for current magnetic recording media. One way to control the magnetic properties in these materials is through the introduction of a third element into the crystal matrix e.g. Rh. When Rh is added to replace Pt in the equiatomic alloy, new magnetic phases emerge. Here neutron diffraction studies on the magnetic properties of different thick $Fe_{50}Pt_{50-x}Rh_x$ films in dependence on temperature and external magnetic fields allowed us to investigate the rich phase diagram of the system for thin films, e.g. the transition from the FM to AF state in the system with increasing Rh concentration. In particular films with a Rh concentration of about 10% show a temperature dependent AF-FM transition. From the neutron data it was moreover possible to determine the magnetic configurations in dependence on concentration, temperature and magnetic field on a microscopic scale. Based on the observed results a theoretical model considering the changes in the anisotropies could be developed. In a next step magnetic multilayer consisting of $Fe_{50}Pt_{50-x}Rh_x$ bilayers with different Rh concentrations were grown and studied by polarized neutron reflectivity to investigate the magnetic interactions along the lattice matched interfaces. First results will be presented here.

9:00am NT+AS+MI-WeM4 Spectroscopic and Magnetic Characterization of the Spin-Crossover Transition in Thin Films of $Fe(C_{12}H_8N_2)_2(NCS)_2$. *E.C. Ellingsworth, G.J. Szulcowski, The University of Alabama, Tuscaloosa, V. Lauter, Oak Ridge National Laboratory*
The octahedral complex bis(1,10-phenanthroline)dithiocyanate iron(II), $Fe(phen)_2(NCS)_2$, is known

to exhibit an abrupt transition between a high and low magnetic spin state from 170 – 180 K in the

bulk phase. As a result, $Fe(phen)_2(NCS)_2$ is an interesting organic semiconductor to study charge and

spin transport in thin films. We synthesized and characterized $Fe(phen)_2(NCS)_2$ according to literature

procedures. Thin films of $Fe(phen)_2(NCS)_2$ were made by vapor deposition onto a variety of substrates

including Si, KBr, Au and Al and characterized by infrared and photoelectron spectroscopy, SQUID

magnetometry, optical microscopy, and polarized neutron reflectometry. The films were found to be

very sensitive to water vapor under ambient conditions, which complicates the structural, chemical and

magnetic analysis of the films. However, appropriate capping layers can be deposited onto the

$Fe(phen)_2(NCS)_2$ thin films to protect them from water vapor before removal from the vacuum system. The

differences in the magnetic behavior of the thin films will be compared to the bulk phase.

9:20am NT+AS+MI-WeM5 Nanoscopic Magnetic Phase Separation at the $SrTiO_3(001)/La_{1-x}Sr_xCoO_3$ Interface. *M. Sharma, M.A. Torija, Univ. of Minnesota, J. Gazquez, M. Varela, ORNL, J. Schmitt, C. He, Univ. of Minnesota, J.A. Borchers, M. Laver, NIST, S. El-Khatib, American University of Sharjah, V. Lauter, H. Ambaye, R. Goyette, ORNL, C. Leighton, Univ. of Minnesota*

INVITED

The remarkable functionality of complex oxides, when combined with the favorable lattice matching that is possible at their interfaces, provides many opportunities for new physics and applications. The perovskite manganites and cobaltites are excellent examples, being of interest in gas sensing, catalysis, and as electrodes in ferroelectric memory and solid oxide fuel cells. From the magnetism perspective they have potential for high conduction electron spin polarization, and a variety of functional ground states. However, the same delicate balance between phases that provides such impressive functionality also leads to a serious problem; it can be difficult to maintain desired properties (e.g. high spin polarization and conductivity) close to the interface with a dissimilar oxide. This is exemplified by magnetic tunnel junctions for example, where the interface spin polarization is suppressed and drops rapidly with temperature. In this work, using $SrTiO_3(001)/La_{1-x}Sr_xCoO_3$ [1] as a model system, we have combined epitaxial growth by high pressure oxygen sputtering with atomic-level structural characterization (including STEM/EELS imaging [2]), conventional magnetometry, electronic transport, small-angle neutron scattering, and polarized neutron reflectometry. We observe the usual degradation in magnetization and conductivity in the very thin film limit. We demonstrate that this is due to nanoscopic magnetoelectronic phase separation in the interface region [3]. Essentially, nanoscopic ferromagnetic (FM) clusters form in an insulating non-FM matrix near the interface, resulting in reduced magnetization and conductivity, even at compositions that display no such phase separation in bulk. STEM/EELS depth profiling of the chemical composition reveals that this effect has a chemical origin, being due to subtle depth-wise variations in Sr and O content, resulting in reduced hole doping near the interface. Simple thermodynamic and structural arguments for the origin of these variations are provided, based on Sr dissolution energies and the critical link between strain state and O vacancy concentration provided by O vacancy ordering [2,3].

Work at UMN supported by NSF and DoE (neutron scattering). Work at ORNL supported by DoE. Work at UCM supported by the European Research Council.

[1] Torija, Sharma, Fitzsimmons, Varela, Wu and Leighton, *J. Appl. Phys.* **104** 023901 (2008).

[2] Gazquez, Luo, Oxley, Prange, Torija, Sharma, Leighton, Pantiledes, Pennycook and Varela, *Nano. Lett.* **11** 973 (2011).

[3] Torija, Sharma, Gazquez, Varela, He, Schmitt, Borchers, Laver, El-Khatib, Maranville and Leighton, published online, *Adv. Mater.* (2011).

10:40am NT+AS+MI-WeM9 Study of $L1_0$ Ordering in $^{57}Fe/Pt$ Multilayers. *K. Srikanti, Ugc-Dae, Csr, India*

Ordered $L1_0$ FePt, FePd and CoPt alloy thin films have large magnetic anisotropy constants suitable for high-density recording media. The $L1_0$ ordered phase is obtained with post growth annealing at high temperatures. However, the high temperature annealing leads to grain growth. The present work is an attempt to lower the transition temperature starting with multilayer precursors. The evolution of the structural and magnetic properties of Si(sub) [$^{57}Fe(19\text{\AA})$

]/Pt (25\AA)] $_{x10}$ multilayers as a function of vacuum annealing at different temperatures is studied. The film thickness is selected to have equi-atomic stoichiometry. The multilayers are prepared by ion beam sputtering. X-ray reflectivity (XRR), X-ray diffraction (XRD), and magneto optical Kerr effect (MOKE) and conversion electron Mössbauer spectroscopy (CEMS) are used to characterise the as-deposited and annealed multilayers. Using XRR it is observed that due to intermixing FePt alloy formation takes place with annealing. The XRD indicated the presence of superstructure peaks at 350°C and above. Mössbauer measurements indicated a clear evidence for the strong exchange coupling between the soft fcc FePt and hard fct FePt phase. The results indicate that the multilayer structure does not transform directly to the ordered fct FePt, rather first an fcc FePt phase is formed and subsequently it gets converted in to the fct FePt phase as a function of annealing. A detailed study on stoichiometric FePt system embedded in Carbon matrix prepared by ion beam sputtering technique will also be discussed.

Few preliminary results of polarised neutron reflectivity measurements on FePt/FeNi exchange spring magnets will be discussed.

11:00am **NT+AS+MI-WeM10 Influence of Capping Layer Rigidity on Properties of Supporting Temperature Sensitive Hydrogel Polymers Using Neutron Reflectivity.** *M. Dubey*, Los Alamos National Laboratory, *M.S. Jablin*, Carnegie Mellon University, *M. Zhernenkov*, Los Alamos National Laboratory, *R. Toomey*, University of South Florida, *J. Majewski*, Los Alamos National Laboratory

Temperature sensitive hydrogel polymers are utilized as responsive layers in various applications. While the polymer's native characteristics have been studied extensively, details concerning its properties during interaction with bio-related structures are lacking. This work investigates the interaction between a thermoresponsive polymer cushion and different lipid membrane capping layers probed by neutron reflectometry. N-isopropylacrylamide copolymerized with methacryloylbenzophenone first supported a lipid bilayer composed of 1,2-Dipalmitoyl-*sn*-Glycero-3-Phosphoethanolamine (DPPE) and subsequently 1,2-Dipalmitoyl-*sn*-Glycero-3-Phosphocholine (DPPC). The polymer-membrane systems were investigated above and below the polymer lower critical solution temperature (37 and 25 °C). While the same cushion supported each lipid membrane, the polymer hydration profile and thickness were markedly different for DPPE and DPPC systems. Since DPPE and DPPC have different bending rigidities, these results establish that the polymer-membrane interaction is critically mediated by the mechanics of the membrane, providing better insight into cell-hydrogel interactions. There has been increased interest in the effect of matrix elasticity on cell lineage specification. Polymeric matrices with known stiffness are used as supports to understand the physical effects of *in vivo* tissue microenvironment for therapeutic uses of stem cells. This work focuses on the influence of a capping layer on the mechanical properties of the underlying support.

Plasma Science and Technology Division

Room: 201 - Session PS+SE-WeM

Atmospheric Plasma Processing and Micro Plasmas

Moderator: P.L.S. Thamban, University of Texas at Dallas

8:00am **PS+SE-WeM1 2011 AVS Peter Mark Award Lecture - Microscale, Atmospheric-Pressure Plasmas: A Platform for Nanomaterials Synthesis at Different Length Scales.** *M. Sankaran**, Case Western Reserve University **INVITED**

Large-scale, low-pressure plasmas play an essential role in the processing of materials for a wide-range of applications including integrated-circuit (IC) manufacturing. In recent years, new challenges have arisen for these top-down approaches to materials processing. Advanced electronic devices will be comprised of nanomaterials such as nanoparticles and carbon nanotubes that cannot be fabricated by current plasma technology because of limitations associated with photolithography. In addition, emerging applications in sensors, energy, and medicine require nanomaterials that must be prepared from the "bottom-up" and assembled into macroscale structures. The aim of our research is to develop a new class of plasmas, termed microplasmas, for nanomaterials synthesis and assembly.

Microplasmas are electrical discharges formed in geometries where at least one dimension is less than 1 mm. As a result of their pD scaling (p is the gas pressure and D is the smallest dimension), microplasmas operate stably at atmospheric pressure. These properties open up unique opportunities for nanomaterials synthesis and assembly. For example, vapor-phase metal-organic precursors can be dissociated near ambient conditions to homogeneously nucleate metal [1] and alloyed [2] nanoparticles. The formation of well-defined metal nanoparticles in the gas phase allows direct introduction of these materials as catalysts for chiral-enriched carbon nanotube growth [3]. Recently, we have also coupled microplasmas with liquids to electrochemically synthesize nanoparticles from aqueous metal salts [4]. By extending this strategy to thin films, microscale patterns of nanoparticles are fabricated in a single step [5]. In this talk, I will discuss these topics in detail, highlighting the advantages of microplasma-based systems for the synthesis of well-defined nanomaterials at various length scales.

1. W-H. Chiang and R. M. Sankaran, *Appl. Phys. Lett.* **91**, 121503 (2007).

2. P. A. Lin and R. M. Sankaran, in review.

3. W-H. Chiang and R. M. Sankaran, *Nat. Mater.* , 882 (2009) .

4. C. Richmonds and R. M. Sankaran, *Appl. Phys. Lett.* , 131501 (2008).

S. W. Lee, D. Liang, X. P. A. Gao, and R. M. Sankaran, *Adv. Func. Mater.*, available online: doi: 10.1002/adfm.201100093.

* Peter Mark Memorial Award Winner

8:40am **PS+SE-WeM3 Surface and In-Depth Modification of LDPE using an Atmospheric Plasma Torch.** *S. Abou Rich*, *P. Leroy*, Universite Libre de Bruxelles, Belgium, *N. Wehbe*, University of Namur, Belgium, *N. Avril*, *L. Houssiau*, University of Namur, Belgium, *F. Reniers*, Universite Libre de Bruxelles, Belgium

In order to improve the adherence of a coating onto a polymer, the substrate surface must be properly functionalized. Plasma techniques are more and more used for that purpose. However, plasma treatments do not only modify the polymer surface, as active species can penetrate into its bulk.

In the present study, polyethylene samples are surface-functionalized by an atmospheric plasma torch, using argon and a mixture of argon-oxygen. The surface is characterized by dynamic water contact angle, atomic force microscopy and X-ray photoelectron spectroscopy. The changes in the bulk of the polymer have been characterized using infrared spectrometry, angle-resolved X-ray photoelectron spectroscopy (ARXPS), and secondary ion mass spectrometry (SIMS).

It is shown that both plasma treatments (argon or argon-oxygen) lead to an increase in the hydrophilicity of the surface by the grafting of oxygen-containing polar functions. AFM reveals also a change in surface roughness induced by the plasma treatment, depending on the operational conditions. FTIR, ARXPS and SIMS evidenced that the plasma treatment also modifies a significant zone under the surface. The diffusion depth of oxygen as a function of the plasma parameters (power, treatment time, oxygen ratio in the gas phase) is determined.

The ageing of the plasma-modified polymers during storage in air is also studied

9:00am **PS+SE-WeM4 Surface Analysis of Polymers Treated by Remote Atmospheric Pressure Plasma.** *R.F. Hicks*, University of California Los Angeles, *E. Gonzalez*, Intel Corporation, *T.S. Williams*, University of California Los Angeles

Atmospheric plasma treatment is a key process for improving the adhesive bond strength of polymers in many products, such as thermoplastic composites on jet aircraft and helicopters, molded plastic parts in automobiles, and plastic tubing and stents in implantable medical devices. In this study, the surfaces of high-density polyethylene (HDPE), poly(methyl methacrylate) (PMMA), and polyethersulfone (PES) were treated with a low-temperature, atmospheric pressure oxygen and helium plasma. The polymers were exposed to the downstream afterglow of the plasma, which contained primarily oxygen atoms and metastable oxygen molecules ($^1\Delta_g O_2$), and no ions or electrons. X-ray photoelectron spectroscopy of HDPE revealed that 20% of the carbon atoms were converted into oxidized functional groups, with about half of these being carboxylic acids. Attenuated total reflection infrared spectroscopy of all three polymers was obtained in order to determine the types of functional groups formed by atmospheric plasma exposure. It was found that the polymers were rapidly oxidized with addition of alcohols, ketones, and carboxylic acids to the carbon backbone. Chain scission occurred on HDPE and PMMA, while on PES the aromatic groups underwent ring-opening and insertion of carboxylic acid. The implications of this work for forming strong adhesive bonds to these polymers will be discussed at the meeting.

9:20am **PS+SE-WeM5 Deposition of SiO_x Films by Means of Atmospheric Pressure Microplasma Jets: Study of Deposition Mechanism.** *J. Benedikt*, *R. Reuter*, *D. Ellerweg*, *K. Ruegner*, *T. de los Arcos*, *A. von Keudell*, Ruhr-University Bochum, Germany **INVITED**

Deposition of thin films with plasmas at atmospheric pressure is always a challenging task because of high collision rates, absence of ion bombardment, filamentary behavior of the plasma and limited knowledge of plasma chemistry. The preparation of high quality thin films is therefore still the main domain of low pressure plasmas. One of films, which can be prepared at atmospheric pressure, is SiO₂. Hexamethyldisiloxane (HMDSO) and O₂ (or N₂O) are usually used as precursors fed into the plasma.

We have shown in the past that a good quality SiO₂ films can be prepared by means of microplasma jets driven by RF voltage and operated in Ar or He as plasma forming gas. Here we concentrate on the study of plasma chemistry and surface reactions leading to the film growth. The geometry of the microplasma jet and the localization of the plasma treatment allow studying of gas phase reactions and plasma-surface interaction separately. Molecular beam mass-spectrometry is used to measure HMDSO depletion and stable products in the gas phase. Depletion below 15% and limited fragmentation is observed even under conditions with high O₂ density, which leads to formation of carbon free SiO₂ films. The plasma-surface interaction is studied by application of several jets with different gas mixtures (He/HMDSO, He/O₂, He/H₂...) to the same trace on the rotating substrate in controlled helium atmosphere. It is shown that surface reactions are responsible for the carbon removal from the grown film. Infrared spectroscopy, spectroscopic ellipsometry and X-ray photoelectron spectroscopy measurements are performed to analyze film properties and

compare them with plasma measurements. A fluid model of gas flow and reaction kinetics in the effluent of the plasma is used to reproduce observed trends and measured deposition rates. Good agreement is achieved with relatively simple model of plasma chemistry and surface reactions.

11:00am **PS+SE-WeM10 Synthesis of $\text{Li}_4\text{Ti}_5\text{O}_{12}$ Nanoparticles Using an Atmospheric Pressure Plasma Jet, S.M. Chang, E.F. Rodriguez, H.C. Li, Y.J. Yang, N.L. Wu, C.C. Hsu, National Taiwan University, Taiwan, Republic of China**

Nanocrystalline spinel $\text{Li}_4\text{Ti}_5\text{O}_{12}$ (LTO) is a promising anode material for Li-ion batteries due to its zero-strain during intercalation/deintercalation and the 1.5 V (vs. Li+/Li) potential plateau. Development of a process that allows for rapid synthesis with controllable microstructure has been challenging. In this work, LTO nanocrystalline particles synthesized by an atmospheric pressure plasma jet (APPJ) will be presented. The APPJ is sustained using a repetitive pulsed power source with N_2 gas. Ti and Li ions-containing solution of specific formula is used as the precursor solution. The precursor is ultrasonically nebulized and is then carried into the downstream of the APPJ using a carrier gas. With this process, nanocrystalline LTO can be fabricated in one step with a short contact time (a few ms) between the precursor and the plasma jet without an additional annealing process. The LTO particle size can be effectively controlled using the precursor solution concentration and the carrier gas flow rate. 100-300 nm dense spherical particles can be fabricated under an optimized condition. The microstructure and porosity of the particles is strongly influenced by the pre-heat process for the nebulized precursor droplets prior to entering the jet downstream. Dense spherical and porous particles are fabricated under conditions with and without preheating, respectively. Finally, full battery performance test will be presented and key factors that dominate the fabricated nanoparticle characteristics will be discussed.

11:20am **PS+SE-WeM11 Laser-Assisted Plasma Coating at Atmospheric Pressure: Production of Yttria-Stabilized Zirconia Thermal Barriers, Z. Ouyang, P. Raman, Y.L. Wu, L. Meng, T.S. Cho, D.N. Ruzic, University of Illinois at Urbana-Champaign**

A laser-assisted plasma-coating technique at atmospheric pressure (LAPCAP) for use in thermal-barrier coatings (TBC) deposition has been developed. This technique allows PVD-quality depositions to be done at atmospheric pressure. The microwave source employed has a working frequency at 2.45 GHz, and a maximum input power of 6 kW, and the attached plasma torch head has the ability to generate various types of atmospheric-pressure plasmas at the temperatures of room temperature (20°C) to more than 2,000 °C. Optical emission spectroscopy (OES) technique has been used to spatially analyze some critical characteristics of plasma, such as electron density ($n_e > 10^{14} \text{cm}^{-3}$), electron temperature ($T_e \sim 1 \text{ eV}$), and plasma gas temperature ($T_g \sim 400\text{-}3,000 \text{ K}$), under different operating conditions (gas type, input power and gas flow rate). A helium atmospheric plasma has been used to assist in Nd:YAG laser ablation ($f = 100 \text{ Hz}$, Energy/pulse = 20 mJ at 266 nm; 120 mJ at 532 nm; 325 mJ at 1064 nm) of a 3% yttria-stabilized zirconia (3YSZ) target, to provide a means to deposit high quality, adhesive thin films on René N5 superalloy substrates with better lamination at a relatively higher deposition rate ($\sim 1,000 \text{ nm/min}$), in comparison to traditional PVD methods. The morphology and characteristics of the films have been compared at three laser wavelengths (266 nm, 532 nm and 1064 nm), different laser energy densities ($1\text{-}10 \text{ J/cm}^2$) and substrate temperatures (20-1100 °C), using microanalysis techniques such as scanning electron microscope (SEM), focused ion beam (FIB), X-ray photoelectron spectroscopy (XPS), and X-ray diffraction (XRD).

11:40am **PS+SE-WeM12 Investigation on the Discharge Formation Mechanisms and Surface Analysis of SiO_2 -like Layers on Polymers Synthesized using High Current Dielectric Barrier Discharge at Atmospheric Pressure, M.C.M. van de Sanden, FOM-Inst. for Plasma Phys. Rijnhuizen & Eindhoven Univ. of Tech., Netherlands, A. Premkumar, Eindhoven Univ. of Tech. & M2i, Netherlands, S. Starostin, H. de Vries, Fujifilm Tilburg, Netherlands, M. Creatore, Eindhoven Univ. of Tech., Netherlands**

The dielectric barrier discharge is recognized as a promising tool for PECVD of thin films at atmospheric pressure. Emerging applications including encapsulation of flexible solar cells and flexible displays requires low costs production of transparent uniform and dense layers with low level of coating defects. Among the two discharges Townsend like discharge (TD) and glow like discharge (GD) the latter offers more flexibility for the high growth rates in plasma enhanced deposition. In this investigation we demonstrate the utilization of glow like discharge in, He free, industrially relevant gas mixture comprising $\text{Ar/N}_2/\text{O}_2/\text{HMDSO}$ for the deposition of high quality silica like films on large area polymeric substrates (PET or PEN) in a roll-to-roll configuration. While the discharge physics exhibiting the glow like behaviour is investigated via fast ICCD camera, voltage-

current waveforms and optical emission spectroscopy, the deposited silica like films is comprehensively analyzed using AFM, SEM, XPS, SE and FTIR. The time evolution of the diffuse atmospheric discharge showed several phases starting from the initial ignition of the low current Townsend-like mode followed by the transition to glow like discharge which then undergoes lateral expansion providing uniform treatment of the whole substrate width. As a generic characteristic of the developed technology, it is observed that, irrespective of precursors (TEOS or HMDSO) and process gases (Ar , N_2 or air) employed, the films are smooth, both locally and globally, and of near stoichiometric silica with very low carbon content ($< 2\%$). Detailed AFM morphology description and surface statistical analysis on SiO_2 dynamics showed that no film roughening in growth front and lateral directions observed and the synthesized layers ($\sim 350 \text{ nm}$) grow in a self-similar fashion following the topology of the substrate. The films are uniform with no defects or particle being incorporated during the deposition process and exhibit excellent barrier performances towards O_2 and H_2O permeation.

**Plasma Science and Technology Division
Room: 202 - Session PS+SS-WeM**

**Plasma Surface Interactions (Fundamentals & Applications) I
Moderator: C. Labelle, GLOBALFOUNDRIES**

8:00am **PS+SS-WeM1 Investigation of Sidewall Passivation Mechanism in a 'CMOS-compatible' Plasma Etching Process for InP-based Photonic Devices, S. Bouhoule, CNRS-LPN, France, L. Vallier, CNRS-LTM, France, L. Gatilova, G. Patriarche, S. Guilet, L. Le Gratiet, CNRS-LPN, France**

Inductively coupled plasma (ICP) etching of II-V semiconductors is now widely used for the development of high-performance emitters, and various chlorine- or HBr- containing chemistries have been proposed for the patterning of InP-based heterostructures required to reach the NIR region. Smooth and anisotropic etching is generally a key-requirement, but only few studies exist on the understanding of the sidewall passivation mechanisms occurring during the etching of InP and related materials. We have shown for the $\text{Cl}_2\text{-H}_2$ and HBr chemistries [JVSTB 26, 666 (2008)] that a silicon oxide layer acting as a lateral etch-inhibitor can build-up on the etched sidewalls of InP-based heterostructures, when a Si wafer is used as the sample tray. This configuration corresponds to most commercial ICP etch systems having an electrode diameter of 4-in or more, used to etch III-V samples of 2-in or less size. However, this may not be the case for future large surface processing of III-V when the III-V wafer will have the same size as the electrode or when III-V dies bonded onto a 200/300 mm wafer have to be etched, where most of the wafer surface is covered by a protecting layer that is not silicon. This may occur in III-V/Si photonic technologies. We have shown that high-aspect-ratio etching of the photonic patterns via a SiO_x sidewall passivation mechanism independent of the electrode surface can be obtained when a Si-containing gas such as SiH_4 , or SiCl_4 added [JVSTB 29, 020601 (2011)]. A more detailed analysis of the plasma has shown that hydrogen may promote the deposition of a Si-rich passivation layer on the sidewalls of the etched patterns. SiOCl sidewall passivation takes place during Si ICP etching using $\text{Cl}_2\text{-HBr-O}_2$ chemistry in CMOS technology. We have therefore investigated $\text{SiCl}_4/\text{Cl}_2/\text{HBr-O}_2/\text{Ar}$ plasma for the etching of InP dies in a 300-mm CMOS etching tool. This gas mixture provides the Si_iO_x and H species required for the build-up of a SiO_x passivation layer on the InP sidewalls. We show that the passivation mechanism is enhanced when the HBr concentration is increased in the feed gas. We have performed a local analysis of the passivation layer deposited on the InP sidewalls using EDX spectroscopy coupled to TEM. We show that the nature of the passivation layer can be changed from a-Si or nc-Si to SiO_2 depending on the hydrogen and oxygen concentrations in the gas mixture. Finally we demonstrate smooth and anisotropic etching of ridge waveguide and vertical Bragg reflector patterns in the CMOS etching tool.

8:20am **PS+SS-WeM2 Coupling of Surface Mixed-Layer Kinetics and Monte Carlo Modeling for Profile Evolution in Patterning Complex Oxides, N. Marchack*, C.D. Pham, J.P. Chang, University of California Los Angeles**

As the downscaling of integrated circuit devices continues, minute variations in the feature profiles from processing techniques such as plasma etching significantly affect device performance. With the increasing introduction of novel materials into integrated circuits, the need to predict

* Coburn & Winters Student Award Finalist

surface response during etching of these materials, such as complex oxides, becomes critical to attainable device performance. In this work, a phenomenological model¹ based on high-k oxide etching in chlorine based plasmas is adapted into a translated mixed layer (TML)² kinetics-based format to be used a Monte Carlo-based feature profile simulator. To accurately represent the kinetics involved, experiments are conducted in this work in an inductively coupled plasma (ICP) reactor equipped with a quadrupole mass spectrometer (QMS) for analyzing etch products and a quartz crystal microbalance (QCM) for measuring the etch rate *in situ*. This reactor is connected to a UHV transfer tube which allows the surface composition to be studied via x-ray photoelectron spectroscopy (XPS) without exposure to ambient conditions. In the TML model, surface reactions such as ion impingement, neutral adsorption, physical sputtering and chemically enhanced ion etching are accounted for, and reaction parameters are either measured directly or extracted by comparing the model to etch yield data. The MC model used ion incident angle dependence and an elliptical energy deposition model to capture the effects of surface morphology on the profile evolution under the bombardment of energetic and directional ions. The material systems studied include HfLaO and HfSiON etched in Cl₂/BCl₃ plasmas, for both blanket films and trenches patterned by e-beam lithography. Very good agreement was demonstrated between the phenomenological and TML models, as well as between simulated profiles and cross-sectional SEM images of the patterned material systems.

¹ Martin et al. Journal of Vacuum Science and Technology A 27(2) 2009

² Kwon et al. Journal of Vacuum Science and Technology A. 24(5) 2006

8:40am **PS+SS-WeM3 Plasma Diagnostics and Nanoscale Surface Processing - Application to SiO₂, High-k PVD and ALD, T. Kitajima, National Defense Academy, Japan**

INVITED

Introduction

Reactive plasmas are widely used for surface processings due to its controllable ion energy and radial fluxes.

Nano size feature control with plasma processing requires nonthermal chemistry with low energy ion exposure. Metastable atoms with internal energy of a few eV become important for the quality and throughput of deposition as ion energy is reduced.

Minimizing the processing target to the nanoscale also reveals the new properties of materials interacting with plasmas due to the size effect. Namely, sticking coefficients of radicals on metal significantly increase.

In the presentation, some recent results on metastable radical induced deposition including HfO₂ ALD are shown. The latest findings of nano particle interaction with reactive plasmas are introduced for the model case of PVD based HfSiON film growth.

Reactive metastables for oxide growth : SiO₂ and HfO₂

The density of metastable O(1D) (1.9eV) in Ar-diluted O₂ ICP shows maximum at O₂ fraction of 1% and the flux shows significant increase due to the reduced quenching by O₂. O(1D) density is measured by Vacuum UltraViolet Absorption Spectroscopy (VUVAS). The XPS analysis shows the stoichiometry of the grown SiO₂ is comparable to the thermal oxide as well as the electrical breakdown.

The scheme is applied to the plasma enhanced atomic layer deposition (PEALD) of HfO₂. The reagent is TEMA and the oxidant is Ar-diluted O₂ ICP. The increased O(1D) flux enables less particle film surface with fewer carbon contamination.

Reactive surface nano particles interacting with plasma : HfSiON growth

Hf nanoparticles self assembled on SiO₂/Si(100), origin of HfSiON, have sticking coefficient of N radicals close to 1 in the initial stage of N₂ ICP exposure. The reactivity of the nanoparticles with underlying SiO₂ is enhanced by the plasma exposure, results in the formation of carbon free HfSiON film.

Concluding remarks

Metastables are important reactant for low temperature non-biased deposition processes

Metastable flux is controllable with the base gas chemistry

Nanoscale surface features are current concerns for plasma deposition

Nano sized surface has totally different reaction kinetics including interface with underlayer

Nano size effect of the surface is evident for radical reactivity

Self assembly (bottom up scheme) is highly important for next generation nano scale plasma processing as well as lithographic techniques (top down scheme)

Acknowledgement

This work was supported by MEXT Grant-in-Aid for Scientific Research on Innovative Areas (22110520) and JSPS Grant-in-Aid for Young Scientists (B) (21760033).

9:20am **PS+SS-WeM5 Nitric Oxide Reactivity Investigation via Plasma Processing, J.M. Blechle, E.R. Fisher, Colorado State University**

With increasing concern about environmental health, there is a greater need to investigate fundamental reactivity of pollutant species with and without the influence of surface effects. Here, inductively coupled plasmas are used to examine the catalyzed conversion of industrial exhaust, with an emphasis on elucidating the surface and gas-phase chemistry. Literature studies have thus far failed to explore the primary driving forces present in these catalytic plasma systems. The present work focuses on investigating the properties of nitric acid within plasmas formed from a collection of precursor gases including NO, NO₂, N₂O, and N₂+O₂. The behavior of the NO radical is determined by various methods that include catalytic surface reactivity measurements via the imaging of radicals interacting with surfaces (IRIS) technique as well as kinetic formation and destruction via time-resolved optical emission spectroscopy (TR-OES). Species density, surface scatter coefficients (S), along with vibrational and rotational temperatures establish inherent characteristics of NO. Results from these studies show the density of NO is strongly dependent on system pressure, which is in part attributable to formation of gas-phase dimers. In addition, S(NO) using non-catalytic surfaces (e.g. Si) increases with increasing plasma power. Additional results from studies of NO formation through bimolecular reactions in N₂/O₂ plasmas will be presented. Collectively, these data allow for unparalleled insight into the properties of atmospheric species during plasma processing and the interactions they undergo in the presence of catalytic substrates.

9:40am **PS+SS-WeM6 Near-Threshold Ion-Enhanced Silicon Etching, H. Shin, W. Zhu, V.M. Donnelly, D.J. Economou, University of Houston**

Nearly mono-energetic ion energy distributions (IED) were obtained on the substrate electrode in a Faraday-shielded inductively couple plasma. This was accomplished by pulsing the plasma, and applying a synchronous DC bias on a "boundary" electrode, during a specified time window in the afterglow. Both the peak ion energy and the width of the IED could be controlled.[1] The ability to precisely control the IED enabled a study of ion-enhanced etching of silicon with chlorine, at near-threshold ion energy. Unlike "beam" experiments, where there is no plasma over the substrate, this work involves etching under "realistic" plasma conditions. The progress of etching in an argon-diluted chlorine plasma was monitored as a function of pressure and ion energy using optical emission spectroscopy. The silicon etch rate was measured using infrared laser interferometry. The etch rate of a p-type blanket silicon substrate was proportional to Cl-atom density, but did not depend on ion energy for sub-threshold (less than ~ 20 eV) ions. Under these conditions, however, the etch rate was much higher than that expected based on reported experiments in downstream plasmas where the surface is exposed to Cl atoms alone. Above threshold, the etch rate increased with the square root of ion energy. A comparison with n-type silicon substrate was also made. The carrier-mediated mechanisms of p-type Si etching in a plasma under very low energy ion bombardment will be proposed and discussed.

Work supported by the DoE Plasma Science Center and NSF.

[1] H. Shin et al., to appear in *Plasma Sources Science and Technology*.

10:40am **PS+SS-WeM9 Atomic Chlorine Absolute Densities and Surface Recombination Coefficients in Inductively-Coupled Plasmas in Pure Cl₂, J.-P. Booth, LPP-CNRS, France, N. Sirse, NCPST Dublin City University, Ireland, Y. Azamoum, P. Chabert, LPP-CNRS, France**

Two-photon laser-induced fluorescence (TALIF) at 233.2nm was used to measure the density of Cl atoms in a 13.56MHz Inductively-coupled plasma in pure chlorine. Initial attempts to use the technique proposed by Ono et al [1], to calibrate the signal using photolysis of CCl₄ gave unphysically high values, probably due to poor knowledge of the laser spatial profile at the focal point. Therefore we developed a new technique, based on 355nm (tripled YAG) photolysis of Cl₂ to generate a known density of Cl atoms. The variation of the absolute Cl density at the reactor centre was measured as a function of pressure and RF power in the range 3-90 mTorr and 20-500W. We also used the TALIF technique to determine the recombination coefficient, γ_{Cl} , of atomic chlorine at the reactor walls from the rate of decay of the Cl density in the afterglow of a pulsed discharge. The signal to noise ratio is good enough to make measurements far into the afterglow (50 ms), when the gas has cooled to the wall temperature, making a precise measurements possible. We found that γ_{Cl} varies in the range 0.05-0.15, decreasing with increased pressure and RF power, and increasing with gas residence time. We show that the latter effect is due to the increased proportion of O₂ due to inevitable small air leaks: the presence of 0.5% O₂

was shown to double the value of γ_{Cl} . The origin of the pressure and power dependencies will be discussed.

Work partly supported by Agence Nationale de la Recherche project INCLINE (ANR-09 BLAN 0019)

[1] K. Ono, T. Oomori, M. Tuda, and K. Namba, *Journal of Vacuum Science & Technology a-Vacuum Surfaces and Films*, **10**, 1071, (1992).

11:00am PS+SS-WeM10 Silicon Etching Characteristics by Hydrogen Halide Ions (HCl^+ and HBr^+) and Ions of Desorbed Species ($SiCl_x^+$). T. Ito, K. Karahashi, Osaka University, Japan, S.-Y. Kang, Tokyo Electron Ltd., Japan, S. Hamaguchi, Osaka University, Japan

In recent reactive ion etching (RIE) processes for Si, halogen and hydrogen halide gases, such as Cl_2 and HBr , have been widely used to achieve high selectivity, etching anisotropy, and high etching rates. Furthermore, in some highly selective silicon etching processes, higher gas-pressure processes have been found to be more effective. In higher-pressure systems, chemical compounds formed from the input gas and some of desorbed species containing Si may serve as additional etchants. To develop etching equipments based on such plasma chemistry, it is important to understand basic etching reactions on silicon surfaces by energetic ion species associated with silicon and/or hydrogen containing species. To clarify the roles of $SiCl_x$, $SiBr_x$, HCl , and HBr in silicon etching processes, we have employed a mass-analyzed ion beam system that can irradiate a sample surface with a specific ionic species under an ultra-high vacuum condition and evaluated the etching yields. The change in chemical nature of the substrate surface during the process can be observed *in situ* by X-ray photoelectron spectroscopy (XPS) installed in the reaction chamber. Time of Flight (TOF) measurement of species desorbed from the sample surface in a pulsed ion beam operation is also possible with the use of a differentially pumped quadrupole mass spectrometer (QMS). In this study, etching yields of silicon by Cl^+ , $SiCl^+$, $SiCl_3^+$, Br^+ , H^+ , HCl^+ , and HBr^+ ion beams were evaluated with incident energies of 100 – 1000 eV. A typical ion dose for each ion irradiation was $2-4 \times 10^{17}/cm^2$. Yields by some of these ionic species have been known and our etching yield data are confirmed to be in good agreement with the earlier data. It is found that, for a given incident energy, the etching yield by $SiCl_3^+$ ions is higher than that by Cl^+ ions whereas the etching yield by $SiCl^+$ ions is lower than that of Cl^+ ions, which may be accounted for by the number of Cl atoms and a possible deposition effect of Si. It has been also observed that deposition occurs under $SiCl^+$ ion irradiation when the injection energy is lower than 300eV. Energy dependence of etching yields and effects of hydrogen will be discussed in detail.

11:20am PS+SS-WeM11 Interaction of Chlorine Plasma with Si_xCl_y Coated Plasma Reactor Chamber Walls, R. Khare*, A. Srivastava, V.M. Donnelly, University of Houston

The interplay between chlorine plasmas and silicon chloride (Si_xCl_y) coated reactor walls has been studied by line-of-sight mass spectrometry in a radio frequency (rf) inductively coupled Cl_2 plasma (ICP), using the spinning wall method. A bare silicon wafer was etched in a 400 Watt Cl_2 ICP, with rf power applied to the stage resulting in a -110 VDC self-bias. Etch products were deposited on the plasma reactor walls and the rotating substrate surface, resulting in a thick layer of Si_xCl_y that was characterized *in situ* by Auger electron spectroscopy. Some oxygen also incorporated into the film due to erosion of the fused silica discharge tube. The reactions of chlorine plasmas with this prepared surface were then studied by line-of-sight mass spectrometry. Without substrate bias, the chlorine plasma etches the Si_xCl_y layer to form products that result in detection of $SiCl_x$ ($x = 1-4$) m/e components, as well as oxy-silicon-chloride products ($m/e = 177, 247, 307, 361$). In one experiment, after the deposition of dense Si_xCl_y layer on reactor and substrate surfaces, substrate rotation was stopped and the film was etched from the reactor walls with the chlorine plasma, leaving only the Si_xCl_y layer on $2/3^{rd}$ of the substrate surface that was out of the plasma. Upon resuming rotation, and exposing the Si_xCl_y loaded surface to the Cl_2 plasma, $SiCl_x$ products were detected, but at suppressed levels, indicating that the evolution of etch products is a complex “recycling” process in which these species deposit and desorb from the walls many times, and repeatedly fragment in the plasma. These and other experiments will be discussed. This work is supported by the National Science Foundation and Lam Research Corporation.

11:40am PS+SS-WeM12 Numerical Simulation of Enhanced Oxygen Diffusion in Silicon as a Cause of Si Recess, K. Mizotani, M. Isobe, Osaka University, Japan, M. Fukasawa, T. Tatsumi, Sony Corporation, Japan, S. Hamaguchi, Osaka University, Japan

In a gate etching process, the formation of hollowed Si profiles around the polysilicon (poly-Si) gates, which is now widely known as “Si recess,” has raised serious concern in the semiconductor processing community as such hollows on a Si surface can severely degrade the device performance and reliability. In a typical process that causes Si recess, a plasma based on HBr and oxygen gases are used to etch polysilicon gates anisotropically. A recent study [1] based on multiple-beam and plasma experiments has shown that Si recess is caused by ion assisted oxygen diffusion, i.e., oxygen diffusion enhanced by hydrogen ion injections. In this study, we have used molecular dynamics (MD) simulations to understand the mechanism of enhanced oxygen diffusion in Si under such conditions. In the simulations, energetic hydrogen ions and low-energy oxygen atoms (with kinetic energies close to room temperature) are simultaneously injected into a crystalline Si substrate initially covered with a native oxide layer. Simulation results are in good agreement with ion beam experiments performed under similar conditions given in Ref. [1]. In our simulations, O atoms are transported into the bulk Si due to momentum transfer from energetic hydrogen ions. In other words, the enhanced ion transport is not typical “diffusion” associated with thermal motion in solid. However, random walk characteristics of O atoms in Si under such conditions are interestingly similar to those of diffusion. In this study, we relate this oxygen transport to diffusion transport and present its effective diffusion coefficient as a function of hydrogen ion injection energy.

[1] T. Ito, K. Karahashi, M. Fukasawa, T. Tatsumi and S. Hamaguchi, “Si recess of Poly-Si Gate Etching: Damage Enhanced by Ion Assisted Oxygen Diffusion,” *Jpn. J. Appl. Phys.* (2011) *in press*.

Advanced Surface Engineering Division Room: 104 - Session SE+SS-WeM

Surface Engineering for Thermal Management

Moderator: A.A. Voevodin, Air Force Research

Laboratory, H. Barankova, Uppsala University, Sweden

8:20am SE+SS-WeM2 Near-Field Radiation Heat Transfer, A. Mavrokefalos, P. Sambegoro, K. Esfarjani, G. Chen, Massachusetts Institute of Technology

INVITED

Radiation heat transfer in nanostructures can differ significantly from that in macrostructures due to wave effects. Max Planck himself realized that the blackbody radiation law that now bears his name was limited to geometries much larger than wavelength of thermal radiation. Theory has predicted that thermal radiation heat transfer between two surfaces separated by tens of nanometers can exceed that of Planck’s blackbody radiation law by several orders of magnitude. We have designed an experiment measuring near-field radiation heat transfer between a sphere and a flat plate using bi-layer atomic force microscope cantilevers as a heat flux and a temperature sensor. We demonstrated experimentally that near-field radiation heat transfer can exceed Planck’s law prediction by four orders of magnitude, mediated by surface phonon polaritons. We will also show that existing fluctuating electrodynamics theory cannot predict experimental results in the extreme limit of small separation between two surfaces. Our experiments raise interesting question on the convergence of radiation heat transfer mechanism and interfacial heat conduction mechanism. Theoretical approaches bridging these two regimes will be discussed.

9:00am SE+SS-WeM4 Atomic Level Temperature Measurements and Near-field Thermal Energy Tunneling, A.A. Voevodin, I. Altfeder, J. Hu, V. Varshney, A. Roy, Air Force Research Laboratory

An atomic level thermometer was developed to study interfacial thermal conductivity using a scanning tunneling microscope with inelastic electron tunneling spectroscopy (STM-IETS), where inelastic peak broadening was used to measure temperature of the CO molecular group at the platinum probe apex, while Au substrate with (111) surface was cryogenically cooled. The experiments led to a discovery of vacuum phonon tunneling across nanometer contact gaps. This discovery showed that contact thermal transport can exceed by 10 orders of magnitude Planck’s radiation Law for heat transfer in vacuum [1]. This indicated that there should be an alternative mechanism for thermal energy transfer, where near field effects support energy tunneling across such small vacuum gaps. A hypothesis about mirror charge coupling at the interfaces was formulated and tested in the experiments with varied tip-sample temperature gradients. Based on these developments, the STM-IETS experimental approach was further extended to study interfaces made of the surfaces with different Debye

* Coburn & Winters Student Award Finalist

temperatures. The second derivative of the tunneling current was used to obtain information on the interfacial thermal coupling and energy transfer. This paper reports on the experimental set-up for atomic scale thermometry, corresponding first principle calculation approaches for small gap interfacial thermal coupling, and discusses experimental and modeling results for different tip-surface combinations toward understanding near-field effects for thermal energy transfer.

1. "Vacuum phonon tunneling", I. Altfeder, A. A. Voevodin, A. K. Roy, *Physical Review Letters*, 105, 166101 (2010).

9:20am **SE+SS-WeM5 Two-Color Time-Domain Thermoreflectance with an Optical Parametric Oscillator**, *J. Gengler*, Spectral Energies, LLC, *C. Muratore*, Air Force Research Laboratory, *S. Roy*, Spectral Energies, LLC, *J.R. Gord*, Air Force Research Laboratory

Conventional single-color laser pump-probe methods for measuring thermal properties are limited by sample requirements that arise from considerations of surface roughness and compatible thermoreflectance transducers. Here we describe a new experimental arrangement for performing two-color time-domain thermoreflectance (TDTR). The technique is a variation of traditional pump-probe spectroscopy that is based on a femtosecond Ti:sapphire oscillator of fixed wavelength and an optical parametric oscillator (OPO), with the goal being to create an independently tunable probe wavelength. This method offers two advantages: 1) spectral filtering of diffusely scattered pump light (to prevent it from reaching the detector), and 2) generation of thermoreflectance signal from different metal thin films. The wavelength tunability of the system allows enhancement of TDTR signal generation for multiple thermoreflectance transducer materials. This wavelength-adjustable feature, in turn, facilitates direct measurement of the thermal transport properties of various thin films and substrates, which would be difficult with single-color femtosecond pump-probe systems. Demonstrated results include optimization of the probe wavelength for different metals, measurement of metal-graphite interfacial conductances on relatively rough samples, and two orders-of-magnitude calibration of thermal conductivity measurements using copper as a thermoreflectance transducer.

9:40am **SE+SS-WeM6 Low-Friction V-alloyed ZrO₂ Thin Films with Temperature Homogenization Functions for High Temperature Sliding Interfaces**, *O. Jantschner*, *C. Walter*, *C. Mitterer*, University of Leoben, Austria, *C. Muratore*, *A.A. Voevodin*, Air Force Research Laboratory

The effect of vanadium on reactively magnetron-sputtered zirconia coatings was investigated with respect to its structural and mechanical properties as well as its thermal management abilities for high temperature sliding interfaces. ZrO₂ coatings with different V-content (0, 2.2, 5.8 and 17.4 at%) were co-sputtered from Zr and V targets using an Ar/O₂ discharge. The X-ray diffraction pattern of the as-deposited coatings show a change in crystal structure from monoclinic (0-2.2 at% V) to cubic/tetragonal (5.8 at% V) and finally X-ray amorphous structure at even higher V content (17.4 at% V). Hardness and Young's modulus were evaluated by nanoindentation showing a decrease beyond 2.2 at% V from 17.4 to 7.5 GPa and from 230 to 150 GPa, respectively. The tribological investigations by ball-on-disc tests against alumina balls were carried out at three different temperature levels (25, 600 and 800°C). Additional in-situ Raman analyses have been done to study the formation of tribolayers in the sliding contact. At 25°C, the coefficient of friction (COF) is about 0.2 for low V contents (≤ 2.2 at%). For higher V contents, the COF increases up to 0.5 and higher. At 600°C, the COF measured was between 0.4 and 0.8. At the even higher temperature of 800°C, the COF decreased to below 0.2 for V contents of 17.4 at%, where a self-lubricating film was formed in the sliding contact. Differential scanning calorimetry (DSC) measurements of virgin powder samples showed a characteristic exothermic peak at ~600°C which is due to the formation of a stoichiometric ZrV₂O₇ phase. This phase was found to decompose at ~800°C by an endothermic reaction in ZrO₂ and V₂O₅. The re-runs of the DSC measurements indicated melting of V₂O₅ at 670°C.

In summary, alloying of V to ZrO₂ coatings has on the one hand been proven to result in self-lubricious properties at temperatures above 700°C. On the other hand, the endothermic reactions needed for formation of the self-lubricious phase have the potential to reduce high local temperatures in the sliding contact, enabling thermal management abilities of these coatings.

10:40am **SE+SS-WeM9 Thermal Characterization of Metal/Carbon Interfaces: Comparison of Metallized Nanotubes and Graphite**, *C. Muratore*, *S. Shenogin*, *A. Waite*, *A. Reed*, *J. Gengler*, *T. Smith*, *J. Hu*, *J. Bultman*, *A.A. Voevodin*, Air Force Research Laboratory

Most applications of carbon nanotubes require contact with more ordinary materials, such as metals or polymers. Unfortunately, the extraordinary thermo-electro-mechanical properties of nanotubes are often negated at the interface between the nanotubes and whatever they touch, resulting in a major shortfall between the measured and predicted performance of

nanotube-based materials. One of the most troubling discrepancies in projected versus measured properties is found in thermal conductivity measurements of nanotube-containing composite materials. For example, a continuous network of thermally conductive nanotubes (or about 1 percent, by volume) within an organic matrix ($k = 0.3$ W m⁻¹ K⁻¹) should yield a 30-fold increase in thermal conductivity over the pure matrix phase alone, based on simple effective medium theory. Despite this potential increase, experimental results typically show an increase of only a factor of 2 at best in composites with nanotube additives. To better understand the nature of interfacial resistance in carbon nanotubes, modeling and experimental studies investigating engineered interfaces on highly oriented pyrolytic graphite (HOPG) samples were conducted. This substrate was selected as a practical 2-dimensional analog for nanotube sidewalls to facilitate modeling and experimentation. Molecular dynamics simulations of heat transfer through metal carbon interfaces were conducted, and measurements of thermal conductance at these interfaces were made by analysis of the two-color time domain thermoreflectance (TDTR) data from the samples. The TDTR analysis of the different metals on HOPG was made possible by having an optical parametric oscillator on the probe beam which allows for tuning the wavelength to match absorption bands for each metal studied. Comparison of simulation and experimental results between graphite and nanotubes is highlighted. Metal films were selected to identify effects of atomic mass, chemical interactions and mechanical properties. For example, metals known to exhibit in situ formation of an interfacial carbide layer when in contact with a carbon source and heated, such as titanium and boron, were investigated, and the effect of this carbide layer formation on interfacial conductance was examined. Graded and sharp interfaces were also considered with computational and experimental efforts.

11:00am **SE+SS-WeM10 The Experiment of Surface Tension Driven Flow with Various Parameters on JEM/ISS**, *S. Yoda*, Japanese Aerospace Exploration Agency, *S. Matsumoto*, JAXA, Japan, *A. Komiya*, Tohoku University, Japan

The surface tension driven flow (Marangoni) experiments were carried out by using 50mm diam. with liquid bridge of Silicones oil under microgravity condition on Japanese Experiment Module on International Space Station. The parameters in these experiments were liquid bridge length being corresponded to aspect ratio which is defined as liquid length/liquid diam., and temperature difference between hot and cold disks which sustains the liquid bridge. The particles coated by gold to fit with the density of the liquid silicones were inserted into the liquid bridge. Observing the movement of the particles by three CCD camera, we can determine the flow behavior of Marangoni with different temperature as 3 dimension observation of the flow. Moreover, two ultrasonic transducers were attached in the cold disk to measure the particles velocity. The number of experiments done on JEM were more than 40 times with around 6 hr for all each experiment. The Marangoni number was changed with aspect ratio. The smaller aspect ratio around showed smaller critical Marangoni numbers, whereas the larger those were larger the numbers.

11:20am **SE+SS-WeM11 Enhanced Thermal Transport at Covalently Functionalized Carbon Nanotube Interfaces**, *S. Kaur*, Lawrence Berkeley National Lab, *N. Ravivikar*, Intel Corporation, *D.F. Ogletree*, Lawrence Berkeley National Lab

Thermal transport is restricted in systems including carbon nanotubes (CNT) due to high thermal interface resistance. We have substantially improved thermal transport at CNT-metal interfaces by functionalizing the contacting surfaces with amino-propyl silane to form covalent chemical bonds bridging the CNT-metal gap. This strategy was suggested by molecular dynamics calculations of Hu *et al.* (1)

We have characterized the resulting interface using multi-frequency and multi-wavelength time-domain thermo-reflectance (TDTR) measurements, which are able to independently determine interface and bulk CNT contributions to thermal transport. TDTR analysis showed that thermal contacts were made between a functionalized Al surface and 4-5% of the CNTs in an array grown on silicon. The intrinsic CNT interface conductivity exceeded 300 MW/m²-K, resulting in an effective thermal interface resistance of less than 0.8 mm²-K/W. Successful interface functionalization was independently verified by mechanical adhesion testing, which showed a correlation between interface strength and thermal transport, as discussed by Prashar. (2).

(1) Ming Hu, Pawel Keblinski, Jian-Sheng Wang, Nachiket Ravivikar, *J. Appl. Phys.* **104** 083503 (2008).

(2) Ravi Prashar, *Appl. Phys. Lett.* **94** 041905 (2009).

Surface Science Division

Room: 107 - Session SS1-WeM

Atomistic Control of Structure & Evolution

Moderator: T.S. Rahman, University of Central Florida

8:40am **SS1-WeM3 Destabilization of Ag Nanoislands on Ag(100) by Adsorbed Sulfur**, *M. Shen, S.M. Russell*, Iowa State University, *D.-J. Liu*, Ames Laboratory - US DOE, *P.A. Thiel*, Iowa State University & Ames Laboratory - US DOE

Studies of chalcogen (O, S) interactions with coinage metal surfaces elucidate how those interactions affect mass transport on the surface and whether a general mechanism exists for these systems. Sulfur accelerates coarsening of Ag nanoislands on Ag(100) at 300 K, and this effect increases with sulfur coverage over a range spanning a few hundredths of a monolayer, to nearly 0.25 monolayers. We propose that acceleration in this system is strongly tied to the formation of AgS₂ complexes at step edges. These complexes can transport Ag more efficiently than Ag adatoms (due to a lower diffusion barrier and comparable formation energy), hence leading to enhanced coarsening. The mobility of isolated sulfur on Ag(100) is very low, so that complex formation is kinetically-limited at low sulfur coverages, and thus enhancement is minimal. However, higher sulfur coverages force the population of sites adjacent to step edges, so that formation of the complex is no longer limited by diffusion of sulfur.

9:00am **SS1-WeM4 Pt Terminated Mono- and Multilayer CuPt Alloys Supported on Ru(0001) Single Crystals as Model System for Core Shell Particles**, *A.K. Engstfeld, R.J. Behm*, Ulm University, Germany

A popular concept to improve the catalytic activity of metal particles is the utilization of core shell particles. This means that a metal/alloy core is encapsulated by an additional metal in the shell of the particle. An interesting example has recently been published by R. Srivastava et al. [1], who found that Pt enclosed alloy particles containing Cu, Co and Pt, have a much better activity towards oxygen reduction than pure Pt. Whereas the principle concept is thus proven to work, the "optimum catalyst" for oxygen reduction has not yet been found.

For a better understanding of the structure and the formation of such core shell particles we prepare nanostructured planar model surfaces under well defined conditions, such as in ultra high vacuum (UHV). The surfaces consist of mono- and multilayer CuPt alloys on a Ru(0001) single crystal. They can be prepared by subsequent evaporation of the single metals and annealing at elevated temperatures. By this means the composition of the core can be well defined. The shell can be achieved by terminating the alloy by an additional Pt layer.

In this work we focus on the preparation of mono and bimetallic CuPt layers. They are characterized via STM to elucidate the morphology as well as the atom distribution. From the atom distribution within the alloy we will discuss the dominant factor for alloy formation, in view of the different size of the atoms and difference in their intermetallic bonding. Furthermore we will elucidate the surface segregation behavior of Pt in the bilayer alloy during the alloying process.

[1] Srivastava, R., P. Mani, N. Hahn, and P. Strasser, 'Efficient Oxygen Reduction Fuel Cell Electrocatalysis on Voltammetrically Dealloyed Pt-Cu-Co Nanoparticles', *Angewandte Chemie*, 8988 (2007).

9:20am **SS1-WeM5 Carbon-induced Nano-Faceting of Re(11-21): Synthesis and Performance of a Pt ML-C/Re(11-21) Electrocatalyst**, *X.F. Yang*, Lehigh University, *H. Wang*, Columbia University, *W. Chen, R.A. Bartynski*, Rutgers University, *B.E. Koel*, Princeton University

Faceted surfaces can provide unique opportunities to explore how catalytic reactions respond to changes in the catalyst surface structure. In this study, using LEED, XPS, AES, and STM, we report on how the presence of surface carbon significantly modifies the surface structure of a Re(11-21) single crystal and causes faceting, *i.e.*, an initially planar Re(11-21) surface becomes "nano-textured" to expose new crystal faces and form "pyramids" on the nanometer scale. In addition to describing these nanostructures, we identify different states of surface carbon and describe their dependence on the coverage of carbon. We also utilized the faceted Re(11-21) surface containing these nanoscale pyramids to explore for unusual catalytic properties. Here, we describe the synthesis of a model electrocatalyst by deposition of one monolayer of Pt on the faceted C/Re(11-21) surface and investigation of its performance for the hydrogen evolution reaction (HER). This Pt ML-C/Re(11-21) surface displayed higher activity for the HER than pure Pt. This is particularly promising since Re is only one-fifth the price of Pt. This study is the first application of using a nanoscale faceted surface as a template for electrocatalyst synthesis, and illustrates the potential for other such investigations. It is also of interest to further explore the catalytic

activity of such faceted surfaces for heterogeneous catalytic reactions, *e.g.*, selective reduction of NO_x with NH₃ and selective oxidation of methanol, in order to understand the various effects of facet size, orientation, and low-coordination sites that are available for reaction.

W.C. and R.A.B. acknowledge support under DOE Contract No. DE-FG02-93ER14331. B.E.K. acknowledges support by NSF Grant No. CHE-1129417.

9:40am **SS1-WeM6 Nucleation and Growth of Ag Islands on the (√3x√3)R30° Phase of Ag on Si(111)**, *A. Belianinov*, Iowa State University & Ames Laboratory - US DOE

Using STM, we measure densities and characteristics of Ag islands that form on the (√3x√3)R30°-Ag phase on Si(111), as a function of deposition temperature between 50 and 300 K. Assuming that Ag diffusion occurs via thermally-activated motion of single atoms between adjacent sites, the data can be explained as follows. At 50-125 K, islands are relatively small, and island density decreases only slightly with increasing temperature; the island density does not follow conventional Arrhenius scaling, probably due to limited mobility and lack of steady-state between deposition and consumption of Ag atoms. At higher temperatures there is a transition to conventional Arrhenius scaling, from which a diffusion barrier of 0.20-0.23 eV can be derived. At 300 K Ag atoms can travel for distances on the order of 1 μm, and they nucleate preferentially at step bunches. We have used this information to nanopattern the surface with Ag. We have done this by creating artificial defects in the √3-Ag structure with the STM tip, and then subsequently depositing Ag at 300 K. This leads to strong preferential aggregation at these sites.

10:40am **SS1-WeM9 Surface Diffusion of In and Sn on Si(001) at Room Temperature**, *N. To, S. Dobrin, J. Nogami*, University of Toronto, Canada

A self-aligning nanostencil mask was used to pattern circular features of tin and indium on an atomically clean Si(001) substrate. The shadow mask limited material deposition to below where the membrane was open, leaving adjacent areas of clean surface for material to diffuse. STM was used to study the room temperature surface diffusion of these metals in UHV and DFT was used to calculate relevant activation barriers. The comparison of these two metals is significant since they have the same atomic structure in the first atomic layer when grown on Si(001). The diffusion of tin is limited in comparison with indium, and remains so even at increasing metal coverage. Indium forms unstable 3D islands that dissolve over time and contribute to the spreading of a single atomic layer thick film on the surrounding clean surface. The difference in behavior between the two metals can be attributed to the energy balance between 3D islands and the 2D wetting layers, as well as differences in activation energy for diffusion of atoms on top of the first atomic layer of metal. These results also show the potential for stencil patterning to provide insight into aspects of thin film growth.

11:20am **SS1-WeM11 The Effect of Surface Fluoride on the Crystallization and Photocatalytic Activity of Titania**, *J.I. Brauer, G.J. Szulcowski*, University of Alabama

A two-step strategy to improve the photocatalytic activity of titania is reported. First, nitrogen doped titanium dioxide, denoted N-TiO₂, has been synthesized by sol-gel methods to increase the absorption of visible radiation. Second, surface hydroxyl groups of the as-synthesized powders are replaced with fluoride ions. The two-step strategy gives independent control of "bulk" doping and surface modification. The as-synthesized and annealed powders were characterized by x-ray photoelectron spectroscopy, x-ray diffraction, diffuse reflection UV/Vis spectroscopy, IR spectroscopy, and scanning electron microscopy. Surface fluorination has two important consequences: it lowers the temperature to crystallize the as-synthesized powders into the photoactive anatase phase and improves the retention of nitrogen-dopants upon annealing. The photoactivity of the titania powders were characterized by assessing the ability to degrade aqueous solutions of methylene blue, a common dye molecule, with visible radiation greater than 420 nm. The photodegradation experiments show that the rate of methylene blue decomposition follows the trend: F, N-doped TiO₂ > N-TiO₂ > undoped TiO₂. A mechanism to explain the observed effects will be presented.

11:40am **SS1-WeM12 Microscale Corrosion of an Aerospace Al 2024 Alloy with Low Mg and the Effect of Chromate and Cerium Based Conversion Coatings**, *J.A. DeRose, T. Suter*, EMPA, Switzerland, *A. Balkowiec, J. Michalski, K.J. Kurzydowski*, Warsaw University of Technology, Poland, *I. De Graeve, H. Terryn*, Vrije Universiteit Brussel, Belgium, *P. Schmutz*, EMPA, Switzerland

An aluminum alloy, AA2024-T351 (Al 2024), with a composition having a higher proportion of Cu to Mg (Cu/Mg = 3.7), which is used in the

aerospace industry, has been studied for corrosion simulation development. Results show that the Al 2024 alloy's microstructure and corrosion behavior is quite different from that reported for Al 2024 alloy with higher Mg, a more common composition (normally Cu/Mg = 2.9) [1]. Characterization of the Al 2024 indicates a dominant presence of 2nd phase (AlCuFeMnSi) intermetallic particles (>70%), but that the S phase (Al₂CuMg) and θ phase (Al₂Cu) precipitate particles are much smaller in population (<30%). Microscale corrosion studies show that open circuit (OCP) and pitting potential (PP) values extracted from micropolarization curves [2] measured for Al 2024 (Cu/Mg = 3.7) 2nd, S, or matrix phase have a large variation within a similar range of values. These results are in contrast to those already reported for Al 2024 with a more common composition (Cu/Mg = 2.9) where the electrochemical potential values separate with respect to the alloy phase and the microstructure shows S phase particles to be in the majority (>60%) [2]. Nanoscale dispersoid particles and, to a much lesser degree, nanoscale 2nd phase particles were also found present throughout the matrix of the Al 2024 studied. The impact of chromate and cerium based conversion coatings, which inhibit corrosion, on the microscale corrosion properties of the Al 2024 alloy has been studied. Electrochemical current density data extracted from micropolarization curves measured for Al 2024 2nd, S, and matrix phase exposed to electrolytic solutions containing chromate (Na₂Cr₂O₇) or cerium based (Ce(NO₃)₃) molecules show the chromate coating to be more efficient as a corrosion inhibitor. However, other cerium based molecules, such as cerium dibutylphosphate (Ce(dbp)₃) and cerium chloride (CeCl₃), which have shown more promising results [3], deserve further investigation. [1] R.G. Buchheit, R.P. Grant, P.F. Hlava, B. McKenzie, G.L. Zender, J. Electrochem. Soc. 144 (1997) 2621. [2] T. Suter, R.C. Alkire, J. Electrochem. Soc. 148 (2001) B36. [3] S.J. Garcia, T.H. Muster, Ö. Özkanata, N. Sherman, A.E. Hughes, H. Terryn, J.H.W. de Wita, J.M.C. Mol, Electrochim. Acta 55 (2010) 2457.

Surface Science Division

Room: 109 - Session SS2-WeM

Chemisorption on Metal & Oxide Nanoparticles

Moderator: B. Roldan Cuenya, University of Central Florida

8:00am **SS2-WeM1 Temperature Program Desorption and X-ray Photoelectron Spectroscopy Study of Cu_x on CeO₂/YSZ (111)**, *J.C. Lofaro, Jr.*, Stony Brook University, *M.G. White*, Stony Brook University and Brookhaven National Laboratory

Energy research has increased in importance in the past decade due to our growing understanding of climate science and rising oil prices. Many catalysts center around expensive and rare transition metals, such as Pt and Pd, supported on oxide substrates. However, copper, a relatively cheap and abundant metal, supported on metal oxides has been used as a heterogeneous catalyst in industrial settings for various chemical processes.^{1,2} Recent works have shown that copper nanoparticles supported on metal oxides (ZnO, CeO₂, TiO₂) have higher activity for the water gas shift reaction (WGS) as well as other important chemical reactions when compared to their individual components.^{3,4} Understanding how these complex catalysts work on a fundamental level will allow for the design and implementation of more efficient and selective systems in the future. Here, using a homemade thermal evaporator, a model system of copper nanoparticles deposited on CeO₂ films (200 nm thick) grown on YSZ (111) single crystals is used. X-ray photoelectron spectroscopy (XPS) is used to characterize the oxidation state of supported copper nanoparticles and temperature programmed desorption (TPD) is used to probe their reactivity and thermal stability. Copper coverages ranging from 0.25ML to 1ML are investigated. Carbon monoxide and water are used as probe molecules since they are the reactants involved in the WGS. We have found that copper's stability is highly temperature dependent and have found evidence of its encapsulation by the support.

1. K. Klier, Adv. Catal., 1982, 31, 243.
2. J. C. Bart and R. P. A. Sneedon, Catal. Today, 1987, 2, 124.
3. J. A. Rodriguez, P. Liu, J. Hrbek, J. Evans, M. Pérez, Angew. Chem. Int. Ed., 2007, 46, 1351.
4. X. Zhao, J. A. Rodriguez, J. Hrbek, M. Pérez, Surface Science, 2005, 600, 229.

8:20am **SS2-WeM2 X-ray Photoelectron Spectroscopy and Scanning Tunneling Microscopy Characterization of the Active Edge Sites of MoS₂ Nanoclusters**, *A. Tuxen, S. Porsgaard, H. Goebel, F. Besenbacher, J.V. Lauritsen*, Aarhus University, Denmark

The atomic and electronic structure of MoS₂ nanoclusters is of considerable interest due to the catalytic application of MoS₂ in e.g. hydrotreating catalysis of crude oil and in photocatalysts and hydrogen evolution reactions. Previous atom-resolved STM results have shown in great detail that both the overall morphology and in particular the edge structure of MoS₂ nanoclusters, which are known to contain the most catalytically active sites for hydrotreating and H₂ dissociation, adopt a structure which is very dependent on the conditions under which the cluster are kept. Under sulfiding conditions, atom-resolved STM images show that the MoS₂ nanoclusters expose fully sulfide edges, whereas activation by H₂ or mixed H₂/H₂S exposures show that sulfur vacancies and S-H form on the cluster edges reflecting the MoS₂ catalyst in its active state. To dynamically follow such structural changes at the MoS₂ edges induced e.g. by hydrotreating reaction conditions we have here combined high-resolution x-ray photoelectron spectroscopy (XPS) and scanning tunneling microscopy (STM) studies of single-layer MoS₂ nanoclusters with a well known structure. The XPS studies done on well-characterized samples reveal a set of edge specific core level shifts in the Mo3d photoemission peak that can be uniquely associated with the fully sulfide edges, edge with S vacancies or fully reduced edges. The XPS fingerprint thus allows us to dynamically follow changes between the catalytically active states of MoS₂ when exposed to sulfiding of sulforeductive conditions. Preliminary *in-situ* XPS results on the same MoS₂ samples obtained under a 10⁻² torr H₂ atmosphere on the Ambient Pressure X-ray Photoelectron Spectroscopy on beamline 11.0.2 of the Advanced Light Source Berkeley show a characteristic sequence of sulfur reduction steps on the catalytically interesting edges followed by decomposition of MoS₂ at higher temperatures. The present studies thus successfully shows that XPS in combination with STM can be successfully used as a tool to characterize the chemistry of highly dispersed active sites of well-defined nanoclusters, such as the active edges on MoS₂.

8:40am **SS2-WeM3 Charge-Mediated Chemisorption on Supported Clusters**, *M. Sterrer*, Fritz-Haber-Institute of the Max-Planck-Society, Germany **INVITED**

Among the many factors that influence catalytic activity of supported metal clusters, the effects of size and charge state of the clusters are most frequently discussed, e.g., in CO oxidation over supported gold. In this contribution, I will present results of our recent experimental efforts to characterize metal clusters supported on single-crystalline model oxide surfaces, using Au on MgO thin films as example. Using a combination of various surface science techniques including low-temperature scanning tunneling microscopy, infrared spectroscopy, X-ray photoelectron spectroscopy, and electron paramagnetic resonance, the properties of supported Au atoms and clusters were addressed in detail. Starting with the unusual CO chemisorption behavior of single Au atoms on the perfect MgO(001) surface, I will move on and show how the charge state of Au particles on the MgO surface, which in most cases is inferred from distinct CO chemisorption features, may be influenced by modification of the oxide surface, e.g. by their interaction with defects or hydroxyl groups, or by the MgO film thickness.

9:20am **SS2-WeM5 The Structure and Chemical Activity of Two-dimensional Gold Islands on Single-layer Graphene/Ru(0001)**, *L. Liu*, Texas A&M University, *Y. Xu*, Oak Ridge National Laboratory, *Z. Zhou*, Texas A&M University, *Q. Guo*, Chinese Academy of Sciences, China, *Z. Yan*, *Y. Yao*, Texas A&M University, *L. Semidey-Flecha*, Oak Ridge National Laboratory, *D.W. Goodman*, Texas A&M University

Single-layer graphene supported on transition metals provides a unique substrate for synthesizing metal nanostructures due to the high crystallographic quality, thermal stability, and chemical inertness of the graphene. Contrary to its formation of three-dimensional (3-D) nanoclusters on graphene supported on a SiO₂ substrate, Au forms two-dimensional (2-D) islands on graphene moiré/Ru(0001). These Au islands maintain their 2-D structures up to 1 monolayer (ML) equivalent of Au dosage and are stable at room temperature. Our scanning tunneling microscopic study further shows that the 2-D Au islands are most likely two layers high, and conform to the graphene moiré in the lateral direction. Spin- and angle-resolved photoemission studies indicate even though these Au islands are largely electronically isolated, a weak through-graphene coupling exists between the Au islands and the Ru(0001) substrate. The structure for these 2-D Au islands and the corresponding electronic band structures are proposed based on DFT calculations.

Parallel studies using polarization modulation infrared reflection absorption spectroscopic (PM-IRAS) and high resolution electron energy loss spectroscopic (HREELS) indicate that CO adsorbs on these 2-D gold islands at 85 K with a characteristic CO stretching feature at 2095 cm⁻¹ for a

saturation coverage. Preliminary data obtained by dosing molecular oxygen onto this CO pre-covered surface suggest that the 2-D gold islands catalyze the oxidation of CO. These electron-rich, weakly coupled 2-D Au islands provide a unique platform to study the intrinsic catalytic activity of low-dimensional Au nanostructures.

9:40am **SS2-WeM6 Spatially Resolved Measurements of Catalytic Activity on Variable-Composition Pd-Cu and Pd-Cu-Au Thin Films using a Microfluidic Reactor Array**, *P. Kondratyuk, G. Gumushu, Carnegie Mellon University, B.D. Morreale, National Energy Technology Laboratory, J.B. Miller, A.J. Gellman, Carnegie Mellon University*

A new experimental approach to mapping the relationship between composition and catalytic activity in metal alloy catalysts is presented. We apply this methodology to study H₂-D₂ exchange reaction on Pd-Cu and Pd-Cu-Au alloys. The activity measurements were performed on thin alloy films deposited in such a way that the elemental composition varied continuously across the film. We refer to these films as composition spread alloy films (CSAFs). CSAFs were prepared by co-deposition of Pd, Cu and Au onto a molybdenum substrate under UHV conditions. The top-layer and near-surface composition of the CSAFs were determined by low-energy ion scattering (LEIS) and X-ray photoemission spectroscopy (XPS) respectively. The activity of the alloy films in the H₂-D₂ exchange reaction was analyzed at atmospheric pressure using a 100-channel glass microfluidic device. During the spatially-resolved activity measurements, the microfluidic device delivers reactant gases to a 10x10 array of measurement points on the CSAF surface covering an area of 1 cm², each measurement point corresponding to a different catalyst composition. After coming in contact with the catalyst, the gases are withdrawn for mass-spectrometric analysis through a separate set of channels. The activity-composition relationship can then be established by correlating the XPS (or LEIS) data with the product concentration in each channel of the microfluidic device.

10:40am **SS2-WeM9 Surface Structure Dependence by Monofaceted CeO₂ Nanoparticles: Catalytic Oxidation Reactions**, *M. Li, Z. Wu, F.C. Calaza, D.R. Mullins, S.H. Overbury, Oak Ridge National Laboratory*

Reducibility of pure and doped CeO₂ is of interest in emission control catalysts because of the ability of the CeO₂ to store and supply oxygen during oxidation catalysis. But, it is not known how the structure or crystallographic termination of the CeO₂ affects the catalytic reaction rates and selectivity. Using CeO₂ nanoparticles with controlled shapes including cubes, octahedra and rods that are terminated on (100), (111) and (110) surfaces respectively, we have investigated this structure dependence. Temperature programmed desorption, temperature programmed reaction, flow reactor rates, and in situ DRIFTS were used to probe adsorption states, desorption, reaction, oxidation rates and product selectivity for CO and ethanol oxidation. Results show pronounced differences between the three different morphologies. All morphologies show evidence of surface ethoxide species at room T, but during subsequent TPD, the DRIFTS exhibits variation in surface species between the different surfaces with evidence for formation of adsorbed acetaldehyde and acetate. Temperature induced changes in the C-H stretching regions, different also for each polymorph, suggest competing dehydrogenation and dehydration of surface species. Desorption temperatures and product distributions also vary. The ratio of H₂/H₂O, and the H₂ peak desorption temperature is highest for the octahedra, consistent with its highest vacancy formation energy and therefore least available oxygen. This ratio is lowest for high surface area multi-faceted nanoparticles, and its variability has important implications for tailoring and understanding CeO₂ catalysts or supports for production of H₂ in ethanol fuel cells. Product profiles during TPR of ethanol in O₂ were also dependent upon the surface structure. Octahedra show the highest selectivity to acetaldehyde and an onset of H₂ evolution above 400 °C while the cubes and rods showed lower temperatures for the onset of H₂, indicating that the hydrogen is evolved by two different pathways on different shaped ceria. Similarly, in a steady state flow reactor, the ratio of selective oxidation product (acetaldehyde) to the total oxidation product (CO₂) followed the order (111) > (100) > (110). Such results provide a basis for fundamental understanding of how surface coordination, bonding, decomposition and reaction are affected by the atomic structure of an oxide surface, especially important for reducible oxides.

Research sponsored by the Division of Chemical Sciences, Geosciences, and Biosciences, Office of Basic Energy Sciences, US DOE.

11:00am **SS2-WeM10 Tuning the Adsorption Properties of an Oxide Material Via Doping: Au Clusters onto Cr-doped MgO(001) Films**, *F. Stavale, N. Nilus, H.-J. Freund, Fritz-Haber-Institute of the Max-Planck-Society, Germany*

The doping of metal oxides has been explored in several investigations with the aim to prepare better materials for catalysis, optics and electronic

applications. Doping of wide-gap oxide materials can be realized by the controlled introduction of various types of lattice defects, including point defects such as oxygen vacancies, line defects (e.g. grain boundaries and dislocations) and impurity atoms. In this study, we have exploited photon-scanning tunneling microscopy used in imaging as well as in cathode-luminescence mode to investigate Au clusters supported on thin, single crystalline MgO(001) and Cr-doped MgO(001) films grown on Mo(001). First of all, we have prepared Cr-doped MgO films on a Mo(001) support as a model system for a transition-metal doped wide-gap insulator with interesting applications in catalysis. To elucidate the role of the Cr in the MgO matrix, the morphological and optical properties of the system were analyzed as a function of the Cr load, using the STM. The Cr was incorporated into the film either by Cr-Mg co-deposition in oxygen or post-evaporation followed by an annealing step. From the distinct light emission properties of the doped oxide, a detailed picture has been developed on the Cr³⁺ position inside the MgO lattice and the associated modifications in the electronic structure. The role of the Cr dopants on the adsorption behaviour of the oxide film was investigated by depositing small amounts of Au. While on pristine MgO films, Au nucleates into 3D particles, mainly 2D aggregates form on the doped oxide support. We assign this change in the Au growth mode to charge transfer processes from the Cr centres into the Au clusters and will discuss possible consequences on the chemical activity of the doped metal-oxide system.

11:20am **SS2-WeM11 Hydrogen Adatom Manipulation on the Rutile TiO₂(110) Surface using LT-STM**, *P. Sutter, D. Acharya, N. Camillone III, Brookhaven National Laboratory*

Characterization and control of the structure of TiO₂ surfaces at the single-atom level are vital to the development of a fundamental understanding of the chemistry and physics of this technologically important oxide. In this work we investigate the use of a low-temperature scanning tunneling microscope (LT-STM) tip to manipulate individual hydrogen adatoms on the rutile TiO₂(110) surface at 77 K. We show that applied voltage pulses are effective for transferring hydrogen atoms from the surface to the STM tip with single-atom control. This tip-induced ‘desorption’ is useful for unambiguously distinguishing between surface hydroxyls (OH_{br}) and bridging oxygen (O_{br}) vacancies—two common surface defects whose appearance in STM images is quite similar. In addition we show that individual atoms can be redeposited on the surface precisely at selected O_{br} sites, allowing for the controlled preparation of arbitrary hydrogen adatom assemblies. Such control is a prerequisite for the investigation of the structural dependence of surface photo- and thermal reactivity at the single-molecule level.

11:40am **SS2-WeM12 Reaction of Water with Terminal Hydroxyls on TiO₂(110) Surface**, *I. Lyubinetsky, Y.G. Du, Pacific Northwest National Laboratory, N.A. Deskins, Worcester Polytechnic Institute, Z. Zhang, Baylor University, Z. Dohnalek, M. Dupuis, Pacific Northwest National Laboratory*
We report a combined experimental and theoretical investigation of the reaction of molecular water with terminal hydroxyls (OH_t) on reduced TiO₂(110)-(1x1) surface at 300 K. We show that OH_t's have a significant effect on the water reactivity and extract molecular-level details about the underlying reaction mechanisms. By tracking the same surface area with high-resolution scanning tunneling microscopy before and after water exposure, we demonstrate that there are two distinctive reaction pathways involving multiple proton transfers [1]. For water interaction with OH_t on an adjacent Ti row, the proton can be transferred through bridging oxygen to OH_{br}, which leads to the formation of a new water molecule and apparent across-row motion of OH_t due to O scrambling. This process further manifests the existence of the equilibrium between molecular and dissociated states of water on TiO₂(110) [2]. If H₂O interacts with OH_t along the same Ti row, fast multi-step OH_t motion along the Ti row is observed. Our density functional theory results show that this process is caused by the fast diffusion of (OH_t + H₂O) pairs, whereby the underlying mechanism involves proton transfer and H₂O hopping over OH_t.

[1] Y. Du, N. A. Deskins, Z. Zhang, Z. Dohnálek, M. Dupuis, and I. Lyubinetsky, *Phys. Chem. Chem. Phys.* 12 (2010) 6337.

[2] Y. Du, N. A. Deskins, Z. Zhang, Z. Dohnálek, M. Dupuis, and I. Lyubinetsky, *Phys. Rev. Lett.* 102 (2009) 096102.

This work was supported by the U.S. Department of Energy (DOE) Office of Basic Energy Sciences, Division of Chemical Sciences, and performed at EMSL, a national scientific user facility sponsored by the DOE's Office of Biological and Environmental Research and located at PNNL.

Thin Film Division

Room: 110 - Session TF1+EM-WeM

ALD/MLD: Hybrid Organic Films

Moderator: Q. Peng, Duke University

8:00am **TF1+EM-WeM1 Vapor-Phase Fabrication of Organic-Inorganic Hybrid Thin Films Using Molecular Layer Deposition with Atomic Layer Deposition, M.M. Sung**, Hanyang University, Korea
INVITED

We report a vapor phase deposition method of high quality organic thin films, called molecular layer deposition (MLD). MLD is a gas phase process analogous to ALD and also relies on sequential saturated surface reactions which result in the formation of a self-assembled monolayer in each sequence. In the MLD method, the high quality organic thin films can be quickly formed with monolayer precision under ALD conditions (temperature, pressure, etc). The MLD method can be combined with ALD to take advantages of the possibility of obtaining organic-inorganic hybrid thin films. The advantages of the MLD technique combined with ALD include accurate control of film thickness, large-scale uniformity, excellent conformality, good reproducibility, multilayer processing capability, sharp interfaces, and excellent film qualities at relatively low temperatures. Additionally, a vast library of materials is accessible by ALD methods, ranging from single elements to compound semiconductors to oxides, nitrides, and sulfides. Therefore, the MLD method with ALD is an ideal fabrication technique for various organic-inorganic nanohybrid superlattices.

8:40am **TF1+EM-WeM3 Metalcone and Metalcone/Metal Oxide Alloys Grown Using Atomic & Molecular Layer Deposition Techniques, B.H. Lee, V.R. Anderson, S.M. George**, University of Colorado, Boulder

A new class of films known as the "metalcones" can be grown using atomic layer deposition (ALD) and molecular layer deposition (MLD) techniques. Metalcones are hybrid organic-inorganic materials derived from the sequential, self-limiting reactions of metal and organic alcohol precursors. The first metalcones were the "alucones" based on trimethylaluminum and ethylene glycol (EG) and the "zincones" based on diethylzinc and EG. Other metalcones can be fabricated with various properties using different metal precursors together with organic alcohols. This talk reports new metalcones known as the "zircones" using zirconium tert-butoxide (ZTB) and EG. In addition, this talk will discuss two new tunable ALD:MLD films based on alloys of alucone MLD/Al₂O₃ ALD and zircone MLD/ZrO₂ ALD. Zircone MLD films were grown by using zirconium tert-butoxide (ZTB) and EG. MLD growth was observed at temperatures ranging from 105 to 195°C. *In situ* quartz crystal microbalance and *ex situ* X-ray reflectivity (XRR) experiments confirmed linear growth of zircone MLD versus number of ZTB/EG reaction cycles. Zircone MLD growth rates decreased versus temperature and varied from 1.6 Å per cycle at 105°C to 0.3 Å per cycle at 195°C. A constant density of ~2.3 g/cm³ was measured for all growth temperatures. XRR measurement also showed that zircone MLD films were very stable under ambient conditions. The metalcones will have useful mechanical, optical and electrical properties that can be tuned by growing alloys of the metalcones and their parent metal oxides. For example, this tuning allows the density of alucone MLD/Al₂O₃ ALD alloys to be varied from 1.6 g/cm³ to 3.0 g/cm³. The density of zircone MLD/ZrO₂ ALD alloys could also be varied from 2.3 g/cm³ to 4.0 g/cm³. The reflective index of zircone MLD/ZrO₂ MLD alloys was also tuned continuously between 1.63 and 1.86. These new metalcone materials provide a tool set for engineering the functional properties of thin films. These materials can be grown with atomic control of thickness and excellent conformality. The metalcones and metalcone alloys can also be thermally annealed to remove the organic constituent and create porous metal oxide films.

9:00am **TF1+EM-WeM4 Sequential Vapor Infiltration and Atomic Layer Deposition on Surfactant Films for Mesoporous Metal Oxide, B. Gong, D. Kim, G.N. Parsons**, North Carolina State University

Mesoporous materials are critical for applications such as catalyst support, energy storage and conversion, and chemical separations. Conventionally, solution based approaches are employed for the preparation of these materials, and amphiphilic molecules are widely used as templates to form well defined pore size and surface area. In these methods, the interaction between the hydrophilic block of the surfactant molecules and the metal oxide precursors direct the self-assembly of ordered micelles/metal oxide hybrid materials, and porous inorganic structures were recovered after removal of the organic template. Recently, this selective interaction was also discovered during vapor phase sequential vapor infiltration and atomic

layer deposition (ALD) of metal oxide onto polymers, where precursor infusion and reaction depends strongly on the interaction between the precursor and polymer starting substrate. We therefore believe that sequential vapor infiltration or ALD on amphiphilic surfactant molecule films could also yield ordered inorganic/organic hybrid materials and porous metal oxides.

In this work, mesoporous aluminum oxide and titanium oxide materials were prepared by the vapor phase infiltration and ALD on two kinds of surfactants: the ionic cetyltrimethylammonium bromide (CTAB) and poly ethylene oxide based nonionic surfactant F127 (PEO-PPO-PEO). The nitrogen adsorption and desorption measurement was employed to measure the specific surface area and the pore size distribution of the resulted material. In-situ FTIR was used to monitor the chemistry change during the vapor infiltration, SEM TEM and XRD were used to characterize the structure and the morphology of the porous material.

We find that both sequential vapor infiltration and ALD produced mesoporous materials. However, the vapor phase infiltrated films show a relative higher specific surface area and narrower pore size distribution. This can be explained by the more uniform distribution of metal oxide into the surfactant layer compared to ALD. These results demonstrate a new vapor phase approach for well defined mesoporous materials, which would potentially important for many advanced applications.

9:20am **TF1+EM-WeM5 Flexibility and Water Vapor Transmission Rates for Al-, Hf-, and Zr-based ALD Films and Nanolaminates Utilizing Water and Glycerol Co-Reactants, M.J. Sowa, E.W. Deguns**, Cambridge NanoTech, Inc.

Organic electronics constructed on flexible substrates stand to revolutionize the display and lighting markets due to the low potential cost of manufacturing inherent to roll-to-roll manufacturing. A significant downside to organic electronics is their sensitivity to atmospheric oxygen and moisture. Various encapsulation techniques have been demonstrated, some of which have achieved Water Vapor Transmission Rates (WVTR) better than 1e-6 g/m²/d, which has been suggested to be the maximum allowable rate to give a minimum usable lifetime of 10,000 hours for Organic Light Emitting Diodes (OLEDs). However, most of the encapsulation technologies that provide these low WVTRs lack the flexibility of the underlying plastic substrate or the organic electronics, limiting the actual flexibility of the final product.

Here we will report on the flexibility of aluminum-, hafnium-, and zirconium-based ALD films deposited on representative substrate material samples of polyethylene naphthalate (PEN) at 115°C. Metal precursors used were trimethyl aluminum (TMA), tetrakis(dimethylamino)hafnium (TDMAH), and tetrakis(dimethylamino)zirconium (TDMAZ). Water was used as the ALD co-reactant for producing inorganic films while glycerol was utilized as the co-reactant for depositing hybrid organic films. Various nanolaminate combinations of the inorganic/organic materials were also investigated for their response to various levels of strain. Inorganic Al₂O₃ films subjected to 2% strain were observed to begin cracking at thicknesses below 27nm. A 2% strain did not cause any cracking on organic films deposited with TMA and glycerol to the thickest film studied at 245nm. Organic films were always observed to be more flexible than inorganic films of the same thickness. Nanolaminates were observed to have flexibility intermediate to their pure inorganic and organic constituents.

WVTR measurements were performed on inorganic, organic, and nanolaminate aluminum films. A WVTR of 6.1e-6 g/m²/day was obtained for a 100nm inorganic Al₂O₃ film. A substantially more flexible 100nm TMA + glycerol film gave a WVTR of 9.2e-6 g/m²/day.

The technical issues associated with uniformly delivering glycerol to a 115°C ALD reactor will also be discussed.

9:40am **TF1+EM-WeM6 Polymer Wires Containing Quantum Dots with Different Lengths Grown by Molecular Layer Deposition: Potential Applications to Sensitization in Photovoltaics, T. Yoshimura, R. Ebihara, A. Oshima**, Tokyo University of Technology, Japan

[Introduction] Molecular layer deposition (MLD) grows tailored polymer wires with designated molecular arrangements by connecting different kinds of molecules with monomolecular steps. We grew polymer wires with quantum dots (QDs), called as "polymer multiple quantum dot (polymer MQD)," by MLD using three kinds of molecules, terephthalaldehyde (TPA), *p*-phenylenediamine (PPDA) and oxalic dihydrazide (ODH), and proposed their potential applications to sensitized photovoltaic devices.

[Polymer MQDs] As a preliminary work, polymer MQDs of OTPTPT, OTPT and OT were grown. In OTPTPT, molecules are connected in a sequence of -ODH-TPA-PPDA-TPA-PPDA-TPA-ODH---. The region

between two ODHs is a QD of ~3-nm long. In OTPT, ~2-nm-long QDs are constructed with a molecular sequence of -ODH-TPA-PPDA-TPA-ODH---. In OT, ~0.8-nm-long QDs are constructed by connecting ODH and TPA alternately. A polymer MQD with three kinds of QDs, "3QD-MQD," in which OT-like QD [OT], OTPT-like QD [OTPT] and OTPTPT-like QD [OTPTPT] are formed in one polymer wire, was grown with a sequence of -ODH-TPA-ODH-TPA-PPDA-TPA-ODH-TPA-PPDA-TPA-PPDA-TPA-ODH---. For polymer MQD growth, we used the carrier-gas type MLD, where carrier gas of nitrogen was employed to give molecular gas blows onto substrates through valves for molecular gas switching.

[Light Absorption Spectra] Light absorption measurements revealed that the peak energy of the absorption spectra shifts toward the high energy side with decreasing the QD length, namely, in the order of OTPTPT, OTPT, and OT. This effect is attributed to the quantum confinement. The absorption spectrum of 3QD-MQD is broad extending from ~480 nm to ~300 nm, which is a superposition of the spectra of [OTPTPT], [OTPT], and [OT]. This result indicates that the polymer MQD with different QD lengths could be an efficient sensitizer. In addition, the molecular orbital calculation confirmed that the electron density is high in the QD regions of 3QD-MQD.

[Proposal of Polymer MQD Sensitization] In the polymer MQD sensitization, polymer MQD is on a ZnO surface as a sensitizer. QDs exhibit narrow absorption bands comparing with bulk semiconductors like Si due to their zero-dimensional characteristics. The absorption peak energy can be adjusted by QD lengths. Therefore, polymer MQD containing different-length QDs enables us to divide the wavelength region for light absorption into narrow regions. Each QD absorbs lights of wavelengths matched to its own energy gap, and injects the excited electrons into ZnO. This might suppress the energy loss arising from the heat generation in the light absorption process. The structure is regarded as a molecular tandem structure.

10:40am **TF1+EM-WeM9 Hybrid Materials by Vapor Phase Infiltration**, *M. Knez*, Max-Planck-Institut für Mikrostrukturphysik, Germany **INVITED**

Atomic layer deposition (ALD) is a thin film deposition technique which was developed in the 1970s to meet the needs for processing thin film electroluminescent displays (TFEL). Technically and chemically it is similar to chemical vapor deposition (CVD). However, in contrast to CVD, ALD incorporates as a specific feature the separation of the chemical reaction into two half-reactions. The ALD is not only able to perform thin film coatings of inorganic materials, but also allows coatings with organic-inorganic hybrid materials and, due to the separated exposure of the substrate to the precursors, infiltration of soft matter.

This talk will show top-down approaches to hybrid organic-inorganic and bio-inorganic materials obtained by infiltration with metals from the vapor phase. With tiny amounts of metals infiltrated, biological materials, such as spider silk or collagen, can positively change their mechanical properties after being treated with pulsed vapors of metal-organic precursors. The improvement of mechanical properties is related to changes in the molecular structure of the protein-based materials. However, not only biopolymers undergo changes after infiltration. With the example of some synthetic polymers, analogous routes to modify their mechanical properties will be shown.

11:20am **TF1+EM-WeM11 Titanicene Molecular Layer Deposition Using TiCl₄ and Sugar Alcohols and Porous TiO₂ Films Produced by Annealing**, *R.A. Hall, A.I. Abdulagatov, S.M. George*, University of Colorado, Boulder

Metalcone molecular layer deposition (MLD) can be performed using metal precursors and organic diols or triols. The first metalcone MLD films were the alucones and zincones grown using trimethylaluminum and diethylzinc, respectively, with ethylene glycol (EG). In this work, we report the growth of titanicone MLD films using TiCl₄ and two sugar alcohols: EG and glycerol (GL). The titanicones may have useful photocatalytic properties and may form valuable porous TiO₂ frameworks upon annealing to remove the organic constituent. Titanicone films were grown using TiCl₄ and EG at temperatures between 90-135°C. Quartz crystal microbalance (QCM) measurements observed a growth rate of ~83 ng/cm²-cycle from 90 to 115°C before decreasing significantly at 135°C. X-ray reflectivity (XRR) studies obtained a growth rate of 4.5 Å/cycle with a density of 1.84 g/cm³ at 115°C. Titanicone films were grown using TiCl₄ and GL at higher temperatures between 130-210°C. The GL is believed to lead to more cross-linking that stabilizes the MLD film. QCM measurements observed growth rates that varied slightly with temperature from 49 ng/cm²-cycle at 130°C to 34 ng/cm²-cycle at 210°C. XRR studies yielded a growth rate of 2.2 Å/cycle at 150°C. QCM measurements revealed that the surface chemistry for titanicone MLD was self-limiting. XRR studies indicated that the titanicone films were stable in air. The titanicone films were absorptive in the

ultraviolet and consistent with an optical bandgap of ~3.5 eV. Annealing the titanicone films removed the carbon component and yielded porous TiO₂ films. Ultraviolet exposures also appear to be able to produce porous TiO₂ films. The ability to deposit conformal porous TiO₂ films on high surface area substrates could produce "super" high surface area substrates. These substrates may serve as TiO₂ scaffolds for dye-sensitized solar cells or photocatalytic membranes.

Wednesday Lunch, November 2, 2011

Exhibitor Technology Spotlight

Room: West Exhibit Hall - Session EW-WeL

Find out more at the Spotlight Session on SpringerMaterials at AVS 58

Exhibitor Technology Spotlight

Moderator: Langley

12:20pm EW-WeL2 Granville Phillips Autoresonant Ion Trap Mass Spectrometer, *S. Lass*, Brooks Automation, Inc.

Granville-Phillips®, the Instrumentation Center for Brooks Automation Inc., recently introduced the VQM830 Vacuum Quality Measurement (VQM) System for gas analysis at high and ultra-high vacuum levels that is comprised of a high-speed Autoresonant Ion Trap Mass Spectrometry (ART MS) Sensor and High Performance VQM Controller. With advantages in speed, power consumption, simple calibration, accurate low mass reporting, and UHV performance, the VQM surpasses the traditional RGA products. In addition to explaining the advantages of this next generation mass spectrometer, new additions to the VQM family since initial product shipment will be covered.

12:40pm EW-WeL3 Combining NEG and Sputter Ion Pump Technologies to Meet the Challenges of UHV-XHV Systems, *B. Garcia, F. Siviero, A. Conte, L. Viale, A. Bonucci, P. Manini, L. Caruso, A. Cadoppi*, SAES Getters

Current UHV and XHV vacuum technology requires better vacuum, lower power consumption and smaller components. The NEX Torr pumping system meets these requirements by providing large pumping, good gas capacity, low power consumption and vibration free pumping in an unprecedented small size. Specifications and data will be presented to discuss advantages of the NEX Torr pumping system.

1:00pm EW-WeL4 EW - No Title - EW - No Title, *S. Palmer*, Agilent - Varian Vacuum Division

1:20pm EW-WeL5 Faster, Higher Resolution and More Accurate Imaging with the Cypher™ Atomic Force Microscope, *K. Jones*, Asylum Research

Within four years of the invention of the AFM, micro-fabricated cantilevers with integrated tips appeared, saving early practitioners from the joys of hand-assembling their cantilevers. However, even though many researchers soon understood the benefits of further miniaturization of the lever, standard commercial levers remained at the same 100 to 300 μm size for nearly the next two decades, in part because making a commercial instrument capable of using much smaller levers presented significant technical challenges.

Within the past few years, commercial instruments like the Cypher AFM, from Asylum Research, have appeared which are capable of using cantilevers as small as 10 μm in length and with resonance frequencies 5 MHz and higher and those levers are now readily available. Small levers bring two major benefits to AFM. The first is much smaller thermal noise, enabling quieter force measurements and higher resolution imaging with Angstrom-scale cantilever amplitudes. The second is a major speed boost for AC modes (tapping, non-contact) in both air and liquid. When coupled with other instrumental improvements such as a high-speed scanner, the shorter levers allow scanning with good tracking at rates 20X to 40X what was possible with conventional levers. I will talk about the technical details behind both these improvements. I will also present images and movies highlighting the improvements, including images showing individual vacancy defects on crystals and movies showing fast scanning on polymers, crystals, and biological samples.

1:40pm EW-WeL6 SpringerMaterials – An Online Resource Facilitating Vacuum Research and Development, *M. Shaikh*, SpringerMaterials

SpringerMaterials is an invaluable database for research both exploring and requiring vacuum science, as well as for the development of equipment that harnesses vacuum technology. Use this online resource to search for data on materials' interactions with photons and electrons, molecular constants, coupling constants via nuclear magnetic resonance data, band structures via Photoelectron Spectroscopy, electronic transport, thermal and optical properties for a huge range of semiconductors, surface sciences and properties, characterization methods, metallic and organic thin films, particle detector systems, and so much more! With over 100,000 critically evaluated documents on properties of about 250,000 different substances, a robust metacontent system and advanced search engine, you are sure to find what you are looking for vacuum research and development.

Wednesday Afternoon, November 2, 2011

Actinides and Rare Earths Focus Topic

Room: 209 - Session AC+MI-WeA

Magnetic and Electron Correlation Effects in Actinides and Rare Earths

Moderator: J.G. Tobin, Lawrence Livermore National Laboratory

2:00pm AC+MI-WeA1 Electronic Structure Theory of Complex Ordered Actinide Materials, *P.M. Oppeneer*, Uppsala University, Sweden **INVITED**

Actinide materials display many complex and correlated behaviors that originate from the special properties of the open f-shell atom embedded in a specific material's environment. First-principles investigations provide a route to assess these anomalous phenomena in a materials specific way, providing direct, fundamental insight.

Here we consider recently obtained *ab initio* modeling results for actinide materials that are in the focus of current interest: actinide oxides, such as NpO₂, PuO₂, and higher-oxides, U₃O₈, and Np₂O₅, the hidden order (HO) material URu₂Si₂, and correlated plutonium compounds.

NpO₂ is one of the very few materials in which complex multipolar order has been identified. Using the density-functional theory (DFT)-based LDA+*U* method we provide a first-principles theory of multipolar order and superexchange in NpO₂. DFT+*U* calculations offer a precise microscopic description of the 3*q*-antiferro ordered phase. We find that the usually neglected higher-order multipoles (electric hexadecapoles and magnetic triakontadipoles) are at least equally significant as the electric quadrupoles and magnetic octupoles [1].

We further investigate light actinide oxides in higher oxidation states, such as U₃O₈, PuO_{2+x}, and Np₂O₅, for which non-collinear magnetic ordering is predicted. The possible further oxidation of PuO₂ to PuO_{2+x} is studied using DFT+*U* calculations in combination with x-ray absorption measurements [2].

The Pu monochalcogenides are intriguing materials, in which a correlated temperature gap develops, reminiscent of the behavior seen in Kondo insulators. Using dynamical mean field theory (DMFT) in comparison to LDA+*U* calculations, we show that dynamical self-energy fluctuations are important for the formation of an unusual gap. Static approximations to the self-energy as the LDA+*U* fail to provide a gap.

For URu₂Si₂ we report extensive electronic structure investigations [3], using full-potential LSDA, LSDA+*U*, and DMFT approaches to assess the origin of the hidden order. Our investigation show that the itinerant f-electron picture provides an excellent description of the materials properties of this fascinating compound. The Fermi surface which is crucial for the HO transition and the occurrence of unconventional superconductivity is accurately given. Our study points to the formation of long-lived spin fluctuations that are the driving quasiparticles for the HO.

1. M.-T. Suzuki, N. Magnani, and P.M. Oppeneer, Phys. Rev. B **82**, 241103(R) (2010).
2. A. Modin, Y. Yun, M.-T. Suzuki et al., Phys. Rev. B **83**, 075113 (2011).
3. P.M. Oppeneer, J. Ruzs, S. Elgazzar, M.-T. Suzuki, T. Durakiewicz, and J.A. Mydosh, Phys. Rev. B **82**, 205103 (2010).

2:40pm AC+MI-WeA3 Anomalous Quasiparticle Dynamics in the Hidden Order state of URu₂Si₂, *T. Durakiewicz, G.L. Dakovski, Y. Li, S.M. Gilbertson, G. Rodriguez, A.V. Balatsky, J.X. Zhu, K. Gofryk, E.D. Bauer, P.H. Tobash, A. Taylor, J.L. Sarrao*, Los Alamos National Lab, *P.M. Oppeneer*, Uppsala Univ., Sweden, *P.S. Riseborough*, Temple Univ., *J.A. Mydosh*, Leiden Univ., the Netherlands **INVITED**

An exotic phase of unknown nature emerges from a heavy fermion state in URu₂Si₂ at T₀ = 17.5 K. The nature of this hidden order (HO) state is being vigorously debated, while the massive removal of entropy due to the HO transition evades explanation. Here we use time- and angle-resolved photoemission spectroscopy (tr-ARPES) to elucidate the itinerant nature of HO. We show how the Fermi surface is renormalized by shifting states away from the Fermi level at specific hot spots. By measuring the ultrafast dynamics we identify the location and lifetime of the quasiparticle states forming at the hotspots. We find that the quasiparticle lifetime increases from 42 fs to few hundred fs across the HO transition, and the hidden order parameter is related to the anisotropic gapping of the Fermi surface.

4:00pm AC+MI-WeA7 Advanced X-ray Spectroscopies on 4f and 5f Systems, *J. Bradley, M. Lipp*, Lawrence Livermore National Laboratory, *A. Sorini*, SLAC National Accelerator Laboratory

Photon-in photon-out x-ray spectroscopies allow for a bulk-sensitive, high-pressure compatible look at rare earth and actinide electronic structure. The techniques couple to well-defined and meaningful quantum mechanical observables, including orbital occupation number and magnetic moment. These observables are key differentiators between theoretical treatments of strongly correlated systems, and they also provide meaningful and correct intuitive understanding. Here we will present a selection of measurements, both at ambient and high pressure, that exemplify the kind of insight these techniques can provide. In particular, we will address the question of rare earth volume collapse, where considerable controversy has existed between competing (Mott vs. Kondo) theoretical treatments.

4:20pm AC+MI-WeA8 Hard X-Ray Photoelectron Spectroscopy and Electronic Structure of Single Crystal UPd₃, UGe₂, and USB₂, *M.F. Beaux, T. Durakiewicz, J.J. Joyce, E.D. Bauer, J.L. Sarrao*, Los Alamos National Laboratory, *L. Moreschini, M. Grioni*, Ecole Polytechnique Federale, Switzerland, *F. Offi*, Universita Roma Tre, Italy, *M.T. Butterfield*, KLA-Tencor, *G. Monaco*, European Synchrotron Radiation Facility, France, *G. Panaccione*, Laboratorio Nazionale TASC-INFN-CNR, Italy, *E. Guziewicz*, Polish Academy of Sciences

Hard X-ray Photoelectron Spectroscopy (HAXPES) with 7.6 keV photons has been performed on single crystals of UPd₃, UGe₂, and USB₂ at the European Synchrotron Radiation Facility (ESRF). The greatly reduced surface sensitivity of HAXPES enabled observation of the bulk core levels in spite of surface oxidation. An 800 meV splitting within the Sb 3d core level was observed. The splitting of the Sb core levels is attributed to manifestations of two distinct Sb binding sites within the USB₂ single crystal as supported by consideration of interatomic distances and enthalpy-of-formation. Photoelectron mean-free-path vs oxide layer thickness considerations were used to model the effectiveness of HAXPES for probing bulk features of in-air cleaved samples.

4:40pm AC+MI-WeA9 Actinide Dioxides under Pressure, *L. Petit*, Daresbury Laboratory, UK

The self-interaction corrected local spin density approximation is used to investigate the oxidation of actinide dioxides under pressure. The methodology enables us to determine the ground state valency configuration of the actinide 5f electrons and to study the localization/delocalization transition that occurs under pressure. We argue that this delocalization facilitates the oxidation of the actinide dioxides and present results for the estimated transition pressures.

5:00pm AC+MI-WeA10 Hybridization and Electronic Structure in Pu Compounds, *J.J. Joyce, T. Durakiewicz, K.S. Graham, M.F. Beaux, E.D. Bauer, J.N. Mitchell, T.M. McCleskey, E. Bauer, Q.X. Jia, R.L. Martin, J.X. Zhu, J.M. Wills*, Los Alamos National Laboratory, *L. Roy*, Savannah River National Laboratory, *G.E. Scuseria*, Rice University

The electronic structure of Pu materials is directly tied to the details of the 5f electron bonding and hybridization. In compounds where direct 5f-5f bonding is negligible due to crystal structure and wavefunction overlap, hybridization is the key component for 5f electron influence on electronic properties. We examine two strongly correlated materials, PuCoGa₅ and PuO₂ that span the range of interesting materials from Mott insulator to heavy fermion superconductor. The synergy between synthesis, spectroscopy and modeling has provided a unique opportunity to explore details of the energy and crystal momentum dependence of Pu compound electronic structure through angle-resolved photoemission on single crystal samples and advanced modeling based on theories beyond density functional theory.

The strength of the 5f electron hybridization may be quantified through dispersion in 5f electron peaks from the angle-resolved photoemission. In the case of PuO₂, we see over two eV of dispersion in the hybridized (O 2p - Pu 5f) valence band. For PuCoGa₅, the quasiparticle peak at the Fermi energy shows 50 meV or more of dispersion in reciprocal space over a range covering slightly less than half the zone center to zone boundary. We are unable to follow the peak dispersion beyond this point as it crosses above the Fermi energy. These energy dispersions place significant constraints on models, which might be used to describe the electronic structure of these strongly correlated materials. For PuCoGa₅, models, which place the 5f electrons in a localized configuration without significant hybridization, would not agree with the experimental results. In the case of PuO₂, the dispersion measured in photoemission agrees well with the

hybrid functional calculations for PuO₂ and further support the increase in hybridization moving from ionic UO₂ to covalent PuO₂.

5:20pm **AC+MI-WeA11 Structure and Magnetic Properties of Actinide-Based Thin Films**, *L. Havela*, Charles University, Czech Republic, *N.-T. Kim-Ngan*, Pedagogical University Cracow, Poland, *A. Adamska*, Charles University, Czech Republic, *A.G. Balogh*, TU Darmstadt, Germany, *T. Gouder*, European Commission, JRC Institute for Transuranium Elements, Germany

INVITED

Actinide-based sputter deposited films were so far used in the context of surface-science studies (such as [1]) and for exploration of electronic structure by photoelectron spectroscopy (e.g. [2,3]). In addition, sputter deposition was used in attempts to synthesize amorphous uranium alloys for ex-situ studies of magnetic properties. Such early (late 1980's) attempts in U.S. [4] or Japan [5] were undertaken in simple setups and lack proper diagnostics of the deposited material. Considering strong electropositivity of U, oxidation has to be suspected for films prepared in HV conditions. More recently, U metal in multilayers with possibility of epitaxial growth were sputter deposited with the aim to induce uranium magnetic moments [6]. We have used sputter deposition to investigate structure and magnetic properties of various U-based compounds as a function of deposition conditions (deposition rate, substrate type and temperature). Employing diagnostics by XPS, Glancing Angle XRD, and RBS, it was established that UN films have a long-term stability, which allows comfortably to make ex-situ studies over months. The reason can be seen in pronounced compressive residual strains, imposed during the deposition, which prevent progressing the surface oxidation into the bulk of several hundred nm thick films. Departing more from a fully crystalline state, the antiferromagnetism of UN is masked by a weak ferromagnetism, as usual for nanograined AF structures, and finally both moments and their order disappears [7]. Similar suppression of magnetism was found for ferromagnetic US [8].

Recently we undertook sputter-deposition experiments on Fe-rich U-Fe alloys derived from the Laves phase UFe₂, which combines the 3d and 5f magnetism in a compound with a relatively high Curie temperature ($T_C = 162$ K). An Fe-excess is expected to increase the T_C value markedly. Nanocrystalline material obtained up to the stoichiometry UFe_{2.3} by splat cooling, with the excessive Fe atoms entering the U sublattice has T_C enhanced up to 230-240 K. More Fe leads to the segregation of α -Fe. We succeeded to synthesize amorphous films by U and Fe co-sputtering, with stoichiometry up to UFe₃. T_C is enhanced up to 450 K in this case.

- [1] T. Gouder et al., Surface Science 601 (2007) L77.
- [2] T. Gouder et al., Phys.Rev.Letters 84 (2000) 3378.
- [3] L. Havela et al., Phys.Rev.B 65 (2002) 235118.
- [4] P.P. Freitas et al., J.Appl.Phys. 63 (1988) 3746.
- [5] S. Itoh et al., Physica B 281-282 (2000) 230.
- [6] R. Springell et al., Phys. Rev. B 77 (2008) 064423.
- [7] D. Rafaja et al., J.Alloys Comp. 386 (2005) 87.
- [8] L. Havela et al., J. Alloys Comp. 408-412 (2006) 1320.

Applied Surface Science Division
Room: 102 - Session AS-WeA

Correlative Analysis - A Multi-technique Approach for Identification and Structure-Property Relationships

Moderator: K. Artyushkova, The University of New Mexico

2:00pm **AS-WeA1 Complementary Ultra Thin Film Analysis using Low Energy Ion Scattering (LEIS) and TOF-SIMS**, *T. Grehl*, P. Bruener, ION-TOF GmbH, Germany, *N. Havercroft*, ION-TOF USA, Inc., *H. Brongersma*, *E. Niehuis*, ION-TOF GmbH, Germany

Ultra-thin film structures have become increasingly important and simultaneously gained complexity with regard to the number of layers and the elemental composition. Understanding the processes occurring during deposition is crucial for improving the film quality. Especially during the first stages of film growth, analytical techniques with high surface sensitivity and good detection limits are required to study the growth process.

Low Energy Ion Scattering (LEIS) lends itself well to these tasks with its ultimate surface sensitivity of a single monolayer and detection limits of down to 10 ppm. This is accomplished by bombarding the surface with noble gas ions of a few keV and measuring the energy loss of the backscattered ions at a fixed scattering angle. The energy spectrum is

converted into a mass spectrum of the elements present at the sample surface. The absence of matrix effects allows a straightforward quantification.

Besides the composition analysis of the outermost atomic layer, depth profiling is available via two distinct methods. Static depth profiling exploits the fact that ions scattered in deeper layers lose additional energy proportional to the penetration depth. As this process involves neutralization and re-ionization, intensities are lower than for the ions scattered at the surface. Thus, these ion can be distinguished, giving information about the elemental distribution in the first few nm in a non-destructive way. Alternatively, dynamic depth profiling is available by using a second, low energy sputter ion beam to erode the surface while recording surface spectra at different depths. This yields a quantitative, high depth resolution depth profile. By observing the change in the static in-depth signal during sputtering, the sputter rate can be intrinsically and continuously determined.

The unique advantages of LEIS complement established techniques like TOF-SIMS. The latter is often hampered by sputter transients at interfaces and difficult quantification especially of matrix species, but excels as far as the detection of trace elements or the gaining of chemical composition information is concerned. We applied both LEIS depth profiling modes to a number of thin film sample systems. Hereby we show the possibilities arising from each of the two modes, as well as from the combination with TOF-SIMS. Specifically, we worked on model samples relevant to the semiconductor industry (high-k, SiGe). Some of these samples were designed for studying the response function of the in-depth signal in order to improve the understanding and to allow the application to real-world samples, e. g. to correct for varying erosion rates.

2:20pm **AS-WeA2 Multi-technique Characterization of Polymer Surfaces and Diamond-Like Carbon Films**, *P. Mack*, *R.G. White*, *A.E. Wright*, Thermo Fisher Scientific, UK

Surface treatment of polymers produces materials that exhibit a wide range of surface compositions, properties and structures. The chemical and structural properties of these novel materials can be exploited for the fabrication of devices for bio-medical and electronics applications. Additionally, the wear-resistant properties of steel can be modified by coating the surface with a diamond-like carbon (DLC) film.

The combination of a variety of complementary surface-sensitive electron spectroscopies maximises the information available to the analyst for full quantitative surface characterisation of polymer surfaces and DLC films. The silicon content of a DLC film can affect its hardness, for example, and XPS is the ideal technique for chemical quantification of the silicon. The concentration of hydrogen in a DLC film also modifies its wear properties, but XPS cannot quantify this element. It is possible, however, to detect and quantify hydrogen using Reflected Electron Energy Loss Spectroscopy (REELS). When used together, XPS and REELS can provide a total quantification for polymer surfaces and DLC films.

This presentation will show how Thermo Scientific tools can be used to investigate the chemistry and structure of various polymer and DLC samples. Chemical changes produced by surface treatments were examined by high energy resolution XPS and argon profiling (both monomer and gas cluster). Complementary REELS measurements were used to examine the level of carbon unsaturation at the uppermost surface of each sample and to detect and quantify hydrogen.

2:40pm **AS-WeA3 Challenges Associated with Mathematically Correlating Data from Multiple Surface Characterization Techniques**, *K.G. Lloyd*, *D.J. Walls*, *L. Zhang*, *J.P. Wyre*, DuPont Corporate Center for Analytical Sciences

INVITED

There are now many examples of multivariate analysis of surface-specific technique data[1,2]. These include multivariate statistical methods such as Principal Components Analysis (PCA), Partial Least Squares (PLS), or Multivariate Curve Resolution (MCR) applied to so-called "hyperspectral" mapping data, in which hundreds of channels of spectral data are collected at each pixel of a two-dimensional pixel array spanning an area of interest. The idea of trying to mathematically correlate different sets of mapping data from the same area is not new[3], and falls under the broader category of 'image fusion' used in conjunction with remote sensing applications[4]. However, this approach is not prevalent in the surface science literature, with the notable exception of Fulghum and Artyushkova[5,6].

There are good reasons for this, from both the experimental and modeling perspectives. This talk will discuss the challenges associated with mathematically correlating spectroscopic and mapping data from multiple surface-specific techniques. Examples from the literature and the analytical lab will be discussed.

- [1]V. S. Smentkowski, J. A.Ohlhausen, P. G. Kotula, M. R. Keenan, *Applied Surface Science* **2004**, 231, 245.

[2] M. S. Wagner, D. J. Graham, B. D. Ratner, D. G. Castner, *Surface Science* **2004**, 570, 78.

[3] H. Hutter, M. Grasserbauer, *Chemometrics and Intelligent Laboratory Systems* **1994**, 24, 99.

[4] C. Pohl, J. L. Van Genderen., *International Journal of Remote Sensing* **1998**, 19, 823.

[5] K. Artyushkova, J. E. Fulghum, "XPS and Confocal Microscopy Data Fusion for Polymer Characterization," talk presented at American Vacuum Society 50th International Symposium held in Baltimore, MD November 2-7, **2003**.

[6] K. Artyushkova, S. Pylypenko, J. Fenton, K. Archuleta, L. Williams, J. Fulghum, *Microscopy and Microanalysis* **2006**, 12(Suppl. 02), 1402.

4:00pm AS-WeA7 Multi-technique Characterization for Interfacial Analysis, Depth Profile and Chemical Imaging, S.V.N.T. Kuchibhatta, V. Shuithanandan, B.W. Arey, C.M. Wang, M.L. Nandasiri, N. Ponnusamy, T. Varga, S. Thevuthasan, Pacific Northwest National Laboratory, **F. Liu, L. Huang, L. Porter, R.F. Davis,** Carnegie Mellon University, **T. Prosa,** CAMECA Instruments Inc.

Nanoscale interfaces are finding use in a multitude of applications including fuel cells, LEDs etc. In addition, our group at EMSL, Pacific Northwest National Laboratory is interested in understanding the influence of interfaces on energy and environmental applications, in particular, radiation tolerance, and oxygen ion conduction. While a number of techniques are available to synthesize interfaces, their analysis is often challenging. Hence, the fundamental understanding required to develop next generation devices with controlled interfaces is not widely available in the literature. In this context, it is imperative to intelligently combine more than one analytical technique and as appropriate use new techniques with improved spatial and chemical resolutions (better chemical sensitivity and improved mass resolution) to achieve such a goal. Atom Probe Tomography (APT), a relatively new technique that compliments various surface and interfacial analysis tools, is capable of providing 3D-chemical images of various materials including multi-layer thin films with sub-nanometer spatial and a ppm level chemical resolution. This talk will focus on combining the information obtained from high-resolution scanning transmission electron microscopy, high-resolution Rutherford backscattering spectrometry, x-ray photoelectron spectroscopy, atom probe tomography, x-ray reflectivity and diffraction analysis of two sets of multi-layer thin films. The first set of multi-layer thin films is synthesized using oxygen plasma-assisted molecular beam epitaxy consisting of samaria doped cerium oxide and scandia stabilized zirconium oxide. These films are expected to provide significantly enhanced oxygen-ion conduction relative to the films that are made of either of the materials. The second set of films, consisting of GaN, InGaN multi-quantum well structures, is prepared using metal-organic chemical vapor deposition. These structures as green LED active regions were shown to have significant improvements in internal quantum efficiency when employing an InGaN buffer layer to modulate MQW interface roughness. The information such as layer thickness, elemental composition of the layers and interfacial roughness/mixing would be compared from various techniques mentioned earlier. Dopant distribution and any possible intermixing of the layers will be of major interest in the case of ceria-zirconia system. The interfacial roughness and any preferential segregation or clustering of In along with 2D/3D uniformity of the layers will be of most interest in the GaN-InGaN system.

4:20pm AS-WeA8 Characterization of Lubricant Coated Cartridges Using Multiple Surface Analytical Techniques, X. Dong, Z. Xiao, C. Kemp, Eli Lilly and Company

Glide force is a key performance attribute for pharmaceutical injection devices. It is directly impacted by lubricant amount, lubricant distribution, and surface chemistry. However, obtaining accurate information on these lubricant properties has been a challenge within the industry because all of the surfaces are curved. Although ellipsometry has been routinely applied to measure the thickness of individual layers within flat samples, the analysis of multi-layered, curved samples, especially non-destructively, remains difficult. We have modified the sample stage and sample holder of a conventional ellipsometer to make it possible to examine lubricant distribution within drug containers with different geometric configurations and components, including those made of plastic and glass. To overcome the challenge introduced by curved surface, the area of the surface analyzed in any individual experiment is reduced to allow effective focusing of the beam. The mapping of large, curved areas may then be accomplished by assembling multiple individual analyses. The relationship between sprayed volume and lubricant thickness can thus be established through non-destructive analysis by ellipsometry. The surface chemistry of a fluorine containing lubricant was evaluated by FTIR-ATR and XPS, both before and after post-spray treatment. Fluorine concentration remains stable with mild treatment, but lubricant was depleted from the surface after severe

treatment. This work demonstrated that the combination of multiple surface analytical tools can enhance our understanding of the device lubrication process.

4:40pm AS-WeA9 Challenges in Surface and Interface Analysis of Thin Films, H. Piao, General Electric Co., **Y.F. Hu,** Canadian Light Source Inc., Canada, **J. Fronheiser,** General Electric Co., **V. Tilak,** General Electric Co., India, **M. Karadge, M. Morra,** General Electric Co.

Surface analysis methods play an important role in the characterization of thin films. The analysis of "nano-structured" films requires further development of existing surface analysis methods and exploration of new techniques. The aim of this presentation is to identify some of the challenges that exist in understanding surface and interface states of thin films using conventional X-ray Photoelectron Spectroscopy (XPS). Unique advances in thin film analysis using synchrotron-based X-ray Photoemission (XPS) and X-ray Absorption Near Edge Structure (XANES in both TEY and FLY modes) techniques are discussed. The presentation gives an emphasis on how these methods complement each other. Examples describing the characterization of thin films are given in two areas of technology that are growing in importance: (1) Gate oxide development on SiC and (2) corrosion inhibitor coatings.

5:00pm AS-WeA10 A Comparison of AES and XPS Depth Profiling for Characterization of Multicomponent Thin Films, B.R. Rogers, R.R. Harl, Vanderbilt University

Auger electron spectroscopy (AES) depth profiling has been used to characterize thin films for decades. Thin film depth profiling using x-ray photoelectron spectroscopy (XPS) has become increasingly common due to recent advances in XPS instrumentation. Often the choice of which depth - technique is best for a particular sample is not clear. In this presentation I will compare the logistics and results of AES and XPS depth profiling of insulating and metallic multicomponent thin films. Depth profiles of SiO₂, C_{1s} and CrSi_xN_y thin films acquired using both techniques will be presented. Sample preparation, analysis set-up, and analysis time will be compared. Signal to noise and interface sharpness of the resulting profiles will be compared. The ability to determine chemical state information from the acquired data will also be discussed.

5:20pm AS-WeA11 Characterization and Fabrication of Patterned, Infiltrated Carbon Nanotube Forests with Applications to Thin Layer Chromatography, M.R. Linford, D. Jensen, R. Davis, S. Kanyal, Brigham Young University, **A. Dadson, M. Vail,** US Synthetic Corporation

Patterned forests of carbon nanotubes (CNTs) were used as a template to fabricate novel silica-based thin-layer chromatography plates (TLC). The resulting CNTs are infiltrated with elemental silicon by low pressure chemical vapor deposition of silane. Silicon coated CNTs are annealed in air to remove the CNTs and convert the silicon to silica. The resulting material is white, which is indicative and characteristic of silica. This process produces TLC plates that are porous and robust. The microfabricated TLC plates are characterized extensively by scanning electron microscopy (SEM), which shows the precise placement of the adsorbent material. Plates are also characterized by X-ray photoelectron spectroscopy, time-of-flight secondary ion mass spectrometry, and BET isotherm measurements. Unlike almost all other commercially available plates, these microfabricated structures do not require a binder to hold the adsorbent material together. Baseline separation of a CAMAG (Muttenz, Switzerland) five-component dye test mixture using toluene as the mobile phase was obtained. The chromatographic efficiencies of these microfabricated TLC plates are typically 70% higher than commercially available high-performance TLC plates, and sometimes much higher, also showing a 150% reduction in development time; these microfabricated TLC plates allow for both improved efficiency and speed of analysis.

Biomaterial Interfaces Division

Room: 108 - Session BI+AS+NS+SS-WeA

Functionalization and Characterization of Nanostructures

Moderator: A. Belu, Medtronic, Inc.

2:00pm BI+AS+NS+SS-WeA1 Characterization of Nano-objects by Cluster-SIMS, E.A. Schweikert, Texas A&M University **INVITED**

Secondary ion mass spectrometry, SIMS is a method of choice for the chemical analysis of nanodomains embedded in solids. We examine here a case which has received little attention, the analysis of individual, free-standing nano-objects. Our approach uses a variant of SIMS. The nano-

objects are bombarded with a sequence of individual projectiles resolved in time and space, in the present case Au₄₀₀⁴⁺ of up to 520 keV impact energy. The successive projectiles impact stochastically the nano-objects dispersed on a solid support. Typically tens of secondary ions are ejected from each impact. They are identified with time-of-flight mass spectrometry and recorded individually. This approach reveals molecules co-located within the 10-20 nm diameter area of emission from one Au₄₀₀⁴⁺ impact. We demonstrate that the event-by-event bombardment-detection mode is sensitive to the chemical and/or physical nano-scale separation of molecular species. The performance is illustrated with the determination of the relative abundance of the oxide layer in the near surface of 50-100 nm nanoparticles; the nature and abundance of different nano-objects (5-20 nm in diameter) in mixtures of nano-sized solids; the composition of bio-objects such as a bacteriophage including the amino acids of the proteins surrounding the phage and the bases from the encapsulated DNA. The distinct feature of the nanoprobe technique presented here is in the detection of co-emitted ejecta from individual projectile impacts which allows to test chemical composition, in a nonimaging mode, yet at an exquisite level of spatial resolution. Moreover the co-emission of fragment and parent ions enhances the accuracy of molecular identification.

Work supported by NSF grant CHE-0750377

2:40pm **BI+AS+NS+SS-WeA3 Strategies for Studying the Surface Chemistry of Engineered Nanoparticles with SIMS**, *C. Szakal, J. McCarthy*, National Institute of Standards and Technology, *K. Louis, R.J. Hamers*, University of Wisconsin-Madison, *R.D. Holbrook*, National Institute of Standards and Technology

The environmental toxicity of engineered nanoparticles (ENPs) is of increasing importance as these materials become more widely used in manufacturing processes and consumer products. Nanoparticles have extremely high surface-to-volume ratios, which makes the surfaces more critical than their corresponding bulk materials in terms of reactivity, aggregation, and toxicity to various life forms. Therefore, it is critical that we develop methods to distinguish small chemical changes on nanoparticle surfaces in order to understand how these materials will interact outside of controlled laboratories. Conventional approaches of nanoparticle characterization have focused on high resolution morphological imaging (TEM, SEM) and physical property measurements such as surface charge. However, chemical information is generally only inferred from these materials with most current methods. If it is possible to obtain both elemental and molecular information from ENP surfaces, we may be able to determine the eventual fate of ENPs in the environment.

We have developed a comprehensive approach for studying the surface chemistry of ENPs, including 1) preparation of ENPs to controllably study desired variables, 2) development of methods such as time-of-flight secondary ion mass spectrometry (ToF-SIMS) and environmental scanning electron microscopy (ESEM) to probe small changes in ENP surface chemistry and/or aggregation, and 3) development of methods to improve the speed and reproducibility of ENP aggregation for batch studies. These approaches will be utilized as the basis of future toxicity studies of selected ecosystems.

3:00pm **BI+AS+NS+SS-WeA4 Unusual Hydrogenation Isotherms for Pd Nanoring Model Systems Observed Via Nanoplasmonic Sensing**, *C.B. Langhammer, E.M.K. Larsson, I.L. Zoric*, Chalmers University of Technology, Sweden, *V.P. Zhdanov*, Boreskov Institute of Catalysis, Russian Federation

Nanostructured materials have been proposed as a solution for the development of efficient hydrogen storage systems. As the size of the system gets reduced in the nanometer range enthalpies and entropies of hydrogen dissolution in the metal (α -phase) and hydride formation (β -phase) as well as activation barriers for diffusion and desorption of hydrogen become size dependent thus influencing both thermodynamics (pressure-composition isotherms) and kinetics (loading/unloading kinetics). The pressure-composition isotherms for a H₂/M system show a well-known behavior typical for an α -phase in the low pressure-composition range followed by a plateau signaling the onset of a hydride formation (β -phase) via a first order phase transition and a coexistence of the two over a wide composition range. At higher pressure a pure β -phase exists characterized by a pressure-composition curve with a steep slope. The plateau pressure of the H₂/M system is determined by the requirement of equilibrium between the three phases in coexistence, thus primarily by the enthalpy and entropy of hydride formation. In case of more than one hydride type a coexistence region exhibits multiple plateaux determined by appropriate energetics as described above. In all known cases the same multiple plateaux features were observed both during the charging and discharging process, i.e. when hydrogen pressure was increased/decreased, accompanied of course by a perennial hysteresis.

In this work we report unusual pressure-composition isotherms for H₂/Pd nanosized rings where a double plateau isotherms are observed during the charging process and a single plateau one during the hydrogen discharging. The Pd nanorings were fabricated using colloidal lithography. Hydrogen isotherms were followed by monitoring the shift in the ring Localized Surface Plasmon Resonance, LSPR, upon exposing the system to increasing/decreasing hydrogen pressure steps (and equilibrating the sample at each pressure step). The shift of the LSPR resonance was calibrated by preparing the same ring structure on a quartz crystal microbalance and "weighing" directly absorbed hydrogen. A linear relation between the LSPR shift and QCM frequency shift (proportional to hydrogen concentration) was observed.

We present a simple model, based on the observed heterogeneity of the nanorings (as seen in TEM) and by taking into account the defect induced lattice strain, that accounts for the unusual behavior of the observed isotherms.

4:00pm **BI+AS+NS+SS-WeA7 Surface Functionalization and Analysis of Functional "Soft" Nanostructures: From 2 to 3 Dimensions**, *H. Schönherr*, University of Siegen, Germany **INVITED**

The local properties of soft matter, e.g. for the fabrication of functional biointerfaces or nanostructures, are of tremendous importance for ultimate functionality. In this presentation, the closely interrelated areas of surface chemical functionalization / engineering and analysis of properties will be discussed based on three key examples. These examples include: (i) synthesis and modification of polymer brushes with particular focus on the nanomechanical properties, (ii) ultra small diameter nanotubes obtained by the layer-by-layer assembly of polyelectrolytes inside a sacrificial porous template and (iii) block copolymer nanocapsules that are developed for advanced wound management. In all examples, confinement effects are expected to play a significant role in determining e.g. the mechanical properties, as assessed by atomic force microscopy (AFM) nanoindentation.

For thin polymer films (2D) the dependence of the mechanical properties on the film architecture was unraveled. Compared to spin-coated films, brushes synthesized on gold surface by surface initiated polymerization showed higher elastic moduli, which is attributed to entropy effects. Upon chemical crosslinking tunable elastic properties are obtained, which provides interesting pathways for the fabrication of defined cell - surface contacts.

Similarly important are defined nanoscale objects that can be obtained via the replication of small templates by the so-called layer by layer (LbL) deposition of polyelectrolytes (G. Decher Science 1997, 277, 1232). LbL deposition in porous Anodic Aluminum Oxide (AAO) was only very recently expanded to the 100 nm length scale due to an alleged entropic barrier caused by adsorbed polyelectrolytes close to the pore orifice [Y. Cho et al. Small 2010, 6, 23, 2683.]. However, in contrast to this report, we show that the adsorption of polyelectrolytes on the top plane of the AAO and polymer sedimentation have been identified as main bottlenecks. Suppressing these processes enabled us to produce free standing polymer nanotubes with external diameters of < 55 nm.

Finally, first steps in the development of active nanocapsules filled with a reporter dye or an antimicrobial agent for applications in burn wound management will be presented. In particular the case of burn wounds and the devised biomimetic strategy of BacterioSafe will be introduced. Subsequently, the fabrication and characterization of a polystyrene-block-poly(acrylic acid) amphiphile-based model vesicle system, in particular the loading and release behavior and mechanical properties will be discussed.

4:40pm **BI+AS+NS+SS-WeA9 Large Area Fabrication of Biological Nanostructures**, *G. Tizazu, O. El-Zubir*, University of Sheffield, UK, *S. Brueck*, University of New Mexico, *D. Lidzey, G. Leggett*, University of Sheffield, UK, *G.P. Lopez*, Duke University

There has been enormous interest in the control of biological interactions at interfaces with nanometer spatial resolution, but important challenges still remain to be addressed. Of the established fabrication techniques, electron beam lithography is expensive, and requires exposure under vacuum, while scanning probe methods are slow and (with few exceptions) do not permit fabrication over large areas. In contrast, interferometric lithography (IL) is a simple approach that uses inexpensive apparatus to fabricate sub-wavelength structures over macroscopic areas. When two coherent laser beams interfere, they yield a sinusoidal pattern of intensity that may be used to modify photosensitive materials. Previously IL has been used extensively for semiconductor nanofabrication, but our recent data show that combined with self-assembled monolayer resists it provides a fast, simple method to create molecular nanostructures over macroscopic areas. Illustrations will be provided of bionanofabrication using interferometric modification of protein-resistant (oligo ethylene glycol) functionalised surfaces, where feature sizes as small as 30 nm ($\lambda/8$) have been achieved over square cm areas, and the controlled growth of protein-resistant brush structures from patterns of initiators for atom-transfer radical polymerisation. The

fabrication of metallic nanostructures over macroscopic regions, including Ti structures as small as 35 nm, and gold nanostructures of controlled size and periodicity will also be demonstrated.

5:00pm **BI+AS+NS+SS-WeA10 Functionalization of Mesoporous Silicon Biosensors to Achieve Tunable DNA Bioreceptor Density**, *J. Lawrie, R.R. Harl, B.R. Rogers, P. Laibinis, S.M. Weiss*, Vanderbilt University

Porous silicon has become a widely studied material for sensing over the last decade based on its large surface to volume ratio and easily tunable morphology. With growing interest in the detection and analysis of genetic material, DNA oligos have become an increasingly important bio-recognition element in porous silicon and many other sensor platforms. As aptamers, nucleic acids serve as high affinity bioreceptors to a wide range of small molecules and biological materials, opening up a number of potential applications in environmental science, chemical and biological defense, and medical diagnostics. In this work, tuning of the porous silicon surface chemistry is described. Controlling surface silanization, bioreceptor density, and bioreceptor charge and secondary structure enables the fabrication of reusable, label-free optical sensors toward specific nucleic acid targets. Detection limits in the nanomolar range have been demonstrated.

We have previously shown that in situ DNA synthesis via the phosphoramidite method in porous silicon produces high bioreceptor coverage for label-free optical biosensing applications. Low hybridization efficiency, despite high sensitivity, for such sensors indicated that tuning the receptor surface density could further improve detection limits. To modify surface receptor density, two-component trichlorosilane monolayers were deposited from solution onto porous silicon. One monolayer component remained active to phosphoramidite chemistry while the second component was inert. This method enabled a range of surface probe densities to be achieved and controlled via silanization conditions. Monolayer composition and DNA receptor density were verified using XPS, contact angle, and UV-Vis spectrophotometry. For a 16mer DNA oligo bound within a porous silicon waveguide, detection of the complementary target nucleic acid was maximized when 25% of the internal pore surface area was active toward DNA synthesis. Tuning surface DNA density increases sensitivity by a factor of 2-3. Label-free, target-specific detection of oligos was observed at concentrations of 25nM.

We will present results from hybridization efficiency studies in which DNA bioreceptor surface density, length, and secondary structure are varied. These parameters are vital to nucleic acid aptamer sensing strategies in label-free optical biosensors. Predicting appropriate receptor surface density for aptamer sensors based upon oligo sequences will provide advantages in achieving fast and sensitive waveguide sensors for detection in complex media.

Acknowledgements: This work is supported in part by the Army Research Office (W911NF-08-1-0200).

5:20pm **BI+AS+NS+SS-WeA11 Composite Fluorocarbon Membranes by Surface-Initiated Polymerization**, *C.A. Escobar, A.R. Zulkifli, G.K. Jennings*, Vanderbilt University

This presentation describes the fabrication and characterization of a novel composite membrane that consists of two types of nanoporous materials, namely, nanoporous gold leaf (NPGL) and nanoporous alumina, and a selective poly(perfluorohexyl norbornene) (pNBF6) polymer. Integration of the three materials is achieved by means of silane and thiol chemistry, and the use of surface-initiated ring-opening metathesis polymerization (SI-ROMP). The former two provide functionalization of the nanoporous substrates, and the latter promotes the generation of the polymer film within and atop of the alumina-NPGL membrane. The synthetic process is versatile in that simultaneous or selective growth of the polymer film in each nanoporous layer is straightforward. The use of SI-ROMP allows tailoring of the extent of polymerization of pNBF6 throughout the structure by varying polymerization time. Advancing contact angle measurements show that the surface of these composite membranes exhibits both hydrophobic and oleophobic behavior. Scanning electron microscopy (SEM) images indicate that the thin polymer films cover the porous substrates entirely. Results from electrochemical impedance spectroscopy (EIS) confirm that the membranes provide effective barriers to aqueous ions and that sulfonation of the polymer backbone substantially enhances ion transport through the composite membrane. Ion transport and selectivity of the membrane change by regulating the polymerization time. The fluorinated nature of the polymer thin film renders the membrane selective towards molecules with similar chemical characteristics.

Electronic Materials and Processing Division Room: 210 - Session EM-WeA

Defects in Electronic Materials

Moderator: B.D. Schultz, University of California, Santa Barbara

2:00pm **EM-WeA1 Controlling Schottky Barriers and Doping with Native Point Defects**, *L.J. Brillson, Y. Dong*, The Ohio State Univ., *F. Tuomisto*, Helsinki Univ. of Tech., Finland, *B. Svensson, A.Yu. Kuznetsov*, Univ. of Oslo, Norway, *D. Doust*, The Ohio State Univ., *H.L. Mosbacher*, Trayer Diagnostic, *G. Cantwell, J. Zhang, J.J. Song*, ZN Technology, *Z.-Q. Fang*, Univ. of Dayton, *D.C. Look*, Air Force Research Lab **INVITED**

Native point defects in semiconductors have until now not been considered a major factor in Schottky barrier formation or doping due to their relatively low bulk densities. Likewise, efforts to control doping type and density usually treat point defects as passive, compensating donors or acceptors. Recent advances in the rapidly emerging semiconductor ZnO include a deeper understanding into the nature of native point defects at its surfaces, interfaces, and epitaxial films. Key to ZnO Schottky barrier formation is a massive redistribution of native point defects near its surfaces and interfaces. It is now possible to measure the energies, densities and in many cases the type of point defects below the semiconductor free surface and its metal interface with nanoscale precision. Using depth-resolved cathodoluminescence spectroscopy (DRCLS) of deep level emissions calibrated with electrical techniques, we find that native point defects can (i) increase by orders-of-magnitude in densities within tens of nanometers of the semiconductor surface, (ii) alter free carrier concentrations and band profiles within the surface space charge region, (iii) dominate the Schottky barrier formation for metal contacts to ZnO, and (iv) play an active role in semiconductor doping. Among major roadblocks to ZnO optoelectronics have been the difficulty of both n- and p-type doping. Oxygen vacancies (V_O), V_O complexes, Zn interstitial-related complexes, and residual impurities such as H and Al are all believed to be shallow donors in ZnO, while Zn vacancies (V_{Zn}) and their complexes are acceptors. While their impact on free carrier compensation and recombination is recognized, the physical nature of the donors and acceptors dominating carrier densities in ZnO and their effect of carrier injection at contacts is unresolved. How these defects impact ZnO optoelectronics at the nanoscale is only now being explored. We address these issues using a combination of depth-resolved and scanned probe techniques to clearly identify the optical transitions and energies of V_{Zn} and V_{Zn} clusters, Li on Zn sites, Ga on Zn site donors, the effects of different annealing methods on their spatial distributions in ion-implanted as well as Ga grown-in ZnO, and how V_{Zn} , V_{Zn} clusters, and V_O complexes contribute to near- and sub-surface carrier density. Defects also couple to nanostructures, which form spontaneously on ZnO polar surfaces and create sub-surface V_{Zn} locally with Zn diffusion that feeds the growth. These results reveal the interplay between ZnO electronic defects, dopants, polarity, and surface nanostructure, and they highlight new ways to control ZnO Schottky barriers and doping.

2:40pm **EM-WeA3 High Level of Mg Alloying Effects on the Deep Level Defects in $Mg_xZn_{1-x}O$** , *E. Gur*, The Ohio State University, *G. Tabares*, Ciudad Universitaria, Spain, *A. Arehart*, The Ohio State University, *J.M. Chauveau*, University of Nice Sophia Antipolis, France, *A. Hierro*, Ciudad Universitaria, Spain, *S.A. Ringel*, The Ohio State University
The $Mg_xZn_{1-x}O$ material system is very promising for ultraviolet emission and detection applications because of its direct band-gap, band-gap tunability, low lattice mismatch, and low polarization field. Using molecular beam epitaxy, a-plane 1.5 micron thick n-type $Mg_xZn_{1-x}O$ films ($x=0, 0.26, 0.36, 0.43, 0.52$) were grown on r-plane sapphire. Semi-transparent 100 Å thick Au Schottky contacts were used for deep level optical spectroscopy measurements (DLOS). The Schottky diodes (SD) exhibited rectification with low leakage currents and barrier heights between 1.00-1.19 eV from $Mg_{0.52}Zn_{0.48}O$ to ZnO. The frequency dependence of the capacitance caused by the high series resistance of the SDs required low frequency lock-in based capacitance measurements for accurate determination of capacitance. Lock-in 1kHz DLOS measurements revealed six deep levels in $Mg_xZn_{1-x}O$ samples while only three deep levels were observed in ZnO. In all samples, the energy of the deep levels relative to the conduction or valence band was independent of Mg content. The $\sim Ec-1.4$ eV, $\sim Ec-1.85$ eV, and $\sim Ec-2.50$ eV levels follow the conduction band while $\sim Ev+1.20$ eV, $\sim Ev+0.60$ eV, and $\sim Ev+0.28$ eV follow the valence band. Because of high concentration of two dominant deep levels, lighted capacitance-voltage measurements was applied on all the samples in order to obtain true values of the concentration of the traps. The concentration of the two dominant compensating centers at $\sim Ev+0.28$ eV and $\sim Ev+0.60$ eV are $\sim 3 \times 10^{16} \text{ cm}^{-3}$ and $\sim 1 \times 10^{16} \text{ cm}^{-3}$, respectively.

3:00pm **EM-WeA4 Comparative Depth Resolved Cathodoluminescence and X-ray Excited Optical Luminescence Studies of SrTiO₃**, *R.A. Rosenberg, Y. Choi, V. Kalyanaraman*, Argonne National Laboratory, *M. Kareev, J. Tchakhalian*, University of Arkansas at Fayetteville, *S. Balaz, L.J. Brillson*, Ohio State University

SrTiO₃ and related perovskite materials are increasingly being utilized in a wide range of electrical applications. Furthermore, SrTiO₃ is often used as a substrate for growth of thin film structures. Thus, knowledge of its defect structure and, in particular, their depth dependence is crucial for understanding their impact on conductivity and optical phenomena. In the present work we utilize the limited penetration depth of x-rays to study the near-surface properties of SrTiO₃ substrates and epilayers and compare the results to analogous measurements using electrons. For an incidence angle of 10 degrees, the x-ray penetration depth varies between 22 and 207 nm as the energy changes from 600 to 1500 eV. For electrons the mean penetration depth varies from 3 to 90 nm as the energy changes from 0.5 to 5 keV. Thus, by obtaining x-ray excited optical luminescence (XEOL) and cathodoluminescence (CL) spectra as a function of x-ray or electron energy, it is possible to probe the near-surface region with nm-scale resolution. We will present energy-dependent XEOL and CL data from several SrTiO₃ samples. The luminescence spectra show features that can be assigned to Ti³⁺ (~1.6 eV) and oxygen-related (1.9-2.9 eV) defects, but the relative intensities differ between XEOL and CL. We will discuss the results in terms of the respective mechanisms, previous CL studies [1,2] and theoretical models.

This work was performed at the Advanced Photon Source and was supported by the U.S. Department of Energy, Office of Science, Office of Basic Energy Sciences under Contract No. DE-AC02-06CH11357. We gratefully acknowledge

Ohio State University support from Army Research Office Grant

W911NF-10-1-0220

1. J. Zhang, et al, J. Vac. Sci. Technol. B 26, 1456 (2008).
2. J. Zhang, et al, Appl. Phys. Lett. 94, 092904 (2009).

4:00pm **EM-WeA7 Quantifying the Surface Generation Rate for Bulk Point Defects in TiO₂**, *K. Pangan-Okimoto, A. Hollister, P. Gorai, E.G. Seebauer*, University of Illinois at Urbana Champaign

The defect and surface properties of titania have been well-studied for its potential use in memory resistors and nanoelectronic gas sensors but the control of these properties in such fields has still not been fully realized. Such control of defect mobility and concentration in titania is essential for improving the operation of these technologies. Previous work in our research group has found that controlling the rutile (110) surface has opened up a new pathway for oxygen self-diffusion via an oxygen-interstitial mechanism in conditions where oxygen vacancies and titanium interstitials are thought to dominate. The present work models the detailed diffusion-reaction network of point defects in rutile to simulate interstitial-mediated self-diffusion of oxygen and to calculate a generation rate of bulk point defects at the surface. The model explicitly incorporates gas adsorption onto the (110) surface, interstitial generation at the surface/near surface, and diffusion of the oxygen in an interstitial-mediated mechanism through the bulk. In addition, the model employs techniques drawn from systems engineering to estimate the key kinetic parameters. Simulated diffusion profiles were compared to experimental profiles obtained by exposing annealing single-crystal rutile to isotopically labeled oxygen gas and then measuring isotopic oxygen concentration with secondary ion mass spectrometry. The simulated diffusion profiles matched experimental results, verifying that oxygen interstitials do indeed mediate oxygen self-diffusion in our experiment. More importantly, our model allows us to calculate the oxygen interstitial generation rate at the (110) surface, a first for titania.

4:20pm **EM-WeA8 Metastable Defects and Recoverable Degradation in InAs/AlSb HEMTs**, *X. Shen, S. DasGupta, R.A. Reed, R.D. Schrimpf, D.M. Fleetwood, S.T. Pantelides*, Vanderbilt University

It is known that some defects undergo a structural transformation to a metastable configuration when capturing a carrier. However, their roles in affecting device performance are not widely recognized. Here we show that metastable oxygen defects can cause recoverable degradation of InAs/AlSb HEMTs (high-electron mobility transistors).

Recently, we performed electrical stress tests on InAs/AlSb HEMTs and observed a recoverable degradation in some of the devices. The degradation is manifested as negative shifts of the transconductance peak and threshold voltage, which nearly completely recover after two days at room temperature. The recoverable nature of the degradation suggests that metastable defects are involved. The threshold shift indicates an increase of donor concentration or a decrease of acceptor concentration in the device.

No degradation of mobility in the channel is observed, indicating that the responsible defects are in the AlSb barrier instead of the InAs channel.

We propose that the recoverable degradation is caused by a pre-existing defect in the top AlSb barrier being converted into more positive metastable configurations upon capturing the injected holes that are generated by impact-ionization in the channel. To identify the responsible defects, we performed a thorough survey of the defects in AlSb such as intrinsic defects, dopants, and contaminants, using first-principles calculations. We found that among all the candidates, oxygen impurities, both substitutional and interstitial, can account for the observed degradation. More specifically, both oxygen defects undergo large structural changes upon capturing two holes and the resulting states are metastable.

It is notable that the metastability of the oxygen defects in these devices does not originate from an energy barrier, but instead from a totally different mechanism. The Fermi level in the AlSb layer is pinned in the lower part of its band gap by the adjacent InAs layer, which ensures low electron concentration in AlSb. This leads to slow electron capture by the metastable defects. Furthermore, upon capturing two holes, the emptied electronic level associated with an oxygen defect is shifted far above the Fermi level due to the large structural relaxation. This energy-level shift ensures slow hole emission from the defect and slow electron tunneling from the adjacent layer. This mechanism results in lifetimes of metastable defects that are consistent with the experiments, and is further confirmed by additional annealing experiments that are done under bias.

The work was supported by ONR MURI under Grant No. N-00014-08-10665 and by the McMinn Endowment at Vanderbilt University.

4:40pm **EM-WeA9 Room-Temperature Native Defect Diffusion in Semiconductors**, *K.H. Warnick, Y.S. Puzryev, T. Roy, D.M. Fleetwood, R.D. Schrimpf*, Vanderbilt University, *S.T. Pantelides*, Vanderbilt University and ORNL

Diffusion mediated by native point defects does not generally occur in semiconductors at room temperature (RT) because of high activation energies. However, recent observations of plastic deformation in AlGaIn/GaN High Electron Mobility Transistors (HEMTs) in AlGaIn epilayers on GaN in the presence of strain and electric fields have been attributed to diffusive processes. Here we report the results of first-principles density-functional calculations of formation and migration energies of vacancies under strain and electric fields that allowed us to identify the enablers of self-diffusion at RT in AlGaIn/GaN structures: triply-negative cation vacancies with near-zero formation energy, driven by an electrostatic potential gradient. We show that the formation energies of Ga and Al vacancies in unstrained n-type AlGaIn are near zero but their migration energies are too large, >1.5 eV, for appreciable diffusion at RT (typically the diffusion activation energy, i.e., sum of formation and migration energies, must be ~1 eV or lower for diffusive processes to be appreciable at RT). We find that application of strain, even at substantial levels, has little effect on either formation or migration energies. However, the Ga and Al vacancies are triply negative, and application of an electric field lowers the barrier for migration by more than 0.5 eV. At the observed critical values of the field, the net activation energy is lowered down to approximately 1 eV which makes thermally-activated atomic migration possible at RT. Simulation of the AlGaIn/GaN HEMT shows that the electric field is highest in the region where the plastic deformation is observed. These results provide a mechanism for plastic deformation mediated by vacancies, much like Nabarro-Herring creep and dislocation climb, but with an electric field being the main driver (vacancy drift). In addition, unusually high local strain can also lead to dislocation glide and further dislocation formation via strain relaxation, compounding the role of vacancy migration processes.

The work was supported in part by ONR MURI grant N-00014-08-1-0655 and by the McMinn Endowment at Vanderbilt University.

5:00pm **EM-WeA10 Defect Interactions at Grain Boundaries in Polycrystalline Graphene**, *Y.S. Puzryev, B. Wang*, Vanderbilt University, *S.T. Pantelides*, Vanderbilt University and ORNL

The properties of polycrystalline graphene largely depend on the properties of the grain boundaries (GB) [1,2]. Classical molecular dynamics simulations coupled with density functional calculations of vacancies and self-interstitials at grain boundaries show that lower formation energies are induced by the local strain near the GB. The vacancies interact with each other as well as the interstitials. Vacancies and interstitials [3] can diffuse in graphene due to their low migration barrier. We investigated the time scale of vacancy and interstitial dynamics in pristine graphene and at grain

boundaries at the distances where defect-defect and defect-GB interactions are found to be significant. GB-558 consists of pentagon and octagon pairs, whereas GB-575 is formed by repeated pentagon-heptagon pairs. We show that recombination of vacancies and interstitials can occur at grain boundaries resulting in efficient annealing of defects. The compression (stretch) for GB-558 is up to 3%, while in GB-575, the stretch reaches 9% at the C-C bonds between pentagon and heptagon or between hexagon and heptagon. We find that single vacancies can diffuse towards a grain boundary, attach to a pentagon, then merge into the grain boundary to release the compressive strain and cause local reconstruction. Molecular dynamics simulations show that if a single vacancy exits at 1nm from the grain boundary GB-558, it diffuses towards the grain boundary and attaches at the pentagon ring after 160 ps at 3000 K. It takes another 40 ps to merge into the grain boundary. Similar phenomena occur in GB-575. Stretched C-C bonds at the heptagon, on the other hand, accumulate interstitials. An interstitial that was initially positioned 7 Å above the graphene sheet, was adsorbed on the grain boundary. Once the vacancy coalesces into the grain boundary, the carbon adatom fills the reconstructed vacancy and recovers the original grain boundary structure. This recombination takes only ~ 0.5 ns at 2000 K. The results suggest a new mechanism of defect annealing with a two-step procedure, i.e. point defects (single vacancies and interstitials) diffuse and recombine locally at grain boundaries. This work was supported by DTRA Grant No. HDTRA1-10-1-0016, the US Department of Energy, Basic Energy Sciences, and the William A. and Nancy F. McMinn Endowment at Vanderbilt University. The calculations were performed at ORNL's Center for Computational Sciences and the Air Force Research Laboratory DoD Supercomputing Resource Center

[1] P. Y. Huang et al, *Nature* 469, 389-393, 2011.

[2] Q. X. Pei, Y. Z. Zhang, V. B. Shenoy, *Carbon* 48, 898-904, 2010.

[3] A. Hashimoto, et al, *Nature* 430, 870-873, 2004.

5:20pm **EM-WeA11 X-ray Induced Defect Formation in Graphene**, **E.X. Zhang**, A.K.M. Newaz, S. Bhandaru, M.L. Alles, D.M. Fleetwood, R.D. Schrimpf, K. Bolotin, R.A. Reed, R.A. Weller, S.M. Weiss, S.T. Pantelides, Vanderbilt University

Graphene is a truly two-dimensional material that consists of carbon atoms connected by sp² bonding and arranged in a honeycomb lattice. Due to its unique properties and potential applications in future electronic devices, graphene has received much attention recently from the scientific community. Initial studies of the effects of electron-beam and proton irradiation have been performed on graphene materials, but there remain significant questions about the nature of the conductivity and of the defects.

In this work, the responses of graphene materials to 10-keV x-ray radiation are evaluated with Raman spectroscopy. A defect related peak (D-peak) appears (~1345 cm⁻¹) after x-ray irradiation in air; the intensity of the D-peak increases with increasing total dose, and decreases with post-irradiation vacuum annealing at 350 °C. (See supplemental figures.) These results suggest that new defects can be created and/or that weak bonds at defect precursor sites can be scissioned and decorated with impurities (e.g., H, O) during x-ray exposure. The charge neutral point of graphene transistors made from similar material shifts positively with increasing x-ray dose, suggesting that similar defects may contribute to shifts in the Dirac point and degradation in the conductivity.

It has been shown previously that ozone can react with C-C bonds to degrade graphene layers. We have measured significant ozone generation during x-ray irradiation, suggesting that the x-rays may not directly create the defects sensed by Raman, but that x-ray generated ozone may lead to at least some of the observed defects. However, it is likely that there is an additional source of degradation, since in previous work the ozone reaction typically has been shown to lead to irreversible degradation, but we find that vacuum annealing at elevated temperature leads to partial recovery. Hydrogen annealing treatments of graphene have shown reversible degradation. Thus, it seems likely that hydrogen released by x-ray exposure in the SiO₂ substrate reacts with defect precursors (e.g., weak bond sites) in the graphene. Hydrogen reactions with C-C bonds can enhance the intervalley scattering, thereby increasing the D line intensity. Much of the hydrogen may be driven out by annealing in vacuum at 350 °C, leading to recovery of the degradation, consistent with our experimental results.

This work was supported by the DTRA Basic Research Program through Grants HDTRA1-10-1-0016 and HDTRA1-10-1-0041.

5:40pm **EM-WeA12 Influence of Point Defects on the Properties of Highly Mismatched Alloys**, R.L. Field III, T. Dannecker, Y. Jin, C. Kurdak, C. Uher, R.S. Goldman, University of Michigan

It has been suggested that alloy films composed of highly immiscible solute atoms in a solvent, termed "highly-mismatched alloys" (HMAs), are promising for energy conversion devices due to their ability to efficiently absorb light and heat, and to subsequently transport charge carriers. The

properties of HMAs are often described with models focusing on the influence of individual solute atoms, assuming that all solute atoms "see" the same atomic environment. In the case of GaAsN alloys, the single local environment models predict a N composition-dependence of the energy band gap which agrees *qualitatively* with experiment. However, such models do not *quantitatively* explain several extraordinary electronic and optical properties. In this talk, I will discuss our investigations of the growth [1], structure [2-3], and properties [4-6] of GaAsN alloys. I will focus on correlations between the presence of N-N, N-As, and N-Si pairs [2,5-6] and extraordinary physical phenomena, including non-monotonic composition-dependent effective masses [7] and persistent photoconductivity [8]. I will also discuss our preliminary work on complementary alloys in the GaAsBi system.

[1] M. Reason, et al, *J. Appl. Phys.* **101**, 083520 (2007).

[2] M. Reason, et al, *Appl. Phys. Lett.* **85**, 1692 (2004).

[3] M. Reason, et al, *J. Appl. Phys.* **97**, 103523 (2005).

[4] M. Reason, et al, *J. Appl. Phys.* **102**, 103710 (2007).

[5] Y. Jin, et al, *Appl. Phys. Lett.* **95**, 062109 (2009).

[6] Y. Jin, et al, *Appl. Phys. Lett.* **95**, 092109 (2009).

[7] T. Dannecker, et al, *Phys. Rev. B* **82**, 125203 (2010).

[8] R.L. Field III, et al., to be submitted (2011).

Energy Frontiers Focus Topic

Room: 103 - Session EN1+TF-WeA

Thin Film Chalcogenide Solar Cells (CIGS, CZTS, CdTe and Related Materials)

Moderator: L.W. Rieth, University of Utah

2:00pm **EN1+TF-WeA1 Comparative Study of Structure and Morphology of CuIn_{1-x}Ga_xS₂ and CuIn_{1-x}Ga_xSe₂ Thin Film Absorbers Using EBSD**, A. Kaul, E. Schneller, N.G. Dhere, Florida Solar Energy Center, H.R. Moutinho, National Renewable Energy Laboratory

Electron backscatter diffraction (EBSD) in scanning electron microscopy (SEM) is a powerful technique that allows crystallographic information such as the grain orientation, grain boundaries and also the grain size to be obtained. Crystalline maps are formed in EBSD while the electron beam of a SEM scans the sample surface providing information about crystalline orientation of individual grains as well as features such as twin boundaries. This study relates to EBSD investigation of CuIn_{1-x}Ga_xSe₂ (CIGSe) and CuIn_{1-x}Ga_xS₂ (CIGS₂) samples that were prepared by a two stage process which is easily scalable to large area manufacturing. Since sample polishing is very critical for generation of very good quality Kikuchi pattern formed by back scattered electrons, the earlier work was focused on optimizing the sample polishing technique. Efforts were also made to develop a database to facilitate proper indexing and corresponding accurate determination of preferred orientation of the pseudo-quaternary compound absorber films. Eventually, high quality Kikuchi patterns and EBSD maps have been obtained. It is essential for the research and development of the chalcopyrite thin film absorbers to elucidate the effect of variation of processing conditions (temperature, time and composition) on the growth and development of microstructure. Therefore, in the current work, CIGSe and CIGS₂ absorber films were synthesized under different processing conditions and their EBSD maps and patterns are being compared in terms of grains size, grain orientation and grain boundaries as a necessary and vital step prior to undertaking the study of the still more complex compound CuIn_{1-x}Ga_xSe_{2-y}Se_y (CIGSeS) being used in large-volume production of photovoltaic solar cells and modules.

2:20pm **EN1+TF-WeA2 Improving the Damp-Heat Stability of Copper Indium Gallium Diselenide Solar Cells**, B.S. Tosun, University of Minnesota, R.K. Feist, The Dow Chemical Company, S.A. Campbell, E.S. Aydil, University of Minnesota

While copper indium gallium diselenide (CIGS) thin film solar cells with laboratory efficiencies exceeding 20 % have been reported, these high efficiencies may degrade with time as the devices are exposed to humid environments. It is well known that grain boundary diffusion of water through the ZnO to the CIGS-CdS interface is implicated in long-term degradation of the solar cell performance.¹ This penetration must be reduced or stopped to increase the solar cell lifetime. Herein, we show that amorphous tin dioxide (SnO₂) layers deposited by radio frequency (RF) magnetron sputtering on top of the completed CIGS solar cells can significantly increase the device lifetime by forming a barrier against water diffusion. Specifically, with approximately 0.2 micron and thicker SnO₂

layers deposited on top of the completed CIGS solar cells we have demonstrated that initially 11.1 % efficient CIGS solar cells lose less than 7 % of this peak efficiency and still exhibit efficiencies greater than 10 % (factor of 10%) after 150 hours at 85 °C and 85 % relative humidity. In comparison, under identical test conditions, the solar cells without the SnO₂ layer lost nearly 80 % of their initial efficiency within 24 hours after commencing the test. We studied the effects of deposition conditions and film thickness for different film structures on the solar cell stability in damp-heat tests. The deposited SnO₂ films tend to be amorphous when deposited at room temperature or when the films are thin, but show increased crystallinity for thicker films and films deposited at 150 °C. We found that solar cells coated with polymorphous SnO₂ films exhibit better damp-heat stability than those coated with polycrystalline films. By polymorphous we mean films that consist of nanocrystalline SnO₂ embedded in amorphous SnO₂. We attribute this difference to the lack of grain boundary diffusion in polymorphous SnO₂ films. Replacing the crystalline ZnO window layer with a SnO₂ film can provide further protection of the CIGS solar cells. We demonstrate a 8.2±0.2 % efficient CIGS solar cell with a SnO₂ window layer. Same solar cell fabrication process and CIGS film with ZnO window layer resulted in 8.2±0.6 % overall efficiency. The open circuit voltages of the two cells were the same indicating that the band alignment with the SnO₂ film is suitable for CIGS. These SnO₂ films were deposited using magnetron sputtering at 5 mTorr and 150-250 W RF power using Ar as the sputtering gas without substrate heating.

¹R. Feist et al, IEEE Photovoltaic Specialist Conference, 2009.

2:40pm EN1+TF-WeA3 Progress Towards a High-Efficiency Cu-Zn-Sn-S-Se Thin-Film PV Technology. *D.B. Mitzi, O. Gunawan, T.K. Todorov, D.A.R. Barkhouse, S. Bag, R. Haight, T. Gokmen, T. Goisard de Monsabert, S.J. Chey, S. Thiruvengadam,* IBM T.J. Watson Research Center

INVITED

A key criteria for achieving terawatt-compatible photovoltaic (PV) technology is the ability to fabricate high power conversion efficiency (>10%) solar cells using a low-cost process (< \$1/watt) and readily available, abundant and preferably non-toxic materials. The kesterites, Cu₂ZnSn(S,Se)₄ (CZTSSe), are considered a promising PV technology for meeting this goal because of similar electronic properties to the two leading thin-film chalcogenide technologies, CdTe and Cu(In,Ga)(S,Se)₂ (CIGSSe), achieved while employing low-cost, readily-available constituents. This talk will discuss recent developments that have enabled the demonstration of the first CZTSSe solar cells with certified power conversion efficiencies of over 10%, using a glass/Mo/CZTSSe/CdS/i-ZnO/ITO structure and a simple liquid-based deposition approach. We also present a device characterization study that compares the CZTSSe devices with higher-performing CIGSSe analogs, elucidating some of the key performance bottlenecks in CZTSSe cells, including dominant buffer-absorber recombination, high series resistance and a relatively short minority carrier lifetime. These studies help to elucidate key areas for improvement for the CZTSSe cells in the effort to develop a high performance pervasive technology.

4:00pm EN1+TF-WeA7 Solar Cells from Colloidal Dispersions of Cu₂ZnSnS₄ Nanocrystals. *A. Khare, Y. Li, B. Chernomordik, B.S. Tosun, A.W. Wills, D.J. Norris, E.S. Aydil,* University of Minnesota

Copper zinc tin sulfide (Cu₂ZnSnS₄ or CZTS) is emerging as a promising photovoltaic material for thin film solar cells. CZTS has a band gap of ~1.4 eV, the ideal value for converting the maximum amount of energy from the solar spectrum. In addition, CZTS has a high absorption coefficient (> 10⁴ cm⁻¹ in the visible region of the electromagnetic spectrum) and its constituent elements are all abundant in the earth's crust and are non-toxic. We have synthesized CZTS nanocrystals from metal dithiocarbamate complexes. The diameter of the nanocrystals can be varied from 2-7 nm by changing the temperature and synthesis time. A suite of methods including Raman spectroscopy, optical absorption, electron energy loss spectroscopy and X-ray diffraction were used to characterize these nanocrystals and show that they are phase-pure CZTS. Nanocrystals with diameters less than 3 nm exhibit quantum confinement. These quantum dots were used to assemble quantum dot solar cells. In a second approach to making solar cells, thin films of CZTS nanocrystals are annealed to form thin films with large grains. Nanocrystals melt at temperatures much less than the bulk temperature and recrystallize to yield larger CZTS grains. These films were then used for making conventional thin film solar cells.

4:20pm EN1+TF-WeA8 Surface Structure of Pyrite Thin Films Grown by MOCVD. *M. Cheng, Y. Liu, N. Berry, A. Margarella, J.C. Hemminger, M. Law,* University of California, Irvine, *H. Bluhm, Z. Liu,* Lawrence Berkeley National Laboratory

Iron pyrite (FeS₂) has been considered one of promising materials for use in solar cells due to its large absorption coefficient, suitable band gap and elemental abundance. In-lab X-ray photoelectron spectroscopy and tunable-energy synchrotron X-ray photoelectron spectroscopy were used to explore the surface structure of pyrite thin films grown by metal organic chemical vapor deposition (MOCVD). The influence of sodium diffusion on the growth of pyrite thin films on glass substrates was examined. By using synchrotron X-ray photoelectron spectroscopy, the different types of sulfur chemical states on the surface of pyrite thin films were resolved. The mechanism of pyrite oxidation after exposure to different oxidizing environments indicated that the surface monosulfide species were oxidized first. In addition, the band gap of pyrite thin films was determined by combining valence band spectroscopy with X-ray absorption spectroscopy compared to traditionally ultraviolet-visible absorption spectroscopy. The discrepancy between the two measurement techniques will be discussed.

4:40pm EN1+TF-WeA9 Effect of the Use of a c-CdS Nanocrystalline Layer on the Photovoltaic Characteristics of the Screen Printed CdS/CdTe Heterostructure. *L.G. Rangel-Chavez,* UAM-Azcapotzalco, Mexico, *M. Garcia-Aguirre, F.A. Cuevas-Ortiz,* Cinvestav-IPN, Mexico, *M.I. Neria-Gonzalez,* Instituto Tecnológico de Estudios Superiores de Ecatepec, Mexico, *M.A. Melendez-Lira,* Cinvestav-IPN, Mexico

The fact that the efficiency for the CdS/CdTe system has remained without any change for several years until now requires employing new approaches in order to increase it. In this work it is reported the effect on the photovoltaic characteristics of the CdS/CdTe system by employing as source of the CdS the one obtained as a by-product from bio-remediation of heavy metals in residual waters. By using a novel sulfate-reducing bacterium (*Desulfovibrio alaskensis* 6SR) particles of the CdS semiconductor are obtained. Structural and optical characterization by XRD, UV-vis, Raman and photoluminescence spectroscopies shown that nanoparticles of cubic CdS are obtained. The nanoparticles of cubic CdS are deposited on CdTe films by screen printing and then subject to a mild thermal treatment. It is expected that the employment of CdS with cubic rather than hexagonal crystal structure will reduce the number of defects at the CdS/CdTe interface improving the transport of minority carriers through it. We will report the effects on the spectral response and filling factor obtained for the CdS/CdTe heterostructure by employing nanostructured cubic CdS as compared to those obtained employing hexagonal CdS.

*: Work partially supported by CONACYT-Mexico.

5:00pm EN1+TF-WeA10 Surface Structure and Chemistry of AgInSe₂ Studied by Scanning Tunneling Microscopy. *P. Peña Martin, J.W. Lyding, A. Rockett,* University of Illinois at Urbana-Champaign

Chalcopyrite semiconductors such as (Cu,Ag)(In,Ga)(S,Se)₂ show great promise in thin film solar cells as they exhibit high optical absorption and excellent performance even as polycrystalline layers. The alloy AgInSe₂ (AIS) is a promising candidate for solar applications, as it has a nearly ideal energy gap (1.2 eV), high absorption coefficient, and shows sharper photoluminescence emissions than do the Cu-containing alloys. The surface of the material forms the heterojunction and determines many aspects of device performance. These semiconductors also contain a large number of intrinsic point defects, which are probably responsible for minority carrier recombination in the depletion region. Therefore understanding the surface and near surface nanostructure and nanochemistry are critical to device optimization. To characterize the structure and buried point defects near the surface, we used ultra high vacuum scanning tunneling microscopy (UHV-STM) to obtain atomic-scale topographic and electrical information.

We report the first atomically-resolved STM images and current-voltage profile measurements of AIS. Epitaxial layers were grown on epi-ready substrates of p-GaAs(111)A by hybrid technique, in which Ag and In are sputtered concurrently with effusion cell evaporation of Se. The resulting film was transported in a N₂ ambient to the STM laboratory, mounted under normal lab air as quickly as possible, and introduced to vacuum, with a total atmosphere exposure of about 20 minutes. The sample was degassed at ~100°C to drive off water and other contaminants. Electrochemically-etched W tips were used for scanning. The STM measurements were carried out in a home-built system with a base pressure of 1.2x10⁻⁸ Pa (9x10⁻¹¹ Torr). Topographic images reveal atomically-resolved regions on the surface with the periodicity expected for the polar metal-terminated [112] plane, 0.34 and 0.36 nm along rows oriented 60° from each other. This indicates that the surface does not reconstruct, unless by swapping one type of metal atom for another. Current-voltage spectra confirm that the material exhibits n-type behavior with an energy gap close to the bulk value of 1.2 eV. Some regions exhibit more fluctuations in the bandgap for a series of

current spectra taken along a different line, indicating that there are variations in the electronic properties due to defects. We attempt to correlate these with topographic features in order to identify the defect responsible. Understanding and controlling these defects should lead to improved device performance, and some of the results may even carry over to CIGS devices.

5:20pm **EN1+TF-WeA11 Imaging and Phase Identification of $\text{Cu}_2\text{ZnSnS}_4$ Thin Films using Confocal Raman Spectroscopy.** A.-J. Cheng, M. Manno, A. Khare, C. Leighton, S.A. Campbell, E.S. Aydil, University of Minnesota

Copper zinc tin sulfide ($\text{Cu}_2\text{ZnSnS}_4$ or CZTS) is a potential candidate for next generation thin film solar cells because it contains abundant and nontoxic elements and exhibits high light absorption. Thin films of CZTS are typically synthesized by sulfidizing a stack of zinc, copper and tin films. In addition to CZTS, a variety of binary and ternary metal sulfides can form and distinguishing among phases with similar crystal structure can be difficult. Herein, we show that confocal Raman spectroscopy and imaging can distinguish between CZTS and the other binary and ternary sulfides [1]. Specifically, Raman spectroscopy was used to detect and distinguish between CZTS (338 cm^{-1}), Cu_2SnS_3 (298 cm^{-1}) and Cu_4SnS_4 (318 cm^{-1}) phases through their characteristic scattering peaks. Confocal Raman spectroscopy was then used to image the distribution of coexisting phases and is demonstrated to be a useful tool for examining the heterogeneity of CZTS films. We show that, during sulfidation of a zinc/copper/tin film stack, ternary sulfides of copper and tin, such as Cu_2SnS_3 form first and are then converted to CZTS. The reason for formation of Cu_2SnS_3 as an intermediary to CZTS is the strong tendency of copper and tin to form intermetallic alloys upon evaporation. These alloys sulfidize and form copper tin sulfides first, and then eventually convert to CZTS in the presence of zinc. As a consequence, films sulfidized for 8 hours at $400\text{ }^\circ\text{C}$ contain both CZTS and Cu_2SnS_3 while films sulfidized at $500\text{ }^\circ\text{C}$ contain nearly phase-pure CZTS. In addition, using Cu *K α* radiation, we identify three CZTS X-ray diffraction peaks at 37.1° [(202)], 38° [(211)] and 44.9° [(105) and (213)], which are absent in ZnS and very weak in Cu_2SnS_3 .

[1] A.-J. Cheng, M. Manno, A. Khare, C. Leighton, S. A. Campbell, and E. S. Aydil, *J. Vac. Sci. Technol. A*, *in press* (2011).

5:40pm **EN1+TF-WeA12 Synthesis of CZTS Solar Cells using Non-Toxic Sulfur Precursor.** P. Vasekar, L. Ganta, D. Vanhart, T. Dhakal, C.R. Westgate, The State University of New York at Binghamton

Thin film solar cells based on $\text{Cu}(\text{In,Ga})(\text{S,Se})_2$ and CdTe have demonstrated significant improvement in last few years and they are also being transferred to production level. However, both CIGS and CdTe based thin film solar cells are hindered by potential environmental hazard issues and scarcity issues associated with the constituent elements, mainly Te, In, Ga and to some extent Se. Recent research trends are moving towards finding alternatives based on earth-abundant and non-toxic elements. An alternative material $\text{Cu}(\text{Zn,Sn})(\text{S,Se})_2$ is being explored these days by the thin film photovoltaics community which contains earth abundant materials like Zn and Sn. CZTS structure can be derived from CuInS_2 chalcopyrite structure by replacing one half of the constituent indium atoms by zinc and other half by tin. The resulting bandgap varies in the range of 0.8 eV for a selenide structure to 1.5 eV for a sulfide structure. Copper and sulfur in earth's crust are 50 and 260 ppm respectively and while abundance of zinc and tin is 75 and 2.2 ppm in respectively. As compared to this, indium in earth's crust is 0.049 ppm and selenium 0.05 ppm. CZTS also has a large absorption coefficient in the order of 10^4 cm^{-1} . There are vacuum-based as well as non-vacuum based approaches for the synthesis of CZTS solar cells. Among vacuum based approaches, generally sulfurization in H_2S atmosphere is carried out on sputtered CuZnSn precursors. However, there are toxicity issues involved with the use of H_2S gas. We subscribe to the philosophy of sticking to a non-toxic approach of synthesizing thin film solar cells and for the first ever time introduced a non-toxic sulfur precursor called di-tertiray-butyl-disulfide (TBDS) for the sulfurization of CZT layer. Initial results are quite encouraging and device quality CZTS cells are already being synthesized. The CZTS cells are characterized using materials characterization techniques such as SEM, XRD, XPS and photovoltaic parameters are being extracted under AM 1.5 conditions and also analyzed using quantum efficiency measurement. This is the very first attempt to successfully synthesize CZTS solar cells using a non-toxic sulfur source.

Energy Frontiers Focus Topic
Room: 106 - Session EN2+TF-WeA

Thin Films for Solar Fuels

Moderator: A.J. Muscat, University of Arizona

4:00pm **EN2+TF-WeA7 N-doped $\text{SrTiO}_3(100)$ Epitaxial Films for Fundamental Studies of Visible Light Active Photocatalysts.** T. Luttrell, M. Batzill, University of South Florida

N-doping of photocatalysts, in particular TiO_2 , has been extensively studied for its ability to increase visible light activity. However, the solubility of N in TiO_2 is limited to $\sim 2\%$ and thus limits the visible light absorption. One reason for the low solubility of nitrogen is the different preferred charge state of nitrogen (3-) compared to the substituted oxygen (2-) anions. Here, we investigate the less studied perovskite SrTiO_3 , which has similar photocatalytic activity to TiO_2 . Because a wide range of oxides crystallize in the perovskite structure, we anticipate that charge compensating co-doping in N: SrTiO_3 can be more easily accomplished than in TiO_2 . Such co-doping may result in a higher achievable N-concentration. In our studies, the stability of N-doping in SrTiO_3 and the effect of co-doping have been investigated in thin films. High quality pure and N-doped epitaxial films of SrTiO_3 have been grown on $\text{LaAlO}_3(100)$ substrates by pulsed laser deposition (PLD). The structural and electronic properties have been investigated, by x-ray and UV photoemission spectroscopy (XPS and UPS) and ex-situ atomic force microscopy (AFM). N-doping was accomplished by deposition in an ammonia atmosphere. N^{3-} ions are substituting for O^{2-} ions in the SrTiO_3 matrix and thus cause a charge imbalance that is compensated for in pure films by formation of oxygen vacancies. To avoid this defect formation, substitution of the quadrivalent cations in SrTiO_3 by co-doping with La^{3+} is investigated. La co-doping allows a higher nitrogen solubility in SrTiO_3 . Nitrogen doping causes a band gap narrowing due to formation of filled N-2p states at the top of the valence band and thus an increase in visible light adsorption. The UV and visible light photocatalytic activity is assessed by decomposition of methyl orange.

4:20pm **EN2+TF-WeA8 Photoelectrochemical Water Splitting by Hematite Nanostructures Prepared by Chemical Bath Deposition.** R. Morrish, Colorado School of Mines, M. Rahman, J.M.D. MacElroy, University College Dublin, C.A. Wolden, Colorado School of Mines

Hematite ($\alpha\text{-Fe}_2\text{O}_3$) is a promising material for sustainable generation of H_2 due to its low cost, widespread availability, chemical stability, and ability to absorb a significant fraction of visible light. However numerous challenges remain in order for this material to approach its theoretical potential of 15% solar to hydrogen efficiency. Nanorod geometries are an ideal configuration for this material, decoupling the different length scales required for photon absorption and efficient carrier transport. Unfortunately such structures have historically yielded poor photoelectrochemical performance ($<5\text{ mA/cm}^2$).¹ We recently demonstrated that nanorods synthesized by chemical bath deposition (CBD) could be activated through the use of appropriate annealing treatments.² Photocurrents $>500\text{ mA/cm}^2$ were achieved at 1.23 V versus RHE, and the photoanodes displayed low onset potentials. These changes were correlated with significant amount of tin diffusion from the underlying FTO substrate into the Fe_2O_3 matrix occurs during high temperature annealing process. The benefits of this process may include enhanced conductivity as well as improvement of the FTO/ Fe_2O_3 interface. Despite these advancements, significant room remains for further improvement. In this paper we describe a number of strategies to reach this goal. First, the nanostructure of the hematite can be further improved. This is explored by varying the CBD chemistry, optimizing the post-deposition annealing conditions, and through subtractive processing. A second issue is electron transport at the hematite/FTO interface, and this is explored through the use of novel treatments of the FTO prior to deposition. Finally, the addition of an electrocatalyst can further reduce the onset potential. Each of these three strategies has demonstrated enhanced photocurrent over our previous results. We plan to integrate these advancements in order to maximize performance. Detailed characterization of the structure, composition, and electrochemical changes observed with these processes will be used to provide fundamental insight into the mechanisms underlying the improvements.

References

- [1] N. Beermann, L. Vayssieres, S.-E. Lindquist & A. Hagfeldt, "Photoelectrochemical Studies of Oriented Nanorod Thin Films of Hematite", 2456-2461, (2000).
- [2] R. Morrish, M. Rahman, J. M. D. MacElroy & C. A. Wolden, "Activation of hematite nanorod arrays for photoelectrochemical water splitting", 474-479, (2011).

4:40pm **EN2+TF-WeA9 Nanostructured Thin Films for Solar Water Splitting.** *K. Sivula*, Ecole Polytechnique Federale de Lausanne, Switzerland **INVITED**

Solar energy can be converted to chemical energy stored in hydrogen through water splitting using a photoelectrochemical device. However, decades of research have failed to identify one semiconducting electrode material that can perform the water splitting reaction with adequate efficiency, stability and material cost. Here I present a system that overcomes the limitations of conventional materials to afford direct solar hydrogen production by taking inspiration from natural photosynthesis and using two photosystems in tandem. In addition, to reach the terawatt energy scale needed to have a global impact, I describe the use of abundant and inexpensive semiconducting materials. Specifically, progress developing hematite (Fe_2O_3) photoanodes and cuprous oxide (Cu_2O) photocathodes will be presented. I will show that our water splitting tandem cell, using these materials and inexpensive processing techniques, is capable of solar-to-hydrogen conversion efficiencies of over 5 % at standard conditions. I will further detail how the progress in developing the electrode thin films has been enabled by exploiting recently developed techniques like aerosol-assisted chemical vapor deposition and atomic layer deposition.

5:20pm **EN2+TF-WeA11 TiO_2 N-doped Nanofibers Deposited by Electrospinning for Photocatalytic Applications.** *D. Di Camillo, F. Ruggieri, L. Lozzi, S. Santucci*, University of L'Aquila, Italy

Titanium dioxide (TiO_2), thanks to its interesting properties as nontoxicity, low cost and high chemical stability, has been extensively investigated for several application in which, following light absorption, the generated charges can be usefully applied, as for photovoltaic applications or for photocatalytic devices. However, due to the wide intrinsic energy gap of TiO_2 (between 3.0 and 3.2 eV, depending on the crystalline structure), only a small fraction of the solar spectrum can be used to promote the light absorption [6]. In the photocatalytic devices one of the most important goal of the recent research is to be able to prepare photocatalyst which can be active by absorbing the visible light, in order to increase the application of TiO_2 -based system in poor regions (where it could be difficult to use UV light sources) or to reduce the application cost. In order to increase the fraction of the solar spectrum that can be absorbed, different approaches have been used, mainly by doping TiO_2 with metals or anions.

One of the most studied doping is using nitrogen. TiO_2 doped with nitrogen atoms can be prepared in different ways, as powders, as thin films by sol-gel or reactive sputtering.

In this paper we will show the photocatalytic results obtained depositing TiO_2 N-doped nanofibers (NF) prepared by means of electrospinning (ES) and near-field electrospinning (NF-ES) techniques for the photo-degradation of methylene blue (MB) in water under visible light. The ES preparation technique allows a quick deposition of fibers on wide surfaces using a cost-effective system. Instead NF-ES method allows the growth of a well ordered NF net, with a spacing lower than few microns.

The NFs were deposited using different deposition and post-deposition parameters (solution composition, annealing temperature and atmosphere) and have been characterized by using X-ray photoemission spectroscopy (XPS), X-ray diffraction (XRD) and Secondary Electron Microscopy (SEM). The photocatalytic properties have been studied recording the variation of the optical absorption of MB when the sample is illuminated by an halogen lamp (visible spectrum).

The annealing process determines a partial loss of nitrogen and the formation of the Anatase crystalline phase. The TiO_2 N-doped NFs have shown interesting degradation properties, which are much better than those observed when TiO_2 NFs are used.

5:40pm **EN2+TF-WeA12 Fabrication of Palladium Nanoscale Structures for Hydrogen Sensing Applications.** *D. Rodriguez-Vindas*, University of Puerto Rico at Rio Piedras, *C. Ortiz, V. Pantojas*, University of Puerto Rico at Cayey, *W. Otaño*, University of Puerto Rico at Cayey and Institute for Functional Nanomaterials

Palladium (Pd) metal is one of the most prominent materials studied for the detection of hydrogen gas. Hydrogen rapidly dissociates on its surface and diffuses into subsurface layers forming palladium hydride with consequent changes in optical, mechanical and electrical properties that are easily detected. Materials with nanoscale morphologies are promising to improve sensor performance as they provide large surface areas for adsorption, and smaller crystallite size reducing the time needed for "bulk" diffusion. The amount of sites available for hydrogen adsorption per Pd atom is also higher in the surface and subsurface layers resulting in higher sensitivity. In this project, Pd nanoribbons and nanoshells are prepared by magnetron sputtering deposition on top of the mat of polymer fibers, which act as a template that shapes the morphology of the palladium being deposited while providing support to the metallic scaffold that is created. Sputtering is a line-of-sight deposition process and the fibers become a variable angle-

substrate for the incoming Pd flux. A larger amount of palladium is deposited on top of the fiber where the incoming flux is perpendicular to the surface compared to the sides where the flux is incident at a glancing angle. The top and sides of the fibers shadow their bottom parts closer to the substrate preventing any substantial deposition there. The end result of the deposition is the formation of Pd nanostructures, thicker in the middle region than at the edges, with a large void network. Process parameters such as deposition time, sputtering pressure, and power can be used to produce nanoshells with different thickness and crystallinity. The high sensitivity and response time shown to 1% or less of hydrogen in nitrogen is understood to result from the reduced dimensions combined with this unique nanostructure. A description will be given of the conductance changes with hydrogen concentration as result of the competing mechanisms of percolation and scattering. This work shows the use of nanotechnology combined with unique processing approaches to produce new sensor geometries with different behavior and morphology than simple thin film or wire approaches.

Graphene and Related Materials Focus Topic
Room: 208 - Session GR-WeA

Graphene Characterization including Microscopy and Spectroscopy

Moderator: J.T. Robinson, Naval Research Laboratory

2:00pm **GR-WeA1 Scanning Probe and Optical Microscopy and Spectroscopy of Graphenes on (sub-) Molecular Layers on Atomically Flat Substrates.** *J. Rabe, N. Severin, P. Lange, M. Dorn, S. Eilers*, Humboldt University Berlin, Germany **INVITED**

Graphenes were used to cover solid substrates, including silicon wafers and atomically flat mica, pre-coated with molecularly thin liquids as well as single macromolecules. Optical reflection microscopy was employed to identify single graphenes on optically transparent substrates in optical reflection microscopy with a contrast of more than 12% [1]. A combined fluorescence and scanning force microscopy study revealed that that graphene is not only a highly conductive and transparent electrode, but also a most effective barrier to protect conjugated polymers against degradation through water and oxygen [2]. Time resolved pump-probe spectroscopy revealed ultrafast nonequilibrium carrier dynamics [3]. Finally, scanning force and electrostatic force microscopy, and also STM/STS were used to characterize structure and electronic properties of single graphenes with molecules either on top or below the graphene, revealing a remarkable stability of the electronic properties of these hybrid systems.

[1] M. Dorn, P. Lange, A. Chekushin, N. Severin, J.P. Rabe, *J. Appl. Phys.* **108** (2010) 106101.

[2] P. Lange, M. Dorn, N. Severin, D. Vanden Bout, J.P. Rabe, *Verhandlungen DPG Regensburg* 2010.

[3] M. Breusing, S. Kuehn, T. Winzer, E. Malic, F. Milde, N. Severin, J.P. Rabe, C. Ropers, A. Knorr, T. Elsaesser, *Phys. Rev. B* (2011) 153410.

2:40pm **GR-WeA3 Scanning Tunneling Microscopy and Spectroscopy of Suspended Graphene Membranes.** *N.N. Klimov*, PML/CNST/NIST and Maryland NanoCenter UMD, *S. Jung*, CNST/NIST and Maryland NanoCenter UMD, *N.B. Zhitenev*, CNST/NIST, *D.B. Newell*, PML/NIST, *J.A. Stroscio*, CNST/NIST

The discovery of graphene, a unique two-dimensional electron system with extraordinary physical properties, has ignited tremendous research activity in both science and technology. Graphene interactions with a substrate such as, for example, SiO_2/Si are known to strongly limit the electrical performance of graphene devices. Suspended graphene devices, where the interaction with substrates can be strongly reduced, have been studied by macroscopic transport measurements and shown to have a 10-fold increase in mobility. However, a detailed investigation of electronic properties of suspended graphene on a microscopic scale is still missing. In this talk we present a scanning tunneling microscopy/spectroscopy (STM/STS) study of free-standing graphene membranes. The device was fabricated from a graphene flake exfoliated over an array of 1 μm holes etched in SiO_2/Si substrate. Electronic spectra of both suspended and supported regions of single-layer graphene can be probed using STM/STS in a perpendicular magnetic field with varying back gate voltages applied to the Si substrate. We found that both the scanning probe tip and applied back gate voltage induce mechanical deformations in the suspended graphene membrane, which, in turn, influences the graphene electronic spectrum. The significant differences found in the electronic spectra of suspended and non-suspended graphene will be discussed.

3:00pm **GR-WeA4 Moiré Twist and Absence of Chirality in Graphene on Ru(0001)**, *K.L. Man, M.S. Altman*, Hong Kong University of Science and Technology, China

The strength of the interaction between graphene and a supporting metal substrate is revealed in its influence on electronic structure and properties. Knowledge of structure is of elementary importance for understanding the nature of this interaction. The structure of a single layer of graphene (g) on the Ru(0001) surface has been controversial, beginning with the elementary matter of its lateral periodicity. It was eventually shown using surface x-ray diffraction (SXRD) that a superstructure forms from the moiré-like superposition of (25x25) graphene on (23x23) Ru units [1]. Although corrugation was detected within the supercell, the predominant origin of corrugation in this system, whether physical or electronic, has been disputed. Intriguing evidence from SXRD was also put forth that g/Ru(0001) exhibits chirality, whereby the weakly bound, protruding regions of a physically corrugated graphene layer are rotated in-plane by up to two degrees [2]. We have investigated single layer g/Ru(0001) using low energy electron microscopy (LEEM) and micro-low energy electron diffraction (μ LEED) in order to verify the existence of chirality. Chirality should give rise to differences between the intensities of diffraction spots mirrored across the high symmetry directions. However, this broken mirror symmetry will be very difficult to detect using laterally averaging techniques such as SXRD because of the presence of two chiral enantiomers and two terminations of the hcp substrate. Using LEEM and μ LEED we have successfully obtained diffraction information from an area with a diameter of 250 nm within a single surface termination. While no evidence is found with such high spatial resolution diffraction measurements that confirms chiral features within the unit cell, we do in fact observe rotation or twist of the moiré-like superposition over long length scales. Moiré twist causes the entire ensemble of satellite diffraction spots around each integer order spot to rotate as a group about their respective stationary foci. When the μ LEED beam is scanned across the surface, the rotation angle undulates randomly. The data also suggest that the ground state configuration comprises a graphene layer that is slightly rotated with respect to the underlying substrate surface. Conceivably, the orientational variations that are observed here over sub-micron length scales might produce a signature in laterally averaging measurements that could be construed as evidence of chiral features on the short length scale within the unit cell.

[1] D. Martoccia *et al.*, Phys. Rev. Lett. **101**, 126102 (2008).

[2] D. Martoccia *et al.*, New J. Phys. **12**, 043028 (2010)

4:00pm **GR-WeA7 Scanning Tunneling Microscopy Study on a Graphene Layer Grown on a Single-crystal Cu(111) Surface by Using Chemical Vapor Deposition**, *W. Kim*, Korea Research Institute of Standards and Science, Republic of Korea, *K.-E. Yang*, KRISS and Chunnam National Univ., Republic of Korea, *K. You, S.J. Kim, E.K. Seo, C. Hwang*, Korea Research Institute of Standards and Science, Republic of Korea

We investigated the surface atomic structure of a graphene layer grown on a single-crystal Cu(111) surface by using a chemical vapor deposition method. The low-energy electron diffraction pattern shows a clear ring structure, which indicates the existence of multiple domains with different in-plane orientations. In the scanning tunneling microscopy (STM) experiment, two domains showing different Moiré patterns and a domain boundary between them are observed. The misorientation angle between the domains was estimated from the quantum interference pattern around the domain boundary and the atom-resolved image of each domain. In the STM images of the domain boundary, the chain of protrusions was observed, which indicates the existence of localized electronic states originated from the pentagon or heptagon structures at the boundary.

4:20pm **GR-WeA8 Interface Structure of Graphene on SiC(000-1)**, *N. Srivastava, G. He, R.M. Feenstra*, Carnegie Mellon University

The graphene/SiC interface structure is quite well understood on the SiC(0001) surface (the *Si-face*) but the situation is less clear on the SiC(000-1) surface (the *C-face*). For the C-face some groups report a 3x3 and/or 2x2 interface structure with weak interaction with the underlying substrate.¹ A single study however found an interface layer that was strongly bonded to the SiC.² We demonstrate that the interface layer on the C-face depends on the means of graphene formation. For graphitization in vacuum we observe a 3x3 interface in agreement with other groups. However for graphitization in a Si-rich environment we observe a new interface indicative of a buffer layer similar to that seen on the Si-face.

In this work, graphene films are formed by heating the C-face in vacuum or in a disilane environment. It is found that different interface structures occur for the two preparation conditions. In particular, in 5×10^{-5} Torr of disilane we find a graphene-like buffer layer forming at the interface, analogous to the well known behavior of the Si-face. We therefore find that graphene formation on the C-face and Si-face are not so much different (although

they appear to be when using vacuum preparation): A buffer layer that acts as a template for graphene formation exists in both cases, so long as equilibrium conditions are employed (i.e. with the disilane environment).

Studies are performed using atomic force microscopy (AFM), low-energy electron diffraction (LEED), and low-energy electron microscopy (LEEM). For graphene prepared in vacuum, LEED patterns show a characteristic 3x3 pattern together with graphene streaks. In contrast, for the graphene produced in 5×10^{-5} Torr of disilane, LEED patterns reveals a complex $\sqrt{43} \times \sqrt{43}$ -R $\pm 7.6^\circ$ arrangement. This structure is somewhat similar to the well known $6\sqrt{3} \times 6\sqrt{3}$ -R30° “buffer layer” of the Si-face, with satellite spots surrounding the primary Si spots, and is interpreted as arising from a C-rich buffer layer with 8x8 graphene unit cells on the SiC (with rotation angle of $\pm 7.6^\circ$ rather than 30° for the Si-face). After air exposure the $\sqrt{43} \times \sqrt{43}$ -R $\pm 7.6^\circ$ pattern changes, with the intensity of the graphene streaks increasing and the $\sqrt{43} \times \sqrt{43}$ spots themselves disappearing and being replaced by $\sqrt{3} \times \sqrt{3}$ -R30° spots. This latter behavior is interpreted as oxidation of the SiC surface beneath the buffer layer,³ again similar to what occurs on the Si-face. LEEM reflectivity curves on the surface reveal features similar to those for the $6\sqrt{3} \times 6\sqrt{3}$ -R30° layer on the Si-face.⁴ Importantly, selected area diffraction on those surface areas, after oxidation, reveals a wavevector magnitude precisely equal to that of graphene, thus proving that a decoupled buffer layer does indeed exist on the surface. It is argued that the C-face buffer layer represents the equilibrium structure of the interface, whereas the 3x3 interface forms due to kinetic limitations.

[1] Emtsev *et al.*, Phys. Rev. B **77**, 155303 (2008).

[2] Varchon *et al.*, Phys. Rev. Lett **99**, 126805 (2007).

[3] Oida *et al.*, Phys. Rev. B **82**, 041411 (2010).

[4] Hibino *et al.*, Phys. Rev. B **77**, 075413 (2008).

4:40pm **GR-WeA9 Thermionic Emission of Graphene on Metal Surfaces**, *E. Starodub, N.C. Bartelt, K. McCarty*, Sandia National Laboratories

We employ low-energy electron microscopy (LEEM) to study the thermionic emission of graphene on representative metals, Ru(0001) and Ir(111). In traditional LEEM, an image is produced using low-energy electrons reflected from a surface. The unique capabilities of LEEM allow us to image directly electrons thermionically emitted from graphene at high temperatures, above 1100K, using the same imaging optics. Due to the strong dependence of emission current on temperature, given by the Richardson-Dushman equation, we determine the work function of graphene-covered Ru(0001) and Ir(111) surfaces. The work function of graphene on Ru(0001) is determined to be 3.4 ± 0.1 eV, which is considerably smaller than work function of clean Ru (5.4 eV) and graphene (4.6eV). The obtained value is in good agreement with the result of first principles calculations, 3.6 eV [1], where strong graphene/metal interaction leads to significant film-to-substrate charge transfer and, as a result, reduced work function.

In contrast to the strong interaction with Ru, graphene bounds weakly to the Ir surface reducing the work function. The work functions of graphene on Ir(111) measured for two in-plane orientations on the Ir surface [2], R0 and R30, are 4.5 ± 0.1 eV and 4.7 ± 0.1 eV, respectively. Thus, the in-plane orientation noticeably changes the work function on Ir. It is consistent with our previous observation of the effect of electronic structure on orientation by electron reflectivity [3] and ARPES [4].

Our finding shows that graphene has another application in addition to be a promising candidate for future electronics. One-monolayer graphene on metals such as Ru and Ir can be used as a chemically inert electron emitter with large surface area and low work function, comparable to lanthanum hexaboride, LaB₆.

Acknowledgement: This work is supported by the Office of Basic Energy Science, Division of Materials Sciences and Engineering of the U.S. DOE under Contract No. DE-AC04-94AL85000.

[1] B. Wang, S. Günther, J. Wintterlin and M.-L. Bocquet, New Journal of Physics **12** (2010) 043041

[2] E. Loginova, S. Nie, K. Thürmer, N. C. Bartelt, and K. F. McCarty, PRB **80** (2009) 085430

[3] S. Nie S, A. L. Walter, N. C. Bartelt, E. Starodub, A. Bostwick, E. Rotenberg, K. F. McCarty, ACS NANO **5** (2011) 2298-2306

[4] E. Starodub, A. Bostwick, L. Moreschini, S. Nie, F. El Gabaly, K. F. McCarty, and E. Rotenberg, PRB **83** (2011) 125428

5:00pm **GR-WeA10 Imaging Epitaxial Graphene on SiC(0001) using STM with Functionalized W Tips**, *S.H. Rhim, Y. Qi, G.F. Sun, Y. Liu, M. Weinert, L. Li*, University of Wisconsin-Milwaukee
Epitaxial graphene on SiC(0001) is studied using scanning tunneling microscopy with W tips functionalized by transition metal (Cr, Fe) coating,

which enables the imaging of states within a few meV of the Fermi level that are not accessible with conventional W tips. Modeling of these tips using X/W(110) (X=Cr, Fe, W) by first-principles calculations indicates that states responsible for enhanced tunneling are located 0.4~0.6 eV above and below E_F for Fe/W tips, and 0.3 eV above E_F for Cr/W tips. Further calculations show that the formation of an apex atom is not stable for W/W(110) or Fe/W(110) tips, but is stable for Cr/W(110) tips, resulting in point-like iso-density of states contours that are ideal for the selective imaging of the complex electronic properties of the epitaxial graphene on SiC(0001).

5:20pm **GR-WeA11 Hydrogenation of Epitaxial Graphene on 6H-SiC(0001): The Formation of Hydrogen-Vacancy Complex**, *Y. Liu, M. Weinert, L. Li*, University of Wisconsin-Milwaukee

In this work, we have studied the hydrogenation of epitaxial graphene on 6H-SiC(0001) by Ar/H₂ plasma at room temperature. Two predominant types of defects are observed, and their atomic and electronic structures are studied by scanning tunneling microscopy/spectroscopy (STM/STS) and first principles calculations. The results suggest that vacancies are created with hydrogen atoms trapped nearby between the graphene sheets, forming H-vacancy complexes. In addition, changes in the electronic structures of the defects are also observed during STM imaging, which can be attributed to the dissociation and recombination of these complexes by the electric field of the STM tip. These results and their impact on the gap opening in hydrogenated graphene will be presented at the meeting.

5:40pm **GR-WeA12 Many-Body Interactions in Quasi-Freestanding Graphene**, *D.A. Siegel**, *C.H. Park*, University of California, Berkeley, *C.G. Hwang*, Lawrence Berkeley National Laboratory, *J. Deslippe*, University of California, Berkeley, *A.V. Fedorov*, Lawrence Berkeley National Laboratory, *S.G. Louie*, *A. Lanzara*, University of California, Berkeley

Until recently it had been extremely difficult to experimentally address one of the most fundamental questions about graphene: How do the quasiparticles behave in neutral graphene, i.e. when the chemical potential coincides with the Dirac point energy? Here we address this question by investigating graphene on a particularly interesting substrate, the carbon face of SiC, with high-resolution angle-resolved photoemission spectroscopy (ARPES). We present the first direct measurements of the self-energy in graphene near the neutrality point, and show that the many-body physics in graphene differ from those of an ordinary metal. These exciting findings set a new benchmark in our understanding of many-body physics in graphene and a variety of novel materials with Dirac fermions.

Magnetic Interfaces and Nanostructures Division

Room: 105 - Session MI-WeA

Spintronics, Magnetoelectronics, Multiferroics, and Dilute Magnetic Semiconductor Applications

Moderator: E. Vescovo, Brookhaven National Laboratory

2:00pm **MI-WeA1 Novel Properties of Topological Insulator Thin Films Prepared by Molecular Beam Epitaxy**, *Q.-K. Xue*, Tsinghua University, China

INVITED

We have grown topological insulator thin films of Bi₂Te₃, Bi₂Se₃ and their alloys on Si(111), 6H-SiC(0001) and sapphire substrates by using state-of-art molecular beam epitaxy (MBE). We studied nontrivial surface states and their thickness-dependence of the films by *in situ* angle resolved photoemission spectroscopy (ARPES) and scanning tunneling microscopy/spectroscopy (STM/STS). By direct imaging standing waves associated with magnetic and nonmagnetic impurities and steps on Bi₂Te₃ and Bi₂Se₃ (111) surfaces, we show that the topological states have a surface nature and are protected by the time reversal symmetry. We demonstrated the high mobility of the Bi₂Se₃ films by direct observation of Landau quantization. We also studied the growth of superconducting and magnetic thin films on the topological insulator films. Implication on probing Majorana fermions and topological magneto-electric effect will be discussed.

2:40pm **MI-WeA3 Kondo Effect in a Molecular Machine**, *U.G.E. Perera†*, *Y. Zang*, *H. Kersell*, Ohio University, *G. Vives*, *G. Rapenne*, CNRS, Cemes, France, *S.-W. Hla*, Ohio University

Due to the continuous miniaturization of existing devices, artificial molecular machines have emerged as a new field in nano-science with the aim of developing novel motion systems on a single-molecule level. Here, we report the spin-electron interactions and local vibration signature of an artificially synthesized double-decker molecular rotor 4Fc3SEt on Au(111) surface for the first time using a low temperature scanning tunneling microscopy and spectroscopy at 5 K. The 4Fc3SEt molecule has an upper-deck capability of rotating around the sandwiched metal ion as its rotational axis. The upper-deck has five arms and four of these have ferrocene units attached to pi-ring. A spin-active iron atom is caged at the center of each ferrocene unit. The lower-deck of the molecule is the stator and includes three SEt groups which are designed to anchor on to the Au(111) substrate. At 80 K temperature, most of the molecular rotors were found to be rotating due to thermal excitation. However, when the sample was cooled down to 5 K temperature, stationary conformation of the molecular rotors was determined by high resolution STM images. We probe the spin-electron interactions between the spin of the iron atom inside the molecule, and the surface state free electrons of Au(111) by monitoring the differential conductance (dI/dV) tunneling spectroscopy. Furthermore, by measuring dI²/dV²-V spectroscopy on the ferrocene units, the vibration signature of M(Cp)₂ was identified. Both signatures reveal a site dependent orbital effect in the upper rotator arm. This work opens a novel avenue of molecular machines future nanoscale spintronic and mechanical applications. This work is supported by the US Department of Energy Basic Energy Sciences grant no. DE-FG02-02ER46012 and NSF OSIE 0730257.

3:00pm **MI-WeA4 Spin-Polarized Photoemission of Long-Range Metal-Organic Supramolecular Networks**, *S.Z. Janjua*, University of Missouri - Kansas City, *E. Vescovo*, Brookhaven National Laboratory, *K.I. Pokhodnya*, North Dakota State University, *A.N. Caruso*, University of Missouri - Kansas City

Preliminary spin-resolved photoemission studies of in-situ deposited supramolecular networks were completed at the National Synchrotron Light Source, beamline U5UA. The molecular networks were grown on metallic surfaces with and without a remanent magnetic moment with the intention of studying the influence of the interfacial dipole on the induced moment of the molecules and their long-range order.

4:00pm **MI-WeA7 Spin Transport Phenomena in Nanostructures with Non-Collinear Magnetic Moments**, *M. Chshiev*, SPINTEC, UMR 8191 CEA/CNRS/UJF Grenoble, France

INVITED

Spintronic phenomena in magnetic nanostructures with non-collinear spin configurations have been of major interest for scientists and engineers. Among the most important phenomena arising from non-collinearity of magnetic moments and which has tremendous impact on spintronics [1] is current induced magnetization switching caused by spin transfer torque [2] (STT). The latter continues to generate interest for spin electronic applications such as magnetic random access and domain wall racetrack memories, spin torque oscillators and detectors. Among the most favorable candidates for realization of STT devices are crystalline magnetic tunnel junctions (MTJ) where Bloch state symmetry based spin filtering may lead to extremely high TMR ratios [3] (MTJ).

The first part of this talk will include theory of non-equilibrium spin currents and the corresponding spin transfer torques in MTJs with non-collinear moments. Calculations are based on the Keldysh formalism in which the non-equilibrium Green functions are calculated within a tight-binding model and free electron models. The properties of spin transfer torque and spin currents as a function of applied bias, barrier thickness and distance from the interface in the free layer will be discussed [4].

The second part of the presentation will be devoted to phenomenon of interlayer exchange coupling which also results from equilibrium spin currents in non-collinear magnetic configurations. In particular, using ab-initio and tight-binding approaches, we will address the impact of interfacial oxidation conditions on amplitude of IEC in MTJs [5] as well as the importance of occupation numbers on period of IEC oscillation as a function of ferromagnetic electrode thickness [6] and dynamics of exchange coupled magnetic moments.

In conclusion, theory of voltage induced switching in magnetically frustrated bulk materials will be presented [7].

* Morton S. Trau Award Finalist

† Postdoc Award Finalist

- [1] A. Fert et al, *Mat. Sci. Eng. B*, **84**, 1 (2001); S. A. Wolf, *Science*, **294**, 1488 (2001).
- [2] J. C. Slonczewski, *J. Magn. Magn. Mat.* 159, L1 (1996); L. Berger, *Phys. Rev. B* 54, 9353 (1996).
- [3] W. H. Butler et al, *Phys. Rev. B*, **63**, 054416 (2001); J. Mathon et al, *Phys. Rev. B*, **63**, 220403(R) (2001).
- [4] I. Theodonis et al, *Phys. Rev. Lett.* 97, 237205 (2006); M. Chshiev et al. *IEEE Trans. Mag.* **44** (11) (2008); A. Kalitsov et al, *Phys. Rev. B* 79, 174416 (2009); S.-C. Oh et al, *Nature Physics* 5, 898 (2009).
- [5] H. X. Yang et al, *Appl. Phys. Lett.* 96, 262509 (2010).
- [6] L. E. Nistor et al, *Phys. Rev B* 81, 220407 (2010).
- [7] A. Kalitsov et al, *Phys. Rev. B* 82, 094420 (2010).

4:40pm **MI-WeA9 Concepts based on Magnetoelectrics and Half-Metals for Spintronic Applications**, *K.D. Belashchenko*, University of Nebraska-Lincoln **INVITED**

I will discuss two new concepts of interest for voltage-controlled magnetism and for efficient high-current spin injection in semiconductors, as well as our computational studies of magnetic materials that may be employed in such devices.

First, I will explain the concept of a boundary magnetization carried by a magnetoelectric antiferromagnet, which can be used to induce a switchable equilibrium exchange bias in a proximate ferromagnet. This effect, demonstrated experimentally using magnetoelectric Cr₂O₃, can be utilized in non-volatile magnetoelectric memory and spin field-effect transistors. However, for these purposes the Cr₂O₃ Néel temperature of 307 K is too low. Using first-principles calculations, we predict that it can be increased by introducing boron as a substitutional dopant in the anion sublattice, whereas transition-metal dopants are detrimental. Compressive in-plane strain was also found to be favorable.

Next, I will discuss the possibility of Ohmic spin injection in semiconductors without using Schottky or tunnel barriers. Usually such a high-resistance interfacial barrier is used to overcome the conductivity mismatch problem, but this barrier limits the injected current density. A half-metal used as a spin injector overcomes this problem at zero temperature, but the situation at finite temperatures is nontrivial. I will argue that the two-current model is inapplicable to half-metals, and that barrier-free spin injection from a half-metal may be possible even at finite temperatures. I will present an intuitive model summing up multiple scatterings at the interface, as well as direct calculations of the spin injection efficiency in a simple tight-binding model with averaging over thermal spin fluctuations.

There is much interest in Gd-doped EuO as a half-metal that could be used as a spin injector. Gd doping (and, more controversially, O deficiency) sharply enhances the Curie temperature from 69 K up to as much as 170 K. I will report the results of first-principles studies of exchange interaction in Gd-doped EuO. In the virtual crystal approximation the indirect exchange through the conduction band qualitatively explains the observed doping dependence of the Curie temperature. We also considered EuO supercells with one or more substitutional Gd atom, as well as with an oxygen vacancy, and found deviations from the virtual-crystal behavior that can be associated with local lattice relaxations.

Time permitting, I will also show how first-principles calculations for large supercells with noncollinear spins can be used to analyze the spin-disorder contribution to the electric resistivity of magnetic metals.

5:20pm **MI-WeA11 Magnetic, Structural and Morphological Characterization of Self Assembled Dilute Magnetic Mn₂Ge_{1-x} Quantum Dots**, *J.K. Kassim, J.A. Floro, P. Reinke, C.A. Nolph*, University of Virginia

Group IV dilute magnetic semiconductors (DMS) are candidates for the development of spin based devices due to their compatibility with the traditional semiconductor technology. We have grown heteroepitaxial Ge_{1-x}Mnx quantum dots (QDs) on Si (001) by molecular beam epitaxial co-deposition, with x ranging from 0.02 – 0.22. There is evidence in the literature for room-temperature ferromagnetism in Mn-doped Ge quantum dots. Using atomic force microscopy, in situ scanning tunneling microscopy, transmission electron microscopy, and in situ scanning Auger mapping, our goal is to clearly ascertain how and where Mn incorporates in our films, especially where the magnetically-active Mn resides, and in so doing to contribute to our understanding of the basic origin of ferromagnetic (FM) ordering in this system. Morphology of the QD's up to 5 at.% nominal Mn atomic fraction mirror those observed in pure Ge QDs grown at identical temperatures and deposition rates. The standard "hut cluster" islands bound by {105} facets are observed followed by the introduction of dome clusters at larger Ge thicknesses. Noticeable changes in morphology,

QD's density and mean volume become apparent for the highest Mn contents. Further increase in Mn content promotes introduction of rods believed to be a germanide phase. Field cooled hysteresis loops obtained by vibrating sample magnetometry with an in-plane external magnetic field demonstrate ferromagnetic behavior at 5K, with a maximum magnetization saturation of 2.1μB per Mn ion and a coercivity of 250 Oe recorded for x=0.02. Ferromagnetism disappears above 70K, and is not improved by increasing average Mn content of the films. The saturation moment on a per atom basis is seen to decrease with an increase in Mn content. While we cannot yet isolate any specific island type, or the wetting layer, as being primarily responsible for the ferromagnetism, we have shown that dome clusters are not a prerequisite to ferromagnetism. This work is supported by the National Science Foundation under grant number DMR-0907234.

5:40pm **MI-WeA12 Alterations in the Electronic Band Structure and Magnetic Properties of EuO Films via Rare Earth Doping**, *J.A. Colón Santana*, J. An, N. Wu, K.D. Belashchenko*, University of Nebraska-Lincoln, *X. Wang, P. Liu, J. Tang*, University of Wyoming, *Ya. Losovyj*, Center for Advanced Microstructure & Devices, *I.N. Yakovkin*, National Academy of Science of Ukraine, *P.A. Dowben*, University of Nebraska-Lincoln

High quality films of EuO, Eu_{0.99}Ce_{0.04}O and Eu_{0.99}Gd_{0.04}O were successfully grown on a p-type Si (100) substrate via pulsed laser deposition (PLD). X-ray diffraction (XRD) results show that the addition of Gd changes the growth texture orientation from [001] to [111] with both films crystallizing in the expected rock-salt structure. Angular-resolved photoemission spectroscopy (ARPES) measurements confirms that the doping with Gd atoms have a strong influence in the electronic band structure of these films as well, revealing the presence of electron pockets around some of the high symmetry point in Eu_{0.99}Gd_{0.04}O and Eu_{0.99}Ce_{0.04}O films. There is confirmation of the indirect nature of the EuO electronic band gap suggesting a near semi-metallic character for the Eu_{0.99}Gd_{0.04}O surface. Combined photoemission and inverse photoemission measurements suggests that under some circumstances the surface appears p-type apparent rather than the expected n-type and this unexpected result is likely due to a reconstruction of the highly polar (111) surface. The combination of Gd doping and oxygen vacancies does lead to an appreciable density of states at the Fermi level and is seen to affect the magnetic properties of these films.

Neutron Scattering Focus Topic
Room: 207 - Session NT+AS-WeA

Applications of Neutron Scattering II

Moderator: J. Majewski, Los Alamos National Laboratory

3:00pm **NT+AS-WeA4 Probing Fractals by the Combined Ultra-Small- and Small-Angle Neutron Scattering (USANS/SANS) Technique**, *M. Agamalian*, Oak Ridge National Laboratory

Many natural and man-made materials exhibiting multi-level morphology (atoms – molecules – aggregates – agglomerates), in other words, existence of intermediate structural units between atomic/molecular and macroscopic levels, usually call hierarchical structures. The combined USANS/SANS is one of the best techniques using at present time for characterization of the hierarchical structures, which in many cases shows fractal behavior. The current presentation is focused at the mass and surface fractals discovered experimentally in the sedimentary rocks, attractive colloidal glasses and aggregates of soot particles in MCT-30 engine oil. Some of the fractal structures, particularly the surface fractals in rocks, are extended over three orders of magnitude in the length scale; therefore, application of the combine USANS/SANS technique, which covers the Q-range extended over five orders of magnitude in the reciprocal space ($2 \times 10^{-5} \text{ \AA}^{-1} < Q < 1 \text{ \AA}^{-1}$), is required to obtain complete structural information for complicated hierarchical structures with fractals.

4:20pm **NT+AS-WeA8 Interaction of Alzheimer's Disease Tau Protein with Model Lipid Membranes**, *E.M. Jones*, Univ. of New Mexico, *M. Dubey*, Los Alamos National Lab, *P.J. Camp, B.C. Givler*, Univ. of New Mexico, *J. Biernat, E. Mandelkow*, Max Planck Unit for Structural Biology, Germany, *J. Majewski*, Los Alamos National Lab, *E.Y. Chi*, Univ. of New Mexico **INVITED**

In addition to amyloid plaques, tau neurofibrillary tangles comprise another pathological hallmark of Alzheimer's disease (AD). The mechanism of tau's misfolding and aggregation is unknown, but evidence suggests that tau in AD brains may abnormally interact with the neuronal cell membrane. Using

* Falicov Student Award Finalist

lipid monolayers at the air/water interface and supported lipid bilayers as model membrane systems, we characterized the interaction between 4 tau constructs with membranes of different lipid compositions and elucidated the structure of the protein-membrane films using a combination of biophysical techniques, including pressure-area isotherms, fluorescence microscopy, and x-ray and neutron scattering. Our data show that the full length human tau (hTau40) and its constructs are highly surface active and exhibited strong association with negative DMPG lipids and induced morphological changes observed with fluorescence microscopy, while exhibiting weaker and no interactions with positive DMTAP and neutral DMPG lipids. To elucidate molecular-scale structural details, we used X-ray scattering techniques to study tau and lipid monolayer association. X-ray reflectivity modeling indicated hTau40's presence under a DMPG monolayer and partial insertion into the lipid headgroup region, while grazing incidence X-ray diffraction data showed hTau40 insertion disrupted lipid packing. We also used neutron reflectivity assays to investigate hTau40's ability to disrupt lipid bilayers. The protein completely disrupted a DMPG bilayer while not affecting a neutral DPPC bilayer. These results indicate hTau40 has a propensity to interact with a negatively charged membrane surface and disrupt lipid packing, suggesting a possible protein-aggregate induced mechanism for aggregation and toxicity.

5:00pm NT+AS-WeA10 Stabilization of a Lipid Multilayer System by Polysaccharides. *M. Kreuzer, M. Strobl*, University of Heidelberg, Germany, *M. Reinhardt, R. Steitz*, Helmholtz-Zentrum Berlin für Materialien und Energie, Germany, *R. Dahint*, University of Heidelberg, Germany

Hyaluronic acid (HA) is a high molecular weight polysaccharide. It is involved in a wide range of processes in the human body, such as wound healing, tumor progression and joint lubrication. Here we show that HA also stabilizes a lipid multilayer system at physiological conditions. The observed effect may be an important contribution to joint lubrication as lipid films covering the cartilage of natural joints are assumed to reduce internal friction. Neutron reflectometry investigations were carried out at V6 and the new BioRef neutron reflectometer at Helmholtz-Zentrum Berlin. Measurements against excess D₂O verified, that an oligolamellar DMPG lipid bilayer coating remains stable on a silicon substrate at 21 °C in its ordered state (L_{β} , P_{β}) with a d-spacing of 66 Å, but detaches almost completely from the solid support at 38 °C in its chain-disordered state (L_{α}). By contrast, oligolamellar lipid bilayers remain stable on a substrate at 38 °C when incubated with a solution of HA in D₂O. Lamella transformations occur over time, resulting in a new lamella phase with a d-spacing of 233 Å. This effect has to our knowledge not been reported before on solid-supported oligolamellar systems. We will discuss potential consequences of the "new" lamella phase with respect to further insight into joint lubrication.

5:20pm NT+AS-WeA11 Neutron Reflectometry, QCM-D, and TIRF Study of the Interaction of Endoglucanases with Films of Amorphous Cellulose. *M. Kent*, Sandia National Laboratories **INVITED**

Cellulase enzyme cocktails include exoglucanases that digest cellulose chain ends and endoglucanases that cleave randomly at interior points along the chains. While it is known that these enzymes work synergistically, the details are not fully understood. In addition, cellulose binding domains (CBDs) are known to play an important role in the digestion of crystalline cellulose but much less is known about the benefit of CBDs in the digestion of amorphous cellulose. Amorphous cellulose is of interest as pretreatment of biomass with ionic liquids, a promising next generation technology, results in a combination of amorphous cellulose and cellulose II. Determining the full effects of endoglucanase activity is challenging because these enzymes can alter the structure of insoluble cellulose in addition to releasing soluble oligomers. To unravel the actions of endoglucanases and the role of cellulose binding domains in enhancing activity on amorphous cellulose, we have combined studies of the profile of water through cellulose films during digestion by neutron reflectivity, measurements of changes in mass and film stiffness using a quartz crystal microbalance (QCM), and visualization of the motion of individual enzymes by total internal reflection fluorescence (TIRF) microscopy.

Plasma Science and Technology Division Room: 202 - Session PS+EM-WeA

Low-K Materials & Integration Moderator: S. King, Intel Corporation

2:00pm PS+EM-WeA1 Electric and Optical Characterization of Leakage and Breakdown in Low-k Dielectric Materials. *J.M. Atkin, R. Laibowitz*, Columbia University, *T.M. Shaw*, IBM T.J. Watson Research Center, *T.F. Heinz*, Columbia University **INVITED**

Low-k dielectric thin films are finding increased use in integrated circuits for the faster signal speed that they permit. These materials, however, have higher leakage currents and shorter lifetimes than SiO₂-based dielectrics. With the continued push to lower values of k, these problems are becoming more acute.

In this paper, we present results of several complementary characterization techniques for determining key physical properties, such as trap densities and barrier heights, that influence leakage and time-dependent dielectric breakdown (TDBD) phenomena. Electrical characterization techniques include impedance spectroscopy and the measurements of transient currents. In addition, we make use of distinctive optical characterization techniques to obtain specific information about the underlying material properties. Internal photoemission (or photocurrent) spectroscopy yields information on interfacial barrier heights from the photon energies required to induce a current. Optical second-harmonic generation (SHG) provides a sensitive, non-contact method for measuring both photo-driven and spontaneous charge transport. From these methods, we show that the increase in current with long time biasing, which is in turn a precursor to electrical breakdown, can be directly correlated with increased trap densities. Conduction models accounting for the early failure mechanism will be discussed. Partial support for this work from the Semiconductor Research Corporation is gratefully acknowledged

2:40pm PS+EM-WeA3 Electron Spin Resonance Study of Low-K Dielectrics and Etch Stop Layers. *B.C. Bittel, P.M. Lenahan, T.A. Pomorski*, Penn State University, *S. King*, Intel Corporation

The electronic properties of thin film low-κ interlayer dielectric (ILD) and etch stop layers (ESL) are important issues in ULSI development. However as the semiconductor industry looks to transition to 16 nm and beyond technology nodes, numerous concerns with low-κ materials need to be addressed. Leakage currents, time dependent dielectric breakdown and stress induced leakage currents are critical problems that are not yet well understood in ILD. A topic of current interest is ultraviolet light (UV curing) of low-κ materials.

We have made electron spin resonance (ESR) and current density versus voltage measurements on a moderately extensive set (over 50 films) of dielectric/silicon structures involving materials of importance to low-κ interconnect systems. Most of the dielectrics studied involve various compositions of SiOC:H. In addition we have also made measurements on other dielectrics including SiO₂, SiCN:H and SiN:H, some of which are utilized as ESLs. In our study we have made ESR and current density versus voltage measurements both before and after exposing the dielectrics to UV light ($hc/\lambda \leq 5$ eV), and films that have experienced an industrial UV curing process. We observe extremely gross differences in the ESR spectra and leakage current versus voltage response of these low-k films. We find that UV exposure consistently increases both the density of paramagnetic defects and the leakage current density at a given field. Paramagnetic point defects observed in these films include, E' centers, silicon dangling bond defects in which the silicon is back bonded to oxygen, the 74 gauss doublet which is E' center complexed to a hydrogen atom, the 10.4 gauss doublet which is a hydrogen coupled E' center, the K-center which are silicon vacancies back bonded to three nitrogens, and possibly silicon and carbon dangling bond centers and likely organic radicals. We have also made electrically detected magnetic resonance (EDMR) spin dependent trap assisted tunneling measurements on some ILD films. The close correspondence between the ESR and SDT result establishes a direct link between the defects observed in ESR and the defects responsible for the increased tunneling currents. We have also observed a correspondence between ESR amplitudes and leakage currents. Our preliminary results suggest the UV curing process creates paramagnetic centers which take part in trap assisted tunneling. Our results indicate quite clearly that the processing parameters have extremely gross effects upon defect densities within these films.

4:00pm **PS+EM-WeA7 The Nature of Defects in Low-*k* Organosilicate Glass and their Response to Plasma Exposure**, *H. Ren, M.T. Nichols*, University of Wisconsin-Madison, *G. Jiang, G.A. Antonelli*, Novellus Systems, *Y. Nishi*, Stanford University, *J.L. Shohet*, University of Wisconsin-Madison

Defect concentrations in low-*k* organosilicate glass [SiCOH] films deposited on high-resistivity silicon were measured with electron-spin resonance. Both plasma exposure and ultraviolet exposure were used. During argon electron-cyclotron resonance plasma exposure, ion and photon bombardment increased the measured defect concentrations. Ultraviolet lamp exposure was also shown to increase the defect concentrations. SiCOH samples with several dielectric constants were examined showing that as the value of the dielectric constant was lowered, the defect concentrations were shown to increase significantly.[i] In addition, the nature of the defects in SiCOH was investigated using air and nitrogen plasma exposure. The defects were found to be silicon dangling bonds. Air-plasma exposure increases the defect concentrations by breaking silicon-hydrogen bonds, measured by Fourier-transform infrared spectroscopy. Nitrogen-plasma exposure as well as free-radical exposure have only a small influence on the bond breaking. It was also shown that UV curing improves the chemical-damage resistance of the dielectric.

Work Supported by the Semiconductor Research Corporation under contract 2008-KJ-1781 and the National Science Foundation under Grant CBET-1066231.

[i] H. Ren, M. T. Nichols, G. Jiang, G. A. Antonelli, Y. Nishi, and J.L. Shohet, *Applied Physics Letters* **98**, 102903 (2011).

4:20pm **PS+EM-WeA8 The Effects of Plasma Exposure on the Time Dependent Dielectric Breakdown of Low-*k* Porous Organosilicate Glass**, *M.T. Nichols, H. Sinha*, University of Wisconsin-Madison, *G.A. Antonelli*, Novellus Systems, Inc., *Y. Nishi*, Stanford University, *J.L. Shohet*, University of Wisconsin-Madison

Time dependent dielectric breakdown (TDDB) is a major concern for newly emerging low-*k* organosilicate (SiCOH) dielectrics. TDDB degradation can be caused by changes in electrical, chemical, and mechanical properties of the dielectric materials.[i] [ii] [iii] [iv] In order to examine the effect of plasma exposure on TDDB degradation, time-to-breakdown measurements were made on porous SiCOH before and after exposure to a variety of plasma exposure conditions. Plasma parameters were changed between exposures such that each sample was subjected to different charged particle and vacuum ultraviolet photon fluxes in order to determine how TDDB degradation was affected by each of them during plasma exposure. By utilizing a capillary-array window to separate charged particle and photon bombardment, it is possible to show that each process is responsible for causing different types of TDDB degradation.

A constant voltage TDDB measurement technique was implemented to analyze unexposed, VUV-irradiated and plasma (charged-particle and photon bombardment) exposed samples to examine the degradation in TDDB. It was observed that the time to breakdown reduces as the electric field stress in increased, which is consistent with what has been previously predicted. It was also found that the unexposed samples exhibit longer time-to-breakdown, indicating highest reliability. Capillary-array-window covered samples exhibited marked degradation in leakage currents and time-to-breakdown relative to the unexposed samples. However, samples exposed to both charged particle and VUV photon bombardment exhibited the most significant degradation, resulting in substantially reduced breakdown times and increased leakage currents. Thus both charged particle and photon bombardment degrade TDDB.

This work has been supported by the Semiconductor Research Corporation under Contract 2008-KJ-1871 and by the National Science Foundation under Grant CBET-1066231.

[i] E. T. Ogawa, J. Kim, G. S. Haase, H. C. Mogul, and J. W. McPherson, *Proc. IEEE Int. Rel. Physics Symp.*, p. 166. (2003)

[ii] Kok-Yong Yang, H. W. Yao, A. Marathe, and O. Auel, *Reliability Physics Symposium Proceedings, 44th Annual IEEE International* (2009).

[iii] F. Chen, O. Bravo, K. Chanda, P. McLaughlin, T. Sullivan, J. Gill, J. Lloyd, R. Kontra, J. Aitken, *Reliability Physics Symposium Proceedings, 44th Annual IEEE International* (2006)

[iv] C. Guedj, E. Martinez and G. Imbert, *Mater. Res. Soc. Symp. Proc.* **990** (2007)

4:40pm **PS+EM-WeA9 Modeling the Penetration of Vacuum Ultraviolet Photons in Porous-ULK Films**, *J. Lee, D.B. Graves*, University of California, Berkeley

VUV radiation inherent in plasma discharges have been shown to be a concern during plasma processing of low-*k* materials [1, 2]. VUV photons are known to break Si-C bonds, thereby transforming the material into a SiO_x-like material post-exposure. Damage to samples exposed to a Xe VUV lamp ($\lambda = 147$ nm) in a vacuum chamber compared to corresponding effects in an Ar/O₂ plasmas ($\lambda = 104, 106,$ and 130 nm) suggests that chemical modification is limited by the penetration depth of the VUV photons, which is in turn dependent on wavelength. The formation of a SiO_x-like layer near the surface of the material, which deepens as more carbon is lost, introduces a dynamic change of integrated VUV absorption throughout the material over time. As a result, the rate of carbon loss is continuously changing during the exposure. We present a model that captures this dynamic behavior and compare the model to experimental data by fitting a parameter that represents the effective carbon photolysis using a procedure described previously [3]. For sample exposures to argon plasmas, the model shows good agreement with the experimentally obtained carbon loss profile, inferred from post-processing, ex-situ Fourier transform infrared spectroscopy (FTIR). For O₂ plasma, there is evidence that an additional effect, perhaps oxygen radicals, plays a major role in chemical modification at short times near the surface of the material. By contrast, we conclude that VUV photons contribute more to damage in the bulk. By exposing samples to VUV radiation in He plasmas ($\lambda = 58$ nm), it may be possible to treat and modify the surface of low-*k* films with high energy, low penetrating VUV photons to limit damage to the near-surface.

[1] B. Jinnai, T. Nozawa, and S. Samukawa, *J. Vac. Sci. Tech. B* **26**, 1926 (2008).

[2] J. Lee and D. B. Graves, *J. Phys. D: Appl. Phys.* **43**, 425201 (2010).

[3] M. J. Titus, D. G. Nest, and D. B. Graves, *J. Phys. D: Appl. Phys.* **42**, 152001 (2009).

5:00pm **PS+EM-WeA10 Characterization of Plasma-Induced Damages on Low-*k* during Interconnection Integration by Scatterometric Porosimetry**, *R. Hurand*, STMicroelectronics, France, *M. Darnon, T. Chevolleau, D. Fuard, CNRS-LTM, France, F. Bailly, R. Bouyssou, STMicroelectronics, France, T. David, CEA Leti, France, O. Joubert, CNRS-LTM, France, F. Leverd, STMicroelectronics, France*

With the continuous downscaling of devices, interconnects get narrower and narrower, and necessitate using porous low-*k* as insulator. Plasma processes required for the integration of low-*k* may cause damage at the sidewalls of the patterns, which degrades the dielectric properties of the material. The impact of the modified layer on the low-*k* sidewalls is becoming more critical when interconnects dimensions are scaled down. Developing low-damage plasma processes for porous low-*k* materials integration is compulsory, but requires a trustworthy characterization technique. Electron microscopy which leads to material shrinkage and does not precisely reveal the damaged layers is reaching its limitations. A new characterization technique, so-called Scatterometric Porosimetry has been recently proposed (Bouyssou et al. JVSTB, 2010). In this paper, we explain the principles of the method and demonstrate it can be used on complex industrial-relevant dielectric patterns (more than 9 dielectric layers, 140nm pitch). This technique can also be used to determine fundamental mechanisms of plasma induced modification to porous low-*k* dielectrics.

Scatterometric Porosimetry (SP) is a combination of scatterometry and porosimetric ellipsometry. Scatterometric measurements under vacuum give access to the pattern dimensions while measurements under controlled partial pressure of solvent give access to the material porosity or permeation (with low-polar solvent) or to the thickness of the hydrophilic damaged layer when water is used as a solvent.

Using this technique on an industrial stack, we determined the pattern profile and damaged layer thickness at the pattern sidewalls after each step of the etch process in a non destructive and high accuracy way. We identified that low-*k* main etch step is more damaging than barrier open or post etch plasma treatments: the damaged layer thickness representing 28% of the low-*k* width. On the contrary, the pattern profile is mostly controlled by the barrier opening step. A similar trend is measurable by SEM using decoration technique (measure before and after HF dip) but with less accuracy. We also investigated by SP the kinetic of sidewall modification during standard plasma processes including fluorocarbon-based processes or oxidizing or reducing plasma treatments.

5:20pm **PS+EM-WeA11 Photon Effects in Damage of Porous Low-*k* SiOCH During Plasma Cleaning**, *J. Shoeb*, Iowa State University, *M.J. Kushner*, University of Michigan

Porous dielectric materials offer lower capacitances that reduce RC time delays in integrated circuits. Typical low-*k* materials include SiOCH –

silicon dioxide with carbon groups, principally CH₃, lining the pores. Fluorocarbon plasmas are often used to etch *low-k* materials, a process that leaves a fluorocarbon polymer on the *low-k* surface that must be removed. With porosities as high as 0.5, pores which are internally connected provide pathways for reactive species to enter into the porous network. During cleaning using oxygen plasmas, reactions of O atoms with the CH_x groups, can remove carbon as CO/CO₂. After the process, H₂O from air can form hydrophilic Si-OH which can further adsorb H₂O through hydrogen bonding or physisorption.[1] As such, O₂ plasmas can degrade the low *k* value of the porous SiCOH. Plasma cleaning with He/H₂ mixtures causes less damage to SiCOH as reaction of H atoms with -CH₃ is endothermic. These damage scenarios are complicated by the UV/VUV photons produced by the plasma. Photons produced by the plasma can break Si-C bonds and separate -CH₃ radicals from SiO₂ to enhance the C removal rate.[2] 130 nm photons of Ar/O₂ plasmas can penetrate into SiCOH ≈100 nm but photons of He/H₂ plasmas (<100 nm) penetrate ≈20 nm. As a result, VUV photons from O₂ plasmas can produce Si-C bond scission approximately 5 times deeper in the *low-k* material compared to the VUV photons from He/H₂ mixtures. These penetration depths are sensitive functions of porosity and interconnectivity. For example, penetration depth increases nearly linearly with increases in interconnectivity due to the alignment of pores. In this talk, we discuss results from modeling of the plasma damage of porous SiOCH in He/H₂ and Ar/O₂ plasmas. The HPEM (Hybrid Plasma Equipment Module) was employed to obtain the ion energy and angle distributions of reactive fluxes from inductively coupled plasmas. These are used as input to the MCFPM (Monte Carlo Feature Profile Module) with which profiles of the *low-k* materials after the plasma exposure are predicted. The role of photons in porous SiCOH damage and validation of numerical results will be discussed in terms of treatment time, interconnectivity and photon flux. Overall, we found that due to its lower photon penetration depth and less reactivity, He/H₂ plasmas cause approximately 3 times less damage than Ar/O₂ plasmas, which is in agreement with experiments.

1. J. Proost, E. Kondoh, G. Vereecke, M. Heyns, and K. Maex, J. Vac. Sci. Technol. B **16**, 2091 (1998).
2. B. Jinnai, S. Fukuda, H. Ohtake, and S. Samukawa, J. Appl. Phys. **107**, 43302 (2010).

* Work supported by Semiconductor Research Corp.

5:40pm **PS+EM-WeA12 X-ray Photoelectron Spectroscopy Investigation of the Schottky Barrier at BN/Cu Interfaces.** *M. French, M. Jaehnig, M. Kuhn, J. Bielefeld, S. King, B. French*, Intel Corporation

Due to a low dielectric constant (4-4.5) and high density (1.8-2.0 g/cm³), Plasma Enhanced Chemically Vapor Deposited (PECVD) boron nitride (BN) is an intriguing material for use in *low-k*/Cu interconnect structures as a Cu diffusion barrier material. However, relatively little is known about the electrical leakage performance of BN in Cu interconnects or the Schottky barrier formed at the interface between these two materials. In this regard, x-ray photoelectron spectroscopy (XPS) was utilized to determine the Schottky barrier formed at the interface between polished Cu substrates and PECVD BN thin films. Our measurements indicate a barrier height of 3.0±0.2 eV for the BN/Cu interface. This barrier height is nearly 2X that determined for a-SiCN:H and a-SiOC:H Cu capping layers and is attributed to the significantly larger band gap of BN (> 5 eV).

Plasma Science and Technology Division

Room: 201 - Session PS-WeA

Plasma Sources

Moderator: S.C. Shannon, North Carolina State University

2:00pm **PS-WeA1 Integrated Power Delivery Systems for Next Generation Plasma Processes.** *F.G. Tomasel, M. Watanabe, D. Carter*, Advanced Energy Industries

The continued drive for ever shrinking features in semiconductor manufacturing poses significant challenges for tool manufacturers and process developers alike. Requirements such as higher uniformity, tighter control of critical dimensions, reduced plasma damage, thinner layers, and shorter process times, combined with the introduction of new materials demand higher sophistication in the development of semiconductor processing tools, starting at the plasma chambers and going all the way down to the power delivery systems. As an example, major advances in etch processes have been enabled by the introduction of a recent generation of RF power supplies with advanced capabilities, including frequency tuning while pulsing and multi-generator synchronized pulsing [1]. While significant improvement to a variety of plasma processes has been realized

through the use of these high performance generators, a more holistic analysis of current power delivery systems seems to indicate that the characteristics and quality of the power delivered to the plasma load could be partly limited by power delivery system architectures based on autonomous building blocks. This observation suggests that a higher level of integration in communication, measurement and control among the components of the power delivery system could further benefit the development of next generation processes and tools. In this presentation we will show results from a new generation of power delivery systems where the matching networks and generators are fully integrated from a communication, measurement and control point of view. Although certainly possible, this integration scheme does not necessarily imply full physical integration. The performance of the integrated hardware combined with high performance control algorithms on both fixed and dynamic loads will be discussed in terms of electrical measurements performed at the loads under various operating regimes, including match and frequency tuning while pulsing. The results will demonstrate the potential for these integrated systems to enable processes with stringent requirements such as highly accurate power regulation in a wide dynamic range, faster power stabilization during transients, and minimal reflected power, both in pulsing and CW modes.

- [1] C. Petit-Etienne, M. Darnon, L. Vallier, E. Pargon, G. Cunge, F. Boulard, O. Joubert, S. Banna, and T. Lill, J. Vac. Sci. Technol. B **28**(5), 926 (2010).

2:20pm **PS-WeA2 Remote VHF Source for High Efficiency Plasma Generation.** *D. Carter, D.J. Hoffman, R. Grilley, K. Peterson*, Advanced Energy Industries

Remote plasma sources have evolved through the years and have generally been designed around traditional MF/HF frequencies in the 0.5 to 13 MHz range or at microwave frequencies around 2 GHz. Remote plasma sources can offer benefits including high dissociation rates, segregation of ionic and neutral species and reduced damage compared to in-situ generated plasmas. Due to the complexities of operating a microwave discharge or the difficulties achieving and maintaining H-mode ICP coupling, these devices are commonly designed for specific applications, such as chamber cleaning, organic layer ashing or PFC destruction in process effluent. As a result, many existing remote source technologies suffer from operating range and/or scaling constraints and so utilization in processes outside their specified purpose is often restricted.

This paper describes a new remote source technology employing a high efficiency VHF electrostatic coupling method to produce a versatile and robust remote plasma generator. The design approach is shown capable of producing high density discharges across a broad range while operating at relatively low voltages. The concept is scalable and adaptable to most any chemistry used for cleaning, etching and even deposition. This paper describes some of the important design elements incorporated into these new source devices along with early results illustrating a broad performance range exceeding many capabilities of the alternative technologies.

2:40pm **PS-WeA3 Study of Radio Frequency Breakdown Mechanisms in a Plasma Environment.** *J.B.O. Caughman, R.H. Goulding, D.A. Rasmussen*, Oak Ridge National Laboratory, *C.H. Castano Giraldo, M. Aghazarian*, University of Illinois at Urbana Champaign, *E.H. Martin, S.C. Shannon*, North Carolina State University

INVITED

Radio frequency (RF) breakdown/arcing is a major power-limiting factor in antenna systems used for RF heating and current drive in magnetic fusion experiments and is also an issue for high voltage substrate operation in process plasmas. The factors that contribute to breakdown include gas pressure, gas type, magnetic field, materials, ultraviolet light, and local plasma density. The effects of these factors on RF breakdown are being studied in a resonant 1/4-wavelength section of vacuum transmission line terminated with an open circuit electrode structure with a well-defined electric field. A small plasma source is used to inject plasma into the high-field region of the electrodes. Changes in the electrical parameters, such as input impedance and the voltage at the electrodes, are being monitored to detect the breakdown events. Measurements of the light emission prior to and during an arc are also being made. For high vacuum conditions using copper electrodes, bright spots (unipolar arcs) appear on the electrode surfaces prior to a breakdown event. The voltage-current characteristic in this regime is consistent with Fowler-Nordheim field emission. An increase in the RF field results in an arc and a flash of light corresponding to copper line emission. Analysis of the electrode surfaces show large areas of melting and formation of micron-sized rounded protrusions, especially along the sharp edges of small scratches or at impurity inclusions on the surface. The maximum electric field that can be sustained without breakdown is on the order of 30-40 kV/mm for vacuum conditions, but this value is substantially reduced in the presence of plasma and magnetic field.

An increase in the chamber pressure results in a decrease in the maximum RF electric field that can be sustained without breakdown as the pressure approaches a few mTorr. The breakdown event leads to formation of a plasma in the structure, and the addition of an external magnetic field causes the formation of a plasma at lower pressures. Ultra-violet light, with an energy greater than the work function of the electrode material, has been shown to induce electron emission from the surface and initiate multipactor discharges. In addition, we are using optical emission spectroscopy to determine the magnitude of the DC and RF electric fields near the electrode structure by utilizing the dynamic Stark effect. Experimental details and future research directions will be presented.

4:00pm PS-WeA7 A Narrow Ion Energy Distribution Bias System, V. Brouk, Advanced Energy Industries, S.C. Shannon, North Carolina State University, D.J. Hoffman, D. Carter, W. Hattel, Advanced Energy Industries

Conventional bias systems use sine wave voltage systems to achieve ion energy distribution functions for the creation of thin films. By combining dual frequency sine waves, the mean energy and its spread can be independently controlled¹. Arbitrary wave-shaping has been suggested to create single energy near-delta function distributions². We investigate a system where the waveform is defined a priori where two elements are run in a feed forward system to control the instantaneous IEDF. We evaluate the effectiveness of this system in an argon/oxygen plasma at typical operating pressures inside the 10-150 mT range at plasma densities in the low 10^{10} cm⁻³ range.

1 S. Shannon et al.; J. Appl. Phys. 97, 103304 (2005)

2 Wendt A. et. al., "Method and apparatus for plasma processing with control of ion energy distribution at the substrates", US Patent 6201208, March 13, 2001

4:20pm PS-WeA8 Effect of Multi-frequency Bias on Ion Energy Distribution in Inductively Coupled Plasma, A. Agarwal, A. Balakrishna, S. Rauf, K. Collins, Applied Materials, Inc.

Inductively coupled plasma (ICP) sources, commonly used for semiconductor and conductor etching, embody the concept of functional separation between plasma production and ion energy control, wherein the inductive coupling through the coils is only responsible for the plasma generation while the bias determines the ion energies. Plasma etching of microelectronics structures at advanced technological nodes (< 3x nm), especially complicated structures such as multi-gate MOSFETs and 3D memory stacks, are placing great emphasis on control of ion energy distributions (IEDs) to finely discriminate etching thresholds.[1] Sinusoidal biases typically provide broad IEDs, making such control difficult to achieve. One promising alternative is non-sinusoidal bias waveforms, which have been demonstrated to provide such control.[2] However, there are issues associated with passing non-sinusoidal signals through the finite impedance of the match, transmission line, and the substrate.

Multi-frequency bias is compatible with current manufacturing hardware, and has been successfully used for controlling IEDs in capacitively coupled plasmas.[3] This approach may be utilized to enable IED control in ICP etchers as well. We investigate the impact of multiple bias frequencies in this paper. A high frequency applied in addition to a relatively low frequency bias causes the sheath potential to vary in a complicated manner due to the non-linear nature of the sheath. As a result, IED exhibits a complex dependence on relative bias voltages and frequencies.

In this work, the effect of applying bias at multiple frequencies will be discussed using results from a computational investigation. The 2-dimensional plasma equipment model, HPEM[4], has been modified to enable power deposition at multiple frequencies on the same electrode. Results will be discussed for Ar/Cl₂ plasma utilizing a 13.56 MHz bias in addition to a bias at a different frequency in an ICP chamber. The additional frequency is varied over a wide range and its consequences assessed on the ion and radical flux and IEDs incident on the wafer. We found that, in addition to modulating the IEDs, the flux composition is different depending on the frequency due to the secondary plasma generation by the alternate frequency.

[1] A. Nitayama and H. Aochi, ECS Trans. **18**, 89 (2009).

[2] A. Agarwal and M.J. Kushner, J. Vac. Sci. Technol. A **27**, 37 (2009).

[3] S. Shannon, D. Hoffman, J.-G. Yang, A. Paterson, and J. Holland, J. Appl. Phys. **97**, 103304 (2005).

[4] M.J. Kushner, J. Phys. D: Appl. Phys. **42**, 194013 (2009).

4:40pm PS-WeA9 Electron Energy Distribution at Electrode in a Low Pressure Capacitively Coupled Plasma, S. Rauf, L. Dorf, A. Agarwal, K. Collins, Applied Materials, Inc.

Low pressure (sub-20 mTorr) capacitively coupled plasmas (CCP) are playing an increasingly important role in technological applications. As the mean free path becomes commensurate with the discharge dimensions, the fluid assumptions inherent in plasma and sheath models start to break down and ought to be reexamined. We focus on one aspect of the CCP operation in this paper, namely the electron energy distribution (EED) at electrodes and surfaces, and use kinetic particle-in-cell (PIC) models to understand the temporal behavior of the EED. Kinetic results are compared to fluid representation of the EED at electrodes to identify deficiencies in the fluid model at low pressures and propose solutions.

The sheath at the plasma-surface interface ensures that the electrons remain confined in the bulk plasma. However, during certain phases of the radio-frequency (RF) cycle in a CCP, the sheath collapses and the electrons exit at the surface. Energy distribution of these electrons contains useful information about the bulk plasma and the sheath. One can probe into the energy characteristics of these electrons using dc probes embedded in the electrode. Analysis of the resulting probe data can be used to determine the electron temperature, the electron density, and the EED in the bulk plasma. If a fluid model is used for this analysis, the electrons are assumed to be governed by the Boltzmann relation where their density and flux depend exponentially on the sheath voltage. Electrons are however highly non-equilibrium near the sheaths in CCPs and the Maxwellian distribution assumption (implicit in the Boltzmann relation) is questionable. Furthermore, most probe analysis models are dc-based. Low pressure situations demand further scrutiny as even the bulk plasma EED tends to become non-Maxwellian.

1 and 2-dimensional PIC model of CCPs are used for this investigation. These models consider plasma chemistry using the Monte Carlo technique. Simulations are done for Ar and N₂ plasmas under a variety of conditions (13.56 – 60 MHz RF frequency, RF voltage of 100 – 500 V, 5 – 100 mTorr gas pressure). The 1-dimensional PIC model is used to examine the EED at the electrodes where the sheath undergoes substantial variation during the RF cycle. The 2-dimensional model is used to investigate the EED at small metal surfaces (e.g., a probe) away from the primary electrodes. Dc voltage is also applied to the probe electrode in the 2-dimensional simulations. It is found that, in addition to a non-Maxwellian contribution from electrons adjacent to the sheath, the EED also contains high energy electrons which are the remnant of electrons that were accelerated at the opposite sheath.

5:00pm PS-WeA10 The Control of Electron Shading and Plasma EEDf in a DC/RF Parallel-Plate Etcher, L. Chen, Tokyo Electron America
INVITED

There are several principles in the consideration of plasma etcher design. This paper addresses two important areas: (1) the ability of tailoring the electron energy distribution function (EEDf), (2) the ability of adjusting the charging and neutralization of surface features (the electron shading effect). Stochastic heating by high frequency RF (VHF) energizes the Maxwellian bulk into the energetic tail population for efficient ionization. Such energetically bottom-up heating also indiscriminately populates the below-ionization energetic group that drives chemistry such as molecular dissociation and VUV production. A generic DC/RF system has a RF biased wafer-electrode with a high-negative DC superimposed opposing electrode. The DC/RF system dominates its electron heating with an energetically top-down process. The secondary electrons emitted from the high-negative DC surface disseminate the beam-energy into a distribution of energetic-electrons through collisions and more importantly, various beam-wave instabilities. These energetic electrons are trapped between the sheaths of the two parallel plates when the RF sheath field is sufficiently strong, dissipating their energies mainly into ionization. The energetic part of the EEDf reveals (in descending order) a group of ballistic-electron associated with the applied -DC voltage, an energy continuum, and finally stop at a lower middle-energy peak in the range of ~ 40eV to 300eV depending on the process. The data show extremely efficient ionization by these energetic electrons and as a result, the Maxwellian bulk remains relatively unchanged at $T_e \sim 1.8$ eV regardless the bias RF power and process pressure. Such energetically decoupled EEDf enables increased ionization without increasing molecular dissociation. In one RF period, the trapping of these energetic electrons diminishes as the RF sheath collapses. By pulse-synchronizing the -DC voltage and the bias RF voltage, ion-bombardment excitation of the wafer surface can alternate with high-energy electron-bombardment neutralization of the wafer surface. Ion-bombardment of the wafer surface occurs when the bias RF pulse is high and the -DC pulse is at a medium level. As the RF and the DC pulses are synchronously altered to a low RF voltage and a high-negative DC voltage, ion-bombardment excitation of the wafer diminishes and the wafer surface sees an increased current of energetic (>25eV) electrons. High aspect ratio SEM data show that the signatures of electron shading (e.g., bending and twisting of the

features) are eliminated when synchronous DC/RF pulsing is implemented allowing energetic electrons to reach the bottom of high aspect ratio features.

5:40pm **PS-WeA12 Negative Plasma Potentials Produced by Electropositive Plasmas in a Multi-Dipole Chamber**, *N. Hershkovitz*, University of Wisconsin-Madison, *L. Oksuz*, Suleyman Demirel University, Turkey, *J.P. Sheehan*, University of Wisconsin-Madison

Negative plasma potentials were obtained in DC hot filament unmagnetized electropositive argon plasma in two configurations. For sufficiently low plasma density ($<10^9 \text{ cm}^{-3}$) bounded by conducting walls, double layers provide ion and electron confinement near the walls. Similar results were observed in higher density plasmas ($\sim 10^9 \text{ cm}^{-3}$) when a thin dielectric coating of oil covered the surface of the conducting walls. The potential profiles, measured using emissive probes in the limit of zero emission, from the center of the plasma to the potential minima are quite similar in shape to those observed when the plasma has positive plasma potentials. The primary electrons emitted from the filaments are important for charge conservation and for modification of the Bohm criteria but are not important for current balance.

This work was supported by US Department of Energy grants No. DE-AC02-09CH11466 and No. DE-FG02-97ER54437, and the Fusion Energy Sciences Fellowship Program administered by Oak Ridge Institute for Science and Education under a contract between the U.S. Department of Energy and the Oak Ridge Associated Universities.

Advanced Surface Engineering Division

Room: 104 - Session SE+PS-WeA

Atmospheric Pressure Plasmas

Moderator: H. Barankova, Uppsala University, Sweden

2:00pm **SE+PS-WeA1 An Investigation of the Influence of Hybrid Current Modes on the Plasma Behavior during Plasma Electrolytic Oxidation (PEO) Coating Process on Mg and Mg-Alloys**, *R.O. Hussein*, *D.O. Northwood*, *X. Nie*, University of Windsor, Canada

The increased use of magnesium alloys is considered one of the more promising methods for light-weighting in the automotive industry since, for a given strength level, Mg represents a 57% weight reduction over steel and 8% weight reduction over aluminum. However, due to its high chemical and electrochemical activity, magnesium has poor corrosion resistance in aqueous and other environments. In order for Mg and its alloys to find increased usage, there is a need to surface engineer these materials for improved corrosion and wear resistance. Plasma Electrolytic Oxidation (PEO) is an electrochemical process working at atmospheric pressure that uses an environmentally-friendly aqueous electrolyte to oxidize the metal surfaces to form ceramic oxide coatings which impart a high corrosion and wear resistance. The properties and structure of PEO coatings are dependent on parameters such as substrate metallurgy, composition of the electrolyte and the process conditions including current density, current mode and processing time. In this study we investigated the effect of current mode on plasma temperature and coating properties of PEO coatings formed on pure magnesium and an AM60B magnesium alloy (mass fraction: Al 5.6–6.4%, Mn 0.26–0.4%, Zn \leq 0.2%, balance Mg). Unipolar, bipolar and hybrid (combination of both) current modes were used in this work. Optical Emission Spectroscopy (OES) was employed to study the plasma species, and electron temperature of the plasma. The morphology and microstructure of the coatings were investigated using Scanning Electron Microscopy (SEM). Potentiodynamic polarization in a 3.5% NaCl solution was used for the corrosion investigations.

2:20pm **SE+PS-WeA2 Aging Mechanism of the Hydrophilic Silicon (100) Native Oxide Surface**, *T.S. Williams*, *R.F. Hicks*, University of California Los Angeles

The wetting behavior of surfaces is important in many applications, such as for example, microfluidic devices that are fabricated on silicon wafers. In this study, silicon native oxide surfaces were cleaned with a radio frequency, atmospheric pressure helium and oxygen plasma and with ammonium hydroxide, hydrogen peroxide, and deionized water in a 1:1:5 ratio (RCA SC-1). Both processes created a hydrophilic state with water contact angles of $<5^\circ$ and $16.2 \pm 1.7^\circ$, respectively. During subsequent storage in a chamber purged with boil off from a liquid nitrogen tank, the water contact angle increased over several days at a rate dependant on the cleaning method used. Internal reflection infrared spectroscopy revealed that the change in water contact angle was due to the adsorption of organic molecules with an average hydrocarbon chain length of 10 ± 2 . The rate of the adsorption process decreased with the fraction of hydrogen-bonded

hydroxyl groups on the surface relative to those groups that were isolated. On Si (100) surfaces that were cleaned by RCA SC-1 and the plasma, 96% of the silanol groups were hydrogen bonded. The first-order rate constant for adsorption of the organic contaminant on this surface was $0.182 \pm 0.008 \text{ hr}^{-1}$. Several methods have been explored for keeping the silicon dioxide surface in a hydrophilic state for extended periods of time, and these will be presented at the meeting.

2:40pm **SE+PS-WeA3 Polyimide Surface Treatment to Hydrophobic Surface with Self Assembled Mask Layer for Direct Inkjet Patterning Process**, *J.B. Park*, *G.Y. Yeom*, Sungkyunkwan University, Republic of Korea

The inkjet printing technology is emerging as one of the important process technologies for electronics, because it can significantly reduce the manufacturing process cost, materials waste, and number of process steps. Especially, many researchers investigating the inkjet-printed process have focused their attention on the printing of conductive films on a polymer film. The technique is not suitable for applying to organic transistors yet, because its pattern width is limited to several dozens μm by statistical variations of the flight direction of droplets and their spreading on the substrate.

In this study, polyimide film was treated to hydrophobic surface using modified atmospheric pressure plasma system (double discharge system). Especially, for keeping the surface characteristics permanently, surface of the polymer film was etch/textured with self assembled mask layer to form the textured polymer surface. The texturing process is progressed for 4 process step. The mask layer (HMDS) is deposited and agglomeration/oxidation by using atmospheric discharge of HMDS/He/O₂ gas mixture through 1st step and 2nd step. And Etch and texturing process is progressed with atmospheric discharge of He/O₂/Ar gas mixture in 3rd step. And the mask layer is removed in 4th step using NF₃/N₂ gas mixture of remote atmospheric plasma. In the 2nd process, the HMDSO mask layer is formed specific tissue layer as the input power was increased. And the morphology is also varied with the whole size of the HMDSO mask layer. And this whole process is possible because of perfect etch selectivity between the polyimide film and HMDSO layer. The contact angle of textured polyimide film was measured over the 100 degree and varied with textured surface morphology. And keeping the pattern width of inkjet printing was clearly improved compare with normal polymer surface.

3:00pm **SE+PS-WeA4 In Situ Fabricating Blue Ceramic Coatings on Al Alloy by Plasma Electrolytic Oxidation**, *Z.J. Wang*, *R.O. Hussein*, *X. Nie*, *H. Hu*, University of Windsor, Canada

In-situ formation of novel blue ceramic coatings on Al alloy with a controllable blue color was successfully achieved using a plasma electrolytic oxidation (PEO) process working at atmospheric pressure. This novel blue ceramic coating overcomes the shortcomings of surface treatments resulting from traditional dyeing process by depositing organic dyes into the porous structure of anodic film, such as poor resistance of abrasion and rapid fading when exposed to light. X-ray diffraction, scanning electron microscopy and energy dispersive spectroscopy were employed to characterize the microstructure of the blue ceramic coating. The main compositions of the coating are CoAl₂O₄ and Al₂O₃. This work shows that the working current density plays significant roles on CoAl₂O₄ phase in the ceramic coating which has a controllable influence on the coating color. Low current density reduces the percentage of CoAl₂O₄ component in the coating, and light blue ceramic is produced. On the other hand, higher current density increases CoAl₂O₄ component in the coating, hence deep blue ceramic is fabricated. Electrochemical test, ball-on-plate sliding wear tester and thermal shock method were utilized for the corrosion, wear and thermal shock resistance analysis of the fabricated ceramic coatings. The results indicate that the developed blue coating via PEO process superiorly improves the tribological property, anti-corrosion property and thermal shock resistance. The fabricated blue ceramic coating tends to be applied to colored light cast alloys for applications used in relatively harsh and severe working environments.

4:00pm **SE+PS-WeA7 Cold Atmospheric Plasma Sources for Treatment of Cell-Containing Surfaces**, *M.G. Kong*, Loughborough University, UK

INVITED

Low-temperature gas discharges generated at atmospheric pressure, commonly known as cold atmospheric plasmas, are a relatively new member of the processing plasma family. Without the need for a vacuum chamber, they offer a much more cost-effective route to material processing and open up opportunities for chamber-less processes and vacuum-incompatible materials such as moist objects. With a mean electron energy at a few eV and a gas temperature close to room temperature, cold atmospheric plasmas are ideally placed for effective chemical dissociation and hence for a wide range of materials processing applications. In this

contribution, a review of the current cold atmospheric plasma sources will be presented in terms of their underpinning science and their current technology capability. These include the traditional dielectric barrier discharges, radio-frequency glow discharges, and cold atmospheric plasma jets and jet arrays. Through discussion of their plasma characteristics, their applications are exemplified through treatment of cell-containing surfaces, including living tissues. The interaction of cold atmospheric plasmas with individual microorganisms and indeed microbial communities will be discussed, and its implications to treatment of skin diseases and wounds will be presented. This will also be supported with data of plasma interaction with mammalian cells.

4:40pm SE+PS-WeA9 High Performance of 60-Hz Atmospheric Pressure Plasma: Basic Characteristics and Applications, F. Jia, K. Takeda, K. Ishikawa, H. Inui, S. Iseki, Nagoya University, Japan, H. Kano, NU Eco-Engineering Co., Ltd., Japan, H. Kondo, M. Sekine, M. Hori, Nagoya University, Japan

In this paper, the spatial distribution of atomic oxygen density in a 60-Hz non-equilibrium atmospheric pressure plasma[1] is diagnosed by two-photon absorption laser induced fluorescence (TALIF)[2]. The plasma unit is made of ceramics comprised three regions: gas diffusion region, main discharge region, and plasma jet in the open air. The discharge gases were Ar and a small amount of O₂. The plasma could offer electron density as high as 10¹⁵ cm⁻³ with a low gas temperature[1,3], and have been successfully used to clean glass surface[1] and inactivate the spores of *Penicillium digitatum*[4]. In the above applications, we find that atomic oxygen plays an important role[1,4], and the samples are usually treated in the open air; therefore it is necessary to investigate the behavior of atomic oxygen, especially in the open air, in order to achieve high performance. A dye laser pumped by an excimer laser is used to generate nanosecond UV laser pulses at around $\lambda = 226$ nm for the two-photon excitation of atomic oxygen ($2p\ 3P-3p\ 3P$). The laser power is adjusted to 0.1 mJ/pulse to make sure that the effect of photo dissociation of ozone can be negligible in the experiment. The results showed that the effect of O₂ admixture variation on the atomic oxygen density is totally different in the main discharge region and in the plasma jet. In the main discharge region where the discharge gas are only Ar and O₂, the density of atomic oxygen increased quickly with adding only 0.25% O₂, became saturated with adding 1% O₂, and reduced quickly when adding 1.5% O₂. The discharge was stable until adding 2.5% O₂. However, in the plasma jet that was in the open air, the density of atomic oxygen remained almost same while adding O₂ from 0% to 2.5%. This is because the mechanisms of generation and recombination of atomic oxygen are different in the main discharge region and plasma jet. More work will be done to study the behavior of atomic oxygen in the plasma jet, the data and results will be very useful to understand the behavior of atomic oxygen and improve the applications of non-equilibrium atmospheric pressure plasma. [1] M. Iwasaki, H. Inui, Y. Matsudaira, H. Kano, N. Yoshida, M. Ito, and M. Hori, *Appl. Phys. Lett.* **92**, 081503 (2008). [2] K. Niemi, V. Schulz-von der Gathen, and H. F. Dobeles, *Plasma Sources Sci. Technol.* **14**, 375 (2005). [3] Fengdong Jia, Naoya Sumi, Kenji Ishikawa, Hiroyuki Kano, Hiroto Inui, Jagath Kularatne, Keigo Takeda, Hiroki Kondo, Makoto Sekine, Akihiro Kono, and Masaru Hori, *Appl. Phys. Express*, **4**, 026101 (2011). [4] S. Iseki, T. Ohta, A. Aomatsu, M. Ito, H. Kano, Y. Higashijima, and M. Hori, *Appl. Phys. Lett.* **96**, 153704 (2010).

5:00pm SE+PS-WeA10 Dense Atmospheric Pressure Discharges for Surface and Gas Treatment, M.J. Kelly, B.D. Schultz, W.M. Hooke, International Technology Center

Dielectric barrier discharge (DBD) plasmas have been formed in atmospheric pressure gases exhibiting peak currents in excess of 100 amperes. Power densities during the pulse routinely exceed 100 kilowatts per cubic centimeter for moderately sized electrodes (>100 square centimeters) with ionization densities of 10¹⁴ per cubic centimeter. Charge transfer of 100 microcoulombs per pulse has been repeatedly generated at frequencies up to 100 hertz, and the charge delivery is found to scale in proportion to the electrode area for a given dielectric consistent with a homogeneous discharge. Diffuse discharges have been formed over larger areas (exceeding 1 meter in length and 500 square centimeters) as well. These results were obtained using a custom high voltage driving source and in the absence of helium, argon, or any other easily ionized gas. The source readily achieves an overvoltage in excess of the DC breakdown voltage prior to the onset of breakdown in which 20-30 kV is delivered with rise times shorter than the lag time between the pulse crossing the threshold voltage and the onset of a discharge. Electrical modeling of the discharge characteristics has produced correlations relating power and charge transfer to various electrical and geometrical parameters of the system which will be discussed in this paper.

5:20pm SE+PS-WeA11 Investigation of Discharge Modes of Cylindrical Dielectric Barrier Discharge Configuration for Surface Treatment at Atmospheric-Pressure, T.S. Cho, Y.L. Wu, J.M. Hong, Z. Ouyang, D.N. Ruzic, University of Illinois at Urbana Champaign

To date, various structural concepts of atmospheric-pressure dielectric barrier discharge had been studied and some of the concepts have already been commercialized for surface treatment processes because of its simplicity and scalability. In this study, cylindrical dielectric barrier discharge configurations for treating the powder particles or controlling the air pollutants at atmospheric-pressure have been investigated. The electrical characteristics of the cylindrical dielectric barrier discharge structure as a capacitive load have been experimentally measured for the mixture of helium and nitrogen and its flow rate with voltage-charge lissajous analysis method. Also, it has been compared with remote plasmas from the commercial planar dielectric barrier discharge system of which capacitance has been 280pF for driving conditions of 5kV and 30 kHz. Emissions from the atmospheric-pressure dielectric barrier discharge plasma have been analyzed for varied gas conditions with the optical emission spectroscopy. For comparison purposes, the glass substrates treated with commercial planar and cylindrical dielectric barrier discharge plasmas have been analyzed. In addition, the sugar-alcohol particles have been treated with atmospheric-pressure plasma from the cylindrical dielectric barrier discharge system, and compared with the untreated particles.

Surface Science Division

Room: 107 - Session SS-WeA

Adsorption & Reactions on Oxide Surfaces

Moderator: S.L. Scott, University of California, Santa Barbara

2:00pm SS-WeA1 Direct Observation of O₂ Molecular Chemisorption at Two Distinctive Sites of TiO₂(110), Z.T. Wang, Y.G. Du, Z. Dohnálek, I. Lyubinetzky, Pacific Northwest National Laboratory

The chemistry of oxygen on TiO₂ surfaces is an important component in many catalytic and photocatalytic processes, such as water splitting and waste remediation, and has been extensively studied. So far, the majority of fundamental research has been carried out on the model transition-metal oxide surface of the rutile TiO₂(110). The investigation of molecular adsorption of O₂ can be considered as a natural first step providing information about possible O₂ surface chemistry on TiO₂(110). Both experiment and theory have demonstrated that O₂ dissociatively adsorbs at bridging oxygen vacancies (V_O) sites and five-fold coordinated terminal titanium atoms (Ti_{5c}) at elevated temperatures. At sufficiently low temperatures, the majority of the ensemble-averaging technique studies suggested that O₂ molecularly chemisorbs at V_O sites on reduced surfaces (at $T < 150$ K). However, recent STM studies reported a contradict result that the O₂ dissociation at V_O sites has been observed at temperatures as low as ~ 110 K.

In this work, we investigated the initial stages of oxygen adsorption on reduced TiO₂(110) with high-resolution scanning tunneling microscopy (STM) at 50 K. Molecularly chemisorbed O₂ species, not directly observed until now on TiO₂(110), have been imaged at two distinctive adsorption sites (V_O and Ti_{5c}) using "extremely mild" tunneling conditions. While O₂ species at Ti_{5c} site appears as a single protrusion centered on the Ti_{5c} row, the O₂ at V_O manifests itself by a disappearance of the V_O feature. The dissociation of chemisorbed O₂ can be readily induced by tunneling conditions that are normally used for TiO₂(110) imaging, and the dissociation details strongly depend on the scanning parameters and the type of the O₂ adsorption site. The O₂ molecules chemisorbed at low temperatures at these two distinct sites are the most likely precursors for the two O₂ dissociation channels, observed at temperatures above 150 and 230 K at the V_O and Ti_{5c} sites, respectively. In general, our results provide a molecular level insight into the thermal chemistry of O₂ on reduced TiO₂, and assist in understanding of the surface reactivity of transition-metal oxides.

2:20pm SS-WeA2 The Interaction of Carboxylic Acids with Rutile TiO₂ (110) Single Crystal Surfaces: Results from IR-Spectroscopy, M. Buchholz, Karlsruhe Institute of Technology (KIT), Germany, M.C. Xu, Y.M. Wang, Ruhr-University Bochum, Germany, A. Nefedov, C. Wöll, Karlsruhe Institute of Technology (KIT), Germany

The role of oxides is central in many technological areas such as gas sensing, catalysis and thin film growth. Zinc oxide and titanium oxide are also important for photocatalysis and photooxidation, e.g. of CO to CO₂^[1]. In the Graetz cell, organic molecules bound to TiO₂-substrates via carboxylate bonds effectively convert photons into electric energy. In last

decades numerous IR investigations of oxide powders, including the different modifications of TiO₂, have been reported. An unambiguous assignment of the features in the complex IR spectra recorded for molecules bound to the oxide powder particle surfaces, however, is only possible on the basis of data recorded for well-defined reference systems, e.g. surfaces of single crystals. Unfortunately, studies on oxide single crystals are extremely scarce due to the fact that the sensitivity of reflection IR-spectroscopy for molecular adsorbates is two orders of magnitude lower for oxides than for metal single crystals. Only recently was it possible to overcome these technical problems by employing a novel, optimized spectrometer.^[2] Here, we will demonstrate the performance of this highly sensitive IRRAS-setup by presenting high-quality IR-spectra obtained for two molecules, benzoic acid and terephthalic acid, adsorbed on rutile TiO₂ (110). Owing to the fact that many Dye Sensitized Solar Cells (DSSCs) consist of dyes grafted to the oxide support via carboxylate groups determining and controlling the adsorption of carboxylic acids on oxidic substrates is fundamental to understanding the energy transfer from the molecule to the substrate. For the present experiments, monolayers of terephthalic acid (TPA) and benzoic acid (BA) were first deposited under UHV-conditions on a rutile TiO₂ (110) surface at room temperature. Subsequently the sample was transferred in the main chamber and subjected to an analysis in a highly sensitive UHV IRRAS system. While for BA the expected bidentate carboxylate bonding is observed, for TPA the presence of two carboxylic acid groups leads to interesting complications. The IR-spectra allow, in particular, answering the question whether for the flat-lying TPA species observed in scanning probe techniques^[3] the carboxylic acid group is still protonated, a question which could not be answered by the results from x-ray absorption spectroscopy^[3].

[1] M. C. Xu, Y. K. Gao, E. M. Moreno, M. Kunst, M. Muhler, Y. M. Wang, H. Idriss, C. Wöll, *Phys. Rev. Lett.* **2011**, *106*, 138302.

[2] Y. M. Wang, A. Glenz, M. Muhler, C. Wöll, *Rev. Sci. Instrum.* **2009**, *80*, 113108.

[3] P. Rahe, M. Nimrich, A. Nefedov, M. Naboka, C. Wöll, A. Kühnle, *Journal of Physical Chemistry C* **2009**, *113*, 17471.

2:40pm SS-WeA3 The Adsorption Dynamics and Interfacial Charge Trapping Behavior for Acetic Acid on Rutile TiO₂ Surfaces, J. Tao, T. Luttrell, M. Batzill, University of South Florida

Using temperature programmed desorption (TPD), scanning tunneling microscopy (STM) and ultraviolet photoemission spectroscopy (UPS), we have observed very different adsorption dynamics for acetic acid on rutile TiO₂(110) and (011)-2×1 surfaces at room temperature. While the bidentate adsorption of carboxylic acids on the (110) surface is well-established, we find a monodentate adsorption on the (011)-2×1 surface as the most likely adsorption geometry. On the (011)-2×1 surface, the initial sticking of adsorbed acetic acid is low. It appears that initial adsorption occurs at defects. These adsorbed acetates then act as nucleation sites for further adsorption. This adsorption mechanism results in the formation of quasi-1D acetate clusters running along direction. The role of acetate adsorption in the formation or annihilation of excess charges in TiO₂ is also found to be different on these two surfaces. We find that bidentate adsorption of acetate on the (110) surface results in extraction of excess charges from the substrate, while mono-dentate adsorption on the (011)-2×1 surface causes net-charge donation to the substrate. More interestingly, a difference in the binding energy of excess charges, or Ti-3d band gap states, has been observed. On the TiO₂(011)-2×1 surface the binding energy is ~0.3 eV higher than on the (110) surface. This difference is explained by the different crystal fields on the reconstructed (011) surface compared to the bulk-truncated (110) surface. At the rutile TiO₂(011)-2×1 surface, Ti-ions are located in a distorted square pyramidal coordination environment, which we propose causes the shift in binding energy of excess electrons at the Ti-site. The differences in binding energy of electrons trapped at the surface for the two surfaces may contribute to the face dependent photocatalytic activity of rutile TiO₂.

References:

1. J. Tao, T. Luttrell, J. Bylsma, and M. Batzill, *J. Phys. Chem. C* **2011**, *115*, 3434

2. J. Tao and M. Batzill, *J. Phys. Chem. Lett.* **2010**, *1*, 3200.

3:00pm SS-WeA4 Effect of the Adsorption Geometry of Zinc-Tetraphenylporphyrin Derivatives on ZnO and TiO₂, on the Exciton Delocalization Pathways, S. Rangan, S. Coh, R.A. Bartynski, K. Chitre, J. Rochford, E. Galoppini, Rutgers University, C. Jaye, D.A. Fischer, National Synchrotron Light Source

ZnTPP derivatives are attractive candidates for photoinduced electron-transfer mediators in dye sensitized solar cells (DSSCs). Many fundamental properties of the dye/metal oxide interface are not known and need careful consideration. In particular, the influence on solar cells efficiency, of the

energy alignment and of the molecular packing at the surface, remains unclear. In this work, using x-ray, UV and inverse photoemission spectroscopies in conjunction with density functional theory (DFT) calculations, we have determined the energy alignment of molecular levels with respect to the substrate band edges for several ZnTPP derivatives adsorbed on ZnO(11-20) and TiO₂(110) surfaces. The ZnTPP derivatives were functionalized with COOH anchoring groups, to allow a priori either upright or flat adsorption on the surfaces. While the energy alignment, a critical parameter to allow charge separation at the dye/semiconductor interface, is found similar for all of these systems, large differences in solar cells efficiencies are observed. We have thus explored the adsorption geometry of the same ZnTPPs at the surface of ZnO and TiO₂ using UV-visible absorption and NEXAFS spectroscopies and scanning tunnel microscopy. It is found that that dye/dye interactions is an important factor, for electron transfer to the substrate. For ZnTPPs, upright adsorption opens deleterious exciton delocalization pathways, due to dipole/dipole interactions competing with electron transfer to the substrate. Choosing the adsorption geometry is thus critical for the electronic pathway control.

4:00pm SS-WeA7 Adsorption of Trimethylacetic Acid on Stoichiometric and Reduced CeO₂(111) Surfaces, S.P. Sanghavi, A.S. Karakoti, M.I. Nandasiri, W. Wang, P. Nachimuthu, P. Yang, S.V.N.T. Kuchibhatla, S. Thevuthasan, Pacific Northwest National Laboratory

The use of nanoparticles in energy, environmental and medical applications has been growing significantly in recent years. In most of these applications, the nanoparticles are being used in as-synthesized form and/or functionalized through ligand conjugation. When particle size decreases to nanometer scale, a large percentage of the atoms are at or near the surface which makes the surface highly dynamic and reactive in nature. Consequently, these particles exhibit unique properties that make their characterization more difficult by conventional spectroscopic methods. Furthermore, knowledge on how the ligand molecules bind to the surface of nanoparticles is very limited. To better understand the interactions between ligand molecules and the surface of nanoparticles, we used a model system approach to study the interaction between the carboxylate anchoring group from trimethylacetic acid (TMAA) and CeO₂(111) surfaces as a function of oxygen stoichiometry. The epitaxial CeO₂(111) thin films 50nm in thickness were grown on YSZ(111) by oxygen plasma-assisted molecular beam epitaxy at 650°C under 2.5×10⁻⁵ Torr of oxygen plasma. The sample films from MBE system were transferred to X-ray photoelectron spectroscopy (XPS) system and sputter cleaned to remove any surface contamination during the transfer. Following sputtering, stoichiometric CeO₂(111) surface was obtained by annealing the thin film under 2.0×10⁻⁵ Torr of oxygen at ~550°C for 30 min. In order to reduce the CeO₂(111) surface, the thin film was annealed in ~5.0×10⁻¹⁰ Torr vacuum at 550°C, 650°C, 750°C and 850°C for 30 min to progressively increase the oxygen defect concentration on the surface. XPS was used to characterize these surfaces prior to and following dissociative adsorption of TMAA on these surfaces using a molecular doser. The saturated TMAA coverage and the oxygen defect concentration were determined from XPS elemental composition. The saturated TMAA coverage on CeO₂(111) surface is found to increase with increasing oxygen defect concentration. This is attributed to increase in under coordinated cerium sites on the surface with increase in the oxygen defect concentrations. In parallel, we studied the interactions of TMAA adsorbed at various sites on the stoichiometric CeO₂(111) surface using periodic density functional theory (DFT) calculations. Both energetics and electronic properties of the surface and TMAA will be presented and correlated with experimental observations.

4:20pm SS-WeA8 Reactivity Differences between CeO₂(100) and CeO₂(111) Thin Films, D.R. Mullins, F.C. Calaza, S.H. Overbury, M.D. Biegalski, H.M. Christen, Oak Ridge National Laboratory

Cerium oxide is a principal component in many heterogeneous catalytic processes. One of its key characteristics is the ability to provide or remove oxygen in chemical reactions. The different crystallographic faces of ceria present significantly different surface structures and compositions that may alter the catalytic reactivity. The structure and composition determine the availability of adsorption sites, the spacing between adsorption sites and the ability to remove O from the surface.

To investigate the role of surface orientation on reactivity, CeO₂ films were grown with two different orientations. CeO₂(100) films were grown *ex situ* by pulsed laser deposition on Nd-doped SrTiO₃(100). The structure was characterized by RHEED, XRD and reflectometry. CeO₂(111) films were grown *in situ* by thermal deposition of Ce metal onto Ru(0001) in an oxygen atmosphere. The structure of these films has been studied by LEED and STM. Attempts to grow CeO₂(100) *in situ* by physical vapor deposition on Pt(100) and Pd(100) failed due to preferential growth of CeO₂(111) on these supports.

The chemical reactivity was characterized by the adsorption and decomposition of various molecules such as methanol, water and acetaldehyde. Reaction products were monitored by TPD and surface intermediates were determined by soft x-ray photoelectron spectroscopy. In general the CeO₂(100) surface was found to be more active, i.e. molecules adsorbed more readily and reacted to form new products, especially on a fully oxidized substrate. However the CeO₂(100) surface was less selective with a greater propensity to produce CO, CO₂ and water as products. The differences in chemical reactivity are discussed in light of possible structural terminations of the two surfaces.

Research sponsored by the Division of Chemical Sciences, Geosciences, and Biosciences, Office of Basic Energy Sciences, U.S. Department of Energy. Portions of this work were conducted at the National Synchrotron Light Source, Brookhaven National Laboratory, and Oak Ridge National Laboratory's Center for Nanophase Materials Sciences, which are sponsored by the Office of Basic Energy Sciences, U.S. Department of Energy.

4:40pm SS-WeA9 Adsorption and Photo-Reactivity of CO on TiO₂(110), N.G. Petrik, G.A. Kimmel, Pacific Northwest National Laboratory

We have studied the low-temperature adsorption and reactions of CO on reduced, oxidized, hydroxylated, and electron-irradiated TiO₂(110) using temperature programmed desorption, photon-stimulated desorption (PSD) and reflection-absorption infrared spectroscopy (RAIRS). Changing the condition of the crystal surface and the adsorbate coverage provides insight into the interactions of adsorbed CO with 5-fold coordinated Ti sites, (Ti_{5c}), bridge-bonded oxygen (BBO) sites, and defect sites (oxygen vacancies, bridging hydroxyls and radiation-induced surface defects). Infrared spectra were obtained for light with the plane of incidence parallel and perpendicular to the [001] azimuths of TiO₂(110). For adsorption on Ti_{5c} sites, the RAIRS spectra are consistent with CO adsorbed nearly perpendicular to the surface. For adsorption on BBO sites, the molecules adsorb parallel to the surface and perpendicular to the rows of BBO atoms. The reactivity of various molecular adsorption forms of CO is probed using PSD. In CO photo-oxidation, the PSD yields of CO and CO₂ change dramatically with initial CO coverage, indicating the importance of the relative position and orientation of O₂ and CO molecules for the photochemical reaction.

5:00pm SS-WeA10 Adsorption of Carbon Dioxide on Rutile TiO₂(110): A Scanning Tunneling Microscopy Study, X. Lin, B.D. Kay, Z.T. Wang, I. Lyubintsev, Z. Dohnalek, Pacific Northwest National Laboratory

Understanding the fundamental aspects of CO₂ adsorption and reaction on well-characterized oxide surfaces is critical in providing fundamental understanding on how to control catalytic carbon sequestration and CO₂ conversion to fuels. A model oxide surface, rutile TiO₂(110) is used to investigate the adsorption properties of CO₂ using scanning tunneling microscopy (STM). STM images obtained before and after *in-situ* doses of CO₂ at 50 K reveal that the CO₂ molecules preferentially bind in bridge-bonded oxygen vacancy (V_O) defect sites. We show that electron injection from the STM tip can induce CO₂ reduction to CO and V_O annihilation. After the saturation of V_O's, CO₂ molecules preferentially adsorb on five-fold coordinated Ti sites, where they remain mobile even at 50 K. The mobile CO₂ molecules may be corralled by other immobile species such as CO. The contrast observed in the STM images suggests that the distribution of mobile CO₂ molecules tracks the distribution of the subsurface charge as demonstrated by the CO₂ induced standing wave patterns along the Ti rows. The adsorption behavior of CO₂ on hydroxylated TiO₂ surfaces will also be presented.

5:20pm SS-WeA11 Interaction of ZnO-supported Cu Oxides with CO and CO₂, Z. Zhang, F. Wang, M. Le, M. Ren, J. Flake, P. Sprunger, R. Kurtz, Louisiana State University

Cu and Cu-oxide nanoclusters supported on ZnO are prototypical catalysts for the electrochemical reduction of CO and CO₂ to methanol. In this report we describe the interaction of CO and CO₂ with Cu oxide nanoclusters on ZnO(10 $\bar{1}$ 0) with a combination of surface sensitive tools including STM for structural information, EELS for electronic and vibrational studies as well as synchrotron-based photoemission for electronic properties. Cu is deposited onto ZnO and oxidized with a combination of O-exposure and annealing procedures to result in two distinct Cu-oxide (CuI and CuII) clusters, which preferentially nucleate and grow at step edges. Photoemission shows a large charge transfer between the oxide cluster and the substrate surface as well as significant band bending. It is believed that the CO₂ adsorption, forming a carbonate species, and consequent reduction, is coupled to the induced defects and electronic perturbation of the Cu_x/ZnO nanoclusters, absent in the case of Cu/ZnO nanoclusters. In

addition to vibrational EELS and TDS to characterize the adsorption of the CO and CO₂ adsorption species, similar results from Au on ZnO(10 $\bar{1}$ 0), which shows a lack of cluster formation growth, will be compared and contrasted.

This material is based upon work supported as part of the Center for Atomic Level Catalyst Design, an Energy Frontier Research Center funded by the U.S. Department of Energy, Office of Science, Office of Basic Energy Sciences under Award Number DE-SC0001058

5:40pm SS-WeA12 Microfabricated Nitrogen-Phosphorus Detectors: Surface Work Function and Thermionic Emission, M.T. Brumbach, R.F. Hess, R.J. Simonson, M.W. Moorman, T.J. Boyle, Sandia National Laboratories

Chemically selective sensors are required for detection of chemical warfare agents with ever increasing demands on the selectivity, sensitivity, lifetime, speed, and reduced power consumption of these devices. Strategies for reducing the scale of these sensors have been explored to produce microfabricated Nitrogen-Phosphorus Detectors (NPDs) to accommodate these many requirements. The device incorporates sol-gel derived alkali metal silicate thin films on low thermal mass silicon substrates for field portable gas chromatography applications. In spite of the long history of NPDs, the details of the chemically-mediated emission related to their selectivity are not well understood. The NPD signal current ultimately depends on the transfer of electrons across the surface potential barrier of the thermionic cathode emitter. Two classes of competing mechanisms have been described in the literature to account for the chemically-selective ionization observed in NPDs: (a) gas-phase ionization models and (b) surface mediated electron emission. The latter mechanism has been the focus of our measurements of the surface work function of candidate emitter materials as a function of composition, structure, temperature, and ambient atmosphere. Specifically, both the local work function variations by scanning probe measurements and effective average work function by measuring total emission will be discussed.

Thin Film Division

Room: 109 - Session TF1+EM-WeA

Nonvolatile Memory

Moderator: T. Karabacak, University of Arkansas at Little Rock

2:00pm TF1+EM-WeA1 Application of Amorphous Zinc Tin Oxide for Memristor Devices, G.S. Herman, J.S. Rajachidambaram, S. Murali, J. Conley, Oregon State University, **S.P. Sanghavi, P. Nachimuthu, V. Shuthanandan, T. Varga, S. Thevuthasan,** Pacific Northwest National Laboratory

Amorphous zinc tin oxide semiconductor materials have been studied primarily as the active semiconducting material for thin film transistors with applications including transparent and flexible electronics. Due to the amorphous nature of these materials excellent uniformity can be obtained over a large area, while still having reasonably high electron mobilities (>10 cm²/Vs). Furthermore, considerable control over the electrical properties can be maintained, where insulating, semiconducting, and conductive properties can be obtained by varying the processing conditions. We have recently used sputter-deposited zinc tin oxide as a bipolar switching element in memristor devices. Memristors are a two-terminal nonvolatile data memory device that is very promising for the replacement of silicon-based Flash. A significant benefit is that memristors can be manufactured with high areal densities with potentially low manufacturing costs. A variety of oxide-based materials are being evaluated for memristors, however many of these are nanocrystalline which can lead to non-uniformity of devices. We have found that the switching properties of zinc tin oxide are closely related to the process conditions, the electrical test conditions, and the electrode materials. In this presentation we will discuss the physical and electrical characterization of the zinc tin oxide films and the switching mechanisms for these materials.

2:20pm TF1+EM-WeA2 PE-MOCVD of GeTe Materials for Phase Change Memory Applications, E. Despiou-Pujo, L. Dussault, C. Vallée, LTM/CNRS-UJF, France, E. Gourvest, ST Microelectronics, France, D. Jourde, S. Maitrejean, P. Michallon, CEA Leti Minatoc Campus, France Phase-Change Random Access Memories (PCRAM) are very promising candidates for next generation of non-volatile memories. Those devices store information using the high electrical contrast between the amorphous and crystalline phases of chalcogenide alloys such as Ge₂Sb₂Te₅ (also called GST) which are mainly deposited by physical vapor deposition (PVD) [1].

However, two important drawbacks have to be overcome: a too short archival life for GST at high operating temperatures and a too high power consumption. The binary compound GeTe seems to be a promising candidate for high temperature applications since it has an estimated archival life up to ten years at 110°C. A pronounced increase in thermal stability of N- and C-doped GeTe was also demonstrated [2].

Concerning the power consumption, it was shown that a way to reduce the high operating currents is to confine the material. In this way, several groups try to develop a new deposition process to achieve the gap filling of the confined structure. Atomic Layer Deposition (ALD) of GST has shown very good step coverage but the deposition rate remains very low. Therefore, we proposed to study the deposition of GeTe in a shower-head type 200mm plasma-enhanced pulsed liquid injection CVD reactor (AltaCVD200). Ge and Te liquid precursors are introduced into the deposition chamber as vapours through a pulsed injection system and an evaporating furnace. A capacitively-coupled RF plasma is applied between the shower head and the substrate heater to decompose the precursors. Chamber walls are maintained at 70°C to avoid condensation of precursors vapours. The deposition chamber is mounted on a cluster tool which allows quasi *in situ* analysis of the deposited films by angle-resolved XPS while the plasma is analyzed by optical emission spectroscopy (OES).

In this paper, we investigate the optical emission spectra of high pressure (2-20 Torr) Ge- and Te-containing plasmas. Reference UV-visible emission spectra (200-800 nm) are recorded for various conditions of RF power, pressure, and flow rate. The role of electrons and H atoms in the decomposition of Ge and Te precursors is discussed by correlating the OES of the plasma with the chemico-physical properties of the deposited material. It is shown that H atoms induce a competitive effect between deposition (due to the decomposition of the precursors) and etching of Ge and Te atoms at the growing film surface. Role of C contamination in the phase change properties is also discussed and phase transitions of plasma deposited GeTe-C materials are compared with sputtered GeTe-C.

[1] G. W. Burr et al, J. Vac. Soc. Technol. B 2010, 28 (223)

[2] A. Fantini et al, IEDM 2010

2:40pm TF1+EM-WeA3 Embedded HfO₂ based 1T1R Cells for Future RRAM Applications, Ch. Wenger, T. Bertaud, Ch. Walczyk, D. Walczyk, M. Malgorzata, IHP, Germany **INVITED**

The integration of various functionality to (Bi)CMOS circuits is in the focus of the "More than Moore" approach. Here, we demonstrate the incorporation of nonvolatile memories (NVM) into the Back end of line (BEOL) of Bi(CMOS) circuits. The added functionalities open new technological possibilities for high value microelectronics systems.

Embedded nonvolatile memories (NVM) with high-density, high-speed, and low-power are attractive for a growing number of applications. One promising candidate for next-generation nonvolatile memories is based on the electrically switchable resistance change between a high (OFF-state) and a low (ON-state) resistive state of a metal-insulator-metal (MIM) structure. This approach is often termed resistance random access memory (RRAM) technologies. Due to the cost effectivity and BEOL compatibility with (Bi)CMOS technologies, this approach is highly attractive. By combining the MIM devices (R) with selection transistors (T), the 1T-1R cells offer good scalability, long retention time, and rapid read/write times. In this letter, the reliable bipolar resistive switching of TiN/HfO₂/Ti/TiN devices embedded into 1T-1R cells is demonstrated.

The current-voltage (I-V) characteristics of the TiN/HfO₂/Ti/TiN diodes and 1T-1R cells were studied by DC voltage sweep measurements. By applying a positive voltage at the top electrode, the resistance is reduced for $V > V_{set}$. The device can be switched back into the OFF-state when a negative voltage is applied beyond V_{reset} . In case of the 1T-1R cell, the forming and set processes can be controlled by changing the gate voltage (V_G) of the select transistor.

4:00pm TF1+EM-WeA7 Synthesis and Characterization of Multiferroic Oxides by Radical Enhanced Atomic Layer Deposition, C.D. Pham, J.H. Choi, J.P. Chang, University of California Los Angeles

Multiferroic materials exhibit two or more forms of ferroic order such as (anti)ferroelectricity, (anti)ferromagnetism, ferroelasticity, or ferrotoroidicity. Materials containing both ferroelectricity and ferromagnetism will exhibit some amount of magnetoelectric coupling which is a desirable aspect for the future of non-volatile memory, as these materials could potentially be used for devices that will be written magnetically and read electronically or vice versa, as well as the prospect of four-state memory devices. Materials which exhibit magnetoelectric coupling have been well studied, however, the synthesis methods may not easily translate into large scale integration.

One possible route for synthesis on a commercial scale, atomic layer deposition (ALD) is a thin-film processing technique which involves

alternatively flowing non-self reacting precursor vapors or gases onto a substrate. As a result of the self limiting reaction, the precursors only form a single monolayer per cycle. The sequential and self-limiting nature of the deposition is used to deposit thin films with good compositional control, high conformity, high uniformity, and excellent thickness control.

To create multiferroic crystal structures, a 1:1 stoichiometric ratio between cations is desired with low contamination by organic ligands in order to form the crystal phases that permit multiferroicity. Therefore, in this work, multiferroic YMnO₃ and BiFeO₃ on various substrates are synthesized by radical enhanced atomic layer deposition (RE-ALD) using Y(tmhd)₃ (tmhd = 2,2,6,6-tetramethylheptane-3,5 dione), Mn(tmhd)₃, Fe(tmhd)₃, and Bi(tmhd)₃ as metal precursors and oxygen radicals as the oxidizer. By varying the cycle sequences, controlled composition is demonstrated and verified through XPS. Growth rates are shown on a thickness per cycle basis as a function of deposition temperature, precursor pulse times, and substrate. The crystal structure as well as atomic environment are examined by XRD and extended x-ray absorption fine structure spectroscopy (EXAFS) respectively and are accompanied by TEM micrographs. Finally, magnetic measurements made by a super conducting quantum interference device (SQUID) magnetometer, zero-field cooled and field cooled (ZFC-FC) M vs. T and M vs. H, are shown on 1:1 YMnO₃ stoichiometric films showing a Néel temperature $T_N = \sim 45$ K and a coercive magnetic field $H_C = 130$ Oe for Si(111) and $H_C = 300$ Oe for YSZ(111).

4:20pm TF1+EM-WeA8 Perpendicular Magnetic Tunnel Junctions based on Thin CoFeB Free Layer and Co-based Multilayer SAF Pinned Layers, A. Natarajarathinam, S. Gupta, University of Alabama

We have previously reported on fully perpendicular Co/Pd multilayers (ML)-based CoFeB/MgO/CoFeB magnetic tunnel junctions (MTJ's)^{1, 2}. However, Co/Pd ML-based MTJ's have rarely exhibited TMR ratios greater than about 10%. This has been attributed to the inability to pull a sufficiently thick CoFeB layer perpendicular on top of MgO, as well as the incomplete bcc templating of CoFeB from MgO owing to the adjacent fcc Co/Pd ML's³. Recent results³⁻⁷ have generated great interest in MTJ's with pinned perpendicular synthetic antiferromagnets (SAF), of the form AP1/Ru/AP2 where AP1 and AP2 are Co-based multilayers, for instance, Co/Ni or Co/Pd. We report on fully perpendicular MTJ's with a thin CoFeB free layer and a Co/Pd(Pt) ML-based SAF pinned layer. For Co/Pd ML SAF's, strong antiferromagnetic coupling was seen at t_{Ru} of 1.1nm, with a coupling strength of 0.017 mJ/m². For Co/Pt ML SAF's the optimum antiferromagnetic coupling was found at slightly higher Ru thickness of 1.3 nm, with a coupling strength of 0.013 mJ/m². Improved MTJ properties are expected from using a thin Ta-seeded CoFeB bottom free layer, along with a thin, amorphous Ta layer used to transition from bcc CoFeB to fcc Co/Pd(Pt) for the top pinned layer⁶. The full stack is of the form: bottom lead/Ta

(2)/CoFeB(1)/MgO(1.6)/CoFeB(0.8)/Ta(0.3)/[Co(0.3/Pd(1))/5/Co(0.3) or {Co(0.5)/(Pt(2))}5/Co(0.5)/Ru1.1 or 1.3/[Co(0.3/Pd(1) or Co(0.5)/(Pt(2))]/top lead. CIPT measurements indicated TMR values as high as 20% for as-deposited stacks. Magnetometry of blanket stacks showed a large separation in the switching fields of free and pinned layers, with free layer switching close to zero field and pinned layer switching at 0.8-1.8 kOe (Fig.1). This symmetric extended plateau of constant magnetization offers a large dynamic range over which the magnetic configuration remains stable⁷. The stacks were patterned into MTJ's, annealed at 240° C in an in-plane field of 0.5 T, and characterized magnetically and electrically.

Acknowledgements:

This work is partially supported by a U.S. Department of Defense DARPA-MTO STT-RAM Universal Memory contract, and Grandis Technology, Milpitas. Dr. David Abraham of IBM is gratefully acknowledged for CIPT measurements.

References:

1. Z. R. Tadisina et al., J. Vac. Sci. Technol. A **28**, 973 (2010).
2. Z. R. Tadisina et al., J. Appl. Phys. **107**, 09C703 (2010).
3. K. Mizunuma et al., Appl. Phys. Lett. **95**, 232516 (2009).
4. H.He et al., IEEE Trans. Magn. **46**, 1327 (2010).
5. D. C. Worledge et al., Proc. Int'l. Electron. Dev. Mtg. 10-296, (2010).
6. D. C. Worledge et al., Appl. Phys. Lett. **98**, 022501 (2011).
7. J. Sort et al. Appl. Phys. Lett. **83**, 1800 (2003).

4:40pm **TF1+EM-WeA9 Characterizing the Effects of Processing on Materials for Phase Change and Spin Torque based Non-Volatile Memory Technologies.** *E.A. Joseph, R.M. Martin, J.S. Washington, D.W. Abraham, S. Raoux, J.L. Jordan-Sweet, IBM T.J. Watson Res. Ctr., D. Miller, IBM Almaden Res. Ctr., H.-Y. Cheng, Macronix International Co., Ltd, Taiwan, R.O.C., M.C. Gaidis, M. Gajek, M. Breitwisch, IBM T.J. Watson Res. Ctr., S.-C. Lai, Macronix International Co., Ltd, Taiwan, R.O.C., Y. Zhu, R. Dasaka, R. Sawant, D. Neumayer, IBM T.J. Watson Res. Ctr., R.M. Shelby, IBM Almaden Res. Ctr., H.-L. Lung, Macronix International Co., Ltd, Taiwan, R.O.C., C.H. Lam, N.C.M. Fuller, IBM T.J. Watson Res. Ctr.* **INVITED**

Phase change memory (PCM) and spin-torque magnetic random access memory (ST-MRAM) have recently garnered significant interest for future non-volatile memory applications due to their promise for scalability beyond that of conventional DRAM and flash memory technologies. In addition, both PCM and ST-MRAM have potential to enable improvements in programming speed, low voltage operation and high endurance, as compared to current devices. However, the introduction of each technology not only brings with it new device challenges, but the fabrication process itself can also alter the properties of the materials, leading to performance degradation. In this work, we explore the effects of integration and processing on Ge₂Sb₂Te₅ (GST) and CoFeB for PCM and ST-MRAM devices respectively, with relevance towards scaling to the 14nm node and beyond. Using multiple analysis techniques including time resolved laser reflectivity and X-ray diffraction, we determine that exposure to various etch and ash plasma chemistries can cause a significant reduction in the (re)crystallization speed of GST, while concurrently increasing the transition temperature from the rocksalt to the hexagonal phase. Furthermore, by utilizing optical emission spectroscopy, X-ray absorption spectroscopy (XAS) and X-ray photoelectron spectroscopy (XPS) we are able to link the changes in crystallization to etch-induced modification of the GST stoichiometry. For CoFeB materials, vibrating sample magnetometry is used to determine the effect that plasma exposure (as used for both patterning and encapsulation) has on the magnetic moment. We find that even when relatively thick capping layers are present, magnetic moment can still be significantly degraded. The severity of this effect is heavily dependent on plasma chemistry. Further results of process-induced material modification and device degradation as a function of etch, encapsulation, and thermal processing will be presented, focusing primarily on the impact on scaling of these technologies. Finally, potential integration and processing solutions to circumvent these issues will also be discussed.

Thin Film Division

Room: 110 - Session TF2+EM-WeA

Nanostructuring Thin Films

Moderator: A.V. Melechko, North Carolina State University

2:00pm **TF2+EM-WeA1 Templated Solid-State Dewetting for Patterning of Films.** *C.V. Thompson, J. Ye, A.L. Giermann, Massachusetts Institute of Technology* **INVITED**

Most crystalline thin films are metastable in the as-deposited state, and will dewet to form islands when they are heated to temperatures that lead to sufficiently high atomic mobilities. This can happen well below the melting temperature of the film, so that the material remains in the form of a crystalline solid throughout the dewetting process. When unpatterned films dewet on flat substrates, the resulting islands have widely varying sizes and spacings. However, we have shown that substrate patterning can be used to control the solid-state dewetting process and to produce ordered arrays of monodispersed and crystallographically aligned islands from polycrystalline films. Recent experiments on patterned single-crystal films have allowed independent study of the various mechanisms that control structure evolution during solid-state dewetting. These include fingering instabilities, edge faceting, corner instabilities, pinch-off processes, and Rayleigh-like instabilities. Surface energy anisotropy plays a very important role in these processes, and for single-crystal films, leads to the formation of crystallographically aligned complex patterns of lines and islands that can be reproducibly controlled through pre-patterning.

2:40pm **TF2+EM-WeA3 Dynamics of Solid Thin-Film Dewetting in the Silicon-On-Insulator System.** *E. Bussmann, F. Cheynis, F. Leroy, P. Müller, CINaM-CNRS, France*

Thin-film dewetting is a process wherein a film on a substrate spontaneously agglomerates into 3D islands, which in some instances are ordered. A detailed understanding of the mechanism and dynamics of dewetting is crucial, either to avoid the agglomeration, or to engineer

organized arrays of nanostructures. Silicon-on-Insulator (SOI) films, which are promising substrates for microelectronics, undergo dewetting when annealed at >700°C under ultrahigh vacuum conditions. The Si film spontaneously transforms into an assembly of ordered nano-sized Si islands. Previous *ex-situ* studies of dewetted SOI films provided a qualitative description of the dewetting process [1-4]. However, the dewetting dynamics, as well as the thermodynamic driving forces and atomistic mechanisms at work, remained largely unclear. We simultaneously measure the real-time dewetting dynamics and the motion of surface atomic-steps (surface self-diffusion) using low-energy electron microscopy (LEEM) [5]. We observe the following scenario: (i) dewetting voids nucleate at defects in the Si(001) layer. In the early stages of dewetting, the area of the opening voids grows linearly with time, and the Si ejected from the voids accrues into a rim surrounding the dewetted area. (ii) As dewetting progresses, the rim undergoes an instability that leads to the formation of elongated Si fingers. Once the first fingers have formed, the void area grows as the square of time. (iii) Finally, the Si fingers undergo a Plateau-Rayleigh instability, breaking apart into 3D Si nano-islands. We compare our measurements of the morphological evolution of dewetting to a simple analytical model for dewetting void growth (based on surface diffusion, nucleation on the top of the 3D structures, and mass-conservation), and to Kinetic Monte Carlo simulations. The KMC simulations reproduce the qualitative features of the complex void shape evolution in detail, while the analytical model of void growth allows us to connect the void growth rate with the dewetting driving force. These approaches unambiguously show that the SOI dewetting process is surface-diffusion-limited and driven by surface and interface free-energy-minimization.

[1] D. T. Danielson *et al.*, J. Appl. Phys. 100, 83507 (2006).

[2] R. Nuryadi *et al.*, J. Vac. Sci. Technol. B, 20(1), 167 (2002).

[3] B. Yang *et al.*, Phys. Rev. B 72, 135413 (2005).

[4] E. Dornel *et al.*, Phys. Rev. B 73, 115427 (2006).

[5] E. Bussmann *et al.*, New J. Phys. 13 043017 (2011).

3:00pm **TF2+EM-WeA4 Self and Directed Assembly of Thin Metallic Films by Pulsed Laser Induced Dewetting.** *Y. Wu, University of Tennessee, J.D. Fowlkes, Oak Ridge National Laboratory, L. Kondic, New Jersey Institute of Technology, J. Diez, Universidad Nacional del Centro de la Provincia de Buenos Aires (UNCPBA), Argentina, N.A. Roberts, P.D. Rack, University of Tennessee*

The synthesis and assembly of functional metallic nanomaterials is critical for realizing many important applications of nanoscience and nanotechnology, and metallic thin film dewetting has been an effective and low-cost approach to this end. In this study, we investigated dewetting of metal thin films via pulsed nanosecond laser melting. We also explore the dewetting and nanopattern formation of nanolithographically pre-patterned thin films of various shapes to understand initial and boundary conditions in guiding the assembly. More recently, nanolithography was used to impose the perturbation which ultimately led to an organized nanoparticle array. Specifically, liquid-phase pulsed laser induced dewetting (PLiD) was used to transform metallic thin film strips into nanoparticle arrays. We demonstrated that the assembly accuracy and precision could be drastically improved by merely imposing a synthetic sinusoidal perturbation onto the lateral surfaces of the thin film strip. The synthetic perturbations in the strip translated into an unstable varicose oscillation on the rivulet during retraction – a precise nanoparticle diameter and pitch emerged thereby superseding the otherwise naturally evolving modes predicted by the modified Rayleigh-Plateau instability. A nanoscale, synthetic perturbation was usefully imposed to “nudge” the natural, self-assembly dispersion toward significantly higher order.

4:00pm **TF2+EM-WeA7 Directed Self-Assembly of Ge Heteroepitaxial Quantum Dots with sub-35nm Spacing.** *C. Petz, University of Virginia, D. Yang, J. Levy, University of Pittsburgh, J.A. Floro, University of Virginia*

Artificially ordered Ge quantum dot (QD) arrays, where confined carriers can interact via spin coupling, may create unique functionalities such as spintronic bandgap systems. Development of such arrays for quantum computing requires fine control over QD size and spatial arrangement on the sub-35 nm length scale. We employ fine-probe electron-beam irradiation to locally decompose ambient hydrocarbons onto a bare Si (001) surface. These carbonaceous patterns are annealed in UHV, forming ordered arrays of nanoscale SiC precipitates that serve as templates for subsequent Ge quantum dot nucleation via strain-induced self-assembly during heteroepitaxy. The nanoprecipitates effectively reduce the critical thickness for Ge QD formation to below the 3-4 monolayers typical of Stranski-Krastanov growth in the Ge/Si (001) system. Thus, Ge QDs in the SiC-patterned regions nucleate prior to formation of randomly located QDs

in the unpatterned areas. It is critically important to ascertain the variability in Ge QD size and placement, and ultimately to determine the crystalline quality and interface properties of these ultrasmall Ge dots on SiC nanoprecipitates. Using atomic force microscopy and cross-sectional transmission electron microscopy, we investigate the patterned surface morphology and internal structure of patterned QDs to develop a fundamental understanding of the Ge adatom behavior in the vicinity of local high lattice-mismatch nanoprecipitates. We find that Ge self-assembly at SiC sites depends on QD spacing and that the QD size is surface diffusion limited, suggesting that local alteration of the intermediate Si surface may repel Ge to higher lattice mismatched SiC sites. Support from the DOE Office of Basic Energy Sciences is gratefully acknowledged under grant number: DE-FG02-07ER46421.

4:20pm TF2+EM-WeA8 Surface Functionalization of Zeolites and Nanoparticles: Understanding and Applying Plasma Modification Strategies for Unusually Shaped Particles, J.C. Shearer, E.R. Fisher, Colorado State University

Unusually shaped micron- and nanometer-sized particles are becoming key components in catalytic and biological applications. Zeolite particles are typically modified for ion-exchange and catalytic applications. Fe₂O₃ nanoparticles are widely used in biological applications such as MRI imaging and site-specific drug delivery, thereby creating a need for surface functionalization techniques to ensure biocompatibility. Plasma processing can effectively modify and implant functional groups onto flat substrates, and is non-directional. Thus, the primary focus here is on applying these plasma processes to unusually shaped materials and understanding the gas-phase chemistry and surface reactions that make these coatings viable. Previous work in our lab employed plasma-enhanced chemical vapor deposition to create composite SiO₂/TiO₂ nanoparticles. Here, we use plasma processing methods for the modification of zeolite surfaces and functionalization of Fe₂O₃ nanoparticles. Compositional and morphological data demonstrate that the conformal treatment of particles was achieved and that the use of PECVD methods allowed for advanced control over surface modification and specific tailoring of the structure, composition, and growth characteristics of any deposited film. Insight into the modification and deposition process is provided by actinometric optical emission spectroscopy (AOES) and laser induced fluorescence spectroscopy (LIF), which allow characterization of the gas-phase species and their energetics (i.e. internal energies) for each system. To further investigate the functionalization of nanoparticle surfaces, additional studies explore the contributions of gas-phase OH radicals to the creation of SiO₂/Fe₂O₃ composite nanoparticles. Scatter coefficients and gas-phase density measurements derived from our imaging of radicals interacting with surfaces technique (IRIS) provides additional insight on the molecular-level chemistry occurring at the interface between gaseous plasma species and nanoparticle substrates. The operation and design of an in-house rotating drum reactor will be discussed as a potential method for adapting the composite nanoparticle fabrication to an industrial scale.

4:40pm TF2+EM-WeA9 Role of Ion Flux on Alignment of Carbon Nanofibers Synthesized by DC Plasma on Transparent Insulating Substrates, R.C. Pearce, North Carolina State University, A.W. Vasenkov, CFD Research Corporation, D.K. Hensley, M.L. Simpson, T.E. McKnight, Oak Ridge National Laboratory, A.V. Melechko, North Carolina State University

A key factor to the implementation of vertically aligned carbon nanofibers (VACNFs) in devices is a more fundamental understanding of how to control fluctuations in the growth direction of the fibers. It has previously been hypothesized that the electric field is the primary factor in determining the orientation of fibers grown catalytically using plasma enhanced chemical vapor deposition (PECVD). Here we present results of carbon nanofiber synthesis on insulating substrates by dc plasma in the vicinity of grid electrodes. To perform these observations, VACNFs were synthesized on a fused silica substrate using direct current PECVD. To maintain continuous glow discharge above the substrate, a metal grid electrode layer (Cr) was deposited over silica with windows of exposed silica ranging in size from 200 μm to 1 mm. Observed trends in nanofiber alignment at the window-electrode interface suggests that the alignment is governed by the direction of the ion flux rather than the electric field at the substrate level. The proposed alignment mechanism is that ion sputtering of the carbon film on a catalyst particle the growth direction of the nanofibers. With this development, fiber growth direction can be better manipulated through changes in ionic flux direction, opening the possibility for growth of nanofibers on substrates with unique geometries.

5:00pm TF2+EM-WeA10 High-Performance Poly-3-alkylthiophene-Carbon Nanotube Composites for Transparent Electrodes, S.L. Hellstrom, R.Z. Jin, R.M. Stoltenberg, Z. Bao, Stanford University

Flexible transparent electrodes are crucial for flat panel display and solar cell technologies. While carbon nanotube network electrodes show promise, their fabrication often involves insulating surfactants which worsen conductivity. As an alternative, we show that small amounts of conjugated semiconducting polymer added to nanotube dispersions enables straightforward solution deposition of uniform electrodes by spin-coating or drop casting. After doping, electrodes as good as 120 ohm/sq with 81% transmittance at 550 nm are obtained. Tuning system chemistry and deposition parameters allows control of tube bundle size, density, and alignment, and these may be correlated with electrode performance.

We also employ the selectivity of P3HT:CNT composites in wetting of and adhesion to different dielectric surfaces, to simultaneously fabricate and pattern organic electrodes with unprecedented nanotube density gradients and excellent feature resolution. We employ these to drive pentacene and C₆₀ transistors that are competitive with those made using Au electrodes. We thereby suggest that this material system and fabrication technique has promise in applications requiring flexible, semitransparent, low-cost complementary circuits.

5:20pm TF2+EM-WeA11 SiGe Nanomembranes: Defect-Free Single-Crystalline Growth Substrates for High-Quality Strained Epitaxial Materials, D.M. Paskiewicz, B. Tanto, D.E. Savage, M.G. Lagally, University of Wisconsin Madison

Silicon-Germanium semiconductor alloys are important in improving Group IV opto- and microelectronics. Typically, SiGe is used as a stressor to introduce strain into Si, thereby altering the electronic band structure [1, 2] or changing optical properties [3]. The SiGe stressor can be incorporated locally to strain small areas of Si uniaxially [2], or relaxed SiGe can be used as a substrate for growth of biaxially strained Si over large areas [1]. We will focus on the latter: using relaxed SiGe to induce global biaxial strain in Si. Conventional methods for creating relaxed SiGe substrates involve epitaxial growth on Si substrates and relaxation of the alloy *via* dislocations. The density of defects that reach the top relaxed SiGe layer can be limited through various techniques [4], but strain inhomogeneities and surface roughness created by the dislocations remain. We demonstrate the fabrication of SiGe nanomembranes (NM): fully *elastically* relaxed, smooth, single-crystalline sheets of SiGe alloy. A thin SiGe layer (less than the kinetic critical thickness for dislocation formation) is grown on a silicon-on-insulator (SOI) substrate with molecular beam epitaxy (MBE), followed by a Si capping layer of similar thickness to the Si template layer of the SOI. The SiO₂ layer of the SOI is selectively etched away, leaving the Si/SiGe/Si trilayer heterostructure free to strain share [5]. The Si layers of the trilayer are then selectively etched away, leaving a fully elastically relaxed SiGe NM. These SiGe NMs can be transferred to new handling substrates, bonded, and used as templates for growth of new defect-free materials.

A specific application involving strained Si/relaxed SiGe heterostructures is fabrication of 2-dimensional electron gas devices (2DEGs) that can be patterned and gated to confine individual electrons into quantum qubits with long spin coherence times [6]. These devices are very sensitive to changes in the electrostatic potential and thus require superb material quality. We compare the material quality of strained Si/SiGe heterostructures grown on SiGe NMs with those created on SiGe substrates relaxed *via* dislocations.

Research supported by DOE. Facilities support from NSF-MRSEC is acknowledged. DMP is supported by a NSF Graduate Research Fellowship.

1. Schäffler, *Semicond. Sci. Technol.* **12** (1997) 1515.
2. Chu et al., *Annu. Rev. Mater. Res.* **39** (2009) 203.
3. Jacobsen et al., *Nature* **441** (2006) 199.
4. Fitzgerald et al., *J. Vac. Sci. Technol., B* **10** (1992) 1807.
5. Roberts et al., *Nat. Mater.* **5** (2006) 388.
6. Simmons et al., *Phys. Rev. Lett.* **106** (2011) 156804.

5:40pm TF2+EM-WeA12 Multilayer Barrier Coatings for Organic Photovoltaics, A.M. Coclite, K.K. Gleason, Massachusetts Institute of Technology

Barrier coatings, which prevent the permeation of water into OPV devices fabricated on flexible plastic substrates, are essential to extend the device lifetime. Such protective coatings are made of multilayer stacks where multiple dense, inorganic layers are alternated with soft, organic ones. The inorganic layer contains inevitably some pinholes and defects. The roles of the organic layer are (i) creating a tortuous and longer path among the defects of two successive inorganic layers (ii) filling the pores of the inorganic underlayer limiting the propagation of defects from one inorganic layer to the other and (iii) smoothening the substrate surface roughness.

In the past, we obtained good barrier properties ($WVTR = 10^{-2} \text{ g/cm}^2/\text{day}$) with a hexalayer obtained by coupling initiated CVD (iCVD) and plasma enhanced CVD (PECVD). iCVD layers resulted in effective defect decoupling and good planarization of the substrate.¹

Now a similar approach is investigated for the multilayer deposition in a large-area reactor (0.16 m²), maintaining the same organosilicon precursor and the same reactor configuration for both deposition of silica-like and organosilicon layers.

SiO_x layers were deposited through PECVD in MW plasma at high power and high oxygen dilution. The silanol and organic groups were not detectable by IR spectroscopy, resulting in denser film if compared with the previous results.

A new process was used for the formation of organosilicon polymers with enhanced monomer structure retention compared to a conventional plasma deposition and faster deposition rate if compared to conventional iCVD processes from organosilicon monomer. We demonstrate that the monomer molecule remains substantially preserved in fact the C/Si ratio calculated from XPS data on the polymer was 4.3, close to the 3.7 C/Si elemental ratio of the monomer molecule.

The deposition of smoothing organic layers is demonstrated by depositing the coating on the top of a microsphere (1 μm in diameter) monolayer deposited over silicon wafers. Increasing the thickness of the coating, the degree of planarization (DP), both local (DLP) and global (DGP), increases. The DLP increases much faster than the DGP: when the coating is 1 μm-thick the DLP is already 99%, for the global planarization instead a 1.8 μm-thick-coating is needed to reach DGP=99%.

The high density of the inorganic layer, the smoothness and planarization properties of the organic one make this approach particularly promising for the deposition of effective multilayer barrier coatings.

¹ Coclite, Ozaydin-Ince, Palumbo, Milella, Gleason, *Plasma Proc. Polym.*, **2010**, *7*, pp. 561

Tribology Focus Topic

Room: 111 - Session TR-WeA

Emerging Interfaces of Tribological Importance

Moderator: T. Scharf, The University of North Texas

2:00pm **TR-WeA1 Highly Wear-Resistant Surfaces Based on Fluorinated Alkyne-Derived SAMs on Si(111)**, *S.P. Pujari, H. Zuilhof*, Wageningen University, The Netherlands

Micro-electro-mechanical systems (MEMS) are considered to be an important technology for the development of several products in daily life such as electronics, medical devices, and packaging. Even after tremendous progress in fabrication of miniaturized devices based on silicon materials, the development of highly robust surfaces with low friction and resistance against wear is still a challenging subject of accomplishment. To accomplish this goal, new fluorine-containing terminal alkynes were synthesized and self-assembled onto Si(111) substrates to obtain fluorine containing organic monolayers. Such covalently bound organic monolayers have similar surface properties as polytetrafluoroethylene (Teflon), but these monolayers are more stable than traditionally coated PTFE. The combination of these properties yields a highly improved wear resistance.

A combination of spectroscopic (XPS, IR), microscopic (AFM), and contact angle measurements shows these monolayers were to be ordered and highly hydrophobic. Increasing the amount of fluorine on the alkyne precursor resulted in monolayers with a greatly reduced adhesion to silica probes, as well as an almost 5-fold decrease in the coefficient of friction on the surface. Overall, this yields a friction coefficient that is – to the best of our knowledge – lower than reported for any other fluorine-containing monolayer. In addition, these fluorinated monolayers displayed no sign of wear at high loads. Therefore, the use of such highly durable fluorine-containing monolayers can significantly expand the range of applications for MEMS. Therefore, this work opens a route to design new materials with tailor-made properties for a wider range of applications in MEMS-based devices.

2:20pm **TR-WeA2 Composition and Friction Analysis of Copolymer Solution Treatments of Silicone Hydrogel Contact Lens Surfaces**, *S. Perry, Y. Huo, A. Rudy*, University of Florida

The surface chemical compositions of three major brands of silicone hydrogel (SH) contact lenses were analyzed using X-ray photoelectron spectroscopy (XPS) prior to and following treatment in a test solution of diblock copolymer of polyethylene oxide and polybutylene oxide. Atomic

force microscopy (AFM) was also employed to evaluate the surface topography and frictional properties of these lenses prior to and following similar solution treatments. For surface compositional analysis with XPS, lens surfaces have been prepared through a vacuum drying procedure, in which the hydrogel is taken from a fully hydrated state directly to an ultraclean, ultrahigh vacuum environment. Contact and tapping mode AFM were used to measure the frictional and topographical properties in aqueous environments. Prior to treatment, differences in surface elemental composition of the various lenses were found to reflect known bulk compositions and/or respective surface treatments. Following solution treatment, surface chemical modifications were apparent in balafilcon A (PureVision®) and lotrafilcon B (O₂ OPTIX®), especially in the distribution chemical functionalities present at the surface. Only modest changes in surface composition were observed for the senofilcon A (ACUVUE® Oasys®) system. AFM measurements in saline revealed large disparities between the coefficients of friction of the three lenses, with balafilcon A and lotrafilcon B exhibiting coefficients of friction approximately five times greater than that of senofilcon A. Lens surface treatment with the diblock copolymer test solution produced a significant reduction in the coefficients of friction of the two lenses exhibiting higher friction, yet only a small reduction in friction was observed for senofilcon A lens. Together, these results depict a strong correlation between the surface chemistry and frictional response of the lens systems as they relate to solution treatment with this specific diblock copolymer. This study indicated that diblock copolymers containing polyethylene oxide and polybutylene oxide may have a positive impact on the lubrication and wetting properties of silicone hydrogel lenses.

2:40pm **TR-WeA3 In Situ Studies of Cartilage Microtribology**, *D.L. Burris, E.D. Bonnevie, V.J. Baro, L. Wang*, University of Delaware
INVITED

The progression of local cartilage surface damage toward early stage osteoarthritis (OA) likely depends on the severity of the damage and its impact on the local lubrication and stress distribution in the surrounding tissue. It is difficult to study the local responses using traditional methods; *in-situ* microtribological methods are being pursued here as a means to elucidate the mechanical aspects of OA progression. While decades of research have been dedicated to the macrotribological properties of articular cartilage, the microscale response is unclear. An experimental study of healthy cartilage microtribology was undertaken to assess the physiological relevance of a microscale friction probe. Normal forces were on the order of 50 mN. Sliding speed varied from 0 to 5 mm/s, and two probes radii, 0.8 mm and 3.2 mm, were used in the study. *In-situ* measurements of the indentation depth into the cartilage enabled calculations of contact area, effective elastic modulus, elastic and fluid normal force contributions, and the interfacial friction coefficient. This work resulted in the following findings: 1) at high sliding speed ($V=1-5 \text{ mm/s}$), the friction coefficient was low ($\mu = 0.025$) and insensitive to probe radius (0.8 mm – 3.2 mm) despite the 4-fold difference in the resulting contact areas; 2) The contact area was a strong function of the probe radius and sliding speed; 3) the friction coefficient was proportional to contact area when sliding speed varied from 0.05 mm/s-5 mm/s; 4) the fluid load support was greater than 85% for all sliding conditions (0% fluid support when $V=0$) and was insensitive to both probe radius and sliding speed. The findings were consistent with the adhesive theory of friction; as speed increased, increased effective hardness reduced the area of solid-solid contact which subsequently reduced the friction force. Where the severity of the sliding conditions dominates the wear and degradation of typical engineering tribomaterials, the results suggest that joint motion is actually beneficial for maintaining low matrix stresses, low contact areas, and effective lubrication for the fluid-saturated porous cartilage tissue. Further, the results demonstrated effective pressurization and lubrication beneath single asperity microscale contacts. With carefully designed experimental conditions, local friction probes can facilitate more fundamental studies of cartilage lubrication, friction and wear, and potentially add important insights into the mechanical mechanisms of OA.

4:00pm **TR-WeA7 "Going No Wear?"**, *W.G. Sawyer*, University of Florida
INVITED

There is a need for the development of wear-resistant, low-friction materials, and understanding the fundamental origins of wear across length scales will be necessary to guide the development of such materials. The events at buried interfaces that lead to wear entail extreme variability in interaction strength, contact duration, and frequency of occurrence. It has been long postulated that the ensemble of these transient interactions at weak buried interfaces ultimately lead to the ever-present macroscopic phenomena of wear. The quest to find high performance solid lubrication solutions continues. Traditional solid lubrication techniques rely on a pre-deposited coating of a lubricous and/or a protective material, but since these materials wear during operation, the life of the system is finite. In order to

extend the operational life indefinitely and to potentially negate any mechanical contributions to wear, a stable lubricating tribofilm of sufficient chemistry and thickness must be maintained during operation. However, because sliding occurs in a buried interface, it has proven challenging to determine what materials processes are actively enabling stable performance and/or what to add to the system to improve lubrication. In this talk, results from a number of ultra-low wear systems (polymers, metals, and ceramics) that have been studied using a variety of active and *in situ* tribological instrumentation will be presented, along with a discussion of the various mechanisms that we believe to be responsible for this unique behavior.

5:00pm **TR-WeA10 Study on the Fatigue Wear Behaviour of TiN and WC DLC-coated Stainless Steel under Inclined Impact-Sliding Load Tests**, *Y. Chen, X. Nie*, University of Windsor, Canada

WC/C diamond-like carbon (DLC) coatings and Titanium Nitride (TiN) coatings are widely used in industrial machinery and tools. Both of the two coatings have extremely hard surfaces comparing to the stainless steel substrate SS316L. The W: DLC coating gives low coefficients of friction against a number of counterfaces, has relatively high lubricity and resistance to adhesive wear comparing to the TiN coating. In this study, a new method which is called cycled inclined impact-sliding test is introduced and utilized to study the coating durability under a combined force of an Impact force F_i and Pressing force F_p ($F_i/F_p=200N/400N$ and $200N/200N$) and the fatigue wear behaviors after up to 1000 cycles impact tests. A 10mm steel (AISI 52100) bearing ball is used as the impact indenter. Due to the low coefficient of friction of W:DLC coating against steel counterface, greater impact cycle was endurable before the failure of the coating when impacted in dry air condition. Under inclined impact and sliding forces, fatigue cracking was first initiated, followed by chipping and peeling of the coatings. The SEM showed that different types of fatigue wear cracks were found which distributed in the different areas (head and tail parts) of the impact scars. Most of those scars, observed by 45° tilted cross-sectional SEM, penetrated the coating and caused hardening of the under layer (interface layer). Material transfer from the indenter ball could also be detected by EDX in some areas of the impact scar on both of the coating materials.

5:20pm **TR-WeA11 Scaling Laws of Structural Lubricity for Amorphous and Crystalline Nanoparticles**, *D. Dietzel, T. Moeninghoff, M. Feldmann*, Westfaelische Wilhelms-Universitaet Muenster, Germany, *U.D. Schwarz*, Yale University, *A. Schirmeisen*, Justus-Liebig University Giessen, Germany

In an effort to reduce the friction between sliding components scientists and engineers have developed a multitude of lubrication schemes. One of the most intriguing concepts is referred to as 'structural lubricity', where flat surfaces are thought to slide past each other virtually frictionless if their atomic structures are incommensurate. In this talk, we analyze the fundamental mechanisms that govern the area-dependence of friction in extended but atomically flat contacts of dissimilar materials with a particular emphasize on the relation between structure (crystalline vs. amorphous) and friction. The resulting sublinear power laws, which link mesoscopic friction to atomic principles, are then confirmed by measuring the sliding resistance of gold and antimony particles on graphite [1,2]. The findings suggest that engineering surfaces with unprecedented low friction can be realized.

[1] A. Schirmeisen and U. D. Schwarz, ChemPhysChem 10 (2009) 2358

[2] D. Dietzel et al., Physical Review Letters 101 (2008) 125505

5:40pm **TR-WeA12 Auger Surface Analysis of Deposits Formed on Magnetic Tape Recording Head Surfaces**, *F.E. Spada*, University of California, San Diego, *D.F. Paul, J.S. Hammond*, Physical Electronics

The 2008 International Magnetic Tape Storage Roadmap¹ projects that the total magnetic spacing between the recording head and the tape magnetic layer must decrease from the current 43 nm spacing to about 23 nm by the year 2018 in order for tape to maintain its cost advantage as an information storage medium. Because tape drives are contact recording systems, interactions between head materials and components in the tape magnetic layer can detrimentally affect the head-tape separation via deposit formation on head surfaces as well as preferential erosion of critical recording head elements. Understanding the nature of these interactions is therefore essential for mitigating undesirable increases in the magnetic spacing. This study shows that deposition and erosion phenomena in tape heads can be varied *at the local level* by changing the electrical configuration of adjacent pole tip structures in multichannel heads, and that the composition of the head deposits depends on the electrical configuration of the pole tips. Using atomic force and electric force microscopy, we show that conductive deposits form on the "trailing edge" of pole tips which are electrically connected to earth ground or to the head substrate. The conductive deposits

become non-conductive further "downstream" from the pole tips. Deposits adjacent to electrically isolated poles are always non-conductive. Auger analysis shows that the surfaces of the conductive deposit regions contain high levels of Fe and Co, and small amounts of P and Y, whereas the surfaces of the non-conductive deposits contain predominantly P and Y, with very low levels of Fe. Because all of these elements are present in the magnetic coating of the tape, and because the compositions of the deposits on heads having NiFe pole tips is similar to those on heads having CoZrTa pole tips, these results suggest that the deposits originate from components in the tape and not from metallic structures in the tape head.

1. *International Magnetic Tape Roadmap*, Information Storage Industry Consortium, September, 2008.

*Supported by the Information Storage Industry Consortium Tape Program

Thursday Morning, November 3, 2011

Actinides and Rare Earths Focus Topic

Room: 207 - Session AC+SS-ThM

The Surface Science of Actinides and Rare Earths

Moderator: R. Schulze, Los Alamos National Laboratory

8:00am AC+SS-ThM1 **The XPS of Heavy Metal Oxides: New Insights Into Chemistry**, P.S. Bagus, University of North Texas, E.S. Ilton, Pacific Northwest National Laboratory, C.J. Nelin, Consultant **INVITED**

The XPS of Rare Earth and Actinide oxides are commonly used to obtain information about the oxidation state of the metal by taking various features of the spectra as fingerprints of the metal oxidation state. However, it is possible to obtain detailed information about the nature of the chemical interactions from these features by using the predictions of rigorous theoretical analyses. One of our important concerns is to make direct assessments of the covalent character of the metal-ligand interaction; i.e., the mixing of O(2p) with partly occupied, or unoccupied, metal levels to form bonding and anti-bonding orbitals. We relate this covalent character to the XPS features. In particular, we investigate the connection between the covalent character of the interaction and the satellite intensity. We also investigate the characterization of the satellites and discuss their assignment as shake satellites, an assignment that is naturally connected with the extent of the covalent mixing of the metal and oxygen levels. Furthermore, we examine how vibrational excitations can lead to broadening of the XPS features and suggest that the observed broadening of XPS peaks may contain, hitherto not utilized, information about the chemical interactions in an oxide. Our focus will be on the XPS of two Rare Earth oxides, CeO₂ and LaAlO₃, and two actinide oxides, UO₂ and UO₃; these systems have different electronic character that permit the mechanisms discussed above to be explored and compared. Our theoretical analyses are based on relativistic molecular orbital wavefunctions, WF's, for both initial states, before ionization, and final states, after ionization. The WF's are for materials models that contain explicit cations and anions embedded in a point charge field. With the variationally optimized orbitals for these WF, covalent mixing is naturally taken into account. The cluster WF's include one-body and many-body effects and do not use parameters that are adjusted to make calculated relative energies and intensities fit to experiment.

8:40am AC+SS-ThM3 **New Insights into the Oxidation/Corrosion of Plutonium**, D.L. Pugmire, H.G. Garcia Flores, D.P. Moore, A.L. Broach, Los Alamos National Laboratory, P. Roussel, Atomic Weapons Establishment, UK **INVITED**

An understanding of the oxidation and corrosion processes of plutonium metal at room temperature is important to the safe, effective use and storage of this reactive metal. The oxidation rate for the δ -phase stabilized, plutonium/gallium alloy (a commonly employed alloy) can be significantly affected by a number of parameters including the gallium content and the composition of the oxidizing atmosphere (O₂, O₂/H₂O, H₂O). The nature of plutonium oxidation has typically been thought of as the growth of a dioxide (PuO₂) overlayer on the metal to a thickness at which the film begins to spallate (μ 's). Based on thermodynamic arguments, it has been pointed out that a relatively thin layer of the sesquioxide (Pu₂O₃) should exist at the dioxide/metal interface for thick oxide films.

Historically, the oxidation/corrosion of plutonium has been studied by oxygen uptake of samples at elevated temperatures inferred from mass gain measurements. Accuracy of these experimental setups likely limited measurements to oxide films thicker than ~0.05 to 0.1 μ (50 - 100 nm). This is at the upper-limit of the thicknesses typically observed for plutonium oxide films. Little work has been published for studies of plutonium oxide thin-films (< 50 nm) on metal substrates. Additionally, very little is known about the role that gallium plays during the oxidation of the alloy other than it can significantly slow the rate.

We report here our studies of the initial stages of plutonium oxidation with O₂ in the thin-film regime with x-ray photoelectron spectroscopy (XPS) and Auger electron spectroscopy (AES). The results indicate that not only does a Pu₂O₃ layer exist in thin plutonium oxide films, but that the sesquioxide exists as a substoichiometric species on a metal substrate, and is probably best described as Pu₂O_{3-y}. It also appears that the oxide thin-film is comprised mainly of the sesquioxide species, with PuO₂ accounting only for a relatively thin portion of the overall oxide film thickness. While the surface sensitive techniques employed here suffer from relatively high limits of detection, we have also been able to qualitatively, and in some cases quantitatively, study the behavior of gallium during the oxidation of the δ -plutonium alloy. The gallium content relative to plutonium is observed to decrease within the oxide film during oxidation, with the

displaced gallium moving to the oxide/metal interface to form a thin gallium rich region. These new results will be compared and contrasted with existing literature. Additionally, how these results have altered our understanding of the Pu/O thin-film system and the oxidation/corrosion of plutonium will be discussed.

9:20am AC+SS-ThM5 **The Oxidation of Uranium Dioxide at High Pressures in Pure Oxygen**, J.C. Crowhurst, Z. Dai, J.M. Zaig, K.B. Knight, A.J. Nelson, W.J. Siekhaus, I.D. Hutcheon, Lawrence Livermore National Laboratory

The oxidation of uranium dioxide has received much experimental and theoretical attention over the last several decades in large part because of its relevance to the operation and storage of uranium-based nuclear fuel. The oxidation process is inherently complicated, involving the formation of multiple different phases via distinct mechanisms even at relatively low temperatures. In the range of a few hundred degrees centigrade oxidation is generally assumed to be a two step process[1]: UO₂ \rightarrow U₃O₇/U₄O₉ \rightarrow U₃O₈. At low pressures the intermediate phases adopt crystal structures that are modifications of the UO₂ fluorite structure and are slightly denser. By contrast, U₃O₈ forms a considerably less dense orthorhombic structure (by some 23%). The large volume expansion resulting from the oxidation of UO₂ to U₃O₈ is a potentially serious concern in the event of oxidation of a fuel element, with consequent splitting of protective sheaths and the spalling of powder.

While attention has been focused on the oxidation of UO₂ at elevated temperatures, the associated experiments have all been performed at low partial pressures of oxygen. It is unclear how pressure affects the oxidation process – particularly in the context of the formation of U₃O₈, with its large volume change with respect to UO₂. We have examined the oxidation of a nominal single crystal of UO₂ in pure oxygen at elevated pressures up to approximately 0.9 GPa (9000 atm) and temperatures of up to 450 °C. In-situ Raman scattering measurements were made as a function of temperature in order to monitor the oxidation. Recovered material was examined using electron based techniques including SEM, TEM, and electron diffraction and also using x-ray photoelectron spectroscopy.

Material synthesized under high pressure has a Raman spectrum that is different from both the UO₂ starting material and the common form of U₃O₈. Also, compared with common U₃O₈, we find that it has fewer crystalline defects and mostly adopts a hexagonal rather than orthorhombic form. Figure 1 of the supplemental document compares Raman spectra of UO₂ in oxygen with synthesized material. Fig. 2 compares electron diffraction obtained from recovered material with U₃O₈ synthesized at ambient pressure.

Lawrence Livermore National Laboratory is operated by Lawrence Livermore National Security, LLC, for the U.S. Department of Energy, National Nuclear Security Administration under Contract DE-AC52-07NA27344. This work is funded by Laboratory Directed Research and Development (LDRD) Program (10-SI-016) of Lawrence Livermore National Laboratory.

[1] R. J. McEachern and P. Taylor, *JNM*, **254**, 87, (1998).

9:40am AC+SS-ThM6 **Radiation Effects on Hydrogen Reactivity in Narrow Uranium-Uranium and Uranium-LiD (or Air) Gaps using MCNPX Code**, M.A. Schildbach, W.J. Siekhaus, Lawrence Livermore National Laboratory

Preferential uranium hydriding occurs frequently in narrow gaps. There are different hypotheses about its causes, one of which could be radiation-induced chemistry in gaps. Both ²³⁸U and ²³⁵U generate ionizing α , β , and γ radiation capable of vibrationally or translationally exciting, ionizing, or dissociating H₂, all of which increase the reactivity of H₂ with uranium. Dissociation of H₂ is necessary to initiate hydriding, and it has been shown that the sticking coefficient of H atom is about 1200 times higher than H₂'s[1]. Here we use the MCNPX radiation transport code to calculate the energy dependent electron flux generated from the ^{234m}Pa β decay and from photoelectrons generated by brems-strahlung. We apply the code to gaps occurring in two ²³⁸U cylindrical pieces welded together and filled on the inside with LiD with a 100 μ m gap between ²³⁸U and LiD, and having a 100 μ m gap in ²³⁸U itself, typical for step-joint-welded uranium shells.

The MCNPX Monte Carlo Code - as configured now - tracks the life cycle of electrons throughout the material and calculates the electron flux as a function of energy, putting results into "energy bins" 1 keV wide. We find that at 2 keV (\pm 5 keV, the last energy bin) the calculated electron flux in the U-U gap is approximately 19 times larger than in the U-LiD gap, and fifty two times larger than in the U-air gap on the outside of the cylindrical

shells. Cross-sections for electron-hydrogen collisions peak, however, below 1 keV energy. We establish the upper limit of the effect of electron-hydrogen collisions by extrapolating the MCNPX electron flux results from the last bin to energies as low as 1 eV by fitting a function to the flux between 2 and 20 keV. To calculate the fraction of H₂ vibrationally or translationally excited, ionized, or dissociated per cm²/s, we integrate the product of the energy dependent cross sections (listed in reference [2]) and the energy dependent electron flux over the relevant energy range. The fraction of H₂ molecules calculated to be dissociated is small, but significant during long-time exposure. Future work will extend the MCNPX code below 1keV (as is done for biological radiation damage), to avoid energy extrapolation.

This work performed under the auspices of the U.S. Department of Energy by Lawrence Livermore National Laboratory under Contract DE-AC52-07NA27344.

References

1. Balooch M, Hamza AV. "Hydrogen and water vapor adsorption on and reaction with uranium." *Journal of Nuclear Materials*, **230**, 3, 259-270, 1996.
2. Yoon JS et al., "Cross sections for electron collisions with hydrogen molecules." *Journal of Physical and Chemical Reference Data*, **37**, 2, 913-931, 2008.

10:40am **AC+SS-ThM9 Study of the Gd₅Ge₄ (010) Surface**, *C. Yuen, G. Miller, P.A. Thiel*, Ames Laboratory - US DOE

Certain intermetallics of Gd, Ge, and Si exhibit giant magnetocaloric effects, yet very little is known about their surfaces. We have investigated one such system, Gd₅Ge₄, with the goal of elucidating its clean and oxidized surface structure, using STM and XPS. The clean Gd₅Ge₄ (010) surface exhibits a step-terrace morphology after repetitive sputtering and annealing at 900 K. Step heights are equal to half the bulk unit cell length in the <010> direction, consistent with the existence of an equivalent plane in the middle of the unit cell. Surface compositions of Gd and Ge are close to the bulk composition. However, at higher temperatures—between 900 K and 1200 K—the surface becomes Gd poor by 10 at.%. In STM, at these temperatures, the fine structure on the terraces changes, and a different type of terrace with a different step height emerges. We propose that the preferred surface termination is rich in Gd (which has lower surface energy than Ge), and that this termination is exposed after annealing at 900 K. At higher temperature, we propose that Gd (which has higher vapor pressure than Ge) evaporates preferentially, leading to the changes described above and exposing a Ge-rich surface termination. Finally, we find that Gd oxidizes preferentially.

11:00am **AC+SS-ThM10 Using Spatially Controlled Thin-Films Coatings Around Rare-Earth doped Nanophosphors for High Efficiency Energy Applications**, *J.A. Dorman, A. Joshi, G. Kuzmanich, J.H. Choi, J.P. Chang*, University of California Los Angeles

The development of rare-earth (RE) doped phosphors allows for the conversion of photons to energies that are more usable for the desired application. Additionally, these RE phosphors have long lifetimes, on the order of ms, which offer potential in many energy conversion and energy transfer devices. Currently, RE phosphors are used in fiber optics amplifiers, broad absorption solar cells and various other lighting applications. Energy transfer mechanisms of the excited RE states, such as defect quenching and sensitizer/emitter interactions, must be understood in order to achieve high efficiency energy conversion and propagation.

In order to increase the efficiency of solar cells, high efficiency phosphors need to synthesize in order to convert photons at the edge of the absorption band into higher energy photons while avoiding undesired quenching effects. In effort to produce these high efficiency phosphors, spatially controlled RE doped thin films are deposited around nanoparticles (NP) to produce a core-shell nanophosphor. Reduction in luminescent quenching can be achieved by increasing the distance between the surface quenching site and active ions through the deposition of a precisely controlled thin film around the NP. Secondly, the luminescent fingerprint can be further controlled through doping of the shell structure by increasing the absorption spectrum or the introduction of emission peaks. Deposition of a thin film around an Y₂O₃:Er³⁺ core NP is achieved via atomic layer deposition or sol-gel synthesis to compare the effect of a spatially controlled vs. a random dopant distribution. Primarily, this work focuses on the emission of visible photons through upconversion, making them ideal components in broad absorption solar cells. By spatially controlling the position and concentration of the RE ions within the nanostructure, increased luminescence is observed due to energy transfer between the dopant ions within a critical interatomic distance. Passivation of surface sites with increasing film thickness was shown to increase luminescent lifetimes up to 53%, with a critical shell thickness of 8 nm, while lowering the theoretical lifetimes extracted from Judd-Ofelt parameters. The effect of the spatially

controlled Yb ions was probed through the extraction of the upconversion photon requirement, showing a statistical decrease in photons from 2.16 to 1.43, or ~30 %. Finally, the effective energy transfer distance and energy transfer coefficients were studied as a spacer layer is added to the system, showing energy transfer up to ~3 nm, confirming the Förster-Dexter theory.

11:20am **AC+SS-ThM11 Growth and Characterization of Scandia Stabilized Zirconia and Samaria Doped Ceria Multi-Layer Thin Films**, *S. Thevuthasan*, Pacific Northwest National Laboratory, *M.I. Nandasiri*, Western Michigan University, *T. Varga, V. Shuthanandan, S.P. Sanghavi, S.V.N.T. Kuchibhatla*, Pacific Northwest National Laboratory, *A. Kayani*, Western Michigan University

Recent studies showed a colossal enhancement in the ionic conductivity of multi-layer oxygen-ion conducting thin films compared to most commonly used solid oxide fuel cell (SOFC) electrolytes. It has been observed that, the oxygen ionic conductivity of nano-scale hetero-structures increases with the increase in number of layers. However, some of these findings were questioned due to the inability to distinguish electronic and ionic conductivity. Thus, here we investigated the scandia stabilized zirconia and samaria doped ceria (SDC/ScSZ) multi-layer system to understand the oxygen-ion conductance in multi-layer hetero-structures.

In this study, the growth of SDC and ScSZ multi-layer thin films was carried out using the optimized growth conditions, dopant concentrations and film properties established for single-layer SDC and ScSZ epitaxial thin films. The epitaxial SDC and ScSZ multi-layer thin films were grown on Al₂O₃(0001) substrates by oxygen plasma-assisted molecular beam epitaxy (OPA-MBE) at 650°C. The number of layers in the multi-layer hetero-structures was varied from 2 to 20 by keeping the total film thickness constant at 140 nm. Following the growth, thin films were characterized by various in-situ and ex-situ characterization techniques including reflection high energy electron diffraction (RHEED), x-ray diffraction (XRD), Rutherford backscattering spectrometry (RBS), and x-ray photoelectron spectroscopy (XPS). The initial streaky RHEED pattern indicates the epitaxial growth of SDC/ScSZ multi-layer thin films. Furthermore, RHEED patterns indicate the transition of the initial smooth surface to a rough surface with the increase in number of layers. The individual layer thickness was found to be approximately 7 nm for the twenty-layer film as confirmed by x-ray reflectivity data. RBS was also used to find the composition and thickness of the films. HRXRD patterns of ScSZ/SDC thin films exhibit only CeO₂(111) and ZrO₂(111) reflections, indicating the growth of epitaxial SDC(111) and ScSZ(111) multi-layers. XPS depth profile confirmed the uniform dopant concentration in both SDC and ScSZ layers, which was found to be 7 and 6 atom % for Sc and Sm, respectively. In the near future, the ionic conductivity of SDC and ScSZ multi-layer thin films will be measured by four probe conductivity method.

Applied Surface Science Division

Room: 102 - Session AS-ThM

Analysis of Insulators and Challenging Samples

Moderator: D.J. Gaspar, Pacific Northwest National Laboratory

8:00am **AS-ThM1 Imaging and Differentiation of Epicuticular Waxes on *Arabidopsis thaliana* Organs by TOF-SIMS**, *G.L. Fisher*, Physical Electronics, *P. Wong, C. Buschhaus, R. Jetter*, University of British Columbia, Canada

TOF-SIMS has emerged as an important tool for imaging mass spectrometry of biological samples due to its unique capability to detect molecular ion fragments and elemental ions at sub-micron spatial resolution and without the sample treatments required by e.g. the MALDI technique. For many biological specimens, the ability to image samples having a large degree of surface topography is also highly desired. The resulting elemental and molecular images provide important information regarding the composition of biointerfaces, for example between plant tissues and their natural environment. This TOF-SIMS study involves the differentiation and characterization of epicuticular waxes present at the surfaces of *Arabidopsis thaliana* organs including the flower, stem, adaxial (top) leaf surface and the abaxial (bottom) leaf surface.

High spatial resolution images obtained from a flower petal, an adaxial leaf surface, and an abaxial leaf surface revealing spores, trichomes and respiratory pores, respectively, demonstrate the capability of TOF-SIMS to image molecular ion fragments with a spatial resolution of < 0.3 microns. Total ion images, and molecular fragment ion images of epicuticular wax components, demonstrate the capability to image entire organ surfaces without topographical artifacts. High mass range spectra in both the positive

and negative secondary ion polarities reveal that the epicuticular surface of each *Arabidopsis thaliana* organ is comprised of distinct wax components. Mass spectra acquired from specialized cells forming the 1 μm x 7 μm respiratory pores of the abaxial leaf surface indicate that, even within a single organ surface, the epicuticular wax composition may vary. The differences in wax composition on each of the interrogated organs of *Arabidopsis thaliana* will be presented and discussed. Structural assignments for characteristic mass spectrometric features related to the wax composition will also be presented and discussed.

8:20am **AS-ThM2 Aqueous SIMS – Towards in Situ Detection of Chemical Reaction Intermediates in Aqueous Solutions**, *Z. Zhu, L. Yang, X. Yu, M.J. Iedema, J.P. Cowin*, Pacific Northwest National Laboratory

This research provides the first in-situ detection of aqueous surfaces using time-of-flight secondary ion mass spectrometry (ToF-SIMS). ToF-SIMS provides a molecular recognition capability with super-low detection limits, making it a great choice to detect short-lifetime chemical reaction intermediates in aqueous solutions. However, it is difficult to detect aqueous solutions by ToF-SIMS because ToF-SIMS is a high vacuum technique, and the vapor pressure of water is about 2-3 kPa at room temperature. We designed and fabricated a self-contained microfluidic module, allowing in-situ analysis of aqueous surfaces by ToF-SIMS. Microfluidic channels were prepared on top of a block of polydimethylsiloxane (PDMS) using a patterned silicon template with soft lithography techniques, and then a \sim 100nm thick silicon nitride film was placed on top of the microfluidic channels, on which a small hole with a diameter of \sim 2-3 microns could be drilled using a focused primary ion beam in a ToF-SIMS instrument. De-ionized water, heavy water, a 0.5% (weight ratio) formic acid aqueous solution, a 0.5% glycerol aqueous solution, and a 0.5% glutamic acid aqueous solution were successfully analyzed through the small hole using our ToF-SIMS instrument (IONTOF-V). The pressure in the analysis chamber was usually at \sim 5E-7 mbar during measurements, and this value was sufficient for ToF-SIMS analysis. Our device could be safely staying in vacuum for more than 8 hours, and 1 hour continuous SIMS measurements were practical. Molecular signals (M-H⁺) from formic acid (HCO₂⁻), glycerol (C₃H₇O₃⁻), and glutamic acid (C₃H₈NO₄⁻) were clearly observed in the small hole, but not elsewhere. Based on current data, the detection limits of formic acid, glycerol, and glutamic acid were estimated to be $<0.01\%$ (weight ratio).

8:40am **AS-ThM3 Challenges of the XPS Analysis of the Ionic Liquid [BMIM][PF₆]**, *R.R. Harl, B.D. Booth, G.K. Jennings, B.R. Rogers*, Vanderbilt University

Room temperature ionic liquids (ILs) are ionic compounds that are liquids at ambient conditions due to a bulky, asymmetric organic ion that inhibits crystalline packing. The inhibition of crystalline packing results in ILs having a vapor pressure that is negligibly low. The properties of ILs make them candidates for applications such as nonvolatile solvents, electrolytes, and lubricants. The ionic liquid pair 1-butyl-3-methylimidazolium hexafluorophosphate [BMIM][PF₆] is being investigated for use as a lubricant in micro-electrical mechanical systems (MEMS). Surface properties are important in tribological applications like lubrication and the negligible vapor pressure of the [BMIM][PF₆] ionic liquid makes it compatible with traditional surface analysis tools like x-ray photoelectron spectroscopy (XPS).

XPS analysis of ILs is challenging due to the ability of the ionic molecules within the ILs to freely move within the sample. Also, since the ILs are comprised of charged molecules, the motion of the molecules and their relative position within the sample may be affected by changes in surface charging brought about by photoelectron emission or by the electron and ion beams used to neutralize surface charging.

We will present results of our XPS analyses of [BMIM][PF₆] ionic liquid drop-cast onto a silicon substrate. We dropped enough of the IL to form an approximately 150 nm thick film to mimic a film that would be used for lubricating a MEMS device. However, the IL drop-cast in this manner did not form a continuous film, but rather beaded up on the silicon substrate. Under certain analysis conditions we can force the IL droplets to coalesce into a continuous film.

Preliminary results show that when the surface is positively charged the PF₆ molecule segregates to the liquid/vacuum interface. This observation is consistent with previous studies. When the IL surface is negatively charged the C1s peak shape changes from that indicative of the imidazole ring C-N bonding to that indicative of C-C bonding, most likely from the butyl chains of the BMIM molecules. This change in the C1s spectrum suggests the BMIM molecules are segregating to the liquid/vacuum interface. A corresponding drop in the F1s peak intensity suggests that the PF₆ molecules are moving deeper into the sample.

Along with the XPS results we will propose a mechanism by which the charge and/or energy provided by the x-ray, electron and ion beams induce the change from dispersed droplets to a continuous film. We will also provide insight into how these results could be used in developing or using ILs for MEMS lubricants.

9:00am **AS-ThM4 Working with Difficult Samples - Preparation, Damage, Charging and Data Analysis**, *D.R. Baer, M.H. Engelhard, A.S. Lea, P. Nachimuthu, Z. Zhu*, Pacific Northwest National Laboratory
INVITED

X-ray Photoelectron Spectroscopy (XPS) and other surface analysis methods (e.g. AES and SIMS) are playing increasingly important roles in the analysis of many materials ranging from ancient artifacts, geological minerals and even biological specimens to modern very complex nanostructured materials. Samples that need to be analyzed can be made up of components with a wide variety of physical and chemical properties that impact how they can be handled, prepared, mounted and analyzed without destroying the information that is sought from the analysis. During this presentation a variety of the methods and approaches needed to characterize a range of sample and analysis challenges that we have faced in the EMSL, a US Department of Energy user facility, will be discussed. Analysis challenges discussed will include: inexperienced users and their expectations; sample handling, preparation (including extraction of particles from aqueous solution) and mounting (including anaerobic transfer and freezing); identifying and dealing with damage; identifying and controlling impacts of charging (which are not always obvious); and analysis approaches used to extract information about the nanostructure of complex materials. The materials and materials systems to be discussed will include the impact of processing on catalyst surface composition and chemistry, the oxidation state of species adsorbed on mineral surfaces, the nature and properties of organic layers on inorganic substrates, and the nature of the surfaces and intentional as well as inadvertent coatings (shells) on nanoparticles. Some of the methodology and special capabilities developed in EMSL for controlling sample environments, the value of more rapid and enhanced data analysis, and the importance of procedural guides and standards will be noted. Although many of the topics discussed relate to a variety of surface analysis and other methods, the talk will focus on XPS and use TOF-SIMS to provide an example of challenges associated with measurement of hydrogen. The importance of complementary measurements by a variety of methods (including XRD, TEM, APT, SEM and RBS) will be highlighted.

Aspects of the work have been supported by the Offices of Basic Energy Sciences and Biological and Environmental Research of the US DOE and by the National Institute of Environmental Health Science under grant NIH U19 ES019544. Portions of this work were conducted in the Environmental Molecular Sciences Laboratory (EMSL), a DOE user facility operated by Pacific Northwest National Laboratory for the Office of Biological and Environmental Research of the DOE.

10:40am **AS-ThM9 Transient Electron Emission from Insulators under Pulsed Electron Beam Injection**, *Y. Kimura, H. Koyama, H. Makino, H. Shinada, Hitachi, Ltd., Japan, Y. Mochizuki, H. Kazumi, Hitachi High-Technologies Corp., Japan*

Electron emissions from poorly conductive specimen stimulated by photon and electron injections result in charging phenomena. These can cause distortion of data in electron spectroscopy and image artifacts in scanning electron microscopy because surface potential which influence the motion of emitted electron is modified by charging and change time dependently. Therefore, time dependence of electron emission yields are important for understanding of radiation induced charging of resistive materials.

In this study, we present the transient characteristics of electron emission from SiO₂ using a new experimental facility (Pulsed Electron Microscope: PULSEM) built in the present work. Main feature of the PULSEM, as with electron beam testing system, is a beam blanking system attached below the condenser lens. The beam blanking pulses electron beam into the minimum number of 6 electrons under the condition of primary beam current $I_p = 20$ pA and beam-pulse-width $t_p = 50$ ns. The Everhart-Thornley detector with high response scintillator, afterglow time of which is 0.5 ns, and with a photomultiplier is synchronized to the beam blanking system. Transient SE signal as a function of the number of injected electrons is obtained.

Time-dependent electron emission yield (σ) with the resolution of 30 ns is investigated as a function of the primary electron dose which is controlled by pulse duration (Δt) as well as primary energy (E_p). Quasi static emission yield, which assumed to be intrinsic electron emission in the absence of charging, is obtained under low dose condition of below 60 electrons with $I_p = 20$ pA and $\Delta t = 500$ ns. The maximum yield (σ_m) and its corresponding energy (E_m) are 2.5 and 300 eV, respectively. With the increase in electron dose, σ approaches unity due to a charging effect. Finally, we will present

total electron emission yield curves in the range of $E_p < 6$ keV and 50 ns < $\Delta t < 500$ ms.

11:00am **AS-ThM10 High Resolution XPS Chemical State Imaging of Fuel Cell Membranes**, S.N. Raman, P.E. Larson, J. Moulder, J.S. Hammond, S. Alnabulsi, Physical Electronics USA

Nafion based membranes are being developed for applications in fuel cells. These fuel cell membranes are multi-layer structures with a permeation membrane and two thin layers of noble metal in a polymer matrix acting as the anode and the cathode of the fuel cell. The cross-sectional chemical analysis of these membranes, both new and used, may be extremely useful in improving the performance of the fuel cells. In this study we will highlight new and advanced scanning XPS microprobe based techniques to provide cross-sectional line scans and high resolution chemical mapping of these membranes. The line scan and chemical mapping results elucidate the modifications of the membrane chemistry as a function of use.

11:20am **AS-ThM11 Gas-Cluster Ion Beam Secondary Ion Mass Spectrometry Characterization of Thin Films for Organic Electronics Applications**, D.J. Gaspar, Pacific Northwest National Laboratory, S.R. Bryan, Physical Electronics USA, T. Miyayama, ULVAC-PHI, Japan, A.B. Padmaperuma, J.S. Swensen, E. Polikarpov, Pacific Northwest National Laboratory

Organic light emitting devices (OLEDs) have the potential to dramatically change the way we light our living spaces. OLEDs offer the potential for high efficiency lighting from a large area source, with the possibility of transparent and flexible lighting as well. Currently, OLED displays are found commercially in cell phones and in televisions in limited production. One of the key barriers holding back widespread adoption of OLEDs for both lighting and other products is the challenge of generating long-lived devices, particularly for high-efficiency phosphorescent blue OLEDs (a necessary component of high-efficiency white OLEDs). Challenges in the design of stable materials are hampered by our relatively poor ability to measure degradation products in situ, or in ways that ensure we have not damaged the material in the measurement process. To this end, we have generated thin films of single blue phosphorescent OLED components, multilayer films, and working OLEDs before and after aging. These components including the well-studied bis[2-(4,6-difluorophenyl)pyridyl-N,C2']iridium (III) (FIrpic), 2,8-bis(diphenylphosphoryl)dibenzothiophene (PO15), 4-(diphenylphosphoryl)-N,N-diphenylaniline (HM-A1) and di-[4-(N,N-ditolyl-amino)-phenyl]cyclohexane (TAPC). Based on previous experiments in our lab and literature reports, FIrpic and PO15 are known to undergo degradation reactions under conditions similar to those used in this series of experiments. Analysis of these films and systems by gas cluster ion beam secondary ion mass spectrometry (GCIB-SIMS) and other methods show degradation products, which permit the development of useful models for their degradation pathways. These results clearly demonstrate the utility of GCIB-SIMS in the characterization and analysis of OLED devices and materials, and should enable better design and screening of stable materials for high-efficiency OLEDs.

Biomaterial Interfaces Division

Room: 108 - Session BI-ThM

Biomedical Materials

Moderator: S.L. McArthur, Swinburne University of Technology, Australia

8:20am **BI-ThM2 Surface Characterization: A Critical Component in Understanding the Biocompatibility of Biomaterials**, L. Salvati, S. Vass, DePuy Orthopaedics **INVITED**

A biomaterial is defined as "any synthetic material or device—e.g. implant or prosthesis-intended to treat, enhance or replace an aging or malfunctioning native tissue, organ or function in the body" David Williams, states that "*Biocompatibility is largely about the chemical interactions that take place between the materials and the body fluids, and the physiological responses to these reactions.*" These reactions are dominated by the initial events at the molecular level, the interface, thus it is not hard to see the relationship between the implant surface properties and it's in vivo. It is clear that the performance of a biomaterial is directly linked to the surface chemistry, composition and topography of the device. However, despite the preponderance of evidence, biomedical device companies as a whole do not utilize surface analytical methods nearly enough. Why is that?

In orthopaedics, most of the implants are fabricated from metals which directly contact biological fluids that are typically complex aqueous mixtures. Consequently corrosion and/or corrosion prevention are important

considerations in device manufacturing. For the most part, orthopaedics manufacturers utilize the same passivation methodologies used to impart corrosion resistance to stainless materials. Numerous researchers have characterized the impact of acid passivation on stainless materials, but little has been done to study the effect of these treatments on the CoCr alloys. One of the topics in this presentation deals with the effects of passivation on CoCr alloys. Specifically, the presentation will correlate specific surface treatments with surface chemistry and ultimately to metal ion release. The study will also address questions relating to the use of Citric acid as a green replacement for nitric acid passivation. There is no argument that the process is much greener, but there are plenty of questions as to its effectiveness. Considering that the "changes" imparted by the passivation solutions effect the outer most 10-100Å, the only means to characterize the affects of passivation requires surface analysis methodologies. The importance of surface analysis methods, especially XPS, will be highlighted by this example.

In addition to the discussion of metal alloy passivation, this presentation will also deal with other surface related issues that could impact the biocompatibility of biomaterials. The talk will show the potential impact of packaging materials and cleaning processes on the surface chemistry and composition of biomaterials.

9:00am **BI-ThM4 XPS Sputter Depth Profiling of Organic Materials Using a Coronene Ion Source**, S.J. Hutton, C.J. Blomfield, A.J. Roberts, S.C. Page, S.J. Coultas, Kratos Analytical Ltd, UK, C.E. Moffitt, D.J. Surman, Kratos Analytical Inc

Controlled release of active pharmaceutical molecules from biocompatible polymers over defined time periods is an area of intense study. Present applications include drug eluting stents and other drug delivery systems. One of the most important parameters which govern drug dosing is the drug concentration depth profile in the supporting polymer matrix. In a previous study we have shown that combining X-ray photoelectron spectroscopy (XPS) with a coronene ion source is a very powerful tool for investigating the drug distribution with depth of a model system [1].

The use of cluster ion sources for sputter depth profiling of thin film or multilayer organic materials during XPS analysis has become routine. A wide range of organic systems are amenable to profiling and there is a good understanding of the experimental parameters which contribute to successful analysis. Here we report on extending the aforementioned study to materials which closely resemble real world samples intended for use in vivo.

[1] A. Rafati, M.C. Davies, A.G. Shard, S. Hutton, G. Mishra, M.R. Alexander, *J. Controlled Release*, **2009**, *138*, 40–44

9:40am **BI-ThM6 Amino-rich Plasma Polymer Films Prepared by RF Magnetron Sputtering**, J. Hanuš, G. Ceccone, F.J. Rossi, European Commission, JRC. Institute for Health and Consumer Protection, Italy

RF magnetron sputtering of nylon 6.6 was used for the deposition of nitrogen rich films. Deposition was followed by N₂ H₂ plasma post-treatment to enhance primary amine concentration on the surface. Maximal reached NH₂ concentration was 11 % with aminoselectivity 13.5 %. The films exhibited small negative z-potential at basic pH with isoelectric point ~ pH 4.5. Bio properties of the films were tested by QCM in terms of ability to adsorb different proteins and their antigens. The interaction between the film and the buffer solution was also studied and compared to other films such as poly-acrylic acid and PEO plasma polymers. The results show that these films are stable and can be used as a platform where positively charged surfaces are needed

10:40am **BI-ThM9 Surface Analysis in Biotech & Pharma: A Surfeit of Frontiers**, E. Johnston, Genzyme **INVITED**

Surface and interfacial analytical tools continue to provide new value and find unexpected new uses in the biotech and medical device industries. Some uses are investigational in nature and help solve critical problems within manufacturing and quality control. Other applications fall squarely within the realm of R&D - tilting the balance between feasibility of a product or obsolescence of a project, or providing fresh insight into the nature of biomaterial/biological interactions. By way of example, a study will be presented illustrating how TOF-SIMS was used to image a phosphate-binding drug particle in the complex matrix of the rat gastrointestinal tract. Sample preparation was challenging due to the highly hydrated nature of the tissue material. The results yielded surprising information about the ions that bind to this cationically charged particle and opened new avenues for inquiry and study.

11:20am **BI-ThM11 Enhancing Monoclonal Antibody Drug Detection by Developing a Microparticle-based Immunoassay**, *N. Mendez, M.E. Ruidiaz, A.B. Sanchez, B.T. Messmer, A.C. Kummel*, University of California San Diego

Monoclonal antibodies are a notable and rising class of cancer therapeutics due to their enhanced targeting and immune system stimulation properties. Dosage guidelines are typically developed with many uncertainties which may affect treatment outcome and cause unwanted side effects. The requirement for an assay that can quickly and precisely measure the concentration of the monoclonal antibody in a serum sample of a patient during therapy is needed. The present study has demonstrated that the key to detection is compensation for variation in non-specific binding of serum to the assay surface. A microparticle-based assay with peptide antigen mimetics has been developed to rapidly determine the concentration of antibody drug present in serum specimens with high sensitivity. Alemtuzumab (anti-CD52) and rituximab (anti-CD20) antigen peptides, as discovered by phage display, were synthesized on 10 µm TentaGel resin beads using conventional solid phase peptide synthesis techniques. The microparticle beads were modified to allow for multiplexing and microfluidic handling via fluorescent labeling and magnetic functionalization. The antigen-displaying fluoromagnetic particles were incubated with spiked serum samples which allowed free antibody to be captured. Primary antibody detection was performed on alemtuzumab while rituximab detection was used to compensate for non-specific serum binding to the beads. After washing, the beads were incubated with a fluorescently tagged secondary antibody for detection by flow cytometry. Serum from thirty (30) individual donors with various spiked serum concentrations of antibody drug were assessed using this assay. Analysis of bead fluorescence data allows for a limit of quantitation down to 0.5 µg/ml of serum antibody drug concentration. Using detection of an antibody known to be absent in serum, an accurate compensation technique for non-specific binding has been developed on multifunctional antibody assay beads in realistic samples. The developed assay is robust against donor serum variation.

11:40am **BI-ThM12 Controlling the Hydroaffinity of Silicone/Hydrophobic Acrylic Surfaces of Intraocular Lenses using Visco-Elastic Colloids and Blood Proteins**, *N.X. Herbots, ASU / SiO2 NanoTech Inc. / SiO2 Associates, LLC, R.J. Culbertson, Q.X. Bradley, D.A. Sell, A.M. Murphy, Arizona State U., C.H. Sell, Arizona Vitro-Retinal Consultants, H.M. Kwong, Arizona Vitro-Retinal Consultants / ASU, T. Kutz, A.S. Benitez, M.A. Hart, B.J. Wilkens, R.B. Bennett-Kennett, Arizona State U.*

Over 15 million cataract surgeries are performed each year world wide. 2-6 % of cataract patients suffer subsequently from diabetic and other retinal issues post surgery due to aging and accidents and must undergo a secondary eye surgery. Secondary surgery performed after implantation of artificial intra-ocular lenses (IOLs) can fail due to the fogging of IOL's from condensation of bodily fluids. New, high performance accommodating silicone and hydrophobic acrylic IOL's can fog during such surgery. This work solves the problem by modifying water affinity of IOL's using a polymer emulsion, VitreOx™ [1-5] with a 100% success rate in the lab. Ten clinical trials yielded a success rate of 80% in the year 2010-211 with failure inferred to be due to blood proteins on IOL's.

Thus, the role of hydro-affinity of blood proteins preventing coagulation, heparin, present during surgery, has to be investigated. Our results show that heparin behaves identically to H₂O on hydrophobic surfaces. Heparin simply de-wets on silicone IOL's and hydrophobic acrylic lenses. It does not prevent fogging on IOL's nor interfere with our anti-fogging emulsion.

Fibrinogen is the other protein investigated because it enhances blood coagulation and is often present in trauma situations. Fibrinogen applied to IOL's in various dilutions does prevent fogging. However, it cannot be removed after application on the IOL's, thus remaining as a potent coagulant agent in the eye. Thus fibrinogen can indeed prevent fogging, but is not viable since it cannot be removed after application like VitreOx™. Fibrinogen could explain why some IOL's fog while others do not during emergency secondary eye surgery.

[1] U. S. Patent Application "Molecular Films for Hydrophobic Implant Surfaces" N. Herbots, J. D. Bradley, M.A. Hart, D.A. Sell, S. D. Whaley, Q. Xing Bradley Filed 11/9/10

[2] "Modeling Mechanisms of Water Affinity & Condensation on Si-based Surfaces via Experiments & Applications" by Q. Xing, ASU (2011).

[3] N. Herbots, Q. Xing, M. Hart, J. D. Bradley, D. A. Sell, R. J. Culbertson, B. J. Wilkens; "IBMM of OH Adsorbates and Interphases on Si-based Materials" Nucl. Instr. & Meth. B, IBMM 17 (2010), accepted.

[4] Q. Xing, M. A. Hart, R. J. Culbertson, J. D. Bradley, N. Herbots, B. J. Wilkens, D. A. Sell, C. F. Watson, "Particle-Induced X-ray Emission of Silicate Coatings on High Impact Resistance Polycarbonates". 21st ICAARI (2010), accepted

[5] Q. Xing, N. Herbots, M. Hart, J. D. Bradley, B. J. Wilkens, D. A. Sell, C. H. Sell, H. M. Kwong, R. J. Culbertson, S. D. Whaley; "Ion Beam Analysis of Silicon-Based Surfaces and Correlation with Surface Energy Measurements?". 21st ICAARI (2010), accepted.

Spectroscopic Ellipsometry Focus Topic **Room: 209 - Session EL+AS+EM+MS+PS+TF-ThM**

Spectroscopic Ellipsometry of Biological Materials and Organic Films

Moderator: M. Creatore, Eindhoven University of Technology, the Netherlands, K.G. Lloyd, DuPont Corporate Center for Analytical Sciences

8:00am **EL+AS+EM+MS+PS+TF-ThM1 Application of Various Spectroscopic Ellipsometry Techniques for In Situ Studies of Thin Polymer Films on Solid Substrates**, *K.-J. Eichhorn*, Leibniz-Institut für Polymerforschung Dresden e.V., Germany **INVITED**

Thin films of functional polymers are not only widely integrated into modern micro- and nanoelectronic devices, but also used to modify solid surfaces for biosensor, biomedical and antifouling applications.

Therefore, in the first part I will report on improved temperature-dependent spectroscopic Vis-ellipsometry experiments to study confinement effects on the polymer dynamics in thin films to address a question which is controversially discussed in the polymer physics community for a long time past: Is there really a significant change of the glass transition temperature T_g of polymers when confined in nanoscopic films (studied here down to about 10 nm thickness)? We compared well-known linear polystyrenes of different molecular weights /1/ and hyperbranched polyesters having different architectures and functional groups /2/. Films of different thickness were prepared by spin-coating on silicon wafers, carefully equilibrated and measured in dependence on temperature (up to 250°C) in an inert gas atmosphere. The T_g data were determined from the ellipsometric results and discussed.

In the second part, "smart" surfaces will be presented which can be used for controlled adsorption and release of biomolecules. For that, different types of stimuli-responsive polymer brushes were prepared on solid substrates by a "grafting-to" procedure. The brush properties (e.g. swelling/collapsing) as well as the resulting adsorption/desorption of model proteins (e.g. Human Serum Albumin, Chymotrypsin) can be switched in an appropriate aqueous medium with temperature (PNIPAAm) and/or pH (PAA-P2VP). The corresponding processes at the solid-liquid interface were studied in-situ by spectroscopic Vis- and IR-ellipsometry /3,4/.

/1/ M. Tress, M. Erber, E.U. Mapesa, H. Huth, J. Müller, A. Serghei, C. Schick, K.-J. Eichhorn, B. Voit, F. Kremer, *Macromolecules* 43 (2010), 9937-9944

/2/ M. Erber, A. Khalyavina, K.-J. Eichhorn, B. Voit, *Polymer* 51 (2010), 129-135

/3/ E. Bittrich, M. Kuntzsch, K.-J. Eichhorn, P. Uhlmann, J. Polym. Sci. B, *Polym. Phys.* 48 (2010), 1606-1615

/4/ Y. Mikhailova, L. Ionov, J. Rappich, M. Gensch, N. Esser, S. Minko, K.-J. Eichhorn, M. Stamm, K. Hinrichs, *Anal. Chem.* 79 (2007) 20, 7676-7682

8:40am **EL+AS+EM+MS+PS+TF-ThM3 Hard Matter Meets Thin Polymer Films-Spectroscopic Ellipsometry as a Versatile Tool to Investigate Properties of Responsive Poly(N-isopropylacrylamide) Systems with Incorporated Magnetic Nanoparticles**, *S. Rauch*, Leibniz-Institut für Polymerforschung Dresden e. V., Germany

Responsive polymer systems designed by using polymer brushes or hydrogels are interesting systems, which can exhibit reversible or irreversible changes in their physical and structural properties to special environmental conditions (e.g. temperature or magnetic fields). The temperature responsive poly(N-isopropylacrylamide) (PNIPAAm) is one of such polymers. It undergoes a phase transition in aqueous solution at its lower critical solution temperature (LCST) of 32 °C which induces an increase in hydrophobicity. Combined with the properties of magnetic nanoparticles (NP) (e.g. Fe₃O₄ or CoFe₂O₄) these systems can lead to new surface functionalities with new interesting properties for many applications, as sensing, wettability or (bio)adhesion.

For the design of such thin film systems a basic knowledge of the film characteristics is essential. Therefore it is first necessary to know how much nanoparticles are inside or attached to the system. By using spectroscopic

Vis-Ellipsometry (SE) it is not only possible to investigate optical properties of these films but also the composition of it, e.g. volume fraction of Fe₃O₄-NP.

We studied two types of films and present results for a thin NP-composite film prepared by pre-mixing of the PNiPAAm with hydrophobic Fe₃O₄-NP, spin-coated and grafted to a silicon substrate (System 1) and a film prepared by adsorption of hydrophilic functionalized Fe₃O₄-NP onto PNiPAAm brushes (System 2). The former system was chosen to develop an optical model starting from a simple two component effective-medium-approach (Maxwell-Garnett-EMA) using the optical constants of the pure polymer measured by SE and of Fe₃O₄ with averaged data taken from three different publications. The SE best fit-results were validated against scanning electron microscopy (SEM), atomic force microscopy (AFM) and X-ray photoelectron spectroscopy (XPS).

After transferring this optical model to System 2, the adsorption of hydrophilic functionalized Fe₃O₄-NP onto PNiPAAm brushes was investigated and will be discussed with additional results obtained from contact angle (CA) and phase transition (LCST) measurements.

9:00am **EL+AS+EM+MS+PS+TF-ThM4 The White Scarab Beetle *Cyphochilus insulanus* –Scattering and Polarization Properties.** C. Akerlind, Swedish Defence Research Agency / Linköping University, Sweden, H. Arwin, Linköping University, Sweden, T. Hallberg, H. Kariis, Swedish Defence Research Agency, Sweden, J. Landin, K. Järrendahl, Linköping University, Sweden

Three methods were used to characterize the optical properties of the light scattering white scarab beetle *Cyphochilus insulanus*. Spectral directional hemispherical (DH) reflectance measurements in the wavelength region 250 nm to 25 μm were performed using integrating spheres. The general spectral appearance shows a relatively strong reflectance band in the range 400 - 1600 nm. The Bidirectional Reflection Distribution Function (BRDF) was measured over a semi-circle in the plane of incidence at the wavelengths 633 nm and 3.39 μm, using s- and p-polarized light. In the visible the BRDF data shows a near Lambertian behaviour with a constant BRDF for most angles, i.e. the light is diffusely scattered. For large incident angles and in the infrared the BRDF is more specular. Full Mueller-matrix spectroscopic ellipsometry (MMSE) measurements were performed in the wavelength range 250 - 1000 nm at angles of incidence between 45° and 75° using a dual rotating compensator ellipsometer. The Mueller data show that the reflected light in general has a high degree of polarization *P* even for nonpolarized incident light. The angular dependence of *P* was pronounced for incident p-polarized light and was very low near the Brewster angle. In comparison, *P* was high for all measured angles for incident s-polarized light. Close to the Brewster angle, the reflected light showed a high ellipticity for incident p-polarized light. The optical data is used to model the structure and optical response of the beetle cuticle. With input from the DH and BRDF-data analysis of the Mueller Matrix data was made using Fresnel-based layer modelling. 2-, 3- and n-phase models are compared. The obtained optical properties are also used to calculate color data in terms of chromaticity and whiteness. The scattering properties of the *Cyphochilus insulanus* cuticle are also discussed by combining the BRDF and MMSE data as well as recently obtained Mueller matrix imaging polarimetry results.

9:20am **EL+AS+EM+MS+PS+TF-ThM5 Real-time Spectroscopic Ellipsometry and Quartz Crystal Microbalance with Dissipation Characterization of Biomolecule Adsorption within Sculptured Thin Films.** T. Kasputis, D. Schmidt, K.B. Rodenhause, H. Wang, A.K. Pannier, M. Schubert, University of Nebraska - Lincoln

Recent improvements in nanofabrication strategies have led to the development of precisely crafted nanostructures with intricate features. Incorporating biomolecules such as proteins, DNA, drugs, and even whole cells could allow for functionalization of nanostructured surfaces for biological applications including biosensing, tissue engineering scaffolds, and drug and gene delivery. Along with the nanofabrication of biological devices, there is a need to develop instrumentation capable of probing and characterizing the dynamic evolution of these bio-functionalized interfaces. Spectroscopic ellipsometry combined with quartz crystal microbalance with dissipation (SE/QCM-D) is a non-destructive optical/mechanical characterization technique that reveals dynamic properties, including average film thickness (with sub-angstrom resolution), adsorbed mass, and porosity.

Nanostructures in the form of sculptured thin films (STF) were fabricated by glancing angle deposition via electron beam evaporation of titanium onto gold-coated quartz sensors. The sensors were then mounted within an SE/QCM-D liquid cell, and proteins of varying sizes were deposited and characterized, *in-situ*. Protein adsorption was detected shortly after introducing the protein solutions by SE and QCM-D as a change in the optical response and decrease of vibration frequency, respectively. QCM-D

reported greater adsorbed mass for larger proteins (fibronectin) than smaller proteins (bovine serum albumin). The adsorbed mass of proteins within the nanostructured scaffold exceeded that of proteins on flat surfaces, confirming that the STFs are capable of trapping proteins. Analysis of the anisotropic optical response from the nanostructures, which is very sensitive to environmental changes, adds complementary information on protein adsorption; the optical quantification is in agreement with QCM-D results. In addition, the adsorption of other biomolecules, such as cells and DNA complexes, has also been accomplished. The use of combinatorial SE/QCM-D to characterize and monitor the attachment of biomolecules on complex nanotopographies will improve the design and fabrication strategies for a wide array of biotechnological devices.

9:40am **EL+AS+EM+MS+PS+TF-ThM6 Characterization of Multilayer Organic Thin Film for Use as an Aptamer Biosensor with Hybrid Spectroscopic Ellipsometry and Quartz Crystal Microbalance with Dissipation.** J.Y. Gerasimov, K.B. Rodenhause, H. Wang, R.Y. Lai, M. Schubert, University of Nebraska - Lincoln

DNA aptamer molecules passivated by alkanethiols can be used for biological detection and screening. Through the use of spectroscopic ellipsometry (SE, optical) and quartz crystal microbalance with dissipation (QCM-D, mechanical) techniques, selective binding of analytes to chemisorbed aptamer probes can be observed *in-situ*. The system analyzed consists of a gold-coated quartz substrate, a multilayer organic thin film (containing aptamer probe, alkanethiol, and single-stranded DNA analyte), and physiological buffer solution. The attachment and detachment of material, the hybridization efficiency of the aptamer probes, and changes in the porosity of the multilayer organic thin film were all determined by SE/QCM-D.

In this contribution, we present the real-time SE/QCM-D characterization of (a) the formation of the aptamer probe layer, (b) the subsequent chemisorption of alkanethiol, and (c) the interrogation of single-stranded DNA that is non-complementary or complementary to the sequence found on the aptamer probe. The aptamer DNA sequence encodes codon 12 of the *K-ras* gene; mutations of this gene are frequently found among pancreatic cancer patients. We found that introduction of either complementary or non-complementary DNA caused increases of the multilayer organic thin film thickness. However, our SE/QCM-D analysis showed that the porosity of the multilayer organic thin film responded differently depending on the compatibility of the DNA analyte. The SE/QCM-D technique provides evidence for different surface attachment mechanisms and can be useful in characterizing biological interfaces.

10:40am **EL+AS+EM+MS+PS+TF-ThM9 Contamination Processes of EUV Optics Characterized by Spectroscopic Ellipsometry.** L.J. Richter, C. Tarrío, S. Grantham, S.B. Hill, T.B. Lucatorto, National Institute of Standards and Technology, N.S. Faradzhev, University of Virginia

Extreme ultraviolet (EUV) lithography using 13.5 nm light is emerging as a viable tool for semiconductor fabrication at design rules below 32 nm. Tool performance critically depends on limiting and mitigating degradation of the EUV optical elements. A primary degradation mechanism is the EUV induced deposition of carbon from ambient species originating from outgassing of the unbaked vacuum system and/or outgassing from the EUV irradiation of the resist. Using the high brightness of the Synchrotron Ultraviolet Radiation Facility (SURF-III) at NIST both fundamental studies of EUV induced contamination and practical (“witness plate”) studies of resist out gassing are performed. Typical deposits are hydrogenated amorphous carbon features with peak thicknesses of about 1 nm and nominal lateral extent of 1 μm. Both ex-situ, small spot mapping spectroscopic ellipsometry (SE) and in situ single-wavelength imaging nulling-ellipsometry are used for rapid, sensitive, contamination metrology. Fundamental studies of contamination by admitted gases indicate that the process is a complex function of both gas pressure and photon dose. Correlations between SE and XPS are suggestive that, at high EUV fluxes, densification can occur resulting in spatial variation in the deposit dielectric function. The use of principal component analysis of the SE images to highlight the spatial diversity will be discussed.

11:00am **EL+AS+EM+MS+PS+TF-ThM10 Characterization of Organic Solar Cells Materials and Structures by Spectroscopic Ellipsometry.** J.P. Piel, L. Kitzinger, A. Bondaz, C. Defranoux, SEMILAB-SOPRALAB, France

Spectroscopic Ellipsometry (S.E) is a well known optical technique widely used for the characterisation of all types of thin films for determination of film thickness and optical indices on glass or plastic substrates.

S.E. is also being applied to the characterization of materials and multilayer structures of organic materials like organic light-emitting diodes (OLEDs) or Organic Solar Cells.

We present the determination of the refractive indices of organic Solar Cells materials like P3HT, PCBM, Pentacene, Perylene, and their blends. Complex organic materials can be analyzed accurately and fully characterized from their absorption bands in the visible and UV range (190nm to 900nm).

Transmission and absorption can be also measured at the same time and be used to determine the optical properties of these materials.

Using these refractive indices, analysis of real multi-layer stacks can be done. The refractive indices can be used afterwards to automatically optimise and balance the energy flow dissipation Q inside an organic solar cell composed of a thin film stack. We present an example performed on a single cell and on a tandem bi-layer cell structure.

Since these materials are sensitive to moisture and pollution, it can be necessary to measure their optical properties and thickness values through an encapsulated media. We will demonstrate how we can measure single layer properties and multi-layer stacks, through encapsulated samples, from the back side of the substrate. This technique can be applied to test structure or real Organic Solar Cell monitoring. Backside measurement combined with a water vapour cell used for ellipsometry porosimetry is used to test the efficiency of the thin film encapsulation.

We also present the characterization of ITO and ZnO transparent electrodes by S.E. and how near infra-red ellipsometry is used to determine the ITO resistance, without contact, by using the Drude behaviour on encapsulated samples.

Electronic Materials and Processing Division Room: 210 - Session EM+TF-ThM

Hybrid Electronic Materials and Interfaces

Moderator: A.J. Muscat, University of Arizona

8:00am **EM+TF-ThM1 Chemical Modification of Surfaces for Biological Applications**, *W.G. McGimpsey*, Kent State University
INVITED

The chemical and physical characteristics of surfaces can have profound and useful effects on the behavior of biological systems. We describe here several methods for modifying the surfaces of a variety of biocompatible materials, including metals, glass and polymers, in order to produce desired chemical and physical properties. The effects of surface chemistry and surface morphology on the growth and proliferation of mammalian cells as well as bacteria are also reported. Applications investigated include control of the growth of microbial biofilms, the growth of three-dimensional tissue assemblies, the patterned growth of neurons and other cell types and the functionality of primary neurons deposited on surfaces.

8:40am **EM+TF-ThM3 Modification of Oxide-Free Silicon Surfaces with Phosphonic Acid Self-Assembled Monolayers**, *P. Thissen, T. Peixoto, A. Vega, Y.J. Chabal*, University of Texas at Dallas

Phosphonic acid self-assembled monolayers (SAMs) are being considered as versatile surface modification agents due to their ability to attach to surfaces in different configurations, including mono-, bi- or even tri-dentate arrangements. Different chemical strategies for grafting SAMs on oxide-free silicon have been developed. Recently, a novel method for preparing OH-terminated, on otherwise oxide-free silicon has been reported [1] and further expanded for this work. This atomically flat surface contains precisely 1/3 OH and 2/3 H termination groups.

Using this model surface, we demonstrate that the phosphonic group of organic molecules can be chemically grafted to the OH group on the surface using a single chemical step, leaving the Si-H termination unaffected, without oxidation of the Si surface. We also show that the nature of solvents is important as they can act as a catalyst. The perfection of the surface (that remains atomically flat throughout the modification) makes it possible to use first principles DFT-based calculations to model the IR and XPS data obtained for this surface. Thus, a detailed structure for the SAMs can be derived on an atomic level. It is found that phosphonic acids are chemically attached to the Si(111) surface as mono-dentate via Si-O-P bond upon reaction with the OH groups. The remaining groups of P=O and P-OH are further oriented by forming a 2D network of hydrogen bonds.

[1] D. J. Michalak, S. R. Amy, D. Aureau, M. Dai, A. Esteve and Y. J. Chabal, Nanopatterning Si(111) surfaces as a selective surface-chemistry route, NATURE MATERIALS, Vol. 9, March 2010

9:00am **EM+TF-ThM4 Competing Effects of Interfacial Organic Layers on the Nucleation of Inorganic Thin Films Deposited Via Atomic Layer Deposition**, *K.J. Hughes, J.R. Engstrom*, Cornell University

Over the past several years a number of groups have been investigating the use of interfacial organic layers (IOLs) in the form of self-assembled monolayers (SAMs) and/or surface grown or bound oligomers to promote the subsequent growth of inorganic thin films. Work in our group has initially focused on determining the relative importance of the type, density and dimensionality of the organic functional groups present in IOLs on the subsequent growth of the thin film, particularly via ALD^[1]. Here we shall report on two perhaps less well-studied aspects concerning the use of SAMs or IOLs to promote nucleation and growth via ALD: (i) the effects of the underlying substrate on the IOL, and its ability to promote growth; and (ii) given the same IOL/substrate combination, the effects on ALD for a series of inorganic thin film deposition processes. To examine these systems we have made use of a variety of experimental tools, including a conventional viscous flow ALD tool, and also an ultrahigh vacuum (UHV) molecular beam based ALD process, where we employ *in situ* x-ray photoelectron spectroscopy. Concerning the first of these, we have examined the effect of a thin (< 10 Å) organic layer, poly(ethylene-imine) (PEI) on the ALD growth of TaN_x, where the underlying substrate is a chemically oxidized SiO₂ thin film, or a porous SiO₂ based low-κ dielectric thin film. Here we observe essentially the same result from conventional viscous flow, and molecular beam UHV ALD: PEI acts to attenuate TaN_x ALD on SiO₂, while it enhances growth on a low-κ dielectric thin film. From a practical point of view, most importantly, we find that PEI stops infiltration/penetration of the TaN_x ALD thin film into the porous low-κ dielectric. Concerning the second major issue, we have examined the effect of PEI on the subsequent growth via ALD of a series of inorganic thin films, namely: Al₂O₃, HfO₂, Ta₂O₅, and TaN_x. Here PEI has the effect of attenuating growth to different degrees depending on the subsequently grown ALD thin film, leading to no attenuation of growth for Al₂O₃, but significant incubation periods, in increasing order, for Ta₂O₅, HfO₂ and TaN_x. The length of the incubation time is found to correlate with both the total enthalpy change of the overall ALD reaction, as well as the net internal energy change of a single ligand exchange reaction representative of the second half of the ALD reaction, suggesting that these factors associated with the ALD process play a key role in determining the length of the incubation period caused by PEI.

[1] K. J. Hughes and J. R. Engstrom, J. Vac. Sci. Technol. A **28**, 1033-1059 (2010)

9:20am **EM+TF-ThM5 Towards Molecular Electronics: Solution-Based Methods for Selective Deposition of Metals and Semiconductors**, *Z. Shi, J. Yang, P. Lu, A.V. Walker*, University of Texas at Dallas

Robust methods for the chemically selective deposition of metals, semiconductors, biomolecules and other substances are developed and applied in the construction of complex two- and three-dimensional structures. This work has important applications in molecular and organic electronics, sensing, biotechnology and photonics. These methods are easily parallelized, afford precise nanoscale placement and are compatible with photolithography. Two examples are discussed in detail: the chemical bath deposition (CBD) of CdSe on functionalized self-assembled monolayers (SAMs), and the electroless deposition of Ni nanowires on micron-scale patterned surfaces.

CBD is a solution-based method for the controlled deposition of semiconductors. The formation of CdSe nanocrystals are of particular interest for a wide range of applications because their photoluminescence spans visible wavelengths. Using CdSe chemical bath deposition (CBD) we demonstrate the selective growth and deposition of monodisperse nanoparticles on functionalized self-assembled monolayers (SAMs). On -COOH terminated SAMs strongly adherent CdSe nanoparticles form via a mixed ion-by-ion and cluster-by-cluster mechanism. Initially, Cd²⁺ ions form complexes with the terminal carboxylate groups. The Cd²⁺-carboxylate complexes then act as the nucleation sites for the ion-by-ion growth of CdSe. After a sufficient concentration of Se²⁻ has formed in solution via the hydrolysis of selenosulfate ions, the deposition mechanism switches to cluster-by-cluster deposition. On -OH and -CH₃ terminated SAMs monodisperse CdSe nanoparticles are deposited via cluster-by-cluster deposition and they do not strongly to the surface. Thus under the appropriate experimental conditions CdSe nanoparticles can be selectively deposited onto -COOH terminated SAMs. We illustrate this by selectively depositing CdSe on a patterned -COOH/-CH₃ terminated SAM surface.

Our approach for the construction of Ni nanowires begins with a single SAM layer deposited and UV-photopatterned using standard techniques. We exploit the different deposition rates of nickel electroless deposition on -CH₃ and -OH terminated SAMs to deposit nanowires. The deposited nanowires are long (centimeters) and uniform in diameter, and can be patterned in arbitrary shapes. SAMs are ideal for the construction of nano- and micro- structures since their surface chemistry can be easily tuned to

form the needed structures. Further the micron-scale UV photopatterning of SAMs does not require a clean room or expensive lithography equipment.

9:40am **EM+TF-ThM6 Sensing Mechanism for Peroxide and Hydroperoxide Vapors in Phthalocyanine Thin Film Transistors, J. Royer, E. Kappe, W. Trogler, A.C. Kummel**, University of California San Diego

Organic thin-film transistors (OTFTs) are promising candidates for selective chemical sensors due to numerous chemical and electrical parameters which govern sensor response. Analyte selectivity can be obtained using multiparameter electrical monitoring of a single OTFT which is sensitive to changes in mobility, I_{on}/I_{off} ratio, and/or threshold voltage. The present study demonstrates selective hydrogen peroxide and organic peroxide sensors based on irreversible metal-phthalocyanine (MPc) OTFT threshold voltage shifts. The irreversible threshold voltage shift is not evident with non-oxidizing analytes such as di-methyl methylphosphonate (DMMP) and common background analytes such as water vapor. Furthermore, the threshold voltage shift responds linearly to the dose time which permits dosimetric sensing analysis. A proposed mechanism for peroxide sensing is determined using simultaneous monitoring of mobility and threshold voltage. The data reveal reversible mobility and irreversible threshold voltage response. Mobility response time is fast and saturates quickly whereas threshold voltage response is dosimetric, and irreversible, suggesting an accumulation of uncompensated positive charge in the MPc film. The results are consistent with a dual response adsorption/decomposition mechanism in which the peroxide reversibly decreases mobility through a molecular chemisorption event and irreversibly shifts threshold voltage due to electron transfer from the MPc to peroxide. The electron transfer from the MPc to peroxide dissociates the peroxide to form hydroxyl products and leaves an uncompensated MPc⁺. This detection method is exclusive for the OTFT platform and permits high selectivity at low peroxide concentrations.

10:40am **EM+TF-ThM9 Organic/Oxide Hybrid Thin-Film Applications for Photo-detector Cells and Complementary Inverters, S.I. Im**, Yonsei University, Republic of Korea **INVITED**

Due to the distinct advantages and functionalities, oxide and organic devices on glass or flexible substrates have extensively been studied in such basic forms as thin-film transistors (TFTs) and light emitting diodes. As a more revolutionary approach to realize advanced thin-film devices using both oxide and organic layers, organic/inorganic hybrid layer techniques were also employed, so that hybrid p-n diodes, image sensors, nonvolatile memory, and complementary inverters have recently been demonstrated. *These hybrid approaches are an interesting and attractive way to extract a unique device performance which may not be possible with organics or with inorganics alone, compensating some weakness of organics with inorganics or vice versa. The most representative example among the organic/inorganic hybrid devices may be complementary thin-film transistor (CTFT) inverters with an organic p-channel thin-film transistor (TFT) and an oxide n-channel TFT.* In particular, a vertically stacked CTFT (VS-CTFT) inverter for logic operation on a glass substrate is very impressive since the vertical stacking of organic p-TFT on oxide n-TFT improves device integration or device area reduction. For the VS-CTFT inverter for logic and photo-gating, we used a thermally-evaporated p-channel pentacene layer, sputter-deposited n-channel GaZnSn-based oxide (GZTO), and atomic layer deposited (ALD) Al₂O₃ dielectric. Our VS-CTFT inverter nicely displays effective photo- and electrical-gating with a high voltage gain, dynamically operating in the low-voltage regime of 3, 5, and 8 V (the thin pentacene channel receives blue photons). As a more advanced hybrid approach, we have successfully fabricated transparent image pixels that operate at 3 V as composed of pentacene thin-film transistor (TFT) and semitransparent pentacene/ZnO photodiode with a transparent top electrode in the interest of a light detectable smart functional windows. Our transparent pixels was equipped with an additional 6,13-pentacenequinone phosphor layer as deposited on the pentacene/ZnO photodiode. The organic phosphor transmits most of visible photons but absorbs ultra-violet (UV) photons to convert them to yellow-green photons, so that the emitted yellow-green lights excite the pentacene/ZnO diode under a reverse bias state. Our approach to the transparent pixel adopting such an organic phosphor layer certainly makes the pixel operations efficient under not only visible photons but also UV, protecting the organic pentacene from direct UV.

11:20am **EM+TF-ThM11 Near-ideal Schottky-Mott Behavior of n-Si / Hg Diodes with Hydroquinone-Alcohol Monolayers, A. Vilan, R. Har-Lavan, O. Yaffe, P. Joshi, R. Kazaz, D. Cahen**, Weizmann Institute of Science, Rehovot Israel

The Schottky-Mott model predicts that the eventual energy barrier formed when metal and semiconductor are brought into intimate contact, will be equal to the difference between the metal work function and the

semiconductor's electron affinity (for n-type). 60 years of extensive experiments have clearly shown that this ideal picture, that seems to hold for wide bandgap ionic semiconductors such as ZnO, GaS etc., is far from being adequate for the more covalent narrow bandgap Si, Ge, InP, and GaAs. Following Bardeen, who attributed this deviation from the model to surface states energetically located within the semiconductor's forbidden gap, different explanation were raised as for the source of those surface states.

One commonly used model for surface states formation at the interface of semiconductor and metal is the intrinsic Metal Induced Gap State (MIGS) model, stating that gap states are inevitably formed due to the decay of metal electronic states' wavefunction into the semiconductor's bandgap.

We have examined the presence of such MIGS using Hg, which is one of the few metals that doesn't interact chemically with Si, as an electrode. Furthermore, in order to eliminate surface states which are just due to Si dangling bonds, we have used state of the art mixed molecular monolayers of hydroquinone and alcohols that were shown to be the best chemical passivation for Si surfaces.

Using alcohols of different alkyl chain lengths we succeeded to effectively change the electron affinity of the Si over 400 mV range while maintaining firm surface passivation. Current-voltage measurements of diodes formed that way, with Hg on organically modified n-Si surface, demonstrated near ideal Schottky-Mott characteristics with index of interface behavior $S=0.9$ (compared to a common value for Si $S=0.1$).

11:40am **EM+TF-ThM12 Electroless Deposition of Metals on SiO₂ Surfaces Modified by a Self-Assembled Monolayer, R. Jain, A. Ng, A.J. Muscat**, University of Arizona

Self-assembled monolayers (SAMs) are used to both chemically activate and deactivate semiconductor surfaces. For instance, octadecyltrichlorosilane prevents atomic layer deposition of high-k films, and 3-aminopropyltriethoxysilane promotes metal deposition. The formation of a uniform and defect free monolayer is essential for nano-scale device fabrication. SAMs could serve as an adhesion layer, which is required for the electroless deposition of metals on some dielectric surfaces. Electroless deposition processes in particular are known to be sensitive to the surface termination and are not robust. In this work, the thickness and density of an aminosilane SAM formed on a SiO₂ surface were monitored as a function of solvent, concentration, and time, and the metal to N ratio was quantified.

A 3-aminopropyltrimethoxysilane (APTMS) SAM was formed on a well-hydroxylated SiO₂ surface. SAM formation was studied as a function of solvent (methanol and toluene), APTMS concentration (5.72 mM and 57.2 mM), immersion time, solution agitation (stirring and sonication), and post-deposition rinsing in methanol or chloroform depending on the solvent used. The thickness of the APTMS SAM using ellipsometry was 7.8 ± 0.2 Å after 15 min when prepared by stirring an APTMS-methanol solution. This thickness corresponds to the expected length of an APTMS molecule. The roughness was 0.3 ± 0.1 nm measured over 2×2 μm² regions using atomic force microscopy. These thickness and roughness values indicate that thin, uniform layers were formed using this method. The absence of a peak for methoxy groups in the high resolution C 1s x-ray photoelectron spectroscopy (XPS) spectrum suggests that all of the methoxy groups were hydrolyzed on the APTMS molecules that reacted with the surface. A single peak in the N 1s spectrum at 399.7 eV indicates the presence of a primary amine when the SAM was prepared in methanol. A second peak was also observed at 400.4 eV corresponding to a hydrogen-bonded amine when the SAM was prepared in toluene. These results suggest that all the SAM molecules were bonded to the surface by siloxane (Si-O-Si) linkages and that amine groups were directed away from the surface with the methanol solvent. Based on XPS peak areas, the molecular density in the SAM layer was 5.4 ± 1.9 molecules/nm². A layer of Pd atoms was successfully deposited by immersing the APTMS SAM surfaces in an 80 mM PdCl₂-HCl solution for 2 min, yielding one Pd atom bonded to two amine groups based on XPS peak areas. These results demonstrate that an adhesion layer can be formed that will bind metal. Future work will be done to determine how strongly the metal layer adheres to the SAM.

Nanostructures for Energy Storage and Fuel Cells I**Moderator: J. Lewis, RTI International**

8:00am **EN+NS-ThM1 Exploring Intercalation Chemistry of Modified Graphene with Ionic Liquids for Energy Storage Applications**, *M. Acik*, The University of Texas at Dallas, *D.R. Dreyer*, *C. Bielawski*, The University of Texas at Austin, *Y.J. Chabal*, The University of Texas at Dallas

One of a real-world application of Electrochemical Double Layer Capacitors (EDLCs) is their use in prototype electric vehicles. An EDLC simply consists of two non-reactive, porous electrodes and an electrolyte separated with a membrane. Activated charcoals are one of a commonly used electrode systems which has drawbacks such as limited energy storage due to their large ion size. Therefore, a replacement electrode system with a higher surface area is necessary for a superior EDLC performance. Modified graphene is one of a promising candidate with its high theoretical surface area (2630 m²/g). EDLC working principle also depends on how effectively it can polarize the electrolyte solution. In principle, ionic liquids are promising electrolyte systems with their high non-volatility, non-flammability, thermal stability and good solvating ability.

This study focuses on the intercalation studies of ionic liquids such as N-methyl-N,N,N-tris(2-hydroxyethyl)ammonium iodide, N-methyl-N,N,N-tris(2-hydroxyethyl)ammoniummethyl sulfate, 1-butyl-3-methylimidazoliummethylsulfate and N-octyl-N-methylpiperidinium methylsulfate. To achieve a high surface area material with modified graphene, it is essential to understand the interfacial interactions upon intercalation of ionic liquids.

We study powder X-Ray Diffraction Analysis to characterize the interlayer distance of modified graphene. For instance, its d-spacing increases by about 4-12 Å after intercalating as-synthesized graphite oxide (GO, ~9Å) with N-methyl-N,N,N-tris(2-hydroxyethyl)ammonium methylsulfate (IL) at room temperature. Annealing at 300-500°C, (002) orientation of GO disappears as a result of thermal exfoliation. In addition, *in-situ* Infrared Absorption Spectroscopy (IRAS) measurements were performed to explore the intercalation chemistry of modified graphene in the presence of ionic liquids. Therefore, we perform thermal reduction studies in vacuum coupled with IRAS measurements to characterize the chemical interactions during thermal exfoliation of reduced GO. After annealing GO intercalated with this IL, the loss of C-N and C-O containing species is identified at ~1000-1500 cm⁻¹ and 800-1200 cm⁻¹ with contribution from C-OH groups at 3000-3700 cm⁻¹. Complete removal of these species is observed after a ~500°C anneal resulting in a weak infrared absorbance intensity of sp²-hybridized C=C species at ~1580 cm⁻¹. The presence of new formation of sheet-to-sheet linking or bonding motifs was also studied with X-ray Photoelectron Spectroscopy (XPS).

*Research supported by the U.S. Department of Energy, Office of Basic Energy Sciences, Division of Materials Sciences and Engineering under Award DE-SC001951.

8:20am **EN+NS-ThM2 Electronic Structure and Chemical Composition of Candidate Conversion Material Iron Oxyfluoride**, *R. Thorpe*, *S. Rangan*, *R.A. Bartynski*, *O. Celik*, *N. Pereira*, *G. Amatucci*, Rutgers University

Transition metal fluorides have recently gained interest as possible electrode materials in lithium ion conversion batteries. Owing to their large band gaps, they operate at high voltages and enable high energy densities. However this large band gap inhibits charge conduction and thus impedes efficient charge and discharge. One path to overcome this limitation is the use of metal oxyfluorides, which are characterized by a slightly smaller energy gap and thus a higher electronic conductivity. Currently, little is known about the electronic structure of metal oxyfluorides, particularly the relation between chemical structure, composition, and energy gap. Hence, we have produced model oxyfluoride systems in order to characterize the conversion mechanism using surface science tools.

Of all metal fluorides, iron-based compounds are the most promising to maximize energy density. Ultra-thin FeF₂ films have been synthesized via the fluorination of clean Fe foil exposed to XeF₂, following a self-limited Mott-Cabrera mechanism. The FeF₂ films have then been sequentially exposed to a partial pressure of O₂ of 2x10⁻⁶ Torr at 285°C in order to produce iron oxyfluoride. Using x-ray and ultraviolet photoemission as well as inverse photoemission, we have probed the electronic structure of these FeO_xF_y samples and characterized the occupied and unoccupied states near the band gap of the material.

It has been found that oxygen insertion into the FeF₂ matrix can be controlled until complete oxidation occurs. As expected for a Mott-Hubbard insulator, the valence band and conduction band of FeF₂ can be interpreted using a simple crystal field approach. In the case of Fe₂O₃, strong charge transfer effects need to be taken into account in order to interpret the band edges. To explore the conversion process, Li has been evaporated onto these iron oxyfluorides *in-situ*. Preliminary results addressing the reactivity of lithium at the surface of these materials will also be presented.

8:40am **EN+NS-ThM3 Lithium Ion Batteries: Present and Future Technologies**, *K. Amine*, *W. Wu*, *I. Belharouak*, *A. Abouimrane*, *Z. Zhang*, *J. Lu*, Argonne National Laboratory

INVITED

In its goal of developing more fuel efficient vehicles, the US Department of Energy in collaboration with the US auto industries are focusing on high-power and high energy lithium-ion batteries to meet the energy storage requirements for HEV and PHEV applications. Under these auspices, Argonne National Laboratory is investigating several different lithium ion chemistries in order to address the calendar life, cost and safety of high power and high energy lithium ion batteries for transportation applications

To meet the high-energy requirement that can enable the 40-miles electric drive P-HEVs, It is necessary to develop very high energy cathode or anode that offers 5,000 charge-depleting cycles, 15 years calendar life as well as excellent abuse tolerance. These challenging requirements make it difficult for conventional cathode materials to be adopted in P-HEVs. In this paper, we report on several advanced battery chemistry that could be used to power Hybrid electric vehicles. We also discuss several future high energy battery technologies that can enable 40 miles Plug in Hybrid and long range electric vehicles.

9:20am **EN+NS-ThM5 Templating of Porous Materials for Energy Storage and Generation**, *A. Stein*, *J. Davidson*, *N. Petkovich*, *Y. Qian*, *S. Rudisill*, *L. Venstrom*, *A. Vu*, University of Minnesota

INVITED

Materials containing pores in size ranges from micropores to macropores offer interesting features for a number applications involving energy storage and conversion, such as batteries, fuel cells, hydrogen storage, and sunlight-to-fuel conversion. Depending on the specific application, they can provide large surface areas for reaction, interfacial transport, or dispersion of active sites; they can provide nanostructured features which enhance reactivity, alter materials properties, or shorten diffusion paths; they can act as host materials to stabilize other active components; or, in the case of porous carbons, they can provide electrically conductive phases as well as intercalation sites. However, the higher reactivity brought about by nanostructured features can also lead to decreased stability, particularly in applications where phase changes may alter the structure of the material or where high temperatures are employed. This talk will focus on two redox systems (lithium-ion batteries and sunlight-to-fuel conversion) in which templated porous materials provide a platform for either electrical energy storage or light-to-chemical energy conversion. In the first system the role of pore architecture in carbon-based electrodes will be discussed. Improved rate capabilities for lithiation/delithiation are observed for hierarchically porous carbon electrodes. In composites with tin or tin oxide for anodes these structures maintain electrical contact between tin-based particles, even when those particles undergo significant volume changes during cycling, and hence the composite anode maintains good capacities over multiple cycles. Composites of hierarchically structured carbon with poorly conducting but otherwise desirable electrode materials (like sulfur or LiFePO₄) can be used to overcome limitations in electrical conductivity of those materials, increasing the choice of useful electrode materials. In the second system, we investigate the role of porosity in ceria-based materials of interest for solar thermal splitting of water or carbon dioxide to produce hydrogen or carbon monoxide fuels, respectively. Dopants for ceria are examined to stabilize the porous structures at the high reaction temperatures. The interplay between composition and morphology of these materials, thermal stability, and conversion efficiencies will be discussed.

11:00am **EN+NS-ThM10 Exploration of the Effects of Si Nanowire Length and Doping on Li-ion Battery Anode Performance**, *F. Rusli*, *V. Chakrapani*, *M.A. Filler*, *P.A. Kohl*, Georgia Institute of Technology

Silicon nanowires have recently garnered significant attention as a potential candidate to replace graphite as the negative electrode in a lithium-ion battery. Silicon's earth abundance, extensive knowledge base, and its theoretical capacity of 4200 mAh/g make it an attractive material for this purpose. While the high incorporation of lithium presents a problem as silicon undergoes a significant specific volume expansion upon intercalation (up to 400%), nanowires permit facile radial strain relaxation and allow lithiation without pulverization. In this work, we report on the first systematic study of nanowire length and doping on the cycling performance of NW electrodes. Silicon nanowires were grown on stainless steel substrates via the vapor-liquid-solid technique in a cold-wall low

pressure chemical vapor deposition reactor. Growth times ranging from 5-60 minutes and doping concentrations between 10^{18} – 10^{20} atoms cm^{-3} were studied. The half cells were cycled against lithium metal between (1) 0.01 and 2.0 V and (2) 0.07-0.7 V at a C/20 rate for 20 cycles. Cycling performance at different depths of discharge was also studied. Nanowires grown at short and long times both exhibit lower capacities than those grown at intermediate times. We attribute this effect to the loss of nanowire contact at the interface between the stainless steel and nanowire array for long nanowires, while the percolation network formed by short nanowires is not sufficiently robust to prevent loss of electrical connectivity upon wire breakage further from this interface. Nanowires at higher doping concentrations were not found to improve cycling performance drastically, which we attribute to the dopant effects on the growth mechanism of the nanowires and placement of dopant atoms in the silicon matrix that may have inhibited lithium atom insertion. We will present novel electrode fabrication routes that overcome these two challenges.

11:20am **EN+NS-ThM11 In Situ TEM Electrochemistry of Anode Materials in Lithium Ion Batteries, J.Y. Huang**, Sandia National Laboratories **INVITED**

We created the first nano-battery inside a transmission electron microscope (TEM), allowing for real time atomic scale observations of battery charging and discharging processes. Two types of nano battery cells [1], one ionic liquid based, and the other all solid based, were created. The former consists of a single nanowire anode, an ionic liquid (IL) electrolyte and a bulk LiCoO_2 cathode; the latter uses Li_2O as a solid electrolyte and metal Li as anode. Four case studies will be presented: 1) Upon charging of SnO_2 nanowires in an IL cell, a reaction front propagates progressively along the nanowire, causing the nanowire to swell, elongate, and spiral. The reaction front contains high density of dislocations, which are continuously nucleated at the moving front and absorbed from behind. This dislocation cloud indicates large in-plane misfit stresses and is a structural precursor to electrochemically-driven solid-state amorphization. 2) In charging Si nanowires, the nanowires swell rather than elongate. We found the highly anisotropic volume expansion in lithiated Si nanowires, resulting in a dumbbell-shaped cross-section which developed due to plastic flow and necking instability. Driven by progressive charging, the stress concentration at the neck region led to cracking, eventually splitting the single nanowire into sub-wires. 3) Carbon coating not only increases rate performance but also alters the lithiation induced strain of SnO_2 nanowires. The SnO_2 nanowires coated with carbon were charged 10 times faster than the non-coated ones. Intriguingly, the radial expansion of the coated nanowires was completely suppressed, resulting in reduced tensile stress at the reaction front, as evidenced by the lack of formation of dislocations. 4) The lithiation process of individual Si nanoparticles was observed in real time in a TEM. A strong size dependent fracture behavior was discovered, *i.e.*, there exists a critical size with a diameter of ~ 150 nm, below which the particles neither cracked nor fractured upon lithiation, above which the particles first formed cracks and then fractured due to lithiation induced huge volume expansion. For very large particles with size over 900 nm, electrochemical lithiation induced explosion of Si particles was observed. This strong size-dependent fracture behavior is attributed to the competition between the elastic energy and the surface energy of the nanoparticles. These results highlight the importance of in-situ studies in understanding the fundamental sciences of lithium ion batteries.

1. J.Y. Huang *et al.*, *Science* 330, 1515-1520 (2010); *Nano Lett.* (revised); *ACS Nano* (in press).

Graphene and Related Materials Focus Topic
Room: 208 - Session GR+NS+PS+SS-ThM

Graphene: Surface Chemistry, Functionalization, Plasma Processing and Sensor Applications

Moderator: G.G. Jernigan, U.S. Naval Research Laboratory

8:00am **GR+NS+PS+SS-ThM1 Tailoring Graphene's Properties through Chemistry, J.T. Robinson**, Naval Research Laboratory **INVITED**
Graphene's unique electron transport properties have motivated intensive research and development to mold it into the electronic material of the future. However, graphene can be much more than an electrical switch. Its high structural integrity and chemical flexibility enable extensive control of its optical, mechanical, and electronic properties. The most scalable and inexpensive route to modify these properties is chemical functionalization. Consequently, chemically modified graphenes (CMGs) have emerged as a system of materials whose many attractive properties complement and extend those of unmodified graphene.

In this talk I will describe efforts at NRL to synthesize and characterize new CMGs as well as first steps towards applications such as sensors and nanomechanical resonators. To begin, I will discuss the interaction of small molecules (CCl_4 , CS_2 , H_2O and acetone) with single-layer graphene under steady-state conditions using infrared multiple-internal-reflection. Adsorption-induced changes in the IR spectra suggest the formation of in-plane strain, where we observe important differences arising between species that form liquid-like layers under steady-state conditions and those that do not. Second, I will discuss graphene oxide, a well known derivative of graphene that has a rich ensemble of oxygen-based functional groups and related defects. These defects are readily tunable through chemical or thermal treatments and facilitate the formation of vapor and bio-sensors with parts-per-billion and nanomolar sensitivities, respectively. Third, I will discuss the stoichiometric addition of fluorine atoms to graphene and describe their resulting properties. Experiments indicate fluorinated graphene derivatives become highly resistive and optically transparent, while DFT calculations show band gaps open depending on the fluorine coverage and ordering. Finally, through combining these two material systems, I will discuss the fabrication and performance of CMG-based nanomechanical resonators. Through chemical modification, the frequency of CMG-based resonators is tunable over 500% and their quality factors can exceed 20,000 at room temperature.

8:40am **GR+NS+PS+SS-ThM3 Water Splits Epitaxial Graphene on Ru(0001) from Domain Boundaries, X. Feng, S. Maier, M. Salmeron**, Lawrence Berkeley National Laboratory

Epitaxial growth of graphene on metal substrates has recently been demonstrated as a rational synthesis route for producing macroscopic graphene domains and may hold the key to realizing the potential of large-scale applications. However, the epitaxial graphene is generally polycrystalline, with domain boundaries that may severely affect its structure and properties. Here we report that water adsorption splits epitaxial graphene on Ru(0001) and results in nanoscale graphene flakes at temperatures as low as 90K. Scanning tunneling microscopy studies indicated that the splitting starts primarily from domain boundaries followed by water intercalation underneath graphene. The mechanism proposed is that Ru-induced water dissociation provides hydroxyl species that break the graphene starting at the dangling and stretched bonds at the boundaries.

9:00am **GR+NS+PS+SS-ThM4 Novel Strategies for the Chemical Functionalization of Graphene: Towards Graphene/Molecular Nanosheet Heterostructures, A. Turchanin, C.T. Nottbohm, Z. Zheng, M. Schnietz, A. Beyer**, University of Bielefeld, Germany, M. Heilemann, M. Sauer, Julius-Maximilians-University Würzburg, Germany, A. Götzhäuser, University of Bielefeld, Germany

Chemical functionalization of graphene is essential for implementations of the 2D carbon sheets in various functional devices (e.g. chemical and biochemical sensors, nanoelectromechanical components, etc.) and for tuning their electrical properties. However, the functionalization is difficult to achieve due to the chemical inertness of graphene sheets with high structural quality. On the other hand, ultrathin (~ 1 nm) molecular nanosheets made from self-assembled monolayers (SAMs) possess well-defined chemical groups intrinsically. Moreover, due to the directionality of the constituting molecules both faces of the free-standing nanosheets -*Janus nanomembranes*- can be independently and specifically functionalized. Simple mechanical stacking of the nanosheets allows fabricating ultrathin layered structures with tunable physical and chemical properties. Upon annealing these stacks are converted into graphene sheets with adjusted thickness. The engineering of graphene/nanosheet heterostructures opens up novel routes towards chemically functionalized graphene sheets for functional applications. A potential of this approach will be discussed.

Z. Zheng, C.T. Nottbohm, A. Turchanin, H. Muzik, A. Beyer, M. Heilemann, M. Sauer, A. Götzhäuser, "Janus nanomembranes: A generic platform for chemistry in two dimensions", *Angew. Chem. Int. Ed.* 49 (2010) 8493-8497

C.T. Nottbohm, A. Turchanin, A. Beyer, R. Stosch, A. Götzhäuser, "Mechanically stacked 1 nm thick carbon nanosheets: 2D layered materials with tunable optical, chemical, structural and electrical properties", *Small* 7 (2011) 874-883

A. Turchanin, D. Weber, M. Bünenfeld, C. Kisielowski, M. Fistul, K. Efetov, R. Stosch, T. Weimann, J. Mayer, A. Götzhäuser, "Conversion of self-assembled monolayers into nanocrystalline graphene: structure and electric transport", *ACS Nano* 5 (2011) DOI: 10.1021/nn200297n

9:20am **GR+NS+PS+SS-ThM5 Biosensors Based on Chemically Modified Graphene**, *R. Stine, J.T. Robinson, P.E. Sheehan, C.R. Tamanaha*, U.S. Naval Research Laboratory

The sensitive and specific detection of biomolecules without using a label is a long-standing goal of the biosensors community. Several promising advances of the past several years formed biological field effect transistors (bioFETs) that have as the gate nanoscale materials such as nanowires and carbon nanotubes. The nanoscale dimensions of these materials allow the small charges associated with biomolecules to significantly change conduction through the gate. These conduction changes can be correlated with solution concentration to give precise readouts. While bioFETs are a promising way forward, there are many processing difficulties associated with these 1-D materials that inhibit large scale, reproducible fabrication of devices. Here, we will discuss our efforts to develop biosensors based on 2-D chemically modified graphene. These devices impart the sensitivity gains seen from other nanoscale materials, but offer a configuration that is amenable to processing techniques that are common in the semiconductor industry. We will focus primarily on chemically modifying graphene for attachment of biomolecular probes. Devices utilizing both graphene and graphene oxide will be covered, and surface spectroscopic studies of the material modification will be discussed. Successful results for the detection of specific DNA hybridization will also be presented, with detection limits that compare favorably with the best results reported from nanowire bioFETs.

Acknowledgements: R.S. is an employee of Nova Research Inc., Alexandria, VA, USA. This project received support from the Defense Threat Reduction Agency-Joint Science and Technology Office for Chemical and Biological Defense.

9:40am **GR+NS+PS+SS-ThM6 Controllable Defect Healing and N-doping of Graphene by CO and NO Molecules**, *B. Wang*, Vanderbilt University, *S.T. Pantelides*, Vanderbilt University and ORNL

Point defects alter strongly the physical and chemical properties of graphene, e.g. they degrade electrical transport and enhance chemical reactivity. Defects could also be used to achieve graphene functionalization, e.g. N atoms, as n-type dopant, can be introduced to obtain n-type graphene. Thus, controllable defect healing and N-doping in graphene would be very valuable for potential device applications. Here we report first-principles molecular dynamic simulations that suggest a procedure for defect healing and N-doping with fast dynamics and low thermal budget. Vacancies in graphene can be healed by sequential exposure to CO and NO molecules. A CO molecule gets adsorbed at a vacancy site and a NO molecule subsequently removes the extra O by forming NO₂, which desorbs quickly resulting in a defect-free graphene sheet. Controllable N-doping can be achieved by sequential vacancy creation (e.g. by electron or ion beam) and subsequent exposure to NO molecules at room temperature. NO molecules are trapped at vacancies and other NO molecules remove the extra O atoms simultaneously, leaving N atoms incorporated in graphene. Both reactions (healing and doping) are exothermic. We suggest that a combination of CO and NO molecules can potentially provide simultaneous healing and doping. Adjusting the ratio could fine-tune the N-doping level. The proposed strategy introduces no extra defects and is promising for graphene-based electronic materials in radiation environments. Finally, we propose that NH₃, which is normally used in experiments to introduce N atoms, may not be a good choice for N-doping since the dissociated H atoms can be trapped at vacancies and act as impurities that increase the resistivity of graphene.

This work was supported by DTRA Grant No. HDTRA1-10-1-0016 and the William A. and Nancy F. McMinn Endowment at Vanderbilt University. The calculations were performed at ORNL's Center for Computational Sciences.

10:40am **GR+NS+PS+SS-ThM9 Aptamer Modified Graphene Bio Sensor**, *K. Maehashi, Y. Ohno, K. Matsumoto*, Osaka University, Japan

Since graphene has high mobility and a large surface area, it is suitable for the application of the high sensitive sensor. In the present paper, we have first succeeded in the selective detection of the bio molecule such as IgE using the aptamer modified graphene FET.

The graphene was formed using the conventional mechanical exfoliation method on the SiO₂/Si substrate. The source and drain electrode were formed by the electron beam lithography and Ti/Au evaporation. The silicon rubber pool was formed on the fabricated graphene FET, and phosphoric buffer solution was poured into the silicon rubber pool. The Ag/AgCl reference electrode was introduced into the phosphoric buffer solution, which works as a top gate electrode for the graphene FET.

As a first step of the biosensor, three bio molecule such as Immunoglobulin E(IgE), Streptavidin(SA), and Bovine serum albumin(BSA) were introduced into the phosphoric buffer solution of pH of 6.8, and the change of the drain current of the graphene FET was detected. In this case, the IgE

and SA shows the decrease of the drain current, while the BSA the increase of the drain current. Because, in the phosphoric buffer solution of pH of 6.8, IgE and SA are positively charged, while BSA negatively charged. Therefore, the hole current of the graphene FET change the drain current following the charge of the bio molecule. As a result, bare graphene FET can detect the bio molecule following the charge of the molecule, but it does not have the selectivity

As a second step, in order to get the selective sensing of the bio molecule, the surface of the graphene was modified by the IgE aptamer, which was connected to graphene using the linker(1-pyrenebutanoic acid succinimidyl ester). IgE aptamer was known to selectively couple to IgE. When the BSA and SA were introduced into the phosphoric buffer solution on the aptamer modified graphene FET, there occurred no change in the drain current, while the IgE was introduced in the solution, the drastic decrease of the drain current was observed. This means the BSA and SA do not couple to IgE aptamer, and only IgE couple to the IgE aptamer on the graphene FET. Therefore, the selective sensing of the IgE was successfully carried out.

We have first succeeded in the selective sensing of IgE using the modified graphene FET.

11:00am **GR+NS+PS+SS-ThM10 A Molecular Dynamics Study of Chemical Modification of Graphene Oxide Sheets**, *T. Liang, B. Devine, S.R. Phillpot, S.B. Sinnott*, University of Florida

Graphene, the single-layered graphite, has attracted tremendous attention owing to its fascinating physical properties. One of the main obstacles in this field is to find an efficient and consistent approach to produce graphene sheets in large quantities. In addition to the mechanical exfoliation method, many chemical approaches have been developed to synthesize graphene on a large scale. The key intermediate product in these chemical approaches is the graphene oxide sheets, which are often heavily oxygenated with hydroxyl or epoxide functional groups on the surface and carbonyl or carboxyl groups at the edge. However the energetic and kinetics associated with graphene oxide sheets have not been elucidated in detail due to the inherent chemical complexity of the system. Here, a new dynamic charge empirical potential is presented that is used in classical molecular dynamics simulations to elucidate the dynamics of graphene oxidation and the resulting influence on their mechanical and structural properties. In addition, the oxygenating and hydrogenating processes of defective graphene sheets at room temperature in addition to elevated temperatures are presented. The findings are compared to the results of first principles density functional theory findings and to experimental data.

11:20am **GR+NS+PS+SS-ThM11 Enhancing and Controlling the Chemical Reactivity of Epitaxial Graphene via Growth Induced Strain**, *J.E. Johns*, Northwestern University, *Md.Z. Hossain*, Gunma University, Japan, *M.C. Hersam*, Northwestern University

The high electrical and thermal conductivity of graphene, as well as its two dimensional nature, has led to its rapid incorporation into any practical applications including high frequency analog transistors and transparent conductors. However, many other potential applications, such as excitonic switches, pseudospin devices, or digital logic circuits, require covalent chemical modification of graphene. Due to the chemical inertness of its pi bonded network, previous methods for covalently modifying graphene have required extreme, irreversible conditions including acidic treatments, high energy radical polymerization, and ion beam implantation. Here we present an alternative method for increasing the chemical reactivity of graphene by systematically altering the compressive strain of epitaxial graphene (EG) on SiC(0001). Depending on its annealing history, EG has been shown to have a compressive strain of 0% to 1% due to a mismatch of thermal expansion coefficients with the underlying buffer layer and silicon carbide substrate. Using differing thermal treatments, we show that the amount of strain in EG can be tailored, as verified by characteristic peak shifts of the 2D Raman band. The resulting chemical reactivity of the strained EG is studied at the atomic-scale using ultra-high vacuum scanning tunneling microscopy following reversible gas phase reactions of EG with oxygen and fluorine. These results suggest a new method for controlling the electronic properties of graphene, and provide fundamental insight into the nature of chemical bonding on EG.

11:40am **GR+NS+PS+SS-ThM12 Plasma-based Functionalization of Graphene with Primary Amines for Biomaterials Applications**, *S.G. Walton, M. Baraket, S.C. Hernandez, R. Stine, W.K. Lee, C.R. Tamanaha, P.E. Sheehan, J.T. Robinson, C.E. Junkermeier, T.L. Reinecke*, Naval Research Laboratory (NRL)

Graphene, a sp²-structured monolayer of carbon atoms, has attracted much interest for its fundamental science and its potential in many device applications. By tailoring its surface chemistry, material properties can be regulated and thus broaden the number of potential applications. In this work, we demonstrate that by chemically functionalizing graphene the

electrical properties and its interaction with adsorbates may be controlled. Electron beam generated plasmas produced in ammonia-containing gas, is used to controllably introduce nitrogen and primary amines. A study of the chemical, electrical and structural properties of the chemically-modified graphene at different functional group concentrations is discussed. In addition, the use of amine-functionalized graphene as a bio-sensing platform for DNA detection using a field-effect-transistor-based sensor is demonstrated. This work is supported by the Office of the Naval Research.

Magnetic Interfaces and Nanostructures Division

Room: 105 - Session MI-ThM

Emerging Magnetic Characterization and Results

Moderator: A.N. Caruso, University of Missouri-Kansas City

8:00am **MI-ThM1 The X-ray View of Ultrafast Nano Magnetism, H.A. Durr**, SLAC National Accelerator Laboratory **INVITED**

Polarized soft x-rays have been used over the past 20 years to obtain fascinating new insights into nanoscale magnetism. The separation of spin and orbital magnetic moments, for instance, enabled detailed insights into the interplay of exchange and spin-orbit interactions at the atomic level. X-ray and photoelectron imaging techniques have revolutionized our understanding of magnetism of the ULTRA SMALL. In addition the now available polarized soft x-ray pulses with only few ps down to 100 fs duration allow us to observe the magnetic interactions at work in real time, i.e. they open the door to study ULTRA FAST magnetism. The ultimate goal of such studies is to understand how spins may be manipulated by ultrashort magnetic field, spin polarized current or light pulses. In this talk I will give an overview of achievements and the current status of probing magnetism of the ultra small and ultra fast using x-rays from synchrotrons [1-3] and more recently from x-ray free electron lasers.

[1] I. Radu, K. Vahaplar, C. Stamm, T. Kachel, N. Pontius, H. A. Durr, T. A. Ostler, J. Barker, R. F. L. Evans, R. W. Chantrell, A. Tsukamoto, A. Itoh, A. Kirilyuk, Th. Rasing, A. V. Kimel, *Transient ferromagnetic-like state mediating ultrafast reversal of antiferromagnetically coupled spins*, Nature **472**, 205 (2011).

[2] M. Wietstruk, A. Melnikov, C. Stamm, T. Kachel, N. Pontius, M. Sultan, C. Gahl, M. Weinelt, H. A. Dürr, U. Bovensiepen, Hot-Electron-Driven Enhancement of Spin-Lattice Coupling in Gd and Tb 4f Ferromagnets Observed by Femtosecond X-Ray Magnetic Circular Dichroism, Phys. Rev. Lett. **106**, 127401 (2011)

[3] C. Boeglin, E. Beaurepaire, V. Halté, V. Lopez-Flores, C. Stamm, N. Pontius, H. A. Dürr, J.- Y. Bigot, *Distinguishing the ultrafast dynamics of spin and orbital moments in solids*, Nature **465**, 458 (2010).

8:40am **MI-ThM3 Spectroscopy of Magnetic Thin Films, S.N. Gilbert, N.H. Tolk**, Vanderbilt University

Recent studies of magnetic thin films and spintronic devices will be presented. Time-resolved Kerr Effect measurements of ferromagnetic/antiferromagnetic interfaces as a function of film layer thickness and antiferromagnetic spin orientation will be discussed. Magnetic and time-resolved spin characterization of novel spintronic devices and materials will also be shown.

9:00am **MI-ThM4 Detection and Control of Electronic Phase Competition in Complex Oxides, T.Z. Ward**, Oak Ridge National Laboratory **INVITED**

Electronic phase separation is present in many complex material systems and has been linked to colossal magnetoresistance, high T_c superconductivity, and multiferroicity. Here, nanometer to micron sized regions of vastly different electronic and magnetic properties can coexist and compete within single crystal materials. We will discuss recent work on fabricating single crystal wires of electronically phase separated manganites to a size comparable to the domains of the electronic phases residing in the material; thereby allowing finite emergent regions to dominate device characteristics. This has given us a means to probe, observe and exploit properties which are *hidden* in unconfined systems. Transport measurements on simple confined structures reveal new properties such as ultrasharp jumps in resistivity, a reemergent metal-insulator transition, and discreet resistive hopping that are unseen in larger samples. We have found that these properties are also tunable through doping, strain, electric field and magnitude of confinement. This ability to control key elements of the underlying complex electronic correlations and observe the resulting changes in a material's behavior help answer questions about the

fundamental physics that rule emergent phenomena in complex materials while opening the door to new device functionality.

9:40am **MI-ThM6 Room-Temperature Spin-Polarized Scanning Tunneling Microscopy of Topological Antiferromagnetic Nanopyramids on Mn₃N₂(001) Surfaces, K. Wang*, A.V. Chinchore, W. Lin, A.R. Smith**, Ohio University

Antiferromagnets play a critical role in spintronic applications such as pinning layers in magnetic memories. The development of spin-polarized scanning tunneling microscopy and spectroscopy (SP-STM/STS) has shown its unprecedented power in resolving the local spin and domain structures of antiferromagnetic surfaces down to atomic level.¹⁻⁶ While most efforts have been made on imaging metal surfaces at cryogenic temperatures, only a few have been devoted to the study of room-temperature magnetic systems.^{4,6} Here we apply SP-STM/STS to study the local spin and magnetic properties of a technologically driven material system which exhibits layer-wise antiferromagnetism with a very high Néel temperature (>900 K)⁷. Mn₃N₂(001) thin films have been grown on MgO(001) substrates using ultra high vacuum plasma-assisted molecular beam epitaxy and transferred *in situ* to a home-built room-temperature SP-STM⁸ for magnetic imaging. Results have shown that the surface exhibits a *topological spin pyramid* structure with alternating single Mn- and double MnN- layers, where the magnetism is strongly correlated with the surface topography. Using SP-STM with *dl/dV* mapping, different layers can be clearly distinguished due to their different conductance. These differences in the conductance are a result of not only the different chemical environments, but also the spin ordering and the broken symmetry at the surface. We will show that it is possible to separate the contributions from both the electronic and the magnetic structure by applying a small magnetic field. The field rotates the tip magnetization axis causing concomitant change in the magnetic sensitivity while keeping the electronic structure unchanged. The demonstrated ability of direct imaging at room-temperature of the surface antiferromagnetic terraces allows further (ongoing) studies on the interplay between structural defects such as anti-phase domain boundaries and the formation of intriguing antiferromagnetic domains. We gratefully acknowledge support from the Department of Energy and the National Science Foundation.

1. R. Wiesendanger, Rev. Mod. Phys. **81**, 1495 (2009)

2. M. Bode *et al*, Nature Materials **5**, 477 (2006)

3. S. Heinze *et al*, Science **288**, 1805 (2000)

4. R. Wiesendanger *et al*, Science **255**, 583 (1992)

5. T. Kawagoe *et al*, Phys. Rev. Lett. **95**, 207205 (2005)

6. H. Yang *et al*, Phys. Rev. Lett. **89**, 226101 (2002)

7. A. Leineweber *et al*, J. Mater. Chem. **10**, 2827 (2000)

8. K. Wang *et al*, Rev. Sci. Instrum. **82**, 053703 (2011).

10:40am **MI-ThM9 Growth Strategies for Mn Doping of Ge Quantum Dots: An STM Study of Reactions, Bonding and Phase Formation, C.A. Nolph†††††, K.R. Simov, P. Reinke**, University of Virginia

Manganese doped, magnetic germanium quantum dots are predicted to be important building blocks for the future of spintronic devices. The combination of quantum confinement and carrier mediated ferromagnetism make these structures particularly interesting. The goal of this work is to understand and control the Mn environment within the Si(100), Ge wetting layer and Ge quantum dot (QD) systems and understand how it influences the magnetic properties. Samples were investigated primarily using scanning tunneling microscopy followed by magnetic analysis using a vibrating sample magnetometer and one sample with x-ray magnetic circular dichroism. An important materials question is the competition to form secondary phases in this system at elevated temperatures, particularly Mn₅Ge₃ and Mn₁₁Ge₈ which are both ferromagnetic (TC = 294 – 296 K). We investigate three routes for Mn doping of Ge QDs : (1) The investigation of the stability and evolution of Mn nanostructures on a Si(100)-(2x1) reconstructed surface as a function of annealing temperature up to temperatures typical for Ge QD growth. At an annealing temperature of approximately 316°C, Mn adatoms move into Si sub-surface sites and we observe an electronic effect consistent with acceptor dopants. (2) The use of a surface driven approach where Mn is deposited on the Ge QD surface and forms well-defined islands on the QD and wetting layer surface. We observed the behavior of the Mn islands during STM measurement with increasing annealing temperatures and how the islands evolved via ripening and migration across the surfaces. In addition the structure and bonding of the Mn islands specifically on the Ge {105} facets will be discussed. (3) The co-deposition of Ge and Mn throughout the Ge QD growth process. For route (3) the highest Mn concentration is 23% which results in only minor perturbations in the Ge QD growth (fewer and smaller Ge QDs), albeit

* Falicov Student Award Finalist

secondary phases form on the surface. Lower concentration samples (5% and 8% Mn) yielded high quality quantum dots and no observable secondary phases on the surface. We presume that when secondary phases form, the majority of the Mn deposited is consumed to form the secondary phases. The competition to form secondary phases is investigated further utilizing scanning auger microscopy to map Mn and low energy electron microscopy to study the growth sequence as a function of Mn concentration. Magnetism results from one particular sample (Mn_{0.05}Ge_{0.95} QD) indicate a ferromagnetic material with a Curie temperature above room temperature. We'd like to acknowledge our funding support from NSF CHE-0828318 and DMR-0907234.

11:00am **MI-ThM10 Novel Iron-Induced Structures on Gallium Nitride (0001) and (000-1) Studied Using Scanning Tunneling Microscopy and First Principles Theory**, *W. Lin*, Ohio University Nanoscale and Quantum Phenomena Institute, *H.A.H. Al-Britihen*, Ohio University Nanoscale and Quantum Phenomena Institute and KAIN, King Saud Univ., Saudi Arabia, *K.K. Wang, A.V. Chinchore, M. Shi, Y. Liu, N. Takeuchi, A.R. Smith*, Ohio University Nanoscale and Quantum Phenomena Institute

There is much interest in the field of spintronics in which magnetic phenomena are combined with electronic properties to form a new class of materials with added device functionality. An essential area is that of magnetic nanostructures on the surface of semiconductors. Gallium nitride represents one of the most important next generation semiconductors. The possibility for long spin lifetimes in GaN make it attractive as a spintronic material as well.[1] From this perspective, it is important to explore the epitaxial growth of ferromagnetic layers such as Fe at the surface of GaN. New results for the growth of Fe-induced structures on wurtzite GaN will be presented in this talk.

These investigations are carried out using a custom-designed, home-built molecular beam epitaxy/scanning tunneling microscopy (MBE/STM) facility. Growth of iron on GaN is carried out using an Fe effusion cell and at a substrate temperature which is carefully selected in order to produce the highest quality atomically-smooth Fe-induced structures. It is found that the Fe-induced structures on Ga-polar GaN(0001) strongly depends on the presence of the pseudo-1×1 surface structure as a starting surface, and that under the correct conditions a clear 6×6 reconstructed island structure grows outward from the GaN step edges, as revealed in scanning tunneling microscopy images. First-principles theoretical calculations have been carried out which suggest a low-energy model for the 6×6 structure consisting of Fe atoms embedded within the pseudo-1×1 layer and with Ga adatoms at the top.

The results for N-polar GaN(000 $\bar{1}$) are quite different. In this case, deposition of Fe onto a Ga-rich surface results in the formation of uniform-height Fe-induced islands having a 4×2 zigzag row structure. The zigzag rows orient along the high symmetry [11 $\bar{2}$ 0] directions of the surface.

Efforts are also underway to investigate the chemical stoichiometry, and electronic and magnetic properties of these Fe-induced structures and to explore the evolution of these monolayer films as additional Fe and/or Ga is added to the surface.

This work has been supported by the U.S. Department of Energy, Office of Basic Energy Sciences (Grant No. DE-FG02-06ER46317). Additional support from the National Science Foundation (Grant No. 0730257) is also acknowledged.

Y.L. is now at Los Alamos National Laboratory, Los Alamos, NM.

N.T. was a visiting Presidential Scholar from the Universidad Nacional Autónoma de México during 2010-11.

[1] J.H. Bub, J. Rudolph, F. Natali, F. Semon, and D. Hagele, "Anisotropic electron spin relaxation in bulk GaN," *Appl. Phys. Lett.* **95**, 192107 (2009).

11:20am **MI-ThM11 Scanning Tunneling Microscopy and Spectroscopy Performed on Single Mn Monolayer on Wurtzite (000-1) GaN**, *A.V. Chinchore, K.K. Wang, A.R. Smith*, Ohio University, *V. Ferrari, A. Barral*, University of Buenos Aires, Argentina

The III-V diluted magnetic semiconductors (DMS) are a new class of materials with promising applications in spintronics.[1] The low solubility of transition metal atoms into III-V semiconductor host has been a key concern in the successful development of DMS. This low solubility however was used to advantage by Lu et.al. to develop an ideal magnetic/semiconductor bi-layer [2]. Wang et.al. recently reported high density 2D Mn-Ga stripe phases on Ga-Polar GaN(0001) surface, with interesting atomic spin arrangement. [3] The N-Polar GaN(000 $\bar{1}$) 1×1 structure offers an added advantage over the Ga-Polar structure, as the Mn atoms deposited on this surface are in closer proximity to the N atoms favoring the GaMnN bonding.

We have conducted a series of experiments aimed at understanding the behavior, electronic and magnetic properties of Mn atoms on N-Polar GaN(000 $\bar{1}$) 1×1 surface. The experiments were conducted in a custom built MBE-STM system with *in-situ* sample transfer ability. The growth is monitored with reflection high energy electron diffraction (RHEED). The standard GaN(000 $\bar{1}$) 1×1 surface was prepared and was exposed to sub monolayer doses of Mn at various temperatures. It was observed that the behavior of Mn atoms on GaN(000 $\bar{1}$) 1×1 surface is highly sensitive to the substrate temperature (T_s). The low temperature Mn deposition, $T_s \sim 100$ °C, led to the formation of a metastable 3×3 structure which transformed to a more stable $\sqrt{3} \times \sqrt{3}$ R30° structure, when the sample is heated to $T_s \sim 120$ °C, as confirmed by RHEED. It was observed that the $\sqrt{3} \times \sqrt{3}$ R30° structure is stable up to 750 °C. The temperature dependent behavior of the structures suggests that the Mn atoms are *physisorbed* while forming the metastable structure and they are *chemisorbed* in the case of the stable $\sqrt{3} \times \sqrt{3}$ R30° structure. The STM measurements performed on the Mn 3×3 structure showing the metastable nature of the structure are presented as well as the STM and STS results showing the characteristics of $\sqrt{3} \times \sqrt{3}$ R30° surface. RHEED simulations confirming the surface atomic arrangement for the structure are presented. The theoretical calculations are performed using the first principles and the Tersoff-Hamann simulation method. The results indicate that the Mn atoms push the Ga atoms laterally in the surface ad-layer forming bonds directly with the bilayer N atoms. The funding from NSF and DOE for the project is greatly acknowledged.

References.

- [1] T. Dietl et.al. *Science* 287, 1019 (2000).
- [2] E. Lu et.al. *Phys. Rev. Lett.* 97, 46101 (2006).
- [3] K. Wang et.al. *Phys. Rev. B* 83, 165407 (2011)

11:40am **MI-ThM12 Designing of Engineered Multiferroic Composites by Radical Enhanced Atomic Layer Deposition**, *J.H. Choi, T.E. Quickel, S. Tolbert, J.P. Chang*, University of California Los Angeles

Multiferroic materials induced polarization under external magnetic field H, or induced magnetization under external electric field E. Magnetolectric (ME) phenomena in multiferroic materials holds considerable promises because of their potential applications in spintronics, such as magneto-electric sensors, magneto-capacitive devices, and electrically driven magnetic data storage. The ultimate goal for practical device application of multiferroic materials is dependent on how to create strong ME coupling between different types of ferroic order. The strictive interaction between the piezoelectricity of the ferroelectric (FE) phase and the magnetostriction of the ferromagnetic (FM) phase lead to produce larger ME coefficients than single phase multiferroic materials. Thus, the research has been directed towards designing engineered multiferroic composite materials in the form of horizontal multilayer (2-2), vertical superstructures (3-1) or other nanoparticle composite structures (3-0) in a precise controlled manner.

In this work, the BiFeO₃ (BFO) and Pb(ZrTi)O₃ (PZT) thin film were synthesized by radical enhanced atomic layer deposition (RE-ALD). RE-ALD is a gas-phase technique in which precursor vapors are pulsed alternately into the reaction chamber and the thin film growth proceeds through surface reactions in a self limiting manner. The advantages of ALD include excellent conformality, simple and accurate thickness control and good uniformity on large areas. In order to demonstrate conformal deposition of engineered multiferroic materials in the form of 3-0 or 2-2 configuration, PZT and BFO was deposited onto a mesoporous CoFe₂O₄ (CFO) substrate by RE-ALD.

The mesoporous CFO films were found to be fully filled by ALD PZT and BFO. The composition and crystal structure of the PZT-CFO and BFO-CFO systems were confirmed by X-ray Photon Spectroscopy and X-ray Diffraction (XRD), respectively. More detail crystal structure were investigated by synchrotron XRD and extended x-ray absorption fine structure spectroscopy (EXAFS). The magnetic and ferroelectric properties for the PZT-CFO or BFO-CFO systems were characterized by a superconducting quantum interference device (SQUID) magnetometer and piezoresponse force microscopy (PFM). Magnetic properties such as coercive magnetic field (H_c) and saturation moment (M_s) were systematically analyzed on composite systems and the pure CFO substrate. In addition, The P-E loops for PZT-CFO and BFO-CFO thin films were measured at room temperature and the saturation polarization (P_s) and coercive field (E_c) were investigated with respect to thickness and crystal plan.

Molecular Assembly and Devices

Moderator: W. Gao, Brigham and Women's Hospital and Harvard Medical School

8:20am **NS-ThM2 Chemical Modification and Patterning of Self Assembled Monolayers using Scanning Electron and Ion-Beam Lithography**, *M.J. Perez Roldan, C. Pascual Garcia, G. Marchesini, D. Gilliland, G. Ceccone, P. Colpo, F.J. Rossi*, European Commission, JRC Institute for Health And Consumer Protection, Italy

We present chemical modification of self assembled monolayers (SAMs) using electron and ion-beam lithographies. We used thiolated polyethylene oxide (PEO) SAMs on gold to fabricate chemically contrasting patterns at the nanoscale. Patterned surfaces were characterized by X-ray photoelectron spectroscopy (XPS), time of flight-secondary ion mass spectrometry (ToF-SIMS). Results showed a chemical modification of surfaces patterned by means of electron beam (e-beam) lithography and a removal of PEO SAMs on the areas treated with the ion beam. The chemical modification of PEO SAMs converted the non-fouling surfaces on fouling surfaces.

8:40am **NS-ThM3 Interlocking Pinwheel Chains Formed by Self Assembly of Aromatic Cyanides**, *M. Luo, W. Lu, E. Chu, D. Kim, Z. Cheng, D. Sun, K. Cohen, Y. Zhu, J. Wyrick*, University of California, Riverside, *T.L. Einstein*, University of Maryland, College Park, *L. Bartels*, University of California, Riverside

As part of a bottom-up strategy, molecular self assembly can be a promising technique to create surface patterns with ultimately small feature sizes in an economic efficient fashion. Understanding of the factors which guide molecules into different patterns thus become an important goal for prediction and control of molecular patterns structures.

Here we present the formation of interlocked arrays ('gear chains') of pinwheels through self-assembly of 3-phenyl-propynenitrile (PPN) molecules on a Cu(111) surface. Variable temperature scanning tunneling microscopy (STM) reveals upon molecular deposition a pattern of small hexagonal features, which coalesce into sequences of larger, interlocking pinwheel-shaped structures. The pinwheels have an outer diameter as large as ~4nm. The driving force of this entropically disfavored pinwheel formation is discussed.

9:00am **NS-ThM4 Electronics and Mechanics of Single Molecule Circuits**, *L. Venkataraman*, Columbia University **INVITED**

Understanding and controlling electron transfer across metal/organic interfaces is of critical importance to the field of organic electronics and photovoltaics. Single molecule devices offer an ideal test bed for probing charge transfer details at these interfaces. Results from these single-molecule measurements can be directly related directly theoretical models, unlike measurements at the ensemble level. The ability to fabricate single molecule devices and probe electron transfer reliably and reproducibly has enabled us to study and model transport through them.

In this talk, I will review the scanning tunneling microscope break-junction technique we use to measure electronic transport through single molecule junctions. I will discuss our measurements using novel metal-molecule link chemistries, including amines, phosphines[1] and results from recent work using tri-methyl tin linkers, which yield direct Au-C coupled single molecule junctions[2]. I will show how the intrinsic molecular properties influence measured single molecule conductance and bond rupture forces[3]. Finally, I will show how a mechanically controlled binary single molecule switch can be created using bipyridine molecules[4].

[1] Y. S. Park et al., *J. Am. Chem. Soc.* 129, 15768 (2007).

[2] Z.-L. Cheng et al., *Nat. Nano.* In Press (2011).

[3] M. Frei et al., *Nano Lett.* 11, 1518 (2011).

[4] S. Y. Quek et al., *Nat. Nano.* 4, 230 (2009).

9:40am **NS-ThM6 Complex Rotation Mechanisms of a Molecular Machine Probed by STM**, *H. Kersell, U.G.E. Perera, Y. Zhang*, Ohio University, *C. Joachim, G. Rapenne, G. Vives, X. Bouju*, CNRS, Cemes, France, *S.-W. Hla*, Ohio University

The complex rotation of a ruthenium based double-decker molecular rotor is resolved via ultrahigh vacuum low temperature scanning tunneling microscopy. The study was performed at temperatures of 4.2 K and 77 K on a Au(111) substrate. Inelastic electron tunneling (IET) was utilized to induce stepwise rotation of the molecule with respect to the surface. Subsequent rates of molecular switching, induced via tunneling currents,

display sets of discrete energy minima with respect to the molecular stator and to the surface. The molecular rotator is composed of a set of semi-rigid arms whose non-rigid components, upon IET induced rotation, are observed to change conformation to the particular energy minima of the rotor. The resulting STM images were compared to calculated images of the same molecule. Additionally, the rotator was dissociated, revealing an intact stator adsorbed on the Au(111) surface. We acknowledge the financial support of US-DOE; DE-FG02-02ER46012, and NSF-PIRE; OISE 0730257 grants.

10:40am **NS-ThM9 Self-Assembled Double Strand DNA Monolayers as Spin Filters**, *Z. Xie, S.R. Cohen, T.Z. Markus, R. Naaman*, Weizmann Institute of Science, Rehovot Israel

Spin control provides new and interesting opportunities for control and study of the factors governing electron transport. Recent work by Naaman and co-workers has shown that self-assembled monolayers of double stranded DNA (ds-DNA) can act as a spin filter for electrons photoemitted from a gold substrate.[1,2] This phenomenon depends on the helicity of the ds-DNA, which leads to spin polarization and consequent capture of filtered electrons that tunnel back to the substrate. In this work, this effect is investigated for electron flow between two electrodes, a bottom Ni electrode to which one strand of the DNA is bound, and a top gold nanoparticle electrode which serves to identify the ds-DNA and provide good electrical contact through binding to the complementary strand. The current characteristics are measured by conductive scanning probe microscopy, as applied in a previous study of electron transport in DNA monolayers.[3] A magnetic field of approximately 0.3 T at the surface is provided by a permanent magnet placed below the sample. The results are consistent with the photoemission work, namely marked differences in the current flow depending on magnetic field alignment. Furthermore, the effect depends on length of DNA chain, with longer chains providing a more significant effect relative to shorter ones. These experimental findings, together with a physical model will be presented.

[1] Goehler, et al, *Science* 331, p. 894 (2011).

[2] Ray, et al, *Phys. Rev. Lett.*, 96, 03101 (2006).

[3] Nogues et al, *J. Phys. Chem. B* 110, 8910 (2006).

11:00am **NS-ThM10 Controllable Phase Transition Using a Probing Tip**, *Q. Li*, Oak Ridge National Laboratory

Molecular Self-assembled monolayers have applications in many different fields, such as sensing, lubrication and molecular electronics. In our study, a movie containing more than 50 STM images is acquired to investigate the dynamic behavior of the phenyl-acetylene molecular assembly process on Au(111) surface at LN2 temperature. Besides that, we found the phenyl-acetylene molecules are very sensitive to the polarity of the bias voltage. Therefore, phase transition between molecular ordered and disordered structure can be controllably achieved by applying positive or negative bias voltage. Systematically study of the phase transition process turned out it may be related to the charging effect of the molecules.

11:20am **NS-ThM11 How Size, Shape, and Bond Strain Affect Electronic Structure in sp³ Carbon-Cage Molecules**, *T.M. Willey, J.R.I. Lee*, Lawrence Livermore National Lab, *L. Landt, D. Wolter*, Technische Univ. Berlin, Germany, *M. Bagge-Hansen*, Lawrence Livermore National Lab, *P.R. Schreiner, A.A. Fokin, B.A. Tkachenko, N.A. Fokina*, Justus-Liebig Univ. Giessen, Germany, *T. van Buuren*, Lawrence Livermore National Lab, *D. Brehmer*, Stanford Synchrotron Light Source

Novel nanocarbons such as fullerenes, nanotubes, graphene, and nanodiamond reside at the cutting edge of nanoscience and technology. This paper presents a fundamental study of how size, shape, chemical functionalization, and bond strain affect electronic structure in several benchmark series of chemically pure, novel carbon-cage compounds ranging from diamondoids (a fully sp³ form of nanodiamond) to cubane. Size and shape are studied with the diamondoid series from adamantane to hexamantane, where the observed gap changes are primarily due to evolution in occupied states, as measured with photoelectron spectroscopy (XPS & UPS). Bond strain is studied with dodecahedrane, octahedrane, and cubane, where increasing bond strain leads to two major changes in the near-edge x-ray absorption fine structure (NEXAFS) spectra. First, a broad C-C σ^* resonance in the absorption splits into two more narrow and intense resonances with increasing strain. Second, the first manifold of states previously associated with tertiary C-H σ^* in the diamondoid series appears to broaden and shift to lower energy. This feature is more than twice as intense in cubane as octahedrane, even though these two molecules have similar stoichiometries (C₁₂H₁₂ vs. C₈H₈). We attribute the additional intensity to π^* states, indicating a high degree of p interaction between parallel C-C bonds in the cubane.

11:40am **NS-ThM12 Effect of Acetylene Concentration and Thermal Ramp Rate on the Growth of Spin-capable Carbon Nanotube Forests.** *K.H. Lee, D. Burk, L.J. Overzet, G.S. Lee*, The University of Texas at Dallas

Spin-capable multi-walled carbon nanotube (MWCNT) forests that can form webs, sheets, and yarns provide a promising means for advancing various technologies [1-4]. The important factors enabling the growth of the spin-capable forests are still not well understood. Growing spin-capable CNT forests depends on several growth factors such as the catalyst film thickness, the growth temperature, and the carrier and reactant gases [5-9]. Other factors still remain to be investigated more thoroughly. These include the flow rate (or ratio) of the reactant gas, the reactant gas species, and the pressure.

Herein we show how both the spinning capability and morphology of MWCNT forests are changed significantly by controlling the acetylene (C_2H_2) concentration and the thermal ramp rate. The acetylene gas flow is varied in the range of 0.25 ~ 7.5 % in volume. The MWCNTs grown at C_2H_2 concentrations between 1.5 ~ 3.5 % are well-aligned and are spin-capable. The well-aligned forests have higher areal density and shorter distances between the CNTs caused by strong Van der Waals interactions. CNTs grown at C_2H_2 concentrations under 1.5 % or over 3.5 % are curled and have random orientation. The resulting forests have reduced areal density and have poor spinnability. The thermal ramp rate is varied from 30 °C/min to 70 °C/min. Only the CNT forests grown with 50 °C/min condition are well-aligned and spinnable due to high areal density and closer spacing between adjacent CNTs. This condition alone results in Fe nanoparticles which have the proper size and density to produce spin-capable CNT forests.

Figure 1 shows SEM images and picture of spin-capable CNTs grown at 1.5 vol.% of acetylene and 50 °C/min on 70kΩ/sq Fe film at 780°C for 5min with mixture of He, H_2 , and C_2H_2 . The spinnable CNTs of 330 μm have good alignment which is dependent on the ability to form ribbons. From a 1 × 1 cm substrate, the CNTs can form a 4 m length sheet.

- [1] M. Zhang et al., *Science* **306**, 1358 (2004).
- [2] X. Zhang et al., *Adv. Mater.* **18**, 1505 (2006).
- [3] M. Zhang et al., *Science* **309**, 1215 (2005).
- [4] A. E. Aliev et al., *Science* **323**, 1575 (2009).
- [5] M. Zhang et al., *Science*, **306**, 1358 (2004).
- [6] X. Zhang et al., *Adv. Mater.*, **18**, 1505 (2006).
- [7] X. Zhang et al., *Small*, **3**, 244 (2007).
- [8] K. Liu et al., *Nano Lett.*, **8**, 700 (2008).
- [9] J-H. Kim et al., *Carbon*, **48**, 538 (2010).

Plasma Science and Technology Division Room: 202 - Session PS+TF-ThM

Plasma Deposition and Plasma Enhanced ALD Moderator: S.-P. Tay, Mattson Technology Inc.

8:00am **PS+TF-ThM1 High Quality SiNx by Microwave RLSA Plasma Enhanced Atomic Layer Deposition.** *T. Karakawa, M. Oka, N. Fukiage, H. Ueda, T. Nozawa*, Tokyo Electron Technology Development Institute, INC., Japan

Shrinking critical dimensions of Ultra Large Scale Integration (ULSI) and optical device structures continue to drive advances in semiconductor fabrication processes. Three dimensional (3D) and metal gate structures for example, require low temperature dielectric layers (e.g., SiO₂ and SiN_x) with dimensions and film quality that may be met only by Plasma Enhanced Atomic Layer Deposition (PEALD) [1]. In addition to film quality and conformality, minimizing plasma damage in the PEALD process sequence is imperative. Prior to this work we characterized PEALD SiO₂ deposition in a Radial Line Slot Antenna (RLSA) plasma source using bis-tertiarybutyl-amino-silane (BTBAS) as a precursor [2]. In this study, we determined RLSA ALD process conditions favorable for SiN_x film formation. The Si ALD precursor was dichlorosilane (DCS) and nitridation employed a NH₃, N₂ and Ar RLSA plasma. The wafer temperature was controlled below 400°C during the ALD process. Precursor adsorption time, process temperature, nitration time, plasma power were varied in order to determine the RLSA Plasma conditions resulting in the best SiN_x ALD film quality. We obtained very high quality SiN_x films having almost the same HF wet-etching rate as thermal LP-CVD SiN_x (720°C) film. In this presentation, the results of Angle Resolved X-ray Photoelectron Spectroscopy (ARXPS) analyzed RLSA ALD deposited SiN_x films will be presented. We found that the sub-nitride bonding ratio of the SiN_x film was

strongly correlated with the HF wet-etching rate, a measure of the film quality. The lower sub-nitride bonded SiN_x film such as Si₃N₄ was created by the RLSA plasma at low temperature with low plasma damage. The reason so little damage occurs is the low rate of ion bombardment on new Si₃N₄ surfaces during plasma nitridation.

- [1] S. Yokoyama et al., *Applied Surface Science* **112** (1997) 75-81
- [2] Y. Osawa et al., *Proceedings DPS-2009*, 2-P51

8:20am **PS+TF-ThM2 Composition, Morphology and Optical Dispersion of Plasma Polymerized Titanium Oxide Derived Using PECVD.** *L. Sun*, General Dynamics Information Technology, *A. Reed*, Air Force Research Laboratory, *H. Jiang*, General Dynamics Information Technology, *J.T. Grant*, University of Dayton Research Institute, *R. Jakubiak*, Air Force Research Laboratory

In this work plasma-polymerized (PP-) TiO_xC_y films derived from titanium (IV) isopropoxide (TTIP) were deposited onto Si and KBr substrates using remote, room temperature plasma enhanced chemical vapor deposition (PECVD). The composition and morphology of the films was varied by systematically changing the ratio of Ar to O₂ in the carrier gas. Chemical compositions were investigated by FTIR and X-ray photoelectron spectroscopy (XPS). Morphological data derived atomic force microscopy (AFM) and scanning electronic microscopy (SEM) studies showed that the morphology was strongly dependent on the ratio of oxygen to total carrier gas composition. The films grown with Ar as the majority carrier gas have a featureless, smooth, one phase 3-D crosslinking morphology due to the incomplete oxidation of Ti to the most stable Ti⁴⁺ valence state during deposition in an oxygen poor environment. As the mixture of carrier gas became more O₂ rich a second phase evolved that had a columnar structure attributed to TiO₂. This increase in oxidation was also noted in high resolution XPS measurements where a peak corresponding to a carboxyl group in the C 1s spectrum increases with increasing O₂ concentration. Development of the structured second phase was also noted in the optical dispersion obtained by spectroscopic ellipsometry. In order to fit the data, an anisotropic model has to be used that took into account the surface roughness determined from the AFM and SEM studies.

8:40am **PS+TF-ThM3 Plasma Deposition of Carbide-Based Composite Membranes for Hydrogen Purification.** *C.A. Wolden*, Colorado School of Mines **INVITED**

We introduce a new class of composite membranes based on transition metal carbide as economical alternatives to palladium for high temperature purification of H₂. In this talk we describe two membrane concepts that were synthesized using plasma-enhanced chemical vapor deposition (PECVD) and magnetron sputtering. The first is a surface diffusion membrane comprised of nanostructured Mo₂C deposited on porous ceramic supports. Stoichiometric Mo₂C was fabricated using a two step synthesis process. Dense molybdenum oxide films were first deposited by plasma-enhanced chemical vapor deposition (PECVD) using mixtures of MoF₆, H₂, and O₂. Oxide films 100 – 500 nm in thickness were then converted into molybdenum carbide using temperature programmed reaction using mixtures of H₂ and CH₄. Permeation testing of these membranes showed very high flux, but limited selectivity. To address this issue we describe a counterflow PECVD approach that we are developing which is used to both modify the pore size of the original supports as well as to repair pinholes that develop during the carburization.

The second strategy is to produce dense composite membranes comprised of Mo₂C layers sputtered onto BCC metal foils. BCC metals (V, Ta, Nb) and their alloys have extremely high permeability for atomic hydrogen, but negligible catalytic activity for hydrogen dissociation. Platinum group metals have been used as catalysts, particularly palladium, but at elevated temperature they alloy with the underlying metal and rapidly lose their activity. In contrast, the Mo₂C/V membranes described in this work displayed no change in permeability when operated at high temperature for >160 hours, and transmission electron microscopy confirmed that negligible interdiffusion occurs between these materials during testing. Hydrogen dissociation is the primary factor limiting hydrogen transport, as evidenced by the sensitivity of performance to carbide morphology. Sputter parameters were systematically varied to optimize the crystal structure and morphology. These composite membranes are perfectly selective to H₂, with permeability values approach and in fact exceed that of pure palladium. These findings demonstrate the potential of low cost group V metals for H₂ separations with simultaneous carbon capture at temperatures compatible with the processes used for H₂ generation.

9:20am **PS+TF-ThM5 Quantum Dot Sensitized Solar Cells using Nanoparticles of Si Compounds Fabricated by Multihollow Discharge Plasma CVD**, *M. Shiratani, G. Uchida, M. Sato, Y. Wang, K. Koga, N. Itagaki*, Kyushu University, Japan

Quantum dot sensitized solar cells using semiconductor nano-particles have attracted much interest because they are expected to have a high efficiency and a low manufacturing cost. Narrow band-gap semiconductors such as CdS, PbS, and CdSe are employed as sensitizers, and they transfer photo-generated electrons in them to large band-gap semiconductors such as TiO₂ under light excitation. Our interest has been concerned with quantum dot solar cells using Si compound nano-particles because Si is abundant and has little toxicity. We have succeeded in producing Si nano-particles of a narrow size dispersion using a multi-hollow discharge plasma CVD method [1], and have applied them to Si quantum dot sensitized solar cells [2]. In our CVD system, discharges were sustained in 8 small holes of 5 mm in diameter at SiH₄ and H₂ flow rates of 2 and 448 sccm. Si nano-particles were nucleated, grew in SiH₄/H₂ plasma produced inside small holes, and were transported to the downstream region by neutral gas flow. We also performed surface nitridation of Si nano-particles to terminate dangling bond of the surface. Our experiments clearly demonstrated advantages of nitridation of Si nano-particles on the device performance; the short circuit current of Si QDs sensitized solar cells showed 1.3 times higher value by the nitridation and a photon to current conversion efficiency (PCE) achieved a high value of 40% at short wavelength of 350nm [3, 4]. Moreover, quantum dot sensitized solar cells using FeSi nanoparticles show better performance than those using Si nanoparticles. We will compare characteristics of three kinds of quantum dot sensitized solar cells using Si, Si/SiN core shell, and FeSi nanoparticles and discuss relationship between optical and electrical properties of the nanoparticles and the device performance.

- [1] T. Takeya, et al.: Thin Solid Films 506-507 (2006) 288.
- [2] Y. Kawashima, et al.: Trans. Mater. Res. Soc. Jpn. 35 (2010) 597.
- [3] G. Uchida, et al.: Phys. Status Solidi C, (2011) at press.
- [4] G. Uchida, et al.: submitted to Jpn J. Appl. Phys.

9:40am **PS+TF-ThM6 Structure of Organosilicon Polymeric Films Obtained by Expanding Thermal Plasma Chemical Vapor Deposition**, *P.H. Tchoua Ngamou, M.C.M. van de Sanden, M. Creatore*, Eindhoven University of Technology, the Netherlands

Organosilicon polymeric thin films (SiC_xHyOz) have attracted considerable interest due to their wide range of applications such as interlayers in gas/moisture diffusion multi-layer systems, low dielectric constant interconnect materials in microelectronic circuits and biocompatible coatings for medical implants, to name a few. An accurate control of the microstructure and composition of the films is generally required to meet specific requirements in the above-mentioned applications.

In this contribution, we report on the control of the composition and structure of films deposited in Ar/organosilicon precursor mixtures by using a remote plasma, i.e. the expanding thermal plasma, CVD process. The characterization of the deposited layers has been carried out by means of Fourier-transform infrared spectroscopy (FTIR), spectroscopic ellipsometry and X-ray photoelectron spectroscopy (XPS). The characterization of thin films showing a tunable chemical composition and optical properties has allowed identifying the main dissociation paths of the deposition precursor as controlled by the argon ions and electrons emanating from the plasma source, i.e. a cascaded arc, in the downstream region, where the monomer is injected. In particular, Ar ions are responsible for the charge exchange reaction with the monomer and electrons participate to the dissociative recombination with the molecular ions generated in the first reaction, as already proven in the case of other molecular gases [1]. An optimum in the monomer structure retention of 35 % has been observed under conditions of low plasma reactivity, i.e. high monomer flow-to-(Ar⁺,e⁻) flow rate ratio.

- [1] M. Creatore, Y. Barrell, J. Benedikt, M.C.M. van de Sanden, Plasma Sources Science & Technology 15 (2006) 421-431.

10:40am **PS+TF-ThM9 Impact of VUV Photons and Ions on Metal Oxide Films Prepared by Plasma-Assisted ALD with Substrate Biasing**, *H.B. Profijt*, M.C.M. van de Sanden, W.M.M. Kessels*, Eindhoven University of Technology, Netherlands

The interest in plasma-assisted atomic layer deposition (ALD) has increased rapidly over the last

years, since it has been demonstrated that the presence of a plasma step can improve material

properties and ease processing conditions. Although it is known from other plasma-based techniques that

the photons and ions can play an important role during processing, their presence and influence have not

systematically been addressed so far for the specific case of plasma-assisted ALD. In this contribution,

we present a detailed investigation of the impact that VUV photons and energetic ions can have on the

properties of metal oxide thin films prepared by plasma-assisted ALD. We will demonstrate the

detrimental impact that VUV photons can have on electrical properties and we show that structural

material properties can be controlled by tuning the ion energy through substrate biasing. Optical

emission, retarding field energy analyzer, and Langmuir probe measurements were carried out in three

R&D plasma-assisted ALD reactors. In the O₂ plasmas employed, vacuum ultraviolet (VUV) photons with

energies up to 9.5 eV were detected and these photons were found to be able to generate electronic

defects at thin film interfaces. This was demonstrated by experiments in which Al₂O₃ passivated Si(100)

samples were exposed to O₂ plasmas. By exposing the samples through quartz and MgF₂ windows, the

role of ions was excluded and the specific role of the high energy VUV photons was confirmed

unambiguously. Furthermore, during regular ALD conditions, an ion energy of ~30 eV was measured.

This energy is sufficient to contribute to the ALD process by, e.g., the displacement of lattice atoms and

enhancement of the ALD surface reactions, however, it is low enough to prevent substantial damage to

the deposited layers. The impact of the ions was further explored by enhancing the energy of the ions

through the implementation of substrate biasing, either through substrate self-biasing or by RF biasing.

By enhancing the ion energy up to 230 eV, these experiments demonstrated that at 300°C the crystallinity

of TiO₂ films can be changed from the anatase to the rutile crystalline phase. Moreover, at a substrate

temperature of 200°C the rutile phase can be obtained when employing substrate biasing while normally

amorphous TiO₂ is obtained. These results are particularly significant as generally the deposition of rutile

TiO₂ is difficult to achieve by ALD due to substrate temperature limitations imposed by the precursors

used. It is therefore evident that substrate biasing is a promising method to extend the possibilities of ALD.

11:20am **PS+TF-ThM11 Plasma Enhanced Atomic Layer Deposition and Plasma Etching of Gadolinium Oxide High-k Gate Dielectrics**, *S.A. Vitale*, MIT Lincoln Laboratory, *C. Hodson*, Oxford Instruments Plasma Technology, UK

Lanthanide series oxides are being evaluated as second-generation high-k gate dielectric materials. In addition to improving transistor electrostatics by reducing the equivalent oxide thickness (EOT), using lanthanide series gate oxide capping layers allows the effective metal gate workfunctions to be tuned toward the silicon band edges, providing the correct transistor threshold voltages. However these non-traditional CMOS materials have several integration challenges that must be overcome, including depositing a thermally-stable, high quality film with low fixed charge and high-k, without damage to the underlying layers of the gate stack. In addition, in some gate-first and gate-last approaches, the oxide must be etched from the source/drain regions prior to silicidation.

In this work, plasma-enhanced atomic layer deposition (PE-ALD) of gadolinium oxide is reported for the first time. Using Gd(iPrCp)₃ as the organometallic precursor and a pure O₂ plasma as the oxygen source, Gd₂O₃ growth is observed from 150°C to 350°C, though the optical properties of the film improve at higher temperature. True layer-by-layer ALD growth of Gd₂O₃ does not occur under all conditions, in fact only a relatively narrow

* Coburn & Winters Student Award Finalist

window of self-limiting ALD growth of 1.4 Å/cycle was observed at 250°C and below under certain precursor dose conditions. As the temperature increases, high-quality films are deposited, but the growth mechanism appears to become CVD-like. At 250°C, the refractive index of the film is stable at ~1.80 regardless of other deposition conditions, and the measured dispersion characteristics are comparable to those of bulk Gd₂O₃. The electrical characteristics of the films, such as fixed charge and dielectric constant, are extracted from C-V measurements using TiN metal gate capacitors, and will be reported.

The plasma etching rate of the ALD Gd₂O₃ film in a high-density helicon reactor is very low. Little difference is observed in etching rate between Cl₂ and pure Ar plasmas, suggesting that physical sputtering dominates the etching at high bias power. A threshold bias power exists below which etching does not occur, thus it may be possible to etch a metal gate material and stop easily on the Gd₂O₃ gate dielectric. The threshold bias power is lower in a Cl₂ plasma compared to an Ar plasma, which suggests there is a small ion-enhanced chemical component to the etching as well.

*This work is sponsored by the Department of the Air Force under Air Force Contract #FA8721-05-C-0002. Opinions, interpretations, conclusions and recommendations are those of the author and are not necessarily endorsed by the United States Government.

11:40am **PS-TF-ThM12 Nano- & Micro-Hybrid Materials by a Novel Plasma Deposition Method**, *M. Gulas, A. Felten*, Research Center in Physics of Matter and Radiation (PMR) Facultés Universitaires Notre-Dame de la Paix (FUNDP), Belgium, *A. Mansour, J. Guillot*, Centre de Recherche

A novel low temperature plasma method using organometallic precursors has been tested and optimised to produce various hierarchical nano-hybrid and micro-hybrid materials. Very fast, operating at low or ambient temperature, this original "one pot" physical method is extremely simple, not requiring any pre- or post-treatment. The plasma-based technique can use any kind of electric discharge (direct current, radio or microwave frequency), does operate at low pressure or at the atmosphere, and can be combined with a large choice of plasma gases and organometallic precursors. Examples of the versatility of the method will be shown, including Pt and Ni-decorated carbon nanotubes (CNTs), Ag and Ti-decorated latex beads, and Pd-decorated clay sheets.

One focus of the presentation will be the preparation and full characterisation of bimetallic Pd/Rh - CNT hybrids. The x-ray diffraction (XRD) and TEM (EDX) analyses were used to confirm that the deposited nano-particles are indeed truly Pd/Rh bimetallic, excluding the possibility of a simple physical aggregate/mixture of the two metals; complementary analytical tools such as x-ray photoelectron spectroscopy (global information) and scanning transmission x-ray microscopy (truly local information) reveal that the particles contain a metal/oxide ratio depending of the processing gas; they testify also of the possibility of a nano-particle core-shell structure and of a reorganisation of its structure depending of the processing gas.

Plasma Science and Technology Division Room: 201 - Session PS-ThM

Neutral Beam and Low Damage Processing Moderator: S. Bouchoule, CNRS-LPN

8:00am **PS-ThM1 2010 Plasma Prize Lecture - Super-low Damage Top-down Processing for Future Nanoscale Devices**, *S. Samukawa**, Tohoku University, Japan **INVITED**

For the past 30 years, plasma process technology has led in the efforts to shrink the pattern size of ultralarge-scale integrated (ULSI) devices. However, inherent problems in the plasma processes, such as charge build-up and UV photon radiation, limit the process performance for nanoscale devices. To overcome these problems and fabricate nanoscale devices in practice, we have proposed damage-free neutral-beam process. In this presentation, I introduce our developed damage-free etching, structure-designable deposition of super low-*k* SiOC film and low-temperature Si oxidation (thin SiO₂) processes using neutral beams and discuss the actual applications of neutral beam processing for future nanoscale devices (such as, Fin-MOSFET, and Quantum Dot Solar Cell). Neutral beams can perform atomically damage-free etching, deposition and surface modification. Then, the neutral beam process can precisely control the atomic layer chemical reaction and defect generation. This technique is a

promising candidate for the nano-fabrication technology in future nanoscale devices.

8:40am **PS-ThM3 A Numerical Simulation Method for Plasma-induced Damage Profile in SiO₂ Etching**, *N. Kuboi, T. Tatsumi, S. Kobayashi, J. Komachi, M. Fukasawa, T. Kinoshita, H. Ansai*, Sony Corporation, Japan

To create high performance metal-oxide semiconductor devices, it is necessary to reduce variations in the critical dimension, the etching profile, and the amount of damage caused. Recent advancements in plasma processing for the gate electrode, sidewall, and high aspect contact hole have highlighted the importance of fully understanding how plasma induces damage and how to control this damage. We also need to find a way to quantitatively predict the damage depth profile using a numerical simulation that takes a realistic surface reaction into consideration, because it is quite difficult to observe the distribution of damage in the patterns with high aspect ratios. One commonly used simulation method, molecular dynamics (MD) calculation, unfortunately has a very limited range and cannot simultaneously consider a time-dependent etching profile in the 100 nm scale.

We developed a numerical simulation method for the distribution of plasma-induced physical damage to the SiO₂ and Si layers during fluorocarbon plasma (C₄F₈/O₂/Ar) etching. In our method, the surface layer is assumed to consist of two layers: a C-F polymer layer and a reactive layer. Physical and chemical reactions in the reactive layer divided into radical-quantum approach in the parent source. Fluorocarbon plasma etching processes are considered in detail considering reactivity of radicals, dangling bonds ratio, and generation of by-products (CF₂, SiF₂, and SiF₄) with ion energy dependence. As for ion and radical fluxes, we used the results from our previous experiments.

We used our simulation method to calculate the SiO₂ etch rate, the thickness of the C-F polymer layer (T_{C-F}), the selectivity of SiO₂ to Si layer, and the O₂ dependence of both the SiO₂ etch rate and the selectivity during C₄F₈/O₂/Ar plasma etching in the steady state. Results demonstrated that calculation of the absolute values as well as their behaviors were consistent with those of our experimental data. We also successfully predicted depth profiles of physical damage to the Si and SiO₂ layers in the steady state introducing our re-gridding method, which were affected by the T_{C-F} value. When we calculated the time-dependence of the amount of Si damage, we found that much of the damage was generated in the pre- and early stages of the over etching step during the SiO₂/Si layer etching, in spite of the high selectivity. After that, the amount of damage was gradually decreased by etching and finally became constant.

These results demonstrate that the T_{C-F} value and the over etching time must be carefully controlled by process parameters to reduce the amount of damage during fluorocarbon plasma etching.

9:00am **PS-ThM4 Theoretical Analysis of Electron Transfer during the Process of Neutral Beam Generation**, *N. Watanabe, S. Ohtsuka, T. Iwasaki, K. Ono, Y. Iriye*, Mizuho Information & Research Institute, Inc., Japan, *S. Ueki*, BEANS Project 3D BEANS Center, Japan, *O. Nukaga*, Fujikura Ltd., Japan, *T. Kubota*, Tohoku University, Japan, *M. Sugiyama*, University of Tokyo, Japan, *S. Samukawa*, Tohoku University, Japan

We have developed numerical simulation software named QuickQD[1,2] that calculates the time-evolution of wave functions of electrons based on the First principles Quantum Mechanics. We have applied QuickQD for analyzing neutral-beam generated by the neutral-beam etching system developed by Samukawa, et al [3]. Positive or negative ions passing through a graphite aperture of this etching system are converted to neutral atoms by exchanging their valence electrons during a collision with the aperture sidewall.

Our numerical model consists of an ion (Cl⁻ or Cl₂⁺) and 24 carbon atoms forming a graphite sheet. The ion has been moved to collide with the graphite sheet and then bounce back to its original position. QuickQD has simulated the time-evolution of several ten wavefunctions of both the ion and carbon electrons during the whole process of the collision. We have evaluated the distribution of electron density around the ion, and we have determined the probability of neutralization.

We have obtained some numerical results that agree well with experiment results, for example,

a negative Cl⁻ ion transfers its valence electrons to the graphite and is converted to a neutral Cl atom with high probability, meanwhile a positive Cl₂⁺ ion receives valence electrons from the graphite and is converted to a neutral Cl₂ molecule with low probability[4].

To understand the quantum process of electron transfer and the difference of neutralization efficiencies between a negative ion and a positive ion, we have investigated the behavior of each time-evolving electron wave function. We have found that some electrons that existed in the orbital of

* 2010 Plasma Prize Winner

Cl- before the collision were mainly transferred after the collision to some orbitals of graphite whose orbital energies were close, namely, resonant transitions whose transition rates are relatively high. Meanwhile, some electrons that existed in the orbitals of graphite before collision of Cl₂⁺ were transferred after the collision to the orbital of Cl₂⁺ whose orbital energies were not close, namely, Aujer like complicated transitions, whose transition rates are relatively low.

In this talk, we will show the time-evolution of wave functions based on the First principles Quantum Mechanics, which simulated the neutralization processes that occurred in the neutral beam etching system.

[1] N. Watanabe and M. Tsukada, Phys. Rev. E. 65 036705 (2002).

[2] <http://www.mizuho-ir.co.jp/solution/research/semiconductor/nano/meso>

[3] S. Samukawa et al., Jpn. J. Appl. Phys., 40, L779 (2001).

[4] T. Kubota, N. Watanabe, et al., J. Phys. D. 44 125203 (2011)

9:20am **PS-ThM5 Energy and Angular Distribution Analysis for Neutral Beam and Application for Etching Simulation**, S. Ohtsuka, N. Watanabe, T. Iwasaki, K. Ono, Mizuho Information & Research Institute, Inc., Japan, Y. Iriye, O. Nukaga, S. Ueki, BEANS Project 3D BEANS Center, Japan, T. Kubota, Tohoku University, Japan, M. Sugiyama, University of Tokyo, Japan, S. Samukawa, Tohoku University, Japan

The neutral-beam etching system developed by Samukawa et al [1] has a carbon plate which has numerous apertures, where positive or negative ions pass through. In this system, most of those ions passing through the apertures are efficiently converted into neutral atoms. We consider ions are neutralized by the collision with aperture sidewall. A negative ion transfers some of their valence electrons to the aperture sidewall by the collision, and a positive ion receives some valence electrons from the aperture sidewall. The dynamical process of electron transfer by the collision can be described by the Quantum Mechanics as a time-evolution of wave-function during the collision, and we have developed computational simulation software named QuickQD [2].

To realize more practical neutral-beam etching system, we also have to analyze the energy and angular distribution passing through the aperture. Those distributions characterize the ability of etching system. In other words, to achieve efficient etching system, we have to develop optimized aperture configurations (i.e. arrangement and aspect ratio of apertures) and get conditions for suitable energy and angular distribution of neutral beam.

In this study, we calculate the trajectory of particles generated by Monte-Carlo method, and analyze the energy and angular distribution of neutral beam at aperture outlet. To analyze energy and angular distribution at outlet, we have to determine the initial conditions of incident beam at aperture inlet, and have to describe the scattering process for collision between incident particles and side wall of aperture. We determine initial beam condition at inlet using the experimental data fitting. And we use the inelastic surface scattering model known as Hard-Cube model [3] for treating collision between particles and side wall of aperture. Particles injecting into aperture which have broad angular distribution are collimated by this inelastic scattering process.

Using above simulation scheme, we analyze the energy and angular distribution for specific aperture configuration (i.e. aperture aspect ratio) and compare with experimental data. We also analyze the particle distribution of neutral beam at silicon wafer injecting from aperture outlet and discuss the uniformity of neutral beam etching. Using above angular distribution of neutral beam and etching simulator, we predict etching shape by neutral beam generated by various aperture configurations (i.e. aperture aspect ratios).

[1] S. Samukawa et al., Jpn. J. Appl. Phys., 40, L779 (2001).

[2] N. Watanabe and M. Tsukada, Phys. Rev. E. 65 036705 (2002).

[3] R. M. Logan and R. E. Stickney, J. Chem. Phys., 44, 195 (1966).

9:40am **PS-ThM6 High-Aspect-Ratio Silicon Etching using Large-Diameter Neutral Beam Source**, T. Kubota, Tohoku University and BEANS Project, Japan, A. Wada, Tohoku University, Japan, S. Ohtsuka, K. Ono, Mizuho Information & Research Institute, Inc., Japan, H. Ohtake, Tohoku University, Japan, S. Ueki, Y. Nishimori, BEANS Project, Japan, G. Hashiguchi, Shizuoka University and BEANS Project, Japan, S. Samukawa, Tohoku University, Japan

Plasma etching is widely used for fabricating semiconductor electronic devices and microelectromechanical systems (MEMS), but plasma etching is known to cause damages due to the charge-up and UV irradiation. To overcome plasma-induced damages, we have developed a neutral beam source with very high neutralization efficiency. The neutral beam source achieved high neutralization efficiency by using negative ions from pulsed-time modulation plasma, and UV irradiation was drastically reduced. To apply this neutral beam source to mass production, we have developed a large-diameter neutral beam (NB) source by using an 8-inch-diameter

inductively coupled plasma etcher (Panasonic Factory Solutions Co., Ltd. E620) as an ion source. In the previous study, the beam flux of argon NB was more than 1 mA/cm² in equivalent current density and the neutralization efficiency was more than 99%. Vertical Si etching using F₂ gas chemistry was also achieved. Also, beam was successfully accelerated by bias applied to the aperture plate [1].

In this study we investigated high-aspect-ratio silicon etching. At first, angular distribution of NB was measured. As a result, Gauss-function-like distribution was observed and the width of the distribution was determined by aspect ratio of the aperture. On the other hands, angular distribution of incoming ions from plasma to the aperture was almost uniform. Also, plasma parameters such as source power and gas flow rate did not affect the distribution. From these results, it is supposed that aperture plays a dominating role in generation of collimated NB. Then, silicon etching by chlorine (Cl₂) NB was performed using apertures with aspect ratio of 10 and 20. By using the aperture with aspect ratio of 10, almost vertical sidewall with a slight positive taper of 6 degree was achieved. The aperture with aspect ratio of 20 led to almost vertical etching. Silicon trench etching with aspect ratio of about 22 was achieved using the aperture and chlorine NB.

A part of this work was supported by the New Energy and Industrial Technology Development Organization (NEDO). This work is partly supported by Formation of Innovation Center for Fusion of Advanced Technologies, Special Coordination Funds for Promoting Science and Technology, Ministry of Education, Culture, Sports, Science and Technology.

[1] T. Kubota et al., J. Vac. Sci. Technol. A 28(5), 1169 (2010).

10:40am **PS-ThM9 Improvement in the Evaluation Technique for Plasma-Etch Si Damage using Photoreflectance Spectroscopy with Temperature Control**, A. Matsuda, Y. Nakakubo, Y. Takao, K. Eriguchi, K. Ono, Kyoto University, Japan

In etching processes during MOSFET fabrication, bombardment of high-energy ions from plasma creates damaged structures in layers near the substrate surface, characterized by defect sites in the crystalline structure such as vacancies, interstitials, displacements, and dangling bonds. The negative effects of the damage on device characteristics (such as drain current degradation) have become increasingly significant as devices scale down rapidly [1]. To realize low-damage process, an advanced damage evaluation technique is essential. Photoreflectance spectroscopy (PRS) is an optical technique capable of detecting damage with high sensitivity. The surface is perturbed with an electric field by a modulation laser beam, and the reflectivity of a probe beam is measured. PRS has been studied as an advanced technique for contactless damage evaluation.

In this study, we employed an improved technique, where the temperature of the sample is controlled with liquid N₂ during PRS measurement. N-type Si (100) wafers were exposed to an inductively coupled plasma using argon gas, under various rf-bias powers to control the incident ion energies (E_i). At room temperature, the amplitude of the spectral peak decreased with the increase in E_i . This feature is explained in earlier literature that carriers trapped at defect sites lower the surface potential (V_s), resulting in a decrease of the amplitude [2]. Over $E_i \approx 400$ eV, the peak became smaller than background fluctuation, rendering quantitative characterization impossible. When the sample was cooled to 90 K, the spectra were enhanced and the peak of the high- E_i sample was revealed. By fitting the spectra to a functional form [3] and modeling the parameters' temperature dependences, we found that the amplitude enhancement is related to the temperature dependence of the spectral broadening parameter (Γ). We also found that, at a fixed temperature, Γ for damaged surfaces were larger than that of the control sample. These results show that the damage causes changes in V_s and Γ , but by controlling the sample temperature, we were able to lower Γ , which increased the amplitude and revealed the peak.

The PRS-based damage evaluation technique discussed here expands the range of the applicable plasma damage conditions. Furthermore, temperature dependences of the spectra and its parameters (e.g. Γ and/or optical band gap) give us an insight into the band structures of damaged Si. This PRS-based technique is expected to be potentially useful as a future *in-situ* monitoring technique.

[1] K. Eriguchi *et al.*, IEDM Tech. Dig., 2008, p. 436

[2] H. Wada *et al.*, J. Appl. Phys. **88**, 2336 (2000)

[3] D. E. Aspnes, Surf. Sci. **37**, 418 (1973)

11:00am **PS-ThM10 The Mechanism of Thin SiO₂ and GeO₂ Film Formation during Low-Temperature Neutral Beam Oxidation Process**, A. Wada, Tohoku University, Japan, K. Endo, M. Masahara, AIST, Japan, S. Samukawa, Tohoku University, Japan

The thermal oxidation process is usually used to form the gate dielectric films of MOSFETs. However, it involves high temperatures (usually > 800°C), which causes problems. For example, after using the high-

temperature oxidation process to form SiO₂ films, residual compression stress between the Si substrate and SiO₂ remains due to the difference in the thermal expansion coefficient between Si and SiO₂. This residual stress degrades the sub-threshold characteristics of MOSFETs because it increases interfacial state density. Especially, in case of future 3-dimensional transistors such as FinFETs, stress concentration occurs at corner and edge of 3D structures, which may cause drastic increase of leakage current. There have been recent active investigations on the thermal oxidation of Ge to enable the fabrication of high-mobility Ge MOS transistors. After high-temperature thermal processes, however, Ge oxide has poor thermal stability and a large amount of suboxide.

We developed an alternative oxidation process to solve these problems using a low temperature neutral beam (NB) technique to form the gate dielectric film. In this study, we investigated the mechanism to form thin oxide films using a low-temperature neutral beam oxidation (NBO) process. Arrhenius plot has shown that activation energy of NBO was extremely low, which enabled low-temperature oxidation at 300°C or even at room temperature. This should be because bombardment energy of oxygen beam assisted the oxidation reaction. Also, we investigated that the suboxide in thin oxide film using NBO process. As a result, there was little suboxide at the interface between oxide films and semiconductor using NBO process even at low-temperature. These results demonstrate the outstanding potential of the low-temperature NBO process for fabricating gate dielectric films.

11:20am PS-ThM11 Room Temperature Radical Annealing of Plasma Damaged Gallium Nitride. *S. Chen**, *Y. Lu, K. Takeda, K. Ishikawa, H. Kondo*, Nagoya University, Japan, *H. Kano*, NU Eco-engineering Co., Ltd, Japan, *H. Amano*, Nagoya University, Japan, *Y. Tokuda*, Aichi Institute of Technology, Japan, *T. Egawa*, Nagoya Institute of Technology, Japan, *M. Sekine, M. Hori*, Nagoya University, Japan

This paper reports an attempt of low-temperature recovery for gallium nitride (GaN) damaged by the exposure of a chlorine-based etching plasma. The work is motivated by the challenge for manufacturing highly-reliable GaN based devices which have a great deal of potential in optical, high-frequency, and high-power electronics field. So far, high temperature annealing or nitrogen plasma were used as the post-process. However, the high-temperature treatment could not restore the reduced atomic ratio of nitrogen on the damaged surface. The nitrogen plasma introduces damage by the ion bombardment. In this study, a high-density radical annealing in room temperature was newly proposed and evaluated in all in-situ experimental system consisted of etching, radical annealing, and surface analysis.

Radicals and ions extracted from a chlorine plasma were irradiated to n-GaN with an ion dose of $5 \times 10^{16} \text{cm}^{-2}$ at 500 eV [1]. Then the radical annealing using nitrogen radical (N*) or hydrogen radical (H*) with a radical dose of $1 \times 10^{18} \text{cm}^{-2}$ was applied using a high-density radical source [2] at room temperature. The X-ray photoelectron spectroscopy (XPS) and atomic force microscopy (AFM) evaluation carried out after each process.

In N* annealing case, the surface chloride was removed and N/Ga was improved, but there was no change in the composition ratio of oxygen (O). On the other hand, hydrogen radical (H*) could efficiently remove O, and N/Ga was improved greatly. Other characteristic findings were that Ga-Ga (metallic Ga) was observed in the Ga 3d spectra and the surface roughness increased from 0.335 to 0.646 nm rms.

As a result, the radical annealing at room temperature was shown to be very effective for improving GaN stoichiometry to achieve a better interface, whereas the condition should be optimized very carefully.

Acknowledgments

This work was supported by the knowledge Cluster Initiative (the Second Stage), the MEXT, Japan.

[1] S. Chen, et al., Proc. 63rd GEC/7th ICRP (Paris, 2010), BT1-005.

[2] S. Chen, et al., Jpn. J. Appl. Phys. 50, 01AE03 (2011).

11:40am PS-ThM12 Effect of Rapid Thermal Annealing on Si Surface Damage by HBr/O₂- and H₂-Plasma. *Y. Nakakubo, A. Matsuda*, Kyoto University, Japan, *M. Fukasawa*, Sony Corporation, Japan, *Y. Takao*, Kyoto University, Japan, *T. Tatsumi*, Sony Corporation, Japan, *K. Eriguchi, K. Ono*, Kyoto University, Japan

Plasma-induced Si substrate damage has become one of the critical issues in advanced MOSFETs with shallower junction in source/drain extension (SDE) regions, since the damaged layer thickness will be in conflict with the device design margin (e.g. ~ 5 nm in 32-nm technology node). This damage causes the device performance degradation by forming Si loss (Si recess structure) [1]. Ohchi et al. have reported that the damaged layer by hydrogen-containing plasma is thicker than that by plasma without hydrogen, resulting in deeper Si recess [2]. Eliminating the damaged layer by wet etch and reconstructing the crystalline structure by thermal processes are strongly required, but there have been few studies on these issues. In this study, we report the effect of rapid thermal annealing on the damaged layer by HBr/O₂- and H₂- plasmas.

P-type silicon substrates with thermal-oxide layer (2 nm) were exposed to the capacitively coupled plasma (CCP) by applying a dual bias frequency (60/13.56 MHz). HBr/O₂ and H₂ gases were used. Damaged samples were cleaned by the dilute-HF solution (DHF) for 2 min before rapid thermal annealing (RTA) at 1035 °C for 10 s in a N₂ gas ambient. The structure and the electrical conductivity were identified using spectroscopic ellipsometry (SE) and current-voltage (I-V) measurement, respectively. Capacitance-voltage (C-V) method was performed to analyze the features of the defect site in the damage samples.

Although all the damaged samples after RTA had a thicker oxide layer (~ 1.4 nm) compared with that of the native oxide layer (~ 0.6 nm) grown on the Si surface treated by SC2, a much higher current through the thick oxide (~ 20 mA at -0.1 V) was observed in comparison with that through the native oxide (~ 0.7 mA at -0.1 V). This feature is due to the nitrided Si that may be assigned by SE. This nitrided layer was found to be difficult to remove (etch) even by the DHF-treatment of several minutes, and thus the damaged MOSFETs may suffer from performance degradation by the presence of the nitrided layer. These findings imply that in the case of H-plasma, the process recipe for RTA targeted to cure the plasma-induced Si damage should be carefully optimized.

[1] K. Eriguchi *et al.*: IEEE Electron Dev. Lett. **30** (2009) 712.

[2] T. Ohchi *et al.*: Jpn. J. Appl. Phys. **47** (2008) 5324.

Advanced Surface Engineering Division Room: 104 - Session SE-ThM

Nanostructured Thin Films and Coatings

Moderator: C. Mitterer, University of Leoben, Austria

8:00am SE-ThM1 Characterization of Solution-Processed HfO₂, HfSiO₄, and ZrSiO₄ Thin Films on Rigid and Flexible Substrates for Memristive Applications. *J.L. Tedesco, W. Zheng, O.A. Kirillov, S. Pookpanratana, A.A. Herzing, H.-J. Jang, P.P. Kavuri, N.V. Nguyen, C.A. Richter*, National Institute of Standards and Technology

Memristors, nonvolatile bipolar resistive switching devices first intentionally fabricated in 2008 [1], have attracted attention for use in a wide range of applications. To date, most memristors have been fabricated from either TiO_x [1] or TaO_x [2]. However, it is necessary to explore other dielectric materials, because the memristive properties of these dielectrics have not yet been explored.

In this study, memristors were fabricated on both silicon and flexible polyethylene terephthalate (PET) substrates by using HfO₂, HfSiO₄, and ZrSiO₄ thin films and thermally evaporated aluminum contacts. The dielectric films were formed from sol-gel precursors synthesized based on the recipe of Meena et al. [3]. Following synthesis, the precursors were spun on to substrates, exposed to an oxygen plasma, and annealed in air at 150°C for 24 hours. Memristors with cross sectional areas ranging from 2×2 mm² to 0.5×0.5 mm² were fabricated.

The dielectric films were extensively characterized by using optical profilometry and microscopy, x-ray photoelectron spectroscopy (XPS), and deep ultraviolet spectroscopic ellipsometry (SE). The optical profilometry measurements demonstrate that the films show no evidence of significant inhomogeneities due to the solvent-based sol-gel synthesis methods. According to the XPS measurements, the films are ~50% carbon. Such high levels of carbon are reasonable given the synthesis approach employed, and

* Coburn & Winters Student Award Finalist

similarly high levels of carbon have been observed previously in TiO₂ films synthesized from sol-gels [4]. From the SE measurements, it is evident that the bandgaps of the HfO₂, HfSiO₄, and ZrSiO₄ films are similar to their predicted values, but the densities of the films are ≈0.5 due to the high amounts of excess carbon. Transmission electron microscopy measurements of the films will also be discussed.

Current-voltage (I-V), capacitance-voltage (C-V), capacitance-frequency (C-f), and conductance-frequency (G-f) measurements were performed at room temperature in a commercial probe station. The I-V measurements indicate that devices fabricated from these films exhibit bipolar resistive switching. Furthermore, optical microscopy images indicate that the switching events are often accompanied by significant changes to the morphology of the active region of the device, particularly when the switching occurs at high voltages. These changes suggest the formation of localized conduction pathways through the dielectric. The C-f and G-f measurements indicate that the capacitive properties of the devices also change following switching events. Additionally, after 24 days, retention tests show the devices are still in the ON state, thus, they may be considered nonvolatile.

References

- [1] D.B. Strukov et al., *Nature* **438**, 80 (2008).
- [2] J.J. Yang et al., *Appl. Phys. Lett.* **97**, 232102 (2010).
- [3] J.S. Meena et al., 2010 3rd International Nanoelectronics Conference (INEC), **1-2**, 992, 2010.
- [4] J.L. Tedesco et al., *ECS Trans.* **35**, 107 (2011).

8:20am SE-ThM2 Tensile Testing of Substrate for Fracture Toughness of Thin Films, S. Zhang, X. Zhang, Nanyang Technological University, Singapore

INVITED

Measurement of fracture toughness for bulk materials is a routine but extremely difficult and still not standardized for thin films (or coatings). The difficulties in clamping a freestanding thin film and the requirement of a critical dedicate loading system are the main obstacles. In this talk, a method is proposed to carry out tensile loading of the substrate to avoid both problems. The film is deposited on a rectangular silicon wafer on which an edge crack is fabricated beforehand. The film is then "micromachined" into microbridges perpendicular to and ahead of the initial substrate crack. A displacement controlled tensile force is applied to propagate the substrate crack and fracture the "microbridges". The critical fracture strain of the microbridge is measured through measuring the strain of the substrate at the respective location of the microbridge. The fracture toughness of the film is thus obtained in between the un-fractured and the last fractured bridge. A case study is also presented.

9:00am SE-ThM4 Structure and Properties of TaN-(Ag,Cu) Nanocomposite Thin Films, J.H. Hsieh, S.Y. Hung, Ming Chi University of Technology, Taiwan, Republic of China, S.Y. Chang, National Chung Hsing University, Taiwan, Republic of China, C. Li, National Central University, Taiwan, Republic of China

TaN-(Ag,Cu) nanocomposite thin films with various Ag/Ti ratios were deposited by reactive co-sputtering on Si(001) substrates. The samples were then annealed using RTP (Rapid Thermal Processing) at 400 °C to induce the nucleation and growth of Ag/Cu nano-particles in TaN matrix and on film surface. One set of TaN-(Ag60,Cu40) were annealed at various temperatures. The structure and morphologies were examined using XRD, FESEM, and HRTEM. Nano-indenter was used to study the variation of mechanical properties. The results reveal that the mechanical properties were affected by the annealing temperature rather than the atomic ratios of Ag/Cu. However, the anti-bacterial behaviors against *E. coli* and *S. aureus* were significantly affected by the Ag/Cu ratios.

9:20am SE-ThM5 Nanoporous Osmium-Ruthenium Thin Film Coatings for Dispenser Cathodes, P. Swartzentruber, T.J. Balk, University of Kentucky

Nanoporous osmium-ruthenium may be applicable as an improved coating for dispenser cathodes used in travelling wave tubes and other various vacuum tube devices. Osmium-Ruthenium (OsRu) was co-deposited with either magnesium (Mg) or scandium (Sc) as a sacrificial element to form an intermetallic thin film. The sacrificial element was then selectively etched away, which dealloyed the film and left behind a nanoporous structure. Electron microscopy, x-ray diffraction, and x-ray photoelectron spectroscopy were used to characterize the morphology, structure, and composition of the films in both the as-deposited and dealloyed states. Various film compositions and dealloying conditions were studied to determine the optimal conditions for creating a nanoporous film structure.

9:40am SE-ThM6 Influence of Chemistry and Structure on the Thermal Stability and Oxidation Resistance of Ti-Al-N, P.H. Mayrhofer, L. Chen, J. Paulitsch, Montanuniversität Leoben, Austria, Y. Du, Central South University, China

The excellent hardness, good abrasive and sliding wear resistance and high thermal stability and oxidation resistance favor Ti_{1-x}Al_xN to be used as hard protective coating in a variety of industrial applications such as advanced machining and forming tools, automobile and aerospace industry or for semiconductor electronics. Although, thin films based on this material system are investigated in detail, only little is known on the sequential relations between deposition conditions, chemistry, structure and physical and mechanical properties.

Here we show that Ti_{1-x}Al_xN coatings can be synthesized by magnetron-sputtering in single-phase cubic (NaCl, c) structure for x = Al/(Ti+Al) ratios up to 0.62 and single-phase hexagonal (ZnS-wurtzite, w) structure for x ≥ 0.75. These critical values for the individual favored structures strongly depend on the deposition conditions used such as N₂-partial pressure and resulting growth rate. Generally, a low N₂-partial pressure and a high growth rate favor the cubic structure. Increasing Al content of the single-phase cubic coatings results in increased hardness (to ~35 GPa for c-Ti_{0.38}Al_{0.62}N), earlier onset of the decomposition towards the stable phases c-TiN and w-AlN (across the formation of Ti-rich and Al-rich cubic nm-sized domains) and increased oxidation resistance. The single-phase wurtzite-structure coatings exhibit a high thermal stability and better oxidation resistance as compared to the single-phase cubic structure coatings. Even after 40h at 800 °C in ambient atmosphere the w-Ti_{0.25}Al_{0.75}N coating exhibits only an ~1 μm thin dense oxide layer on top of the ~2 μm remaining nitride, whereas the other coatings are already fully oxidized.

The coatings with a dual-phase or mixed-phase structure in the as deposited state show a reduced thermal stability and oxidation resistance as compared to the single-phase cubic or wurtzite structure coatings.

Furthermore, we show that a post-deposition annealing treatment of c-Ti_{0.48}Al_{0.52}N to 900 °C results in a hardness increase from 29 to 32 GPa (due to the formation of cubic nm-sized domains) as well as an increased oxidation resistance. Hence, our results provide insight in designing-strategies for coatings with increased mechanical, thermal stability and oxidation resistance.

10:40am SE-ThM9 Design of Catalytically Active Nanostructured Coatings for Severe Tribological Applications, A. Erdemir, O.L. Eryilmaz, Argonne National Laboratory

Nanostructured and composite coatings are very unique in the field and offer many attractive properties for a wide range of demanding applications. They can also provide the kind of flexibility that is needed for achieving highly protective, super-slippery boundary films on lubricated tribological surfaces. In this study, we explored the possibility of nano-scale designing of a new class of catalytically active super-hard nitride coatings which when used under boundary lubricated sliding conditions can produce a carbon-rich boundary film. The Raman spectra of the carbon film are similar to that of the diamondlike carbon coatings typically produced by CVD and PVD methods. In a wide range of tribological test systems, such carbon-rich boundary films were shown to provide extreme resistance to scuffing and provide very low friction and wear even under the harshest tribological conditions. In this paper, we will mainly concentrate on the structural and chemical nature of these films and present a hypothetical model to explain their unusual tribological properties under severe contact conditions.

11:00am SE-ThM10 Structure and Electrical Properties of Nb-Ge-C Nanocomposite Coatings, O. Tengstrand, Linköping University, Sweden, N. Nedfors, Uppsala University, Sweden, L. Fast, SP Tech. Res. Inst. of Sweden, A. Flink, Impact Coatings AB, Sweden, A.M. Andersson, ABB AB, Corporate Research, Sweden, U. Jansson, Uppsala University, Sweden, P. Eklund, L. Hultman, Linköping University, Sweden

Nanocomposite ceramic coatings are being explored based on their good tribological and electrical properties, which can be tailored by changing e.g. the composition, microstructure, and surface morphology. For example, the nc-TiC/a-SiC nanocomposite system has shown promising properties for electrical contact applications [1, 2]. The tendency to form oxides and carbides greatly influences these properties. For instance, NbC has similar electrical properties as TiC, but has a lower tendency to form oxides. Especially for low force electrical contact applications, this makes NbC a suitable choice as replacement for TiC. Ge is in the same group as Si, but does, as a more noble element, not form carbides or oxides as easily. Here, we investigate the Nb-Ge-C material system with respect to nanostructure and electrical properties.

Nb-Ge-C thin films were deposited onto Si(001) and Ni-electroplated bronze substrates using dc magnetron sputtering in an Ar discharge at a low temperature (200 °C). By use of three elemental targets in current-regulating

mode both the Nb/C ratio and the Ge content was varied to study the effect of composition. XRD, TEM, and SEM showed that the NbC films are columnar and exhibit a preferred 111 crystallographic orientation. With increasing Ge content up to 10 at.%, the NbC grain size was reduced to ~5 nm with a random orientation. While the nc-NbC/Ge nanocomposites have no discernable amorphous tissue phase, XPS showed predominantly Ge-Ge with only little Ge-C bonds. In contact resistance measurements the films performed well (1.7-3.7 mΩ) in comparison to Ag reference (1.2 mΩ) at a contact force of 10 N.

[1] Eklund, P., Surface Engineering, 23, (2007), 406

[2] Lauridsen, J.; et al. Surf. Coat. Technol., 205, (2010), 299

11:20am SE-ThM11 Tuning the Properties of Chromium Oxynitride Coatings, L. Castaldi, Oerlikon Balzers AG, Liechtenstein, J. Patscheider, EMPA, Switzerland, V. Shklover, ETH Zurich, Switzerland, D. Kurapov, A. Reiter, Oerlikon Balzers AG, Liechtenstein

Cr_xN_{1-x} coatings deposited by reactive cathodic arc evaporation were investigated for concentration levels oxygen between 0 and 1. The present study shows some of the possibilities for tuning the crystallographic and electronic properties of chromium oxynitride films by progressively increasing the oxygen concentration. Upon oxygen addition the Cr_xN_{1-x} films remain in the face-centered cubic B1 structure of CrN for oxygen fractions of up to x = 0.70. At higher oxygen contents the properties of the films approach those of Cr₂O₃ and crystallize in the corundum structure. The gradual decrease of the stress-free lattice parameter of the films with the B1 structure at higher oxygen concentrations is consistent with oxygen substituting progressively nitrogen atoms. The almost random orientation of oxygen-free CrN films transforms to a distinct (001) preferred orientation with the increase of oxygen concentration in the films. XPS investigations prove enhanced charge transfer from Cr to O 1s with increasing x with respect to N by changes in the core-level binding energies (BE) of the Cr 2p_{3/2} and N. A shift of the valence band edge toward higher BE indicates a decrease of electrical conductivity of the films with increasing oxygen content.

11:40am SE-ThM12 Synthesis of Al-Cr-O and Al-Cr-O-N Thin Films in Corundum-Type Structure by Reactive r.f. Magnetron Sputtering, M. Stueber, Karlsruhe Institute of Technology (KIT), Germany, D. Diechle, Walter AG, Germany, H. Leiste, S. Ulrich, Karlsruhe Institute of Technology (KIT), Germany

The PVD synthesis of wear and oxidation resistant aluminum oxide and derivative coatings is currently attracting large scientific and technical interest. Ternary Al-Cr-O thin films with mechanical properties comparable or superior to binary Al-O thin films can be deposited at moderate deposition temperatures. New coatings from the quaternary Al-Cr-O-N system could even offer increased strength, hardness and toughness. A combinatorial approach to the growth of Al-Cr-O-N thin films by means of reactive r.f. magnetron sputtering will be presented. For specific deposition conditions well adherent, nanocrystalline Al-Cr-O-N thin films with high Vickers hardness and elastic modulus values were grown at non-equilibrium conditions on cemented carbide and silicon substrates. Detailed results on the coatings composition, constitution, microstructure and properties will be presented and discussed in comparison to ternary Al-Cr-O thin films deposited under identical conditions.

Surface Science Division

Room: 107 - Session SS-ThM

Oxide Surface Structure & Reactivity

Moderator: G.A. Kimmel, Pacific Northwest National Laboratory

8:00am SS-ThM1 Bond Activation of Alkanes on CaO(100), A. Chakradhar, U. Burghaus, North Dakota State University

The molecular and dissociative adsorption kinetics, respectively, of ethane, butane, pentane, and hexane are studied on CaO(100) using thermal desorption spectroscopy (TDS) and Auger electron spectroscopy (AES). After adsorption/desorption cycles, AES scans show no carbon residuals on the surface. Molecular adsorption as well as bond breaking is observed for all alkanes studied, except for ethane. Molecular desorption of these alkanes is characterized by two TDS peaks while recording the parent mass. These two features are assigned to different adsorption sites/configurations of the alkanes. In addition, the binding energies of the bound alkanes, based on their desorption temperatures, are calculated by using Redhead equation. The bond activation is evident from desorption of hydrogen and mostly methane and ethylene fragments in multi-mass TDS experiments. Bond

activation of hydrocarbons is pertinent for the petroleum industry, providing transportation fuels and other petrochemical products.

8:20am SS-ThM2 Reaction Chemistry of Methyl and Methylene Species on Cr₂O₃(0001), Y. Dong, D.F. Cox, Virginia Tech

The reactions of methyl (CH₃) and methylene (CH₂) surface species formed from the dissociation of halogenated methanes have been studied with temperature programmed desorption over Cr₂O₃(0001). Methyl fragments undergo a rate-limiting dehydrogenation to methylene and produce methane (CH₄) and ethylene (CH₂=CH₂) as the primary products. Comparison to earlier results for the Cr₂O₃(1012) surface show that methyl dehydrogenation is a structure-insensitive reaction, with the barrier to dehydrogenation being insensitive to the surface cation coordination number and/or local Cr-O site pair geometry. The ethylene formed from the dehydrogenation of CH₃ is associated with the surface diffusion of methylene species and subsequent coupling (C-C bond formation) reactions.

Separate studies of the reaction of methylene show that surface diffusion and coupling to ethylene can occur at lower temperatures than required for CH₃ dehydrogenation. The diffusion-limited coupling of CH₂ appears to be a structure-sensitive reaction, with the barrier to surface diffusion about 25 kJ/mol higher on Cr₂O₃(0001) than the (1012) surface.

8:40am SS-ThM3 Organometallics as Probes of Functional Group Distribution on Oxide Surfaces, S.L. Scott, University of California, Santa Barbara

INVITED

The reactivity of the hydroxyl-terminated surface of silica is important for constructing tailored interfaces in many applications, including catalysis, separations, and microelectronics. Amorphous silicas are particularly interesting because of their high surface areas. The hydroxyl content of their surfaces can be reduced thermally, but it decreases slowly because the hydroxyls have very low mobility. Their mutual condensation requires proximity, and, frequently, the formation of strained siloxane rings. Since these silicas have no long-range order, it is often postulated that the hydroxyl groups are distributed randomly, and that when the nominal hydroxyl density is low (e.g., after thermal treatment at temperatures exceeding 500 °C), these hydroxyls can be considered essentially isolated. Curiously, the Ga K-edge EXAFS shows that the reaction of Ga(CH₃)₃ with such a silica pretreated at 800 °C generates only digallium sites, requiring that the hydroxyls be organized pair-wise, likely as vicinal silanols linked by a single siloxane bond. The origin of the preferred vicinal disposition may be hydrolysis of a strained siloxane bond. Where isolated hydroxyls do exist, they appear to be located on reactive 2-rings whose reactivity resembles that of a masked silanol. Consequently, it is unwise to assume that site isolation results from grafting onto these silicas, although the vicinal disposition of silanols provides an opportunity to create tailored bifunctional surfaces.

9:20am SS-ThM5 Are MgO Thin Films More Reactive Than Bulk MgO Surfaces?, G. Cabailh, R. Lazzari, H. Cruguel, J. Jupille, UPMC and CNRS, France, L. Savio, IMEM-CNR, France, M. Smerieri, A. Orzelli, L. Vattuone, M. Rocca, Università di Genova, Italy and IMEM-CNR, France

The ubiquity of the interface between water and oxide materials has prompted a tremendous activity to determine the adsorption mechanisms at the microscopic scale on crystalline surfaces of simple oxides. Among these, magnesium oxide MgO offers the advantage of having various morphologies of good crystalline quality, involving cleaved crystal surfaces, high surface area samples and supported films, all of these dominated by the low index (100) orientation. On bulk MgO, the fivefold coordinated atoms of the basal (100) surface do not dissociate isolated H₂O molecules. Conversely, H₂O is easily dissociated at low-coordinated sites such as steps and kinks. A puzzling case is the adsorption of H₂O on metal-supported MgO films in the submonolayer range of which coverage by OH groups has been estimated to 60 to 70% of a monolayer [1,2]. Similar OH coverages were obtained by aging freshly prepared films in the residual atmosphere of the vacuum chamber [1], although the observation was contradicted by the finding of a more modest effect that cast doubt on OH being the cause of aging [2]. The extraordinary uptake of OH groups was attributed to the peculiarities of the electronic properties of the thin supported MgO films [3]. However, density functional theory hardly supports this view. Little changes in both the electronic structure and the capacity to dissociate H₂O are predicted for monolayer-thick MgO(100) islands that, at variance with experiment, are only expected to dissociate H₂O molecules along their borders [4].

In an attempt to solve the discrepancies between experiments and between experiment and simulation, MgO films of different stoichiometry were grown on Ag(100) by reactive deposition of Mg in an O₂ partial pressure, prior to being exposed to H₂O vapor and/or aged in vacuum [5]. Films were observed by scanning tunneling microscopy (STM) and water uptake was analyzed by x-ray photoemission spectroscopy (XPS). The stoichiometry

and, consequently, the chemical activity towards hydroxylation of the MgO(100) films, was shown to strongly depend on the O₂ pressure during the film growth. Oxygen-deficient films undergo dramatic oxygen uptake either by exposure to H₂O or by aging in vacuum. Conversely, on stoichiometric MgO islands, XPS analysis and STM images are consistent with the prediction that H₂O only dissociates at the island edges.

- [1] S. Altieri et al., Phys. Rev. B. 76 (2007) 205413.
- [2] L. Savio et al., J. Phys. Chem. B 108 (2004) 7771.
- [3] S. Altieri et al., Thin Solid Films 400 (2001) 9.
- [4] A. M. Ferrari et al., Phys. Chem. Chem. Phys. 9 (2007) 2350.
- [5] G. Cabailh et al., J. Phys. Chem. C, in press (2011).

9:40am **SS-ThM6 The Adsorption of Silver on Fe₃O₄(111) Studied by Adsorption Microcalorimetry, LEIS, and AES, J.C. Sharp, Y.X. Yao, C.T. Campbell, University of Washington**

Noble metals supported on oxide surfaces are of interest due to their catalytic activity and their sintering resistance is a subject of concern in terms of their long-term stability under reaction conditions. The heat of adsorption of silver on Fe₃O₄(111) grown on Pt(111) was measured using adsorption microcalorimetry, and its growth morphology was measured with low-energy ion scattering spectroscopy (LEIS) and Auger electron spectroscopy (AES). The initial sticking was 0.96 rising to 0.99 after 1 monolayer of Ag deposited. The LEIS and AES data were fitted to a hemispherical cap model for the Ag nanoparticles, which were found to grow with a particle density of 4×10^{12} particles per cm². The initial heat of adsorption was found to be 220 kJ/mol, rising to 285 kJ/mol after 1 monolayer of deposited Ag. From these data, we extracted the energy of metal atoms versus the Ag particle size to which they attach on Fe₃O₄(111), and compare it to results on other single crystalline oxide surfaces.

10:40am **SS-ThM9 Properties of TiO₂ Nanoparticle Arrays Functionalized with Pt Photodeposition, Y. Liu, J. Taing, M. Cheng, University of California, Irvine, H. Bluhm, Lawrence Berkeley National Laboratory, J.C. Hemminger, University of California, Irvine**

Titanium(IV) oxide (TiO₂), acting as a stable support for photocatalysts and sensitizers, has applications in catalysis and energy science. Metal nanoparticles supported on TiO₂ have been shown to have unusual reactivity. The deposition of metal nanoparticles can alter the electronic properties of the TiO₂ nanoparticles. To understand the influence of metal deposition, we photodeposit platinum (Pt) onto ordered linear arrays of TiO₂ nanoparticles grown at the step edges of highly oriented pyrolytic graphite. X-ray photoelectron and absorption spectroscopies were used to explore the electronic structure of the TiO₂ nanoparticle arrays with and without photodeposited Pt. The titanium L-edge spectra, supported by multiplet calculations, provide crucial information about crystal field effects, atomic multiplet interactions, and the phase of the TiO₂ particles. Valence photoemission results and band structure calculations using density-functional theory indicate a narrowing of the TiO₂ band gap when Pt is loaded onto the TiO₂ nanoparticle surface. This suggests that Pt photodeposition onto linear TiO₂ nanoparticle arrays may enhance the solar absorption of TiO₂ due to narrowing of the TiO₂ bandgap.

11:00am **SS-ThM10 Atomic-scale Structure of the Polar Spinel MgAl₂O₄(100) Surface, M.K. Rasmussen, K. Meinander, Aarhus U., Denmark, A.S. Foster, Tampere Univ. of Tech., Finland, B. Hinnemann, Haldor Topsøe A/S, Denmark, F.F. Canova, Tampere Univ. of Tech., Finland, S. Helveg, Haldor Topsøe A/S, Denmark, N.M. Martin, J. Knudsen, Lund U., Sweden, A. Vlad, Max-Planck-Institut für Metallforschung, Germany, E. Lundgren, Lund U., Sweden, A. Stierle, Max-Planck-Institut für Metallforschung, Germany, F. Besenbacher, J.V. Lauritsen, Aarhus U., Denmark**

Metal oxide spinels are an important class of materials in both ceramics technology and materials science. Although the prototypical ternary metal oxide spinel, magnesium aluminate spinel (MgAl₂O₄), is widely used, for instance, as a membrane in solid oxide fuel cells and in heterogeneous catalysis, either as a support for active metal nanoclusters or as a catalyst in its own right [1], many of the intricate details of its surface structure still remain unresolved. The atomic-scale surface characterization of similar spinel-type metal oxides has generally been challenging, due to the insulating nature of these materials, a property which limits the use of many standard surface science techniques.

Using a combination of non-contact atomic force microscopy (NC-AFM) and surface X-ray diffraction (SXRD), coupled together with density functional theory (DFT) structure calculations and NC-AFM simulations based on DFT, we have unraveled the complex structure of the polar MgAl₂O₄ (100) surface. Surprisingly, we find that the surface is terminated by an Al and O-rich structure, with a thermodynamically favored amount of Al atoms interchanged with Mg. These cation antisites, which are low-

density defects in the bulk, may be a key element in determining the substrate properties of MgAl₂O₄, among others its basicity and the likelihood for formation of OH-groups, which are believed to be anchoring sites for metallic nanoclusters, such as Ni, commonly used in steam reforming catalysts.

- [1] J. R. Rostrup-Nielsen, J. Sehested, and J. K. Nørskov, Adv. Catal. 47, 65 (2002).

11:20am **SS-ThM11 Growth and Characterization of Cu/ZnO on Au(111) as a Model Catalyst System, X. Deng, J. Lee, C. Matrangola, National Energy Technology Laboratory**

Model Cu/ZnO catalysts have been grown on a single crystal Au(111) substrate and characterized with X-ray photoelectron spectroscopy (XPS) and scanning tunneling microscopy (STM). Growth of ZnO on Au(111) is achieved by oxidation of Zn that has been deposited onto the substrate or by reactive evaporation of Zn in the presence of an oxidizer. XPS confirms that Zn has been oxidized and STM reveals that ZnO forms a uniform overlayer on Au(111) with an apparent height of ~6 Å. STM also reveals that the ZnO overlayer on Au(111) forms an ordered hexagonal Moiré pattern with a periodicity of 25 Å, possibly due to the lattice mismatch between the oxide and growth substrate. The atomic structure of the ZnO overlayer is also resolved with STM, showing a hexagonal unit cell with a lattice constant of 3.2 Å. Cu is then deposited onto the ZnO overlayer by evaporation, and STM is used to characterize the structure and morphology of the Cu/ZnO system. The model Cu/ZnO on Au(111) system will be compared to “real world” Cu/ZnO catalysts used for CO₂ hydrogenation and low temperature water gas shift reactions.

11:40am **SS-ThM12 Iron Oxide Growth on YSZ(001) and YSZ(111), I. Ermanoski, G.L. Kellogg, Sandia National Laboratories**

We have used low energy electron microscopy (LEEM) to study in real time the growth of iron oxides on the fully oxidized and partially reduced (001) and (111) surfaces of yttria-stabilized zirconia (YSZ). The FeO_x-YSZ system is currently used as a working material for solar thermochemical splitting of H₂O and CO₂ [1], but little fundamental information is available concerning the structure and composition of the mixed oxides and their surfaces. Upon Fe deposition in ~10⁻⁶ Torr of O₂ background pressure, iron oxides grow on the surface. Low energy electron diffraction (LEED) patterns, dark field LEEM imaging, and LEEM I-V measurements show that the composition and morphology of the surface oxide is very diverse, and depends on the substrate stoichiometry, crystallographic orientation, as well as on the deposition conditions and film thickness.

This work was supported by the LDRD program at Sandia National Laboratories, in the form of a Grand Challenge project entitled Reimagining Liquid Transportation Fuels: Sunshine to Petrol. Sandia is a multi-program laboratory operated by Sandia Corporation, a wholly owned subsidiary of Lockheed Martin Company, for the U.S. Department of Energy's NNSA under contract DE-AC0494AL85000.

- [1] Diver, R.B., Miller, J.E., Allendorf, M.D., Siegel, N.P., Hogan, R.E., “Solar thermochemical water-splitting ferrite-cycle heat engines”, Journal of Solar Energy Engineering, 130 (2008) 041001

**Transparent Conductors and Printable Electronics
Focus Topic**

Room: 106 - Session TC+AS+EM-ThM

Transparent / Printable Electronics Part 1

Moderator: R. Haasch, University of Illinois at Urbana
Champaign

8:00am **TC+AS+EM-ThM1 Growth Characteristic and Films Properties of Ga doped ZnO (GZO) by Low Temperature Atomic Layer Deposition, T.W. Nam, J.M. Kim, W.S. Lee, H. Kim, Yonsei University, Republic of Korea**

Atomic layer deposition (ALD) has great benefits over other deposition techniques since its growth mechanism controlled by a self-limited surface reaction exhibits excellent conformality, large area uniformity, and atomic scale thickness controllability. In particular, ALD becomes increasingly more promising thin film deposition method for future flexible electronics. Recently, there have been many research efforts on the investigation of doped ZnO for transparent conducting oxides (TCOs) due to their higher mobility than that of undoped ZnO. Ga doped ZnO (GZO) is one of the promising material for substitution of ZnO. As a representative TCO for applications to the transparent thin film transistor (TTFT) or flexible electronic, GZO thin films by PVD or CVD have been extensively studied.

Nevertheless studies on GZO films grown by ALD at low temperature condition which can be applied to flexible devices were still not carried out as far as we know in spite of its potential importance. Hence, for this study, we investigated the growth characteristics and film properties of low temperature ALD (LT-ALD) GZO films by varying deposition method. Field emission scanning electron microscopy (FE-SEM) observation of the GZO films deposited on 5:1 via patterns showed that the film has excellent conformality with over 95 % coverage even at room temperature growth. Additionally, the chemical and microstructural analysis was studied by various analytical techniques including X-ray photoelectron spectroscopy (XPS), X-ray diffraction (XRD) and atomic force microscope (AFM). Also spectrophotometer was used to measure a transmittance of the film and showed high transmittance that could be applicable to transparent devices.

8:20am TC+AS+EM-ThM2 Enhancement of C-Axis Orientation of Ga-doped ZnO Films Deposited on Unintentionally Heated Glass Substrates using Nanosheet Seed Layers, H. Makino, Kochi Univ. of Tech., Japan, T. Shibata, NIMS, Japan, N. Yamamoto, Kochi Univ. of Tech., Japan, T. Sasaki, NIMS, Japan, T. Yamamoto, Kochi Univ. of Tech., Japan

Ga-doped ZnO (GZO) film is one of promising candidates as substitute for ITO transparent electrodes in optoelectronic devices. Control of structural properties, especially c-axis orientation, is crucial issue to improve electrical properties of polycrystalline GZO films on glass or plastic substrates [1]. Recently, nanosheet seed layers were proposed to control crystal orientation of oxide films on amorphous substrates [2]. In this study, we employed a seed layer of tungsten oxide nanosheets with two-dimensional hexagonal lattice structure for deposition of GZO thin films on unintentionally heated glass substrates.

The nanosheets were assembled on glass substrates by Langmuir-Blodgett method. The GZO films with thickness of 100 nm were deposited by an ion-plating with direct current arc discharge on unintentionally heated glass substrates with and without the nanosheet seed layers.

The crystal structural properties were characterized by x-ray diffraction measurements. The c-axis orientation of the GZO films was drastically enhanced by the nanosheet seed layers. The intensity of (002) diffraction peak of GZO films deposited with the seed layers was about 40 times as strong as that deposited without the seed layers. The degree of c-axis orientation was evaluated by the (002) x-ray rocking curve (XRC). The full-width half-maximum of XRC of the GZO films on the nanosheet seed layers was 2.6 °, which is even lower than that of GZO films deposited on bare glass substrate at 200 °C.

The electrical properties were characterized by Hall effect measurements at room temperature. The GZO films deposited on the nanosheet seed layers showed the resistivity of $2.9 \times 10^{-4} \Omega\text{cm}$ with the Hall mobility of $24 \text{ cm}^2/\text{Vs}$ and the carrier concentration of $9.0 \times 10^{20} \text{ cm}^{-3}$. On the other hand, the GZO film deposited without the nanosheet seed layers showed the resistivity of $5.0 \times 10^{-4} \Omega\text{cm}$ with the Hall mobility of $17 \text{ cm}^2/\text{Vs}$ and the carrier concentration of $7.2 \times 10^{20} \text{ cm}^{-3}$. Both the Hall mobility and the carrier concentration were improved by the nanosheet seed layers.

[1] T. Yamada et al., J. Appl. Phys. 107, 123534 (2010). [2] T. Shibata et al., Adv. Mater. 20, 231 (2008).

8:40am TC+AS+EM-ThM3 Multi-component Transparent Conducting Oxides: Progress in Materials Modeling, S.-H. Wei, National Renewable Energy Laboratory **INVITED**

Transparent conducting oxides (TCOs) play an essential role in modern optoelectronic devices through their combination of electrical conductivity and optical transparency. We review recent progress in our understanding of multi-component TCOs formed from solid solutions of ZnO, In₂O₃, Ga₂O₃ and Al₂O₃, with a particular emphasis on the contributions of materials modeling, primarily based on Density Functional Theory. In particular, we highlight three major results from our work: (i) the fundamental principles governing the crystal structures of multi-component oxide structures including (In₂O₃)(ZnO)_n, named IZO, and (In₂O₃)_m(Ga₂O₃)_l(ZnO)_n, named IGZO; (ii) the relationship between elemental composition and optical and electrical behavior; (iii) the origin of high-performance of amorphous oxide semiconductors. From these advances, the challenge of the rational design of novel electroceramic materials is discussed.

9:20am TC+AS+EM-ThM5 Composition Control of Electron Beam Deposited Nb-TiO₂ Thin Films, N.A. Beckers, R.T. Tucker, University of Alberta, Canada, M.D. Fleischauer, NRC-National Institute for Nanotechnology, Canada, M.J. Brett, University of Alberta, Canada

Nb-doped TiO₂ has been identified as a potential indium-free transparent conductor, and has been fabricated by pulsed laser deposition and sputtering with good success.^{1,2} Other deposition methods, such as electron beam evaporation, are of interest for this material but have had limited

demonstration to date. It would be advantageous to be able to use electron beam evaporation because in addition to planar films, the collimated flux allows for structured thin films via glancing angle deposition (GLAD). Composition control is essential for doped functional materials, which is typically difficult to obtain through physical mixing of source materials. Here we show that using a sol gel approach to prepare the source materials provides a possible route to circumvent this issue. The facile, solution based sol gel process for the synthesis of ceramic and glassy materials allows for precise composition control by controlling the amounts and ratios of the metal oxide precursors. A sol gel methodology was used to prepare a series of Nb-doped TiO₂ deposition source materials with the following compositions: Nb_{0.06}Ti_{0.94}O₂, Nb_{0.12}Ti_{0.88}O₂, and Nb_{0.24}Ti_{0.76}O₂. We will show that XPS results confirm the composition of the electron beam deposited films and reflects the composition of the source materials. Premixed powders of Nb₂O₅ and TiO₂ do not show the same translation of composition as the sol-gel derived source material. Details on the effects of the post-deposition annealing environment on the thin film optical and electrical properties will also be presented.

References:

1. Yamada, N.; Hitosugi, T.; Hoang, N. L. H.; Furubayashi, Y.; Hirose, Y.; Konuma, S.; Shimada, T.; Hasegawa, T. *Thin Solid Films* **2008**, *516*, 5754-5757.
2. Ishida, T.; Okada, M.; Tsuchiya, T.; Murakami, T.; Nakano, M. *Thin Solid Films* **2011**, *519*, 1934-1942.

9:40am TC+AS+EM-ThM6 Laboratory and Production-Scale Low-Temperature Transparent Conducting Oxide Deposition, E. Ritz, University of Illinois at Urbana Champaign, G.B. Rayner, Kurt J. Lesker Company, D. Andruczyk, University of Illinois at Urbana Champaign, T. Dockstader, Kurt J. Lesker Company, D.N. Ruzic, University of Illinois at Urbana Champaign

Transparent conducting oxides (TCOs) are a class of materials that are becoming increasingly ingrained in our daily lives due to their use in electronic displays and mobile devices. There is a strong need to develop an economical deposition technique that allows for high transparency films with high electrical conductivity while replacing costly materials such as Indium Tin Oxide (ITO) with alternatives such as Aluminum-doped Zinc Oxide (AZO). In addition, a low-temperature deposition method would allow creation of TCOs on flexible plastic substrates, such as polyethylene terephthalate (PET). By using a dual DC magnetron system with a secondary RF antenna running at 13.56 MHz, a process has been developed that can deposit TCO films without significantly heating the substrate while maintaining high transmission and electrical properties. This capability has been demonstrated on a small-scale experimental setup utilizing 3-inch diameter circular magnetrons as well as a prototype production-scale chamber operating with 18x3.5 inch rectangular magnetrons aimed at flexible photovoltaic manufacturing. Using an immersed inductive RF antenna, ionization fraction can be increased to over 80%, measured by a gridded energy analyzer, and plasma density increased by an order of magnitude from 10^{10} cm^{-3} to 10^{11} cm^{-3} , as measured by Langmuir probe. The secondary plasma deposits energy in the film without heating the substrate above 100°C while still achieving film resistivity on the order of 10^{-3} - 10^{-4} Ohm-cm (measured by four-point probe method) and transparency of greater than 90% in the visible wavelengths (measured by spectrophotometry.) Adjusting the RF power (0-1000W) and the oxygen content (0-5%) in the plasma enables the ability to tune the film transparency and conductivity to desired levels. Crystal formation of films analyzed by x-ray diffraction (XRD) and elemental composition determined by x-ray photoelectron spectroscopy (XPS).

10:40am TC+AS+EM-ThM9 Optical and Electronic Properties of Photonic Crystal Based Transparent Conductors, S. Narayanan, M. Bockstaller, L. Porter, Carnegie Mellon University

Transparent conductors are becoming ubiquitous in a host of civil and military applications, including transparent electrical contacts in solar cells and LEDs, heated glass for aircraft and automobile windows, and electrochromic devices and smart windows. However, finding abundant materials with optimal electrical and optical properties and that can be produced economically is a particular challenge. Moreover, limited supply and large demand, of late, for indium has inspired focused research on finding alternatives to ITO as a transparent conductor. We report here a novel approach to control optical properties such as absorption, transmission and reflection in multilayered structures (based on [1-2]) with absorbing components. Appropriate combination of materials could, among others, allow for applications like transparent electrodes, transparent electromagnetic shielding, flexible transparent conductors, etc. Through this study, we have demonstrated the validity of this approach using a few different materials combinations including polymer/metal and metal/ceramic systems. In these realizations the approach was shown to

increase the transparency in the visible frequency range by ~ 3 orders of magnitude as compared to the reference materials. For example, transmittances of 30-50% of incident light in the visible region were measured for films containing a polymer (polystyrene – PS) and an amount of metal (gold – Au) that was 3-4 times as thick as its skin depth (~ 40-50 nm). We have also found compatibility between the observed experimental results and numerical simulations. Apart from enhanced optical transmittance, resistivity values of ~ 10⁻⁴ Ωcm (comparable to Au films having ~ 10⁻⁵ Ωcm) have also been discovered in structures having insulating components. Our ongoing and future work is focused on alternative structures to enhance conductivity in the transverse direction as well as incorporate flexibility in the same. **References:** [1] M. Scalora *et al.*, *J. Appl. Phys.* **83** 5 (1998) 2377-2383 [2] M. Scalora, M. J. Bloemer, C. M. Bowden, *Optics and Photonics News* **10** 9 (1999) 24-27

11:00am **TC+AS+EM-ThM10 Effect of Plasma Treatment and Annealing on the Electrical Properties of Spin-Coated Colloidal ITO Films**, **S.M. Joshi**, *G.W. Book, R.A. Gerhardt*, Georgia Institute of Technology

Colloidal ITO based inks may be an attractive route to direct writing transparent circuits and also be useful for the fabrication of transparent conductive ITO films on complex shaped substrates. The presence of stabilizing ligands and minimal contact between the ITO nanoparticles in the deposited films can be a challenge in obtaining the optimum electrical properties. This study investigates the effect of plasma treatment and annealing on the electrical properties of colloidal ITO films. Crystalline colloidal ITO nanoparticles were synthesized in-house by a non-aqueous technique. The solutions were spin coated onto glass and quartz substrates and their electrical and optical properties were evaluated. All films were found to be completely transparent, while the as-deposited films had resistivities more than 10⁸ ohm-cm. Plasma treatments were shown to be effective in removing residual organics in the films, and even without annealing, some recipes were able to reduce the film resistivity by more than four orders of magnitude. Plasma treatments, when done in combination with annealing, resulted in films with resistivities less than 1 ohm-cm.

11:20am **TC+AS+EM-ThM11 Hybrid Organic/Inorganic Materials and Devices for Flexible Electronics Applications**, **M.A. Quevedo-Lopez**, *J.I. Mejia, A. Salas-Villasenor, A. Carrillo-Castillo, B.E. Gnade*, University of Texas at Dallas, *D. Allee*, Arizona State University **INVITED**

The field of flexible electronics has expanded tremendously over the past few years. Similar to what happened in silicon integrated circuit technology 40 years ago; flexible electronics are now at a point where system design and process integration will drive the technology. Flexible electronics will likely push the limits of material performance, process integration, circuit design, and system integration to demonstrate the full potential of flexible electronics. In general, key components for any flexible electronic application include thin film transistors. In order to be competitive with state-of-the-art a:Si:H thin film transistors, any other thin film transistor technology must show reproducible transistor parameters such as mobility, threshold voltage, drive current and reliability.

A grand challenge in flexible, thin-film-transistor (TFT) circuitry is the development of complementary metal oxide semiconductor (CMOS) circuits. Although flexible digital circuits, flexible sensors, flexible batteries and solar cells have already been demonstrated, the missing technology piece that must be developed is flexible analog circuitry. For example, an operational amplifier will enable the interface to most sensors and actuators, significantly expanding the functionality of flexible electronic systems. In this paper, we will present n- and p-type chalcogenide-based materials that can be used as the building blocks for analog CMOS-based circuits. In particular, we will introduce the use of chemical bath deposition as an alternative to deposit these materials and will discuss the correlation between device characteristics and materials properties. Photolithography-based chalcogenide-based TFTs processed by chemical bath deposition achieved mobilities in the order of 10-25 cm²/V-s. In addition, we demonstrate hybrid CMOS for a:Si-Pentacene, CdS-Pentacene and CdS-TIPS Pentacene.

We also present the impact of semiconductor thickness, gate dielectrics and contact in device performance. In addition, NAND, NOR and Inverters are demonstrated using chalcogenide-based materials integrated with either a-Si or pentacene. Device processing is carried out at a maximum processing temperature of 110oC, which is compatible with most plastic substrates.

Thin Film Division

Room: 109 - Session TF1-ThM

Post-Deposition Processing and Characterization of Thin Films

Moderator: C. Vallée, LTM/CNRS-UJF, France

8:00am **TF1-ThM1 Protrusions, Surface Grains and Extended Single-Crystalline Plates**, **A. González González**, Instituto de Ciencia de Materiales de Madrid, Consejo Superior de Investigaciones Científicas, Spain, *G.M. Alonzo Medina, A.I. Oliva*, Centro de Investigaciones y de Estudios Avanzados del IPN, CINVESTAV Unidad de Mérida, Mexico, *C. Polop*, Universidad Autónoma de Madrid, Facultad de Ciencias, Spain, *E. Rodríguez Cañas, J.L. Sacedón, E. Vasco*, Instituto de Ciencia de Materiales de Madrid, Consejo Superior de Investigaciones Científicas, Spain

The processes controlling shape transformations during post-deposition treatments attract great interest due to their technological implications. As an example, residual stress relaxation during thermal annealing could influence component lifetime and performance in applications ranging from microelectronics to mechanical coatings, affecting their functional properties [1]. In this work, we investigate the morphology evolution during thermal annealing at 0.2 T_{melting} in polycrystalline Au(111) films using atomic force [scanning electron] (AFM [SEM]) microscopies and x-ray diffraction in order to follow both shape and structural transformations of surface features for different annealing times. Before annealing, a high density of round-like surface grains —which are surface components of an underlying competitive columnar microstructure—, is observed. During annealing, surface grains merge together into “multigrain” structures that expand laterally up to a saturation size, suggesting a size-dependent phenomenon controlling surface recrystallization. By comparison with Au polycrystalline growth fronts for the same temperature range [2] (T zone of the zone models [1]), we can relate the annealing-generated multigrain structures to the incipient formation of extended sub-micrometric-sized plates that are observed for thinner films. They contain many small surface grains with low-angle or no inner grain boundaries [2]. The small amount of material to be recrystallized for each component favors the multi-component extension of recrystallized zone. Interestingly, results here reported concerning the recrystallization phenomenon are discussed on the basis of local interactions between surface grains triggering plausible elastic/plastic mechanisms of stress accommodation (grain zipping and shear strain) and relaxation by surface diffusion processes [1,3], which in principle seems not to be very different from those expected in the coalescence stage at the T zone.

[1] L. B. Freund and S. Suresh, *Thin Film Materials: Stress, Defect Formation and Surface Evolution* (Cambridge University Press, Cambridge, England, 2003) and references therein.

[2] C. Munuera *et al.*, *J. Vac. Sci. Technol. A* **22**, 1767 (2004)

[3] A. González-González *et al.*, “*Morphology evolution of thermally annealed polycrystalline thin films*” (submitted)

8:20am **TF1-ThM2 Characterization of Mg Acceptors in GaN:Mg Grown by Metal Modulated Epitaxy and MOCVD**, **J.E. Lowder**, *M.W. Moseley, B. Gunning, W.A. Doolittle*, Georgia Institute of Technology, *M.E. Zvanut, J. Dashdorj*, University of Alabama

Acceptor doping of III-Nitrides has been the subject of many studies due to the relatively low hole concentration (~10¹⁷-10¹⁸ cm⁻³) material commonly grown in contemporary devices. This limitation is thought to be one of the contributing factors to efficiency droop in LED's. Recently, extremely high hole concentration (p>4x10¹⁹ cm⁻³) material with very high (>50%) ionization efficiency (see Fig. 1) has been demonstrated by metal modulated epitaxy (MME), an application of MBE where surface chemistry is controlled via shuttering of the source material [*J. Appl. Phys.* **106**, 014905]. The samples in this study are characterized by temperature dependent Hall measurement to elucidate the reduction in the acceptor activation energy. Electron paramagnetic resonance spectroscopy (EPR) was used to show the microscopic view of the Mg acceptor without influence of the surrounding crystal as well as the effect of annealing temperature on the EPR signal. It is found that the primary transport mechanism is likely due to impurity band conduction, consistent with a distributed acceptor band as opposed to an isolated acceptor energy level as is generally observed in p-type GaN. Likewise, the interaction of the Mg with hydrogen shows different annealing behavior when compared to MOCVD p-type GaN.

The samples analyzed by EPR were annealed at various temperatures in forming gas (H₂:N₂). Fig. 2 shows the relative intensity from the EPR signal of the neutral Mg acceptor as a function of forming gas anneal temperature.

It is clear that there is a sharp decrease in signal for the MME grown samples (doped $>10^{20}$ Mg as seen in fig. 1) at 525 °C as compared to the drop observed at 750 °C for the MOCVD grown samples (doped $\sim 10^{19}$ Mg). The exact nature of this temperature dependent decrease in signal is not fully understood, however it is suggested the different growth kinetics and resulting surface leads to a change in H₂ transport. A second mechanism may be the formation of Mg-H complexes with varying activation energies.

Preliminary temperature dependent Hall results (Fig. 3) show an as-grown activation energy of 70 meV in the MME samples as well as 5×10^{18} cm⁻³ holes remaining at cryogenic temperatures. This extremely low activation energy and lack of carrier freeze out is evidence of impurity band conduction and shows the degenerative nature of the material. The full effect of the annealing temperature on this degenerative material will be presented in further detail as it pertains to device processing.

8:40am TF1-ThM3 Post Deposition Annealing Effects on Thin Film Material, Process, and Device Properties, Y. Kuo, Texas A&M University

INVITED

Thermal annealing is a critical but often neglected step in semiconductor production. It has been routinely used to activate the ion implanted dopant and at the same time, to restore the single crystal structure. However, it is also a powerful tool in repairing damages in bulk films as well as at film-film interfaces, which are caused by the plasma-related deposition or etching process. In addition, the thermal annealing step can change film characteristics, which affects the subsequent process result. In this talk, the author will review some of his recent work related to thermal annealing, which involves three types of solid-state devices and thin films. First, an example on repairing the RIE damaged a-Si:H TFT with a low temperature thermal annealing process will be given. This step reduced defects in the bulk a-Si:H and SiN_x layers as well as at the gate-dielectric interface. This result has been interpreted in all TFT LCD productions around the world. In the second example, it will be shown that the thermal annealing step changed the grain size of the sputter deposited copper thin film. It resulted in the change of the copper-Cl reaction mechanism and therefore, the copper consumption rate. This is critical to a new plasma-based copper etch process that has been interpreted in large-area TFT LCDs and BiCMOS chips. In the third example, it will be shown that the post deposition annealing (PDA) condition is the key to the realization of a new type of nonvolatile memory device, i.e., the nanocrystals embedded high-k capacitors or MOSFETs. Furthermore, an addition low temperature annealing step removed the defects generated in the gate and back-contact sputtering processes. In summary, the thermal annealing effects are non-negligible because they are directly involved in product reliability and yield.

(1) Y. Kuo, "TFT and ULSIC – Competition or Collaboration," *Jpn. J. Appl. Phys.*, 47(3), 1845-1852 (2007).

(2) G. Liu, Y. Kuo, S. Ahmed, D. N. Buckley, and T. Tanaka-Ahmed, "Grain Size Effect on Plasma-based Copper Etch Process," *J. Electrochem. Soc.*, 155(6) H432-H437 (2008).

(3) Y. Kuo, "Status Review of Nanocrystals Embedded High-K Nonvolatile Memories," *ECS Trans.* 35(3), 13-31(2011).

9:20am TF1-ThM5 Semiconductor Thin Film Metrology using Coherent Acoustic Phonon Spectroscopy, A.D. Steigerwald, K. Varga, A.B. Hmelo, Vanderbilt University, L. Feldman, Rutgers University, N.H. Tolk, Vanderbilt University

Here we discuss the use of coherent acoustic phonon spectroscopy as a noninvasive and nondestructive measurement tool for semiconductor thin films. Specifically we emphasize its usefulness in studying the optoelectronic structure of materials with various types of structural defects. We discuss in-depth studies of ion-implanted GaAs, demonstrating that the technique may be used to quantitatively determine depth profiles of lattice disorder. Our optoacoustic measurements are shown to be 2-3 orders of magnitude more sensitive in defect concentration than channeling techniques, and establish a quantitative dependence between the change in optical response and defect concentration between 10^{18} - 10^{21} defects/cm³. Further, we demonstrate the entire range over which the coherent acoustic phonon technique is applicable in defect studies, and show results ranging from no noticeable change in optical response to complete damping of the phonon wave. We also discuss the electronic nature of the CAP response, which can provide insight into the interplay between lattice disorder and electronic structure.

9:40am TF1-ThM6 On the Phase Formation of Reactively Sputtered ZrO₂ Thin Films, R. Snyders, G. Geumez, S. Konstantinidis, UMons, Belgium

ZrO₂ is a material used as thin films in numerous applications. One of the applications with the highest added value is its use as ionic conductor in, for example, fuel cell devices. Nevertheless, only the tetragonal and cubic

polymorphs of ZrO₂ exhibit these ionic conduction properties. Therefore, effort have to be made in order to synthesis phase pure tetragonal or, ideally, cubic ZrO₂ thin films. It has been demonstrated that these polymorphs are generated when about 10% of oxygen vacancies are introduced in the material lattice. Recently, some works have demonstrated that it was possible to synthesize, by reactive high power impulse magnetron sputtering, cubic HfO₂ (a compound very close to ZrO₂) containing, as for cubic ZrO₂, 5% of oxygen vacancies when working in the transition region of the poisoning curve. This implementation of this strategy was possible thanks to the smoothness of this transition using this peculiar sputtering technology.

In this work, we aim to apply such a strategy to grow tetragonal (or cubic) ZrO₂ by reactive DC magnetron sputtering. Due to the very sharp metallic-to-poisoned mode transition, we used a plasma monitoring system (PEM) to work in stable conditions in that region.

A pure Zr metallic target is sputtered at constant current (0.2 A) at 10 mTorr in Ar/O₂ mixtures using a DC magnetron sputtering source with an unbalanced magnetic field configuration. A PEM system is implemented in order to grow films in the transition region. The Zr line at 340 nm is monitored in real time. The deposited films were characterized by grazing angle X-Ray diffraction (GAXRD) and X-Ray photoelectron spectroscopy (XPS).

Discharge parameters (voltage, current) and XPS data reveal that the transition occurs for $4\% < \%O_2 < 6\%$. For $\%O_2 < 4\%$, the films are under-stoichiometric with a metallic character. In the transition, we measure a stoichiometry of about ZrO_{1.8}. Finally, $\%O_2 > 6\%$, the films are stoichiometric. In term of phase constitution, it has been demonstrated that working in the poisoned mode, the monoclinic phase is synthesized while in the transition, for which the compound is under-stoichiometric, the tetragonal (and maybe cubic) phase is grown. These data support, for the first time, the theoretical assumption about the oxygen vacancies-generated tetragonal (or cubic) phase of ZrO₂. Finally, the thermal stability of the coatings has been studied: the as-grown samples have been annealed up to 1200°C. For annealing temperature up to 600°C, no modification of the phase constitution is observed while for an annealing temperature of 1200°C, the films experience a phase transition towards the monoclinic structure.

10:40am TF1-ThM9 Effect of 10 keV X-rays on Silicon Oxidation, S. Bhandaru, S.M. Weiss, E.X. Zhang, D.M. Fleetwood, R.A. Reed, R.A. Weller, B.R. Rogers, R.R. Harl, Vanderbilt University

In the past few decades, studies have been conducted to investigate photon assisted oxidation of silicon substrates. Most of these efforts have focused on understanding and modeling the oxide growth mechanism using photon energies spanning the visible (1.55 eV – 3.0 eV) to the UV range (3.0 eV – 6.5 eV). In this work, we study the influence of higher energy x-rays (10 keV) on silicon oxidation. We found that x-ray irradiation of silicon substrates, performed at ambient temperature and atmospheric pressure conditions, can significantly affect the formation of silicon oxide. The oxide formation is influenced by the dose rate and total dose of x-ray irradiation, as well as the initial silicon surface preparation.

Boron doped silicon samples (0.01 Ω-cm - 0.02 Ω-cm) were irradiated at dose rates ranging from 5.8 krad(SiO₂)/min to 31.5 krad(SiO₂)/min using a 10 keV x-ray source (ARACOR Model 4100). The samples were cleaned in dilute HF acid to remove the initial native oxide and obtain a clean surface prior to irradiation. The resulting silicon oxide thickness was estimated using spectroscopic ellipsometry (J. A. Woolam M-2000). Different models for the optical properties of the surface layer were evaluated. Oxide growth on the irradiated samples was compared to oxide growth on control samples, which were placed in ambient air at room temperature. The ellipsometry analyses suggest that the oxide growth on the irradiated samples was greater than that on the control samples. Initial XPS analysis showed that the oxide layers on the irradiated and control samples were chemically different, suggesting that differences observed in the ellipsometry analyses may be due, in part, to differences in the optical properties of the oxide layers and not purely due to a change in thickness.

We will present the results of the oxidation study in addition to XPS and AES characterization of the resulting oxide films. The impact of heating the silicon substrate up to 150°C during x-ray irradiation will also be discussed. A mechanism to explain the experimental observations is proposed based on ozone concentration measurements performed during irradiation. The possible generation of atomic oxygen, due to dissociation of molecular oxygen, by the high energy x-rays is suggested as a key factor in the observed x-ray irradiation induced silicon oxidation.

Acknowledgement: This work was supported in part by the DTRA Basic Research Program (Grant No. HDTRA1-10-0041).

11:00am **TF1-ThM10 Investigating the Local Physical Structure of Amorphous Hydrogenated Boron Carbide**, *M.M. Paquette, W. Li, M.S. Driver, S. Karki, N.A. Oyler, A.N. Caruso*, University of Missouri - Kansas City

The unique physical structure of boron-rich carbides, based on an extended molecular network of covalently bound icosahedral cages, has distinguished this material with an exceptional set of thermal, electrical, and mechanical properties. Technologically, boron carbide has generated interest for applications in solid-state neutron detectors, interlayer low- k dielectrics for ultra-large-scale integrated circuits, and high-temperature thermoelectric power converters. A method that has proven amenable to thin-film heterostructure device fabrication is the plasma-enhanced chemical vapor deposition (PECVD) of high-resistivity amorphous hydrogenated boron carbide ($a\text{-B}_x\text{C:H}_y$; $x \approx 2\text{--}5$) from the single-source precursor orthocarborene ($\text{C}_2\text{B}_{10}\text{H}_{12}$). However, although the physical structure of bulk crystalline boron carbide (e.g., $\text{B}_{4.3}\text{C}$) is nowadays well-understood, the short-range physical structure of the hydrogenated material (e.g., the number and types of atoms/bonds) has remained unsatisfactorily characterized, likewise for the intermediate-range physical structure of the amorphous lattice (e.g., how molecular subunits are bound together and arranged on a short sub-nm length scale)—structural modifications which have important consequences on the properties of the $a\text{-B}_x\text{C:H}_y$ films. Herein, we investigate the short- and intermediate-range physical structure of $a\text{-B}_x\text{C:H}_y$ films using solid-state magic angle spinning nuclear magnetic resonance (MAS-NMR) and Fourier transform infrared (FTIR) spectroscopies, backed by density functional theory (DFT) molecular structure calculations. The comparison of experimentally observed spectral features with theoretical predictions for model molecular compounds provides valuable insight into the different local chemical environments and intermediate-range networks that make up the $a\text{-B}_x\text{C:H}_y$ films. We demonstrate how applying these combined analyses provides an important stepping stone to understanding and optimizing the chemical, electrical, and mechanical properties of $a\text{-B}_x\text{C:H}_y$ films for next-generation device fabrication.

11:20am **TF1-ThM11 Characterization of Amorphous and Nanocomposite Nb-Si-C Thin Films Deposited by dc-Magnetron Sputtering**, *N. Nedfors*, Uppsala University, Sweden, *O. Tengstrand*, Linköping University, Sweden, *A. Flink*, Impact Coatings AB, Sweden, *A.M. Andersson*, ABB AB, Corporate Research, Sweden, *P. Eklund, L. Hultman*, Linköping University, Sweden, *U. Jansson*, Uppsala University, Sweden

Thin films of Me-Si-C (Me = early transition metal) have interesting multifunctional properties, see, e.g., [1]. We have in the present study investigated thin films in the Nb-Si-C system deposited by dc-magnetron sputtering using elemental targets. The microstructure and composition of the films have been characterized with x-ray diffraction, x-ray photoelectron spectroscopy (XPS) and transmission electron microscopy. Nanoindentation and atomic force microscopy were used to investigate the mechanical properties of the thin films while the electrical contact resistance was measured using a four wire set-up with an Au-coated probe pressed against the film surface.

Our results show that films with a silicon content less than 20 at.% exhibit a nanocomposite (nc-NbC/a-SiC) structure with nanocrystalline NbC grains embedded in an amorphous matrix phase. The size of the carbide grains decrease with the carbon content increase. A transition to a completely amorphous structure occurs with a Si content above 20 at.%. The transition in microstructure is reflected in the properties of the films with an abrupt increase in contact resistance (from 30 m Ω to 200 m Ω at 1 N) and a change in the mechanical behavior of the thin films. The XPS spectra show a change of chemical bonding from mainly C-Nb to a significant amount C-Si bonds as the Si and C content increase in the films. This results in harder films and an increase in the electrical resistivity. The amorphous films can be described as a metal carbide-based glass and the formation of this type of structures in sputtered Me-Si-C films will be discussed.

[1] J. Lauridsen et al., *Surf. Coat. Technol.*, 205, 299-305, 2010

11:40am **TF1-ThM12 Evaluation of Mn-based Cu Barriers for Interconnect Applications**, *E. Van Besien, N. Jourdan*, IMEC, Belgium, *L. Zhao*, Intel assignee at IMEC, Belgium, *K. Croes, Y.K. Stew, S. Van Elshocht, Zs. Tökei*, IMEC, Belgium

Diffusion barrier layers with a uniform thickness and good step coverage in narrow lines are needed to enable the continuing scaling of Cu

interconnects. Since physical vapor deposition (PVD) processes have limitations in respect of conformality, atomic layer deposition (ALD) and chemical vapor deposition (CVD) might become the preferred alternatives. Among others, Mn-based CVD barriers have been proposed [1], but up to now, Cu barrier properties for such films have not been proven electrically.

In this study, MnOx layers were deposited by CVD, on top of an O3/TEOS SiO2 layer. Deposition was done at two different temperatures: 200 °C and 350 °C. The effect of a post-plating anneal of one hour at 300 °C or 430 °C was studied. A test structure based on planar capacitors was used, in which first wide areas were patterned, followed by the deposition of the oxide and CVD MnOx layers, metallization, and CMP, respectively [2]. After passivation, voltage ramp (at 25 °C and 100 °C) and TDDB measurements (at 100 °C) were conducted. The electrical data were compared with those from a known good TaN/Ta-barrier reference system.

Voltage ramp measurements at 25 °C show a similar behaviour for all Mn-based films under study, except for the one deposited at 350 °C, with a post-plating anneal at 430 °C. For the latter a leakage current of about 1 order of magnitude lower is found, comparable to the leakage current of our TaN/Ta reference. For the film deposited at 200 °C, and annealed at 430 °C, voltage ramp measurements only showed shorts.

TDDB lifetimes were in all cases higher than for a reference without barrier, but lower than for a TaN/Ta reference. For the Mn-based films deposited at 350 °C, a post-plating anneal at 430 °C clearly improved the reliability properties. In this case, the extrapolated lifetime at user conditions (using the E-model), is above 10 years. A γ value of -3.4 cm/MV was found. However, for the films deposited at 200 °C, an anneal at 300 °C already degraded the reliability properties.

In conclusion, voltage ramp and TDDB measurements on planar capacitors structures show that, with optimised processing, CVD Mn-based barriers are promising candidates as Cu barriers in advanced interconnects.

[1] K. Neishi, S. Aki, K. Matsumoto, H. Sato, H. Itoh, S. Hosaka, J. Koike, *Appl. Phys. Lett.* 93 (2008) 032106

[2] L. Zhao, Zs. Tökei, G. Gai, Gischia, M. Pantouvaki, K. Croes, G. Beyer, *IEEE International Reliability Physics Symposium*, 2009, 848-850

Thin Film Division

Room: 110 - Session TF2-ThM

Modeling and Analysis of Thin Films

Moderator: P.D. Rack, University of Tennessee Knoxville

8:00am **TF2-ThM1 Aluminum Molecular Model for DSMC Simulations of Thin Film Deposition**, *A. Venkatraman, A. Alexeenko*, Purdue University

The direct simulation Monte Carlo (DSMC) technique has been shown to be able to predict various properties of thin films grown using vacuum deposition methods such as CVD, PVD, EBPVD. Such simulations can also provide information about the energy distribution and orientation of vapor molecules striking the substrate which are critical inputs to the prediction of the grain size, residual stress and other properties of the deposited films. One of the most important inputs to a DSMC simulation is the molecular model that determines the interaction between the simulated particles. The variable hard sphere (VHS) model that is widely used due to its combination of simplicity and accuracy is typically determined by fitting to viscosity data obtained from experiments. In the absence of direct measurements of transport coefficients for metal vapors such as Aluminum, one needs to resort to other techniques to determine a set of accurate molecular model parameters. In this work, we compare DSMC simulations with Aluminum thin film deposition experiments to determine the VHS model parameters. The growth rate of the thin films at the substrate location depends strongly on the transport properties of the metal vapor – viscosity being one of the most important – and hence can be compared with the DSMC simulations to determine a suitable molecular model. In a similar analysis for copper published earlier, we used experimental data available in literature while the experiments for this study are performed in the electron-beam evaporator in the Birck Nanotechnology Center at Purdue University.

8:20am **TF2-ThM2 ISSG Chemistry Modeling to Understand Uniformity Issues in RTP**, *S. Gupta, U. Kelkar*, Applied Materials, Inc.

This paper describes three-dimensional flow/thermal/chemistry modeling efforts to study the silicon oxidation using In-Situ Steam Generation (ISSG). This 3D model incorporates 27 step gas phase reaction mechanism which is responsible for ISSG chemistry. The complex 3D geometry, supersonic flow, detailed chemistry pose major challenges to the model convergence and results in unrealistic results due to H2 and O2 exothermic

reaction. Complex 3D geometry causes CFD model mesh size to become more than a million cells. The computational times to include all chemical reactions on a 3D complex flow problem are exorbitant. Thus a simple 2D RTP chamber model was built to examine the validity of gas phase reaction mechanism by comparing in-house simulation results with Professor Robert J. Kee, Colorado School of Mines [1] and to set the solver control parameters for stable solution in 3D. After a working 2D model, simple representative 3D model was built with very good quality structured mesh and the further geometric complexity was added in steps. The oxygen radical distribution predicted from the model matched very well with the oxide growth uniformity over a wide range of chamber pressure, gas flow rate, hydrogen fraction, and gas distributor geometry. At 5 torr, temperature distribution is dominated by wafer temperature as gas phase reaction is weak. At higher pressure exothermic gas phase reaction causes higher temperature above the wafer. There is weak gas phase reaction at 5 torr, resulting in low O atom number density. The O radicals diffuse in the chamber due to higher velocity at 5 torr where they recombine. At higher pressure flame ignites right at the edge of the wafer due to higher residence time resulting in very high O atom number density at the edge. This well calibrated simulation model was used in understanding and expanding process space by optimizing on several hardware and process variables using virtual prototyping before building the hardware.

8:40am **TF2-ThM3 Composition and Finite Size Effects in Thin Magnetic Films for Data Storage Applications: Magnetic and Transport Properties**, *O.N. Mryasov*, University of Alabama **INVITED** Scaling of magneto-resistance (MR) and resistance area product (RA) with thickness is one of a critical materials specific properties of hard disk drive sensors. We consider fundamental aspects of MR-RA scaling with two planar FM/NM/FM hetero-structures: (i) Fe/MgO/Fe tunneling junctions and (ii) all Heusler alloy giant-magneto-resistance (GMR) spin valves [1-3]. In both cases we focus on the electronic structure contributions to RA(MR). Third example motivated by rapidly decreasing grain size of data storage media where material specific finite size effects originate from magnetic interactions of 3d-5d(4d) elements [4,5]. First, we show that calculated within the QSGW theory [6] decay constant controlling thickness dependence of RA are consistent with experiment [7]. We also present results of direct spin dependent electronic transport simulations for two types of GMR structures (i) non-magnetic Heusler alloy spacers [1,2] and (ii) Ag spacer [3]. The (110) textured Co_2MnGe (CMG) and Rh_2CuSn (RCS) [1] have been used to build test hard disk drive reader and yielded MR of about 7 % and DRA of about $4.0 \text{ mW}\cdot\text{mm}^2$ [2]. The (001) textured FM $\text{Co}_2\text{Fe}(\text{Ge-Ga})$ with Ag spacer yielded MR values in excess of 45 % and DRA of $9.5 \text{ mW}\cdot\text{mm}^2$ [3]. Ab-initio electronic structure methods used to account for composition effects are shown to reproduce experimentally observed trends [1-3]. Finally we investigate finite size effects in the recording media granular films using model of magnetic interactions proposed to explain temperature dependence of magnetic anisotropy energy (MAE) observed in highly order L1_0 FePt thin films [4]. We discuss measurements protocol to quantify single vs. two ion contributions to MAE responsible for particular contributions to finite size effects in of 3d-5d(4d) thin films.

References:

- [1]. T. Ambrose and O. Mryasov, US Patent 6, 876, 522 (April 5, 2005).
- [2]. K. Nikolaev, P. Kolbo, T. Pokhil, X. Peng, Y. Chen, T. Ambrose and O. Mryasov, APL., v.94, p. 222501 (2009).
- [3]. Y. K. Takahashi, A. Srinivasan, B. Varaprasad, A. Rajanikanth, N. Hase, T.M. Nakatani, S. Kasaki, T. Furubayashi and K. Hono, Appl. Phys. Lett. **98**, 152501 (2011).
- [4]. O. N. Mryasov, U. Nowak, K. Guslienko, R.W. Chantrell, EuroPhysics Letters, v. **69**(5), 805 (2005).
- [5]. U. Nowak, O. N. Mryasov, R. Weiser, K. Guslienko, R.W. Chantrell, Phys. Rev. B, v. **72** p.172410, (2005).
- [6]. S. Faleev, O. Mryasov and T. Mattsson, Phys. Rev. B., v.81, p. 205436 (2010) and references therein
- [7]. S. Yuasa and D.D. Djayaprawira, J. Phys.D: Appl. Phys. v40, R337 (2007).

9:20am **TF2-ThM5 Large Scale TiN Thin Films Growth Simulations via Improved Modified Embedded Atom Parameterization**, *D.G. Sangiovanni, V. Chirita, L. Hultman*, Linkoping University, Sweden, *I. Petrov, J.E. Greene*, University of Illinois at Urbana Champaign Significant advancements within the last decade in the Modified Embedded Atom Method (MEAM) formalism, present the opportunity to perform, previously not possible, realistic large scale simulations of important model material systems such as TiN. The currently limited number of TiN MEAM parameterizations yield reasonable description of general bulk/surface properties of the material. However, to perform Molecular Dynamics (MD)

simulations of TiN thin films growth, a number of critical nucleation and diffusion phenomena have to accurately be accounted for in addition to basic properties. Herein, an improved TiN MEAM parameterization is reported, which not only correctly predicts bulk/surface properties, but also reproduces the experimentally observed trends in the diffusion of single species (Ti, N), Ti-N dimers and other complexes, on most representative, (100) and (111), steps/surfaces for TiN growth. The calculated activation energies for diffusion, and the all-important Ehrlich-Schwoebel (ES) step-edge barriers, are in good agreement with ab-initio calculations and experimental observations. To demonstrate the potential of this MEAM parameterization for simulations of TiN thin films growth, illustrative case simulation studies are presented, which successfully reproduce experimentally documented crucial processes in the initial stages of TiN nucleation, known to dramatically affect growth modes, and ultimately, properties of thin films. The implications of these results, and perspectives for large scale simulations of this extremely important material model system, are discussed.

9:40am **TF2-ThM6 Hard, yet Tough, Transition Metal Nitride Thin Films by Alloying and Valence Electron Concentration Tuning**, *D.G. Sangiovanni, V. Chirita, L. Hultman*, Linkoping University, Sweden

Improved toughness in hard and superhard thin films is a primary requirement for present day ceramic hard coatings, known to be prone to brittle failure during *in-use* conditions, in modern applications. Based on the successful approach and results obtained for TiN- and VN-based ternary thin films [1,2], we expand our Density Functional Theory (DFT) investigations to TiAlN-based quaternary thin films. $(\text{TiAl})_{1-x}\text{M}_x\text{N}$ thin films in the B1 structure, with $0.06 \leq x \leq 0.75$, are obtained by alloying with $\text{M} = \text{V}, \text{Nb}, \text{Ta}, \text{Mo}$ and W , and results show significant ductility enhancements, hence increased toughness, in these compounds. Importantly, these thin films are also predicted to be hard/superhard, with similar and/or increased hardness values, compared to TiAlN. For $(\text{TiAl})_{1-x}\text{W}_x\text{N}$ these results have experimentally been confirmed recently [3]. As previously demonstrated [1], the ductility increase originates in the enhanced occupancy of d-t_{2g} metallic states, induced by the valence electrons of substitutional elements (V, Nb, Ta, Mo, W). This effect is more pronounced with increasing valence electron concentration (VEC), and, upon shearing, leads to the formation of a layered electronic structure, consisting of alternating layers of high and low charge density in the metallic sublattice. This, in turn, allows a selective response to tetragonal and trigonal deformation: if compressive/tensile stresses are applied, the structure responds in a “hard” manner by resisting deformation, while upon the application of shear stresses, the layered electronic arrangement is formed, bonding is changed accordingly, and the structure responds in a “ductile/tough” manner as dislocation glide along the $\{110\}\langle 1-10 \rangle$ slip system becomes energetically favored [2].

[1] D. G. Sangiovanni et. al. Phys. Rev. B **81** (2010) 104107.

[2] D. G. Sangiovanni et. al. Acta Mater. **59** (2011) 2121.

[3] T. Reeswinkel et. al. Surf. Coat. Technol. (2011) in press.

10:40am **TF2-ThM9 Using Crystallographic Space Group-Subgroup Relations to Analyze Phase Selection and Transition in HfO₂ and Hf-based Ternary Oxide Films**, *C.R. Aita*, University of Wisconsin-Milwaukee

HfO₂ and Hf-based ternary oxides are important candidates for ultrathin high permittivity dielectric applications. However, technological aspects of their use in actual devices far outstrips our knowledge of the fundamental science that governs phase selection and transition in these materials. The latter is important for predicting both initial device performance and long term stability. One big issue is that pure HfO₂ readily forms nanocrystallites in thin films. These crystallites exhibit finite size effects on two different length scales: (1) *Two* metastable phases initially form in crystallites $\sim 7\text{nm}$ in size [1] and transform to monoclinic (m) HfO₂, the standard state, as crystallites grow. (2) Upon transformation from the metastables, m-HfO₂ nanocrystallites whose size is $\sim 11 \text{ nm}$ exhibit a lattice expansion concurrent with surface dipole repulsion [2]. A second issue involves the stability of Hf-based ternaries that are either intentionally grown or inadvertently form as a result of cation mixing during thermal processing or heating upon device use. These questions are being addressed from an experimental viewpoint through controlled isochronal and isothermal annealing studies. In this paper, we use crystallographic space group-subgroup analysis to examine phase selection and transition in three sputter deposited nanolaminates, HfO₂-Al₂O₃, HfO₂-TiO₂, and HfO₂-ZrO₂. The goal is demonstrate how this tool connects phase transitions between seemingly unrelated structures by symmetry considerations. We show that several important transitions observed in these materials are 2nd order and can be described by a simple relation between a parent group of higher symmetry and a daughter group of lower symmetry. Using the suite of programs in the Bilbao Crystallographic Server [3], first, conjugacy classes associated with

the parent → daughter transition are identified, and then using the operations within each class, the general atom positions of the parent are decomposed into cosets of symmetry elements expressed the daughter's basis. Symmetry elements that are “lost” in the decomposition are used to identify a twin domain structure in the daughter resulting from the transition. Using these formalisms, we discuss metastable phase→m-HfO₂ transition in pure HfO₂, the robustness of an entropy-stabilized HfAl-oxide phase, and the initiation HfTiO₄demixing.

Support from UWM Foundation Catalyst Grant / Rockwell Automation Charitable Trust.

[1] E.E. Hoppe et al. APL 91, 203105 (2007); APL 92, 109903 (2008).

[2] M.C. Cisneros-Morales et al., APL 96, 191904 (2010).

[3] M.I. Aroyo et al., Z. Kristallogr. 221, 15 (2006); M. Nespolo, Acta Crystall. A64, 96 (2008).

11:00am TF2-ThM10 Experimental and Theoretical Investigations Using SiO₂ Nanotemplates to Relieve Stress Caused by Thermal Expansion Coefficient Mismatch in Epitaxial Germanium Grown on Silicon, S. Ghosh, D. Leonhardt, S.M. Han, University of New Mexico

High-quality Ge-on-Si (GoS) heterostructures are pursued for many applications, including near-infrared photodetectors, high-mobility devices with Si-based integrated circuits, and virtual substrates for III-V multijunction solar cells. Growing low-dislocation-density GoS and subsequently integrating III-V layers present two significant engineering challenges: lattice mismatch and thermal expansion coefficient mismatch. The materials engineering solutions to circumvent the lattice mismatch include metamorphic growth, graded buffer layers, selective epitaxial overgrowth, aspect ratio trapping (ART), and a variety of defect filtering strategies. The ART technique, in particular, utilizes high-aspect-ratio holes or trenches etched through dielectric films to trap dislocations, greatly reducing the dislocation density. However, one shortcoming of ART is that it has been demonstrated to be effective only for small holes or narrow strips with dimensions less than 1 μm. In this study, we demonstrate that a combination of ART with selective epitaxial growth can produce large areas of high-quality GoS. We focus on the use of SiO₂-based templates with nanoscale windows placed on GoS to relieve the thermal stress. We observe that voids form around the top and sidewalls of SiO₂ template deposited by chemical vapor deposition, further relieving the thermal stress. The same templates also filter threading dislocations propagating from the underlying Ge-Si interface. The Ge layer grown and coalesced over the template is analyzed by transmission electron microscopy and etch pit density measurements. When the template is used, the threading dislocation density near the Ge film surface is approximately 10^7 cm^{-2}, while the twin defect density is approximately $5 \times 10^7\text{ cm}^{-2}$. Finite element modeling based on a commercial software package COMSOL is used to calculate the thermal stress occurring in the epitaxial Ge due to differences in thermal expansion coefficients among Ge, Si, and SiO₂. The simulation results, comparing Ge grown on Si with and without SiO₂ templates, show that the nanoscale templates can effectively reduce the thermal stress. The resulting stress results obtained using the simulation model corroborate the experimental observations. In summary, the simulation results suggest that the SiO₂ nanotemplates can reduce the stress caused by the thermal expansion coefficient mismatch, while simultaneously reducing the lattice-mismatch-induced dislocations in Ge grown on Si.

11:20am TF2-ThM11 Controlling Heteroepitaxy through Surfactant-Enabled Growth: An Ab Initio Thermodynamics Study, B.E. Gaddy, E.A. Paisley, M.D. Losego, J.S. Tweedie, North Carolina State University, R. Collazo, North Carolina State University, Z. Sitar, D.L. Irving, J.-P. Maria, North Carolina State University

We demonstrate that surfactant-assisted epitaxy is a useful method for stabilizing the growth of {111} CaO films on (0001) GaN. Surface free energies, calculated by ab initio thermodynamics, for configurations of CaO surfaces with varying surfactant coverage will be presented. These results explain the recent experimental observation that incorporating water vapor during CaO deposition produces a hydroxylated surface. Hydroxylation changes the preferred habit of CaO from (001) to (111), which enables layer-by-layer growth of (111) CaO on (0001) GaN. Together with experiment, these results demonstrate a new approach, applicable to numerous materials systems, where chemical boundary conditions are engineered to regulate the growth mode. Unique opportunities to integrate highly heterogeneous materials of dissimilar structure and symmetry are consequently available.

11:40am TF2-ThM12 Deposition and Modeling of Nanoscale Organic Porous Polymeric Layers and their Characterization with Visual and Electrical Methods, G. Franz, F. Schamberger, Munich University of Applied Sciences, Germany

To act as long-term antibacterial coating on the interior of hollow implants like artificial bladders or flexible pipes which can act as urethrae, silver layers have to be partly protected against aggressive solutions of the human body, e.g. urine or gall. One of these organic polymers is poly-p-xylylene, commonly known as polyparylene. In order to control this process of dissolution from metallic silver to silver ions which is responsible for the toxic impact, the layers should exhibit an adjustable hole density. This requires the growth control of very thin layers between zero and about 250 nm. By application of the conventional Gorham method, only thicknesses beyond 2 microns are accessible. We present a completely new method to control the growth of these very thin layers with defined porosity for which exact knowledge of vapor pressure and evaporation rate is required which have been measured and modeled using statistical rate theory (SRT) [1]. Applying a digital evaluation procedure of the micrographs gained with AFM, the hole density is correlated with the breakdown voltage and the capacitance which can both easily applied to the samples. Whereas the coating of open surfaces is controlled by flow, this mechanism is not applicable for coating of narrow holes which takes place as a diffusive process with losses due to deposition. In a series of experiments, the growth behavior in thin, narrow pipes with an aspect ratio between 10 and 30 has been obtained, and a theoretical model is presented which reflects the crossover of these two transport mechanisms as function of chamber pressure and temperature. [1] C.A. Ward, and G. Fang, Phys. Rev. E59, 429 (1999)

Tribology Focus Topic

Room: 111 - Session TR+AS+SS-ThM

Atomic-scale Characterization of Tribological Interfaces

Moderator: S. Perry, University of Florida

8:00am TR+AS+SS-ThM1 Electrochemical Control of Atomic Friction, F. Hausen, INM - Leibniz Institute for New Materials, Germany, A. Labuda, McGill University, Canada, N.N. Gosvami, R. Bennewitz, INM - Leibniz Institute for New Materials, Germany

Electrochemical methods allow for fast and reversible modification of metal surfaces through deposition and dissolution of metal films, adsorption and desorption of anions, as well as oxidation and reduction. The surface composition and structure undergo dramatic changes in these processes, which should cause significant changes in the friction on the surface.

We present friction force measurements at the nanometer scale on Au(111) and Au(100) single crystal electrodes performed by means of friction force microscopy in various electrolytes. The resolution of atomic stick-slip events in an electrochemical cell is improved by the development of a dedicated instrument [1]. A significant difference in friction is found for the bare electrodes compared to the modified surfaces. Friction is extremely weak and exhibits almost no load dependence on clean Au(111) surfaces. Upon electrochemical oxidation of the surface, significant friction with linear load dependence is observed. This process is reversible and allows switching repeatedly between high and low friction [2]. In the regime of anion adsorption our results indicate a frictional response with threshold behaviour. The threshold depends on both applied normal load and the electrochemical potential [3].

After deposition of copper on gold by underpotential deposition in perchloric acid, the atomic stick-slip changes into a periodicity which indicates frictional response of CuCl with a linear load dependence. In chloride-free sulphuric acid a different behaviour is found, indicating competing effects of ion adsorption on friction forces at small scales.

[1] A. Labuda et al., Rev. Sci. Instruments 81, 083701 (2010)

[2] A. Labuda et al., Langmuir (2011, available online)

[3] F. Hausen et al., Electrochimica Acta (2011, in print)

8:20am **TR+AS+SS-ThM2 Surface Alterations Effects on Ice Adhesion Strength**, *C. Ellis-Terrell, M. Miller*, Southwest Research Institute, *M. Zou*, University of Arkansas at Fayetteville, *R. Wei*, Southwest Research Institute, *S. Beckford*, University of Arkansas at Fayetteville, *G. Hatton*, Shell Global Solutions, Inc.

Ice adhesion is a serious problem in areas such as the oil, gas, and automotive industry, telecommunications and power line transmission. There is a significant amount of research directed towards designing a coating to reduce ice accumulation. This study focuses on measuring the effects of surface roughness and surface energy on ice adhesion strength. Surface texturing ranged from high to low surface roughness. A sandblasting technique was applied to the aluminum surface creating a high surface roughness. Surface energy changes were created by depositing a silicon doped hydrocarbon film, using plasma enhanced vapor deposition. A custom built apparatus was employed to specifically measure the adhesion force of an ice droplet. The results illustrate that the smoother as-received surfaces have lower ice adhesion strength than the rougher sandblasted surfaces.

8:40am **TR+AS+SS-ThM3 Atomistic Simulations of Nanoindentation and Nanoscratching of SiO₂/Si and HfO₂/Si Systems using COMB Potentials**, *T.-R. Shan, X. Sun, S.R. Phillpot, S.B. Sinnott*, University of Florida

Oxides such as SiO₂, Al₂O₃ and HfO₂, are typically used together with Si in many high-performance electronic devices, including metal-oxide-semiconductor (MOS) devices/junctions and micro- and nano-electromechanical systems (MEMS/NEMS). The lack of precise control over mechanical properties can lead to the degradation of these materials. It is therefore critical to understand the nanometer-scale mechanical properties of materials or complex systems being considered for use in electronic devices. Nanoindentation and nanoscratching are important methods for investigating the mechanical behavior of small volumes of materials, such as thin film systems. Here, classical molecular dynamics simulations are used to examine the responses to nanoindentation and nanoscratching of thin films of SiO₂ and HfO₂ on silicon substrates. The goal is to determine the influence of thin film types and the structure of thin film and substrate interface on the responses. Because these systems consist of heterogeneous interface with significant changes in bonding as one crosses from one side of the interface to the other, the empirical charge optimized many-body (COMB) potential as implemented in large-scale atomic/molecular massively parallel simulator (LAMMPS) program is used to model the structural evolution, mechanical response and charge transfer in these systems in response to a nanometer-scale spherical indenter. Aspects of the SiO₂/Si and HfO₂/Si interfaces during nanoindentation and nanoscratching, including the mechanisms by which fracture and plasticity occurs, will also be addressed. We gratefully acknowledge the support of the National Science Foundation through grant numbers DMR-0426870 and DMR-1005779).

9:00am **TR+AS+SS-ThM4 Accelerated Molecular Dynamics Simulations of Nanoscale Friction**, *W.K. Kim*, University of Minnesota, *M.L. Falk*, Johns Hopkins University **INVITED**

Accelerated molecular dynamics simulations are implemented to model the sliding process of atomic force microscope experiments and to lower the sliding speeds below those in a conventional MD simulation. In this study the hyperdynamics method, originally devised to extend MD time scales for non-driven systems, is applied to the frictional sliding system. This technique is combined with a parallel algorithm that simultaneously simulates the system over a range of slider positions so that the overall acceleration rate is approximately the number of processors multiplied by the boost factor from the hyperdynamics method. The new methodologies are tested using two-dimensional and three-dimensional Lennard-Jones AFM models. The methodology is then applied to simulated sliding between an oxidized silicon tip and surface achieving a range of six decades of velocity and reproducing the experimentally observed velocity dependence of the friction force. In doing so we learn something new about this system and about friction between amorphous surfaces in general. Unlike in the crystalline case, as increasing force is applied to the amorphous tip intermediate states arise. These intermediate states serve as critical transition pathways. The emergence of such states leads to the emergence of a plateau in sliding velocity at lower sliding speeds and higher temperatures. A simple theory based on these observations successfully describes both the experimental and the simulated data.

9:40am **TR+AS+SS-ThM6 Molecular Dynamics Simulations of Contact between Carbon-Based Materials: Isolating the Effects of Experimental Variables**, *J.A. Harrison, K.E. Ryan, P.L. Keating*, US Naval Academy, *D.S. Grierson, J. Liu, K.T. Turner*, University of Wisconsin Madison, *R.W. Carpick*, University of Pennsylvania

The behavior of nanoscale contacts is complex and often cannot be understood through continuum mechanics alone. Here, parallel molecular dynamics (MD) simulations using the AIREBO potential for hydrocarbons to model indentation and friction, are used to investigate nanoscale contacts of carbon-based materials, such as diamond, DLC, and ultrananocrystalline diamond (UNCD). Specifically, the contact of carbon-based AFM probes is simulated to understand the effects of experimental parameters, including tip geometry and material selection, on the adhesion between the tip and sample. Results from the MD simulations will be compared to and discussed within the context of the complementary atomic force microscope experiments and finite element simulations. The tribological response of carbon-based materials is very sensitive to environmental conditions. For example, the presence of water has been shown to negatively impact the friction performance of hydrogenated DLCs but to improve the performance of nanocrystalline and ultrananocrystalline diamond. We have been working to develop a potential energy function that is capable of modeling carbon-based materials in the presence of water. This talk will also outline our current efforts at potential development.

10:40am **TR+AS+SS-ThM9 Modeling the Pressure Dependence of Shear Strength in Sliding, Boundary-Layer Friction**, *M. Garvey, M. Weinert, W.T. Tysoc*, University of Wisconsin-Milwaukee

The pressure dependence of the shear strength of model alkali halide lubricant systems has been investigated at the density functional theory level. This is compared to the experimental dependence given by $S = S_0 + \alpha P$, where P is the contact pressure, S_0 is the zero-pressure shear-strength and α is the coefficient of pressure dependence. Sliding potentials were calculated and shear is found to occur between the film and the sliding interface. The heights of the potentials were calculated as a function of compression, allowing the lateral force to be calculated as a function of pressure. The calculated values of S_0 and α are in good agreement with experimental data.

11:00am **TR+AS+SS-ThM10 Lubrication Mechanisms of MoS₂ Fullerene-Like Nanoparticles: Coupling Computer and Experimental Works**, *E.W. Bucholz*, University of Florida, *I. Lahouij, F. Dassenoy*, Ecole Centrale de Lyon, France, *S.B. Sinnott*, University of Florida, *J.M. Martin*, Ecole Centrale de Lyon, France

Inorganic fullerene (IF)-like MoS₂ nanoparticles have been shown to be good lubricating and anti-wear additives when dispersed in a base oil. This improved tribological performance appears to be a result of the size and structure of the nanoparticles along with the test conditions. Possible lubrication mechanisms include pure rolling to sliding to the exfoliation of lamellar MoS₂ sheets inside the contact. *In situ* transmission electron microscopy (TEM) experiments have been used to manipulate individual MoS₂ nanoparticles and investigate their responses to compression and friction under different conditions. However, the very small scale of the MoS₂ nanoparticles makes distinguishing the properties which affect the lubrication mechanism exceedingly difficult; thus, a computational approach is used to more fully understand the most important mechanisms. Therefore, classical molecular dynamics (MD) simulations of individual nested MoS₂ nanoparticles are performed where they are subjected to compression and shear forces between sulfur-terminated molybdenum surfaces. Two specific nanoparticle configurations are considered, with both structures containing three layers. The first configuration is a curved, ellipsoidal MoS₂ nanoparticle structure with a major and minor diameter of approximately 8.9 and 6.6nm, respectively. The second nanoparticle configuration is an octahedron with grain boundaries that are approximately 6.2 nm in length. MD simulations of these structures indicate the role of curved and faceted morphologies as well as grain boundaries on the rolling/sliding behavior and nanosheet exfoliation of the particles. The results are used to interpret the experimental TEM findings and predict the dominant mechanisms associated with enhanced lubrication through the addition of these particles to base oils. This work is supported by the Office of Naval Research.

11:20am **TR+AS+SS-ThM11 Shape-Independent Lateral Force Calibration**, *E.V. Anderson, N.A. Burnham*, Worcester Polytechnic Institute

The primary problem with lateral force microscopy (LFM) has been the difficulty in calibrating the cantilever and tip in order to obtain quantitative friction data. Two recent review articles and several research articles have expressed this difficulty and the need for a simple, universally-accepted method [1,2]. The available procedures have numerous limitations. Some require specialized samples or setups. Others are difficult to perform. A

number are indirect, or only suitable for certain cantilevers. Several risk damage to the tip or sample, or both, and might require the geometry of the cantilever, which can be hard to measure. We present a procedure that alleviates these problems [3]. The linear relationship between the detected voltage and lateral force is exploited to obtain the slope (calibration factor) and intercept that convert voltage to lateral force. The method is independent of sample shape, probe shape, and scan parameters (load force, gain, and scan rate). The accuracy was investigated on an order-of-magnitude level and was within 50% of torsional spring constants obtained from geometry, and the precision was under 10%. Small scan areas were also found to produce accurate calibration factors and could help to limit tip-sample wear. Quantification of nano-Newton friction forces might now become routine.

1. M. L. B. Palacio, B. Bhushan, *Crit. Rev. Solid State Mater. Sci.* **2010**, *35*, 73-104.
2. M. Munz, *J. Phys. D: Appl. Phys.* **2010**, *43*, 063001.
3. E.V. Anderson, S. Chakraborty, T. Esformes, D. Eggiman, C. DeGraf, K. M. Stevens, D. Liu, and N.A. Burnham, "Shape-Independent Lateral Force Calibration," submitted April 2011.

11:40am **TR+AS+SS-ThM12 Atomic Stick-Slip Friction Studied by Optimally-Matched Accelerated MD Simulations and AFM Experiments**, *Y. Dong*, Purdue University, *Q. Li, R.W. Carpick*, University of Pennsylvania, *A. Martini*, Purdue University

Atomic-scale stick-slip friction of platinum on gold (111) surface is quantitatively studied both experimentally and through optimally-matched accelerated molecular dynamics (MD). In order to make a direct comparison between simulation and experiment, many other factors are matched as closely as possible, such as misalignment, size effect of the tip, cantilever compliance, normal load and so on. The Parallel Replica Dynamic Method (ParRep) is used to accelerate the simulation so scan velocities can be decreased to scales approaching those used in atomic force microscope experiments. A logarithm dependence of friction on scanning velocity is observed both in Atomic Force Microscope (AFM) and MD reveals that at low speed the atomic friction lies in thermal activation regime. A further comparison shows that AFM and MD provide consistent energetics, which supports that MD can be used to interpret AFM results; but attempt frequencies differ by orders of magnitude, which is attributed to the inertia discrepancy.

Thursday Afternoon, November 3, 2011

Actinides and Rare Earths Focus Topic

Room: 207 - Session AC+TF-ThA

The Structure, Properties and Chemistry of Thin Films of Actinides and Rare Earths

Moderator: L. Havela, Charles University, Czech Republic

2:00pm AC+TF-ThA1 **Plutonium Sorption and Reactivity at the Solid/Water Interface**, M. Schmidt, P.A. Fenter, S.S. Lee, R.E. Wilson, L. Soderholm, Argonne National Laboratory **INVITED**

Reliable long-term predictions about the safety of a potential nuclear waste repository must be based on a sound, molecular-level comprehension of the geochemical behavior of the radionuclides. We apply *in situ* crystal truncation rod (CTR) measurements and resonant-anomalous X-ray reflectivity (RAXR) in combination with alpha-spectrometry to elucidate the sorption behavior of tetravalent actinides on muscovite under varying solution conditions.

Key retention mechanisms, particularly in clay formations, are surface mediated processes. In order to be able to understand these processes analytical techniques that allow selectively probing the mineral/water interface and elucidating processes at the interface under *in situ* conditions are required. X-ray reflectivity techniques (CTR, RAXR) have proven to be valuable tools for geochemical studies concerning the sorption behavior of metal ions [1]. More recently they have also been applied to study the sorption behavior of actinides [2].

From CTR measurements the complete adsorption structure, consisting of adsorbed water and the ions adsorbed as inner sphere, outer sphere or extended outer sphere complex can be derived. RAXR extends this approach by providing elemental specificity to the CTR measurements, thus characterizing the contribution of a particular element to the structure.

Using a purpose-built sample cell for radiological experiments, X-ray reflectivity data was collected *in situ* from muscovite ($(\text{KAl}_2(\text{OH})_2[\text{AlSi}_3\text{O}_{10}])$) in contact with the actinide-bearing solutions varying in composition (ionic strength, actinide concentration and speciation, background electrolyte). The data is complemented by precise quantitative analysis by means of alpha-counting experiments. The results clearly show the strong influence of the actinides' aqueous chemistry on their sorption behavior. It will be shown that a full description of the sorption behavior requires parameters such as the hydration enthalpy, complexation constants, hydrolysis constants, and polymer formation constants. At low actinide concentrations the formation of hydrated surface complexes is observed in good agreement with the large hydration enthalpies of the highly charged ions. At large excess of background electrolyte sorption occurs under preservation of the complexation by the anion. When a threshold metal ion concentration is exceeded sorption of polymers is observed which grow up to 150Å in size, while covering only small fractions of the surface.

1. Fenter, P., Reviews in Mineralogy and Geochemistry 2002, 49, 149-220.
2. Fenter, P.; Lee, S. S.; Park, C.; Soderholm, L.; Wilson, R. E.; Schwindt, O., GCA, 2010, 74, 6984-6995.

2:40pm AC+TF-ThA3 **Crystal Chemistry of Thorium Oxy Compounds Containing Tetrahedral Oxyanions**, A.J. Albrecht, P.C. Burns, University of Notre Dame

Here we examine the crystal chemistry and structural topologies of Th compounds containing various cations that are coordinated by oxygen atoms in tetrahedral arrangements. We define the structural unit to be the part of the structure that consists of those polyhedra that contain higher valence cations, with an emphasis on their connectivity. In most cases, structures also contain interstitial units that balance the charge of the structural unit. In the compounds under study, which include both new structures and those from the literature, we find structural units ranging from clusters and chains, through sheets, to extended frameworks. The structural units in thorium compounds are of particular interest because they provide insights into the possible structures of compounds consisting of tetravalent transuranium cations, especially Np and Pu.

3:00pm AC+TF-ThA4 **Solution Route to High Quality Epitaxial Actinide Films Form Oxides to Carbides**, T.M. McCleskey, E. Bauer, A.K. Burrell, B.L. Scott, Q.X. Jia, T. Durakiewicz, J.J. Joyce, S.A. Kozimor, S.D. Conradson, R.L. Martin, Los Alamos National Laboratory
We report on the solution based synthesis of epitaxial thin films of neptunium oxide and plutonium oxide. Actinides represent a tremendous

challenge to first principle calculations of orbital energies due to the complicating features that arise from f orbital interactions. Theoretical development from first principle calculations relies on predictions of continuous materials with no boundaries. To test these theories requires experimental results using high quality single crystals. For many materials this can be a straight forward process. For actinide oxides the experimental work is complicated by the radioactivity that makes CVD processes challenging from a safety perspective and by the recalcitrant nature of the oxides. The challenge of modeling actinide oxides is best represented in Mott insulators such as UO_2 . Theoretical calculations that worked with transition metals predict UO_2 to be a metal as opposed to an insulator with a 2.3 eV band gap. Recent reports predict the same metallic behavior for NpO_2 . Many theoretical reports have highlighted the need for experimental work on single crystals. In the absence of single crystals they rely on work done on powders as in the case of PuO_2 . We report here on epitaxial films of PuO_2 that are thin enough to measure the optical band gap directly. XRD has been used to determine the alignment of the PuO_2 relative to the substrate and EXAFS confirm the stoichiometry.

3:40pm AC+TF-ThA6 **U(VI) Uranyl Cation-Cation Interactions in Framework Germanates**, J.M. Morrison, P.C. Burns, University of Notre Dame

The crystal structure determinations of four highly complex U(VI) germanate framework compounds reveal three distinct U(VI) sites—two that are coordinated by five equatorial oxygen atoms each to form pentagonal bipyramids and one that is coordinated by six oxygen atoms to form a distorted octahedron without the uranyl ion [1]. This is uncommon as most inorganic U(VI) compounds contain the uranyl ion, $(\text{UO}_2)^{2+}$. Also present are cation-cation interactions which occur when an oxygen atom of the uranyl ion also acts as an equatorial oxygen atom in a neighboring U(VI) polyhedron. CCI's are present in fewer than 2% of U(VI) compounds. Finally, a disordered system with the possibility of a one-dimensional GeO_5 chain has led us to suggest three structural models with regard to Ge coordination. The interesting structural and chemical complexities of these CCI-bearing compounds will be presented along with a discussion of the densities of CCI-bearing U(VI) compounds.

[1] Morrison, J.M.; Moore-Shay, L. J.; Burns, P.C. *Inorg. Chem.* **2011**, 50, 2272-2277.

4:20pm AC+TF-ThA8 **The Crystal Chemistry of Uranyl Selenates and their Relations with Uranyl Sulfates**, E.M. Wylie, P.C. Burns, University of Notre Dame

Uranyl sulfate minerals have been studied for several decades owing to their importance in understanding ore genesis, as well as the interaction of uranium mine and mill workings with the environment. In contrast, no uranyl selenate minerals have been described, although several uranyl selenites are known. We are exploring the crystal chemistry of synthetic uranyl selenates produced under mild hydrothermal techniques. We have obtained crystals of several compounds and characterized them with single-crystal X-ray diffraction. They contain a sheet of edge-sharing uranyl pentagonal bipyramids and selenate tetrahedra that is topologically identical to those found in the zippeite group of uranyl sulfate minerals. These synthetic materials provide further insights into layered uranyl phases, including the relationships between the configurations of the structural sheets and their corresponding interlayer complexes. These structures will be placed in the context of known synthetic and natural uranyl sulfate and selenate compounds.

4:40pm AC+TF-ThA9 **Radiation-Induced Degradation of Photoluminescence in YAG:Ce**, S.G. Gollub, D.G. Walker, S.L. Weeden-Wright, Vanderbilt University

Thermographic phosphors are ceramic based materials whose photoluminescence is temperature dependent. We fabricated the phosphor YAG:Ce to determine its sensitivity and selectivity to various radiation environments. In particular we investigated the effects of non-ionizing radiation on the photoluminescent spectra. No change to the spectrum was observed after exposure to 1 MRad of x-ray radiation. Because x-rays are typically ionizing, we did not expect to see any significant degradation. When the material was bombarded with protons, which are known to cause displacement damage in many materials, a degradation was observed. Results of damage cross section and stopping power were commensurate with predicted values using SRIM. Results are shown as a function of proton energy and dose.

5:00pm **AC+TF-ThA10 The Behavior of Uranyl Peroxide Pyrophosphate Nanoscale Cage Clusters in Aqueous Solution, K.L. Pellegrini, P.C. Burns, J. Szymanski, J. Ling, J. Qiu**, University of Notre Dame

Twenty-six nanoscale cage clusters built from uranyl polyhedra have been reported to self-assemble in aqueous solutions over a range of pH conditions [1]. All contain peroxide groups that bridge between uranyl polyhedra, and some contain additional linkages such as pyrophosphate and oxalate. The focus of the current study is the U24P12 cluster that consists of 24 uranyl hexagonal bipyramids and 12 pyrophosphate groups. We have optimized the synthesis of this cluster to obtain pure yields. Subsequently, we have examined the behavior of the cluster in solution using electrospray ionization mass spectroscopy and small angle X-ray scattering. These studies are emphasizing the persistence of this cluster under a variety of conditions, as well as their aggregation in solution. Such materials are of considerable interest because of potential applications in an advanced nuclear energy system, including in fuel recycling. Results to date show that the U24P12 cluster persists in aqueous solution for several days under a range of conditions, and can be induced to aggregate via addition of various counterions.

1. Burns, P.C. *Mineralogical Magazine*. **2011**, 75, 1-25 Open Access on peterburns.com

Spectroscopic Ellipsometry Focus Topic

Room: 209 - Session EL+AS+EM+MS+PS+TF-ThA

Spectroscopic Ellipsometry for Photovoltaics, Metals and Oxide Thin Films

Moderator: M. Creatore, Eindhoven University of Technology, the Netherlands

2:00pm **EL+AS+EM+MS+PS+TF-ThA1 Applications of Ellipsometry in Photovoltaics, D. Levi**, National Renewable Energy Laboratory **INVITED**

With the growing possibility of anthropomorphic-induced climate change there has come increasing concern over energy-related emissions of carbon dioxide into the atmosphere. The search for low or no-carbon energy sources has intensified. This has led to a twenty first century gold rush into photovoltaics research and technology startups. Although the PV industry has maintained its exponential growth rate through the global economic downturn, electricity from photovoltaics is still a long ways from economic competitiveness with fossil fuel-based electricity sources. The U.S. Department of Energy recently announced the Sunshot program, with the expressed goal of \$1/Watt installed cost for utility scale PV plants by 2017. This aggressive goal will require radical advances in new and existing PV technologies.

This presentation will begin with an overview of the major PV technologies and the state of the rapidly evolving global photovoltaics industry. Photovoltaics is a natural arena for application of spectroscopic ellipsometry. Nearly all PV devices are made of multiple thin films of semiconductors and transparent conducting oxides. New materials are constantly being introduced. Film thickness, optical properties, interfaces, electronic properties, and film growth dynamics are all critical aspects of these devices and lend themselves to investigation through the use of spectroscopic ellipsometry. I will present several case studies of how we have applied spectroscopic ellipsometry in our research in photovoltaics at the National Renewable Energy Laboratory.

2:40pm **EL+AS+EM+MS+PS+TF-ThA3 Comparison between Ex Situ and Real Time Spectroscopic Ellipsometry Measurements of Structurally Graded Si:H Thin Films, N.J. Podraza**, University of Toledo

Analysis of spectroscopic ellipsometry measurements of graded thin films remains challenging, although analysis procedures and software have improved over the past several decades. Practical use of these processes remains somewhat time consuming and is often not fully utilized by the casual user. In this work, ex situ ellipsometric spectra collected for static samples and real time spectroscopic ellipsometry (RTSE) measurements collected during film growth will be compared to illustrate differences in results arising from the measurement procedures and analysis. As an application, consider hydrogenated silicon (Si:H) thin films used for solar cells. Devices typically incorporate either amorphous silicon (a-Si:H) or "nanocrystalline" silicon (nc-Si:H) absorber layers, although the best "nanocrystalline" absorber layers actually consist of mixed-phase amorphous+nanocrystalline (a+nc) material. Si:H thin films may initially (i)

nucleate as amorphous and remain amorphous throughout growth; (ii) immediately nucleate as nanocrystallites; or (iii) initially evolve in the amorphous regime but nucleate crystallites which subsequently grow preferentially over the surrounding amorphous material until nanocrystallite coalescence. Analysis of ellipsometric spectra collected for (i) or (ii) simply involve using a substrate / bulk film / surface roughness model and complex dielectric function spectra ($\epsilon = \epsilon_1 + i\epsilon_2$) for the bulk material. For (iii), RTSE is ideally used to monitor the growth of Si:H that evolves through the amorphous, nanocrystalline, and mixed-phase regimes and a virtual interface analysis (VIA) procedure is used to extract ϵ for the amorphous and nanocrystalline components, the bulk and surface roughness thicknesses versus time, and the nanocrystalline fraction depth profile in the (a+nc) growth regime. For (a+nc)-Si:H films only measured with a single static ex situ measurement at the end of the deposition, obtaining ϵ and structural parameters of the film become less precise. Specifically, sensitivity to the variation in the nanocrystallite fraction with thickness may be lost and inaccurate ϵ for the component materials may be obtained. This work seeks to compare the structural and optical properties of (a+nc)-Si:H obtained by RTSE and VIA with those from analysis of static ex situ spectra with models using different structures, parameterizations in ϵ , and spectral range restrictions. These comparisons will be used to identify appropriate structural and dielectric function models to more accurately analyze structurally graded thin films under different material and measurement circumstances.

3:00pm **EL+AS+EM+MS+PS+TF-ThA4 Real-Time Spectroscopic Ellipsometry of Cu(In,Ga)Se₂ Thin Film Deposition: Copper Transition in 3-Stage Co-Evaporation Process, D. Attygalle**, University of Toledo, V. Ranjan, Old Dominion University, P. Aryal, University of Toledo, S. Marsillac, Old Dominion University, R.W. Collins, University of Toledo

With record efficiencies above 20%, Cu(In,Ga)Se₂ (CIGS) based solar cells have shown the greatest potential for success among the thin film photovoltaics technologies. Thermal co-evaporation of individual elements has proven to produce extremely high quality CIGS materials, provides a high level of flexibility, but also generates greater challenges in process optimization. The limitations of existing process monitoring capabilities, hence the challenge of correcting process fluctuations in real time, has led the industrial community toward more controllable CIGS deposition processes. Real time spectroscopic ellipsometry (RTSE) can be used successfully in the monitoring of complicated processes -- including CIGS film preparation by co-evaporation using precursor films of (In_xGa_{1-x})₂Se₃. Information extracted from RTSE includes the evolution of bulk layer and surface roughness layer thicknesses, the composition and phase, as well as the layer dielectric functions, all of which can assist in understanding the fabrication process and in optimizing solar cells. In this study, the focus is on the transitions of Cu-poor to Cu-rich CIGS and vice versa by observing the changes in (ψ , Δ) spectra obtained by RTSE. The commonly used monitoring method, which involves observing the changes in emissivity of the film, largely depends on the apparatus design, the substrate, and the bulk layer thickness. When a CIGS film is prepared by exposing a precursor film of (In_xGa_{1-x})₂Se₃ to Cu and Se fluxes, thereby becoming Cu-rich, a semi-liquid Cu_{2-x}Se phase is believed to form on top of a bulk layer consisting of mixed phases of Cu(In,Ga)Se₂ and Cu_{2-x}Se [1]. A multilayer optical model, with appropriate effective medium approximation layers to represent this scenario, has shown good agreement with the observed (ψ , Δ) spectra. Since RTSE is highly sensitive to monolayer-level changes in the top-most layer, RTSE gives superior sensitivity in Cu-rich to Cu-poor end point detection, which occurs when the top Cu_{2-x}Se phase drops below detectable limits. Furthermore this method is less affected by the substrate and bulk layer thickness. Although careful analysis of RTSE can give a wealth of information about CIGS material properties and their evolution, this type of end point detection can be successful simply by monitoring the real time changes in the (ψ , Δ) spectra.

[1] J. AbuShama, R. Noufi, Y. Yan, K. Jones, B. Keyes, P. Dipppo, M. Romero, M. Al-Jassim, J. Alleman, and D.L. Williamson, "Cu(In,Ga)Se₂ Thin-film evolution during growth from (In,Ga)₂Se₃ precursors", *Mat. Res. Soc. Symp. Proc.* paper H7.2.1, (2001).

3:40pm **EL+AS+EM+MS+PS+TF-ThA6 Bulk Heterojunction Solar Cell Characterization by Phase Modulated Spectroscopic Ellipsometry, K. Uppireddi, L. Yan**, HORIBA Scientific

The blend morphology, phase separation as well as crystallinity of organic photovoltaic solar cell are important properties to increase the efficiency. The performance of such cells is strongly influenced by blend composition and thermal annealing conditions. In this work we demonstrate the use of ellipsometry as a powerful and sensitive metrology means of monitoring organic solar cell based on the blend of poly(3-hexylthiophene) (P3HT) and [6,6]-phenyl C61-butyric acid methyl ester (PCBM). Ellipsometric measurements were performed on P3HT/c-Si, PCBM/c-Si and P3HT:PCBM/c-Si at an angle of incidence of 70 degree, across the spectral

range 190 – 2100 nm (0.6-6.5 eV). Two different analysis protocols were used to model the P3HT:PCBM blend structure. In the first protocol effective medium theory was used to represent the optical constant of layer, where as in the second one the blend was treated as one single homogenous material. The approach renders investigation of final morphology and composition.

4:00pm **EL+AS+EM+MS+PS+TF-ThA7 *In Situ* Spectroscopic Ellipsometry during Atomic Layer Deposition of Pt, Pd and Ru.** N. Leick, J.W. Weber, M.J. Weber, A.J.M. Mackus, H.C.M. Knoop, W.M.M. Kessels, Eindhoven University of Technology, Netherlands

The precise thickness control of atomic layer deposition (ALD) and its conformal growth make ALD the method of choice for nanometer thin film deposition. Platinum-group metals such as Pt, Pd and Ru have many applications in the areas of nanoelectronics and catalysis and recently there has been considerable interest to deposit films of these materials by ALD. Spectroscopic ellipsometry (SE) is a powerful, noninvasive optical technique that can be used *in situ* during ALD to precisely monitor the thickness of the films. SE also provides information on the optical and electrical properties of the films which is very relevant for their applications. Choi et al. [1] previously investigated the dielectric functions of Pt-group metal films with a thickness of ~400 nm as prepared by physical vapor deposition. For the aforementioned applications, however, the films are required to be much thinner, which leads to differences in film morphology as well as to dielectric functions that can be different from those of bulk films. In the spectroscopic ellipsometry work to be presented in this contribution we have therefore focused on films with thicknesses from 5 nm to 35 nm. *In situ* data was obtained during ALD in the photon energy range of 0.7 – 6.5 eV. Using a Kramers-Kronig consistent B-spline model to account for the thickness-dependent dielectric functions, we were able to obtain accurate ALD growth-per-cycle values for Ru, Pt and Pd ($1.00 \pm 0.06 \text{ \AA}$, $0.47 \pm 0.04 \text{ \AA}$, $0.14 \pm 0.02 \text{ \AA}$). Furthermore, the contributions from free-carriers (Drude term) and interband absorptions (Lorentz-oscillator contributions) were investigated by combining the SE data with FT-IR reflectance data such that the photon energy range of 0.04 eV – 6.5 eV was covered. In this range, it was possible to represent each film with a unique Drude-Lorentz model although some ambiguities about the Lorentz oscillator contributions remained in the case of Ru. It will be shown that the extracted thicknesses and electrical resistivities from this model are in line with data obtained from X-ray reflectometry and four-point probe measurements (for example Ru: $\rho_{SE} \sim 23 \mu\Omega\text{cm}$ and $\rho_{PPP} \sim 16 \mu\Omega\text{cm}$). Furthermore, in the case of Ru also the influence of the film roughness will be addressed.

[1] Choi et al., Phys. Rev. B **74**, 205117 (2006)

4:20pm **EL+AS+EM+MS+PS+TF-ThA8 Manipulating the Optical Properties of Metals: Sculptured Thin Films Coated by Atomic Layer Deposition.** D. Schmidt, N. Ianno, E. Schubert, M. Schubert, University of Nebraska - Lincoln

The fabrication of three-dimensional metal nanostructures with tailored geometry is one of the central challenges of nanotechnology because geometrical and material parameters are responsible for the optical, electrical, mechanical, chemical, or magnetic properties of such nanostructured thin films. Engineered artificial sculptured thin films (STFs) with designed anisotropies are potential candidates for applications in various fields such as optics, magneto-optics, as well as chemical and biological sensing and detection. However, in order to utilize metallic nanostructures for novel applications their size-, structure-, and material-driven physical properties have to be understood and quantified.

We utilize glancing angle electron-beam deposition, which exploits physical atomic-scale shadowing and dynamically varying particle flux azimuth for fabrication of three-dimensional highly spatially coherent STFs with different morphologies. Subsequently, nanostructures are individually covered with a thin conformal coating (cladding) by means of atomic layer deposition (ALD).

We will present the anisotropic optical properties of highly anisotropic ALD coated metal STFs determined by generalized spectroscopic ellipsometry in the visible and near-infrared spectral region. The analysis of our multilayer slanted columnar thin films deposited at glancing angle ($\theta_i = 85^\circ$) revealed that such STFs possess monoclinic optical properties, and the optical response may be described by an effective medium dielectric homogenization approach. It will be discussed how the anisotropic Bruggeman effective medium approximation (AB-EMA) allows for determination of structural parameters as well as fractions of individual film constituents. Furthermore, the AB-EMA analysis reveals that the anisotropic dielectric properties of the metal core changes upon deposition of a dielectric cladding.

4:40pm **EL+AS+EM+MS+PS+TF-ThA9 Ellipsometric Characterisation of Porous Aluminium Oxide Supports.** W. Ogieglo, N.E. Benes, H. Wormeester, MESA+ Institute for Nanotechnology, University of Twente, Enschede, The Netherlands

Porous aluminium oxide is widely used as a support material for thin film inorganic micro- and mesoporous membranes. Such membranes are used in energy-efficient gas separation, pervaporation and nanofiltration processes. Ellipsometry can be used to determine material properties of the thin membrane films, as well as the penetrant loading [1]. Interpretation of the ellipsometry data requires a detailed knowledge of the porous aluminium oxide support. This support is made of aluminium oxide particles that are sintered together. In between the particles voids are present that amount to 38% porosity. We have studied the influence of the size of the voids on the optical response of the support material. For this study, voids with a diameter of around 60, 80 and 160 nm were used. We noted a strong decrease of the normal incidence specular reflection with void size and a subsequent increase in off specular reflection. In ellipsometry, only a limited depolarization of the specular reflected light was noted in the wavelength range between 300 and 1750 nm. The angle dependent ellipsometry measurements showed that the optical properties of these supports can not be obtained from a direct inversion. The reason for this is that at the interface the more or less spherical voids are cut, which leads to a distribution of openings at the surface, i.e., a substrate with a very rough surface. This roughness was modelled with a graded porosity changing from 38% in the bulk to 75% at the outer surface. This measured variation in porosity is very similar to the cumulative height distribution of the surface layer obtained from AFM. The validity of this graded porosity model was verified from the analysis of a sample with a thin poly sulfone (PSU) layer deposited on the support. The PSU layer partly fills the open pores at the surface. This results in an interface with a graded variation in aluminium oxide, void and PSU.

The proper treatment of the surface layer also provides the optical properties of the porous aluminium oxide bulk material itself. These optical properties can in a limited wavelength range be modelled with Bruggeman's effective medium approximation. As a consequence of the size of the inclusions, their diameter is no longer negligible with respect to the wavelength of light in the UV part of the spectrum. For the material with the largest pore size, also a large part of the visible range has to be excluded. A more elaborate approach than the standard effective medium approach has to be used in this case.

[1] H. Wormeester, N.E. Benes, G.I. Spijksma, H. Verweij and B. Poelsema Thin Solid Films **455-456**, 747-751 (2004)

5:00pm **EL+AS+EM+MS+PS+TF-ThA10 Optical Properties and Structure of Vanadium Oxide Thin Films.** M.A. Motyka, M.W. Horn, Pennsylvania State University, N.J. Podraza, University of Toledo

Vanadium oxide (VO_x) thin films are common materials used as imaging layers in uncooled microbolometer based thermal imaging devices. These films are used in this application largely due to the controllable resistivity of the film (ρ), the high temperature coefficient of resistance (TCR), and the low electrical noise. One of the main difficulties of this material system relates to the multiple valence states of vanadium, each of which results in materials with different electrical properties. Bolometer quality VO_x may consist of a composite of nanocrystalline face centered cubic (FCC) VO phase and amorphous materials. The thin film oxygen content via Rutherford back scattering (RBS) has suggested that the typical ratio V:O should be near 1:1.7-2.0, significantly higher than the stability window of the FCC phase. This off-stoichiometry ratio suggests that the amorphous material is a mixture of higher oxygen valence states similar to V_2O_5 and VO_2 . The higher quality VO_x thin film material also has been observed via transmission electron microscopy (TEM) to contain $\text{VO}/\text{V}_2\text{O}_5$ nano-twin crystalline domains. The presence of each of these phases impacts the electrical and optical properties of the resulting VO_x film. Films with various oxygen contents and structures were studied with spectroscopic ellipsometry (SE) over a spectral range of 0.05 to 5.15 eV using a multichannel dual rotating compensator near-ultraviolet to near infrared instrument in conjunction with Fourier transform infrared spectroscopic ellipsometry (FTIR-SE). Thus, the complex dielectric function spectra ($\epsilon = \epsilon_1 + i\epsilon_2$) can be obtained for these materials over the full spectral range. Differences in ϵ due to variations in the film structure are observed as functions of processing, indicating that SE is a means of probing the material composition and structure. Specifically, ϵ are compared for various film composites fabricated by unbiased pulsed DC magnetron sputtering as well as composite films prepared by reactive ion beam sputtering and pulsed DC magnetron sputtering with a substrate bias. The microstructure and ϵ are correlated with films exhibiting the desirable device electrical properties. In situ real time spectroscopic ellipsometry (RTSE) has shown that environmental conditions alter the as-deposited VO_x thin films grown via pulsed DC-magnetron reactive sputtering of a metallic vanadium target. In order to prevent undesired atmospheric effects to the thin film, it is a

common practice to encapsulate the thin film with a more environmentally stable material. In this study, the material chosen was SiO₂ grown in the same deposition chamber, pre-atmospheric exposure, via rf sputtering.

5:20pm **EL+AS+EM+MS+PS+TF-ThA11 Sensitivity of Dielectric Properties of Vanadium Dioxide Thin Films to Growth Conditions**, *D.W. Ferrara, R.E. Marvel, J. Nag, R.F. Haglund*, Vanderbilt University

Vanadium dioxide (VO₂) is a strongly-correlated electron material with a well-known semiconductor-to-metal transition (SMT) that can be induced thermally (T_c = 68°C), optically, or electrically. Recently, VO₂ films have attracted attention as a component in active metamaterials, especially in conjunction with metal nanostructures. Since these structures are highly sensitive to the dielectric properties of the embedding material, the SMT of VO₂ can be used to tune the optical response of the structure. Accurately modeling the behavior of these structures requires detailed knowledge of the dielectric function of VO₂ as it undergoes the SMT; however, previous measurements of the optical constants of VO₂ reveal significant variations between experiments.

To understand systematic variations due to growth conditions, films of VO₂ were deposited on either silicon, glass, or sapphire substrates by pulsed laser ablation of vanadium metal targets in 10 mTorr oxygen (O₂) background gas, followed by annealing at 450°C in 250 mTorr of O₂. Anneal times were varied from 30 to 90 depending on film thickness; deposition thickness was varied from 20 nm to 200 nm. For each sample, temperature-dependent spectroscopic ellipsometry measurements at optical and near-infrared wavelengths were conducted to determine the dependence of the optical constants on film thickness, substrate and crystallinity, and temperature.

Bruggeman and Maxwell-Garnett effective-medium formulations were used to account for three constituent materials: semiconducting VO₂, metallic VO₂, and vanadium pentoxide (V₂O₅). The effective dielectric functions were modeled using Lorentz and Tauc-Lorentz oscillators. Our results show that the contribution of V₂O₅ to the effective dielectric function increases with annealing time, consistent with previous studies. The results are also substantiated using Rutherford backscattering, X-ray photoelectron spectroscopy and X-ray diffraction.

Energy Frontiers Focus Topic

Room: 102 - Session EN+MS+VT-ThA

Photovoltaics Manufacturing

Moderator: V. Ku, Satcon Technology Corporation

2:00pm **EN+MS+VT-ThA1 Waste Not, Want Not**, *L.V. Maness, Jr.*, South Park Platinum, Inc. **INVITED**

Rapidly increasing demand for certain geological commodities, in particular semi-conductors, rare earth elements (REE) and those with other desirable characteristics, are making the extraction of formerly ignored elements of significant financial interest for miners, recyclers and other commodity producers. This need is tempered by legal and regulatory requirements that minimize pollution. Historically, miners, smelters and others have used almost all the physical, chemical and electromagnetic characteristics of ores as a means of extraction and concentration – with the exception of the unique benefits afforded by processing in vacuums. Vacuum use enables the clean separation and capture of many commodities that heretofore were wasted, either up smokestacks, in water, or in waste dumps, etc. As a side-benefit, the coating with certain REE, etc., of heated surfaces will enable the selective emission of optimized thermal frequencies for use in generating electricity using Thermal PhotoVoltaics (TPV) technologies: this major improvement in TPV efficiency will result from the suppression in a vacuum of transfer of energy via conduction and convection. In addition, for the many commodities that vaporize selectively in vacuums, a vacuum-smelter would enable the non-polluting capture of all processed materials. Such capabilities will enable revolutionizing the economics of many operations, since the removal of one component from a mix will increase proportionally the relative percentages of the other components. This development will bring closer the goal of “*No Waste Mining*” and of the separation and use of certain otherwise useful constituents, such as arsenic, which are considered harmful, are tightly regulated and whose disposal is presently a very high cost-item.

2:40pm **EN+MS+VT-ThA3 The U.S. PV Manufacturing Consortium – Bringing the Supply Chain Together**, *P. Haldar, H. Efstathiadis*, College of Nanoscale Science & Engineering and U.S. Photovoltaic Manufacturing Consortium **INVITED**

The U.S. Photovoltaic Manufacturing Consortium (PVMC) – a \$300 million partnership between SEMATECH and the College of Nanoscale Science and Engineering (CNSE) of the University at Albany – will bring together the entire supply chain of companies to enable the development of advanced PV-related manufacturing processes. Created as part of the U.S. Department of Energy’s (DOE) SunShot initiative, which is designed to reduce the cost of photovoltaic solar energy systems by about 75 percent over the next decade, the PVMC will engage over 40 companies and organizations from throughout the solar community. Through PVMC, SEMATECH and CNSE will spearhead a unique research and development collaboration through which industry, academia and government will accelerate the development, commercialization and manufacturing of next-generation copper indium gallium selenide (CIGS) thin film PV manufacturing technologies, increasing performance while driving down the cost and risk of bringing them to the marketplace. By integrating the industrial research consortium and manufacturing development facilities models, PVMC offers lab-to-fab capabilities that will support rapid commercialization of new technologies and incubation of new start-up firms. PVMC offers the Federal government an unparalleled opportunity to promote the competitiveness of the U.S. PV industry.

4:20pm **EN+MS+VT-ThA8 Potentials and Challenges for High Efficiency Multi Junction Solar Cells**, *Bedair*, North Carolina State University **INVITED**

The developments of multi junction solar cell will be outlined. The major challenges facing this structure will be discussed. There are several current approaches to improve the efficiency of MJ solar cells. They include: lattice matched structure, metamorphic s structure, inverted structure and GaAsN based approach. We will discuss the concept of strain balanced strained layer super lattices in improving the conversing efficiencies of lattice matched MJ solar cells.

The advantages and the limitations of each of these approaches will be presented and discussed. We also discuss the limitations facing the applications of MJ solar cell at high solar concentrations. We will address the tunnel junction issues for concentration exceeding 1000 suns. Series resistance and heat dissipation issues will also be outlined.

Finally the cost issues will be addressed with their limitations on the potential applications of this approached.

Energy Frontiers Focus Topic

Room: 103 - Session EN+NS-ThA

Nanostructures for Energy Storage and Fuel Cells II

Moderator: J. Lewis, RTI International

2:00pm **EN+NS-ThA1 Charge-Storage Processes in Model MnO₂-Li-HOPG Systems: UHV-STM Investigations**, *S.C. Bharath, W. Song, J.E. Reutt-Robey*, University of Maryland, College Park, *K.R. Zavadil*, Sandia National Laboratories

Nanostructured materials have the potential to substantially improve the speed, efficiency, and cyclic lifetime of energy storage systems such as the lithium-ion battery (LIB). Nanometer-scale oxide cathodes elements allow for greater extent of lithium incorporation due to improved strain accommodation relative to conventional cathode structures. Exposed surface facets in structures with high surface/volume ratio will act as gateways to lithium insertion, playing an important kinetic role in charge storage. However, detailed mechanisms of lithium insertion and their dependence on oxide facet orientation and grain size and shape are largely unknown. As a platform for fundamental investigations of charge-transfer processes in nanocrystalline materials, we have developed a MnO₂-Li-HOPG model system. This system consists of low-dimensional β-MnO₂ and cubic spinel Li_{1+x}Mn_{2-x}O₄ nanocrystallites, synthesized by the reactive co-deposition of elemental Mn and molecular oxygen on native and modified graphite (C(0001)) supports under ultrahigh vacuum conditions. Nanocrystallite phase and composition has been confirmed using single particle electron diffraction, as well as TOF-SIMS and scanning AES. Morphology of individual nanocrystallites, and their registration to the C(0001) support, have been determined with ambient AFM and UHV STM methods. The morphological response of β-MnO₂ nanocrystallites to Li⁺ insertion has been preliminarily explored under solid-state conditions with UHV-STM. The sensitivity of these methods are currently limited by low β-MnO₂ – C(0001) electrical conductivity, and efforts to overcome this limitation will be described. Additionally, alkali seeded growth of MnO₂

nanocrystals will be presented as a means to guide the formation of alternative MnO₂ polymorphs.

Supported by the Science of Precision Multifunctional Nanostructures for Electrical Energy Storage (NEES), an Energy Frontier Research Center funded by the U.S. Department of Energy (DOE), Office of Science, Office of Basic Energy Sciences (BES) under award DESC0001160.

2:20pm EN+NS-ThA2 The Influence of Surface Chemistry as a Function of Salt Composition on the Rate Capability of LiNi_{0.5}Mn_{0.5}O₂ Composite Electrodes for Li-ion Rechargeable Batteries as Investigated using XPS, R.A. Quinlan, Naval Surface Warfare Center, Carderock Division, Y.C. Lu, Massachusetts Institute of Technology, A.N. Mansour, Naval Surface Warfare Center, Carderock Division, Y. Shao-Horn, Massachusetts Institute of Technology

LiCoO₂ is currently the most commonly used cathode material in commercial Li-ion battery technology because of its high working voltage, structural stability and long cycle life. However, cobalt is expensive and there are safety and toxicity concerns. Therefore, there has been a considerable amount of work on developing cheaper alternatives for the positive electrode of large-scale lithium ion batteries. LiNi_{0.5}Mn_{0.5}O₂ (LNMO) has emerged as one of the best options due to its high specific capacity, thermal stability and low material costs. Previous studies have illustrated that decreasing the interlayer mixing can increase the rate capability and that increasing the heat-treatment temperature can also increase the rate capability. Recently, the influence that surface chemistry has on the rate capability of LNMO composite electrodes was investigated and it was shown that an additional annealing treatment after quenching the material during synthesis increased the device performance from 50 mAh/g to 180 mAh/g at 55°C and 8C. Via an inspection using X-ray diffraction (XRD) and X-ray photoelectron spectroscopy (XPS), it was shown that the annealing treatment did not result in significant changes in the lattice parameters or in the cation distributions of the layered structure. However, the annealing treatment was shown to be responsible for removing surface impurity phases such as lithium carbonate species and Mn³⁺-containing species, which was associated with the observed increase in performance.

In this study, we further investigate the role that surface chemistry, as developed during the operation of the cell, has on the device performance. LNMO electrodes were constructed using quenched and annealed LNMO starting material. Both the quenched and annealed electrodes were cycled in the range of 2.0 V – 4.6 V in 1M LiPF₆/EC:DMC (1:1) or 1M LiClO₄/EC:DMC (1:1). The composite electrodes (in the discharged state) were disassembled in an Ar environment glove box and transported to the XPS analysis chamber without exposure to ambient. Cycling performance shows enhanced capacity retention and device performance for annealed electrodes cycled in LiPF₆, with the little to no enhancement observed for annealed electrodes when cycled in LiClO₄. Our initial analysis indicates the formation of both Ni and Mn fluorides/oxyfluoride species on the surface of electrodes cycled in LiPF₆. Additional changes in the surface chemistry and the influence on the rate capability will be discussed.

2:40pm EN+NS-ThA3 Hydrogen Storage in Metal Organic Frameworks (MOFs), N. Nijem, University of Texas at Dallas, L. Kong, H. Wu, Y. Zhao, J. Li, D.C. Langreth, Rutgers University, Y.J. Chabal, University of Texas at Dallas

Hydrogen storage is one of the most challenging problems in hydrogen-based energy technologies. One of the goals of hydrogen storage is the ability to store a high volumetric density of hydrogen at room temperature. As a result, studies exploring molecular hydrogen interaction in storage materials are important to facilitate further development of materials. Metal-organic Frameworks (MOFs) are promising candidates for hydrogen storage because their high surface area and porosity facilitate high hydrogen physisorption on specific sites of the structures and because many options are possible to enhance the interaction of molecular hydrogen with the host.

This work explores the incorporation of hydrogen into MOFs using infrared (IR) absorption spectroscopy to characterize its interaction. IR spectroscopy can distinguish possible H₂ binding sites based on the perturbation of the internal H₂ stretch mode. IR measurements are performed on saturated metal center MOFs varying the ligand and/or the metal center and on unsaturated metal center MOF-74-M (M=Zn, Mg and Ni). We combine room temperature, high pressure with low temperature (20-100K) measurements and theoretical van der Waals density functional (vdW-DF) calculations to derive quantitative information from IR shifts and dipole moment strengths.

Our results show that, in contrast to the current understanding, IR shifts are independent of binding energies and depend instead on the chemical environment of the molecule, including effects such as H₂-H₂ interactions. For example, we see little difference in IR shifts between saturated MOFs with low binding energy (~4kJ/mol), and unsaturated MOFs with higher binding energy (~10kJ/mol) sites at room temperature. Furthermore, we

show that dipole moments of adsorbed H₂ depends greatly on parameters such as geometry of adsorption site and H₂-H₂ interactions. Measurements performed at low temperatures on MOF-74 show that IR shifts of H₂ is greatly red shifted (an additional ~30 cm⁻¹) due to H₂-H₂ interactions on close proximity adsorption sites, and that dipole moments of adsorbed H₂ can appreciably vary with loading.

Our analysis indicate that the intensity of H₂ IR band cannot always be a measure of the amount of adsorbed H₂, therefore methods such as variable temperature IR (VTIR) used to deduce binding energies cannot always be implemented.

3:00pm EN+NS-ThA4 Nanostructure Engineering and Modeling of 3D Electrostatic Nanocapacitors, L.C. Haspert, G.W. Rubloff, S.B. Lee, University of Maryland, College Park

Increasing energy demands require innovative nanofabrication techniques for efficiently storing and supplying available energy. This talk discusses how anodic aluminum oxide (AAO) and atomic layer deposition (ALD) technologies are implemented and designed for creating high performance nanoelectrostatic metal-insulator-metal (MIM) capacitors. The densely porous (~10¹⁰ pores/cm²) self-aligned, self-assembled AAO nanostructure serves as a complex nanostructured template in which the self-limiting and conformal ALD process can uniformly coat this complex 3D structure. Thus, combining these two technologies results in a nano-capacitor with high power density and increased energy density, comparable to electrochemical batteries.

AAO template fabrication is a two-step anodization process, in which pores self-order in the first anodization. Then, the oxide is removed, leaving in a pre-patterned scalloped Al surface. Peak asperities are rounded with a barrier anodic alumina (BAA) and the rounded structures are retained during the subsequent anodization. Mild anodization (MA) chemistries provide interpore spacings, D_{int} (in nm), equal to 2.5x the anodization voltage, V_{anod} (in V), whereas hard anodization chemistries provide D_{int}~2xV_{anod}. In this work, oxalic acid MA results in pores spaced 100nm apart and 40nm in diameter. A final step etches pore sidewalls, increasing pore diameters up to 85nm. MIM layers are deposited by sequentially depositing 10nm of Al-doped ZnO (AZO), 8nm of Al₂O₃ and ~100nm AZO.

The porous structure increases the available surface area on which charge is stored, thus increasing the energy density since E=½CV². The capacitance increases with increasing depth, where planar, 1µm, 1.5µm and 2µm pore depth have capacitance of ~1, 11, 19 and 26µF/cm², respectively. Introducing the BAA reduces leakage currents to ~10⁻¹⁰A/cm² and breakdown fields are increased to 9.3MV/cm. A model simulates performance of the 3D nanogeometry, distributed resistances and dielectric capacitances, and internal non-linear resistance of the capacitor as a function of voltage. Additionally, trade-offs between pore size vs. layer thickness, AAO template interpore spacings vs. capacitance, pore depth vs. electrode series resistance are considered.

The ability to create scalable nano-structured devices is highly desirable for integrating with energy harvesting technologies. The fully self-aligned, self-assembled and self-limiting MIM nanocapacitors fabricated with ALD deposition in AAO templates demonstrate excellent electrical performance. Simulating device performance will aid in further increasing device performance and energy densities.

3:40pm EN+NS-ThA6 Atomic Scale Engineering for Energy Conversion Efficiency, F. Prinz, N.P. Dasgupta, C.-C. Chao, Stanford University

INVITED

The benefits of utilizing nanoscale materials include high surface to volume ratios, short transport lengths, tunable optical and electronic properties, and the ability to take advantage of quantum mechanical effects in low-dimensional structures. Simple scaling laws indicate how nano scale structures may help improving energy conversion efficiency.

Our group has been focusing on two primary application areas of ALD for energy conversion: fuel cells and photovoltaics. In the area of fuel cells, ALD presents several opportunities for reducing efficiency losses. By fabricating oxide-ion conducting electrolyte materials with thicknesses below 100nm which are pinhole free, we have been able to minimize ohmic losses due to ionic transport, allowing for a reduction in the operating temperature of solid oxide fuel cells (SOFCs)[1]. Furthermore, by fabricating 3-D fuel cell architectures[2] and modifying the surface of the electrolyte with a thin ALD layer[3], we have been able to reduce activation overpotentials in these cells and increase power density.

In the field of solar cells, we have been applying ALD to build quantum confinement structures for bandgap engineering. ALD of PbS thin films was performed, and measurements of the localized density of states (DOS) show the ability to tune the bandgap simply by controlling the number of ALD cycles[4]. We have demonstrated a new technique to directly fabricate

quantum dots (QDs) during the initial nucleation cycles of ALD PbS[5]. These QDs were deposited directly on nanowire surfaces, suggesting the ability to combine light trapping in nanostructured templates with quantum confinement effects.

- [1] J. H. Shim, C.-C. Chao, H. Huang and F. B. Prinz, *Chem. Mater.* **19**, 3850 (2007).
[2] P.-C. Su, C.-C. Chao, J. H. Shim, R. Fasching and F. B. Prinz, *Nano Lett.* **8**, 2289 (2009).
[3] C.-C. Chao, Y. B. Kim and F. B. Prinz, *Nano Lett.* **9**, 3626 (2009).
[4] N. P. Dasgupta, W. Lee and F. B. Prinz, *Chem. Mater.* **21**, 3973 (2009).
[5] N. P. Dasgupta, H. J. Jung, O. Trejo, M. T. McDowell, A. Hryciw, M. Brongersma, R. Sinclair and F. B. Prinz, *Nano Lett.* **11**, 934 (2011).

4:20pm EN+NS-ThA8 Nanoscale Characterization of Water Distributions in PEM Fuel Cell Membrane Electrode Assemblies Measured by Scanning Transmission Soft X-ray Microscopy. *A.P. Hitchcock, V. Berejnov*, McMaster University, Canada, *D. Susac, J. Stumper*, Automotive Fuel Cell Cooperation Co, Canada

Successful water management in proton exchange membrane (PEM) fuel cells requires a delicate balance of fuel, oxidant and water transport through a variety of length scales from ~ 1 mm in fuel channels, through ~ 10 -100 mm in the gas diffusion media, to 1-10 nm in the catalyst layer. The combination of a high degree of porosity in the reaction zone, complex composition, heterogeneous wetting properties, and the presence of water in two phases (gas, liquid) makes optimization of the performance of PEM fuel cell challenging. We are studying water distributions *in situ* in thin sections of membrane electrode assemblies (MEA) equilibrated with water vapor under feed-back controlled relative humidity conditions using scanning transmission X-ray microscopy (STXM). The intrinsic soft X-ray absorbance properties of the constituent materials allows direct *in-situ* visualization of water uptake into MEAs and the differentiation and mapping of the gaseous and liquid/sorbed water. The method provides maps of liquid and gaseous water distributed over the catalyst layer, with coincident maps of the ionomer and carbon support in the catalyst layer, as well as the polymer electrolyte membrane. Condensation at specific sites is observed when the relative humidity at the MEA is higher than $\sim 80\%$.

Research funded by AFCC and NSERC. Measurements were also made at the Canadian Light Source (supported by NSERC, NRC, CIHR, and the University of Saskatchewan) and at the Advanced Light Source (supported by the Division of Basic Energy Sciences of U.S. DoE.)

4:40pm EN+NS-ThA9 Optimization of the Delta Phase in Bismuth Oxide Thin Films. *P. Silva-Bermudez, O. Garcia-Zarco*, Universidad Nacional Autónoma de México, *E. Camps, L. Escobar-Alarcón*, Instituto Nacional de Investigaciones Nucleares, México, *S.E. Rodil*, Universidad Nacional Autónoma de México

Bismuth oxide Bi_2O_3 has interesting technological applications, which have not been largely used due to the particular polymorphism of the material. Bismuth Oxide has five polymorphic forms: α , β , γ , δ and ω - Bi_2O_3 . Among them, the low-temperature α and the high-temperature δ phases are stable and the others are metastable phases, as has been established by bulk solid-state studies. Each polymorph possesses different crystalline structures and various electrical, optical and mechanical properties. The face-centered cubic δ - Bi_2O_3 is stable over a narrow temperature range 729–825 °C (melting point) and it has the peculiarity of being among the few materials presenting high ionic conductivity at moderate temperatures (600-700°C). In this research, we aim to obtain δ - Bi_2O_3 thin films as possible ionic conductors for the development of micro solid state fuel cells. However, the first challenge is to find the deposition conditions of the magnetron sputtering system to ensure the formation of the desired δ - Bi_2O_3 , which is only thermodynamically stable at high temperatures. Based on previous results of Fan et al. (Fan 2006), we choose as the deposition variables the substrate temperature (room temperature to 300 °C) and the power (100-200 W). Our target was pure Bi_2O_3 , but the first results indicated that it was necessary to compensate oxygen losses; therefore the atmosphere was a mixture of Argon and Oxygen, where the Oxygen flow was 20% of the total. The results from the different characterization techniques suggested that substrate temperatures between 150 and 200°C are appropriate to obtain the δ - Bi_2O_3 phase at a high deposition rate, between 1.5 to 2 nm/s. X-ray diffraction (XRD) as a single technique to identify the film crystalline structure demonstrated to be rather difficult, since there is a large overlapping between the diffraction peaks corresponding to the α , β , γ and δ phases. However, we showed that by combining XRD and Raman spectroscopy, it was possible to clearly prove the presence of the δ -phase. The explanation for the stabilization of the high temperature phase might be related to the 2-dimensional confinement and/or then effect of the small

crystalline size. The physical properties of the δ - Bi_2O_3 thin films were further investigated; optical properties by transmission spectroscopy and ellipsometric spectroscopy in the ultraviolet-visible range, surface resistivity by the four-points method, composition by X-ray photoelectron spectroscopy and X-ray energy dispersion.

Fan H. T, et al. Thin Solid Films 513 (2006) 142.

5:00pm EN+NS-ThA10 Probing Physical and Interfacial Confinement Effects on Multilayered Piezoelectric Polymeric Films using Second Harmonic Generation Laser Spectroscopy. *J. Jones*, Fisk University, *H. Park*, Vanderbilt University, *L. Zhu*, Case Western Reserve University, *N.H. Tolk*, Vanderbilt University, *R. Mu*, Fisk University

Piezoelectric materials may arguably be the most functional, versatile and widely used materials with a wide range of applications including mechanical sensors, actuators, energy storage and energy harvesting devices. The well established applications are largely based on inorganic piezoelectric materials. The successful employment of polymeric piezoelectric materials, such as polyvinylidene fluoride (PVDF) and its related co-polymers, although light weight, flexible, optically transparent and cost effective, are limited by relatively low piezoelectric coefficients, thermal stability, and durability. The focus of the group is to develop a multilayered piezoelectric PVDF system for improved energy harvesting and energy storage efficiency. These systems are fabricated using enabling technology in co-extrusion which allows more cost effective and large area device production as opposed to more conventional layer-by-layer techniques. Many efforts have been made by the team to fabricate these micro- and nano-layered systems resulting in much improved device performance. A three-time improvement of capacitive electrical energy density has been demonstrated. The focus of this research is to understand the physics of why these multilayered systems perform better than a single layer by developing a characterization technique using both confocal second harmonic generation (SHG) and electric field induced second harmonic (EFISH) laser spectroscopy. Our results have shown that SHG is a very sensitive, non-destructive and versatile technique that can be used to study the piezoelectric and structural properties of layered systems. When combined with EFISH this technique allows the interrogation of electrical properties within the individual layers and at the interfaces between the layers. Further, the proposed techniques can be readily employed *in-situ* which can provide information in real time during sample processing with static and time-resolved spectroscopic measurements.

5:20pm EN+NS-ThA11 Electrical Transport in Ultrathin Ruthenium Films formed by Atomic Layer Deposition. *K.E. Gregorczyk, P. Banerjee, G.W. Rubloff*, University of Maryland, College Park

Next generation nanostructured devices require ultrathin layers of different materials (e.g. current collectors found in solar cells, batteries, and charge storage and memory devices, etc.). However, in the ultrathin regime, expectations from bulk resistivity can be misleading in designing such nanostructures. Here, we show the example of ultrathin (5-24nm) Ru films produced by atomic layer deposition (ALD), where resistivity is dramatically increased: at 5nm resistivity is $\sim 7\text{X}$ higher ($\sim 135 \mu\Omega \text{ cm}$) than at 24nm ($\sim 20 \mu\Omega \text{ cm}$) and $\sim 18\text{X}$ higher than bulk Ru ($7.4 \mu\Omega \text{ cm}$). The drastic differences seen here are explained through Mayadas-Shatzkes (MS) theory, which defines the increase in resistivity through geometrical constraints (e.g. film thickness and grain boundaries). Using MS theory the grain boundary reflection coefficients were calculated as ~ 0.32 for a 18nm thick film and ~ 0.66 for a 5nm film. Furthermore, the electrical transport properties of these films were studied as a function of both temperature (80-340K) and film thickness (5-24 nm). Finally, we show that the ALD Ru films are p-type, in agreement with the theory of compensated metals, and report both the temperature coefficient of resistivity and charge carrier mobility as a function of film thickness.

**Graphene and Related Materials Focus Topic
Room: 208 - Session GR+TF+NS-ThA**

Graphene Nanoribbons and Related Structures

Moderator: Y.J. Chabal, University of Texas at Dallas

2:00pm GR+TF+NS-ThA1 Rationally Patterned Large-Area Semiconducting Graphene Materials from the Top-Down and the Bottom-Up. *N. Safron, M. Kim, P. Gopalan, M. Arnold*, University of Wisconsin-Madison

INVITED

We are experimentally investigating self-assembling lithography (e.g. block co-polymer and nanosphere lithography) to create nanostructured graphene materials with feature sizes below what is easily achieved using optical and electron-beam lithography (< 20 nm), with the motivation of opening up a

technologically relevant band gap in graphene. We are particularly interested in a novel form of semiconducting graphene that we call nanoporated graphene, which consists of graphene perforated by regular hexagonal arrays of nanoscale holes. Unlike nanoribbons, nanoporated graphene advantageously retains a large-area two-dimensional form factor. In this talk, we will discuss the inter-relationship between the physical structure of nanoporated graphene and its electronic properties, with specific emphasis on how its band gap experimentally varies with feature size and how charge transport is affected by structure (including the role of edge defects and the observation of single-electron charging effects). We will also report on efforts in our group to realize nanostructured graphene materials with well controlled edge structure and superior properties via scalable and rationally controlled bottom-up growth that avoids top-down etching without sacrificing arbitrary pattern forming ability.

2:40pm **GR+TF+NS-ThA3 Quantum Pumping in Graphene Nanoribbons**, *T. Kaur*, Ohio University, *L. Arrachea*, Universidad de Buenos Aires, Argentina, *N. Sandler*, Ohio University

The interest in the development of devices at the nanoscale has intensified the search for mechanisms that provide tailored control of transport properties while reducing effects of heat dissipation and contact resistance. For instance, *charge pumping* is one of the current generating methods that allows for minimizing the effects of contact resistance. *Charge pumping* is the mechanism used to generate DC currents in open-quantum systems by applying local de-phased time-dependent potentials.

We analyze the properties of non-equilibrium zero-bias current through nano-ribbons using tight-binding Hamiltonians and the *Keldysh formalism*. This theoretical treatment, based on non-equilibrium Green's function techniques, is the most appropriate one to address questions for systems in non-linear, out of equilibrium conditions. We develop a numerical implementation for the models described below in a wide range of non-equilibrium regimes.

After reviewing results for quantum pumping in a one-dimensional chain attached to two reservoirs, with two local single-harmonic potentials oscillating in time, we study finite-width ribbons of square and graphene lattices. The transmission function reveals the value of the *resonant frequency* and explains how the quantum charge pumping works. We analyze the dependence of the *DC current* as a function of different parameters such as chemical potential, pumping amplitude, frequency, etc. In addition, the role of reservoirs is fully described. Pumped currents can also be generated by application of laser fields. We present the comparison between these two pumping methods. Possible extensions for disordered systems will be discussed.

3:00pm **GR+TF+NS-ThA4 First-principles Study of Field Emission from Graphene Nanoribbons**, *J. Driscoll*, *K. Varga*, Vanderbilt University

A real-space, real-time implementation of time-dependent density functional theory [1,2,3] is used to study electron field emission from graphene nanoribbons. The structures are shown to be good field emitters with spatial variation of the emission current influenced by the presence of passivating hydrogen. The nanoribbons are seen to produce slightly lower currents than nanotubes formed from the ribbons. Spin-polarized field emission from carbon nanotubes has been calculated with and without Fe adsorbates (atoms and clusters). It was observed that various adsorbates cause the separation of density into spin-polarized regions. The calculations predict that carbon nanotubes with various adsorbates can be used as spin-polarized current sources. The spin-polarized results for nanotubes will be compared to similar

calculations for graphene nanoribbons.

References

- [1] J.A. Driscoll and K.Varga, Phys. Rev. B 80, 245431 (2009).
- [2] J.A. Driscoll, S. Bubin, W. French, and K. Varga (submitted).
- [3] J.A. Driscoll, B. Cook, S. Bubin, and K. Varga (submitted).

Acknowledgments

This work is supported by NSF grant CMMI0927345.

3:40pm **GR+TF+NS-ThA6 Quantum Transport Properties of Modified Graphene Nanoribbons with Boron Nitride Domains at the Nanoscale**, *A. Lopez-Bezanilla*, Oak Ridge National Laboratory

Carbon-based systems are being widely investigated as potential candidates for nanoelectronic interconnects and transistors. The control of electric current is, therefore, an important challenge in nanostructures engineering. The possibility of creating hybrid one-atom thick layers containing C, B and N atoms have attracted much attention as they can provide an efficient way to create new materials with properties complementary to those of graphene and h-BN.

Here we present a theoretical methodology and study of charge transport through GNRs with BN domains randomly distributed along the ribbon surface. We resort to both first principles calculations, to obtain a suitable parametrization of the electronic structure, and a transport approach based on the ab initio results to explore conduction regimes through large and disordered systems. The quantum transport modeling is based on the Green's function formalism, combining an iterative scheme for the calculation of transmission coefficients with the Landauer's formula for the coherent conductance.

Our results describe how the conductance of the hybrid systems is altered as a function of incident electron energy and BN domain density. We explore the transport regimes comparing different degrees of BN doping and BN domain size for ribbons of various widths and lengths on the order of the micrometer. A comparison with other types of defects such as atoms in epoxy configuration and functional groups covalently attached to the ribbon surface will be also discussed.

4:00pm **GR+TF+NS-ThA7 Simple and Scalable Route for the 'Bottom-Up' Synthesis of Few-Layer Graphene Platelets and Thin Films**, *K. Coleman*, University of Durham, UK

Graphene has generated much interest owing to its exceptional electronic properties and high mechanical strength. This has enabled new types of electronic devices and composite materials to be envisaged. The main problem is the availability of the material and the difficulties associated with its synthesis. Here we present a simple, convenient and scalable chemical vapour deposition method involving metal alkoxides in ethanol to produce few-layer graphene platelets. The graphene platelets have been fully characterised using TEM, SEM, AFM, XPS and XRD. The methodology used has the added flexibility in that it can be used to grow conducting transparent thin films on inert substrates such as silicon wafer and quartz glass. Importantly, no heavy metal catalysts were required to produce the few-layer graphene platelets or graphene films and all non-carbon by-products are soluble in water.

4:20pm **GR+TF+NS-ThA8 Approaching the Intrinsic Bandgap in Suspended High-Mobility Graphene Nanoribbons**, *M.-W. Lin*, *C. Ling*, Wayne State University, *L.A. Agapito*, *N. Kioussis*, California State University Northridge, *Y. Zhang*, *M.-C. Cheng*, Wayne State University, *W.L. Wang*, *E. Kaxiras*, Harvard University, *Z.X. Zhou*, Wayne State University

We report the first variable-temperature electrical-transport study of suspended ultra-low-disorder GNRs with nearly atomically smooth edges. Suspension of the GNRs not only removes the substrate influence but also allows a thorough removal of impurities, including those trapped at the interface between the GNR and the substrate, leading to a substantial increase of the carrier mobility. We observe high mobility values over $3000 \text{ cm}^2 \text{ V}^{-1} \text{ s}^{-1}$ in GNRs that are $\sim 20 \text{ nm}$ wide, the highest reported to date on GNRs of similar dimensions. Furthermore, we demonstrate that the activation gap extracted from the simple activation behavior of the minimum conductance and residual carrier density at the charge neutrality point approaches the intrinsic bandgap in ultra-low-disorder GNRs. Comparison of the bandgap values of multiple samples shows that the bandgap in our ultra-low-disorder samples is approximately inversely proportional to the ribbon width, consistent with theoretical predictions. On the other hand, non-negligible disorder in GNRs obscures the observation of the intrinsic bandgap in transport measurements. In addition, the size of the bandgap derived from the transport measurements is in *quantitative* agreement with the results of our complementary tight-binding calculations for a wide range of chiral angles characterizing the GNR structure, suggesting that the underlying electronic origin of bandgap enhancement is the magnetism of the zigzag edges.

4:40pm **GR+TF+NS-ThA9 Fabrication of Polymer-Protected Graphene Nanoribbons by Thermal Dip-Pen Nanolithography (tDPN)**, *W.K. Lee*, *J.T. Robinson*, *R. Stine*, *A.R. Laracuenta*, Naval Research Laboratory, *W.P. King*, University of Illinois at Urbana Champaign, *P.E. Sheehan*, Naval Research Laboratory

The lithographic patterning of graphene nanoribbons (GNRs) to engineer band gaps has gained much attention as one path to realizing graphene-based devices. We employed thermal dip-pen nanolithography (tDPN)¹ to pattern GNRs on CVD single-layer graphene (SLG) that had been transferred onto a SiO₂ substrate. In tDPN, a heatable AFM cantilever regulates the deposition of an ink through controlled melting, much like a nanoscale soldering iron. tDPN has been successful at depositing polymers ranging from semiconductors to insulators on a variety of surfaces. To create the nanoribbons, we deposited polystyrene (PS) ribbons via tDPN on a SLG film between the source and drain electrodes. The areas of the graphene not protected by the polymer were then modified to isolate thin graphene nanoribbons. We show that the PS protected ribbon was the only

conductive pathway for active device. This method allows a wide range of nanoribbon widths to be created and avoids electron beams which can damage graphene. The impact of the polymer choice on conductivity as well as the choice of isolation will be discussed. For instance, we find that the PS ribbon can serve not only as an etch mask to pattern GNRs but also a stable dopant layer. The detailed fabrication and characterization of these structures will be presented.

1. WK Lee, et al. (2010) "Maskless Nanoscale Writing of Nanoparticle-Polymer Composites and Nanoparticle Assemblies using Thermal Nanoprobes", *Nano Letters*, 10, 129

5:00pm **GR+TF+NS-ThA10 Edge Termination of Modified Graphene Oxide during Thermal Exfoliation**, *M. Acik**, *Y.J. Chabal*, The University of Texas at Dallas

Nanopore formation in carbon materials (e.g. exfoliated nanostacks of graphite) has been widely studied through mechanical exfoliation, intercalation, electrochemical separation, chemical or thermal exfoliation of graphite oxide (GO) via expansion with partial oxygen removal. Amongst all these methods, exfoliation of modified graphene (GO), a solution-processable precursor compound where aromatic and heterocyclic rings with embedded oxygen functionalities exist, by thermal processing still remains elusive for the following reasons: (1) poor control of GO composition (initial oxygen content), (2) poor understanding of the chemical composition, (3) unknown role of oxygen, adjoining oxygen interactions, and edge termination with oxygen. Infrared absorption spectroscopy coupled with *in-situ* thermal annealing process [1] makes it possible to examine the chemical changes taking place during thermal reduction to identify and understand interacting molecular environment and the edge functionalization. To unravel the complex mechanisms leading the removal of oxygen in GO, we have performed *in-situ* transmission infrared absorption spectroscopy (IRAS) measurements of graphene/graphite oxide (GO) thin and bulk films upon thermal annealing (60-850°C) in vacuum (10^{-3} - 10^{-4} Torr). Control of the edge geometry of finite-sized modified graphene flakes depends very much on the control of the processing methods. This edge reconstruction further determines electronic, electric, optical and mechanical properties of the exfoliated modified graphene flakes. Therefore, we not only perform studies deriving a thermal reduction mechanism, but also examine the edge reconfiguration with oxygen. We report here the observation of a surprisingly strong IR absorption band that occurs only upon thermal reduction of GO. After annealing at 850°C in vacuum, the strong enhancement of the new IR active absorbance band is observed at ~ 800 cm^{-1} [2]. The intensity of this band is 10-100 times larger than what is expected for the oxygen content of the reduced GO, namely between 5 and 8 at.%. This band is assigned to a specific oxidation state, involving oxygen located in the basal plane (forming C-O-C bonds) and at *atomically straight* edges of reduced graphene. The large enhancement in IR absorption is attributed to the direct participation of electrons, induced by the asymmetric C-O-C stretch mode displacement. These findings open new possibilities in the field of nanoelectronics for all sensor and energy storage applications. [1] M. Acik, *et al.* J. Am. Chem. Soc. (2011), *in preparation*. [2] M. Acik, *et al.* Nat. Mater. 9, 840-845 (2010).

5:20pm **GR+TF+NS-ThA11 Study of Ridges on Epitaxial Graphene on 6H-SiC(0001)**, *Y.Y. Li, Y. Liu, L. Li*, University of Wisconsin-Milwaukee

The graphitization of hexagonal SiC surfaces provides a viable alternative for the synthesis of wafer-sized graphene for mass device production. During the later stages of growth, ridges are often observed on the graphene layers as a result of bending and buckling to relieve the compressive strain between the graphene and SiC substrate, which also introduce ripples in the otherwise atomically flat graphene sheet. In this work, we show, by atomic resolution STM imaging, that ridges are in fact bulged regions of the graphene layer, forming one-dimensional (nanowire) and zero-dimensional (quantum dot) nanostructures. We further demonstrate that their structures can be manipulated and even new ones created by the pressure exerted by the STM tip during imaging. These results and their impact on the electronic properties of epitaxial graphene on SiC(0001) will be presented at the meeting.

MEMS and NEMS Group **Room: 105 - Session MN-ThA**

Multi-scale Interactions of Materials and Fabrication at the Micro- and Nano-scale

Moderator: A.V. Sumant, Center for Nanoscale Materials, Argonne National Laboratory

2:00pm **MN-ThA1 Heterogeneous Microsystem Integration with Self-Assembly**, *K. Bohringer*, University of Washington **INVITED**

Self-assembly is the spontaneous and reversible organization of components into ordered structures, representing an alternative to the conventional manufacture of systems made of components from milli to nano scales. First commercial applications of self-assembly have appeared in recent years, for example in the fabrication of radio frequency identification (RFID) tags.

However, the full impact of this new approach towards hetero system integration will only be realized once self-assembly can be programmed on demand. This presentation gives an overview of several projects that aim at programmable self-assembly. A key concept is the "programmable surface" an interface whose properties can be controlled with high spatial and temporal resolution. Several crucial topics are discussed: real time control of interfacial properties; optimization of binding site designs; and algorithms for the modeling and control of self-assembly. Promising novel manufacturing methods are emerging that combine the precision and reproducibility of semiconductor fabrication with the scalability and parallelism of stochastic self-assembly and with the specificity and programmability of biochemical processes.

2:40pm **MN-ThA3 A Study of Solder Bridging for the Purpose of Assembling Three Dimensional Structures**, *M.R. Rao, J.C. Lusth, S.L. Burkett*, The University of Alabama

Recently, dip soldering has been used as a mechanism for driving the assembly of three-dimensional (3D), microscale structures. Solder is deposited on adjacent metallic faces of planar polyhedral patterns, bridging the small gaps between individual faces. When all but one face of a polyhedral pattern are freed from the substrate and solder is reheated to a liquid state (reflow), the free faces of the pattern fold upwards, out of the plane, to form the desired polyhedron. The wetting of solder with regards to coverage of metallic faces has been described previously, but the lateral bridging between the metal faces remains relatively unexplored. The goal of this work is to characterize the parameters influencing the bridging and folding process for two different ways of dip-soldering: face and edge soldering. Face soldering refers to the complete wetting of metal faces while edge soldering refers to selectively applying solder on the edges of a face that come in contact with other faces when folded. Our work explores bridging yield for various gap sizes and face thicknesses for eight different polyhedral patterns. Experiments show that the thickness and gap size strongly influence successful bridging. Experiments also show that improved control over the bridging process increases the yield of folded structures. In particular, gap size is positively correlated to face thickness for successful folding. Moreover, face soldering results in higher yields than edge soldering for all patterns.

3:00pm **MN-ThA4 Fabricating Arrays of Graphene Nanomechanical Resonators with High, Size-Dependent Quality Factors**, *R.A. Barton, A.M. van der Zande, R.B. Ilic, C.S. Ruiz-Vargas, J.S. Alden, W.S. Whitney, J. Park, P.L. McEuen, J.M. Parpia, H.G. Craighead*, Cornell University

Graphene's unparalleled strength, stiffness, and low mass per unit area make it an ideal material for nanoelectromechanical systems (NEMS), but graphene resonators have been challenging to fabricate in large numbers and have exhibited poor quality factor. Here, we present simple methods of fabricating large arrays of graphene resonators from CVD-grown graphene and discuss their properties. We focus on circular graphene resonators with diameter of up to 30 microns, for which we observe highly reproducible resonance frequencies and mode shapes, as well as a striking improvement in the membrane quality factor with increasing size. The largest graphene resonators display quality factors as high as 2400 ± 300 , about an order of magnitude greater than previously observed quality factors for monolayer graphene. These measurements shed light on the mechanisms behind dissipation in monolayer graphene resonators and demonstrate that the quality factor of graphene resonators relative to their thickness is high compared to nanomechanical resonators demonstrated to date. We conclude by providing an outlook for graphene NEMS and their applications.

* Morton S. Traum Award Finalist

3:40pm **MN-ThA6 Modal Dependence of Dissipation in Ultra Thin Silicon Nitride Drum Resonators**, *V.P. Adiga, R.B. Ilic, R.A. Barton*, Cornell University, *I. Wilson-Rae*, Technische Universität München, Germany, *H.G. Craighead, J.M. Parpia*, Cornell University

We have fabricated up to 1 mm diameter high tensile stress (1.2 GPa) circular SiN membranes. Stoichiometric amorphous high tensile stress SiN is a useful material for nanomechanical devices and resonators made from it have shown extremely high Q ($> 1,000,000$) at room temperature.¹ We used both optical and electron beam lithography to define circular structures and measured their resonant frequency and Q using optical interferometric detection methods. The measured mechanical Q shows a strong modal dependence, indicating the influence of clamping losses. Azimuthal harmonics of circular resonators with diameter $s > 200$ nm show an exponential drop in dissipation within an individual modal family ($n = 1, 2, 3, \dots, m$) apparently due to the destructive interference between the waves radiated by adjacent sections of periphery.² However, still higher order modes of large resonators and modes of smaller resonators are strongly influenced by a characteristic fQ limit of 2×10^{13} possibly indicating the presence of intrinsic dissipation in the high frequency limit. These findings pave the way for identifying optimum high Q modes of stressed oscillators for applications in mass sensing and fundamental research in optomechanics.

1) D. Southworth et al, PRL, 2009

2) I. Wilson-Rae et al PRL, 2011

4:00pm **MN-ThA7 Stress-based Flammable Gas Sensing with Nanocoated Resonant Microbridge at Critically-Buckled State**, *D.J. Joe, Y. Linzon, V.P. Adiga, R.A. Barton, M. Kim, B. Ilic*, Cornell University, *S. Krylov*, Tel Aviv University, Israel, *J.M. Parpia, H.G. Craighead*, Cornell University

In this work we demonstrate robust flammable gas sensing using stress-based resonant microelectromechanical systems (MEMS) bridges at ambient pressure and temperature. In contrast to previously reported works, which were based on either measuring a static deflection or changes in frequency due to added mass, we report a method of tracking shifts in resonant frequency of microbridges in real time due to alteration of stress from swelling of a reactive polymer coating near the Euler buckling configuration. Experimental results clearly demonstrate that the suggested approach is efficient for selectively sensing trace vapor. We show projected vapor content sensitivity as low as ~ 13.4 ppm for ethanol vapor in low concentration regime, and demonstrate actualized proven sensitivity of less than 1 part per thousand, with a few seconds response time for the functionalized microbridge.

4:20pm **MN-ThA8 Rapid Serial Prototyping of Magnet-Tipped Attonewton-Sensitivity Cantilevers**, *J.G. Longenecker, E.W. Moore, J.A. Marohn*, Cornell University

There is a critical need for a technique capable of non-invasive high resolution imaging of single copies of delicate biomolecules and as-fabricated semiconductor and spintronics devices. Magnetic resonance force microscopy (MRFM) is a non-invasive, three-dimensional imaging technique that employs attonewton-sensitivity cantilevers to mechanically detect electron spin resonance [1] and nuclear magnetic resonance [2]. The recent demonstration of 4 nm resolution imaging of a virus using MRFM establishes that the technique can achieve single-particle imaging with resolution competitive with cryo-electron microscopy [2]. The sample-on-cantilever geometry used in the experiment of Ref. 2, however, requires small, robust samples and is inapplicable to as-fabricated devices. We propose to image semiconductor devices by instead affixing to the cantilever the submicron magnetic particle required to achieve high spin sensitivity and spatial resolution. To minimize surface dissipation and achieve high signal to noise, the magnet must overhang the leading edge of the cantilever [3]. We recently demonstrated an approach to fabricating cantilevers with such integrated overhanging nanomagnets that achieves high yield [4]. Moreover, the novel tip fabrication method enabled the prototyping of new tip designs in less than sixteen hours of processing time [4], compared to the more than two weeks of processing time required for the best previous method [3].

Here we report harnessing this rapid prototyping technique to fabricate and characterize nickel and cobalt-iron-boron (CoFeB) nanorods. All nanomagnets are defined using electron beam lithography. The nickel nanorods are evaporated followed by liftoff, whereas the CoFeB nanorods are deposited by conformal sputtering and patterned by ion milling. The magnetic properties of the nanomagnets are determined using frequency-shift cantilever magnetometry and superconducting quantum interference device measurements. The elemental composition – paying particular attention to the extent of surface damage – is determined by scanning transmission electron spectroscopy and electron energy loss spectroscopy.

We will detail work to develop a protocol for improved encasement of nanorods overhanging the cantilever leading edge to protect against damage, as well as our progress in implementing the nanomagnet-tipped cantilevers in MRFM experiments to rapidly detect single electron spins.

[1] EW Moore *et al.*, *Proc. Natl. Acad. Sci.* **106**(52), 22251 (2009).

[2] C Degen *et al.*, *Proc. Natl. Acad. Sci.* **106**(5), 1313 (2009).

[3] SA Hickman *et al.*, *ACS Nano* **4**(12), 7141 (2010).

[4] JG Longenecker *et al.*, *J. Vac. Sci. Technol. B*, in press.

4:40pm **MN-ThA9 Microfabrication of On-Chip Electrodeposited CoNiP Micromagnets and Integration into MEMS Sensors**, *D. Schreiber, O. Berkh, S. Krylov, Y. Shacham-Diamand*, Tel Aviv University, Israel

Motion sensing of microelectromechanical systems (MEMS) devices is often a problem due to limited available chip footprint. On-chip thin film hard magnetic materials, when used as elements of integrated induced current displacement sensors, can help significantly simplify the designs and reduce device footprint due to the relatively high field density attainable. Device element spacing can also be increased thereby reducing fabrication tolerance requirements and improving robustness.

Electrochemical deposition is an attractive method for batch processing of magnetic films in patterned structures. Electroplating is a relatively simple process with a wide variability and control of film thickness and good scalability and compatibility with most of the MEMS microfabrication processes. Additionally, electrochemical deposition allows for the controlling of magnetic film anisotropy a key factor for the design of devices that operate in-plane or out-of-plane. Interest has been shown in CoNiP thin films for use in a number of MEMS applications however, the issues of integration were not addressed.

The integration of CoNiP magnetic films into MEMS sensors was studied. Through-mask electrodeposition of 1-2 μm thick magnetic films from concentrated ammonium chloride electrolyte was carried out at current densities of 30-150 mA/cm² using both direct current and pulse plating modes. The effects of current density, seed layer, passivation layer, pattern size and geometry on magnetic properties and feature-scale thickness distribution were investigated. Geometries included various arrays of micron scale stripes and dots, and large 1-4 mm² square areas. Feature scale profiles and magnetic properties of the films are influenced by current density as well as by feature size and geometry. Magnetic properties of CoNiP films after post-electrodeposition processing remain in the range suitable for sensor operation and are therefore shown to be suitable for integration in MEMS sensor.

Micropatterned CoNiP magnetic thin films have been integrated into silicon-on-insulator (SOI) MEMS devices. The patterned micromagnets – large square areas, stripes and dots – were characterized for feature-scale thickness distribution in relation to pattern geometry and current density, the effects on magnetic properties due to post-electrodeposition processing and their compatibility with standard MEMS process chemicals. Thickness distribution is strongly correlated with pattern geometry and current density. Magnetic properties remain in a range suitable for integration into MEMS devices following post-electrodeposition fabrication processes such as lithography, sputtering and etching.

5:00pm **MN-ThA10 Towards an Integrated Nano-optomechanical Platform for Molecular Sensing and Magnetometry**, *W.K. Hiebert, Z. Diao, J.N. Westwood, V.T.K. Sauer, M.R. Freeman*, National Institute for Nanotechnology (NRC Canada) and University of Alberta, Canada

Nanoelectromechanical systems (NEMS) have exquisite potential in fields ranging from quantum measurement to ultrasensitive mass sensing. Signal transduction has remained an important challenge for NEMS where applications demand fast, parallel, sensitive, and low-noise drive and detection of motion in ever smaller and faster devices. The burgeoning field of nano-optomechanical systems (NOMS) has offered a promising solution to this challenge in the form of unprecedented displacement sensitivity with almost unlimited bandwidth. Nanophotonic circuits provide strong local concentration of optical forces and optical phase changes interacting with embedded NEMS devices. The combination is fully integratable with modern opto-electronic and semiconductor technology paving the way to large-scale-integrated lab-on-a-chip NEMS sensing arrays.

We will present our preliminary efforts in building an integrated NOMS platform for molecular sensing and for magnetometry applications. The results include a novel measurement geometry that allows accessing

nanophotonic NOMS chips in vacuum via free-space focusing onto grating couplers. The external-to-vacuum optics arrangement gives independent control over the position and input/output angles of both the input and output laser beams. This geometry allows us to directly compare photonic readout of NEMS motions with conventional free-space Fabry-Perot interferometry. Finally, we will update our progress in 3D integration of NEMS and photonics.

Nanometer-scale Science and Technology Division

Room: 203 - Session NS-ThA

Biological Nanomaterials

Moderator: N.A. Burnham, Worcester Polytechnic Institute

2:20pm **NS-ThA2 Biologically-Inspired Reversible Adhesives: Where Are We Now?**, S. Gorb, Zoological Institute at the University of Kiel, Germany **INVITED**

Biological hairy attachment systems demonstrate their excellent adhesion and high reliability of contact. The structural background of various functional effects of such systems is discussed in the present paper. Additionally, it is demonstrated here, how comparative experimental biological approach can aid in development of novel adhesives. Experimental studies show that the effective elastic moduli of fiber arrays and spatula-like terminal elements are low, and this is of fundamental importance for adhesion enhancement on rough substrata and for an increased tolerance to defects at the level of individual contacts. Based on the broad structural and experimental studies of biological attachment devices, the first industrial bioinspired reversible adhesive foil was developed, which adhesive properties were characterised using variety of measurement techniques and compared with the flat surface made of the same polymer. The microstructured foil demonstrates considerably higher pull off force per unit contact area. The foil is less sensitive to contamination by dust particles, and after washing with water, its adhesive properties can be completely recovered. This glue-free, reversible adhesive is applicable in dynamic pick-and-drop processes, climbing robots, and other systems even under vacuum conditions. The foil represents therefore a considerable step towards development of industrial dry adhesives based on the combination of several principles previously found in biological attachment devices.

3:00pm **NS-ThA4 Ultrastable Superparamagnetic Nanoparticle Design for Membrane Assembly and Triggered Release**, E. Amstad, M. Textor, ETH Zurich, Switzerland, E. Reimhult, University of Natural Resources and Life Sciences Vienna, Austria

Application of superparamagnetic iron oxide nanoparticles as biomedical imaging contrast agents and as actuators in smart materials, e.g. for drug delivery and release, require them to retain high stability even in extremely dilute suspensions, high salt and at elevated temperatures. These requirements can only be met by steric repulsive stabilization through irreversibly binding, low molecular weight dispersants of e.g. poly(ethylene glycol) or a similarly irreversibly bound organic shell which stabilizes the nanoparticle into another matrix material.

We have recently demonstrated that we can stabilize magnetic nanoparticles which fulfil these stability criteria using self-assembling dispersants with nitrocatechol anchors (1-2). This allows us free control over the dispersant type by simple co-adsorption of dispersants to as-synthesized core Fe_3O_4 particles. Combined with independent control over the Fe_3O_4 core size in the range 3-15 nm a versatile toolbox for assembly of various smart materials and for biomedical applications has been created.

This presentation is focussed on recent results demonstrating and characterizing assembly of such nanoparticles into membranes of stealth liposomes (3). We show that there are strict requirements for the size of particles that can be assembled into lipid bilayer membranes and that a requirement for efficient assembly and actuation as well as liposome stability is to ensure stability of the hydrophobic shell surrounding the nanoparticle within the membrane. Encapsulated molecules were released multiple times by application of short bursts of alternating magnetic fields through a localized phase change in the membrane without heating of the surrounding aqueous environment. This allowed control of both timing and dose of release. The highest efficiency of release and encapsulation was obtained for irreversibly stabilized superparamagnetic iron oxide nanoparticles with diameters <6 nm inserted into the lipid membrane.

1. E. Amstad et al., Nano Lett, 9:4042 (2009)
2. E. Amstad et al., J Phys Chem C 115:683-691 (2011)
3. E. Amstad et al., Nano Lett, 11:1664-1670 (2011)

3:40pm **NS-ThA6 Nanoscale Electrical Interaction between Carbon Nanotubes and DNA**, Y. Cao, Y. Xu, Vanderbilt University

Carbon nanotube-biomolecule hybrids have emerged as one of the most promising materials for biological and biomedical applications, such as biosensors, drug delivery, and imaging. Recently, Carbon nanotubes (CNTs) have shown the ability to protect bound DNA cargos from enzymatic cleavage both during and after delivery into cells. This ability may result from the interaction between CNTs and DNA, which makes DNA unrecognizable to enzyme binding pockets. Therefore, it is important to study the interaction between CNTs and DNA. In this work, we have developed a nanoscale optoelectronic probing system by combining highly-sensitive CNT transistors with advanced dual-trap optical tweezers to investigate the interaction between CNTs and DNA at the single-molecule level. We tightly bonded both ends of a DNA molecule with microbeads, which could be held and manipulated by optical tweezers. When the DNA molecule was moved close to a suspended CNT transistor, the negative charge from the DNA molecule would change the local electrostatic environment around the CNT. Through scanning photocurrent measurements, the electrical coupling between individual DNA molecules and CNTs could be investigated.

4:00pm **NS-ThA7 Surface Functionalization of Nanomaterials: From Heterogeneous Catalysis to Nanoparticle Drug Delivery**, W. Gao, Brigham and Women's Hospital and Harvard Medical School **INVITED**

The advent of nanotechnology has vastly advanced our fundamental understandings on nanomaterials, in particular their surface properties. It has also revolutionized the way we functionalize these materials to exploit novel properties and applications. For example, metallic nanoclusters can be processed into different morphologies on support surfaces and subsequently allow desired reaction pathways to occur. In addition, a great number of metal oxides have been grown into single crystal surfaces with precisely controlled atomic arrangements. They have aided researchers to unlock principles governing the extraordinary chemical and electronic properties of oxides. Furthermore, various functionalities can be introduced to polymers and have resulted in multifunctional nanoparticles with superb surface properties. These nanoparticles can therefore overcome biological barriers and effectively deliver therapeutic agents to the disease sites. Using examples from my research in surface functionalization of metals, oxides, and polymeric nanoparticles, I would like to show how the surface functionalization of diverse materials can be guided by a common principle of understanding material structure-property relationship. The continuing effort in studying surface functionalization of nanomaterials will lead them to a brighter future in the fields of biomedicine, energy, and environment.

4:40pm **NS-ThA9 Perfluoropentane Filled Boron Doped Hollow Silica Microspheres for Ultrasound Guided Surgery**, A. Liberman, H.P. Martinez, Z. Wu, S.L. Blair, Y. Kono, R.F. Mattrey, A.C. Kummel, W. Trogler, University of California, San Diego

The reported positive margin rate from wire localized excisions of breast cancers is approximately 20-50%; however, using radioactive seeds and a radiation detector the excision rate is halved because the surgeon can constantly reorient the dissection to place the seed in the center of the specimen. Unfortunately, radioactive seed localization has several safety challenges, only single foci can be localized, and incisions are required to implant the seeds, so it is rarely employed. As a safe alternative, gas-filled hollow boron-doped silica particles have been developed, which can be used for ultrasound-guided surgery for multiple foci. The function of the boron doping is to increase the mechanical strength of the silica shell. The particles are synthesized through a sol-gel method on a polystyrene template, and subsequently calcined to create hollow, rigid microspheres. The boron doped silica shell is derived from tetramethoxy orthosilicate (TMOS) and trimethyl borate (TMB), which forms a rigid, mesoporous shell upon calcination. The microspheres are filled with perfluoropentane vapor. The perfluorocarbon vapor is contained within the porous shell due to its extremely low solubility in water. In addition, the high surface tension of water may serve to seal the fluorocarbon phase within the pores of the shell wall as water enters the outer surface of the porous shell by capillary action. Considerable testing of particle functionality, signal persistence and acoustical properties have been performed in various phantoms including ultrasound gel, chicken breast, and excised human mastectomy tissue. Furthermore, preliminary particle injection longevity studies have been performed in a rabbit animal model. *In vitro* studies have shown that continuous particle imaging time is up to approximately 45 minutes. *In vivo* studies have shown consistent signal presence even 48 hours post injection in rabbits with an injection volume of 50 μl carrying only 100 μg of particles. As a result these particles may provide a significant improvement over current methods in terms of patient comfort in having a small injection 1-2 days prior to surgery. On going studies are currently aimed at improving the understanding of the mechanism by which these microspheres are capable of producing such robust signal under color doppler ultrasound.

Plasma Surface Interactions (Fundamentals & Applications) II

Moderator: A. Kumar, Case Western Reserve University

2:00pm PS+SS-ThA1 Plasma Prize Lecture - The Role of Atomic Hydrogen on Plasma Synthesis of Carbon Nanotubes, E.S. Aydil*, University of Minnesota

INVITED

Hydrogen containing discharges are used widely in plasma synthesis of a variety of nanostructures including nanoparticles and carbon nanotubes. We developed a method for measuring the H-atom flux at the plane of the substrate surface during H₂ plasma exposure. Our method is based on infrared measurements of the change in free-electron absorption in a polycrystalline ZnO film when this film exposed to H atoms. Hydrogen acts as an electron donor in ZnO, and thus the concentration of hydrogen-generated free carriers can be extracted from their absorption in the infrared. The change in the concentration of free carriers can in turn be related to the flux of H atoms impinging on a ZnO film placed on the substrate platen. Using this and a suite of additional plasma and material characterization techniques, including optical emission, infrared, and Raman spectroscopy and electron microscopy we systematically investigated the interrelation among plasma gas phase composition, catalyst morphology, catalyst structure, and carbon nanotube structure in plasma enhanced chemical vapor deposition of carbon nanotubes. The structures of carbon nanotubes grown from catalytic nanoparticles via PECVD in CH₄/H₂ mixtures show a strong dependence on the H₂-to-CH₄ ratio in the feed gas. Hydrogen plays a critical role in determining the final carbon nanotube structure through its effect on the catalyst crystal structure and morphology. At low H₂-to-CH₄ ratios, iron catalyst nanoparticles are converted to Fe₃C and well-graphitized nanotubes grow from elongated Fe₃C nanoparticles. High H₂-to-CH₄ ratios in the feed gas result in high atomic hydrogen concentrations in the plasma and strongly reducing conditions, which prevents conversion of Fe to Fe₃C. In the latter case, poorly-graphitized nanofibers grow from ductile bcc iron nanocrystals that are easily deformed into tapered nanocrystals that yield nanotubes with thick walls. In the limit of pure hydrogen the cylindrical graphene walls of a nanotube are etched and amorphized by the H atoms. Etching is not uniform across the length of the CNT but rather, small etch pits form at defective sites on the CNT walls along the entire nanotube length. Once an etch pit is formed, etching proceeds rapidly, and the remainder of the CNT is quickly etched away.

2:40pm PS+SS-ThA3 CF and CF₂ Contributions to Plasma-Enhanced Chemical Vapor Deposition of Fluorocarbon Films in C_xF_y Systems, M.F. Cuddy, E.R. Fisher, Colorado State University

Inductively coupled fluorocarbon (FC) plasmas produced from C_xF_y (x,y ≥ 1) precursors are widely employed in industrial processes ranging from circuitry fabrication to preparation of low-k optical coatings. The utility of the plasma system is largely dictated by the y/x ratio, specifically in that precursors with lower ratios tend to more efficiently deposit FC films. Film growth is thought to be related to the behavior of radical species within the plasma, such as CF and CF₂. We report here on gas-phase behavior of these radicals in FC plasma systems with precursor y/x ratios ≤ 4, including relative gas-phase concentrations and kinetics and subsequent contributions to Si wafer processing. Our imaging of radicals interacting with surfaces (IRIS) experiment reveals that the propensity for scatter of CF and CF₂ declines dramatically with decreases in precursor y/x ratio. Similarly, with decreasing y/x ratios, we observe increases in FC film surface energies, suggesting that avenues to tailor specific film properties are feasible. High-resolution x-ray photoelectron spectra and surface sum frequency vibrational spectra which corroborate the relationship between the choice of precursor and characteristics of deposited FC films will also be discussed. Ultimately, this work aims to establish a connection between species behavior near surfaces and resulting film properties during FC plasma processing.

3:00pm PS+SS-ThA4 Polymer Surface Modification: Real-time In Situ Electron Spin Resonance Study for Plasma Processes, K. Ishikawa, N. Sumi, Nagoya University, Japan, A. Kono, H. Horibe, Kanazawa Institute of Technology, Japan, K. Takeda, H. Kondo, M. Sekine, M. Hori, Nagoya University, Japan

A comprehensive understanding of interaction between plasmas and soft-materials is essential for advanced plasma processing technology. Simultaneous measurements of the gas-phase ESR signals and the surface

dangling bond signal [1,2], and kinetics analysis of radical formation were performed using *in situ* real-time electron spin resonance (ESR). Chemical reactions under plasma are very complicated, due to the simultaneous irradiation of electrons, ions, radicals, and photons. Therefore, the individual contributions of each of these reactive species in the plasma must be elucidated.

An ESR system was connected to a plasma discharge system (2.45 GHz, 50 W) using a quartz tube with an inner diameter of approximately 9 mm. Gas (H₂, O₂, etc.) was flowed into the quartz tube and the pressure was maintained at approximately 10 Pa in the down-flow region. ESR measurements were conducted using a standard X-band (9 GHz) spectrometer (Bruker Biospin, EMX plus) with a microwave resonator. The quartz tube and polymer (PTFE, PMMA, etc.) film sample were inserted inside the ESR cavity in the down-flow region, typically 20 cm from the plasma discharge.

Individual contributions from gaseous radicals and plasma emission light have been studied in a similar manner using pallets for plasma process evaluation (PAPE) [3].

For irradiation with both atomic H and VUV on the PTFE film, significant acceleration in the rate of C-DB formation was observed at the beginning of irradiation.

Moreover, the surface radicals produced immediately changed to peroxy-radicals when the treated PTFE films were exposed to air. This suggests high reactivity of C-DB with oxygen and the peroxy-radical species can contribute to enhancement of the surface biocompatibility.

In summary, during exposure of gaseous radicals on the polymer surface, the *in situ* real-time ESR technique was demonstrated as a new experimental approach to the microscopic understanding of chemical reactions on surfaces with gaseous radicals during plasma processes. We have successfully obtained information regarding the reaction mechanism with radicals generated by plasma induced surface interactions.

ACKNOWLEDGMENT

This work was supported in part by the Knowledge Cluster Initiative (Second Stage) of the Tokai Region Nanotechnology Manufacturing Cluster.

REFERENCES

- [1] S. Yamasaki, *et al.*, Appl. Phys. Lett. 70, 1137-1139 (1997).
- [2] K. Ishikawa, *et al.*, Appl. Phys. Lett. 81, 1773-1175 (2002).
- [3] S. Uchida, *et al.*, J. Appl. Phys. 103, 073303:1-5 (2008).

3:40pm PS+SS-ThA6 Control of Hydrocarbon Surface Density during H₂/D₂/Ar Low Temperature Plasma Interaction, N. Fox-Lyon, G.S. Oehrlein, University of Maryland, College Park, N. Ning, D.B. Graves, University of California, Berkeley

Control of surface properties of hydrocarbon materials during interaction with H₂/D₂/Ar low temperature plasma has applications in diverse areas including: thin film synthesis, electronic device manufacturing, nuclear fusion reactor design, and plasma sterilization. Plasma processing/exposure of hydrocarbon materials can cause large changes to the surface chemistry and morphology due to interaction with ions, reactive neutrals, and UV/VUV photons. Hard hydrocarbon materials such as amorphous hydrocarbon (a-C:H) and diamond-like carbon (DLC), suffer a loss of density and a thick modified layer with reactive plasma etching through reactant saturation of the surface and an increase in density and formation of a thin modified layer by inert plasma etching through selective sputtering of H, whereas soft hydrocarbon materials (polymers, biomaterials) exposed to reactive and inert plasmas have been shown to increase in density and become chemically modified. In this work we have explored the plasma/surface interaction with hard/soft hydrocarbon films using different H₂/D₂/Ar gas feedstock compositions along with different ion energy/fluence to the surface. The time dependent changes in optical properties and the etch yields were found using real time *in-situ* ellipsometry. Using multilayer films (e.g., soft a-C:H over hard a-C:H) we monitored dynamic changes in the penetration/modification depths for different plasma chemistries.

Shallow modifications by inert plasmas (such as Ar) are well understood. Ar plasma depletes H from the surface of a-C:H films through selective sputtering, scaling with ion energy. H₂ plasmas have been shown to cause deep hydrogenation of the surface not predicted with TRIM models. Mixing the processing gas (Ar/H₂) can be used to control the surface density from H depleted to H saturated. To better understand the roles of ion mass, etch rate and diffusion on the depth/degree of modification seen for H₂ plasmas, we performed comparable studies using D₂. We find that increasing the mass of the ions (by using H isotopes such as D) causes a large change in the etching and surface modification behavior. The etch rate of hard a-C:H in D₂ plasma is ~2 times the rate in H₂ plasma, and surfaces show a lower degree of modification (hydrogenation) than for H₂ plasma. In soft

* 2009 Plasma Prize Winner

hydrocarbon materials exposed to D₂, H₂, and Ar plasmas (listed in order of modification, least to greatest), we find that the density increase is dependent on the ion chemistry, energy, penetration depth, and mass. The data will be compared with molecular dynamics simulation results.

4:00pm PS+SS-ThA7 Atomic Force Microscopy Determination of the Elastic Modulus of Nanometer Thick, Ultra-Stiff Modified Layers after Plasma Etching of a Polymer Film. *T. Lin*, University of Maryland, College Park, *H.C. Kan*, National Chung Cheng University, Taiwan, Republic of China, *R.L. Bruce*, *G.S. Oehrlein*, *R.J. Phaneuf*, University of Maryland, College Park

We report on a determination of the elastic modulus for ultrathin (< 2nm) stiff damaged layers produced by argon plasma etching of the model photoresist polymer, polystyrene (PS). Measured force curves allow a direct determination of the effective modulus of the damaged layer plus polystyrene underlayer within a model which accounts for adhesive forces. The modulus of the modified layer is then extracted via comparison with numerical simulations for contact between a spherical AFM probe and a bilayer-structured film system in a Hertzian mechanics model. Our results show directly that an extremely stiff modified layer is formed, with the modulus increasing with Ar-ion energy during etching, in good quantitative agreement with estimations based upon measurement of the dominant corrugation wavelength and buckling theory.

4:20pm PS+SS-ThA8 Polymer Hardening Technique for Enhancement in Etch Selectivity/Durability Using DC Superimposed Capacitively-Coupled Plasma. *S. Okamoto*, *A. Nakagawa*, *F. Inoue*, *H. Oka*, Tokyo Electron Miyagi Ltd., Japan, *H. Mochiki*, *K. Yatsuda*, Tokyo Electron Ltd., Japan

Higher aspect ratio of DRAM capacitor is required in order to maintain enough capacitance as the device structure is scaled down. The electrode of DRAM capacitor is generated in mold by metal CVD – typically TiN, and the mold is fabricated by RIE – typically dielectric. Thus, it is necessary to develop new techniques to fabricate higher aspect ratio dielectric mold for further DRAM scaling. RIE challenges for mold fabrication are high dielectric etch selectivity to mask, minimum bowing, and sustainment of enough bottom CD.

Generally speaking, mold etch process is optimized by accurate polymer control. However, conventional polymer control technique became marginal in highly scaled DRAM structure. Even slightly excessive polymer makes bottom CD smaller, and sometimes clogs the top portion of mold. On the other hand, slightly lacking polymer bridges neighboring molds at the top and/or sidewall portion due to lack of etch selectivity to mask and/or bowed etch profile.

In this paper, we suggest DC superimposed capacitively-coupled plasma (CCP) etch technique as a breakthrough of high aspect ratio dielectric etch. High energetic electrons emitted and accelerated by superimposed DC harden the polymer generated on mask and sidewall. This hardening technique works in two roles. The first role is etch selectivity enhancement of undesired etch material. Since polymer is maintained thin enough with good etch selectivity to mask, the top portion of mold is not clogged by polymer. The second role is etch durability enhancement of undesired etch portion. Normally, ultra high aspect ratio dielectric etch needs very high ion energy, which results in bowing etch profile due to incoming angular ions. But, superimposed DC hardens the sidewall polymer, and prevents etch profile from bowing. Bottom CD can be enlarged in the over etch step after etch front reaches etch stop layer. In general, bowing etch profile becomes significant during the over etch step. However, this effect can be avoided with stiff polymer enhanced by superimposed DC.

In conclusion, etch selectivity/durability of the undesired etch material/portion can be enhanced by superimposed DC as long as polymer is generated in the desired area by etch process optimization. Superimposed DC allows us to enhance etch selectivity/durability not with thickness of polymer but stiffness of polymer.

4:40pm PS+SS-ThA9 H₂O Plasma Surface Modification of Track-Etched Polycarbonate Membranes Leading to Polar Surface Functionalization and Improved Wettability. *B.D. Tompkins*, *J.M. Dennison*, *E.R. Fisher*, Colorado State University

Plasma surface modifications have the ability to improve performance and realize new applications for polymer membranes in a variety of areas including: microfiltration, gas separation, and water treatment. Past studies in our labs have shown that although some polymer membranes can be successfully modified and are stable after treatment, many partially revert to their untreated state when aged. We are developing a technique that utilizes inductively coupled H₂O plasmas to implant polar functional groups onto the surface of track-etched polycarbonate membranes free of wetting agents. Water contact angle results on freshly treated and aged membrane samples show that the treated membranes have improved wettability compared to

untreated samples and that the effects persist after treatment. Analysis of freshly treated samples using x-ray photoelectron spectroscopy (XPS) shows increases in oxygen incorporation, whereas high resolution XPS spectra of the C1s region shows that the fundamental polycarbonate structure is maintained near the surface. Treatment effectiveness under different plasma conditions, aqueous flux used to evaluate the performance of modified membranes, analysis of gas phase plasma species using optical emission spectroscopy (OES) to probe the processes that lead to surface modification, and a comparison with a similar plasma system using a mixture of O₂ and NH₃ as feedgases will be discussed along with comparisons to other polymer membrane materials treated under similar conditions.

5:00pm PS+SS-ThA10 Plasma Printing: A New Inline Technology for Polymers Surface Modification. *E.A.D. Carbone*, *M.W.G.M. Verhoeven*, Eindhoven University of Technology, Netherlands, *W.J.M. Brok*, *A. Stevens*, Innophysics B.V., Netherlands, *J.J.A.M. van der Mullen*, Eindhoven University of Technology, Netherlands

Fast and easy tunable patterning of surfaces has become of growing interest in the last couple of years in different fields like surface functionalization, thin film coatings and biomedical applications.

The concept of *Plasma Printing* combines the advantages given by the non-equilibrium character of pulsed corona discharges (tunability of surface chemistry), their creation and propagation along small volumes (local plasma treatment) and the mobility of the plasma source as a conventional printer (inline processing). This unique combination allows to treat (in real time) surfaces with arbitrary patterns design with limited restrictions unlike in the use of atmospheric pressure (dielectric barrier discharge) DBD for patterning of surface (also called DBD stamping).

InnoPhysics developed a proprietary Digital-on-Demand PlasmaPrint hardware solution that enables software patterned surface functionalization, etching and deposition of functional coatings on thin (plastic) substrates. A few kV sinusoidal pulse is applied on the electrode gap (pin to plate geometry configuration) in the 50-100 kHz range which generates a 1-10 μs pulsed plasma of about ~ 200 μm diameter in contact with the surface.

In order to assess the performances of the setup, a parametric study of polymers with respect to gas mixtures was performed to detect optimum of surface hydrophilization as well as selective chemistry groups grafting like OH, NH and CO.

PE, PET, FEP as well as PTFE (and PCTFE) were treated by nitrogen and different admixtures of gas/solution namely oxygen, ethanol, water and ammonia (NH₄OH solution). The surfaces were analyzed by water contact angle (WCA), X-ray photoelectron spectroscopy (XPS) and IR spectroscopy in attenuated total reflectance mode (FTIR ATR).

WCA was used to measure the surface energy of the surface and significant improvements of wetting properties were found for a few seconds of treatment time (i.e. <30° in the case of PET treated by N₂/NH₃). Grafting of N species up to a few percents was also found for various plasma compositions. The deconvolution of high resolution C1s, N1s and O1s spectra combined with the analysis of the IR spectra for the same conditions allowed eventually to get more insight in the chemical groups grafting at the surface following the plasma treatment.

5:20pm PS+SS-ThA11 Design of a Plasma Cleaning Unit to Clean Backside Contamination on Substrates. *F.T. Molkenboer*, *N.B. Koster*, *A.J. De Jong*, *J.C.J. van der Donck*, *A.M.C.P. de Jong*, *O. Kievit*, TNO, Netherlands

In this presentation we will report our work on the design and experimental results of a plasma unit to clean the backside of substrates. Backside contamination of substrates can limit the quality of the front side process. Outgassing of backside contaminants can influence the front side process, or particles on the backside can influence the image quality in a wafer stepper. The complete backside cleaning unit uses three modules to remove both organic and an-organic particles as well as organic contamination layers. This is all done in a high vacuum environment. To remove particles we will use a commercial available tacky roller. The second method to remove particles uses an UV lamp that will charge the particles on the substrate and a strong electric field to remove these charged particles from the substrate.

To remove organic contamination, for example resist residues after processing, we will use a RF plasma. The design of the RF plasma unit makes continuous cleaning over a large surface area possible. The gas in the plasma unit itself will have a pressure of 0.5 to 1 mbar. The vacuum chamber in which the complete backside cleaning unit is placed will have a pressure of around 10⁻³ mbar when the plasma unit is in use. This difference in pressure is achieved by placing the inlet of the gas in the RF plasma unit and making the outlet to the vacuum chamber very small. This design leads to a large expansion of the gas at the outlet of the RF plasma unit. The

benefits of this design are that the pressure within the RF plasma unit is high enough for creating plasma and the pressure within the vacuum chamber is low enough to prevent that the whole vacuum chamber is filled with plasma.

This project focuses on backside cleaning of wafers within the "European Equipment & Materials Initiative for 450 mm" (EEMI450) under the ENIAC research program.

Within this European project, TNO is responsible for addressing contamination control issues. The concept of this backside cleaning unit can also be used to clean substrates used in roll to roll lines for solar cells or other processes that need continuous cleaning at high speed.

Plasma Science and Technology Division Room: 201 - Session PS-ThA

Plasma Diagnostics, Sensors and Control II

Moderator: J.-P. Booth, CNRS/Ecole Polytechnique, France

2:00pm **PS-ThA1 Characterization of Atomic Oxygen Emission by PROES and Ion-Flux Measurement in an ECR Plasma Etcher**, *V. Milosavljevic*, Dublin City University, Ireland and University of Belgrade, Serbia, *B. Dolinaj, D. Gahan*, Impedans Ltd., Ireland, *N. Macgarraill*, Dublin City University, Ireland, *MB. Hopkins*, Impedans Ltd., Ireland, *S. Daniels*, Dublin City University, Ireland

For many years, optical emission spectroscopy (OES) has been successfully used for the measurement and control of plasma products in industrial plasma reactors. We have extended this technique using phase resolved optical emission spectroscopy (PROES), in a industrial electron cyclotron resonance (ECR) plasma etcher.

Experiments were conducted in a pure argon discharge with a SiO₂ wafer on the biased electrode. Argon ion bombardment of the wafer liberates oxygen atoms to the discharge. Therefore, oxygen is only present at the beginning of a discharge in solid state, i.e. in the SiO₂ lattice. The ECR etcher used in this experimental study has a 2.45 GHz microwave generator with a maximum power of 2kW, variable magnetic field of up 90 mT and 2MHz RF bias with maximum power of 250 W. The SiO₂ wafer is mechanically clamped to the chuck to which the RF bias is applied.

In order to study the behavior of oxygen in the sheath region above the wafer an iCCD camera and high resolution spectrograph are employed and the iCCD camera is gated with respect to the 2MHz RF bias frequency. The production of oxygen is mostly due to RF voltage oscillation across the wafer induced by argon ion bombardment of its surface. The atomic oxygen spectral line intensity, from the 777 triplet, is monitored with respect to phase of the RF bias. Ion energy distribution functions, at the wafer surface, are measured using a floating retarding field energy analyzer (RFEA). The floating RFEA is placed on the rf biased wafer surface and signal cabling is taken out through the reactor vacuum pump tunnel. This prevents the need for any modification to the reactor configuration. The RFEA sensor is 7 cm in diameter and the wafer on which it sits is 200 mm in diameter resulting in significant exposure of the wafer to ion bombardment. Phase resolved measurements are made using the iCCD camera which is operated with a repetition rate of 2 MHz synchronously (triggered) with the RF bias. The integration gate of 3.90625 ns is locked to a fixed phase position within the RF cycle (500 ns). This gives exactly 128 intervals over the 2Pi RF cycle. A variable delay between the fixed phase and the gate allows one to cover the complete RF cycle. We record strong correlation between the ion-flux and the PROES data.

This work was a partly funded by SFI under the Precision project.

2:20pm **PS-ThA2 Optical Diagnostics of Electron Energy Distributions in Low Temperature Plasmas**, *J. Boffard, L.E. Aneskevich, R.O. Jung, C.C. Lin, A.E. Wendt*, University of Wisconsin-Madison

Passive, non-invasive optical emission measurements provide a means of probing important plasma parameters without introducing contaminants into plasma systems.* Due to the dominant role of electron-impact collisions in gas-phase reactions, our investigation focuses on characterization of the electron energy distribution function (EEDF). In particular, we highlight the ability to observe EEDFs under non-equilibrium conditions in which the EEDF deviates from the Maxwell-Boltzmann form. The energy dependence of the EEDF, which varies with plasma generation method and operating conditions, has significant implications for gas phase reaction rates and is thus critical to the predictive control of plasma process outcomes. EEDFs

are determined using measurements of argon emission intensities in the 650-1150 nm wavelength range and measured metastable and resonance level concentrations, in conjunction with a radiation model that includes contributions from often neglected but critical processes such as radiation trapping and electron-impact excitation from metastable and resonance levels. Results using argon emission spectra will be presented for an inductively-coupled plasma (ICP) over a wide range of operating conditions (pressure, RF power, Ar/Ne/N₂ gas mixtures), which show a depletion of the EEDF relative to the Maxwell-Boltzmann form at higher electron energies, in good agreement with measurements made with Langmuir probes and predictions of a global discharge model. These results are consistent with predictions of electron kinetics and can be explained in terms of reduced life times for energetic electrons due to wall losses and inelastic collisions. For Ne/Ar plasmas, analysis of neon emission spectra in addition to the argon analysis provides enhanced sensitivity to the presence of high-energy electrons. This example highlights the potential utility of this method as a tool for probing kinetics of many types of low-temperature plasma systems, which are typically characterized by non-Maxwellian EEDFs.

Plasma Sources Sci. Technol.* **19, 065001 (2010).

This work was supported by the Wisconsin Alumni Research Foundation (WARF) and by NSF Grant CBET 0714600.

2:40pm **PS-ThA3 Two Dimensional Laser-Collision Induced Fluorescence Measurements in Low Pressure Plasmas**, *E.V. Barnat*, Sandia National Laboratories **INVITED**

Laser-collision induced fluorescence (LCIF) is utilized to produce two-dimensional maps of electron densities and electron temperatures in helium plasmas. In this presentation, the basics of the technique are discussed and means of implementing the technique are described. To correlate the measured intensities of light emitted from the various probed states to electron densities and temperatures, a collisional-radiative model (CRM) is employed. Comparison of predictions made by this CRM to measured LCIF emanating from well characterized plasma constitutes as the calibration process of the LCIF technique. After describing the development and implementation of the LCIF technique, application of the technique to temporally and structurally interesting plasmas are discussed. Examples include ion sheaths, electron sheaths that form around biased electrodes immersed in a plasma. Also discussed are striated structures formed in a pulsed positive column. Transient evolution of these systems is discussed and future extensions of the LCIF technique are considered. "This work was supported by the Department of Energy Office of Fusion Energy Science Contract DE-SC0001939".

3:40pm **PS-ThA6 Controlled Electron Beam Excitation Method to Study Process Chemistries**, *P.L.S. Thamban, G. Padron-Wells*, University of Texas at Dallas, *J. Hosch*, Verity Instruments Incorporated, *M.J. Goeckner*, University of Texas at Dallas

We describe a method to conduct optical emission spectroscopy (OES) measurements, electron beam excitation, that can be adopted to study and quantify process chemistry species. Our method and experiment, designed to be incorporated as a diagnostic system in process tools, relies on extracting electron beam from an inductively coupled plasma. First we will present and discuss results that show electron energy dependent cross section measurements in gas mixtures specifically Fluorocarbon process chemistries. Energy dependent optical excitation cross sections of Fluorine, Oxygen and ionic species as measured with this method will be presented. The controllable excitation method and its applications to quantitative measurements of species in process chamber/exhaust will then be presented. Comparative measurements of species densities as measured with Fourier Transform Infrared Spectroscopy (FTIR) and e-beam excitation will be presented. This project is funded by NSF-Grant (CBET-0922962) and Verity Instruments.

4:00pm **PS-ThA7 Experimental Implementation of Robust Multivariable Real-time Feedback Control Design for RIE Plasma Processing System**, *Y. Zhang, B.J. Keville, A. Holohan, S. Daniels*, NCPST Dublin City University, Ireland

A robust multivariable real-time feedback control strategy for improving output characteristics of a reactive ion etching (RIE) plasma system is presented. Semiconductor fabrication is one of the major applications of low-pressure plasmas. During the course of manufacturing of semiconductor devices, it is often necessary to etch dielectric and/or metal layers to provide features in the layers for subsequent semiconductor processing steps. Reducing process variation is becoming ever more critical and challenging due to shrinking IC device feature dimensions and an increase in wafer size. Developments in process control are struggling to keep pace with these more stringent demands due to the fact that most semiconductor manufacturing tools are run in open loop mode. In this case,

key plasma parameters such as ion flux and radical densities at the substrate surface are sensitive to drift in tool subsystems, changes in wall condition and wafer loading, for example. Disturbances to key plasma parameters may affect process metrics such as etch depth and anisotropy and result in a significant degradation in device yield and performance.

In this paper, we report the development of a robust multivariable, real-time feedback controller for the improvement of process repeatability and reproducibility of a RIE tool. Key plasma variables are sensed and their responses to the process inputs are identified experimentally. A MIMO controller then is developed and implemented to control these variables. *H-infinity* control theory and software are used for a systematic tuning procedure. This controller can effectively reduce cross-coupling effects and cope with parameter uncertainties and external disturbances in real-time in order to achieve robustness and optimal performance of the multivariable system.

4:20pm PS-ThA8 Real Time, Multivariable Control of an SF₆/O₂/Ar Plasma, B.J. Keville, M.M. Turner, Dublin City University, Ireland

Plasmas of sulphur hexafluoride, SF₆, mixed with oxygen and argon have been used for silicon etching in microelectronics manufacturing. Fluorine atoms produced by dissociation of SF₆ etch Si with very high rates. Lateral etching, which reduces feature anisotropy, may be inhibited by the formation of a silicon oxide passivating layer on feature sidewalls. It has been demonstrated experimentally that feature profile shape is determined to a large extent by the balance between O and F radical densities at the surface of the substrate. In general, etch recipes are specified in terms of inputs such as gas flow rates, RF power and pressure and processes are run 'open loop'. 'Chamber matching', which entails *ex situ* statistical analysis of metrics such as etch depth, uniformity, anisotropy and selectivity, is required to ensure that each chamber produces acceptable results. However, process reproducibility may be degraded due to real-time disturbances such as MFC and match network drift, wall seasoning and substrate loading. An alternative approach which would reduce the need for chamber matching and reduce process sensitivity to disturbances would be to specify a recipe in terms of plasma parameters such as O and F radical densities, and the fluxes and energies of ions at the wafer surface and to regulate these in real time by adjusting the inputs with a suitable real time control algorithm. This presentation describes how a real time, multivariable control algorithm for an SF₆/O₂/Ar plasma may be designed with the aid of a control-oriented process model. The stability and efficacy of the control algorithm is demonstrated using a model of the process and a variety of simulated disturbances. Experimental implementation of the control algorithm on a laboratory capacitively coupled plasma is described.

4:40pm PS-ThA9 Maxwell Demon and its Instabilities, CS. Yip, N. Hershkowitz, University of Wisconsin-Madison

Previous experiments[1] have shown that in a low pressure, low temperature plasma, positively biasing an array of thin wires can increase electron temperature by creating an angular momentum trap to absorb cold electrons. In this experiment, such a Maxwell demon device was reproduced by welding 0.025mm tungsten wires onto stainless steel shafts, which were then covered with ceramic. This device was used to more than double the plasma electron temperatures in a multi-dipole chamber operating in the mTorr regime. Moreover, the demon is observed to reduce the cold electron population in a plasma with a bi-Maxwellian electron distribution, leaving a single Maxwellian electron distribution. However, at high positive voltage, instabilities in the kHz range prevent acquisition of meaningful temperature data. The conditions of this instability are investigated by varying neutral pressure, plasma density and applied voltage up to 150V in an argon plasma.

References

[1] K. R. MacKenzie, R.J. Taylor, D. Cohn, E. Ault, and H. Ikezi. *App. Phys. Lett.* Vol. 18, #12, 1971.

5:00pm PS-ThA10 Reliable Arc Detection and Arc Mitigation in RF Plasma Systems, D. Coumou, R. Chouviery, MKS, ENI Products

1. Introduction

Arc disturbances in an RF plasma source are typically short duration transients arising from discharges between the plasma and the electrode, the plasma and the chamber sidewall, or discharges within the plasma that are induced by the build-up of polymer structures. When these transients occur, a reliable means is necessary to detect the presence of the arc and to intercept the RF power delivery system to mitigate the arc event. We present a novel solution of arc detection using suitable tools from a communications equivalent paradigm that supersedes conventional heuristic methods. The proposed arc detection scheme is a quantitative approach measuring the relative arc energy of the plasma arc transient. A receiver operating characteristics (ROC) curve demonstrates the robust detection of

arc transients relative to a ground truth source and yields insightful information contrasting the detection of arc disturbances in different RF sensing locations in the RF power delivery system. When an arc event is detected, arc mitigation is deployed based on suppressing the RF power with duration proportional to the detected arc energy. The rapid, and if necessary, repeated control of the RF source results in a reduction in the plasma potential to extinguish the arc source and alleviate subsequent damage. Results from PECVD and PVD tools corroborate the impact of this new scheme to significantly ameliorate thin-film manufacturing.

2. Brief Theory of Operation

A correlation function is applied to the voltage and current signals representative of the main-line electromagnetic fields sampled by an RF sensor. Analogous to a digital communication system deploying a correlation receiver, the voltage and current signals are digitally sampled, and the power between these signals is derived using well known properties of the correlation function. From the power measurement in the presence of a detected arc transient, arc energy is accumulated from fixed, non-overlapping correlation block functions. By measuring the amount of energy at the moment of detection, an RF counter mechanism is initiated by the RF power supply to reduce the plasma potential and suppress the arc source.

3. Results

Laboratory experiments are conducted and analytically summarized through an ROC curve to demonstrate the efficacy of our detection method by low false-positive occurrences. Field trials for PECVD and PVD tools outline the broad utilization of this arc detection and accompanying arc mitigation for all RF processes associated with photovoltaic device fabrication.

Advanced Surface Engineering Division

Room: 104 - Session SE+PS-ThA

Pulsed Plasmas in Surface Engineering

Moderator: J. Patscheider, EMPA, Switzerland

2:00pm SE+PS-ThA1 High-Power Impulse Magnetron Sputtering of WO₃ - Influence of the Pulse Parameters on the Discharge, A. Hemberg, F. Renaux, J.P. Dauchot, Materia Nova, Belgium, R. Snyders, S. Konstantinidis, UMons, Belgium

Metal oxides as WO₃, SnO₂ and TiO₂ are widely used as active layers in gas sensor applications. The sensor performances (sensitivity, selectivity, and ageing) are strongly dependent grain size, phase constitution, and material microstructure. It is accepted that in magnetron sputtering, these properties can be modified by controlling the energy and the flux of ions impinging the growing films. The ion bombardment allows modifying the nucleation process, increasing the film density, and changing texture, stress and microstructure of the coating, and ultimately improving its performances. Compared to other techniques used for thin films deposition, HiPIMS (High Power Impulse Magnetron Sputtering) enables the sputtered material to be strongly ionized. Therefore, using HiPIMS, the film properties can be altered to a larger extent as compared to conventional DC magnetron.

In this study, WO₃ films have been synthesized using reactive HiPIMS of a metallic tungsten target in Ar/O₂ mixtures. A comparison is made between results obtained in HiPIMS with those obtained with a conventional DC reactive magnetron discharge (RDCMS) at identical mean power (*PD*). We discuss the influence of the pulse duration (*t*) and the target voltage (*VD*) on both the film deposition rate (*RD*) and the hysteresis behaviour. During the HiPIMS experiments, *t* is varied between 10 and 50 μs and *VD* between 800 and 1500 V. *PD* is kept constant by adjusting the frequency. In reactive mode, for a given value of *PD*, *RD* increases as *t* and *VD* are increased. Comparing the HiPIMS data with those recorded during the RDCMS process, it is found that for *t* = 50 μs and *VD* = 1500 V, *RD* in HiPIMS is larger than for the RDCMS discharge. In order to understand this behaviour, the target current waveforms associated with these working conditions have been studied. For this particular condition (*t* = 50 μs, *VD* = 1500 V), the discharge current waveforms in metallic and reactive mode are similar. This observation would reveal that the target surface chemistry is identical, although the discharge is ignited either in a pure Ar or in an Ar/O₂ mixture.

The ion flux composition was also studied with a mass spectrometer located in front of the magnetron target. Time-resolved and time-averaged measurements were carried out.

2:20pm **SE+PS-ThA2 A Versatile Magnetized Pulsed Cascaded Arc Source for Surface Modifications and Efficient Material Deposition, G. De Temmerman, J.J. Zielinski**, FOM Institute for Plasma Physics Rijnhuizen, Netherlands, *L. Marot, D. Mathys*, University of Basel, Switzerland, *W. Melissen*, FOM Institute for Plasma Physics Rijnhuizen, Netherlands, *M.C.M. van de Sanden*, FOM-Instituut for Plasma Physics Rijnhuizen & Eindhoven University of Technology, Netherlands

The interaction of low-temperature plasmas with solid surfaces is at the core of numerous applications such as thin film deposition or materials processing. On the other hand, the interaction of the confined plasma with the plasma-facing materials in a nuclear fusion device can have a serious impact on the operations of a fusion device. This is especially true during plasma instabilities where surfaces are exposed to high transient heat and particle fluxes (several MJ.m⁻² for 0.2-1ms). A pulsed cascaded arc source has been developed [1] to produce fusion-relevant plasmas and study the surface modifications induced by simultaneous continuous and pulsed plasma exposure.

The cascaded arc source, extensively used for thin film deposition by PECVD is used, in the Pilot-PSI linear plasma device to reproduce the plasma conditions expected in a fusion reactor with particle and heat fluxes of 1024.m⁻²s⁻¹ ~10 MW.m⁻² respectively. Magnetic field of up to 1.6T is used to confine the plasma. The plasma source has been modified to allow for combined pulsed/continuous operations [1]. Parallel to the DC power supply, the plasma source is connected to a capacitor bank (5kV, 8.4mF, 100kJ), which is discharged in the source to transiently increase the input power. Peak surface heat fluxes in excess of 1 GW.m⁻² have been generated with pulse duration of about 1 ms (up to 1MJ.m⁻²). To provide more flexibility, the shape and the duration of the pulse can be adapted to the needs. The plasma conditions during the continuous and pulsed phases can be varied independently. The source can be operated in a variety of gases (Ar, H, He, N) as well as with mixed gases. Plasma properties are studied using Thomson scattering, fast visible and infrared imaging.

We will describe how synergistic effects arising from the simultaneous exposure to continuous and pulsed plasma affect the surface of a polycrystalline tungsten surface. The field of applications of the pulsed cascaded source is however not restricted to fusion-related research. Using a slightly altered configuration, the pulsed plasma source system has also opened a new route for the efficient deposition of metallic nano-particles and nano-structured thin films. Complete coverage of the surface by 10-15nm diameter nano-particles can be obtained with only a few pulses (5-10). Under different conditions, deposition rates as high as 50nm per pulse (1ms duration) have been achieved for copper and aluminium films. With a possible repetition rate of 10Hz, the system combines unprecedented deposition rates and the possibility of in-situ surface processing in between pulses.

[1] G. De Temmerman et al., *Appl. Phys. Lett.* 97 (2010) 081502

2:40pm **SE+PS-ThA3 Pulsed Magnetron Sputtering Systems for Reactive Deposition of Oxide and Nitride Films, J. Vlcek, J. Rezek, P. Steidl**, University of West Bohemia, Czech Republic **INVITED**

In recent years, novel high-power pulsed dc magnetron systems have been used for sputtering of films[1].

In the presentation, we report on discharge and deposition characteristics, and on film structure and properties for two different pulsed magnetron sputtering techniques.

High power impulse magnetron sputtering of zirconium target in argon-oxygen gas mixtures was investigated at a high average target power density in a pulse, being up to 2kWcm⁻². The repetition frequency was 500Hz at duty cycles ranging from 2.5 to 10%. The total pressure of the argon-oxygen gas mixture was around 2 Pa. An effective reactive gas flow control, developed by us, was used for high-rate reactive deposition of insulating, highly optically transparent ZrO₂ films. In addition to the ZrO₂ films, high power impulse magnetron sputtering was also successfully used for high-rate reactive deposition of highly optically transparent Al₂O₃ and Ta₂O₅ films. Details of the process and measured properties of the films will be presented.

Pulsed dc magnetron sputtering of B₄C-Si (25:75%) target in an argon-nitrogen (50:50%) gas mixture at the total pressure of 0.5Pa was used for deposition of Si-B-C-N films with extremely high thermal stability (even above 1500°C). The repetition frequency was 10kHz at an 85% duty cycle to avoid microarcs at the target and thus, to produce high-quality defect-free films. Prior to the deposition, target atoms were subplanted into various substrates, being at a high negative rf potential, during their etching using pulsed magnetron sputtering of the B₄C-Si target in argon gas (the same

repetition frequency and the duty cycle of 20%) to enhance adhesion of the Si-B-C-N films.

[1] K. Sarakinos, J. Alami, S. Konstantinidis, *Surf. Coat. Technol.* 204 (2010) 1661.

3:40pm **SE+PS-ThA6 Structure Evolution and Wear Mechanism in TiAlCN/VCN Nanoscale Multilayer Coatings Deposited by Reactive High Power Impulse Magnetron Sputtering Technology, P. Hovsepian, A.P. Ehiasarian, G.K. Kamath**, Sheffield Hallam University, UK, *R. Haasch, I. Petrov*, University of Illinois at Urbana Champaign

2.5 μm thick TiAlCN/VCN coatings were deposited by reactive HIPIMS process. XTEM showed gradual evolution of the structure of the coating with thickness. The initial structure is nanoscale multilayer with sharp interlayer interfaces. This transforms to nanocomposite of TiAlCN and VCN nanocrystalline grains surrounded by C-rich tissue phase and finally changes to an amorphous carbon rich Me-C phase. In contrast deposition in similar conditions using standard magnetron sputtering produces a well defined nanoscale multilayer structure. Depth profiling by AES showed that the carbon content in the HIPIMS coating gradually increased from 25% at the coating substrate interface to 70% at the top thus supporting the TEM observations.

Energy-resolved mass spectrometry revealed that HIPIMS plasma is a factor of 10 richer in C¹⁺ ions, and therefore more reactive, as compared to the plasma generated by standard magnetron discharge at the same conditions. The peculiar structure evolution in HIPIMS is discussed in relation to target poisoning effect and carbon outward diffusion during coating growth.

Highly abrasive AISi9Cu1 alloy was dry machined using TiAlCN/VCN coated 25 mm diameter end mills to investigate the coating-work piece material interaction. Green (532 nm excitation) and UV (325 nm excitation) Raman spectroscopy was employed to identify the phase composition of the built up material on the cutting edge and swarf surfaces produced during machining. These analyses revealed formation of lubricious Magnéli phases namely V₂O₅ and graphitic carbon as well as highly abrasive SiO₂ and Al₂O₃ thus shedding light on the wear processes and coating tribological behaviour during machining.

4:00pm **SE+PS-ThA7 Plasma Study and Interconnect Metallization using a Modulated Pulse Power (MPP) Hollow Cathode Magnetron, L. Meng, H. Yu, T.S. Cho, S. Jung, D.N. Ruzic**, University of Illinois at Urbana Champaign

Modulated pulse power (MPP) magnetron sputtering, as a derivative of high power pulsed magnetron sputtering (HPPMS), was applied to a 200 mm hollow cathode magnetron (HCM) with a Cu target. The aim was to develop a more advanced ionized physical vapor deposition (IPVD) tool for applications such as interconnect metallization for sub-32 nm technologies. The MPP plasma generator, featured with 1000 V maximum pulse voltage and 550 A maximum pulse current, has a unique advantage of flexibly adjusting on- and off-time for each individual pulse, so that a long pulse packet of several milliseconds with desired waveform shapes can be generated. Distinct discharge stages were normally observed in one MPP pulse packet. Time-dependent plasma parameters were investigated using a triple Langmuir probe to help understand the MPP discharge characteristics and its performances. Plasma behaviors were shown to closely depend on the pulse waveforms and various other parameters including pulse current, repetition frequency, pressure, and distance from the target. A high electron density (n_e) of $3 \times 10^{18} \text{ m}^{-3}$ and an electron temperature (T_e) of 5 eV during the pulse were obtained at the substrate level, with an average power less than 8 kW. Compared with the DC magnetron sputtering at the same average power, the pulsed plasma density was an order of magnitude higher, which resulted in an enhanced ionization of the sputtered flux. As measured by an electrostatic gridded energy analyzer combined with a quartz crystal microbalance, the Cu ionization fractions above 30% were easily achieved by the MPP sputtering on the substrate level, twice higher than those by the DC sputtering. Increasing the pulse duty ratio or reducing the pressure resulted in a stronger ionization. The performance of Cu deposition in narrow trenches (70-100 nm) using the MPP sputtering was further studied, which exhibited an improvement over the DC sputtering. Stronger pulses with higher duty ratios and a lower gas pressure were preferred to reduce the overhang and achieve better step coverage and bottom coverage.

4:20pm **SE+PS-ThA8 Structural and Optical Properties of Ultra-Thin Silver Films Deposited via High Power Impulse Magnetron Sputtering (HiPIMS) on Various Adhesion Layers**, *R. Jakubiak*, Air Force Research Laboratory, *L. Sun*, General Dynamics Information Technology, *N. Murphy*, Air Force Research Laboratory, *A. Waite*, Universal Technology Corporation, *J. Jones*, Air Force Research Laboratory

Multilayer metal-dielectric stacks containing noble metals such as gold, silver, and copper have myriad applications in the areas of linear and nonlinear optics and photonics. The optical dispersion of Ag makes it particularly attractive for optical interference filters and metamaterials applications. In this regard, it is essential for the Ag layers be sufficiently thin as to not inhibit transparency in the visible spectral region yet still exhibit the favorable optical dispersion of bulk Ag. This can prove difficult due to the Volmer-Weber island growth process noble metals exhibit on dielectric materials. Island formation occurs at the initial growth stages, followed by nucleation and coalescence with increasing material deposition. Below the coalescence threshold the optical dispersion does not follow that of bulk Ag and that has a detrimental effect on the optical performance of the coating. In order to lower the thickness at which coalescence occurs we've explored highly energetic deposition techniques such as high power impulse magnetron sputtering (HiPIMS) alone or in conjunction with deposition on adhesion layers of Ti, Ge or transition metal nitrides. The adhesion layers also act as barriers to oxidation of the Ag from dielectric materials incorporated in the interference coatings. Using *in-situ* spectroscopic ellipsometry the coalescence threshold of the Ag was easily monitored by noting when during the growth process the optical dispersion of the film matched that of bulk Ag. A systematic study of the how the adhesion layers and deposition parameters affected the optical properties of the Ag films was achieved by correlating structural and compositional data gather from XPS and X-ray diffraction (XRD) to the optical transmission and optical dispersion obtained by UV-Vis spectroscopy and spectroscopic ellipsometry, respectively.

4:40pm **SE+PS-ThA9 Inductively Coupled Impulse Sputtering (ICIS): A Novel Technique for Ionised PVD**, *A.P. Ehasarian*, *D. Loch*, Sheffield Hallam University, UK

One limitation of magnetrons is their use of inhomogeneous magnetic fields which constrains deposition of magnetic materials to thin targets, complex (magnetic) alloys by erosion-dependent stoichiometry, and oxides by build-up of arc-prone insulating layers on the target edge. Inductively Coupled Impulse Sputtering (ICIS) is a new technology for physical vapour deposition based on sputtering without magnetic fields. A plasma is generated in front of the target via an inductively coupled coil driven with a 13.56 MHz radio frequency (RF) power supply. The target is then biased to a high voltage to initiate sputtering. In order to ionise significant fractions of the sputtered flux, the RF power density is pulsed with peak values in excess of 30 Wcm^{-2} to produce plasma density of the order of 10^{12} cm^{-3} . A low duty cycle of $< 25\%$ is used to achieve high peak powers and plasma densities at low average power. The degree of ionisation of ICIS of Cu and Ti in Ar atmosphere were evaluated using optical emission spectroscopy and atomic absorption spectroscopy and the film microstructure and coverage of vias was studied with cross sectional SEM. The effect of peak RF power density (P) was to increase metal ionisation degree hyperbolically. The rate of production of Ti^{1+} metal ions was proportional to $\sim P^{1.1 \pm 0.2}$ and was significantly faster than that of metal neutrals of $\sim P^{0.66 \pm 0.08}$ indicating enhanced ionisation of the vapour with power. The mechanisms of ionisation will be discussed. The influence of pressure on the process was studied at a constant peak RF power density of $P = 30 \text{ Wcm}^{-2}$. The intensity of copper and argon neutral emission rose linearly for pressures of $2.95 \times 10^{-2} - 1.2 \times 10^{-1} \text{ mbar}$ and saturated at higher pressures. The deposition rate was 2 nm min^{-1} for RF-power density of 30 Wcm^{-2} , average target power of 67 W and a pressure of $1.2 \times 10^{-1} \text{ mbar}$. The microstructure of Cu films was globular at $2.95 \times 10^{-2} \text{ mbar}$ and large-grain columnar at $1.2 \times 10^{-1} \text{ mbar}$. Bottom coverage of unbiased vias with width $0.36 \mu\text{m}$ and aspect ratio of 2.5:1 increased from 15 % to 20 % as pressure increased from 2.95×10^{-2} to $1.2 \times 10^{-1} \text{ mbar}$. The current work has shown that the concept of combining a high powered RF coil with a magnet-free cathode is feasible and produces very stable plasma and uniform target erosion. The experiments have shown a significant influence of power and pressure on the plasma and coating microstructure. The process is suitable for Fe, Ni and FeCo alloy deposition.

Surface Science Division
Room: 107 - Session SS-ThA

Semiconducting & Ferroelectric Surface
Moderator: J. Millunchik, University of Michigan

2:00pm **SS-ThA1 Polarization Dependence of the Surface and Interfacial Chemistry of Ferroelectric Oxides**, *E.I. Altman*, Yale University
INVITED

In analogy to ferromagnets, ferroelectric materials develop remnant macroscopic electric fields that can be switched by applying an external field. The bulk electronic polarization is stabilized by compensating charges at the surface that can be supplied by adsorption or electronic and structural reconstructions. Because opposite compensating charges are required on oppositely poled surfaces, ferroelectric materials offer unique opportunities to create surfaces with switchable chemical properties. Further, thin ferroelectric films would be expected to switch their polarization in the presence of molecules that preferentially adsorb on one of the polar surfaces, suggesting a new avenue for chemical sensing. It will be shown that the adsorption of polar molecules such as alcohols and carboxylic acids depends on the ferroelectric polarization direction, with stronger adsorption on positively poled LiNbO_3 . The differences in adsorption strengths are comparable to the energy required to switch 20 nm thick ferroelectric films, thus ferroelectric chemical sensing is feasible. This possibility is further explored through *in situ* measurements of changes in polarization of thin epitaxial titanate ferroelectric films in response to oxidizing and reducing environments. A limitation to switchable chemistry, however, is the low reactivity of typical ferroelectric oxides. Efforts to increase the reactivity through deposition of catalytic metals fail because the metals form three-dimensional clusters whose surfaces are too far from the ferroelectric substrate to be affected. Results of a combined experimental/theoretical approach to identifying catalytic oxides that form stable, atomically thin layers whose reactivity is influenced by the polarization direction of the ferroelectric will be presented. Specific examples include $\text{Cr}_2\text{O}_3/\text{LiNbO}_3$ and perovskite layers on ferroelectric titanates.

2:40pm **SS-ThA3 Surface Reconstructions of $\text{BaTiO}_3(001)$: STM Study**, *E.H. Morales*, *D.A. Bonnell*, University of Pennsylvania

BaTiO_3 is currently used in Random Access Memories and is a versatile material with many potential applications. Ferroelectricity at a surface provides unique possibilities to examine mechanisms of molecular adsorption. Experimentally, the polarization can be manipulated *in situ* by negatively and positively poling the surface. In this manner, the interaction with foreign gaseous species can be controlled. It is necessary to develop fundamental understanding of BaTiO_3 surfaces in order to control the ferroelectric polarization and consequent interactions with adsorbates and in devices. Recent advances have indeed shown that polarization affects molecular adsorption of a variety of molecules; however, the mechanistic processes are not yet understood. Here we present STM of atomically resolved reconstructions, $(\sqrt{5} \times \sqrt{5}) R26.6^\circ$ and (3×1) and relate water adsorption to local polarization. Structural variations and adsorption sites will be discussed in terms of Density Functional Theory predictions. Preliminary results of the interaction of $\text{BaTiO}_3(001)$'s surface and CO_2 will be presented as well.

3:00pm **SS-ThA4 Polarization Dependent Interactions at Ferroelectric Surfaces**, *J. Garra*, *M. Zhao*, *J.M. Vohs*, *E.H. Morales*, *D.A. Bonnell*, University of Pennsylvania

Ferroelectric polarization at surfaces has been exploited over the last several years to mediate reactions in aqueous solutions. More recently studies have shown that ferroelectric polarization at surfaces affects molecular adsorption. The study presented here uses a variety of surface techniques (scanning tunneling microscopy and spectroscopy, low energy electron diffraction, temperature programmed desorption) to examine molecular adsorption on ferroelectric surfaces. Various molecules and various substrates are chosen to determine the effect of polarization orientation and magnitude on physisorption, disassociative chemisorption, defect mediated adsorption and chemical reactions. Specifically, results of interactions of small molecules on LiNbO_3 , and BaTiO_3 surfaces will be compared. We show that ferroelectric polarization can affect both physisorption and chemisorption bond energies as well as the sticking coefficients.

3:40pm **SS-ThA6 An Atomic View of ALD of Dielectrics on Semiconductors Using STM**, *A.C. Kummel, W. Melitz, J.B. Clemens, J.S. Lee, T. Kaufman-Osborn, T. Kent, E.A. Chagarov, J. Shen*, University of California, San Diego, *R. Droopad*, Texas State University-San Marcos

INVITED

Scaling of gate oxides on MOSFETs requires nucleating oxide ALD in every unit cell of the semiconductor channel surface without disrupting the semiconductor surface (high mobility) while eliminating dangling bond states (low D_{it}). The reaction of TMA on the group III rich (4×2) reconstructions of the InAs(0 0 1) and InGaAs(0 0 1) surfaces were been studied using in-situ STM, scanning tunneling spectroscopy (STS), in-situ XPS, and density functional theory (DFT). When an As₂ capped III-V sample is decapped in UHV and the substrate is dosed to with TMA at 300K at annealed at 200C, the TMA reaction products (dimethyl aluminum, DMA) spontaneously forms monolayer islands insuring ALD nucleation in each unit cell. For integration of III-V MOSFETs on 300 mm silicon wafers, it is possible that a gate last process may be required for which As-decapping is not suitable. A combination of atomic hydrogen dosing, annealing, and TMA dosing is observed to produce an ordered unpinned passivation layer on air exposed InGaAs(001)-(4x2) surface with only monatomic steps. This TMA passivation layer on H cleaned air exposed III-V has the same horizontal rows of dimethyl aluminum (STM) and the same unpinned interface (STS) observed with the TMA/decapped InGaAs(100). While TMA directly reacts to create a high density of sites to nucleate gate oxide ALD on III-V surface, for Ge(100) surface functionalization is required. The direct reaction of TMA on a Ge(100) surface and the effect of monolayer H₂O pre-dosing were investigated. At 300K, a saturation TMA dose produced 0.8 monolayer (ML) of semi-ordered species on a Ge(100) surface due to the dissociative chemisorption of TMA. XPS analysis of the 200°C annealed TMA/Ge(100) surface showed that only carbon content was reduced during annealing, while the Al coverage was maintained at 0.15 ML, consistent with the low density of nucleation sites due to site blocks by reaction products. Conversely, saturation TMA dosing at RT on the monolayer H₂O pre-dosed Ge(100) surface followed by annealing at 200°C formed a saturation layer of Al-O bonds with an Al coverage a factor of two greater than the TMA only dosed Ge(100). The Ge-OH sites catalyze the dissociative chemisorption of TMA even at 300K to create a semiordered surface of Ge-O-Al bonds with an Al coverage double the coverage from a TMA surface without the H₂O pre-dose.

4:20pm **SS-ThA8 Electrostatic Coupling of Surface Charge to Bulk Defect Behavior in Metal Oxides**, *P. Gorai, K. Pangan-Okimoto, A. Hollister, E.G. Seebauer*, University of Illinois at Urbana-Champaign

The technologically useful properties of semiconductor oxides such as titania and zinc oxide often depend on the concentration and diffusion of point defects. Near-surface effects are particularly important in nanoscale devices because most of the bulk is located in the vicinity of the surface. Past work in our laboratory with silicon and titania has shown that semiconductor surfaces serve as efficient pathways for generation and annihilation of point defects in the underlying bulk. Surfaces can, in addition, support electrically charged defects which create near-surface strong electric fields that can influence the local motion of charged defects resulting in the formation of space-charge layers. The electric field-driven accumulation or depletion of charged oxygen defects in such space-charge regions in metal oxides have direct implications on the performance of nanoscale devices such as gas sensors and memory resistors. Oxygen diffusion behavior was studied by exposing natural-abundance single-crystal rutile to isotopically labeled oxygen gas. The resulting profiles were measured by secondary ion mass spectrometry and subsequently modeled with continuum equations for the reaction, Fickian diffusion and electric field-driven diffusion of the key point defects. The degree of charge build-up at the surface can be quantified by an electric potential (V_s). The profiles calculated show a characteristic steep concentration gradient near the surface followed by a normal bulk diffusion profile. By identifying the charge-mediated field-driven diffusion mechanism as the controlling factor for the near-surface pile-up of oxygen, we demonstrate that this method allows the spatially resolved characterization of space charge regions near the surfaces of crystalline semiconductor metal oxides. The capability to predict oxygen pile-up in nanoscale metal oxide devices may be beneficial in device improvement via defect engineering of surfaces.

4:40pm **SS-ThA9 Surface Photovoltage Behavior of n-type GaN as a Function of Orientation**, *M. Foussekis, A.A. Baski, M.A. Reshchikov*, Virginia Commonwealth University

GaN is a wide-bandgap semiconductor (3.4 eV) which has approximately 1 eV of upward surface band bending for n-type material, thereby producing a depletion region that can be detrimental to device performance. This band bending can be indirectly measured using the surface photovoltage (SPV) effect. By illuminating the surface with above-bandgap light, electron-hole pairs are created in the depletion region and holes are swept to the surface to

reduce the negative charge and band bending. This change in surface charge is measured by a Kelvin probe in an optical cryostat. When the samples are illuminated with a HeCd laser, the SPV signal immediately rises to approximately 0.6, 0.3 and 0.4 eV for the Ga-polar (c-plane), N-polar, and m-plane sample orientations, respectively. The noticeably smaller SPV value for N-polar GaN indicates that this particular orientation has a smaller value of band bending. After this immediate rise, the SPV signal then begins to slowly change due to photo-induced surface processes. In an oxygen environment, the Ga-polar and m-plane orientations demonstrate a slow decrease in SPV of about 0.1 to 0.2 eV, which is attributed to the photo-induced adsorption of oxygen species [1]. There is no observable change for N-polar GaN, indicating that N-polar GaN is less reactive under UV illumination. In vacuum, all three orientations show a slow increase in the SPV signal of 0.1 to 0.2 eV over 1 h, which is due to the photo-induced desorption of charged surface species. When illumination is ceased after 1 h and the surface is restored in vacuum, subsequent illumination results in a constant, steady-state SPV signal, confirming that the photo-induced removal of any surface contamination layers is complete after approximately 1 h. The restoration behavior of the SPV can be fit for all three orientations using a thermionic model with logarithmic time decay [2]. The N-polar GaN is significantly faster, however, and fully restores in only minutes, as opposed to hours or days for the other orientations. It therefore appears that N-polar GaN has the most distinctive SPV behavior among these orientations, with the lowest SPV value, least amount of photo-induced surface reactivity, and fastest restoration behavior.

[1] M. Foussekis, A. A. Baski, and M. A. Reshchikov, *Appl. Phys. Lett.* **94**, 162116 (2009).

[2] M. A. Reshchikov, M. Foussekis, and A. A. Baski, *J. Appl. Phys.* **107**, 113434 (2010).

5:00pm **SS-ThA10 The Surface States of Lithium Tetraborate**, *L. Wang, W.-N. Mei*, University of Nebraska at Omaha, *D. Wooten, J. McClory, J. Petrosky*, Air Force Institute of Technology, *V. Adamiv, Ya. Burak*, Institute of Physical Optics, Ukraine, *I. Ketsman*, University of Nebraska - Lincoln, *Ya. Losovyj*, The J. Bennett Johnston Sr. Center for Advanced Microstructures and Devices, *P.A. Dowben*, University of Nebraska - Lincoln

The different low index surface terminations of lithium tetraborate, Li₂B₄O₇, are dominated by electronic states that fall within the projected band gap of the bulk states. As a pyroelectric material, Li₂B₄O₇ is a wide band gap dielectric, yet the (110) surface has a much smaller band gap because of occupied surface states that fall at binding energies between the valence band maximum and the Fermi level. The (100) surface is dominated, however, by unoccupied surface states that also fall in the gap between the conduction band minimum and valence band maximum, but at binding energies just below the conduction band minimum. These states have been identified in photoemission studies of Li₂B₄O₇(110) and inverse photoemission studies of Li₂B₄O₇(100) [1]. There is good qualitative agreement between these experiments and the electronic band structure calculations showing that the different surface terminations of lithium tetraborate yield very different surface electronic states.

[1] D. Wooten, I. Ketsman, J. Xiao, Ya.B. Losovyj, J. Petrosky, J. McClory, Ya. V. Burak, V.T. Adamiv, J.M. Brown and P.A. Dowben, *European Physical Journal: Applied Physics* **52** (2010) 31601

Transparent Conductors and Printable Electronics

Focus Topic

Room: 106 - Session TC+EM+NS-THA

Transparent / Printable Electronics Part 2

Moderator: S. Durbin, University at Buffalo

2:00pm **TC+EM+NS-ThA1 ZnO-based Schottky Diodes and Their Utilization in Transparent Electronics**, *H. von Wenckstern*, Universität Leipzig, Germany

INVITED

Transparent conducting oxides (TCO) have found application as electrode in emerging markets like that of thin films solar cells or flat panel displays. For this passive functionality the TCO material must combine high transparency preferentially over a wide spectral range and high conductivity. In the last years active transparent devices like photodetectors, transistors or a complete transparent circuitry are envisioned and rely on semiconducting properties of the material. Besides a precise control of the doping level in the active part of devices the creation of space charge regions by rectifying contacts is a prerequisite for active devices. In the emerging field of transparent electronics, only metal-insulator-semiconductor field-effect transistors (MISFETs) were considered so far. In

this contribution transparent, high-performance MESFETs, inverters etc. based on ZnO and related ternaries are presented. We discuss design prospects as well as limitations regarding device performance, reliability and stability.

The influence of the contact metal and dielectric passivation layers on the properties of ZnO Schottky diode, used as gate electrode within the MESFETs, as well as sources of non-idealities will be highlighted.

2:40pm TC+EM+NS-ThA3 Photoresponse of Amorphous In-Ga-Zn-O / Pt Schottky Junction, D.H. Lee, K. Nomura, T. Kamiya, H. Hosono, Tokyo Institute of Technology, Japan

Amorphous oxide semiconductors (AOSs) are expected as an alternative to amorphous/poly-Si for thin-film transistors (TFTs) in next-generation flat-panel displays (FPDs) because AOS TFTs have many advantages such as large field-effect mobilities ($>10 \text{ cm}^2(\text{Vs})^{-1}$) and low-temperature process [1]. For more advancing AOS optoelectronic technology, it is important to develop more various devices other than TFTs, and to study some remaining issues such as operation characteristics of AOS devices under light illumination.

In this study, we fabricated good and stable metal-AOS Schottky contacts made of amorphous In-Ga-Zn-O (a-IGZO) and bottom Pt electrodes at temperatures below 200°C even though it is generally difficult to make high performance oxide Schottky junctions [2]. It was found that the a-IGZO/Pt Schottky contacts have an ideality factor $n \sim 1.1$ and a Schottky barrier height $\phi_b \sim 0.9 \text{ eV}$, which were evaluated from their J-V curves using the thermionic emission model. From C-V results, the Schottky junctions operate at the full-depletion condition, whose C corresponds to the geometrical capacitance of the a-IGZO layer, and relative permittivity ϵ_s of a-IGZO was obtained approximately 13. However, the results of temperature dependences of J-V characteristics were unexplained if we take a simple uniform Schottky barrier model; we found that the barrier potential fluctuations model [3] explained them well, and the mean barrier height $\phi_{b,m}$ of 1.2 eV and the net electron affinity χ_s of a-IGZO of 4.2 eV were obtained. On the other hand, the Schottky contacts showed very small open circuit voltages (V_{OC} 's) $< 0.1 \text{ V}$ under 100 mWcm^{-2} AM1.5 light illumination, which are far smaller than the built-in potential ($V_{bi} \sim 0.4 \text{ eV}$) estimated from the C-V measurements in dark. We also observed that V_{OC} decays with time after starting the light illumination. We will discuss the mechanism of the small V_{OC} based on these results.

[1] T. Kamiya et. al. *Sci. Technol. Adv. Mater.* **11** 044305 (2010).

[2] K. Ip et al., *J. Cryst. Growth* **287**, 149 (2006).

[3] J. H. Werner and H. H. Güttler, *J. Appl. Phys.* **69**, 1522 (1991).

3:00pm TC+EM+NS-ThA4 Novel Metal-organic Precursors for Printed Electronics - Synthesis, Implementation, and Properties, J.A. Belot, R.A. Potash, R.D. McCullough, K.A. Singh, L. Porter, Carnegie Mellon University

Printed electronics is a rapidly growing industry and within this emerging field there are three required material categories critical to fabricating active and passive circuitry – insulators (dielectrics), semiconductors (polymers), and conductors (metals). The increased interest in printable electronics as alternatives to silicon-based technologies is fueled by the promise of large-area, flexible, and ultra-low-cost devices. To enable the growing demands of printing processes this work develops metal-containing inks for the deposition of the coinage metals - copper, silver, and gold. These metals are chip components ranging from interconnects to source and drain contacts in organic field effect transistors. The liquid ink approach is based on fundamental advances in coordination chemistry to fabricate discrete metal complexes that can be heated or irradiated to yield metallic films. Ultimately inkjet printing technologies were employed to deposit these metal inks in specific, predetermined patterns that were directly transformed into active and passive devices. The versatility of this approach holds the possibility of printing any metallic design and pattern on virtually any type of substrate.

3:40pm TC+EM+NS-ThA6 A New Application for a-IGZO TFTs: An Addressable Microfluidic Electrowetting Channel Device, J. Noh, J.H. Noh, University of Tennessee, E. Kreit, J. Heikenfeld, University of Cincinnati, P.D. Rack, University of Tennessee

An electrowetting (EW) microfluidic platform designed for control and transport of aqueous and polar species has been fabricated on passive electrodes as well as an active matrix thin film transistor (TFT) array. To drive the EW devices we integrated the micro fluidic platform on a base-plane of transparent TFTs. Specifically, we have used an InGaZnO (IGZO) active layer for the TFT device which has superior performance and offers the benefit of transparent devices for biological and display applications. The TFTs are fabricated with a bottom-gate staggered structure with Cr gate and SiO₂ gate dielectrics deposited via plasma enhanced chemical vapor

deposition (PECVD). The a-IGZO semiconducting active layers are deposited using rf magnetron sputtering in a reactive Ar-O₂ atmosphere. Finally, source and drain electrodes are formed by e-beam evaporating Ti/Au. Finally the device is annealed in an N₂ ambient for electrical activation. For the EW device integration, Al electrodes are have been deposited various passivation layers. Subsequently a top dielectric and a hydrophobic Fluoropel layer are applied. In this presentation we will review the process flow and will discuss the materials integration issues of EW device and its effect on the TFT performance. We will illustrate the EW characteristics based on standard planar electrowetting on dielectric (EWOD) platforms and compare them to a new concept we have termed the “Laplace Barrier” which includes post arrays and enhances electrowetting characteristics.

4:00pm TC+EM+NS-ThA7 Amorphous Oxide Semiconductor Thin-Film Transistors, J.F. Wager, K. Hoshino, Oregon State University, B. Yeh, R.L. Hoffman, Hewlett-Packard Company

INVITED

Amorphous oxide semiconductor (AOS) thin-film transistors (TFTs) are transitioning towards commercialization for active-matrix liquid crystal display flat-panel display backplane applications. They also appear to be well-positioned to meet the more demanding challenges associated with active-matrix organic light-emitting device backplanes. Additionally, AOS TFTs offer an attractive approach to printed electronics. The primary focus of this talk will be to discuss our novel approach to top-side passivation of bottom-gate indium gallium zinc oxide (IGZO) and zinc tin oxide (ZTO) AOS TFTs. Device performance between passivated and unpassivated AOS TFTs will be compared. Passivation mechanisms will be considered in the context of induced-gap state and device physics electrostatic modeling.

4:40pm TC+EM+NS-ThA9 Why Optimum Oxygen Pressure Range Exists for Fabricating Amorphous In-Ga-Zn-O Thin-Film Transistor and How it Should be Optimized, K. Ide, K. Nomura, T. Kamiya, H. Hosono, Tokyo Institute of Technology, Japan

Amorphous oxide semiconductors (AOSs) represented by amorphous In-Ga-Zn-O (a-IGZO) are expected for large-area high-performance flexible electronic devices, because AOSs have large electron mobilities greater than $10 \text{ cm}^2(\text{Vs})^{-1}$ even if fabricated at room temperature (RT). In particular, a-IGZO has good controllabilities of carrier concentration, and their thin-film transistors (TFTs) exhibit superior properties including long-term stability.

In this study, we investigated effects of oxidation on operation characteristics of a-IGZO TFTs. Bottom gate, top-contact a-IGZO TFTs were fabricated on SiO₂/c-Si substrates by RF magnetron sputtering. Sputtering conditions were the RF power of 70 W and the total pressure of 0.55 Pa. Two oxidation treatments were examined; (i) ozone annealing and (ii) varying a mixing gas ratio of Ar : O₂ from 18 : 2 to 19.8 : 0.2 in standard cc per minute (sccm) during the channel deposition.

For the ozone annealed TFTs, annealing at $\leq 250^\circ\text{C}$ produced good TFTs, while those annealed at 300°C caused large hysteresis and S slope. After applying a high V_{GS} larger than 40 V, the transfer characteristics showed the large V_{th} of 40V and the small hysteresis. Trap state around Fermi level of the large S state and the large V_{th} state were $\sim 4 \times 10^{17}$ and $\sim 1 \times 10^{17} \text{ cm}^{-3} \text{ eV}^{-1}$, which were estimated by C-V analysis. The large V_{th} state is very stable in the dark, but the TFT recovers to the initial large S state by light illumination. The photoresponse measurements revealed that deep trap states were formed at 2.3 eV below the conduction band minimum by applying a high V_{GS} . Thermal desorption spectra showed that weakly-bonded excess oxygens were incorporated in the a-IGZO layer. From these results, we built a subgap DOS model of the trap states of the excess oxygens. We also confirmed similar behaviors in a-IGZO TFTs fabricated in high oxygen pressure conditions.

This study reveals that the control of oxygen stoichiometry is important for obtaining good performance and stability of AOS TFTs.

5:00pm TC+EM+NS-ThA10 Effects of Low-Temperature Annealing and Deep Traps in Operation Characteristics of Amorphous In-Ga-Zn-O Thin-Film Transistors, T. Kamiya, Y. Kikuchi, K. Ide, K. Nomura, H. Hosono, Tokyo Institute of Technology, Japan

Amorphous oxide semiconductors (AOSs) represented by a-In-Ga-Zn-O (a-IGZO) are expected for channel materials in thin-film transistors (TFTs) for next-generation flat-panel displays such as jumbo-size / fast / ultrahigh-resolution liquid-crystal displays and organic light-emitting diode displays. These are also expected for flexible electronics devices because they may be fabricated on unheated substrates, and thus produce flexible displays and circuits on inexpensive plastic substrates such as PET. On the other hand, it is known that, although room-temperature fabrication is possible for AOS TFTs, post-deposition thermal annealing at $\geq 300^\circ\text{C}$ is better employed to obtain good stability. To employ this technology to the flexible electronics, the annealing temperature should be lowered to 200°C or far below. We reported that wet O₂ annealing produces the best performance TFTs when

annealed at $\geq 300^\circ\text{C}$, while it caused serious negative threshold voltage (V_{th}) shift at $\leq 200^\circ\text{C}$. In this paper, we report the origin of the negative V_{th} shift by employing photoresponse spectroscopy of TFT characteristics. It revealed that the near-valence band maximum (VBM) states are reduced significantly even by the low-temperature 200°C annealing, and implied that the negative V_{th} shift originates from free electrons released by annihilation of the near-VBM states.

5:20pm **TC+EM+NS-ThA11 β -alumina (SBA): A Promising High Dielectric Constant Gate Material for Solution Processed, Transparent and Low Voltage Transistor Devices**, *B. Zhang, Y. Liu, H. Katz*, Johns Hopkins University

β -alumina (SBA) has been discovered as a promising high dielectric constant gate material for solution processed, transparent and low voltage transistor devices. Some experimental evidence indicates that the mobile Na ion within two spinel blocks made by Al and O is responsible for the high dielectric constant. Transistors (W/L ratio 10) using SBA as gate layer and zinc tin oxide (ZTO) as active layer only need 2V to obtain 0.7mA output current. SBA material is compatible with organic semiconductors such as PQT12 and pentacene as well. Some key issues regarding using SBA for real applications, such as device stability in the ambient atmosphere, response under high frequency, and threshold voltage shift under gate bias have also been studied. It is found that encapsulating the device with CYTOP fluorinated polymer is an effective way to increase the operational stability of the devices in the ambient environment.

Thin Film Division

Room: 110 - Session TF+EM+SS-ThA

Applications of Self Assembled Monolayers

Moderator: M.R. Linford, Brigham Young University

2:00pm **TF+EM+SS-ThA1 Organic Monolayers on Silicon-rich Substrates: Methods and Mechanisms**, *H. Zuilhof*, Wageningen University, Netherlands

INVITED

SAMs on silicon-containing substrates including silicon, silicon nitride and glass widely expand the applicability of such materials. The presentation will focus on 3 recent developments:

1) The surface modification of H-terminated Si has functioned as a stepping-stone for the construction of a wide-range of hybrid materials. Recent synthetic improvements and detailed mechanistic studies have shown how to optimally construct such modified substrates. These results will be presented in the light of further developments.

2) Silicon nitride can be modified by covalent SAM attachment to achieve chemically highly robust systems. Biofunctionalization thereof with oligosaccharides and antibodies provides novel diagnostic applications in terms of specific bacterial capture in combination with generally antifouling substrates when combined with lithographic structuring of the material. Proof-of-principle and remaining challenges will be demonstrated based on recent experimental progress.

3) A photochemical method we recently developed to modify glass (SiO_2), and the application thereof within the field of modified glass microchannels will be shown, e.g. via the on-chip embedding of enzymatic cascade reactions using a combination of local SAM attachment and DNA-enzyme hybrids. Finally, generalizations to the modification of other oxidic surfaces will be provided.

Key references:

H. Zuilhof and co-workers, *J. Am. Chem. Soc.* **2011**, *133*, 4998–5008.

H. Zuilhof, J. C. M. Van Hest and co-workers *Chemical Science* **2011**, *2*, in press (DOI: 10.1039/C1SC00146A).

H. Zuilhof and co-workers, *Angew Chem.* **2011**, *50*, in press (DOI: 10.1002/anie.201100835).

2:40pm **TF+EM+SS-ThA3 Molecularly Modulated Electrical Transport at Chemically Passivated Silicon Surfaces**, *G. Dubey*, NRC-SIMS, Canada, *F. Rosei*, INRS-EMT, Canada, *G.P. Lopinski*, NRC-SIMS, Canada

Adsorption of charged or polar species on semiconductor surfaces can modulate the electrical properties through long-range field effects. Hydrogen-terminated silicon-on-insulator (SOI-H) is an interesting model system for investigating this sensitivity to surface processes [1,2]. Accumulation mode SOI-H pseudo-MOSFETs [3] have been used to probe molecular adsorption and reaction events. Current-voltage characteristics of such n -channel devices are found to be sensitive to the environment, with the accumulation threshold voltage, or flat-band voltage (V_{FB}), exhibiting

large reversible changes upon cycling between ambient atmosphere, high vacuum ($<10^{-5}$ Torr) and exposure to water and pyridine vapour at pressures in the torr range. Both these adsorbates act as effective electron donors, shifting the flat band potential to more negative values. The field-effect mobility is found to be comparatively less affected through these transitions. Adsorption of the well known electron acceptor tetracyanoethylene (TCNE), is shown to cause depletion, with ppm levels of TCNE vapour in ambient atmosphere found to rapidly decrease the saturation current by over two orders of magnitude. The effect is only partially reversible on the hydrogen terminated surface, due to the accumulation of strongly bound TCNE molecules on the surface. In addition, oxidation of the H-terminated surface is seen to result in irreversible shifts in both the flat-band voltage and field-effect mobility. In order to passivate the surface from these irreversible processes, a photochemical gas phase reaction [4] with decene was used to form a decyl monolayer on the SOI(100)-H surface. Formation of this monolayer is found to result in a relatively small shift of threshold voltage and only a slight degradation of the field effect mobility. Decyl passivation only slightly decreases the response of the FET to TCNE adsorption while significantly improving the reversibility of the response. These results suggest that alkyl monolayer dielectrics formed by the gas phase photochemical method can function as good passivating dielectrics in field effect sensing applications.

[1] G. Dubey, G.P. Lopinski, and F. Rosei, *Appl. Phys. Lett.* **91**, 232111 (2007).

[2] G. Dubey, F. Rosei, and G.P. Lopinski, *Small* **6**, 2892 (2010).

[3] S. Cristoloveanu, and S. Williams, *IEEE Elec. Dev. Lett.* **13**, 102 (1992).

[4] B.J. Eves, and G.P. Lopinski, *Langmuir* **22**, 3180 (2006).

3:00pm **TF+EM+SS-ThA4 Micrometer- and Nanometer-Scale Patterning of Azide-Functionalized Self-assembled Monolayers on Gold and Aluminum Oxide Surfaces**, *O. El Zubir, I. Barlow, G. Leggett, N. Williams*, University of Sheffield, UK

Self-assembled monolayers (SAMs) have been prepared by the adsorption of [11-(4-azido-benzoylamino)-undecyl] phosphonic acid on aluminum oxide and by the adsorption of 11-(4-azido-benzoylamino)-undecylthiol. Exposure to near UV radiation causes elimination of nitrogen and the creation of a reactive nitrene species. Quantitative studies by X-ray photoelectron spectroscopy (XPS) and contact angle measurement show that the reaction is complete after an exposure of 20 J cm^{-2} . The reaction enables selective introduction of primary amines to the surface. By exposure of the azide under a solution of the amine, derivatization may be carried out with high efficiency, providing a simple pathway for the creation of a variety of multiple-component surface chemical patterns. Micropatterned surfaces were fabricated by exposure the SAMs to UV-laser ($\lambda=325 \text{ nm}$) through a mask in presence of amines. Photopatterning was carried out at the nanometer scale by using scanning near-field photolithography (SNP) in which a scanning near-field optical microscope (SNOM) coupled to a UV laser ($\lambda=325 \text{ nm}$) is utilized as the light source. Selective modification of azide terminated monolayers on aluminum oxide by protein-resistant molecules enabled the fabrication of protein nanopatterns that could be imaged by fluorescence microscopy.

3:40pm **TF+EM+SS-ThA6 Free-standing, SAM-based, Hybrid Biocompatible Nanomembranes for Biological Applications**, *N. Meyerbröker, W. Eck, M. Zharnikov*, Universität Heidelberg, Germany

Functional monomolecular films - so-called self-assembled monolayers (SAMs) - represent a broad platform for nanofabrication, sensor design, and molecular electronics, as well as a framework for Chemical Lithography, and a model system for organic interfaces and molecular, macromolecular and biological assemblies. These films can be prepared on different substrates which provide necessary support and guarantee the persistence of the 2D molecular assembly. Since the intermolecular interaction within the SAMs is relatively weak, such films cannot exist without support, dissipating into the individual constituents upon the separation from the substrate. However, as far as the individual molecules within a SAM can be cross-linked extensively by physical means such as electron irradiation, the resulting quasi-polymer film can be separated from the substrate and exist as a free-standing monomolecular membrane on its own. In this presentation we describe the formation of such free-standing membranes on the basis of aromatic SAMs. In contrast to the previous work, we used not only non-substituted but nitro- and nitrile-substituted SAM constituents which, due to either nitro-to-amine or nitrile-to-amine transformation, become chemically reactive after the irradiation treatment and can be subsequently coupled to further species. As such species we used oligo(ethylene glycol)-based molecules with a specific anchor group providing the coupling to the amine groups of the monomolecular template. After the attachment, these templates and respective hybrid membranes

become protein-repelling and as such can be used as a non-disruptive and highly transparent support for proteins and cells in transmission electron microscopy (TEM) experiments. Whereas the ultimate thinness of this support guarantees a high imaging quality, protein-repelling ensures the lack of protein denaturing, which extends essentially the possibilities of TEM experiments in their specific application to sensitive biological targets.

4:00pm **TF+EM+SS-ThA7 Development of Nanoscale Heterostructures: From Single Component Nanostructures to Multicomponent Nanosystems, N. Chopra**, The University of Alabama, Tuscaloosa **INVITED**

Chemical vapor deposition (CVD) and solution synthesis was coupled to realize a unique surfactant-free approach for the direct nucleation of nanoparticles on 1-D nanostructures. Towards this end, skeleton nanostructures such as carbon nanotubes and oxide nanowires were successfully utilized as a selective nucleation sites for nanoparticles. Carbon nanotubes (CNTs)-Ni/NiO nanoparticles and oxide nanowires -(Au or Co₃O₄) nanoparticles were synthesized. Morphological evolution of nanoparticles as a function of various growth parameters was studied using TEM, SEM, and XRD. New kinds of lattice relationships, interfaces, and morphologies were established. For example, CuO nanowire-Co₃O₄ nanoparticles showed unique optical characteristics leading to enhanced absorbance in visible light. Growth mechanisms of heterostructures revealed various competing phenomena at nanoscale including thermodynamic stability and chemical potential, and surface migration of nanoparticles on high curvature 1-D nanostructures as opposed to flat surface. These heterostructures also hold great promise as novel sensors and energy technologies.

4:40pm **TF+EM+SS-ThA9 Physical and Electrical Characterization of Metal Incorporated SAM-based Molecular Electronic Junctions, S. Pookpanratana, M.A. Walsh, C.A. Richter, C.A. Hacker**, National Institute of Standards and Technology

Molecular electronics is attractive for next-generation applications because of the flexibility in tailoring the organic functionality and the facile formation of uniform monolayers by using thiol-Au chemistry for self-assembly. Added functionality can be achieved by using thiol self-assembled monolayers (SAMs) containing terminal carboxylic acid functional groups to chelate with metal ions [1], and thus can incorporate d-orbital transition metals with the SAMs. One challenge in molecular electronics has been the reliable formation of a top contact to the organic layer. Fabrication techniques involving metal evaporation of the top contact often result in penetration to the substrate [2] or into the SAM [3], either of which influences the measured electrical properties across the junction. Here, we utilize flip chip lamination (FCL), a soft metallization technique by nanotransfer printing, to form a top contact onto SAMs on Au [4].

Based on previous work by Ulman et al. [5] and Allara et al. [6], we have incorporated metal ions (Cu and Ni) with mercaptohexadecanoic acid (MHA) and formed a molecular junction by FCL. SAMs of MHA were prepared on Au on Si and Au on polyethylene terephthalate (PET) substrates. The MHA/Au/Si was exposed to metal ion (M) containing solution. The M-MHA/Au/Si samples were then laminated to MHA/Au/PET to create a 'molecular sandwich' which resulted in the following structure: PET/Au/MHA-M-MHA/Au/Si where the PET substrate is removable.

The SAMs on Au were investigated by using X-ray photoelectron spectroscopy (XPS) and p-polarized reflection absorption infrared spectroscopy (p-RAIRS), and both methods confirm the initial presence of carboxylic acid on the (pre-FCL) surface. Successful incorporation of metal ions into the SAM were directly confirmed by XPS (occupying 30-50% of the -COOH sites), and indirectly by p-RAIRS with the appearance of C=O bands in an acid salt environment. Electrical and physical characterization (using backside p-RAIRS and near edge X-ray absorption fine structure (NEXAFS)) measurements to investigate the monolayer after FCL are currently ongoing. With these results, we are able to obtain a thorough picture linking electrical properties with physical characterization of the buried molecular junctions.

- [1] A. C. Templeton et al., *Langmuir*, 2000, 16, 6682-6688.
- [2] A. V. Walker et al., *J. Am. Chem. Soc.*, 2004, 126, 3954-3963.
- [3] C. A. Richter et al., *Solid-State Electron.*, 2006, 50, 1088-1096.
- [4] M. Coll et al., *J. Am. Chem. Soc.* 2009, 131, 12451-12457.
- [5] S. D. Evans et al., *J. Am. Chem. Soc.*, 1991, 113, 5866-5868.
- [6] T. A. Daniel et al., *Langmuir*, 2007, 23, 638-648.

5:00pm **TF+EM+SS-ThA10 Examining the Role of Laminin-Derived Peptides in Neuronal Attachment, N.A. LaFranzo, J.A. Maurer**, Washington University in St. Louis

Laminin-1 is a 900kD glycoprotein that is a major component of the extracellular matrix (ECM). Laminin is known to be involved in many cellular processes including cell adhesion, migration and differentiation *in vivo* and is often used in *in vitro* experiments to encourage neuronal attachment. While laminin contains some integrin-receptor binding sites, multiple domains on the protein including the peptide sequences IKVAV, YIGSR and RGD have also been shown to bind to non-integrin neuronal receptors, encourage cell adhesion, and encourage neurite outgrowth in the absence of the full protein structure. However, previous experiments performed using these peptides as substrates for neuronal culture fail to consider the effects of excretion of the cells own ECM proteins onto the surface, which we have shown can occur on surfaces with high peptide concentrations. By utilizing self-assembled monolayers (SAMs), we have created a substrate that prevents the non-specific adsorption of proteins excreted by neurons, while introducing a low-concentration of the peptide sequences to encourage neuronal attachment.

A pair of alkane-thiol monomers for assembly on a gold substrate have been designed which contain a tetra-ethylene glycol moiety at the tail to prevent the non-specific adsorption of proteins. One of the monomers is terminated with an azide moiety that can be used to specifically attach molecules with an alkyne group by a copper-mediated azide-alkyne cycloaddition (CuAAC) reaction, also known as the "click" reaction. By introducing 5-pentynoic acid at the N-terminus of each of the peptides during synthesis, we have introduced a bioorthogonal attachment point for reaction with the azide-terminated monomers on the surface. Once prepared, these surfaces have been confirmed to be resistant to adsorption of proteins by quartz-crystal microbalance (QCM) experiments. Primary culture neurons dissected from embryonic mice have been cultured on the surface and the effects of the peptides on neurite outgrowth have been quantified. To better understand the role of these peptides in cell adhesion, neurons transfected with a plasmid encoding EGFP-vinculin or EGFP-paxillin have been cultured on the surface and the focal adhesion morphologies have been observed in live-cell imaging experiments. These results are compared to those observed for a surface where the full laminin protein has been adsorbed. Together, these experiments help to design a surface resistant to non-specific protein adsorption that allows for neuronal adhesion, sheds light on laminin-mediated attachment, and aids in developing better small-molecule mimics of receptor-mediated cellular adhesion.

5:20pm **TF+EM+SS-ThA11 Contact-Free Electrical Characterization of Molecular Layers using CREM, H. Cohen**, Weizmann Inst. of Science, Israel

While generally recognized as a powerful analytical tool, XPS is insensitive to hydrogen atoms and, in many cases, to fine variations in the environment of carbon atoms. As such, XPS characterization of organic molecular layers is rather limited, in particular under demands for high overlayer quality. On the other hand, a recent XPS-based technique for chemically resolved electrical measurements (CREM) proposes high sensitivity to even small amounts of defects or organization imperfections [1,2].

Here, CREM application to monolayers self-assembled on metallic or semiconducting substrates is overviewed, demonstrating some of the unique capabilities offered by this non-contact probe. Damage evolution under irradiation is specifically discussed; two of its extreme limits being modeled, yielding the effect of corresponding defect sites on the CREM-derived I-V curves. Potential applications to molecular electronics, approaching *atomic* resolution in the electrical data, will be discussed.

References

- I. Doron Mor et al., *Nature* **406**, 382 (2000).
- H. Cohen, *Applied Physics Letters* **85**, 1271 (2004).

Tribology Focus Topic
Room: 111 - Session TR-ThA

Advanced Tribological Materials
Moderator: S. Perry, University of Florida

2:00pm **TR-ThA1 Nanomechanics and Nanotribology of ZrB₂ Thin Films Deposited by DC Magnetron Sputtering, E. Broitman, H. Högberg, L. Hultman**, Linköping University, Sweden
The microstructure, nanomechanical and nanotribological properties of ZrB₂ thin films grown by DC magnetron sputtering have been studied as a

function of Ar pressure, substrate bias, and substrate temperature. Films, ~ 500 nm thick, were deposited onto Si (001) and Al₂O₃ (0001) substrates from a compound target using an industrial chamber CC-800/9 from CemeCon operated at a fixed target-to-substrate distance of 7 cm.

X-ray diffraction patterns show that 0001-oriented films can be obtained on both substrates at a substrate bias of -80 V without any external heating. Transmission electron microscopy of samples grown at different conditions reveal the presence of an amorphous 100-300 nm thick layer close to the substrate, followed by the nucleation of ZrB₂(0001). The same oriented structure appears for samples grown up to 150 °C, but at higher temperatures this orientation is gradually degraded. At 500 °C, cross-sectional scanning electron microscopy shows a columnar microstructure with re-nucleation during the growth. For films grown at 100 °C, little impact on the texture is observed when the substrate bias is changed from floating to -200 V.

Nanomechanical and nanotribological properties measured with a Hysitron Triboindenter™ TI 950 reveal that the films have high hardness and elastic recovery, and low friction. For films grown at low temperature, the hardness, reduced elastic modulus, and elastic recovery decrease from 25 to 19 GPa, 290 to 200 GPa, and 96 to 92%, respectively, when the amorphous interface increases from 100 to 300 nm. Nano-frictional tests were done in a load-controlled feedback mode using a force of 1 mN; a total of 40 reciprocating passes were performed for each test using a diamond 90° probe with a 1 μm tip radius. The friction tests reveal a friction coefficient μ in the range 0.10-0.13 for ZrB₂ samples grown at different conditions, in contrast of $\mu = 0.6$ for a pure Zr film.

2:20pm TR-ThA2 Structural and Tribological Properties of CrN_{MPP}/TiN_{DCMS} Multilayer Coatings, J. Paulitsch, C. Maringer, D. Holec, P.H. Mayrhofer, Montanuniversität Leoben, Austria

Deposition processes like the high power impulse magnetron sputtering (HIPIMS) indicate high metal ion ratios in the plasma, which result in increased structural and mechanical properties. The generally low deposition rate, compared to direct current magnetron sputtering (DCMS), narrows the industrial application range of this technology. The modulated pulse power (MPP) deposition technique on the other hand uses multiple complex pulsing steps to increase the metal ion ratio in the plasma without dramatically reducing the deposition rates as compared to DCMS.

Recently we showed that a multilayer architecture of CrN and TiN, deposited using the hybrid HIPIMS/DCMS deposition technique, results in coatings exhibiting friction coefficients in the range of diamond-like-carbon (DLC) coatings when tested at RT and ambient air conditions. Here we show results of MPP/DCMS deposited CrN/TiN multilayer coatings indicating comparable mechanical and tribological properties, hardness values around 25 GPa and coefficient of friction below 0.05. Furthermore, investigations on their dependence to the atmospheric conditions used during dry sliding as well as theoretical investigations of the layered structure using density function theory simulations were carried out.

2:40pm TR-ThA3 Tribological Properties of Plasma Electrolytic Oxidation (PEO) Coatings on an Aluminum A356 Alloy, J.F. Su, X. Nie, University of Windsor, Canada

To reduce the fuel consumption and pollution of passenger vehicles, the aluminium engines have been increasingly used throughout the last 30 years. Since most technical aluminium alloys provide only poor wear resistance, various technical solutions exist to generate a wear-resistant cylinder bore surface against the sliding piston ring. A Plasma Electrolytic Oxidation (PEO) process has been developed in our group to produce oxide coatings on an Al alloy A356 for Al engine block, to battle against the wear attack. Primary results showed that the PEO coatings, thinner than 8 μm, are promising candidates to resist wear at elevated temperature. In this work, further study was carried on a series of PEO coatings on the A356 alloy. The surface morphology, coating thickness and tribological properties were tailored by adjusting the PEO process parameters. The tribological performance of the PEO coatings was better than a Plasma Transferred Wire Arc (PTWA) coating which is currently used for engine applications. Based on this study, selections on optimal thickness and morphology of PEO coatings for better wear resistance were proposed.

3:40pm TR-ThA6 Tribochemical and Microstructural Evolution during Friction and Wear of Nanocomposite Coatings, T. Scharf, The University of North Texas

INVITED

Friction and wear mitigation is typically accomplished by introducing a shear accommodating layer (e.g., a thin film of liquid) between surfaces in sliding and/or rolling contacts. When the operating conditions are beyond the liquid realm, such as in extreme environments, attention turns to solid coatings. The focus of this talk is how contacting surfaces and subsurfaces change both structurally and chemically in order to accommodate interfacial shear for two multifunctional coating systems: nanocomposite

MoS₂/Sb₂O₃/Au and Ni/TiC/graphite. It was determined that the coatings exhibit velocity accommodation modes (VAM) of interfacial sliding and intrafilm shear, as determined by advanced electron microscopy (3-D focused ion beam serial cross-sectioning, HAADF-STEM, and HRTEM) and spectroscopy (Raman, Auger and EDS wear maps) techniques.

In the case of amorphous-based MoS₂/Sb₂O₃/Au nanocomposite sputtered coatings, the main mechanism responsible for low friction and wear in both dry and humid environments is governed by the interfacial sliding between the wear track and the friction-induced transfer film on the counterface ball. In dry environments, the nanocomposite has the same low friction coefficient as that of pure MoS₂ (~0.007). But unlike pure MoS₂ coatings which wear through in air (50% RH), the composite coatings showed minimal amount of wear with wear factors of ~1.2-1.4 x 10⁻⁷ mm³/Nm in both dry nitrogen and air. Cross-sectional TEM of wear surfaces revealed that frictional contact resulted in amorphous to crystalline transformation in MoS₂ with 2H-basal (0002) planes aligned parallel to the sliding direction. In air, the wear surface and subsurface regions exhibited islands of Au. The mating transfer films were also comprised of (0002)-orientated basal planes of MoS₂ resulting in predominantly self-mated 'basal-on-basal' interfacial sliding, and thus low friction and wear.

In the case of laser deposited Ni/TiC/graphite composite coatings, it was determined during sliding that a wear-induced tribochemical and structural change from microcrystalline graphite to amorphous carbon/nanocrystalline graphite hybrid layer resulted in decreased friction and wear. Other novel insights were determined from 3-D microstructural evolution during wear, such as a mechanically mixed layer developed consisting of predominantly refined nanocrystalline Ni grains (~10 nm grain size) and disordered carbon below this hybrid layer. The formation of these low interfacial shear strength films and recrystallized zones were responsible for intrafilm shear VAM to achieve low friction coefficients (~0.09) and wear factors (~6.8 x 10⁻⁷ mm³/Nm).

4:20pm TR-ThA8 Study of Failure Mechanisms of a PVD TiAlN Coating by an Impact-Sliding Tester, J.F. Su, X. Nie, University of Windsor, Canada

Physical vapor deposition (PVD) coatings usually have high hardness and wear resistance and have been considered as necessary top layers of a wide variety of mechanical components to battle the wear problems. One of applications of hard PVD coatings is used as much-needed protective top layers on surfaces of stamping dies thereby to extend the tool life and improve the quality of the stamped products. Impact fatigue tests have been carried out to investigate the failure behavior of coating-substrate systems under simulated stamping force conditions in our group. However, machining forces on the work pieces are not always only perpendicular to the surface. Tangential or parallel forces are usually involved such as in stamping, milling and turning. In this work, an impact-sliding fatigue tester was proposed as an experimental technique to investigate the failure behavior of coating-substrate systems under shear combined conditions. Each impact-sliding cycle consisted of an 200 N impact force and a 200 N pressing force, respectively. One PVD TiAlN coating on D2 substrates was tested at this combination of impact/pressing loads for 1,500 cycles. Impact-sliding wear track was then observed at cross section obtained by Electrical discharge machining (EDM). Coating failure mechanisms were found to be chipping, peeling, fatigue cracks and material transfer. Fatigue cracks were particularly discussed from the point of view of fracture toughness.

4:40pm TR-ThA9 A Study of Sliding Friction Across Velocity Regimes for Alternative MEMS-type Interfaces using Atomic Force Microscopy and Combined Nanoindentation / Quartz Microbalance, N. Ansari, Auburn University, S. Barkley, Luther College, C. Bouxsein, M. Deram, N. Eigenfeld, Saint Olaf College, O. Matthews, Luther College, A. Poda, W.R. Ashurst, Auburn University, E.E. Flater, Luther College, B.P. Borovsky, Saint Olaf College

As mechanical devices have shrunk to microscopic sizes, the need for a more fundamental understanding of friction and other surface phenomena has become urgent. While the emerging technology of microelectromechanical systems (MEMS) shows promise as the mechanical counterpart to integrated circuits, progress remains slow as structural materials and lubricant strategies continue to be developed. We report on the results of a collaborative effort to study the frictional properties of organic monolayers deposited on metal oxide surfaces. These interfacial systems have the potential to offer an alternative to silicon-based device fabrication. Both a nanoindenter-quartz crystal microbalance (NI-QCM) as well as an atomic force microscope (AFM) in lateral force mode have been used to perform tribological experiments at sliding velocities spanning the range from microns per second to meters per second. Our studies have investigated two different self-assembled monolayers chemisorbed onto aluminum oxide surfaces with realistic contact roughnesses and sizes: octadecylphosphonic acid (ODP) and octadecyltrichlorosilane (OTS). Both monolayers are observed to exhibit substantially reduced friction as

compared to the bare interface, at both low as well as high sliding speeds. However, the films appear to fail upon exceeding a threshold contact pressure. We compare the tribological responses of the bare and monolayer coated interfaces of different systems and discuss insights into the molecular-level mechanisms responsible for the observed behaviors.

5:00pm **TR-ThA10 Nanotribological Characterization of Percolating Lead Films Above and Below T_c .** *K. Stevens, J. Krim*, North Carolina State University

Friction at the nanoscale shows a strong and complex relationship to surface roughness and atomic disorder [1]. Recent research in superconductivity dependent friction [2-5], along with reports that quantum size effects [6] can influence diffusion (and thus friction) of adsorbed layers, has motivated our investigation. In particular, we have performed friction measurements of adsorbed nitrogen and helium films sliding on nanostructured lead films substrates that have been deposited on titanium, a substrate that lead does not wet. Varying the lead coverage results in a spectrum of percolated morphologies. We prepare these films on a quartz crystal microbalance (QCM) and probe their topologies by means of adsorption onto the surface [7].

Measurements have been recorded on nanoclustered lead films with coverages crossing the critical concentration for percolation. We study the substrate in the superconducting and normal states, which allows us to isolate and quantify the contribution of electronic and phononic dissipation to the total friction present [2]. Submonolayer adsorbate coverages have allowed us to probe the edge effects of surface nanoclusters, while multilayer coverages have let us explore the strength and proximity effects of surface roughness. We compare our measurements to those reported by Pierno et al. on films of ordered Pb(111) terraces, where atomic step edges are present [3], and conclude that the variation in reported values of friction on nanostructured lead is due to phononic effects at the step edges.

Funding provided by NSF DMR.

- [1] Y. Braiman et al., *Physical Review E* **59**, R4737-40 (1999).
- [2] M. Highland and J. Krim, *Physical Review Letters* **96**, 1-4 (2006).
- [3] M. Pierno et al., *Physical Review Letters* **105**, 1-4 (2010).
- [4] Q. Ding et al., *Wear* **265**, 1136-1141 (2008).
- [5] M. Kisiel et al., *Nature Materials* **10**, 119-122 (2011).
- [6] M. Özer et al., *Physical Review B* **72**, 3-6 (2005).
- [7] V. Panella and J. Krim, *Physical Review E* **49**, 4179-4184 (1994).

5:20pm **TR-ThA11 Advanced SP³EC Carbon Nanocomposite Coatings.** *J. Larson*, United Protective Technologies

United Protective Technologies (UPT) has developed a room temperature plasma assisted chemical vapor deposition (PACVD) coating process to build carbon based coatings. Versions of this coating are in use for infrared optical applications, galvanic corrosion barriers and tribological modifications to critical components. The process used to produce SP³ECTM coatings is compatible with a wide range of materials including semiconductors, metals, polymers and composites. Deposition parameters for the SP³ECTM process can be controlled to produce a wide range of carbon based thin films, ranging from 120 nm diamond crystalline grains to low friction glassy amorphous carbon films. Layered “nano-composite” structures constructed of these films have been proven to improve the life, performance and reliability of components under high wear conditions and corrosion conditions. Additionally, the SP³ECTM process is non-toxic and environmentally friendly.

Current applications for SP³ECTM coatings include targeting optics with improved durability for the AH-64 along with corrosion and wear coatings for UH-60 rotor components. Tribological coatings for improved efficiency of helical gears have been developed in conjunction with advanced wear coatings for aluminum and steel components. This presentation will include details on the mechanical and barrier characteristics of SP³ECTM coatings for various applications, current process capabilities and developmental applications of this coating process.

Biomaterial Interfaces Division

Room: East Exhibit Hall - Session BI-ThP

Biomaterial Interfaces Poster Session

BI-ThP1 Physicochemical Characterization of Loop Polymer Brushes Prepared by Immobilization of End-Functionalized Poly(dimethylsiloxane). *S. Sakurai, H. Watanabe, Jst, Erato, Japan, A. Takahara, Kyushu University, Japan*

A loop polymer brush is surface-tethered polymer chain of which both ends were anchored on the substrate surface to form a loop at a molecular level. The dynamics and physicochemical characterization of the loop brush has been a hot topic of several theoretical and experimental studies for polymer physics because the formation and interaction of loop brushes are key processes in many important biological and engineering processes. In this study, we synthesized loop polymer brushes by using end-functionalized poly(dimethylsiloxane) (PDMS) with various molecular weights as follows. A commercially available amino-terminated PDMS was fractionated by size exclusion chromatography (SEC) in the molecular weight from $M_n = 7,000$ to 100,000 with narrow molecular weight distributions ($M_w/M_n \sim 1.2$), and transformed to a triethoxysilane (TES) end-functionalized PDMS on both ends. The silicon wafer was immersed in dichloromethane solution of the telechelic TES-terminated PDMS at 293 K for 24 h to immobilize both chain ends of the PDMS. The surface morphology of the telechelic PDMS-immobilized silicon wafer was observed by atomic force microscopy (AFM) under air at room temperature. The root mean square (rms) of the surface roughness was 0.6 nm in a $2 \times 2 \mu\text{m}^2$ scanning area. The smooth morphology indicated that loop structure was formed without cross-linking and gelation of TES. Mono-functionalized PDMS was also synthesized to fabricate a linear brush on the silicon wafer. The thickness of these brushes in a dried state determined by ellipsometry increased from 2 to 5 nm with an increase in the molecular weight of $M_n = 5,000$ to 100,000. The loop and linear polymer brushes with same molecular weight showed the almost same thickness in a dried state. Apparent difference derived from a topology effect was not observed in a dried state. AFM measurement of the swollen thickness of the loop and linear brushes in a solution is in progress.

BI-ThP2 Surface Modification of Polylactic Acid (PLA) Fibers for Use as Tissue Engineering Scaffolds. *N.M. Tambe, M.W. King, A. El Shafei, North Carolina State University*

Organ failure is one of the major problems faced by patients around the world. In the USA, there are currently millions of people waiting for organ transplantation with the annual healthcare costs for the treatment of these patients exceeding \$500 billion. The goal of this study is to develop an innovative, resorbable porous tissue engineering (TE) scaffold with controlled biodegradability, good cytocompatibility, suitable surface chemistry for cell growth and optimum mechanical properties. Most scaffold materials do not possess any bioactivity and do not have the ability to promote extracellular matrix (ECM) secretion and support cell growth. So, the surface chemistry is very important as the outermost functional group is responsible for binding cells to the material.

In order to achieve these goals, there are a series of specific objectives:

- 1) To identify and compare various polymer surface modification techniques
- 2) To determine and study the process and material variables for those techniques
- 3) To characterize these techniques for changes in surface chemistry
- 4) To attach bioactive coatings onto the surface successfully.

Polylactic acid (PLA) was chosen as the scaffold material due to the fact that it has most of the desired TE scaffold properties. A PLA nonwoven web from Ahlstrom Nonwovens was used as the material. Surface modification was performed by thermally initiated free radical polymerization using vinyl monomers such as maleic acid and maleic anhydride. Potassium persulfate was used as the initiator and Mohr's salt was added to reduce the extent of homopolymerization. The grafted surfaces were coated with a bioactive coating of collagen using a spacer molecule called genipin. The grafted surfaces were then evaluated via Fourier transform infrared spectroscopy (FTIR), contact angle measurements, X-ray photoelectron spectroscopy (XPS), and dyeing with a basic dyestuff and using visible spectrophotometry.

The FTIR spectra show the grafting of carboxylic acid groups of maleic acid onto the surface of the PLA. The effect of monomer concentration is seen in the contact angle measurements. With increase in the monomer concentration, the contact angle fell, indicating an increase in the hydrophilicity of the material. The collagen was also successfully coated onto the grafted surface which is confirmed by the FTIR spectra showing the characteristic amide bands. Further evaluation of the surfaces is continuing with dyeing, XPS, and measuring the biological performance. In addition, other surface modification methods like plasma, atom-transfer radical polymerization (ATRP), are being undertaken.

BI-ThP3 Application of Layer-By-Layer Coatings to Tissue Scaffolds – A Novel Approach for Developing a Pro-Angiogenic Biomaterial. *C.D. Easton, CSIRO Materials Science and Engineering, Australia, S.L. McArthur, Swinburne University of Technology, Australia, A.J. Bullock, S. MacNeil, University of Sheffield, UK*

Development of flexible coating strategies for angiogenesis promotion is critical for the health care industry to effectively treat chronic non-healing wounds. This need will continue to intensify in light of the increasing number of patients diagnosed with diabetes and an ageing population. In addition, such strategies are required within the tissue engineering community to overcome issues associated with engineered materials failing to engraft as a result of delays in neovascularisation.

An important requirement for a pro-angiogenic biomaterial is the ability to maintain a regulated release of bioactive growth factors to the wound site through the use of heparin. A number of strategies for the use of natural and synthetic heparin-mimetics have been developed, however in general they fail as the heparin can be rapidly lost from the wound site. Therefore new strategies to effectively immobilise heparin for the release of bioactive growth factors are being developed.

This work describes a layer-by-layer (LBL) approach that provides a platform for immobilising a significant amount of heparin to the substrate of choice. The LBL coating prevents desorption of immobilised heparin as a result of 'covalent bond-like' interactions from the electrostatic attraction between the multiple layers of polyelectrolytes. Employing plasma polymerisation, a thin functional coating was applied to the substrate to provide the necessary surface charge in order to build the LBL architecture. In this particular case, plasma polymerised acrylic acid (ppAAc) was deposited onto Si wafer and two different tissue scaffolds, a commercially available polypropylene type, and an electrospun PLGA (75:25) type previously reported in the literature. The LBL structure was then created by physically absorbing alternative layers of polyethyleneimine (PEI) and poly(acrylic acid) (pAAc), and once the desired number of layers was achieved, heparin was immobilised to the structures. The kinetics of the fabrication procedure was examined using a quartz crystal microbalance with dissipation (QCM-D) system, while the resulting structures were probed using X-ray Photoelectron Spectroscopy (XPS) and Atomic Force Microscopy (AFM). The effect of pH of the LBL solutions (PEI and pAAc) on the resulting structure and ability to immobilise and retain heparin were examined. This technique allowed for the immobilisation of a significant amount of heparin to the test substrates explored, more so than that previously reported using similar approaches. This approach therefore provides an inexpensive and easily expandable coating methodology for applying a pro-angiogenic interface to tissue engineered materials

BI-ThP4 In Situ Surface Initiated Enzymatic DNA Polymerization: Potential for Multiplexed Molecular Detection. *L. Tang, V. Tjong, A. Chilkoti, S. Zauscher, Duke University*

We present a new technique called surface initiated enzymatic polymerization (SIEP), which uses terminal deoxynucleotidyl transferase (TdT), a template-independent DNA polymerase that catalyzes the sequential addition of deoxynucleotides (dNTPs) at the 3'-OH group of an oligonucleotide primer. We utilized TdT's ability to polymerize a long DNA chain while incorporating non-natural chemically reactive dNTPs to create new functional materials and to generate signal amplification. Previously, we have shown that fluorescent-dNTP can be directly polymerized by TdT. In this work, we will show the incorporation of amine- and aldehyde-modified dNTPs to impart reactive moieties into the polymerized DNA chain. We quantified the number of reactive dNTPs and their effect on the polymerization efficiency. We then further investigated the reactivity of the functional group for subsequent reactions, which include fluorescent dye conjugation for signal amplification, selective DNA metallization, and oligonucleotide conjugation to create a branched structure. We found that multiple reactive groups can be incorporated and they are active for subsequent reactions. For characterization of SIEP, we utilized a quartz crystal microbalance with dissipation monitoring (QCM-D) to monitor increase in surface mass during DNA polymerization in real-

time. The mass increase versus concentrations of dNTP allows us to determine the reaction constant, which reflects the growth kinetics of DNA polymerization on the surface. In addition, we examined the effect of grafting density on the polymerization reaction and the conformation of DNA brushes.

BI-ThP5 Plasma-based Approaches for Biointerface Preparation, E.H. Lock, S.H. North, S.G. Walton, C.R. Taitt, Naval Research Laboratory (NRL)

The ability to predict and manipulate biomolecule behavior at the biointerface determines the success of biomaterials in applications ranging from biosensing to medical devices and therapeutic products. However, precise biointerface engineering will remain elusive until the roles of physical and chemical properties of surfaces on abiotic and biotic interfacial interactions are well understood. We have shown that plasma treatment of polymers generates chemically reactive surfaces for successful silanization and biomolecule immobilization [1, 2]. The focus of this work is to investigate the influences of surface chemistry and surface morphology on biomolecule attachment. We fine-tune our plasma system to favor the production of specific functional groups that promote subsequent biomolecule attachment. The effects of surface morphology on biomolecule immobilization are also assessed. Plasma diagnostics and modeling allows us to elucidate the effects of plasma parameters (plasma density, electron temperature and the resulting kinetic ion energy) on the polymer surface modifications. The work was supported by the Office of Naval Research.

References:

- 1) E. H. Lock, J. Wojciechowski, S. H. North, S. G. Walton, C. R. Taitt, "Exploring the mechanism of biomolecule immobilization on plasma treated polymer substrate", to be published NATO Science for Peace and Security Series by Springer.
- 2) S. H. North, E. H. Lock, C. J. Cooper, J. B. Franek, C. R. Taitt, S. G. Walton, "Plasma-based surface modification of polystyrene microtitre plates for covalent immobilization of biomolecules", *ACS Appl. Mater. & Interfaces* 2, 2884-91 (2010).

BI-ThP6 A Novel ALD Al₂O₃-Parylene Bi-Layer Encapsulation for Biomedical Implantable Devices, X. Xie, L.W. Rieth, F. Solzbacher, University of Utah

Atomic layer deposited (ALD) Al₂O₃ has been widely used as encapsulation material for organic LEDs and solar cells due to its low water vapor transmission rate (WVTR) (~5×10⁻⁶ g-H₂O/m²-day). However, its coating performance for implantable devices still needs investigation. Parylene has been commonly applied as encapsulation for implantable devices, such as Utah Electrode Arrays (UEAs). The idea of combining Al₂O₃ and parylene is based on the concept that Al₂O₃ works as moisture barrier and parylene as ion barrier. In this paper, Al₂O₃ was deposited by both thermal and plasma-enhanced ALD on interdigitated electrodes (IDEs) for comparison. AFM micrographs (Fig. 1) show that Al₂O₃ films deposited on silica substrate (RMS surface roughness of 0.17 nm) by thermal and plasma-enhanced ALD have RMS surface roughness of 0.51 nm and 0.48 nm, respectively. XPS shows that ALD films had an oxygen to aluminum ratio of 1.2 while thermal ALD Al₂O₃ is 1.09, indicating that the former is closer to Al₂O₃. A 6-μm thick parylene-C layer was deposited by CVD using Gorman process on top of Al₂O₃ and saline A-174 (Momentive Performance Materials) was used as adhesion promoter. The samples were soaked in 1× PBS at 37 °C and 57 °C for accelerated lifetime test. Electrochemical impedance spectroscopy (EIS) and chronoamperometry were used to evaluate the performance of the encapsulation. Preliminary data shows that the leakage current (Fig. 2) remained very small (~ 7 pA) and the electrochemical impedance (Fig. 3) was consistently high (~ 3 MΩ at 1 kHz) after 5 days of soaking test at 57 °C (equivalent to at least 20 days of soaking test at 37 °C). Comparing with parylene and Al₂O₃ control samples, the Al₂O₃-parylene coated sample showed lower leakage current (Fig. 2). The impedance for three different types of samples was almost the same. However, the phase of parylene-C coated sample slightly declined after 5 days of soaking test (Fig. 3), suggesting that sample coated with Al₂O₃ had lower WVTR. No obvious difference has been observed yet for samples soaked at different temperatures since the soaking period is relatively short. Parylene came off after one day of soaking test for one sample, which might be caused by the poor adhesion between Al₂O₃ and parylene. In conclusion, preliminary results shows that the Al₂O₃-parylene bi-layer encapsulation scheme is promising encapsulation in terms of leakage current and electrochemical impedance. Long-term soaking tests are being performed to further investigate the functionality of this novel encapsulation scheme.

BI-ThP7 Complementary Electronic and Vibrational Circular Dichroism Analysis of Bovine Serum Albumin Adsorbed on Hydroxyapatite Microspheres, K.P. Fears, Naval Research Laboratory, D.E. Day, Missouri University of Science and Technology, D.Y. Petrovykh, International Iberian Nanotechnology Laboratory, T.D. Clark, Naval Research Laboratory

Bovine serum albumin (BSA) is a widely studied globular protein that contains ca. 68% of alpha-helices and <2% of beta-sheets in its native conformation. The well characterized secondary structure of BSA is commonly used as a benchmark for electronic (ECD) and vibrational (VCD) studies of proteins in solution. Both ECD and VCD indicated a substantial loss of helical structure accompanied by an increase of beta-sheet character in BSA thermally denatured in solution. In surface adsorption experiments, hydroxyapatite microspheres were incubated in solutions with low (1.0 mg/mL) or high (50.0 mg/mL) concentrations of BSA for one hour, then triple rinsed and re-suspended in buffer for analysis. The ECD spectra were similar for BSA adsorbed from low and high concentration solutions, both showing a sizeable increase in beta-sheet character upon adsorption, while being dominated by alpha-helical features. The VCD spectra also exhibited stronger peaks in the beta-sheet region upon adsorption of BSA on hydroxyapatite. VCD signal enhancement, however, was observed upon adsorption from the high concentration BSA solution, indicating the formation of macroscopic chiral structures. The analysis of proteins adsorbed on surfaces thus can be enhanced by taking advantage of the complementary sensitivities of ECD and VCD spectroscopies to the secondary structures of biomolecules.

BI-ThP9 Binding Affinities of wt and H93R PTEN to Lipid Membranes Containing PS and PI(4,5)P₂, S. Shenoy, Carnegie Mellon University, A. Gericke, Kent State University, A.H. Ross, University of Massachusetts Medical School, M. Lösche, Carnegie Mellon University and National Institute of Standards and Technology

PTEN is a phosphatidylinositolphosphate (PIP) phosphatase frequently mutated in human cancer [1]. By lowering PI(3,4,5)P₃ levels in the plasma membrane, it functions as an antagonist to PI3-kinase in the regulatory circuit that controls cell proliferation and survival. wt PTEN has only weak affinity to zwitterionic phosphatidylcholine (PC) membranes but a strong interaction with anionic lipids. Its C2 domain was shown to bind in a Ca²⁺ independent manner to phosphatidylserine (PS) and phosphatidylglycerol (PG), whereas a short N-terminal domain binds specifically to PI(4,5)P₂ [2,3]. H93R PTEN is an autism related mutant which has decreased phosphatase activity [4].

Using Surface Plasmon Resonance (SPR), we characterized the affinity of wt and H93R PTEN to tethered bilayer lipid membranes (tBLMs) that contain PC and PS, PC and PI(4,5)P₂, and PC, PS and PI(4,5)P₂. As compared with wt PTEN, we find that the H93R mutation is sufficient to cause significant increases in the protein's association with lipid membranes containing PS. PI(4,5)P₂ enhances the apparent binding constant for both proteins and leads to intriguing binding kinetics of the protein to the membrane. The binding of either protein to membranes containing both PS and PI(4,5)P₂ shows a biphasic behavior, suggesting two independent binding sites. This supports the hypothesis of non-competitive binding of the protein to PS and PI(4,5)P₂ [5]. We also performed neutron reflectivity experiments to determine the structure and orientation of PTEN bound to the membrane.

1. R. J. Shaw, L. C. Cantley, *Nature* **441** (2006), 424-430.
2. J. O. Lee, *et al.*, *Cell* **99** (1999), 323-334.
3. S. Das, J. E. Dixon, W. Cho, *Proc. Natl. Acad. Sci. USA* **100** (2003), 7491-7496.
4. R. E. Redfern, *et al.*, *Protein Sci.* **19** (2010), 1948-1956.
5. R. E. Redfern, *et al.*, *Biochemistry* **47** (2008), 2162-2171.

BI-ThP10 Membrane Binding and Structure for Cytoplasmic Domain of Zeta Subunit of T Cell Receptor, P. Shekhar, Carnegie Mellon University, F. Heinrich, Carnegie Mellon University and National Institute of Standards and Technology, K. Zimmerman, University of Massachusetts Medical School, M. Lösche, Carnegie Mellon University and National Institute of Standards and Technology, L.J. Stern, University of Massachusetts Medical School

The cytoplasmic domain of the T-cell receptor zeta subunit, ζ_{cyt}, a cell surface protein complex responsible for binding peptide fragments of foreign antigens bound to major histocompatibility complex (MHC) proteins, is sufficient to couple receptor ligation to intracellular signaling cascades [1]. These domains carry immunoreceptor tyrosine-based activation motifs (ITAMs), *i.e.* signaling motifs that are phosphorylated by tyrosine kinases following receptor crosslinking. The phosphorylation of ITAMs is a first and obligatory step in signal transduction. ζ_{cyt} has been shown to be unstructured in aqueous solution and to assume a helical

conformation in the presence of anionic lipid vesicles [2,3]. Membrane binding and membrane-induced conformational changes likely plays an important role in signal transduction, but no direct structural information on these functionally important lipid-bound states was available so far. Using a synthetic membrane model, *i.e.*, fluid lipid bilayers tethered to planar solid supports [4,5], we report surface plasmon resonance (SPR) results on the binding kinetics and neutron reflectivity investigations of the association of the disordered ζ_{eyt} with membranes. We determine the extent to which the protein penetrates into the bilayer and discuss structural details of the ζ_{eyt} -lipid interaction.

1. M. E. Call, K. W. Wucherpfennig, *Annu. Rev. Immunol.* **23** (2005), 101-125.
2. A. Sigalov, *Semin. Immunol.* **17** (2005), 51-64.
3. D. Aivazian, L. J. Stern, *Nat. Struc. Biol.* **7** (2000), 1023-1026.
4. D. J. McGillivray, *et al.*, *Biointerphases* **2** (2007), 21-33.
- F. Heinrich, *et al.*, *Langmuir* **25** (2009), 4219-4229.

BI-ThP11 Microfluidic Bacterial Adhesion Assay to Characterize the Easy to Clean Properties of Surfaces, M.P. Arpa Sancet, C. Christophis, S. Bauer, A. Rosenhahn, M. Grunze, Universität Heidelberg, Germany

Biofouling, the undesired growth of marine organisms on submerged surfaces, is a global problem with both economic and environmental consequences. The attachment of bacteria to surfaces is an important step in the biofouling process, and the development of ways to attenuate microbial attachment or to achieve their easy removal is desirable. We built a microfluidic system and applied it to determine the adhesion strength of bacterial biofilms. Marine bacteria, *e.g. Cobetia marina* are cultivated in this microfluidic device on the surfaces of interest. The bacterial detachment is caused by a hydrodynamic shear flow which is continuously increased and the removal is recorded via video microscopy. The adhesion strength is determined as the shear stress needed to detach 50% of the bacteria. The parameters incubation time, medium and increase of shear stress were varied in order to find the optimal conditions to carry out the biological assays. The applicability of the technique is demonstrated using self assembled monolayers with a different ability to bind water. Well hydrated surfaces lead to decreased adhesion strength while bacteria stick stronger to less hydrated surfaces. Based on these findings, a range of polysaccharide hydrogels were tested towards their potential to reduce adhesion strength.

Spectroscopic Ellipsometry Focus Topic Room: East Exhibit Hall - Session EL-ThP

Spectroscopic Ellipsometry Poster Session

EL-ThP1 Microstructure and Dispersive Optical Parameters of Tungsten, Titanium and Tungsten-Titanium Films, V.V. Atuchin, T.I. Grigorieva, A.S. Kozhukhov, V.N. Kruchinin, L.D. Pokrovsky, Institute of Semiconductor Physics, Russian Federation, R.S. Vemuri, Pacific Northwest National Laboratory, C.V. Ramana, University of Texas at El Paso

Tungsten (W) and titanium (Ti) films are widely used in electrochemistry, microelectronics, energy conversion and nanotechnology. In integrated optics, the nanometric Ti films are used as a source for doping LiNbO₃ and LiTaO₃ substrate and optical waveguide fabrication by thermal diffusion. Because effective refractive indices of the waveguide modes are strongly dependent on the optical profiles in doped layer, precise control of Ti film thickness (*h*) is needed in the range *h*~10-50 nm. Ellipsometry can be successfully applied for nondestructive determination of the thickness of a dielectric and semi-transparent metal film when optical constants of the material are known. Regrettably, noticeable scattering was found for optical constants reported earlier in literature for W and Ti films and crystals. As it seems, this scattering appeared due to different film quality and surface state. The focus of the present work is centered on W, Ti and W-Ti film fabrication and evaluation of their optical parameters with spectroscopic ellipsometry. Tungsten and tungsten-titanium films were prepared by magnetron sputtering deposition in vacuum below 10⁻⁵ Torr. Titanium films were fabricated by thermal evaporation method in vacuum below 10⁻⁵ Torr. The substrate temperature was *T*=100 °C. For precise determination of optical parameters, thick metal films (*h*~100 nm by as determined from optical interferometry) were prepared on silica substrate. To increase the metal adhesion, the substrate was subjected to RCA chemical cleaning just before insertion into vacuum chamber. Structural parameters of metal films were studied with reflection high-energy electron diffraction (RHEED). Surface micromorphology was controlled with atomic force microscopy (AFM). Spectral dependencies of refractive index *n*(λ) and extinction coefficient *k*(λ) were determined with the help of spectroscopic ellipsometry

in the spectral range, λ ~250-1030 nm. A relation between optical constants of pure metal W and Ti and mixed metal W-Ti films is discussed.

EL-ThP2 Temperature Dependences of the Dielectric Response of InSb Measured by Spectroscopic Ellipsometry, J.J. Yoon, T.J. Kim, S.Y. Hwang, M.S. Diware, Y.D. Kim, Kyung Hee University, Republic of Korea, Y.C. Chang, Academia Sinica, Taiwan, Republic of China

InSb is a promising material for optical devices, particularly for high-frequency and nonlinear-optical applications. InSb has a high electron mobility and offer excellent design flexibility as a result of its large conduction-band offset in multilayer structures. Consequently, InSb offers significant potential for devices such as quantum-well lasers, laser diodes, and heterojunction bipolar transistors. A knowledge of the dielectric function at various temperatures is required for optimizing the properties for specific device applications. In-situ control of growth is also becoming an important technique. Therefore, the dielectric function at growth temperatures is also needed. On the other hand, critical point (CP) energies can be better identified from low-temperature data, where the decreased electron-phonon interaction allows separation of CP structures that are nearly degenerate at room temperature.

Although the optical properties of InSb have been well studied, there are only a few reports of their temperature dependence in the 1.2 to 5.6 eV spectral ranges [1]. Here, we report results of an investigation of the temperature dependence of the dielectric response of InSb from 22 K to 700 K and from 0.74 to 6.57 eV.

Spectroscopic ellipsometric (SE) data were obtained on a bulk semi-insulating InSb (100) substrate. The cryostat consisted of a stainless-steel chamber with high-quality stress-free fused-quartz windows. To avoid condensation at low temperatures, the sample was maintained in ultrahigh vacuum during measurement. SE data were obtained at an angle of incidence of 70.41° using a conventional rotating-compensator system with a diode-array detector. The influence of the oxide overlayer was removed mathematically by a multilayer calculation. In the *E*₂ energy region only four structures are clearly resolved at 300 K. However, at 22 K the *E*₂' and *E*₂ structures are seen to consist of five CPs. We identified the origin of these structures with band-structure calculations using the LASTO method. Separation of the *E*₀', *E*₀' + Δ_0 ', *E*₂, *E*₂ + Δ_2 , *E*₂', *E*₁' and *E*₁' + Δ_1 ' CPs was clearly found in the region of the *E*₂ peak. Two saddle-point transitions, Δ_5^{cu} - Δ_5^{vu} and Δ_5^{cl} - Δ_5^{vu} , are clearly seen. We also determined the temperature dependences of the newly observed transitions near 5.9 eV. These results will be useful in a number of contexts, including the design of optoelectronic devices based on InSb, as data for improved band structure calculations, and for in-situ monitoring.

[1] S. Logothetidis, L. Vina and M. Cardona, *Phys. Rev. B* **31**, 947 (1985).

EL-ThP3 Tailored Helical Nanostructures Investigated with Mueller Matrix Ellipsometry, R. Magnusson, J. Birch, C.-L. Hsiao, P. Sandström, H. Arwin, K. Järrendahl, Linköping University, Sweden

Metamaterials showing chiral features in the optical spectral range have been fabricated with the aim to obtain polarized reflection with high ellipticity.

A series of tailored anisotropic and transparent structures of helical Al_{1-x}In_xN nanorods were grown using UHV magnetron sputtering on sapphire substrates. Due to an internal in-plane composition gradient across the crystalline structure, the nanorods will tilt relative to the substrate normal. By rotating the substrate step-by-step around its normal during deposition 'staircase' helical structures are obtained. The layer thickness for each step is controlled to tailor the nanorods. Samples with different pitch and layer thickness and with right-handed as well as left-handed chirality were grown.

Ellipsometric measurements were performed using a dual rotating compensator ellipsometer providing the full Mueller matrix in the spectral range 245-1700 nm at multiple angles of incidence and 0-360° sample orientation. The relation between the optical characteristics of the samples, specifically the ellipticity, and structural parameters such as number of layers, layer thickness and nanorod pitch of the samples, was studied. For certain wavelengths, near circular polarization is observed both for right- as well as left-handed helical structures.

Based on the Mueller matrix data, descriptions of the polarization states and degree of polarization in reflection for different incoming states of polarization will be presented.

EL-ThP4 Study of the Thin Film Growth of Volatile Condensable Material via In Situ Ellipsometry and Quartz Crystal Microbalance Measurements, J. Pu, F. Zhou, N.J. Ianno, The University of Nebraska

DC-93-500, SCV-2590 and SCV-2590-2 silicone/siloxane based copolymer serve as adhesive components in communications satellites and other spacecraft under adverse low-earth and geo-synchronous orbits. The outgassing and deposition of Volatile Condensable Materials (VCM's) from these adhesives onto optically-sensitive surfaces of satellites is of significant interest to spacecraft-contamination engineers. In our work, samples of these materials are heated to 100 C in a liquid nitrogen (LN2) cooled cryo-shroud lined high vacuum chamber. One MK-18 quartz crystal microbalance (QCM) sensor is placed above the effusion cell which is mounted on the bottom of the chamber. At various QCM temperatures from 120K to 180K, we observed the formation of a thin film of volatile contaminant material on the gold coated QCM crystal. Spectroscopic ellipsometric data is simultaneously acquired from the depositing film. Generally, quartz crystal microbalance measures an areal mass density which is related to the density and the geometric thickness of the film, while in-situ spectroscopic ellipsometric can determine either thickness or refractive index for very thin film. Therefore, a reasonable assumption for the density of the film must be made in order to determine the thickness. By using these two techniques in combination, we can find the actual mass condensed at different temperatures. Our findings for the optical constants of materials condensed from different bulk compounds as a function of temperature will be presented.

EL-ThP5 Combined Electrochemical Impedance Spectroscopy and In Situ Spectroscopic Ellipsometry of Anodically Grown SiO₂, E.A. Montgomery, University of Nebraska - Lincoln, T.E. Tiwald, J.A. Woollam Co., Inc., E. Schubert, M. Schubert, University of Nebraska - Lincoln, C. Beasley, Gamry Instruments, C. Briley, University of Nebraska - Lincoln

Electrochemical oxidation of silicon (n-type) at room temperature in a mixture of ethylene glycol, water and potassium nitrate has been performed by applying constant current densities to prepare thin SiO₂ layers. In-situ Electrochemical Impedance Spectroscopy (EIS) and Spectroscopic Ellipsometry (SE) are employed during the SiO₂ film growth. Using EIS and SE techniques in-situ one is able to monitor the capacitive changes and also the film thickness change of the oxide. The thickness of the oxides is also measured ex-situ before and after growth using SE. Equivalent circuit models corresponding to the electrolyte-oxide-silicon interfaces and optical models are fit to EIS and SE data respectively, to gain insight into the quality of the anodically grown SiO₂.

EL-ThP7 In Situ Spectroscopic Ellipsometry of Nanoscale Germanium Films Deposited via High Power Impulse Magnetron Sputtering, N. Murphy, Air Force Research Laboratory, L. Sun, Air Force Research Laboratory and General Dynamics Information Technology, A. Waite, Air Force Research Laboratory and Universal Technology Corporation, J. Jones, R. Jakubiak, Air Force Research Laboratory

Germanium films were deposited on both glass and silicon substrates using high power impulse magnetron sputtering (HiPIMS). Throughout the deposition process, the optical constants and thicknesses were measured and recorded via *in-situ* spectroscopic ellipsometry. Preliminary analysis of the films' optical behavior has indicated that the refractive index is highly sensitive to changes in thickness. As film thickness increases from 100 to 500 Å, the refractive index displays the tendency to slowly decrease due to void porosity, lack of crystalline order and surface roughness. The preservation of the refractive index seen in the HiPIMS deposited Ge films is a direct result of their high density and low void fraction, following the relationship between density and refractive index as given by the Gladstone-Dale approximation.

**Electronic Materials and Processing Division
Room: East Exhibit Hall - Session EM-ThP**

Electronic Materials and Processing Poster Session

EM-ThP1 Novel Quantized Edge States on Ag(111), A.R. DiLullo, Ohio University, D. Acharya, Pacific Northwest National Laboratory, N. Takeuchi, Universidad Nacional Autonoma de Mexico, S. Ulloa, S.-W. Hla, Ohio University

A one-dimensional electronic edge state has previously been observed using ultra-high-vacuum low-temperature scanning tunneling microscopy (UHV-LT-STM) methods at a sample tunneling bias of approximately 4V on Cu(111) and explained in terms of an image state at the step with energy modified by a dipolar potential[1]. Presented here are new measurements using sample bias dependent UHV-LT-STM imaging techniques of step

edges on a Ag(111) surface which show numerous higher order states with correlated energy spacing. Measurements are additionally made at tip induced vacancy locations (holes in the surface) to examine effects of confinement on the newly observed one dimensional states. Experimental results are supported by density functional theory (DFT) calculations, and a framework for explanation of the newly observed energy correlated one dimensional and confined states is explored.

Supporting funding is supplied in part by the grants DOE DE-FG02-02ER46012 and NSF OSIE 0730257.

[1] L. Bartels, S. Hla, A. Kühnle, G. Meyer, K.-H. Rieder, and J. Manson, *Physical Review B* **67**, 1-5 (2003).

EM-ThP2 Fabrication of Multilayered Bi₂Te₃/Sb₂Te₃ and Bi₂Te₃/Bi₂Te_{3-x}Se_x Thin Film Cooling Devices, M. Hines, J. Lenhardt, Alabama A&M University, M. Lu, Brookhaven National Laboratory, Z. Xiao, Alabama A&M University

In this paper, we report to fabricate multilayered Bi₂Te₃/Sb₂Te₃ and Bi₂Te₃/Bi₂Te_{3-x}Se_x thin film cooling devices using the microfabrication techniques. The multilayered Bi₂Te₃/Sb₂Te₃ and Bi₂Te₃/Bi₂Te_{3-x}Se_x thin films will be grown using the e-beam evaporation. The in-plane and cross-plane micro cooling devices will be fabricated using the standard integrated circuit (IC) fabrication process; pn junction diodes will be fabricated as thermometers for the measurement of temperature in the devices. The electrical and thermal properties of the e-beam-grown Bi₂Te₃/Sb₂Te₃ and Bi₂Te₃/Bi₂Te_{3-x}Se_x thin films and the cooling efficiency of the fabricated cooling devices will be measured, and the measurement results will be reported in the conference. The developed devices could be a good candidate for the application of high-efficiency solid-state micro-cooling.

EM-ThP3 Solution-Based High Performance and Fully Patterned Chalcogenide Thin Film Transistors, J.I. Mejia, A. Salas-Villasenor, A. Carrillo-Castillo, B.E. Gnade, M.A. Quevedo-Lopez, University of Texas at Dallas

In recent years, the development of novel processes for inexpensive and flexible electronics has become an increasing research area where low-cost and low temperature deposition techniques are key point to fabricate large area and flexible circuits. Here, we demonstrate fully photolithography defined thin film transistors using cadmium sulfide (CdS) and lead sulfide (PbS) as n-type and p-type semiconductors, respectively. These chalcogenides materials are deposited using chemical bath deposition (CBD) which is a low cost solution-based process that requires temperatures below 70° C. Extracted mobility for CdS was 25 cm²/V-s and 0.14 cm²/V-s for PbS. These mobilities are among the highest reported for a fully patterned TFT made with either CdS or PbS as semiconductor. The maximum temperature used in the complete fabrication process was kept below 100° C. In addition, we studied how the device performance (mobility, threshold voltage and contact resistance) is affected depending on the semiconductor thickness, thermal annealing and the metal used as drain-source electrodes. Our fabrication approach can be integrated in complex designs such as CMOS logic gates, pixel arrays, etc., complying with all the requirements for a flexible electronics technology.

EM-ThP4 Novel Materials and Device Structures for Solid-State Charged Particle Detectors, J.W. Murphy, J.I. Mejia, B.E. Gnade, M.A. Quevedo-Lopez, University of Texas at Dallas

Detectors for charged particle spectroscopy are typically fabricated from crystalline silicon, germanium, or gallium arsenide, which are high-cost materials. However, if the purpose of the device is particle detection rather than spectroscopy, then it is possible to use less expensive materials and deposition techniques to fabricate electrically-sensing, solid-state particle detectors. Particularly, we are interested in detecting alpha particles emitted from a 210-Polonium source. In this work we investigate ZnO nanostructures in combination with poly(3-hexylthiophene) (P3HT) to form hybrid inorganic/organic p-n diodes which are as charged particle sensors. The ZnO nanostructures are grown from solution on a Cr electrode, and the P3HT is subsequently deposited via the drop-casting technique to achieve bi-layer film thicknesses on the order of microns. We evaluate the devices' performance in terms of leakage current, capacitance, and alpha particle detection efficiency as a function of thickness, DC bias, and annealing treatment. The structures are investigated using x-ray diffraction and cross-sectional electron microscopy. We also study the materials degradation upon exposure to radiation by monitoring the leakage current.

EM-ThP5 Structural and Electrical Characteristics of TaN Film Deposited by DC Sputtering for MOS Capacitor and Schottky Diode Upper Electrodes, L.P.B. Lima, J.A. Diniz, State University of Campinas, Brazil, C. Radtke, Federal University of Rio Grande do Sul, Brazil, I. Doi, J. Miyoshi, A.R. Silva, J. Godoy Fo, State University of Campinas, Brazil

Tantalum nitride (TaN) films have been obtained by DC sputtering deposition in a nitrogen/argon ambient on Si substrates. TaN film have been used as gate electrodes in MOS capacitors and in Schottky diodes on Si substrates. 20nm and 100nm thick TaN layers were deposited by DC sputtering in N₂:Ar (20:60 sccm) ambient, with a sputtering power of 1000 W. These films presented electrical resistivity of 327 Ω.cm and polycrystalline structure. XPS analysis evidence TaN and Ta₂O₅ formation in both 20 nm (Fig. 1) and 100 nm (Fig. 2) thick films. Ta₂O₅ formation could be related with the exposure the metal electrode to air. To get MOS capacitors with TaN/SiO₂/Si/Al and Al/TaN/SiO₂/Si/Al structures, the Si substrates were used and were cleaned with a standard RCA method. After, dry thermal oxidation at 1000°C for 2 min was carried out and a 8 nm thick SiO₂ layer on Si was obtained. 20 nm and 100nm thick TaN layer was deposited on SiO₂/Si by DC sputtering. Finally, in some devices a 200nm thick aluminium (Al) layer was deposited on TaN layer by DC sputtering, in order to reduce these contamination of the metal electrode. MOS capacitor pattern was defined by a mask composed of an array of 200 μm diameter dots. These devices were sintered in conventional furnace in forming gas at 450 °C for 30 minutes and were electrical characterized by capacitance-voltage (C-V) measurements. Figure 3 and 4 presents MOS capacitor C-V characteristics. TaN work function values and flat-band voltage were extracted from all C-V measurements using CVC software and 1/C² method. The extracted TaN work function values and flat-band voltage were between 4.3 and 4.4 eV (Fig. 3-4), 0.1 and 0.2 V (Fig. 3-4), respectively. The variations on work function values are related with the dipole variations due the interface between metal and dielectric. To investigate the TaN work function, Schottky diodes were fabricated in the same substrate of MOS capacitors. TaN layer were deposited by DC sputtering in a N₂:Ar (20:60 sccm) ambient, with a sputtering power of 1000 W. TaN/Si/Al and Al/TaN/Si/Al diodes were formed with TaN (20nm and 100nm) gate electrodes and Al layer (200nm) were deposited by DC sputtering process. These diodes were sintered in conventional furnace in forming gas at 450 °C for 30 minutes. The electrodes were patterned with a mask composed of an array of 200 μm diameter dots. These diodes were electrical characterized by current-voltage (I-V) measurements, and the ideality factor between 1.1 and 1.5, and work function values between 4.4 and 4.5 eV were extracted, which is near the work function values for mid-gap electrode application.

EM-ThP6 TiAlO and TiAlON Obtained by e-Beam Evaporation with Additional Electron Cyclotron Resonance (ECR) Plasma Oxidation and Oxynitridation on Si for MOS Gate Dielectric, J. Miyoshi, A.R. Silva, F.A. Cavarsan, J.A. Diniz, L.P.B. Lima, State University of Campinas, Brazil

Titanium-Aluminum Oxide (TiAlO) and Titanium-Aluminum Oxynitride (TiAlON) high *k* films have received considerable attention due to their electrical and physical properties, which are from the composition of Titanium Oxide and Aluminum Oxide properties, such as higher permittivity (*k*~80) and higher band gap (E_g~8.8 eV), respectively, than others high *k* (such as HfO₂ and ZrO₂) films [1,2]. Furthermore, this composition can reduce the undesirable effects on sub-32 nm MOS devices, which are high leakage current, due to the value of band offset of 2.8 eV to Al₂O₃, and EOT higher than 2 nm, due to relatively low *k* between 8 and 10, respectively. In this work, Titanium-Aluminum Oxide (TiAlO) and Titanium-Aluminum Oxynitride (TiAlON) were obtained on Si wafers as follow: 0.75 nm Titanium (Ti) and 0.25 nm Aluminum (Al) were sequentially deposited by vacuum e-beam evaporation, without any substrate heating. The evaporation pressure was 3x10⁻⁸ Torr, and the Ti and Al evaporation rates were of 0.1 nm/min, resulting in Al/Ti/Si structures. ECR (electron cyclotron resonance) plasma oxidation and oxynitridation process were carried out on these structures using O₂/Ar and O₂/N₂/Ar gases, respectively, to get the TiAlO and TiAlON films on Si. Physical thickness values between 6.3 and 6.9 nm were determined by ellipsometry. XPS (X-Ray Photoelectron Spectroscopy) analysis was performed and the formation of TiAlO and TiAlON films was confirmed. These films were used as gate insulators in MOS capacitors fabricated with TiN (20nm)/Al (180 nm) electrodes, and they were used to obtain capacitance-voltage (C-V) measurements. A relative dielectric constant of 3.9 was adopted to extract the equivalent oxide thickness (EOT) of films from C-V curves under strong accumulation condition, resulting in values between 0.5 and 1.4 nm, and effective charge densities of about 10¹¹ cm⁻². Because of these results, nMOSFETs with TiN/Al gate electrode and TAON gate dielectric were fabricated and characterized by current-voltage (I-V) curves. These results indicate that the obtained TiAlON and TiAlO films are suitable gate insulator for the next generation (MOS) devices.

Reference:

- [1] Miyoshi J., Diniz J.A., Barros A.D., Doi I., Von Zuben A.A.G., (2010) *Microelectronic Engineering*, 87 (3), pp. 267-270.
- [2] A. P. Alekhin, A. A. Chouprik, S. A. Gudkova, and A. M. Markeev, Yu. Yu. Lebedinskii, Yu. A. Matveyev, and A. V. Zenkevich, 01A302-1 *J. Vac. Sci. Technol. B* 29(1), Jan/Feb 2011.

EM-ThP7 Exploring Thermal Reduction Efficiency of Reduced Graphene Oxide with Alcohols Studied by First - Principles Calculations and Infrared Spectroscopy, R.M. Abolfath, C.G. Gong, M. Acik, Y.J. Chabal, K. Cho, The University of Texas at Dallas

Graphite oxide (GO) is convenient to be used as a precursor for functionalization studies and explore the chemistry in solution. Since GO is solution-processable and hygroscopic, tuning the chemical properties by reduction therefore tailors the electronic and electric properties of thermally/chemically reduced GO. The reduction processes of GO sheets have gained much interest since improvement and systematic investigation of the graphitic structure-electrical property relationship is particularly required for graphene nanoelectronics applications. The excellent electrical conductivity of the reduced GO sheets therefore promises potential electronic applications.

It was reported by Su *et al.* in (*ACS Nano*, 4, 5285-5292, 2010) that the use of high-temperature alcohol vapor for reducing GO increases the conductivity dramatically which improves the graphitic domains. However, details of understanding reduction mechanisms behind the interactions of alcohol molecules within the reduced defective sites of reduced GO still remains elusive.

One of our recent study in (*ACS Nano* 4, 5861-5868, 2010) shows that trapped water molecules intercalate in the interlayers of as-synthesized GO and interacts with the carbon dangling bonds of the etch holes upon reduction. In this study, formation of carbonyl groups and production of CO₂ from the structural decomposition is a key experimental observation. Replacing intercalated water with methanol and ethanol and performing thermal reduction of GO at 60-300°C, *in-situ* infrared spectroscopy measurements in transmission demonstrate that the thermal reduction efficiency of reduced GO changes dramatically within two different alcohol environment. In the presence of methanol in the interlayers of reduced GO, an increase of infrared absorption could be observed which is attributed to a stable carbonyl concentration during annealing. In contrast, compared with methanol, carbonyl formation at ~1750-1850 cm⁻¹ is absent when there is ethanol in the interlayers of reduced GO. To understand differences in these experimental observations, we simulate the reduction mechanisms by both MD and DFT calculations which show a faster diffusion of methanol in the interlayer of GO that facilitate its reaction with etch holes, inducing a competing mechanism. In the case of ethanol intercalation, simulations confirm that the carbonyl formation which tends to enlarge the etch hole upon annealing can be blocked.

EM-ThP8 Characterization of Ion Implantation-Induced Vacancy Defects and Graphitization in Diamond Lattices by Coherent Acoustic Phonon Spectroscopy, J.M. Gregory, A.D. Steigerwald, Vanderbilt University, H. Takahashi, Japan Advanced Institute of Science and Technology, Japan, N.H. Tolk, Vanderbilt University

We describe implantation damage experiments on single-crystal diamond samples and subsequent characterization using optical pump-probe techniques. Samples are irradiated using He⁺ ions with energies on the order of 1 MeV, generating lattice defects and buried layers of graphitic carbon under high pressure. Using the time-resolved optical technique known as coherent acoustic phonon spectroscopy, these samples are characterized in a depth-dependent manner. The resulting oscillation patterns reveal clues about the optical and electronic structure of the defects and the graphitic layers.

EM-ThP9 New Reconstruction Mechanism of Dense SiC(111) on Sparse Si(110) Interface, E. Abavare, University of Tokyo, Japan, J.-I. Iwata, University of Tsukuba, Japan, A. Oshiyama, University of Tokyo, Japan

SiC grown on Si substrates is a promising candidate for mass production of Graphene, an emerging material in technology. SiC(111) on Si (110) with particular alignments of the two planes offers almost perfect matching of the lattice periodicity, albeit dense SiC and sparse Si. We here report the total-energy electronic-structure calculations based on the Real-Space Density Functional Theory (RSDFT), that elucidate new reconstruction mechanism of the dense 3C-SiC(111) on the sparse Si(110) interface with the relaxed superstructures displaying undulating structures near the interface. We have explored a variety of candidate interface structures and

reached two distinctive types called type I and II which shows bistability at the interface. In type I, the silicon-silicon interface energy is calculated as 9.57 eV whereas that of silicon-carbon is 10.41 eV. Similarly, in type II, silicon-silicon interface energy is 9.89 eV and that of silicon-carbon is 10.84 eV. We argue that in both types, the silicon-silicon interface is energetically favorable compared with the silicon-carbon interface.

EM-ThP10 The Influence of the Layer Thickness on the Optoelectronic Properties of InN. *M.K.I. Senevirathna, S. Gamage, R. Atalay, Georgia State University, J. Hong, Georgia Institute of Technology, N. Dietz, A.G.U. Perera, Georgia State University*

Indium nitride (InN) and indium-rich group III-nitride alloys may have great potential for high efficient energy conversion devices such as solar cells, high speed optoelectronic devices, and various types of light emitting device structures. Scientists are exploring several different growth methods and various characterization methods to improve the material quality and to understand the optical, structural, and electronic properties of these epilayers. However, till today, the growth of high quality InN alloys and epilayers is still a challenge, mainly due to low InN dissociation temperature and due to stoichiometry instabilities at optimum growth conditions. InN epilayers exhibit significant different physical properties depending on the growth techniques (PAMBE, MBE, MOCVD, etc.) and the substrate material used. At present, low-pressure CVD based growth methods are limited to InN growth temperatures at or below 600°C, which creates problems related to a suited nitrogen precursor, since the ammonia decomposition at these growth temperatures is insufficient. To stabilize InN at higher growth temperature, we explored the growth of InN by high-pressure chemical vapor deposition (HPCVD) at 10 bar and 15 bar reactor pressures. Under these growth conditions the growth temperature can be increased to around 800 °C, resulting in improved ammonia decomposition and smaller group III/N precursor ratio.

This contribution presents results on the effect of the layer thickness on the physical properties of epitaxial InN layers. All InN layers were grown on GaN/sapphire (0001) templates under identical growth conditions, only the growth time was varied. Fourier transform IR reflectance (FTIR) spectroscopy was used to analyze the film thickness and the optoelectronic layer properties. We will present results on the free carrier concentration and mobility as a function of layer thickness. The reflectance spectra were simulated using a Lorentz-Drude model and a multilayer stack model, which allows determining the phonon frequencies, dielectric function, plasma frequency, and damping parameters. From these, the free carrier concentration and mobility for each layer can be calculated. The crystalline quality of the epilayers has been characterized by XRD 2theta- omega scans and by Raman spectroscopy analysis.

EM-ThP11 The Effect of Reactor Pressure on the Optoelectronic Properties of InN Epilayers Grown by HPCVD. *M.K.I. Senevirathna, S. Gamage, M. Buegler, R. Atalay, Georgia State University, J. Hong, Georgia Institute of Technology, N. Dietz, A.G.U. Perera, Georgia State University*

The dependency of the optoelectronic and structural properties of InN epilayers on the reactor pressure is presented. The InN epilayers were grown by high-pressure chemical vapor deposition (HPCVD) varying the reactor pressure from atmospheric pressure to 18.5 bar. The optoelectronic properties such as free carrier concentration and mobility have been studied using Fourier transform IR reflection spectroscopy. The film thickness, growth rate, free carrier concentration and carrier mobility of the InN layer are obtained by simulating the IR reflectance spectra, using a multilayer stack layer model and a Lorentz-Drude model. XRD 2theta- omega scans and Raman spectroscopy were used to evaluate the structural properties of the epilayers.

EM-ThP12 Effect of Buffer Layers on Structural and Optical Properties of InN Films by RF-MOMBE. *W.C. Chen, National Applied Research Laboratories, Taiwan, Republic of China, S.Y. Kuo, Chang Gung University, Taiwan, Republic of China, F.-I. Lai, Yuan-Ze University, Taiwan, Republic of China, C.-T. Lee, C.N. Hsiao, D.P. Tsai, National Applied Research Laboratories, Taiwan, Republic of China*

Hexagonal InN films were prepared on sapphire by RF-MOMBE using AlN, GaN and ZnO buffer layers. Also, we have investigated the effect of buffer layers on optical, structural and electrical properties of InN films. The crystalline quality of the InN film is sensitive to the underlying buffer layer when the film is grown under the high effect V/III ratio condition. The structural, optical and electrical properties of InN films were investigated by X-ray diffraction (XRD), Field emission scanning electron microscopy (FE-SEM), transmission electron microscopy (TEM), UV/VIS/IR spectrum measurements, and Hall effect, respectively. The XRD pattern indicated all InN films along c-axis growth. Optical absorption edge by spectrophotometer confirms that the band gap of wurtzite InN films were 1 to 1.2 eV. A Hall mobility of more than 170 cm²/V-s with a carrier

concentration of 9.2×10^{19} cm⁻³ at room temperature can be routinely obtained on InN/GaN film. Also, the average later thicknesses range measured about 800 to 1000 nm, and high growth rate about 1.6 mm/hr at InN/GaN, 2 mm/hr at InN/ZnO and 1 mm/hr at InN/AlN, respectively. We suggest that the reduced lattice mismatch between the InN epilayer and top buffer layer is responsible for improvement of sample quality using the buffer-layer technique.

EM-ThP13 The Influence of Ammonia - MO Precursors Pulse Separation on the Gallium Incorporation in Indium-Rich In_xGa_{1-x}N Epilayers. *S. Gamage, R. Atalay, M.K.I. Senevirathna, Georgia State University, J. Hong, Georgia Institute of Technology, J.S. Tweedie, R. Collazo, North Carolina State University, N. Dietz, Georgia State University*

Ternary In_xGa_{1-x}N alloys and embedded epilayers are of great interest due to their large band gap tenability, which enables new applications in the fields of advanced optoelectronic devices. Here, the growth of ternary In_xGa_{1-x}N epilayers is explored by high-pressure chemical vapor deposition (HPCVD) and pulsed precursor injection in order to reduce the temperature gap between the binary alloys GaN and InN and to improve the phase stability on the ternary alloys. In the pulsed precursor injection approach, the precursor separation times between the metal organic (MO) sources (TMI and TMG) and ammonia (S₁), and ammonia and MO (S₂) are two critical process parameters. Previous studies on InN growth showed that the precursors separation critically influences the surface chemistry and the resulting structural and physical layer properties.

In this contribution, we present results on indium-rich InGaIn epilayers grown by simultaneous MO injection and with different S₂ timings, with the aim to find the optimum S₂ separation for high quality, single-phase InGaIn epilayers. We will show that the S₂ separation is critical for the incorporation of gallium into the epilayers. In order to maintain single-phase epilayers, the S₂ separation has to be increased from S₂=400 ms for InN to over 1200 ms for In_xGa_{1-x}N with x=0.2. Raman spectroscopy and X-ray diffraction (XRD) are used to study the structural properties and the Fourier Transform Infra-red (FTIR) and transmission spectroscopy are used to study the electrical and optical properties of the epilayers.

EM-ThP14 Thermal Stability of HPCVD Grown InN Epilayers. *A.R. Acharya, S. Gamage, N. Dietz, B.D. Thoms, Georgia State University*

The thermal stability of InN layers grown on sapphire by high-pressure chemical vapor deposition (HPCVD) was studied using isothermal desorption measurements and Auger electron spectroscopy (AES). The desorption of hydrogen-, carbon-, and nitrogen-containing species was analyzed using a differentially-pumped mass spectrometer while the sample temperature was ramped from room temperature to a target value, where it was held constant for ten minutes before cooling back to room temperature. Experiments were performed with increasing target temperatures from 500 °C and 700 °C. No significant evaporation of nitrogen and other species was observed until the samples were annealed to 600 °C. However, during isothermal heating to 650 °C or above, the evaporation of molecular nitrogen commenced around 450 °C and an abrupt increase occurred above 600 °C indicating serious degradation of the film. The stability of InN layers was found to be dependent on V/III ratio, being more stable for the film grown in higher V/III ratio growth conditions. After annealing to 700 °C, the AES spectra showed carbon, oxygen, and traces of indium but no nitrogen indicating the complete desorption of nitrogen from the InN film.

EM-ThP15 Substrate Template and V/III-Ratio Effects on the Surface and Structural Properties of HPCVD Grown InN Films. *A.R. Acharya, M. Buegler, R. Atalay, S. Gamage, Georgia State University, J.S. Tweedie, R. Collazo, North Carolina State University, N. Dietz, B.D. Thoms, Georgia State University*

Nucleation and growth processes in chemical vapor deposition determine the crystalline quality and orientation which also affect the surface configuration. The bulk and surface structural properties of InN layers grown by high-pressure chemical vapor deposition (HPCVD) were investigated by Raman spectroscopy, x-ray diffraction (XRD), and high resolution electron energy loss spectroscopy (HREELS). HREEL spectra of InN grown on GaN/sapphire with a group V/III precursor ratio of 630 showed surface NH species and nitrogen-termination. For this layer Raman spectroscopy and x-ray diffraction (XRD) showed c-axis film orientation. In contrast, HREEL spectra of InN grown directly on sapphire with a higher group V/III precursor ratio of 3000 revealed that the dominant surface species is NH₂. For this sample, the Raman and XRD analysis indicate the existence of micro-crystallites oriented in the (01-11) direction. Two factors suggested to account for the appearance of these tilted planes are slower surface diffusion under more nitrogen-rich conditions and strain due to the larger lattice mismatch when growing on sapphire substrates.

EM-ThP16 P-Si / N-type GaN Heterojunction, J. Kim, J. Ahn, Korea University, Republic of Korea

P-N heterojunction from P-Si thin film / N-GaN microstructures have been demonstrated. To control the position of GaN microstructures, a mechanical method or electric-field assisted method was employed. Firstly, thermally-grown SiO₂(300nm) on top of p-Si substrate was wet-etched to define the mesa structures. Then, the metal was deposited on both front (on top of the SiO₂) and backside. Finally, GaN microstructures were moved to form p-n heterojunction. When P-Si thin film / N-GaN microstructures were forward-biased, the electroluminescence from p-n heterojunction was observed. The details of the fabrication and the characterizations of P-Si thin film / N-GaN microstructures will be presented.

EM-ThP17 CIGS Thin Film Prepared by One-Step Sputtering Process by Using a Powder Target, S. Oh, G. Cho, N. Kim, Chosun University, Republic of Korea

CIGS thin film with cells reported the highest efficiency up to 20% in the thin film solar cells, which is generally considered as the most promising thin film solar cell. It has been fabricated by using the three stage process in evaporation process with four sources of Cu, In, Ga, and Se pure elements. This preparation method requires very strict controls during the deposition process of CIGS thin film. Recently, there are two widely used methods for CIGS thin film fabrication: selenization with H₂Se or Se after sputtering and thermal co-evaporation. Although the sputtering process was the most suitable method for the deposition of CIGS thin film over the large area with a good uniformity, the two-step selenization shows the critical drawbacks including the additional manufacturing steps, higher materials costs, and the less efficiency. The co-evaporation for CIGS thin film is hard to manage the sources in sequence and to deposit over the large area. For this reason, the novel method for CIGS preparation was demonstrated by using the sputtering process with the powder target. This method has the advantages of the production of target, change of stoichiometry, and easy doping of impurities. The composition of the powder-sputtered CIGS thin film with 1 μm-thickness were analyzed and compared to that of the starting powder target with a composition of Cu, In, Ga, and Se at 25, 15, 10, and 50 at% by electron probe microanalysis (EPMA). The crystal structure, surface morphology, optical properties, and electrical characteristics of CIGS thin film were analyzed by using X-ray diffraction (XRD), atomic force microscope (AFM), UV-Visible spectrophotometer, and a Hall effect measurement system.

EM-ThP18 Effects of Ta Addition on the Characteristics of ITO Thin Film Transistors by Sputtering, S.M. Chung, J.H. Shin, C.H. Hong, W.S. Cheong, ETRI, Republic of Korea

Thin-film transistors (TFTs) using amorphous oxide semiconductors (AOSs) as an active layer have shown remarkable performances including low-temperature processing, high transparency, environmental stability, and high mobility for alternative display backplanes of active-matrix organic light emitting displays (AM-OLEDs), thin-film-transistor liquid crystal displays (TFT-LCDs) and opto-electronic components. Oxide material combinations such as InZnO (IZO), InGaZnO (IGZO), ZnSnO (ZTO), and GaZnSnO (GZTO) have been vastly studied for enhancing the mobility and stability. Though the mobility of the amorphous oxide TFTs has been much improved for several years, the instability under prolonged on-current status is still critical issue to substitute for Si-based technology. Recently, other elements of high oxygen affinity such as Al, Zr, Si, and Hf were added to oxide based TFTs for improving the stability characteristics, which, however, results in a mobility reduction problem. In order to overcome the problem, we used Ta dopant. This work reports on the characteristics of bottom-gate Ta-doped InSnO (ITO) TFTs. An amorphous ITO:Ta channel layer was deposited at room temperature by sputtering. The devices were annealed at 50 ~ 200°C in oxygen condition for 1 hours. Optical transmittance data in the visible range reveal average transmittance higher than 80% including the glass substrate. The field-effect mobility of 15.9 cm²/V-s, the ON/OFF ratio of >10⁸, and the sub-threshold slope of 0.81 V/decade are achieved in the n-channel ITO:Ta TFTs. Effects of ITO:Ta preparation conditions on the resulting TFT performances were discussed. Stability experiments and further device optimizations through processes are under investigation. The detailed results will be revealed in this presentation.

EM-ThP19 Infrared Absorption Enhancement in Silicon via Silicidation and Nanoparticle Incorporation, C.M. Gonzalez, R. Sachan, G. Duscher, R. Kalyanaraman, P.D. Rack, University of Tennessee, Knoxville

Conventional silicon photovoltaics lack the ability to absorb the full electromagnetic spectrum arriving from the sun. Nickel silicides are small band-gap semiconductors that effectively engage the near-infrared region, whereas bare silicon does not. Ultra-thin (<100nm) silicon structures incorporated with nickel silicides have been synthesized and characterized

and have shown enhanced absorption from 750-3000nm wavelengths. Four different structures were constructed via a combination of sputtering, co-sputtering and laser irradiation and their optical and electrical characteristics were compared. In one case, the nickel is deposited and reacted between the p and the n+ silicon regions; in another, nickel is co-sputtered along with p-Si and co-sputtered with n+ silicon; and finally nickel is co-sputtered with silicon followed by laser irradiation to form nickel silicide nanoparticles via pulsed laser induced dewetting. This last structure contains non-patterned nanoparticles (<50nm) in close proximity to a pn junction after capping the former with the p and n+ silicon. In this presentation we will correlate the material composition and micro and nanostructure by STEM and EELS to the observed optical and photovoltaic responses and demonstrate effective media approximations for the observed optical properties.

EM-ThP20 Fabrication of Shape-Controlled Metal Nanodot Array by Electrostatically-Driven Self-Assembly as well as their Charge Injection Properties, R. Sumi, Nagoya University, Japan, T. Hosoi, H. Watanabe, Osaka University, Japan, X. Hu, O. Takai, N. Saito, N. Zettsu, Nagoya University, Japan

Nanometer-sized inorganic particles play an important role in modern nanotechnology owing to their superior characteristics that can lead to fascinating function that are difficult to be realized using conventional used bulk materials. Recently the development of shape-controlled synthesis techniques make possible to obtain various well-defined shapes of nanoparticles with high yield. To determine their surface-to-volume ratio and crystal structure are expected to lead to improvement in performance in given application.

In this paper, we demonstrated fabrication of various metal nanodots MOS capacitors for floating nanodot gate memory using a evaporation-based colloidal self-assembly in order to attain a tight control over the size, shape, and density of metal nanodots, as well as the study of their effects on the charge injection characteristics of the nanodot arrays.

We synthesized Au nanoparticles with 2nm diameter by solution plasma processing in aqueous solution. The surface was modified with organic surfactants which tuned their zeta-potential to be approximately -40mV. We have recently proposed a versatile method for the fabrication of self-assembled metallic nanodot arrays onto a SiO₂/Si substrate with dimension of 50 x 100mm² by using a newly developed electrostatically-driven self-assembly. The substrate surface was modified with amino-silane agents prior to use assembly. In order to make MOS capacitor containing Au nanodot array as a charge trapping layer, the Au nanodot array was embedded in a gate oxide.

By precise control of the velocity of the leading edge of a liquid slug, the volume ratio of the particles, and the deposition rate, we were able to reproducibly form an array consisting of a single layer of Au nanodot array with density of 1012particles/cm². We further demonstrated the charge injection characteristics of the Au nanodot array, embedded in the ultra-thin SiO₂ layer consisting of both thermally grown tunnel oxide and RF-driven sputtered control oxide layer. Counterclockwise hysteresis was observed reproducibly, whereas there was no hysteresis in the C-V curve of the MOS capacitor without Au nanodots. This hysteresis indicates the charging and discharging of the embedded Au nanodots. This electron confinement caused the flat-band voltage shift observed as the capacitance hysteresis.

EM-ThP21 Small-Molecule Scaffolds for Directed Self-Assembly, P. Mancheno-Posso, A.J. Muscat, University of Arizona

Self-assembled monolayers (SAMs) are often used as scaffolds for the deposition of a subsequent layer. This process allows the surface properties to be tailored to a specific application and facilitates the construction of functional nanostructures. For instance, copper electrodes and graphene have been deposited on carboxyl-terminated and on 3-aminopropyltriethoxysilane (APTES) monolayers, to create metallic electrodes for electronic devices and a lubricating layer for nanoelectromechanical systems, respectively. Small silane molecules in particular could be used to direct the self-assembly of another layer and keep it in close proximity to a silicon surface. Vinyltrichlorosilane (VTCS, CH₂=CH-SiCl₃) is a candidate and contains a carbon-carbon double bond. A vinyl C=C bond is a versatile functional group because it can be reacted in situ to generate a variety of terminations, including -COOH, -SH, and -NH₂, and could also direct the assembly of new molecules on the surface. While VTCS SAMs have been studied previously, a reproducible and self-limiting process to form a single monolayer from solution has not yet been achieved. In this work we adsorbed VTCS from solution on a Si(100) substrate and characterized the layer with ellipsometry, X-ray photoelectron spectroscopy (XPS), and atomic force microscopy (AFM). Silicon wafers were cleaned and hydroxylated in a piranha solution. After drying, the samples were dipped for different times into a 1:1000 solution of VTCS in toluene, hexane, chloroform and acetone. The thickness of the monolayer was monitored ex situ using ellipsometry. Toluene and hexane yielded

multilayers with a thickness greater than 10 Å, whereas chloroform and acetone produced more consistent monolayers with a thickness of about 6 Å. A bromination was performed to demonstrate the presence of the unsaturated bond. We are in the process of making XPS and AFM measurements to determine whether VTCS is covalently attached to the Si substrate and to assess whether the vinyl group is suitable to graft molecules to the substrate.

EM-ThP22 Deposition of Organic and Inorganic Hybrid Laminates using Ozone Based ALD (Atomic Layer Deposition). *S. Lee*, NCD Technology, *J. Huang, M. Lee*, University of Texas at Dallas, *P.-R. Cha*, University of Texas at Dallas and Kookmin Univ., Korea, *J. Kim*, University of Texas at Dallas

Recently, organic materials have been attracting attention due to the large area, low cost, and flexibility. On the other hand, inorganic conducting materials have several benefits such as high conductivity, functional properties, and rigid characteristics, etc. A novel technique for building an organic and inorganic hybrid stack has been introduced by M. M. Sung et al. using a modified ALD method.¹ It has advantages to minimize the defects during growth of organic and inorganic films because hybrid films are deposited by an in-situ process through the sequential self-limiting surface reaction like atomic layer deposition (ALD), while maintaining their flexibility and functionality.

In this study, we investigate the growth characteristics of organic/inorganic conducting material, ZnO, and 7-octenyltrichlorosilane (7-OTS) thin film using an ozone based ALD. 7-OTS is grown by exchange reaction between functional group and water and then the terminal vinyl group of 7-OTS is converted into a carboxylic group through ozone activation.¹ The deposition rate and the contact angle of the organic films are about 7Å/cycle and 60°, respectively. In case of the ZnO, it is deposited using diethylzinc (DEZ) source and H₂O oxidant under the temperature of 120°C. The deposition rate is about 2 Å/cycle. The organic/inorganic hybrid laminate films will be analyzed by TEM, AFM, Ellipsometer and FTIR. The electrical characteristics of laminate structure will be discussed.

This research has been partially funded through Korea-US collaboration R/D program by MKE-COSAR-KETI.

References

[1]. B. H. Lee, et al., *J. Am. Chem. Soc.*, 129, 16034 (2007).

EM-ThP23 Simple Methods to High Quality Self-Assembled Monolayers of Alkylsilanes on Oxides. *B.D. Gates, Y. Gong, A. Liu, H.W. Ng, M. Wang*, Simon Fraser University, Canada

The interfacial properties of a material can be easily modified by modifying its surfaces with self-assembled monolayers. These single-molecule thick coatings can be used to prevent non-specific adsorption of biomolecules, protect the underlying material from chemical attack, serve as a masking layer to prevent or direct the deposition of a coating material, and reduce friction between two materials. Interest in the use of self-assembled monolayers continues to grow. The applications being pursued for these molecular coatings are increasingly interested in the robustness and uniformity of these films. An important aspect of their resilience is the density and size of defects within the monolayers, which can have a large role in their overall performance. One type of monolayer for which it is particularly challenging to achieve high quality coatings are those films based on the assembly of alkylsilane molecules. Often these coatings are pursued for the modification of oxidized surfaces, but form either a sub-monolayer or a multilayered film. A primary goal of the work that will be presented is to further optimize the conditions in which monochloro alkylsilane-based molecules are assembled into monolayers. Considerations for the development of these refined methods include the ease of scaling the technique to cover larger areas and the ability to avoid stringent requirements for environmental control during growth of the monolayer. Additional work is being pursued to identify and repair defects within the silane-based films. One approach that will be discussed uses solvent extraction techniques to remove adsorbed molecules, followed by further assembly of alkylsilane molecules onto the unprotected regions of these surfaces. The 'repaired' surfaces exhibit improved resistance to chemical attack. A key aspect of this work has been the development of new analytical methods for determining the density and size of the defects. These methods are used to also monitor the success of repairing the defects. The talk will cover these and other aspects of our progress towards developing simple methods that will produce high quality monolayers of alkylsilane-based molecules.

EM-ThP24 Deposition and Characterization of Hydrophobic Coatings on Electronic Devices. *V. Gupta, S.C. Kunzler, M.R. Linford*, Brigham Young University

More cell phones are damaged by water than by any other means, and this damage often requires the devices to be discarded. The number of damaged phones is also increasing because these phones are now taken almost everywhere. Chemical vapor deposition may provide a solution to this problem, which is large (100.9 million Smartphones were shipped in Q4 2010). For example, the phones may be coated with a hydrophobic monolayer or multilayer of fluorosilanes. Bonding of the fluorosilane may be improved using of a primary adhesion layer, which may be a different silane monolayer, e.g., an isocyanatosilane, and/or by introduction of hydroxyl groups via plasma treatment. The latter process is typically rapid and economical and can take place both on oxide and polymeric materials. The presence of OH groups can be assayed by XPS, ToF-SIMS and ATR-FTIR. The density of surface hydroxyl groups can be varied by changing the proportions of etch gases, the time and intensity of the plasma treatment, and the system base pressure. The hydrophobicity of the surface can be characterized by contact angle goniometry and XPS and ToF-SIMS analysis of fluorine. Resistance to abrasion can be tested with a Martindale abrasion tester. This work can be further extended to touch screen panels in equipment used under water.

EM-ThP25 Impact of Substrate Type on the Formation of Si Nanocrystals in the Annealed SiO_x and SiO_x:Er,F Films. *A.S. Nikolenko, M.V. Sopinsky, V.V. Strelchuk, L.I. Veligura, N.A. Vlasenko, V. Lashkaryov* Institute of Semiconductor Physics, Ukraine

Erbium doped nc-Si/SiO₂ nanosystems are considered as possible candidates for the manufacturing of light emitting sources compatible with silicon technology [1]. Fluorine, like other halogens, has a tendency to enhance recrystallization processes. Therefore, one could hope that introduction of F will intensify the transformation of amorphous silicon nano-inclusions formed on initial stage of SiO_x, thermal decomposition into Si nanocrystallines, and reduce the low-temperature threshold of this process. Lowering of the process temperature is the essential advantage of every technology. In case of SiO_x:ErF₃ films this is principally important because at $T_{ann} > 900^{\circ}\text{C}$ the segregation of erbium ions into metallic clusters takes place. Consequently, the final stage of forming the erbium-doped light-emitting system should not exceed 1000 °C.

In this work the silicon nanoparticle formation due to the structural-phase transformations in the SiO_x and SiO_x:Er,F films evaporated onto c-Si and sapphire substrates is studied. These transformations are induced by moderate temperatures annealing (650–1000°C). For this study the methods of Micro-Raman scattering and multi-angle ellipsometry are used. It was established that more intensive formation of a-Si nanoparticles takes place in the doped films as compared to undoped SiO_x films on both c-Si and sapphire substrates. Besides, it was found that the crystallization of a-Si nanoparticles is much more intensive and occurs at lower temperatures ($\geq 750^{\circ}\text{C}$) in the annealed SiO_x:Er,F films on sapphire substrate as compared to the annealed SiO_x:Er,F films on c-Si substrate.

Analysis of available literature data which deal with behaviour of Er and F in silicon, Si–O, and Al–O systems allows explaining the obtained results by the influence of F. In our opinion, the mechanism of F influence on the crystallization of a-Si nanoparticles is similar to the mechanism of hydrogen-induced crystallization of amorphous Si thin films [1]. Fluorine diffuses into Si–O and c-Si extremely fast. Therefore, during the annealing of SiO_x:Er,F films deposited on c-Si the significant part of mobile fluorine easily diffuses into c-Si substrate and its concentration in the film drops considerably. On the contrary, F very slowly diffuses into Al₂O₃ – even the thin native aluminum oxide layer provides very good protection against fluorine diffusion. Accordingly, fluorine concentration in the film on sapphire substrate stays significant, and its crystallization action manifests itself stronger.

Conclusions.

1) It is shown that the formation of erbium doped nc-Si/SiO₂ nanosystems at the temperatures $\geq 750^{\circ}\text{C}$ is possible by annealing of SiO_x:Er,F films on sapphire substrate.

2) This work, together with the work [2], demonstrates the wide variety of mechanisms by which a substrate can impact upon the formation of nc-Si–SiO_x nanosystems.

[1] S. Sriraman, M. S. Valipa, E. S. Aydil, and D. Maroudas. *J. Appl. Phys.* 100,

053514 (2006).

[2] M.V. Sopinsky, I.Z. Indutnyi, K.V. Michailovska, P.E. Shepeliavii. AVS-58. Abstract SE-TuP1 (2011).

Energy Frontiers Poster Session

EN-ThP1 Development of Analysis System for Evaluating Carrier Lifetime in Organic Thin Film Solar Cell. *K. Naito*, KAST, Chuo Univ., Japan, *M. Sakai, H. Takei*, KAST, Japan, *K. Nakata*, KAST, Tokyo Univ. Sci., Japan, *K. Katayama*, Chuo University, Japan, *K. Takagi*, KAST, Japan, *A. Fujishima*, KAST, Tokyo Univ. Sci., Japan

Recently, photovoltaic cell is expected as new green technology replacing fossil fuel. Because of a next-generation photovoltaic cell with flexibility, portability and low cost, organic thin film solar cell (OTFSC) is currently the subject of great interest and intensive study. OTFSC is composed of organic electronic materials, which have differences in electron affinity and ionization energy, between two metallic conductive electrodes. The layer of the material with higher electron affinity and ionization potential is electron acceptor, and the other layer is electron donor. The hole-electron pairs (exciton) generated in either material, when OTFSC was photoinduced. When most of excitons reach the interface of the electron acceptor and electron donor, excitons break into carriers of electrons and holes efficiently. Electrons and holes move in the acceptor and donor, respectively. The carriers are collected by the electrode in contact with each layer. In the latest report, OTFSC has exceeded 8 percent of conversion efficiency. However, it was difficult to increase the area of OTFSC with high conversion efficiency. For instance, the conversion efficiency depended on the layer defects, which was caused by contamination of dust and H₂O, oxidation and inhomogeneous coating. The defects influenced the carrier lifetime in OTFSC. Hence, the inspection technique, which was evaluated in two dimensions XY, was required to measure the carrier lifetime. The present inspection technique (Laser beam induced current method) had to contact electrodes with electric wires and pass an electric current through OTFSC. Because the carrier lifetime was measured by the decay of electric current, the value was influenced by every interface of circuitry in OTFSC. Therefore, it was necessary to detect the pure carrier lifetime in the organic semi conductivity layer. In this study, to investigate the pure carrier lifetime in the OTFSC, we developed the analysis system employing micro wave photoconductivity decay (μ PCD). The carrier lifetime was discussed from the viewpoints of electrochemistry and quantum mechanics.

EN-ThP2 Reactivation of Thermionic Electron Emission from Nitrogen Doped Diamond Films by Atomic Hydrogen Exposure. *M. Zumer, V. Nemanic, B. Zajec*, Jozef Stefan Institute, Slovenia, *F.A.M. Koeck, R.J. Nemanich*, Arizona State University

Thermionic electron emission from nitrogen doped hydrogen terminated diamond film has been evaluated 18 months after it had been deposited on a 25 mm diameter molybdenum substrate by microwave plasma assisted chemical vapour deposition. A hydrogen enriched surface layer, enabling a negative electron affinity, was formed during the film deposition procedure. The initial thermionic emission current density of the aged film obtained at 500 °C and 0.2 V/micrometer electric field was stable but relatively low compared to the value measured on a freshly deposited film. The value at a base pressure of 2×10^{-7} mbar was $\sim 1.4 \times 10^{-9}$ A/cm². Such a low current density is presumed to be a consequence of oxidation, surface adsorption of contaminants and hydrogen depletion from the surface layer, all processes which proceed during ambient atmosphere exposure since the manufacturing date. Reactivation of the surface was achieved by introducing atomic hydrogen, generated by the hot filament cathode of the ionization gauge. A stable current density of $\sim 2 \times 10^{-6}$ A/cm² (an increase factor of ~ 1400) was achieved after exposure to hydrogen at the base pressure of 2.2×10^{-4} mbar for 2 hours again at 500 °C and 0.2 V/micrometer. The atomic hydrogen exposure rate was estimated by subsequent measurement of the change in optical transmittance of the tungsten phosphate glass plates. The increase in emission with hydrogen was ascribed to two effects: 1) reactivation of the surface, and 2) molecular assisted emission.

Research at ASU is supported through the Office of Naval Research and at JSI through the Slovenian Research Agency (grant B1-US/09-12/021).

EN-ThP3 Self-powered Environmental Sensor System Driven by Nanogenerators. *M. Lee, J. Bae*, Georgia Institute of Technology, *J.H. Lee*, Seoul National University, Republic of Korea, *C. Lee*, Korea Electronics Technology Institute, Republic of Korea, *S. Hong*, Seoul National University, Republic of Korea, *Z. Wang*, Georgia Institute of Technology

A self-powered sensor for toxic materials can be the most desirable and promising prototype of the future monitoring systems for environmental protection/detection. Wiring power-source to sensors that are placed in

every corner of our surroundings not only causes a vast amount of labours, resources and budget, but also potential contamination to be produced by the batteries. Although solar energy is most attractive, it depends on the weather, season and has day and night difference. However, regardless of day and night, mechanical energy is one of the most abundant/sustainable sources practically to be utilized through piezoelectric materials. ZnO nanowires (NWs) not only have piezoelectricity, but also are environmental friendly and biological compatible, which make it a strong candidate for energy-harvesting for environmental sensors. Here, we have demonstrated a fully stand-alone, self-powered environmental sensor driven by nanogenerators with harvesting vibration energy. Such a system is made of ZnO nanowire-based nanogenerator, a rectification circuit, a capacitor for charge storage, a signal transmission LED light and a carbon nanotube-based Hg²⁺ ion sensor. The circuit lights up the LED indicator when it detects mercury ions in water solution. It is the first demonstration of nanomaterial-based, self-powered sensor system for detecting a toxic pollutant.

EN-ThP4 Effect of Inserting a Thin Buffer Layer on Obtainable Efficiency in n-ZnO/p-Cu₂O Heterojunction Solar Cells. *T. Minami, T. Miyata, Y. Nishi, J. Nomoto*, Kanazawa Institute of Technology, Japan

The effect of inserting a thin-film buffer layer on the obtainable efficiency in n-ZnO/p-Cu₂O heterojunction solar cells was investigated with a transparent conducting Al-doped ZnO (AZO) thin film/Cu₂O sheet structure. To improve conversion efficiency, various heterojunction solar cells were fabricated by forming an AZO/thin-film buffer layer/Cu₂O structure on the front surface of thermally oxidized Cu₂O sheets that function as the active layer as well as the substrate. It was found that achieving higher efficiency Cu₂O-based heterojunction solar cells fabricated by depositing various thin films on Cu O sheets requires that the surface of the Cu₂O sheets always be treated using a low-damage deposition technology at a low deposition temperature.

The Cu₂O sheets, with electrical properties such as resistivity on the order of 10³ Ω cm, hole concentration on the order of 10¹³ cm⁻³ and Hall mobility above 100 cm²/Vs, were prepared by a thermal oxidation of copper sheets under appropriate conditions. The AZO thin film and the thin-film buffer layer were prepared by a pulsed laser deposition (PLD) using an ArF excimer laser. As an example of AZO/buffer layer/Cu₂O heterojunction solar cells, AZO/ non-doped ZnO (ZO)/Cu₂O solar cells were fabricated by inserting a ZO thin film as the buffer layer. It was found that the obtainable conversion efficiency in AZO/ZO/Cu₂O heterojunction solar cells increased markedly as the deposition temperature of the AZO and ZO thin films was decreased from approximately 300°C to room temperature (RT), *i.e.*, non-intentionally heated Cu₂O sheets. In addition, when the ZO thin films were prepared on non-intentionally heated Cu₂O sheets by PLD, the efficiency (η) increased considerably as the introduced O₂ gas pressure was increased; η , approximately 3 % with a ZO thin-film layer deposition at an O gas pressure of 0.1 Pa, gradually increased as the O₂ gas pressure was increased up to approximately 1.2 Pa, and then decreased markedly at a pressure of approximately 1.5 Pa. The optimal thickness of the ZO thin-film layer was in the range from 30 to 50 nm. The obtained increase of η as the ZO film thickness was increased up to approximately 50 nm may be attributable to an improvement of film quality; in contrast, the decrease of η as the ZO film thickness was increased above approximately 50 nm may be attributable to the short lifetime of minority carriers in the n-ZO thin film. An AZO/ZO/Cu₂O heterojunction solar cell fabricated under optimal preparation conditions exhibited an efficiency of 3.83% under simulated AM1.5G solar.

EN-ThP5 Surface Texturing of Silicon for Solar Cells for CMOS Technology. *A.R. Silva, J. Miyoshi, F.A. Cavarsan, L.P.B. Lima, J.A. Diniz*, State University of Campinas, Brazil

The solar cell efficiency is hardly connected with device fabrication processes, such as texturing silicon surface, which increases the surface absorption area of incident radiation on the cell and, consequently, reduces the substrate reflectance. Nowadays, solar cells based on silicon substrate are fabricated with texturing surfaces to increase the device efficiency. These surfaces are obtained by anisotropic wet etching in KOH and NaOH alkaline solutions [1]. The disadvantage of these solutions are K⁺ and Na⁺ ions from KOH and NaOH, which are mobile charges in Metal-Oxide-Silicon structures. Thus, these solutions are not compatible for CMOS technology, which is used for integration circuits and devices on silicon surface. As an advantage, using these alkaline solutions, the <111> planes of silicon substrate with (100) crystallographic orientation are exposed, resulting in groups of pyramid on silicon surface. The pyramids induce many reflections and scatterings of the incident radiation, which increase the light absorption on the surface. This effect is defined as light trapping [1]. In this work, the silicon substrate texturing is carried out by an anisotropic wet etching, with an alkaline solution based on NH₄OH, because this solution can form pyramids on the surface, does not release alkaline

products/reagents on the silicon surface and is fully compatible with the CMOS technology. With this solution (concentration of 9%wt of NH_4OH and four magnetic stirring velocities) the $\langle 111 \rangle$ planes of silicon substrate with (100) crystallographic orientation are exposed and these planes can form some pyramids on surface. Scanning Electron Microscopy analysis presents that these pyramids are observed all long on the surface, indicating that the wet etching was uniform on the substrate. Furthermore, the pyramid height values are between 3.5 and 7.2 μm , and the silicon etching wet rate was about of 0.7 $\mu\text{m}/\text{minute}$. The reflectance measurements show that the surfaces with and without texturing present reflectance values of about 16% and 38%, respectively. The reflectance values of about 16% with texturing are similar to the results from references [1], which have used KOH solution. This result indicated that our texturing process based on NH_4OH , which is fully compatible with the CMOS technology, can be used to fabricate Si-based solar cells [2].

REFERENCES

- [1] L.A. Dobrzański, A. Drygala, Surface texturing of multicrystalline silicon solar cells, *JAMME*, Volume 31 ISSUE1, November 2008.
- [2] J.Lu, W.Liu, C.H.M. van der Werf, A.Y. Kovalgin, Y. Sun, R. E. I. Schropp and J. Schmitz, Above-CMOS a-Si and CIGS Solar Cells for Powering Autonomous Microsystems, *IEDM*, December 2010

EN-ThP7 Carrier Life Time of Several Organic Photovoltaic Cells by using Micro Wave Photoconductive Decay, *M. Sakai*, Kanagawa Academy of Science and Technology (KAST), Japan, *K. Naito*, KAST, Chuo Univ., Japan, *H. Takei*, KAST, Japan, *K. Nakata*, KAST, Tokyo Univ. Sci., Japan, *K. Katayama*, Chuo University, Japan, *K. Takagi*, KAST, Japan, *A. Fujishima*, KAST, Tokyo Univ. Sci., Japan

Recently, the importance of developing the future energy is recognized in various industries. In one of the green innovations, there are great expectations to develop organic photovoltaic cells; Dye sensitized solar cell (DSSC) and Organic thin film solar cell (OTFSC). Organic photovoltaic cells with inexpensive and low resource constraint are currently the subject of great interest and intensive study. DSSC is composed of photo-sensitized anode using molecular dye placed on a porous layer of titanium dioxide nanoparticles, and an electrolyte solution. The photo electrochemical system was known as the Grätzel cell. Electrons at the dye excited because of sunlight move into the titanium dioxide, and are collected by the electrode. On the other hands, OTFSC is composed of organic electronic materials, which have differences in electron affinity and ionization energy, between two metallic conductive electrodes. The layer of the material with higher electron affinity and ionization potential is electron acceptor, and the other layer is electron donor. The hole-electron pairs (excitons) generated in either material, when OTFSC was photoinduced. When most of excitons reach the interface of the electron acceptor and electron donor, excitons break into carriers of holes and electrons efficiently. Electrons and holes move in the acceptor and donor, respectively. The carriers are collected by the electrode in contact with each layer. In either solar cell, the carrier life time would influence the performance of the solar cell, because the carriers (electrons) move through the semiconductor and reach the electrode. Therefore, we investigated the carrier life time of several organic photovoltaic cells by using micro wave photoconductive decay (μPCD). The difference of the carrier life time was discussed from the viewpoints of electrochemistry and quantum mechanics.

EN-ThP8 Making Molecular Multilayers using "Click" Chemistry: Growth, Characterization, and Application in p-Type Dye Sensitized Solar Cells, *P.K.B. Palomaki*, *P.H. Dinolfo*, Rensselaer Polytechnic Institute

Bottom-up approaches to creating molecular multilayer assemblies using layer-by-layer (LbL) techniques give one the ability to tailor the surface properties of an interface through molecular control. LbL assembly methods can provide molecular level control of structure in one dimension from simple solution deposition processes. We have developed a versatile LbL fabrication method using copper(I)-catalyzed azide-alkyne cycloaddition (CuAAC) or "click" chemistry in the construction of multilayer assemblies on oxide surfaces. 1,2 These reactions occur in minutes at room temperature allowing for the facile creation of complex, covalently attached multilayer assemblies. Multilayers containing synthetic porphyrins, perylenes, and mixtures of the two have been constructed in order to highlight the versatility of this method. The fabrication of this new type of molecular multilayer thin film will be discussed along with characterization of the photophysical, electrochemical, and structural properties. Initial results pertaining to the use of these films as light harvesting systems in p-type dye sensitized solar cells will be presented.

1. Palomaki, P.K.B. and Dinolfo, P.H. *Langmuir* **2010**, 26 (12), 9677-9685.

2. Palomaki, P.K.B.; Krawicz, A.; Dinolfo, P.H. *Langmuir* **2011**, 27 (8), 4613-4622.

EN-ThP9 Powder-Sputtered $\text{Cu}(\text{In,Ga})\text{Se}_2$ Thin Films: Nonstoichiometric Influences on Optical and Electrical Characteristics, *N. Kim*, *J. Jeon*, *W. Lee*, Chosun University, Republic of Korea

The thin film solar cell efficiency of 19.2% (0.41 cm^2) was accomplished by using $\text{Cu}(\text{In,Ga})\text{Se}_2$ (NREL, 2003), which has been fabricated by using the three stage co-evaporation process. There are two general methods for $\text{Cu}(\text{In,Ga})\text{Se}_2$ thin film fabrication: selenization after sputtering and thermal co-evaporation. The novel method of powder-sputtering was employed for the preparation of $\text{Cu}(\text{In,Ga})\text{Se}_2$ to deposit the thin film over the large area with a good uniformity without selenization of toxic H_2Se because the co-evaporation method requires very strict controls during the deposition process of $\text{Cu}(\text{In,Ga})\text{Se}_2$ thin film. This method has the advantages of the production of target, change of stoichiometry, and easy doping of impurities. The composition of the starting powder target was changed by $x = 0.1, 0.3, 0.5, 0.7$, and 0.9 in the deposition process of $\text{Cu}(\text{In}_x\text{Ga}_{1-x})\text{Se}_2$ thin film while $\text{Cu}/(\text{In}+\text{Ga})$ ratio was '1'. The compositions of the starting powder target and the deposited samples with 1 μm -thickness were comparatively analyzed by electron probe microanalysis (EPMA). The crystal structure, surface morphology, optical properties, and electrical characteristics of $\text{Cu}(\text{In}_x\text{Ga}_{1-x})\text{Se}_2$ thin films were analyzed by using X-ray diffraction (XRD), atomic force microscope (AFM), UV-Visible spectrophotometer, and a Hall effect measurement system to investigate the influence of nonstoichiometry on the characteristics. The optimized composition was selected through the comprehensive analysis of the characteristics.

EN-ThP10 Indium-Doped CdS Thin Film by He-Ne Laser Exposure for CIGS Solar Cells, *K. Myung*, *N. Kim*, *W. Lee*, Chosun University, Republic of Korea

Cadmium sulfide (CdS) is a direct and wide band gap (2.42 eV at room temperature) II-VI semiconductor, which is a very desirable window layer for many photovoltaic solar cells including CIGS solar cell. CdS thin film has been paid to the considerable attention due to its band gap, high absorption coefficient, reasonable conversion efficiency, stability and low cost. It is generally known that the undoped CdS thin film has the high electrical resistivity. Some impurities were employed for doping CdS to produce less resistive films. Especially, indium (In) showed the improvement of resistivity and optical transmittance when it was doped into the sputtering-deposited CdS thin film. In this study, the structural, optical, electrical, and morphological properties of indium-doped CdS thin films prepared by the effective method with He-Ne laser at room temperature. Indium was deposited on the 200 nm-thickness of CdS thin film by the sputtering method with 10 nm-thickness. He-Ne laser (632.8 nm) was exposed with a small energy by a change of exposure time. The remained indium layer was removed with the chemical solutions. The doping effects of indium on the CdS thin films were investigated by analyzing the structural, optical, electrical, and morphological properties of CdS thin films by using X-ray diffraction (XRD), Auger electron spectroscopy (AES), UV-Visible spectrophotometer, Hall effect measurement system, and atomic force microscope (AFM). AES depth profile was employed to examine the indium-doped CdS thin film with a change of He-Ne laser exposure time. The doping uniformity and amount of indium into the depth of CdS thin film was compared to the characteristics of CdS thin film. The optimization of indium-doping process was achieved to enhance the electrical and optical characteristics including resistivity and optical transmittance.

EN-ThP11 Three-Terminal Tandem Devices for PV, TPV and CPV Applications, *M. Emziane*, Masdar Institute, United Arab Emirates

One of the key approaches for achieving very-high efficiency for photovoltaic (PV) devices is to use, instead of single junctions, double or multi-junction devices due to an extended solar spectral coverage leading to an enhanced overall power output from the multi-junction PV devices.

In this study, we investigated two-junction solar cells based on group IV materials, i.e. Si and Ge, for top and bottom sub-cell, respectively. Unlike the conventional and widely used monolithic series-connected two-terminal device configuration that was shown to deliver a slightly lower output, these double-junction cells were assembled with three terminals and operated independently [1, 2].

The main advantages of choosing these materials and device configuration are: (i) cheapest, largest and easiest group IV substrates; (ii) extended spectral coverage leading to more photons being converted; and (iii) no

current matching or the associated tunnel junctions between the two sub-cells.

We have undertaken a comprehensive modeling analysis for the device optimization and performance prediction. n/n/p as well as p/p/n device structure configurations were investigated and optimized with regard to the thicknesses and doping levels of both top and bottom active junctions that lead to the highest device performance. Due to the split of the incident solar spectrum between the top and bottom sub-cells, the latter only receives the light to which the former is transparent (mainly in the near infrared) and therefore behaves differently from the single-junction cell counterpart.

Optimal current-voltage and power-voltage characteristics were generated for individual cells together with the corresponding quantum efficiency spectra. The applications of these devices in conventional PV, concentrator PV and thermal PV were assessed and the output PV parameters were predicted as a function of the simulated operating conditions.

References:

- [1] M. Emziane, R. J. Nicholas, *Journal of Applied Physics*, 102 (2007) 074508.
- [2] M. Emziane, *Mater. Res. Soc. Symp. Proc.*, Vol 1165 (2009) M08-13.

EN-ThP12 The Advantage of State of the Art DC Power Supplies Over the Pulsed DC Power Supplies for TCO Magnetron Sputtering. P. Rozanski, P. Ozimek, M. Zelechowski, P. Lach, W. Glazek, J. Abraham, Huettinger Electronic Company, Poland

Non-pulsing DC power supplies for highly arcing processes are gaining more and more interest slowly pushing out older pulsing DC power supplies as more efficient and more cost optimal. The importance of arc management in DC power supplies is taking on a new meaning as most advanced DC generators are more and more successful in sputtering highly arcing and difficult materials, providing high deposition rates at competitive investment.

It has been developed as the answer to the market's demand to limit arc energy during an arc occurrence in sputtering. Industrial implementation has been already successfully performed with air-cooled DC power supplies that have been on the market for years. The possibility of using DC power supplies for sputtering highly-arcing materials is the result. It is the beginning of a new age in magnetron sputtering technology. Further improvement and optimization by using more efficient water cooling and faster transistors has resulted in a new generation of power supplies with state-of-the-art arc management parameters. A complementary feature of the newly-developed arc management circuitry is software that supports efficient arc handling: self-adjusting arc management settings and an internal oscilloscope.

EN-ThP13 Photogenerated Current Enhanced by Surface Plasmon Resonance in Metal Grating. D.J. Lee, Inha University, Republic of Korea

Photogenerated current enhanced by surface plasmon resonance excited in metal grating was confirmed in Au/p-type a-Si Schottky structures. Conduction electrons in metal absorb the incident photon of energy $h\nu$ (h is the Planck's constant and ν is the optical frequency) through the a-Si film, gaining enough energy to cross over the Schottky barrier into the semiconductor, where they are swept across the depletion region and collected as photocurrent under reverse bias. In addition, the surface plasmon polariton is excited in metal grating fabricated on the photoresist layer, and excited electrons will flow over the Schottky barrier. This additional photocurrent added to that directly induced by incident light and enhanced the responsivity of the photodetector.

EN-ThP14 The Science of Precision Multifunctional Nanostructures for Electrical Energy Storage. A. Predith, University of Maryland, College Park

Nanostructures for Electrical Energy Storage (NEES) is a five-year Energy Frontier Research Center investigating nanoscale behavior in lithium-ion battery materials. Funded by the US Department of Energy, the Center studies the properties of composite nanostructures containing an oxide or silicon as a charge storage material and low dimensional forms of carbon as an electronic conductor or mechanical support. NEES is particularly interested in nanostructures that are precise and regularly ordered. These structures provide a unique test bed for uncovering to the science of electrochemistry at the nanoscale.

The two Science Thrusts of the Center investigate nanotubes, nanowires, and layers of MnO₂, silicon, and carbon electrode materials as well as nanoporous membranes in an electrolyte. They examine the mechanical behavior, electrochemical properties, and interfacial phenomena that arise in heterogeneous material combinations. The two Enabling Thrusts of the Center develop model systems and characterization instruments for the nanoscale. Ultra high vacuum scanning probe microscopy and first principles modeling provide for the study of pristine systems, and in situ transmission electron microscopy and microelectromechanical systems are allowing members of NEES to observe electrochemical processes as they unfold.

NEES is a collaboration of 19 senior investigators, ~35 postdoctoral associates and graduate research assistants, and many staff members at six institutions. The Center integrates their perspectives to pursue a comprehensive examination of electrical energy storage using precision, multifunctional nanostructures. Members include Philip Collins (University of California-Irvine), Michael Fuhrer (University of Maryland), Sang Bok Lee (UMD), Charles Martin (University of Florida), Reginald Penner (UCI), Zuzanna Siwy (UCI), John Cumings (UMD), S. Thomas Picraux (Los Alamos National Laboratory & Center for Integrated Nanotechnologies), Mark Reed (Yale University), Chunsheng Wang (UMD), YuHuang Wang (UMD), Kevin Leung (Sandia National Laboratories), Janice Reutt-Robey (UMD), Kevin Zavadil (SNL), Reza Ghodssi (UMD), Jianyu Huang (SNL, CINT), Robert Hwang (SNL), Gary W. Rubloff (UMD), John Sullivan (SNL, CINT), and Ashley Predith (UMD).

EN-ThP15 Photosystem I-Based Solar Cells. D. Gunther, D.E. Cliffler, G.K. Jennings, Vanderbilt University

The long-term success of photosynthetic organisms has resulted in their global superabundance, which is sustained by their widespread, continual mass-production of the integral proteins that photocatalyze the chemical processes of natural photosynthesis. Here, a fast, general method to assemble wet and dry solar cells composed of one such photocatalytic protein complex, Photosystem I (PSI), onto a variety of electrode substrates, including gold, nanoporous gold, and graphene is reported. The resulting PSI films consist of a protein matrix that is permeable to electrochemical mediators in a wet cell and conducting for electron transfer in a dry cell. These results demonstrate how the assembly of micron-thick coatings of PSI on non-biological substrates yields a biohybrid ensemble that manifests the photocatalytic activity of the film's individual protein constituents, and represent significant progress toward affordable, biologically-inspired renewable energy conversion platforms.

EN-ThP16 Thickness Dependent Photo-Voltaic Effect In Ferroelectric PLZT Thin Films. S. Kotru, H.V. Nampoori, The University of Alabama, Tuscaloosa

Ferroelectrics are emerging as potential candidate materials for energy harvesting. Among the class of ferroelectrics, Lanthanum doped Lead Zirconate Titanate (PLZT) is one which possesses high electro-optic coefficient and exhibits high optical transparency thereby makes it an attractive material for PV applications. In this work ferroelectric thin films of $Pb_{0.95}La_{0.05}(Zr_{0.54}Ti_{0.46})O_3$ (PLZT) of various thicknesses were fabricated using chemical solution deposition method. Structural and ferroelectric properties of these films were studied using standard characterizations methods. Capacitor type solar cells were fabricated from these films using Pt as the top electrode. The IV curves were measured for each device where the thickness of PLZT film ranged from 70 nm to 350 nm. For devices, made with films less than 150 nm thickness, no PV response could be measured as an electrical contact could not be made on such films. From the PV curves measured on films with 140 to 350 nm thickness, the photocurrent density was seen to decrease from 597 to 64 nA/cm², where as no major change was observed for the open circuit voltage. Thus thinner films are seen to enhance the PV response in ferroelectric based capacitor type solar cells.

EN-ThP17 Nanostructure Analysis of Diamond Cold-Cathode Field Emitter. T.C. Wade, N. Ghosh, J.E. Wittig, W.P. Kang, Vanderbilt University, L.F. Allard, K. Unocic, Oak Ridge National Laboratory, J.L. Davidson, N.H. Tolk, Vanderbilt University

Chemical-vapor-deposited diamond is an attractive material for electron field emitters because of its low or negative electron affinity, mechanical strength, and chemical inertness. Arrays of ultra-sharp diamond tips with a radius of curvature less than 5nm have been fabricated [1] and show significant improvement in emission brightness and turn-on field compared

to conventional field emitters [2,3]. Irregularities in emission behavior between tips were historically attributed to anomalies in the fabrication process: “sharp” or “less sharp” tips. However, we observe large differences in electron emission thresholds between tips that appear to be equally well formed. We examine the emitter’s sub-surface structure to provide insight into how surface and subsurface structure affect emission.

Cross-sectional Transmission Electron Microscopy (TEM) samples were prepared by standard Focused Ion Beam (FIB) lift-out techniques with the additional step of using a layer of EBID Pt before the ion-beam Pt deposition in order to preserve the 5 nm field emission tips. TEM images of the emitter tip cross sections were recorded with a sub-angstrom probe in a JEOL 2200FS.

The core of the emitter consists of boron-doped microcrystalline diamond with characteristic diamond cubic twinning. The graphite layers observed are likely specimen preparation artifacts, although the presence of graphitic material in these diamond emitter tips is still an open question. Crystallites on the order of 5 nm in size are evident in the nanocrystalline diamond surface layer. Final thinning using a nanomill (Fischione Co.) with low energy Ar may be the solution for removing any surface artifacts and reducing the sample thickness. Comparison of the nanostructure of emitter tips with variation in field emission characteristics will provide insight into the influence of the nanocrystalline structure on the electronic properties.

[1] K. Subramanian, W.P. Kang, J.L. Davidson, R.S. Takalkar, B.K. Choi, M. Howell, D.V. Kerns, Enhanced electron field emission from micropatterned pyramidal diamond tips incorporating CH₄/H₂/N₂ plasma-deposited nanodiamond. *Diamond and Related Materials*, 15 (2006) 1126-1131.

[2] M.A.R. Alves, P.H.L. de Faria, E.S. Braga, Current-voltage characterization and temporal stability of the emission current of silicon tip arrays. *Microelectronic Engineering*, 75 (2004) 383-388.

[3] K.C. Qi, Z.L. Lin, W.B. Chen, G.C. Cao, J.B. Cheng, X.W. Sun, Formation of extremely high current density LaB₆ field emission arrays via e-beam deposition. *Applied Physics Letters*, 93 (2008) 093503-093503.

EN-ThP18 Microbial Fuel Cells Development on the Base of *Desulfuromonas Acetoxidans* Bacteria. O.M. Vasylyv, O.I. Bihy, S.O. Hnatush, Ivan Franko National University of Lviv, Ukraine

Microbial fuel cells (MFCs) are able to capture the electrons produced during different biochemical microbial processes to generate electricity. They offer the promise of a new sustainable source of energy, produced from biodegradable and reduced compounds. Increased shortcoming of unrenewable fossil fuels causes the need for its less dependence. The enhance of use of renewable fuels requires the development of alternative sources of energy such as waste biomass for environmental benefits. MFCs investigations have attracted substantial interest in development of different devices for generating electricity and removing wastes. The development of processes that can apply bacteria of normal environmental microflora to produce electricity represents a highly effective method for bioenergy production as bacteria are self-replicating, and thus the catalysts for organic matter oxidation are self-sustaining.

Nowadays MFCs is considered to be applied as highly effective and self-sustaining model of wastewater treatment which contains energy in the form of biodegradable organic matter. At the same time wastewater contains high concentrations of xenobiotics, such as different heavy metal ions that have an overwhelming harmful effect towards all living organisms. These elements even in small concentration in the environment cause the intensive inhibition of physiological and biochemical properties of most bacteria. Despite that, some genres of bacteria possess high toxic heavy metals resistance because of highly-efficient defensive systems functioning. There are *Ferroplasma*, *Streptomyces*, *Thiobacillus* etc.

Desulfuromonas acetoxidans are uncoloured gram-negative sulfur-reducing bacteria. These bacteria are considered to be used as the substrate for microbial-anode fuel cells with high electron recovery, which is more than 80%, to electric current by the interaction between processes of acetate oxidation and S⁰ or Fe³⁺ - reduction. Sulfurbacteria have a great effect on the biogeochemistry of aquatic environments because of their ability to reduce and precipitate toxic heavy metals compounds. It’s a result of their particular binding with the final product of bacterial dissimilative sulfur-reduction – H₂S, and formation of the insoluble metal sulfides. It also serves as self-defensive mechanism of these bacteria against toxic influence of toxic heavy metal ions.

The influence of different of Ni²⁺ and Cu²⁺ concentrations on size distribution and relative content of *D. acetoxidans* bacteria during their life cycle on the base of cells’ light scattering properties changes by the new method of measurement has been investigated. The ability of this bacteria to produce electric current in microbial-anode fuel cells under the specific cultivation condition has been shown. Particular heavy metals resistance of *D. acetoxidans* bacteria has been observed. Distribution curves of the cells’

size distribution changes were in the range from 0.3 to 1.9 μm under the influence of investigated metal ions. The maximum of cells’ size distribution of investigated bacteria was changed from 0.55 to 0.62 μm under the influence of 0.01-10 mM of NiCl₂·6H₂O and CuCl₂·2H₂O during five days of bacterial growth.

EN-ThP19 Investigating CdTe/CdS/TCO Inter-diffusion by AES and XPS. L. Le Tarte, A. Barbuto, J. Courmoyer, K. Dovidenko, H. Piao, General Electric, Global Research Center

CdTe has recently received a lot of attention as the material of choice for thin film solar cells as it converts light to electricity more cost effectively than traditional semiconductors and is compatible with manufacturing scale-up. An in-depth understanding of film composition, morphology and interface integrity is critical for CdTe thin film process development. Clear depth profiles of the buried layers by Auger electron spectroscopy (AES) and X-ray photoelectron spectroscopy (XPS) are difficult to obtain due to the rough, and thick (~3μm ± 0.5μm), upper CdTe layer. Sputtering through this layer leads to broadened depth profile interfaces which reduces information about inter-diffusion. We have developed a polishing method to thin and smooth this layer prior to analysis. In this poster we will present how this method has improved the Auger depth resolution and therefore the understanding of inter-diffusion between the CdTe, CdS and TCO layers. A novel FIB preparation method for Auger will also be discussed. XPS imaging analyses on AES sputter crater sidewalls provides additional chemical information about the buried layers and interfaces.

Magnetic Interfaces and Nanostructures Division

Room: East Exhibit Hall - Session MI-ThP

Magnetic Interfaces and Nanostructures Poster Session

MI-ThP1 Investigations of Ni and Co Magnetic Overlayers at the Advanced Photon Source. G.D. Waddill, T. Komatsu, Missouri University of Science and Technology, S.W. Yu, J.G. Tobin, Lawrence Livermore National Laboratory

Magnetic overlayers and bilayers of Ni and Co on Cu(001) have been investigated as a function of coverage, using X-ray Magnetic Circular Dichroism in X-ray Absorption Spectroscopy (XMCD-XAS) and Photoelectron Spectroscopy (PES). These studies were pursued at Beamline 4 at the Advanced Photon Source (APS).

Lawrence Livermore National Laboratory is operated by Lawrence Livermore National Security, LLC, for the U.S. Department of Energy, National Nuclear Security Administration under Contract DE-AC52-07NA27344. This work is funded by the DOE Office of Science, Office of Basic Energy Science, Division of Materials Sciences and Engineering. The Advanced Photon Source (APS) is supported by the Director, Office of Science, Office of Basic Energy Sciences.

MI-ThP2 Microstructure, Static and Dynamic Magnetic Properties of Thin Co Films Obtained using DC-Magnetron Sputtering. S.A. Maklakov, I.A. Ryzhikov, K.N. Rozanov, A.V. Osipov, O.Yu. Kasurkin, Institute for Theoretical and Applied Electromagnetics RAS (ITAE RAS), Russian Federation, V.A. Amelichev, Moscow State University, Russian Federation

Thin Co films possess high value of saturation magnetization, low coercivity and uniaxial magnetic anisotropy. These properties are necessary for high density storage devices, magnetic field sensors and applications for UHF electromagnetic radiation. Consequently Co is perspective material for such employments. There are many influences to affect magnetic film growth. The latter allows one to govern their properties in wide range. Comparative studies of microstructure and magnetic properties (static and dynamic) are essential to develop new approaches for directional obtaining of materials with given frequency dispersion of magnetic permeability.

The results of a comparative study of microstructure (TEM, GIXD), static (VSM) and dynamic (in the range of 0.01 to 10 GHz) magnetic properties of thin Co films are presented. The objects studied were rectangular films (60 x 600 nm) of 20 nm thick on poly(ethylene terephthalate) substrate. High purity (99,95%) cobalt disk target and a rotating drum as a substrate holder was used to obtain Co films.

Under a certain sputtering conditions two different types (with ferromagnetic resonance at 2 and 6 GHz) of Co films were obtained. Both types of films are of nanocrystalline structure. The increase of crystalline size (from 7 to 90 nm) along with the increase of coercivity (from 17 to 110 Oe) and the increase of resonant frequency (from 2 to 6 GHz) was discovered.

Uniaxial crystalline texture discovered was found to effect resonant frequency. When the texture axis is in the film plane, mechanical bending of Co film may cause resonance frequency varying up to 1 GHz. Perhaps the effect is due to magnetostriction mechanism [1].

The relationship obtained allows one to develop new pathways for magnetic materials production.

1. Lagarkov A.N., Kashurkin O.Yu., Maklakov S.A., Osipov A.V., Rozanov K.N., Ryzhikov I.A., Starostenko S.N., Iakubov I.T. Influence of magnetoelastic effect on ultra high frequency magnetic properties of thin Fe-N films. // Journal of Communications Technology and Electronics, 2011 (in press).

MI-ThP3 A Facile and Controllable Two-Step Electrodeposition Technique in Synthesis of Nanostructures of Metal Oxides on Carbon Nanotube S. J. Yang, S. Gunasekaran, University of Wisconsin-Madison

The nano dimensions of materials are comparable to the size of the target analyte biomolecule, higher catalytic reaction, better affinity binding or more efficient molecule-capturing may occur, leading to high sensitivity. And it is possible to use nanoparticle tags for designing electrical bioaffinity assays with remarkable sensitivity and multiplexing ability. So far, efforts have always been made to design novel nanomaterials useful in solving emerging bioanalytical problems such as rapidness, anti-interfering ability, specificity, stability and sensitivity. Synergies of nanocomposite materials, generally retaining the functional properties of each component and possibly yield synergistic effects via cooperative interactions, have exploited a new area to miniaturize and optimize nano-scale sensors and electronics. The synergistic interesting new features include but not limited to increased surface area, enhanced electrocatalytic activities, improved biocompatibility, promoted electron transfer and better invulnerability against intermediate species. A lot of efforts have been made to fabricate nanocomposite materials of metals/metal oxides nanostructures and carbon materials, using a number of techniques, including sputtering, sol-gel, hydrothermal, microwave and electrodeposition from different precursor solutions containing complex agents. Among these, electrodeposition is the easiest, most controllable, environment-friendly and robust technique for synthesis of metal/ metal oxides NPs, in which, the size, density, composition and even the shape of NPs could be well-controlled by electrodeposition potential, time, concentration and composition of metal precursor solutions.

Herein, we report a general two-step approach of electrodeposition useful in facile, controllable and 'green' electrochemical synthesis of metal oxide NPs onto carbon supports, using carbon nanotubes (CNTs) as an example. First, metal nanostructures were electrochemically deposited onto carbon supports at a constant potential with the density, size, shape and electrocatalytic activities of the produced nanostructures well-controlled by the time and deposition potential applied as well as the concentration of the precursor solution. Then the as-deposited metallic nanostructures were oxidized into metal oxide nanostructures by repetitive potential cycling with extent of oxidation and generation of metal oxides controlled by the number of potential circles. The as-synthesized metal oxides-CNTs composites were characterized and applied as a glucose sensor for illustration of their electrocatalytic properties.

MI-ThP4 Magnetic Properties and Size Control of $Zn_{0.95}Mn_{0.05}O$ Nanorods Deposited by Pulsed Laser Deposition, T.C. Wu, Y.C. Yeh, D.R. Liu, D.Y. Chiang, National Applied Research Laboratories, Taiwan, Republic of China

The well-aligned ZnO nanorods with 5 at.% of Mn doping ($Zn_{0.95}Mn_{0.05}O$) were deposited on silicon (100) substrates by pulsed laser deposition at three different substrate temperatures ranged from 600 °C to 700 °C, while the structure with and without a ZnO seed layer were both considered. The magnetic and structural properties of $Zn_{0.95}Mn_{0.05}O$ nanorods has been characterized by X-ray diffraction (XRD), energy-dispersive X-ray spectroscopy (EDX), scanning electron microscopy (SEM), high-resolution transmission electron microscopy (HRTEM), and superconducting quantum interference device (SQUID). We demonstrate that the distribution and diameter of well-aligned $Zn_{0.95}Mn_{0.05}O$ nanorods are controllable, which strongly depend on the substrate temperature. Also, the magnetic properties are directly controlled by the morphologies of $Zn_{0.95}Mn_{0.05}O$ nanorods, and are thus appropriate for further applications.

MI-ThP5 Characterization of Metal Oxides Tunnel Barriers for use in a Non-Local Spin Detection Device, A. Matsubayashi, College of Nanoscale Science and Engineering, the University at Albany-SUNY

Metal oxides can be utilized as interfacial layers between ferromagnetic metals and graphene to achieve spin injection into graphene. Utilizing the spin of the electron as well as its charge has the potential to be utilized for logic devices in the post CMOS era. The goal of our research is to inject and readout spins using a non-local measurement device. However the

efficient spin injection has been realized its difficulty due to the conductivity mismatch problem^{1,2}. In order to achieve the efficient spin injection, it has been determined that the insertion of a few nanometers of a tunnel barrier between the ferromagnetic metal and the graphene increases the contact resistance and measured spin lifetime³. However, non-uniformity of the tunnel barriers (pinholes)⁴ lowers the quality of the interface barrier. In this study, we investigate the fabrication of tunnel barrier on graphene using various metal oxides such as aluminum oxide grown under UHV conditions directly on the graphene. Graphene samples were loaded into an ultrahigh vacuum MBE (Molecular Beam Epitaxy) machine. Desired thickness of metals were deposited from a Knudsen cell. Samples were then transferred back into the load lock and exposed to approximately 130 mTorr of pure O₂ for 20 min. Several measurements were performed including scanning electron microscopy, X-ray photoelectron spectroscopy, and angle resolved XPS characterize the electrical and structural quality of the films and their suitability for to be utilized as a tunnel barrier in graphene spin measurements.

References:

- [1] P. C. van Son, H. van Kempen, and P. Wyder, Phys. Rev. Lett. **58**, 2271 (1987)
- [2] G. Schmidt, D. Ferrand, L. W. Molenkamp, A. T. Filip, and B. J. van Wees, Phys. Rev. B **62**, 4790 (2000)
- [3] E. I. Rashba, Phys. Rev. B **62**, 16267 (2000)
- [4] W. Han, K. Pi, K. M. McCreary, Y. Li, J. J. I. Wong, A. G. Swartz, and R. K. Kawakami, Phys. Rev. Lett. **105**, 167202 (2010)

MI-ThP6 In Situ Scanning Tunneling Spectroscopy on Ordered, Epitaxial $La_{5/8-x}Pr_xCa_{3/8}MnO_3$ Films, Z. Gai, Oak Ridge National Laboratory, M. Gao, Chinese Academy of Sciences, P.C. Snijders, H.W. Guo, T.Z. Ward, Oak Ridge National Laboratory, H.J. Gao, Chinese Academy of Sciences, J. Shen, Fudan University, China

Scanning probe microscopy has been shown to be a potent tool to investigate the structural, electronic, magnetic properties as well as their spatial distributions of strongly correlated perovskite manganites. Differences in tunneling spectra were interpreted to originate from the metallic and insulating phases in the material. However, questions were raised and still remain whether SPM on manganites probes bulk characteristics or is limited to surface properties. Complicating factors in this discussion are that most scanning probe studies either were performed on rather rough or grainy (and thus not very well ordered) surfaces, or on surfaces that were contaminated due to exposure to ambient air. Such ill-defined surfaces exhibit many localized surface states that often give rise to non-equilibrium occupation of states, and associated artifacts in scanning tunneling spectroscopy (STS) data, often masking or overwhelming possible bulk contributions. However, an STM does probe the electronic structure at the surface and this can include both surface and bulk contributions. Therefore, even on ideally ordered surfaces such as *in situ* grown and studied epitaxial manganite films, it is still unclear whether surface states (or even surface ground states that are different from their bulk counterparts) that are induced by the broken symmetry of the surface will overwhelm the bulk contributions in STS. We report temperature dependent scanning tunneling spectra recorded on *in situ* grown, single crystalline epitaxial $La_{5/8-x}Pr_xCa_{3/8}MnO_3$ ($x=0.3$) (LPCMO) films with different thicknesses: 100 nm and 25 nm. On the 100 nm LPCMO film, the tunneling spectra show a higher metal-insulator transition temperature as compared to the 25 nm LPCMO film. Consistently, bulk transport data for the two thicknesses of LPCMO films also show different metal-insulator transition temperatures, thus revealing that tunneling spectroscopy on manganites is sensitive to the bulk electronic structure and not limited to surface effects.

This effort was supported by the US DOE Office of Basic Energy Sciences, Materials Sciences and Engineering Division, and Center for Nanophase Materials Sciences, through the Oak Ridge National Laboratory.

MI-ThP7 Promise of New Multiferroics: Synthesis and Characterization of Epitaxial $NiTiO_3$ Films, T. Varga, T. Droubay, M.E. Bowden, S.A. Chambers, B. Kabijs, W.A. Shelton, P. Nachimuthu, V. Shutthanandan, Pacific Northwest National Laboratory

In a search for new multiferroic materials where the direction of magnetization can be switched by an applied electric field, we have looked for materials in which polarization and magnetization are strongly coupled. Recent theory calculations predicted that the family of compounds $MTiO_3$ ($M = Mn, Fe, Ni$), in a certain polymorphic structure (acentric $R3c$), are promising candidates where a polar lattice distortion can induce weak

ferromagnetism. Guided by these insights, a rhombohedral phase of Ni TiO₃ has been prepared in epitaxial thin film form, whose structure is very close to that predicted to be a multiferroic. The synthesis of such new epitaxial films, their full structural characterization along with our first-principles DFT calculations to predict the desired NiTiO₃ structure and its stability are reported.

Plasma Science and Technology Division Room: East Exhibit Hall - Session PS-ThP

Plasma Science and Technology Poster Session

PS-ThP1 Anomalous Copper Contamination Observed during Hydrogen Plasma Processing. *A. Zakharov*, GlobalFoundries, Germany, *P. Geissbuhler*, *C. Waldfried*, Axcelis Technologies, *R. Sonnemans*, Axcelis Technologies, GmbH, Germany, *I.L. Berry III*, Axcelis Technologies

We report on an investigative study into the anomalous copper contamination observed on silicon test wafers run in hydrogen plasma processing systems using substantially oxygen-free plasmas. The copper is believed to originate from trace copper constituents of aluminum and other alloys used in construction of the vacuum system components. The transport of the copper to the wafer surface is consistent with the formation of meta-stable CuH.

Several plasma-ash systems from multiple vendors were tested using VPD/ICP-MS on silicon test wafers processed using hydrogen plus nitrogen gas mixtures. Anomalously high copper contamination levels in excess of 5×10^{11} atoms/cm² were measured. The copper contamination was found to increase linearly with plasma process time and the rate was highly system dependent. Clean systems tended to have higher contamination rates as compared to systems that have run large amounts of mixed processes, suggesting carbon or hydrocarbon deposits on chamber walls can somewhat suppress the CuH formation. Cycling these systems with oxygen plasmas increased the copper contamination rate. Additionally the contamination rate increased with increasing chamber wall temperature suggesting strongly that the chamber construction materials are the source of the contamination. Additionally several systems exhibited increases of cadmium, germanium and nickel. Each of these metals also has stable or meta-stable metal hydrides.

It was found that adding oxygen to the plasma in excess of 1% by volume, suppressed completely the anomalous copper contamination. VPD/ICP-MS measurement showed that 1% or higher oxygen concentration reduced copper contamination to below 1×10^9 atoms/cm².

PS-ThP2 Real-Time Monitoring of Reactors Wall Status during Silicon and Metal Gate Etching. *A.P. Marchelli*, *G.M. Pietrogrande*, MICRON Semiconductor Italia, Italy

One major challenge in plasma etching processes for sub-65nm integrated circuits is to assure the wafer to wafer repeatability.

Particularly in plasma processes etching for IC fabrication, with metal gate, organic or metallic residues are deposited on the chamber walls. Because of the deposition of these layers a large and uncontrolled shifts in the etch process could be observed. To avoid this problem dedicated dry cleaning of the etching chamber must be developed but this methodology requires the precise knowledge of the layer coated on the reactor walls (1). This is not easy because of complexity of the stacks that need several steps of etching with different chemistries. Particularly the sharing of the equipments among many different process increases the complexity of layer coated. In order to assure that every wafer has been etched correctly a real-time monitoring of plasma impedance has been developed. The experiments were performed in a low pressure inductively coupled plasma reactor supplied with 13.56 MHz rf powers. Through the monitoring of dedicated equipment parameter tightly related to the plasma impedance is possible to activate a dedicated fault detection control. During the wafer process, the check of this parameter along dedicated step that use only oxygen, it is possible to get the status of chamber wall in real-time; therefore is possible to activate a recovery action if necessary and don't process any other wafer. In order to validate the correlation between equipment parameter and reactors wall status etch rate test and XRF spectroscopy tests were performed. The innovation of this method consists therefore in the possibility to directly estimate the state of chamber walls during the process without having to affect measures devoted through sample (2).

(1) R. Ramos, G. Cunge and O.Joubert. *J.Vac. Sci. Technol. B* 26(1), Jan/Feb 2008

(2) O.Joubert, G. Cunge, BPellissier, L. Vallier, M. Kogelschatz and E. Pargon. *J.Vac. Sci. Technol. A* 22(3), May/June 2004

PS-ThP3 Reaction Process of Si Surfaces with Hydrogen Plasma. *K. Hara*, *M. Shinohara*, *Y. Takami*, *Y. Takaki*, *Y. Matsuda*, *H. Fujiyama*, Nagasaki University, Japan

Hydrogen plasma generates hydrogen radicals and ions in it. Both of them are important to Si technologies, such as the deposition of Si-related films, the etching of the films and so on; hydrogen radicals generate the adsorption sites by abstracting hydrogen from hydrogen terminated Si surface, while hydrogen radicals terminated dangling bonds of Si films. On the other hand, hydrogen ions also play an important role in Si etching process. Then, it is important to investigate the reaction process of hydrogen plasma with Si surfaces. We investigated the reaction processes at the different substrate bias conditions. The processes were investigated with infrared spectroscopy in multiple internal reflection geometry (MIR-IRAS). Hydrogen plasma was generated by feeding RF (13.56 MHz) power to the coil wrapped the glass tube. Hydrogen plasma was exposed to chemical oxide covered Si(100) surfaces. After the oxide layer was etched, the surface was terminated with hydrogen. Moreover, the surface was distorted, so that the atomic arrangements on the surface were changed into amorphous layer. With the increase of substrate bias which was fed with RF (800kHz) power, the formation of the amorphous layer was increased. Furthermore, we noticed that the main peak position was changed with the exposure in this process; in the initial stage, the main peak was observed between 2000 and 2030 cm⁻¹. In the middle stage the main peak was located at 2060 cm⁻¹. In the final stage the main peak was located at 2100 cm⁻¹. From the assignment of the peak positions, amorphous SiH components were formed in the initial stage; amorphous SiH₂ components were formed in the final stage. The peak at 2060 cm⁻¹ observed in the middle stage can be assigned to the distorted SiH or hydrogen terminated vacancy. It is suggested that the kinds of hydride components are changed with the exposure.

PS-ThP4 Comparative Study on Atmospheric Pressure Plasma Modification on Packaging Material using Microwave and DBD Sources. *J.M. Hong*, *Y.L. Wu*, *T.S. Cho*, *D.N. Ruzic*, University of Illinois at Urbana Champaign

Atmospheric plasma treatment is a very promising way to get hydrophilic or hydrophobic surface characteristics for many applications. In the food manufacturing industry there have been various kinds of technical approaches for prohibiting oxygen or water vapor penetration into products in order to preserve freshness and prolong shelf life. In this study two different types of atmospheric pressure plasmas, microwave and dielectric barrier discharge, are used on paraffin-wax coated paper. Different process recipes were applied on the packaging material and the surface modification results were evaluated. In the case of the microwave torch, a 10% improvement in hydrophobicity in terms of water contact angle measurement result and relative permeability change for water vapor was measured. The water contact angle was increased to $116 \pm 6^\circ$ from $105 \pm 7^\circ$ through applying a plasma treatment using a He/N₂ mixture. For the permeability, three replications were prepared for each condition and weighed periodically. Each sample was prepared with a cup containing 2.0g of de-ionized water covered with treated or untreated packaging paper. According to its different treatment condition, the water loss of the plasma treated sample was 7-9% less than untreated one. This means the plasma-treated material will do better as a protective barrier against water vapor transmission. With the DBD remote plasma, a highly efficient hydrophilic process was used using nitrogen gas with small amount of air or hydrogen insertion. In order to understand the different surface reaction for the two plasma sources, the surface morphologies of treated samples were characterized by scanning electron microscopy and chemical properties were evaluated.

PS-ThP6 Inductively Coupled Plasma-Enhanced Atomic Layer Deposition of Platinum Nano-particles and Platinum Thin Films Using Ar/O₂ Plasma. *B.H. Liu*, *C.C. Kei*, *C.C. Yu*, *D.Y. Chiang*, *C.N. Hsiao*, National Applied Research Laboratories, Taiwan, Republic of China

Platinum nano-particles (NPs) and platinum thin films were deposited by using inductively coupled plasma atomic layer deposition (PEALD). In this PEALD process, the Ar/O₂ reaction plasma was applied to decompose the ligands of Pt precursor (MeCpPtMe₃) at varied substrate temperatures between 150 to 300 °C. The partial pressures of Ar and O₂ were held at 1.5 and 0.5 Torr during the PEALD Pt NPs process. Next the PEALD Pt thin films deposited by using the lower pressure of Ar and O₂ at 0.3 and 0.1 Torr. X-ray diffraction (XRD) patterns show that Pt NPs and thin films are polycrystalline and a preferred orientation along the (111) plane of the fcc structure. Based on the Transmission Electron Microscopy (TEM) measurement, the growth rate of Pt NPs size and Pt thin films thickness is about 0.04 nm/cycle. The Pt thin film 4f XPS spectra consists with the Pt 4f data that observed metallic Pt peaks deposited at 200 °C on Si wafer using Ar/O₂ plasma of 400 W. The step coverage was approximately 100% coated in 170 nm (open diameter) trench structures with 3.5 : 1 aspect ratio. The

low resistivity of Pt NPs and Pt thin films prepared by using 600 and 200 cycles was 1.83×10^{-5} and 1.62×10^{-5} Ω -cm, respectively.

Keywords: inductively coupled plasma, PEALD, platinum NPs

PS-ThP7 Properties and Performance of TiN, TiCN Coatings on Stainless Steel for Commercial Production Equipment, Y.L. Wu, J.M. Hong, T.S. Cho, D.N. Ruzic, University of Illinois at Urbana Champaign

Commercial production equipment coated with TiN and TiCN films were studied experimentally and their material properties and performance were characterized in detail. The goal is to produce a titanium nitride and titanium cabonitride coating on bare stainless steel surfaces that can resist material adhesion on the equipment surfaces. TiN and TiCN were chosen as the coating material due to their superior performance of low friction coefficient and high wear resistivity. Previous studies have shown that the friction coefficient of the coatings could be as low as 0.15 and wear rate of 6×10^{-6} $\text{mm}^3 \text{N}^{-1} \text{m}^{-1}$ whereas the friction coefficient was 0.6 and the wear rate was about 3 orders of magnitude higher for the bare stainless steel surfaces. In this study the TiN and TiCN coatings were made using magnetron reactive sputtering using a titanium target of 300mm in diameter and 1cm thickness with methane and nitrogen as reactive gases. The coating properties were characterized tribology testing. Adhesions of the coatings on equipment surfaces were determined with single-pass scratch tests and the friction coefficients and wear rates were found using pin-on-disc tests. Resistivity on gum base materials were also characterized with the amount of adhered gum based materials and contact angle measurements.

PS-ThP8 The Dry Etching Properties of $\text{Na}_{0.5}\text{K}_{0.5}\text{NbO}_3$ Thin Films in Inductively Coupled Plasma, Y.H. Joo, J.C. Woo, C.I. Kim, Chung-Ang University, Republic of Korea

Recently, the ferroelectric materials are possible to study many fields for the application of the ferroelectric materials. The application of ferroelectric materials in random access memory devices tends to replace both magnetic core and magnetic bubble memories. And observed high electric field tunability with low losses makes this material suitable candidate for various voltage tunable microwave devices. Ferroelectric materials usually have high dielectric constants. From several published works, it was found that the sodium-potassium niobate, $\text{Na}_{0.5}\text{K}_{0.5}\text{NbO}_3$ (NKN) thin films grown on oxide substrate have a great dielectric and piezoelectric characteristics. Ferroelectric NKN thin films attract attention for their superior dielectric, piezoelectric, and crystalline properties. Therefore, we can use NKN thin films for many applications including non-volatile memory, sensors, optical switches, and ultrasonic transducers. The preferential development of anisotropic etching process for NKN thin films is desirable for highly integrated ferroelectric application. Unfortunately, a small number of papers on NKN etch behavior published. The etch characteristics are not known appropriate accurately. This fact makes some difficulties for integration of NKN in the microelectronic technology.

In this work, we investigated etch characteristics of the NKN thin films in inductively coupled plasma. Both NKN etch rate and NKN/SiO₂ etch selectivity were measured as functions of gas mixing ratio, input RF power, and dc bias voltage. The chemical reaction between plasma and NKN thin film surface were investigated by x-ray photoelectron spectroscopy (XPS). Field emission Auger electron spectroscopy (FE-AES) was used for the elemental analysis of the etched surfaces. Field emission scanning electron microscopy (FE-SEM) was used to investigate the etching profile.

PS-ThP9 The Dry Etching Properties of IZO Thin Films in High Density CF_4/Ar Plasma, J.C. Woo, C.I. Kim, Chung-Ang University, Republic of Korea

The Indium zinc oxide (IZO) is a wide band gap transparent conducting oxide that has provoked a great deal of interest recently, due to its many potential applications. It allows the fabrication of devices with a low operating voltage, and the design of such devices will lead the way to the next generation of display technologies based on transparent and flexible devices. IZO thin films have attracted a great deal of attention because of their excellent optical transmission, high conductivity, chemical stability, thermal stability and low compressive stress. Therefore, amongst the various patterning techniques used for IZO thin films, plasma etching is preferred, because it allows for high resolution pattern transfer for optoelectronic device structures. Recently, although the growth characteristics of IZO thin films have been well optimized, the development of an efficient pattern transfer process remains to be achieved. Among the various patterning techniques, the dry etching process has several advantages over the conventional wet etching process, including high resolution and easy process automation. Moreover, there have only been a few studies relating to IZO dry etching using the high density plasma sources favored by modern microelectronic technology. As a result, the influence of the process parameters on the IZO etch rate has not been explored in detail and the IZO etch mechanism is not quite clear.

In this work, we investigated the etching characteristics of IZO thin film using a high density plasma (HDP) system. The etching characteristics of the IZO thin film were investigated in the terms of the selectivity of IZO over SiO₂ as a function of the etch chemistry. The chemical states on the etched surface were investigated by X-ray photoelectron spectroscopy (XPS). Field emission Auger electron spectroscopy (FE-AES) was used for the elemental analysis of the etched surfaces.

PS-ThP10 The Dry Etching Properties of TaN Thin Film Using Inductively Coupled Plasma, J.C. Woo, Y.H. Joo, C. Li, C.I. Kim, Chung-Ang University, Republic of Korea

PLEASE NOTE YOU MUST IDENTIFY A DIFFERENT PRESENTER FOR THIS ABSTRACT. YOU MAY PRESENT ONE PAPER ONLY (ORAL OR POSTER) AT THE CONFERENCE. J. WOO IS CURRENTLY LISTED AS PRESENTER FOR ABSTRACT #1295Recently, to overcome these problems, conventional poly-Si gates on ultrathin SiO₂ dielectric layers could be replaced by metal gates on high-*k* dielectric materials. Metal electrode/high-*k* gate stacks have already been implemented, but require continuous improvement with scaling. Currently, to integrate HF-based high-*k* dielectric materials including HfO₂, HfAlO, HfON, and HfSiO, the use of various metal gate electrode materials including TaN and TiN is being widely studied. Among these materials, TaN/HfAlO are promising candidates for replacing poly-Si/SiO₂. TaN is very attractive due to its high thermal stability, good adhesion, high melting point, and low resistivity (25 to 250 $\mu\Omega/\text{cm}$). To pattern the metal electrode/high-*k* gate stack structure, etching of the metal electrode against a high-*k* dielectric layer using etching processes can be employed. In this approach, a very high etch selectivity of the metal gate electrode to the high-*k* dielectric is required because of the very thin nature of high-*k* dielectric materials. Therefore, a very high etch selectivity of the metal gate electrode to the high-*k* dielectric is also needed to minimize Si damage loss at ultrashallow source/drain regions.

In this work, the TaN thin films were etched in Cl₂/BCl₃/Ar and O₂/Cl₂/BCl₃/Ar plasma. The effects of adding O₂ to the Cl₂/BCl₃/Ar chemistry were investigated for the purpose of improving the etch selectivity of the TaN to SiO₂ layer. The etching characteristics of TaN thin films were investigated in terms of etch rates and selectivity as a function of the gas mixing ratio. X-ray photoelectron spectroscopy (XPS) and Auger electron spectroscopy (AES) was used for elemental analysis of the etched surfaces.

PS-ThP11 Mass Spectroscopy of Metastable Atomic Species in Gas Analysis and Processing Plasmas at High Spectrometer Source Pressures, D. Seymour, A.J. Rees, C. Greenwood, S. Davies, M. Buckley, Hidden Analytical

The availability of particle counters which may be operated at ambient pressures of up to 2×10^{-4} Torr is highly desirable in many current research applications. In one field in particular, it allows mass spectroscopy of gas analysis and processing plasmas to be performed using pressures of this order in the quadrupole mass spectrometer (QMS). These pressures are much closer to those of many processing plasmas so that the sampling of neutral species, in particular, from the plasma is improved. The sampling of ion and neutral species from magnetron plasmas is a good example. The particle counter used in the present investigation, could be mounted axially so as to have a direct line-of-sight view of the sampling orifice of the QMS. Consequently, energetic neutral species such as metastable atoms of helium, which are produced in helium plasmas and have long lifetimes against spontaneous de-excitation, may travel to the detector and have sufficient energy to be counted there. The detection of metastable helium may be of importance in the study of reaction processes during hydrogen (H/HD)-deuterium (D₂) plasma fusion, of which the residual fusion byproduct is helium ash. Furthermore, collision processes in the ionisation source of the QMS, (including Penning ionisation), which are insignificant at the more usual source pressures of below 1×10^{-5} Torr, generate product ion species whose study helps the interpretation of the processes occurring in the plasma reactor. Typical data from neutral gases and plasmas in a range of gas mixtures which include helium or argon with molecular gases such as hydrogen and nitrous oxide are shown. The majority of the data presented consist of electron impact threshold ionisation efficiency curves obtained by scanning the energy of the electrons in the QMS source. The results presented are discussed in terms of processes which include collisions between metastable species such as He (2^1S and 2^3S) at 20.61eV and 19.82eV respectively^[1] having radiative lifetime states of $20 \pm 2 \text{ms}$ ^[2], and also other plasma constituents. The measurements suggest new avenues of research into gas analysis and processing plasmas in which energetic, long-lived, metastable species may have important roles.

[1] Laborie, P, Rees, J.A. Electronic Cross Sections and coefficients, Hydrogen and rare gases, Dunod, 1968

[2] Van Dyck, Robert, S et al. Phys. Rev. A 4, 1327-1336 (1971)

PS-ThP12 Cutoff Probe Using Fourier Analysis for Electron Density Measurement, *B.K. Na, K.H. You, D.W. Kim*, Korea Advanced Institute of Science and Technology, Republic of Korea, *S.J. You*, Korea Research Institute of Standards and Science, Republic of Korea, *S.H. Seo, H.Y. Chang*, Korea Advanced Institute of Science and Technology, Republic of Korea

Wave-cutoff method is an electron density measurement tool. Most of the diagnostic tools, including cutoff probe, need a few seconds to measure the plasma parameters. In this presentation, a fast measurement method using Fourier analysis will be newly introduced. A wave-cutoff probe system consists of two antennas and a network analyzer. A network analyzer provides the transmission spectrum and the reflection spectrum by frequency sweeping. The plasma parameters such as electron density can be obtained through these spectra. The frequency sweeping time, the time resolution of the wave-cutoff method, is about 1~10 seconds.

We proposed a new method to use an impulse generator and an oscilloscope instead of a network analyzer. This method was named 'Fourier cutoff probe method'. A short impulse signal with a few GHz band and its transmitted signal were detected by an oscilloscope, and the Fourier analysis of the signals made a transmission spectra of plasma. The data acquisition time can be reduced with this method.

In this work, 3 diagnostic methods, Langmuir probe, network analyzer cutoff probe, and Fourier cutoff probe, were also compared. The measurement results were well matched. This method provides electron density with time resolution of 10 nano seconds, and it took about 100 milli seconds to make a measurement. This technique is found to be very useful especially in pulsed plasma. Fourier cutoff probe was 40 times faster than Langmuir probe in a pulsed plasma measurement.

PS-ThP13 Full Wave Simulation Study of Multi-mode Plasma Absorption Probes, *C.Y. Kao, W.C. Chen, K.C. Leou, C.H. Hsieh*, National Tsing Hua University, Taiwan, Republic of China

Measurement of plasma density, a key parameter that control the property of processing plasmas and hence the processing results, has been the focus of extensive studies in recent years, not only for characterization of the plasmas but also for development of tools for monitoring of the plasma based processes¹. In this study, a multi-mode plasma absorption probe² was investigated by employing a full wave electromagnetic simulation using a finite element code, High Frequency Structure Simulation (HFSS, ANSOFT CORP). The spherically-shaped probe was formed by two isolated hemispherical conductors, which was enclosed by a layer of dielectrics (alumina). In the simulation analysis, a coaxial line was attached to the spherical probe head and the "driven mode" was adopted, i.e., the wave was fed into the coaxial line and the absorption spectrum, reflection coefficient vs frequency, was then analyzed. The probe was in a plasma, characterized by the collisional electromagnetic plasma permittivity, determined by plasma density, wave frequency and momentum transfer collisional frequency. Simulation results show that the absorption spectrum exhibits a number of resonances, as a result of cavity-like structure resonant modes, as well as the plasma density, similar to the results reported in a previous work based on an electrostatic analysis³. The electromagnetic analysis adopted in this work, however, reveals that the wave also propagates along the interface between the plasma and the coaxial cable, similar to the characteristics of a conventional plasma absorption probe³. This effect thus contributes to resonant peaks in the absorption spectrum that did not appear in the electrostatic analysis. A parametric study by varying the plasma density, probe size and dielectric thickness have been conducted and the results will be presented.

¹ M. A. Lieberman and A. J. Lichtenberg, *Principle of Plasma Discharges and Material Processing*, Wiley, New York, 2005.

² C. Scharwitz, et al, *Appl. Phys. Lett.*, 94, 011502(2009).

³ H. Kokura, et al, *Jpn. J. Appl. Phys.*, Part 1, 38, 5262, 1999.

* Work supported by the National Science Council of Taiwan, ROC.

PS-ThP14 Characteristics of SiO₂ Etching with Ar/C₄F₈/CHF₃/O₂ Gas Mixture in 60 MHz/2 MHz Dual Frequency Capacitive Coupled Plasmas, *M.H. Jeon, S.-K. Kang, J.Y. Park, G.Y. Yeom*, Sungkyunkwan University, Republic of Korea

As the size of the semiconductor device is drastically scaled down to nano-scale, the etching technology of high aspect ratio contact (HARC) is increasingly important. To etch the nano patterned HARC, the multi-layer resist (MLR) structure conventionally composed of a PR, SiON layer, and amorphous carbon layer has been developed because it is difficult to etch HARC directly using a photoresist mask only. However, even though the etching of HARC tends to show higher etch selectivity and proper etch profile with MLR structures, for the next-generation nano-scale dynamic random access memory devices, the etching of nano-scale SiO₂ HARC using fluorocarbon plasmas is becoming more and more important.

Nanoscale SiO₂ contact holes were etched by using C₄F₈/CHF₃/O₂/Ar gas mixtures in dual-frequency capacitive coupled plasmas (DF-CCPs) where 60 MHz source power is applied to the top electrode while 2 MHz bias power is applied to the bottom electrode. We added CHF₃ and O₂ gases to control the etch rate and improve the etch selectivity. Proper additive gas ratios are needed to get the high etch selectivity and maintain CD size. We measured radical intensity, etch rate and SiO₂ surface by using optical emission spectroscopy(OES), X-ray photoelectron spectroscopy(XPS), field emission scanning electron microscopy(Fe-SEM) respectively.

In this study, we confirm that the etch rate and etch selectivity are varied as a function of CHF₃/O₂ gas ratios. The SiO₂ and amorphous carbon layer(ACL) etch rate are increased with increasing the HF power due to the improvement of gas dissociation. But as increasing the HF power, etch selectivity is saturated. In this study, Highest etch selectivity of about 6 is obtained at HF power 300 W, LF power 500 W, Ar/C₄F₈/CHF₃/O₂ = 150/20/25/5 sccm, process pressure of 20 mTorr.

PS-ThP15 An Experimental Study on Large-Area Multi-Electrode Discharge for the Deposition of Microcrystalline Silicon Thin Film for Solar Cell, *Y.S. Lee, S.H. Seo, H.Y. Chang*, Korea Advanced Institute of Science and Technology, Republic of Korea

Recently, there are many researches in order to increase the deposition rate (D/R) and improve film uniformity and quality in the deposition of microcrystalline silicon thin film. These two factors are the most important issues in the fabrication of the thin film solar cell, and for the purpose of that, several process conditions, including the large area electrode (more than 1.1 X 1.3 (m²)), higher pressure (1 ~ 10 (Torr)), and very high frequency regime (VHF, 40 ~ 100 (MHz)), have been needed.

But, in the case of large-area capacitively coupled discharges (CCP) driven at frequencies higher than the usual RF (13.56 (MHz)) frequency, the standing wave and skin effects should be the critical problems for obtaining the good plasma uniformity, and the ion damage on the thin film layer due to the high voltage between the substrate and the bulk plasma might cause the defects which degrade the film quality.

In this study, we will propose the new concept of the large-area multi-electrode (a new multi-electrode concept for the large-area plasma source), which consists of a series of electrodes and grounds arranged by turns. The experimental results with this new electrode showed the processing performances of high D/R (1 ~ 2 (nm/sec)), controllable crystallinity (~70% and controllable), and good uniformity (less than 10%) at the conditions of the relatively high frequency of 40 MHz in the large-area electrode of 280 X 540 mm². And, we also observed the SEM images of the deposited thin film at the conditions of peeling, normal microcrystalline, and powder formation, and discussed the mechanisms of the crystal formation and voids generation in the film in order to try the enhancement of the film quality compared to the cases of normal VHF capacitive discharges. Also, we will discuss the relation between the processing parameters (including gap length between electrode and substrate, operating pressure) and the processing results (D/R and crystallinity) with the process condition map for μ c-Si:H formation at a fixed input power and gas flow rate.

Finally, we will discuss the potential of the multi-electrode of the 3.5G-class large-area plasma processing (650 X 550 (mm²)) to the possibility of the expansion of the new electrode concept to 8G class large-area plasma processing and the additional issues in order to improve the process efficiency.

PS-ThP16 Qualitative Research on Low-Damage Neutral Beam Etching Effect of Mechanical Properties, *Y. Nishimori, U. Shinji, K. Tomohiro*, BEANS Project, Japan, *S. Masakazu*, University of Tokyo and BEANS Project, Japan, *G. Hashiguchi*, Shizuoka University and BEANS Project, Japan

The Neutral Beam Etching (NBE) system has been expected to provide a damage-free top-down process for organic and inorganic materials and facilitate the practical development of future Nano scale devices

In order to examine the mechanical damage-free effect by NBE, we have conducted NBE surface treatment to microcantilever formed over an 8 – inch wafer from the upper surface several times, and measured the resonance frequency and the quality factor (Q-factor) of 52 cantilevers after each treatment.

The NBE treatment removes about 50nm, 100nm, and 500nm thick silicon surface layer, respectively.

The Q-factor of cantilevers is attributed by summation of various kinds of energy dissipation mechanisms such as air damping, thermo elastic damping, support, and surface dissipation.

Based on the theoretical consideration of mechanical vibration, we have designed the microcantilever having 30 μ m in width, 150 μ m in length and 2 μ m in thickness, by which the surface energy dissipation become dominant compared to other ones in high-vacuum condition.

In general, Q-factor is a function of the resonant frequency (f_r) so that we can't argue the effect of NBE treatment from the Q-factor change as it is. Therefore we adopt the values Q-factor divided by resonant frequency (Q/ f_r value) which becomes independent of the thickness in case that the Q-factor is dominated by the surface dissipation and is a good parameter to represent surface dissipation.

From the viewpoint of transition of Q/ f_r value taken after each NBE treatment, surface dissipation of the cantilever was increased with each treatment process and saturated after adequate NBE treatment.

This indicates that surface damage introduced during fabrication process can be removed completely by slight surface etching using NBE.

In the conference, we will report the precise results of the NBE treatment experiment.

PS-ThP17 Free-standing Anodic Aluminum Oxide on Silicon Substrate by using Neutral Beam Etching, C.K. Kim, K.S. Min, J.S. Oh, G.Y. Yeom, Sungkyunkwan University, Republic of Korea

When the Anodic Aluminum Oxide (AAO) is used as the solid mask, compared to the patterning using electron-beam lithography and block copolymer, the patterning using AAO is cheaper, more reliable, and easier in controlling the size and shape. However, due to the stress at the interface between the aluminum and the substrate, the alumina barrier layer is formed at the bottom of the AAO holes during the formation of AAO and it prevents direct physical and electrical contact to the substrate.

In this work, to study the effect of surface charging on the removal of the barrier layer, the Cl_2/BCl_3 neutral beam etching has been used and the results were compared with the AAO etched by an ion beam etching. By the neutral beam etching with BCl_3 containing gas mixtures, the barrier layer was successfully removed due to the formation of volatile BO_2Cl_2 during the etching. However, when the barrier layer was etched using the ion beam with the BCl_3 containing gas mixtures, even though AAO itself is etched, the barrier layer located near the bottom of the AAO pore was not easily etched due to the charging of the AAO pore similar to the case of conventional reactive ion etching.

PS-ThP18 Synchronous Pulsed Inductively Coupled Plasma Source for Controllable Charged Process, K.S. Min, J.S. Oh, C.K. Kim, G.Y. Yeom, Sungkyunkwan University, Republic of Korea

A high-density ion source derived from an inductively coupled plasma is a useful tool in the fabrication of devices. A disadvantage of the technique is that charge-induced damage can cause irreversible changes in the device properties. In order to avoid or to compensate for the non-uniform accumulation of positive and negative charges near the treated surface, a number of low-damage processes have been proposed. The most promising of these processes uses high-energy 10–1000 eV beams of fast atoms and radicals for surface treatment.

This letter reports on a different method of negative beam formation that has potential application to neutral beam etching. In particular, we obtain a flux of fast neutral atoms with narrow energy and angular distribution from an initially negative ion beam which is extracted from the discharge volume with energy of 10 – 500 eV and then neutralized. By increasing the pulse frequency of the antenna voltage to 20 kHz and applying a synchronized bipolar potential to the accelerating electrodes, it is possible to produce a high-density negative ion beam whose energy level is determined by the amplitude of the extraction potential. During the discharge, a positive potential is applied to the extraction electrode and a negative potential to the focusing electrode. In the afterglow period, these potentials are switched, allowing high-energy negative ions to escape the source. The lower and upper limits of the bipolar extraction potential on the two electrodes can be varied independently, so that the ratio of negative ions to positive ions in the resulting beam can be adjusted from 0% to 100%.

PS-ThP19 Initial Studies of a-Si Deposition and Nano-Crystallization using a Novel Reactor with Rotating Substrates, Z. Chen, J.A. Mucha, V.M. Donnelly, D.J. Economou, University of Houston, Y. Lee, A.J. Akey, I.P. Herman, Columbia University

Amorphous silicon deposition and nano-crystallization experiments were performed in a novel reactor with rotating substrates. Separate plasma sources were used for deposition (a capacitively coupled silane/helium plasma) and crystallization (an inductively coupled hydrogen plasma). Substrates were exposed sequentially and repeatedly to the deposition and crystallization plasmas for different times by varying the rotation speed. Radical concentrations in the plasma were monitored by optical emission spectroscopy while stable products were measured using a mass spectrometer. Films were characterized by spectroscopic ellipsometry (thickness, optical constants), Fourier transform infrared absorption (silicon-hydrogen bonding, hydrogen concentration), Raman spectroscopy and X-Ray diffraction (crystalline structure, degree of crystallization).

Results will be presented for different plasma operating conditions, substrate temperatures, and exposure times in the deposition and crystallization plasmas. The effect of “cross-talk” between the two plasmas and methods to prevent it will also be discussed.

Supported by the University of Houston GEAR Program and DoE

PS-ThP20 Fundamental Overview on a Controllable Optical Emission Spectroscopy Diagnostic System for Analysis of Process Chemistry, G. Padron-Wells, P.L.S. Thamban, The University of Texas at Dallas, J. Hosch, Verity Instruments Incorporated, L.J. Overzet, M.J. Goeckner, The University of Texas at Dallas

An Electron Beam Exciter device has been developed to perform as a controllable optical emission spectroscopy diagnostic system. In this design, a small to moderate amount of current extraction (0-5 mA) is necessary to achieve the desired emission signal to produce reliable optical measurements utilized in etch process monitoring and control. Current extraction from this downstream plasma system is achieved in a Non-ambipolar Flow regime. Non-ambipolar flow occurs when all electron thermal flux, from the exciter plasma system, exits through a uniform electron sheath formed about the perimeter of a Nozzle Aperture (area A_e) while the ions are lost to the Exciter ICP grounded wall (area A_i). Electron extraction from the exciter ICP is maximized when the ratio of the ion loss collection area (A_i) to the electron loss collection area (A_e) is proportionally equal to the square root of the ratio of the ion mass to the electron mass, and the ion sheath potential drop to the Exciter ICP grounded wall is much larger than T_e/e . To investigate the degree of Non-ambipolar Electron flow in our device, we have tested a set of manufactured Nozzle extractors with different geometrical dimensions so as to discern the influence of A_i/A_e on the electron extraction process in low pressure (5-35 mTorr) Ar discharges. Strong agreement is observed between the measured plasma parameters at the ICP extraction region and the total amount of extracted current, I_e . In addition there is a measurable energy dependent response in the ratio of $I_i(E)/I_e(E)$ indicative of electron-atom/molecule collision cross section for ionization. We have measured this ratio response in Ar and O₂ atmospheres. This project is funded by NSF-Grant (CBET - 0922962) and Verity Instruments.

1P. L. Stephan Thamban; J. Hosch; M. J. Goeckner. *Rev. Sci. Instrum.*, 2010, **81**, 013502

2B. Longmier; S. D. Baalrud; N. Hershkovitz. *Review of Scientific Instruments*, 2006, **77**, 113504 (1-8)

3S. D. Baalrud; N. Hershkovitz; B. Longmier. *Physics of Plasmas*, 2007, **14**, 042109 (1-6)

PS-ThP21 Fluid Model Simulation of Controllable E-beam, D. Urrabazo, G. Padron-Wells, P.L.S. Thamban, M.J. Goeckner, University of Texas at Dallas

We have developed a new chemical diagnostic based on a controlled electron beam. Specifically we make use of an inductively coupled plasma, electron extraction optics and traditional optical emission spectroscopy. In the work reported here, a computer simulation was developed which allows the use of three different models: ambipolar, classical, and revised classical. Here, we investigate both the strengths and weakness of the various models as well as determine which system characteristics can be used to enhance the system performance. These simulation results will be compared to electrical probe measurements gathered from the experimental apparatus. This work is supported in part by NSF (Grant CBET- 0922962) and Verity Instruments.

PS-ThP22 Characterization of an ECR Etching Reactor using a Retarding Field Energy Analyzer, B. Dolinaj, D. Gahan, P. Scullin, D. O' Sullivan, MB. Hopkins, Impedans Ltd., Ireland, V. Milosavljevic, S. Daniels, NCPST Dublin City University, Ireland

Microwave plasma sources are widely used in industrial plasma processing devices for their favorable characteristics. In particular, electron cyclotron resonance (ECR) reactors offer a number of desirable characteristics for plasma etching and deposition, including higher plasma density, lower ion energy, lower pressure operation, and higher uniformity compared with the conventional radio frequency (RF) type plasmas. ECR devices designed for commercial use usually provide the user with very limited access for controlling and characterizing the plasma conditions.

Retarding field energy analyzers (RFEAs) are generally used to measure the ion energy distribution function (IEDF) at electrically grounded surfaces. An RFEA can also be used to measure IEDFs at the surface of radio-frequency (RF) driven electrodes by electrically isolating it from the ground reference. The RFEA then “follows” the RF bias without disturbing it. Using the same principle, but applying grid bias signals of opposite polarity, one can also measure the electron energy distribution function (EEDF) at

the surface of RFEA. From the measured IEDFs and EEDFs it is possible to calculate the respective ion and electron flux and energy. These quantities are key parameters in plasma surface processing. Therefore, the metrological capabilities of the RFEA together with its non-perturbing in situ operation makes it a convenient diagnostic tool for characterizing plasmas in devices like ECR etching reactors.

In this work we present IEDF measurements at the surface of an RF driven electrode using a RFEA installed in an industrial ECR etching reactor. The RFEA is mounted at the RF biased electrode (on which the SiO₂ wafer is mounted) and is connected through high input impedance low pass filters to the ground referenced grid bias signals. The RFEA installation does not require any modifications to the reactor since the signal cabling is taken out to atmosphere through an existing unused port located in the vacuum pump tunnel. The discharge control parameters were varied as follows; pressure 5 to 20 mTorr, flow rate 10 to 50 sccm of pure argon and oxygen, microwave input power 750 to 1500 W, RF input power 0 to 250W, and a variety of magnetic field profiles. The radial location of RFEA has also been varied. The measured fluxes and energy distribution of the ions and electrons impacting the wafer surface are presented and discussed.

PS-ThP23 Simulations of the Radial Line Slot Antenna Plasma Source. *P. Ventzek*, Tokyo Electron America, *S. Mahadevan*, *L. Raja*, Esgee Technologies, *T. Iwao*, Tokyo Electron Technology Development Institute, INC., *L. Chen*, *M. Funk*, *B. Lane*, *R. Sundararajan*, Tokyo Electron America, *J. Yoshikawa*, Tokyo Electron Technology Development Institute, INC., *J. Zhao*, Tokyo Electron America, *T. Nozawa*, *C. Tian*, *K. Ishibashi*, Tokyo Electron Technology Development Institute, INC.

The Radial Line Slot Antenna (RLSA) plasma source couples microwave power through a slot antenna structure and window to a plasma characterized by a generation zone adjacent to the window and a diffusion zone that contacts a substrate. The diffusion zone is characterized by a very low electron temperature. This property renders the source useful for soft etch applications and thin film processing for which low ion energy is desirable. Models of the RLSA source typically include ambipolar diffusion as an approximation enabling 2D and 3D simulations to be feasible. While such models have predictive value, they also have shortcomings when surface charging, capacitive coupling through a substrate or electronegativity are important. In this presentation we describe a self-consistent fluid model of the plasma kinetics of the RLSA source and demonstrate 3D source characteristics for benchmark argon and oxygen plasmas with and without capacitive coupling. Comparisons between the ambipolar model and self-consistent model are made.

PS-ThP24 Dual-Coil, Dual-Frequency ICP Source for Plasma Processing. *V. Nagorny*, *D. Lee*, Mattson Technology, Inc.

RF plasma sources used in modern plasma etch applications are required to provide a high plasma uniformity and variety of plasma controls, including independent plasma profile, plasma density and ion energy controls. They must be able to sustain a stable plasma in a very different gases and under very different conditions (gas flow, gas pressure, etc.). Finally, going forward the system has to produce a minimum impact on environment (energy consumption, EM emission). Mattson Technology has developed an etch tool with a new and efficient ICP source that uses two coils operating at significantly different frequencies (13.56 and 2 MHz) by utilizing a ferromagnetic core in a low frequency coil. Tests on the tool revealed that

- It provides high-density plasma generation, with no capacitive coupling between plasma and the source;
- There is no interference between higher and lower frequency RF subsystems;
- It provides good plasma and process profile control;
- It has wide processing window (gas pressure, gas flow, gas composition, source and bias power);
- High efficiency and stability of operation with both electropositive and electronegative gases.

PS-ThP25 Development of Inductively Coupled Hydrogen Plasma Source with a Ceramic Tube. *J. Cho*, *J. Yang*, PSK Inc., Republic of Korea, *S. Park*, *D. Lee*, Inha University, Republic of Korea

Organic photoresist in semiconductor photolithographic process has been removed by downstream oxygen plasma which is generated in a quartz chamber or tube. In case of stripping heavily ion-implanted photoresist whose surface is carbonized by energetic ions, it is sometimes necessary to add CF₄ gas to oxygen. Moreover, hydrogen based plasma begins to be used to strip photoresist coated on low-k dielectric layers, where oxygen plasma is known to degrade low-k dielectric films. However, fluorine or hydrogen ions can attack the quartz walls and generate particles. To solve this problem, plasma generation chamber should be made of materials inert to fluorine or hydrogen ions. In this work we have designed and constructed a

plasma source chamber made of ceramic tube. A 12 cm diameter ceramic tube is surrounded by a Faraday shield and wound by a 4 turn helical coil connected to 13.56 MHz RF power. There are also two turn dummy coils, which are electrically grounded, at the top and bottom sides of the 4 turn power coil. All coils have hollow square cross-section and cooling water flows through the coils. At the bottom of the 25 cm long tube an electrically grounded baffle with many small holes are located and only radicals are fed to the stripping process chamber for 300 mm wafers. Because ceramic materials usually have larger thermal expansion coefficient than quartz, larger thermal stress exists in the ceramic tube across tube thickness and at gaps between cooling coils, which results in breakage of ceramic tube. It is very important to achieve good thermal contacts between cooling water coils and tube wall and thus small temperature gradient in the tube. We have investigated the temperature profiles and thermal stress to the ceramic tube in terms of ceramic tube materials (Al₂O₃ and AlN), types of ceramic paste to glue cooling coils to the ceramic tube, size of cooling coils, thickness of ceramic tube, and RF impedance matching methods. It is found that AlN which has larger thermal conductivity than Al₂O₃ shows no breakage of tube. Size of cooling coils and types of ceramic paste have no effect on tube breakage. In case of Al₂O₃, thinner tube survives from breakage. It is confirmed that little side wall attack is observed after 1000 runs of photoresist strip by H₂/N₂ plasma.

PS-ThP26 Capability of Microwave Plasma Source for 450 mm Etching Apparatus. *S. Obama*, *M. Izama*, *H. Tamura*, Hitachi High-Technologies Corp., Japan, *K. Maeda*, Hitachi Ltd., Japan

To produce semiconductors at low cost, the transition to 450 mm-sized wafers is being considered. For semiconductor fabrication on 450 mm substrates, the etching performance is expected to equal or exceed 300 mm substrate capability with improved productivity requirements. A 450 mm substrate capable apparatus was developed on a proven plasma source using microwave electron cyclotron resonance (ECR) currently utilized for 300 mm equipment. We have evaluated plasma uniformity by using: 1) Single Langmuir probe with -50 V bias to measure ion current flux (ICF) distribution in the plasma reactor. The plasma generated area and the spatial distribution of ICF were scanned in the radial and z-axis directions in the reactor. 2) A 41-point wafer stage to measure ICF distribution. 3) Etch rate uniformity of poly-Si and SiO₂ using coupon samples attached on 450 mm bare Si wafers. We used HBr/Cl₂/O₂/Ar gas and 0.1-10 Pa pressure range as test conditions.

We found that the high density plasma generated at the ECR zone and the shape of the plasma was ring-shaped. This ring-shaped plasma diffused and became increasingly uniform, finally becoming almost flat at a height of 25 mm above the wafer stage. To evaluate ICF distribution of the wafer stage, 41 pads were used to measure plasma density distribution using about 500 test conditions. By controlling the magnetic fields, non-uniformity of ICF below ±5% was achieved for several test conditions of gas and pressure. Poly-Si and SiO₂ etching rate were observed to be very similar to rates seen using 300 mm substrate equipment with non-uniformity below ±1% within a wafer.

In this preliminary study, though we need more process evaluation by using whole blanket wafers and patterned wafers, the microwave ECR plasma apparatus for 450 mm wafers achieved the same level of process performance as the 300 mm equipment.

PS-ThP27 Plasma-based Techniques for Doping Three-Dimensional Structures. *G. Papisoulotis*, *K. Han*, *H. Persing*, *L. Godet*, Varian Semiconductor Equipment Associates, Inc.

Increasingly stringent demands for maximum device speed and control of random dopant fluctuation effects dictate changes in device architecture, with FinFET adoption becoming a viable possibility for device scaling at and beyond the 15 nm technology node. Three-dimensional architectures pose a fundamental challenge for traditional ion beam implant processes, since, depending on the aspect ratio of the structure, certain sections can be inaccessible to the dopant beam. Plasma immersion ion implantation (Plasma Doping), which has been adopted as an enabling, production-worthy technology in the ultra high dose and low voltage regime for advanced DRAM device nodes, can be an alternative capable of overcoming these limitations. In this work, experiments are carried out using a VIISta PLAD system, which uses an ICP source to generate a discharge and a series of negative dc voltage pulses applied to the substrate to accelerate ions towards it. Silicon trenches are implanted using an AsH₃-containing gas mixture in the PLAD reactor. The presence and activation of the N-type dopant onto the #D structures are characterized by physical (Secondary Ion Mass Spectrometry, Transmission Electron Microscopy, Energy Dispersive X-ray spectroscopy) and electrical methods, and discussed in conjunction with analysis of the gas phase in the plasma chamber. Our experimental results indicate the occurrence of a combination of implant and ion assisted deposition processes. It is shown that balancing the constituents of a plasma doping process and plasma characteristics such

as electron temperature and gas phase composition is required to allow dopant incorporation into sidewalls of 3D structures.

PS-ThP28 Study of Low-k Dielectric Damage in a Radial Line Slot Antenna (RLSA) Reactor. *Y. Susa*, Tokyo Electron Technology Development Institute, INC., *R. Sundararajan, J. Zhao, L. Chen*, Tokyo Electron US Holdings Ltd., *T. Nozawa*, Tokyo Electron Technology Development Institute, INC., *J.A. Mucha, D.J. Economou, V.M. Donnelly*, University of Houston, *R. Wise*, IBM Research

Low-k dielectrics are widely used as insulating materials in ULSI circuits. In BEOL processes, etching of low-k layers can cause serious damage, especially during photoresist ashing. In this work, a Radial Line Slot Antenna (RLSA) microwave plasma source was used in an effort to minimize damage to low-k dielectrics as a result of photoresist ashing. The focus of the work was ashing in CO₂-containing gas mixtures of test wafers partially covered with blanket low-k and photoresist layers. Damage to the SiCOH (k=2.5) low-k dielectric was characterized using Spectroscopic Ellipsometry, FTIR and XPS. It was found that low pressure (~5 mTorr) and high bias voltage (~2000 V) were beneficial in terms of minimizing low-k damage. XPS revealed that, under these conditions, an oxide "crust" formed on the surface of the low-k, that apparently protected the underlying material. Low pressure favors an enhancement of the ratio of the ion -to- O-atom flux. Energetic ions can be instrumental in forming this oxide crust by near surface ion implantation. The oxide hinders diffusion of the (already low density) O atoms into the low-k film resulting in minimal damage.

PS-ThP29 New Pulsed Plasma Generator for producing near Arc Free Discharges for Reactive Magnetron Sputter Processes. *R. Chistyakov, B. Abraham*, Zond Inc/ Zpulsar, *J.Y. Park*, SEMICAT Inc

New pulsed plasma generator for reactive magnetron sputter processes was developed. (old sentence)

A new pulsed plasma generator for reactive magnetron sputter processes has been developed. (new sentence)

Compare with existing pulsed DC plasma generators new generator has high current capabilities in the range of 100 – 300 A. (old sentence)

Compared to existing pulsed DC plasma generators, the new generator has high current capabilities in the range of 100 – 300 A. (new sentence)

In proposed method near arc free magnetron discharge in reactive atmosphere can be generated by adjusting the frequency and amplitude and shape of the voltage pulses. (old sentence)

In the proposed method, near arc free magnetron discharge in reactive atmosphere can be generated by adjusting the frequency and amplitude and shape of the voltage pulses. (new sentence)

The application of new pulse plasma generator for reactive sputtering of SiN, SiO₂, AlN and TiO₂ films at ENDURA 200 mm tool (AMAT) will be discussed. (old sentence)

The application of new pulse plasma generator for reactive sputtering of Si₃N₄, SiO₂, AlN and TiO₂ films at ENDURA 200 mm tool (AMAT) will be discussed. (new sentence)

Transparent Conductors and Printable Electronics

Focus Topic

Room: East Exhibit Hall - Session TC-ThP

Transparent Conductors and Printable Electronics

Poster Session

TC-ThP1 A Combinatorial Thin Film Sputtering Approach of the Synthesis and Characterization of Al₂O₃-TiO₂ High-k Dielectrics for Oxide TFT Application. *J.H. Noh, J. Noh, P.D. Rack*, The University of Tennessee

For the last decade, oxide based thin-film transistors (TFTs) have been extensively investigated because of their transparency, high mobility, low process temperature which are expected to serve as the basis for new optoelectronic and flexible devices. However, most of the work on oxide TFTs still rely on conventional dielectrics from Si technology, such as plasma-enhanced chemical vapor deposited (PECVD) SiO₂ or SiN_x with process temperature of 250–300°C. For high performance, low-cost and flexible electronics, high-k dielectrics at low process temperatures are needed. rf sputtering is alternative process for low temperature dielectrics. Usually, the deposition rate with oxide target is very low, so it is not compatible for mass production. In order to overcome this problem, reactive sputtering is adapted in this study. Although oxide TFTs with low-temperature sputtered materials such as Al₂O₃, HfO₂, Y₂O₃, Ta₂O₅ have

already been reported in the literature, TFTs performance are worse than standard higher temperature dielectrics because of high interface trap density due to low temperature. In order to improve the TFT performance, high-k materials are preferable. However, most of the high-k materials show a polycrystalline structure and small bandgap, hence the leakage current is high and breakdown voltage is low. These problems can be overcome through a combination of high-k but low bandgap and low-k but large bandgap materials. In this study, TiO₂ is chosen as a high-k material because of very high dielectric constant of ~80, and Al₂O₃ is chosen as a low-k material because of large bandgap of 8.7 eV. For optimization of high dielectric constant and low leakage current, a combinatorial thin film sputtering approach is used for the synthesis and characterization of Al₂O₃-TiO₂ high-k dielectrics because a combinatorial thin film sputtering approach can yield a wide range of compositions via a single co-sputter deposition process. The composition ranges of the films are simulated using a co-sputtering simulation and compared favorably to compositions measured by the wavelength dispersive spectrometer (WDS). The TFTs are fabricated with a bottom-gate staggered structure using amorphous indium gallium zinc oxide (a-IGZO) and In₂O₃ as the semiconducting active layer. Standard I-V and C-V data on the dielectric multilayers will be compared as a function of composition and finally, the TFTs' performance will be presented according to the relative contents of TiO₂ and Al₂O₃.

TC-ThP2 Fabrication and Characterization of Sub-micron OTFT Using Ink Jet Combined Imprint Process. *K. Kim, N. Kwon, I. Chung*, Sungkyunkwan Univ., Republic of Korea

We fabricated sub-micron organic thin film transistors on polyethersulphone (PES) substrate using ink jet printing combined with an imprint method. The channel lengths of OTFTs were in the range between 500 nm and 1 μm. 6,13-bis(triisopropylsilylethynyl) (TIPS) pentacene was used as an active material and Polyvinyl alcohol (PVA) was chosen as a gate insulator. TIPS pentacene was printed by jetting onto the confined channels which were prepared using imprinting. The surface of confined channel was modified by UV irradiation in order to enhance the crystallinity of tips pentacene. The physical properties were analyzed using SPM, SEM, and XRD. The electrical properties were extracted from the transfer characteristics which were measured using Keithley-4200.

TC-ThP3 Study on Multiple Stacked 6,13-bis(triisopropylsilylethynyl) (TIPS) Pentacene for Improved Organic Thin Film Transistor. *S. Lee*, Sungkyunkwan Univ. & Samsung Mobile Display, Republic of Korea, *J.J. Han, K. Kim, I.J. Bae, I. Chung*, Sungkyunkwan Univ., Republic of Korea

We found that the crystallization of TIPS pentacene thin film plays an important role in determining the electrical property of organic thin film transistor (OTFT). Ink jetted TIPS pentacene film reveals 2 different types of grains namely due to the coffee strain effect. The better electrical properties were obtained from the OTFTs with bigger grains that had been possible due to the multiple stacked TIPS pentacene layer. Poly-4-vinylphenol (PVP) was used as a gate insulator, and Au electrode was evaporated using a shadow mask. The channel lengths of OTFTs with the bottom gate structure were 20-50 μm. The physical properties of the TIPS pentacene films were analyzed using optical microscope (OM), x-ray diffraction (XRD) and secondary electron microscopy (SEM). The electric characteristics of OTFT were obtained using Keithley- 4200.

TC-ThP4 Catalyst-assisted Pulsed Laser Deposition of Tin (IV) Oxide on Si Substrates: Growth Evolution of Low-dimensional Nanostructures. *K.T. Leung*, University of Waterloo, Canada

Single-crystalline nanostructures of SnO₂ have been grown with the aid of size-controllable gold nanoisland catalysts supported on a Si substrate by using the Pulsed Laser Deposition (PLD) method. By changing the gas atmosphere and manipulating the deposition at a relatively low substrate temperature (500-700°C), we produce faceted nanobricks, nanograss, and nanoribbons on oxidized Si and cubic nanoparticles on H-terminated Si. Scanning electron microscopy clearly shows the faceted morphology of these one-dimensional and zero-dimensional nanostructures and suggests a vapour-solid and a vapour-liquid-solid growth mechanisms for nanoparticles and nanobricks and for nanograss and nanoribbons, respectively. X-ray diffraction results reveal the tetragonal crystalline phase of the SnO₂ nanostructures, and the relative intensity ratios obtained for different peaks further show a preferred growth orientation of (101) for the nanoparticles and nanobricks, and of (200) for the nanograss and nanoribbons. For nanograss and nanoribbons, transmission electron microscopy confirms the single-crystalline nature of these nanostructures, and the corresponding high-resolution and selected area electron diffraction data illustrate their different growth orientations that generally lead to the preferred growth directions as inferred from the corresponding X-ray diffraction data. We have also recently used Helium Ion Microscopy to elucidate not only the intricate surface details but also the growth evolution of these SnO₂ nanostructures. These results demonstrate the versatility of

the catalyst-assisted PLD technique in depositing a variety of SnO₂ nanostructures, which can be easily optimized and/or modified by appropriate doping within the PLD method for producing desirable optoelectronic, magnetic, gas-sensing, and semiconducting properties for emerging applications.

TC-ThP5 From Discrete and Hollow Nanocavities to the Formation of Continuous Indium-Filled Indium Oxide Nanotubes. *M. Kumar*, South Dakota State University, *B.R. Mehta, J.P. Singh*, Indian Institute of Technology-Delhi, India

The growth mechanism for single crystalline indium oxide nanotube is still under debate in scientific community. The mechanism was proposed for the growth of nanotubes based on the growth parameters dependent morphological transformation from discrete and hollow nanocavities in nanowires to continuous indium-filled indium oxide nanotubes. The gas flow rate induced change in indium partial pressure and hence supersaturation during reaction of species on substrate decides the growth of two different nanostructures. We discussed a unified growth mechanism based on vapor-solid growth followed by the out diffusion or in-diffusion of metal indium depending on its partial pressure during growth. The out diffusion of indium resulted discrete and hexagonal nanocavity enclosed with minimum surface energy planes, {111} while the higher partial pressure of indium support the merging of discrete nanocavities into continuous connecting and filled with In metal.

Tribology Focus Topic

Room: East Exhibit Hall - Session TR-ThP

Tribology Focus Topic Poster Session

TR-ThP1 Subsurface Characteristics of an Abraded Fe-0.4wt%C Martensitic Steel using Nanoindentation and Cross-Sectional TEM Techniques. *F. Katsuki*, Sumitomo Metal Industries, Limited, Japan

The present investigation of unidirectional abraded surfaces of a martensitic (0.4 wt%C) steel with silicon (1.5wt%Si), chromium (1.5wt%Cr) and molybdenum (1.9wt%Mo) addition elucidates the work hardening and the softening near the surface layer caused by abrasion, particularly its relation to the wear behavior. The abrasion testing was performed using a pin-abrasion apparatus in which a small pin of the specimen was ground on an abrasive paper at an applied load of 2.1N and sliding speed of 0.66m/s. Crushed silica particles (size: 15-67 μ m) were used as the abrasive medium. The abraded surfaces were examined with a nanoindentation apparatus to evaluate the variation of nanohardness with sliding time on a nanometer scale. A cross sectional transmission electron microscope (TEM) technique was also employed to clarify the structural changes in the region close to the abraded surface. It has been found that abrasion induced work hardening with sliding time was observed in the case of chromium and molybdenum addition steels. A fine dispersion of molybdenum carbide (Mo₂C) was observed in the surface of the molybdenum steel after abrasion. Mo₂C precipitates at approximately 550°C, indicates that surface and near surface temperatures would be over the carbide formation temperature by the abrasion induced frictional heating. On the other hand, the softening has been indicated to be caused by the abrasion heating leading to some tempering effects in the case of the silicon addition steel. Work hardening and softening caused by abrasion induced subsurface deformation and frictional heating respectively seem to be two processes taking place simultaneously which counteract each other's effect. Metallurgical reaction such as precipitation and temper by frictional heating has been found to play an important role in controlling the wear characteristics of steels. The influence of the alloying element addition on the wear response of the martensitic steel will be discussed.

TR-ThP2 The Lubrication Characteristics of Molybdenum Disulfide Films by RF Magnetron Sputter. *A. Kasahara, M. Goto, M. Tosa*, National Institute for Materials Science (NIMS), Japan, *T. Mariyama, J. Nakagawa, K. Endo*, Toyama Co., Ltd., Japan

For vacuum applications, lubricants which have low vapor pressure and good tribological performance are required. Solid lubricants have been widely adopted for vacuum applications due to their low vapor pressure. Thin film lubricants and high-temperature solid lubricants are discussed as the latest alternatives to fluorine grease. These lubricants feature lower outgassing for clean and vacuum environments. One big drawback of solid lubrication is limited life. We investigate solid lubricant in order to develop high performance ultra-high vacuum (UHV) manipulation mechanism and high-temperature drive devices. We focused sputtering coating method and Molybdenum Disulfide (MoS₂), since this material has been reported to be suitable in vacuum, but not well been investigated. As a first step, we have

carried out basic study of MoS₂ thin film to find out suitable sputtering parameter. It was deposited on martensite stainless steel (SUS440C) substrates, using radio frequency magnetron sputter. Their tribological characteristics in UHV and high-temperature was evaluated by vacuum friction measurement system, high-temperature friction measurement system based on Bowden-Leben type and abrasion measurements by Stylus Surface Profiler.

TR-ThP3 Structure of Thin Diamond-Like Carbon Films and its Relationship to its Tribological Performance. *F.J. Flores-Ruiz, F.J. Espinoza-Beltran, M.O. Vazquez-Lepe, A. Herrera-Gomez*, CINVESTAV- Unidad Queretaro, Mexico

Diamond-like carbon (DLC) films are promising materials for dry-contact applications where resistance to surface damage or lubricating performance is required. In the present work, the structure of 3 and 10 nm Focus Cathodic Arc (FCA) carbon films and 3 and 10 nm plasma carbon films grown on Si(100) was studied by angle-resolved X-ray photoelectron spectroscopy (ARXPS). The concentration and distribution of sp² and sp³ carbon within the film was assessed with methods described elsewhere [i]. Atomic force microscopy (AFM) with a silicon tip was used to study the friction coefficient μ on the nanoscopic scale. It is defined by the Amonton law, $\mu = F_L/F_N$, where F_N and F_L are the normal and the lateral force applied to a probe [ii]. The calculation of the normal and lateral force applied during the process of sliding the tip over the sample was done according to the methodology proposed by Carpick [iii]. The results suggest a relationship between the chemical structure and the tribological performance for each film tested. The films grown by FCA presented the best tribological performance ($\mu \sim 0.02$) compared to films grown by plasma ($\mu \sim 0.06$) indicating a direct link between the distribution of sp² and sp³ carbon and the nanoscale friction coefficient. Since during the friction tests there was no evidence of damage or wear on either the surface or the tip, the conventional interpretation for the origin of friction proposed by Bowden and Tabor [iv] grossly underestimates the energy loss in the sliding process. On the other hand, the energy loss can be quantitatively explained in terms of heat generation [v]. The tribological performance analysis indicates that the friction is related to the adhesion force between tip and sample. However, the friction coefficient values do not show significant changes as the strength of adhesion varies, indicating that the value of the friction coefficient depend on the contributions of atomic bonds at the surface.

[i] A. Herrera-Gomez, et al., "Structure of ultra-thin diamond-like carbon Films grown with Filtered cathodic arc on Si(001)". *Analytical Sciences* **26**, pp. 267 (2010).

[ii] G. Amonton, "De la resistance cause'e dans les machines". *Mem. Acad. R. A.* **275** (1699).

[iii] R. W. Carpick, "Scratching the Surface: Fundamental Investigation of the Tribology with the Atomic Force Microscopy". *Chemical Reviews*, **97**, pp. 1163 (1997).

[iv] F. P. Bowden, and D. Tabor, "Friction and Lubrication of Solids". Oxford University Press, pp. 52 (1964).

[v] J. Luo, Y. Hu, S. Wen (Editors), "Physics and Chemistry of Micro-Nanotribology." ASTM-International, West Conshohocken, PA, USA. Chapter 9, pp. 167 (2009).

TR-ThP4 Tribological Investigations of Octadecylphosphonic Acid (ODP) and Octadecyltrichlorosilane (OTS) Self-Assembled Monolayers: A Comparative Study of MEMS-type Interfaces. *N. Ansari*, Auburn University, *S. Barkley*, Luther College, *C. Bouxsein, M. Deram, N. Eigenfeld*, Saint Olaf College, *O. Matthews*, Luther College, *A. Poda, W.R. Ashurst*, Auburn University, *B.P. Borovsky*, Saint Olaf College, *E.E. Flater*, Luther College

Microelectromechanical systems (MEMS) are critically-limited by interfacial phenomena such as friction and adhesion. One strategy to reduce friction between MEMS surfaces is to coat them with molecularly-thin self-assembled monolayer (SAM) coatings. Historically, silicon MEMS have been coated with silane-based SAMs, such as octadecyltrichlorosilane (OTS). However, continued progress in the development of MEMS may require new material systems to be employed. Therefore, in this study, we have investigated the frictional properties of octadecylphosphonic acid (ODP) monolayers deposited on aluminum oxide surfaces, across speed regimes. Measurements using an atomic force microscope (AFM) and separately using a nanoindenter-quartz crystal microbalance system were performed each with a microsphere-terminated probe. This allows for a comparative study between different velocity regimes using contacts with similar sizes, pressures, surface roughnesses, and interfacial chemistries. AFM colloidal probe friction measurements indicate that for a bare tip sliding on various substrates, ODP-coated alumina surfaces exert a lower friction force than either bare or OTS-coated alumina substrates. We also

observed strong evidence of transfer of the ODP molecules to the tip when the tip is uncoated. The results presented in this study are significant contributions towards our goal of better understanding the frictional properties of phosphonate SAMs in pursuit of alternative MEMS materials.

TR-ThP6 The Effect of Test Parameters on the Tribocorrosion Behavior of Multilayers, M. Flores, O. Jiemnez, J. Garcia, E. Rodriguez, Universidad de Guadalajara, Mexico, L. Huerta, Universidad Nacional Autonoma de Mexico

The multilayer coatings can improve the corrosion and wear resistance of materials for biomedical applications. The tribocorrosion behavior of TiALN and TiAlPt_xN coatings and TiAlPt_xN-TiAlPt_x multilayers immersed in a corrosive environment was investigated. The coatings were deposited on 316L stainless steel and Ti6Al4V alloys by magnetron sputtering. The period thickness of multilayers was 300 nanometers and the total thickness was 3.6 microns. In order to evaluate the influence of the environment, the corrosion was studied using open circuit potential (OCP) measurements and potentiodynamic polarization techniques in saline and a Ringer's solutions. For the tribocorrosion test a counterbody of Alumina with 10 mm diameter was used. The loads used were from 1 to 5 N, the oscillating frequencies were 1Hz to 5 Hz. The electrochemical noise measurements were performed during, and after the sliding and scratch tests. The structure and composition of multilayers were studied by means of XRD, XPS and RBS techniques. It was found that the codeposition of Pt and TiAlN-TiAl multilayer can improve the wear-corrosion resistance of materials for biomedical applications. The tribocorrosion behavior results in terms of the coefficient of friction showed a dependence against the force and the sliding frequency.

TR-ThP7 Tribological Properties of Electron Beam Excited Plasma Nitrided Surfaces, P. Abraha, J. Miyamoto, Meijo University, Japan

Tribological properties play significant role on the performance of tool steel surfaces. Here, application of electron beam excited plasma nitriding and its effect on tribological properties is described. The technique eliminates the formation of the brittle and rough compound layer that is common in nitriding processes. The hardening process is done through diffusion of the plasma species in to the subsurface of the treated material without altering the initial surface finish. The applications of the process can be in areas of hard coating where adhesion of the coating material with the tool steel is of significant importance.

The experimental tool steel material is SKD 61 with a chemical composition of 0.36% C, 5.05% Cr, 1.21% Mo, 0.83% V, 0.92% Si, 0.43% Mn, 0.008% P, >0.001% S, Fe bal. The sample was heat treated, hardened and triple tempered to a hardness of 630 Hv. The sample was then treated in a nitrogen plasma produced by a beam current of 8 A under a working pressure of 0.4 Pa. The temperature was set at 500 degrees centigrade throughout the treatment time. The experimental set up includes bias terminals that reduce the ion density within the vicinity of the tool steel material. This is done to reduce nitriding due to ion and increase the chance of nitriding due to neutral species within the plasma. The cross sectional hardness distributions and wear measurements of the nitrided tool steels were examined to determine the mechanical and tribological surface properties. The surface has no trace of the compound layer that is usually observed in the ion nitriding processes. This is also confirmed from the X-ray Diffraction peaks, as there is no visible Fe₃N and Fe₄N peaks observed. These results are attractive as they open new areas of application especially in the coating industry where adhesion remains to be the limiting factor in lots of the hard coatings that protect cutting and forming tools against wear.

TR-ThP8 Parameter Optimization of Ion Plated Nickel-Copper-Silver Lubrication, M. Danyluk, A. Dhingra, University of Wisconsin Milwaukee

In this paper we present a connection between argon ion flux with ion mixing and rolling contact fatigue (RCF) life of a thin solid nickel-copper-silver film lubrication on ball bearings tested in high vacuum. Using a Langmuir probe we measure plasma properties and ion flux and then calculate plane stress within the film during deposition using a validated model found in the thin film science literature. Experiments reveal that there is an inverse relationship between ion flux and RCF life for most deposition voltage and pressure combinations tested, specifically, 15.5 to 18.5 mTorr and 1.5 to 3.5 kV. For voltages up to 2.5 kV, RCF life decreases as deposition voltage and ion flux increase. Experiments also confirm that as ion flux increases deposition rate decreases due to sputter removal from the ball surface. For voltages between 2.5 and 3.5 kV interlayer mixing and contamination of the 100 nm thick coating reduces RCF life even as ion flux decreases with decreasing process pressure within a constant power process. At ion energy greater than 2.5 keV and ion flux above 10^{15} cm⁻² s⁻¹, SRIM results suggest elemental mixing of copper and nickel at the interface and this is confirmed using Auger Electron Spectroscopy (AES) on steel and Si₃N₄ 5/16" diameter balls.

TR-ThP9 Shear-induced Tribofilm Formation: Boron Containing Molecules on Copper, B.P. Miller, O.J. Furlong, W.T. Tysoe, University of Wisconsin Milwaukee

The push for greener lubricants has steered focus away from compounds containing sulfur and phosphorus. The tribological chemistry can depend critically on the nature of the substrate so that a good lubricant additive for one type of surface may not be applicable to another. In particular, the lubrication of sliding copper-copper interfaces in electrical motors provides a challenge due to the requirement for a conducting interface. Boron containing molecules have been proposed as potential green lubricants since environmentally safe boric acid is a prominent decomposition product in the presence of water. The following investigates the chemistry and frictional properties of alkoxy dioxaborolane (borolane) on copper surfaces in ultrahigh vacuum (UHV) to determine the precursor at room temperature that can potentially form a tribofilm needed for the lubrication of sliding copper-copper contacts. Temperature programmed desorption (TPD) and X-ray photoelectron spectroscopy (XPS) experiments provide the background information for investigating the frictional properties of borolane. A sliding copper-copper interface is exposed to borolane under UHV conditions, and a significant reduction in friction is found from the clean-surface values. A lasting tribofilm persisted even after the borolane dosing was stopped, and carbon was found on and below the surface in the wear scar region by *in-situ* Auger spectroscopy. Because the interfacial temperature rise under the experimental conditions used to measure friction is <1 K, the tribofilm formation is shear- and not thermal-induced

Friday Morning, November 4, 2011

Spectroscopic Ellipsometry Focus Topic

Room: 209 - Session EL+AS+EM+MS+PS+TF-FrM

Spectroscopic Ellipsometry: Future Directions and New Techniques

Moderator: H. Wormeester, MESA, The Netherlands

8:20am **EL+AS+EM+MS+PS+TF-FrM1 Current Trends and Future Outlook for Spectroscopic Ellipsometry**, *J.N. Hilfiker, B. Johs, C.M. Herzinger, T.E. Tiwald, J.A. Woollam Co., Inc.* **INVITED**

This talk reviews the significant developments in spectroscopic ellipsometry (SE) in areas including extending spectral range, improving accuracy, and enhancing speed. Current SE applications owe much to hardware and software developments of the past. Thus, today's research efforts may reach full potential for applications years or even decades from now. With this in mind, we point to the current state-of-the-art and what this may mean for future SE applications.

Three important areas will be explored. First, there has been a continual trend to expand SE wavelength range. This has included extensions to both shorter and longer wavelengths. For the latter, there is current development into the THz. More immediate benefit may come from smaller SE extensions from the ultraviolet to the near infrared. For example, further near-infrared extensions help to characterize modern transparent conductive oxides (TCOs), used in both inorganic and organic photovoltaic stacks.

Second, we look at the search for improved SE accuracy. Substantial improvements have come with the development of new ellipsometer technologies, progressing from rotating analyzer/polarizer to rotating compensator and now dual-rotating compensator ellipsometers. In addition to improved accuracy, this technology provides advanced measurements, including the complete Mueller-matrix. This will open SE characterization to new applications of anisotropic, nanostructured, and even patterned thin films. Accuracy enhancements must be compatible with the expanding SE spectral range. Infrared SE has overcome many non-ideal optical components to provide measurements competitive to standard FTIR measurements.

Third, we look at the quest for improved measurement speed. This development is constrained by the previous requirements. The benefits of a wide spectral range generally outweigh speed requirements; otherwise laser-based ellipsometry would still have a strong foothold. Thus, compromises are made depending on application. Current instrumentation typically utilizes detector arrays for multi-channel SE measurements.

To conclude, we will look at the SE outlook and how it may take advantage of wavelength range, accuracy, and speed. In-line and in-situ SE measurements show special promise. Significant improvements in instrumentation, computing speed, and software are now making these applications more feasible. In addition, there are novel ideas to provide sample access and overcome non-ideal measurement conditions for in-line and in-situ SE. Significant progress in many different areas promises to extend ellipsometry into new areas – many of which are being studied by researchers today.

9:00am **EL+AS+EM+MS+PS+TF-FrM3 THz Optical Hall-effect and MIR-VUV Ellipsometry Characterization of 2DEG Properties in a HfO₂ Passivated AlGaIn/GaN HEMT Structure**, *S. Schöche, U. of Nebraska - Lincoln, J. Shi, Cornell U., A. Boosalis, P. Kühne, U. of Nebraska - Lincoln, C.M. Herzinger, J.A. Woollam, J.A. Woollam Co., Inc., W.J. Schaff, L.F. Eastman, Cornell U., V. Darakchieva, Linkoping U., Sweden, M. Schubert, T. Hofmann, U. of Nebraska - Lincoln*

Nitride based high electron mobility transistors (HEMT) utilize the formation of a two-dimensional electron gas (2DEG) at the interface between GaN and AlGaIn due to a difference in spontaneous polarization. It is known that surface traps significantly influence the electrical properties of this 2DEG. Accurate knowledge about the influence of surface passivation on the channel properties is crucial. The device performance is governed by the mobility, the sheet charge density, and the effective mass of electrons in the 2DEG. These parameters are typically determined by electrical Hall effect (EHE), Shubnikov-de Haas (SdH), or cyclotron resonance (CR) measurements. Commonly these experiments require very low temperatures and high magnetic fields. Complex contact configurations are required for SdH and EHE and the ability to locate the 2DEG and possible parallel current paths is limited.

We present non-contact, optical measurements of free-charge carrier mobility, sheet density, and effective mass parameters of the 2DEG for a HfO₂-passivated AlGaIn/GaN HEMT structure at room temperature.

Spectroscopic ellipsometry in the spectral range from THz and Mid-IR to VUV and THz optical Hall-effect (generalized ellipsometry in magnetic field) (OHE) are employed.

The MIR measurements are performed for analysis of the heterostructure constituents' layer thickness, phonon modes, and volume free charge carriers. The phonon mode parameters were found to be in excellent agreement with literature values and the existence of significant volume charge carrier concentrations could be excluded. NIR to VUV ellipsometry is used to determine the thickness of the thin top layers. From a line-shape analysis in the VUV spectral range the optical constants of the HfO₂ passivation layer could be extracted. An amorphous structure of the HfO₂ passivation layer could be confirmed by comparison with existing studies in literature.

OHE in the THz spectral range is performed for characterization of the 2DEG channel parameters. A classical Drude model for free charge carrier contribution to the dielectric function was applied to determine the sheet density, the carrier mobility, and the effective mass of the 2DEG electrons. The electron effective mass of $(0.22 \pm 0.04) m_0$ extracted here using OHE corroborates the values found in previous SdH and CR studies. The values for the high-frequency sheet density and carrier mobility obtained by the optical investigations in the THz spectral range are in excellent agreement with results from dc EHE measurements indicative within linear Boltzmann transport theory for frequency-independent carrier scattering mechanisms of the 2D carrier distribution.

9:20am **EL+AS+EM+MS+PS+TF-FrM4 Vector-Magneto-Optical Generalized Ellipsometry on Sculptured Thin Films**, *D. Schmidt, C. Briley, E. Schubert, M. Schubert, University of Nebraska - Lincoln*

Sculptured thin films are self-organized and self-assembled three-dimensional nanostructures with tunable geometries. These artificial nanostructured thin films exhibit highly anisotropic physical properties, which mainly depend on their specific geometry.

Slanted, highly-spatially coherent, columnar nanostructure samples were prepared by glancing angle electron-beam deposition. Glancing angle deposition is a bottom-up fabrication technique that employs a physical vapor deposition process at oblique angles where the trajectory of the incoming particle flux is not parallel to the substrate normal. The technique allows to engineer the columnar film structure and is today amongst the most promising self-organized fabrication processes in micro- and nanotechnology.

We present and discuss the novel approach of vector-magneto-optical generalized ellipsometry on ferromagnetic permalloy nanostructured thin films carried out at room temperature. Investigations have shown that the metal alloy thin films are highly transparent, reveal strong form-induced birefringence, and exhibit intriguing magneto-optical anisotropy. Spatial magnetization orientation hysteresis and magnetization magnitude hysteresis properties are studied using a three-dimensional Helmholtz coil arrangement. This particular octupole setup allows for arbitrary magnetic field directions at the sample position with field strengths up to 200 mT while optical access is granted for reflection and transmission-type ellipsometry measurements. Analysis of data obtained within this unique vector-magneto-optic setup reveals magnetization anisotropy of the permalloy slanted nanocolumns and gives insight into switching behavior of confined magnetic domains.

9:40am **EL+AS+EM+MS+PS+TF-FrM5 THz Dielectric Anisotropy of Metal Slanted Columnar Thin Films**, *T. Hofmann, D. Schmidt, A. Boosalis, P. Kühne, R. Skomski, University of Nebraska-Lincoln, C.M. Herzinger, J.A. Woollam, J.A. Woollam Co., Inc., M. Schubert, E. Schubert, University of Nebraska-Lincoln*

Sculptured thin films (STFs) present an interesting class of self-organized, artificially made materials with three-dimensional, highly spatially coherent arrangements of nanostructures. Contemporary interest in materials for terahertz (THz) electronic, optoelectronic, and optical applications is redrawing attention to STFs that may enable designed optical properties for the THz frequency region.

We report on the anisotropic optical dielectric functions of a metal (cobalt) slanted columnar thin film deposited by electron-beam glancing angle deposition for the THz frequency domain using generalized spectroscopic ellipsometry. A simple anisotropic Bruggeman effective medium dielectric function homogenization approach is successfully employed to describe the observed optical response. This approach describes isolated, electrically conductive columns which render the thin film biaxial (orthorhombic). The anisotropy induced by the columnar film structure is very large. The anisotropic Bruggeman effective medium approach predicts upon slight modifications of Drude, fraction and/or depolarization parameters that

targeted optical properties of STF in the THz range can be achieved by variation of slanting angle, lateral column density, and material.

10:00am **EL+AS+EM+MS+PS+TF-FrM6 A Compact High-speed Spectroscopic Ellipsometer**, *G. Chin*, ULVAC Inc., Japan

Recently, we developed a compact, high-speed spectroscopic ellipsometer. It analyzes the spectrums obtained from the polarization interference occurring between two multiple-order retarders which snapshot the wavelength distribution of the sample's spectroscopic polarization parameters. This innovative spectroscopic ellipsometer can measure the thickness and optical constants of thin films at a dramatically fast speed. Its acquisition time is as short as 10 ms. It does not require the conventional complex mechanical or active components for polarization-control, such as a rotating compensator and an electro-optical modulator. It can open great opportunities for new applications of the spectroscopic ellipsometry in which the compactness, the simplicity and the rapid response are extremely important. For example, it was integrated into the deposition tool and successfully measured thin films in the vacuum chamber.

This paper describes the principle, system configuration and our innovative efforts on developing the compact high-speed spectroscopic ellipsometer. Some typical application data will be also introduced, such as in line and in situ measurements for photovoltaic, flat panel display and semiconductor industries.

10:20am **EL+AS+EM+MS+PS+TF-FrM7 Ellipsometry Porosimetry (EP): In Situ Spectroscopic Ellipsometry Measurements Coupled with Pressure Controlled Adsorption of Organic Vapors to Study Properties of Nano-Porous Thin Films**, *J.P. Piel, L. Kitzinger, A. Bondaz, C. Defranoux*, SEMILAB-SOPRALAB, France

Ellipsometric porosimetry (EP) is a non contact, non destructive technique that is cited as a reference technique for porous thin film analysis [1, 2]. As it is based on a spectroscopic ellipsometric measurement, the technique allows the precise determination of the refractive indices and thickness of the porous films. The advantage of these EP tools is that the combination of this well established spectroscopic ellipsometric (SE) technique with a suitably adapted adsorption chamber permits access to all the information obtained by classic adsorption experiments (e.g. BET) on thin films with an excellent sensitivity. Information such as open and closed porosity, pore size distribution etc... can be thus obtained.

In addition the EP allows access to a multitude of information that the classic equipment does not. For example, Spectroscopic Ellipsometry allows to follow the variation of the sample thickness during the adsorption experiment, leading to the determination of the Young's Modulus for the thin films. This will be presented. The technique is highly sensitive to the detection of interfaces; it is thus possible to detect a porosity gradient or to study a multilayer structure and thereafter simultaneously plot the two corresponding adsorption isotherms [3]. In the same manner, the instrument permits the use of a range of different gases adsorptive in order to tailor the probe molecule to the morphology and to the chemistry of the porous layer at ambient temperature [4]. We thus obtain information on the chemistry of the pores within the layer, before, during and after the adsorption experiment. Recent developments include the implementation of the FTIR interferometer SE extension to the EP system. It allows a precise characterization of the chemistry of the pores within the layer. We thus obtain information on the chemical bonds present in the layers before, during and after the adsorption experiment. Preliminary results will be presented.

Specifically, this fundamental technique permits the thorough characterization of porous thin film samples. We will demonstrate some of the different features of the EP technique with regards to the morphological and chemical properties of the porous thin films. Additionally, we will illustrate the technique for various thin film applications such as solgel thin films, nanofilms for catalysis, photovoltaic cells, fuel cells, optical sensors, and bio-compatible materials to name but a few.

References :

- [1] M.R. Baklanov et al, *J. Vac. Sci. Technol. B* **18**, 1385 (2000).
- [2] C. Wongmanerod et al, *Appl. Surf. Sci.* **172**, 117 (2001).
- [3] A. Bourgeois et al, *Thin Solid Films* **455-456**, 366 (2004).
- [4] A. Bourgeois et al, *Adsorption* **11**, 195 (2005).

Electronic Materials and Processing Division
Room: 210 - Session EM+SS-FrM

Surfaces and Materials for Next Generation Electronics
Moderator: E.X. Zhang, Vanderbilt University, L. Porter, Carnegie Mellon University

8:20am **EM+SS-FrM1 Growth of 3C-SiC Epitaxial Layers on 4H-SiC Step-Free Mesas**, *R.L. Myers-Ward, E.A. Imhoff, J.D. Caldwell, L.O. Nyakiti, V.D. Wheeler, K.D. Hobart, C.R. Eddy, Jr., D.K. Gaskill*, Naval Research Laboratory (NRL)

To avoid defects such as polytype inclusions or dislocations, the epitaxial growth of 3C-SiC requires a lattice-matched, perfect substrate. One solution to this problem is to use step-free mesas of 4H-SiC as 3C-SiC lattice templates [1]. In this work, we describe the formation of large area step-free mesas and the subsequent nucleation and growth of 3C-SiC layers. A powerful array of tools were utilized to characterize the properties of these layers including Nomarski microscopy, secondary electron microscopy (SEM), atomic force microscopy and X-Ray diffractometry. Micro-photoluminescence (μ -PL) was employed to investigate the presence of electronic defects and identification of polytype, enabling us to obtain information about the structural and electronic properties on a micron-sized length scale.

On-axis 4H-SiC substrates were initially patterned and reactive ion etched to produce hexagonal and square shaped mesas with varying widths ranging from 40 to 400 μ m (400% greater area than previous reports), and heights from 2 to 5 μ m. Homoepitaxial layers were grown on the mesas in an Aixtron VP508 horizontal hot-wall chemical vapor deposition reactor using the standard chemistry of silane and propane in order to grow out the steps on the mesas. The homoepitaxial layers were terminated at the mesa step edge and further growth is prohibited. The films were grown at 2 μ m/hr and the pressure and temperature were 100 mbar and 1580 $^{\circ}$ C, respectively. The yields of 200 μ m width 4H-SiC step-free mesas was ~95%. Heteroepitaxial 3C-SiC was grown 2 μ m thick on the homoepitaxy (4H-SiC) by means of reducing the growth temperature to 1450 $^{\circ}$ C, while maintaining 100mbar.

Under Nomarski evaluation, ~ 18% of the 200 μ m wide 3C-SiC mesas appeared to be step-free. Micro-PL maps were used to confirm the presence of 3C-SiC, where uniform 3C-SiC was detected across the entire mesas. X-ray rocking curves also indicated 3C-SiC, with the FWHM of the SiC (111) being ~21", indicating good quality material.

Yield maps for the 200 and 400 μ m mesas will be presented. In addition, real color PL imaging will be used to determine the types of defects within the mesas which displayed lower PL intensity regions of 3C-SiC. Lastly, initial results of Schottky rectifiers performance made on the layers will given.

References

- [1] J. A. Powell, *et al.*, *Appl. Phys. Lett.* **77**, 1449 (2009).

8:40am **EM+SS-FrM2 Growth of Epitaxial Rare Earth Nanostructures in III-V Semiconductors**, *B.D. Schultz, J.K. Kawasaki, C.J. Palmstrom*, University of California, Santa Barbara

Highly ordered embedded nanostructures of rare-earth monopnictides can be formed within III-V semiconductor heterostructures providing a new degree of control over the structural and transport properties of the heterostructures. Materials such as ErAs and ErSb are thermodynamically stable with GaAs and GaSb respectively, and in both cases a common group-V sublattice is maintained throughout the heterostructures. In both the arsenides and antimonides, co-deposition at concentrations above a few atomic percent results in the formation of nanoparticles and nanorods. The shape of the nanostructures is strongly dependent of the growth surface including reconstructions, stoichiometry, temperature, and crystallographic orientation. Codeposition of Er with GaAs can produce nanoparticles or ordered nanorods oriented along either the [111] or [211] directions depending on aforementioned conditions[1]. While codeposition of Er with GaSb produces either particles or nanorods oriented primarily along the [100] direction. STM of the GaAs(311)A and B surfaces during the initial stages of nucleation show that following the deposition of a fractional monolayer of ErAs, embedded growth of ErAs particles are observed on the B surface, while the A surface shows primarily surface cluster formation. MBE growth of GaAs on (311)A and B orientations produces relatively flat surfaces with uniquely different (8 \times 1) reconstructions. Codeposition of Er with GaAs results in significant roughening of the surface during growth due to anisotropic diffusion of Ga and Er along the <233> and <011> directions and the general tendency of GaAs not to wet ErAs(100) surfaces. The [211] orientation of the ErAs nanorods on the surface is found to result from preferential growth along the (1 -1 -1) plane on Ga-polar A surfaces. While the angle between the (1 -1 -1) and surface normal remains less than

or equal to 90°, the [211] orientated growth is supported. The {111} surface of the rocksalt ErAs is typically a high-energy surface; however, the Ga-rich (1 -1 -1) plane provides a flux mediated epitaxial growth surface for the ErAs analogous to a vapor-liquid-solid type of growth. *In-situ* RHEED, LEED and STM surface studies will be presented along with a detailed growth model to explain differences in the growth process and in nanorod formation for different substrates and substrate orientations.

Supported by AFOSR FA9550-10-1-0119 and ARO W911NF-07-1-0547. [1] T.E. Buehl, C.J. Palmström, and A.C. Gossard, *J. Vac. Sci. Technol. B* 29, 03C108-1, 2011.

9:00am **EM+SS-FrM3 Bulk Topological Insulators and Superconductors: Discovery and the Frontier**, *M.Z. Hasan*, Princeton University **INVITED**

While most known phases of matter are characterized by broken symmetries, the discovery of quantum Hall effects (1980s) revealed that there exists an organizational principle based on topology rather than broken symmetry. In the past few years, theory and experiments have suggested that new types of topological states of matter exist in certain insulators without any applied magnetic field. These topological insulators are characterized by a full band gap in their bulk and gap-less conducting edge or surface states protected by time-reversal symmetry. Unlike the quantum Hall systems, the topological insulators can be doped into superconductors and magnets revealing the interplay between topological order and broken symmetry order. In this talk, I will briefly review the basic theory and highlight the experimental developments in topological insulators. I will then conclude by drawing connections between the emergent novel physics and their potential applications.

10:20am **EM+SS-FrM7 Inter-band GaN/InGaN/GaN Tunnel Diodes**, *S. Krishnamoorthy, D.N. Nath, S. Bajaj, S. Rajan*, Ohio State University

The III-Nitride material system has demonstrated its potential for a broad range of optoelectronic and electronic applications. However there are no reports of efficient III-Nitride tunnel junctions due to the large band gaps in this material system. In this work, we show that with unique properties such as the polarization, tunneling can be enhanced using band bending over smaller distances in nitride heterostructures, leading to record reverse and forward tunneling current density for the III-nitride material system.

We have designed and demonstrated GaN/InGaN/GaN tunnel junction with a record high current density of 118 A/cm² at a reverse bias of 1 V by utilizing a 6.4 nm thin In_{0.33}Ga_{0.67}N barrier material. N-polar p-GaN/In_{0.33}Ga_{0.67}N/n-GaN heterostructure designed for tunneling close to zero bias was grown by plasma assisted molecular beam epitaxy by choosing the critical thickness of InGaN barrier appropriately. The tunnel junction sample shows five orders of magnitude higher current at a reverse bias of 1 V as compared to a standard p⁺/n⁺ GaN sample indicating efficient tunneling across the InGaN barrier. The tunneling turn-on close to zero bias, and maximum current density of 9.1 kA/cm² achieved in this work demonstrates the potential of polarization-engineered tunnel junctions.

Two distinct regimes of transport are identified based on the temperature dependent I-V measurements. At lower reverse bias, defect assisted tunneling with strong temperature dependence is found to dominate. In this regime, a plot of ln (I/E) vs E^{1/2} shows a linear behavior suggesting a Frenkel-Poole emission mechanism due to the high field in the InGaN quantum well. A direct band to band tunneling regime resulting in weak temperature dependence that arises from band gap variation with temperature is observed from a reverse bias of 1 V. A decrease in current density is observed with increase in temperature in the range of 77- 150 K and this can be attributed to the presence of band tail states which has been observed previously in In face InGaN.

We discuss the design of these quantum well tunnel junctions. Although higher indium compositions yield higher band to band tunneling probability, calculations using a simplified Kane model reveal that the wider depletion region in n GaN due to higher band offset considerably reduces the net tunneling probability. Calculations also reveal the need for very high doping in the n GaN layer so as to minimize the depletion region thickness in order to achieve very high current densities in such polarization charge assisted tunnel junctions. These calculations can guide future tunnel junctions with better performance characteristics.

10:40am **EM+SS-FrM8 Probing Surface-Induced Fluctuations in Organic Materials using an Atomic Force Microscope**, *N.C. Hoepker, S. Lekkala, R.F. Loring, J.A. Marohn*, Cornell University

The development of organic electronics calls for new tools to study organic thin films. By measuring the frequency noise experienced by a cantilever near a surface, we are able to microscopically probe organic materials. In previous work, we used an Atomic Force Microscope to measure frequency noise due to dielectric fluctuations as a function of cantilever height and

voltage over a thin film of polyvinyl acetate. In parallel, we have developed a zero-free parameter linear-response theory of thermally induced dielectric fluctuations that successfully describes our observations.¹

Having understood dielectric fluctuations, we are now investigating fluctuations induced by carrier motion in polymeric semiconductors. Charge transport in these devices is not well understood. Previous work indicates that the ratio of diffusion constant to mobility in these materials violates what is predicted by the Einstein relation. In addition, there is an ongoing controversy on the charge density and electric field dependence of mobility. While the correlated-disorder model correctly predicts the electric field dependence of mobility, models that predict a density dependence of mobility rely on uncorrelated site-to-site energies.

A resolution of these controversies calls for new tools to study carrier motion in organic semiconductors. By measuring the frequency fluctuations experienced by a cantilever near a surface, we are able to microscopically probe carrier motion in organic materials. Comparing our observations over a poly(3-hexylthiophene) transistor to a calculation based on free diffusion, we find that while theory overestimates the observed fluctuations, it predicts the correct spectral shape and distance dependence of the fluctuations. Even at high gate bias, the observed cantilever frequency fluctuations differ from what we expect based on free diffusion and on the measured carrier mobility. This discrepancy indicates a breakdown of the Einstein relation. Further we present a number of different charge hopping models. We find that the predicted cantilever frequency noise is very sensitive to the details of the model, indicating that frequency noise spectra are a vital tool for selecting appropriate charge transport models.

[1] Nikolas Hoepker, Swapna Lekkala, Roger F. Loring, John A. Marohn (manuscript in preparation). *Quantifying Dielectric Fluctuations over Polymer Films Using an Atomic Force Microscope*.

11:00am **EM+SS-FrM9 2011 AVS Albert Nerken Award Lecture - Electron Spectroscopy of Reconstructed Surfaces: From Silicon to Graphene**, *J.E. Rowe**, North Carolina State University **INVITED**

Surface reconstruction of silicon (and other materials) refers to the process by which atoms at the surface of a crystal assume a different structure than that of the bulk and has been extensively discussed and reported at a number of AVS meetings from the early 1960's until present time. In the 1970's a number of electron spectroscopy methods were applied to study this effect and many atomic models were proposed. Early 1970's experiments using electron energy loss spectroscopy and photoemission spectroscopy are described which along with modern theory methods led to the now accepted dimer model (later confirmed by STM) for the Si(100)2x1 and most other reconstructed (100) semiconductor surfaces. Additional core-level synchrotron spectra are described along with very recent studies which include adsorbate-induced surface reconstruction and the role of interface reconstruction of SiC(0001) used for the growth of graphene and studied by STM and STS. Spectroscopy has continued to play an important role even during the past 25 years after the discovery of atomic-scale imaging by STM of the Si(111)7x7 reconstruction. Both early and more recent studies of reconstruction by the author are reviewed.

11:40am **EM+SS-FrM11 Molecular Motion Confined to Self-Assembled Quantum Corrals**, *E. Yitamben, R.A. Rosenberg, N.P. Guisinger*, Argonne National Laboratory

Engineering molecular superstructures on metals opens great possibilities for the control and exploration of complex nanosystems for technological applications. Of particular interest is the use of chiral molecules, such as alanine, to build self-assembled nanoscale structures for the trapping of the two-dimensional free electron gas of a metal. In the present work, molecules of D- or L-alanine were deposited on Cu(111). Scanning tunneling microscopy and spectroscopy revealed the formation of a uniform network of hexagonal pores of average diameter ~1.2 nm. Each pore acts as a quantum corral by confining the two-dimensional electron gas of the Cu(111) surface state. Furthermore, excess alanine molecules were trapped at the inner perimeter of the hexagonal pore, and were observed as rotating or immobile spatial states. This study demonstrates the engineering of one of the smallest quantum confined structure, and the dynamics of molecular motion within these potential wells.

Acknowledgements: This work was supported by the U.S. Department of Energy, Office of Science, Office of Basic Energy Sciences, under Contract No. DE-AC02-06CH11357

* Albert Nerken Award Winner

Materials Challenges for Nuclear Energy**Moderator:** L. Petit, Daresbury Laboratory, UK**8:20am EN+AC-FrM1 Multi-Electron Correlation in UO₂ from Soft X-ray Spectroscopy, J.G. Tobin, S.W. Yu, Lawrence Livermore National Laboratory**

Resonant Inverse Photoelectron Spectroscopy (RIPES) and X-ray Emission Spectroscopy (XES) have been used to probe the electronic structure of Uranium Dioxide, UO₂. From these variants of soft x-ray spectroscopy, the nature of the main and satellite features at the U4d_{5/2} edge can be ascertained. This leads to important insights into the multi-electronic correlations underlying the ubiquitous satellite features of UO₂ and implications for future experiments with Pu.

Lawrence Livermore National Laboratory is operated by Lawrence Livermore National Security, LLC, for the U.S. Department of Energy, National Nuclear Security Administration under Contract DE-AC52-07NA27344. This work is funded by the DOE Office of Science, Office of Basic Energy Science, Division of Materials Sciences and Engineering. The Advanced Light Source (ALS) is supported by the Director, Office of Science, Office of Basic Energy Sciences.

8:40am EN+AC-FrM2 New Results from the DOE EFRC on the Materials Science of Actinides, P.C. Burns, University of Notre Dame, G. Sigmon, EFRC INVITED

The Materials Science of Actinides EFRC has three major themes: (1) Complex actinide materials, with complexity arising from chemistry, structure, and properties; (2) Nanoscale control of actinides; and (3) Behavior of actinide materials in extreme environments of pressure, temperature and radiation fields (including coupled effects). This presentation will cover several recent results that span the range of themes in the EFRC, with emphasis on those that are most significant to the challenges of nuclear energy.

9:20am EN+AC-FrM4 Proof that UO₂ is an f-f Electron Correlated System, S.W. Yu, J.G. Tobin, J.C. Crowhurst, Lawrence Livermore National Laboratory, S. Sharma, J.K. Dewhurst, Max Planck Institute, Halle, Germany, P. Olalde-Velasco, W.L. Yang, Lawrence Berkeley National Laboratory, W.J. Stekhaus, Lawrence Livermore National Laboratory INVITED

We have performed x-ray absorption experiments on uranium dioxide (UO₂) at the O 1s, U 4d, U 4f, and U 5d edges. After comprehensive energy calibrations for O 1s, U 4d, and U 4f spectra, we have used the U 4d and 4f spectra to sort the energetic positions of the 5f and the 6d states in the unoccupied band unambiguously. This demonstrates conclusively that UO₂ is an f-f Mott-Hubbard insulator, where the electronic repulsion between f electrons is responsible for the insulating state. Calculations performed within the U-corrected generalized gradient approximation of the optical response of UO₂ permit direct comparison with the absorption spectra and confirm the experimental results.

Lawrence Livermore National Laboratory is operated by Lawrence Livermore National Security, LLC, for the U.S. Department of Energy, National Nuclear Security Administration under Contract DE-AC52-07NA27344. This work is funded in part by the DOE Office of Science, Office of Basic Energy Science, Division of Materials Sciences and Engineering. This work is also funded in part by Laboratory Directed Research and Development (LDRD) Program (10-SI-016) of Lawrence Livermore National Laboratory. The Advanced Light Source (ALS) is supported by the Director, Office of Science, Office of Basic Energy Sciences, of the U.S. Department of Energy under Contract No. DE-AC02-05CH11231. We would like to thank Ian Hutcheon, Patrick Allen, Anthony Van Buuren, Trevor Wiley, and Joseph Zaugg for valuable discussions. POV would like to acknowledge CONACyT Mexico.

10:00am EN+AC-FrM6 Atomistic Models for Actinide-Actinide Oxide Interfaces, S.M. Valone, Los Alamos National Laboratory

An important class of materials problems of great interest to nuclear energy production consists of composites of metals and metal oxides, and in particular, actinide metals and actinide oxides. Individually, either type of material, actinide or oxide, can involve strong electron correlation effects. At an interface, the situation becomes even more complex. In traversing a metal-metal oxide interface, a radical compositional change is encountered. Most atomistic models address only metals, or only ceramics, but rarely both. In addition, the actinide oxides themselves enter multiple oxidation states, depending on the composition. Thus, in traversing an interface, the

oxidation state need not change abruptly. As a result, these sorts of interfaces present new challenges that must be met in order to understand this important class of material systems. To address these needs, a new, "fragment" model Hamiltonian is constructed at the atomistic level, as opposed to the one-electron model Hamiltonians that underlie tight-binding and density functional theory methods. The model encompasses both actinides and actinide oxides, and provision is made for transitioning gradually through multiple oxidation states. The extremes of the models, the dioxides and the metals, map closely to existing models for these materials. The model for metals conforms generally to a modified embedded atom method (MEAM), meaning that the embedding function (atomistic site energy model) is analytical. The differences between the fragment Hamiltonian potential and the existing MEAM models appear in the explicit form of the embedding function and in the fact that there are two distinct terms in the embedding energy in the new model. The second term is critical to strongly-correlated-electron materials, as it is an atomistic analog to

terms appearing in Hubbard models. The model also possesses a sense of electron hopping that imparts ways to both regulate the net charge on sites in the material and to change important energy gaps that determine metallic and insulating behavior.

10:20am EN+AC-FrM7 Structure and Properties of New Actinide Oxalates, Precursors of Fuel Materials, C. Tamain, B. Arab-CHapelet, CEA Marcoule, France, M. Rivenet, F. Abraham, UCCS, France, S. Grandjean, CEA Marcoule, France

For future generation nuclear fuel cycle, actinide co-conversion processes are one option for the co-management of actinides. Oxalic acid is a well-known reagent to recover actinides thanks to the very low solubility of An(IV) and An(III) oxalate compounds in acidic solution. Therefore, considering mixed-oxide fuel or considering minor actinides incorporation in ceramic fuel materials for transmutation, oxalic co-conversion is convenient to synthesize mixed oxalate compounds, precursors of oxide solid solutions.

Up to now, only U(IV)-Ln(III) oxalate solid solutions have been completely structurally described started from single-crystals. In these oxalate compounds, a mixed-crystallographic site which accommodates both elements in spite of their different charges has been established. The extent of this study on powder compounds allowed to examine the influence of An(IV) and An(III) nature. The switch of actinide's nature causes unexpected structural modifications underlining the complexity of specific transuranium elements physical chemistry and the need to pursue studies on single crystal on these actinides.

As the existing oxalate single crystal syntheses are not adaptable to the actinide-oxalate system, several original crystal growth methods allowing the formation of mixed actinide oxalate crystals were first developed. Applied to the mixed actinide systems, they lead to the formation of the first mixed An(IV)-An(III) oxalate single crystals. The results, including the different structural resolutions, are presented.

10:40am EN+AC-FrM8 Recent Work on Magnetism, Actinides and Defects at ORNL, G.M. Stocks, B.C. Larson, Oak Ridge National Laboratory INVITED

The extent to which the collective effects of defects can be manipulated and controlled yields the combination of structural materials properties – strength, toughness, and resistance to degradation in extreme chemical and radiation environments. In this presentation I shall outline the scope of studies of the fundamental physics of dislocations and radiation-induced displacement cascades being conducted within the Center for Defect Physics (CDP) at Oak Ridge National Laboratory and its partner institutions. Within the CDP, the focus is on the quantitative measurement and direct quantum simulation of defects at the level of unit dislocation and cascade events. For dislocation interactions, the focus is on high-spatial-resolution techniques such as 3D X-ray microscopy and convergent beam electron diffraction, which measure the local strains/stresses near isolated defects directly and thereby quantify the interactions and dynamics of defects in the bulk. For displacement cascades, the focus is on quantitative measurement of the formation and time evolution of energetic-ion-induced atomic displacement cascades using ultrahigh-resolution time-resolved X-ray diffuse scattering measurements made possible by the ultrahigh brilliance of femtosecond X-ray pulses produced at the Linac Coherent Light Source (LCLS) and the time-averaged brilliance of the Advanced Photon Source (APS). Theoretically, the focus is on developing high-fidelity models that treat spin and ion dynamics on an equal footing and to address system sizes and time scales commensurate with experiments. I will outline early progress with respect to addressing the feasibility of experimentally observing unit events and on developing *ab initio* electronic

structure based theories of combined atomistic and spin dynamics. For the latter, I will show preliminary results for Fe that address the importance of the disruption of the magnetic state of Fe caused by the introduction of defects such as dislocations and displacement cascades that are based on large scale (~10,000 atom) models and order-N electronic structure methods.

Work supported by the "Center for Defect Physics in Structural Materials" which is a Department of Energy, Office of Science, Energy Frontier Research Center (EFRC).

Graphene and Related Materials Focus Topic

Room: 208 - Session GR+MS+EM-FrM

Graphene Device Physics and Applications

Moderator: M. Arnold, University of Wisconsin-Madison

8:20am GR+MS+EM-FrM1 **Fabrication and Characterization of Graphene p-n Junction Devices**, J.U. Lee, University at Albany-SUNY
INVITED

Graphene is a newly discovered material composed of two-dimensional array of hexagonal carbon atoms. It has a number of unique electronic properties, the most remarkable of which is the zero band-gap light-like linear electronic dispersion, giving rise to Dirac fermions. This feature can be used to make devices based on previously unexplored physical properties. For example, in analogy to optics, we describe new devices based on *optics-like manipulation of electrons*.

Our devices are based on graphene and bi-layer graphene *p-n* junctions doped using electrostatic doping techniques from buried split gates. In the present context, graphene *p-n* junctions do not rectify, i.e. behave as semiconductor diodes. Instead, in graphene *p-n* junctions, carriers launched from a point contact from one side of the junction are able to refocus back to a point on the other side of the junction. This behavior, known as the Veselago effect, can be the basis for new logic devices for replacing Si CMOS. In addition, using the same platform, we describe interconnect structures that can be reconfigured. Together, we envision a new circuit paradigm based on components that seamlessly reconfigure between devices and interconnect components.

In this talk, we describe the details of graphene *p-n* junction fabrication and characterization, and circuits that are enabled by the *p-n* junction devices. The devices are fabricated at CNSE's state-of-the-art 300mm Si wafer fabrication line using processing techniques that leave atomically flat top oxide surface above the patterned split gates. For characterizing the *p-n* junctions, we perform transport and SPM measurements.

9:00am GR+MS+EM-FrM3 **Assembled Bilayer Graphene for Electronic Applications**, G.G. Jernigan, T.J. Anderson, J.T. Robinson, J.D. Caldwell, M.D. Ancona, V.D. Wheeler, L.O. Nyakiti, J. Culbertson, A.L. Davidson, A.L. Friedman, P.M. Campbell, D.K. Gaskill, U.S. Naval Research Laboratory

Graphene has shown successful application in RF transistors and frequency doublers where its high mobility and high saturation velocity translate into operation at high frequencies while utilizing little power. However, a major detraction to graphene development for other device applications is that it does not have a band gap. The lack of a band gap means that graphene's current cannot be turned off. Bilayer graphene is regarded as one possible solution to this problem, since bilayer graphene is capable of developing a band gap if the symmetry of the system can be broken. That said, bilayer graphene (from exfoliation or growth) forms a highly ordered A-B stack of the two graphene sheets resulting in little to no band gap, unless a high electric field can be applied.

In this presentation, we will demonstrate a novel method for creating bilayer graphene where a single layer of CVD graphene grown on Cu is bonded to a single layer of epitaxial graphene grown on Si-face SiC. This process results in a bilayer system that has a built-in asymmetry that yields unique physical and electrical properties not previously observed. For example, we demonstrate that the transfer of CVD graphene to epitaxial graphene results in a smoother morphology than transfer onto SiO₂ and that bonding of CVD graphene to epitaxial graphene can avoid the damage caused by the drying step necessary in the poly (methyl methacrylate) transfer method. X-ray photoelectron spectroscopy and Raman microscopy demonstrate that the sheets are coupled together but strained differently, in contrast to a naturally formed bilayer. Electrical characterization of Hall devices fabricated on the novel bilayer show higher mobilities and lower carrier concentrations than the individual CVD graphene or epitaxial graphene sheets alone. Modeling of the electric field produced by opposite

doping in the graphene sheets will also be presented, as CVD graphene is typically p-type and epitaxial graphene is typically n-type.

10:00am GR+MS+EM-FrM6 **Rectification at Graphene / Semiconductor Junctions: Applications Beyond Silicon Based Devices**, S. Tongay, X. Miao, K. Berke, M. Lemaire, B.R. Appleton, A.F. Hebard, University of Florida

Schottky barriers are crucial and necessary device components of metal-semiconductor field effect transistors (MESFETs) and high electron mobility transistors (HEMTs). Here, we report on the formation of Schottky barriers at graphene-multilayer graphene/semiconductor junction interfaces which have been characterized by current density vs. voltage (J-V) and capacitance vs. voltage (C-V) measurements. After graphene transfer onto various semiconductors such as Si, GaAs, GaN and SiC, we observe a strong rectification at the interface, i.e., high (low) resistance in the reverse (forward) bias directions. The J-V characteristics have been analyzed using thermionic emission theory and the extracted barrier height values are consistent with the Schottky-Mott model. When capacitance is plotted as $1/C^2$ vs V, a linear dependence is observed, which by extrapolation to the intercept identifies a built in potential that is consistent with the Schottky barrier height extracted from J-V measurements. Graphene's low Fermi energy together with its robust thermal, chemical, structural and physical properties provide numerous advantages when used to form Schottky barriers in device applications: namely, voltage tunability of the Schottky barrier height, stability to high temperatures, resistance to impurity diffusion across the interface, and the use of absorbates to chemically tune the Fermi energy and hence the Schottky barrier height.

10:20am GR+MS+EM-FrM7 **Imaging of Electron Beam Induced Current in Epitaxial Graphene**, S. Mou, J. Boeckl, W.C. Mitchel, J.H. Park, Air Force Research Laboratory, S. Tellak, Wyle Laboratories, W. Lu, Fisk University

It has been known and observed that there forms a Schottky junction between graphene and SiC in epitaxial graphene due to the work function difference and the charge transfer between them. As a result, it is viable to apply the electron beam induced current (EBIC) technique on the epitaxial graphene directly due to the fact that it needs a built-in field and ample electron generation volume to generate EBIC. EBIC is an important characterization technique, which identifies electrically active impurities/defects, detects local built-in field, and measures minority carrier diffusion length. In this paper, we use a FEI SEM equipped with a current amplifier to investigate the spatial mapping of EBIC generation and collection in a two terminal geometry. The incident electron beam generates excited electron-hole pairs in SiC and the minority carriers are collected through the Schottky junction before flowing into graphene. EBIC imaging reveals mesoscopic domains of bright and dark contrast areas due to local EBIC polarity and magnitude, which is believed to be the result of spatial fluctuation in the carrier density in graphene. We also investigate the electron energy dependence, which modulates the EBIC magnitude. With an analytical drift-diffusion current model, we are able to extract the minority carrier diffusion length in the SiC, which is on the order of micro meter and agrees well with other published data.

10:40am GR+MS+EM-FrM8 **Potassium-Ion Sensors Based on Valinomycin-Modified Graphene Field-Effect Transistors**, Y. Sofue, Y. Ohno, K. Maehashi, K. Inoue, K. Matsumoto, The Institute of Scientific and Industrial Research, Osaka University, Japan

Highly sensitive ion sensors based on valinomycin-modified graphene field-effect transistors (VGFETs) have been developed to selectively detect K ions, which are an essential element for biological activity including human life. Graphene single-layers were obtained by mechanical exfoliation. Graphene FETs were fabricated by conventional e-beam lithography and lift-off method on a thermally grown SiO₂ layer. To demonstrate selective detection of K ions, the graphene channels were covered with ion selective membrane, which consisted of polyvinyl chloride and valinomycin. Transfer characteristics of VGFETs in a 100 mM Tris-HCl buffer solution with various KCl concentrations over the range from 10 nM to 1.0mM. With increasing K ion concentration, the solution-gated voltage at the Dirac point shifted toward negative direction. The shifts are due to the accumulation of positively charged K ions surrounded by valinomycin on the graphene surfaces. The electrostatic potential of graphene surfaces exhibit a rather linear dependence on log[K]. These results indicate that VGFETs effectively detected K ions with concentration from 10 nM to 1.0 mM. To investigate selectivity in VGFETs, Na-ion concentration dependence was also measured. The transfer characteristic in VGFETs remained almost constant over the Na ion concentration range between 10 nM and 1.0 mM. These results indicate that VGFET selectively detected K ions with high sensitivity.

11:00am **GR+MS+EM-FrM9 Band-gap Generation by using Ionic-Liquid Gate in Bilayer Graphene**, *Y. Yamashiro, Y. Ohno, K. Maehashi, K. Inoue, K. Matsumoto*, Osaka University, Japan

Electric fields were applied to a bilayer graphene to generate a band gap using an ionic-liquid gate instead of the general top-gate structures. The ionic-liquid gate can apply higher electric field than other type of the gates because of its large capacitance and electric strength. In this abstract, the graphene layers were extracted from kish graphite by a mechanical exfoliation and were put on highly *n*-doped Si substrates covered with a 300-nm-thick SiO₂ layer. Side-gate electrodes were patterned approximately 20 mm away from the channels. An ionic liquid (DEME-TFSI) was put on the bilayer graphene and the side-gate electrode. Electrical characteristics at 300 K revealed that the electrical double layer in the ionic-liquid, which works as a very thin insulator, had 200 times larger capacitance than a 300-nm-thick SiO₂ layer. The thickness of electrical double layer was estimated to be 3.75 nm. In electric field dependence measurements, an increase in a sheet resistance of the bilayer graphene channel was clearly observed with increasing the magnitude of electric field in bilayer graphene. On the other hand, the increase in the sheet resistance didn't appear in the monolayer- and trilayer- graphene. That is why the increasing of the sheet resistance was caused by a band gap generated in ionic-liquid gated bilayer graphene by the electric field.

11:20am **GR+MS+EM-FrM10 Electronic Transport in Hydrogenated Graphene Films**, *B.R. Matis, J.S. Burgess*, NRC/NRL Postdoctoral Associate, *A.L. Friedman, J.T. Robinson*, Naval Research Laboratory (NRL), *F.A. Bulat*, Sotera Defense Solutions, Inc., *B.H. Houston, J.W. Baldwin*, Naval Research Laboratory (NRL)

Graphene films grown by chemical vapor deposition on copper foils and exfoliated graphene flakes were hydrogenated using low kinetic energy plasma processing. The film sheet resistance can be tuned over a wide range (1 kΩ/square – 300 kΩ/square), increasing proportionally with hydrogen coverage. Variable temperature measurements demonstrate a transition from semi-metallic behavior for graphene to semiconducting behavior for hydrogenated graphene. Sheet resistance measurements as a function of temperature also suggest the emergence of a band gap in the hydrogenated graphene films. Interesting surface doping effects will be discussed in conjunction with the location of the charge neutrality point. This work was supported by the Office of Naval Research.

11:40am **GR+MS+EM-FrM11 First-principles Study of Electronic Properties of Two Dimensional Carbon and Boron Nitride Nanomaterials**, *S. Mukherjee*, S.N. Bose National Centre for Basic Sciences, India

First principles pseudopotential plane wave method was used to study ground state electronic properties of Graphene, hexagonal Boron Nitride (h-BN), Graphene doped with Boron and Nitrogen, and multilayers of Graphene and h-BN. Our results on doped Graphene indicate that upon electron (hole) doping, the Dirac-point in the electronic bandstructure shifts below (above) the Fermi level and a gap appears at the high-symmetric K-point. Upon co-doping of Graphene by both Boron and Nitrogen a small energy gap between the conduction and valence band appears at the Fermi level, making the CBN nanomaterial a narrow band semiconductor. The energy gap depends sensitively on the degree of doping and on the thickness of CBN layer. These results are in agreement with recent experimental measurements [1,2]. Our bandstructure calculations on the multilayers of Graphene and h-BN indicate that these nanostructured multilayers exhibit semiconducting behaviour with band gap in the range 60-600 meV depending on the relative orientation and thickness of the layers. (Author: Sugata Mukherjee, work done in collaboration with T.P. Kaloni)

1. X. wang et al, Science **324**, 768 (2009)
2. L. Cie et al, Nature Materials **9**, 430 (2010).

MEMS and NEMS Group
Room: 105 - Session MN-FrM

Characterization of Materials and Structures at the Micro- and Nano-scale
Moderator: M. Metzler, Cornell University

8:20am **MN-FrM1 Nanomechanics: Controlling Near-Field Interactions between Mechanical Systems**, *D. Lopez*, Argonne National Laboratory **INVITED**

Metallic and dielectric objects are surrounded by fluctuating electromagnetic fields due to thermal and quantum fluctuations of the

charge and current density at the surface of the bodies. Immediately outside the objects, this electromagnetic field exists partly in the form of propagating electromagnetic waves and partly in the form of evanescent waves that decay exponentially with distance away from the body's surface. These fluctuating electromagnetic modes are responsible for a great variety of near-field phenomena such as the Van der Waals force, the Casimir force, near-field heat transfer, and non-contact friction forces. As devices evolve from micro- to nanoscale structures, these forces become relatively stronger, and their effect cannot be disregarded any further. For example, researchers working to develop NEMS devices need to consider the effects caused by Van der Waals and Casimir forces which can lead to compromise in the range of motion or in the voltages required for actuation. To improve our understanding of these near-field interactions and to develop mechanisms to control them is extremely important for a diversity of seemingly different fields, such as nanomechanics, quantum computing with trapped ions, measurements of gravitational forces at the nanometer scale, and detection of single spins for magnetic resonance force microscopy.

In this presentation I will describe the fundamentals of near-field forces, I will review recent scientific advances regarding manipulation of these interactions in the field of nanomechanics, and I will illustrate novel applications that could be enabled once we are capable of control these forces.

9:00am **MN-FrM3 Pull-in Experiments on Electrostatically Actuated Microfabricated Meso Scale Beams**, *Y. Gerson, I. Sokolov*, Tel Aviv University, Israel, *T. Nachmias*, RAFAEL LTD, Israel, *S. Lulinsky, S. Krylov*, Tel Aviv University, Israel

Meso scale (hundreds of micrometers to several millimeters) MEMS sensors and actuators are beneficial in applications where large displacements, manufacturability, and ease of integration with existing mechanical and packaging environments are required.

In this work we report on the results of characterization and modeling of electrostatically actuated meso scale beams. The beams with clamped ends were 5000 μm long, 150 μm thick and 10, 12 and 15 μm wide and were operated by a parallel plate electrode located at the distance of 20 μm from the beam. The goal of the work was twofold. First, we demonstrate the feasibility of electrostatic actuation of the meso scale devices and ability to achieve relatively large displacement. Second, an electrostatically actuated double clamped micro beam is viewed as a kind of benchmark problem and was intensively studied. However, the number of reported experimental results, which can serve for validation of models, is limited. We anticipate that our experimental results, obtained using larger meso scale structures and therefore relatively more accurate, could provide a reliable experimental reference for a double clamped beam actuated by a parallel-plate electrode.

The devices were fabricated by deep reactive ion etching (DRIE)-based process from highly doped Si using a silicon on insulator (SOI) wafer with [111] surface orientation and 150 μm thick device layer. The experimental approach based on the use of SOI wafers allows to fabricate devices with low residual stress and excellent mechanical properties of Si. The devices were operated in ambient air conditions. Linearly increasing (ramp) voltages were applied quasistatically to the actuation electrode and easily visualized in-plane (parallel to the wafer surface) motion of the devices was registered using an optical microscope and a CCD camera. The response was video recorded, the movie was split into separate frames and the voltage-displacement dependence was built using customized edge detection image processing procedure implemented in Matlab. The critical pull-in voltage varied between 70 V in (nominally) 10 mm wide beam and up to 125 V in 15 mm wide beams. In addition, pull-in behavior of the beams was modeled using several approaches, starting from simplified reduced order models based on the Galerkin decomposition with linear eigenmodes as base functions and up to fully coupled nonlinear large deflection three-dimensional simulations. The actual dimensions of each beam, carefully measured using scanning electron microscope (SEM) were used in calculations. Excellent agreement between the results provided by the model and the experimental data was observed.

9:20am **MN-FrM4 Absorption and Emission of Plasmonic Antenna Arrays**, *K.E. O'Brien, P.H. Holloway, M.R. Davidson*, University of Florida

New and more portable means of generating narrow band radiation are of interest, especially in the terahertz (THz) range. One potential method for generating radiation involves photo-mixing over nano/micro scale plasmonic structures. The plasmonic structures can serve as antennas for absorbing incoming photons and conversely emit radiation of a lower frequency. Designs include 2-dimensional arrays of these resonant structures fabricated on Ag thin films using electron-beam lithography and

lift-off. Patterns vary from arrays of linear structures, “bowties,” and interlocking structures. We have shown emission of visible radiation from similar structures when excited by space charge from electrons. The absorption and emission of light by the structures has been measured for micron-scale and nano-scale antenna arrays and has exhibited a polarization dependent behavior. The effect of different antenna structures on the absorption and emission will be discussed.

10:00am MN-FrM6 Fabrication and Characterization of Structural and Electrical Properties of Ultrananocrystalline Diamond Nanowires, X. Wang, University of Puerto Rico, *A.V. Sumant, V. Joshi, L.E. Ocola, B. Kabius, D. Lopez,* Argonne National Laboratory

Due to extraordinary mechanical, optical and electrical properties as predicated by theory, there has been tremendous amount of interest in making diamond nanowires (DNWs) and diamond nano-rods (DNRs). Synthesizing or fabricating these nanostructures is proving to be very challenging. To date, only a few attempts have been reported, either by etching single crystal diamond using focus ion beam (FIB) to produce diamond NRs or by coating Si nanowires with nanocrystalline diamond to produce diamond NWs. We report a top-down method based on e-beam lithography and reactive ion etching of ultrananocrystalline diamond (UNCD) to produce UNCD nanowires (UNCDNWs) with nanowire diameters as small as 30 nm. Since they are produced by lithographic approach (top-down), they can be fabricated at well-defined position with nanometer-scale precision. Compare to other fabrication techniques like FIB, our UNCDNWs maintain intrinsic diamond structure and properties without degradation after fabrication process, which has been confirmed by Raman spectroscopy (ultraviolet and visible), transmission electron microscope (TEM) and electron energy loss spectroscopy (EELS). Preliminary electrical measurement of UNCDNWs will be discussed. The ability to fabricate UNCDNWs provides an opportunity to study the fundamental mechanism of transport processes in UNCDNWs, which will enable new ideas and possibilities for the fabrication of new functional nanoelectronic devices.

10:20am MN-FrM7 Investigation of Heat Transfer Enhancement in Nanofluids with Molecular Dynamics Simulations – Role of Particle Charge and Fluid Polarity, J.D. Schall, Oakland University, *A.S. Comfort,* U.S. Army RDECOM-TARDEC

Thermal loads are increasing in military vehicles because of the greater use of microelectronics,

higher power density engines, and restricted air flow from up-armor kits. Conventional methods

to increase heat dissipation, such as increasing heat exchanger size produce an undesired

increase in vehicle weight and packaging issues. One approach to mitigate these issues is the

development of heat transfer fluids with improved thermal transport properties. Nanofluids are

suspension of nanometer sized particles in solvent, and represent a potential method to increase

the effective fluid thermal conductivity and heat transfer coefficient of coolants without creating

the adverse effects found in larger particle suspensions, such as settling, clogging, and abrasion.

Since their introduction by U.S. Choi in 1995, a great deal of uncertainty about the mechanisms

of enhanced thermal conductivity of nanofluids continues to employ researchers and limits

the development of optimized nanofluids in heat transfer applications. In this paper, molecular

dynamics simulations are used to investigate heat conduction between model particle surfaces

separated by a liquid layer. In particular, effects of base fluid charge, polarity, and nanoparticle

surface charge on the solid-liquid interface liquid structure, thermal (i.e. Kapitza) resistance, and

thermal conductivity are investigated. Results are compared with previous simulations from the

literature which used simple monoatomic models interacting through Lennard-Jones potentials.

10:40am MN-FrM8 Novel CMOS MEMS Double Parallel Plate Capacitive Tactile Sensors For Blood Flow Monitoring, C.J. Hsieh, J.C. Liou, C.T. Sun, Y.C. Lin, W.-C. Tian, National Taiwan University

This research focuses on the developments and characterizations of non-invasive tactile blood flow sensors using CMOS MEMS technologies. The capacitive sensing structure consists of two parallel plate capacitors which can be connected in different configurations in cape with different measuring ranges. Sensor detection scope is set to be from 0 to 150 mmHg according to the estimated maximum human vessel pressure. The sensor is fabricated in commercial 2 polysilicon and 4 metal CMOS technology followed by the self-developed post processes. The dimension of each sensor is 400 μ m in length with the membrane thickness of 1.45 μ m.

An anisotropic inter metal dielectric layer etch step was utilized on CMOS chips to open wet metal etching holes. After this dielectric layer etch, a metal wet etching process was applied to release sensing structures. In order to protect the metal bonding pads in post CMOS MEMS processes, an Au layer was deposited on the pad areas. Based on the experiment results, the lateral metal sacrificial layer etching rate is 1.85 μ m per minute and the lateral etching rate underneath gold layer is 2.9 μ m per minute. We have successfully demonstrated the post CMOS MEMS processes for our sensors.

Initial finite element method analysis results showed that the sensitivities of two different designs are 6.7 and 2.2 fF per mmHg with a dynamic range of 75 and 200 mmHg. The sensor behavior measurement data will be presented.

11:00am MN-FrM9 A Highly Sensitive Nanomachined TiO₂ Gas Sensor for Micro Gas Chromatography, C.H. Chou, C.H. Chen, W.-C. Tian, National Taiwan University, *T.H. Chan, C.-J. Lu,* National Taiwan Normal University

The purpose of this study is to develop a sensitive gas sensor with engineered TiO₂ nanostructures using semiconductor nanotechnologies for micro gas chromatography. Many TiO₂ nanowires for gas sensing nowadays were fabricated by chemical synthesis methods, and the nanowire arrays are in irregular formats and the amount of sensing material may be varied chip to chip. The behavior of sensing repeatability of these TiO₂ nanowires using conventional methods is hard to control.

With the combination of E-beam lithography and the TiO₂ thin film deposition, the TiO₂ sensing nanowire arrays with well-controlled structures (100-300 nm wide with 1 μ m period), were placed in between the Au interdigitated electrodes. A microheater were fabricated by deposition of the 3/50 nm thick Cr/Au films on the backside of the sensor. The great linear heating with increasing input power and uniform heating (329.3 $^{\circ}$ C in average, STDV of 9.3 $^{\circ}$ C, power of \sim 0.8 W) were obtained through an IR camera.

The performance of nanowire detector (100 nm wide, 183.5 M Ω) is compared to the microwire detector (20 μ m wide, 24.6 M Ω) at various ethanol and benzene concentrations or at various operation temperatures. The measured resistance to the initial resistance ratio of the nanowire detector changed from 1 to 0.35 at 284 $^{\circ}$ C at 6.5% ethanol concentration. The effects of the rapid thermal annealing and an O₂ plasma treatment to improve the sensor performances is investigated and will be presented.

11:20am MN-FrM10 Ultra-high Aspect Ratio High-speed Silicon Nanowire and Three-dimensional Formation Using a Hydrogen-assisted Deep Reactive Ion Etching, Z. Sanaee, S. Azimi, M. Poudineh, S. Mohajerzadeh, A. Sandoughsaz, University of Tehran, Iran

We report the formation of ultra-high aspect ratio and three dimensional features on silicon substrates using a novel low-density capacitive-coupled plasma reactive ion etching (13.56MHz). The etching process is based on using three gases of hydrogen/oxygen and SF₆ in two sub-sequences called as passivation and etching sub-cycles. All three gases are used in the passivation step and SF₆ in the etching step. Unlike Bosch process no polymer is used for passivation. By controlling the passivation sub-cycle, one is able to allow desired under-etching followed by “recovery” of the formerly under-etched features to make unique three-dimensional structures directly on silicon substrates [1].

Cleaned silicon samples are placed in an e-beam evaporation unit to deposit a 40nm chromium layer as the mask for the subsequent processing steps. The masking layer is patterned using precision projection lithography to achieve desired features between 100nm and 20 μ m. For ultra-high aspect ratio and scallop-free etching while keeping the etch-rate of 1 μ m/min, it is necessary to include trace values of H₂O₂ during the etching step. Typical flows for H₂/O₂ and SF₆ are 200/200 and 5 sccm in the passivation step while the etching is mainly practiced with SF₆ (35 sccm). The plasma power is set at 250 W for the passivation and 130 W for the etching sub-cycle. By controlling these important parameters, we have realized three-dimensional features where the vertical structures have serpentine surfaces

with desired recessions of 10um. Moreover, we have been able to realize arrays of nano-metric 3-D features using Si/SiO₂ structures with a diameter of 2-3um and features of the order of 100nm.

We realized 9-10um high and 90nm wide nano-wires where the mask undercut is 30nm and the surface of the wires is almost free of "scallop". Scallop is side-effect of time-multiplexed processes where the periodic track of the etching step is seen on side-walls. To avoid this, while obtaining high-rates we have included H₂/O₂ gases during the etching sub-cycle. Normally H₂/O₂ gases act as the passivation layer, however the trace value of these gases does not affect the etching. Instead a slight passivation is formed on side-walls while the etching proceeds, prohibiting further lateral-etching of walls. We have studied the passivation layer using XPS and Ellipsometry. Thickness of the passivation layer is 2-3nm and it is mainly SiOF bonds (XPS). Field-emission SEM has been used to compare the results. Using this process we obtained high etch-rates of 0.8-1.1um/min for features around 100nm. The height of the nano-wires is around 10um, with an aspect ratio of 100 and more. This process uses low-density plasma with rapid steps and apart from MEMS/NEMS applications it can be used for "solar-cells" where nano-wires can significantly affect the efficiency and cost.

[1]. S. Azimi, A. Sandoghsaz, B. Amirsolaimani, J. Naghsh-Nilchi, S. Mohajerzadeh, "Three-dimensional etching of silicon substrates using a modified deep reactive-ion etching technique", *J. Micromech. Microeng.* No. 21, 074005, (2011).

Plasma Science and Technology Division Room: 201 - Session PS-FrM

Plasma Modeling

Moderator: K. Bera, Applied Materials, Inc.

8:20am **PS-FrM1 Delivering Activation Energy to Surfaces in Atmospheric Pressure Plasmas: Local and Remote**, *Z. Xiong, N.Yu. Babaeva, M.J. Kushner*, University of Michigan

Non-equilibrium atmospheric pressure plasmas (APPs) are efficient at producing chemically reactive environments by electron impact dissociation and ionization of feedstock gases. Other than generating UV photon fluxes, APPs are not thought to be sources of non-thermal activation energy in the form of energetic ions or hot atoms. Although mean free paths of ions may be less than 1 micron, the transient production of electric fields of 100s kV/cm to 1 MV/cm when the ionization fronts of streamers intersect with surfaces provide the possibility of accelerating ions to many to tens of eV. This high quality delivery of activation energy is a function of not only the properties of the streamer but also depends on the properties of the surface. For example, delivery of high energy ions to the surface of a bulk polymer may differ from a layered polymer due to differences in their capacitive properties. These differences extend to organic material as well – the delivery of energetic ions to cells and tissue will depend on their respective dielectric properties and those of the surrounding medium. Delivery of high quality activation energy in any form (photons or ions) to remote sites or locations is challenged by line-of-site issues and the charging of surrounding materials that may reduce ion energies. Being able to deliver activation energy to the crevices of rough surfaces may be important in the context of plasma sterilization. In this talk, results from modeling studies of atmospheric pressure plasma streamers and jets intersecting with dielectric surfaces will be discussed. The delivery of activation energy by ions and photons to rough surfaces will be discussed in the context of polymer modification and sterilization. Plasma sources will include directly applied dielectric barrier discharges and remote plasma source delivered by capillary tubes. * Work supported by the Department of Energy Office of Fusion Energy Sciences.

8:40am **PS-FrM2 Kinetic Effects in Low Pressure Capacitively Coupled Plasmas**, *A. Likhanskii, P. Stoltz*, Tech-X Corp.

We present results of particle-in-cell/Monte Carlo collision simulations of kinetic effects in low pressure capacitively coupled plasma discharge.[1] In particular, we examine discharges of various gases (including Ar, Xe, and others) in the pressure range of 10s of mT and the frequency range of 10s of MHz. We track the formation of high energy electrons (*e.g.*, at the ionization threshold or greater) as a marker for enhanced ionization, and look at the effects of elastic and inelastic collisions on the formation of these high energy electron bunches. [2,3] We show results for 2D and 3D simulations where we include density gradient effects, and results for plasma chemistry effects on the bulk electron energy distribution function and the ion energy distribution function at a plasma surface interface. We discuss the role of the bunches on electron heating in the plasma bulk and

on their presence on how electron heating is treated in fluid simulations of plasma sources.

9:00am **PS-FrM3 Challenges in Modeling of Plasma Interactions in Medicine and Biology: What Insights Can You Expect?**, *N.Yu. Babaeva, M.J. Kushner*, University of Michigan **INVITED**

The development of technologies for the plasma treatment of living tissue is in large part based on controlling plasma sources to deliver the desired fluxes of radicals and ions to surfaces. This process is complicated by scientific and technical issues. From a scientific standpoint, although it is generally accepted that reactive oxygen species (ROS) and reactive nitrogen species (RNS) are important in, for example, wound healing, sterilization and cancer treatment, it is not clear which species and in what proportions are optimum for each type of treatment. The situation becomes more complex when considering the UV photons, energetic ions and electric fields produced by the discharge which also interact with the tissue. From a technical view point, the interaction between the tissue (and wounds in particular), the surrounding materials and the plasma can significantly affect the plasma. For example, the shape of the wound and the permittivity of the fluid in a wet wound can warp local electrical fields which then feed back to the plasma. Given this complexity and interdependencies, computer modeling of plasma-tissue interactions might provide insights to these interactions. In this talk, results from computer modeling of plasma-tissue interactions will be discussed. The modeling platform solves for charged particles, neutral and photon fluxes while also solving Poisson's equation, and resolving spatial scales on reactor-to-cellular levels. Plasma transport through gases and liquids are included. Two types of plasma sources will be considered - dielectric barrier discharges (DBDs) where the plasma is in direct contact with the tissue and remote plasma jets, where dominantly neutral species and photons reach the tissue. We will discuss the treatment of wounds through a liquid layer covering exposed cells wherein the blood serum contains blood platelets. The characteristics of the plasma sources, and the interaction of plasma generated species and electric fields with the wound, fluid and underlying cells will be discussed.

* Work supported by the Department of Energy Office of Fusion Energy Sciences.

10:00am **PS-FrM6 Magnetic Field - Plasma Interaction in Low Pressure VHF Capacitively Coupled Plasmas using PIC-MCC/Fluid Hybrid Model**, *K. Bera, A. Agarwal, S. Rauf, K. Collins*, Applied Materials, Inc.

Low pressure magnetized capacitively coupled plasmas are extensively used for advanced microelectronics device fabrication. Due to the long mean free path of electrons in this regime, kinetic effects characterize the plasma dynamics in low pressure discharges. To take into account the kinetic effects, a hybrid 2-dimensional (2D) plasma modeling software has been developed that couples a particle-in-cell (PIC) model for charged species with a fluid method for neutral species. The electron motion due to electric and magnetic fields is incorporated in 3-dimensional velocity space using the Lorentz force law. The PIC model uses the Monte Carlo Collision (MCC) method to account for collision processes. The fluid model for neutral species takes into account species transport in the plasma, chemical reactions, and surface processes. Capacitively coupled rf plasmas in Ar have been computationally investigated for a 2D parallel plate plasma reactor in Cartesian co-ordinates. The inter-electrode gap is 5 cm (in y-direction). The bottom electrode is powered using a 60 MHz very high frequency (VHF) source, and the top electrode is grounded. The two electrodes are separated by quartz inserts. Ar plasma is simulated for a range of magnetic fields (25 - 100 Gauss), pressures (10 - 50 mTorr) and rf voltages (100 - 300 Volts). In this range of magnetic fields, the electrons are magnetized due to a small Larmor radius while the ions remain non-magnetized. For a symmetric reactor configuration without magnetic field, the plasma is symmetric, and the peak in plasma density occurs at the center plane between the top and bottom electrodes. The electron density increases with increase in pressure and rf voltage. With magnetic field in the x-direction (parallel to the electrodes), the plasma becomes more confined. When the magnetic field is applied in the z-direction, orthogonal to the electric field, the $E \times B$ drift is observed, and the plasma becomes asymmetric. When the magnetic field direction is reversed, $E \times B$ drift reverses, therefore, the direction of plasma asymmetry reverses. The effect of magnetic field on plasma symmetry will be examined. In addition, results from the kinetic simulation will be compared to corresponding results from a fluid plasma model.

10:20am **PS-FrM7 Simulations of SF₆ Plasma Etching in the GEC Reference Cell**, *S. Lopez-Lopez*, Quantemol - University College London, UK, *J.J. Munro, D. Brown*, Quantemol Ltd., UK, *J. Tennyson*, University College London, UK

Electrically driven plasmas containing halogens are very used in different material modification and surface cleaning processes. Sulfur Hexafluoride

(SF₆) is used industry-wide in a range of processes for the dry etching of silicon or silicon dioxide for microelectronic feature definition, such as the Bosch process. However, the performance and efficiency of different processes and machines can vary widely, and the use of simulations can give us significant insight into the optimization problem and provide a low cost means for further development. That is especially relevant in the case of SF₆, given its environmental impact, with a Greenhouse Warming Potential that is 22,000 times that of CO₂. It is therefore vital to use SF₆ sparingly and efficiently in every process, and simulation can help to find ways of remediating harmful waste gases and optimize the process for typical processing goals (e.g. etch rate, uniformity) as well as improving SF₆ consumption efficiency and other environmental measures.

A key aspect of the plasma processes here considered is that some type of work is done at the plasma / surface boundary layer, and realistic simulations must therefore incorporate the surface material and the etch product chemistry. This increases drastically the complexity of the problem but is the only way to represent all of the appropriate physics. Radical species from the surface entering the gas phase will take part in the phase and surface reactions that are associated with the parent gas, including negative ion formation and electron dissociation among others.

Here we present 2D simulations of an inductively driven SF₆ silicon etch process in the GEC Reference Cell [1], building upon previous calculations of SF₆ plasma chemistries using Quantemol-P [2]. Etch rate, pressure and power trends along with chamber wide contour plots of gas-phase species concentrations and fundamental plasma properties are considered. We have found a good agreement with experimental results [3], which validates the underlying model and points to the important role of simulation-assisted plasma process development and optimization.

REFERENCES

- [1] P. J. Hargis et al, *Rev. Sci. Instrum.* **65**, 140 (1994).
- [2] J. J. Munro and J. Tennyson, *J. Vac. Sci. Technol. A* **26**, 865 (2008).
- [3] G. A. Hebner, I. G. Abraham, J. R. Woodworth, "Characterization of SF₆/Argon Plasmas for Microelectronics Applications", Sandia Report, Sand2002-0340 Unlimited Release, March 2002.

10:40am **PS-FrM8 Simulation of InP Etching under ICP Ar/Cl₂/N₂ Plasma Discharge: Role of N₂ in the Sidewall Passivation**, R. Chanson, A. Rhallabi, M.C. Fernandez, Ch. Cardinaud, J.P. Landesman, Institut des Matériaux Jean Rouxel (IMN), France, S. Bouchoule, A. Talneau, Laboratoire de Photonique et de Nanostructures (LPN), France

InP-based optoelectronic devices need reliable dry etching processes characterized by high etch rate, profile control and low damages. High density plasma etching, using inductively coupled plasma ICP reactors, has been found to be very important for the transfer of patterns from the mask to InP substrate and InP-based layers. In order to investigate the role of N₂ in the InP etching process under Cl₂/Ar/N₂ plasma discharge, we have developed an InP etching simulator permitting to determine the InP etch profile evolution through the mask as a function of the operating conditions and the initial mask geometry.

The InP etching simulator is divided in three modules: the global kinetic model of Cl₂/Ar/N₂ ICP plasma discharge is based on 0D approach which allows to calculate the averaged densities of neutrals and ions as well as the electron density and electron temperature versus the machine parameters. The resolution of the differential equations associated to the mass balance of each considered specie coupled to charge neutrality equation and the differential power balance equation from t=0 until the steady state allows to determine all reactive specie densities as well as their fluxes into the InP substrate. n_e and T_e calculated from the plasma global kinetic model are introduced in the sheath model to estimate the average sheath thickness. The Monte-Carlo technique is used to study the ion transport in the sheath. The calculation of energies and angles of all positive ions impinging on the substrate allows determining the angular and energy distribution functions of positives ions. Such distribution functions with Cl, N and positives ions fluxes are introduced as input parameters into the etching model. The later is based on the cellular approach combined to the Monte-Carlo method which the considered domain (InP substrate and mask) is discretized on 2D uniform cells which each cell represents a real number of In sites. The fluxes of neutral species and positive ions are introduced as input parameters into the etching model. All the particle surface interaction processes like adsorption of atomic neutrals Cl and N on InCl_xN_y surface sites, desorption of InCl_x sites, sputtering of both InCl_xN_y and mask by positive ions and redeposition of InCl_x sites are described in probabilistic ways. Simulation results show the effect of the N₂ on the passivation of the lateral surfaces and as consequence the improvement of the etch profile anisotropy. However, a diminution of the etch rate by increasing the percentage of N₂ is observed. The simulated etch profiles are compared to those obtained by the experiments and the good agreements are obtained.

11:00am **PS-FrM9 Three-Dimensional Modeling and Formation Mechanisms of Atomic-Scale Surface Roughness during Si Etching in Chlorine-Based Plasmas**, H. Tsuda, Y. Takao, K. Eriguchi, K. Ono, Kyoto University, Japan

Three-dimensional measurement and prediction of atomic-scale surface roughness on etched features become increasingly important for the fabrication of next-generation devices; however, the feature profiles are too small or too complex to measure the surface roughness on bottom surfaces and sidewalls of the etched features. To predict the surface roughness on atomic or nanometer-scale, we have developed our own three-dimensional atomic-scale cellular model (ASCEM-3D) [1] and feature profile simulation. Emphasis is placed on a better understanding of the formation mechanisms of atomic-scale surface roughness during Si etching in chlorine-based plasmas and the relationship between the ion incident energy and angle and etched feature profiles.

In the ASCEM-3D model, the simulation domain is divided into a number of small cubic cells of $L = r_{Si}^{-1/3} = 2.7 \text{ \AA}$, where $r_{Si} = 5.0 \times 10^{22} \text{ cm}^{-3}$ is the atomic density of Si substrates. Ions and neutrals are injected from the top of the simulation domain, and etch and/or sputter products are taken to be desorbed from etching surfaces into microstructural features, where two-body elastic collision processes between incident ions and substrate atoms are also taken into account to analyze ion reflection on etched feature surfaces and penetration into substrates. The ASCEM-3D takes into account surface chemistries based on the Monte Carlo (MC) algorithm [2-4], including adsorption and reemission of neutrals, chemical etching, ion-enhanced etching, physical sputtering, and redeposition of etch and/or sputter products on feature surfaces.

Numerical results indicated that nanoscale convex features increase in size with increasing etching or plasma exposure time, and surface roughness increases with increasing ion incident energy. The ripple structures of etched surfaces were found to occur depending on incident angle of ions. Ion reflection or scattering on etched surfaces strongly affects the evolution of feature profiles and surface roughness on atomic scale.

- [1] H. Tsuda et al., *Jpn. J. Appl. Phys.* (2011), in press.
- [2] Y. Osano and K. Ono, *J. Vac. Sci. Technol. B* **26** (2008) 1425.
- [3] H. Tsuda et al., *Thin Solid Films* **518** (2010) 3475.
- [4] H. Tsuda et al., *Jpn. J. Appl. Phys.* **49** (2010) 08JE01.

11:20am **PS-FrM10 Control of the Ion Energy Distribution on a Plasma Electrode**, P. Diomedede, D.J. Economou, V.M. Donnelly, University of Houston

The energy of ions bombarding the substrate is critical in plasma etching and deposition of thin films, especially when precise etching without damage is required. The ion energy distribution (IED) may be controlled by applying "tailored" bias voltages on the substrate, or on nearby electrodes immersed in the plasma. A Particle-in-Cell simulation with Monte Carlo Collisions (PIC-MCC) was conducted of the application of DC voltage steps (and staircases) on an electrode, during the afterglow of a capacitively-coupled pulsed argon discharge, to control the energy of ions incident on the counter-electrode holding the wafer. Staircase voltage waveforms with selected amplitudes and durations resulted in ion energy distributions with distinct narrow peaks, having controlled peak energies and fraction of ions under each peak. A semi-analytical model was also employed to achieve "tailored" IEDs, i.e., distributions with a desired shape and energy spread (for example a nearly-monoenergetic IED with given FWHM). This was again accomplished by applying judicious voltage waveforms on the substrate electrode. Predicted IEDs were compared with experimental data. Strategies to control the energy flux of bombarding ions or to distribute the total ion energy flux to different energies were identified.

Work supported by DoE Plasma Science Center and NSF.

11:40am **PS-FrM11 Molecular Dynamic Simulation for Selective Etching of Silicon Nitride and Silicon Oxide by Hydrofluorocarbon Ions**, R. Shigekawa, M. Isobe, Osaka University, Japan, M. Fukasawa, T. Tatsumi, Sony Corporation, Japan, S. Hamaguchi, Osaka University, Japan

Selective etching of silicon oxide (SiO₂) over silicon nitride (SiN) has been widely used in microelectronics fabrication processes such as contact hole etching in self-aligned processes, formation of a stress liner, and dual/triple hard mask (DHM/THM) etching processes of dual-damascene structures. Opposite selective etching of SiN over SiO₂ with high selectivity would be also desirable for various processes. In general, when a fluorocarbon gas is used for etching processes, a carbon film tends to be accumulated on SiN surface, which is considered to reduce its etching rate. Therefore, there have been various attempts in plasma processing to increase the SiN etching rate by reducing carbon films over SiN with the use of hydrogen reactions with carbon. In such plasma processing, hydrofluorocarbon gases are typically used. In this study, we have performed molecular dynamics (MD) simulations of SiN and SiO₂ etching by CH_xF_y ions and compared their

etching rates and surface chemistry, especially focusing on effects of hydrogen on the process. The reactive interatomic potential functions for atomic systems of Si, O, F, C, N, and H were developed in-house for the MD simulations code, based on atomic interaction data of small molecules in ground states obtained from ab-initio calculations. Details of the atomic potential functions used in the simulations will be presented elsewhere. Simulations are typically performed on a small block of a model substrate that consists of several thousand atoms and is subject to bombardment of energetic particles such as CH_xF_y . In the simulations, we evaluate sputtering yields, surface modification during the process, and characteristics of sputtered products. From the simulations, it has been found that hydrogen of CH_xF_y ions tends to reduce F accumulation on SiN surface, forming volatile HF, and sometimes promotes formation of cyanides such as HCN. Detailed simulation results, including sputtering yields and surface chemical compositions, will be given in this presentation.

Late Breaking Session

Room: 109 - Session SS2-FrM

Surface Science Late Breaking Session

Moderator: C.R. Eddy Jr., U.S. Naval Research Laboratory, S.B. Sinnott, University of Florida

8:20am **SS2-FrM1 CO Oxidation Facilitated by Robust Surface States on Au-Covered Topological Insulators**, *H. Chen*, The University of Tennessee, Knoxville, *W. Zhu*, The University of Tennessee, Knoxville and ORNL, *D. Xiao*, Oak Ridge National Laboratory, *Z. Zhang*, Univ. of Sci. and Tech. of China and The Univ. of Tennessee, Knoxville

Surface states—the electronic states emerging as a solid material terminates at a surface—are usually vulnerable to contaminations and defects. The robust topological surface state(s) (TSS) on the three-dimensional topological insulators (3DTI) provide a perfect platform for exploiting surface states in less stringent environments. Employing first-principles density functional theory calculations, we demonstrate that the TSS can play a vital role in facilitating surface reactions by serving as an effective electron bath. We use CO oxidation on gold-covered Bi_2Se_3 as a prototype example, and show that the robust TSS can significantly enhance the adsorption energy of both CO and O_2 molecules, by promoting different directions of electron transfer. The concept of TSS as an electron bath may lead to new design principles beyond the conventional *d*-band theory of heterogeneous catalysis.

*H. Chen, W. G. Zhu, D. Xiao, and Z. Y. Zhang, *Phys. Rev. Lett.* 107, 056804 (2011)

8:40am **SS2-FrM2 A Theoretical Study of Methanol Synthesis from CO_2 Hydrogenation on Metal-doped Cu(111) Surfaces**, *Y. Yang*, State University of New York (SUNY) at Stony Brook, *M.G. White*, Stony Brook University and Brookhaven National Laboratory, *P. Liu*, Brookhaven National Laboratory

The synthesis of methanol (CH_3OH) from CO_2 hydrogenation ($\text{CO}_2 + 3\text{H}_2 \rightarrow \text{CH}_3\text{OH} + \text{H}_2\text{O}$) has attracted considerable attention in the past decades. It is not only industrially important, but also of great environmental significance due to its application in the conversion of greenhouse gas, CO_2 . Commercially, the reaction is performed on a catalyst containing Cu, ZnO and Al_2O_3 , on which the conversion of CO_2 to CH_3OH is kinetically limited to 15-25%. To improve the performance of the Cu catalysts, the effect of alloying on CH_3OH synthesis was investigated in this study.

Density functional theory (DFT) calculations and Kinetic Monte Carlo (KMC) simulations were employed to investigate the CH_3OH synthesis reaction from CO_2 hydrogenation on metal-doped Cu(111) surfaces. Both the formate pathway and the reverse water gas shift (RWGS) reaction followed by CO hydrogenation pathway (RWGS + CO-Hydro) were considered. Our calculations showed that the overall CH_3OH yield increased in the sequence: Au/Cu(111) < Cu(111) < Pd/Cu(111) < Rh/Cu(111) < Pt/Cu(111) < Ni/Cu(111). On Au/Cu(111) and Cu(111), the formate pathway dominates the CH_3OH production. Doping Au does not help the CH_3OH synthesis on Cu(111). Pd, Rh, Pt and Ni are able to promote the CH_3OH production on Cu(111), where the conversion via the RWGS + CO-Hydro pathway is much faster than that via the formate pathway. Further kinetic analysis revealed that the CH_3OH yield on Cu(111) was controlled by three factors: the dioxomethylene hydrogenation barrier, the CO binding energy and the CO hydrogenation barrier. Accordingly, two possible descriptors are identified which can be used to describe the catalytic activity of Cu-based catalysts towards CH_3OH synthesis. One is the activation barrier of dioxomethylene hydrogenation; the other is the CO binding energy. An ideal Cu-based catalyst for the

CH_3OH synthesis via CO_2 hydrogenation should be able to hydrogenate dioxomethylene easily and bond CO moderately, being strong enough to favor the desired CO hydrogenation rather than CO desorption, but weak enough to prevent CO poisoning. In this way, the CH_3OH production via both the formate and the RWGS+CO-Hydro pathways can be facilitated.

9:00am **SS2-FrM3 Synthesis and Characterization of Surface Oxide Films on CoGa(100)**, *D.C. O'Connor*, Stony Brook University, *S. Axnanda*, *W.-P. Zhou*, Brookhaven National Laboratory, *M.G. White*, Stony Brook University and Brookhaven National Laboratory

Methanol is currently garnering a lot of attention as both a chemical feedstock for synthesis of organic substances and as a possible source of energy. It is currently produced industrially from a mix of syngas and hydrogen over a copper-zinc oxide catalyst. However, it has been shown that palladium-gallium oxide is a more active catalyst for methanol production, and uses a carbon dioxide-hydrogen feed, which is desirable for efforts toward CO_2 mitigation^{1, 2}. Surface Science characterization of this catalyst poses a problem as a gallium oxide substrate is not conductive enough for use with X-ray photoelectron spectroscopy (XPS) or low energy electron diffraction (LEED). The most straightforward way to circumvent this limitation is to grow Ga_2O_3 on a conductive substrate. It has been shown that a Ga_2O_3 film forms on the surface of CoGa alloy crystals when exposed to oxygen^{3, 4}. In this work we report the results of the characterization of Ga_2O_3 films on the CoGa(100) surface using XPS, LEED, and ion scattering spectroscopy (ISS). The films were synthesized using either O_2 or NO_2 as the oxidant at 300 K or in excess of 700K. ISS scans showed that cobalt was always present in the top surface layer regardless of oxidation conditions. XPS illustrated that depending on the oxidant and the temperature, the composition of the oxide films vary with some being nearly all Ga_2O_3 and ordered and others Co-Ga mixed oxides that gave no diffraction pattern.

1. Fujitani, T., Saito, M., Kanai, Y., Watanabe, T., Nakamura, J., Uchijima, T., *Appl. Catal. A* **1995**, 125, L199.

2. Collins, S. E., Balatanás, M.A., Bonivardi, A.L., *J. Catal.* **2004**, 226, 410.

3. Pan, F. M., Pflitsch, C., David, R., Verheij, L., Franchy, R., *Surf. Sci.* **2001**, 490, L609.

4. Vlad, A., Stierle, A., Marsman, M., Kresse, G., Costina, I., Dosch, H., Schmid, M., Varga, P., *Phys. Rev. B* **2010**, 81, (11), 115402.

9:20am **SS2-FrM4 Apparent Ferroelectricity from Electrochemistry: Local Vacancy Diffusion in Oxides**, *A. Kumar*, *Y. Kim*, *A. Tselev*, *S.V. Kalinin*, *A. Baddorf*, Oak Ridge National Laboratory

Multiple reports of unexpected ferroelectricity in nanoscale systems have been made based on electromechanical hysteresis detected by piezoresponse force microscopy (PFM). These include thin films of ferroelectric materials below theoretical stability limits and materials without bulk ferroelectricity, such as strontium titanate and manganites. However, recent studies of ionic systems, such as Li-ion conductors, suggest that local electrochemistry, usually ignored in these studies, may have an important role to play in the origin of the hysteresis loops. We report the role of local electrochemistry, including surface and bulk oxygen vacancy generation and dynamics on ionic conductors such as Ytria stabilized zirconia (YSZ) and lanthanum strontium cobaltites (LaSrCoO) and compare results with less understood systems including strained and unstrained SrTiO_3 and the lanthanum aluminate - strontium titanate (LAO-STO) interface.

The role of oxygen vacancies in oxides, of obvious relevance in fuel cells, memristors, superconductors, etc., have traditionally been studied in macroscopic volumes and has been limited by high activation temperatures. We have developed an approach for spatially resolved local assessment of the thermodynamics and kinetics involved in the generation and diffusion of oxygen vacancies by utilizing volume variations of these oxides upon application of a concentrated electric field. In band excitation electrochemical strain microscopy (ESM), a strongly confined electric field at a tip is used to drive the oxygen vacancies in these oxide materials and the tip used to detect the resulting local electrochemical strain due to migration of oxygen vacancies. Vacancy diffusion is relatively slow, so that local strain hysteresis loops are open. Mapping the loop opening as a function of the final bias establishes the onset and kinetics of the diffusion process. Signal relaxation experiments locally characterize the diffusion dynamics of the vacancies. In mixed ionic-electronic oxide systems, current-voltage measurements provide complementary information on electronic transport.

Mapping of local oxygen vacancy diffusivity with 30 nm resolution has been achieved on a number of oxides ranging from purely ionic conductors (YSZ) to mixed ionic electronic conductors (LaSrCoO), including ferroelectrics and resistive switching in TiO_2 and SrTiO_3 films. This approach was further applied to the LAO-STO interface, now a prototypical 2D electron gas with ferroelectric behavior proposed due to local hysteresis

loops. While the role of *static* oxygen vacancies has been well discussed, we explore the local *dynamic* processes in the system. We observe two parallel dynamic processes that we tentatively ascribe to surface charge dynamics and bulk vacancy injection. This behavior is unique for LAO-STO and is not observed in YSZ and LaSrCoO. These observations both explain hysteresis without ferroelectricity and provide insight into the behavior of this system.

This research was conducted at the Center for Nanophase Materials Sciences, which is sponsored at Oak Ridge National Laboratory by the Office of Basic Energy Sciences, U.S. Department of Energy.

9:40am SS2-FrM5 Dopant-enhanced Neutralization of Low Energy Li⁺ Scattered from Si(111). *R.D. Gann*, University of California, Riverside, *Z. Sroubek*, Czech Academy of Sciences, Czech Republic, *J.A. Yarmoff*, University of California, Riverside

The role of doping in semiconductor surface reactions is of fundamental scientific and technological importance, yet the effects of doping in atom-surface charge exchange have never been investigated directly. For example, in the dry processing of silicon, a dependence of oxidation, etching, and silicide formation rates on doping has been observed. The doping concentration changes the density of states at the surface by adding excess majority carriers, which could have a large effect on electron tunneling rates between reactants and the surface, leading to the observed doping dependences. In addition to populating the bands, the band gap of Si narrows with increasing dopant density, which may also influence charge exchange.

This work presented here demonstrates that the charge exchange between scattered low-energy Li ions and a passivated Si surface depends strongly on doping. The neutralization of 3 keV Li⁺ ions scattered from Si(111) is measured as a function of doping density, dopant type, and hydrogen coverage using time-of-flight spectroscopy. When the surfaces are saturated with hydrogen to unpin the Fermi level, the neutral fractions decrease for lightly doped samples, but become anomalously large for highly doped *n*-type Si. The neutralization does not correlate with the surface work function, indicating that the models used for metal surfaces are not directly applicable here.

A model is presented that includes the many-body band-gap narrowing effect, which predicts the neutralization to good accuracy using a tunneling mechanism similar to the free-electron gas jellium model normally employed for ion/metal interactions, but excluding levels in the gap. This work demonstrates that the surface of Si behaves, as far as electron transfer is concerned, like a jellium electron gas with states missing in the band gap region.

10:00am SS2-FrM6 Charge Transfer and Diabatic Dissipation of Surface Released Chemical Energy in GaP/Pt Schottky Nanostructures with a Resistively Heated Nanocathode Layer. *E.G. Karpov*, *S.K. Dasari*, *A. Hashemian*, University of Illinois

Recent observations of chemically induced hot electron flow over Schottky barriers in planar nanostructures provides interesting possibilities for electrolyte-free conversion of chemical energy into electricity and novel sensor applications. The work aims to make advantage of the nonthermal nature of the diabatic chemicurrents and explores the low-temperature (340-430K) chemovoltaic effect of hydrogen to water oxidation on Pt/GaP nanostructure surface. The chemicurrent is also studied at high pressures of the oxyhydrogen mixture diluted with nitrogen, all the way to atmospheric pressures. Separation of the diabatic component to the total generated current is performed with an accurate method based on resistive nanofilm heating.

10:20am SS2-FrM7 Utilizations of Low Platinum Loading Pt-Co Bimetallic Alloy Catalyst for Proton Exchange Membrane Fuel Cells (PEM) in UHV Conditions. *A.S. Ahsen*, Gebze Institute of Technology, Turkey, *O.K. Ozdemir*, Yildiz Tech Univ., Turkey, *O. Ozturk*, Gebze Institute of Technology, Turkey

In this ongoing study it has been tailored surface structures and morphologies to increase chemical and structural stability for higher efficiency and improved utilization compared to presently available Pt-based catalysts used for fuel cell application. Pt-Co bi-metallic alloys is selected to explore the electronic and structural properties of tailored surface and interfaces of electrocatalysts, and it is intended to explain surface chemical dynamics and interaction in fuel cell where chemical reaction pathways are influenced by the nature of the underlying support, the surfaces can be designed and modified appropriately to either promote or inhibit particular reaction.

A series of Pt and Pt-Co bi-metallic nanocatalysts alloys films were deposited on glassy-carbon disks and on a commercial hydrophobic carbon paper substrate by dc magnetron sputtering. The electronic structure and

chemical states of surface were investigated by Photoelectron Spectroscopy (XPS and UPS). Cyclic Voltammetry (CV) and Rotating Disc Electrode (RDE) methods were used to investigate Active Surface Area (ASA) and Oxygen Reduction Reaction (ORR) kinetics. Low loading values, 6–22 μg Pt/cm², were observed the kinetic properties of the nanocatalysts. The highest active surface area was observed with an optimum loading of 10 μg Pt/cm² value. Besides that the Pt-Co alloy catalysts showed significant improvement on catalytic activity against pure platinum catalysts. The effects of deposition temperature on alloy formation and reaction kinetics were also observed. A photoelectron spectroscopy study was also used for understanding electronic interaction between Pt and Co by the function of preparation temperature.

CV measurements indicate that carbon supported Pt-Co catalyst on gas diffusion electrode had electrochemical stability in the acidic environment. Also, it was observed that with increasing Co ratio metal oxidation and reduction current peaks rises. The enhancement on the ORR activity for the PtCo/C catalysts to form of the Pt-shell layer as revealed from the CV analysis, where the PtCo/C electrodes show a delayed formation of Pt-OH and faster reduction of the Pt-oxygenated containing species compared to Pt/C. It means that the oxophilicity of the PtCo/C catalysts are low compared to Pt/C. The hydrogen desorption peaks on the CV curve showed that the highest ESA value was obtained from Pt-Co(3:1) ratio. The capacitance region of PtCo catalysts increases with rising Co ratio. This is a strong evidence for that additional Co layers change the catalyst morphology. As a result, gas can reach to the reaction area easily and this reduces the ohmic resistance.

Surface Science Division

Room: 107 - Session SS-FrM

Surface Science on Graphene

Moderator: I.I. Oleynik, University of South Florida

8:20am SS-FrM1 Towards Controlled Growth of a Single-Layer of MoS₂. *D. Sun*, *W. Lu*, *D. Kim*, *J. Mann*, *L. Bartels*, University of California, Riverside

MoS₂ is a semiconducting material consisting of sulfur-molybdenum-sulfur tripledecker layers loose bound by van der Waals interactions. MoS₂ has been used technologically for a long time, for instance as lubricant, where similar to graphite its layered character was employed. Recently, its electronic characteristics have attained increased attention with the finding that it transitions from an indirect bandgap semiconductor at 1.6eV gap to a direct bandgap one at 1.9eV gap at the transition from multilayers to a single layer. A transistor has been constructed from a MoS₂ and shown appreciable properties. The increased bandgap and high fluorescence yield may also suggest applications of the material for photonic or photocatalytic applications.

MoS₂ can be exfoliated mechanically similar to graphene. While this method is simple, it is hard to control and not amendable to mass production of thin films. Solution-based processes have been proposed and may provide a scalable source of a mixture of single and multilayer material. Here we show an alternative avenue for the fabrication of MoS₂ monolayers: growth of MoS₂ on a sulfur-preloaded copper surface. In contrast to all other methods, this route has the potential of providing exclusively monolayer material, as the sulfur source is only available until the substrate is covered. Practically, this approach is related to the growth of graphene monolayers on copper or ruthenium films, where segregation of carbon to the surface is employed in aggregating a carbonaceous layer that transforms into graphene under the correct conditions.

Small MoS₂ triangles of a few nanometers in size have been grown previously on gold in a dilute H₂S atmosphere. Here we show significantly larger patches, tens of nanometers in size. In contrast to gold, copper forms a multitude of sulfur surface coverages and also readily absorbs sulfur into the bulk. Thus, we can preload the substrate with a specific amount sulfur using an easy to handle liquid precursor, benzenethiol. In previous work we have shown that heating to below 400K removes the phenyl group of benzenethiol reliably from copper leaving sulfur coverages behind.

8:40am SS-FrM2 Oxygen Adsorption on Electronically Modified Graphite Surfaces Studied by Molecular Beam Scattering. *J.P. Oh*, *T. Kondo*, *K. Arakawa*, *Y. Saito*, *J. Nakamura*, University of Tsukuba, Japan

The graphite surface consists of π conjugated system. When the π conjugated system is broken, the non-bonding π electronic states are known to form on the surface. Recently, the non-bonding π electronic states at the Fermi level of the graphite-related materials are expected to the active sites

for the specific chemical reaction such as oxygen-reduction reaction in the fuel cell [1]. It is thus important to understand the interaction between an oxygen molecule and the graphite surface for the efficient usage of the graphite-related materials. We have reported previously that the defects induced by Ar⁺ ion bombardment on the graphite surface significantly affects the gas-graphite interaction based on the measurements of the angular intensity distributions of He and Ar beam scattered from the pristine and the defect induced graphite surfaces [2]. The difference in the gas-surface interaction has been ascribed to the local breaking of the π conjugated system of graphite by defect formation. To further investigate the effect of the modification of the graphite electronic states on the gas-surface interaction, especially for the oxygen adsorption, we have measured angular intensity distributions of O₂ from electronically modified graphite surfaces, namely potassium intercalated graphite, nitrogen-doped graphite (graphite bombarded by N₂⁺ ion) and defective graphite (graphite bombarded by Ar⁺ ion). The detail of scattering features as well as the effects of the electronic modification of graphite on the oxygen adsorption will be discussed in detail with our recent STM and STS results.

*E-mail: nakamura@ims.tsukuba.ac.jp
[mailto:nakamura@ims.tsukuba.ac.jp]

[1] S.F. Huang, K. Terakura, T. Ozaki, T. Ikeda, M. Boero, M. Oshima, J. Ozaki and S. Miyata, *Phys. Rev. B*, **80**, 235410 (2009).

[2] J. Oh, T. Kondo, D. Hatake, Y. Honma, K. Arakawa, T. Machida, J. Nakamura, *J. Phys.: Condens. Matter*, **22**, 304008 (2010).

9:00am **SS-FrM3 Interaction and Thermal Stability of Oxygen Species in Graphene Oxide and Graphene Defects**, *M. Acik, C. Gong, G. Lee, K. Cho, C. Mattevi, M. Chhowalla, Y.J. Chabal*, University of Texas at Dallas
INVITED

Graphene devices are based on finite size flakes (e.g. nanoribbons) in contact with dielectrics or other materials, and therefore require control of edges and depend on the control of processing methods (often involving vapor or wet chemistry). Graphene oxide (GO) represents an interesting system from which much can be learned about oxygen interaction with graphene. Furthermore, studying the reduction of GO provides a powerful way to understand the stability of oxygen species and the role of trapped molecules. We have studied both the thermal and chemical reduction of single- and multi-layer GO using *in situ* infrared (IR) absorption spectroscopy under a variety of conditions. For the commonly used as-synthesized GO, we find that water molecules play an important role in both defect formation (evident from CO₂ evolution)¹ and carbonyl-termination of defect edges at intermediate annealing temperatures (150-250 C).² We also find that a very stable edge configuration appears after high temperature anneals (> 850C), involving edge-ether termination of atomically straight zigzag edges and characterized by an anomalously strong IR absorption.³ The situation is dramatically different when water is replaced by alcohols or more complex molecules (e.g. ionic liquids). In general, defect formation is greatly suppressed (no CO₂ evolution) with less carbonyl formation and a reduced density of atomically straight, edge-ether terminated edges. This talk will summarize the current understanding of the mechanisms involved in thermal reduction and suggest pathways for developing stable graphene nanostructures with reasonable electrical properties.

1. Acik et al., Generation and capture of CO₂ and CO in graphite oxide stacks during thermal reduction Mater. Res. Soc. Symp. Proc., **1205E**, 1205 (2010).

2. Acik et al., The Role of Intercalated Water in Multilayered Graphene Oxide. ACS Nano **4**, 5861 (2010).

3. Acik et al., Unusual infrared-absorption mechanism in thermally reduced GO. Nature Materials **9**, 840 (2010).

9:40am **SS-FrM5 Graphene on Pt(111) as a Template for Pt Nanocluster Formation**, *Z. Liang, H. Khosravian, A. Uhl, R. Meyer, M. Trenary*, University of Illinois at Chicago

Graphene on transition metal substrates often forms superlattices that are manifested as Moiré patterns in scanning tunneling microscopy (STM) images. Such graphene superlattices can serve as templates for the formation of periodic arrays of metal nanoclusters with a uniform size distribution, a situation that is ideal for model catalyst studies. We have used an ultra high vacuum (UHV) STM to investigate graphene growth on Pt(111) from precursor hydrocarbon species. Different periodicities in the Moiré patterns are observed corresponding to different orientations of the graphene layer with respect to the Pt(111) lattice. Various graphene orientations are possible because of a relatively weak graphene-Pt interaction. Following Pt deposition onto the graphene-covered areas of the surface, small Pt nanoclusters were observed. While graphene on Pt(111) only weakly interacts with the substrate, which leads to a weak corrugation in the superlattice compared to other transition metals, such as Ru, our results show that even this weak corrugation is sufficient to serve as a

template for the formation of mono-dispersed Pt nanoclusters. These Pt nanoclusters are relatively stable and only undergo agglomeration for annealing temperatures above 600 K.

10:00am **SS-FrM6 Ripening Behavior of Pt Clusters on Monolayer Graphene Supported by Ru(0001) and the System's Thermal Stability**, *C.U. Lorenz, A.K. Engstfeld*, Ulm University, Germany, *H.E. Hoster*, Technische Universität München, Germany, *R.J. Behm*, Ulm University, Germany

The Moiré-type nm-scale patterns of graphene monolayers supported by metal single crystals were recently used for the fabrication of ordered arrays metal nanoclusters by metal vapor deposition under ultrahigh vacuum UHV conditions [1-3]. The corrugation within the adsorption potential of the graphene layer result in virtually monodisperse clusters. These are important for model (electro-)catalysis studies investigating the size dependency of Pt clusters on carbon support.

In this study we analyze the ripening behavior of Pt clusters (formed at room temperature) on monolayer graphene supported by Ru(0001) at temperatures above 450 K by means of STM. The size distribution change of the clusters gives insight into the rate determining step and into the mechanism of the ripening process. Two different annealing step methods (i: a single sample was successively heated to higher temperatures and ii: individual samples reproducibly prepared in the same manner annealed to certain temperatures; both methods using the same heating period of 10 min) bring us to the conclusion that Pt cluster ripening between 450 K and 725 K occurs via a mechanism proposed by M. Smoluchowski. Above 725 K we observe indications for a change in the ripening mechanism, where Smoluchowski ripening is likely in competition with Ostwald ripening. Also above 725 K, we observed an adverse influence of the Pt on the stability of the monolayer graphene. Single defects in the otherwise well ordered graphene appeared, which were absent after annealing to lower temperatures.

[1] A.T. N'Diaye et al., New J. Phys. **11**, 2009, 103045. [2] Yi Pan et al., Appl. Phys. Lett. **95**, 2009, 093106. [3] K. Donner and P. Jakob, J. Chem. Phys. **131**, 2009, 164701.

10:20am **SS-FrM7 Mechanisms of Graphene Growth on Metals**, *N.C. Bartelt*, Sandia National Laboratories
INVITED

Growth on metal substrates is a promising route for synthesizing high-quality graphene films. In addition, moving electronic applications into the real world requires understanding and controlling the properties of graphene in contact with metals. This talk will focus on the properties and growth mechanisms on several metals distinguished by varying binding strengths to graphene sheets. Mechanistic insight comes from observing growth directly using low-energy electron microscopy (LEEM). On the relatively strongly interacting substrate Ru(0001), graphene grows with a single in-plane orientation from a highly supersaturated sea of C adatoms. On the less interacting substrates Ir(111) and Pd(111), graphene forms several but discrete in-plane orientations. Small but significant differences in graphene's electronic properties (i.e., band structure and work function) result from changes in orientation. On Cu foils, graphene islands nucleate with a large range of orientation. Thus, the weak film-Cu interaction leads to a high defect density. Finally, the mechanism of bilayer graphene growth has been explored. Diffraction analysis reveals that the second graphene layer on Ir(111) grows next to the substrate, not on top of the first layer. This "underlayer" growth mechanism occurs when the carbon source is either segregation from the substrate or deposition on top of the first layer. How this unusual mechanism affects thickness uniformity will be discussed.

This work was supported by the Office of Basic Energy Sciences, Division of Materials and Engineering Sciences of the U.S. Department of Energy under Contract No. DE-AC04-94AL85000.

11:00am **SS-FrM9 Graphene Moiré Polymorphism on Hydrogenated Ruthenium Surfaces**, *B. Diaconescu*, University of New Hampshire, *F. Hagelberg*, East Tennessee State University, *K. Pohl*, University of New Hampshire

Graphene has aroused tremendous interest due to its remarkable electronic and mechanical properties. The lack of a band-gap, however, causes a serious challenge for implementing graphene as a material for electrical switches and therefore creative ways of inducing this band-gap are needed. We will present a STM/LEED/DFT study of the monolayer graphene on Ru(0001) system in the presence of hydrogen. STM reveals a diverse array of Moiré superlattice sizes ranging from 0.9 to 2.4 nm in the presence of hydrogen adlayer structures, as confirmed by LEED. Density functional theory calculations show a correlation between the Moiré superstructure

sizes and the hydrogen coverage and the opening of a band-gap in the graphene/H/Ru(0001) system for some of the Moiré/hydrogen adlayer coverages.

This work was supported by the Nanoscale Science and Engineering Center for High-rate Nanomanufacturing (NSF NSEC-425826) and NSF DMR-1006863.

11:20am **SS-FrM10 Modifying Ni(111)/Graphene Interfaces by Sn-Ni Interface Alloy Formation**, *R.Q. Addou, A. Dahal, L. Adamska, I.I. Oleynik, M. Batzill*, University of South Florida

Graphene growth on metal surfaces (Ni, Pt, Ir, Rh and Cu) has been studied extensively [1]. Ni(111) is special among these metals because it is closely lattice matched with graphene ($a_{\text{graphene}} = 0.246$ nm vs. $a_{\text{Ni(111)}} = 0.249$ nm) allowing the growth of graphene with a single domain and in registry with the substrate [2]. However, compared to most other metal substrates the interaction between Ni and graphene is rather large, resulting in a small metal-carbon distance and a large shift of the graphene π -band compared to freestanding graphene. In order to de-couple graphene from the Ni-substrate other weaker interacting metals such as Cu and Au have been successfully intercalated between the graphene and Ni-substrate [3]. These metals have, however, a different lattice parameter and consequently the registry between the substrate and graphene is lost. Here we demonstrate a new approach that weakens the metal-graphene interaction without destroying the lattice registry. By intercalating Sn-atoms an ordered $\sqrt{3} \times \sqrt{3}$ R30° Sn-Ni alloy is formed at the interface. The Sn intercalation process is characterized by Auger electron spectroscopy (AES) and low energy electron diffraction (LEED). In this alloy Sn substitutes for surface Ni atoms without changing the lattice parameter of the substrate and consequently the registry between the metal substrate and graphene is maintained. DFT simulations indicate that Sn alloying with Ni weakens the interaction of graphene with the metal substrate and consequently increasing the graphene-substrate distance and restoring the graphene π -band close to the position of free-standing graphene. Atomic-resolution scanning tunneling microscopy (STM) imaging reveals that the alloy periodicity is reproduced in the graphene layer, i.e. a $\sqrt{3} \times \sqrt{3}$ R30° superstructure is imposed on the graphene by the alloy substrate. This indicates a variation of the local density of states for C-atoms located on top of Sn-substrate sites compared to Ni-sites. Further experimental and theoretical characterization of the influence of the substrate on the electronic and structural properties of graphene is ongoing.

[1] J. Winterlin and M.-L. Bocquet, *Surf. Sci.* **603**, 1841-1852 (2009)

[2] J. Lahiri et al., *Nano Lett.* **11**, 518-522 (2010)

[3] A. Varykhalov et al., *Phys. Rev. Lett.*, **101**, 157601 (2008)

11:40am **SS-FrM11 Silicene Epitaxial Sheets: Silicon New Start**, *P. Vogt*, Aix Marseille Univ, CNRS-CINaM, France and Technische Universität Berlin, Germany, *P. De Padova, C. Quaresima*, CNR-ISM, Italy, *J. Avila, E. Frantzeskakis, M.C. Asensio*, Synchrotron SOLEIL, France, *B. Ealet*, Aix Marseille Univ, CNRS-CINaM, France, *G. Le Lay*, Aix Marseille Univ, CNRS-CINaM, France and CNR-ISM, Italy

We have just synthesized in Marseille silicene sheets [1], i.e., atom-thin two-dimensional graphene-like silicon layers with an in-plane Si-Si interatomic distance of 0.23 nm [2], upon in-situ epitaxial growth on silver (111) surfaces. The honeycomb atomic structure is revealed in Scanning Tunneling Microscopy, while the long-range epitaxial order is confirmed by sharp 4x4 Low Energy Electron Diffraction patterns. Dirac cones at the K and K' points of the silicene Brillouin zone, evidenced in High-Resolution Synchrotron Radiation Angle-Resolved PhotoElectron Spectroscopy measurements, point to massless relativistic fermions with a Fermi velocity of 1.3E6 m/s, as theoretically predicted [3], quite the same as graphene, and four times higher than previously obtained on a one-dimensional grating of silicene nano-ribbons [4]. Density Functional Theory calculations including the *Ag(111)* substrate confirm the stability of the epitaxial arrangement. The demonstration that silicon can form sheets of silicene, a two dimensional honeycomb structure, which does not exist in Nature, is tantalizing for new Physics. Silicon being the workhorse of electronics industry, this synthesis could have a major impact for novel devices because of the compatibility with existing Si technologies.

[1] P. Vogt, P. De Padova, C. Quaresima, J. Avila, E. Frantzeskakis, M.C. Asensio and G. Le Lay, submitted

[2] G. G. Guzman-Verri and L.C. Lew Yan Voon, *Phys. Rev. B* **76**, 75132 (2007).

[3] M. Houssa, G. Pourtois, M. Heyns, V.V. Afanas'ev, and A. Stesmans, *J. Electrochem. Soc.* **158**, H107 (2011)

[4] P. De Padova et al., *Appl. Phys. Lett.*, **96**, 261905 (2010)

Thin Film Division

Room: 110 - Session TF-FrM

Thin Films: Growth and Characterization II

Moderator: S. Gupta, University of Alabama

8:20am **TF-FrM1 Low-temperature CVD with Growth Inhibitors to Afford Uniform, nm-thick Films in Structures with Aspect Ratio ~ 200**, *S. Babar, J. Abelson*, University of Illinois at Urbana Champaign

In order to grow uniform, smooth and pinhole-free films of nm thickness, the nucleation step must occur with high areal density on the substrate and the nuclei must have a narrow size distribution. If the film must be deposited inside of a deep structure of very high aspect ratio, then the growth process must be strictly governed by the surface reaction rate of the precursor species rather than by the rate at which precursor is transported to the growth surface. Here, we present a method of control in chemical vapor deposition that simultaneously meets both of the above criteria.

We previously reported that the steady-state film growth rate is reduced when a molecular species, called the *inhibitor*, is added to the CVD process. The inhibitor interacts transiently with the growth surface but does not decompose and incorporate its elements into the film, i.e., the inhibitor is not consumed. We also reported that the inhibitor greatly improves the film nucleation step, e.g. for the growth of HfB₂, a high performance diffusion barrier, on SiO₂ substrates. In the absence of the inhibitor the nucleation density is low and the size distribution is broad, such that some islands attain a height of > 10 nm before the film even coalesces. In the presence of the inhibitor, nuclei attain a height of ~ 1 nm, but then grow only very slowly. Additional nuclei continue to form and fill in the bare substrate, such that coalescence occurs at a thickness of ~ 2 nm with a rms surface roughness of ≤ 0.5 nm.

The use of a growth inhibitor allows the *nucleation regime of film growth* to afford excellent nm-thick coatings in extremely high aspect ratio features. Note that when the film growth rate is low, so also is the consumption of precursor, such that a partial pressure of precursor species persists to the bottom of the feature. The inhibitor further assures that the nucleation process will be uniform. In features of aspect ratio > 200, we show that a film is deposited on all surfaces with a rms roughness of 0.6 nm. We also discuss the mechanisms that can afford the observed results. We suggest that the ability to reduce (homogenize) the size distribution and increase the areal density of nuclei will greatly extend the useful range of CVD precursor-substrate combinations which can afford nm-thick coatings in very high aspect ratio features.

8:40am **TF-FrM2 Understanding the Role of Hydrogen Impurity Scattering in Manganese Thin Films on the Si(001) Surface**, *A.J. Stollenwerk, B.J. Friend*, University of Northern Iowa

Interest in energy production via hydrogen has been increasing due to the fact that it does not emit harmful greenhouse gases associated with fossil fuels. Unfortunately, hydrogen is an explosive gas that is both colorless and odorless. This will make hydrogen sensors an important piece of safety equipment in a hydrogen based economy. Diffusion of hydrogen to the Mn/Si interface is believed to have an amphoteric effect on the interface characteristics making it a possible hydrogen sensor. This motivates a need to better understand electron transport properties through Mn/Si Schottky diodes. We performed ballistic electron emission microscopy (BEEM) on Mn/Si(001) Schottky diodes to study hot electron transport properties through this system. Samples were fabricated using electron-beam deposition of Mn onto n-type Si(001) with thickness ranging from 10 to 40 Å. Scattering in the Mn films as function of energy has been measured and compared to results obtained on Au/Si(001) Schottky diodes. Schottky heights on these samples were determined from the corresponding BEEM spectra using the Bell-Kaiser model. Future plans include introducing an atmosphere consisting of varying amounts of hydrogen and measuring the resulting effects on hot electron transport in the Mn film as well as the Schottky height. Should electron scattering or the Schottky height be affected by the presence of hydrogen, this system may prove useful as an inexpensive hydrogen sensor.

9:00am **TF-FrM3 Elimination of Indium Surface Segregation in InGaN Grown Throughout the Miscibility Gap**, *M.W. Moseley, B. Gunning, J.E. Lowder*, Georgia Institute of Technology, *G. Namkoong*, Old Dominion University, *W.A. Doolittle*, Georgia Institute of Technology

InGaN alloys have great potential in optoelectronics due to the tunable bandgap which spans the visible spectrum. However, these alloys are difficult to obtain as a result of thermal decomposition, indium surface segregation, and spinodal decomposition. To solve these problems, low growth temperatures, fast growth rates, and in situ surface analysis must be

used. These limitations make Metal-Modulated Epitaxy (MME) a promising growth candidate. Using MME, smooth InGaN has been grown without phase separation throughout the miscibility gap.

MME is a growth technique applied to molecular beam epitaxy of III-nitrides in which metal and dopant cell shutters are periodically opened and closed while active nitrogen flux remains constant. This technique uses metal-rich fluxes that would accumulate droplets in traditional MBE, taking advantage of the enhanced adatom mobility provided by excess metal. The periodic shuttering of the effusion cells allows the excess metal to be consumed, providing smooth, dry surfaces required for devices that demand abrupt interfaces.

In this study, MME is applied to the growth of InGaN and transient RHEED intensities are monitored for differing metal shutter open times (Fig. 1). It is found that these RHEED transients are the result of a RHEED oscillation associated with the buildup and consumption of the metal adlayer. This allows for observation and control of fractions of adsorbed metal layers. However, there is a drastic difference between the RHEED transients of low and high metal shutter open times. This difference is attributed to indium surface segregation, resulting in leftover In on the surface that does not form InN at these elevated temperatures. A model for adlayer buildup and consumption is developed, and a key RHEED signature is identified as the onset of surface segregation. The thickness of the adsorbed metal at this onset is found to be between 1 and 2 ML for various compositions. Samples grown throughout the miscibility gap using this technique exhibited single phase XRD spectra and < 1 nm RMS roughnesses (Fig. 2). High hole concentrations in p-InGaN are also achieved by MME (Fig. 3).

At the low temperatures required for high indium-content InGaN, an intermediate growth regime in MBE does not exist. Thus, traditional MBE cannot produce metal-rich InGaN without droplets or surface segregation. Because the onset of surface segregation ($1 < x < 2$ ML) occurs below droplet accumulation (<2.3 ML), this study confirms that for metal-rich InGaN growth, some form of modulation must be employed.

This work was supported by the Air Force Office of Scientific Research under a basic science grant managed by Kitt Reinhardt.

9:20am **TF-FrM4 Aging Effect on the Hydrophilicity of Metal Nanorod Arrays**, *N. Albarakati, D. Ye*, Virginia Commonwealth University

Time dependent wettability of nickel nanorod arrays were studied by measuring the water contact angles on the samples. Nickel nanorods arrays were deposited on silicon substrates by sputtering oblique angle deposition with an 85° incident angle. The substrates are rotated at a speed of 0.5 rps by a stepper motor. Samples with varying nanorod heights were prepared. Water contact angles were measured for each sample on a sequence of time up to three months. The water contact angles on the fresh nanorod arrays are less than 10°. However, the contact angle increases with time after the samples were exposed to air. We observed that the contact angles on the samples with short nanorods increase quickly to an angle close to hydrophobic and that on the samples with long nanorods increase slowly and remain in the hydrophilic region. X-ray photoelectron spectroscopy was employed to study the change of the surface composition due to oxidation and hydrocarbon contamination. We believe that the change of water contact angles is due to the accumulation of hydrocarbon on the nanorod surface.

9:40am **TF-FrM5 Cubic ZnMgO and NiMgO for UV-C Applications**, *R.C. Boutwell, J.W. Mares, M. Wei, W.V. Schoenfeld*, University of Central Florida

We will report on two new ternary cubic oxides offering close lattice matching to MgO, ZnMgO and NiMgO, and compare the properties of films grown by both RF Plasma-Assisted MBE and a much more economical sol-gel deposition process. Using both methods we have successfully demonstrated band gap tuning in the UV-C spectral region, with ZnMgO films producing band gaps ranging from ~5eV to 7.8eV and NiMgO films having band gaps ranging from 3.5eV to 7.8 eV. XRD revealed 2θ FWHM values as narrow as 0.19°, and atomic force microscopy of ZnMgO films demonstrated surface roughness of 3.4nm with NiMgO films having roughness below 1Å. Optical, compositional, and morphological results from films produced using both synthesis methods will be presented. We will also report on initial photodetectors with 5µm interdigitated fingers that produced peak responsivities of 12 mA/W at 250 nm.

10:00am **TF-FrM6 Growth of Fe-Pd Nanoparticles and Thin Films via Pulsed Laser Deposition and the Matrix Assisted Pulsed Laser Evaporation of Metal Based Acetates**, *M.A. Steiner, J.M. Fitz-Gerald*, University of Virginia

Nanoparticle and thin film magnetic alloys of 3d-4d/5d metals such as Fe-Pt, Co-Pt, and Fe-Pd are of technological interest due to their ordered L1₀ tetragonal phase which exhibits high magnetocrystalline anisotropy. Hard magnetic properties combined with ductility and corrosion resistance make these alloys ideal for applications including micro-electro-mechanical systems and ultra high-density magnetic storage. These materials have also been shown to possess a unique strain-induced chessboard eutectoid microstructure between their hard L1₀ and soft L1₂ magnetic phases that features exchange coupling effects. Within this class of materials Fe-Pd alloys possess a low order-disorder transition temperature making them a good candidate for ordered structure studies.

Nanoparticles and thin films of eutectoid (61.5 at% Pd) Fe-Pd were deposited by pulsed laser deposition. Additionally ordered nanoparticles were deposited utilizing a novel technique involving the matrix assisted decomposition of metal-organic precursors. Nanoparticles and films were subsequently characterized by x-ray diffraction, vibrating sample magnetometry, high resolution transmission electron microscopy, and scanning electron microscopy.

10:40am **TF-FrM8 Surface Plasmon Resonance Excited in RuO₂ Films Grown on Glass and on Crystalline (001) TiO₂**, *L. Wang, K. Yang, C. Clavero, E. Crisman, V. Dinavahi, I. Novikova, R.A. Lukaszew*, College of William and Mary

PLEASE NOTE YOU MUST IDENTIFY A DIFFERENT PRESENTER FOR THIS ABSTRACT. YOU MAY PRESENT ONE PAPER ONLY (ORAL OR POSTER) AT THE CONFERENCE. YOU ARE ALREADY LISTED AS PRESENTER OF ABSTRACT #554Surface Plasmon Resonance (SPR) excitation in metallic thin films and nanostructures has been widely applied to study biomolecules absorption, bio-imaging, bio-sensing, and sensitivity enhanced Raman spectroscopy [1,2,3]. However, although the theoretical principles underlying SPR excitation are applicable to any conductive material, only metals, and in particular Au and Ag, have been considered for practical applications. Here we investigate SPR excitation in a conducting metal oxide such as RuO₂. Due to the optical properties frequency dependence, SPR excitation is more intense in the infrared region for this material. The RuO₂ thin films investigated were grown using reactive magnetron sputtering on two different substrates resulting on amorphous RuO₂ films when deposited on glass and crystalline RuO₂ films when epitaxially deposited on TiO₂ (001) substrates. We have used Atomic Force Microscopy (AFM) and Reflection High-Energy Electron Diffraction (RHEED) to characterize the surface morphology and microstructure of these samples. Four-point probe was used to investigate the electrical conductivity properties and ellipsometry was used to characterize the optical properties of the films. We will show a comparison of the physical properties including the SPR excitation between these two kinds of thin film RuO₂ samples. The investigation of SPR in conducting metal oxide materials provides a significant advancement for thin film characterizations as well as opens new venues for photonic and plasmonic applications.

This work was financially supported by NSF (DMR-1006013).

[1] Amanda J. Haes and Richard P. Van Duyne, *J. Am. Chem. Soc.*, 2002, **124** (35), pp 10596–10604.

[2] Lin He, Michael D. Musick, Sheila R. Nicewarner, Frank G. Salinas, Stephen J. Benkovic, Michael J. Natan, and Christine D. Keating, *J. Am. Chem. Soc.*, 2000, **122** (38), pp 9071–9077.

[3] Lehui Lu, Atsuko Kobayashi, Keiko Tawa, and Yukihiro Ozaki, *Chem. Mater.*, 2006, **18** (20), pp 4894–4901

11:00am **TF-FrM9 Towards Achieving a High Degree of Carbon Ionization in Magnetron Sputtering Discharges**, *A. Aijaz, K. Sarakinos, D. Lundin, U. Helmersson*, Linköping University, Sweden

Physical vapour deposition (PVD) methods, which are characterized by highly ionized deposition fluxes of the film forming species, provide added means for the synthesis of tailor-made materials. They can, for instance, facilitate the growth of meta-stable phases, nanostructures as well as selective deposition on complex-shaped substrates. In such methods, the generation of highly ionized deposition fluxes stems from high electron (plasma) densities. Cathodic arc and pulsed laser deposition are examples of such discharges where electron densities in the order of 10²¹ m⁻³ can be obtained. These techniques, while providing as high as 100% degree of ionization of the deposition flux, exhibit several drawbacks, such as macroparticle ejection from the target, lack of lateral film uniformity, and in some cases are difficult to scale up. Magnetron sputtering based techniques

are technologically more relevant, owing to their inherent advantages of conceptual simplicity, upscalability, and film uniformity. However, electron densities in magnetron discharges are significantly smaller, in the range of 10^{14} - 10^{16} m^{-3} and therefore generation of a highly ionized deposition flux is often difficult. This difficulty is overcome by high power impulse magnetron sputtering (HiPIMS), where plasma densities on the order of 10^{19} m^{-3} are achieved. HiPIMS has been successful in enhancing the ionization for most common metals (Cu, Al, Ta, Ti), but it is challenged when non-metals such as carbon is considered. Previous investigations have shown that C⁺/C ratio in HiPIMS does not exceed 5%, which does not provide efficient control over the physical properties and synthesis of carbon in various technologically relevant forms, e.g. tetrahedral amorphous carbon. In the present study we address the low degree of ionization of carbon in magnetron discharges. We have developed a new HiPIMS based process, which provides a plasma characterized by high electron temperature and plasma density as determined by time-resolved Langmuir probe measurements. The C⁺ ion energy distribution functions (IEDFs) determined by time-averaged energy resolved mass spectrometry demonstrate an energetic C⁺ ion population and an overall five-fold increase of the C⁺ ion fraction as compared to standard HiPIMS methods. The enhanced ionized fraction of carbon facilitates the growth of carbon films with mass densities as high as approx. 2.8 g/cm³ as determined by high resolution x-ray reflectivity measurements. Determination of the D-peak to G-peak ratio (I(D)/I(G)) and full width at half maximum of the G-peak in Raman spectra indicate that the films contain a large fraction of diamond-like bonded (sp³) carbon.

11:20am **TF-FrM10 Kinetics of Sputtered Metal Film Growth on Vertically Aligned Carbon Nanotube Arrays**, *C. Muratore, A. Reed, A. Waite, J. Bultman, J. Hu, T. Smith, A.A. Voevodin*, Air Force Research Laboratory

Controlling the surface morphology of metallized arrays of vertically aligned nanotubes (VACNTs) is useful for diverse technological applications, such as interface materials for thermal management of high-heat flux electronics and electrical contacts for MEMS switches. We have observed variation of the morphology of metal films sputtered on carbon nanotubes, ranging from thin continuous films surrounding individual bundles of carbon nanotubes along their entire length for tubes up to 100 microns in length, to metal canopies covering the surface, with only minimal penetration (10-20 microns) into the nanotube forest. There is a strong link between flux of metal ions and their kinetic energy and the morphology of metal films of technological interest, including titanium, nickel, copper, gold and aluminum. To explore the mechanisms dictating metal film architectures on VACNT arrays, we systematically altered the flux and energy of incident metal and inert gas ions. These processing conditions were characterized using a mass spectrometer and energy analyzer adjacent to VACNT substrates. For conditions of interest, film growth was carried out for different times in an ultra high vacuum processing chamber, followed by electron microscopy of VACNT film cross sections, which were examined to observe different stages of growth and identify mechanisms of film nucleation and growth on nanotube sidewalls and tips. Comparison of growth kinetics of metal films on planar (002) graphite surfaces to that observed on VACNTs was used to identify effects of curvature on film growth. Switch performance was shown to be strongly dependent on morphology.

11:40am **TF-FrM11 Crystallographic Orientation of Vanadium Dioxide Nano-Grains on Various Single-Crystal Sapphire Substrates**, *F. Rivera*, Brigham Young University, *J. Nag, R.F. Haglund Jr.*, Vanderbilt University, *R. Davis, R. Vanfleet*, Brigham Young University

Vanadium dioxide (VO₂) is a material of particular interest due to the reversible semiconductor to metal phase transition that VO₂ exhibits near room temperature (~ 68 °C) and the accompanied hysteresis. Recent studies suggest that external stresses applied to VO₂ crystals have an effect on the transition temperature and hysteresis. Thin films of VO₂ were deposited on three different cuts of sapphire by Pulsed Laser Deposition (PLD). Electron Back-Scattered Diffraction (EBSD) was used to study the orientation of the crystalline VO₂ grains obtained and showed epitaxial relationships between the different single-crystal substrates. A predominant family of crystallographic relationships is present in all cuts of sapphire wherein the rutile VO₂ {001} planes tend to lie parallel to the substrate's {10-10} and the rutile VO₂ {100} planes lie parallel to the substrate's {1-210} and {0001}. This family accounts for the majority of the VO₂ grains observed on all substrates with specific orientations (and stresses) depending upon the substrate's normal direction. Transmission Electron Diffraction patterns taken from cross-section of particles of the A and R cut sapphire substrates helped to lift the ambiguity present in the rutile {100} axes. EBSD showed additional families of relationships in the C and R cuts of sapphire, most related to the aforementioned predominant family. Variations in the

transition temperatures of the deposited thin films mentioned in this study are attributed to the stresses generated by the epitaxial relationships.

Authors Index

Bold page numbers indicate the presenter

— A —

Abavare, E.: EM-ThP9, **241**
Abb, S.: SS2-MoA2, 50
Abdulagatov, A.I.: TF1+EM-WeM11, 157
Abdulgalil, A.: SS1-MoM1, 21
Abel, J.: AS+BI+NS-WeM11, 133; GR+MI-TuA3, **91**
Abelson, J.: TF-FrM1, 270
Abolfath, R.M.: EM-ThP7, **241**
Abou Rich, S.: PS+SE-WeM3, 148
Abouimrane, A.: EN+NS-ThM3, 193
Abraha, P.: TR-ThP7, **257**
Abraham, B.: PS-ThP29, 255
Abraham, D.W.: TF1+EM-WeA9, 181
Abraham, F.: EN+AC-FrM7, 261
Abraham, J.: EN-ThP12, **247**
Acharya, A.R.: EM-ThP14, 242; EM-ThP15, **242**
Acharya, D.: EM-ThP1, 240; NS+AS-TuA10, 98; SS1-TuM11, **75**; SS2-WeM11, 155
Achim, C.: SS2-TuM11, 76
Acik, M.: EM-ThP7, 241; EN+NS-ThM1, 193; GR+TF+NS-ThA10, **222**; SS-FrM3, 269; SS-TuP3, **123**
Acomb, P.D.: VT-TuP5, **130**
Adamiv, V.: SS-ThA10, 231
Adamska, A.: AC+MI-WeA11, 160
Adamska, L.: GR+MI-TuA9, 92; GR+TF+ET-MoA4, **37**; GR-MoM3, 10; SS-FrM10, 270
Adderley, P.A.: VT-TuM1, 80
Addou, R.Q.: GR+TF+ET-MoA4, 37; SS-FrM10, **270**
Adiga, V.P.: MN-ThA6, **223**; MN-ThA7, 223
Afonso, C.R.M.: SS-TuA1, 105
Afzali, A.: BI-MoA8, 31
Agamalian, M.: NT+AS-WeA4, **171**
Agapito, L.A.: GR+TF+NS-ThA8, 221
Agarwal, A.: PS1-TuA4, 99; PS1-TuA9, 100; PS-FrM6, 265; PS-WeA8, **175**; PS-WeA9, 175
Agarwal, S.: TF-TuA3, **107**
Aghazarian, M.: PS-WeA3, 174
Ahmet, P.: NM+MS+NS+TF-MoM5, 16
Ahn, J.: EM-ThP16, 243
Ahn, S.: NM+NS+MS-TuA12, 97
Ahsen, A.S.: SS2-FrM7, **268**
Aijaz, A.: TF-FrM9, **271**
Aita, C.R.: TF2-ThM9, **211**
Ajo, H.M.: AS-TuP12, **112**
Akerlind, C.: EL+AS+EM+MS+PS+TF-ThM4, **190**
Akey, A.J.: PS-ThP19, 253
Aksamija, Z.: ET+EM+NS+GR-TuM5, 63
Aksoy, F.: IS+AS+SS-TuM9, 66
Alaboson, J.M.P.: NS-WeM3, **145**
Alagoz, A.S.: SE+TF-TuA3, **102**
Alam, M.: BI-TuA9, 85
Albarakati, N.: TF-FrM4, 271
Albrecht, A.J.: AC+TF-ThA3, **215**
Al-Brithen, H.A.H.: MI-ThM10, 197
Albu, S.P.: AS-TuP19, 113
Alden, J.S.: MN-ThA4, 222
Aldinger, B.: PS+SE-MoA11, 47
Alexander, M.R.: BI-WeM3, 134
Alexandrov, T.: BI-WeM4, 134
Alexeenko, A.: TF2-ThM1, **210**
Alkemade, P.F.A.: HI+AS-TuA10, 95; HI+AS-TuA12, 96; HI+AS-TuA4, **95**
Allara, D.L.: EN+NS-TuM2, 61
Allard, L.F.: EN-ThP17, 247
Allee, D.: TC+AS+EM-ThM11, 208
Allen, S.: AS+BI+NS-WeM12, 133; PS-TuM12, 73; PS-TuM5, 72
Allen, S.A.: SS2-TuM5, **76**
Allen, T.R.: EN-TuM1, **62**
Alles, M.L.: EM-WeA11, 165
Alnabulsi, S.: AS-ThM10, 188; AS-TuP4, **111**

Alonzo Medina, G.M.: TF1-ThM1, 208
Altamirano-Sanchez, E.: PS+SE-MoA4, **46**
Altfeder, I.: SE+SS-WeM4, 151
Altman, E.I.: NS+AS-TuA4, 97; SS-ThA1, **230**
Altman, M.S.: GR-WeA4, **169**
Amabye, H.: NT+AS+MI-WeM3, 147
Amano, H.: PS-ThM11, 203
Amatucci, G.: EN+NS-ThM2, 193
Ambye, H.: NT+AS+MI-WeM5, 147; NT-TuP2, 121
Ambrosini, A.: AS-MoA8, 29
Amelichev, V.A.: MI-ThP2, 248
Amine, K.: EN+NS-ThM3, **193**
Aminpour, M.: SS2-TuM6, 76
Amstad, E.: NS-ThA4, 224
An, J.: MI-WeA12, 171; PS+SE-MoA10, 47
Ancona, M.D.: GR+MS+EM-FrM3, 262
Andersen, J.N.: IS+AS+SS-MoM4, 13; IS+AS+SS-MoM6, 14; IS+AS+SS-MoM9, 14; NS-WeM2, 145
Anderson, D.G.: BI-WeM3, 134
Anderson, E.V.: TR+AS+SS-ThM11, 213
Anderson, I.M.: AS-TuA8, 84
Anderson, T.J.: GR+MS+EM-FrM3, 262
Anderson, V.R.: TF+EN-TuM2, **77**; TF1+EM-WeM3, 156
Andersson, A.M.: SE-ThM10, 204; TF1-ThM11, 210
Ando, T.: AS+BI+NS-WeM1, **132**
Andruczyk, D.: TC+AS+EM-ThM6, 207
Aneskavich, L.E.: PS-ThA2, 227
Ankner, J.: EM1-MoA6, 33
Anniyev, T.: GR+TF+ET-MoA3, 37
Ansai, H.: PS-ThM3, 201
Ansari, N.: TR-ThA9, 235; TR-ThP4, 256
Antonelli, G.A.: PS+EM-WeA7, 173; PS+EM-WeA8, 173
Aoki, T.: AS-TuM10, 57
Appavoo, K.: NS-MoA2, **42**
Appleton, B.R.: GR+EM-TuM11, 65; GR+MI-TuA11, 92; GR+MS+EM-FrM6, 262
Arab-CHapelet, B.: EN+AC-FrM7, 261
Arahara, S.: SS-TuP27, **126**
Arakawa, I.: SS1-MoA10, **49**
Arakawa, K.: SS-FrM2, 268
Araki, R.: PS2-TuA1, **101**
Arakoni, R.A.: EM-WeM2, **135**
Arehart, A.: EM-WeA3, 163
Aresta, G.: TF-MoM4, **24**
Arey, B.W.: AS-WeA7, 161; HI+AS+BI+NS-WeM11, **142**
Armbrust, N.: SS-TuP12, 125
Árnadóttir, L.: BI-MoM8, **5**
Arnold, J.: PS-MoM9, 20; PS-TuM5, 72
Arnold, M.: GR+TF+NS-ThA1, **220**
Arnold, P.C.: VT-MoM4, **26**
Arpa Sancet, M.P.: BI-ThP11, **239**
Arpa, R.: VT-MoA11, 54
Arrachea, L.: GR+TF+NS-ThA3, 221
Artyushkova, K.: AS-TuA7, **83**; AS-TuP3, 111
Arvin, H.: EL+AS+EM+MS+PS+TF-ThM4, 190; EL-ThP3, 239
Aryal, P.: EL+AS+EM+MS+PS+TF-ThA4, 216
Asano, K.: PS1-TuA11, 101
Asensio, M.C.: SS-FrM11, 270
Ash, J.: BI-MoM4, 4
Ashby, P.: NM+MN+MS+TF-TuM12, 68
Ashurst, W.R.: TR-ThA9, 235; TR-ThP4, 256
Asmar, M.: GR+MI-TuA10, **92**
Assaf, E.M.: SS-TuA1, 105
Asscher, M.: EN+EM+NS-WeM6, **137**
Assoufid, L.: SE-TuP2, 122
Atalay, R.: EM1-MoA4, **32**; EM-ThP10, 242; EM-ThP11, 242; EM-ThP13, 242; EM-ThP15, 242
Atkin, J.M.: PS+EM-WeA1, 172
Atkinson, S.: BI-WeM3, 134

Attili, S.: AS-MoA1, 28
Attygalle, D.: EL+AS+EM+MS+PS+TF-ThA4, **216**
Atuchin, V.V.: EL-ThP1, **239**
Augur, R.: EM-WeM9, 136
Avila, J.: SS-FrM11, 270
Avouris, Ph.: GR+TF+ET-MoA7, 37; NS-WeM4, **145**
Avril, N.: PS+SE-WeM3, 148
Axnanda, S.: SS2-FrM3, 267
Aydil, E.S.: EN1+TF-WeA11, 167; EN1+TF-WeA2, **165**; EN1+TF-WeA7, 166; PS+SS-ThA1, **225**
Azamoum, Y.: PS+SS-WeM9, 150
Azarnouche, L.: PS+SE-MoA3, 46
Azimi, S.: MN-FrM10, **264**
Aznárez, J.A.: SS-TuP29, 127
Azucena, C.: TF-MoM5, 24
Azuma, Y.: NS-TuP2, 119

— B —

Babaeva, N.Yu.: PS-FrM1, 265; PS-FrM3, **265**
Babar, S.: TF-FrM1, **270**
Baddorf, A.: ET+EM+SS-MoM3, **9**; SS2-FrM4, 267
Bae, I.J.: TC-ThP3, 255
Bae, J.: EN-ThP3, 245
Baek, H.: GR-TuA2, **92**
Baek, K.H.: PS+SE-MoA1, 46
Baer, D.R.: AS-MoA6, 28; AS-ThM4, **187**
Baer, M.: SS1-MoM6, 21
Bag, S.: EN1+TF-WeA3, 166
Bagge-Hansen, M.: NS-ThM11, 198
Baglin, V.: VT+MN+NS+SS+AS-TuA12, 110
Bagus, P.S.: AC+SS-ThM1, **185**; IS+AS+SS-MoM5, 13
Bai, X.: ET+EM+NS+GR-TuM6, 63
Bailey III, A.D.: PS1-TuA2, 99
Bailey, C.A.: EN+NS-WeM4, **139**
Bailly, F.: PS+EM-WeA10, 173
Baily, C.: AS-TuP8, **112**
Baio, J.E.: AS-TuA3, **83**; BI-MoM4, 4
Bajaj, S.: EM+SS-FrM7, 260; EM+TF-TuM12, 60
Baker, L.: TF+EN-TuM3, **77**
Baklanov, M.: PS1-TuA7, 100
Balaeff, A.: SS2-TuM11, 76
Balakrishna, A.: PS1-TuA4, 99; PS1-TuA9, **100**; PS-WeA8, 175
Balakrishnan, S.: PS-MoM10, 20
Balandin, A.: GR-TuA10, 93
Balatsky, A.V.: AC+MI-WeA3, 159
Balaz, S.: EM-WeA4, 164
Balci, S.: AS-TuA9, 84; EN+EM+NS-WeM12, 138
Baldo, M.: EN+NS-WeM5, **139**
Baldwin, J.W.: GR+MS+EM-FrM10, 263
Balk, T.J.: SE-ThM5, 204
Bałkowiec, A.: SS1-WeM12, 153
Ballard, J.: IS+AS+SS-MoM10, 14
Ballinger, T.: EW-TuA5, **91**
Bally, M.: BI-TuA10, **85**
Balmes, O.: IS+AS+SS-MoM6, 14
Balogh, A.G.: AC+MI-WeA11, 160
Balsano, R.: AS+BI+NS-WeM11, 133
Balseanu, M.: EM-MoM3, **6**
Baltazar, J.: GR-TuP5, 115; GR-TuP6, 116
Bandeira, N.: BI-WeM4, 134
Banerjee, A.: EN+TF-TuA7, 90
Banerjee, P.: EN+NS-ThA11, 220
Bangsaruntip, S.: NM+MN+MS+TF-TuM10, 68
Banik, A.: PS+SE-MoA6, 47; PS-MoM10, 20
Banna, S.: PS-MoM1, 19; PS-MoM3, 19; PS-MoM5, 19
Bao, K.: PS+SE-MoA11, 47
Bao, Z.: TF2+EM-WeA10, 182

Baraket, M.: GR+NS+PS+SS-ThM12, 195; GR-TuA4, 92; NS-WeM6, 145

Baranger, H.U.: ET+EM+NS+GR-TuM9, **63**

Baranova, N.S.: AS-MoA1, 28

Barbier, C.N.: VT-TuP7, 130

Barbuto, A.: EN-ThP19, 248

Barkhouse, D.A.R.: EN1+TF-WeA3, 166

Barkley, S.: TR-ThA9, 235; TR-ThP4, 256

Barlow, D.E.: BI-WeM1, **133**; MB-MoM8, 15

Barlow, I.: TF+EM+SS-ThA4, 233

Barnat, E.V.: PS-ThA3, **227**

Baro, V.J.: TR-WeA3, 183

Barral, A.: MI-ThM11, 197

Barraza-Lopez, S.: GR+TF+ET-MoA6, **37**

Barriss, L.: HI+AS-TuA3, 94

Bartels, L.: NS-ThM3, 198; SS2-MoA4, **50**; SS-FrM1, 268

Bartelt, N.C.: GR-MoM10, 12; GR-MoM6, 11; GR-WeA9, 169; SS-FrM7, **269**

Bartis, E.: PS+BI-MoA10, 45; PS+BI-MoA7, **44**; PS-TuM6, 73

Bartling, B.: PS+BI-MoA11, 45

Barton, R.A.: MN-ThA4, **222**; MN-ThA6, 223; MN-ThA7, 223

Bartynski, R.A.: EN+NS-ThM2, 193; SS1-WeM5, 153; SS-TuA2, **105**; SS-TuP22, 125; SS-WeA4, 178

Barybin, M.: SS2-MoA3, 50

Baski, A.A.: EM1-MoA3, 32; SS-ThA9, 231

Batzill, M.: EN2+TF-WeA7, 167; GR+MI-TuA9, 92; GR+TF+ET-MoA4, 37; GR-MoM3, **10**; SS-FrM10, 270; SS-WeA3, 178

Bauer, E.: AC+MI-WeA10, 159; AC+TF-ThA4, 215

Bauer, E.D.: AC+MI-WeA10, 159; AC+MI-WeA3, 159; AC+MI-WeA8, 159

Bauer, S.: BI-ThP11, 239

Baughman, W.: AS-TuA9, 84; EN+EM+NS-WeM12, 138

Baumann, P.: AS-MoM11, 3

Baumgart, H.: EM-TuA11, 87; TF-TuA7, **107**

Baur, M.: AS-MoA3, 28

Baxter, J.B.: EN+EM+NS-WeM11, **137**

Baykara, M.Z.: NS+AS-TuA4, **97**

Baylor, L.R.: VT-TuP7, 130

Beasley, C.: EL-ThP5, 240

Beaux, M.F.: AC+MI-WeA10, 159; AC+MI-WeA8, **159**

Beck, K.: NS-MoA8, 43

Becker, J.S.: NM+MS+NS+TF-MoM3, **16**

Beckers, M.: IS+AS+SS-TuM6, 66

Beckers, N.A.: TC+AS+EM-ThM5, **207**

Beckford, S.: TR+AS+SS-ThM2, 213

Bedair: EN+MS+VT-ThA8, **218**

Bedzyk, M.J.: NS-WeM3, 145

Beechem, T.E.: GR+MN-WeM10, 141

Beerbom, M.M.: SS2-TuM11, 76

Behafarid, F.: SS-TuP28, **127**

Behm, R.J.: SS1-WeM4, 153; SS-FrM6, 269

Belashchenko, K.D.: MI-WeA12, 171; MI-WeA9, **171**

Belharouak, I.: EN+NS-ThM3, 193

Belianinov, A.: SS1-WeM6, **153**

Bell, D.C.: HI+AS-TuA7, **95**

Belostotskiy, S.: PS1-TuA9, 100

Belot, J.A.: TC+EM+NS-ThA4, **232**

Benedikt, J.: PS+SE-WeM5, **148**

Benes, N.E.: EL+AS+EM+MS+PS+TF-ThA9, 217

Benítez, A.S.: BI-ThM12, 189

Benítez, J.J.: BI-MoA11, 31

Bennett-Kennett, R.B.: BI-ThM12, 189; SS1-MoA11, 49

Bennowitz, R.: TR+AS+SS-ThM1, 212

Bent, S.F.: EN-TuM9, **62**; SS1-MoA8, 49

Bentley, W.E.: BN+NM-TuM11, 59; BN+NM-TuM2, 57; BN+NM-TuM3, 58; BN+NM-TuM6, 58

Bera, K.: PS-FrM6, **265**

Beratan, D.N.: SS2-TuM11, 76

Berejnov, V.: EN+NS-ThA8, 220

Berg, R.F.: VT-TuM9, **81**

Berger, O.: EN+EM+NS-WeM6, 137

Berger, S.: AS-TuP19, 113

Beringer, D.: VT+MN+NS+SS+AS-TuA9, 109

Berke, K.: GR+EM-TuM11, **65**; GR+MS+EM-FrM6, 262

Berkh, O.: MN-ThA9, 223

Berman, D.: VT+MN+NS+SS+AS-TuA3, **108**

Berrie, C.L.: BN-TuP3, 115; GR+EM-TuM10, 65; NS-TuP6, 120; SS2-MoA3, **50**

Berry III, I.L.: PS-ThP1, 250

Berry, N.: EN1+TF-WeA8, 166

Bersch, E.J.: EM+TF-TuM6, **59**

Bersuker, G.: EM+TF-TuM4, 59

Bertaud, T.: TF1+EM-WeA3, 180

Bertino, M.: NS-TuM12, 70

Bertuch, A.: NM+MS+NS+TF-MoM3, 16

Besenbacher, F.: SS2-WeM2, 154; SS-ThM10, 206

Bettac, A.: NS+AS-TuA11, **98**

Betz, J.: BN+NM-TuM11, **59**; BN+NM-TuM2, 57; BN+NM-TuM6, 58

Beye, M.: SS2-MoM2, 22

Beyer, A.: GR+NS+PS+SS-ThM4, 194; HI+AS+BI+NS-WeM6, **142**; HI-TuP5, 117; HI-TuP6, 117

Bezars, F.J.: GR-MoM11, 12

Bezer, S.: SS2-TuM11, 76

Bhandaru, S.: EM-WeA11, 165; TF1-ThM9, **209**

Bharath, S.C.: EN+NS-ThA1, **218**

Bhatia, R.: NM+MS+NS+TF-MoM3, 16

Bhaviripudi, S.: ET+EM+NS+GR-TuM2, 62

Biedermann, L.B.: GR+MN-WeM10, 141

Biegalski, M.D.: SS-WeA8, 178; TF-MoM2, 23

Bielawski, C.: EN+NS-ThM1, 193

Bielefeld, J.: PS+EM-WeA12, 174

Biernat, J.: NT+AS-WeA8, 171

Biffinger, J.C.: BI-WeM1, 133

Biggs, M.: BN-TuA3, 86

Bilich, D.K.: AS-MoM9, 3

Bilyy, O.I.: EN-ThP18, 248

Binder, J.R.: TF-MoM5, 24

Biolsi, P.: PS+SE-MoA10, 47; PS-TuM10, 73; PS-TuM12, 73

Birch, J.: EL-ThP3, 239

Biswas, R.: EN+NS-TuA7, **88**

Bittel, B.C.: PS+EM-WeA3, **172**

Blair, S.L.: NS-ThA9, 224

Blanc, R.: PS-MoM3, 19

Blankenship, D.W.: AS-TuP12, 112

Blechle, J.M.: PS+SS-WeM5, **150**

Blednykh, A.: VT-TuM2, 80

Blomberg, S.: IS+AS+SS-MoM4, **13**

Blomfield, C.: EW-TuL4, 82

Blomfield, C.J.: AS-MoM10, 3; BI-ThM4, 188

Bluhm, H.: EN1+TF-WeA8, 166; IS+AS+SS-TuM9, 66; SS-ThM9, 206

Bockstaller, M.: TC+AS+EM-ThM9, 207

Bodart, P.: PS-MoM1, 19; PS-MoM3, 19; PS-MoM5, **19**

Boeckl, J.: GR+MS+EM-FrM7, 262

Boffard, J.: PS-ThA2, **227**

Bohringer, K.: MN-ThA1, **222**

Bol, A.A.: GR-MoM9, 12

Bollmann, T.R.J.: IS+AS+SS-MoA7, 38

Bolotin, I.L.: EN+NS-WeM10, 139

Bolotin, K.: EM-WeA11, 165; EW-TuL3, 82; GR+MN-WeM4, **140**

Bondaz, A.: EL+AS+EM+MS+PS+TF-FrM7, **259**; EL+AS+EM+MS+PS+TF-ThM10, 190

Bonnell, D.A.: AS+BI+NS-WeM10, 133; AS+BI+NS-WeM9, 133; NM+AS+MS-WeM9, **144**; NS-MoA10, 43; SS-ThA3, 230; SS-ThA4, 230

Bonnevie, E.D.: TR-WeA3, 183

Bonucci, A.: EW-WeL3, 158; VT-TuM6, 81; VT-TuP6, 130

Bonvalot, M.: EM2-MoA9, **34**

Book, G.W.: TC+AS+EM-ThM10, 208

Boon, J.J.: AS-TuA2, 83

Boosalis, A.: EL+AS+EM+MS+PS+TF-FrM3, 258; EL+AS+EM+MS+PS+TF-FrM5, 258; GR+EM-TuM6, **64**; GR-TuP7, 116

Booth, B.D.: AS-ThM3, 187

Booth, J.-P.: EN+PS-MoM5, 8; EN+TF-TuA4, 90; PS+SS-WeM9, **150**

Borchers, J.A.: NT+AS+MI-WeM5, 147

Borg, A.: IS+AS+SS-MoM4, 13

Boris, D.R.: PS2-TuA2, **101**

Borovsky, B.P.: TR-ThA9, **235**; TR-ThP4, 256

Botton, G.: NS-WeM12, 146

Bouchoule, S.: PS+SS-WeM1, **149**; PS-FrM8, 266

Boufnichel, M.: PS+MN+TF-TuM3, 71

Bouju, X.: NS-ThM6, 198

Boulard, F.: PS-MoM5, 19

Boullart, W.: PS+SE-MoA4, 46

Boutwell, R.C.: TF-FrM5, **271**

Bouxsein, C.: TR-ThA9, 235; TR-ThP4, 256

Bouyssou, R.: PS+EM-WeA10, 173

Bowden, M.E.: MI-ThP7, 249

Boyle, T.J.: SS-WeA12, 179

Boztug, C.: NS-MoA11, 43

Bradley, J.: AC+MI-WeA7, **159**

Bradley, J.D.: SS1-MoA11, 49

Bradley, Q.X.: BI-ThM12, 189; SS1-MoA11, 49

Bratescu, M.A.: PS+BI-MoA4, **44**

Brau, C.A.: AS-TuP6, 111

Brauer, J.I.: SS1-WeM11, **153**

Braun, J.: NS+AS-TuA12, 99

Braunstein, P.: SS+EM-TuA4, 103

Bregliozzi, G.: VT+MN+NS+SS+AS-TuA12, 110

Brehmer, D.: NS-ThM11, 198

Brehmer, F.: EN+PS-MoM3, 7

Breitwisch, M.: TF1+EM-WeA9, 181

Brennan, B.: EM+TF-TuM2, **59**; EM+TF-TuM3, 59; EM-TuA10, 87; EM-TuA9, 87

Brett, M.J.: SE+TF-TuA7, 103; TC+AS+EM-ThM5, 207; TF+SE-TuA4, 79

Brihoum, M.: PS-MoM1, 19; PS-MoM3, 19

Briley, C.: EL+AS+EM+MS+PS+TF-FrM4, 258; EL-ThP5, **240**

Brillson, L.J.: EM-WeA1, **163**; EM-WeA4, 164

Brink, M.: PS+SE-MoA6, 47

Broach, A.L.: AC+SS-ThM3, 185

Brock, R.E.: EN+NS-WeM3, 138

Broitman, E.: TR-ThA1, **234**

Brok, W.J.M.: PS+SS-ThA10, **226**

Brongersma, H.: AS-WeA1, 160

Brons, J.G.: AS-TuA8, **84**

Brouk, V.: PS-WeA7, **175**

Brown, A.: SS2-TuM12, 77

Brown, D.: NS+EM-MoM6, 18; PS-FrM7, 265

Brown, R.D.: SS2-MoM4, **22**

Bruce, R.L.: PS+SE-MoA9, 47; PS+SS-ThA7, 226; PS-MoM10, 20; PS-TuM11, **73**

Brucker, G.A.: VT-MoA6, **54**; VT-MoM4, 26; VT-TuP5, 130

Brueck, S.: BI+AS+NS+SS-WeA9, 162

Brueckel, T.: NT+AS+MI-WeM1, **146**

Bruener, P.: AS-WeA1, 160

Bruggeman, P.J.: PS+BI-MoA2, **44**

Bruix, A.: IS+AS+SS-MoM3, 13

Brukman, M.J.: AS+BI+NS-WeM10, **133**

Brumbach, M.T.: SS-WeA12, **179**

Bruns, M.: TF-MoM5, 24; TF-TuP4, **128**

Bryan, S.R.: AS-ThM11, 188; AS-TuM11, **57**; AS-TuP4, 111

Bubin, S.: GR+MI-TuA12, **92**

Buchholz, M.: SS-WeA2, **177**

Bucholz, E.W.: TR+AS+SS-ThM10, **213**

Buckley, M.: PS-ThP11, 251

Buegler, M.: EM1-MoA4, 32; EM-ThP11, 242; EM-ThP15, 242

Bulat, F.A.: GR+MS+EM-FrM10, 263

Bulkin, P.: EN+PS-MoM8, 8

Bullock, A.J.: BI-ThP3, 237

Bulou, H.: MI-WeM6, 143

- Bultman, J.: SE+SS-WeM9, 152; SE-TuP4, 122; TF-FrM10, 272
- Bunker, K.L.: AS-TuP13, 112
- Bunning, T.J.: AS+BI+NS-WeM6, 132
- Burak, Ya.: SS-ThA10, 231
- Burden, D.K.: MB-MoM8, **15**
- Burek, G.B.: EM-MoM2, 6
- Burgess, J.S.: GR+MS+EM-FrM10, 263
- Burghaus, U.: SS2-MoM9, 23; SS-ThM1, 205
- Buriak, J.M.: TF+SE-TuM4, 79
- Burk, D.: NS-ThM12, 199
- Burkett, S.L.: MN-ThA3, 222
- Burnham, N.A.: TR+AS+SS-ThM11, **213**
- Burns, P.C.: AC+TF-ThA10, 216; AC+TF-ThA3, 215; AC+TF-ThA6, 215; AC+TF-ThA8, 215; EN+AC-FrM2, 261
- Burns, S.: PS-MoM9, 20
- Burrell, A.K.: AC+TF-ThA4, 215
- Burris, D.L.: TR-WeA3, **183**
- Buschhaus, C.: AS-ThM1, 186
- Bushell, A.: EW-TuL2, 82
- Busse, C.: NS-WeM2, 145
- Bussmann, E.: TF2+EM-WeA3, **181**
- Butler, L.: AS-TuA9, 84; EN+EM+NS-WeM12, 138
- Butler, S.: NM+NS+MS-TuA1, 96
- Butler, W.H.: MI-WeM1, **142**
- Butterfield, M.T.: AC+MI-WeA8, 159
- C —
- Cabailh, G.: SS-ThM5, 205
- Cabrini, S.: NM+MN+MS+TF-TuM12, 68
- Cadoppi, A.: EW-WeL3, 158
- Cagg, B.A.: SS-TuA9, 106; SS-TuP5, 123
- Cahen, D.: BI-MoM11, **5**; EM+TF-ThM11, 192; EN+NS-WeM11, 139
- Cai, C.: EN+TF-TuA9, 90
- Calaza, F.C.: SS1-TuM12, **75**; SS2-WeM9, 155; SS-WeA8, 178
- Caldwell, J.D.: EM+SS-FrM1, 259; GR+MS+EM-FrM3, 262; GR-MoM11, 12; GR-MoM4, 11
- Calley, W.L.: IS+AS+SS-MoA6, **38**; TF-MoM6, 24
- Callow, J.A.: MB-MoM10, 15; MB-MoM3, 15
- Callow, M.E.: MB-MoM10, 15; MB-MoM3, 15
- Calvey, J.: VT+MN+NS+SS+AS-TuA11, 109
- Cameron, C.: AS-MoA10, 29
- Camillone III, N.: SS2-WeM11, 155
- Camillone, N.: NS+AS-TuA10, **98**
- Camino, F.E.: NS-TuP9, 120
- Camp, P.J.: NT+AS-WeA8, 171
- Campagna, L.: VT-MoA11, 54
- Campbell, C.T.: SS1-TuM2, 74; SS-ThM6, 206
- Campbell, P.M.: GR+MS+EM-FrM3, 262
- Campbell, S.A.: EN1+TF-WeA11, 167; EN1+TF-WeA2, 165
- Campigilo, P.: MI-WeM6, 143
- Camps, E.: EN+NS-ThA9, 220
- Candler, R.: AS-TuP22, 114
- Canova, F.F.: SS-ThM10, 206
- Cans, A.S.: BI-MoM3, 4
- Cansizoglu, M.F.: TF+SE-TuM5, 79
- Cantwell, G.: EM-WeA1, 163
- Cao, Y.: NS-ThA6, **224**
- Carbone, E.A.D.: PS+SS-ThA10, 226
- Carbonell, L.: PS1-TuA7, 100
- Cardinaud, Ch.: PS-FrM8, 266
- Carlsson, P.-A.: IS+AS+SS-MoM6, 14
- Carnevale, S.D.: NS+EM-MoM2, **17**
- Carpenter, E.: NS-MoA9, 43
- Carpenter, M.A.: NS-TuP3, 120
- Carpick, R.W.: GR+MN-WeM5, 140; TR+AS+SS-ThM12, 214; TR+AS+SS-ThM6, 213
- Carrillo-Castillo, A.: EM-ThP3, 240; TC+AS+EM-ThM11, 208
- Carroll, K.: NS-MoA9, 43
- Carter, A.D.: EM-MoM2, 6
- Carter, D.: PS-WeA1, 174; PS-WeA2, **174**; PS-WeA7, 175
- Caruso, A.N.: EM-WeM6, 135; MI-WeA4, 170; SS-TuP17, 125; TF1-ThM10, 210
- Caruso, L.: EW-WeL3, 158; VT-TuM6, 81
- Casal, P.: BI-MoA4, 30
- Cass, L.: EN+NS-TuM11, 61
- Castaldi, L.: SE-ThM11, 205
- Castano Giraldo, C.H.: PS-WeA3, 174
- Castner, D.G.: AS-MoM8, 3; AS-TuA3, 83; AS-TuM6, 56; BI-MoM4, 4; BI-MoM6, 4; BP-SuA1, 1; SS1-MoA9, 49
- Castro, R.: EN-MoM10, 9
- Caughman, J.B.O.: PS-WeA3, **174**
- Cavanagh, A.S.: TF+EN-TuM2, 77; TF+EN-TuM3, 77
- Cavarsan, F.A.: EM-ThP6, 241; EN-ThP5, 245
- Caymax, M.: EM-TuA4, 87
- Ceballos-Sanchez, O.: AS-TuP20, **114**; EM-TuA12, 88
- Ceccone, G.: BI-ThM6, 188; NS-ThM2, 198
- Celik, O.: EN+NS-ThM2, 193
- Cha, P.-R.: EM-ThP22, 244; GR-TuA7, 92
- Chabal, Y.J.: EM+TF-ThM3, 191; EM-ThP7, 241; EN+NS-ThA3, 219; EN+NS-ThM1, 193; EN+NS-TuM1, 60; GR+TF+NS-ThA10, 222; IS+AS+SS-MoM10, 14; SS1-TuM4, 74; SS-FrM3, **269**; SS-TuP3, 123
- Chabert, P.: PS+SS-WeM9, 150
- Chacon, C.: MI-WeM6, **143**
- Chae, S.-D.: EM-MoM8, 6
- Chagarov, E.A.: SS-ThA6, 231
- Chakradhar, A.: SS-ThM1, **205**
- Chakrapani, V.: EN+NS-ThM10, 193
- Chambers, S.A.: IS+AS+SS-MoM5, 13; MI-ThP7, 249
- Chan, J.: GR-TuA9, **93**
- Chan, M.H.: NM-TuP3, **118**
- Chan, T.H.: MN-FrM9, 264
- Chang, C.M.: NM-TuP7, **118**
- Chang, C.-Y.: BI-WeM3, 134
- Chang, H.Y.: PS-ThP12, 252; PS-ThP15, 252
- Chang, J.: NM+MN+MS+TF-TuM10, 68; PS-MoM10, 20
- Chang, J.P.: AC+SS-ThM10, 186; MI-ThM12, 197; NS-MoA4, 42; PS+SS-WeM2, 149; TF+EN-TuM4, 78; TF1+EM-WeA7, 180; TF-TuA2, 107
- Chang, S.M.: PS+SE-WeM10, **149**
- Chang, S.Y.: SE-ThM4, 204
- Chang, W.S.: EN+PS-MoM9, 8
- Chang, Y.C.: EL-ThP2, 239; EM+TF-TuM9, 60
- Chanson, R.: PS-FrM8, 266
- Chao, C.-C.: EN+NS-ThA6, 219
- Chaudhuri, S.: SS1-TuM4, 74
- Chauveau, J.M.: EM-WeA3, 163
- Chave, F.: PS-MoM6, **20**
- Chawla, J.S.: ET+EM+NS+GR-TuM11, 63
- Chen, C.: EN+EM+NS-MoA9, **36**
- Chen, C.H.: MN-FrM9, 264
- Chen, C.L.: VT-TuM12, 81
- Chen, D.: IS+AS+SS-MoA8, 39
- Chen, D.A.: SS1-TuM3, 74; SS-TuA9, **106**; SS-TuP5, 123
- Chen, F.: NS-MoA11, 43
- Chen, F.Z.: VT-TuP3, 130
- Chen, G.: SE+SS-WeM2, **151**
- Chen, H.: SS2-FrM1, **267**
- Chen, J.R.: VT-TuM12, 81
- Chen, L.: PS-ThP23, 254; PS-ThP28, 255; PS-TuM10, 73; PS-WeA10, **175**; SE-ThM6, 204
- Chen, M.H.: EN+NS-WeM12, **140**
- Chen, N.: NS-TuM1, 68; SS2-MoM8, **23**
- Chen, S.: PS-ThM11, **203**
- Chen, S.T.: PS-MoM9, 20
- Chen, T.: PS-TuM12, 73
- Chen, W.: SS1-WeM5, 153; SS-TuA2, 105
- Chen, W.C.: EM-ThP12, **242**; NM-TuP3, 118; PS-ThP13, 252
- Chen, X.: AS+BI+NS-WeM9, **133**
- Chen, Y.: TR-WeA10, **184**; VT-MoA4, **54**
- Chen, Z.: PS-ThP19, **253**
- Cheng, A.-J.: EN1+TF-WeA11, 167
- Cheng, H.-Y.: TF1+EM-WeA9, 181
- Cheng, M.: EN1+TF-WeA8, **166**; SS-ThM9, 206
- Cheng, M.-C.: GR+TF+NS-ThA8, 221
- Cheng, Y.: BN+NM-TuM11, 59; BN+NM-TuM2, **57**; BN+NM-TuM6, 58
- Cheng, Z.: NS-ThM3, 198; SS2-MoA4, 50
- Cheong, W.S.: EM-ThP18, 243
- Chernomordik, B.: EN1+TF-WeA7, 166
- Cheung, K.P.: EM-TuA11, 87
- Chevolleau, T.: PS+EM-WeA10, 173
- Chey, S.J.: EN1+TF-WeA3, 166
- Cheynis, F.: TF2+EM-WeA3, 181
- Chhowalla, M.: SS-FrM3, 269
- Chi, E.Y.: NT+AS-WeA8, **171**
- Chiang, D.Y.: MI-ThP4, 249; NM-TuP7, 118; PS-ThP6, 250
- Chiba, Y.: PS+SE-MoA10, 47; PS-TuM10, 73; PS-TuM5, 72
- Chiggiano, P.: VT+MN+NS+SS+AS-TuA12, **110**; VT-TuP6, 130
- Chilkoti, A.: BI-ThP4, 237
- Chin, G.: EL+AS+EM+MS+PS+TF-FrM6, **259**
- Chinchore, A.V.: MI-ThM10, 197; MI-ThM11, **197**; MI-ThM6, 196
- Chirita, V.: TF2-ThM5, **211**; TF2-ThM6, 211
- Chistyakov, R.: PS-ThP29, **255**
- Chitre, K.: SS-WeA4, 178
- Cho, E.K.: SS2-TuM12, **77**
- Cho, G.: EM-ThP17, 243
- Cho, J.: PS-ThP25, **254**; TF+EN-TuM4, **78**
- Cho, K.: EM-ThP7, 241; MB-MoM1, 15; NS+EM-MoM5, 18; SS-FrM3, 269
- Cho, S.: AS-TuP23, 114; NS-WeM9, 145
- Cho, T.S.: PS+SE-WeM11, 149; PS-ThP4, 250; PS-ThP7, 251; SE+PS-ThA7, 229; SE+PS-WeA11, **177**
- Cho, W.-H.: NM-TuP3, 118; NM-TuP4, **118**
- Choi, B.K.: AS-TuP6, 111
- Choi, B.L.: NS+EM-MoM5, 18
- Choi, H.J.: NS+EM-MoM1, 17
- Choi, J.: NS-MoA3, **42**
- Choi, J.H.: AC+SS-ThM10, 186; MI-ThM12, **197**; TF1+EM-WeA7, 180
- Choi, S.H.: PS+SE-MoA1, 46
- Choi, T.: PS1-TuA2, 99
- Choi, Y.: EM-WeA4, 164
- Chopra, I.: SS1-TuM4, **74**
- Chopra, N.: TF+EM+SS-ThA7, **234**
- Chou, C.H.: MN-FrM9, **264**
- Chou, M.Y.: GR+TF+ET-MoA6, 37
- Chouier, R.: PS-ThA10, 228
- Christen, H.M.: SS-WeA8, 178
- Christophis, C.: BI-ThP11, 239; BI-WeM11, 135; IS+AS+SS-TuM6, 66
- Chshiev, M.: MI-WeA7, **170**
- Chu, E.: NS-ThM3, 198
- Chu, H.-W.: GR-TuP6, 116
- Chu, J.-W.: PS+BI-MoA10, 45; PS+BI-MoA7, 44
- Chung, I.: NM-TuP8, 119; TC-ThP2, 255; TC-ThP3, 255
- Chung, S.M.: EM-ThP18, **243**
- Chung, T.-Y.: PS+BI-MoA10, **45**; PS+BI-MoA7, 44
- Ciofi, I.: PS1-TuA7, 100
- Cipriani, B.R.: BI-MoA11, 31
- Cirigliano, N.: TF+EN-TuM4, 78
- Civale, L.: VT-TuP10, 131
- Claessens, N.: PS+TF-ThM12, 201
- Clark, E.A.: AS-TuP12, 112
- Clark, K.: BI-MoM9, 5; ET+EM+NS+GR-TuM1, **62**
- Clark, R.D.: EM+TF-TuM6, 59
- Clark, T.D.: BI-ThP7, 238
- Clavero, C.: NS-MoA9, 43; TF-FrM8, 271; VT+MN+NS+SS+AS-TuA8, **109**; VT+MN+NS+SS+AS-TuA9, 109
- Clayton, C.: EM-WeM6, 135

- Clearfield, R.: NS+EM-MoM10, **18**
 Clemens, J.B.: SS-ThA6, 231
 Cliffler, D.E.: EN-ThP15, 247
 Coates, N.: EN+NS-TuA9, 88
 Coclite, A.M.: TF2+EM-WeA12, **182**
 Coffee, R.: SS2-MoM2, 22
 Coh, S.: SS-WeA4, 178
 Cohen, H.: TF+EM+SS-ThA11, **234**
 Cohen, K.: NS-ThM3, 198
 Cohen, P.I.: GR-TuA11, 94
 Cohen, S.: EM-WeM9, 136
 Cohen, S.R.: NS-ThM9, **198**
 Coker, E.: AS-MoA8, 29
 Colburn, M.: PS-MoM9, 20
 Cole, C.: PS-TuM12, **73**
 Coleman, E.: EN+NS-TuA11, 89
 Coleman, K.: GR+TF+NS-ThA7, **221**
 Collazo, R.: EM1-MoA4, 32; EM-ThP13, 242;
 EM-ThP15, 242; TF2-ThM11, 212; TF-MoM2,
 23
 Collings, M.: SS1-MoM1, 21
 Collins, K.: PS1-TuA4, 99; PS1-TuA9, 100; PS-
 FrM6, 265; PS-WeA8, 175; PS-WeA9, 175
 Collins, R.W.: EL+AS+EM+MS+PS+TF-ThA4,
 216
 Colombo, L.: GR-MoM1, **10**; GR-TuA9, 93;
 NM+NS+MS-TuA1, 96
 Colón Santana, J.A.: MI-WeA12, **171**
 Colpo, P.: BN-TuA4, 86; NS-ThM2, 198
 Combs, S.K.: VT-TuP7, 130
 Comfort, A.S.: MN-FrM7, 264
 Coneski, P.N.: MB+BI+PS-MoA10, **40**
 Conklin, D.: NS-MoA10, **43**
 Conley, J.: TF1+EM-WeA1, 179
 Conradson, S.D.: AC+TF-ThA4, 215
 Consiglio, S.P.: EM+TF-TuM6, 59
 Conte, A.: EW-WeL3, 158; VT-TuM6, 81; VT-
 TuP6, 130
 Conway, J.: VT+MN+NS+SS+AS-TuA11, 109
 Cook, B.: ET+EM+SS-MoM11, **10**; GR+TF+ET-
 MoA11, 37
 Cooper, K.: NM+MS-MoA9, **41**
 Costa Pinto, P.: VT+MN+NS+SS+AS-TuA12, 110
 Coultas, S.J.: AS-MoM10, **3**; AS-TuA7, 83; BI-
 ThM4, 188
 Coumou, D.: PS-ThA10, **228**
 Courmoyer, J.: EN-ThP19, 248
 Coutu, R.: NM+MS+NS+TF-MoM3, 16
 Cowell, W.: AS-MoM9, 3
 Cowin, J.P.: AS-ThM2, 187
 Cox, D.F.: SS-ThM2, 205
 Cozza, I.F.: VT-MoA11, **54**
 Craighead, H.G.: BI-MoA11, 31; MN-ThA4, 222;
 MN-ThA6, 223; MN-ThA7, 223
 Creatore, M.: EN+PS-MoM3, 7; EN+TF-TuA3,
89; PS+SE-WeM12, 149; PS+TF-ThM6, 200;
 TF-MoM4, 24
 Crisman, E.: TF-FrM8, 271
 Crittenden, J.A.: VT+MN+NS+SS+AS-TuA11,
 109
 Croes, K.: TF1-ThM12, 210
 Cronin, S.: ET+EM+NS+GR-TuM3, **62**
 Crowhurst, J.C.: AC+SS-ThM5, **185**; EN+AC-
 FrM4, 261
 Croy, J.R.: SS-TuA10, 106
 Cruguel, H.: SS-ThM5, 205
 Cubric, D.: AS-TuP5, **111**
 Cuddy, M.F.: PS+SS-ThA3, **225**
 Cuevas-Ortiz, F.A.: EN1+TF-WeA9, 166
 Cui, D.: EM-MoM3, 6
 Cui, S.: NS-MoA6, 42
 Cui, Y.: AS-MoA4, 28
 Culbertson, J.: GR+MS+EM-FrM3, 262; GR-
 TuA8, 93
 Culbertson, R.J.: BI-ThM12, **189**; SS1-MoA11, 49
 Cunge, G.: PS-MoM1, 19; PS-MoM3, 19; PS-
 MoM5, 19
 Cunningham, G.: EM1-MoA11, 33; EN+EM+NS-
 MoA3, 35
 Czaplewski, D.A.: NM+MN+MS+TF-TuM9, **68**
 — **D** —
 Dadmun, M.: EM1-MoA6, **33**
 Dadson, A.: AS-WeA11, 161
 Dahal, A.: GR+TF+ET-MoA4, 37; SS-FrM10, 270
 Dahint, R.: NT+AS-WeA10, **172**
 Dahn, J.: AS-MoM3, 2
 Dai, F.: EN+TF-TuA9, 90
 Dai, Z.: AC+SS-ThM5, 185
 Dakovski, G.L.: AC+MI-WeA3, 159
 Dalby, M.J.: BI-MoM1, 3
 Daniels, S.: PS-ThA1, 227; PS-ThA7, 227; PS-
 ThP22, 253
 Dannecker, T.: EM-WeA12, 165
 Danyluk, M.: TR-ThP8, **257**
 Darakchieva, V.: EL+AS+EM+MS+PS+TF-FrM3,
 258; GR+EM-TuM6, 64
 Darnon, M.: PS+EM-WeA10, 173; PS-MoM1, 19;
 PS-MoM3, **19**; PS-MoM5, 19
 Dasaka, R.: TF1+EM-WeA9, 181
 Dasari, S.K.: SS2-FrM6, 268
 Dasgupta, N.P.: EN+NS-ThA6, **219**
 DasGupta, S.: EM-WeA8, 164
 Dashdorj, J.: TF1-ThM2, 208
 Dassenoy, F.: TR+AS+SS-ThM10, 213
 Dauchot, J.P.: SE+PS-ThA1, 228
 Dauskardt, R.H.: EM-WeM11, **136**
 David, T.: PS+EM-WeA10, 173; PS-MoM3, 19
 Davidson, A.L.: GR+MS+EM-FrM3, 262
 Davidson, J.: EN+NS-ThM5, 193
 Davidson, J.L.: EN+NS-TuA12, 89; EN-ThP17,
 247
 Davidson, M.R.: MN-FrM4, 263; NS-MoA3, 42
 Davies, M.C.: BI-WeM3, 134
 Davies, S.: PS-ThP11, **251**
 Davis, R.: AS-WeA11, 161; TF-FrM11, 272
 Davis, R.F.: AS-WeA7, 161; EM1-MoA2, 32
 Dawahre, N.: AS-TuA9, 84; EN+EM+NS-WeM12,
 138
 Day, C.: VT-TuM10, **81**; VT-TuM4, 80
 Day, D.E.: BI-ThP7, 238
 De Alwis, A.: SS1-MoA3, 48
 De Graeve, I.: SS1-WeM12, 153
 De Jong, A.J.: PS+SS-ThA11, 226
 de Jong, A.M.C.P.: PS+SS-ThA11, 226
 De Jonge, N.: AS-TuP6, 111; IS+AS+SS-TuM3,
65; IS+AS+SS-TuM5, 66
 de los Arcos, T.: PS+SE-WeM5, 148
 de Marneffe, J.F.: PS1-TuA7, 100
 De Oteyza, D.G.: NM+MN+MS+TF-TuM12, **68**
 De Padova, P.: SS-FrM11, 270
 De Temmerman, G.: SE+PS-ThA2, **229**
 de Vries, H.: PS+SE-WeM12, 149
 Dechawatanapaisal, B.: PS2-TuA3, **101**
 Defibaugh, D.R.: VT-MoM10, 27
 Defranoux, C.: EL+AS+EM+MS+PS+TF-FrM7,
 259; EL+AS+EM+MS+PS+TF-ThM10, 190
 Deguns, E.W.: TF1+EM-WeM5, 156
 Dekeyser, K.: TF-MoM9, 25
 Dela Rosa, A.: SS2-MoA3, 50
 Delabie, A.: EM-TuA4, 87
 Delattre, P.-A.: EN+PS-MoM5, **8**; EN+TF-TuA4,
 90
 Delgado, G.A.: PS1-TuA2, 99; PS-TuM2, **72**
 Dell'Angela, M.: SS2-MoM2, 22
 DelSesto, D.: SS2-MoM10, 23
 Demers-Carpentier, V.: SS1-MoA1, 48
 D'Emic, C.: BI-MoA8, **31**
 Demuynck, S.: PS-TuM1, 72
 Denault, L.: HI-TuP4, **117**
 Deng, X.: SS1-TuM10, 75; SS-ThM11, **206**
 Dennison, J.M.: PS+SS-ThA9, 226
 Deppert, K.: IS+AS+SS-MoM4, 13
 Deram, M.: TR-ThA9, 235; TR-ThP4, 256
 DeRose, J.A.: SS1-WeM12, **153**
 Desai, T.V.: IS+AS+SS-TuM12, 67
 Deshmukh, R.: MB+BI+PS-MoA1, 39
 Desikan, R.P.: BI-MoA7, **31**
 DeSisto, W.J.: SS1-TuM1, 73
 Desjardins, P.: TF-MoM9, 25
 Deskins, N.A.: SS2-WeM12, 155
 Deslippe, J.: GR-WeA12, 170; SS-TuP2, 123
 Despiau-Pujo, E.: TF1+EM-WeA2, **179**
 Detavernier, C.: TF-MoM9, 25
 Devine, B.: GR+NS+PS+SS-ThM10, 195
 Devine, C.K.: TF+EN-TuM9, 78; TF-TuA9, **107**
 Dewhurst, J.K.: EN+AC-FrM4, 261
 Dezelah, C.: NM+MS+NS+TF-MoM6, **16**
 Dhakal, T.: EN1+TF-WeA12, 167
 Dhayal, M.: BI-MoA9, 31; PS+BI-MoA8, 45
 Dhere, N.G.: EN1+TF-WeA1, 165
 Dhingra, A.: TR-ThP8, 257
 Dhuey, S.: NM+MN+MS+TF-TuM12, 68
 Di Camillo, D.: EN2+TF-WeA11, 168
 Di Giacomo, L.: VT-TuM6, 81
 Diaconescu, B.: SS-FrM9, **269**
 Diao, Z.: MN-ThA10, 223
 Dickey, E.: NM+MS+NS+TF-MoM10, **17**
 Diebold, A.C.: EM+TF-TuM6, 59; NM+AS+MS-
 WeM11, **144**
 Diechle, D.: SE-ThM12, 205
 Diesner, M.-O.: BI-MoM5, 4
 Dietz, N.: EM1-MoA4, 32; EM-ThP10, **242**; EM-
 ThP11, 242; EM-ThP13, 242; EM-ThP14, 242;
 EM-ThP15, 242
 Dietzel, D.: TR-WeA11, 184
 Diez, J.: TF2+EM-WeA4, 181
 Dignard, P.: ET+EM+SS-MoM11, 10
 Dillon, A.C.: TF+EN-TuM2, 77
 DiLullo, A.R.: EM-ThP1, **240**
 Dimitrakopoulos, C.: GR+MI-TuA3, 91;
 GR+TF+ET-MoA7, 37
 Dinavahi, V.: TF-FrM8, 271
 Dingemans, G.: EM+TF-TuM11, 60
 Diniz, J.A.: EM-ThP5, 241; EM-ThP6, 241; EN-
 ThP5, **245**
 Dinolfo, P.H.: EN-ThP8, 246
 Diomede, P.: PS-FrM10, **266**
 Dirahoui, B.: PS+SE-MoA10, 47
 Discher, B.M.: AS+BI+NS-WeM9, 133
 Diware, M.S.: EL-ThP2, 239
 Dobrin, S.: SS1-WeM9, 153
 Dockstader, T.: TC+AS+EM-ThM6, 207
 Doering, R.: NM+NS+MS-TuA1, 96
 Doğan, İ.: EN+PS-MoM6, **8**
 Dohnalek, Z.: SS2-WeM12, 155; SS-WeA10, 179
 Dohnálek, Z.: SS1-MoA4, 48; SS1-TuM11, 75;
 SS-WeA1, 177
 Dohnalova, K.: EN+PS-MoM6, 8
 Doi, I.: EM-ThP5, 241
 Dolinaj, B.: PS-ThA1, 227; PS-ThP22, **253**
 Dolocan, A.: NS+AS-TuA10, 98
 Dombrowski, E.: SS2-MoM10, 23
 Donath, M.: MI-WeM11, **143**; NS+AS-TuA12, 99
 Dong, H.: EM+TF-TuM2, 59; EM+TF-TuM3, 59;
 EM-TuA10, **87**; EM-TuA9, 87
 Dong, X.: AS-WeA8, **161**
 Dong, Y.: EM-WeA1, 163; SS-ThM2, **205**;
 TR+AS+SS-ThM12, **214**
 Donghwa, L.: EN+NS-WeM10, 139
 Doniat, F.: PS1-TuA10, 100
 Donnelly, V.M.: PS+SS-WeM11, 151; PS+SS-
 WeM6, 150; PS2-TuA10, **102**; PS2-TuA9, 102;
 PS-FrM10, 266; PS-ThP19, 253; PS-ThP28,
 255
 Doolittle, W.A.: EN+TF-TuA11, 90; IS+AS+SS-
 MoA6, 38; TF1-ThM2, 208; TF-FrM3, 270;
 TF-MoM6, 24
 Doom, L.: VT-TuM2, 80
 Dorf, L.: PS-WeA9, 175
 Dorman, J.A.: AC+SS-ThM10, **186**
 Dorn, M.: GR-WeA1, 168
 Dorrestein, P.C.: BI-WeM4, **134**
 Doudin, B.: SS+EM-TuA4, 103
 Dougherty, D.B.: GR+MI-TuA7, 91
 Doust, D.: EM-WeA1, 163
 Dovidenko, K.: EN-ThP19, 248

- Dowben, P.A.: GR+EM-TuM6, 64; GR-TuP7, 116; MI-WeA12, 171; SS+EM-TuA4, 103; SS-ThA10, **231**
- Dragoi, V.: SE-TuP3, 122
- Dremel, M.: VT-TuP7, 130
- Dresselhaus, M.S.: ET+EM+NS+GR-TuM2, 62
- Drews, S.N.: SS1-MoA11, 49
- Dreyer, D.R.: EN+NS-ThM1, **193**
- Driscoll, J.: GR+TF+NS-ThA4, **221**
- Driver, M.S.: EM-WeM6, 135; SS-TuP17, **125**; TF1-ThM10, 210
- Drobny, G.P.: BI-MoM4, 4
- Droopad, R.: AS-TuP17, 113; SS-ThA6, 231
- Droubay, T.: IS+AS+SS-MoM5, 13; MI-ThP7, 249
- Du, Y.: SE-ThM6, 204
- Du, Y.G.: SS2-WeM12, 155; SS-WeA1, 177
- Dubey, G.: TF+EM+SS-ThA3, **233**
- Dubey, M.: BI-MoM4, 4; NT+AS+MI-WeM10, **148**; NT+AS-WeA8, 171
- Dubon, O.: GR-MoM10, 12; GR-MoM6, 11
- Duckworth, R.C.: VT-TuP7, 130
- Dufrene, Y.F.: BP-SuA5, 1
- Duncan, M.L.: VT-MoM2, **26**
- Dunn, B.: TF+EN-TuM4, 78
- Dupuis, M.: SS2-WeM12, 155
- Durakiewicz, T.: AC+MI-WeA10, 159; AC+MI-WeA3, **159**; AC+MI-WeA8, 159; AC+TF-ThA4, 215
- Duran, A.: SS-TuP23, 126
- Durr, H.A.: MI-ThM1, **196**
- Durr, M.: AS-MoA3, **28**; SS-TuP12, 125
- Durstock, M.F.: EN+NS-WeM2, 138; EN+NS-WeM4, 139
- Duscher, G.: EM-ThP19, 243
- Dussarrat, C.: PS1-TuA10, 100
- Dussart, R.: PS+MN+TF-TuM3, 71
- Dussault, L.: TF1+EM-WeA2, 179
- Dutton, G.J.: EN+NS-WeM9, 139
- **E** —
- Ealet, B.: SS-FrM11, 270
- Eastman, L.F.: EL+AS+EM+MS+PS+TF-FrM3, 258
- Easton, C.D.: BI-ThP3, **237**
- Ebihara, R.: TF1+EM-WeM6, 156
- Eck, W.: TF+EM+SS-ThA6, 233
- Economou, D.J.: PS+SS-WeM6, 150; PS2-TuA9, 102; PS-FrM10, 266; PS-ThP19, 253; PS-ThP28, 255
- Economou, E.N.: GR+EM-TuM4, 64
- Eddy: NS-WeM6, 145
- Eddy Jr., C.R.: GR-MoM11, 12; GR-TuA8, 93
- Eddy, Jr., C.R.: EM+SS-FrM1, 259; GR-MoM4, 11; GR-MoM8, 11
- Edgemon, T.D.: VT-TuP7, 130
- Edwards, C.: GR+EM-TuM10, **65**
- Edwards, E.A.: AS-MoA11, 29
- Efstathiadis, H.: EN+MS+VT-ThA3, **218**
- Egawa, T.: PS-ThM11, 203
- Ehiasarian, A.P.: SE+PS-ThA6, 229; SE+PS-ThA9, **230**
- Eibl, C.: MI-WeM11, 143
- Eichhorn, K.-J.: EL+AS+EM+MS+PS+TF-ThM1, **189**
- Eigenfeld, N.: TR-ThA9, 235; TR-ThP4, 256
- Eigler, D.: NS+AS-TuA2, **97**
- Eilers, S.: GR-WeA1, 168
- Einabad, O.: ET+EM+NS+GR-TuM12, 64
- Einstein, T.L.: NS-ThM3, 198; SS2-MoA4, 50
- Eisenbraun, E.: PS1-TuA10, 100
- Eklund, P.: SE-ThM10, 204; TF1-ThM11, 210
- El Shafei, A.: BI-ThP2, 237
- El Zubir, O.: TF+EM+SS-ThA4, **233**
- Elam, J.W.: NS-WeM3, 145; TF-TuA1, **106**
- Eliad, L.: AS+BI+NS-WeM6, 132
- El-Khatib, S.: NT+AS+MI-WeM5, 147
- Ellefson, R.: VT-MoA8, **54**
- Ellerweg, D.: PS+SE-WeM5, 148
- Ellingsworth, E.C.: NT+AS+MI-WeM4, **147**
- Ellis, D.: AS-TuP10, 112
- Ellis-Terrell, C.: TR+AS+SS-ThM2, **213**
- El-Zubir, O.: BI+AS+NS+SS-WeA9, 162
- Emelli, E.: VT-MoA11, 54
- Emery, J.D.: NS-WeM3, 145
- Emziane, M.: EN-ThP11, **246**
- Endo, K.: PS-ThM10, 202; TR-ThP2, 256
- Endoh, T.: EM-MoM10, 6
- Endres, J.: ET+EM+NS+GR-TuM5, 63
- Engelhard, M.H.: AS-MoA6, **28**; AS-ThM4, 187; TF-MoM1, 23
- Engelman, S.U.: PS+SE-MoA6, 47
- Engelmann, S.: PS+MN+TF-TuM4, 71; PS+SE-MoA9, 47; PS-MoM10, **20**; PS-TuM11, 73
- Engeln, R.: EN+PS-MoM3, 7
- Engstfeld, A.K.: SS1-WeM4, **153**; SS-FrM6, 269
- Engstrom, J.R.: EM+TF-ThM4, **191**; IS+AS+SS-TuM12, 67
- Enomoto, T.: PS-TuM12, 73
- Eralp, T.: IS+AS+SS-TuM9, 66
- Erdemir, A.: SE-ThM9, **204**
- Eriguchi, K.: PS-FrM9, 266; PS-ThM12, 203; PS-ThM9, 202
- Eriksson, M.: ET+EM+NS+GR-TuM5, 63
- Erkens, I.J.M.: IS+AS+SS-MoA9, **39**
- Ermanoski, I.: SS-ThM12, **206**
- Eryilmaz, O.L.: SE-ThM9, 204
- Escamilla, R.: SS-TuP23, 126
- Escano, M.C.: SS-TuP8, 124
- Escobar, C.A.: BI+AS+NS+SS-WeA11, **163**; NM+MN+MS+TF-TuM3, 67
- Escobar-Alarcón, L.: EN+NS-ThA9, 220
- Escudero, C.: IS+AS+SS-TuM1, **65**
- Esfarjani, K.: SE+SS-WeM2, 151
- Espinoza-Beltran, F.J.: TR-ThP3, 256
- Esposto, M.: EM+TF-TuM12, 60; NS+EM-MoM6, 18
- Estrada-Raygoza, I.C.: PS+BI-MoA6, **44**
- Evans, K.R.: EM1-MoA2, 32
- Ezekoye, O.K.: AS-TuP15, **113**
- **F** —
- Faggini, M.F.: PS+SE-MoA11, 47
- Fairbrother, H.: SS1-MoA7, **48**
- Falch, R.M.: NM+MN+MS+TF-TuM12, 68
- Falconi, R.: SS-TuP23, 126
- Falk, M.L.: TR+AS+SS-ThM4, **213**
- Fang, Z.-Q.: EM-WeA1, 163
- Faradzhev, N.S.: EL+AS+EM+MS+PS+TF-ThM9, 190
- Farber, D.: PS-TuM6, 73
- Fast, L.: SE-ThM10, 204
- Faubel, M.: IS+AS+SS-TuM11, 67; SS1-MoM5, 21
- Fay, P.: EM-MoM8, 6
- Fazio, T.: BN-TuA3, 86
- Fears, K.P.: BI-ThP7, **238**
- Fedchak, J.A.: VT-MoM10, **27**
- Fedorov, A.V.: GR-WeA12, 170; SS-TuP2, 123
- Feenstra, R.M.: ET+EM+NS+GR-TuM1, 62; GR-WeA8, 169
- Feibelman, P.J.: NS-WeM2, 145
- Feici, R.: IS+AS+SS-MoM6, 14
- Feist, R.K.: EN1+TF-WeA2, 165
- Feldman, L.: TF1-ThM5, 209
- Feldmann, M.: TR-WeA11, 184
- Fellin, F.: VT-TuM4, 80
- Felser, C.: MI-WeM4, **143**
- Felten, A.: PS+TF-ThM12, 201
- Feltz, A.: AS-MoM11, 3; NS+AS-TuA11, 98
- Feng, J.: VT-MoA3, 53
- Feng, X.: GR+NS+PS+SS-ThM3, **194**; IS+AS+SS-MoA8, 39
- Fenner, C.: HI+AS-TuA3, 94
- Fenske, J.: NT+AS+MI-WeM3, 147
- Fenter, P.A.: AC+TF-ThA1, 215
- Ferguson, J.D.: EM1-MoA3, **32**
- Fernandez, M.C.: PS-FrM8, 266
- Fernsler, R.F.: PS2-TuA2, 101
- Ferranti, D.: HI-TuP2, 116; HI-TuP4, 117
- Ferrara, D.W.: EL+AS+EM+MS+PS+TF-ThA11, 218; NS-MoA1, **42**
- Ferrari, A.C.: GR+EM-TuM1, **64**
- Ferrari, V.: MI-ThM11, 197
- Ferreira, E.S.B.: AS-TuA2, 83
- Ferreira, M.J.: VT-TuM2, 80
- Feulner, P.: EN+NS-TuM2, 61
- Feuprier, Y.: PS-TuM10, 73; PS-TuM5, **72**
- Field III, R.L.: EM-WeA12, 165
- Figueroa, J.: BI-MoA10, **31**
- Filler, M.A.: EN+EM+NS-MoA7, 35; EN+EM+NS-WeM3, **136**; EN+NS-ThM10, 193; NS-TuM11, 70; NS-TuM9, 69
- Fisch, N.J.: PS2-TuA7, 102
- Fischer, D.A.: AS-TuA3, 83; BI-MoM4, 4; SS-WeA4, 178
- Fisher, E.R.: PS+SS-ThA3, 225; PS+SS-ThA9, 226; PS+SS-WeM5, 150; TF2+EM-WeA8, 182
- Fisher, G.L.: AS-ThM1, **186**; AS-TuM11, 57
- Fitz-Gerald, J.M.: TF-FrM6, 271
- Fitzmorris, R.: TF+SE-TuM10, 80
- Flake, J.: SS-WeA11, 179
- Flater, E.E.: TR-ThA9, 235; TR-ThP4, **256**
- Fleetwood, D.M.: EM-WeA11, 165; EM-WeA8, 164; EM-WeA9, 164; TF1-ThM9, 209
- Fleischauer, M.D.: TC+AS+EM-ThM5, 207; TF+SE-TuM4, 79
- Fletcher, B.: BI-MoA8, 31
- Flink, A.: SE-ThM10, 204; TF1-ThM11, 210
- Flood, A.H.: SS-TuP15, 125
- Flores, M.: SS-TuP23, 126; TR-ThP6, **257**
- Flores-Ruiz, F.J.: TR-ThP3, **256**
- Floro, J.A.: MI-WeA11, 171; TF2+EM-WeA7, 181
- Foehlich, A.: SS2-MoM2, 22
- Fokin, A.A.: NS-ThM11, 198
- Fokina, N.A.: NS-ThM11, 198
- Fonda, E.: MI-WeM6, 143
- Foster, A.S.: SS-ThM10, 206
- Fouchier, M.: PS+SE-MoA3, 46
- Foussekis, M.: SS-ThA9, **231**
- Fowlkes, J.D.: NM+NS+MS-TuA11, 97; NS+EM-MoM10, 18; TF2+EM-WeA4, 181
- Fox-Lyon, N.: PS+SS-ThA6, **225**
- Frantzeskakis, E.: SS-FrM11, 270
- Franz, G.: TF2-ThM12, 212
- Franz, S.: AS-TuP22, 114
- Frederick, B.G.: SS1-TuM1, 73
- Frederick, M.: EN+NS-TuM11, 61
- Freeman, M.R.: MN-ThA10, 223
- Freitag, M.: GR+TF+ET-MoA7, 37
- French, B.: PS+EM-WeA12, 174
- French, M.: PS+EM-WeA12, **174**
- French, W.: GR+TF+ET-MoA11, 37
- Frenkel, A.I.: IS+AS+SS-MoM1, **13**
- Freund, H.-J.: SS2-WeM10, 155
- Friedman, A.L.: GR+MS+EM-FrM10, 263; GR+MS+EM-FrM3, 262
- Friend, B.J.: TF-FrM2, 270
- Friend, C.M.: SS2-MoM3, 22; SS-TuA8, 105; SS-TuP1, 122
- Fronheiser, J.: AS-WeA9, 161
- Fu, W.: ET+EM+NS+GR-TuM6, 63
- Fuard, D.: PS+EM-WeA10, 173
- Fuhrer, M.: GR+TF+ET-MoA8, **37**; GR-TuA4, 92
- Fujikawa, S.: SS-TuP9, 124
- Fujimoto, T.: NS-TuP2, 119
- Fujishima, A.: EN-ThP1, 245; EN-ThP7, 246
- Fujita, D.: HI+AS+BI+NS-WeM12, 142
- Fujiyama, H.: IS-TuP1, 117; PS-ThP3, 250
- Fukasawa, M.: PS+SS-WeM12, 151; PS-FrM11, 266; PS-ThM12, 203; PS-ThM3, 201; PS-TuM3, **72**
- Fukiage, N.: PS+TF-ThM1, 199
- Fuller, N.C.M.: PS+MN+TF-TuM4, **71**; PS+SE-MoA6, 47; PS+SE-MoA9, 47; PS-MoM10, 20; PS-TuM11, 73; TF1+EM-WeA9, 181
- Funk, M.: PS-ThP23, 254
- Furlong, O.J.: TR-ThP9, 257

— G —

Gaddam, S.: GR+EM-TuM6, 64
 Gaddy, B.E.: TF2-ThM11, 212; TF-MoM2, 23
 Gahan, D.: PS-ThA1, 227; PS-ThP22, 253
 Gai, Z.: MI-ThP6, **249**
 Gaidis, M.C.: TF1+EM-WeA9, 181
 Gajek, M.: TF1+EM-WeA9, 181
 Galatage, R.V.: EM+TF-TuM2, 59; EM+TF-TuM4, 59; EM-TuA9, **87**
 Galhenage, R.P.: SS-TuP5, 123
 Gall, D.: ET+EM+NS+GR-TuM11, **63**
 Galoppini, E.: SS-WeA4, 178
 Galtayries, A.: TF-MoM10, 25
 Gamage, S.: EM1-MoA4, 32; EM-ThP10, 242; EM-ThP11, 242; EM-ThP13, **242**; EM-ThP14, 242; EM-ThP15, 242
 Gamble, L.J.: AS-MoM8, 3; BI-MoM8, 5; BI-WeM6, 134
 Gann, R.D.: SS2-FrM5, 268
 Ganta, L.: EN1+TF-WeA12, 167
 Gao, H.J.: MI-ThP6, 249
 Gao, M.: MI-ThP6, 249
 Gao, W.: NS-ThA7, **224**
 Garces, N.Y.: GR-MoM11, 12; GR-MoM8, 11; GR-TuA8, 93
 Garcia Flores, H.G.: AC+SS-ThM3, 185
 Garcia, B.: EW-WeL3, **158**
 Garcia, J.: TR-ThP6, 257
 Garcia-Aguirre, M.: EN1+TF-WeA9, 166
 Garcia-Zarco, O.: EN+NS-ThA9, 220
 Garra, J.: SS-ThA4, 230
 Garramone, J.J.: AS+BI+NS-WeM11, **133**; GR+MI-TuA3, 91
 Gartstein, Y.N.: EN+NS-TuM1, 60
 Garvey, M.: TR+AS+SS-ThM9, **213**
 Gaskill, D.K.: EM+SS-FrM1, 259; GR+EM-TuM6, 64; GR+MS+EM-FrM3, 262; GR-MoM11, 12; GR-MoM4, 11; GR-MoM8, **11**; GR-TuA8, 93; NS-WeM6, 145
 Gaspar, D.J.: AS-ThM11, **188**
 Gates, B.D.: EM-ThP23, **244**
 Gates, S.M.: EM-WeM3, 135; EM-WeM9, 136
 Gatilova, L.: PS+SS-WeM1, 149
 Gaudet, S.: TF-MoM9, **25**
 Gaylord, R.: PS-TuM5, 72
 Gazit, E.: AS+BI+NS-WeM6, 132
 Gazquez, J.: NT+AS+MI-WeM5, 147
 Gebhardt, C.R.: AS-MoA3, 28
 Geisler, H.: GR-MoM9, 12; NS-WeM1, 144
 Geissbuhler, P.: PS-ThP1, 250
 Gellman, A.J.: SS1-MoA3, 48; SS2-WeM6, 155; SS-TuA11, **106**
 Gengler, J.: SE+SS-WeM5, **152**; SE+SS-WeM9, 152
 George, A.: HI-TuP3, 116
 George, S.M.: NM+MS+NS+TF-MoM8, 17; TF+EN-TuM2, 77; TF+EN-TuM3, 77; TF1+EM-WeM11, 157; TF1+EM-WeM3, 156
 Gerasimov, J.Y.: EL+AS+EM+MS+PS+TF-ThM6, **190**
 Gerber, T.: NS-WeM2, 145
 Gerhardt, R.A.: TC+AS+EM-ThM10, 208
 Gericke, A.: BI-ThP9, 238
 Germain, J.: NM-TuP11, **119**
 Gerson, Y.: MN-FrM3, 263
 Gesswein, H.: TF-MoM5, 24
 Geumez, G.: TF1-ThM6, 209
 Ghampson, I.T.: SS1-TuM1, 73
 Ghosh, N.: EN-ThP17, 247
 Ghosh, S.: TF2-ThM10, **212**
 Giannuzzi, L.: HI+AS-TuA11, **95**
 Gibbs, J.G.: TF+SE-TuM9, **79**
 Gibson, K.D.: SS1-MoM2, 21
 Gidley, D.W.: EM-MoM5, 6; EM-WeM5, 135
 Giermann, A.L.: TF2+EM-WeA1, 181
 Giewekemeyer, K.: IS+AS+SS-TuM6, 66
 Gilbert, S.N.: MI-ThM3, **196**
 Gilbertson, S.M.: AC+MI-WeA3, 159
 Gildea, A.J.: PS1-TuA10, 100

Gilliland, D.: NS-ThM2, 198
 Gilmore, I.S.: AS-MoA9, **29**; AS-TuM4, 56
 Girard, Y.: MI-WeM6, 143
 Given, U.: NS-TuM10, 70
 Givler, B.C.: NT+AS-WeA8, 171
 Gladh, J.: SS2-MoM2, 22
 Glazek, W.: EN-ThP12, 247
 Gleason, K.K.: TF2+EM-WeA12, 182
 Glodde, M.: PS+SE-MoA6, 47
 Gnade, B.E.: EM-ThP3, 240; EM-ThP4, 240; TC+AS+EM-ThM11, 208
 Goacher, R.E.: AS-MoA11, **29**
 Gobbi, A.L.: TF-MoM10, 25
 Gocalinska, A.: EM+TF-TuM4, 59
 Godet, L.: PS-ThP27, 254
 Godoy Fo, J.: EM-ThP5, 241
 Godyak, V.: PS2-TuA8, **102**
 Goebel, H.: SS2-WeM2, 154
 Goeckner, M.J.: PS+BI-MoA6, 44; PS-ThA6, 227; PS-ThP20, 253; PS-ThP21, 253
 Goel, N.: EM+TF-TuM4, 59
 Gofryk, K.: AC+MI-WeA3, 159
 Goisard de Monsabert, T.: EN1+TF-WeA3, 166
 Gokmen, T.: EN1+TF-WeA3, 166
 Goldman, R.S.: EM-WeA12, **165**
 Gollub, S.G.: AC+TF-ThA9, **215**
 Göllzhäuser, A.: GR+NS+PS+SS-ThM4, 194; HI+AS+BI+NS-WeM6, 142; HI-TuP5, 117; HI-TuP6, 117; SS2-TuM2, 75
 Gomez, D.: BI-MoA10, 31
 Gong, B.: TF1+EM-WeM4, **156**
 Gong, C.: SS-FrM3, 269
 Gong, C.G.: EM-ThP7, 241
 Gong, Y.: EM-ThP23, 244
 Gonon, P.: EM2-MoA9, 34
 González González, A.: SS-TuP29, 127; TF1-ThM1, **208**
 Gonzalez, C.M.: EM-ThP19, **243**
 Gonzalez, D.: BI-WeM4, 134
 Gonzalez, E.: PS+SE-WeM4, 148
 Goodlin, B.E.: NM+NS+MS-TuA1, **96**
 Goodman, D.W.: SS2-WeM5, 154; SS-TuA3, 105
 Goodson, W.J.: BI-WeM1, 133
 Gopalan, P.: GR+TF+NS-ThA1, 220
 Gorai, P.: EM-WeA7, 164; SS-ThA8, **231**
 Gorb, S.: NS-ThA2, **224**
 Gord, J.R.: SE+SS-WeM5, 152
 Gordon, M.: PS+MN+TF-TuM4, 71; PS-MoM10, 20
 Gordon, R.J.: AS-MoA4, 28
 Gordonov, T.: BN+NM-TuM3, **58**
 Gorniak, T.: IS+AS+SS-TuM6, **66**
 Gossard, A.C.: EM-MoM2, 6
 Gosvami, N.N.: TR+AS+SS-ThM1, 212
 Goto, M.: TR-ThP2, 256
 Gouder, T.: AC+MI-WeA11, 160
 Gougousi, T.: TF-TuP5, 128
 Goulding, R.H.: PS-WeA3, 174
 Goundie, B.M.: SS1-TuM1, **73**
 Gouraud, P.: PS-MoM6, 20
 Gourvest, E.: TF1+EM-WeA2, 179
 Goyette, R.: NT+AS+MI-WeM5, 147
 Goyhenex, C.: MI-WeM6, 143
 Graanäs, E.: NS-WeM2, 145
 Graham, D.J.: AS-TuM6, **56**
 Graham, G.W.: AS-TuP15, 113
 Graham, K.S.: AC+MI-WeA10, 159
 Graham, W.S.: PS+SE-MoA6, 47; PS-MoM10, 20; PS-TuM11, 73
 Grampeix, H.: EM2-MoA9, 34
 Granados, B.: TF-TuA12, **108**
 Grandjean, S.: EN+AC-FrM7, 261
 Granneman, E.H.A.: TF-MoA1, 51
 Grant, J.T.: PS+TF-ThM2, 199
 Grantham, S.: EL+AS+EM+MS+PS+TF-ThM9, 190
 Grass, M.E.: IS+AS+SS-MoM4, 13; IS+AS+SS-TuM9, 66

Graves, D.B.: PS+BI-MoA10, 45; PS+BI-MoA7, 44; PS+EM-WeA9, 173; PS+SS-ThA6, 225
 Green, F.M.: AS-MoA9, 29
 Greene, G.W.: SS2-MoA9, 51
 Greene, J.E.: TF2-ThM5, 211
 Greenlee, J.D.: IS+AS+SS-MoA6, 38; TF-MoM6, **24**
 Greenwood, C.: PS-ThP11, 251
 Greenwood, O.: AS-TuA4, 83
 Gregorczyk, K.E.: EN+NS-ThA11, **220**
 Gregorkiewicz, T.: EN+PS-MoM6, 8
 Gregory, C.: EM1-MoA11, 33; EN+EM+NS-MoA3, 35
 Gregory, J.M.: EM-ThP8, **241**
 Grehl, T.: AS-WeA1, **160**
 Grierson, D.S.: TR+AS+SS-ThM6, 213
 Grigorieva, T.I.: EL-ThP1, 239
 Grill, A.: EM-WeM3, **135**; EM-WeM9, 136; GR+MI-TuA3, 91
 Grilley, R.: PS-WeA2, 174
 Grioni, M.: AC+MI-WeA8, 159
 Grönbeck, H.: IS+AS+SS-MoM4, 13; IS+AS+SS-MoM6, 14
 Gronheid, R.: PS+SE-MoA4, 46
 Grundmeier, G.: SS-TuP10, 124
 Grunze, M.: BI-ThP11, 239; BI-WeM11, 135; IS+AS+SS-TuM6, 66; MB-MoM10, 15; MB-MoM3, 15
 Gu, D.: NS-MoA9, 43
 Gu, G.: ET+EM+NS+GR-TuM1, 62
 Gu, X.: GR+MN-WeM3, 140
 Gudeman, C.S.: PS+MN+TF-TuM5, **71**
 Guenther, B.: NS+AS-TuA11, 98
 Guglietta, G.W.: EN+EM+NS-WeM11, 137
 Guha, J.: PS-MoM2, **19**
 Guha, S.: EN+TF-TuA7, 90
 Guilet, S.: PS+SS-WeM1, 149
 Guillorn, M.A.: BI-MoA8, 31; NM+MN+MS+TF-TuM10, **68**; PS+SE-MoA6, 47
 Guillot, J.: PS+TF-ThM12, 201
 Guisinger, N.P.: EM+SS-FrM11, 260; VT+MN+NS+SS+AS-TuA8, 109
 Gulas, M.: PS+TF-ThM12, 201
 Gumuslu, G.: SS2-WeM6, 155
 Gunasekaran, S.: MI-ThP3, 249
 Gunawan, O.: EN1+TF-WeA3, 166
 Gunlycke, D.: GR+TF+ET-MoA1, **36**
 Gunnarsson, A.: BI-MoM3, 4
 Gunning, B.: EN+TF-TuA11, **90**; TF1-ThM2, 208; TF-FrM3, 270
 Gunther, D.: EN-ThP15, **247**
 Guo, D.: GR+MI-TuA4, 91
 Guo, H.W.: MI-ThP6, 249
 Guo, H.X.: HI+AS+BI+NS-WeM12, **142**
 Guo, Q.: SS2-MoA11, **51**; SS2-WeM5, 154
 Guo, T.: EN+TF-TuA9, 90
 Gupta, A.: PS+SE-MoA11, 47
 Gupta, S.: TF1+EM-WeA8, 180; TF2-ThM2, **210**
 Gupta, V.: EM-ThP24, **244**
 Gur, E.: EM-WeA3, **163**
 Gustafson, J.: IS+AS+SS-MoM4, 13; IS+AS+SS-MoM6, **14**
 Gutmann, S.: SS2-TuM11, 76
 Guzewicz, E.: AC+MI-WeA8, 159
 Gyenge, E.: SS-TuP8, 124

— H —

Ha, J.: GR-TuA2, 92
 Ha, R.: NS+EM-MoM1, 17
 Haasch, R.: SE+PS-ThA6, 229
 Haass, M.: PS-MoM1, **19**; PS-MoM3, 19
 Haberkorn, N.F.: VT-TuP10, 131
 Hacker, C.A.: TF+EM+SS-ThA9, 234
 Hadjar, O.: AS-MoA10, **29**
 Haensch, W.E.: NM+MN+MS+TF-TuM10, 68
 Haga, H.: PS+SE-MoA10, 47
 Hagelberg, F.: SS-FrM9, 269
 Hagen, C.: SS1-MoA7, 48
 Haglund Jr., R.F.: NS-MoA2, 42; TF-FrM11, 272

Haglund, R.F.: EL+AS+EM+MS+PS+TF-ThA11, 218; NS-MoA1, 42

Haight, R.: EN1+TF-WeA3, 166

Haldar, P.: EN+MS+VT-ThA3, 218

Halevi, B.: AS-TuP3, 111

Hall, A.R.: HI-TuP2, **116**

Hall, R.A.: TF1+EM-WeM11, **157**

Hallberg, T.: EL+AS+EM+MS+PS+TF-ThM4, 190

Ham, H.C.: SS1-TuM9, 74; SS-TuA12, **106**; SS-TuP14, 125

Hamaguchi, S.: PS+MN+TF-TuM12, 71; PS+SS-WeM10, 151; PS+SS-WeM12, 151; PS-FrM11, 266

Hämäläinen, J.: TF-MoA10, 53

Hamby, M.: BI-WeM4, 134

Hamers, R.J.: BI+AS+NS+SS-WeA3, 162

Hammer, B.: SS1-MoA1, **48**

Hammer, G.E.: AS-MoM8, **3**

Hammond, J.S.: AS-ThM10, 188; AS-TuM1, 56; AS-TuM11, 57; AS-TuP19, 113; EW-TuL5, **82**; NS-TuM10, **70**; TR-WeA12, 184

Hamoudi, H.: EN+NS-TuM2, 61

Han, J.J.: TC-ThP3, 255

Han, K.: PS-ThP27, 254

Han, S.M.: BI-MoA3, 30; TF2-ThM10, 212; TF-MoM8, 24

Hanke, S.: VT-TuM4, **80**

Hanley, L.: AS-MoA4, 28; EN+NS-WeM10, 139

Hannon, J.B.: GR-MoM9, 12

Hanson, J.A.: SS2-MoA8, 50

Hanuš, J.: BI-ThM6, 188

Hao, Y.: GR-MoM1, 10; NS-WeM1, 144

Happel, M.: IS+AS+SS-MoM3, **13**

Hara, K.: IS-TuP1, 117; PS-ThP3, **250**

Haran, B.: PS-MoM9, 20

Hardy, G.: BI-TuA9, **85**

Harl, R.R.: AS-ThM3, **187**; AS-WeA10, 161; BI+AS+NS+SS-WeA10, 163; TF1-ThM9, 209

HarLavan, R.: EN+NS-WeM11, 139

Har-Lavan, R.: EM+TF-ThM11, 192

Harris, K.D.: TF+SE-TuM4, 79

Harris, N.: AS-TuA9, 84; EN+EM+NS-WeM12, 138

Harrison, J.A.: TR+AS+SS-ThM6, **213**

Hart, M.A.: BI-ThM12, 189; SS1-MoA11, 49

Harteneck, B.D.: NM+MN+MS+TF-TuM12, 68

Hartfield, C.D.: NM+NS+MS-TuA11, 97

Hartig, M.: PS-MoM9, 20

Hasan, M.Z.: EM+SS-FrM3, **260**

Hasegawa, S.: ET+EM+SS-MoM1, **9**

Hashemian, A.: SS2-FrM6, 268

Hashiguchi, G.: PS-ThM6, 202; PS-ThP16, 252

Haspert, L.C.: EN+NS-ThA4, **219**

Hattel, W.: PS-WeA7, 175

Hatton, G.: TR+AS+SS-ThM2, 213

Hausen, F.: TR+AS+SS-ThM1, **212**

Havela, L.: AC+MI-WeA11, **160**

Havercroft, N.: AS-TuM5, 56; AS-WeA1, 160

Hayashi, N.: PS+BI-MoA9, 45

Hayashi, T.: PS1-TuA11, 101

Hayden, B.E.: SS-TuA1, 105

Hays, S.M.: NM+AS+MS-WeM6, **144**

He, C.: NT+AS+MI-WeM5, 147

He, G.: ET+EM+NS+GR-TuM1, 62; GR-WeA8, 169

He, K.T.: GR-TuA12, 94

He, W.: SS-TuP5, 123

He, Y.P.: SE+TF-TuA8, 103

Hebard, A.F.: GR+EM-TuM11, 65; GR+MI-TuA11, 92; GR+MS+EM-FrM6, 262

Hechler, M.P.: VT-TuP7, 130

Heikenfeld, J.: TC+EM+NS-ThA6, 232

Heilemann, M.: GR+NS+PS+SS-ThM4, 194

Heinrich, F.: BI-ThP10, 238

Heinrich, H.: SS-TuA10, 106

Heinz, T.F.: PS+EM-WeA1, **172**

Heissler, S.: MB-MoM3, 15

Held, G.: IS+AS+SS-TuM9, 66

Hellman, A.: IS+AS+SS-MoM6, 14

Hellstrom, S.L.: ET+EM+NS+GR-TuM6, 63; TF2+EM-WeA10, **182**

Helmersson, U.: TF-FrM9, 271

Helveg, S.: SS-ThM10, 206

Hemberg, A.: SE+PS-ThA1, **228**

Hemminger, J.C.: EN1+TF-WeA8, 166; IS+AS+SS-TuM11, 67; SS1-MoM3, **21**; SS1-MoM5, 21; SS-ThM9, 206

Henager, C.H.: TF-MoM1, 23

Henderson, C.L.: GR-TuP5, 115; GR-TuP6, **116**

Henderson, W.E.: IS+AS+SS-MoA6, 38

Hendricks, J.H.: VT-MoM1, **25**

Henneken, C.: BI-MoM9, 5

Hennies, F.: IS+AS+SS-MoM9, 14

Henry, K.L.: AS-TuA8, 84

Hensley, D.K.: TF2+EM-WeA9, 182

Heo, J.H.: NS-TuP12, **121**

Heo, S.: PS1-TuA2, 99

Herbots, N.X.: BI-ThM12, 189; SS1-MoA11, 49

Herman, G.S.: TF1+EM-WeA1, **179**

Herman, I.P.: PS-ThP19, 253

Hernandez, G.: AS-TuP22, 114

Hernandez, S.C.: GR+NS+PS+SS-ThM12, 195

Hernández, S.C.: NS-WeM6, **145**

Hernandez-Garcia, C.: HI-TuP7, 117

Herrera-Gomez, A.: AS-MoM5, 2; AS-TuP20, 114; AS-TuP21, 114; EM-TuA12, 88; TR-ThP3, 256

Hersam, M.C.: EN+NS-WeM2, 138; EN+NS-WeM3, 138; EN+NS-WeM4, 139; GR+NS+PS+SS-ThM11, 195; NS-WeM3, 145

Hershkowitz, N.: PS2-TuA3, 101; PS2-TuA7, 102; PS-ThA9, 228; PS-WeA12, **176**

Herzing, A.A.: AS-TuA8, 84; SE-ThM1, 203

Herzinger, C.M.: EL+AS+EM+MS+PS+TF-FrM1, 258; EL+AS+EM+MS+PS+TF-FrM3, 258; EL+AS+EM+MS+PS+TF-FrM5, 258

Hess, R.F.: SS-WeA12, 179

Hess, W.P.: HI-TuP7, 117; NS-MoA8, 43

Hetzl, C.: VT-TuM2, 80

Heyns, M.: EM-TuA1, **86**

Hichri, H.: PS+SE-MoA10, 47

Hickmott, D.: NT-TuP1, 121

Hicks, R.F.: NS-TuM6, 69; PS+SE-WeM4, **148**; SE+PS-WeA2, 176

Hiebert, W.K.: MN-ThA10, **223**

Hierro, A.: EM-WeA3, 163

Hildebrand, H.: AS-TuP19, 113

Hilfiker, J.N.: EL+AS+EM+MS+PS+TF-FrM1, **258**

Hill, I.: EN+NS-WeM1, 138

Hill, S.B.: EL+AS+EM+MS+PS+TF-ThM9, 190

Hillenmeyer, E.: BI-MoM6, 4

Hines, D.: GR-TuA4, 92

Hines, M.: EM-ThP2, **240**; PS+SE-MoA11, **47**

Hingel, K.: SE-TuP3, 122

Hinkle, C.L.: EM+TF-TuM4, 59; EM-TuA9, 87

Hinnemann, B.: SS-ThM10, 206

Hinojos, D.: GR-TuA9, 93

Hirahara, T.: ET+EM+SS-MoM1, 9

Hiramatsu, T.: BN-TuP1, 115; NM-TuP1, 118; NM-TuP9, 119

Hirano, T.: TF-TuP3, 128; TF-TuP7, 129

Hirsch, B.E.: SS-TuP15, **125**

Hisamatsu, H.: VT-TuM5, 80

Hitchcock, A.P.: EN+NS-ThA8, **220**; NS-WeM12, 146

Hite, J.K.: GR-MoM11, 12; GR-MoM4, **11**

Hla, S.-W.: BI-MoM9, 5; EM-ThP1, 240; EN+NS-TuM9, 61; MI-WeA3, 170; NS-ThM6, 198

Hlawacek, G.: HI+AS+BI+NS-WeM5, 141; HI+AS-TuA3, 94; HI-TuP3, **116**

Hmelo, A.B.: AS-TuP6, 111; TF1-ThM5, 209

Hnatush, S.O.: EN-ThP18, 248

Ho, A.D.: BI-WeM11, 135

Ho, W.: NS+AS-TuA8, **98**

Hobart, K.D.: EM+SS-FrM1, 259

Hochrein, J.M.: VT-MoA7, 54

Hockenberry, D.: BI-WeM6, 134

Hodges, T.: VT-MoA1, **53**

Hodson, C.: PS+TF-ThM11, 200

Hoepker, N.C.: EM+SS-FrM8, **260**

Hofer, U.: SS-TuP12, 125

Hoffman, D.J.: PS-WeA2, 174; PS-WeA7, 175

Hoffman, R.L.: TC+EM+NS-ThA7, 232

Hofmann, T.: EL+AS+EM+MS+PS+TF-FrM3, 258; EL+AS+EM+MS+PS+TF-FrM5, **258**; GR+EM-TuM6, 64

Hogan, S.: AS-TuP22, 114

Hogan, W.W.: EN-MoM1, **9**

Högberg, H.: TR-ThA1, 234

Hojo, H.: VT-TuP1, 129

Holbrook, R.D.: BI+AS+NS+SS-WeA3, 162

Holec, D.: TR-ThA2, 235

Hollister, A.: EM-WeA7, 164; SS-ThA8, 231

Holloway, P.H.: EN+EM+NS-MoA8, 35; MN-FrM4, 263; NS-MoA3, 42

Holman, Z.: EN+EM+NS-WeM1, 136

Holmes, S.: PS-MoM9, 20

Holohan, A.: PS-ThA7, 227

Holsclaw, B.: SS1-MoA3, **48**

Hong, C.H.: EM-ThP18, 243

Hong, J.: EM-ThP10, 242; EM-ThP11, 242; EM-ThP13, 242

Hong, J.M.: PS-ThP4, **250**; PS-ThP7, 251; SE+PS-WeA11, 177

Hong, J.S.: PS+SE-MoA1, 46

Hong, M.: EM+TF-TuM9, **60**

Hong, S.: EN-ThP3, 245; NS-TuM12, 70; SS1-TuM3, **74**; SS-TuA9, 106

Hook, A.L.: BI-WeM3, **134**

Höök, F.: BI-MoM3, 4; BI-TuA10, 85

Hooke, W.M.: SE+PS-WeA10, 177

Hopkins, M.B.: PS-ThA1, 227; PS-ThP22, 253

Horak, D.: PS-MoM9, 20; PS-TuM5, 72

Hori, M.: PS+SS-ThA4, 225; PS1-TuA11, 101; PS-ThM11, 203; SE+PS-WeA9, 177

Horibe, H.: PS+SS-ThA4, 225

Horn, M.W.: EL+AS+EM+MS+PS+TF-ThA10, 217

Horvath, B.J.: VT-MoA6, 54; VT-TuP5, 130

Hosadurga, S.: EM-WeM9, 136

Hosch, J.: PS-ThA6, 227; PS-ThP20, 253

Hoshino, K.: TC+EM+NS-ThA7, 232

Hosoi, T.: EM-ThP20, 243

Hosono, H.: TC+EM+NS-ThA10, 232; TC+EM+NS-ThA3, 232; TC+EM+NS-ThA9, 232

Hossain, Md.Z.: GR+NS+PS+SS-ThM11, 195

Hoster, H.E.: SS-FrM6, 269

Houssiau, L.: PS+SE-WeM3, 148

Houston, B.H.: GR+MS+EM-FrM10, 263

Hovsepian, P.: SE+PS-ThA6, **229**

Howell, S.W.: GR+MN-WeM10, 141

Hryn, J.N.: TF-TuA1, 106

Hsaio, C.-L.: EL-ThP3, 239

Hseuh, H.C.: VT-TuM2, **80**

Hsiao, C.N.: EM-ThP12, 242; NM-TuP2, 118; NM-TuP3, 118; PS-ThP6, 250; VT-TuP4, 130

Hsieh, C.H.: PS-ThP13, 252

Hsieh, C.J.: MN-FrM8, **264**

Hsieh, F.C.: VT-TuP3, **130**

Hsieh, J.H.: SE-ThM4, **204**

Hsiung, G.Y.: VT-TuM12, 81

Hsu, C.C.: PS+SE-WeM10, 149

Hsu, S.L.C.: NS-TuP11, **121**

Hsueh, H.P.: VT-TuM12, **81**

Hsueh, W.J.: NM-TuP7, 118

Hu, E.L.: NS-MoA6, 42

Hu, H.: SE+PS-WeA4, 176

Hu, J.: SE+SS-WeM4, 151; SE+SS-WeM9, 152; SE-TuP4, 122; TF-FrM10, 272

Hu, J.P.: VT-TuM2, 80

Hu, S.: IS+AS+SS-MoA8, 39

Hu, W.: SS-TuP9, 124

Hu, X.: EM-ThP20, 243; TF+EN-TuM10, 78; TF-TuP11, 129

- Hu, Y.F.: AS-WeA9, 161
Huang, C.-H.: EN+EM+NS-MoA1, 35
Huang, J.: EM+TF-TuM4, 59; EM-ThP22, 244; HI-TuP2, 116
Huang, J.Y.: EN+NS-ThM11, **194**
Huang, L.: AS-WeA7, 161; EM1-MoA2, 32
Huang, M.J.: NM-TuP7, 118
Huang, M.L.: EM+TF-TuM9, 60
Huang, Y.: SS2-MoM8, 23
Huba, Z.: NS-MoA9, 43
Hudson, E.A.: PS1-TuA2, **99**
Huerta, L.: SS-TuP23, **126**; TR-ThP6, 257
Hughes, K.J.: EM+TF-ThM4, 191
Huh, K.: NM+NS+MS-TuA12, 97
Hultman, L.: SE-ThM10, 204; TF1-ThM11, 210; TF2-ThM5, 211; TF2-ThM6, 211; TR-ThA1, 234
Hung, C.H.: MB+BI+PS-MoA11, 41
Hung, S.Y.: SE-ThM4, 204
Hung, T.-H.: EM+TF-TuM12, **60**
Huo, Y.: TR-WeA2, 183
Hurand, R.: PS+EM-WeA10, **173**
Hurlley, P.K.: AS-TuP17, 113; EM+TF-TuM4, 59
Hurst, K.E.: TF+EN-TuM2, 77
Hussein, R.O.: SE+PS-WeA1, **176**; SE+PS-WeA4, 176
Hutcheon, I.D.: AC+SS-ThM5, 185
Hutton, S.J.: AS-MoM10, 3; AS-TuA7, 83; BI-ThM4, **188**
Hwang, B.: GR-TuA2, 92
Hwang, C.: GR-WeA7, 169
Hwang, C.G.: GR-WeA12, 170; SS-TuP2, 123
Hwang, D.: EN+PS-MoM9, 8
Hwang, G.S.: SS1-TuM9, 74; SS-TuA12, 106; SS-TuP14, **125**
Hwang, H.: NM+NS+MS-TuA12, 97
Hwang, J.: EN+EM+NS-MoA9, 36
Hwang, S.Y.: EL-ThP2, 239
Hwang, W.-S.: EM-MoM8, 6
- **I** —
Iagarashi, M.: EN+EM+NS-MoA1, 35
Ianno, N.: EL+AS+EM+MS+PS+TF-ThA8, 217
Ianno, N.J.: EL-ThP4, 240
Ibrahim, S.: SS-TuP25, 126
Ibuki, S.: AS-TuM10, 57
Ichiki, K.: AS-TuM10, 57
Ide, K.: TC+EM+NS-ThA10, 232; TC+EM+NS-ThA9, **232**
Iedema, M.J.: AS-ThM2, 187
Iijima, T.: HI+AS+BI+NS-WeM3, 141
Ilic, B.: MN-ThA7, 223
Ilic, R.B.: MN-ThA4, 222; MN-ThA6, 223
Illas, F.: IS+AS+SS-MoM3, 13
Illiberi, A.: TF-MoA7, 52
Ilton, E.S.: AC+SS-ThM1, 185
Ilyas, N.: SS+EM-TuA3, 103
Im, S.I.: EM+TF-ThM9, **192**; NS+EM-MoM1, 17
Imhoff, E.A.: EM+SS-FrM1, 259
Inoue, F.: PS+SS-ThA8, 226
Inoue, K.: GR+MS+EM-FrM8, 262; GR+MS+EM-FrM9, 263; NS-WeM10, 146
Inoue, T.: TF-TuP1, **127**
Inui, H.: SE+PS-WeA9, 177
Iriye, Y.: PS-ThM4, 201; PS-ThM5, 202
Irving, D.L.: TF2-ThM11, **212**; TF-MoM2, 23
Is, H.: TF+SE-TuM5, **79**
Iseki, S.: SE+PS-WeA9, 177
Ishibashi, K.: PS-ThP23, 254
Ishibashi, T.: VT-TuM5, 80
Ishii, A.: NM-TuP9, **119**
Ishikawa, K.: PS+SS-ThA4, **225**; PS1-TuA11, 101; PS-ThM11, 203; SE+PS-WeA9, 177
Ishikawa, M.: PS-TuM5, 72
Ishizaki, I.: AS-TuM11, 57
Isobe, M.: PS+SS-WeM12, 151; PS-FrM11, 266
Israealachvili, J.N.: SS2-MoA9, 51
Itagaki, N.: PS+TF-ThM5, 200
Ito, T.: PS+MN+TF-TuM12, 71; PS+SS-WeM10, **151**
- Itoh, H.: HI+AS+BI+NS-WeM12, 142
Itou, A.: PS+MN+TF-TuM4, 71; PS-MoM10, 20; PS-TuM11, 73
Ivanov, B.: AS-TuP6, 111
Ivory, C.F.: BI-MoA3, 30
Iwai, H.: NM+MS+NS+TF-MoM5, 16
Iwao, T.: PS-ThP23, 254
Iwasaki, T.: HI+AS+BI+NS-WeM12, 142; PS2-TuA1, 101; PS-ThM4, 201; PS-ThM5, 202
Iwata, J.-I.: EM-ThP9, 241
Iwatake, K.: GR+MI-TuA4, 91
Iwaya, T.: AS+BI+NS-WeM5, 132
Izawa, M.: PS-ThP26, 254
- **J** —
Jablin, M.S.: NT+AS+MI-WeM10, 148
Jablonski, A.: AS-MoM4, 2
Jacob, D.: EM-WeM5, 135
Jacobson, R.B.: NS-MoA11, 43
Jadhav, P.: EN+NS-WeM5, 139
Jaehnig, M.: PS+EM-WeA12, 174
Jain, R.: EM+TF-ThM12, **192**
Jakubiak, R.: EL-ThP7, 240; PS+TF-ThM2, 199; SE+PS-ThA8, **230**
Jandhyala, S.: GR-TuA7, **92**
Jang, H.-J.: SE-ThM1, 203
Jang, L.: PS-MoM9, 20
Jang, S.: NM+NS+MS-TuA12, 97
Janjua, S.Z.: MI-WeA4, **170**
Jankovic, V.: NS-MoA4, **42**
Jansson, U.: SE-ThM10, 204; TF1-ThM11, 210
Jantschner, O.: SE+SS-WeM6, 152
Järrendahl, K.: EL+AS+EM+MS+PS+TF-ThM4, 190; EL-ThP3, 239
Jarvis, J.D.: AS-TuP6, **111**
Javey, A.: EN+EM+NS-WeM9, **137**
Jayawarna, V.: BI-MoM1, 3
Jaye, C.: AS-TuA3, 83; BI-MoM4, 4; SS-WeA4, 178
Jennings, G.K.: AS-ThM3, 187; BI+AS+NS+SS-WeA11, 163; EN-ThP15, 247; NM+MN+MS+TF-TuM3, **67**
Jensen, D.: AS-WeA11, 161
Jeon, H.T.: TF-MoA6, 52
Jeon, H.Y.: TF-MoA6, 52
Jeon, I.: NM+NS+MS-TuA12, 97
Jeon, J.: EN-ThP9, **246**
Jeon, M.H.: PS-ThP14, **252**
Jeon, S.: NS+AS-TuA1, **97**
Jernigan, G.G.: GR+MS+EM-FrM3, **262**; GR-MoM8, 11
Jetter, R.: AS-ThM1, 186
Ji, B.: PS1-TuA2, 99
Jia, F.: SE+PS-WeA9, **177**
Jia, Q.X.: AC+MI-WeA10, 159; AC+TF-ThA4, 215
Jia, X.T.: ET+EM+NS+GR-TuM2, 62
Jiang, G.: PS+EM-WeA7, 173
Jiang, H.: PS+TF-ThM2, 199
Jiang, W.: AS-TuP15, 113; NS-TuP3, 120; TF-TuP2, 128
Jiang, X.: TF-TuA10, 107
Jienez, O.: TR-ThP6, 257
Jimenez, J.M.: VT+MN+NS+SS+AS-TuA12, 110; VT-TuP6, 130
Jin, R.Z.: TF2+EM-WeA10, 182
Jin, Y.: EM-WeA12, 165
Joachim, C.: NS-ThM6, 198
Joe, D.J.: MN-ThA7, **223**
Johansson, N.: IS+AS+SS-MoM9, 14
Johns, J.E.: GR+NS+PS+SS-ThM11, **195**
Johnson, E.V.: EN+PS-MoM5, 8; EN+TF-TuA4, 90
Johnson, J.: IS-TuP3, **117**
Johnson, M.D.: AS-MoM9, 3
Johnston, E.: BI-ThM9, **188**
Johs, B.: EL+AS+EM+MS+PS+TF-FrM1, 258
Joly, A.: NS-MoA8, 43
Jones, E.M.: NT+AS-WeA8, 171
- Jones, J.: EL-ThP7, 240; EN+NS-ThA10, **220**; SE+PS-ThA8, 230
Jones, K.: EW-WeL5, **158**; TF+EN-TuM2, 77
Jönsson, P.: BI-MoM3, 4
Joo, Y.H.: PS-ThP10, 251; PS-ThP8, **251**
Jordan-Sweet, J.L.: TF1+EM-WeA9, 181; TF-MoM9, 25
Joseph, E.A.: PS+MN+TF-TuM4, 71; PS-MoM10, 20; PS-TuM11, 73; TF1+EM-WeA9, **181**
Joshi, A.: AC+SS-ThM10, 186
Joshi, P.: EM+TF-ThM11, 192
Joshi, S.M.: TC+AS+EM-ThM10, **208**
Joshi, V.: MN-FrM6, 264
Joubert, O.: PS+EM-WeA10, 173; PS+SE-MoA3, 46; PS-MoM1, 19; PS-MoM3, 19; PS-MoM5, 19; PS-MoM6, 20
Jourdan, N.: TF1-ThM12, 210
Jourde, D.: TF1+EM-WeA2, 179
Jousseume, V.: EM2-MoA9, 34
Jousten, K.: VT-MoM8, 26
Joy, N.A.: NS-TuP3, **120**
Joyce, J.J.: AC+MI-WeA10, **159**; AC+MI-WeA8, 159; AC+TF-ThA4, 215
Juang, B.: EN+EM+NS-MoA9, 36
Jung, K.: NM+NS+MS-TuA12, 97
Jung, R.: PS-MoM9, 20
Jung, R.O.: PS-ThA2, 227
Jung, S.: GR+MI-TuA8, **91**; GR-WeA3, 168; SE+PS-ThA7, 229
Jung, S.J.: IS+AS+SS-TuM10, 66
Junkermeier, C.E.: GR+NS+PS+SS-ThM12, 195
Jupille, J.: SS-ThM5, **205**
Jur, J.S.: EM1-MoA9, **33**; TF+EN-TuM9, 78; TF-MoA9, 53; TF-TuA9, 107
- **K** —
Kabius, B.: MI-ThP7, 249; MN-FrM6, 264
Kacher, J.: IS+AS+SS-MoA1, 38
Kafesaki, M.: GR+EM-TuM4, 64
Kafrouni, W.: PS+MN+TF-TuM3, 71
Kaganovich, I.: PS2-TuA7, 102
Kakushima, K.: NM+MS+NS+TF-MoM5, 16
Kalanyan, B.: TF+EN-TuM9, 78
Kalinin, S.V.: SS2-FrM4, 267
Kalyanaraman, R.: EM-ThP19, 243
Kalyanaraman, V.: EM-WeA4, 164
Kamath, G.K.: SE+PS-ThA6, 229
Kamineni, V.K.: NM+AS+MS-WeM11, 144
Kamiya, T.: TC+EM+NS-ThA10, **232**; TC+EM+NS-ThA3, 232; TC+EM+NS-ThA9, 232
Kan, H.C.: PS+SS-ThA7, 226
Kanakasabapathy, S.: PS-MoM9, **20**; PS-TuM12, 73
Kanazawa, K.: VT-TuM5, 80
Kang, H.G.: PS+SE-MoA1, 46
Kang, S.-K.: PS-ThP14, 252
Kang, S.-Y.: PS+SS-WeM10, 151; PS1-TuA1, 99
Kang, W.P.: EN+NS-TuA12, 89; EN-ThP17, 247
Kano, H.: PS-ThM11, 203; SE+PS-WeA9, 177
Kanyal, S.: AS-WeA11, 161
Kao, C.Y.: PS-ThP13, **252**
Kao, P.: EN+NS-TuM2, 61
Kappe, E.: EM+TF-ThM6, 192
Karabacak, T.: SE+TF-TuA3, 102; TF+SE-TuM5, 79
Karadge, M.: AS-WeA9, 161
Karahashi, K.: PS+MN+TF-TuM12, **71**; PS+SS-WeM10, 151
Karakawa, T.: PS+TF-ThM1, **199**
Karakoti, A.S.: NS-TuP7, 120; SS-WeA7, 178
Kareev, M.: EM-WeA4, 164
Kariis, H.: EL+AS+EM+MS+PS+TF-ThM4, 190
Karim, Z.: NM+NS+MS-TuA3, 96
Karki, S.: EM-WeM6, 135; SS-TuP17, 125; TF1-ThM10, 210
Karmel, H.J.: EN+NS-WeM3, 138
Karp, E.M.: SS1-TuM2, 74
Karpov, E.G.: SS2-FrM6, **268**
Kasahara, A.: TR-ThP2, **256**

- Kasai, H.: SS-TuP8, 124
Kasouit, S.: EN+PS-MoM8, **8**
Kaspar, T.C.: IS+AS+SS-MoM5, **13**
Kasputis, T.: EL+AS+EM+MS+PS+TF-ThM5, 190
Kassakian, J.G.: EN-MoA3, **36**
Kassan, S.: AS-MoA10, 29
Kassim, J.K.: MI-WeA11, **171**
Kasurkin, O.Yu.: MI-ThP2, 248
Katayama, K.: EN-ThP1, 245; EN-ThP7, 246
Katayama, T.: SS2-MoM2, 22
Kathan-Galipeau, K.: AS+BI+NS-WeM9, 133
Kato, H.: BN-TuP1, 115; NM-TuP1, 118; NM-TuP9, 119
Kato, K.: PS+SE-MoA2, 46
Kato, M.: PS1-TuA2, 99
Katsuki, F.: TR-ThP1, **256**
Katz, H.: TC+EM+NS-ThA11, 233
Kau, D.: EM2-MoA6, **34**
Kaufman-Osborn, T.: EM-TuA4, **87**; SS-ThA6, 231
Kaul, A.: EN1+TF-WeA1, **165**
Kaur, S.: SE+SS-WeM11, 152
Kaur, T.: GR+TF+NS-ThA3, **221**
Kavanagh, K.L.: ET+EM+NS+GR-TuM12, 64
Kavuri, P.P.: SE-ThM1, 203
Kawai, M.: AS+BI+NS-WeM5, 132
Kawakami, R.K.: GR+TF+ET-MoA10, 37
Kawasaki, J.K.: EM+SS-FrM2, 259
Kaxiras, E.: GR+TF+NS-ThA8, 221
Kay, B.D.: SS1-MoA4, 48; SS1-MoM10, 21; SS1-TuM11, 75; SS-WeA10, 179
Kaya, S.: GR+TF+ET-MoA3, 37; SS2-MoM2, 22
Kayani, A.: AC+SS-ThM11, 186; TF-TuP2, 128
Kazaz, R.: EM+TF-ThM11, 192
Kazumi, H.: AS-ThM9, 187
Keating, C.D.: NS+EM-MoM8, 18
Keating, P.L.: TR+AS+SS-ThM6, 213
Keck, J.A.: VT-MoM2, 26
Kei, C.C.: NM-TuP2, 118; NM-TuP3, 118; NM-TuP4, 118; PS-ThP6, 250
Kelber, J.: EM1-MoA8, 33; GR+EM-TuM6, 64; GR-TuP7, 116
Kelkar, U.: TF2-ThM2, 210
Keller, S.: NS+EM-MoM6, 18
Kelley, M.: VT+MN+NS+SS+AS-TuA4, **108**
Kellogg, G.L.: GR+MN-WeM10, 141; SS-ThM12, 206
Kelly, L.L.: SS+EM-TuA3, 103
Kelly, M.J.: SE+PS-WeA10, **177**
Kemp, C.: AS-WeA8, 161
Kemper, T.: SS1-MoA6, 48
Kenney, J.A.: PS1-TuA4, **99**; PS1-TuA9, 100
Kent, M.: NT+AS-WeA11, **172**
Kent, T.: AS-TuP17, **113**; EM-MoM1, 5; SS+EM-TuA9, 104; SS-ThA6, 231
Kent, T.F.: NS+EM-MoM2, 17
Kern, K.: GR+MI-TuA1, **91**
Kersell, H.: MI-WeA3, 170; NS-ThM6, **198**
Kersevan, R.: VT-MoA9, **54**; VT-TuP7, 130
Kershish, M.D.: SS-TuP30, 127
Kersten, R.: BI-WeM4, 134
Kersting, R.: AS-TuM9, 57
Keshavarz, S.: NT-TuP2, 121
Kessels, W.M.M.: EL+AS+EM+MS+PS+TF-ThA7, 217; EM+TF-TuM11, 60; EN+PS-MoM10, **8**; IS+AS+SS-MoA9, 39; PS+TF-ThM9, 200; TF-MoA4, 52
Ketsman, I.: SS-ThA10, 231
Keville, B.J.: PS-ThA7, 227; PS-ThA8, **228**
Khabibullin, M.: EM-WeM2, 135
Khademhosseini, A.: BN-TuA1, **85**
Khaing, A.: BN+NM-TuM5, **58**
Khalil, M.: TF-MoA3, 51
Khalili, P.: EM2-MoA1, 34
Khan, S.: BI-MoM9, **5**
Khare, A.: EN1+TF-WeA11, 167; EN1+TF-WeA7, **166**
Khare, R.: PS+SS-WeM11, **151**
- Kholine, N.: AS-TuP5, 111
Khosravian, H.: SS-FrM5, 269
Kiantaj, K.: EM-TuA4, 87
Kibelka, G.: AS-MoA10, 29
Kiefer, B.: AS-TuP3, **111**
Kiehlauch, M.: PS+MN+TF-TuM9, **71**
Kiejna, A.: SS2-TuM6, 76
Kievit, O.: PS+SS-ThA11, 226
Kikuchi, Y.: TC+EM+NS-ThA10, 232
Kil, S.C.: SE-TuP5, 122
Kilcoyne, A.L.D.: PS+TF-ThM12, 201
Killelea, D.R.: SS1-MoM2, **21**
Kim, B.: NM+NS+MS-TuA12, 97
Kim, B.I.: SS2-MoA8, **50**
Kim, C.I.: PS-ThP10, **251**; PS-ThP8, 251; PS-ThP9, 251
Kim, C.K.: AS-TuP18, 113; PS-ThP17, **253**; PS-ThP18, 253
Kim, D.: EM-WeM2, 135; EN+PS-MoM9, 8; NS-ThM3, 198; SS2-MoA4, 50; SS-FrM1, 268; TF+EN-TuM9, **78**; TF1+EM-WeM4, 156
Kim, D.H.: IS+AS+SS-TuM10, 66
Kim, D.W.: PS-ThP12, 252
Kim, H.: BI-MoA4, 30; EM1-MoA1, **32**; TC+AS+EM-ThM1, 206
Kim, H.J.: NS-TuP12, 121
Kim, H.T.: SE-TuP5, **122**
Kim, J.: EM+TF-TuM2, 59; EM+TF-TuM3, 59; EM-ThP16, **243**; EM-ThP22, 244; EM-TuA10, 87; GR-TuA7, 92; NS+EM-MoM8, 18
Kim, J.K.: NS+EM-MoM1, 17
Kim, J.M.: NM-TuP11, 119
Kim, J.M.: TC+AS+EM-ThM1, 206
Kim, K.: NM-TuP8, 119; TC-ThP2, **255**; TC-ThP3, 255
Kim, K.-J.: AS-TuP11, 112; SS-TuP13, 125
Kim, M.: GR+TF+NS-ThA1, 220; MN-ThA7, 223
Kim, N.: EM-ThP17, 243; EN-ThP10, 246; EN-ThP9, 246
Kim, R.H.: PS-MoM9, 20
Kim, S.: AS-TuA9, 84; EN+EM+NS-MoA9, 36; EN+EM+NS-WeM12, **138**; IS+AS+SS-TuM10, 66; NM+NS+MS-TuA12, 97; NS+AS-TuA1, 97
Kim, S.J.: GR-WeA7, 169
Kim, T.H.: ET+EM+NS+GR-TuM6, 63; ET+EM+SS-MoM8, **10**
Kim, T.J.: EL-ThP2, 239
Kim, W.: GR-WeA7, **169**
Kim, W.K.: TR+AS+SS-ThM4, 213
Kim, Y.: SS2-FrM4, 267
Kim, Y.D.: EL-ThP2, 239
Kim, Y.-G.: EN+PS-MoM9, 8
Kim, Y.K.: SS1-MoA4, 48
Kimmel, G.A.: SS1-MoM6, **21**; SS-WeA9, 179
Kim-Ngan, N.-T.: AC+MI-WeA11, 160
Kimura, Y.: AS-ThM9, **187**
Kindermann, M.E.: GR+TF+ET-MoA6, 37
King, M.W.: BI-ThP2, 237
King, S.: EM-WeM5, **135**; PS+EM-WeA12, 174; PS+EM-WeA3, 172
King, W.P.: GR+TF+NS-ThA9, 221
Kinoshita, T.: PS-ThM3, 201
Kioussis, D.: EM-WeM9, **136**
Kioussis, N.: GR+TF+NS-ThA8, 221
Kirchen, S.: MB-MoM3, 15
Kirillov, O.A.: SE-ThM1, 203
Kirk, W.P.: EM+TF-TuM4, 59
Kish, E.R.: IS+AS+SS-TuM12, **67**
Kitajima, T.: PS+SS-WeM3, **150**
Kitazaki, S.: PS+BI-MoA9, **45**
Kitzinger, L.: EL+AS+EM+MS+PS+TF-FrM7, 259; EL+AS+EM+MS+PS+TF-ThM10, **190**
Kizilkaya, O.: SS+EM-TuA4, 103
Klem, E.J.D.: EM1-MoA11, 33; EN+EM+NS-MoA3, **35**
Klimov, N.N.: GR+MI-TuA8, 91; GR-WeA3, **168**
Klimov, V.I.: EN+NS-TuM3, **61**
Klose, F.: NT+AS+MI-WeM3, 147
- Klymko, N.: EM-WeM9, 136
Knaapen, R.: TF-MoA7, 52
Knez, M.: TF1+EM-WeM9, **157**
Knezevic, I.: ET+EM+NS+GR-TuM5, 63
Knight, K.B.: AC+SS-ThM5, 185
Knoops, H.C.M.: EL+AS+EM+MS+PS+TF-ThA7, 217; IS+AS+SS-MoA9, 39
Knudsen, J.: IS+AS+SS-MoM9, 14; NS-WeM2, **145**; SS-ThM10, 206
Knutson, C.: AS-MoM9, 3
Ko, A.: PS-TuM12, 73
Ko, K.Y.: NM-TuP11, 119
Ko, Y.B.: TF-MoA6, 52
Koay, C.S.: PS-MoM9, 20
Kobayashi, M.: MB+BI+PS-MoA8, **40**
Kobayashi, N.P.: EN+NS-TuA11, 89
Kobayashi, S.: PS-ThM3, 201
Kobayashi, T.: VT-TuP1, 129
Kobe, H.: BN-TuP1, **115**; NM-TuP9, 119
Kocha, S.: TF+EN-TuM2, 77
Kodambaka, S.: NS-TuM6, 69
Koeck, F.A.M.: EN-ThP2, 245
Koel, B.E.: SS1-WeM5, **153**; SS-TuP4, 123
Koelsch, P.: BI-MoM5, **4**
Koga, K.: PS+BI-MoA9, 45; PS+TF-ThM5, 200
Kohl, P.A.: EN+NS-ThM10, 193
Kohler, J.L.: AS-TuP6, 111
Kohler, R.: TF-TuP4, 128
Koleske, D.: EN+TF-TuA11, 90
Komachi, J.: PS-ThM3, 201
Komarneni, M.: SS2-MoM9, **23**
Komesu, T.: MI-ThP1, 248
Komiya, A.: SE+SS-WeM10, 152
Komori, F.: GR-MoM5, **11**
Kompa, K.-L.: AS-MoA3, 28
Kondic, L.: TF2+EM-WeA4, 181
Kondo, H.: PS+SS-ThA4, 225; PS1-TuA11, 101; PS-ThM11, 203; SE+PS-WeA9, 177
Kondo, T.: GR+MI-TuA4, **91**; SS2-MoM11, 23; SS-FrM2, 268
Kondo, Y.: PS1-TuA11, 101
Kondratyuk, P.: SS1-MoA3, 48; SS2-WeM6, **155**; SS-TuA11, 106
Kong, J.: ET+EM+NS+GR-TuM2, 62
Kong, L.: EN+NS-ThA3, 219
Kong, M.G.: SE+PS-WeA7, **176**
Kongkanand, A.: TF+EN-TuM3, 77
Kono, A.: PS+SS-ThA4, 225
Kono, Y.: NS-ThA9, 224
Konstantinidis, S.: SE+PS-ThA1, 228; TF1-ThM6, 209
Koo, H.J.: TF+EN-TuM9, 78
Korolkov, V.V.: AS+BI+NS-WeM12, **133**; SS2-TuM5, 76
Kortshagen, U.: EN+EM+NS-WeM1, **136**
Kosel, T.: EM-MoM8, 6
Koshy, R.: PS-TuM5, 72
Kostamo, J.: NM+MS+NS+TF-MoM6, 16
Koster, N.B.: HI+AS-TuA12, **96**; PS+SS-ThA11, 226
Kotru, S.: EN-ThP16, **247**
Kouda, M.: NM+MS+NS+TF-MoM5, 16
Kowalik, J.: GR-TuP5, 115; GR-TuP6, 116
Koyama, H.: AS-ThM9, 187
Kozen, A.C.: TF-MoA3, **51**
Kozhukhov, A.S.: EL-ThP1, 239
Kozimor, S.A.: AC+TF-ThA4, 215
Kramer, N.J.: EN+PS-MoM6, 8
Krause, K.M.: TF+SE-TuM4, 79
Kreil, J.: SS+EM-TuA10, **104**
Kreit, E.: TC+EM+NS-ThA6, 232
Kreuzer, M.: NT+AS-WeA10, 172
Krim, J.: TR-ThA10, 236; VT+MN+NS+SS+AS-TuA3, 108
Krishnamoorthy, S.: EM+SS-FrM7, **260**; EM+TF-TuM12, 60
Krishnan, M.: VT-TuP10, 131
Kristiansen, K.: SS2-MoA9, 51
Kroemker, B.: AS-MoM11, 3

- Kruchinin, V.N.: EL-ThP1, 239
 Krupin, O.: SS2-MoM2, 22
 Kruse, P.: SS-TuP6, 123
 Krylov, S.: MN-FrM3, **263**; MN-ThA7, 223; MN-ThA9, 223
 Kubo, A.: AS-TuM11, 57
 Kuboi, N.: PS-ThM3, **201**
 Kubota, T.: PS2-TuA1, 101; PS-ThM4, 201; PS-ThM5, 202; PS-ThM6, **202**
 Kuchibhatla, S.V.N.T.: AC+SS-ThM11, 186; AS-TuP15, 113; AS-WeA7, **161**; EM1-MoA2, 32; HI-TuP7, 117; NS-TuP3, 120; SS-WeA7, 178; TF-MoM1, 23; TF-TuP2, 128
 Kuech, T.F.: SS2-TuM12, 77
 Kuhn, K.: AS-MoA10, 29
 Kuhn, M.: PS+EM-WeA12, 174
 Kühne, P.: EL+AS+EM+MS+PS+TF-FrM3, 258; EL+AS+EM+MS+PS+TF-FrM5, 258
 Kuk, Y.: GR-TuA2, 92; NS+AS-TuA1, 97; NS+EM-MoM5, 18
 Kulshreshtra, P.: NM+MN+MS+TF-TuM12, 68
 Kumar, A.: NS-WeM11, **146**; SS2-FrM4, **267**
 Kumar, K.: PS+SE-MoA10, 47; PS-TuM10, 73; PS-TuM12, 73; PS-TuM5, 72
 Kumar, M.: GR-TuA11, 94; TC-ThP5, 256
 Kumar, N.: PS+SE-MoA9, 47
 Kummel, A.C.: AS-TuP17, 113; BI-ThM11, 189; EM+TF-ThM6, 192; EM-MoM1, 5; EM-TuA4, 87; NS-ThA9, 224; SS+EM-TuA9, 104; SS-ThA6, **231**
 Kung, P.: AS-TuA9, **84**; EN+EM+NS-WeM12, 138
 Kung, S.: NS-TuP1, 119
 Kunzler, S.C.: EM-ThP24, 244
 Kuo, S.Y.: EM-ThP12, 242
 Kuo, Y.: TF1-ThM3, **209**
 Kurapov, D.: SE-ThM11, 205
 Kurczy, M.: BI-MoM3, 4
 Kurdak, C.: EM-WeA12, 165
 Kurihara, M.: NM+MN+MS+TF-TuM4, **67**
 Kurokawa, A.: NS-TuP2, 119; VT-TuP1, **129**
 Kurosu, M.: SS-TuP26, **126**
 Kurtz, R.: SS-WeA11, **179**
 Kurzydowski, K.J.: SS1-WeM12, 153
 Kushner, M.J.: PS+EM-WeA11, 173; PS1-TuA8, 100; PS-FrM1, **265**; PS-FrM3, 265
 Kutz, T.: BI-ThM12, 189
 Kuzmanich, G.: AC+SS-ThM10, 186
 Kuznetsov, A.Yu.: EM-WeA1, 163
 Kuznetsov, V.I.: TF-MoA1, **51**
 Kwo, J.: EM+TF-TuM9, 60
 Kwon, J.: GR-TuA2, 92; NS+EM-MoM5, 18
 Kwon, N.: NM-TuP8, **119**; TC-ThP2, 255
 Kwon, T.: PS-TuM5, 72
 Kwong, H.M.: BI-ThM12, 189
- **L** —
- LaBean, T.: BI-MoM10, 5
 LaBella, V.P.: AS+BI+NS-WeM11, 133; GR+MI-TuA3, 91
 Labelle, C.: PS-TuM12, 73; PS-TuM5, 72
 Labuda, A.: TR+AS+SS-ThM1, 212
 Lach, P.: EN-ThP12, 247
 Ladroue, J.: PS+MN+TF-TuM3, 71
 LaForge, J.M.: SE+TF-TuA7, 103
 LaFranzo, N.A.: TF+EM+SS-ThA10, **234**
 Lagally, M.G.: ET+EM+NS+GR-TuM5, 63; NS-MoA11, 43; TF2+EM-WeA11, 182
 Lagoute, J.: MI-WeM6, 143
 Lahiri, J.: GR-MoM3, 10
 Lahouij, I.: TR+AS+SS-ThM10, 213
 Lai, F.-I.: EM-ThP12, 242
 Lai, R.Y.: EL+AS+EM+MS+PS+TF-ThM6, 190
 Lai, S.-C.: TF1+EM-WeA9, 181
 Laibinis, P.: BI+AS+NS+SS-WeA10, 163
 Laibowitz, R.: PS+EM-WeA1, 172
 Lakhtakia, A.: TF+SE-TuM11, 80
 Lalany, A.: TF+SE-TuM4, 79
 Lam, C.H.: TF1+EM-WeA9, 181
 Lamb, R.: MB-MoM1, **15**; MB-MoM11, 16
 Lambert, C.: BN+NM-TuM5, 58
 Lambert-Milot, S.: TF-MoM9, 25
 Lamsa, A.: BI-WeM4, 134
 Landesman, J.P.: PS-FrM8, 266
 Landheer, K.: SS1-MoA7, 48
 Landie, G.: PS-MoM9, 20
 Landin, J.: EL+AS+EM+MS+PS+TF-ThM4, 190
 Landt, L.: NS-ThM11, 198
 Lane, B.: PS-ThP23, 254
 Lange, P.: GR-WeA1, 168
 Langer, R.: BI-WeM3, 134
 Langhammer, C.B.: BI+AS+NS+SS-WeA4, 162
 Langreth, D.C.: EN+NS-ThA3, 219
 Lanza, G.: VT+MN+NS+SS+AS-TuA12, 110
 Lanzara, A.: GR-WeA12, 170; SS-TuP2, 123
 Laracuenta, A.R.: GR+TF+NS-ThA9, 221
 LaRose, J.D.: EM+TF-TuM6, 59
 Larsen, G.K.: TF+SE-TuM10, **80**
 Larson, B.C.: EN+AC-FrM8, 261
 Larson, G.: BI-TuA10, 85
 Larson, J.: TR-ThA11, **236**
 Larson, P.E.: AS-ThM10, 188; EW-TuL5, 82
 Larsson, E.M.K.: BI+AS+NS+SS-WeA4, 162
 Laskoski, M.: GR-TuA4, 92
 Lass, S.: EW-WeL2, **158**
 Latulippe, D.R.: BI-MoA11, 31
 Lauritsen, J.V.: SS2-WeM2, **154**; SS-ThM10, 206
 Lauter, V.: NT+AS+MI-WeM3, 147; NT+AS+MI-WeM4, 147; NT+AS+MI-WeM5, 147; NT-TuP2, 121
 Laver, M.: NT+AS+MI-WeM5, 147
 Lavoie, C.: TF-MoM9, 25
 Law, J.J.M.: EM-MoM2, **6**
 Law, M.: EN1+TF-WeA8, 166
 Lawrie, J.: BI+AS+NS+SS-WeA10, **163**
 Lazzari, R.: SS-ThM5, 205
 Lazzarino, F.: PS1-TuA7, 100; PS-TuM1, **72**
 Le Gratiot, L.: PS+SS-WeM1, 149
 Le Lay, G.: SS-FrM11, **270**
 Le Tarte, L.: EN-ThP19, **248**
 Le, D.: SS2-TuM6, **76**
 Le, M.: SS-WeA11, 179
 Le, T.P.: EN+EM+NS-WeM11, 137
 Lea, A.S.: AS-ThM4, 187; AS-TuA1, **83**
 LeClair, P.: NT-TuP2, 121; SS+EM-TuA10, 104
 Lecordier, L.: NM+MS+NS+TF-MoM3, 16
 Lee, B.: GR-TuA7, 92
 Lee, B.H.: TF1+EM-WeM3, **156**
 Lee, B.-J.: AS-MoA3, 28
 Lee, C.: EN-ThP3, **245**
 Lee, C.-T.: EM-ThP12, 242; NM-TuP4, 118
 Lee, D.: PS-ThP24, 254; PS-ThP25, 254; SS1-MoA6, 48
 Lee, D.H.: TC+EM+NS-ThA3, **232**
 Lee, D.J.: EN-ThP13, **247**
 Lee, G.: SS-FrM3, 269
 Lee, G.S.: NS-ThM12, 199
 Lee, H.: NT-TuP2, **121**
 Lee, H.-J.: EN+PS-MoM9, 8
 Lee, J.: AS-TuP11, 112; NM+NS+MS-TuA12, 97; PS+EM-WeA9, **173**; SS1-TuM10, **75**; SS-ThM11, 206; SS-TuP13, **125**
 Lee, J.H.: EN-ThP3, 245
 Lee, J.L.S.: AS-MoA9, 29; AS-TuM4, **56**
 Lee, J.R.I.: NS-ThM11, 198
 Lee, J.S.: EM-TuA4, 87; SS-ThA6, 231; TF-MoA6, **52**
 Lee, J.U.: GR+MS+EM-FrM1, **262**
 Lee, K.: NS-TuP4, **120**; TF+EN-TuM9, 78
 Lee, K.H.: NS-ThM12, **199**
 Lee, M.: EM-ThP22, 244; EN-ThP3, 245
 Lee, S.: BI-MoA4, 30; EM-ThP22, **244**; EN+TF-TuA11, 90; NM+NS+MS-TuA12, 97; SS+EM-TuA9, 104; TC-ThP3, **255**
 Lee, S.B.: EN+NS-ThA4, 219
 Lee, S.S.: AC+TF-ThA1, 215
 Lee, S.W.: PS+BI-MoA1, **43**; PS+BI-MoA11, 45
 Lee, T.: NM+NS+MS-TuA12, 97
 Lee, W.: EN-ThP10, 246; EN-ThP9, 246
 Lee, W.C.: EM+TF-TuM9, 60
 Lee, W.K.: GR+NS+PS+SS-ThM12, 195; GR+TF+NS-ThA9, **221**; GR-TuA4, 92; NS-WeM6, 145
 Lee, W.S.: TC+AS+EM-ThM1, 206
 Lee, Y.: AS-TuP11, **112**; PS-ThP19, 253; SS-TuP13, 125
 Lee, Y.S.: PS-ThP15, **252**
 Lee, Y.T.: NS+EM-MoM1, **17**
 Leever, B.J.: EN+NS-WeM2, **138**; EN+NS-WeM4, 139
 Lefaucheux, P.: PS+MN+TF-TuM3, 71
 Leggett, G.: BI+AS+NS+SS-WeA9, **162**; TF+EM+SS-ThA4, 233
 Lehto, T.: NM+MS+NS+TF-MoM6, 16
 Lei, Z.: EN+TF-TuA9, 90
 Leick, N.: EL+AS+EM+MS+PS+TF-ThA7, **217**; TF+EN-TuM2, 77
 Leighton, C.: EN1+TF-WeA11, 167; NT+AS+MI-WeM5, **147**
 Leiste, H.: SE-ThM12, 205
 Lekkala, J.: TF-MoA10, 53
 Lekkala, S.: EM+SS-FrM8, 260
 Lemaitre, M.: GR+EM-TuM11, 65; GR+MI-TuA11, 92; GR+MS+EM-FrM6, 262
 Lenahan, P.M.: PS+EM-WeA3, 172
 Leng, S.: VT-TuM2, 80
 Lenhardt, J.: EM-ThP2, 240
 Lenox, C.: PS-TuM6, 73
 Leonhardt, D.: TF2-ThM10, 212; TF-MoM8, **24**
 Leou, K.C.: PS-ThP13, 252
 Lerner, A.: NT-TuP1, 121
 Leroy, F.: TF2+EM-WeA3, 181
 Leroy, P.: PS+SE-WeM3, 148
 Leskelä, M.: TF-MoA10, 53
 Leung, K.T.: TC-ThP4, **255**
 Leusink, G.J.: EM+TF-TuM6, 59
 Leverd, F.: PS+EM-WeA10, 173
 Levi, D.: EL+AS+EM+MS+PS+TF-ThA1, **216**
 Levine, M.S.: SS-TuA9, 106; SS-TuP5, 123
 Levy, J.: TF2+EM-WeA7, 181
 Lewis, J.: EM1-MoA11, **33**; EN+EM+NS-MoA3, 35
 Lewis, T.: IS+AS+SS-TuM11, **67**; SS1-MoM5, 21
 Li, A.-P.: ET+EM+NS+GR-TuM1, 62; ET+EM+NS+GR-TuM6, 63
 Li, C.: PS-ThP10, 251; SE-ThM4, 204
 Li, F.: SS2-MoA11, 51
 Li, H.: EN+TF-TuA9, 90
 Li, H.C.: PS+SE-WeM10, 149
 Li, J.: EN+NS-ThA3, 219
 Li, K.: BI-MoA4, 4
 Li, L.: EN+TF-TuA9, **90**; GR+TF+NS-ThA11, 222; GR-WeA10, 169; GR-WeA11, **170**; MI-WeM12, 144
 Li, M.: NS+EM-MoM8, 18; SS2-WeM9, 155
 Li, Q.: EN+TF-TuA11, 90; GR+MN-WeM5, 140; NS+AS-TuA7, 98; NS-ThM10, **198**; TR+AS+SS-ThM12, 214
 Li, R.: EM-MoM8, 6
 Li, W.: EN+TF-TuA9, 90; PS-TuM10, 73; TF1-ThM10, 210
 Li, X.: GR-MoM1, 10; PS+SE-MoA10, 47
 Li, Y.: AC+MI-WeA3, 159; EN1+TF-WeA7, 166; TF-TuP11, **129**; VT+MN+NS+SS+AS-TuA11, **109**
 Li, Y.Y.: GR+TF+NS-ThA11, **222**
 Li, Z.J.: SS1-MoA4, **48**
 Liang, T.: GR+NS+PS+SS-ThM10, **195**
 Liang, W.: ET+EM+NS+GR-TuM6, 63
 Liang, Z.: SS-FrM5, **269**
 Libera, J.A.: TF-TuA1, 106
 Liberman, A.: NS-ThA9, **224**
 Libuda, J.: IS+AS+SS-MoM3, 13
 Licciardello, A.: AS-TuM4, 56
 Liddell, K.: NS+EM-MoM8, 18
 Lidzey, D.: BI+AS+NS+SS-WeA9, 162
 Lie, F.L.: TF-TuA12, 108
 Lii, T.: PS-TuM6, 73

- Likhanskii, A.: PS-FrM2, **265**
Lill, T.: PS-MoM3, 19; PS-MoM5, 19
Lim, D.V.: BI-MoA10, 31
Lim, H.: SS2-MoA1, **50**
Lim, S.J.: NS+EM-MoM5, **18**
Lim, W.C.: AS-TuP11, 112
Lima, L.P.B.: EM-ThP5, **241**; EM-ThP6, 241; EN-ThP5, 245
Lin, C.C.: PS-ThA2, 227
Lin, C.-H.: NM+MN+MS+TF-TuM10, 68
Lin, C.P.: VT-TuP4, 130
Lin, M.-W.: GR+TF+NS-ThA8, 221
Lin, P.: NS-TuM2, **69**; NS-WeM11, 146
Lin, P.H.: VT-TuP3, 130
Lin, S.-H.: EN+EM+NS-MoA1, **35**
Lin, T.: PS+SS-ThA7, **226**
Lin, T.D.: EM+TF-TuM9, 60
Lin, W.: MI-ThM10, **197**; MI-ThM6, 196
Lin, X.: SS1-TuM11, 75; SS-WeA10, **179**
Lin, Y.: GR+MI-TuA9, 92; GR+MN-WeM3, 140
Lin, Y.C.: MN-FrM8, 264
Lin, Y.S.: AS-TuP22, **114**
Lin, Y.W.: VT-TuP4, **130**
Linderoth, T.R.: SS2-TuM9, **76**
Linford, M.R.: AS-WeA11, **161**; EM-ThP24, 244
Ling, C.: GR+TF+NS-ThA8, 221
Ling, J.: AC+TF-ThA10, 216
Linzon, Y.: MN-ThA7, 223
Liou, J.C.: MN-FrM8, 264
Lipp, M.: AC+MI-WeA7, 159
Lippuner, M.A.: SS-TuP12, **125**
Lipson, A.L.: NS-WeM3, 145
Lisi, A.: PS-TuM10, 73
Liu, A.: EM-ThP23, 244
Liu, B.H.: NM-TuP2, 118; NM-TuP3, 118; NM-TuP4, 118; PS-ThP6, **250**
Liu, C.: ET+EM+NS+GR-TuM12, **64**; SE-TuP2, **122**
Liu, C.-C.: PS+BI-MoA11, 45
Liu, C.Y.: EN+EM+NS-WeM1, 136
Liu, D.-J.: SS1-WeM3, 153; SS2-MoA10, **51**
Liu, D.R.: MI-ThP4, 249
Liu, F.: AS-WeA7, 161; EM1-MoA2, **32**
Liu, G.: GR-TuA10, 93; IS+AS+SS-MoA1, 38; NM+MS+NS+TF-MoM3, 16
Liu, J.: GR+EM-TuM10, 65; TR+AS+SS-ThM6, 213
Liu, L.: ET+EM+NS+GR-TuM6, 63; SS2-WeM5, **154**
Liu, M.: EM-MoM5, 6; EM-WeM5, 135
Liu, P.: MI-WeA12, 171; SS2-FrM2, 267
Liu, Q.: EM-MoM8, 6
Liu, T.-L.: NS-MoA6, 42
Liu, W.-T.: BI-WeM4, 134
Liu, X.: VT+MN+NS+SS+AS-TuA11, 109
Liu, X.-Z.: GR+MN-WeM5, **140**
Liu, Y.: AS-MoA4, 28; EN1+TF-WeA8, 166; GR+TF+NS-ThA11, 222; GR-WeA10, 169; GR-WeA11, 170; MI-ThM10, 197; MI-WeM12, **144**; SS-ThM9, **206**; TC+EM+NS-ThA11, 233
Liu, Z.: EN1+TF-WeA8, 166; IS+AS+SS-MoM4, 13; IS+AS+SS-TuM9, 66; TF-TuP11, 129
Lloyd, K.G.: AS-WeA3, **160**
Lobb, C.: TF-MoA3, 51
Loch, D.: SE+PS-ThA9, 230
Lock, E.H.: BI-ThP5, 238; GR-TuA4, **92**
Lofaro, Jr., J.C.: SS2-WeM1, **154**
Lohn, A.J.: EN+NS-TuA11, **89**
Lohstreter, L.: AS-MoM3, **2**
Long, J.C.: PS1-TuA10, 100
Longenecker, J.G.: MN-ThA8, **223**
Longo, C.: VT-TuM2, 80
Look, D.C.: EM-WeA1, 163
Lopez, D.: MN-FrM1, **263**; MN-FrM6, 264
Lopez, G.P.: BI+AS+NS+SS-WeA9, 162; MB-MoM9, **15**
Lopez-Bezanilla, A.: GR+TF+NS-ThA6, **221**
Lopez-Lopez, S.: PS-FrM7, **265**
Lopinski, G.P.: TF+EM+SS-ThA3, 233
Lorenz, C.U.: SS-FrM6, **269**
Loring, R.F.: EM+SS-FrM8, 260
Lösche, M.: BI-ThP10, 238; BI-ThP9, 238; BI-TuA7, **84**
Losego, M.D.: TF2-ThM11, 212
Losovyj, Ya.: MI-WeA12, 171; SS-ThA10, 231
Losvyj, Y.B.: SS+EM-TuA4, 103
Lott, D.: NT+AS+MI-WeM3, **147**
Louie, S.G.: GR-WeA12, 170; SS-TuP2, 123
Louis, K.: BI+AS+NS+SS-WeA3, 162
Lowder, J.E.: EN+TF-TuA11, 90; IS+AS+SS-MoA6, 38; TF1-ThM2, **208**; TF-FrM3, 270
Lozzi, L.: EN2+TF-WeA11, **168**
Lu, B.: NM+NS+MS-TuA3, **96**
Lu, C.-J.: MN-FrM9, 264
Lu, J.: EN+NS-ThM3, 193
Lu, J.C.: VT-TuP3, 130
Lu, M.: EM-ThP2, 240
Lu, P.: EM+TF-ThM5, 191
Lu, T.-M.: SE+TF-TuA1, 102
Lu, W.: BI-MoA4, 30; BI-MoA6, 30; EM1-MoA1, 32; GR+MS+EM-FrM7, 262; NS-ThM3, 198; SS-FrM1, 268
Lu, Y.: EM-MoM8, 6; PS-ThM11, 203
Lu, Y.C.: EN+NS-ThA2, 219
Lucaortoro, T.B.: EL+AS+EM+MS+PS+TF-ThM9, 190
Lukaszew, R.A.: NS-MoA9, **43**; TF-FrM8, 271; VT+MN+NS+SS+AS-TuA8, 109; VT+MN+NS+SS+AS-TuA9, 109
Lulinsky, S.: MN-FrM3, 263
Lundgren, E.: IS+AS+SS-MoM4, 13; IS+AS+SS-MoM6, 14; SS-ThM10, 206
Lundin, D.: TF-FrM9, 271
Lundwall, Matt: SS-TuA3, **105**
Lung, H.-L.: TF1+EM-WeA9, 181
Luo, M.: NS-ThM3, **198**
Luo, X.: VT-TuM4, 80
Luo, X.L.: BN+NM-TuM2, 57; BN+NM-TuM6, **58**
Lusth, J.C.: MN-ThA3, 222
Luttrell, T.: EN2+TF-WeA7, **167**; SS-WeA3, 178
Lyding, J.W.: EN1+TF-WeA10, 166; GR-TuA12, 94
Lykhach, Y.: IS+AS+SS-MoM3, 13
Lynch, S.: SE-TuP2, 122
Lysaght, P.: AS-TuP20, 114; EM-TuA12, 88
Lyubinsky, I.: SS2-WeM12, **155**; SS-WeA1, 177; SS-WeA10, 179
— **M** —
Maas, D.J.: HI+AS-TuA12, 96; HI+AS-TuA4, 95
MacElroy, J.M.D.: EN2+TF-WeA8, 167
Macgarrait, N.: PS-ThA1, 227
Machida, M.: NS+AS-TuA1, 97
Machida, T.: GR+MI-TuA4, 91
Mack, P.: AS-TuA4, 83; AS-WeA2, **160**; EW-TuL2, 82
Mackus, A.J.M.: EL+AS+EM+MS+PS+TF-ThA7, 217; IS+AS+SS-MoA9, 39; TF-MoA4, 52
MacNeil, S.: BI-ThP3, 237
MacQuarrie, E.R.: NS-MoA1, 42
Madan, A.: EM-WeM9, 136
Madix, R.J.: SS2-MoM3, 22; SS-TuA8, 105; SS-TuP1, 122
Maeda, K.: PS-ThP26, 254
Maeda, S.: PS+SE-MoA2, 46
Maehashi, K.: GR+MS+EM-FrM8, 262; GR+MS+EM-FrM9, 263; GR+NS+PS+SS-ThM9, **195**; NS-WeM10, 146
Magana, S.: BI-MoA10, 31
Magel, G.A.: NM+NS+MS-TuA11, 97
Magnan, H.: MI-WeM6, 143
Magnuson, C.: GR-MoM1, 10; GR-TuA9, 93
Magnusson, R.: EL-ThP3, **239**
Mahadevan, S.: PS-ThP23, 254
Maier, M.: NS+AS-TuA11, 98
Maier, S.: GR+NS+PS+SS-ThM3, 194
Maitrejean, S.: TF1+EM-WeA2, 179
Majewski, J.: NT+AS+MI-WeM10, 148; NT+AS-WeA8, 171; NT-TuP1, 121
Majidi, H.: EN+EM+NS-WeM11, 137
Makino, H.: AS-ThM9, 187; TC+AS+EM-ThM2, **207**
Maklakov, S.A.: MI-ThP2, **248**
Maksymovych, P.: NS+AS-TuA7, **98**
Malgorzata, M.: TF1+EM-WeA3, 180
Malinen, T.: NM+MS+NS+TF-MoM6, 16
Malko, A.V.: EN+NS-TuM1, 60
Malocsay, C.: EW-WeM8, **140**
Maluf, S.S.: SS-TuA1, **105**
Man, K.L.: GR-WeA4, 169
Mancho-Posso, P.: EM-ThP21, **243**
Mandelkow, E.: NT+AS-WeA8, 171
Mandoc, M.M.: EM+TF-TuM11, 60
Maness, Jr., L.V.: EN+MS+VT-ThA1, **218**
Mani-Gonzalez, P.G.: AS-TuP21, 114
Manini, P.: EW-WeL3, 158; VT-TuM6, 81; VT-TuP6, **130**
Mankey, G.J.: NT+AS+MI-WeM3, 147; NT-TuP2, 121
Mann, J.: SS-FrM1, 268
Mannequin, C.: EM2-MoA9, 34
Manno, M.: EN1+TF-WeA11, **167**
Mansour, A.: PS+TF-ThM12, 201
Mansour, A.N.: EN+NS-ThA2, 219
Marc, D.: PS+SE-MoA4, 46
Marchack, N.: PS+SS-WeM2, **149**
Marchelli, A.P.: PS-ThP2, 250
Marchesini, G.: NS-ThM2, 198
Marchi, A.: BI-MoM10, 5
Marchman, H.M.: NM+NS+MS-TuA11, 97
Mares, J.W.: TF-FrM5, 271
Margarella, A.: EN1+TF-WeA8, 166; SS1-MoM5, **21**
Maria, J.-P.: TF2-ThM11, 212; TF-MoM2, **23**
Maringer, C.: TR-ThA2, 235
Marks, T.J.: EN+NS-WeM2, 138; EN+NS-WeM3, 138; EN+NS-WeM4, 139
Markus, T.Z.: NS-ThM9, 198
Marohn, J.A.: EM+SS-FrM8, 260; MN-ThA8, 223
Marot, L.: SE+PS-ThA2, 229
Marquis, Jr., J.P.: AS-TuP13, 112
Marsillac, S.: EL+AS+EM+MS+PS+TF-ThA4, 216
Mårtensson, N.: IS+AS+SS-MoM9, 14
Martin, E.H.: PS-WeA3, 174
Martin, J.M.: TR+AS+SS-ThM10, 213
Martin, N.M.: IS+AS+SS-MoM4, 13; IS+AS+SS-MoM6, 14; SS-ThM10, 206
Martin, R.L.: AC+MI-WeA10, 159; AC+TF-ThA4, 215
Martin, R.M.: TF1+EM-WeA9, 181
Martin, T.: BN-TuA4, 86
Martinez, H.P.: NS-ThA9, 224
Martini, A.: TR+AS+SS-ThM12, 214
Martin-Palma, R.J.: TF+SE-TuM11, 80
Maruyama, T.: TR-ThP2, 256
Marvel, R.E.: EL+AS+EM+MS+PS+TF-ThA11, **218**
Masahara, M.: PS-ThM10, 202
Masakazu, S.: PS-ThP16, 252
Master, E.R.: AS-MoA11, 29
Masters, A.E.: TF+EN-TuM10, 78
Masuda, H.: EM-WeM9, 136
Mathys, D.: SE+PS-ThA2, 229
Matis, B.R.: GR+MS+EM-FrM10, **263**
Matolin, V.: IS+AS+SS-MoM3, 13
Matranga, C.: SS-ThM11, 206
Matsubayashi, A.: GR+MI-TuA3, 91; MI-ThP5, **249**
Matsuda, A.: PS-ThM12, 203; PS-ThM9, **202**
Matsuda, Y.: IS-TuP1, 117; PS-ThP3, 250
Matsui, K.: BN-TuP1, 115
Matsumoto, D.: SS1-MoA10, 49
Matsumoto, H.: PS+MN+TF-TuM4, 71; PS-MoM10, 20

- Matsumoto, K.: GR+MS+EM-FrM8, 262;
GR+MS+EM-FrM9, 263; GR+NS+PS+SS-
ThM9, 195; NS-WeM10, 146
- Matsumoto, S.: SE+SS-WeM10, 152
- Matsumaga, S.: AS+BI+NS-WeM5, 132
- Matsuo, J.: AS-TuM10, 57
- Matsuoka, D.: SS-TuP11, 124
- Matsuura, G.: PS+MN+TF-TuM4, 71; PS-MoM10,
20; PS-TuM11, 73
- Mattevi, C.: SS-FrM3, 269
- Matthes, F.: NS+AS-TuA11, 98
- Matthews, O.: TR-ThA9, 235; TR-ThP4, 256
- Mattrey, R.F.: NS-ThA9, 224
- Maurer, J.A.: TF+EM+SS-ThA10, 234
- Mavrikakis, M.: SS1-TuM5, 74
- Mavrokefalos, A.: SE+SS-WeM2, 151
- May, R.A.: SS1-MoM10, 21
- Mayer, J.S.: NS+EM-MoM8, 18
- Mayer, T.S.: NS+EM-MoM8, 18
- Mayo, A.T.: NS-TuP8, 120
- Mayo, D.C.: NS-TuP8, 120
- Mayrhofer, P.H.: SE-ThM6, 204; TR-ThA2, 235
- Maziarz, A.: BN+NM-TuM5, 58
- McAllister, D.R.: AS-TuP13, 112
- McAllister, N.M.: AS-TuP13, 112
- McArthur, S.L.: BI-MoM1, 3; BI-ThP3, 237
- McBreen, P.H.: SS1-MoA1, 48
- McCarthy, J.: BI+AS+NS+SS-WeA3, 162
- McCarty, K.: GR-MoM10, 12; GR-MoM6, 11;
GR-WeA9, 169
- McClelland, D.: VT-MoA8, 54
- McCleskey, T.M.: AC+MI-WeA10, 159; AC+TF-
ThA4, 215
- McClory, J.: SS-ThA10, 231
- McCoustra, M.: SS1-MoM1, 21
- McCreary, K.M.: GR+TF+ET-MoA10, 37
- McCullough, R.D.: TC+EM+NS-ThA4, 232
- McDevitt, T.: BI-WeM9, 134
- McDonald, A.: MB-MoM11, 16
- McDonald, K.P.: SS-TuP15, 125
- McDonnell, S.: GR-TuA9, 93; IS+AS+SS-
MoM10, 14
- McEuen, P.L.: GR+EM-TuM9, 65; GR+MN-
WeM1, 140; MN-ThA4, 222
- McFarlane, H.F.: EN-MoA1, 36
- McGimpsey, W.: BN+NM-TuM5, 58
- McGimpsey, W.G.: EM+TF-ThM1, 191
- McIntyre, P.C.: EM-TuA7, 87
- McKnight, T.E.: TF2+EM-WeA9, 182
- McLellan, E.: PS-MoM9, 20
- McQuillan, A.J.: MB-MoM5, 15
- Mebarki, B.: EM-MoM3, 6
- Mecklenburg, M.: NS-TuM6, 69
- Mehl, M.J.: GR+EM-TuM4, 64
- Mehn, D.: BN-TuA4, 86
- Mehta, B.R.: TC-ThP5, 256
- Mei, W.-N.: SS-ThA10, 231
- Meinander, K.: SS-ThM10, 206
- Meisner, G.P.: EN-TuM5, 62
- Meitner, S.J.: VT-TuP7, 130
- Mejia, J.I.: EM-ThP3, 240; EM-ThP4, 240;
TC+AS+EM-ThM11, 208
- Melechko, A.V.: NS+EM-MoM10, 18; TF2+EM-
WeA9, 182
- Melendez-Lira, M.A.: EN1+TF-WeA9, 166
- Melissen, W.: SE+PS-ThA2, 229
- Melitz, W.: AS-TuP17, 113; EM-MoM1, 5; EM-
TuA4, 87; SS-ThA6, 231
- Membreno, D.: TF+EN-TuM4, 78
- Mendez, N.: BI-ThM11, 189
- Mendoza-Galvan, A.: AS-TuP21, 114
- Meng, L.: PS+SE-WeM11, 149; SE+PS-ThA7,
229
- Meng, Y.: EN+TF-TuA9, 90
- Menguelti, K.: PS+SE-MoA3, 46
- Merkle, A.P.: HI+AS-TuA3, 94
- Meseck, G.R.: BI-WeM11, 135
- Messing, M.E.: IS+AS+SS-MoM4, 13
- Messmer, B.T.: BI-ThM11, 189
- Metz, A.: PS-TuM10, 73; PS-TuM12, 73
- Metzler, D.: PS+SE-MoA9, 47
- Meulenberg, R.W.: SS1-TuM1, 73
- Meunier, S.: VT-TuP6, 130
- Meunier, V.: ET+EM+NS+GR-TuM2, 62
- Meyer III, H.M.: AS-TuP14, 113; EW-TuL3, 82
- Meyer, R.: SS-FrM5, 269
- Meyerbröker, N.: TF+EM+SS-ThA6, 233
- Miao, X.: GR+MI-TuA11, 92; GR+MS+EM-
FrM6, 262
- Michallon, P.: TF1+EM-WeA2, 179
- Michalski, J.: SS1-WeM12, 153
- Michely, T.: NS-WeM2, 145
- Migani, A.: IS+AS+SS-MoM3, 13
- Mignot, Y.: PS-MoM9, 20; PS-TuM12, 73; PS-
TuM5, 72
- Mikkelsen, A.: NS-TuM3, 69
- Milasinovic, S.: AS-MoA4, 28
- Milkani, E.: BN+NM-TuM5, 58
- Miller, B.P.: TR-ThP9, 257
- Miller, D.: TF1+EM-WeA9, 181
- Miller, G.: AC+SS-ThM9, 186
- Miller, J.: AS-MoA8, 29
- Miller, J.B.: SS2-WeM6, 155; SS-TuA11, 106
- Miller, M.: TR+AS+SS-ThM2, 213
- Miller, S.: EM1-MoA10, 33
- Millette, J.R.: NM+AS+MS-WeM6, 144
- Mills, M.J.: NS+EM-MoM2, 17
- Milosavljevic, V.: PS-ThA1, 227; PS-ThP22, 253
- Mims, C.A.: AS-MoA11, 29
- Min, K.S.: AS-TuP18, 113; PS-ThP17, 253; PS-
ThP18, 253
- Min, Y.H.: IS+AS+SS-TuM10, 66
- Minami, T.: EN-ThP4, 245; TF-TuP3, 128; TF-
TuP7, 129
- Miro, H.: HI+AS-TuA10, 95
- Mishra, U.K.: NS+EM-MoM6, 18
- Misra, N.: PS1-TuA4, 99
- Mitchel, W.C.: GR+MS+EM-FrM7, 262
- Mitchell, J.N.: AC+MI-WeA10, 159
- Mitterer, C.: SE+SS-WeM6, 152
- Mitzi, D.B.: EN1+TF-WeA3, 166
- Miura, T.: SS1-MoA10, 49
- Miwa, K.: PS2-TuA1, 101
- Miyamoto, J.: TR-ThP7, 257
- Miyata, T.: EN-ThP4, 245; TF-TuP3, 128; TF-
TuP7, 129
- Miyawaki, Y.: PS1-TuA11, 101
- Miyayama, T.: AS-ThM11, 188; AS-TuM1, 56
- Miyazoe, H.: PS+SE-MoA6, 47
- Miyoshi, J.: EM-ThP5, 241; EM-ThP6, 241; EN-
ThP5, 245
- Mizotani, K.: PS+SS-WeM12, 151
- Mochiki, H.: PS+SS-ThA8, 226
- Mochizuki, Y.: AS-ThM9, 187
- Moellers, R.: AS-TuM5, 56; AS-TuM9, 57
- Moennighoff, T.: TR-WeA11, 184
- Moffitt, C.E.: BI-ThM4, 188
- Mohajezadeh, S.: MN-FrM10, 264
- Mohanty, A.: EN+NS-WeM5, 139
- Molas, G.: EM2-MoA3, 34
- Molis, S.: EM-WeM9, 136
- Molkenboer, F.T.: PS+SS-ThA11, 226
- Monaco, G.: AC+MI-WeA8, 159
- Mönig, H.: NS+AS-TuA4, 97
- Montgomery, E.A.: EL-ThP5, 240
- Monti, O.L.A.: SS+EM-TuA3, 103
- Moore, B.: BI-WeM4, 134
- Moore, D.P.: AC+SS-ThM3, 185
- Moore, E.W.: MN-ThA8, 223
- Moore, J.F.: AS-MoA4, 28
- Moore, T.M.: NM+NS+MS-TuA11, 97
- Moorman, M.W.: SS-WeA12, 179
- Morales, E.H.: SS-ThA3, 230; SS-ThA4, 230
- Moravej, M.: PS1-TuA2, 99
- Mordi, G.: GR-TuA7, 92
- Moreau, N.: MI-WeM6, 143
- Moreschini, L.: AC+MI-WeA8, 159
- Morgenstern, K.: SS2-MoM5, 22
- Mori, T.: NM-TuP1, 118
- Morikawa, Y.: PS+MN+TF-TuM1, 70
- Morita, K.: GR-MoM5, 11
- Moroz, P.: PS1-TuA1, 99
- Morra, M.: AS-WeA9, 161
- Morreale, B.D.: SS2-WeM6, 155; SS-TuA11, 106
- Morris-Cohen, A.: EN+NS-TuM11, 61
- Morrish, F.: BI-WeM6, 134
- Morrish, R.: EN2+TF-WeA8, 167
- Morrison, J.M.: AC+TF-ThA6, 215
- Morrow, T.: NS+EM-MoM8, 18
- Mosbacher, H.L.: EM-WeA1, 163
- Moseley, M.W.: EN+TF-TuA11, 90; IS+AS+SS-
MoA6, 38; TF1-ThM2, 208; TF-FrM3, 270
- Motyka, M.A.: EL+AS+EM+MS+PS+TF-ThA10,
217
- Mou, S.: GR+MS+EM-FrM7, 262
- Moulder, J.: AS-ThM10, 188; AS-TuP4, 111
- Moutinho, H.R.: EN1+TF-WeA1, 165
- Mryasov, O.N.: TF2-ThM3, 211
- Mu, R.: EN+NS-ThA10, 220; NS-TuP8, 120
- Mucha, J.A.: PS-ThP19, 253; PS-ThP28, 255
- Muhlberger, S.A.: TF+SE-TuM11, 80
- Mukherjee, S.: GR+MS+EM-FrM11, 263
- Mulders, A.: NT+AS+MI-WeM3, 147
- Müller, P.: TF2+EM-WeA3, 181
- Mullins, D.R.: SS1-TuM12, 75; SS-WeA8, 178
- Mullins, D.R.: SS2-WeM9, 155
- Mulvaney, S.: GR-TuA4, 92
- Mundy, C.J.: SS1-MoM6, 21
- Munro, J.J.: PS-FrM7, 265
- Murali, S.: TF1+EM-WeA1, 179
- Muratore, C.: SE+SS-WeM5, 152; SE+SS-WeM6,
152; SE+SS-WeM9, 152; SE-TuP4, 122; TF-
FrM10, 272
- Murayama, A.: EN+EM+NS-MoA1, 35
- Murayama, T.: PS+MN+TF-TuM1, 70
- Murphy, A.M.: BI-ThM12, 189
- Murphy, J.W.: EM-ThP4, 240
- Murphy, N.: EL-ThP7, 240; SE+PS-ThA8, 230
- Murphy, P.J.: BI-MoA11, 31
- Murray, I.P.: EN+NS-WeM2, 138
- Muscat, A.J.: EM+TF-ThM12, 192; EM1-MoA10,
33; EM-ThP21, 243; TF-TuA12, 108
- Musgrave, C.: TF-MoA3, 51
- Musho, T.D.: EN+NS-TuM10, 61
- Musin, I.R.: EN+EM+NS-WeM3, 136; NS-
TuM11, 70
- Muzik, H.: SS2-TuM2, 75
- Mydosh, J.A.: AC+MI-WeA3, 159
- Myers, R.C.: NS+EM-MoM2, 17
- Myers-Ward, R.L.: EM+SS-FrM1, 259; GR-
MoM11, 12; GR-MoM4, 11; GR-MoM8, 11;
GR-TuA8, 93; NS-WeM6, 145
- Myung, K.: EN-ThP10, 246
- N —
- Na, B.K.: PS-ThP12, 252
- Naaman, R.: NS-ThM9, 198
- Naboka, M.: SS2-TuM2, 75
- Nachimuthu, P.: AS-ThM4, 187; AS-TuP15, 113;
MI-ThP7, 249; NS-TuP3, 120; NS-TuP7, 120;
SS-WeA7, 178; TF1+EM-WeA1, 179; TF-
MoM1, 23; TF-TuP2, 128
- Nachmias, T.: MN-FrM3, 263
- Naef, S.P.: VT-MoM8, 26
- Nag, J.: EL+AS+EM+MS+PS+TF-ThA11, 218;
NS-MoA1, 42; TF-FrM11, 272
- Nagorny, V.: PS-ThP24, 254
- Nagpal, P.: EN+EM+NS-MoA6, 35
- Nahor, A.: EN+EM+NS-WeM6, 137
- Naik, M.: EM-MoM3, 6
- Naik, R.R.: AS+BI+NS-WeM6, 132
- Naito, K.: EN-ThP1, 245; EN-ThP7, 246
- Najafi, E.: NS-WeM12, 146
- Nakagawa, A.: PS+SS-ThA8, 226
- Nakagawa, J.: TR-ThP2, 256
- Nakakubo, Y.: PS-ThM12, 203; PS-ThM9, 202
- Nakamura, I.: TF-TuP9, 129

- Nakamura, J.: EM-TuA3, **86**; GR+MI-TuA4, 91; SS2-MoM11, 23; SS-FrM2, 268
- Nakamura, M.: PS+MN+TF-TuM4, 71; PS-MoM10, 20; PS-TuM11, 73
- Nakanishi, H.: SS-TuP8, 124
- Nakashima, R.: NM-TuP9, 119
- Nakata, K.: EN-ThP1, 245; EN-ThP7, 246
- Nakatsuji, K.: GR-MoM5, 11
- Nakayama, K.S.: NS-TuM1, **68**
- Nalamasu, O.: EN-MoM10, **9**
- Nam, S.: NM+NS+MS-TuA12, 97
- Nam, T.W.: TC+AS+EM-ThM1, **206**
- Namkoong, G.: TF-FrM3, 270
- Nampoori, H.V.: EN-ThP16, 247
- Nanayakkara, S.: AS+BI+NS-WeM10, 133; NS-MoA10, 43
- Nandasiri, M.I.: AC+SS-ThM11, **186**; AS-TuP15, 113; AS-WeA7, 161; HI-TuP7, 117; NS-TuP3, 120; SS-WeA7, 178; TF-TuP2, 128
- Narayanan, S.: TC+AS+EM-ThM9, **207**
- Narkilahti, S.: TF-MoA10, 53
- Nascente, P.A.P.: SS-TuA1, 105; TF-MoM10, **25**
- Nasrollahi, Z.: GR+EM-TuM11, 65
- Natarajarathinam, A.: TF1+EM-WeA8, **180**
- Nath, D.N.: EM+SS-FrM7, 260; EM+TF-TuM12, 60; NS+EM-MoM6, **18**
- Neal, B.: SS2-MoA3, 50
- Nealey, P.F.: NM+MN+MS+TF-TuM5, **68**
- Nedfors, N.: SE-ThM10, 204; TF1-ThM11, **210**
- Nefedov, A.: SS2-TuM2, **75**; SS-WeA2, 177
- Negishi, N.: NM+MN+MS+TF-TuM4, 67
- Nelin, C.J.: AC+SS-ThM1, 185
- Nelson, A.: NS-MoA9, 43
- Nelson, A.J.: AC+SS-ThM5, 185
- Nemanic, V.: EN-ThP2, 245
- Nemanich, R.J.: EN-ThP2, 245
- Neppel, S.: EN+NS-TuM2, 61
- Neria-Gonzalez, M.I.: EN1+TF-WeA9, 166
- Neumayer, D.: TF1+EM-WeA9, 181
- Newaz, A.K.M.: EM-WeA11, 165
- Newell, D.B.: GR+MI-TuA8, 91; GR-WeA3, 168
- Neyman, K.M.: IS+AS+SS-MoM3, 13
- Ng, A.: EM+TF-ThM12, 192
- Ng, H.W.: EM-ThP23, 244
- Ngo, C.: NS-TuM6, **69**
- Nguyen, H.M.: EN+NS-TuM1, 60
- Nguyen, N.V.: SE-ThM1, 203
- Nguyen, S.: EM-WeM3, 135
- Nguyen, V.: EM-MoM3, 6
- Nichols, M.T.: PS+EM-WeA7, 173; PS+EM-WeA8, **173**
- Nie, S.: GR-MoM10, **12**
- Nie, X.: SE+PS-WeA1, 176; SE+PS-WeA4, 176; TR-ThA3, **235**; TR-ThA8, 235; TR-WeA10, 184
- Niehuis, E.: AS-TuM5, 56; AS-TuM9, 57; AS-WeA1, 160
- Nijem, N.: EN+NS-ThA3, **219**
- Nikolenko, A.S.: EM-ThP25, 244
- Nikonov, S.: EM-WeM2, 135
- Nilius, N.: SS2-WeM10, 155
- Nilsson, A.: GR+TF+ET-MoA3, 37; SS2-MoM2, 22
- Ning, N.: PS+BI-MoA10, 45; PS+BI-MoA7, 44; PS+SS-ThA6, 225
- Ning, T.: BI-MoA8, 31
- Nishi, Y.: EN-ThP4, 245; PS+EM-WeA7, 173; PS+EM-WeA8, 173
- Nishida, T.: NM+MN+MS+TF-TuM4, 67
- Nishimori, Y.: PS-ThM6, 202; PS-ThP16, **252**
- Nizamidin, N.: NM+MN+MS+TF-TuM3, 67
- Nogami, J.: SS1-WeM9, **153**
- Noguchi, Y.: TF-TuP3, 128
- Noh, J.: TC+EM+NS-ThA6, **232**; TC-ThP1, 255
- Noh, J.H.: TC+EM+NS-ThA6, 232; TC-ThP1, **255**
- Nolph, C.A.: MI-ThM9, **196**; MI-WeA11, 171
- Nomoto, J.: EN-ThP4, 245; TF-TuP3, 128; TF-TuP7, **129**
- Nomura, K.: TC+EM+NS-ThA10, 232; TC+EM+NS-ThA3, 232; TC+EM+NS-ThA9, 232
- Nordell, B.J.: EM-WeM6, **135**
- Nordlund, D.: SS2-MoM2, 22
- Norris, D.J.: EN+NS-TuA1, **88**; EN1+TF-WeA7, 166
- North, S.H.: BI-ThP5, **238**
- Northwood, D.O.: SE+PS-WeA1, 176
- Nottbohm, C.T.: GR+NS+PS+SS-ThM4, 194
- Notte, J.A.: HI+AS-TuA1, **94**; HI+AS-TuA3, 94; HI-TuP1, 116; HI-TuP2, 116
- Novikova, I.: TF-FrM8, 271
- Nowak, J.: BN-TuA4, **86**
- Nozawa, T.: PS+TF-ThM1, 199; PS-ThP23, 254; PS-ThP28, 255
- Ntwaeaborwa, O.M.: AS-TuP23, **114**
- Nukaga, O.: PS-ThM4, 201; PS-ThM5, 202
- Nunney, T.S.: AS-TuA2, **83**; AS-TuP8, 112; EW-TuL2, 82; EW-TuL3, **82**
- Nyakiti, L.O.: EM+SS-FrM1, 259; GR+MS+EM-FrM3, 262; GR-MoM11, **12**; GR-MoM8, 11; GR-TuA8, 93; NS-WeM6, 145
- O —
- O' Sullivan, D.: PS-ThP22, 253
- O'Connor, D.C.: SS2-FrM3, **267**
- Obama, S.: PS-ThP26, **254**
- Oberg, H.: SS2-MoM2, 22
- O'Brien, K.E.: MN-FrM4, **263**
- Ocola, L.E.: MN-FrM6, 264; NM+MN+MS+TF-TuM9, 68
- Odaka, K.: NS-TuP2, **119**
- Odum, T.W.: NM+MN+MS+TF-TuM1, **67**
- Oehrlein, G.S.: PS+BI-MoA10, 45; PS+BI-MoA7, 44; PS+SE-MoA9, 47; PS+SS-ThA6, 225; PS+SS-ThA7, 226; PS-TuM6, 73
- Oertel, M.: NS+AS-TuA11, 98
- Offi, F.: AC+MI-WeA8, 159
- Ogasawara, H.: GR+TF+ET-MoA3, 37; SS2-MoM2, **22**
- Ogawa, S.: HI+AS+BI+NS-WeM3, **141**
- Ogieglo, W.: EL+AS+EM+MS+PS+TF-ThA9, 217
- Ogletree, D.F.: SE+SS-WeM11, **152**
- Oh, J.P.: SS-FrM2, **268**
- Oh, J.S.: AS-TuP18, **113**; PS-ThP17, 253; PS-ThP18, 253
- Oh, S.: EM-ThP17, **243**
- Oh, Y.: NS+AS-TuA1, 97; NS+EM-MoM5, 18
- Ohashi, Y.: AS-TuM11, 57
- Ohlhausen, J.: AS-MoA8, **29**
- Ohno, K.: GR-TuP3, **115**
- Ohno, Y.: EN+EM+NS-MoA1, 35; GR+MS+EM-FrM8, 262; GR+MS+EM-FrM9, 263; GR+NS+PS+SS-ThM9, 195; NS-WeM10, 146
- Ohresser, P.: MI-WeM6, 143
- Ohta, T.: GR+MN-WeM10, 141
- Ohtake, H.: PS-ThM6, 202
- Ohtsuka, S.: PS-ThM4, 201; PS-ThM5, **202**; PS-ThM6, 202
- Oka, H.: PS+SS-ThA8, 226
- Oka, M.: PS+TF-ThM1, 199
- Okada, S.: GR+MI-TuA4, 91
- Okamoto, S.: PS+SS-ThA8, **226**
- Oksuz, L.: PS-WeA12, 176
- Okuda, S.: NS-WeM10, **146**
- Olalde-Velasco, P.: EN+AC-FrM4, 261
- Oldham, C.J.: EM1-MoA9, 33; TF-TuA9, 107
- Oleynik, I.I.: GR+MI-TuA9, **92**; GR+MN-WeM3, 140; GR+MN-WeM9, 141; GR+TF+ET-MoA4, 37; GR-MoM3, 10; SS-FrM10, 270
- Oliva, A.I.: TF1-ThM1, 208
- Olson, D.A.: VT-MoM1, 25
- Olsson, A.: IS+AS+SS-MoM9, 14
- Olynick, D.L.: NM+MN+MS+TF-TuM12, 68; PS+SE-MoA7, **47**
- Omarjee, V.: PS1-TuA10, **100**
- Onaka, K.: BN-TuP1, 115
- Onishi, K.: HI+AS+BI+NS-WeM12, 142
- Ono, K.: PS2-TuA1, 101; PS-FrM9, 266; PS-ThM12, 203; PS-ThM4, 201; PS-ThM5, 202; PS-ThM6, 202; PS-ThM9, 202
- Ono, L.K.: PS-TuA10, **106**
- Oppeneer, P.M.: AC+MI-WeA1, **159**; AC+MI-WeA3, 159
- Orihuela, B.: MB-MoM8, 15
- Orr, G.: HI+AS+BI+NS-WeM11, 142
- Ortiz, C.: EN2+TF-WeA12, 168
- Orzelli, A.: SS-ThM5, 205
- Osborn, K.D.: TF-MoA3, 51
- Osgood, R.M.: SS2-MoM1, 22
- Oshima, A.: TF1+EM-WeM6, 156
- Oshiyama, A.: EM-ThP9, 241
- Osipov, A.V.: MI-ThP2, 248
- Ostrom, H.: SS2-MoM2, 22
- Otaño, W.: EN2+TF-WeA12, **168**
- Ouyang, Z.: PS+SE-WeM11, **149**; SE+PS-WeA11, 177
- Overbury, S.H.: SS1-TuM12, 75; SS2-WeM9, **155**; SS-WeA8, 178
- Overzet, L.J.: NS-ThM12, 199; PS+BI-MoA6, 44; PS-ThP20, 253
- Owen, J.H.G.: IS+AS+SS-MoM10, 14
- Oyler, N.A.: TF1-ThM10, 210
- Ozdemir, O.K.: SS2-FrM7, 268
- Ozimek, P.: EN-ThP12, 247
- Ozkaya, B.: SS-TuP10, **124**
- Ozturk, O.: SS2-FrM7, 268
- P —
- P. Ryan Fitzpatrick, P.R.: NM+MS+NS+TF-MoM8, 17
- Pachauri, N.: NT-TuP2, 121
- Pachuta, S.J.: AS-MoA7, **28**
- Padmaperuma, A.B.: AS-ThM11, 188
- Padron-Wells, G.: PS+BI-MoA6, 44; PS-ThA6, 227; PS-ThP20, **253**; PS-ThP21, 253
- Page, S.: EW-TuL4, 82
- Page, S.C.: BI-ThM4, 188
- Paiella, R.: NS-MoA11, 43
- Paisley, E.A.: TF2-ThM11, 212; TF-MoM2, 23
- Palma, M.: BN-TuA3, 86
- Palmans, J.: TF-MoM4, 24
- Palmer, M.A.: VT+MN+NS+SS+AS-TuA11, 109
- Palmer, S.: EW-WeL4, **158**
- Palmström, C.J.: EM+SS-FrM2, 259
- Palomaki, P.K.B.: EN-ThP8, **246**
- Pan, M.H.: ET+EM+NS+GR-TuM2, **62**; NS+AS-TuA7, 98
- Pan, X.: AS-TuP15, 113; EN+EM+NS-MoA9, 36
- Pan, Z.: NS-TuP8, 120
- Panaccione, G.: AC+MI-WeA8, 159
- Pandey, R.R.: BI-MoA9, **31**; PS+BI-MoA8, 45
- Pangan-Okimoto, K.: EM-WeA7, **164**; SS-ThA8, 231
- Pannier, A.K.: EL+AS+EM+MS+PS+TF-ThM5, 190
- Pantelides, S.T.: EM-WeA10, 164; EM-WeA11, 165; EM-WeA8, 164; EM-WeA9, 164; GR+NS+PS+SS-ThM6, 195
- Pantojas, V.: EN2+TF-WeA12, 168
- Papaconstantopoulos, D.A.: GR+EM-TuM4, **64**
- Papasoulitiotis, G.: PS-ThP27, **254**
- Paquette, M.M.: EM-WeM6, 135; TF1-ThM10, **210**
- Pargon, E.: PS+SE-MoA3, **46**; PS-MoM3, 19; PS-MoM5, 19
- Park, C.H.: GR-WeA12, 170; SS-TuP2, 123
- Park, D.-G.: BI-MoA8, 31
- Park, E.H.: IS+AS+SS-TuM10, 66
- Park, H.: EN+NS-ThA10, 220
- Park, J.: AS-TuP23, 114; MN-ThA4, 222
- Park, J.B.: SE+PS-WeA3, **176**
- Park, J.G.: TF-MoA6, 52
- Park, J.H.: GR+MS+EM-FrM7, 262; SS+EM-TuA9, **104**
- Park, J.Y.: PS-ThP14, 252; PS-ThP29, 255
- Park, P.S.: NS+EM-MoM6, 18
- Park, S.: PS-ThP25, 254

- Park, S.W.: PS+SE-MoA1, **46**
 Park, T.: NS-MoA10, **43**
 Park, T.Y.: TF-MoA6, **52**
 Park, Y.J.: PS-TuM5, **72**
 Parks, C.: EM-WeM9, **136**
 Parpia, J.M.: MN-ThA4, **222**; MN-ThA6, **223**; MN-ThA7, **223**
 Parsons, G.N.: EM1-MoA9, **33**; NS-TuP4, **120**; TF+EN-TuM9, **78**; TF1+EM-WeM4, **156**; TF-MoA9, **53**; TF-TuA9, **107**
 Pascual Garcia, C.: NS-ThM2, **198**
 Paskiewicz, D.M.: NS-MoA11, **43**; TF2+EM-WeA11, **182**
 Paskova, T.: EM1-MoA2, **32**
 Pasquale, F.: EM1-MoA8, **33**; GR-TuP7, **116**
 Patel, R.: TF-MoM11, **25**
 Patriarche, G.: PS+SS-WeM1, **149**
 Patrinos, A.A.N.: EN-MoM8, **9**
 Patscheider, J.: SE-ThM11, **205**
 Paul, D.F.: AS-TuP19, **113**; NS-TuM10, **70**; TR-WeA12, **184**
 Paulin-Filho, P.I.: TF-MoM10, **25**
 Paulitsch, J.: SE-ThM6, **204**; TR-ThA2, **235**
 Pauric, A.D.: SS-TuP6, **123**
 Paxton, W.F.: EN+NS-TuA12, **89**
 Payne, G.F.: BN+NM-TuM11, **59**; BN+NM-TuM2, **57**
 Pearce, R.C.: TF2+EM-WeA9, **182**
 Pearce, R.J.H.: VT-TuP7, **130**
 Pecht, I.: BI-MoM11, **5**
 Peckys, D.B.: IS+AS+SS-TuM3, **65**; IS+AS+SS-TuM5, **66**
 Pederson, M.R.: GR+EM-TuM4, **64**
 Pehrsson, P.E.: BI-WeM1, **133**
 Peixoto, T.: EM+TF-ThM3, **191**
 Pellegrini, K.L.: AC+TF-ThA10, **216**
 Pellin, M.J.: NS-WeM3, **145**
 Pelucchi, E.: EM+TF-TuM4, **59**
 Peña Martin, P.: EN1+TF-WeA10, **166**
 Pender, J.: EM-MoM3, **6**
 Peng, W.N.: ET+EM+NS+GR-TuM5, **63**
 Penkala, R.: BI-MoM6, **4**
 Penner, R.: NS-TuP1, **119**
 Penzak, J.S.: AS-MoA4, **28**
 Peppernick, S.: NS-MoA8, **43**
 Pereira, N.: EN+NS-ThM2, **193**
 Perera, A.G.U.: EM1-MoA4, **32**; EM-ThP10, **242**; EM-ThP11, **242**
 Perera, P.: NM+MN+MS+TF-TuM12, **68**
 Perera, U.G.E.: EN+NS-TuM9, **61**; MI-WeA3, **170**; NS-ThM6, **198**
 Perez Roldan, M.J.: NS-ThM2, **198**
 Perez, R.: NS+AS-TuA4, **97**
 Perng, Y.-C.: TF+EN-TuM4, **78**; TF-TuA2, **107**
 Perriot, R.: GR+MN-WeM3, **140**; GR+MN-WeM9, **141**
 Perry, S.: TR-WeA2, **183**
 Persing, H.: PS-ThP27, **254**
 Persson, O.: NS-TuM3, **69**
 Petersen, E.R.: BI-WeM1, **133**
 Peterson, E.: SS2-MoM10, **23**
 Peterson, K.: PS-WeA2, **174**
 Petit, L.: AC+MI-WeA9, **159**
 Petit-Etienne, C.: PS-MoM1, **19**; PS-MoM3, **19**; PS-MoM5, **19**
 Petkovich, N.: EN+NS-ThM5, **193**
 Petrik, N.G.: SS1-MoM6, **21**; SS-WeA9, **179**
 Petrosky, J.: SS-ThA10, **231**
 Petrov, I.: SE+PS-ThA6, **229**; TF2-ThM5, **211**
 Petrova, G.P.: IS+AS+SS-MoM3, **13**
 Petrovykh, D.Y.: BI-ThP7, **238**
 Pettersson, L.G.M.: SS2-MoM2, **22**
 Pettitt, M.E.: MB-MoM3, **15**
 Petz, C.: TF2+EM-WeA7, **181**
 Pflieger, W.: TF-TuP4, **128**
 Pham, C.D.: PS+SS-WeM2, **149**; TF1+EM-WeA7, **180**
 Phaneuf, R.J.: PS+SS-ThA7, **226**
 Phillips, J.: EN+EM+NS-MoA9, **36**
 Phillips, M.C.: AS-TuA1, **83**
 Phillips, P.J.: NS+EM-MoM2, **17**
 Phillipot, S.R.: GR+NS+PS+SS-ThM10, **195**
 Phillipot, S.R.: EN+NS-WeM10, **139**; SS1-MoA6, **48**; TR+AS+SS-ThM3, **213**
 Pi, T.W.: EM+TF-TuM9, **60**
 Piao, H.: AS-WeA9, **161**; EN-ThP19, **248**
 Piasecki, J.D.: AS-TuP13, **112**; AS-TuP8, **112**
 Pickard, D.S.: HI+AS+BI+NS-WeM9, **142**
 Piel, J.P.: EL+AS+EM+MS+PS+TF-FrM7, **259**; EL+AS+EM+MS+PS+TF-ThM10, **190**
 Pietrogrande, G.M.: PS-ThP2, **250**
 Pietzsch, A.: IS+AS+SS-MoM9, **14**
 Pilvi, T.: NM+MS+NS+TF-MoM6, **16**
 Piqueras Jover, R.: BN-TuA3, **86**
 Pireaux, J.-J.: PS+TF-ThM12, **201**
 Pirkle, A.: GR-TuA9, **93**
 Plaisant, M.: EN+EM+NS-MoA8, **35**
 Plasencia, A.: AS-TuP8, **112**
 Pleticha, F.D.: EN+NS-WeM10, **139**
 Poda, A.: TR-ThA9, **235**; TR-ThP4, **256**
 Podraza, N.J.: EL+AS+EM+MS+PS+TF-ThA10, **217**; EL+AS+EM+MS+PS+TF-ThA3, **216**
 Poelsem, B.: HI+AS+BI+NS-WeM5, **141**; HI+AS-TuA3, **94**; HI-TuP3, **116**; IS+AS+SS-MoA7, **38**
 Pogliano, K.: BI-WeM4, **134**
 Pohl, K.: SS-FrM9, **269**
 Pokhodnya, K.I.: MI-WeA4, **170**
 Pokrovsky, L.D.: EL-ThP1, **239**
 Polikarpov, E.: AS-ThM11, **188**
 Polop, C.: TF1-ThM1, **208**
 Pomorski, T.A.: PS+EM-WeA3, **172**
 Ponduri, S.: EN+PS-MoM3, **7**
 Ponnusamy, N.: AS-WeA7, **161**
 Poodt, P.: TF-MoA7, **52**
 Pookpanratana, S.: SE-ThM1, **203**; TF+EM+SS-ThA9, **234**
 Pop, E.: GR-TuA12, **94**
 Porsgaard, S.: SS2-WeM2, **154**
 Porter, L.: AS-WeA7, **161**; EM1-MoA2, **32**; TC+AS+EM-ThM9, **207**; TC+EM+NS-ThA4, **232**
 Potapenko, D.V.: SS2-MoM1, **22**
 Potash, R.A.: TC+EM+NS-ThA4, **232**
 Poudineh, M.: MN-FrM10, **264**
 Pouliquen, S.: EN+PS-MoM5, **8**; EN+TF-TuA4, **90**
 Pourtois, G.: EM-TuA4, **87**
 Powell, C.J.: AS-MoM4, **2**
 Powers, K.W.: NM+AS+MS-WeM4, **144**
 Pozuelo, M.: NS-TuM6, **69**
 Preble, E.A.: EM1-MoA2, **32**
 Predith, A.: EN-ThP14, **247**
 Premkubar, A.: PS+SE-WeM12, **149**
 Pret Vaglio, A.: PS+SE-MoA4, **46**
 Prince, K.C.: IS+AS+SS-MoM3, **13**
 Prinz, F.: EN+NS-ThA6, **219**
 Priyadarshini, D.: SS-TuA11, **106**
 Proell, J.: TF-TuP4, **128**
 Profijt, H.B.: PS+TF-ThM9, **200**
 Prosa, T.: AS-WeA7, **161**
 Pruemper, G.: AS-MoM11, **3**
 Pu, J.: EL-ThP4, **240**
 Pugmire, D.L.: AC+SS-ThM3, **185**
 Pujari, S.P.: TR-WeA1, **183**
 Pulsifer, D.P.: TF+SE-TuM11, **80**
 Pushkarev, V.: SS1-MoA3, **48**
 Putkonen, M.: TF-MoA8, **52**
 Puzryev, Y.S.: EM-WeA10, **164**; EM-WeA9, **164**
- **Q** —
 Qi, Y.: GR-WeA10, **169**
 Qian, Y.: EN+NS-ThM5, **193**
 Qin, S.: ET+EM+NS+GR-TuM1, **62**; ET+EM+NS+GR-TuM6, **63**
 Qin, X.: SS-TuP7, **124**
 Qiu, J.: AC+TF-ThA10, **216**
 Quang, N.T.: SS-TuP8, **124**
 Quaresima, C.: SS-FrM11, **270**
 Quevedo-Lopez, M.A.: EM-ThP3, **240**; EM-ThP4, **240**; TC+AS+EM-ThM11, **208**
 Quickel, T.E.: MI-ThM12, **197**
 Quinlan, R.A.: EN+NS-ThA2, **219**
- **R** —
 Rabe, J.: GR-WeA1, **168**
 Rack, P.D.: EM-ThP19, **243**; HI+AS-TuA10, **95**; NM+NS+MS-TuA11, **97**; NS+EM-MoM10, **18**; TC+EM+NS-ThA6, **232**; TC-ThP1, **255**; TF2+EM-WeA4, **181**
 Racke, D.A.: SS+EM-TuA3, **103**
 Radindranath, V.: VT-TuM2, **80**
 Rading, D.: AS-TuM5, **56**; AS-TuM9, **57**
 Radtke, C.: EM-ThP5, **241**
 Raghunathan, S.: PS-MoM9, **20**
 Rahman, F.H.M.: HI-TuP1, **116**
 Rahman, M.: EN2+TF-WeA8, **167**
 Rahman, T.S.: NS-TuM12, **70**; SS1-TuM3, **74**; SS2-TuM6, **76**; SS-TuA9, **106**
 Raitses, Y.: PS2-TuA7, **102**
 Raja, L.: PS-ThP23, **254**
 Rajachidambaram, J.S.: TF1+EM-WeA1, **179**
 Rajan, S.: EM+SS-FrM7, **260**; EM+TF-TuM12, **60**; NS+EM-MoM6, **18**
 Rajasekaran, S.: GR+TF+ET-MoA3, **37**
 Ralph, D.C.: GR+EM-TuM9, **65**
 Raman, P.: PS+SE-WeM11, **149**
 Raman, S.N.: AS-ThM10, **188**; EW-TuL5, **82**
 Ramana, C.V.: EL-ThP1, **239**; TF-MoM1, **23**
 Ramanathan, S.: NM+NS+MS-TuA3, **96**
 Randall, J.N.: IS+AS+SS-MoM10, **14**
 Rangan, S.: EN+NS-ThM2, **193**; SS-WeA4, **178**
 Rangel-Chavez, L.G.: EN1+TF-WeA9, **166**
 Ranjan, A.: PS-TuM10, **73**; PS-TuM12, **73**
 Ranjan, V.: EL+AS+EM+MS+PS+TF-ThA4, **216**
 Ranson, P.: PS+MN+TF-TuM3, **71**
 Rao, M.R.: MN-ThA3, **222**
 Raoux, S.: TF1+EM-WeA9, **181**
 Rapenne, G.: MI-WeA3, **170**; NS-ThM6, **198**
 Ravavikar, N.: SE+SS-WeM11, **152**
 Raschke, M.: AS-TuA1, **83**
 Rasmussen, D.A.: PS-WeA3, **174**; VT-TuP7, **130**
 Rasmussen, M.K.: SS-ThM10, **206**
 Rathbone, J.: VT-MoA6, **54**; VT-TuP5, **130**
 Ratner, B.D.: BP-SuA7, **1**
 Rauch, S.: EL+AS+EM+MS+PS+TF-ThM3, **189**
 Rauf, S.: PS1-TuA4, **99**; PS1-TuA9, **100**; PS-FrM6, **265**; PS-WeA8, **175**; PS-WeA9, **175**
 Rauh, E.: BI-MoM9, **5**
 Rayner, G.B.: TC+AS+EM-ThM6, **207**
 Raynor, M.W.: VT-MoA3, **53**
 Reece, C.: VT+MN+NS+SS+AS-TuA9, **109**
 Reed, A.: PS+TF-ThM2, **199**; SE+SS-WeM9, **152**; SE-TuP4, **122**; TF-FrM10, **272**
 Reed, R.A.: EM-WeA11, **165**; EM-WeA8, **164**; TF1-ThM9, **209**
 Reed, S.M.: BI-TuA11, **85**
 Reeder, L.J.: SS2-MoA8, **50**
 Rees, A.J.: PS-ThP11, **251**
 Regan, B.C.: NS-TuM6, **69**
 Reimhult, E.: NS-ThA4, **224**
 Reinecke, T.L.: GR+NS+PS+SS-ThM12, **195**
 Reinhardt, M.: NT+AS-WeA10, **172**
 Reinicker, A.: SS1-MoA3, **48**
 Reinke, P.: MI-ThM9, **196**; MI-WeA11, **171**
 Reiss, G.: HI-TuP6, **117**
 Reiter, A.: SE-ThM11, **205**
 Remmert, J.L.: AS+BI+NS-WeM6, **132**
 Ren, H.: PS+EM-WeA7, **173**
 Ren, J.: TF-TuP11, **129**
 Ren, M.: SS-WeA11, **179**
 Renaux, F.: SE+PS-ThA1, **228**
 Reniers, F.: PS+SE-WeM3, **148**; PS+TF-ThM12, **201**
 Rentsch, J.: EN+PS-MoM4, **7**
 Repain, V.: MI-WeM6, **143**
 Reshchikov, M.A.: EM1-MoA3, **32**; SS-ThA9, **231**
 Resta, A.: IS+AS+SS-MoM6, **14**
 Restaino, D.: EM-WeM9, **136**

- Rettenmayr, M.: BI-WeM2, 133
 Reuter, R.: PS+SE-WeM5, 148
 Reutti-Robey, J.E.: EN+NS-ThA1, 218; SS+EM-TuA7, **104**; SS+EM-TuA8, 104
 Rezek, J.: SE+PS-ThA3, 229
 Rhallabi, A.: PS-FrM8, **266**
 Rhim, S.H.: GR-WeA10, **169**
 Rhoades, R.L.: SS1-MoA11, 49
 Rice, A.R.: TF-MoM2, 23
 Richmonds, C.: PS+BI-MoA11, 45
 Richter, C.A.: SE-ThM1, 203; TF+EM+SS-ThA9, 234
 Richter, L.J.: EL+AS+EM+MS+PS+TF-ThM9, **190**
 Richter, M.L.: BN-TuP3, 115
 Richter, R.P.: AS-MoA1, **28**
 Ricker, J.E.: VT-MoM1, 25
 Rider, D.A.: TF+SE-TuM4, 79
 Rieth, L.W.: BI-ThP6, 238
 Rignall, M.: AS-TuP2, 111
 Rijnders, G.: IS+AS+SS-MoA3, **38**
 Ringel, S.A.: EM-WeA3, 163
 Riseborough, P.S.: AC+MI-WeA3, 159
 Rittschof, D.: MB-MoM8, 15
 Ritz, E.: TC+AS+EM-ThM6, **207**
 Rivenet, M.: EN+AC-FrM7, 261
 Rivera, F.: TF-FrM11, **272**
 Ro, H.W.: EM-MoM5, 6
 Roach, W.M.: VT+MN+NS+SS+AS-TuA9, **109**
 Roberts, A.: EW-TuL4, 82
 Roberts, A.J.: AS-MoM10, 3; AS-TuA7, 83; BI-ThM4, 188
 Roberts, C.J.: AS+BI+NS-WeM12, 133; SS2-TuM5, 76
 Roberts, N.A.: NM+NS+MS-TuA11, **97**; TF2+EM-WeA4, 181
 Robertson, I.M.: IS+AS+SS-MoA1, **38**
 Robey, S.W.: EN+NS-WeM9, **139**
 Robinson, J.T.: GR+MS+EM-FrM10, 263; GR+MS+EM-FrM3, 262; GR+NS+PS+SS-ThM1, **194**; GR+NS+PS+SS-ThM2, 195; GR+NS+PS+SS-ThM5, 195; GR+TF+NS-ThA9, 221; GR-TuA4, 92; NS-WeM6, 145
 Robinson, M.: AS-TuM6, 56; BI-WeM6, **134**
 Robinson, Z.R.: GR-MoM9, **12**; NS-WeM1, 144
 Roca i Cabarrocas, P.: EN+PS-MoM8, 8
 Rocca, M.: SS-ThM5, 205
 Rochford, J.: SS-WeA4, 178
 Rockett, A.: EN1+TF-WeA10, 166
 Roco, M.: NM+MS-MoA2, **41**
 Rodenhansen, K.B.: EL+AS+EM+MS+PS+TF-ThM5, **190**; EL+AS+EM+MS+PS+TF-ThM6, 190
 Rodil, S.E.: EN+NS-ThA9, **220**
 Rodriguez Cañas, E.: SS-TuP29, 127; TF1-ThM1, 208
 Rodriguez, E.: TR-ThP6, 257
 Rodriguez, E.F.: PS+SE-WeM10, 149
 Rodriguez, G.: AC+MI-WeA3, 159
 Rodriguez-Reyes, J.C.: SS2-MoM3, **22**
 Rodriguez-Vindas, D.: EN2+TF-WeA12, 168
 Rodwell, M.J.W.: EM-MoM2, 6
 Rogers, B.R.: AS-ThM3, 187; AS-WeA10, **161**; BI+AS+NS+SS-WeA10, 163; TF1-ThM9, 209
 Röhrig, M.: MB-MoM10, 15
 Roldan Cuenya, B.: SS-TuA10, 106; SS-TuP28, 127
 Roldán Cuenya, B.: SS-TuA7, **105**
 Roozeboom, F.: IS+AS+SS-MoA9, 39; TF-MoA7, 52
 Rosa, L.G.: SS+EM-TuA4, 103
 Rosei, F.: TF+EM+SS-ThA3, 233
 Rosenberg, R.A.: EM+SS-FrM11, 260; EM-WeA4, **164**
 Rosenberg, S.: SS1-MoA7, 48
 Rosenhahn, A.: BI-ThP11, 239; BI-WeM11, **135**; IS+AS+SS-TuM6, 66; MB-MoM10, 15; MB-MoM3, 15
 Ross, A.: GR+MI-TuA9, 92
 Ross, A.H.: BI-ThP9, 238
 Rossi, F.J.: BI-ThM6, **188**; BN-TuA4, 86; NS-ThM2, 198
 Rossouw, D.: NS-WeM12, 146
 Rothwell, S.: GR-TuA11, **94**
 Rott, K.: HI-TuP6, 117
 Rousseau, R.J.: SS1-MoA4, 48; SS1-MoM6, 21
 Roussel, P.: AC+SS-ThM3, 185
 Rousset, S.: MI-WeM6, 143
 Routaboul, L.: SS+EM-TuA4, **103**
 Rowe, J.E.: EM+SS-FrM9, **260**; GR+MI-TuA7, 91
 Roy, A.: SE+SS-WeM4, 151
 Roy, K.: VT-TuM2, 80
 Roy, L.: AC+MI-WeA10, 159
 Roy, S.: BI-MoM1, 3; SE+SS-WeM5, 152
 Roy, T.: EM-WeA9, 164
 Royer, J.: EM+TF-ThM6, **192**; SS+EM-TuA9, 104
 Rozanov, K.N.: MI-ThP2, 248
 Rozanski, P.: EN-ThP12, 247
 Rubloff, G.W.: BN+NM-TuM11, 59; BN+NM-TuM2, 57; BN+NM-TuM6, 58; EN+NS-ThA11, 220; EN+NS-ThA4, 219; TF+EN-TuM5, **78**; TF-MoA3, 51
 Rudisill, S.: EN+NS-ThM5, 193
 Rudy, A.: TR-WeA2, 183
 Ruegner, K.: PS+SE-WeM5, 148
 Ruggieri, F.: EN2+TF-WeA11, 168
 Ruidiaz, M.E.: BI-ThM11, 189
 Ruiz-Vargas, C.S.: MN-ThA4, 222
 Ruoff, R.S.: GR-MoM1, 10; GR-TuA9, 93; NM+NS+MS-TuA9, **96**; NS-WeM1, 144
 Rusli, F.: EN+NS-ThM10, **193**
 Russell, J.N.: BI-WeM1, 133
 Russell, K.J.: NS-MoA6, **42**
 Russell, S.M.: SS1-WeM3, **153**
 Ruzic, D.N.: PS+SE-WeM11, 149; PS-ThP4, 250; PS-ThP7, 251; SE+PS-ThA7, 229; SE+PS-WeA11, 177; TC+AS+EM-ThM6, 207
 Ryan, E.T.: EM-WeM3, 135; EM-WeM9, 136
 Ryan, K.E.: TR+AS+SS-ThM6, 213
 Ryu, J.H.: TF-MoA6, 52
 Ryyänen, T.: TF-MoA10, **53**
 Ryzhikov, I.A.: MI-ThP2, 248
 — S —
 Saaem, I.: BI-MoM10, 5
 Sa'ar, A.: EN+EM+NS-WeM6, 137
 Sacedón, J.L.: SS-TuP29, **127**; TF1-ThM1, 208
 Sachan, R.: EM-ThP19, 243
 Sadasue, K.: GR-TuP2, **115**
 Safron, N.: GR+TF+NS-ThA1, 220
 Saini, K.K.: BI-MoA9, 31; PS+BI-MoA8, **45**
 Saito, N.: EM-ThP20, 243; GR-TuP2, 115; GR-TuP3, 115; NS-WeM9, 145; PS+BI-MoA4, 44
 Saito, Y.: SS-FrM2, 268
 Sakai, M.: EN-ThP1, 245; EN-ThP7, **246**
 Sakuishi, T.: PS+MN+TF-TuM1, 70
 Sakuma, S.: PS+SE-MoA2, 46
 Sakurai, M.: SS2-MoM11, **23**
 Sakurai, S.: BI-ThP1, **237**
 Salas-Villasenor, A.: EM-ThP3, 240; TC+AS+EM-ThM11, 208
 Salditt, T.: IS+AS+SS-TuM6, 66
 Salmeron, M.: GR+NS+PS+SS-ThM3, 194; IS+AS+SS-TuM1, 65
 Salvati, L.: BI-ThM2, **188**
 Samatova, N.: NS+EM-MoM10, 18
 Sambegoro, P.: SE+SS-WeM2, 151
 Samuelson, L.: NS-TuM3, 69; NS-TuM4, **69**
 Samukawa, S.: EN+EM+NS-MoA1, 35; PS+SE-MoA2, 46; PS2-TuA1, 101; PS-ThM1, **201**; PS-ThM10, 202; PS-ThM4, 201; PS-ThM5, 202; PS-ThM6, 202
 Sanada, N.: AS-TuM1, 56
 Sanaee, Z.: MN-FrM10, 264
 Sanchez, A.B.: BI-ThM11, 189
 Sanchez-Martinez, A.: AS-TuP20, 114; EM-TuA12, **88**
 Sanchez-Perez, J.R.: NS-MoA11, **43**
 Sanderson, R.: AS-MoM3, 2
 Sandin, A.A.: GR+MI-TuA7, **91**
 Sandler, N.: GR+TF+NS-ThA3, 221
 Sandoughsaz, A.: MN-FrM10, 264
 Sandström, P.: EL-ThP3, 239
 Sanghavi, S.P.: AC+SS-ThM11, 186; NS-TuP7, 120; SS-WeA7, **178**; TF1+EM-WeA1, 179
 Sangiovanni, D.G.: TF2-ThM5, 211; TF2-ThM6, **211**
 Sankaran, M.: PS+SE-WeM1, **148**
 Sankaran, R.M.: NS-TuM2, 69; NS-WeM11, 146; PS+BI-MoA1, 43; PS+BI-MoA11, 45
 Santella, G.: VT-TuM6, 81
 Santis, S.De.: VT+MN+NS+SS+AS-TuA11, 109
 Santucci, S.: EN2+TF-WeA11, 168
 Sarabi, B.: TF-MoA3, 51
 Sarakinos, K.: TF-FrM9, 271
 Sarangan, A.: SE+TF-TuA4, 103
 Sarrao, J.L.: AC+MI-WeA3, 159; AC+MI-WeA8, 159
 Sasaki, T.: TC+AS+EM-ThM2, 207
 Satake, M.: NM+MN+MS+TF-TuM4, 67
 Sato, M.: PS+TF-ThM5, 200; SS-TuP24, 126; SS-TuP27, 126; TF-TuP9, 129
 Sauer, M.: GR+NS+PS+SS-ThM4, 194
 Sauer, V.T.K.: MN-ThA10, 223
 Savage, D.E.: ET+EM+NS+GR-TuM5, 63; TF2+EM-WeA11, 182
 Savio, L.: SS-ThM5, 205
 Sawant, R.: TF1+EM-WeA9, 181
 Sawyer, W.G.: TR-WeA7, **183**
 Sazegar, M.: TF-MoM5, 24
 Scannapiego, M.: VT-TuM4, 80
 Scarel, G.: TF+EN-TuM10, **78**
 Schaff, W.J.: EL+AS+EM+MS+PS+TF-FrM3, 258
 Schall, J.D.: MN-FrM7, **264**
 Schamberger, F.: TF2-ThM12, **212**
 Scharf, T.: TR-ThA6, **235**
 Schetz, J.A.: MB+BI+PS-MoA1, **39**
 Scheurer, F.: MI-WeM6, 143
 Schilbach, M.A.: AC+SS-ThM6, 185
 Schirmeisen, A.: TR-WeA11, 184
 Schlaf, R.: BI-MoA10, 31; SS2-TuM11, 76
 Schlotter, W.F.: SS2-MoM2, 22
 Schmalzl, K.: NT+AS+MI-WeM3, 147
 Schmidt, A.B.: MI-WeM11, 143; NS+AS-TuA12, 99
 Schmidt, D.: EL+AS+EM+MS+PS+TF-FrM4, **258**; EL+AS+EM+MS+PS+TF-FrM5, 258; EL+AS+EM+MS+PS+TF-ThA8, 217; EL+AS+EM+MS+PS+TF-ThM5, 190
 Schmidt, D.A.: GR+MN-WeM10, **141**
 Schmidt, M.: AC+TF-ThA1, **215**; NM+MN+MS+TF-TuM12, 68
 Schmidt, W.: NT+AS+MI-WeM3, 147
 Schmidt-Stein, F.: AS-TuP19, 113
 Schmitt, J.: NT+AS+MI-WeM5, 147
 Schmitz, S.: PS-MoM9, 20
 Schmuki, P.: AS-TuP19, 113
 Schmutz, P.: SS1-WeM12, 153
 Schnadt, J.: IS+AS+SS-MoM9, **14**
 Schneider, C.M.: NS+AS-TuA11, 98
 Schneller, E.: EN1+TF-WeA1, 165
 Schnietz, M.: GR+NS+PS+SS-ThM4, 194
 Schoche, S.: GR+EM-TuM6, 64
 Schöche, S.: EL+AS+EM+MS+PS+TF-FrM3, **258**
 Schoenfeld, W.V.: TF-FrM5, 271
 Schönherr, H.: BI+AS+NS+SS-WeA7, **162**
 Schreiber, D.: MN-ThA9, **223**
 Schreiber, D.K.: EM1-MoA2, 32
 Schreiner, P.R.: NS-ThM11, 198
 Schreyer, A.: NT+AS+MI-WeM3, 147
 Schrimpf, R.D.: EM-WeA11, 165; EM-WeA8, 164; EM-WeA9, 164
 Schroder, H.: AS-MoA3, 28
 Schroeter, A.: BI-WeM2, 133
 Schubert, E.: EL+AS+EM+MS+PS+TF-FrM4, 258; EL+AS+EM+MS+PS+TF-FrM5, 258; EL+AS+EM+MS+PS+TF-ThA8, 217; EL-ThP5, 240

- Schubert, M.: EL+AS+EM+MS+PS+TF-FrM3, 258; EL+AS+EM+MS+PS+TF-FrM4, 258; EL+AS+EM+MS+PS+TF-FrM5, 258; EL+AS+EM+MS+PS+TF-ThA8, **217**; EL+AS+EM+MS+PS+TF-ThM5, 190; EL+AS+EM+MS+PS+TF-ThM6, 190; EL-ThP5, 240; GR+EM-TuM6, 64; GR-TuP7, 116
- Schuck, P.J.: NM+MN+MS+TF-TuM12, 68
- Schuette, M.: EM1-MoA1, 32
- Schulte, K.: NS-WeM2, 145
- Schultz, B.D.: EM+SS-FrM2, **259**; SE+PS-WeA10, 177
- Schüpbach, B.: EN+NS-TuM2, 61
- Schuster, S.: BI-WeM2, 133
- Schvartzman, M.: BN-TuA3, 86
- Schwartzberg, A.: NM+MN+MS+TF-TuM12, 68
- Schwarz, T.: MB-MoM3, 15
- Schwarz, U.D.: NS+AS-TuA4, 97; TR-WeA11, **184**
- Schweikert, E.A.: BI+AS+NS+SS-WeA1, **161**
- Schwendemann, T.C.: NS+AS-TuA4, 97
- Schwoeble, A.J.: AS-TuP13, 112
- Scipioni, L.: HI+AS-TuA1, 94; HI+AS-TuA3, 94; HI-TuP4, 117
- Scott, B.L.: AC+TF-ThA4, 215
- Scott, S.: ET+EM+NS+GR-TuM5, 63
- Scott, S.L.: SS-ThM3, **205**
- Scullin, P.: PS-ThP22, 253
- Scuseria, G.E.: AC+MI-WeA10, 159
- Seabaugh, A.: EM-MoM8, **6**
- Seah, M.P.: AS-MoA9, 29
- Seal, S.: TF-TuP2, 128
- Seebauer, E.G.: EM-WeA7, 164; SS-ThA8, 231
- Segalman, R.A.: EN+NS-TuA9, **88**
- Seitz, O.: EN+NS-TuM1, **60**
- Seki, T.: AS-TuM10, 57
- Sekine, M.: PS+SS-ThA4, 225; PS1-TuA11, **101**; PS-ThM11, 203; SE+PS-WeA9, 177
- Sell, C.H.: BI-ThM12, 189
- Sell, D.A.: BI-ThM12, 189; SS1-MoA11, 49
- Sellberg, J.A.: SS2-MoM2, 22
- Semidey-Flecha, L.: SS2-WeM5, 154
- Senevirathna, I.: EM1-MoA4, 32
- Senevirathna, M.K.L.: EM-ThP10, 242; EM-ThP11, **242**; EM-ThP13, 242
- Senkbeil, T.: IS+AS+SS-TuM6, 66
- Seo, E.K.: GR-WeA7, 169
- Seo, S.: PS-MoM9, 20
- Seo, S.H.: PS-ThP12, 252; PS-ThP15, 252
- Seog, J.: PS+BI-MoA10, 45; PS+BI-MoA7, 44
- Sepunaru, L.: BI-MoM11, 5
- Serrano, A.: MB+BI+PS-MoA4, **40**
- Sershen, M.: NM+MS+NS+TF-MoM3, 16
- Settle, J.K.: BN-TuP3, **115**
- Severin, N.: GR-WeA1, 168
- Seymour, D.: PS-ThP11, 251
- Sezen, H.: AS-MoM6, **2**
- Sgammato, W.: AS-TuP13, 112
- Sha, X.W.: GR+EM-TuM4, 64
- Shacham-Diamand, Y.: MN-ThA9, 223
- Shachar, S.: PS-TuM6, 73
- Shafai, G.: NS-TuM12, **70**
- Shah, P.: SE+TF-TuA4, **103**
- Shaikh, M.: EW-WeL6, **158**
- Shaler, R.C.: TF+SE-TuM11, 80
- Shan, T.-R.: TR+AS+SS-ThM3, **213**
- Shannon, S.C.: PS-WeA3, 174; PS-WeA7, 175
- Shao, Q.: SS+EM-TuA8, 104
- Shao-Horn, Y.: EN+NS-ThA2, 219
- Shard, A.G.: BP-SuA3, **1**
- Sharma, K.: EN+TF-TuA3, 89
- Sharma, M.: NT+AS+MI-WeM5, 147
- Sharma, S.: EN+AC-FrM4, 261; VT-TuM2, 80
- Sharp, J.C.: SS-ThM6, **206**
- Shavorskiy, A.: IS+AS+SS-TuM9, **66**
- Shaw, T.M.: PS+EM-WeA1, 172
- Shearer, J.C.: TF2+EM-WeA8, **182**
- Sheehan, J.P.: PS2-TuA3, 101; PS2-TuA7, **102**; PS-WeA12, 176
- Sheehan, P.E.: GR+NS+PS+SS-ThM12, 195; GR+NS+PS+SS-ThM5, 195; GR+TF+NS-ThA9, 221; GR-TuA4, 92; NS-WeM6, 145
- Sheetz, M.: BN-TuA3, 86
- Shekhar, P.: BI-ThP10, **238**
- Shelby, R.M.: TF1+EM-WeA9, 181
- Shelton, W.A.: MI-ThP7, 249
- Shen, G.: AS-TuA9, 84; EN+EM+NS-WeM12, 138
- Shen, J.: AS-TuP17, 113; EM-MoM1, 5; MI-ThP6, 249; SS-ThA6, 231
- Shen, M.: SS1-WeM3, 153
- Shen, Q.: SS-TuA2, 105
- Shen, X.: EM-WeA8, **164**
- Shenogin, S.: SE+SS-WeM9, 152
- Shenoy, S.: BI-ThP9, **238**
- Sheth, P.: MB+BI+PS-MoA1, 39
- Sheves, M.: BI-MoM11, 5
- Shi, J.: EL+AS+EM+MS+PS+TF-FrM3, 258
- Shi, M.: MI-ThM10, 197
- Shi, S.-F.: GR+EM-TuM9, **65**
- Shi, Z.: EM+TF-ThM5, 191
- Shiao, M.H.: NM-TuP7, 118
- Shibata, K.: VT-TuM5, 80
- Shibata, T.: TC+AS+EM-ThM2, 207
- Shida, S.: TF-TuP1, 127
- Shigekawa, R.: PS-FrM11, **266**
- Shimada, K.: BN-TuP1, 115
- Shin, H.: PS+SS-WeM6, **150**; PS2-TuA9, 102
- Shin, J.H.: EM-ThP18, 243
- Shin, K.: AS-TuP11, 112
- Shin, K.S.: PS+SE-MoA1, 46
- Shin, N.: EN+EM+NS-WeM3, 136; NS-TuM9, **69**
- Shin, Y.G.: PS+SE-MoA1, 46
- Shinada, H.: AS-ThM9, 187
- Shindo, H.: PS2-TuA4, 101; PS-MoM11, **20**
- Shinjii, U.: PS-ThP6, 252
- Shinohara, M.: IS-TuP1, **117**; PS-ThP3, 250
- Shirai, M.: VT-TuM5, 80
- Shiratani, M.: PS+BI-MoA9, 45; PS+TF-ThM5, **200**
- Shklover, V.: SE-ThM11, 205
- Shoeb, J.: PS+EM-WeA11, **173**
- Shohet, J.L.: PS+EM-WeA7, 173; PS+EM-WeA8, 173
- Shrestha, P.R.: EM-TuA11, **87**
- Shukur, A.: SS-TuP24, **126**
- Shukur, H.: SS-TuP24, 126; SS-TuP25, 126; SS-TuP27, 126; TF-TuP9, **129**
- Shuler, M.L.: BN+NM-TuM9, **58**
- Shumaker-Perry, J.S.: BI-MoA1, **30**
- Shutthanadan, S.V.: TF-MoM1, 23
- Shutthanandan, V.: AC+SS-ThM11, 186; AS-WeA7, 161; HI+AS+BI+NS-WeM11, 142; HI-TuP7, **117**; MI-ThP7, 249; NS-TuP3, 120; NS-TuP7, 120; TF1+EM-WeA1, 179; TF-TuP2, 128
- Sibener, S.J.: SS1-MoM2, 21; SS2-MoM4, 22
- Siegbahn, H.: IS+AS+SS-MoM9, 14
- Siegel, D.A.: GR-WeA12, **170**; SS-TuP2, **123**
- Siegismund, D.: BI-WeM2, **133**
- Siekhaus, W.J.: AC+SS-ThM5, 185; AC+SS-ThM6, **185**; EN+AC-FrM4, 261
- Siew, Y.K.: TF1-ThM12, 210
- Siewert, J.M.: SE+TF-TuA7, **103**
- Sigmon, G.: EN+AC-FrM2, **261**
- Sikora, J.P.: VT+MN+NS+SS+AS-TuA11, 109
- Sikorski, E.M.: PS+MN+TF-TuM4, 71; PS+SE-MoA6, 47; PS-MoM10, 20; PS-TuM11, 73
- Silbaugh, T.L.: SS1-TuM2, **74**
- Silva, A.R.: EM-ThP5, 241; EM-ThP6, 241; EN-ThP5, 245
- Silva-Bermudez, P.: EN+NS-ThA9, 220
- Sim, J.H.: EM-MoM5, 6
- Simonson, R.J.: SS-WeA12, 179
- Simonsson, L.: BI-MoM3, **4**
- Simov, K.R.: MI-ThM9, 196
- Simpson, M.L.: TF2+EM-WeA9, 182
- Singh, J.P.: TC-ThP5, **256**
- Singh, K.A.: TC+EM+NS-ThA4, 232
- Sinha, H.: PS+EM-WeA8, 173
- Sinnott, S.B.: EN+NS-WeM10, 139; GR+NS+PS+SS-ThM10, 195; SS1-MoA6, **48**; TR+AS+SS-ThM10, 213; TR+AS+SS-ThM3, 213
- Sioncke, S.: EM-TuA4, 87
- Sirard, S.: PS1-TuA2, 99
- Sirse, N.: PS+SS-WeM9, 150
- Sitar, Z.: TF2-ThM11, 212; TF-MoM2, 23
- Sivaram, S.: EN+EM+NS-MoA7, **35**; EN+EM+NS-WeM3, 136
- Siviero, F.: EW-WeL3, 158; VT-TuM6, **81**
- Sivula, K.: EN2+TF-WeA9, **168**
- Skála, T.: IS+AS+SS-MoM3, 13
- Skomski, D.: SS2-MoA2, **50**
- Skomski, R.: EL+AS+EM+MS+PS+TF-FrM5, 258
- Smentkowski, V.S.: AS-TuP10, **112**; HI-TuP4, 117
- Smerieri, M.: SS-ThM5, 205
- Smets, M.: TF-MoA7, 52
- Smith, A.R.: MI-ThM10, 197; MI-ThM11, 197; MI-ThM6, 196
- Smith, D.A.: HI+AS-TuA10, **95**
- Smith, G.: NS-TuP6, **120**
- Smith, J.: NM-TuP11, 119
- Smith, N.J.: EN+EM+NS-WeM5, **137**
- Smith, R.S.: SS1-MoM10, 21
- Smith, T.: SE+SS-WeM9, 152; SE-TuP4, 122; TF-FrM10, 272
- Snijders, P.C.: MI-ThP6, 249
- Snyders, R.: SE+PS-ThA1, 228; TF1-ThM6, **209**
- Soda, E.: PS-TuM5, 72
- Soderholm, L.: AC+TF-ThA1, 215
- Sofue, Y.: GR+MS+EM-FrM8, **262**
- Sokolov, I.: MN-FrM3, 263
- Soles, C.L.: EM-MoM5, 6
- Soloway, P.D.: BI-MoA11, 31
- Solzbacher, F.: BI-ThP6, 238
- Song, J.J.: EM-WeA1, 163
- Song, S.-H.: PS1-TuA8, **100**; SS1-MoA9, **49**
- Song, W.: EN+NS-ThA1, 218
- Sonnemans, R.: PS-ThP1, 250
- Sonnet, A.M.: EM+TF-TuM4, 59
- Sopinsky, M.V.: EM-ThP25, 244
- Sorescu, D.: SS1-TuM10, 75
- Sorgenfrei, F.: SS2-MoM2, 22
- Sorini, A.: AC+MI-WeA7, 159
- Souren, F.M.M.: EN+PS-MoM4, 7
- Souriau, L.: PS1-TuA7, **100**
- Sowa, M.: NM+MS+NS+TF-MoM3, 16
- Sowa, M.J.: TF1+EM-WeM5, **156**
- Spada, F.E.: TR-WeA12, **184**
- Spencer, N.D.: MB+BI+PS-MoA4, 40; MB+BI+PS-MoA9, 40
- Spradlin, J.S.: VT-TuP9, **130**
- Sprunger, P.: SS-WeA11, 179
- Srikanti, K.: NT+AS+MI-WeM9, **147**
- Sriraman, S.: PS-MoM2, 19
- Srivastava, A.: PS+SS-WeM11, 151
- Srivastava, N.: GR-WeA8, **169**
- Srivastava, R.: PS-TuM5, 72
- Sroubek, Z.: SS2-FrM5, 268
- Stacchiola, D.: GR+TF+ET-MoA3, 37
- Stafford, N.: PS1-TuA10, 100
- Staub, P.G.: IS+AS+SS-MoA6, 38
- Starodub, E.: GR-MoM6, 11; GR-WeA9, **169**
- Starostin, S.: PS+SE-WeM12, 149
- Staudt, T.: IS+AS+SS-MoM3, 13
- Stavale, F.: SS2-WeM10, **155**
- Steele, B.: GR+MN-WeM9, **141**
- Steele, M.P.: SS+EM-TuA3, 103
- Stefanov, S.K.: VT-MoM9, 26
- Steidl, P.: SE+PS-ThA3, 229
- Steigerwald, A.D.: EM-ThP8, 241; TF1-ThM5, **209**
- Stein, A.: EN+NS-ThM5, **193**
- Steiner, M.A.: TF-FrM6, **271**
- Steinfeld, E.: EN-MoM3, **9**
- Steitz, R.: NT+AS-WeA10, 172

- Stellacci, F.: SS+EM-TuA1, **103**
 Stemme, F.: TF-MoM5, **24**
 Stephens, J.A.: SS1-TuM9, **74**; SS-TuA12, 106;
 SS-TuP14, 125
 Stern, L.A.: HI+AS-TuA1, 94; HI-TuP1, 116; HI-
 TuP2, 116
 Stern, L.J.: BI-ThP10, 238
 Sterner, O.: MB+BI+PS-MoA9, **40**
 Sterrer, M.: SS2-WeM3, **154**
 Stetcher, J.: NS-MoA10, **43**
 Stevens, A.: PS+SS-ThA10, 226
 Stevens, K.: TR-ThA10, **236**
 Stickle, W.: AS-MoM9, **3**
 Stierle, A.: SS-ThM10, 206
 Stine, R.: GR+NS+PS+SS-ThM12, 195;
 GR+NS+PS+SS-ThM5, **195**; GR+TF+NS-
 ThA9, 221
 Stocks, G.M.: EN+AC-FrM8, **261**
 Stollenwerk, A.J.: TF-FrM2, **270**
 Stoltenberg, R.M.: TF2+EM-WeA10, 182
 Stoltz, P.: PS-FrM2, 265
 Strachan, J.P.: NM+NS+MS-TuA7, **96**
 Stratman, P.: NS-WeM2, 145
 Strelchuk, V.V.: EM-ThP25, 244
 Strobl, M.: NT+AS-WeA10, 172
 Strohmeier, B.R.: AS-TuP13, **112**; AS-TuP8, 112
 Strosccio, J.A.: GR+MI-TuA8, 91; GR-TuA2, 92;
 GR-WeA3, 168; VT+MN+NS+SS+AS-TuA1,
108
 Stueber, M.: SE-ThM12, **205**
 Stumper, J.: EN+NS-ThA8, 220
 Stutzman, M.L.: VT-TuM1, **80**
 Su, J.F.: TR-ThA3, 235; TR-ThA8, **235**
 Sudradjat, F.: NS-MoA11, 43
 Suetsugu, Y.: VT-TuM5, **80**
 Sugiyama, M.: PS-ThM4, 201; PS-ThM5, 202
 Suh, H.: NS+AS-TuA1, 97
 Sullivan, E.: AS-TuA3, 83
 Sumant, A.V.: GR-TuA10, **93**; MN-FrM6, 264
 Sumi, N.: PS+SS-ThA4, 225
 Sumi, R.: EM-ThP20, **243**
 Sun, C.T.: MN-FrM8, 264
 Sun, D.: NS-ThM3, 198; SS2-MoA4, 50; SS-
 FrM1, **268**
 Sun, G.F.: GR-WeA10, 169
 Sun, H.: SS-TuP7, **124**
 Sun, J.C.: MB+BI+PS-MoA11, 41
 Sun, K.: NS+EM-MoM8, 18
 Sun, L.: EL-ThP7, 240; PS+TF-ThM2, **199**;
 SE+PS-ThA8, 230
 Sun, X.: TR+AS+SS-ThM3, 213
 Sun, Z.: EM-WeM9, 136
 Sundaram, G.M.: NM+MS+NS+TF-MoM3, 16
 Sundararajan, R.: PS-ThP23, 254; PS-ThP28, 255;
 PS-TuM10, 73
 Sung: GR+MI-TuA3, 91
 Sung, M.M.: TF1+EM-WeM1, **156**
 Surman, D.: EW-TuL4, **82**
 Surman, D.J.: AS-MoM10, 3; BI-ThM4, 188
 Susa, Y.: PS-ThP28, **255**
 Susac, D.: EN+NS-ThA8, 220
 Sussman, J.: EN+NS-WeM5, 139
 Suter, T.: SS1-WeM12, 153
 Sutter, P.: NS+AS-TuA10, 98; SS2-WeM11, **155**
 Suu, K.: PS+MN+TF-TuM1, 70
 Suyatin, D.: NS-TuM3, 69
 Suzer, S.: AS-MoM6, 2; SS+EM-TuA12, **105**
 Suzuki, H.: SS-TuP25, **126**
 Suzuki, M.: TF+SE-TuM2, **79**
 Suzuki, T.: GR+MI-TuA4, 91; NM+MS+NS+TF-
 MoM5, **16**
 Svensson, B.: EM-WeA1, 163
 Swain, G.: MB-MoM3, 15
 Swanson, S.A.: EN-TuM3, **62**
 Swart, H.C.: AS-TuP23, 114
 Swartzentruber, P.: SE-ThM5, **204**
 Sweet, W.: EM1-MoA9, 33; TF-MoA9, **53**
 Swensen, J.S.: AS-ThM11, 188
 Szakal, C.: BI+AS+NS+SS-WeA3, **162**
- Szulczewski, G.J.: MI-WeM3, **143**; NT+AS+MI-
 WeM4, 147; SS+EM-TuA10, 104; SS1-
 WeM11, 153
 Szymanowski, J.: AC+TF-ThA10, 216
- T —**
- Tabares, G.: EM-WeA3, 163
 Taborelli, M.: VT+MN+NS+SS+AS-TuA12, 110
 Tada, Y.: NM+MN+MS+TF-TuM4, 67
 Taing, J.: SS-ThM9, 206
 Tait, S.L.: SS2-MoA1, 50; SS2-MoA2, 50; SS2-
 TuM3, **75**; SS-TuP15, 125
 Taitt, C.R.: BI-ThP5, 238
 Tajima, T.: VT-TuP10, **131**
 Tajiri, H.: SS-TuP9, 124
 Takagi, K.: EN-ThP1, 245; EN-ThP7, 246
 Takahara, A.: BI-ThP1, 237; MB+BI+PS-MoA8,
 40
 Takahashi, H.: EM-ThP8, 241
 Takahashi, N.: VT-MoM6, **26**
 Takahasi, M.: SS-TuP9, **124**
 Takai, O.: EM-ThP20, 243; GR-TuP2, 115; GR-
 TuP3, 115; NS-WeM9, 145; PS+BI-MoA4, 44
 Takaki, Y.: IS-TuP1, 117; PS-ThP3, 250
 Takami, Y.: IS-TuP1, 117; PS-ThP3, 250
 Takano, I.: SS-TuP24, 126; SS-TuP25, 126; SS-
 TuP26, 126; SS-TuP27, 126; TF-TuP9, 129
 Takao, Y.: PS-FrM9, 266; PS-ThM12, 203; PS-
 ThM9, 202
 Takeda, K.: PS+SS-ThA4, 225; PS1-TuA11, 101;
 PS-ThM11, 203; SE+PS-WeA9, 177
 Takei, H.: EN-ThP1, 245; EN-ThP7, 246
 Takekuma, S.: SS1-MoA10, 49
 Takemura, S.: BN-TuP1, 115; NM-TuP1, 118;
 NM-TuP9, 119
 Takeshita, K.: PS1-TuA2, 99
 Takeuchi, N.: EM-ThP1, 240; MI-ThM10, 197
 Talapin, D.V.: EN+NS-TuA3, **88**
 Tallarico, D.A.: TF-MoM10, 25
 Talneau, A.: PS-FrM8, 266
 Tamain, C.: EN+AC-FrM7, **261**
 Tamaaha, C.R.: GR+NS+PS+SS-ThM12, 195;
 GR+NS+PS+SS-ThM5, 195; NS-WeM6, 145
 Tambe, N.M.: BI-ThP2, **237**
 Tamura, H.: PS-ThP26, 254
 Tamura, M.: EM-TuA3, 86
 Tamura, R.: SS1-MoA10, 49
 Tanaka, S.: GR-MoM5, 11
 Tang, B.: EN+TF-TuA9, 90
 Tang, J.: MI-WeA12, 171
 Tang, L.: BI-ThP4, **237**; SS2-MoA11, 51
 Taniuchi, Y.: PS2-TuA4, **101**; PS-MoM11, 20
 Tanner, D.B.: GR+EM-TuM11, 65
 Tanto, B.: TF2+EM-WeA11, 182
 Tao, J.: SS-WeA3, **178**
 Tapily, K.N.: EM+TF-TuM6, 59
 Tarrio, C.: EL+AS+EM+MS+PS+TF-ThM9, 190
 Tartakowskaya, E.: NT+AS+MI-WeM3, 147
 Tashchuk, M.T.: SE+TF-TuA7, 103; TF+SE-TuM4,
 79
 Tatsumi, T.: PS+SS-WeM12, 151; PS-FrM11, 266;
 PS-ThM12, 203; PS-ThM3, 201; PS-TuM3, 72
 Taubert, I.: BI-WeM11, 135
 Taubman, M.S.: AS-TuA1, 83
 Taylor, A.: AC+MI-WeA3, 159
 Taylor, P.C.: EN+TF-TuA1, **89**
 Tchakhalian, J.: EM-WeA4, 164
 Tchoua Ngamou, P.H.: PS+TF-ThM6, **200**
 Tedesco, J.L.: GR-MoM4, 11; SE-ThM1, **203**
 Telib, H.: VT-MoA11, 54
 Temple, D.: EM1-MoA11, 33; EN+EM+NS-
 MoA3, 35
 ten Elshof, J.E.: HI-TuP3, 116
 Tendler, S.J.B.: AS+BI+NS-WeM12, 133; SS2-
 TuM5, 76
 Tengstrand, O.: SE-ThM10, **204**; TF1-ThM11, 210
 Tenney, S.A.: SS-TuA9, 106; SS-TuP5, **123**
 Tennyson, J.: PS-FrM7, 265
 Terada, M.: MB+BI+PS-MoA8, 40
 Terfort, A.: EN+NS-TuM2, 61
- Terlinden, N.M.: EM+TF-TuM11, **60**
 Terminello, L.J.: NS-TuP7, 120
 Terryn, H.: SS1-WeM12, 153
 Tetlak, S.: GR+MS+EM-FrM7, 262
 Textor, M.: NS-ThA4, 224
 Thamban, P.L.S.: PS+BI-MoA6, 44; PS-ThA6,
227; PS-ThP20, 253; PS-ThP21, 253
 Therien, M.: NS-MoA10, 43
 Thevuthasan, S.: AC+SS-ThM11, 186; AS-TuP15,
 113; AS-WeA7, 161; HI-TuP7, 117; NS-TuP3,
 120; NS-TuP7, 120; SS-WeA7, 178; TF1+EM-
 WeA1, 179; TF-MoM1, 23; TF-TuP2, **128**
 Thibeault, B.: EM-MoM2, 6
 Thiel, P.A.: AC+SS-ThM9, 186; SS1-WeM3, 153
 Thiruvengadam, S.: EN1+TF-WeA3, 166
 Thissen, A.: IS+AS+SS-MoA10, **39**
 Thissen, P.: EM+TF-ThM3, **191**
 Thomas Plach, T.: SE-TuP3, **122**
 Thomas, K.: EM+TF-TuM4, 59
 Thomas, M.: TF+SE-TuM4, 79
 Thomas, W.: BI-MoM6, 4
 Thomé, I.: MB-MoM3, **15**
 Thompson, C.V.: TF2+EM-WeA1, **181**
 Thompson, G.B.: AS-TuA8, 84
 Thompson, S.E.: MB-MoM10, 15
 Thoms, B.D.: EM-ThP14, **242**; EM-ThP15, 242
 Thornberg, S.M.: VT-MoA7, **54**
 Thorpe, R.: EN+NS-ThM2, **193**
 Thundat, T.G.: BI-MoA7, 31
 Tian, C.: PS-ThP23, 254
 Tian, H.C.: BI-MoA11, 31
 Tian, J.: BI-MoM10, 5
 Tian, W.-C.: MN-FrM8, 264; MN-FrM9, 264
 Tilak, V.: AS-WeA9, 161
 Tillocher, T.: PS+MN+TF-TuM3, **71**
 Timm, R.: NS-TuM3, 69
 Timmons, R.B.: MB+BI+PS-MoA1, 39
 Tisdale, W.A.: EN+NS-TuM5, **61**
 Tiwald, T.E.: EL+AS+EM+MS+PS+TF-FrM1,
 258; EL-ThP5, 240
 Tizazu, G.: BI+AS+NS+SS-WeA9, 162
 Tjong, V.: BI-ThP4, 237
 Tkachenko, B.A.: NS-ThM11, 198
 To, B.N.: PS+MN+TF-TuM4, 71
 To, N.: SS1-WeM9, 153
 Tobash, P.H.: AC+MI-WeA3, 159
 Tobin, J.G.: EN+AC-FrM1, **261**; EN+AC-FrM4,
 261; MI-ThP1, 248
 Todorov, T.K.: EN1+TF-WeA3, 166
 Todorovic, M.: NS+AS-TuA4, 97
 Toivola, M.: NM+MS+NS+TF-MoM6, 16
 Tökei, Zs.: TF1-ThM12, 210
 Toker, G.: EN+EM+NS-WeM6, 137
 Tokuda, Y.: PS-ThM11, 203
 Tolbert, L.M.: GR-TuP5, **115**; GR-TuP6, 116
 Tolbert, S.: MI-ThM12, 197
 Tolic, A.: HI+AS+BI+NS-WeM11, 142
 Tolk, N.H.: EM-ThP8, 241; EN+NS-ThA10, 220;
 EN-ThP17, 247; MI-ThM3, 196; TF1-ThM5,
 209
 Tomasel, F.G.: PS-WeA1, **174**
 Tomizawa, H.: PS-TuM5, 72
 Tomohiro, K.: PS-ThP16, 252
 Tompa, G.S.: EN+NS-TuA11, 89
 Tompkins, B.D.: PS+SS-ThA9, **226**
 Tongay, S.: GR+EM-TuM11, 65; GR+MI-TuA11,
 92; GR+MS+EM-FrM6, **262**
 Toomey, R.: NT+AS+MI-WeM10, 148
 Topolancik, J.: BI-MoA11, **31**
 Torija, M.A.: NT+AS+MI-WeM5, 147
 Tosa, M.: TR-ThP2, 256
 Tosado, J.: GR-TuA4, 92
 Tosatti, S.: MB+BI+PS-MoA4, 40; MB+BI+PS-
 MoA9, 40
 Tosun, B.S.: EN1+TF-WeA2, **165**; EN1+TF-
 WeA7, 166
 Tougaard, S.: AS-MoM1, **2**
 Toyoda, S.: PS+MN+TF-TuM1, 70
 Trelles, J.-P.: EM-WeM2, 135

Trenary, M.: SS-FrM5, 269
 Tribby, L.: BI-MoA3, **30**
 Trickett, D.: PS-TuM5, 72
 Trincherio, A.: IS+AS+SS-MoM6, 14
 Trinh, H.D.: NM-TuP2, 118
 Trogler, W.: EM+TF-ThM6, 192; NS-ThA9, 224; SS+EM-TuA9, 104
 Truffert, V.: PS-TuM1, 72
 Tsai, D.P.: EM-ThP12, 242; NM-TuP2, 118; NM-TuP3, 118; NM-TuP4, 118
 Tsao, C.Y.: BN+NM-TuM11, 59; BN+NM-TuM2, 57; BN+NM-TuM6, 58
 Tselev, A.: SS2-FrM4, 267
 Tseung, C.T.: EN+NS-WeM12, 140
 Tseng, W.H.: EN+NS-WeM12, 140
 Tshabalala, K.G.: AS-TuP23, 114
 Tskipuri, L.: SS+EM-TuA8, **104**
 Tsuchiya, Y.: NM+MN+MS+TF-TuM4, 67
 Tsud, N.: IS+AS+SS-MoM3, 13
 Tsuda, H.: PS-FrM9, **266**
 Tsuda, N.: NS-WeM9, **145**
 Tuberquia, J.C.: NM+MN+MS+TF-TuM3, 67
 Tucker, R.T.: TC+AS+EM-ThM5, 207; TF+SE-TuM4, **79**
 Tuominen, M.T.: NM+MS-MoA6, **41**
 Tuomisto, F.: EM-WeA1, 163
 Turchanin, A.: GR+NS+PS+SS-ThM4, **194**; HI+AS+BI+NS-WeM6, 142; SS2-TuM2, 75
 Turmel, O.: PS1-TuA2, 99
 Turner, J.J.: SS2-MoM2, 22
 Turner, K.T.: TR+AS+SS-ThM6, 213
 Turner, M.M.: PS-ThA8, 228
 Turner, M.W.: SS2-MoA8, 50
 Tuxen, A.: SS2-WeM2, 154
 Tweedie, J.S.: EM1-MoA4, 32; EM-ThP13, 242; EM-ThP15, 242; TF2-ThM11, 212
 Tyagi, P.: GR-MoM9, 12; NS-WeM1, **144**
 Tyler, T.P.: EN+NS-WeM3, **138**
 Tysoe, W.T.: TR+AS+SS-ThM9, 213; TR-ThP9, 257

— **U** —

Uchida, G.: PS+TF-ThM5, 200
 Ueda, A.: NS-TuP8, 120
 Ueda, H.: PS+TF-ThM1, 199
 Ueki, S.: PS-ThM4, 201; PS-ThM5, 202; PS-ThM6, 202
 Ueno, T.: GR-TuP2, 115; GR-TuP3, 115; NS-WeM9, 145
 Uesugi, T.: PS+SE-MoA2, **46**
 Uher, C.: EM-WeA12, 165
 Uhl, A.: SS-FrM5, 269
 Uljin, R.V.: BI-MoM1, 3
 Ulloa, S.: EM-ThP1, 240; GR+MI-TuA10, 92
 Ulrich, S.: SE-ThM12, 205
 Unocic, K.: EN-ThP17, 247
 Uppireddi, K.: AS-TuP24, 114; EL+AS+EM+MS+PS+TF-ThA6, **216**
 Urban, J.: EN+NS-TuA9, 88
 Urrabazo, D.: PS-ThP21, **253**
 Utsumi, M.: PS2-TuA4, 101
 Utz, A.: SS2-MoM10, **23**; SS2-MoM8, 23

— **V** —

Vail, M.: AS-WeA11, 161
 Valderrama, E.: VT-TuP10, 131
 Valente-Feliciano, A.-M.: VT+MN+NS+SS+AS-TuA10, **109**; VT-TuP9, 130
 Valla, T.: GR-MoM9, 12; NS-WeM1, 144
 Vallee, C.: EM2-MoA9, 34
 Vallée, C.: TF1+EM-WeA2, 179
 Vallier, L.: PS+SS-WeM1, 149; PS-MoM1, 19; PS-MoM3, 19; PS-MoM5, 19; PS-MoM6, 20
 Valone, S.M.: EN+AC-FrM6, **261**
 Valtiner, M.: SS2-MoA9, **51**
 Vamala, C.: GR+EM-TuM6, 64
 van Asten, A.: TF-MoA7, 52
 Van Besien, E.: TF1-ThM12, **210**
 van Buuren, T.: NS-ThM11, 198

van de Sanden, M.C.M.: EM+TF-TuM11, 60; EN+PS-MoM3, 7; EN+PS-MoM4, 7; EN+PS-MoM6, 8; EN+TF-TuA3, 89; GR+EM-TuM5, 64; PS+SE-WeM12, **149**; PS+TF-ThM6, 200; PS+TF-ThM9, 200; SE+PS-ThA2, 229; TF-MoM4, 24
 van der Donck, J.C.J.: PS+SS-ThA11, 226
 van der Drift, E.W.J.M.: HI+AS-TuA12, 96; HI+AS-TuA4, 95
 van der Marel, C.: TF-MoA4, 52
 van der Mullen, J.J.A.M.: PS+SS-ThA10, 226
 van der Zande, A.M.: MN-ThA4, 222
 Van Dijken, J.G.: TF+SE-TuM4, 79
 Van Elshocht, S.: TF1-ThM12, 210
 van Gastel, R.: HI+AS+BI+NS-WeM5, 141; HI+AS-TuA3, **94**; HI-TuP3, 116; IS+AS+SS-MoA7, 38
 van Langen, K.: HI+AS-TuA4, 95
 Van Neste, C.W.: BI-MoA7, 31
 Van Swol, F.: BI-MoA3, 30
 van Veldhoven, E.: HI+AS-TuA12, 96; HI+AS-TuA4, 95
 Vandervorst: AS-TuA10, **84**
 vanDorp, W.: SS1-MoA7, 48
 Vanfleet, R.: TF-FrM11, 272
 Vanhart, D.: EN1+TF-WeA12, 167
 Varela, M.: NT+AS+MI-WeM5, 147
 Varga, K.: ET+EM+SS-MoM11, 10; GR+MI-TuA12, 92; GR+TF+ET-MoA11, **37**; GR+TF+NS-ThA4, 221; TF1-ThM5, 209
 Varga, T.: AC+SS-ThM11, 186; AS-TuP15, 113; AS-WeA7, 161; MI-ThP7, **249**; NS-TuP3, 120; TF1+EM-WeA1, 179; TF-MoM1, 23; TF-TuP2, 128
 Vargas, J.: GR-TuP5, 115
 Vargas, M.: VT-MoM9, **26**
 Varshney, V.: SE+SS-WeM4, 151; SE-TuP4, 122
 Vasco, E.: SS-TuP29, 127; TF1-ThM1, 208
 Vasekar, P.: EN1+TF-WeA12, **167**
 Vasen, T.: EM-MoM8, 6
 Vasenkov, A.W.: TF2+EM-WeA9, 182
 Vasquez, K.A.: TF+EN-TuM10, 78
 Vass, S.: BI-ThM2, 188
 Vasudev, M.C.: AS+BI+NS-WeM6, 132
 Vasylyv, O.M.: EN-ThP18, **248**
 Vattuone, L.: SS-ThM5, 205
 Vayssilov, G.N.: IS+AS+SS-MoM3, 13
 Vazquez-Lepe, M.O.: AS-TuP20, 114; AS-TuP21, **114**; EM-TuA12, 88; TR-ThP3, 256
 Vega, A.: EM+TF-ThM3, 191
 Veligura, L.I.: EM-ThP25, 244
 Veligura, V.: HI+AS+BI+NS-WeM5, **141**
 Vemuri, R.S.: EL-ThP1, 239; TF-MoM1, **23**
 Venkataraman, L.: NS-ThM4, **198**
 Venkattaraman, A.: TF2-ThM1, 210
 Venstrom, L.: EN+NS-ThM5, 193
 Ventrice, Jr., C.A.: GR-MoM9, 12; NS-WeM1, 144
 Ventzek, P.: PS-ThP23, **254**; PS-TuM10, 73
 Venugopal, A.: GR-TuA9, 93
 Verdonck, P.: PS1-TuA7, 100
 Vereecke, B.: PS-TuM1, 72
 Verheijen, M.A.: EN+PS-MoM6, 8; TF-MoA4, 52
 Verhoeven, M.W.G.M.: PS+SS-ThA10, 226
 Vermont, P.: TF-MoA1, 51
 Vérove, C.: PS-MoM6, 20
 Vescovo, E.: MI-WeA4, 170; MI-WeM9, **143**
 Veyan, J.F.: IS+AS+SS-MoM10, 14; SS1-TuM4, 74
 Viale, L.: EW-WeL3, 158; VT-TuM6, 81
 Vieker, H.: HI-TuP5, 117; HI-TuP6, **117**
 Vilan, A.: EM+TF-ThM11, **192**
 Vincent-Johnson, A.J.: TF+EN-TuM10, 78
 Virwani, K.: EM-WeM9, 136
 Vitale, S.A.: PS+TF-ThM11, **200**
 Vives, G.: MI-WeA3, 170; NS-ThM6, 198
 Vlad, A.: SS-ThM10, 206
 Vlasak, P.R.: AS-MoA7, 28
 Vlasenko, N.A.: EM-ThP25, **244**

Vlcek, J.: SE+PS-ThA3, **229**
 Voci, D.: HI+AS-TuA3, 94
 Voevodin, A.A.: AS+BI+NS-WeM6, 132; SE+SS-WeM4, **151**; SE+SS-WeM6, 152; SE+SS-WeM9, **152**; SE-TuP4, 122; TF-FrM10, 272
 Vogel, E.M.: EM+TF-TuM2, 59; EM+TF-TuM4, **59**; EM-TuA9, 87; GR-TuA9, 93
 Vogt, P.: SS-FrM11, 270
 Vohs, J.M.: SS-ThA4, **230**
 von Keudell, A.: PS+SE-WeM5, 148
 von Wenckstern, H.: TC+EM+NS-ThA1, **231**
 Vu, A.: EN+NS-ThM5, 193

— **W** —

Wada, A.: PS+SE-MoA2, 46; PS-ThM10, **202**; PS-ThM6, 202
 Wada, T.: NS-TuM1, 68
 Waddill, G.D.: MI-ThP1, **248**
 Wade, T.C.: EN-ThP17, **247**
 Wager, J.F.: TC+EM+NS-ThA7, **232**
 Wagner, F.T.: TF+EN-TuM3, 77
 Wagner, M.S.: SS1-MoA9, 49
 Wahl, K.J.: MB-MoM8, 15
 Wainright, J.: PS+BI-MoA11, 45
 Waite, A.: EL-ThP7, 240; SE+PS-ThA8, 230; SE+SS-WeM9, **152**; TF-FrM10, 272
 Walczyk, Ch.: TF1+EM-WeA3, 180
 Walczyk, D.: TF1+EM-WeA3, 180
 Waldeck, D.H.: SS2-TuM11, 76
 Waldfried, C.: PS-ThP1, 250
 Walker, A.R.: AS-TuP2, **111**
 Walker, A.V.: EM+TF-ThM5, **191**
 Walker, D.G.: AC+TF-ThA9, 215; EN+NS-TuM10, 61
 Walker, M.J.: VT+MN+NS+SS+AS-TuA3, 108
 Wall, M.: EW-TuL3, 82
 Wallace, R.M.: EM+TF-TuM2, 59; EM+TF-TuM3, 59; EM-MoM8, 6; EM-TuA10, 87; EM-TuA9, 87; GR-TuA9, 93; IS+AS+SS-MoM10, 14
 Walle, L.E.: IS+AS+SS-MoM4, 13
 Wallentin, J.: NS-TuM3, 69
 Wallin, C.B.: BI-MoA11, 31
 Walls, D.J.: AS-WeA3, 160
 Walsh, M.A.: TF+EM+SS-ThA9, 234
 Walter, C.: SE+SS-WeM6, 152
 Walton, S.G.: BI-ThP5, 238; GR+NS+PS+SS-ThM12, **195**; GR-TuA4, 92; NS-WeM6, 145; PS2-TuA2, 101
 Wandelt, K.R.: SS2-MoA6, **50**
 Wang, B.: EM-WeA10, 164; GR+NS+PS+SS-ThM6, **195**
 Wang, C.M.: AS-WeA7, 161; TF-MoM1, 23
 Wang, E.: ET+EM+NS+GR-TuM6, 63
 Wang, F.: SS-WeA11, 179
 Wang, G.-C.: SE+TF-TuA1, **102**
 Wang, H.: EL+AS+EM+MS+PS+TF-ThM5, 190; EL+AS+EM+MS+PS+TF-ThM6, 190; SS1-WeM5, 153; TF-TuA10, 107
 Wang, J.: NS-MoA8, 43
 Wang, J.Y.: EN+NS-WeM12, 140
 Wang, K.: MI-ThM6, **196**
 Wang, K.K.: MI-ThM10, 197; MI-ThM11, 197
 Wang, K.L.: EM2-MoA1, **34**
 Wang, L.: NS-MoA9, 43; SS-ThA10, 231; TF-FrM8, **271**; TR-WeA3, 183
 Wang, M.: EM-ThP23, 244; EN+NS-WeM1, **138**
 Wang, M.S.: BI-TuA11, **85**
 Wang, P.: NT-TuP1, **121**; SS+EM-TuA11, 104
 Wang, Q.H.: NS-WeM3, 145
 Wang, W.: AS-MoM9, 3; ET+EM+NS+GR-TuM6, 63; SS-WeA7, 178
 Wang, W.L.: GR+TF+NS-ThA8, 221
 Wang, X.: MI-WeA12, 171; MN-FrM6, **264**
 Wang, X.-Y.: EN+EM+NS-MoA1, 35
 Wang, Y.: BI-MoA6, **30**; NS-MoA8, 43; PS+TF-ThM5, 200
 Wang, Y.M.: SS-WeA2, 177
 Wang, Z.: EN-ThP3, 245
 Wang, Z.J.: SE+PS-WeA4, **176**

- Wang, Z.T.: SS-WeA1, **177**; SS-WeA10, 179
Ward, T.Z.: MI-ThM4, **196**; MI-ThP6, 249
Wark, D.: HI-TuP4, 117
Warnick, K.H.: EM-WeA9, **164**
Washington, J.S.: TF1+EM-WeA9, 181
Watanabe, H.: BI-ThP1, 237; EM-ThP20, 243
Watanabe, M.: PS-WeA1, 174
Watanabe, N.: PS-ThM4, **201**; PS-ThM5, 202
Watanabe, Y.: NM-TuP1, **118**; NM-TuP9, 119
Watkins, S.: ET+EM+NS+GR-TuM12, 64
Watrous, J.: BI-WeM4, 134
Watson, D.G.: EW-TuL5, 82
Weber, J.W.: EL+AS+EM+MS+PS+TF-ThA7, 217; GR+EM-TuM5, **64**
Weber, M.J.: EL+AS+EM+MS+PS+TF-ThA7, 217; TF-MoA4, **52**
Webster, D.C.: MB+BI+PS-MoA6, **40**
Weeden-Wright, S.L.: AC+TF-ThA9, 215
Wehbe, N.: PS+SE-WeM3, 148
Wei, M.: TF-FrM5, 271
Wei, R.: TR+AS+SS-ThM2, 213
Wei, S.-H.: TC+AS+EM-ThM3, **207**
Wei, W.D.: NS-MoA8, **43**
Wei, Y.: SS+EM-TuA7, 104
Weidner, T.: AS-TuA3, 83; BI-MoM4, 4; SS1-MoA9, 49
Weilnboeck, F.: PS+SE-MoA9, 47; PS-TuM6, **73**
Weinert, M.: GR-WeA10, 169; GR-WeA11, 170; MI-WeM12, 144; TR+AS+SS-ThM9, 213
Weise, N.K.: MB+BI+PS-MoA10, 40
Weiss, E.A.: EN+NS-TuM11, **61**
Weiss, S.M.: BI+AS+NS+SS-WeA10, 163; EM-WeA11, 165; TF1-ThM9, 209
Weitering, H.H.: ET+EM+SS-MoM5, **10**
Weller, R.A.: EM-WeA11, 165; TF1-ThM9, 209
Wells, I.B.: EM+TF-TuM6, 59
Welzel, S.: EN+PS-MoM3, 7
Wen, H.: SE-TuP2, 122
Wen, X.: BI-MoA4, **30**
Wendt, A.E.: PS-ThA2, 227
Wenger, Ch.: TF1+EM-WeA3, **180**
Wernersson, L.-E.: NS+EM-MoM3, **18**
Westgate, C.R.: EN1+TF-WeA12, 167
Westwood, J.N.: MN-ThA10, 223
Wevers, I.: VT-TuP6, 130
Whaley, S.D.: SS1-MoA11, **49**
Wheeler, M.C.: SS1-TuM1, 73
Wheeler, V.D.: EM+SS-FrM1, 259; GR+MS+EM-FrM3, 262; GR-MoM11, 12; GR-MoM8, 11; GR-TuA8, **93**; NS-WeM6, 145
White, M.G.: SS2-FrM2, 267; SS2-FrM3, 267; SS2-WeM1, 154; SS-TuP30, 127
White, M.L.: VT-MoA7, 54
White, R.G.: AS-WeA2, 160; EW-TuL2, **82**; EW-TuL3, 82
Whitney, W.S.: MN-ThA4, 222
Wi, S.-S.: EN+PS-MoM9, **8**
Wierer, J.: EN+TF-TuA11, 90
Wierzbinski, E.: SS2-TuM11, 76
Wilbert, S.: AS-TuA9, 84; EN+EM+NS-WeM12, 138
Wilkens, B.J.: BI-ThM12, 189
Willeke, F.: VT-TuM2, 80
Willey, T.M.: NS-ThM11, **198**
Williams, E.D.: EN-MoM5, **9**
Williams, N.: TF+EM+SS-ThA4, 233
Williams, P.: BI-WeM3, 134
Williams, R.S.: NM+NS+MS-TuA7, 96
Williams, T.S.: PS+SE-WeM4, 148; SE+PS-WeA2, **176**
Willis, B.G.: TF-TuA10, **107**
Wills, A.W.: EN1+TF-WeA7, 166
Wills, J.M.: AC+MI-WeA10, 159
Wilson, D.P.: SS-TuP30, **127**
Wilson, K.: VT-TuM2, 80
Wilson, R.E.: AC+TF-ThA1, 215
Wilson-Rae, I.: MN-ThA6, 223
Wimplinger, M.: SE-TuP3, 122
Wind, S.: BN-TuA3, **86**
- Winkler, K.: AS-MoM11, **3**
Winter, B.: IS+AS+SS-TuM11, 67; SS1-MoM5, 21
Wise, R.: PS+SE-MoA10, 47; PS-ThP28, 255; PS-TuM12, 73
Wissing, S.N.P.: MI-WeM11, 143
Wistey, M.: EM-MoM8, 6
Wittig, J.E.: EN-ThP17, 247
Witzke, M.: PS+BI-MoA11, **45**
Wnuk, J.: SS1-MoA7, 48
Wofford, J.: GR-MoM10, 12; GR-MoM6, **11**
Wolak, M.A.: SS2-TuM11, **76**
Wolden, C.A.: EN2+TF-WeA8, 167; PS+TF-ThM3, **199**; TF-MoM11, 25
Wolf, M.: SS2-MoM2, 22
Woll, A.R.: IS+AS+SS-TuM12, 67
Wöll, C.: SS2-TuM2, 75; SS-WeA2, 177
Wolter, D.: NS-ThM11, 198
Won, B.: NS+EM-MoM8, 18
Wong, K.T.: SS1-MoA8, **49**
Wong, P.: AS-ThM1, 186
Woo, J.C.: PS-ThP10, 251; PS-ThP8, 251; PS-ThP9, **251**
Wood, J.D.: GR-TuA12, **94**
Woodroof, M.: TF+EN-TuM9, 78
Woollam, J.A.: EL+AS+EM+MS+PS+TF-FrM3, 258; EL+AS+EM+MS+PS+TF-FrM5, 258
Wooten, D.: SS-ThA10, 231
Worfolk, B.J.: TF+SE-TuM4, 79
Wormeester, H.: EL+AS+EM+MS+PS+TF-ThA9, **217**
Wormyo, E.: PS-TuM5, 72
Wornyo, E.: PS-TuM12, 73
Wright, A.E.: AS-TuA4, **83**; AS-WeA2, 160
Wu, A.: MB-MoM1, 15; MB-MoM11, **16**
Wu, A.T.: VT+MN+NS+SS+AS-TuA7, **109**
Wu, C.I.: EN+NS-WeM12, 140; SS+EM-TuA11, **104**
Wu, H.: EN+NS-ThA3, 219
Wu, H.C.: BN+NM-TuM2, 57; BN+NM-TuM6, 58
Wu, I.: SS+EM-TuA11, 104
Wu, J.: GR+EM-TuM10, 65
Wu, J.K.: MB+BI+PS-MoA11, 41
Wu, J.T.: NS-TuP11, 121
Wu, K.R.: MB+BI+PS-MoA11, **41**
Wu, N.: MI-WeA12, 171
Wu, N.L.: PS+SE-WeM10, 149
Wu, T.C.: MI-ThP4, **249**
Wu, W.: EN+NS-ThM3, 193
Wu, Y.: TF2+EM-WeA4, **181**
Wu, Y.L.: PS+SE-WeM11, 149; PS-ThP4, 250; PS-ThP7, **251**; SE+PS-WeA11, 177
Wu, Z.: NS-ThA9, 224; SS2-WeM9, 155
Wüest, M.: VT-MoM5, **26**; VT-MoM9, 26
Wulff, K.: NS+AS-TuA12, **99**
Wurth, W.: SS2-MoM2, 22
Wyllie, E.M.: AC+TF-ThA8, **215**
Wynne, J.H.: MB+BI+PS-MoA10, 40
Wyre, J.P.: AS-WeA3, 160
Wyrick, J.: NS-ThM3, 198; SS2-MoA4, 50
- **X** —
Xia, L.Q.: EM-MoM3, 6
Xiang, T.: ET+EM+SS-MoM10, 10
Xiao, D.: SS2-FrM1, 267
Xiao, J.: SS+EM-TuA4, 103
Xiao, K.: EM1-MoA6, 33
Xiao, L.: MB-MoM10, **15**
Xiao, Z.: AS-WeA8, 161; EM-ThP2, 240; NS-TuP9, **120**
Xie, X.: BI-ThP6, **238**
Xie, Y.: HI+AS+BI+NS-WeM11, 142
Xie, Z.: NS-ThM9, 198
Xing, H.: EM-MoM8, 6
Xing, W.: NS-TuP1, **119**
Xiong, G.: NS-MoA8, 43
Xiong, Z.: PS-FrM1, 265
Xiu, F.: EM2-MoA1, 34
Xu, B.: SS-TuA8, **105**; SS-TuP1, **122**
Xu, M.C.: SS-WeA2, 177
- Xu, Q.: IS+AS+SS-MoA8, 39
Xu, X.: GR+EM-TuM9, 65
Xu, Y.: NS-ThA6, 224; SS1-TuM12, 75; SS2-WeM5, 154
Xu, Z.: EN+TF-TuA9, 90
Xue, Q.-K.: MI-WeA1, **170**
- **Y** —
Yaffe, O.: EM+TF-ThM11, 192; EN+NS-WeM11, **139**
Yakovenko, O.: BI-MoM6, 4
Yakovkin, I.N.: MI-WeA12, 171
Yakshinskiy, B.V.: SS-TuP22, **125**
Yamada, S.: NM+NS+MS-TuA12, 97
Yamada, T.: AS+BI+NS-WeM5, **132**
Yamamoto, A.: AS-TuM11, 57
Yamamoto, N.: TC+AS+EM-ThM2, 207
Yamamoto, T.: TC+AS+EM-ThM2, 207
Yamamoto, Y.: AS-TuM10, 57
Yamanobe, T.: AS-TuM10, 57
Yamashiro, Y.: GR+MS+EM-FrM9, **263**
Yan, B.: EN+TF-TuA7, **90**
Yan, L.: AS-TuP24, **114**;
EL+AS+EM+MS+PS+TF-ThA6, 216
Yan, Z.: SS2-WeM5, 154
Yanagisawa, M.: PS2-TuA4, 101
Yang, C.T.: NM-TuP7, 118
Yang, D.: TF2+EM-WeA7, 181
Yang, F.: GR+TF+ET-MoA3, 37
Yang, H.: GR-MoM9, 12; NS-WeM1, 144
Yang, J.: BI-WeM3, 134; EM+TF-ThM5, 191; EN+EM+NS-WeM1, 136; EN+TF-TuA7, 90; HI-TuP2, 116; MI-ThP3, **249**; NS+EM-MoM2, 17; PS-ThP25, 254
Yang, K.: NS-MoA9, 43; TF-FrM8, 271
Yang, K.-E.: GR-WeA7, 169
Yang, L.: AS-ThM2, 187
Yang, P.: NS-TuP7, 120; SS-WeA7, 178
Yang, W.L.: EN+AC-FrM4, 261
Yang, X.F.: SS1-WeM5, 153; SS-TuP4, **123**
Yang, Y.: SS2-FrM2, **267**
Yang, Y.J.: PS+SE-WeM10, 149
Yang, Z.G.: EN-MoA6, **36**
Yao, Y.: SS2-WeM5, 154
Yao, Y.X.: SS-ThM6, 206
Yarmoff, J.A.: SS2-FrM5, **268**
Yarmush, J.: PS+SE-MoA10, **47**
Yasuda, A.: PS+SE-MoA2, 46
Yasuda, T.: NM+MS+NS+TF-MoM5, 16
Yatsuda, K.: PS+SS-ThA8, 226
Ye, D.: TF-FrM4, **271**
Ye, J.: TF2+EM-WeA1, 181
Ye, L.: TF-TuP5, **128**
Yee, S.: EN+NS-TuA9, 88
Yeh, B.: TC+EM+NS-ThA7, 232
Yeh, C.W.: MB+BI+PS-MoA11, 41
Yeh, Y.C.: MI-ThP4, 249
Yeo, J.: NM+NS+MS-TuA12, **97**
Yeom, G.Y.: AS-TuP18, 113; PS-ThP14, 252; PS-ThP17, 253; PS-ThP18, 253; SE+PS-WeA3, 176
Yeung, K.: NS-MoA6, 42
Yin Vallgren, C.: VT+MN+NS+SS+AS-TuA12, 110
Yin, W.: EM1-MoA6, 33
Yin, Y.: PS-MoM9, 20; PS-TuM5, 72
Yip, C.: AS+BI+NS-WeM3, **132**
Yip, C.S.: PS2-TuA3, 101; PS-ThA9, **228**
Yitamben, E.: EM+SS-FrM11, **260**
Yitzchaik, S.: EN+EM+NS-WeM6, 137
Ylä-Outinen, L.: TF-MoA10, 53
Yoda, S.: SE+SS-WeM10, **152**
Yokoyama, Y.: NS-TuM1, 68
Yoo, S.J.: EN+PS-MoM1, 7
Yoo, W.: NM+NS+MS-TuA12, 97
Yoon, D.Y.: EM-MoM5, **6**
Yoon, J.J.: EL-ThP2, **239**
Yoshida, H.: NM+MN+MS+TF-TuM4, 67
Yoshikawa, J.: PS-ThP23, 254
Yoshimura, M.: SS-TuP11, **124**

- Yoshimura, T.: GR-MoM5, 11; TF1+EM-WeM6, **156**
- You, K.: GR-WeA7, 169
- You, K.H.: PS-ThP12, 252
- You, S.J.: PS-ThP12, 252
- Youn, Y.-S.: IS+AS+SS-TuM10, 66
- Yu, C.C.: NM-TuP2, **118**; NM-TuP3, 118; PS-ThP6, 250
- Yu, H.: SE+PS-ThA7, 229
- Yu, J.: GR-TuA10, 93; NT-TuP2, 121
- Yu, S.W.: EN+AC-FrM1, 261; EN+AC-FrM4, **261**; MI-ThP1, 248
- Yu, X.: AS-ThM2, 187
- Yuan, H.: SS1-MoM2, 21
- Yuen, C.: AC+SS-ThM9, **186**
- Yusuff, H.: PS-TuM12, 73
- **Z** —
- Zaccaria, P.: VT-TuM4, 80
- Zaera, F.: SS-TuP7, 124
- Zafar, S.: BI-MoA8, 31
- Zahl, P.: NS+AS-TuA10, 98
- Zajec, B.: EN-ThP2, 245
- Zakharov, A.: PS-ThP1, **250**
- Zandvliet, H.: HI+AS+BI+NS-WeM5, 141; HI+AS-TuA3, 94; HI-TuP3, 116; IS+AS+SS-MoA7, 38
- Zang, Y.: MI-WeA3, 170
- Zaug, J.M.: AC+SS-ThM5, 185
- Zauscher, S.: BI-ThP4, 237; BI-TuA9, 85
- Zavadil, K.R.: EN+NS-ThA1, 218
- Zelechowski, M.: EN-ThP12, 247
- Zettsu, N.: EM-ThP20, 243; GR-TuP2, 115; GR-TuP3, 115; NS-WeM9, 145
- Zhakhovskiy, V.V.: GR+MN-WeM3, 140; GR+MN-WeM9, 141
- Zhang, B.: GR+MN-WeM5, 140; TC+EM+NS-ThA11, **233**
- Zhang, C.: TF-TuA10, 107
- Zhang, E.X.: EM-WeA11, **165**; TF1-ThM9, 209
- Zhang, F.: EN+TF-TuA9, 90
- Zhang, H.: MB-MoM1, 15
- Zhang, J.: EM-WeA1, 163
- Zhang, J.Z.: TF+SE-TuM10, 80
- Zhang, L.: AS-WeA3, 160; NS-TuP2, 119
- Zhang, M.: EM1-MoA2, 32
- Zhang, Q.: EM-MoM8, 6
- Zhang, S.: SE-ThM2, **204**
- Zhang, X.: HI-TuP5, **117**; SE-ThM2, 204
- Zhang, X.-G.: ET+EM+SS-MoM10, **10**
- Zhang, Y.: EN+NS-TuM9, **61**; GR+TF+NS-ThA8, 221; NS-ThM6, 198; PS-ThA7, **227**; PS-TuM11, 73
- Zhang, Z.: EN+NS-ThM3, 193; SS+EM-TuA4, 103; SS1-TuM11, 75; SS2-FrM1, 267; SS2-WeM12, 155; SS-WeA11, 179
- Zhao, J.: PS-ThP23, 254; PS-ThP28, 255
- Zhao, L.: TF1-ThM12, 210
- Zhao, M.: SS-ThA4, 230
- Zhao, Y.: EN+NS-ThA3, 219
- Zhao, Y.P.: SE+TF-TuA8, **103**; TF+SE-TuM10, 80; TF+SE-TuM9, 79
- Zharnikov, M.: EN+NS-TuM2, **61**; TF+EM+SS-ThA6, 233
- Zhdanov, V.P.: BI+AS+NS+SS-WeA4, 162
- Zheng, W.: SE-ThM1, 203
- Zheng, Z.: GR+NS+PS+SS-ThM4, 194
- Zhernenkov, M.: NT+AS+MI-WeM10, 148
- Zhernokletov, D.M.: EM+TF-TuM2, 59; EM+TF-TuM3, **59**; EM-TuA10, 87; EM-TuA9, 87
- Zhitenev, N.B.: GR+MI-TuA8, 91; GR-WeA3, 168
- Zhong, X.: NS+EM-MoM8, 18
- Zhou, D.: EN+TF-TuA9, 90
- Zhou, F.: EL-ThP4, 240
- Zhou, G.: EM-MoM8, 6
- Zhou, H.: NS-TuM6, 69
- Zhou, K.: EM-MoM3, 6
- Zhou, M.: GR-TuP7, **116**
- Zhou, W.: SS2-MoA11, 51
- Zhou, W.-P.: SS2-FrM3, 267
- Zhou, Z.: SS2-WeM5, 154
- Zhou, Z.X.: GR+TF+NS-ThA8, **221**
- Zhu, J.F.: IS+AS+SS-MoA8, **39**
- Zhu, J.X.: AC+MI-WeA10, 159; AC+MI-WeA3, 159
- Zhu, L.: EN+NS-ThA10, 220
- Zhu, W.: GR+TF+ET-MoA7, **37**; PS+SS-WeM6, 150; PS2-TuA9, **102**; SS2-FrM1, 267
- Zhu, Y.: NS-ThM3, 198; TF1+EM-WeA9, 181
- Zhu, Z.: AS-ThM2, **187**; AS-ThM4, 187; HI-TuP7, 117
- Ziebert, C.: TF-TuP4, 128
- Zielinski, J.J.: SE+PS-ThA2, 229
- Zierath, D.: EM-WeM2, 135
- Zigrosser, D.: VT-TuM2, 80
- Zimmerman, K.: BI-ThP10, 238
- Zoric, I.L.: BI+AS+NS+SS-WeA4, **162**
- Zou, M.: TR+AS+SS-ThM2, 213
- Zuillhof, H.: TF+EM+SS-ThA1, **233**; TR-WeA1, 183
- Zulkifli, A.R.: BI+AS+NS+SS-WeA11, 163
- Zumbülte, A.: MI-WeM11, 143
- Zumer, M.: EN-ThP2, **245**
- Zürcher, S.: MB+BI+PS-MoA4, 40; MB+BI+PS-MoA9, 40
- Zurn, M.: BN-TuA4, 86
- Zvanut, M.E.: TF1-ThM2, 208